SECOND EDITION

Handbook of Laser Technology and Applications

VOLUME III

Laser Applications

Materials Processing and Spectroscopy

edited by

Chunlei Guo • Subhash Chandra Singh

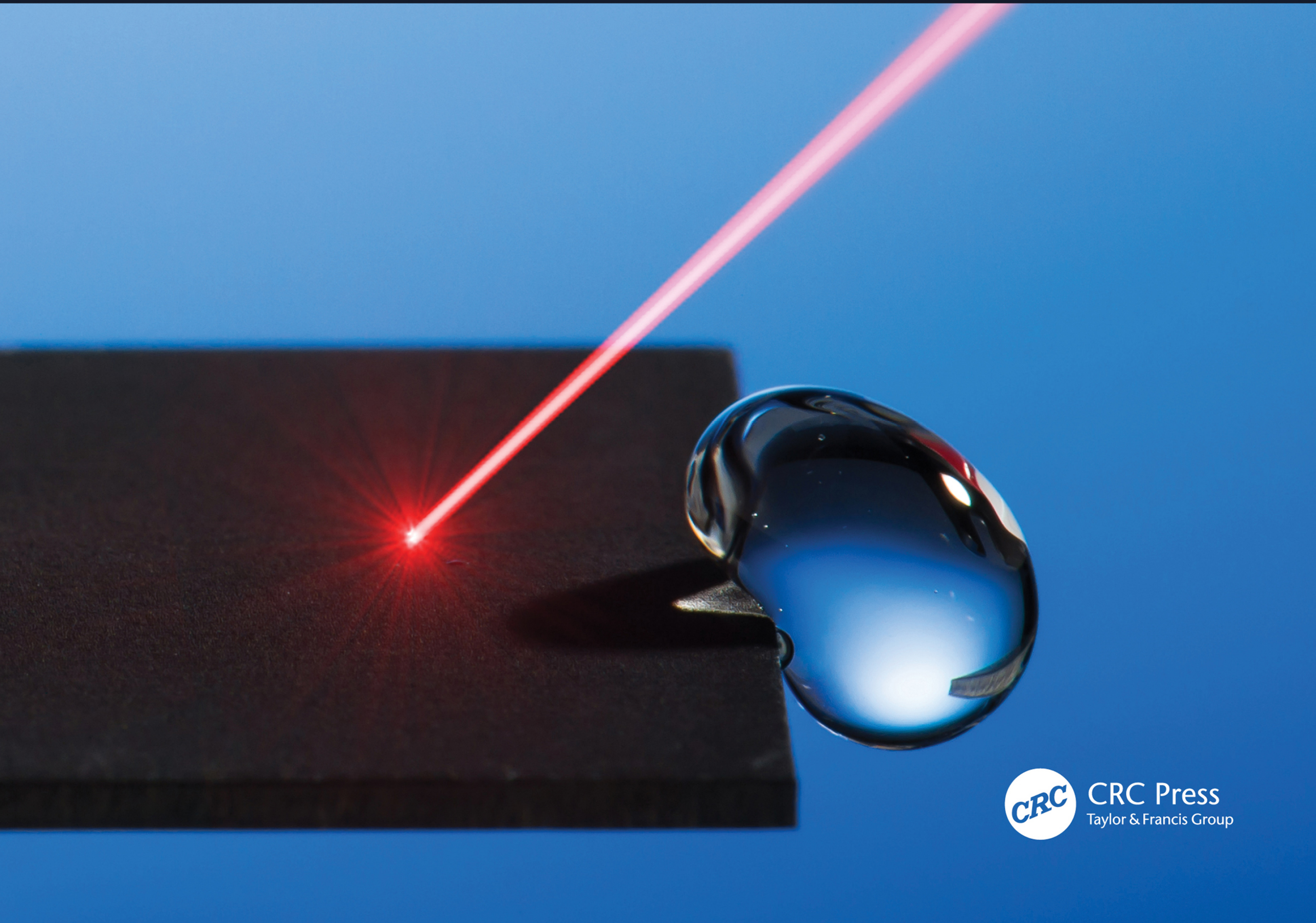

CRC Press
Taylor & Francis Group

Handbook of Laser Technology and Applications

Handbook of Laser Technology and Applications

Lasers: Principles and Operations (Volume One)
Second Edition

Lasers Design and Laser Systems (Volume Two)
Second Edition

Laser Applications: Material Processing and Spectroscopy (Volume Three)
Second Edition

Laser Applications: Medical, Metrology and Communication (Volume Four)
Second Edition

Handbook of Laser Technology and Applications

Laser Applications: Material Processing and Spectroscopy (Volume Three)

Second Edition

Edited by
Chunlei Guo
Subhash Chandra Singh

CRC Press
Taylor & Francis Group
Boca Raton London New York

CRC Press is an imprint of the
Taylor & Francis Group, an **informa** business

Second edition published 2021
by CRC Press
6000 Broken Sound Parkway NW, Suite 300, Boca Raton, FL 33487-2742

and by CRC Press
2 Park Square, Milton Park, Abingdon, Oxon, OX14 4RN

© 2021 Taylor & Francis Group, LLC

First edition published by IOP Publishing 2004

CRC Press is an imprint of Taylor & Francis Group, LLC

Reasonable efforts have been made to publish reliable data and information, but the author and publisher cannot assume responsibility for the validity of all materials or the consequences of their use. The authors and publishers have attempted to trace the copyright holders of all material reproduced in this publication and apologize to copyright holders if permission to publish in this form has not been obtained. If any copyright material has not been acknowledged please write and let us know so we may rectify in any future reprint.

Except as permitted under U.S. Copyright Law, no part of this book may be reprinted, reproduced, transmitted, or utilized in any form by any electronic, mechanical, or other means, now known or hereafter invented, including photocopying, microfilming, and recording, or in any information storage or retrieval system, without written permission from the publishers.

For permission to photocopy or use material electronically from this work, access www.copyright.com or contact the Copyright Clearance Center, Inc. (CCC), 222 Rosewood Drive, Danvers, MA 01923, 978-750-8400. For works that are not available on CCC please contact mpkbookspermissions@tandf.co.uk

Trademark notice: Product or corporate names may be trademarks or registered trademarks and are used only for identification and explanation without intent to infringe.

Library of Congress Cataloging-in-Publication Data
Names: Guo, Chunlei, editor. | Singh, Subhash Chandra, editor.
Title: Handbook of laser technology and applications: four volume set /
[edited by] Chunlei Guo and Subhash Chandra Singh.
Description: 2nd edition. | Boca Raton: CRC Press, 2021- |
Series: Handbook of laser technology and applications |
Includes bibliographical references and index. |
Contents: v. 1. Lasers: principles and operations—v. 2. Laser design and laser systems—
v. 3. Lasers applications: materials processing—v. 4. Laser applications: medical, metrology a [?].
Identifiers: LCCN 2020037189 (print) | LCCN 2020037190 (ebook) |
ISBN 9781138032613 (v. 1; hardback) | ISBN 9781138032620 (v. 2; hardback) |
ISBN 9781138033320 (v. 3; hardback) | ISBN 9780367649173 (v. 4; hardback) |
ISBN 9781138196575 (hardback) | ISBN 9781315389561 (v. 1; ebook) |
ISBN 9781003127130 (v. 2; ebook) | ISBN 9781315310855 (v. 3; ebook) |
ISBN 9781003130123 (v. 4; ebook)
Subjects: LCSH: Lasers.
Classification: LCC TK7871.3 .H25 2021 (print) |
LCC TK7871.3 (ebook) | DDC 621.36/6—dc23
LC record available at https://lccn.loc.gov/2020037189
LC ebook record available at https://lccn.loc.gov/2020037190

ISBN: 9781138033320 (hbk)
ISBN: 9780367649852 (pbk)
ISBN: 9781315310855 (ebk)

Typeset in Times
by codeMantra

Contents

Preface vii
Editors ix
Contributors xi

1. **Laser Material Processing: Section Introduction** 1
   Subhash C. Singh and Chunlei Guo

2. **Laser Welding** 3
   M. Sparkes and W.M. Steen

3. **High-Power Laser Cutting** 17
   John Powell and Dirk Petring

4. **Laser Marking** 35
   Terry J. McKee

5. **Laser Micromachining** 47
   Beat Neuenschwander

6. **Rapid Manufacturing** 71
   Gary K. Lewis

7. **Laser Printing** 81
   Zacharias Vangelatos and Costas P. Grigoropoulos

8. **3D Printing and Additive Manufacturing** 89
   V. Melissinaki and M. Farsari

9. **Photolithography** 105
   Shinji Okazaki

10. **Pulsed Laser Deposition of Thin Films** 111
    Binod Subedi, Venkata S. Puli, Ian W. Boyd, and Douglas B. Chrisey

11. **Surface Micro- and Nano-structuring on Metals with Femtosecond Lasers** 125
    Jianjun Yang and Chunlei Guo

12. **Laser Ablation in Liquids for Nanoparticle Generation and Modification** 137
    Subhash C. Singh and Chunlei Guo

13. **Laser-Induced Forward Transfer** 149
    Alexandra Palla Papavlu and Thomas Lippert

14. **Laser Pyrolysis** 161
    Mohammad Malekzadeh, Parham Rohani, and Mark T. Swihart

15. **Laser Spectroscopy: Section Introduction** 169
    Subhash C. Singh, Pavel Redkin, and Chunlei Guo

16. **Laser Raman Spectroscopy: Fundamentals to Applications** 171
    Siva Umapathy Deepak Ranjan Nayak, Khokan Roy, and Sanchita Sil

17. Laser Scattering Spectroscopy: Rayleigh Scattering and Dynamic Light Scattering 197
Haruhisa Kato

18. Laser-Induced Breakdown Spectroscopy 207
Parviz Parvin and Seyedeh Zahra Mortazavi

19. Laser-Induced Fluorescence (LIF) for the Detection of Microbes 219
Frank Duschek, Lea Fellner, and Karin Grünewald

20. Harmonic Generation—Materials and Methods 233
David J Binks

21. Non-linear Optical Properties of Novel Nanomaterials 255
Soma Venugopal Rao, K. Naga Krishnakanth, C. Indumathi, and T.C. Sabari Girisun

22. Lasers in Imaging: Section Introduction 289
Pavel Redkin, Subhash C. Singh, and Chunlei Guo

23. Lasers in Microscopy 291
Peng Xi

24. Laser-based Coherent Diffractive Imaging 299
Garth J. Williams

25. High-Speed Imaging 307
Adam Whybrew

26. Ultrafast Optical Imaging 315
Jinyang Liang and Lihong V. Wang

27. Transient Absorption Microscopy Measurements of Single Nanostructures 329
Gary Beane, Tuphan Devkota, Brendan S. Brown, and Gregory V. Hartland

Index 339

Preface

This updated Handbook comes at the time when the world just celebrated the 60th anniversary of the laser. Compared to most fields in science and technology, the laser is still a relatively young one, but its developments have been astonishing. Today, hardly any area of modern life is left untouched by lasers, so it is almost impossible to provide a complete account of this subject.

As challenging as it is, this updated Handbook attempts to provide a comprehensive coverage on modern laser technology and applications, including recent advancements and state-of-the-art research and developments. The main goal of developing this Handbook is to provide both an overview and details of ever-expanding technologies and applications in lasers.

We want this Handbook to be useful for both newcomers and experts in lasers. To meet these goals, the chapters in this Handbook are typically developed in a style that does not require advanced mathematical tools. On the other hand, they are written by the experts in each area so that the most important concepts and developments are covered.

The first edition of the Handbook was released in 2003. It has been hugely popular and ranked as one of the top ten most referenced materials by the publisher. Eighteen years later, although a relatively short period for many more established scientific fields, the Handbook has become outdated, and an update is overdue. The rapid changes in lasers are certainly reinforced by my own experience of teaching and researching the subject in the Institute of Optics at University of Rochester. Flipping through my old lecture notes on lasers, I am often amazed at how much progress we have witnessed in this field over the years.

I am indebted to the editors of the first edition, Colin Webb and Julian Jones, who brought this original Handbook into existence. When I was asked to take over this second edition, it laid before me a daunting task of how to rejuvenate the Handbook while keeping its original flavour. Since many of the fundamental principles of the laser are well established, we tried to honour the original authors by keeping the chapters on fundamental concepts where possible. If a revision is needed, we usually started by asking the original authors for the revision but if impossible, we brought in new authors to revise these chapters.

As the laser shines in modern applications, we added a large number of new chapters reflecting the most recent advancements in laser technologies. Throughout the Handbook, entirely new sections were added, including sections on materials processing, laser spectroscopy and lasers in imaging and communications. Nearly all chapters in these sections are either entirely new or substantially revised. On the other hand, some of the topics previously included have seen dwindling relevance today. We had to make the hard decision to let go of some of these outdated chapters from the first edition. Despite these deletions, this new Handbook still grows significantly from the original three volumes to the current four volumes.

Bringing this large project to its conclusion is the collective effort of many individuals. It began with the encouragement and guidance of Lu Han, the then managing editor of this Handbook. I know how much Lu cared about this project. I still remember an initial phone call with Lu; we finished it at a late afternoon past 5 pm. Over the phone, I was told that I would receive the first edition of this Handbook. To my surprise, I had the handbooks in my hand the next morning. At CRC press, this project was later passed onto Carolina Antunes and finally to Lara Spieker, who has been essential in bringing this project to its conclusion.

Many people have provided me with indispensable help. My co-editor, Subhash C. Singh, at the University of Rochester, helped chart the layout of this new edition and worked along with me throughout this project. Ying Zhang, who was a senior editor at Changchun Institute of Optics, Fine Mechanics, and Physics (CIOMP) in China, spent a half year with us in Rochester, where his years of professional editorial experience helped move this project forward significantly. Lastly, my thanks go to Pavel Redkin of CIOMP, who made significant contributions in communicating with the chapter authors and guiding them throughout the project. Additionally, my appreciation goes to Kai Davies, Sandeep K. Maurya, Xin Wei, and Wenting Sun for their help in this Handbook project.

Chunlei Guo
Editor-in-Chief
University of Rochester

Taylor & Francis
Taylor & Francis Group
http://taylorandfrancis.com

Editors

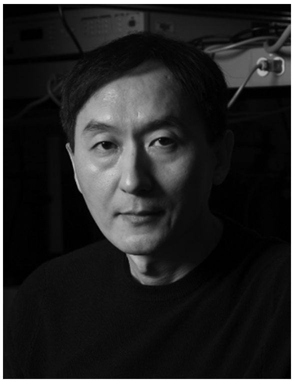

Chunlei Guo is a Professor in The Institute of Optics and Physics at the University of Rochester. Before joining the Rochester faculty in 2001, he earned a PhD in Physics from the University of Connecticut and did his postdoctoral training at Los Alamos National Laboratory. His research is in studying femtosecond laser interactions with matter, spanning from atoms and molecules to solid materials.

His research at University of Rochester has led to the discoveries of a range of highly functionalized materials through femtosecond laser processing, including the so-called black and colored metals and superhydrophillic and superhydrophobic surfaces. These innovations may find a broad range of applications, and have also been extensively featured by the media, including multiple New York Times articles. Lately, he devoted a significant amount of efforts to developing technologies for global sanitation by working with the Bill & Melinda Gates Foundation. Through this mission, he visited Africa multiple times to understand humanitarian issues. To further expand global collaboration under the Gates project, he helped establish an international laboratory at Changchun Institute of Optics, Fine Mechanics, and Physics in China. He is a Fellow of the American Physical Society, Optical Society of America, and International Academy of Photonics & Laser Engineering. He has authored about 300 referred journal articles.

Subhash Chandra Singh is a scientist at the Institute of Optics, University of Rochester and an Associate Professor at Changchun Institute of Optics, Fine Mechanics, and Physics. Dr. Singh earned a Ph.D. in Physics from University of Allahabad, India in 2009. Prior to working with the Guo Lab, he was IRCSET-EMPOWER Postdoctoral Research Fellow at Dublin City University, Ireland for 2 years and a DST-SERB Young Scientist at University of Allahabad for 3 years. He has more than 10 years of research experience in the fields of laser-matter interaction, plasma, nanomaterial processing, spectroscopy, energy applications, plasmonics, and photonics. He has published more than 100 research articles in reputable refereed journals and conference proceedings. His past editor experience includes serving as the main editor for Wiley-VCH book *Nanomaterials; Processing and Characterization with Lasers* and guest editor for special issues of a number of journals.

Taylor & Francis
Taylor & Francis Group
http://taylorandfrancis.com

Contributors

Gary Beane
David J Binks
Ian W. Boyd
Brendan S. Brown
Douglas B. Chrisey
Tuphan Devkota
Frank Duschek
M. Farsari
Lea Fellner
Costas P Grigoropoulos
Karin Grünewald
Chunlei Guo
Gregory V. Hartland
C. Indumathi
Haruhisa Kato
K. Naga Krishnakanth
Gary K Lewis
Jinyang Liang
Thomas Lippert
Mohammad Malekzadeh
Terry J McKee
V. Melissinaki
Seyedeh Zahra Mortazavi
Deepak Ranjan Nayak
Beat Neuenschwander
Shinji Okazaki
Alexandra Palla Papavlu
Parviz Parvin
Dirk Petring
John Powell
Venkata S Puli
S. Venugopal Rao
Pavel Redkin
Parham Rohani
Khokan Roy
T.C. Sabari Girisun
Sanchita Sil
Subhash C. Singh
M. Sparkes
W.M. Steen
Binod Subedi
Mark T. Swihart
Siva Umapathy
Zacharias Vangelatos
Lihong V. Wang
Adam Whybrew
Garth J. Williams
Peng Xi
Jianjun Yang

Taylor & Francis
Taylor & Francis Group
http://taylorandfrancis.com

1

Laser Material Processing: Section Introduction

Subhash C. Singh and Chunlei Guo

Applications of lasers in materials processing, such as cutting, drilling, and welding, started right after the invention of the laser in 1960. Even before the laser was invented, focused electron beam-based sources were used for welding and other machining applications [1]; however, the discovery of lasers significantly increased the speed for the machining of workpiece. In the year 1962, just after the invention of laser, a range of industrial applications of lasers have been proposed, including cutting, welding, and fusing of metals; drilling of deep holes with precision; removal of materials from surface with precise locations; localized heat-induced control of chemical processes; localized sterilization of surfaces; and isotope separation [2].

Chapters 2–8 of this section describe major laser material processing technologies for the machining of workpieces. Each of these chapters presents a specific application of the laser starting from the physical principles used, the experimental set-up, equipment required, and the results obtained.

Along with processing and machining of bulk materials, lasers have also shown their potential roles in the synthesis, modification, organization, and assembling of nanoscale materials. For example, photolithography is an important application of the laser for micro- and nanoscale electronics. Availability and rapid development of VUV/EUV lasers in the spectral range of 10–50 nm can make pattern and devices of nanoscale sizes and is a unique way for the validation of Moore's law. Chapter 9 presents recent advances and challenges associated with photolithography.

Pulsed laser ablation (PLA) of solid and liquid targets is used for the processing of plasmas for a number of scientific and industrial applications (Chapter 10). The PLA-processed plasma in different environments can be used for thin-film deposition and synthesis of nanoparticles. More recently, ultrafast lasers have shown their tremendous capacity in surface nano-/microstructuring that in turn can alter the surface optical, wetting, mechanical, and chemical properties. For example, femtosecond laser pulses can turn a shiny piece of metal pitch black or a certain colour, and render regular surfaces either superhydrophobic or superhydrophilic (see Figure 1.1) [3–6]. Surface nano-/microstructuring using femtosecond laser pulses is the subject of Chapter 11 of this section.

Parallel to the laser surface processing in the air, liquid-assisted laser processing also started right after the invention of the laser. The presence of liquid not only helps to avoid redeposition of debris to make sharper edges and cleaner surfaces, but also increases the rate of surface processing through laser-plasma-induced etching [7]. PLA/irradiation of solid targets or suspended particles in liquids exhibits much simpler and low-cost experimental arrangements as compared to gas-phase laser ablations, and provides a simple and scalable way for the generation of colloidal solution of particles [8,9]. Laser ablation/irradiation in liquid for the generation and modification of nanoparticles is the subject of discussion of Chapter 12. Nanoparticles from the solution of liquid media can be transferred to a desired substrate in the form of thin film using laser-induced forward transfer (LIFT) for fabricating nanomaterial-based devices. Any type of nanomaterials in controlled size, shape, and distribution can be synthesized in powder form using laser pyrolysis of corresponding gaseous precursors. LIFT and laser pyrolysis are discussed in Chapters 13 and 14, respectively.

REFERENCES

1. W. L. Wyman, High vacuum electron beam fusion welding, *Welding Res. Suppl.* 37, 49–53 (1958).
2. R. T. Berg, Electron beam machining, *American Machinist*, 115–116 (1959).
3. A. Y. Vorobyev and C. Guo, Direct femtosecond laser surface nano/microstructuring and its applications, *Laser Photonics Rev.* 7, 385–407 (2013).

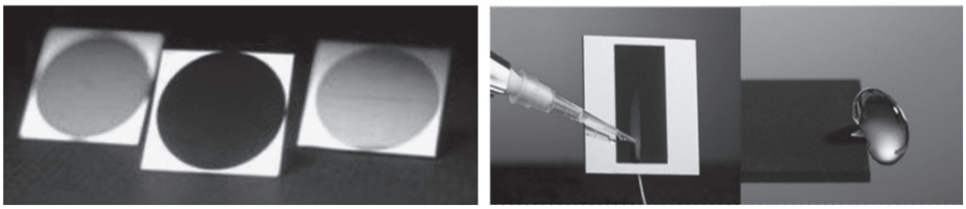

FIGURE 1.1 (a) Coloured metals following femtosecond laser treatment [4]. (b) Super-wicking [5], and (c) superhydrophobic metal surfaces [6].

4. A. Y. Vorobyev and C. Guo, Colorizing metals with femtosecond laser pulses, *Appl. Phys. Lett.* 92, 041914 (2008).
5. A. Y. Vorobyev and C. Guo, Metal pumps liquid uphill, *Appl. Phys. Lett.* 94, 224102 (2009).
6. A. Y. Vorobyev and C. Guo, Multifunctional surfaces produced by femtosecond laser pulses, *J. App. Phys.* 117, 033103 (2015).
7. A Kruusing, *Handbook of Liquids-Assisted Laser Processing*, First Edition, Elsevier (2007). ISBN: 9780080444987.
8. S. C. Singh, H. Zeng and S. Yang, Nanomaterials: Laser based processing in liquid media, in *Nanomaterials: Processing and Characterization with Lasers* (Ed.) S.C. Singh et al., First Edition, Wiley-VCH Verlag GmbH & Co. KGaA, Weinheim (2012).
9. H. Zeng, X. W. Du, S. C. Singh, S. A. Kulinich, S. Yang, J. He, W. Cai, Nanomaterials via laser ablation/irradiation in liquid: A review, *Adv. Func. Mater*, 22, 1333–1353 (2012).

2

Laser Welding

M. Sparkes and W.M. Steen

CONTENTS

2.1 Introduction ... 3
2.2 What Are the Basic Mechanisms for Laser Welding? ... 4
  2.2.1 Light–matter Interaction ... 4
    2.2.1.1 Laser Energy Is Absorbed by the Material ... 4
    2.2.1.2 Melt Is Generated ... 4
    2.2.1.3 After Cooling ... 4
  2.2.2 Continuous and Pulsed Welding ... 5
  2.2.3 Laser Sources ... 5
  2.2.4 Practical Considerations ... 6
    2.2.4.1 Beam Delivery ... 6
    2.2.4.2 Gas Shrouding ... 6
    2.2.4.3 Filler Materials ... 7
    2.2.4.4 Defects ... 7
2.3 Why Use Laser Welding? ... 7
2.4 What Is Being Done to Ruggedize the Process and Expand Its Implementation? ... 8
  2.4.1 Dissimilar Materials ... 8
    2.4.1.1 Metal–metal Welding ... 8
    2.4.1.2 Dissimilar Materials ... 8
  2.4.2 Plastics and Transmissive Materials ... 8
  2.4.3 Micro-welding ... 9
  2.4.4 Process Developments ... 9
    2.4.4.1 Hybrid Processing ... 9
    2.4.4.2 Melt Pool Manipulation ... 9
    2.4.4.3 Short Wavelength ... 10
    2.4.4.4 Short Pulse ... 11
    2.4.4.5 Multiple Beams ... 11
    2.4.4.6 Melt Pool Support ... 11
    2.4.4.7 Aluminium to Steel ... 13
  2.4.5 Implementations ... 13
    2.4.5.1 Remote Laser Welding ... 13
    2.4.5.2 Process Set-up and Diagnostics ... 13
2.5 Future Opportunities ... 14
References ... 14

2.1 Introduction

Laser welding is now a mature technology and has moved away from the initial implementations of metal seam welding in the applications like cans and double glazing spacer bars through its second phase of industrialization, laser-welded tailored blanks, and is now prevalent in the joining of not just metals but plastics and ceramics. This has been principally driven by the developments in laser technology, the obvious changes are smaller, high brightness, high-efficiency fibre lasers; now more recently, pulsed lasers (including ultrafast) and the expansion of affordable reliable laser wavelengths.

Typical book chapters on this subject would concentrate on the CO_2 and Nd:YAG lasers and their light–matter interaction, discuss melt flows and then perhaps look at a case study. Given that the subject is broad and mature (and yet still being developed) and we could easily fill a book with any part of the process we are going to skim through the background (clear introductory material being given by Steen [1], Ready [2], and Ion [3]) giving only a general introduction to the process and jargon, with good references! Instead of repetition we will outline the absolute basics of the laser welding mechanism on metals, discuss why the laser may be the best solution to a problem, examine the application space of laser welding, and look in more detail at modern implementations. This will hopefully present a very informal guide to help the reader appreciate the scope of the process and have enough understanding of the jargon to delve in a targeted manner into the vast amount of information now available.

2.2 What Are the Basic Mechanisms for Laser Welding?

2.2.1 Light–matter Interaction

2.2.1.1 Laser Energy Is Absorbed by the Material

The laser energy is absorbed by a process that involves the interaction of the electromagnetic wave stream with the electric structure of the material causing internal forces resulting in vibrations that we perceive as heat. When the vibrations are strong enough the interatomic bonding is broken and the material is said to have melted. Greater excitation loosens the structure further to cause boiling; further absorption within the vapour may result in electrons being stripped from their atoms producing a plasma, which both absorbs incoming radiation and reradiates.

2.2.1.2 Melt Is Generated

The most basic weld is the *conduction weld* (Figure 2.1), in which all of the energy is coupled to the material from absorption at the surface; all further heat transfer is via conduction and convection, typically limiting the weld depths below a couple of millimetres.

If the laser irradiation is intense enough and the speed slow enough, then boiling will occur in the melt pool and a *keyhole weld* may be formed (Figure 2.2). The keyhole is a void in the melt sustained by the pressure of the vaporized material, typically quoted at being around 1.5 times the diameter of the laser incident spot diameter. There are two efficiency benefits of having a keyhole, and are often considered a black body in many basic models of thicker-section welding. The first benefit is the potential for multiple absorption opportunities as a photon is reflected off successive surfaces down the keyhole; the second for most materials is that the plasma generated absorbs the laser and the energy is reradiated onto the edges of the keyhole.

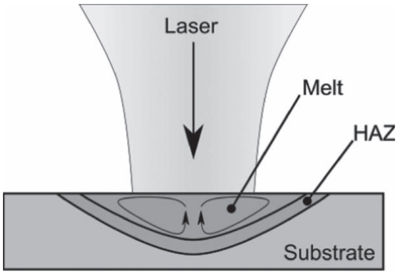

FIGURE 2.1 Conduction welding with melt circulation.

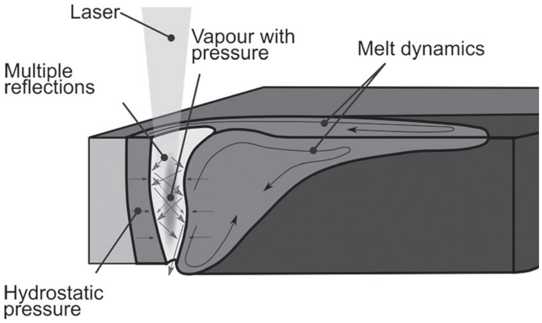

FIGURE 2.2 Keyhole welding phenomena.

Melt pool dynamics is one among the two primary forces (the other being cooling) that dominate the weld structure; possessing microstructure, grain orientation, porosity, or the mixing of dissimilar materials. In *conduction welding*, the primary flow mechanism is due to Marangoni flow [4] (Figure 2.1), caused by the variation in surface tension with temperature. Within the small size of the melt pool, the temperature will vary from boiling in the middle to melting at the edge, and the flow can produce swift mixing in the pool. The Marangoni effects in the melt cause stirring and sharp movement towards the edges of the pool. This may produce a raised hump at the start and a hollow at the end of a weld run; in between, it defines the melt pool surface and hence the bead shape. The strength of the Marangoni flow is also dependent on the material composition. For example, when small quantities of sulphur are added to steel, the flow can reverse the direction [5].

Keyhole welding couples Marangoni flow with a range of additional dynamics. The fluid flow within the keyhole is crucial in determining the quality of the weld bead and formation of porosity as well as the depth of penetration. Some ingenious experiments have been done to determine the flow within the keyhole, in particular the work of Matsunawa [6] who not only filmed the surface flow around the keyhole but by using a high-speed X-ray camera was able to observe the turbulent flow within the keyhole by imaging the trajectory of tungsten particles. He showed that the melt is forced around the keyhole flowing both horizontally and vertically downwards on the leading edge, oscillating with the keyhole throat occasionally closing. This feature seems to be related to the wave formation on the leading edge of the keyhole, whereby a wave would change the angle of incidence of the incident radiation and cause an explosive evaporation, causing ejection. This ejection is directed into the back face of the pool causing oscillations or even particle generation. Stabilizing the keyhole is a feature of successful keyhole welding and is primarily achieved by the careful selection of laser power and speed; an additional refinement the balance with external gas jets used to blow the plasma or dust away.

2.2.1.3 After Cooling

After joining, the heat is dissipated from the melt by conduction into the substrate; there is relatively little loss due to reradiation or convection as a result of the small weld bead surface

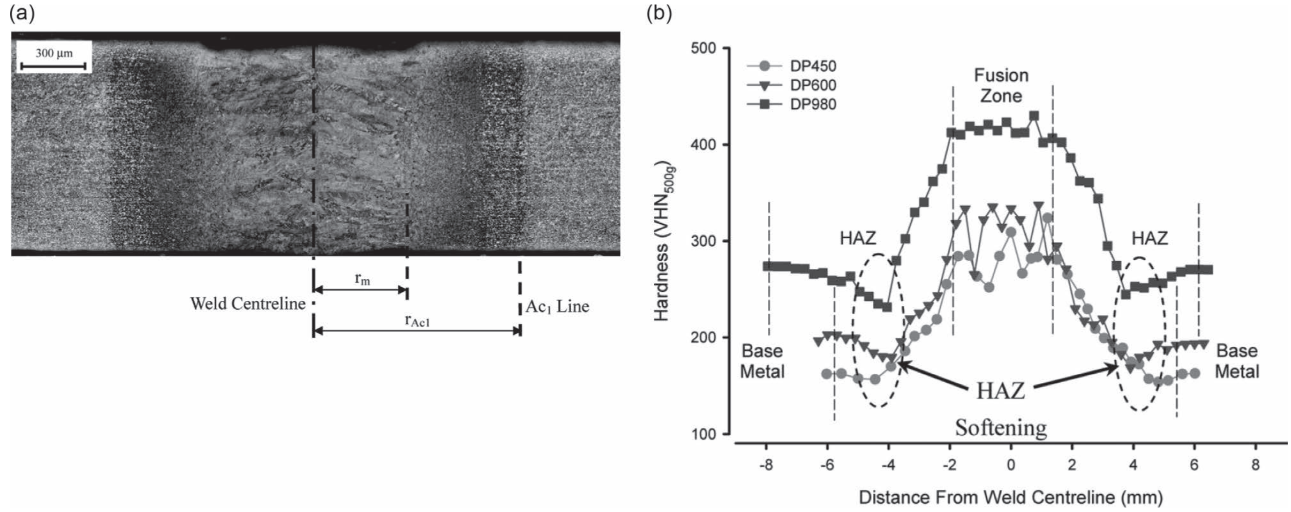

FIGURE 2.3 Diode laser welding of dual-phase (DP600) steel, (a) micrograph, (b) effect on hardness [7].

area. The extent of the region that can be identified as being affected by the process is termed the "heat-affected zone" (HAZ) and is typically determined by looking at the grain structure (phase/orientation, etc.) of a cross section of a weld or its materials properties (e.g. hardness) (Figure 2.3). The extent of the HAZ constrains the source of any residual stress and distortion that may result and is small due to the well-defined narrow welds usually generated by the laser.

The HAZ can be estimated from standard thermal conduction as stated in Fourier's equation, an approximation of which can be made by using the Fourier number (a dimensionless group defining heat flow) $F = \alpha t/x^2 = 1$; such a value would define the thickness of the temperature gradient away from the pool edge, where α is the thermal diffusivity ($m^2 s^{-1}$), t the interaction time (s) (D/V, D defining beam diameter (m) and V the welding speed (m)), and x the extent of HAZ (m).

2.2.2 Continuous and Pulsed Welding

One of the advantages of the laser is the ease with which the power can be controlled, being variable from continuous to pulsed with optional shaping, the power profile during each pulse.

Continuous laser welding is the simplest form of laser welding using a continuously on laser of uniform power, termed "continuous wave" (CW). The process speed and laser power are optimized for specific materials with the material thickness describing the operating regime; a basic analytical model describing the process is summarized by Ducharme [8]. The model delineates where there is insufficient penetration, or problems with the weld bead. To define some examples of power boundaries, at the minimum for fibre laser welding metals, this means lasers with powers above >200 W for ferrous materials and >600 W for high reflectors (e.g. Al) when processing mm-range materials. Increasing power gives greater speed or thickness. CW welding is essential for a sustained keyhole operation, and as such, it is the most efficient process and used whenever possible for commercial joining if the material is not excessively sensitive to heat.

In its simplest form *pulsed laser welding* is simply turning the laser on and off to produce discrete weld pools and weld seams, which are made of a collection of these spots. This does not mean that there cannot be a keyhole, just it is not sustained. The process has the advantage that the thermal load on the part can be managed by allowing time for cooling. It has been known for many years that pulsed laser welding allows for the benefits of using high-gain laser cavities. For example, during square pulsing at 100–500 Hz having a peak power twice the average power gives an improvement of 30% penetration when welding 304 stainless steel has been reported [9]. The increased peak power also means that welding high-reflectivity material, such as Au or Al, is easier since the keyhole will be established quicker.

2.2.3 Laser Sources

Historically, the industrial laser of choice was the CO_2 laser having high average powers and relatively high wall plug efficiency. Overtime the Nd:YAG replaced some of the applications of the CO_2 laser; despite having lower average power the shorter wavelength, and greater peak power and pulse control opened up new materials processing options and levels of precision. These lasers are now all constrained to niche applications (e.g. certain types of plastic welding for the CO_2) with the advent of the fibre laser. The high efficiency of fibre lasers (some quoted at around 50%), diffraction-limited focusability, and varied pulse control coupled with telecom levels of reliability make it the first choice for all mainstream applications, particularly when one adds the smaller footprint for the machinery and less demand for cooling systems.

The fibre laser is not going to be alone in the welding market for long. While they may be necessary for high speed or fine features developments in direct diode technology are now giving multi-kilowatt beams which can propagate through fibres with claims of beam quality approaching that of CO_2 lasers [10] (≈2 kW, in fibres down to 50 μm). Combined with efficiencies touching 65% (in the commercial units), they are highly suited to many applications, e.g. <3 mm steel [11].

There are three primary types of fibre laser operating in a pulsed form. The lowest power units (traditionally <20 W average, but the latest high power units now promise which >250 W) of master oscillator power amplifier (MOPA) lasers amplify complex seed laser power profiles with short pulse lengths (<20 ns) and very high peak power capabilities. These lasers are used only for very delicate work being capable of producing very small welds, but with a high degree of thermal control – peak powers are too high for most welding applications. Next in power are the fibre grating Q-switched lasers (≈ <100 W average, >15 kW peak, >20 ns), which while being designed for marking and engraving are being used to demonstrate new ways to mix metals. The latest incarnation of the pulsed laser is the quasi-CW (QCW) laser. These lasers reduce the optical and thermal load on the laser by only pulsing the diodes for a period of time (in the ms regime), but as a result can be driven harder when on, typically around ×10 higher than in CW mode. As the pulse length is long, and the repetition rate is high (in the 10's kHz), many processes are slow enough to effectively operate as if the laser was CW, but with the benefits of high peaks affecting surface temperature/absorption, etc.

Finally, there is a big push to move both further down in wavelength for higher absorption in metals, and further up for plastics and glass, discussed later.

2.2.4 Practical Considerations

For those looking for practical advice on how to weld there can be no better place to start then Dawes [12]; while the laser sources are a little dated the theory and application techniques stay the same – just the numbers change with the selection of laser.

2.2.4.1 Beam Delivery

For CO_2 radiation at 10.6 μm beam delivery is via a series of guidance mirrors, for shorter wavelengths as with 1.06 μm from Nd:YAG or fibre lasers beam delivery is through an optical fibre. The laser is then focused using lenses (or for extreme high powers a concave/off-axis parabolic mirror) through a cover slide (to protect the optics from fume and splatter) and finally through a gas nozzle (protecting the lens and usually shielding the workpiece) onto/inside the material (Figure 2.4).

Laser spots are compromises. General rules are for thin sheet the spot is small giving high-speed welds. As the thickness increases, the spots need to be larger to make a more stable keyhole and longer depth of focus. The focal position for thin sheet (<3 mm) will typically be on the surface of the material. As the thickness increases moving the focus through the material helps to distribute the energy down the weld and make the weld more uniform by stabilizing the keyhole.

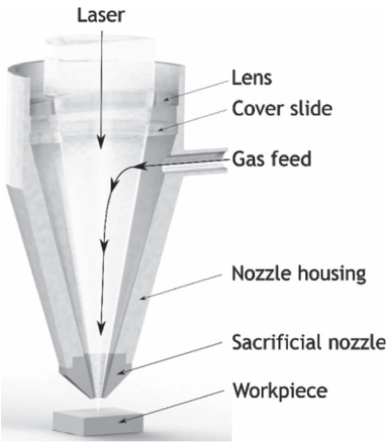

FIGURE 2.4 Simple welding configuration.

2.2.4.2 Gas Shrouding

Gas shrouding is usually needed to avoid oxidation of the weld pool, which gives rise to oxide inclusions. A further problem is the formation of plasma, which prevents laser propagation and can starve energy from the base of the weld. Gas selection is a compromise between laser absorption, ionization potential, and cost.

In the simplest form the gas is delivered either co-axially with the laser or at an angle to help push the plasma away from the beam path (Figure 2.5) (note "squashed" plasma and reduced penetration depth with co-axial jet); the off-axis arrangement has the additional benefit that the flow rate can be far higher without affecting the weld geometry. Particularly, sensitive materials (e.g. Ti that readily forms nitrides when heated) may need an additional jet at the base of the weld or for a length of the fresh weld to protect from atmospheric gases.

The selection of shroud gas species can make significant differences to both the weld geometry and the penetration of the laser, and is discussed at some length by Kugler [2] (Section 10.2.8), which comes to the conclusion that each material should be assessed on a case-by-case basis for optimum quality at a given price. In summary, gases with a high ionization potential are less likely to form a plasma. N_2, O_2, and CO_2 frequently react or are soluble with metals, and as such they can compromise weld quality. Ar and He rise to the top of the list as potential general-purpose process gases, before He is then discounted due to its excessive price.

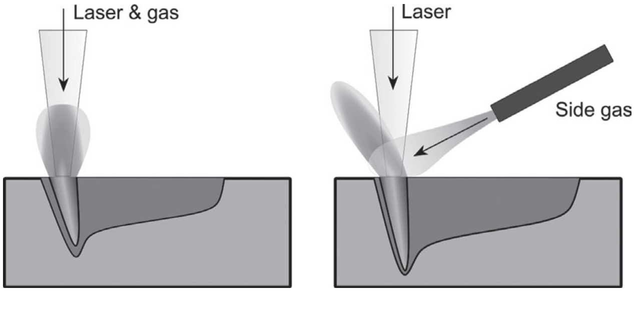

FIGURE 2.5 Shrouding gas designs.

2.2.4.3 Filler Materials

Filler materials can be added to a weld to control the metallurgy of dissimilar welds, reduce tolerances on fit, or for multipass welding of thick sections where a fillet has to be filled. While in theory the material can be either preplaced or added in either powder or wire form, in reality wire is used whenever possible due to significant reduction in cost, and flexibility of delivery [13].

2.2.4.4 Defects

2.2.4.4.1 Geometric Defects

Even with the correct parameters the principal defect, *lack of fusion* (Figure 2.6a), will occur as a result of poor fit-up when the laser is not correctly aligned with the workpiece or the gap is too large. With insufficient power it is possible to produce welds with only partial penetration; while these may look cosmetically pleasing from the upper surface they are particularly weak and a perfect source of stress concentration on the opposite side. Gravitational *sagging*, or *drop-out*, occurs when the laser spot is too large or the speed is too low, generally giving welds which have a high tendency to cracking. Taken to the extreme *perforation* is observed. A similar looking fault can also be found when the shielding gas pressure is too high (a form of laser cutting), but with a narrower weld bead. The inverse of sagging is *suck-back*, where the material is sucked from the base of the plate to form a bridge on the upper surface, typically when the speed is too fast and the gap too wide. *Humping* (Figure 2.6b) occurs when instability as a result of Marangoni and pressure-driven forces in the weld pool cause excessive flow to the back of the pool. This melt freezes as a lump and the smooth bead is spoilt, again often as a result of excessive speed [14]. The weld bead may be proud of the surface due to the shrinkage of the weldment squeezing the melt out of the joint due to a form of shrinkage distortion, or by the addition of excess filler material.

2.2.4.4.2 Internal Defects

The simplest internal defects to be identified are *porosity* and *cracking*. Small pores in the weld are often formed by the generation of bubbles from keyhole collapse or extreme turbulence. Cracking occurs during the cooling phase as the material crystallizes and shrinks. It is basically a material composition/structure problem (lack of strength or ductility), which can be a real challenge during the welding of certain alloys, notably certain Al alloys and high-strength Ni alloys.

More difficult to quantify is *residual stress* (forces within the body of a material not as a result of thermal or external loads), which can cause a range of issues in a component, including cracking, bending, localized corrosion enhancement, and reduced fatigue strength. The primary mechanism for the generation of bubbles during laser welding is dissimilar volumes of melt on the upper and lower surfaces coupled with an excess of heat in the upper surface. During molten process, there are no stresses, the lower surface then cools first and is put under compressive stress by the upper as the temperature of the part becomes uniform. There is a vast array of modelling on the subject, which looks to find processing strategies for reducing the effects; alternative approaches are the addition of specialist filler materials and heat treatment of the final part – some of which is summarized by De and DebRoy [15].

2.3 Why Use Laser Welding?

There are plenty of mature welding technologies – why did we need another? Conventional welding processes by MIG, TIG, ARC, resistance, oxy-acetylene, etc. use much lower-cost equipment and are far more energy efficient, but the large welds add considerable heat to the part. Electron beam welding is also much more efficient than laser, cheaper, comes at higher powers with fidelity not too dissimilar to laser, but has the substantial drawback of needing to operate in vacuum.

The laser is the compromise for materials below 10 mm thick Considering standard materials (e.g. steels) most texts on laser welding outline speed, quality, precision, and limited HAZ, leading to low material deformation (while being amenable to automation) as the primary benefits. Additional reasons for the use of a laser are as follows:

- Wide range of materials weldable (e.g. plastic/ceramic/glass);
- Dissimilar materials
- Subsurface welding;
- Chemically clean.

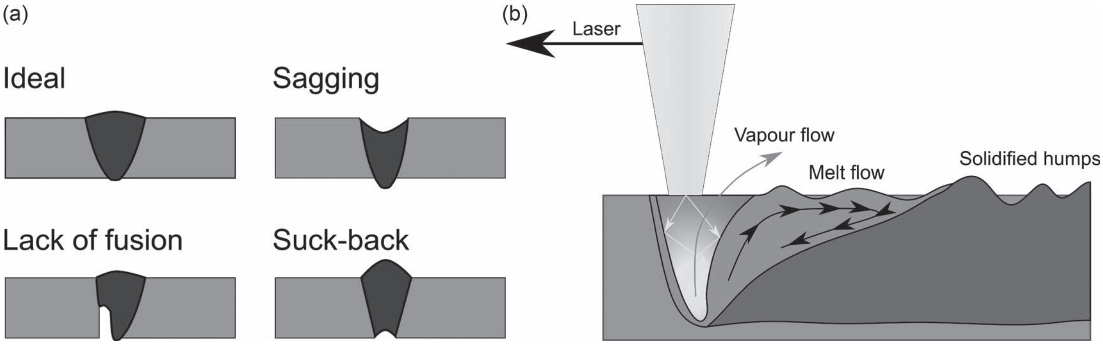

FIGURE 2.6 (a) Weld forms, (b) hump formation mechanism.

The short answer is that laser welding saves money. You can get a fast weld generally with no preparation of the surface. The weld finish is of sufficient quality that little or no further cleaning is required on a wide range of materials. Additionally, laser welding can be easily monitored and both the position and power of the laser can be rapidly controlled, thereby making the process amenable to automation reducing waste and minimizing defects.

Once you get over the cost of the machine the primary downside is poor gap filling (due to the narrow bead width of the keyhole weld), resulting in the need for a high degree of part preparation/fit-up and alignment. One further consideration is laser safety for anyone in the vicinity, eyes and lasers don't mix so the welding process has to be behind a shield. An additional challenge can be getting the energy into some materials. Metals that are highly reflective to the laser wavelength (e.g. Al, Cu, Ag, Au) were used as the mirror components in some of the early lasers. This can cause problems if the laser intensity is not high enough to generate a keyhole and enhance the coupling, in which case care has to be taken that when there is back reflection it does not reflect back into the laser cavity causing damage. High reflectivity is being alleviated by using shorter-wavelength lasers (later). Similarly, excessive transmission (typically in plastics or glass where there is insufficient laser absorption for the generation of melt) is being tackled with new longer-wavelength sources (again more later).

2.4 What Is Being Done to Ruggedize the Process and Expand Its Implementation?

2.4.1 Dissimilar Materials

2.4.1.1 Metal–metal Welding

There is a vast array of metal laser welding processes, with examples ranging from the mundane spot and seam welds in the automotive industry to the exotic joining of precious metals in craft industries. For this review, we will ignore all processes where the two parts being joined are of the same metal as the laser process only adds value in areas already discussed.

2.4.1.2 Dissimilar Materials

Many metals cannot be welded together using conventional means due to their differing chemical and physical properties (principally melt temperature and thermal behaviour). On cooling there may be the formation of brittle intermetallic phases and the inclusion of mechanical stress resulting from differing thermal expansion. Laser welding minimizes some of these problems allowing a wider range of materials to be joined as the narrow kerf (and associated minimal heat input) causes faster solidification and reduces the amount of mixing and diffusion. Other non-melting processes such as resistance, diffusion bonding, ultrasonic, and stir welding may offer joining on materials not possible with laser.

The quality of a binary joint is subjective – one often quoted early "map" of the weld space ranks joining materials from excellent to fail. It is interesting to note the differences between those in Steen [1] and Dawes [12] and how many materials marked as fair or poor are now routinely joined using slight adaptions to the technique (more in *Process Developments*).

2.4.2 Plastics and Transmissive Materials

Welding transparent materials with a laser sounds like an impossible task, but even this has become routine by either the addition of an intermediate absorption layer or intense multiphoton absorption. The first welding applications of plastics could not work through a transparent material as CO_2 lasers are highly absorbed by plastics. Some "welding" was done; laser pressure bonding, where one or both sides of a seam were surface-heated and pressed together to form a join, now still being researched as a route for flexible thermoplastic composite manufacture (Figure 2.7).

With the advent of mainstream Nd:YAG lasers transmission, laser lap welding joints became possible either by ensuring that one of the materials was transparent to the laser and the second absorptive, or by the addition of a interstitial coating transparent to the human eye but highly absorbent to 1 μm radiation, e.g. Clearweld [17]. Moving into this space and new to the industrial scene is mid-infrared laser welding. Thallium lasers operating around 2 μm can be absorbed more readily by plastics and permit the generation of melts within an optically transmissive material [18]. It should be noted that most of these processes benefit from the addition of mechanical pressure during the melt process as there is very little melt movement.

The most flexible solution, which also does not need an absorbing layer, is ultrashort laser pulse welding. Ultrashort pulses (typically <15 ps, down to ≈200 fs, material/process dependent) are capable of delivering GW of peak power in an extremely short period of time. Transmissive welding is made possible as the energy is absorbed only when the photon density is above a threshold level and non-linear absorption at the beam focus occurs resulting in a hot plasma being "instantaneously" created [19]. The weld is characterized by having an inner teardrop region, where the laser has directly melted the material under high pressure, and an outer ring that has been melted by conduction (Figure 2.8). Due to the excessive cost for commercial application of ultrafast lasers, alternative "short-pulse" solutions (10's to 100's ns) are being researched – one solution is the addition of a Ti film when welding borosilicate

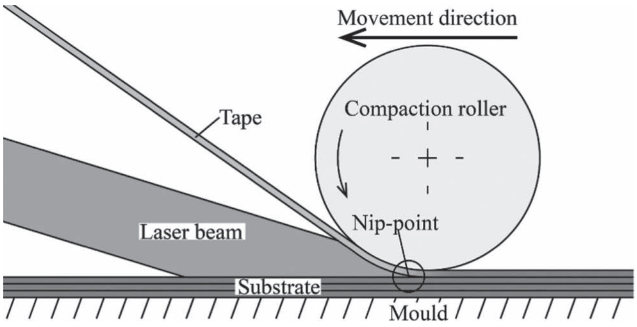

FIGURE 2.7 Laser-assisted fibre placement [16].

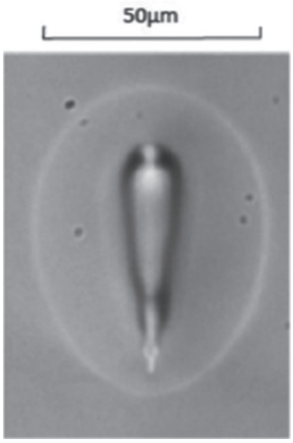

FIGURE 2.8 Characteristic weld shape of an ultrafast laser pulse in glass [21].

glass which forms a Ti-rich bond interface within the glass giving a reduced defect join [20].

2.4.3 Micro-welding

A general trend in all manufacturing is miniaturization primarily for the reduction of material and weight, medical devices and sensors being examples. For welding seams in materials below 200 μm, the laser is a particularly useful tool; the controlled energy delivery and small melt volumes prevent excessive surface tension balling the material and producing voids. The challenging metal combinations are particularly suited to this type of weld as the melts are kept very small with exceedingly short lifetimes producing few intermetallics.

Many of these components also contain electrical connections which require reliable welds for the service life of the component, i.e. microspot welding. The connection between Cu and Al deserves special mention due to a drive to reduce material cost by substituting Al for Cu; Al – while being inferior to Cu in both thermal and electrical conductivity – is acceptable for some applications as it is significantly lighter and cheaper. At the micro-level, the joins are usually strong enough making for a simple process; larger >200 μm connections may need the addition of filler materials to increase ductility and give longer service life [22].

2.4.4 Process Developments

2.4.4.1 Hybrid Processing

Typical of laser applications after the first incarnation of the process described by Steen in 1978 [23], it took over 20 years for the technology to become stable enough for commercial implementation, an oil tank factory in 2000 [24]. The technique uses a combination of both laser and arc welding to produce a hybrid process that has the benefits of the two. It is more efficient than the laser and more tolerant to fit-up errors while being deeper with reduced heat input than the arc alone.

There are two implementations [25]: the first is commonly called "laser-assisted arc welding" or "laser-guided and stabilized welding". A relatively low-power laser (typically <300 W) is used to change the conductivity of a gas discharge, i.e. the opto-galvanic effect, which guides and stabilizes the arc which does the welding. The primary application of this technique is welding thin sheet (<2 mm), where the laser steers the arc deeper into the material giving higher speeds. In the second implementation, i.e. the arc-augmented laser welding (frequently called "hybrid laser welding"), the laser and arc source combine to work on a common melt pool (Figure 2.9). The arc provides bulk energy on the surface of the material, while the laser generates a keyhole allowing for high aspect ratio welding.

2.4.4.2 Melt Pool Manipulation

Oscillating beam welding, more recently coined "wobble welding", is a term used to describe a process of rapid movement of a laser keyhole across a weld seam. The process combines the benefits of keyhole welding, namely efficient high aspect

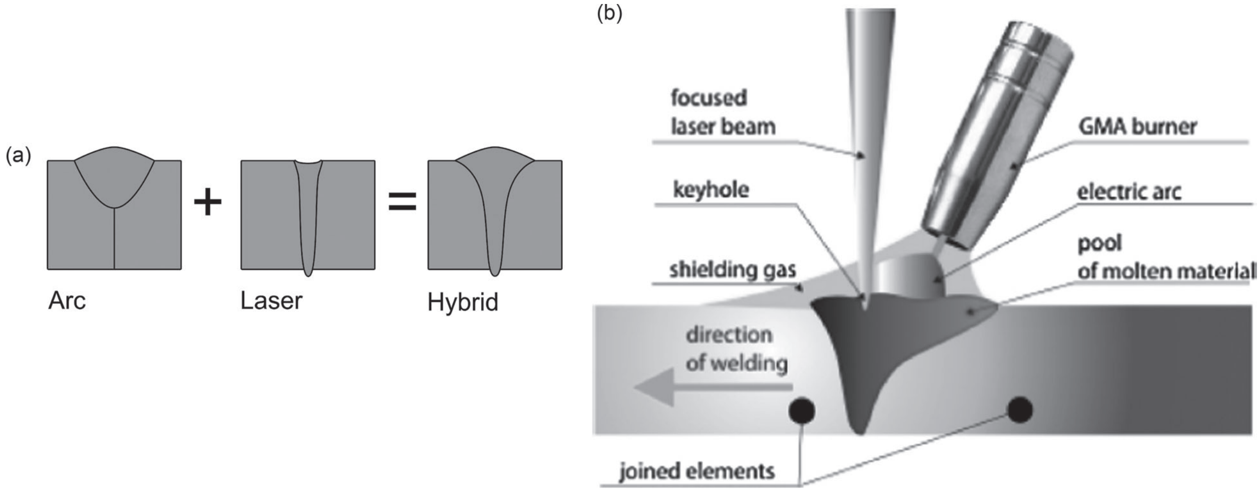

FIGURE 2.9 (a) Hybrid laser-arc process [25], (b) comparative weld forms.

welds, with the need to produce wide melt tracks. Changing the pattern has an effect on the flow of melt giving significant control [26] (Figure 2.10).

The resultant technique has many benefits:

1. As a keyhole is used highly reflective materials can be joined.
2. The melt pool stirring can be used to optimize the strength of a dissimilar weld joint.
3. The melt width is independent of beam shape allowing for optimization of weld properties.
4. Cosmetic adjustments can be made to the weld.
5. Join defects can be removed/prevented.
6. There is a significant reduction in alignment and fit-up tolerances making for a more reliable process (Figure 2.11).
7. Equiaxial grains or some degree of grain size control can be achieved [26].

This is well demonstrated by the corner welding (Figure 2.12), which would appear as two sharp corners with a thin joining weld without aid of the oscillation.

2.4.4.3 Short Wavelength

Most materials become more absorbent to radiation at shorter wavelengths. High-reflectivity materials such as Cu, Ag, Au, and Al particularly benefit from the higher coupling efficiencies (Figure 2.13). The challenge to welding these materials is made even harder by their material properties; considering Cu, there is not only the high-reflectivity melt but also a low-viscosity melt (prone to sagging/dropout forcing lower powers) and high thermal conductivity

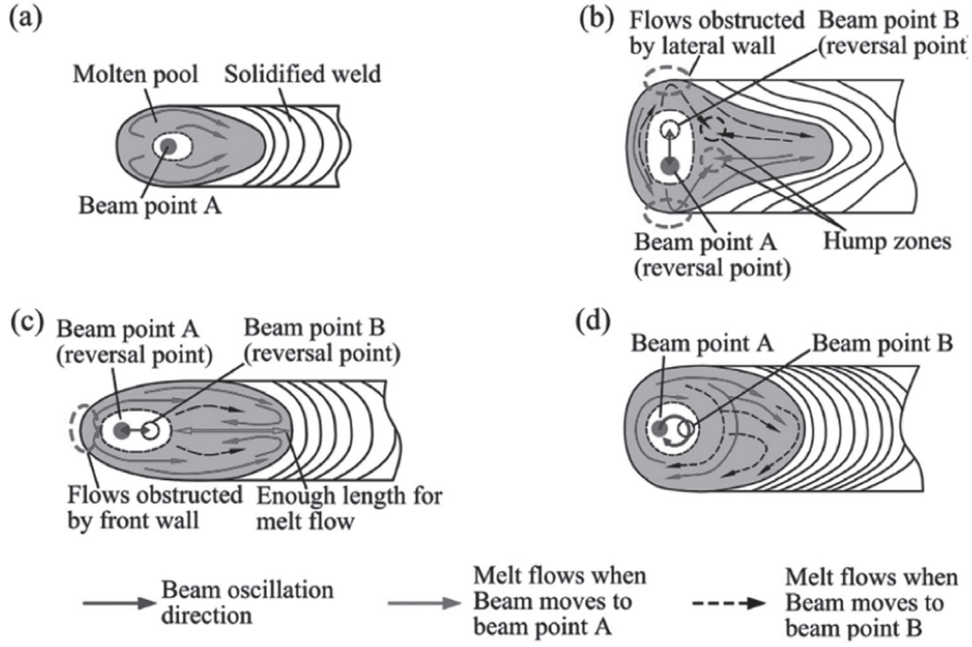
(a)
Molten pool
Solidified weld
Beam point A
(b)
Flows obstructed by lateral wall
Beam point B (reversal point)
Beam point A (reversal point)
Hump zones
(c)
Beam point A (reversal point)
Beam point B (reversal point)
Flows obstructed by front wall
Enough length for melt flow
(d)
Beam point A
Beam point B
Beam oscillation direction
Melt flows when Beam moves to beam point A
Melt flows when Beam moves to beam point B

FIGURE 2.10 Selection of melt pool flows for an oscillating laser (a) without oscillation, (b) transverse, (c) longitudinal, (d) circular [26].

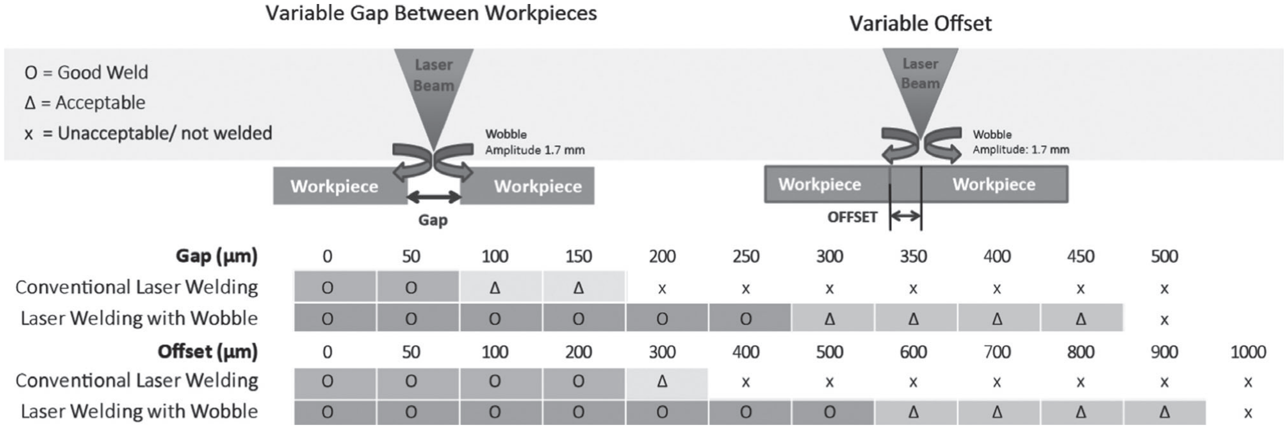
Variable Gap Between Workpieces
Variable Offset
O = Good Weld
Δ = Acceptable
x = Unacceptable/ not welded
Laser Beam
Wobble Amplitude 1.7 mm
Workpiece
Workpiece
Gap
Laser Beam
Wobble Amplitude: 1.7 mm
Workpiece
Workpiece
OFFSET

Gap (µm)	0	50	100	150	200	250	300	350	400	450	500
Conventional Laser Welding	O	O	Δ	Δ	x	x	x	x	x	x	x
Laser Welding with Wobble	O	O	O	O	O	O	Δ	Δ	Δ	Δ	x

Offset (µm)	0	50	100	200	300	400	500	600	700	800	900	1000
Conventional Laser Welding	O	O	O	O	Δ	x	x	x	x	x	x	x
Laser Welding with Wobble	O	O	O	O	O	O	O	Δ	Δ	Δ	Δ	x

FIGURE 2.11 Extended gap or offset tolerance when using oscillation welding [27].

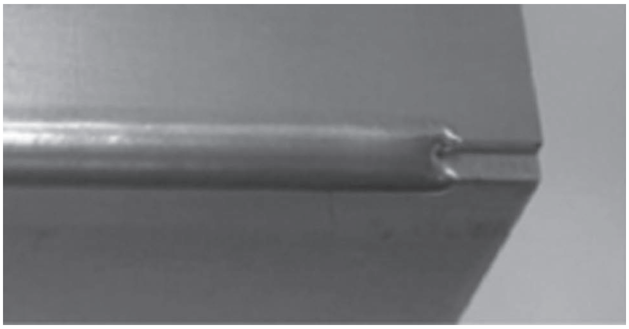

FIGURE 2.12 Wobble corner weld of 6061-T6 aluminium [27].

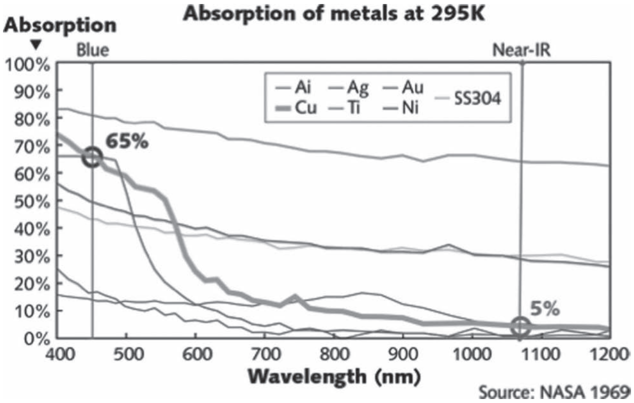

Source: NASA 1969

FIGURE 2.13 Change in absorption coefficient with wavelength at room temperature, highlighting "blue" processing of Cu [28].

(conversely giving premature weld failure with lower powers). While the first problem is reduced by the use of, say, green radiation in the 500 nm range, the low viscosity makes waves in the melt pool more likely, and therefore, a poor weld bead and the high thermal conductivity result in the wave structure becoming frozen into the final bead – a fine-balancing act for seam welding.

While shifting to the shorter wavelengths offers the potential for bulk welding of these materials, the lasers are still in their infancy. Green lasers are only just becoming available in the 500 W bracket costing >$70 k, while blue lasers (usually diodes) are available at a similar price but with very low brightness. As such, these wavelengths are typically only used for small specialist applications, like jewellery, where precision and not high power is required.

2.4.4.4 Short Pulse

The low-power (<100 W) MOPA-based ns lasers offer unique pulse control at low cost being mass-produced for many markets, e.g. marking, and as such, the application of these lasers to welding is desirable. By configuring the pulse energy to have peaks above 10 kW, the bonding of dissimilar metals up to 1 mm thick can be achieved. Gabzdyl [29] has demonstrated joining of a range of traditionally challenging materials to steel using a 70 W laser. Each weld site *mixes* a very small amount of material which quench rapidly, substantially reducing the formation of intermetallics associated with higher-energy processes. By patterning the weld spots to produce a larger area of join, a structurally sound connection can be made, as an example. Figure 2.14 shows a section of a spiral weld connecting Cu to Fe.

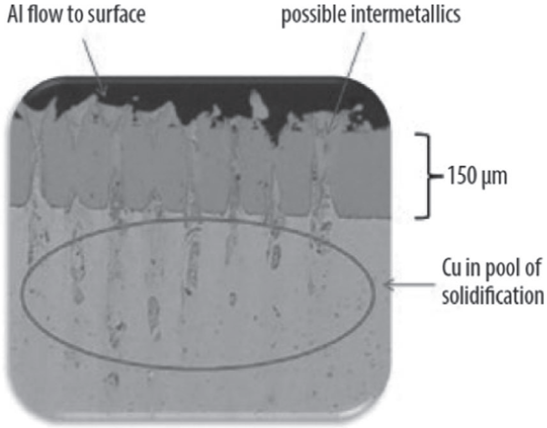

FIGURE 2.14 Spiral welding section, copper to steel [29].

2.4.4.5 Multiple Beams

Dual beam welding was quickly identified as a method to allow for greater control of the welding process. Two beams (parallel) beside each other [30] permit wider melt seams, and reduce sensitivity to fit. Two beams inline [31] (tandem) give a longer cooling cycle and reduced temperature gradients, typically characterized by a smaller leading keyhole followed by the primary joining keyhole (Figure 2.15). For steel, this configuration gives reduced hardness and cracking of the weld as the quench is less severe, with by-products of faster welding (before humping) and reduced defects (porosity and sag). Al also shows reduced defects with enhanced cosmetic quality. A more subtle implementation of the inline technique permits enhanced welding of lap joint zinc-coated mild steel (automotive body components) where the long interaction time and large keyhole give the zinc vapour time to be expelled from the weld and not be a source of porosity/poor coupling [32]. In another incarnation, the second beam can be used not to generate a keyhole, but instead to heat the surface and extend the life of the melt pool, which is shown to reduce the Rt (range from the lowest valley to the highest peak) of a weld by 20% [33] (Figure 2.16). Despite the promising nature of this work, it appears that developments in monitoring and control (and oscillation) have overtaken optical manipulation and industrial uptake is minimal.

Multiple laser beams may also be combined as a combination of different wavelengths. As an example, when welding Cu, a combination of green (515 nm) and fibre (around 1 μm) gives an enhanced performance. The low-power (<100 W) green is preferentially absorbed, heats the surface, and increases the absorptivity to the high-power 1 μm beam.

2.4.4.6 Melt Pool Support

The evolution of the fibre laser to ever greater powers gives the capability to weld ever thicker plate, e.g. >30 mm for

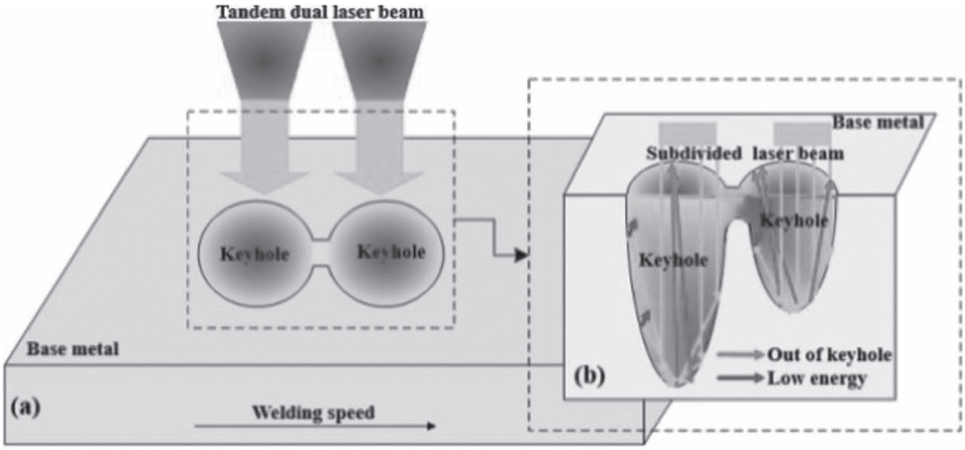
Tandem dual laser beam
Keyhole
Keyhole
Base metal
(a)
Welding speed
Base metal
Subdivided laser beam
Keyhole
Keyhole
(b)
Out of keyhole
Low energy

FIGURE 2.15 Tandem laser welding: (a) layout, (b) example ray tracing [34].

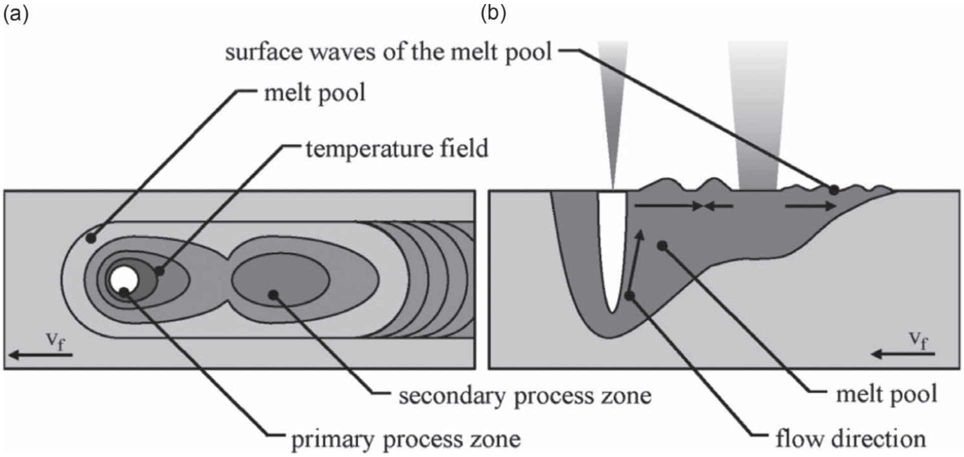
(a)
(b)
surface waves of the melt pool
melt pool
temperature field
v_f
v_f
secondary process zone
primary process zone
melt pool
flow direction

FIGURE 2.16 Melt pool forms: (a) top view of isotherms, (b) longitudinal melt section [33].

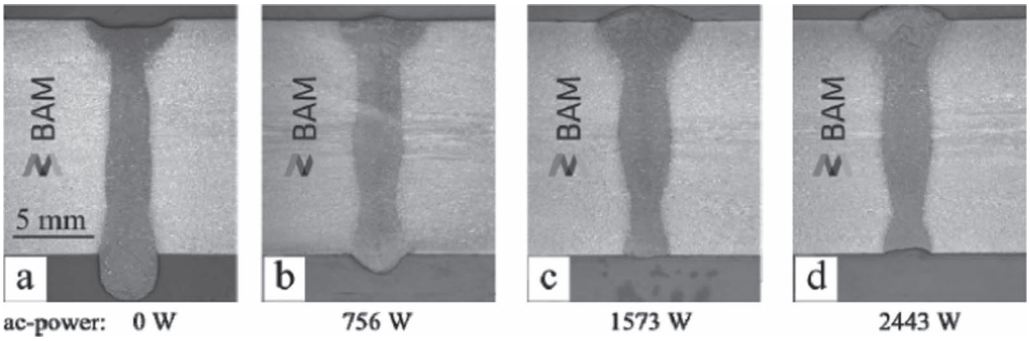
BAM
5 mm
a
b
c
d
ac-power: 0 W
756 W
1573 W
2443 W

FIGURE 2.17 Root curvature evolution with increasing ac power (1180 Hz) 15 mm duplex steel AISI 2205 (left no support) [37].

aluminium and steel using a 20 kW laser, enabling welds previously in the realm of e-beam only. One consequence is there comes a point where the Laplace pressure is exceeded and the melt begins to sag or even drop from the base of the joint, about 20 mm thick for steel plates [35]. This is particularly so for low-viscosity melts such as Cu and Al.

Unlike when using an electron source, you can use magnetohydrodynamics to control the flow of the melt pool, which is often used in processes like metal casting to control the movement/cooling rate of the material. A high-frequency magnetic field is used to generate a surface pressure and avoid melt sagging. This can not only help keep the melt supported (Figure 2.17), but also control the mixing of filler materials [36].

The addition of ultrasonic vibration [38,39] to the weld bead has also been shown to give additional control of the final melt bead, thus reducing porosity, increasing mixing, and changing grain growth.

2.4.4.7 Aluminium to Steel

The joining of Al to steels deserves special mention being a key application for the automotive industry driven by the need to shed weight and hence reduce emissions for combustion engines and increase range in electric vehicles. This is notoriously difficult because of weak intermetallics and a tendency to form porosity – a clear description of the problem is given by Schubert [40].

One method to achieve this is laser joining (flux-less brazing), where the laser is used to heat the steel to a temperature where the aluminium in contact melts and then solidifies on the steel surface producing a joint, but with a limited strength. A range of fillers may also be used to enhance the process.

One promising route for an automated process is another form of dual beam laser welding [41], which uses a combination of CW and pulsed lasers to produce a lap joint. The CW laser maintains a melt on the upper surface of the steel, and the pulses force intermittent stirring of the steel into the Al with root-like tendrils. While not a fully developed process, initial results show a greater degree of mechanical coupling giving an increased strength joint, rising from a shear strength of 71 MPa without the pulse stirring to 128 MPa in this study (Figure 2.18).

2.4.5 Implementations

2.4.5.1 Remote Laser Welding

In remote laser welding, a laser is projected in free space either from a robot arm or from a galvanometer onto the workpiece without the benefit of nozzles and shrouding. The implementation is being targeted as a replacement for resistance spot welding as it offers greater flexibility, speed, cosmetic appearance, and deeper penetration for a given spot with the corresponding reductions in distortion [42]. The primary application area being targeted is automotive, there being numerous case studies looking into the economics of the process, weighing up floor space, energy costs and safety issues, etc. Taking one typical study by Fysikopoulos [43] the conclusions appear to be that it is a technology with potential that has yet to prove itself in industry. Perhaps it will suddenly take off as the new generation of multi-kilowatt-capable high-precision scanners reduce in cost from the high premiums they currently claim (>$35 k).

2.4.5.2 Process Set-up and Diagnostics

As previously discussed, one way to reduce the amount of failure within the welding cycle is to generate wider welds, the alternative is to be more accurate with the position of the laser. A visit to a laser-welded tailored blanking line in the early 1990s would have revealed a camera pointing to the feedstock and a monitor with marker pen or tape showing the ideal position of the joint. Operator skill would have been used to monitor and adjust this during the shift and maintain weld integrity. Over time, this was automated, but is still a very simple process. As part shape has become more complex, there has been increased acceptance of the process and multi-axis robots have become more common; there has been a need for greater automatable position control.

One of the first in-process weld monitoring systems used spectroscopic analysis of the plasma plume [44]; lower-cost, higher-speed systems are being achieved by looking at relative changes in specific areas of the spectrum [45]; another early technique is acoustic analysis [46] of the plate. For those interested in the state of the art a quick search will show that they are all being actively revisited with the advances in computing, big data, neural networks, and machine learning (and being applied to metal additive manufacturing).

The current industrial push seems to be to combine as many analysis techniques as possible into one tool to maximize

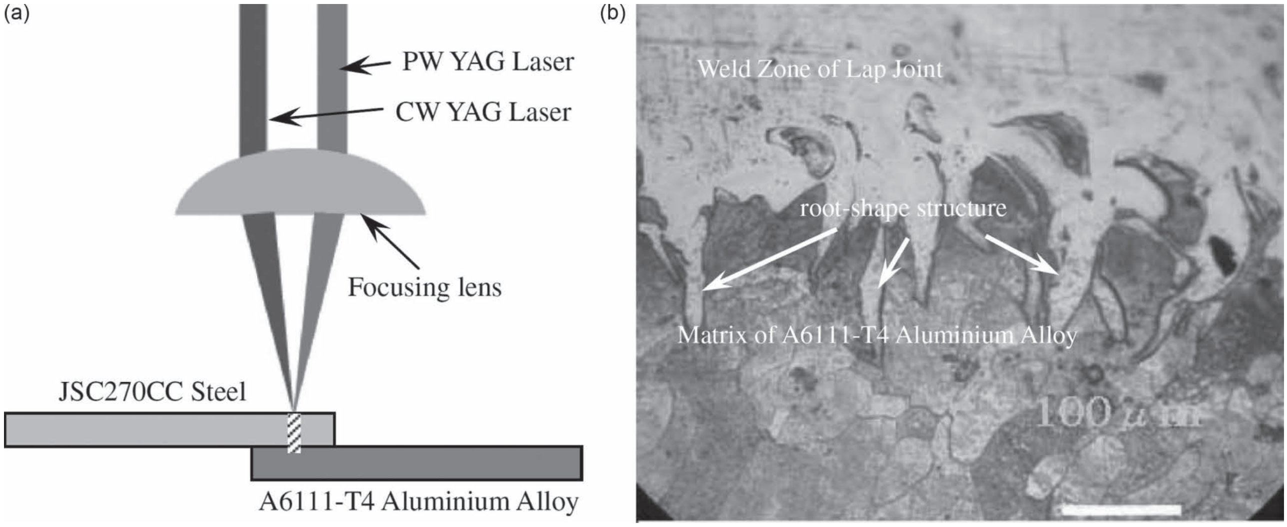

FIGURE 2.18 (a) CW/pulsed dual beam optical configuration, (b) Al-steel join morphology [41].

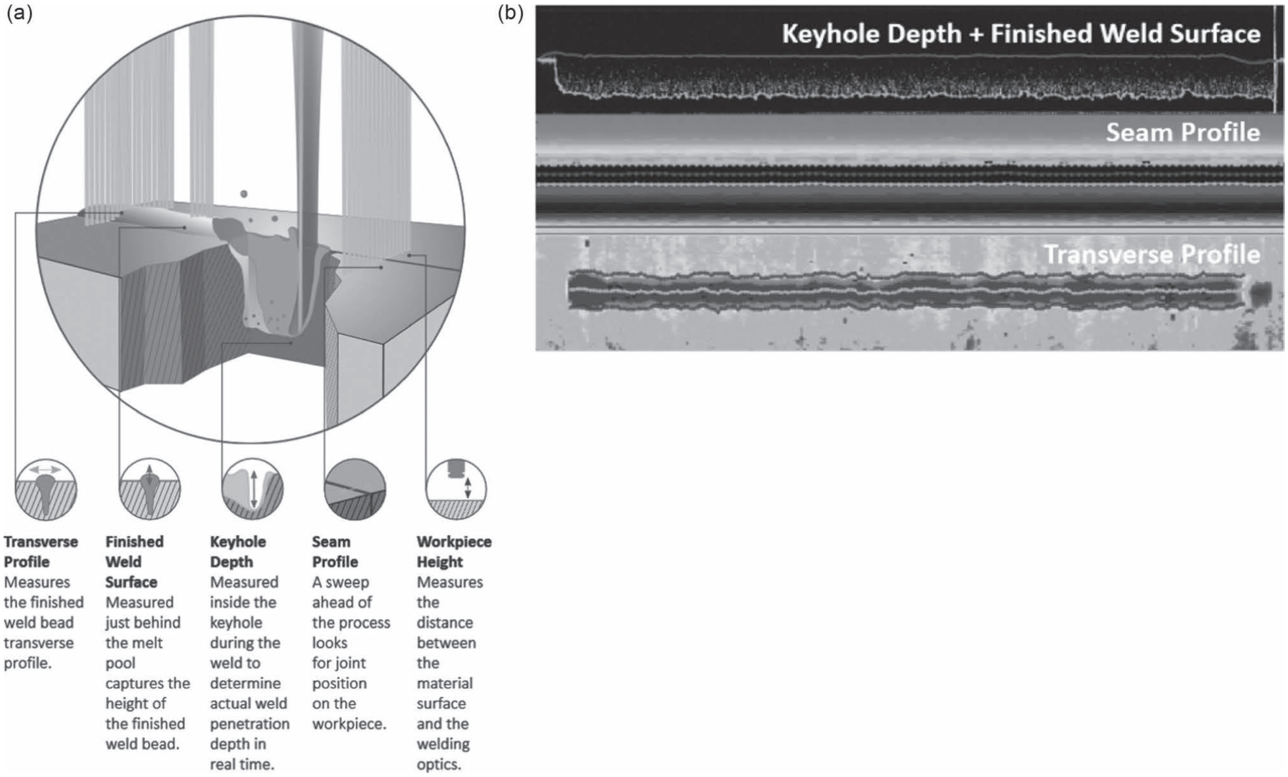
(a)
(b)
Transverse Profile
Measures the finished weld bead transverse profile.
Finished Weld Surface
Measured just behind the melt pool captures the height of the finished weld bead.
Keyhole Depth
Measured inside the keyhole during the weld to determine actual weld penetration depth in real time.
Seam Profile
A sweep ahead of the process looks for joint position on the workpiece.
Workpiece Height
Measures the distance between the material surface and the welding optics.
Keyhole Depth + Finished Weld Surface
Seam Profile
Transverse Profile

FIGURE 2.19 (a) Omni-WELD optical configuration and measurements, (b) Example data [48].

reliability [47]. Omni-WELD is a geometry measuring system that can measure the location of the joint (*X*, *Y*, and *Z*), melt profile, and most importantly the depth of the keyhole at 250 kHz by using swept source optical coherence tomography within a galvanometer scanner (Figure 2.19). Data can then be used to control the position of the laser and traverse rates, and subsequently confirm the integrity of the weld.

2.5 Future Opportunities

Laser welding is now a very mature technology. It seems reasonable to assume that the major developments will come from the development of new laser sources and the inclusion of new materials into mainstream engineering. Looking at the sources, we have seen the transition of the laser from the CW CO_2 "heat gun" to the 1 μm fibre laser CW, ns, QCW, and ps now being mainstream, with ruggedized high power fs not far away. There are clear benefits for welding many materials moving to shorter wavelengths, mirrored in the blue [49] and green lasers; we are starting to see offered by the laser manufacturers.

Material and scale developments are even more extreme, with a progression to lighter cheaper "exotic" energy-efficient materials in all parts of our lives. Globally, we are spending significant research resources on graphene and carbon nanotubes for the manufacture of the next-generation sensors and electronics but still have no effective way of connecting them to metal much better than silver paint!

REFERENCES

1. W. Steen, J. Mazumder, *Laser Material Processing*, 4th ed. Springer London, 2010.
2. J. F. Ready, D. F. Farson, and T. Feeley, *LIA Handbook of Laser Materials Processing*. Laser Institute of America, Orlando, FL, 2001.
3. J. C. Ion, *Laser Processing of Engineering Materials*. Butterworth-Heinemann, Oxford, 2005.
4. M. Courtois, M. Carin, P. L. Masson, S. Gaied, and M. Balabane, 'A new approach to compute multi-reflections of laser beam in a keyhole for heat transfer and fluid flow modelling in laser welding', *J. Phys. Appl. Phys.*, vol. 46, no. 50, p. 505305, Dec. 2013.
5. G. Tsotridis, H. Rother, and E. D. Hondros, 'Marangoni flow and the shapes of laser-melted pools', *Sci. Nat.*, vol. 76, no. 5, pp. 216–218, May 1989.
6. A. Matsunawa, J.-D. Kim, N. Seto, M. Mizutani, and S. Katayama, 'Dynamics of keyhole and molten pool in laser welding', *J. Laser Appl.*, vol. 10, no. 6, pp. 247–254, Dec. 1998.
7. M. Xia, E. Biro, Z. Tian, and Y. N. Zhou, 'Effects of heat input and martensite on HAZ softening in laser welding of dual phase steels', *ISIJ Int.*, vol. 48, no. 6, pp. 809–814, 2008.
8. R. Ducharme, K. Williams, P. Kapadia, J. Dowden, B. Steen, and M. Glowacki, 'The laser welding of thin metal sheets: an integrated keyhole and weld pool model with supporting experiments', *J. Phys. Appl. Phys.*, vol. 27, no. 8, pp. 1619–1627, Aug. 1994.

9. M. Naeem, and T. Kugler, 'Material processing with super modulation', in *Proceedings of the 21st International Congress on Applications of Lasers and Electro-Optics (ICALEO 2002), Scottsdale, Arizona, USA*, 2002.
10. R. K. Huang et al., 'Direct diode lasers with comparable beam quality to fiber, CO_2, and solid state lasers', presented at the *SPIE LASE*, San Francisco, California, USA, 2012, p. 824102.
11. A. Lisiecki, 'Diode laser welding of high yield steel', presented at the *Tenth Symposium on Laser Technology*, Szczecin - Świnoujście, Poland, 2013, p. 87030S.
12. C. Dawes, *Laser Welding*, 1st ed. Woodhead Publishing, Cambridge, 1992.
13. W. W. Duley, *Laser welding*. Wiley, New York, 1999.
14. Y. Ai, et al., 'Investigation of the humping formation in the high power and high speed laser welding', *Opt. Lasers Eng.*, vol. 107, pp. 102–111, Aug. 2018.
15. A. De, and T. DebRoy, 'A perspective on residual stresses in welding', *Sci. Technol. Weld. Join.*, vol. 16, no. 3, pp. 204–208, Apr. 2011.
16. T. Kok, W. J. B. Grouve, L. L. Warnet, and R. Akkerman, 'Effect of ply orientation on bond strength in fiber-placed composites', in *International Conference on Composite Materials*, Copenhagen, Denmark, 2015, p. 12.
17. I. A. Jones and R. J. Wise, 'Weblding method', EP117502B1, Jan–2003.
18. I. Mingareev, F. Weirauch, A. Olowinsky, L. Shah, P. Kadwani, and M. Richardson, 'Welding of polymers using a 2 µm thulium fiber laser', *Opt. Laser Technol.*, vol. 44, no. 7, pp. 2095–2099, Oct. 2012.
19. T. Tamaki, W. Watanabe, J. Nishii, and K. Itoh, 'Welding of transparent materials using femtosecond laser pulses', *Jpn. J. Appl. Phys.*, vol. 44, no. 22, pp. L687–L689, May 2005.
20. A. de Pablos-Martín, and Th. Höche, 'Laser welding of glasses using a nanosecond pulsed Nd:YAG laser', *Opt. Lasers Eng.*, vol. 90, pp. 1–9, Mar. 2017.
21. I. Miyamoto, K. Cvecek, and M. Schmidt, 'Simple evaluation procedure of nonlinear absorptivity in glass welding using USLP with high-pulse repetition rates', *Phys. Procedia*, vol. 39, pp. 526–533, 2012.
22. M. Weigl, F. Albert, and M. Schmidt, 'Enhancing the ductility of laser-welded copper-aluminum connections by using adapted filler materials', *Phys. Procedia*, vol. 12, pp. 332–338, 2011.
23. W. M. Steen, and M. Eboo, 'Arc augmented laser welding', *Met. Constr.*, vol. 11, pp. 332–333, 335, 1979.
24. D. Petring, and C. Fuhrmann, 'Recent progress and innovative solutions for laser-arc hybrid welding', in *Pacific International Conference on Applications of Lasers and Optics*, Melbourne, Australia, 2004, p. P702.
25. B. Acherjee, 'Hybrid laser arc welding: State-of-art review', *Opt. Laser Technol.*, vol. 99, pp. 60–71, Feb. 2018.
26. L. Wang, M. Gao, C. Zhang, and X. Zeng, 'Effect of beam oscillating pattern on weld characterization of laser welding of AA6061-T6 aluminum alloy', *Mater. Des.*, vol. 108, pp. 707–717, Oct. 2016.
27. 'D50 Wobble and Seam Tracking Head'. [Online]. Available: https://www.ipgphotonics.com/en/products/beam-delivery/process-heads/welding/d50-wobble-and-seam-tracking-head. [Accessed: 24-Apr-2019].
28. 'Novel Lasers: Blue direct-diode lasers extend industrial laser capability'. [Online]. Available: https://www.laserfocusworld.com/articles/print/volume-54/issue-09/features/novel-lasers-blue-direct-diode-lasers-extend-industrial-laser-capability.html. [Accessed: 26-Apr-2019].
29. J. Gabzdyl, and D. Capostagno, 'Joining dissimilar materials with pulsed nanosecond fiber lasers: Industrial use of nanosecond lasers for welding and joining', *Laser Tech. J.*, vol. 14, no. 3, pp. 38–41, Jun. 2017.
30. C. M. Banas, and E. Hartford, 'Twinspot Laser Welding', 4,691,093, Sep 1987.
31. J. Xie, 'Dual beam laser welding', *Weld. J.*, vol. 10, no. 81, pp. 223–230, 2002.
32. M. G. Forrest, and F. Lu, 'Fundamental study of dual beam laser welding of zinc coated steel sheets in lap joint configuration with zero-gap', presented at the *ICALEO 2003*, Jacksonville, Florida USA, 2003, p. 1402.
33. A. Haeusler, S. Hollatz, A. Olowinsky, A. Gillner, and R. Poprawe, 'Quality improvement of the surface of laser micro welds by using a dual beam setup', *J. Laser Appl.*, vol. 30, no. 3, p. 032423, Aug. 2018.
34. S. Pang, W. Chen, J. Zhou, and D. Liao, 'Self-consistent modeling of keyhole and weld pool dynamics in tandem dual beam laser welding of aluminum alloy', *J. Mater. Process. Technol.*, vol. 217, pp. 131–143, Mar. 2015.
35. F. Vollertsen, S. GrÜnenwald, M. Rethmeier, A. Gumenyuk, U. Reisgen, and S. Olschok, 'Welding thick steel plates with fibre lasers and GMAW', *Weld. World*, vol. 54, no. 3–4, pp. R62–R70, Mar. 2010.
36. M. Gatzen, Z. Tang, and F. Vollertsen, 'Effect of electromagnetic stirring on the element distribution in laser beam welding of aluminium with filler wire', *Phys. Procedia*, vol. 12, pp. 56–65, 2011.
37. A. Fritzsche, V. Avilov, A. Gumenyuk, K. Hilgenberg, and M. Rethmeier, 'High power laser beam welding of thick-walled ferromagnetic steels with electromagnetic weld pool support', *Phys. Procedia*, vol. 83, pp. 362–372, 2016.
38. J. S. Kim, T. Watanabe, and Y. Yoshida, 'Ultrasonic vibration aided laser welding of Al alloys: improvement of laser welding-quality', *J. Laser Appl.*, vol. 7, no. 1, pp. 38–46, Mar. 1995.
39. S. Jia, and L. Nastac, 'The influence of ultrasonic stirring on the solidification microstructure and mechanical properties of A356 alloy', *Chem. Mater. Eng.*, vol. 1, no. 3, pp. 69–73, 2013.
40. E. Schubert, I. Zerner, and G. Sepold, 'Laser beam joining of material combinations for automotive applications', presented at the *Lasers and Optics in Manufacturing III*, Munich, Germany, 1997, pp. 212–221.
41. S. Yan, Z. Hong, T. Watanabe, and T. Jingguo, 'CW/PW dual-beam YAG laser welding of steel/aluminum alloy sheets', *Opt. Lasers Eng.*, vol. 48, no. 7–8, pp. 732–736, Jul. 2010.
42. P. Kah, J. Lu, J. Martikainen, and R. Suoranta, 'Remote laser welding with high power fiber lasers', *Engineering*, vol. 05, no. 09, pp. 700–706, 2013.
43. A. Fysikopoulos, G. Pastras, J. Stavridis, P. Stavropoulos, and G. Chryssolouris, 'On the performance evaluation of remote laser welding process: an automotive case study', *Procedia CIRP*, vol. 41, pp. 969–974, 2016.

44. S. Palanco, et al., ‘Spectroscopic diagnostics on CW-laser welding plasmas of aluminum alloys.’, *At. Spectrosc.*, vol. 56, p. 9, 2001.
45. H. B. Chen, L. Li, D. J. Brookfield, K. Williams, and W. M. Steen, ‘Laser process monitoring with dual wavelength optical sensors’, presented at the *ICALEO*, San Jose, CA, 1991, pp. 113–122.
46. H. Gu, and W. W. Duley, ‘A statistical approach to acoustic monitoring of laser welding’, *J. Phys. Appl. Phys.*, vol. 29, no. 3, pp. 556–560, Mar. 1996.
47. P. Stritt, et al., ‘Comprehensive process monitoring for laser welding process optimization’, presented at the *High-Power Laser Materials Processing: Lasers, Beam Delivery, Diagnostics, and Applications*, San Francisco, CA, US, 2016, vol. 9741, p. 10.
48. ‘Real Time Weld Process Monitoring | IPG Photonics’. [Online]. Available: https://www.ipgphotonics.com/en/products/beam-delivery/process-monitoring. [Accessed: 30-Apr-2019].
49. M. Tsukamoto, S. Masuno, Y. Sato, R. Higashino, K. Tojo, and K. Asuka, ‘Development of high intensity blue diode laser system for materials processing (Conference Presentation)’, presented at the *Proceedings of the SPIE*, 2018, vol. 10514.

3

High-Power Laser Cutting

John Powell and Dirk Petring

CONTENTS

3.1 The Basics of the Laser Cutting Process 17
  3.1.1 Introduction 17
  3.1.2 Why Use Laser Cutting? 18
  3.1.3 Types of High-power Laser Cutting Machines 19
    3.1.3.1 Three-dimensional Laser Cutting 20
  3.1.4 Differences between CO_2 and Fibre Laser Cutting 20
    3.1.4.1 General 20
    3.1.4.2 Cutting Speeds 20
    3.1.4.3 Cut Quality 21
    3.1.4.4 Laser Absorption in the Cutting Zone 21
3.2 How Lasers Cut Different Materials 22
  3.2.1 General Notes 22
  3.2.2 Cutting Stainless Steels 23
  3.2.3 Cutting Mild and Carbon Steels 24
    3.2.3.1 Cutting Mild Steel with Oxygen 24
    3.2.3.2 Cutting Mild Steel with Nitrogen 25
  3.2.4 Cutting Alloy Steels 26
  3.2.5 Cutting Non-ferrous Metals 26
    3.2.5.1 Aluminium and Copper Alloys 26
    3.2.5.2 Titanium Alloys 27
    3.2.5.3 Nickel Alloys 28
    3.2.5.4 Other Alloys 28
  3.2.6 Cutting Non-metals with CO_2 Lasers 28
    3.2.6.1 General Notes 28
    3.2.6.2 Polymers 28
    3.2.6.3 Other Non-metals 30
3.3 Cutting Speeds 31
  3.3.1 Mild and Carbon Steels 31
  3.3.2 Stainless Steels 31
  3.3.3 Aluminium Alloys 31
  3.3.4 Non-metals – CO_2 Lasers Only 31
Acknowledgements 33

3.1 The Basics of the Laser Cutting Process

3.1.1 Introduction

Note: This entire section on high-power laser cutting is an excerpt taken (with permission) from the 'LIA Guide to High Power Laser Cutting' – published by the Laser Institute of America March 2017 (ISBN 978 1940168 111).

Laser cutting has become a standard industrial process since its initial development in the early 1970s. The technique is commonly used in job shop environments and in the manufacturing sector for applications as diverse as cutting steel engineering components and yacht sails.

Tens of thousands of laser cutting machines are active all over the world, and several thousands more are sold every year. The main two types of laser involved are as follows:

a. The carbon dioxide (CO_2) laser, the traditional workhorse of the industry, which has been under constant development since the 1970s;

b. The fibre laser[1], which started to appear on the market in 2005 and has experienced a rapid industrial uptake, primarily driven by its superior performance in cutting thin-section metals.

These complementary technologies have different strong points, which will be discussed later in this section. The basic mechanism by which both types of laser-cut materials are extremely simple is as follows:

a. The laser beam is focused down to a small spot on, or below, the surface of the workpiece.
b. The intense heat of the focused beam melts its way all the way through the workpiece in a very narrow area, typically 0.1–1.0 mm.
c. A gas jet acting with the laser pushes the melt out of the bottom of the cutting zone, as shown in Figure 3.1. (Note 1: When cutting certain materials, the gas jet can be chosen to react chemically with the workpiece to produce heat and accelerate the cutting process. The most common application of this is the cutting of mild or carbon steel with an oxygen jet. Note 2: Some of the materials are vaporized during cutting but in most cases, the dominant material removal mechanism is melting.)
d. The cutting zone is moved around the workpiece to produce the desired profile. Either the laser head, the workpiece or both can be moved, depending on the machine design.

3.1.2 Why Use Laser Cutting?

Before moving on to a more detailed description of the cutting process, here is a summary of the benefits of laser cutting:

A. The process cuts at high speed compared to other profiling methods. For example, 5 kW of CO_2 laser power can cut 5-mm-thick stainless steel at approximately 3 m min^{-1}. 1200 W of CO_2 laser power will cut 5-mm-thick acrylic sheet at ~10 m min^{-1}. Note: These are not thickness limits – just random examples. In most cases (e.g. the examples given above), the cut components will be ready for service immediately after cutting without any subsequent cleaning operation.
B. The cut width (kerf width) is extremely narrow, typically 0.1–1.0 mm wide, so detailed work can be carried out without the restriction of a minimum internal radius imposed by flame cutting, plasma cutting or milling machines and similar mechanical methods.
C. The process is fully CNC-controlled. This, combined with the lack of necessity for complex jigging arrangements, means that a change of job from cutting component 'A' out of steel to cutting component 'B' out of brass can be carried out in seconds.
D. Although laser cutting is a thermal process, the amount of material heated by the laser is very small, and most of this heated material is removed during cutting. Thus, the thermal input to the bulk of the material is very low. This means that heat-affected zones (HAZs) are minimized and thermal distortion is generally avoided.
E. It is a non-contact process, which means that the material only needs to be lightly clamped or merely positioned under the beam. Flexible or flimsy materials can be cut with great precision and do not distort during cutting as they would when cut by mechanical methods (although they might need to be supported and clamped to avoid being distorted by the gas jet).
F. Since the kerf width is extremely narrow and there is no mechanical force on the sheet being cut, components can be arranged to 'nest' very close together. Hence, material waste is reduced to a minimum (see Figure 3.2). In some cases, this principle can be extended until there is no waste material at all between edges of adjacent components. For example, the laser cut separates the two components, which will 'share' the cut line. This is an extremely effective use of material and laser time, but is generally only applicable where two components can be arranged to share a straight-line cut.
G. Although the capital cost of a laser cutting machine is substantial, the running costs are generally low. Many industrial cases exist where a large installation has paid for itself in under a year.
H. The process is generally extremely quiet compared to competing techniques, a factor that improves the

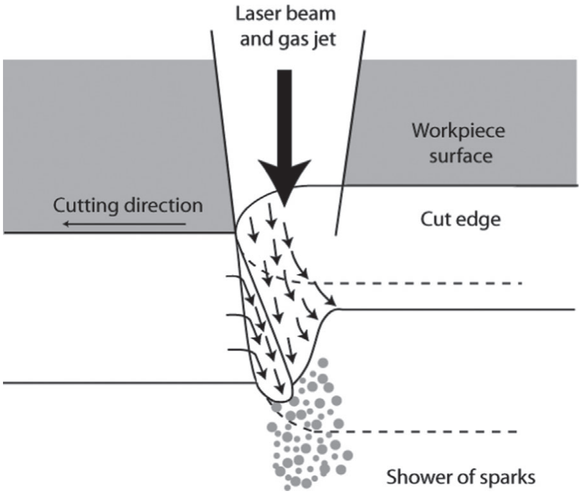

FIGURE 3.1 The basic mechanism of laser cutting. The laser generates a localized melt, and the liquid is ejected from the cutting zone by a gas jet. In some cases (e.g. when cutting carbon steel with oxygen), the gas jet reacts chemically with the workpiece to produce extra heat, which speeds up the cutting process. (LIA Guide to High Power Laser Cutting. Pub; Laser Institute of America 2017.)

---

[1] In this section, the term 'Fibre laser' will be used to describe both fibre and disk lasers as the differences between these technologies are trivial as far as the cutting process is concerned.

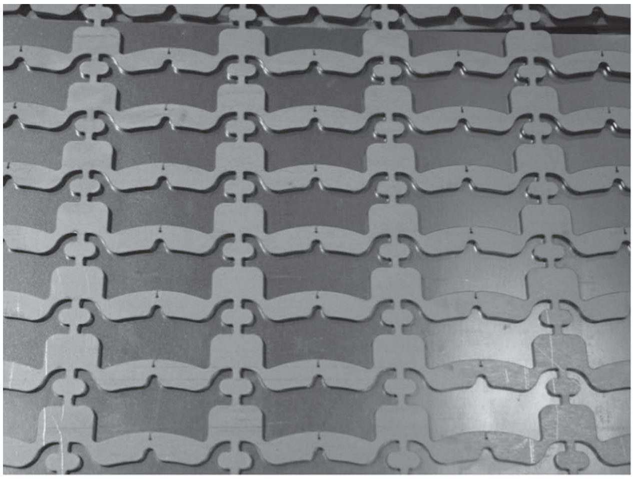

FIGURE 3.2 Components can be nested close together on a sheet to minimize wasted material. Here is shown the 'skeleton' of a sheet from which a number of nested components have been cut (the 'skeleton' in this photo is resting on an un-cut sheet of steel). (LIA Guide to High Power Laser Cutting. Pub; Laser Institute of America 2017.)

working environment and the efficiency of the operating staff. Although cutting often involves a rather noisy, high-pressure gas jet, the machine enclosure limits the noise experienced by the machine operator.

I. Laser cutting machines are extremely safe to use in comparison with many of their mechanical counterparts.

3.1.3 Types of High-power Laser Cutting Machines

The infrared light generated by a CO_2 or fibre laser is invisible to the naked eye in the same way as the sound made by a dog whistle can't be heard by human ears. In every other way, it behaves as a normal light beam which can be reflected off mirrors and focused by lenses. The light from a fibre laser can also be passed down an optical fibre.

There are six main ways of moving a cut around the workpiece. The most common systems employ only three axes and are used to cut flat sheets. If three-dimensional objects are being cut, five- or six-axis robots are employed:

A. Moving optics systems

Figure 3.3 demonstrates the principle of a 2D machine which uses moving mirrors to reflect the laser beam to the cutting head. In this case, the material remains stationary. This technology is the most common design for CO_2 laser cutting machines.

B. Fibre optic systems

These systems cannot be used with CO_2 lasers but are the most common choice for fibre or disk lasers. In this case, the light from the laser is piped down an optical fibre before being focused by a cutting head which is moved across the workpiece.

C. Hybrid systems

A single moving mirror or fibre optic is used to move the laser beam in one direction and the material is moved in the other.

D. Tube cutting systems

In this case, the tubular workpiece is rotated and moved to and fro along its axis. The laser (via moving optics or fibre) moves perpendicular to the axis of the tube (this is a specific type of hybrid system). Figure 3.4 shows examples of tube cut junctions that have been developed specifically for laser tube cutting.

E. Moving workpiece systems

In this case, the laser cutting head remains stationary and the workpiece is moved.

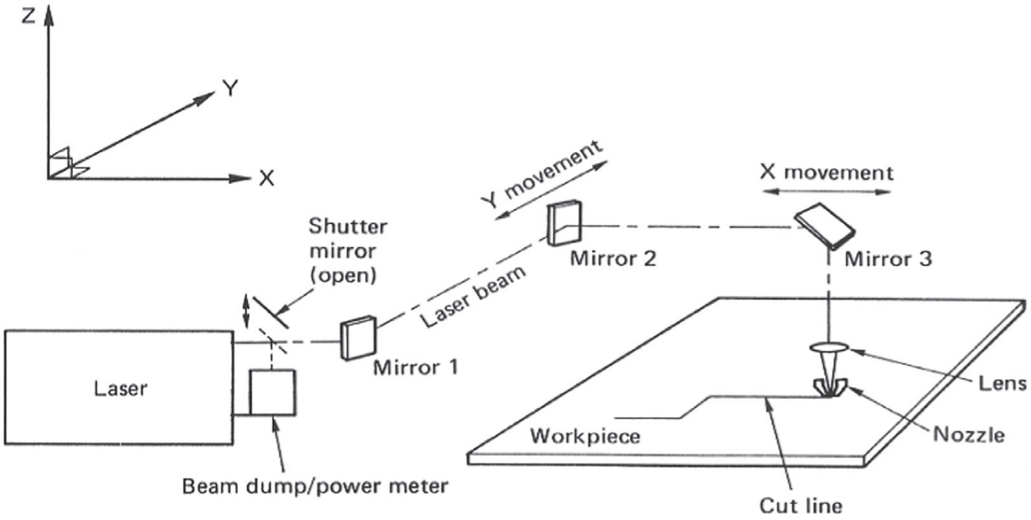

FIGURE 3.3 A schematic of a cutting table with moving mirrors in the *X*- and *Y*-axes. The laser beam path is shown as a broken line. Mirror 1 is stationary; mirror 2 moves into and out of the page together with mirror 3 and its attached cutting head (lens + nozzle). Mirror 3 and the attached cutting head can move towards and away from mirror 2 (left and right in this diagram). The head also has a limited movement in the Z direction (usually controlled by a sensor) to allow for non-flatness of the workpiece. This type of machine is usually referred to as a 'moving optics' table. (LIA Guide to High Power Laser Cutting. Pub; Laser Institute of America 2017.)

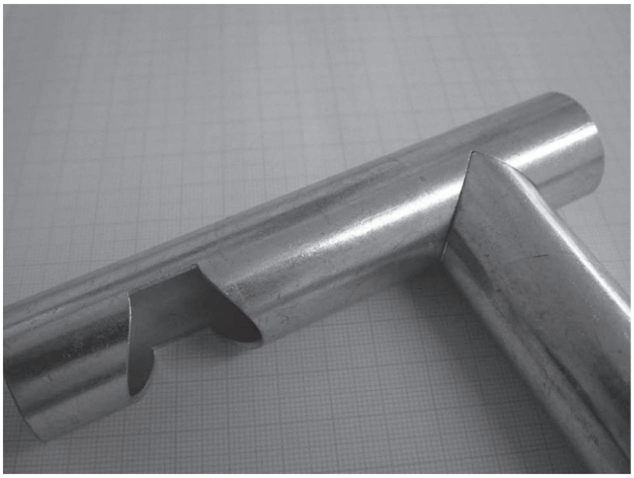

FIGURE 3.4 Examples of laser tube cutting demonstrating the design flexibility available. The joint type on the left (second tube not inserted into the joint for clarity) was developed with laser cutting in mind. (LIA Guide to High Power Laser Cutting. Pub; Laser Institute of America 2017.)

F. Moving laser systems

The laser itself is moved over the workpiece with its cutting head.

Computer software is used to define the tool path and cutting speed; to add tool compensation to a chosen path; and to control additional functions such as laser power, laser pulsing and cutting gas pressure.

Laser powers for cutting range from ~50 W to ~10 000 W. CO_2 laser powers below 200 W are generally only suitable for non-metals. The lasers can produce a continuous beam of energy (continuous wave or cw), or they can be used to generate a stream of pulses of energy (pulsed wave or pw). Both types of output can be used for cutting although pulsed beam cutting is preferred where a high degree of control is necessary (e.g. when cutting fine detail in steels).

3.1.3.1 Three-dimensional Laser Cutting

In some cases, a standard flatbed cutting machine can carry out work on pre-formed workpieces. For example, cuts can easily be achieved in boxes or square-section tubing if one face is cut at a time. Circular cross-sectional tubing can also have slots or details cut-out if the profile does not vary too far from the top-centre of the cross section. If the work involves profiling all around a circular or rectangular cross-sectional tube, a computer-controlled chuck attachment can be fitted to a flatbed cutter. This attachment takes the place of one of the axes and rotates the tube under the laser beam as the remaining axis moves backwards and forwards. However, dedicated tube cutting machines have much higher productivity rates than chuck-adapted flatbed machines, and they can profile a wide range of tube cross sections.

If the work does not involve tubing or two-dimensional surfaces, then it will require the use of a five- or six-axis cutting machine. There are two basic designs of this type of machine:

A. A robotic arm holding a laser cutting head. The laser beam is fed to the head via a system of mirrors in the case of CO_2 lasers, or via an optical fibre for fibre lasers.

B. A gantry system, which consists of a large, box-like structure. Within this frame, the cutting head is suspended from a moving *x*–*y*–*z* system similar to a gantry crane. The cutting head involves a wrist-like mechanism containing several mirrors or a fibre to direct the beam to the nozzle.

The advantage of five- or six-axis cutting machines is obviously that they can profile three-dimensional shapes. There are, however, a number of special issues to be taken into account:

A. Five- and six-axis machines are more expensive than flatbed cutters.

B. They take a lot longer to programme and set up for a job.

C. Cutting speeds and acceleration rates tend to be lower.

D. Positional and dynamic accuracy is generally reduced.

In spite of these considerations, machines of this type have become increasingly popular over recent years. They have proved a major benefit in the aerospace and automobile industries.

3.1.4 Differences between CO_2 and Fibre Laser Cutting

3.1.4.1 General

Since their introduction into the laser profiling industry in approximately 2005, sales of high-power fibre lasers have been rising rapidly, and they are now more popular than the more traditional CO_2 laser technology. However, CO_2 laser cutting machines have retained some market share because they produce better-quality cut edges on thicker-section metals without the need for specialist techniques. They can also cut plastics, wood-based products and other non-metals, which cannot be cut by fibre laser because, at the fibre laser wavelength of approximately one micron, these materials do not absorb enough energy for a cut to be generated.

A typical capital outlay in the range of half a million dollars (or Euros) will buy a multi-kilowatt CO_2 or fibre machine with a working area of approximately 3 m × 1.5 m.

3.1.4.2 Cutting Speeds

Maximum cutting speeds quoted for the fibre lasers for thin-section metals will be very much higher than for CO_2 lasers. It is true that the machines are faster, but this maximum speed differential may be misleading. For example, the quoted maximum cut speed for 1mm stainless steel might be twice as fast for a fibre laser as for the comparable CO_2 machine, but these high speeds will only be achieved for a fraction of the time when profiling actual components. The cutting machine needs to spend a considerable amount of its time accelerating as well as decelerating around details and small holes. Also, the machine needs to stop whenever it pierces a material of more than 2–3 mm thickness to produce a cut. Depending on the component geometry, this brings the average cutting speed for the item down to a value well below the maximum speed for that thickness of material.

The productivity of a laser cutting machine is, of course, related to how much time it takes to produce a cut item. This time is made up of the following components in addition to the time spent cutting the component at its nominal programmed speed:

1. The time spent piercing the component before cutting begins.

   A profile that involves 20 cut-out holes needs 21 piercing events – one for each hole and a final one for the profile itself.
2. The time taken to accelerate into and out of detailed features.

   If the laser is cutting refrigerator doors, then this extra time might be trivial. If, on the other hand, saw blade teeth are being cut, then the machine will be constantly accelerating or decelerating and might never reach its nominal programmed speed.
3. The time taken to move between cut-outs in the component – when the laser is off. The time taken in this case is solely dependent on the machine mechanics and has nothing to do with the laser.
4. The time taken to remove a cut sheet and replace it with the next one to be cut (most machines have two tables and the changeover is an automated process). If a machine is cutting 500 small components out of each sheet, this sheet-change time might be a trivial component of the overall production time. However, cutting large refrigerator doors out of thin-section steel might result in the sheet-change time being more than half of the production time.

Even for a manufacturer who will be cutting thousands of the same component all year, productivity cannot be predicted accurately from theoretical cutting speeds. Although cutting machine manufacturers can use software to calculate the component cut time (taking into account most of the points above), contributions like the sheet-change time might not be included. Therefore, the only truly reliable way of getting accurate component cut times is by having a series of samples cut. This is also the best way of checking the quality, dimensional accuracy and reproducibility of the cut product.

3.1.4.3 Cut Quality

The subject of cut edge quality will be discussed in more depth in the next section, but a quick note on the differences in cut quality between CO_2 and fibre lasers is useful here.

When cutting mild steel with oxygen, the cut edge quality produced by a fibre laser is similar to that produced by a CO_2 laser. Figure 3.5 shows examples of cut edges cut by both types of machine (the left-hand image in each case was cut by fibre laser, and the right-hand image was cut by CO_2 laser).

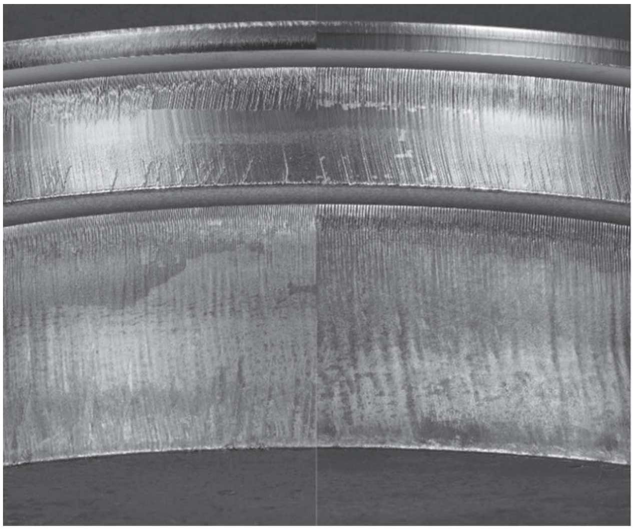

FIGURE 3.5 Mild steel cut with oxygen. Left-hand side: samples cut with a fibre laser. Right-hand side: samples cut with a CO_2 laser. Sample thickness: top, 3 mm; middle, 12 mm; bottom, 25 mm. Photos courtesy of Trumpf GmbH (LIA Guide to High Power Laser Cutting. Pub; Laser Institute of America 2017.)

CO_2 and fibre lasers also produce similar-quality cut edges in stainless steel up to a thickness of about 4 mm. Above that thickness, the fibre laser produces a rougher cut edge, which is, nevertheless, generally acceptable for most customers (see Figure 3.6).

Special techniques that produce a higher-quality edge for thicker sections (using slightly slower speeds, increased gas flow and special laser beam shaping techniques) are offered by some fibre laser machine manufacturers (see Figure 3.7).

3.1.4.4 Laser Absorption in the Cutting Zone

The cutting zones created by fibre and CO_2 lasers have different geometries, and this results in different cut qualities when sections thicker than 4 mm are cut with nitrogen.

Both types of laser arrive at the cutting front at a glancing angle – as shown in Figure 3.8.

The size of the glancing angle is determined by the physics of the laser–material interaction and is different for different wavelengths of laser light. The glancing angle which gives the highest absorptivity for a CO_2 laser is approximately 3°, and for a fibre laser, it's approximately 11°. This difference in preferred angle means that CO_2 laser light creates a smoother cutting front (and therefore a better cut edge quality) than a fibre laser when cutting thicker-section steels (except when oxygen is used as the assist gas). On the other hand, the higher preferred angle for fibre lasers means that they are better suited to thin-section material and higher cutting speeds are possible.

When thicker-section metals are being cut by CO_2 laser, the very shallow glancing angle of 3° means that the laser beam can directly interact with the whole of the cut front. However, when thicker sections are being profiled by fibre laser, this is

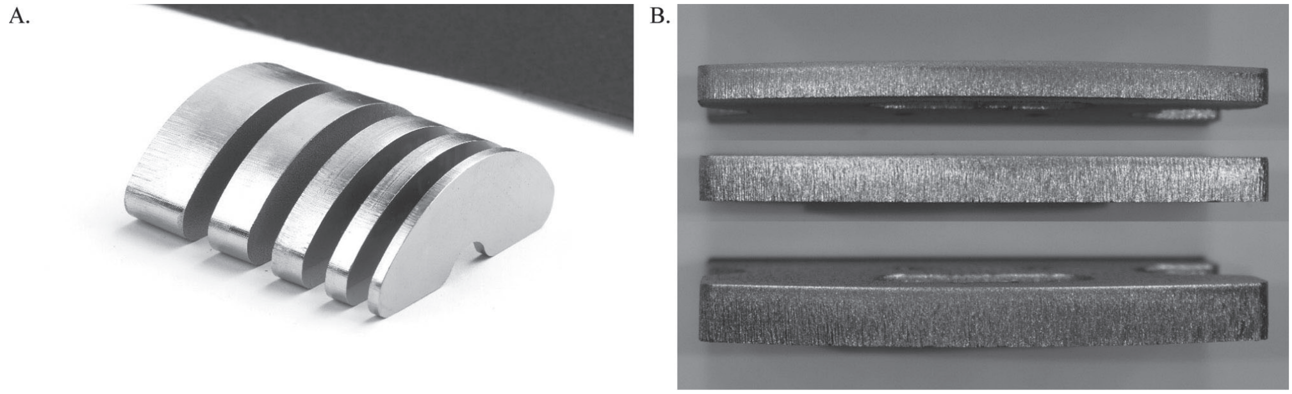

FIGURE 3.6 Stainless steel cut with nitrogen. (a) Samples cut with a CO_2 laser, thickness: 4–20 mm. (b) Samples cut with a fibre laser, thickness: 6, 8 and 10 mm. (Photos courtesy of Amada. Amada, like most suppliers, also offer a specialized parameter set which optimizes fibre laser cut edge quality – see figure 1.7.) (LIA Guide to High Power Laser Cutting. Pub; Laser Institute of America 2017.)

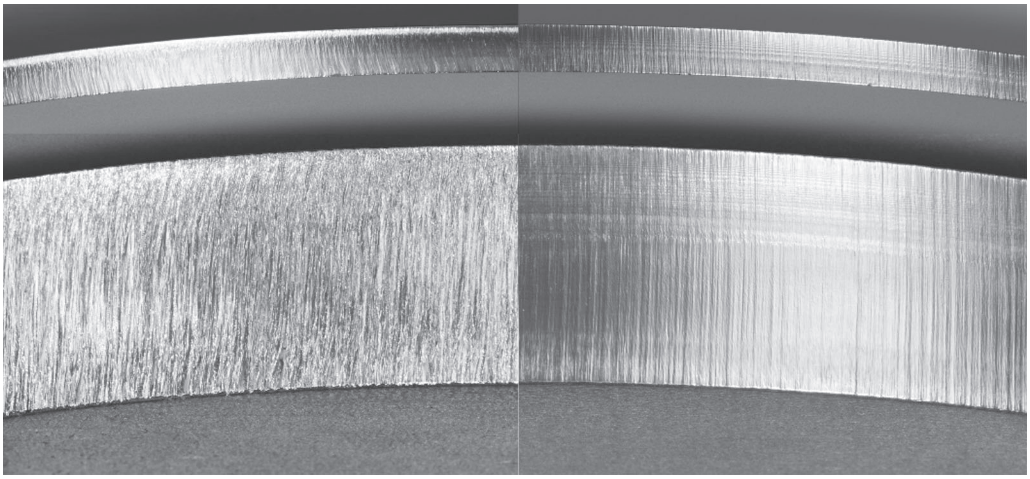

FIGURE 3.7 Typical cut edges produced when cutting stainless steel with nitrogen assist using optimum quality parameters. Left-hand samples were cut by fibre laser. Right-hand samples were cut by CO_2 laser. Top samples 3 mm thick. Bottom samples 15 mm thick. Photos courtesy of Trumpf GmbH. (LIA Guide to High Power Laser Cutting. Pub; Laser Institute of America 2017.)

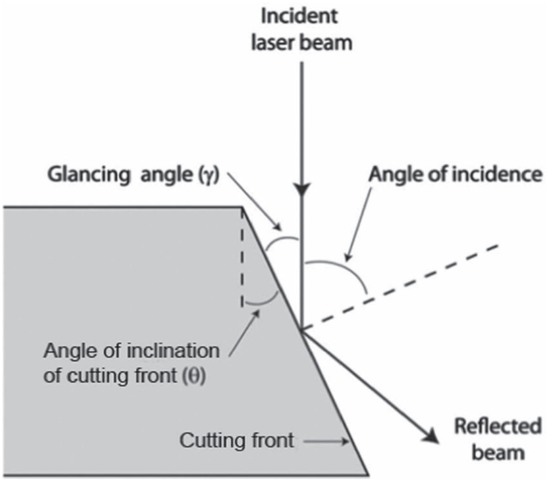

FIGURE 3.8 Lasers interact with the cutting front at a glancing angle. (LIA Guide to High Power Laser Cutting. Pub; Laser Institute of America 2017.)

not the case. Only the top part of the cutting zone is inclined at approximately 11°. Below this, the beam makes its way down the cutting front by bouncing off the sides of the cutting zone. A process known as ‘multiple reflections’ is illustrated in Figure 3.9.

This multiple reflection process for fibre lasers at thicker sections tends to produce rougher cut edges than those generated by CO_2 lasers.

3.2 How Lasers Cut Different Materials

3.2.1 General Notes

Lasers can cut materials by a variety of mechanisms, depending on the material involved and the type of laser used. These mechanisms are as follows:

a. *Melting* (*also known as ‘fusion cutting’*). In fusion cutting, the laser melts the material and the gas jet pushes the melt out of the bottom of the cutting zone.

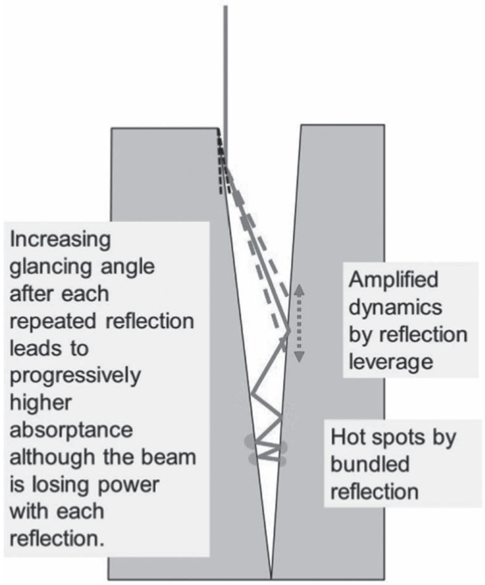
Increasing glancing angle after each repeated reflection leads to progressively higher absorptance although the beam is losing power with each reflection.
Amplified dynamics by reflection leverage
Hot spots by bundled reflection

FIGURE 3.9 Multiple reflections inside the cutting zone of a fibre laser. (D. Petring, T. Molitor, F. Schneider and N. Wolf. Diagnostics, modelling and simulation: three keys towards mastering the cutting process with fibre, disk and diode lasers. *Physics Procedia*, 39, pp. 186–196.)

This is the simplest mechanism of laser cutting and is the one which is dominant when cutting stainless steels and non-ferrous alloys.

b. *Evaporation* (*also known as 'vaporization cutting'*). During evaporation cutting, the laser heats the material in the cutting zone up to the point where it becomes a vapour or gas. This process is dominant when CO_2 lasers cut some plastics (acrylic or polyacetal) and can play a part in metal cutting at high speeds when material thicknesses are low. Evaporation also takes place to some extent when cutting metals with pulsed lasers (the high intensities achieved at the peak of the pulses can give rise to evaporation). Generally, however, when cutting metals, most of the materials leave the cutting zone as liquid droplets.

c. *Oxidation* (*also known as 'oxygen cutting'*). If mild steel is being cut, the process can involve either oxygen or nitrogen as the cutting gas. When nitrogen is used, the cutting mechanism is simply one of fusion cutting techniques. If oxygen is used, then the chemical reaction between the iron in the mild steel and the oxygen has two beneficial effects on the cutting process:

   i. The oxidation reaction adds a considerable amount of energy to the cutting zone.
   ii. The liquid generated in the cutting zone when oxygen is present is a mixture of iron oxide and iron. This mixture has a much lower viscosity than liquid iron and can easily be blown out of the cutting zone to produce a clean cut edge.

d. *Chemical degradation*. This type of cutting is generally restricted to CO_2 laser cutting of non-metals which do not melt. Such materials (e.g. wood products, thermoset polymers and fibre-reinforced epoxy) are cut by heating up the workpiece until the molecules of the material involved are broken up and ejected as dust, gas and vapour. For example, wood is broken down into carbon, water, CO_2, etc.

Note: This chemical degradation of materials during cutting will be referred to as 'decomposition' in the rest of this discussion.

Each of these processes will now be discussed in more detail while examining how lasers cut various materials.

3.2.2 Cutting Stainless Steels

Stainless steel is one of the mainstays of the laser cutting industry and is a good place to start a more detailed description of the laser cutting process, because it involves the simplest cutting mechanism of all – fusion cutting. In this case, the laser generates a liquid layer on a cutting front and a high-pressure nitrogen jet blows the liquid out of the bottom of the cutting zone as shown in Figure 3.10. The nitrogen also protects the melt and the edges of the cut from atmospheric oxygen, which ensures an oxide-free, shiny cut edge.

Fusion cutting gives a high-quality cut edge which is covered in microscopic ripples (see Figure 3.11). High-pressure nitrogen (10–20 bar pressure – increasing with material thickness) is used to propel the melt out of the cutting zone.

When thin-section material is being cut (up to 3 mm thick), the laser is focused on the top surface of the material and a narrow cut is produced at high speed. With thicker sections, the laser is progressively focused deeper and deeper into the material. This defocusing makes the cut width (known as the 'kerf width') wider and allows more gas to enter the kerf and contribute to the melt removal process. In addition to this, the defocused laser beam permits a better distribution of laser energy within the cutting zone – giving a better-quality cut. One disadvantage of using a defocused beam is that because

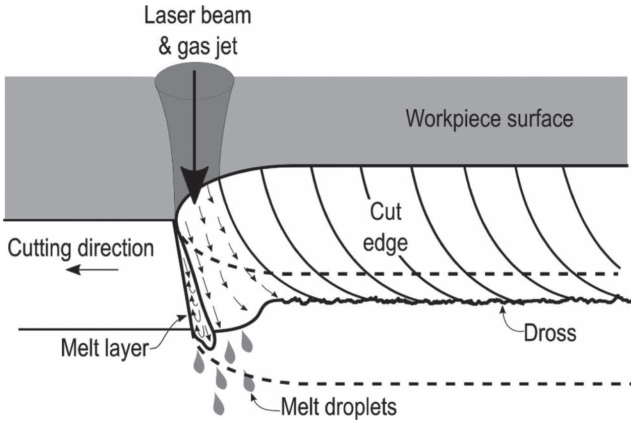

FIGURE 3.10 Fusion cutting stainless steel with the aid of a high-pressure nitrogen jet (dross may be present or not, depending on laser parameters and material thickness). Note: The laser beam is focused into the body of the material at thicknesses above 3 mm. (LIA Guide to High Power Laser Cutting. Pub; Laser Institute of America 2017.)

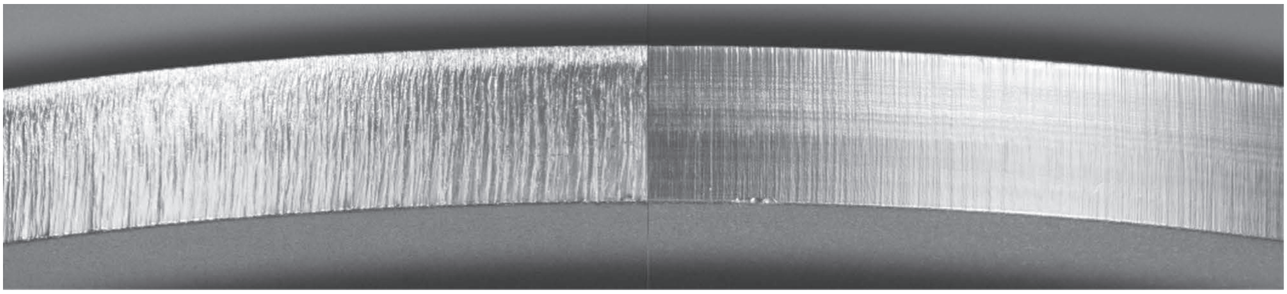

FIGURE 3.11 Typical cut edges produced when cutting 8-mm-thick stainless steel with nitrogen assist using optimum quality parameters. Left-hand sample was cut by fibre laser. Right-hand sample was cut by CO_2 laser. Photos courtesy of Trumpf GmbH. (LIA Guide to High Power Laser Cutting. Pub; Laser Institute of America 2017.)

the cut is wider, more materials need to be melted and removed from the cutting zone. This results in a reduction in cutting efficiency and cutting speeds. Also, the cut sides tend to become less perpendicular to the surface of the sheet if the laser is focused deep into the material.

Stainless steels are available in a range of surface finishes, some of which are decorative (brushed, polished, etc.). In order to protect these high-quality surfaces, the steel is often supplied with a plastic coating. Fortunately, it is possible to laser-cut the steel with the coating in place, and this protects cut components during subsequent fabrication operations such as bending (see Figure 3.12). CO_2 lasers cut plastics as readily as metals so any protective plastic covering (e.g. polyethylene) can be cut at the same time as the steel. However, the light produced by fibre lasers passes straight through most plastics, so specialist plastic coatings have been developed which absorb this type of beam so that they can be cut at the same time as the steel.

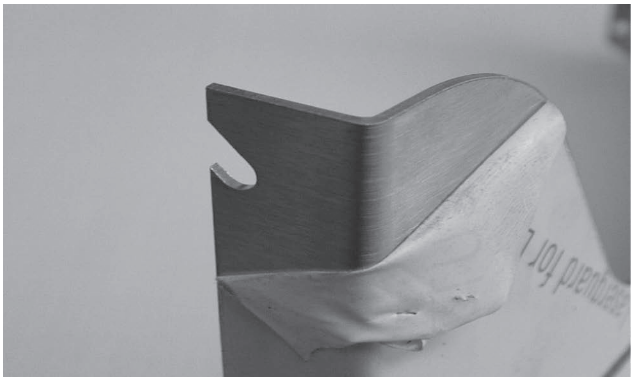

FIGURE 3.12 Cutting can be carried out on plastic-covered metals. The laser cuts the covering and metal together, and the material surface is thus protected during any fabrication operations like bending. This is particularly important for metals that have a high-quality surface finish. (LIA Guide to High Power Laser Cutting. Pub; Laser Institute of America 2017.)

3.2.3 Cutting Mild and Carbon Steels

3.2.3.1 Cutting Mild Steel with Oxygen

Back in 1967, an engineer from the UK Welding Institute[2] (TWI) was asked to try to cut steel using the institute's new laser. The initial trials weren't very encouraging but eventually the engineer – Peter Houldcroft – had a great idea. He was familiar with how flame cutting worked, and he thought he'd try to use oxygen with the laser. Perhaps the laser could do the heating instead of the flame and the oxygen would do the rest of the work?

Within hours, he had laid the cornerstone of the process which eventually changed laser cutting from a laboratory oddity to an industrial tool. In those days – and right through until the 1980s – laser powers for cutting machines were fairly low (1 kW was considered 'high power') and the laser cutting of steel would have been a slow, expensive and inefficient process without the help of oxygen. The oxidation reaction not only speeded up cutting but, as was seen with flame cutting, also made it much easier to blow the melt out of the cutting zone because the oxidized melt flows like water and it doesn't stick well to solid steel. (When cutting stainless steel with a nitrogen jet, the un-oxidized liquid metal has a relatively high viscosity and it sticks to solid stainless steel rather well, which is why the cutting process requires cutting gas pressures in excess of 10 bar.)

In summary, when iron is heated by a focused laser, it will burn in oxygen, producing heat and an easily removable melt. This is one of the major reasons behind the tremendous growth of the laser cutting market. The easy ejection of the oxidized melt from the mild steel cutting zone means that a clean edge is produced, as exhibited in Figure 3.13.

In Figure 3.13, it is clear to see that although the cut edge is of high quality, it is covered in parallel ridges or 'striations'. In laser-oxygen cutting, these striations are caused by the cyclic nature of the chemical and physical interactions involved in the cutting zone as it experiences the combination of laser heating and the oxidation/burning reaction.

During the laser cutting of steel, the laser acts as the heating source, which warms the steel up to its ignition temperature of ~1100°C. The steel (iron) starts to burn in the oxygen jet but, as it does so, it moves away from the laser and the fire is partially extinguished by the surrounding cold metal. The laser moves on to regenerate the localized 'fire', and by repeating this process, a cut line is produced. Figure 3.14, taken from the

---

[2] The TWI was called the 'British Welding Research Association (BWRA)' in those days.

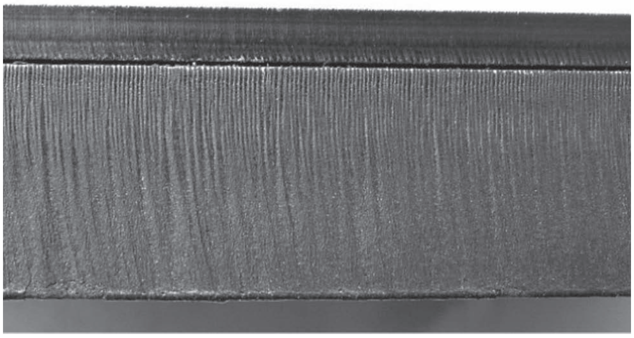

FIGURE 3.13 Typical mild steel cut edges produced by CO_2 laser-oxygen cutting. Note the overall high quality of the cut surface and the presence of parallel striations. Top sample thicknesses: 3 mm, lower sample thickness: 12 mm. (LIA Guide to High Power Laser Cutting. Pub; Laser Institute of America 2017.)

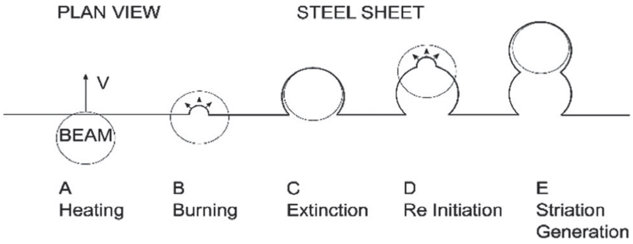

FIGURE 3.14 The burning cycle that takes place when laser-oxygen cutting mild steel. Depending on cutting speed, this cycle can take place over one hundred times a second. The resulting edge ripples or striations are almost microscopic, and cut edges are of high quality. The cut width is usually in the range of 0.1–1.0 mm. (LIA Guide to High Power Laser Cutting. Pub; Laser Institute of America 2017.)

work of Japanese scientists[3], demonstrates a very simplified description of the type of repeated burning reaction, which is responsible for the fact that all mild steel cut edges are covered in parallel ripples running from top to bottom of the cut edge. These ripples are produced by the beam even in its un-pulsed mode of operation. Striations that are similar in appearance but closer together, and therefore generally smoother, can be produced by using a pulsed laser beam at the correct frequency. Fortunately, the striations in either case are very small and shallow so the cut edge is of high quality.

The burning/extinction cycle takes place over one hundred times per second in a very small area producing a cut between 0.1 and 1.0 mm wide.

Although the oxidation reaction gives us high speeds and good edge quality, it also makes the process rather sensitive to some of the process parameters, particularly when cutting fine details. This sensitivity can give rise to unwanted burning of the product (see Figure 3.15), which can be avoided by using the correct laser pulse parameters.

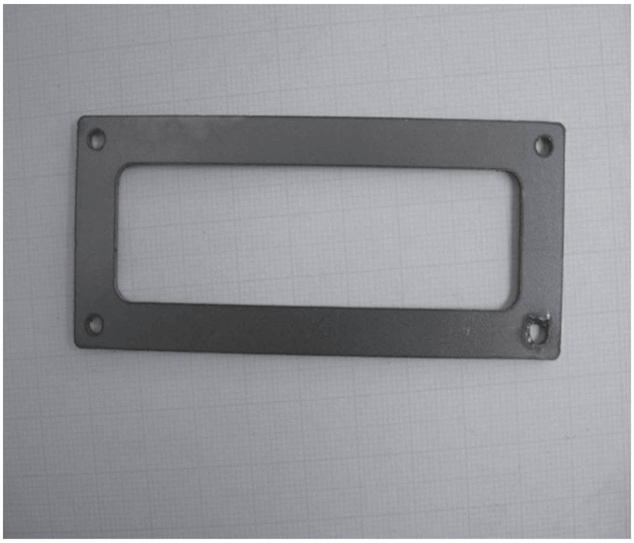

FIGURE 3.15 Laser cutting small details in mild steel with oxygen can lead to overheating and ‘burning’ of the component in question. In this case, the lower right-hand hole is burned. (LIA Guide to High Power Laser Cutting. Pub; Laser Institute of America 2017.)

3.2.3.2 Cutting Mild Steel with Nitrogen

In recent years, nitrogen is being used as the cutting gas more often than oxygen when cutting mild steel at thicknesses below about 4 mm. Nowadays, sufficient laser power exists for the laser to do all the cutting work at high speed without the assistance of the oxidation reaction. In fact, at thicknesses of 4 mm and below, nitrogen cutting can deliver both higher speeds and a better quality cut edge.

3.2.3.2.1 Improved Edge Quality When Cutting Mild Steel with Nitrogen Rather than Oxygen

Although the oxidation reaction produces a liquid which is easy to remove from the cutting zone, it leaves behind a thin skin of iron oxide on the cut edge – a dark grey, brittle material which is not firmly attached to the underlying steel. Figure 3.16 shows a cross section of a cut edge showing the hard, cracked oxide surface, which in this case is approximately 20 µm thick.

The brittle, loosely attached nature of the oxide becomes very apparent if laser-oxygen-cut mild steel items undergo a bending operation. Figure 3.17 shows a typical example of what happens. During the bending operation of this item, the hard brittle oxide layer has broken off in the area where the bending took place. The oxide can also break off if a component is flexed or rubbed in service. In some cases, this is not a problem, but this flaking off is a more serious concern if it happens after the component has been painted or plated. Many mild steel components are designed to flex slightly during service (supermarket shelf brackets for example). If such items are laser-oxygen-cut and then painted or plated, the oxide layer forms an unreliable link between the paint or plating and the steel along the cut edge. Under these conditions, the paint or plating can, at some point, break off with the oxide layer. A typical example of this is shown in Figure 3.18.

---

[3] Y. Arata, H. Maruo, I. Miyamoto and S. Takeuchi. Dynamic behaviour in laser-gas cutting of mild steel. *Transactions JWRI*, 8(2), pp. 15–26, 1979.

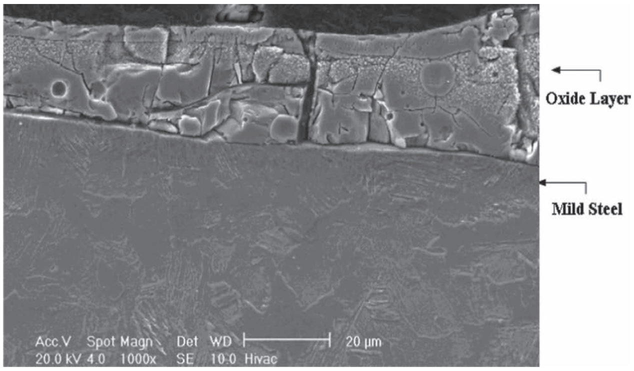

FIGURE 3.16 Laser-oxygen cutting of mild steel produces a brittle oxide layer on the cut edge, which can break off in service or if the component undergoes a bending operation. This has given rise to the use of nitrogen as a cutting gas for items that are eventually painted. (LIA Guide to High Power Laser Cutting. Pub; Laser Institute of America 2017.)

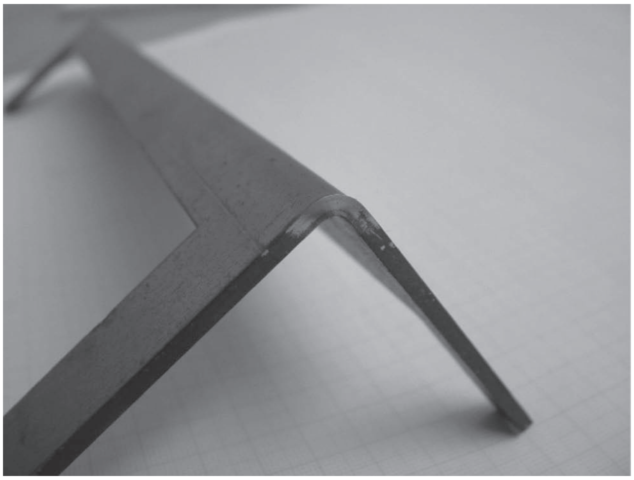

FIGURE 3.17 The brittle oxide coating on the cut edge will break off during any bending operation to reveal the bright metal underneath. (LIA Guide to High Power Laser Cutting. Pub; Laser Institute of America 2017.)

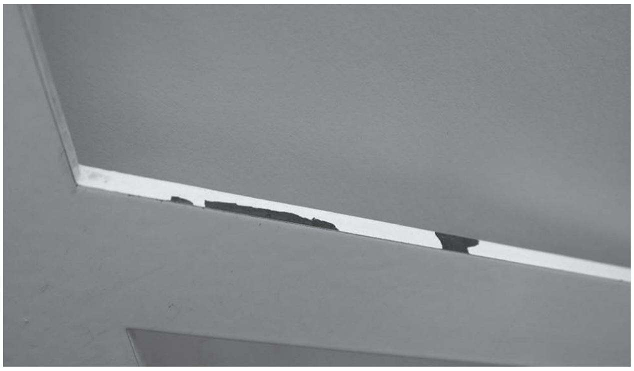

FIGURE 3.18 If the brittle oxide coating breaks off after painting or plating, it will expose the unprotected metal beneath which can then corrode. (LIA Guide to High Power Laser Cutting. Pub; Laser Institute of America 2017.)

3.2.4 Cutting Alloy Steels

A material is a steel if the major component of its alloy mixture is iron. There are hundreds of different steel alloys which have been developed for various properties from high temperature strength to ease of formability. Whatever their chemical composition, it will be possible to cut these steels (in thin to medium sections) using a CO_2 or fibre laser. If the iron content of the material is over 98%, it will usually cut like mild steel and oxygen can be used if required (see previous section). At lower iron contents, the material should be treated as a variant on stainless steel as far as cutting is concerned.

Steels that can be hardened by heat treatment will achieve their maximum hardness on the cut edge as a result of the heating and cooling cycle associated with laser cutting. In this condition, operations such as reaming, tapping or bending might be very difficult to carry out. However, this hard surface –HAZ – is generally rather thin, with a depth of between 5% and 25% of the material thickness.

If a high tolerance hole is required, a common practice is to laser-cut the hole undersize and then drill it out to size before reaming. It is often advantageous to laser-cut the original hole *considerably* undersize (e.g. if a high tolerance 12-mm-diameter hole is required in 10-mm-thick carbon steel, the laser might be used to cut a hole of only 8 mm in diameter). In this case, the drill will be cutting through the softer material beyond the HAZ. If such a hole was laser-cut only just undersize, the drill (and subsequent reamer or tap) would be continuously dealing with very hard material.

3.2.5 Cutting Non-ferrous Metals

3.2.5.1 Aluminium and Copper Alloys

Aluminium and copper alloys can be cut by the fusion cutting method (Figure 3.10) using nitrogen as the cutting gas. If the gas pressure is high enough, the cut edge will be dross-free and shiny in appearance for thin sections. Cutting speeds and maximum thicknesses can be increased if oxygen is used as the cut gas, but in this case, the cut edge will be rougher and dross may be noticeable on the lower edge of the cut.

Aluminium and copper alloys have high thermal conductivities and are very reflective, especially to CO_2 laser light. Both of these properties have the effect of reducing cutting speeds and the maximum thickness that can be cut, as the following notes will explain.

3.2.5.1.1 The Effect of High Reflectivity

If a material has a high reflectivity, then most of the laser light will bounce back off the surface without heating the workpiece. Although this phenomenon has some effect on the cutting process, it is even more important during the piercing event that happens at the start of each cut.

At the beginning of the piercing event, the material reflectivity is at its maximum because it is cold and solid. A small amount of laser energy is absorbed, and this begins to heat the material. As the material gets hotter, it becomes less reflective and more energy is absorbed until it melts. Eventually, a cutting zone is developed as shown in Figure 3.10. Inside the cutting zone, the material has two differences from the original cold solid, which result in relatively low reflectivity:

A. The surface of the cutting front is hot and molten (hot, molten metal absorbs laser light better than cold, solid metal).
B. The surface of the cutting front is at a glancing angle to the laser beam's direction of travel (see Figure 3.10). When light hits a surface at a particular shallow, glancing angle, reflectivity is reduced to a minimum, especially in the case of CO_2 laser radiation.

During cutting, most of the laser beam interacts with the liquid in the cut zone. There is, however, a small portion of the beam that hits the solid metal surface just in front of the cut zone. It is here where the material reflectivity is important and can result in interruptions to the cutting process[4] if cutting speeds are too high or laser powers too low. It is one of the advantages of fibre lasers that the absorptivity of metals at the perpendicular incidence is much higher than it is for CO_2 laser radiation.

It is important to realize that in some cases, piercing may not be possible. This is particularly true if a high-reflectivity material is above a limiting thickness for the laser in question. It is interesting to note that if piercing could be accomplished, then cutting would be possible because a lower-reflectivity cutting zone would be established.

Safety Note:

High-reflectivity materials can reflect the beam back onto machinery and operators. This is a particular hazard if the beam, in its unfocused state, reflects off an already-cut component or piece of scrap. Do not let components or scrap accumulate on the cutting table as they can result in unwanted beam reflections.

3.2.5.1.2 The Effect of High Thermal Conductivity

If a material has a high thermal conductivity, it means that energy can easily move away from the cutting zone to heat up the surrounding material. This, of course, reduces the amount of energy available for the cutting process. The problem becomes worse when cutting speeds are low.

It was noted in the previous section that the reflectivity of the cutting zone is far lower than that of the original solid surface. However, the thermal conductivity of the material does not appreciably change once a cutting zone has been established. For this reason, a high thermal conductivity affects the cutting process more than a high reflectivity. Unfortunately for laser cutting, reflectivity and thermal conductivity are usually related to each other, and both are high in certain metals (e.g. aluminium, copper, silver and gold).

Finally, it is important to note that, from a technical and commercial point of view, the low melting point of aluminium and its alloys greatly helps the laser cutting process (less energy is required to melt low melting point materials). In spite of their high reflectivity and thermal conductivity, aluminium alloys can be laser-cut at high speeds, especially when the thickness is below 3 mm.

3.2.5.2 Titanium Alloys

It has already been noted that an oxygen jet can be used to add energy to the cutting process in the case of carbon steels. Titanium reacts with oxygen even more energetically than steel. Unfortunately, in the case of titanium, there are major drawbacks to the use of oxygen:

A. The burning reaction is so vigorous that it is almost uncontrollable and results in widespread burning and poor edge quality. The process is, in fact, dangerous and should not be attempted.
B. The presence of oxygen in the cutting zone makes the eventual cut edge hard and brittle.

The first of these drawbacks can be overcome by using a less reactive gas like nitrogen. In this case, cutting speeds remain high, but the cut quality improves. The second drawback is, however, more serious and is not helped by using nitrogen as it also makes the cut edge hard and brittle.

Titanium alloys are strong, tough, light and corrosion resistant. They are used extensively by aerospace and other high-demand industries. If a cut edge has been contaminated with oxygen, nitrogen or a mixture of these gases (i.e. air), the mechanical properties of the titanium alloy will be badly affected. The hard, brittle edge will be susceptible to cracking, and this reduces the toughness of the material. The fatigue life of the material is also severely reduced (fatigue life is a measure of the material's ability to withstand millions of very small bending or stretching operations).

There are applications where the reduction in toughness and fatigue life of titanium does not matter, for example, in the production of replaceable skids underneath racing cars. In cases such as this, titanium alloys can be cut at high speed using nitrogen as the cutting gas. In most cases, however, the customer is using titanium because they require high levels of toughness and fatigue strength. It is therefore important that the cutting zone is kept free of reactive gases such as oxygen or nitrogen. For this reason, a chemically inert (unreactive) gas (argon) is used when laser profiling titanium alloys. Once the cut edge has solidified and cooled, it is safe to expose it once more to the air. Depending on the thickness of the material and the cutting speed, this 'safe zone' starts 1.5–6 mm or so behind the cut zone. The cutting gas may therefore require a bigger diameter nozzle than normal in order to keep the area around the cutting zone free of air until the melt has solidified and cooled down. Contamination of the cut titanium surface is self-diagnostic: If the cut edge is uncontaminated with air, it will be shiny silver in appearance. Contamination gives the edge the blue, yellow or grey colours often seen on titanium jewellery. When cutting titanium with argon, it is particularly important to use high gas pressures (10–20 bar) in order to remove any dross from the bottom edge of the cut. Any residual dross tends to remain hot and can be contaminated by the surrounding air once the inert gas jet has moved on to continue the cut.

---

[4] In the days before multi-kilowatt fibre lasers, the reflectivity of the material could be decreased by abrasive sanding of the surface or by covering it with a non-reflective coating. Commonly used coatings included the type of household cleaner which is applied wet and then dries before it is cleaned off (e.g. Brasso). The dry powder absorbed the laser very effectively, so cutting became more reliable.

Commercial note. Argon is expensive compared to oxygen and nitrogen.

Safety note. Although nitrogen and argon are not toxic, they must not be used in large quantities in confined, unventilated spaces because they dilute the air that is needed to breath. Ensure that the workplace is well ventilated and that the cutting machine extraction system is working properly. Argon is denser than air and will fill low-lying chambers.

3.2.5.3 Nickel Alloys

Nickel alloys include a wide range of materials such as Monels, Nimonics, Inconels, Hastalloys and Renes, all of which contain different mixtures of nickel, chromium and cobalt + molybdenum, among other alloying ingredients.

As far as laser cutting is concerned, these materials cut in a similar way to stainless steels (see Section 3.2.2). The cutting speeds table for stainless steels in Section 3.3.2 can be used as a starting point for identifying process parameters. However, cutting speeds will be up to 50% lower as will the maximum thickness possible.

As always, HAZ along the cut edge will be present no matter what process parameters are used. Nickel superalloys are frequently used in aerospace applications where the fatigue life of a component is important. In such cases, the customer should be advised that the HAZ may affect fatigue life. Generally, however, this is not a problem.

3.2.5.4 Other Alloys

There are hundreds of commercially available metal alloys ranging in properties from low strength, low melting point (solder) to high strength, high melting point (Nimonics). To produce a long list of alloys and laser parameters would be out of place in a chapter of this size. One practical way to find the cutting parameters for an unfamiliar alloy is by trial and error. The parameters given for stainless steels in Section 3.3.2 would be a good starting point if no information is available. On the other hand, any information that can be obtained from the customer or metal suppliers could be useful (e.g. if it's a titanium alloy, then the laser operator will know to avoid oxygen and nitrogen).

Trade names of alloys are not usually very informative. Since the basic alloying elements of the metal will influence cutting parameters, it should be determined if the material is steel (mostly iron) or a copper alloy, etc. A phone call to the applications laboratory of the laser supplier may also prove useful.

3.2.6 Cutting Non-metals with CO_2 Lasers[5]

3.2.6.1 General Notes

There are three main groups of non-metallic materials that are commonly cut by CO_2 lasers: polymers (plastics), wood-based products and ceramics. These will be discussed separately in the following sections.

Although Figure 3.10 is a good starting point for a description of laser cutting, it does not give a complete picture. It was mentioned earlier that lasers are capable of cutting by mechanisms other than simple melting. In some cases, the material (acrylic, polyacetal) is vaporized rather than melted in the cutting zone, and in other cases, the material (epoxy resins, wood products) cannot melt and must be locally decomposed. These different cutting mechanisms affect the quality of the eventual cut edge in ways that are described below.

3.2.6.2 Polymers

Polymers (or plastics as they are more commonly called) can be divided up into two main groups:

A. *Thermoplastics*. These are polymers that can be repeatedly melted down and cast into new shapes. They include polypropylene, polystyrene, polyethylene (polythene), polyamide (nylon) and others. CO_2 lasers are used commercially to cut these materials as solid sheets, foam sheets or fabrics.

B. *Thermosets*. These materials cannot be remelted once they have been made into their initial shape. They sometimes involve the mixing of two liquids which then set hard. This group includes epoxy adhesives, phenolic resins (kitchen worktop surfaces) and most natural rubber products. These materials can also be cut by a CO_2 laser.

3.2.6.2.1 Thermoplastics

Figure 3.10 shows a good description of how most thermoplastics are cut by a CO_2 laser. The laser produces a melt which is then blown out of the cutting zone by a gas jet (usually air). However, the viscosity of the melt combined with its low thermal conductivity means that a proportion of the material leaving the cutting zone is actually evaporated or chemically decomposed as it flows out of the cutting zone. This evaporation and chemical degradation take place towards the centre line of the cut where the temperatures are highest. At the edge of the cut zone, where the cut edge is being created, liquid flow is dominant, as in 'fusion cutting'. The resulting cut edge is of good quality but covered in microscopic ripples (see Figure 3.19).

In many cases not all the liquid is blown out of the cutting zone, and it is common to have a residue of resolidified melt on

---

[5] At the time of writing (2017), fibre lasers have a negligible industrial role in non-metal cutting although there are some promising developments in this area.

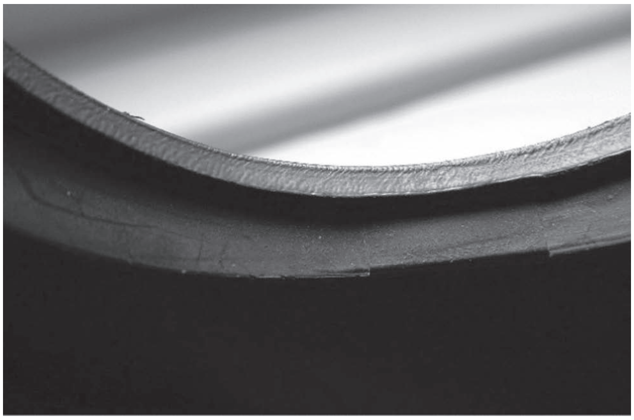

FIGURE 3.19 The microscopically rippled edge typical of laser-cut thermoplastics. This photo shows part of an oval cut-out made in an injection-moulded part. The material is 3mm thick along the cut line. (LIA Guide to High Power Laser Cutting. Pub; Laser Institute of America 2017.)

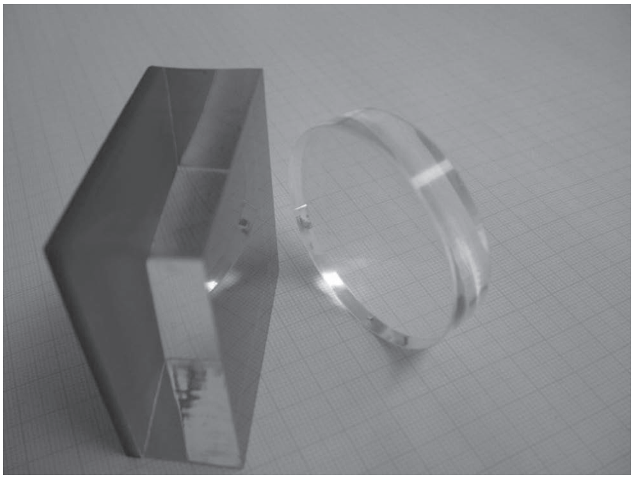

FIGURE 3.20 The 'polished' cut edge achievable when cutting acrylic (Plexiglas) with a CO_2 laser. This quality of edge is only possible if the cutting gas jet (see figure 2.1) is set to a very low pressure. Both the objects above have been balanced on their cut edges. The square on the left consists of a 3 mm sheet of blue acrylic which was glued to a 20 mm clear sheet before cutting. (LIA Guide to High Power Laser Cutting. Pub; Laser Institute of America 2017.)

the lower edge of the cut. This material is generally known as 'dross'. Thermoplastics cut at high speed and relatively thick sections can be profiled (see Section 3.3.4).

There are two important thermoplastics that do not cut by the melt shearing mechanism:

A. *Polyvinyl chloride* (*PVC*). This material degrades chemically when heated by the laser. The fumes given off contain high levels of hydrogen chloride, which is extremely corrosive and very toxic. For this reason, **PVC sheet material must never be cut by a laser**. If there is suspicion that the material might be PVC, always check with suppliers or customers. The material gives off a choking, smoky, green-brown fume, and the cut edge is dark brown-black, flat and dusty.

B. *Polymethyl methacrylate* (*acrylic, Plexiglas etc.*). This material boils[6] rather than melts during the cutting process, and under the correct conditions, a polished cut edge can be produced (see Figure 3.20).

C. The process involved in profiling acrylic is known as 'cutting' by vaporization. As the boiling vapour is blown away from the cutting zone, it leaves a thin liquid layer on the cut edges. If the gas jet blowing the vapour away flows gently over this liquid layer, the liquid will dry like paint to produce a glossy edged cut (see Figure 3.20). If, however, the gas jet is above a certain velocity, the solidifying liquid will become frosted. If a polished edge is required, it is necessary to use low gas supply pressures (0.1–0.3 bar) and larger than normal nozzle diameters of 2–3 mm.

3.2.6.2.2 Thermoset Plastics

These materials are not cut by the melt shearing mechanism as shown in Figure 3.10 for the simple reason that they cannot melt. In this case, the laser decomposes the material in the kerf, reducing the plastic to a smoke made up of carbon and all the other chemicals which were contained in the original material. This process is known as 'cutting' by chemical degradation. Because this process takes more energy than simple melting, cut speeds and maximum thicknesses for thermosets are lower than for thermoplastics (see Section 3.3.4).

The cut edge of such materials is generally flat, smooth and covered with a thin layer of carbon. These materials are sometimes used as electrical insulators (circuit board material, glass fibre boxes, etc.), and it must be borne in mind that the carbon dust on the cut edge is electrically conductive. For general engineering applications, however, it is often sufficient to wipe the carbon dust off the cut edge.

3.2.6.2.3 Fibre-reinforced Plastics

Thermoset plastics (and some thermoplastics) are often reinforced with strong fibres such as glass, carbon fibre or Kevlar. These materials have the effect of slowing the cutting speed. In the case of carbon fibre, the cut edge can have exposed fibres because the carbon conducts heat, which burns the surrounding polymer material. High-speed cutting techniques with scanner optics using repeated passes along the contour to be profiled are under development to solve this problem.

3.2.6.2.4 Wood-based Products

Wood and wood-based products are cut by a similar mechanism to thermoset plastics (see previous section). The laser decomposes the material in the kerf to produce a cut, and the carbon-based smoke is blown out of the cutting zone by a gas jet which is usually air. The top and bottom surfaces of the workpiece retain their original appearance but the cut edge is covered in a layer of carbon which darkens it (see Figures 3.21 and 3.22). Low-density woods like pine are cut faster than

---

[6] To be scientifically accurate, it should be mentioned that this is not a standard boiling process: The laser heats up the solid polymer until it becomes a liquid which then depolymerizes, giving off a vapour of the monomer (methyl methacrylate).

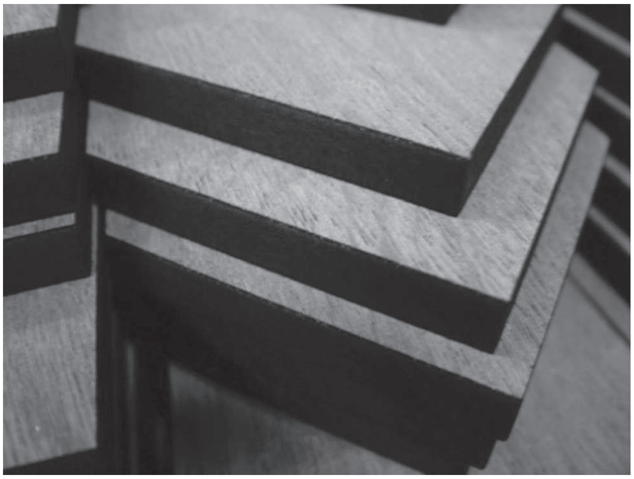

FIGURE 3.21 Laser-cut plywood. Note that the cut edge is darkened by the cutting process but the top (and bottom) faces of the wood remain clean and uncharred. (LIA Guide to High Power Laser Cutting. Pub; Laser Institute of America 2017.)

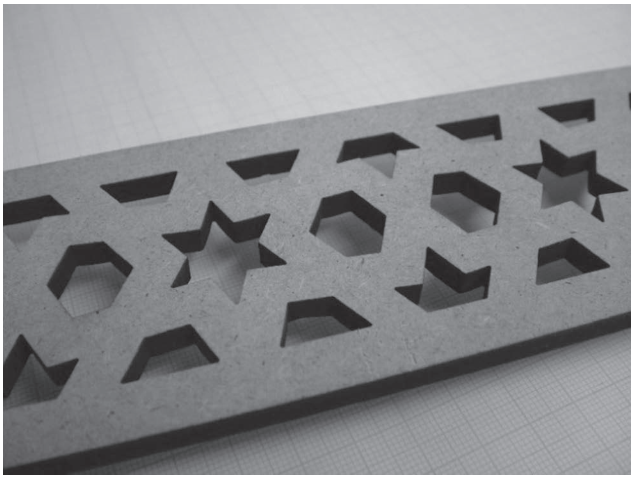

FIGURE 3.22 Decorative panel cut from medium-density fibreboard (MDF). (LIA Guide to High Power Laser Cutting. Pub; Laser Institute of America 2017.)

high-density material like teak (see Section 3.3.4). Also, the cut edge becomes darker as the density is increased.

Wood batches vary in density because of piece-to-piece variations in water content, etc. Within a single piece, the density may also change especially if knots (high density) are present. For this reason, the cut speeds presented in Section 3.3.4 should be taken only as rough guidelines. If a large batch of boarding has to be cut, productivity may be improved by weighing each board beforehand and adjusting the cutting speed accordingly. (The lighter boards are less dense and will cut faster.) Adequate drying of the wood will also help cutting speeds. Fibreboards (MDF) and plywood cut at a much more uniform rate that is, once again, determined by the density of the material.

3.2.6.2.5 Ceramics and Glass

3.2.6.2.5.1 Ceramics Ceramics are usually hard, high melting point materials produced by the reaction of metals with elements such as oxygen, nitrogen and carbon. Common industrial ceramics include the following:

A. Alumina (Al_2O_3),
B. Tungsten carbide (WC),
C. Titanium nitride (TiN),
D. Titanium carbide (TiC).

Tungsten and titanium carbides are used in the manufacture of drill bits, and although they could be laser-cut, it is rarely appropriate. The ceramic of most interest to laser cutting is alumina, which is used to produce some types of microelectronic substrate. This high melting point material cuts very slowly if full penetration cutting by the melt shearing method is employed (see Section 3.3.4). Fortunately, most applications merely require cutting sheets of the material into rectangles, and another, faster, technique called 'scribing' can be used. Scribing involves drilling lines of small blind holes in the material surface using a single pulse of energy for each hole (see Figures 3.23 and 3.24). The lines of holes are mechanically weak and can be used to accurately snap the workpiece into the rectangles required. Scribing speeds can be more than ten times as fast as full penetration cutting. Full penetration cutting is useful, however, for cutting curves or circles.

3.2.6.2.5.2 Glasses Most glasses have a high absorptivity to CO_2 laser light and can be cut by the melt shearing process (Figure 3.10). The problem with these materials is that of cracking along the cut edge as a result of the rapid thermal cycle associated with laser cutting. Most glasses are not generally laser-cut, but quartz and heat-resistant glasses can be cut effectively. Scribing (see previous section) can also be used to produce lines for subsequent snapping.

3.2.6.3 Other Non-metals

The range of non-metals which can be cut by a CO_2 laser is enormous. Cutting speeds exist in the literature for materials

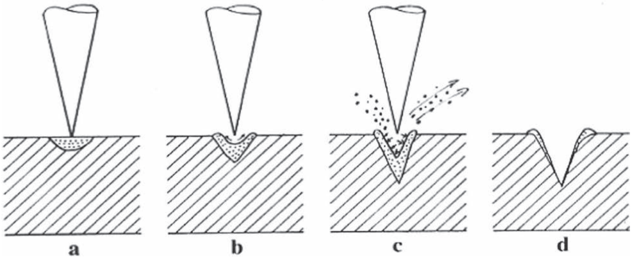

FIGURE 3.23 A cross section showing a blind hole being scribed in the surface of a ceramic during a single pulse. The centre of the melt boils suddenly, and the vapour pressure expels the melt. A row of such holes produces a weak line in the material, which can then be accurately snapped. (LIA Guide to High Power Laser Cutting. Pub; Laser Institute of America 2017.)

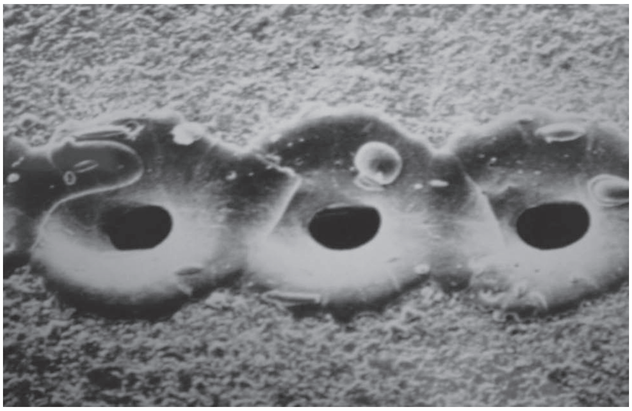

FIGURE 3.24 A magnified photo of a line of scribed holes on a ceramic substrate. (The entrance to each hole is of the order of tens of microns in diameter). (LIA Guide to High Power Laser Cutting. Pub; Laser Institute of America 2017.)

as diverse as boron–epoxy composites and leather. It is not in the scope of this chapter to list hundreds of cutting speeds, and in any case, such a list would be of little help without exact descriptions of the materials ('Leather from which animal? Of what density? or How much boron? What type of epoxy?' etc.).

Trial and error is really the only way to investigate a new material, but a literature search or contact with the laser supplier may help. Be cautious of the fumes given off from any unknown material, particularly if it might contain PVC (see earlier section).

One final note of interest: CO_2 laser cutting of foodstuffs is generally pointless. Good cut speeds and cut qualities may be achievable but the charred nature of the cut edge makes it taste unpleasant.

3.3 Cutting Speeds

3.3.1 Mild and Carbon Steels

See Tables 3.1 and 3.2.

3.3.2 Stainless Steels

See Table 3.3.

3.3.3 Aluminium Alloys

See Table 3.4.

3.3.4 Non-metals – CO_2 Lasers Only

Unlike fibre lasers, CO_2 laser light is readily absorbed by plastics and a wide range of non-metals. The following tables therefore only refer to CO_2 lasers (Tables 3.5–3.7).

TABLE 3.1

Mild/Carbon Steel 5 kW Laser Cutting Machine – Oxygen Assist Gas

Thickness (mm)	Cutting Speed – CO_2 Laser (m min^{-1})	Cutting Speed – Fibre Laser (m min^{-1})
1.0	8.0	9.0
2.0	5.5	5.6
3.0	5.0	4.2
4.0	4.0	3.5
5.0	3.5	3.2
6.0	3.0	2.9
8.0	2.8	2.5
10.0	2.3	2.2
12.0	1.8	1.7
15.0	1.5	1.3
20.0	1.0	0.9
25.0	0.8	0.7

Source: LIA Guide to High Power Laser Cutting. Pub; Laser Institute of America 2017.

Notes:

Cutting gas pressure is highest at thin sections (3–4 bar), falling to less than 1 bar at thicker sections.

Nozzle diameters rise from approximately 1 mm at thin sections up to approximately twice that value at the thickest sections.

Power settings rise from approximately 1 kW at the thinnest sections up to full power (5 kW) at medium to thick section.

TABLE 3.2

Mild/Carbon Steel 5 kW Laser Cutting Machine – Nitrogen Assist Gas

Thickness (mm)	Cutting Speed – CO_2 Laser (m min^{-1})	Cutting Speed – Fibre Laser (m min^{-1})
1.0	20.0[a]	40.0[a]
2.0	10.0[a]	22.0[a]
3.0	5.0	10.0
4.0	4.0	6.2
5.0	3.0	4.4
6.0	2.5	3.2
8.0	1.8	1.5
10.0	1.2	1.0

Source: LIA Guide to High Power Laser Cutting. Pub; Laser Institute of America 2017.

Notes:

Cutting gas pressure is lowest at thin section (10–13 bar), rising to over 15 bar at thicker sections.

Nozzle diameters rise from approximately 0.06 in (1.5 mm) at thin sections up to approximately twice that value at the thickest sections.

Power settings are generally set to maximum but may be lower at the thinnest sections.

[a] Cutting speeds on some commercially available '5 kW' machines can be less than half these values because the laser power is automatically reduced at thin sections.

TABLE 3.3

Stainless Steels 5 kW Laser Cutting Machines – Nitrogen Assist Gas

Thickness (mm)	Cutting Speed – CO_2 Laser (m min^{-1})	Cutting Speed – Fibre Laser (m min^{-1})
1.0	20.0[a]	48.0[a]
2.0	12.0[a]	24.0[a]
3.0	5.0	11.0
4.0	4.0	6.5
5.0	3.0	5.0
6.0	2.4	3.7
8.0	1.6	2.0
10.0	1.2	1.0
12.0	0.9	0.75
15.0	0.6	0.45
20.0	0.4	0.22

Source: LIA Guide to High Power Laser Cutting. Pub; Laser Institute of America 2017.

Notes:

Cutting gas pressure is lowest at thin section (10–13 bar), rising to over 18 bar at thicker sections.

Nozzle diameters rise from approximately 1.5 mm at thin sections up to approximately twice that value at the thickest sections.

Power settings are generally set to maximum but may be lower at the thinnest sections.

[a] Cutting speeds on many commercially available '5 kW' machines can be less than half these values because the laser power is automatically reduced at thin sections.

TABLE 3.4

Aluminium Alloys 5 kW Laser Cutting Machine – Nitrogen Assist Gas

Thickness (mm)	Cutting Speed – CO_2 Laser (m min^{-1})	Cutting Speed – Fibre Laser (in min^{-1} (m min^{-1}))
1.0	40.0[a]	65.0[a]
2.0	20.0[a]	27.0[a]
3.0	9.5	12.0
4.0	4.0	6.0
5.0	3.0	5.0
6.0	2.0	4.2
8.0	1.2	2.8
10.0	0.9	2.0
12.0	0.7	1.1
15.0		0.8
20.0		0.5

Source: LIA Guide to High Power Laser Cutting. Pub; Laser Institute of America 2017.

Notes:

Cutting gas pressure is lowest at thin sections (8–10 bar), rising to over 15 bar at thicker sections.

Nozzle diameters rise from approximately 1.5 mm at thin sections up to approximately twice that value at the thickest sections.

Power settings are generally set to maximum but may be lower at the thinnest sections.

Dross or burr on the bottom of the cut edge is common in aluminium cutting – particularly at sections over 5 mm.

[a] Cutting speeds on many commercially available '5 kW' machines can be less than half these values because the laser power is automatically reduced at thin sections.

TABLE 3.5

Typical Cutting Speeds for Thermoplastic Polymers Using a 500 W CO_2 Laser

Thickness (mm)	Acrylic (PMMA) (m min^{-1})	Polyethylene (m min^{-1})	Polypropylene (m min^{-1})
1	35.0	11.0	17.0
2	15.0	4.0	7.0
3	8.0	2.2	4.0
4	5.5	1.5	2.8
5	4.5	1.2	2.0
6	3.5	1.0	1.6
7	3.0	0.8	1.3
8	2.3	0.6	1.1
9	1.9	0.5	0.9
10	1.5	0.4	0.7
12	1.2	0.3	0.4

Thickness (mm)	Polystyrene (m min^{-1})	Nylon (m min^{-1})	ABS (m min^{-1})	Polycarbonate (m min^{-1})
1	19.0	20.0	21.0	21.0
2	7.4	8.0	8.2	8.2
3	4.2	4.8	5.0	5.0
4	3.0	3.5	3.6	3.6
5	2.3	2.6	2.7	2.7
6	1.8	2.0	2.1	2.1
7	1.6	1.6	1.7	1.7
8	1.2	1.2	1.3	1.3
9	1.0	1.0	1.1	1.1
10	0.9	0.8	0.9	0.9
12	0.7	0.5	0.6	0.6

Source: LIA Guide to High Power Laser Cutting. Pub; Laser Institute of America 2017.

Notes:

Air or nitrogen assist gas.

Cutting speeds can be changed dramatically by changes in molecular weight, degrees of crystallinity and porosity.

As a first approximation, cutting speeds and maximum material thickness can be assumed to vary in a linear manner with laser power for polymers (between 100 and 1500 W). Maximum material thickness for 500 W = 15 – 30 mm depending on material type.

The cutting gas is usually air at moderate pressures (1–4 bar). Nozzle diameters: 1–2 mm. If a glossy edge is required on acrylic, gas pressures may be dropped to below 0.25 bar and nozzle diameters increased.

TABLE 3.6

Cutting Speeds for Selected Thermoset Plastics, Rubbers and Fibre-Reinforced Materials with a CO_2 Laser

Material	Laser Power (W)	Thickness (mm)	Cutting Speed (m min^{-1})
Formica	400	1.6	7.8
	1200	1.6	14.0
	400	3.0	2.8
Phenolic resin	400	3.0	2.9
	400	6.0	1.1
Rubber	400	3.0	4.0
	400	6.0	1.6
	400	9.0	0.9
Rubber (carbon filled, black)	400	3.0	3.0
	400	6.0	1.2
	400	9.0	0.7
	400	12.0	0.4
Glass fibre-reinforced plastics (GFRP)	1200	1.6	15.0
	400	3.2	2.4

Source: LIA Guide to High Power Laser Cutting. Pub; Laser Institute of America 2017.

Notes:

Air or nitrogen assist gas.

a. Cutting speeds for materials such as glass fibre-reinforced plastics (GFRP) depend on the relative proportion of glass, resin and trapped air in the material.
b. Cutting gas is usually high-pressure air (3–10 bar), nozzle diameters: 1–2 mm.
c. Cutting speeds will increase dramatically if porous grades of rubber are cut – figures given here are for fully dense material.

TABLE 3.7

Cutting Speeds for Wood and Wood-Based Products Using a CO_2 Laser

Material	Thickness (mm)	Cutting Speed (m min^{-1})	Laser (Power) (W)
Poplar	10	5.0	500
Douglas fir	10	3.5	500
Yellow pine	10	3.2	500
Walnut	10	3.8	500
Cherry	10	4.3	500
Scotch pine	10	3.3	500
Beech	10	5.0	500
Teak	10	3.5	500
Mahogany	10	3.1	500
Oak	10	2.9	500
Ash	10	2.6	500
Ebony	10	1.2	500
Pine	6	8.0	1000
Pine	12	3.2	1000
Pine	20	1.6	1000
Plywood	6	7.0	1000
Plywood	12	3.0	1000
Plywood	20	1.5	1000
MDF[a]	6	9.0	1000
MDF[a]	12	4.0	1000
MDF[a]	20	2.0	1000
Hardboard	3	10.0	500
Hardboard	4	7.0	500
Corrugated card	3	25.0	500
Paper	0.1	500.0	500

Source: LIA Guide to High Power Laser Cutting. Pub; Laser Institute of America 2017.

Notes:

Air or nitrogen assist gas.

Cut with high-pressure (5–10 bar) air.

[a] Medium-density fibreboard.

Acknowledgements

The support of this work by the European Commission through the Seventh Framework Programme (FP7) within the HALO project (Grant Agreement Number 314410) is gratefully acknowledged. The authors would also like to thank the Laser Institute of America for permission to use these excerpts and images from their 'LIA Guide to High Power Laser Cutting' (ISBN 978 1 940168 111)

Taylor & Francis
Taylor & Francis Group
http://taylorandfrancis.com

4

Laser Marking

Terry J. McKee

CONTENTS

4.1 Introduction 35
4.2 Laser-marking Equipment 37
  4.2.1 CO_2 Lasers (10.6 µm IR Wavelength) 37
  4.2.2 Excimer Lasers 38
  4.2.3 YAG Lasers 39
4.3 Materials 40
  4.3.1 Plastics 40
  4.3.2 Glass and Ceramics 41
  4.3.3 Metals 42
  4.3.4 Semiconductors 42
4.4 Competitors for Laser Marking 42
4.5 Case Study: Decorative Marking of Plastics 43
References 45

4.1 Introduction

This chapter presents a discussion of various aspects of laser marking:

1. A physical description of the laser-marking process,
2. A description of the various lasers used to mark in typical industrial applications,
3. A discussion of materials that are laser-markable,
4. A comparison of laser marking with other marking techniques,
5. A case study describing techniques that can be used for decorative marking of plastics.

Using a laser to mark or code information on a product—*laser marking*—is one of the most common industrial applications of lasers [1,2]. Laser marking often takes the form of an alphanumeric code imprinted on the label or on the surface of the product to describe date of manufacture, best-before, serial number or part number, but the mark can also be a machine-readable barcode or 2D symbol (ID matrix) [3]. This type of marking is often specified as laser coding. Since the equipment used for surface processing of a macroscopic nature (e.g. scribing, melting, smoothing or roughening, and annealing) is basically the same equipment sold for laser marking, the term 'laser marking' has taken a more general meaning than simple coding. Hence, similar to coding, laser marking also includes functional marking (such as scribing gradation lines on a syringe) or decorative marking (such as engraving a logo or graphic image on an integrated circuit).

Laser coding is one 006Ff, which is the final process in the assembly of a product, taking place during the final filling cycle at a brewery, for example, or on a finished integrated-circuit chip before it is boxed for shipment. Compared to other online marking techniques such as inkjet, hot stamping or mechanical scribing, laser coding offers many advantages: indelibility, reliability, no consumables and high speed. Laser coding is usually the best marking solution with one proviso: *not all materials mark well with every laser.*

Laser marking is a surface process. Typically, the light absorbed during the optical pulse is transformed into heat, thereby creating a high 'instantaneous' temperature rise in the material on a time scale very short compared to the thermal conduction time constant of the material being marked. Pulse lengths of industrial lasers typically used for marking are in the range of 0.02–10 µs. The resultant mark can take a number of forms with an actual groove being cut or a colour change through carbonization being the two most common marks. Other forms include physical modification of the surface finish such as smoothing within the marked region; highly controlled and reproducible modification of the surface by thermal melting with no other damage; bleaching or colour change of a plastic whereby a white or other colour hidden by a darker pigment shows through foaming after melting of a plastic surface leading to a light coloured mark; and photochemical decomposition of a pigment in a plastic leading to another colour or a combination of these effects. A general description of a laser-marked surface would include a crater of shallow depth, surface modification within the crater and around the heat-affected zone, a raised ridge or kerf around

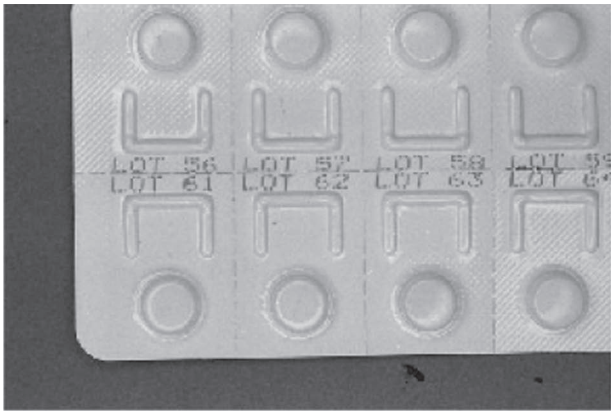

FIGURE 4.1 Lot/batch code laser-marked on a pill blister pack using a dot-matrix CO_2 laser marker.

the crater and debris scattered nearby. A kerf may be present only for cases where melting and material flow have occurred. Depending on the laser and beam delivery process used, the depth of the crater can be negligible or as much as 0.010 in. (Figure 4.1 and 4.2).

Absorption of light in dielectrics follows an exponential form such that the absorbed energy E (per unit volume) at depth z is given by

$$E(z) = I_0 a e^{-az} \Delta t$$

where a is the absorption coefficient at that wavelength for the material being marked, I_0 is the laser peak power density (per unit area) incident on the material and Δt is the time duration of the laser pulse. A simple description of the heating process and temperature rise ΔT (per unit mass) for a volume of material at depth z is

$$\Delta T = \frac{(\text{heat added}) - (\text{heat conducted away})}{(\text{specific heat of material})}$$

where the heat added is determined by the light absorbed in the material at depth z, the heat lost is determined by the thermal conductivity of the material and the temperature rise is determined by the specific heat capacity of the material. Since the laser pulse is finite in duration, this description must be integrated over time.

This simple thermal description helps to explain laser marking qualitatively. However, it is evident that melting and material removal would add other terms to the energy balance. Absorption may be strongly temperature dependent as, for example, in silicon marking at the wavelength of 1.06 µm, or strongly time dependent as, for example, in marking metals reflective at the laser wavelength (where plasma formation and initiation of surface damage may occur before a significant portion of the energy can be absorbed). Absorption of radiation from lasers such as pulsed CO_2 with very high peak power can be highly non-linear. In fact, although a qualitative understanding of how a laser mark takes place is fairly intuitive, quantitative predictions of the marking interaction of light at various wavelengths with different materials can be quite complex [4–7].

Reasonably strong absorption of the laser light is the key not only to efficient, cost-effective marking but also aesthetically attractive marking. Light that penetrates too deeply will either not raise the surface temperature enough to have any effect or may cause incomplete or non-continuous marking (e.g. bubbling in plastics). For example, radiation from the Nd:YAG laser at 1.06 µm passes through a transparent PET (polyethylene terephthalate) water bottle but radiation from the CO_2 laser at 10.6 µm will mark clear PET bottles very nicely. For this reason, it is important to choose the laser wavelength which will best interact with the material to be marked. In many cases, it will be necessary to try a variety of lasers available to the user to determine which type of laser provides the desired mark. Although it should be possible to predict the absorption as a function of wavelength for a given material, in practice the material is not pure but contains additives such as colourants or fillers which radically alter the absorption process, and in fact, the use of such additives is common to improve the marking process. Some general observations are possible:

1. Ultraviolet light from an excimer laser or from the harmonics of a solid-state laser is strongly absorbed by most materials.
2. Radiation from a Nd:YAG laser at 1.06 µm will typically have low absorption in any visually transparent material except in the case where it is focused very tightly.
3. A CO_2 gas laser at the wavelength of 10.6 µm will not mark any metal since it is usually strongly reflected, so Nd:YAG lasers are typically used to mark metals.
4. Radiation from a CO_2 laser will mark thin coatings of ink and other materials on paper or metal even though the light is not strongly absorbed in the coating.

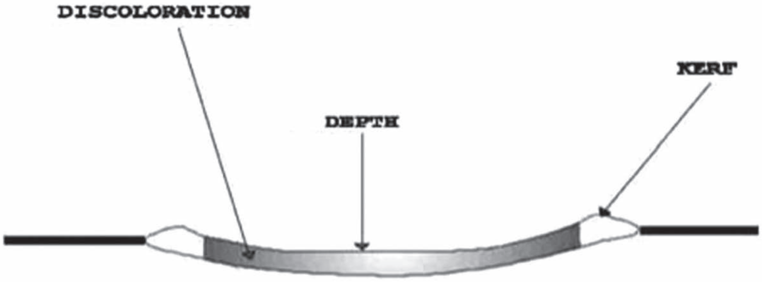

FIGURE 4.2 Schematic drawing of typical marked surface.

As a typical sample, consider a white polymer insulating coating on wire, which might give the following results: the CO_2 gas laser marks the coating by cutting a groove into the material with modest colour change grey against white; the Nd:YAG laser penetrates too deeply into the polymer causing an unsatisfactory irregular bubbling interaction; the ultraviolet excimer laser makes a sharp but very shallow black mark against white, which is susceptible to scratching unless the polymer is hard, such as a fluoropolymer or high-density polyethylene. Thus, although two of three lasers give a readable mark, the user will have to make the choice of laser based on a number of criteria, including readability, indelibility, speed and cost.

Although strong absorption of the laser radiation is a definite prerequisite to a good mark, the effect of the radiation on the material once it is absorbed is also very important. Radiation from an ultraviolet excimer laser, even though it is strongly absorbed in a dielectric, may not have enough energy density to melt the material so no mark will occur. Or, even if the material melts, there may be no colour change so that the mark is not visible. Radiation from an Nd:YAG laser, although strongly absorbed in a coloured elastomer, may always create an unsatisfactory irregular bubbling interaction because that is the way that material melts. In many cases, the effect of the absorption of laser light on the material can be improved by the use of additives, which modify the interaction. For example, a thermochromic pigment whose colour is changed at a temperature below the melting temperature of the elastomer would allow marking without the necessity of melting the plastic. The process of optimizing a laser mark on a given material includes not only increasing the absorption but also improving the resultant material response to the deposition of light energy.

4.2 Laser-marking Equipment

As of the start 1999, there was an installed base of approximately 22 000 laser-marking units worldwide. The approximate breakdown among the major laser types used is:

CO_2 lasers	33%
Nd:YAG lasers	63%
excimer lasers	4%

With about 40% of the installed laser-marking base, the electronics market has been the largest historically. Other important markets are consumer packaging and the automotive, medical and aerospace industries as shown in Table 4.1.

4.2.1 CO_2 Lasers (10.6 μm IR Wavelength)

CO_2 lasers mark most materials except metals. Imaged-mask pulsed CO_2 markers are very effective in marking electronic components encapsulated in thermoset epoxy such as integrated circuits, transistors and capacitors when a relatively small mark is needed on-the-fly at high speed [8,9]. A typical speed to mark low-cost electronic parts is 500 parts min^{-1}. Imaged-mask CO_2 laser markers are relatively unsophisticated, low-cost and simple systems with very high speed but a limited programmability.

TABLE 4.1

Major Marking Applications by Laser Type

a.	Laser Type	Market/application
b.	CO_2	Electronics
		ICs
		Transistors, capacitors
		TV tubes
		Packaging
		Beverage containers, paper labels cosmetics, soaps, pharmaceuticals
	Nd:YAG	Electronics
		ICs
		Keyboards, moulded parts, switches control panels, consumer items
		Automotive
		Metal parts, dashboard displays
		Medical
		Moulded parts, syringes, containers
		Aerospace
		Displays, metal parts, wire
	Excimer	Electronics
		Capacitors
		Aircraft wire

Because the imaged-mask technique is optical imaging, very sharp marks can be made, depending primarily on the surface smoothness. Characters as small as 0.012 in. in height are possible for very small parts such as ceramic chip capacitors. But the 'webs' in each character caused by the supportive elements in the metal mask result in a less attractive mark.

For marking larger electronics parts, the maximum size of the marked area is typically restricted to 1/4 in.×3/4 in. and possibly even smaller if the material does not mark readily. Additives and coatings can dramatically reduce the energy density required to achieve an acceptable mark so that larger marks can then be achieved in those cases.

CO_2 lasers are widely used to mark packaged goods [10,11] using both the imaged-mask and dot-matrix formats. The most common application is to code a date or batch code on an inked paper label whereby the laser removes a dark ink showing the white paper underneath; thus, the characters are seen as white against dark. Both formats will mark samples on the fly, i.e. as they move along an assembly line (Figures 4.3–4.5).

Other examples of consumer packages marked with the CO_2 laser include plastic bottles marked directly with the laser; anodized or inked metal containers such as toothpaste tubes; glass parts such as TV tubes where the CO_2 laser marks the glass directly; plastic film labels; and thermoplastic elastomer items such as wiper blades (Figures 4.6 and 4.7).

The imaged-mask CO_2 laser-marking system is designed in a similar manner to a slide projector: laser light passing through a metal mask is imaged using a lens to produce an image of reduced size at the sample. For materials requiring high energy density to make a good mark, the size of the image

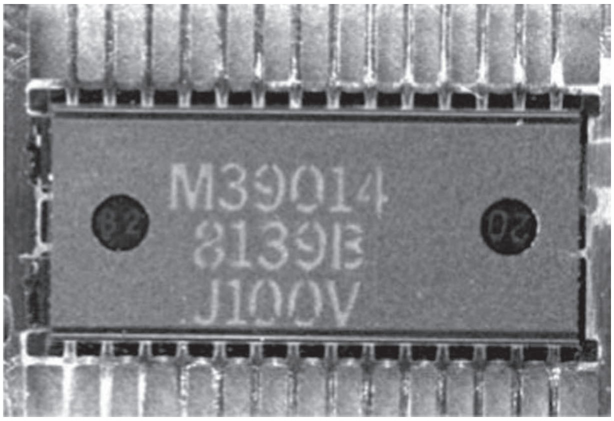

FIGURE 4.3 Pulsed CO_2 laser-marked integrated circuit.

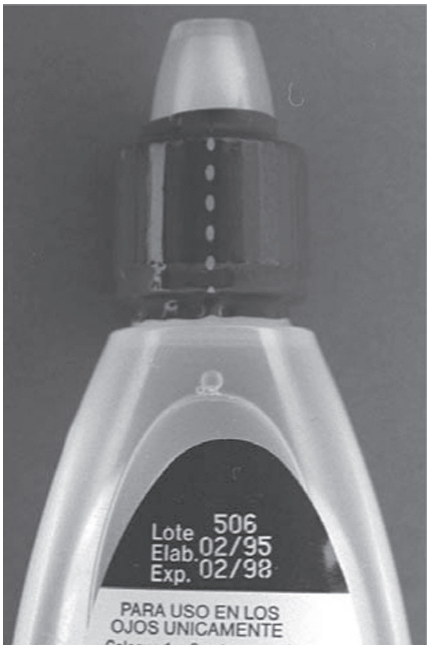

FIGURE 4.4 Pulsed CO_2 laser-marked label.

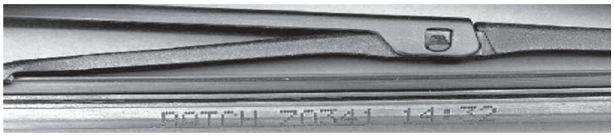

FIGURE 4.5 CO_2 laser dot-matrix mark on a black elastomer wiper blade.

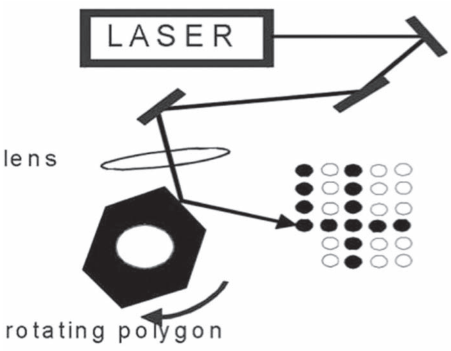

FIGURE 4.7 Schematic layout of dot-matrix CO_2 marker.

marked at the sample is ‘demagnified’ or reduced substantially so a smaller mark is made. A demagnification of between two to three is typical for easy-to-mark materials such as inked paper, sensitized plastics and anodized aluminium; a demagnification as high as 10 may be required to mark glass. The imaged-mask CO_2 laser will make marks at speeds typically up to 30 marks s^{-1}.

The dot-matrix CO_2 laser-marking system is designed in a similar manner to an inkjet printer: pulses of laser light sufficient to burn a single dot are scanning linearly as the sample passes by. The resultant dot-matrix mark relies on the motion of the part along an assembly line, and line speeds exceeding 1 m s^{-1} can be accommodated depending on character size. Since no pre-fabricated mask is required, the message printed by the dot-matrix marking system is programmable in real time. The system is small, portable and has a strong resemblance to a medical CO_2 system, including the articulated arm delivery component.

4.2.2 Excimer Lasers

Excimer lasers are used for marking in a few niche areas where the ultraviolet wavelength is necessary to make a mark. Ultraviolet light is strongly absorbed by many materials so that it typically makes a very shallow mark. The two main markets are as follows:

1. Marking part numbers on very small ceramic chip capacitors,
2. Marking the jacket of fluoropolymer-coated aircraft wire and medical catheters.

In the latter case, the ultraviolet wavelength marks the polymer by virtue of the use of small amounts of titanium dioxide additive in the plastic [12] (Figure 4.8).

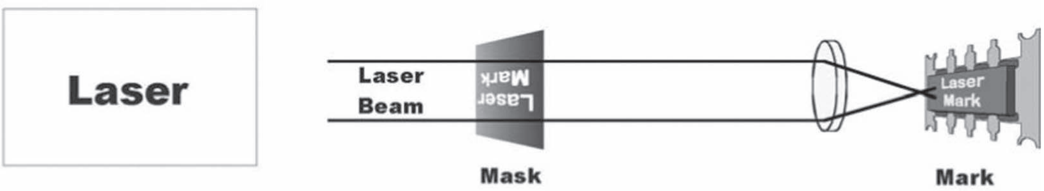

FIGURE 4.6 Schematic layout of pulsed CO_2 laser-marking system with imaged-mask marking.

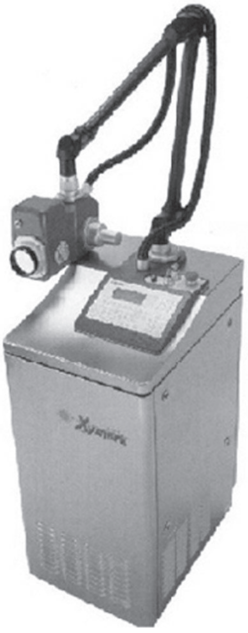

FIGURE 4.8 GSI Lumonics Xymark® CO_2 dot-matrix marker.

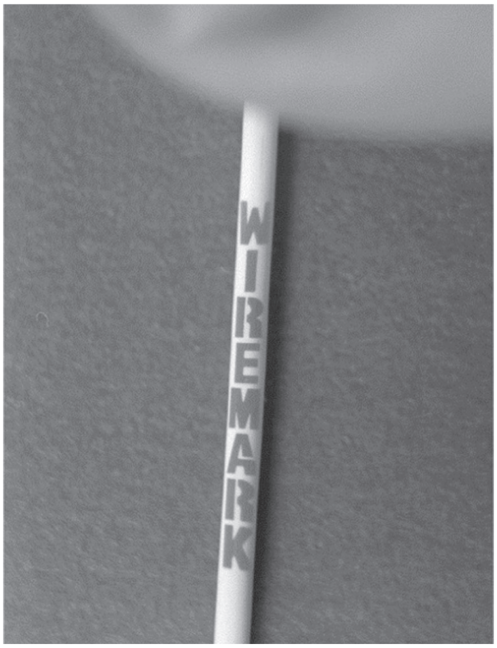

FIGURE 4.9 Tefzel®-coated aircraft wire marked by an excimer laser.

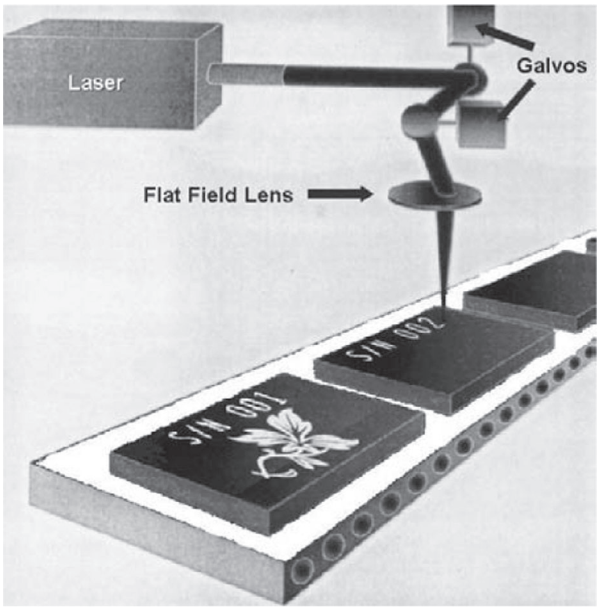

FIGURE 4.10 Schematic diagram of a YAG-based laser marker.

The imaged-mask marking technique described earlier for pulsed CO_2 laser marking is also used for excimer marking although, due to the markedly different wavelength, optical components such as lenses and mirrors are made from different materials. Because the excimer laser is a high-average-power, high-repetition-rate source, it is capable of marking at very high speeds. However, since its pulse energy is low, the mark made by an excimer laser is small.

Excimer lasers are widely used for precise material processing applications, many of which are similar to marking. For example, KrF excimer lasers are used to inscribe gratings inside doped optical fibres for use in optical telecommunications equipment [13]. In this case, the ultraviolet light is imaged inside the fibre using a diffractive mask.

4.2.3 YAG Lasers

The most common industrial solid-state laser—the Nd:YAG laser operating at about 1.06 μm wavelength—is widely used for marking electronics [8,9,14–16], medical [17] and metal [18] components. This is a very versatile laser choice since the wavelength can be frequency-doubled, frequency-tripled or frequency-quadrupled to provide other wavelengths in the green and in the ultraviolet. This is an important advantage for marking materials such as plastics where the absorption may change dramatically at different wavelengths (Figures 4.9 and 4.10).

Typically, the YAG-based marker uses a Q-switched Nd:YAG source pumped by lamps or, later, by high-power laser diodes. The laser produces a train of short light pulses at about 20 000 pulses s^{-1}, and each pulse, when focused onto the sample to be marked, makes a small dot. By directing the spot advantageously over the sample using galvo-mounted mirrors controlled by a computer, the YAG-based marker can efficiently make a very high-quality mark in which lines, circles and patterns are actually a series of contiguous dots too small to separate visually. This technique is variously described as ‘directed beam’ marking, ‘scanned spot’ marking or simply ‘laser writing’. As well, barcodes or ID matrix codes are commonly marked (Figure 4.11).

The largest market for YAG-based laser markers is in the electronics industry where they are commonly used to mark part number and serial code information on integrated circuits. Although ink marking may provide a higher-speed process and a bolder mark, the main advantages of laser marking in this market are indelibility and reliability. As companies move

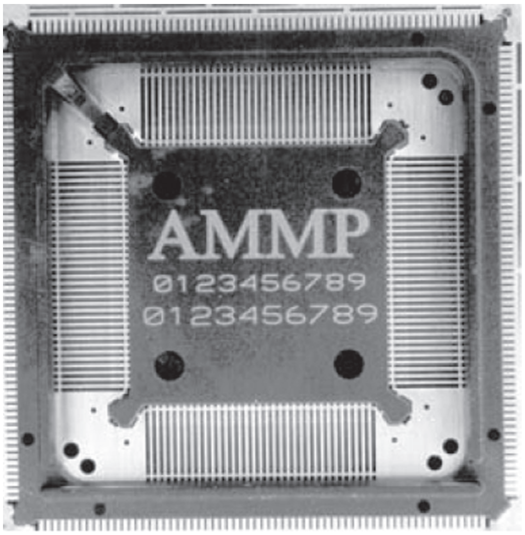

FIGURE 4.11 YAG-marked integrated circuits.

toward achieving 6σ reproducibility in their manufacturing process, lasers are typically the marking choice. In addition to alphanumerics, barcodes or ID matrix codes are also commonly marked.

At the front end of the integrated-circuit manufacturing process, YAG lasers are commonly used to mark silicon wafers prior to the wafer fabrication process. These lasers provide debris-free and very reproducible surface marks which are used to track each wafer through wafer fabrication and up to the dicing process. As well, these markers are beginning to be used for 'backside marking' to mark the diced silicon chip mounted on a surface mount structure.

YAG-based markers are also used to mark plastics and metals in consumer electronics, automotive, aerospace and medical markets. Since the marking process is basically identical to the scribing process, these systems can also be used for material processing applications such as scribing, cutting, drilling and etching where the beam is scanned across the surface to cut a groove in a ceramic or glass material, is trepanned to cut a hole through a thin metallic sheet, etc. Although these applications are not strictly marking, the process and the equipment used are similar.

4.3 Materials

Most materials can be marked with a laser of one kind or another. The key to cosmetically attractive laser marking is to have the laser light absorbed within less than 0.1 mm of the surface of the material to be marked. Usually, a laser with the optimal wavelength can be found to achieve an attractive mark. Sometimes, however, it is necessary to change the composition of the material by using additives, coatings, or other schemes to promote adequate absorption at the surface (Figure 4.12).

4.3.1 Plastics

Both thermoplastic polymers and thermoset plastics are commonly marked using lasers [2,19,20]. The marking applications include not only coding and serialization but also increasingly sophisticated custom decorating using logos and images. Depending on the polymer and additives used, visually stunning laser marks can be obtained in some thermoplastics.

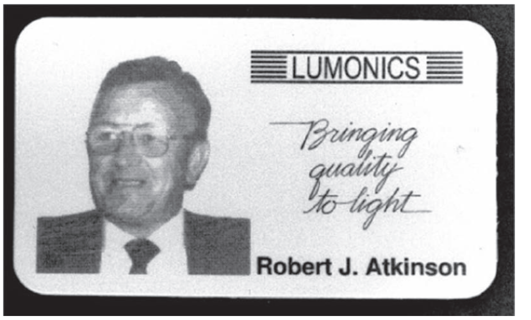

FIGURE 4.12 Facial image marked on white polyethylene card containing AFFLAIR®.

Some plastics mark well even in their raw state. Because it is strongly absorbing at the 10.6 μm wavelength, polyvinyl chloride (PVC) always marks well with CO_2 lasers to produce a characteristic yellow/orange mark. Vinyl films and labels are often marked using CO_2 lasers. Another polymer that marks well using the CO_2 laser is clear PET commonly used for beverage bottles.

The markability of most other plastics primarily depends on what laser is used and what additives are present. It is not possible to provide a definitive table of markability since the composition of any given polymer used varies widely depending on the additives present. Additives such as fillers, colourants, release agents, UV retardants and flame retardants can have the dominant effect on absorption and thus markability in plastic marking applications [1,2,21–25]. Thus, to determine laser markability and especially the cosmetic appearance of the laser mark on such polymers as ABS, polycarbonates, polyamides (e.g. nylon), PBT (polybutylene terephthalate) and the polyolefins (polyethylene, polypropylene, polystyrene), it is often a case of try-it-and-see. And it is always wise to do marking tests with a variety of wavelengths as well.

In some cases, inadequate absorption of the laser light will lead to bubbling and edge roughness of the mark, making it unattractive. Some inert additives that can be used to improve the absorption of polymers include carbon black, mica, kaolin and titanium dioxide. AFFLAIR® pigment (called IRIODIN® in Europe) [1,25] is a mica-based additive, which has been widely used to improve the laser markability of polyolefins used in packaging and bottling applications. Carbon black [26] is a very strong absorber of light at any wavelength and can aid in laser marking if used in low concentrations; however, carbon black can also very effectively dampen out any whitening effect of laser marking in concentrations above 1%. The accompanying Figure 4.13 shows the reduction of mark contrast as the concentration of carbon black additive increases when marking VALOX® black PBT using the YAG laser. In addition to inert additives, colourants have a marked effect on laser markability, especially for the Nd:YAG laser since its wavelength (1.06 μm) is very close to the visible spectrum. Some chemical companies specializing in plastics now

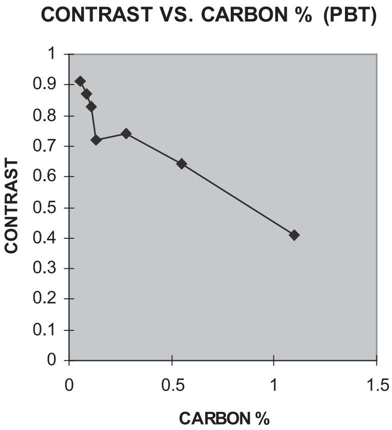

FIGURE 4.13 Mark contrast *versus* carbon black concentration for black PBT.

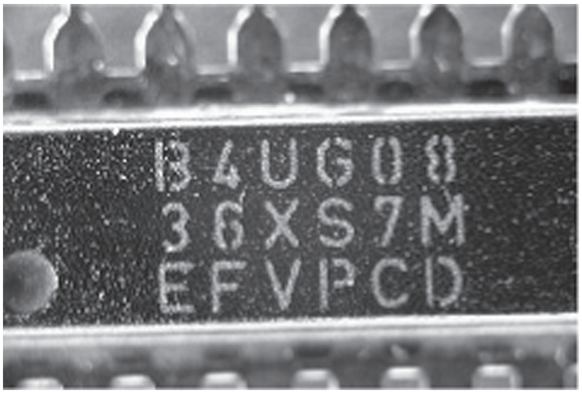

FIGURE 4.14 CO_2 laser marks on coated integrated circuits.

provide 'laser-enhanced' grades of their trade-named polymers. For example, Hoechst offers laser-markable grades of black Celcon® acetal copolymer, which allows Nd:YAG marking with contrasts as high as 95%. M A Hanna offers laser-markable plastics where a coloured mark can be made against a dark background (Figure 4.14).

Ultraviolet lasers such as excimers or frequency-tripled YAG lasers can mark most white plastics by virtue of the titanium dioxide present as the white pigment [12]. Fluoropolymers, such as Teflon and Tefzel® in particular, which are used as lightweight insulation for aircraft wire, are commonly marked using UV lasers. Because the UV light is absorbed very close to the surface, the penetration of the laser mark into the polymer can be as small as a few μm. Although a shallow mark with a minimal mechanical effect can be a desirable feature for thin samples like lightweight wire insulation, some soft plastics like LDPE (low-density polyethylene) are susceptible to abrasion so a shallow mark is removed by a scratch.

Thermoset epoxy materials and phenolics are commonly used in the electronics industry as encapsulants and in moulded parts such as switches [9,27]. Carbon black is the most prevalent additive for thermosets, and it is a strong absorber of laser radiation at all wavelengths. Both CO_2 and YAG lasers have been used to mark black thermoset epoxy materials for years. However, since the laser-induced colour change is largely a function of controlled burning of the plastic resins, the marks tend to be off-white in colour, rather than the brilliant white, which can often be achieved in thermoplastics. As for thermoplastics, the major suppliers of thermosets such as Nitto and Sumitomo Bakelite offer 'laser-enhanced' grades of their resins. Less commonly used are laser-markable coatings such as those available from Nippon Kayaku (Figure 4.15).

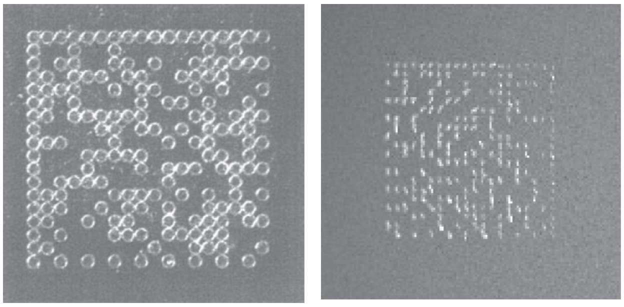

(*a*) (*b*)

FIGURE 4.15 Two ID matrix marks on glass: (a) ID matrix 2D code marked on glass using an ArF excimer laser, dot diameter 0.1 mm, spacing 0.125 mm; and (b) ID matrix 2D code marked inside glass using a green frequency-doubled YAG laser, spacing 0.085 mm.

4.3.2 Glass and Ceramics

CO_2 lasers are frequently used to mark glass; marking television tubes and glass bottles is a common application for the dot-matrix CO_2 marker. The marking process actually creates microcracking at the surface of the glass due to the melt/freeze cycle induced by the laser, and the visibility of the marks arises not from any colour change but from light scattered from the microcracks. Time-resolved measurements show that the microcracks form about 120 ms after the laser radiation—hence the theory regarding freezing. Extensive measurements of laser-marked glass have shown [28] that the melted region is typically within 18 μm of the surface of the glass. Some heat-resistant glasses like borosilicates (e.g. Pyrex®) do not mark.

The microetching caused by CO_2 lasers is undesirable for precise applications like marking flat-panel display glass. Ultraviolet lasers such as the ArF excimer laser and short-pulse femtosecond lasers have been shown to provide a much more controlled etching or marking process in glass. Very fine features can be precisely etched with no evident effect on the glass outside the marked region.

Another interesting development in glass marking is the phenomenon of inner glass marking where the laser is focused to a spot inside the glass [29,30]. If a very short focal length lens is used, the light will not have enough energy density to mark the surface of the glass but will reach a higher energy density inside the glass, thereby leading to a mark within the material. Ideally, a wavelength that is transmitted by the glass is used. The inner glass mark can be the result of microcracking within the glass or, in more controlled situations, can appear as regions of melting but without microcracks emanating from the region. Marks can be so subtle that subsequent thermal annealing will remove the mark. In addition to the novelty of a three-dimensional mark visible within a glass material, the advantage of inner glass marking is the absence of any debris on the surface.

4.3.3 Metals

Metals are commonly marked using Nd:YAG lasers. Although polished metals are reasonable reflectors for wavelengths in the region of 0.4–1.2 μm, enough radiation is absorbed from a focused laser beam to initiate some surface damage, which results in an efficient coupling of the energy from the remainder of the pulse to mark the metal. For longer wavelengths, the reflectivity of polished metals is even higher and it becomes very difficult to make a mark with a longer-wavelength laser. Deep grooves can be cut in metals using the YAG laser by overlapping successive pulses to melt the metal to a greater depth. Melted material can sometimes splatter over the surface nearby, thereby detracting from the contrast and appearance of the mark. Since heat deposition is usually high, a heat-darkened zone and a kerf may also be present around the groove. Fine dust particles of some metals can be injurious to health (Figure 4.16).

Since polished metal is an excellent reflector of CO_2 laser radiation, this laser cannot mark metals. However, both CO_2 and YAG lasers can mark painted and anodized metal exceptionally well. Aluminium oxide is a very strong absorber at 10.6 μm so it is easy to remove a dark coloured anodized layer from aluminium to create an attractive mark of polished metal against black. Sequential laser marking/colour anodizing of aluminium can result in an attractive multi-coloured marking [31]. Ink-washed metal containers such as toothpaste tubes are frequently date-coded using dot-matrix CO_2 lasers.

4.3.4 Semiconductors

Marking of semiconductor wafers prior to the wafer fabrication process is an important application of YAG lasers [32,33]. Typically, an alphanumeric or ID matrix code is marked along one edge of the wafer, and alignment karats can also be placed on the sides of the wafer using the same technique. A SuperSoftMark® mark consists of dot-matrix characters such that the dots are all about 70 ± 10 μm in diameter and about 2.6 μm deep. Although silicon actually has a linear absorption depth of >250 μm at 1.06 μm wavelength (right at the band edge), non-linear absorption caused by a strong temperature dependence of absorption results in a shallow mark about 2.6 μm deep. Laser parameters can be adjusted to optimize the absorption in the case of doped silicon so that consistent debris-free marks can be made. In order to obtain marks of consistent depth and size with no debris, the laser pulse energy must be maintained constant to better than ±0.2% pulse to pulse with the result that YAG lasers used to mark wafers are almost always pumped by laser diodes rather than lamps in modern equipment. By maintaining the pulse energy stable to this degree, each pulse just melts the surface without imparting any extra kinetic energy to the molten silicon so that ejection of dust and debris is minimized. The prime criteria for marking silicon wafers at about 250 wafers per hour are (i) debris-free marking and (ii) a readable mark after successive process steps in wafer fabrication.

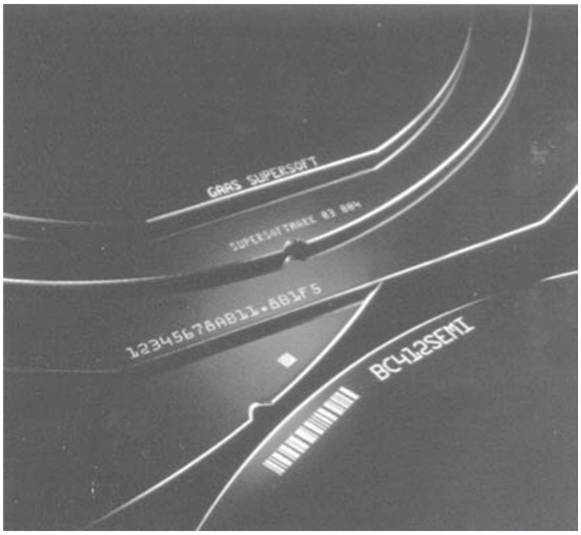

FIGURE 4.16 Wafers with typical laser marks, including barcode and ID matrix.

Marking the back side of diced silicon wafers (backside die marking) is also done using YAG lasers. This process occurs after the wafer is diced and the die is bonded to a conductor substrate so debris-free marking is not a strict requirement. Backside die part line speeds are significantly faster than wafer marking speeds.

Other semiconductor materials such as GaAs wafers are also marked using solid-state lasers. Often, because of stronger absorption, the green or UV wavelengths are used. It is important for health reasons to implement careful ventilation when marking some of these materials.

4.4 Competitors for Laser Marking

In the general arena of commercial labelling, printing and decorating, laser marking is a high-end, niche application. The advantages of laser marking over competitive techniques include the following:

1. High reliability, low downtime;
2. Mark indelibility;
3. High speed;
4. Non-contact process;
5. High-tech reputation;
6. Real-time programmability;
7. Low operating and consumables costs.

Laser coding is usually the highest capital cost coding solution although the payback in added speed and reliability with little operating cost can more than compensate for the high initial capital cost over the lifetime of the product. The goal to lower the price for laser-marking equipment in order to capture a larger part of the high-speed marking market has not been realized; the CO_2 laser dot-matrix marker, at about US $20,000, still costs approximately twice as much to buy as a typical inkjet marker.

In the majority of applications, laser marking is an online process. Laser coding is often one of the final steps in the manufacture of a product, taking place during the final filling cycle at a bottling plant or just before a finished product is boxed for shipment. Competitive online coding techniques [34] include (i) inkjet printing, (ii) thermal transfer printing, (iii) pad printing, (iv) stick on decals, (v) mechanical stamping, (vi) hot stamping, (vii) nameplates, (viii) mechanical scribing and (ix) chemical etching.

Lasers can also be used to decorate a product offline although this is not a common application. In order to mark a larger area, the decorating step usually takes a significant amount of time, which is the reason it is done offline. However, once speed becomes a less important issue, there are a number of other cost-effective techniques to decorate. Competitive decorating techniques [35] include (i) silk screen printing, (ii) dry offset printing, (iii) clear and coloured film labels and decals, (iv) painting, (v) chemical etching, (vi) in-mould film for plastics and (vii) coloured anodizing or dyes for metals. Lasers find a place in decorating for reasons of indelibility, reliability and novelty.

The nemesis of laser coding is inkjet marking [36,37]. Both compete for the high-speed, high-end marking market in both packaging and electronics. Inkjet can mark in a variety of colours, and the marking speed and font can be changed over a wide range. Inkjet markers are programmable in real time and can mark on the fly. The dot-matrix CO_2 markers are designed to compete head-to-head with inkjets in terms of size and portability but are significantly more pricey to buy. Studies of the total cost over the lifetime of an inkjet marker, however, show that the operating outlay for inks will quickly eat into any saving in capital cost and then some. The profits for companies which make inkjet markers come primarily from selling the inks, which are quite sophisticated chemically, and a large fraction of their R&D costs are spent to design inks (Figure 4.17).

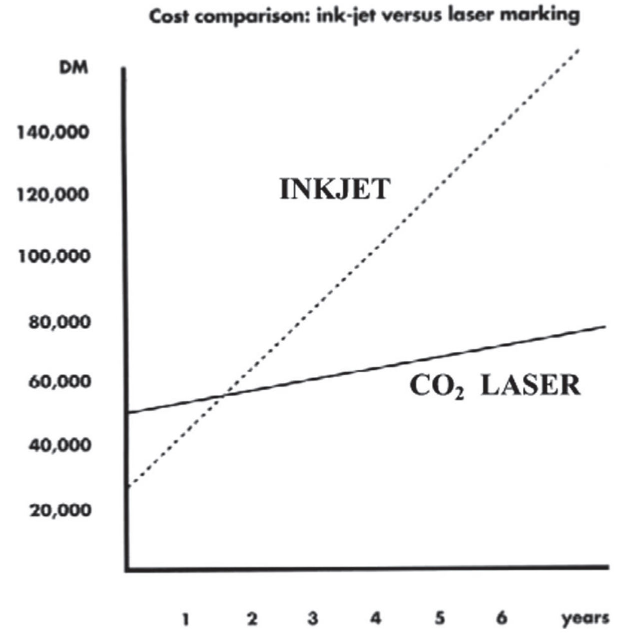

FIGURE 4.17 Cost comparison: inkjet *versus* laser in the DM (Deutschmark) [38].

Because inkjets have a tendency to clog when inactive, lasers have a deserved reputation for higher reliability. An inkjet marker installed in an industrial environment is usually accompanied by a big blob of ink on the floor underneath as a result of several hurried cleanings while the assembly line is stopped. Reliability is the key reason to choose a laser-marking solution over inkjet. Other reasons include indelibility and safety. Although inks may stick well, they and even their protective coatings wear off in time; in contrast, the laser mark penetrates below the surface and will not wear away. Inkjet marks can be made impervious to water but the solvents used are quite dangerous. To maximize adhesion and minimize drying time, the solvent of choice has overwhelmingly been MEK (methyl ethyl ketone), which has been blamed for causing health problems in plants where it is used. In order to address this issue, inkjet suppliers are moving to other solvents such as water, which are safe but smear easily and take longer to dry. The solvent problem for inkjets has been a small boon to laser marker suppliers, especially in large facilities such as breweries. Nevertheless, based primarily on their lower price tag, inkjet markers continue to capture a larger overall market share than lasers.

4.5 Case Study: Decorative Marking of Plastics

The best product in an unattractive package risks anonymity. The design and manufacture of attractively decorated packaging accounts for a significant portion of product development cost not only in consumer packaging but also in electronics, automotive and many other industries. Packaging engineers are always looking for the new package that will set their product apart. The use of lasers for decorating, and particularly customized decorating, of polymers has been a topic of some interest [39–42]. Although there are many excellent technologies for decorating, laser decorating can offer a distinctive mark not achievable any other way: a colour-change indelible decorative graphic image marked into the surface of a plain polyethylene cosmetics container, a personalized logo applied to an electronic device like a personal digital assistant, or a facial image marked into a credit card or bank card.

The most sophisticated laser-marking technology, which is most suitable for marking-customized decorative images, is the Nd:YAG laser-directed beam or ‘light writing’ technology. As opposed to the common printer which raster prints a bitmap matrix of dots on the page to form an image, a laser writer marks a vector image composed of lines, closed polygons and fill patterns usually associated with ‘writing’. By focusing the laser beam to a smaller spot, the resolution of the marked image can be increased at the expense of the time taken to mark the whole image. Since the PC directing the beam is the brains for the laser writing technique, fast and complex manipulation of graphic images is feasible and laser marking of sophisticated images becomes possible (Figure 4.18).

An equally important aspect of decorative laser marking is the response of the polymer being marked to the deposited laser energy. In order to achieve a grey scale or coloured image

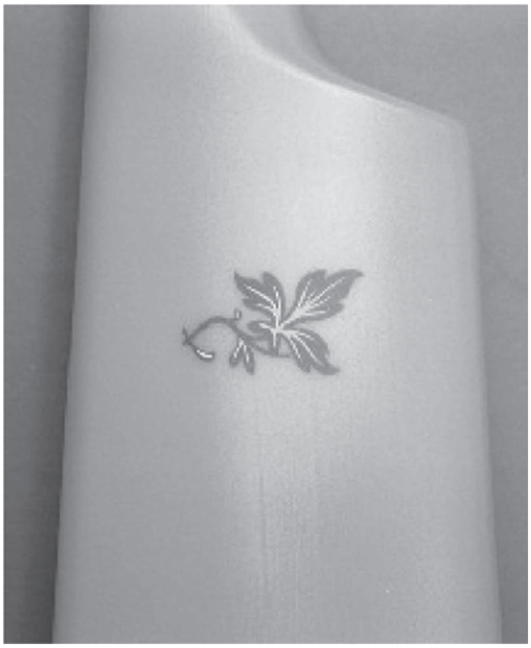

FIGURE 4.18 Black-and-white laser mark on yellow polyethylene bottle.

with good resolution and contrast, the polymer should exhibit some or all of the following properties:

1. The laser induces a colour-change mark in the polymer with little or no material removal.
2. The laser can induce various shades of the same colour (e.g. grey, dark grey, black) depending on the energy density of the laser light used; that is, the mark contrast is a linear function of the laser energy density.
3. The laser can induce two or more distinct colours in a material (e.g. white and black in a yellow plastic or white and green in a black plastic).

One advantage of the Nd:YAG laser is that it can be operated at the fundamental wavelength of 1.06 μm but the wavelength can also be changed using non-linear harmonic crystals so that wavelengths of green (0.53 μm) and ultraviolet (0.35 μm) can also be used. The use of different wavelengths is a very important tool in tailoring the response of the polymer being marked to the deposited laser energy, especially if a photochemical reaction is desired.

In practice, the polymers with higher melting points tend to be the best choice for decorative marking. The response to the deposited laser energy can be controlled without undue bubbling or splatter. Suitable polymers include the engineering polymers such as acetal copolymer, PBT, nylon and polyamides, as well as other hard polymers such as polyethylene. Low melting point elastomers are not good candidates. Controlled marking can take a number of routes. A black or dark marking often results from controlled pyrolization without melting right on the surface at low energy density. As the energy density is increased, melting begins and the mark becomes lighter, then white due to the phenomenon of foaming: the melted polymer re-solidifies quickly freezing 'waves' in place on the surface giving a white appearance to the mark. In some polymers, foaming can yield a very high contrast white against black mark. In polymers that exhibit both of these effects, a white-and-black graphic image can be simply marked by controlling the pulse energy of the laser as the beam is scanned across the surface (Figures 4.19 and 4.20).

Colour marking (other than black and white) requires more sophisticated control of the polymer using additives, primarily pigments, with appropriate properties. One technique to make coloured marks on dark polymers involves including a colour pigment in a formulation containing a black or dark pigment which masks the colour. When the laser energy is deposited and melting occurs, the foaming reaction previously described draws the colour pigment into the 'waves', making the mark

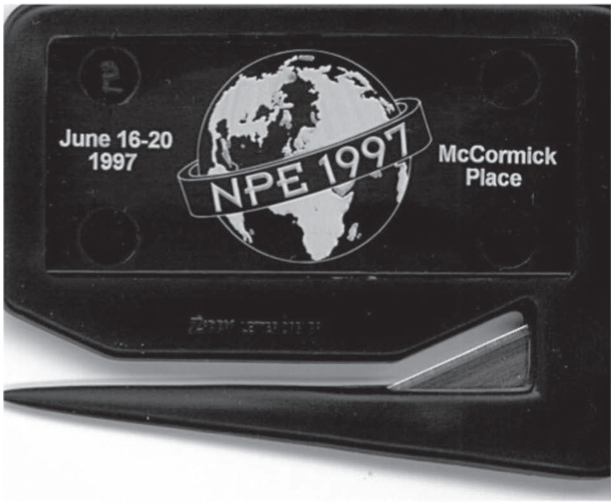

FIGURE 4.19 Yellow mark on black using Nd:YaG fundamental wavelength (provided by M A Hanna Inc at NPE 97).

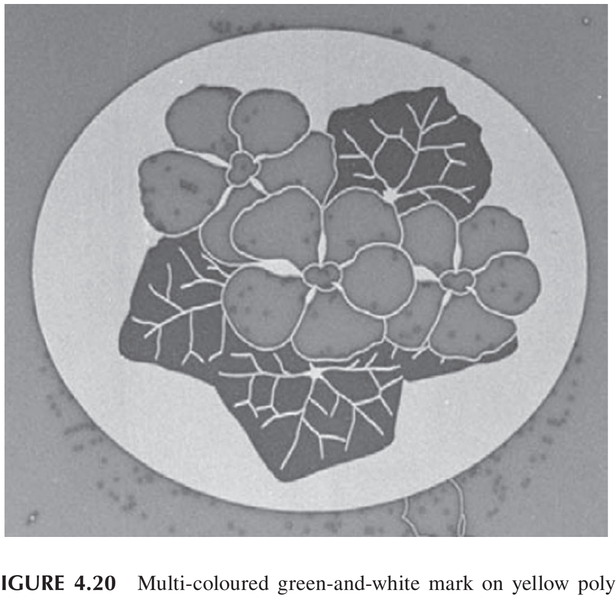

FIGURE 4.20 Multi-coloured green-and-white mark on yellow polyamide 66 (BASF Ultramid® A3K) nylon.

take on the colour of the coloured pigment still against the dark background. This technique has been demonstrated on a number of different polymers.

A more sophisticated concept involves the use of a colour pigment which changes colour after being exposed to laser radiation. Thermochromic materials are designed for this purpose but, in many cases, the colour change is not permanent. The ideal reaction would involve a permanent photochemical change to the pigment so that the colour change is permanent, e.g. from yellow to green. It is conceivable that a pigment could be found, which exhibits a whole range of colours depending on the laser energy deposited. Even more sophisticated, one could envisage a whole set of additives, each addressed by a laser of different wavelengths, so that each laser wavelength would write a different colour.

Laser decorating of polymers using grey-scale and multi-coloured images is an intriguing concept which, however, has a long way to go before it becomes a standard technique in the packaging industry. Many of the chemical companies such as BASF, Hoechst, M A Hanna, GE Plastics and E Merck already offer laser-markable grades of their standard polymers. These companies have begun to fund R&D programmes to understand better and optimize the laser-marking process so that in future they may be able to provide polymers with marking properties, including colour marking, on demand. For their part, the companies supplying laser markers would love to break into the decorating market because the money budgeted to decorate a product is usually much higher than the budget to apply a date code.

REFERENCES

1. McKee T. J. 1995 *Plast. Formulating Compound.* **1** 27–32.
2. McKee T. J. 1996 *Electrotechnol.* 7 27–31.
3. Klein R. H. 1995 *New Electron.* **26** 20–4.
4. Bechtel J. H. 1975 *J. Appl. Phys.* **46** 1585.
5. Hu S. C. et al. 1980 *Metall. Trans. B* **11** 29.
6. Hill D. A. and Soong D. S. 1987 *J. Appl. Phys.* **61** 2132.
7. Jundt H. and Junghans J. 1987 *Proc. SPIE* **744** 147–55.
8. Koller K., Hoang D. and White S. 1991 *Semiconductor Int.* **June** 106–7
9. Bosnos C. et al. 1998 *Adv. Packag.* **7** 54–62.
10. Bosnos C. et al. 1982 *Package Eng.* **February** 62.
11. Hunter J. 1994 *Good Packag. Mag.* **April** 30–2.
12. Birmingham J. et al. 1996 US patent 5,560,845.
13. Hill K. O. et al. 1993 US patent 5,216,739.
14. Bosnos C. 1996 *Electron. Eng.* **July** 146–50.
15. Lee L. Y. et al. 1995 *Proceedings of the International Wire and Cable Symposium* (Philadelphia, PA) pp 823–8.
16. Battis R. D. et al. 1998 *Adv. Packag.* **7** 61–8.
17. Bosnos C. et al. 1998 *Med. Dev. Diagn. Indust.* **February** 86–95.
18. Farrell J. and Verzani G. 1994 *Mod. Appl. News* **August** 76–7.
19. Schlather P. M. 1992 *Indust. Laser Rev.* **March** 11–14.
20. Stevenson R. L. 1997 *Plast. Eng.* **February** 23–5.
21. Hofmann H. et al. 1987 *Proc. SPIE* **744** 156–80.
22. Wildmann D., Pietsch B. and Jundt H. F. 1989 *Proceedings of the Lasers '89 Optoelektronik in der Technik* (Berlin: Springer) pp 687–90.
23. Kilp T. 1991 *Proceedings of Antec'91 (Society of Plastics Engineers)* pp 1901–3.
24. Graff G. 1996 *Mod. Plast.* **April** 24–5.
25. McKee T. 1995 *Packag. Technol.* **August** 48–52.
26. Spanjer K. G. 1987 US patent 4,654,290
27. McKee T. 1997 *Proceedings of the RETEC Conference on Thermoset Materials (Society of Plastics Engineering).*
28. Allcock G. et al. 1995 *J. Appl. Phys.* **78** 7295.
29. Clement R. M., Nevill R. L. and Sunman R. P. 1993 US patent 5,206,496.
30. Erokhin A. I. 1997 US patent 5,637,244.
31. Mann C. O. 1987 Canadian patent 1,219,122.
32. Kuhn-Kubnenfeld F. 1985 US patent 4,522,656.
33. Scaroni J. and McKee T. J. 1997 *Solid State Technol.* **40** 245–51.
34. Scaroni J. and McKee T. J. 1996 *Plast. Technol.* **April** 68–71.
35. Elber G. 1994 *Plast. Des. Forum* **September** 22–6.
36. Larson M. 1984 *Packaging* **July** 33–6.
37. Larson M. 1994 *Packag. Technol. Eng.* **February** 32–3.
38. Larson M. 1992 *Effekte* vol 3 (Darmstadt: Merck) p 2.
39. Herkt-Maetzky C. and Robers W. 1995 *Macromol. Symp.* **100** 57–63.
40. McKee T., Toth L. and Sauerer W. 1997 *Packaging Technol. Eng.* **6** 26–40.
41. Maniscalco M. 1998 *Injection Molding* **March** 44–8.
42. Feng K., Burgess A. and Harris R. M. 1998 PCT patent application WO 98/56594 Chapter originally submitted 11 November 1999.

Taylor & Francis
Taylor & Francis Group
http://taylorandfrancis.com

5

Laser Micromachining

Beat Neuenschwander

CONTENTS

5.1 Introduction 47
5.2 Basics 48
  5.2.1 Energy Transfer 48
  5.2.2 Absorption of Light 48
  5.2.3 Heat Transfer for Long (Nanosecond) Pulses 49
    5.2.3.1 Heat Diffusion Equation 49
    5.2.3.2 Point Source in Infinite Homogeneous 3D Body 49
    5.2.3.3 Linear Heat Conduction 50
    5.2.3.4 Enthalpy Model 50
  5.2.4 Heat Transfer for Ultra-short Pulses 51
    5.2.4.1 Two-temperature Model 51
    5.2.4.2 Metals 51
    5.2.4.3 Dielectrics and Semiconductors 52
  5.2.5 Heat Accumulation 53
5.3 Optimized Material Removal 54
  5.3.1 Problem 54
  5.3.2 Ablation Efficiency 54
    5.3.2.1 Top Hat Intensity Distribution 54
    5.3.2.2 Gaussian Beam 55
  5.3.3 Specific Removal Rate 55
  5.3.4 Consequences from the Model 56
  5.3.5 Incubation 57
  5.3.6 Influence of the Pulse Duration 57
  5.3.7 Influence on the Machining Quality 58
    5.3.7.1 Metals 58
    5.3.7.2 Semiconductors: Silicon and Germanium 60
5.4 Power Scale-up for Surface Structuring: Demands, Solutions and Limiting Factors 62
  5.4.1 Surface Structuring 62
  5.4.2 Marking Speed and Power Scale-up 62
  5.4.3 Limiting Factors 64
    5.4.3.1 Heat Accumulation 64
    5.4.3.2 Plasma and Particle Shielding 65
  5.4.4 Pulse Bursts 66
  5.4.5 Alternative Approaches 68
5.5 Summary and Future Challenges 68
References 69

5.1 Introduction

For the last two decades of the previous century the field of laser micromachining was dominated by µs- and ns-pulsed laser systems. Q-switched or free running solid-state lasers with IR or green radiation were often used for melt-dominated processes like micro-welding and fine-cutting, whereas pulsed UV lasers (frequency-tripled/quadrupled systems or excimer lasers) were the tool of choice for evaporation-based and almost debris-free processes as, for example, deep engraving or drilling of shaped ink-jet printer nozzles.

The situation totally changed in the early noughties when first industrial-ready *ultra-short pulsed* (USP) laser systems became available. For these systems, it is assumed that due to the very short interaction time, the deposited energy cannot distribute into the environment and the material is then ablated

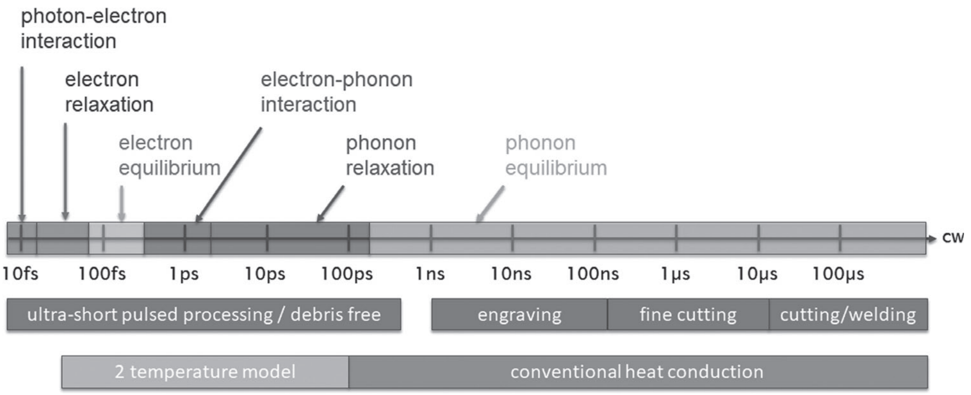

FIGURE 5.1 Processes and corresponding time scales for the energy transfer from the laser photon to the lattice material together with the corresponding typical laser micromachining processes and the physical model used to describe the energy transfer process.

(removed) with almost vanishing *heat-affected zone* (HAZ), which created the term *cold ablation*. Although this picture is definitively an oversimplification and the ablation process is far away from being cold, it describes the advantages of USP laser systems well. The significantly reduced losses into the surroundings lower the energy per pulse needed to drive a process, thereby increasing the accuracy/precision of machining and reducing the wavelength dependency of many processes. Figure 5.1 shows a brief overview together with the corresponding electron/phonon states as well as the corresponding physical models discussed in the following section. USP laser systems also offered the development of many new processes like nano-manufacturing by two-photon processes or fast cutting of glasses by induced processes.

5.2 Basics

5.2.1 Energy Transfer

Figure 5.1 gives a brief overview about the energy transfer mechanism from the photons in a laser pulse to the lattice (phonon excitation) of the material to be machined. Within the first few fs, the photons of a laser pulse are absorbed by the electrons of the material, thus leading to a thermal disequilibrium of excited and not excited electrons. Within the next tens of fs, relaxation of the excited electrons leads to an equilibrium state of the electrons with temperature T_e. Via electron–phonon interactions, the energy transfer from the electrons to the lattice starts, taking from ps to several tens of ps, depending on the material. Within the next hundreds of ps (Klett and Rethfeld 2018), the phonons, i.e. the lattice, reach an equilibrium state with the temperature T_l by the relaxation of phonons. Finally, the thermalization between the electron subsystem and the lattice takes place, and the electrons and lattice can be described by a common temperature $T_e = T_l = T$, where the energy transport is described by conventional heat conduction. During the transfer phase of the energy from the electrons to the lattice, both are described with individual temperatures T_e and T_l – i.e. the two-temperature model is applied.

5.2.2 Absorption of Light

For moderate values of the incoming intensity I_{in} the light is absorbed by a material following Beer's law:

$$I(z)=(1-R)\cdot I_{\text{in}}\cdot e^{-\alpha\cdot z}=(1-R)\cdot I_{\text{in}}\cdot e^{-\frac{z}{\delta}} \tag{5.1}$$

where R is the surface reflectivity, α is the absorption coefficient and $\delta = 1/\alpha$, which is the optical penetration depth. All values are given by the complex refractive index $\tilde{n} = n + i\cdot k$:

$$R=\frac{(n-1)^2+k^2}{(n+1)^2+k^2}\,, \qquad \alpha = 1/\delta = \frac{4\cdot\pi\cdot k}{\lambda} \tag{5.2}$$

For metals like silver, gold, copper, iron and nickel, the reflectivity in general increases with the wavelength and δ has values between 10 and several tens of nm (see Figure 5.2), which is very short. Materials like semiconductors or dielectrics can show a completely different behaviour; for example, silicon and silicon carbide show a decreasing reflectivity and an increasing optical penetration depth (up to 10 µm for silicon carbide and several mm for silicon) with increasing wavelength.

Following (5.1) the deposited power per unit volume as a function of the depth z reads

$$dP/dV = -dI/dz = (1-R)/\delta\cdot I_{\text{in}}\cdot e^{-\alpha\cdot z} \tag{5.3}$$

i.e. for a fixed intensity I_{in}, the absorbed power per unit volume directly scales with $(1-R)/\delta$. Figure 5.2 shows the reflectivity R, the optical penetration depth δ and the upper scaling factor for silver, copper, iron, nickel, silicon carbide and silicon.

For USP lasers, pulses, semiconductors as well as dielectrics the assumption of a linear absorption (5.1) often fails as non-linear effects like multiphoton absorption, free carrier absorption, impact ionization and Auger recombination can take place. For example, following van Driel (1987), the deposited energy per unit volume for a wave travelling in z-direction within silicon is determined by

$$\frac{dI}{dz} = -\alpha\cdot I - \Theta\cdot n_{\text{el}}\cdot I - \sigma_2\cdot I^2 \tag{5.4}$$

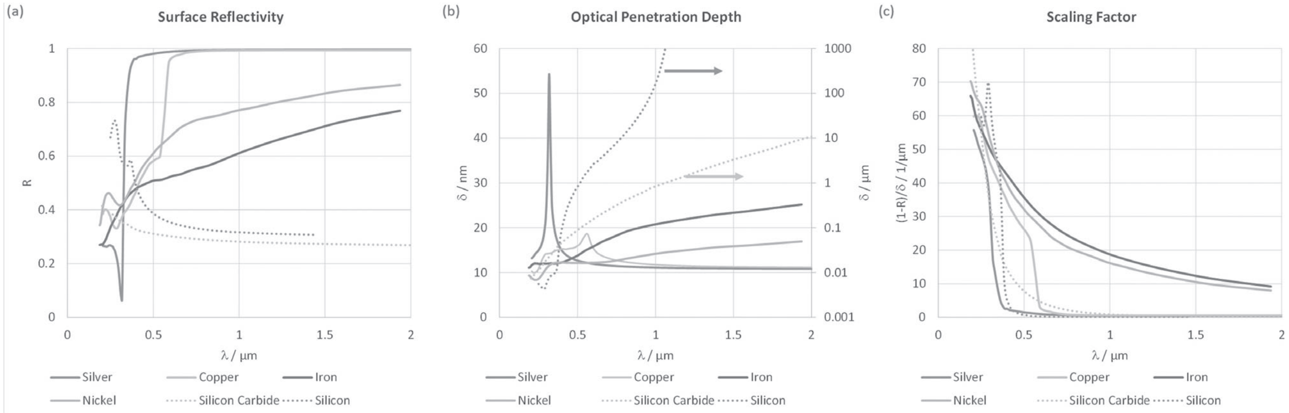

FIGURE 5.2 Reflectivity of a polished surface (a), optical penetration depth (b) and scaling factor $(1-R)/\delta$ (c) as a function of the wavelength from 200 nm up to 2 μm for silver, copper, iron, nickel, silicon carbide and silicon. The presented values are based on n and k obtained via the public domain database refractiveindex.info.

where α is the linear absorption coefficient following (5.2), Θ the carrier absorption coefficient, n_{el} the free carrier density and σ_2 the two-photon absorption coefficient. The free carrier density itself depends on the absorption (5.4) as well as impact ionization and Auger recombination (Derrien et al. 2010):

$$\frac{dn_{\mathrm{el}}}{dt} = \frac{(1-R)\cdot\alpha\cdot I}{\hbar\omega} + \frac{(1-R)^2\cdot\sigma_2\cdot I^2}{2\cdot\hbar\omega} + \beta\cdot n_{\mathrm{el}} + \gamma_{\mathrm{Auger}}\cdot n_{\mathrm{el}}^3 \tag{5.5}$$

where ω is the angular frequency of the laser field, β the coefficient representing the impact ionization and $\gamma_{\mathrm{Auger}}$the coefficient representing the Auger recombination.

For glasses, Preuss et al. (1993) describe the deposited energy per unit volume for a laser pulse travelling in z-direction by multiphoton processes:

$$\frac{dI}{dz} = \sum -\sigma_m \times i \tag{5.6}$$

where $\sigma_1 = \alpha$ is the linear absorption coefficient of (5.3) and σ_m the absorption coefficient for the m-photon process.

The strong non-linearities in (5.4)–(5.6) often prevent an analytical solution and numerical approaches as finite differences or finite elements must be applied.

5.2.3 Heat Transfer for Long (Nanosecond) Pulses

5.2.3.1 Heat Diffusion Equation

For long pulses thermalization between the electron subsystem and the lattice takes place already during the laser pulse. In this case, the heat transfer can be described by the well-known heat diffusion equation:

$$C_l \times \frac{\partial T}{\partial t} = \vec{\nabla} \times k_l \times \vec{\nabla} T + Q(x,y,z \tag{5.7}$$

where C_l is the lattice heat capacity per unit volume $\left(C_l = \rho.c_p\right)$, k_l the thermal conductivity and Q the source term reading, following (5.3), for a given intensity distribution $I(x,y,z,t)$ of a wave propagating in z-direction: $Q = -dI/dz$.

For special cases analytical solution or approximations of (5.7) exist; two of them will be discussed in the following.

5.2.3.2 Point Source in Infinite Homogeneous 3D Body

For an infinite homogeneous 3D body instantaneously heated at $t=0$ with a point source of energy Q at $r=0$, the temperature raise ΔT as a function of the time $t > 0s$ reads:

$$\Delta T(r,t) = \frac{Q}{\rho\cdot c_p\cdot\sqrt{(4\cdot\pi\cdot\kappa\cdot t)^3}}\cdot e^{-\frac{r^2}{4\cdot\kappa\cdot t}} \tag{5.8}$$

where ρ is the mass density, c_p is the specific heat capacity, k is the heat conductivity and $\kappa = k/\left(\rho\cdot c_p\right)$, which is the temperature conductivity. Thus, the temperature raise is described by a Gaussian distribution having a decreasing peak value and increasing spread as a function of the time t. The thermal diffusion length l_D defines the distance where ΔT drops to $1/e$ of its maximum value:

$$l_D = 2\cdot\sqrt{\kappa\cdot t} \tag{5.9}$$

It sha × ll be mentioned here that (5.8) also holds for a point source in the centre $(x = y = 0)$ on the surface $(z = 0)$ of an isolated semi-infinite domain by replacing the source term Q with $2Q$. Based on this, ΔT for any surface heat source and assuming an infinite short pulse duration can be composed by:

$$\Delta T(r,t) = \frac{2}{4\cdot\rho\cdot c_p\cdot\sqrt{(\pi\cdot\kappa\cdot t)^3}}\cdot \iint_{-\infty}^{\infty} \phi(\tilde{x},\tilde{y})\cdot e^{-\frac{(x-\tilde{x})^2+(y-\tilde{y})^2+z^2}{4\cdot\kappa\cdot t}}\cdot d\tilde{x}\cdot d\tilde{y} \tag{5.10}$$

where $\phi(\tilde{x},\tilde{y})$ defines the local fluence (energy per unit area per pulse).

5.2.3.3 Linear Heat Conduction

The limitation to an infinite short pulse duration can, for example, be overcome by considering a 1D semi-finite $(0 \le z < \infty)$ domain and a constant intensity $I_a = (1-R)\cdot I_{in}$ during the pulse of duration τ on the surface $(z=0)$. In this case, the analytical solution of (5.7) reads:

$$\Delta T(z,t) = \frac{I_a}{k}\cdot \begin{cases} 2\sqrt{\kappa t}\cdot \mathrm{ierfc}\left(\frac{z}{2\sqrt{\kappa t}}\right) & 0 \le t \le \tau \\ 2\sqrt{\kappa t}\cdot \mathrm{ierfc}\left(\frac{z}{2\sqrt{\kappa t}}\right) - 2\sqrt{\kappa(t-\tau)}\cdot \mathrm{ierfc}\left(\frac{z}{2\sqrt{\kappa(t-\tau)}}\right) & t > \tau \end{cases} \tag{5.11}$$

with

$$\mathrm{ierfc}(x) = \frac{1}{\sqrt{\pi}}\cdot e^{-x^2} - x\cdot \mathrm{erfc}(x) \text{ and}$$

$$\mathrm{erfc}(x) - \frac{2}{\sqrt{\pi}}\cdot \int_0^x e^{-\tilde{x}^2}\,d\tilde{x} \tag{5.12}$$

This approximation is valid for laser pulses where the lateral extension is dominating compared to the depth where the desired process (melting, evaporation etc.) takes place. For any time t, the highest temperature $\Delta T_{\max}$ is located at the surface $(z=0)$. There the expressions in (5.11) simplify as the ierfc functions can all be replaced by $1/\sqrt{\pi}$ and the value of $\Delta T_{\max}$ is given by:

$$\Delta T_{\max}(t) = \frac{(1-R)\cdot I_{in}}{k\cdot\sqrt{\pi}}\cdot 2\cdot\left(\sqrt{\kappa\cdot t} - (t>\tau?)\cdot\sqrt{\kappa\cdot(t-\tau)}\right) \tag{5.13}$$

Figure 5.3 shows the results for a pulse with a pulse energy of 500 µJ and a pulse duration of 10 ns focused to a radius of 25 µm on a copper surface having a reflectivity of 90%. Figure 5.3a shows the temperature as a function of the depth exactly at $t = \tau = 10$ ns. Figure 5.3b shows the maximum temperature on the surface as a function of the time.

5.2.3.4 Enthalpy Model

The calculations do not take phase transitions into account but are finally virtual temperatures based on constant values of c_p, ρ and k. In a first approximation, the phase transitions can be considered with the enthalpy model, including the latent heat of melting L_m and evaporation L_{ev}, as illustrated in Figure 5.4. The calculated temperature (5.11)–(5.13) follows the light grey line and must be converted to the corresponding value on the dark grey line. Figure 5.3c shows the corresponding result for the temperature as a function of the depth at the end of the pulse from Figure 5.3a. The parts with constant temperatures represent the melting and evaporating sections with the fluid phase between. The solid phase is located in higher depth below the melting phase. The thermal diffusion length l_D for the pulse duration of $\tau = 10$ ns, also sketched in Figure 5.3c, corresponds very well with the melting depth. Thus, l_D represents a good approximation for the dimension of the HAZ and the depth the thermal energy is penetrating in, when a material is treated with a pulse of pulse duration τ.

The discussion of other analytical solutions would go beyond the scope of this chapter. Many helpful cases can, for example, be found in Bäuerle (2000), Ready (2001) or vonAllmen and Blatter (1995).

Following (5.13), the highest temperature is obtained just after the pulse at $t = \tau$. For short and ultra-short pulses it is much more convenient to use the fluence (pulse energy per unit area), $\phi_{\text{in}} = I_n \cdot \tau$, instead of the intensity to characterize the pulse. With this and by replacing $\Delta T_{\max}$ with the virtual temperature $T_v - T_0$, which has to be achieved for a process (e.g. melting or vaporization), one obtains an expression for the threshold fluence ϕ_{th}, the fluence which has minimum to be applied for the desired process:

$$\phi_{\text{th}} = \phi_{\text{in}} = (T_v - T_0)\cdot\frac{\sqrt{\pi\cdot k\cdot\rho\cdot c_p}}{2\cdot(1-R)}\cdot\sqrt{\tau} \rightarrow \phi_{\text{th}} \propto \sqrt{\tau} \tag{5.14}$$

Thus, the threshold fluence depends on the square root of the pulse duration. This dependence is confirmed down to pulse durations of 100 ps for gold, fused silica and calcium fluoride (Stuart et al. 1996). Additionally, it is shown that the dependence of the threshold fluence on the pulse duration becomes weaker for pulses shorter than about 10 ps and almost vanishes for gold.

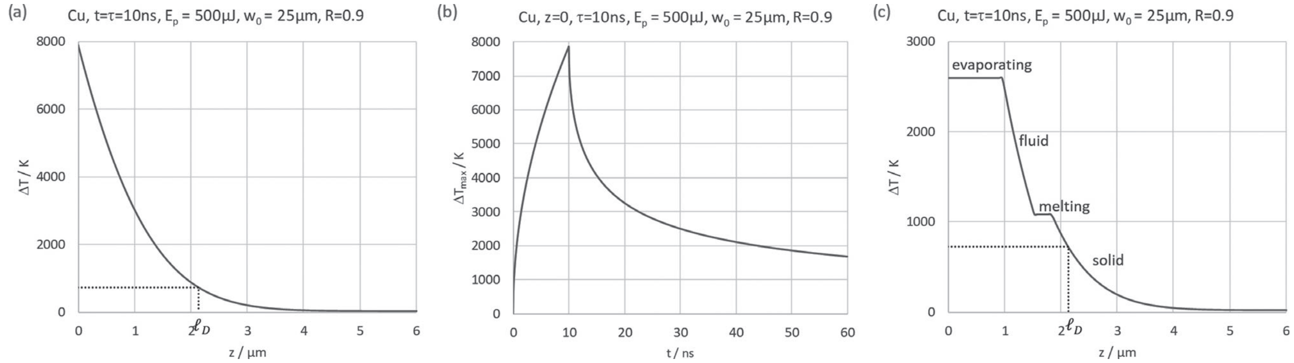

FIGURE 5.3 Temperatures following the linear heat conduction for copper with a reflectivity of 90% and a laser pulse of 10 ns duration having an energy of 500 µJ and focused to a radius of 25 µm.

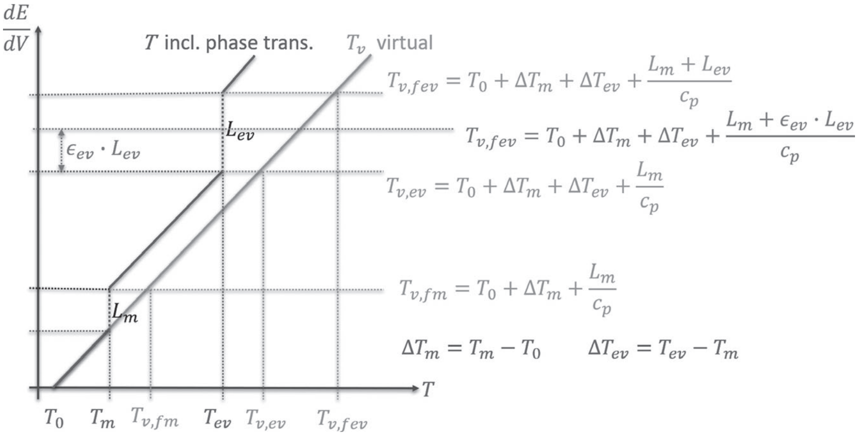

FIGURE 5.4 Sketch of the enthalpy model. The calculated temperatures on the light gray line are the virtual values from the model and have to be converted to the ones on the dark gray lines taking phase transitions into account by considering the latent heat of melting and evaporation. $T_{v,\text{fm}}$, $T_{v,\text{ev}}$ and $T_{v,\text{fev}}$ represent the virtual temperatures where the material is fully melted, starts to evaporate and is fully evaporated, respectively.

5.2.4 Heat Transfer for Ultra-short Pulses

5.2.4.1 Two-temperature Model

In case of ps and fs pulses the electron and the lattice subsystems have to be treated separately with a two-temperature model. The equations for the electron and the lattice temperatures T_e and T_l then read:

$$\begin{aligned} C_e \times \frac{\partial T_e}{\partial t} &= \vec{\nabla}\left(k_e \times \vec{\nabla} T_e\right) - G \times \left(T_e - T_l\right) + Q\left(x, y, z, t\right) \\ C_l \times \frac{\partial T_l}{\partial t} &= \vec{\nabla}\left(k_l \times \vec{\nabla} T_l\right) + G \times \left(T_e - T_l\right) \end{aligned} \tag{5.15}$$

where C_e and C_l are the heat capacities; k_e and k_l are the thermal conductivities of the electrons and the lattice subsystem, respectively; G is the electron–phonon coupling coefficient; and Q denotes the source term which reads for a given intensity distribution $I\left(x, y, z, t\right)$ of a wave propagating in z-direction, following (5.3): $Q = -dI / dz$.

5.2.4.2 Metals

A detailed discussion for metals is given in Chichkov et al. (1996), Momma et al. (1996) and Nolte et al. (1997): The laser energy is first absorbed by the free electrons due to inverse Bremsstrahlung followed by a fast energy relaxation and thermal diffusion in the electron subsystem. Finally, the energy is transferred to the lattice subsystem by electron–phonon coupling. As the heat diffusion through the electron subsystem is much faster than through the lattice, the thermal conductivity of the latter can be neglected. For the 1D case and assuming linear absorption (5.15) can be significantly simplified to:

$$\begin{aligned} C_e \cdot \frac{\partial T_e}{\partial t} &= \frac{\partial}{\partial z}\left(k_e \frac{\partial T_e}{\partial z}\right) - G \cdot \left(T_e - T_l\right) + I\left(t\right) \cdot \left(1 - R\right) \cdot \alpha \cdot e^{-\alpha . z} \\ C_l \cdot \frac{\partial T_l}{\partial t} &= G \cdot \left(T_e - T_l\right) \end{aligned} \tag{5.16}$$

where $I(t)$ the temporal shape of the pulse intensity. In the abovementioned references, analytical solutions and approximations for T_e and T_l are presented. One finding is that the highest lattice temperature (have in mind that the thermal conductivity of the lattice was neglected) can be described by:

$$T_l = \frac{\left(1 - R\right) \cdot \phi_{\text{in}}}{C_l} \cdot \frac{1}{l^2 - \delta^2} \cdot \left(l \cdot e^{-z/l} - \delta \cdot e^{-z/\delta}\right) \tag{5.17}$$

where l is the heat penetration depth (the heat is transported by the hot electrons) depending on the absorbed fluence and the pulse duration, and δ is the optical penetration depth. For $\delta \ll l$ and $\delta \gg l$, the deposited energy per unit volume can then be approximated by:

$$\frac{dE}{dV} = \left(1 - R\right) \cdot \phi_{\text{in}} \cdot \begin{cases} \frac{1}{\delta} \cdot e^{-\frac{z}{\delta}} & \delta \gg l \\ \frac{1}{l} \cdot e^{-\frac{z}{l}} & \delta \ll l \end{cases} \tag{5.18}$$

Assuming that the energy per unit volume for significant evaporation and ablation has to fulfil the condition $C_l \cdot T_l \geq \rho \cdot \Omega$, where Ω is the specific heat of evaporation per unit mass leading to the well-known logarithmic ablation law:

$$z_{\text{abl}} = \begin{cases} \delta \cdot \ln\left(\frac{\phi_a}{\phi_{\text{th}}^{\delta}}\right) & \phi_{\text{th}}^{\delta} \approx \rho \cdot \Omega \cdot \delta & \delta \gg l \\ l \cdot \ln\left(\frac{\phi_a}{\phi_{\text{th}}^{l}}\right) & \phi_{\text{th}}^{l} \approx \rho \cdot \Omega \cdot l & \delta \ll l \end{cases} \tag{5.19}$$

with $\phi_a = \left(1 - R\right) \cdot \phi_{\text{in}}$. The fluence values in the natural logarithm in (5.19) refer to absorbed fluences who scale with $\left(1 - R\right)$ compared to the incoming values. This factor reduces in the quotient, and the logarithmic law can also be expressed by the incoming fluences ϕ_{in}:

$$z_{\text{abl}} = l_p \cdot \ln\left(\frac{\phi_{\text{in}}}{\phi_{\text{th}}}\right) \tag{5.20}$$

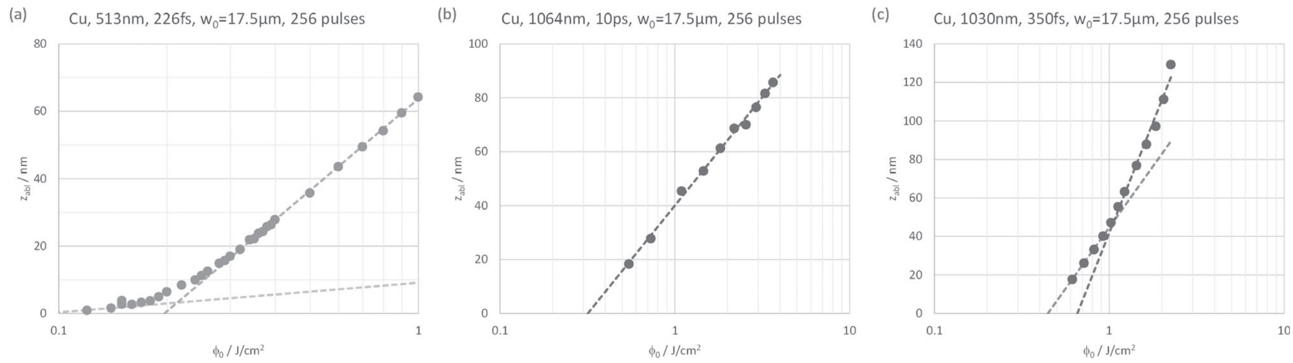

FIGURE 5.5 Ablation depth per pulse for copper and a focus radius of 17.5 µm as a function of the peak fluence of a Gaussian beam and corresponding least-square fits with the logarithmic model for (a) 226 fs pulses at 513 nm, (b) 10 ps pulses at 1064 nm and (c) 350 fs pulses at 1030 nm.

where l_p is the energy penetration depth and ϕ_{th} the incoming value of the threshold fluence for the corresponding regime. This logarithmic ablation law was confirmed by many experimental works as in Preuss et al. (1995) for UV (248 nm) 500 fs pulses on nickel, indium, copper, molybdenum, tungsten and gold. But the existence of different ablation regimes (5.19) depends on the material, the pulse duration and the wavelength as illustrated in Figure 5.5. For a wavelength of 800 nm on copper, Nolte et al. (1997) show that first regime where the optical penetration depth is dominating vanishes for pulses longer than 1 ps due to electronic heat diffusion during the laser pulse. Figure 5.5b shows the ablation depth for 10 ps pulses and a wavelength of 1064 nm. Figure 5.5c shows the ablation depth for 350 fs pulses and a wavelength of 1030 nm. The optical regime where δ is dominating is not observed because fluences below 0.6 J cm^{-2} were not investigated in this experiment. For fluences higher than 1.2 J cm^{-2}, it seems as a third regime with even higher penetration depth and threshold would exist as also shown, for example, by Schille et al. (2015).

5.2.4.3 Dielectrics and Semiconductors

For dielectrics and semiconductors the non-linear absorption (5.4), (5.6) can become significant or even dominating, and the source term in the two-temperature model (5.15) will then depend on the material state during the pulse, e.g. the free carrier density, and the ablation depth does not longer follow the logarithmic ablation law (5.20). This is often the case for glasses and crystals or in general pure materials with a high gap between the conduction and the valence band. For silicate glasses, Grehn et al. (2014) showed that the crater depth obtained with 120 fs pulses at 800 nm wavelength can be well modelled with a pure three-photon absorption process.

The results of a 1D two-temperature model simulation according to (5.15) for a 750-nm-thick silicon layer with an incoming fluence $\phi_{\text{in}} = 1.5\,\text{J}\,\text{cm}^{-2}$ and a temporally Gaussian-shaped pulse of 10 ps duration are shown in Figure 5.6. The absorption process is strongly non-linear as it can be seen from Figure 5.6b: The absorbed power per unit volume just at the surface does not follow the pulse shape as it would be expected with linear absorption but it starts to increase with the free carrier density as it can be expected from (5.4). The strong change in the free carrier density has also an influence onto the complex refractive index and changes the surface reflectivity (5.2) as illustrated in Figure 5.6c. The transmission is given by the absorption in the layer and the surface reflectivity on the front and back surface of the layer. It drops from about 45% down to about 2% during the pulse, also demonstrating that the absorption process is strongly non-linear. After thermalization the lattice temperature rests almost

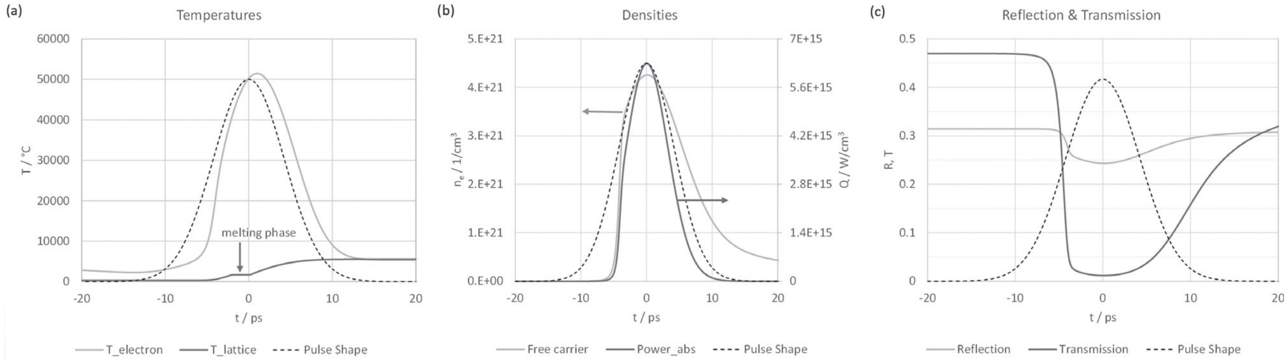

FIGURE 5.6 Results from a 1D two-temperature model simulation for a 750-nm-thick silicon layer and a 10 ps (Full With Half Max, (FWHM)) pulse at 1064 nm wavelength having a fluence of ϕin = 1.5 J cm^{-2}. (a) Surface temperature of the electron and the lattice subsystem. The short plateau in the temperature of the lattice subsystem denotes the melting phase occurring already during the pulse. (b) Free carrier density and absorbed power per unit volume just at the surface. (c) Surface reflectivity and transmission through the silicon layer. In all graphs, the black dashed line represents the Gaussian pulse shape.

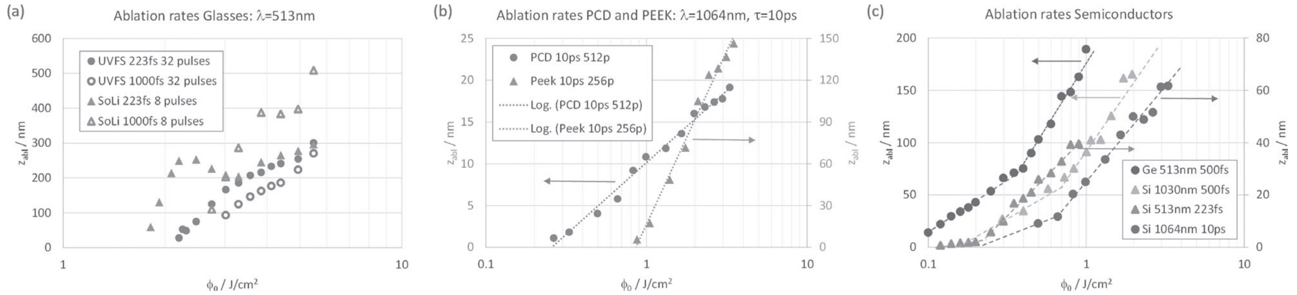

FIGURE 5.7 Measured ablation depths per pulse as a function of the applied peak fluence of a Gaussian beam with a spot radius of $w_0 = 17.5\,\mu m$. (a) For fused silica (32 pulses) and soda–lime glass (8 pulses). (b) For PCD (512 pulses) and PEEK (256 pulses). (c) For germanium (64 pulses), silicon with 256 223 fs and 10 ps pulses as well as 32 500 fs pulses and a spot radius of $w_0 = 13.5\,\mu m$.

constant; i.e., the heat diffusion through the lattice is much slower than through the electron subsystem, and the approximation to neglect the lattice thermal conductivity in (5.16) is valid.

Figure 5.7 shows experimental results for the crater depth of a Gaussian beam as a function of its peak fluence for different materials. For fused silica and soda–lime glasses, the ablation depth does definitively not follow the logarithmic ablation law (5.20). Polycrystalline diamond (PCD), a material used in the tool industry, and polyether ether ketone (PEEK), an industrial plastic, approximately follow the logarithmic law (5.20) for moderate fluences. Although the absorption process is strongly non-linear, silicon and germanium seem to follow (5.19) with two regimes for moderate fluences.

Thus, for many dielectric materials and for moderate fluences, the logarithmic ablation law (5.20) holds too with one or multiple regimes.

5.2.5 Heat Accumulation

In any repetitive process with a pulsed laser, a part of the absorbed energy per pulse is thermalized and remains in the material as residual heat. This problem can be treated by convection and heat conduction following (5.7). The residual heat is continuously accumulating from pulse to pulse, thus leading to an increasing temperature until the heat transfer via conduction into the material and convection into the surrounding air between two pulses is high enough that the material sufficiently cools down between the two pulses and a steady-state situation is obtained. Steady state in this case means that the temperature just before the next pulse impinges on the surface, at the point it will be located, is constant, which includes also the situation of a moving heat source.

Weber et al. (2014) used analytical solutions analogous to (5.8) to describe 1D, 2D and 3D situations for a non-moving heat source. For the 1D case in steel, the results for a 16-µm-radius spot, a pulse energy of 60 µJ and 71% of it converted to heat are shown in Figure 5.8a for the repetition rates of 250, 1250 and 2500 kHz. In Weber et al. (2017), an analytical approximation to calculate the temperature raise due to heat accumulation after N pulses just before the next pulse impinges on the surface is presented. It reads for the 1D case:

$$\Delta T_{H,\mathrm{acc}} = \frac{Q_1}{\rho \cdot c_p \cdot \sqrt{\dfrac{4 \cdot \pi \cdot \kappa}{f}}} \cdot \left(2 \cdot \sqrt{N} + C_1\right), \tag{5.21}$$

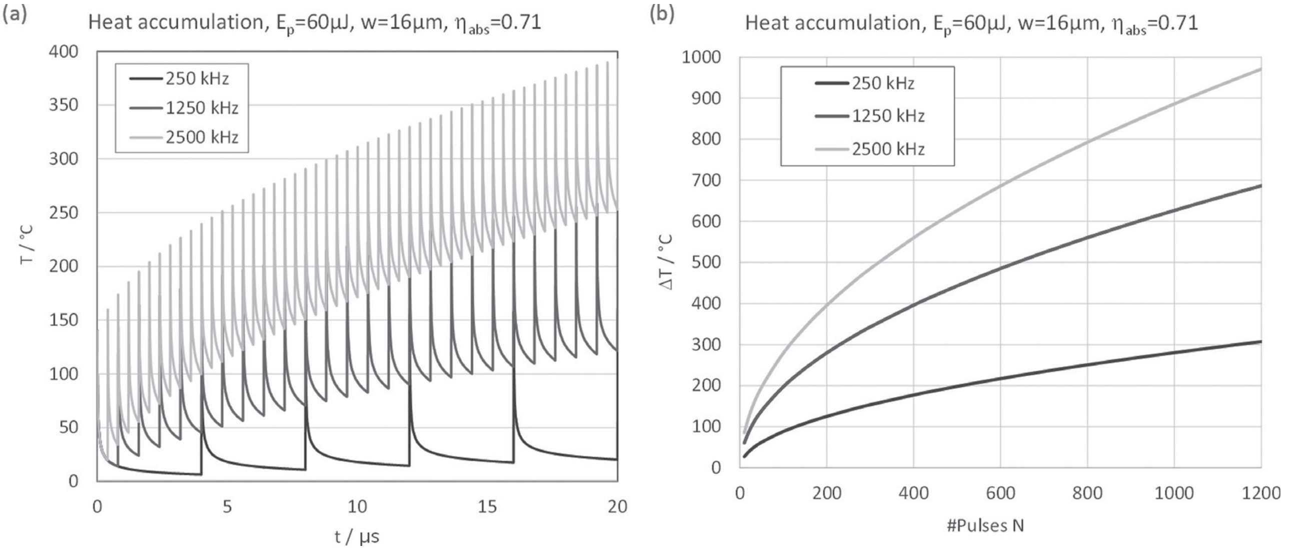

FIGURE 5.8 Illustration of heat accumulation on steel for pulses with an energy of 60 µJ, a spot radius of 16 µm, 71% converted to heat and a repetition rate of 250, 1250 and 2500 kHz.

where $C_1 = -1.46$, f the laser repetition rate and $Q_1 = 2 \cdot \frac{Q_{\text{Heat}}}{A} = 2 \cdot \frac{\eta_{\text{abs}} \cdot P_{\text{av}}}{f \cdot \pi \cdot w^2}$. The corresponding temperature raises as a function of the numbers of pulses are shown in Figure 5.8b. Although the presented solutions are approximations, the results are very valuable for estimations of the heat accumulation for many situations.

Bauer et al. (2015a) showed for ps pulses that energy distribution of the residual heat source follows the intensity distribution of the beam. With this, an analytic solution for a Gaussian-shaped beam was developed (Bauer et al. 2015b), which can also be applied in the situation of a moving pulsed beam. But no closed-form solutions for the temperature raise after N pulses can be developed with this model and mathematical software like MATLAB is demanded.

5.3 Optimized Material Removal

5.3.1 Problem

A user has often the challenge to increase the throughput of a laser machining process by keeping its quality. The throughput is finally, besides many other process parameters, a question of the average power. As the average power of a pulsed system is given by $P_{\text{av}} = f \cdot E_p$ with f being the laser repetition rate and E_p its pulse energy, it is essential to know if the pulse energy or the repetition rate should be increased. Often a laser system has a given average power but a variable repetition rate, which finally ends in the identical problem to identify the best suited pulse energy for a process. The next subsections will demonstrate that there exists an optimum fluence or pulse energy for the ablation process; i.e., the efficiency of the ablation process can be optimized.

5.3.2 Ablation Efficiency

5.3.2.1 Top Hat Intensity Distribution

Following (5.18)–(5.20) and assuming only one ablation regime, the deposited energy per unit volume or the 1D case (corresponding to a top hat intensity distribution) reads $\frac{dE}{dV} = \frac{\phi_a}{l_p} \cdot e^{-z/l_p}$ and a minimum energy per unit volume $dE/dV\big|_{\min} = \rho \cdot \Omega = \frac{\phi_{a,\text{th}}}{l_p}$ is needed to remove the material. The totally absorbed energy per unit area, represented by the light gray area in Figure 5.9a and assuming a thickness $d \gg l_p$ (all energy absorbed within the material), exactly equals to ϕ_a. But to remove the material down to the depth z_{abl}, only the energy per unit area of $\frac{\phi_{a,\text{th}}}{l_p} \cdot z_{\text{abl}}$, represented by the dark gray area in Figure 5.9b and c, is really needed. The energy in the red tail only heats the material without ablation, and the one in the red upper part overheats the ablated material. Following (5.20), the really needed energy per unit area reads: $\phi_{a,\text{need}} = \frac{\phi_{a,\text{th}}}{l_p} \cdot z_{\text{abl}} = \phi_{a,\text{th}} \cdot \ln\left(\frac{\phi_a}{\phi_{a,\text{th}}}\right)$. The efficiency η of the ablation process can be expressed by dividing $\phi_{a,\text{need}}$ (represented by green area in Figure 5.9b and c) by ϕ_a (represented by the red area in Figure 5.8a), leading to:

$$\eta_{1D} = \frac{\phi_{a,\text{th}}}{\phi_a} \cdot \ln\left(\frac{\phi_a}{\phi_{a,\text{th}}}\right) = \frac{\phi_{\text{th}}}{\phi_{\text{in}}} \cdot \ln\left(\frac{\phi_{\text{in}}}{\phi_{\text{th}}}\right) \tag{5.22}$$

For a too low incoming fluence the part of the energy remaining in the material is dominating (Figure 5.8b), and for a too high incoming fluence too much energy is used to overheat the ablated material (Figure 5.8c). The efficiency of the ablation process is therefore maximum, which can easily be calculated from (5.22):

$$\eta_{\max,1D} = \frac{1}{e} = \frac{\phi_{\text{th}}}{\phi_{\text{in,opt}}} \tag{5.23}$$

This means that for the 1D case or a top hat intensity distribution, the highest efficiency of $\frac{1}{e} = 36.8\%$ is obtained when the incidence fluence equals e times the threshold fluence. The ablation depth in this optimum case exactly equals the energy

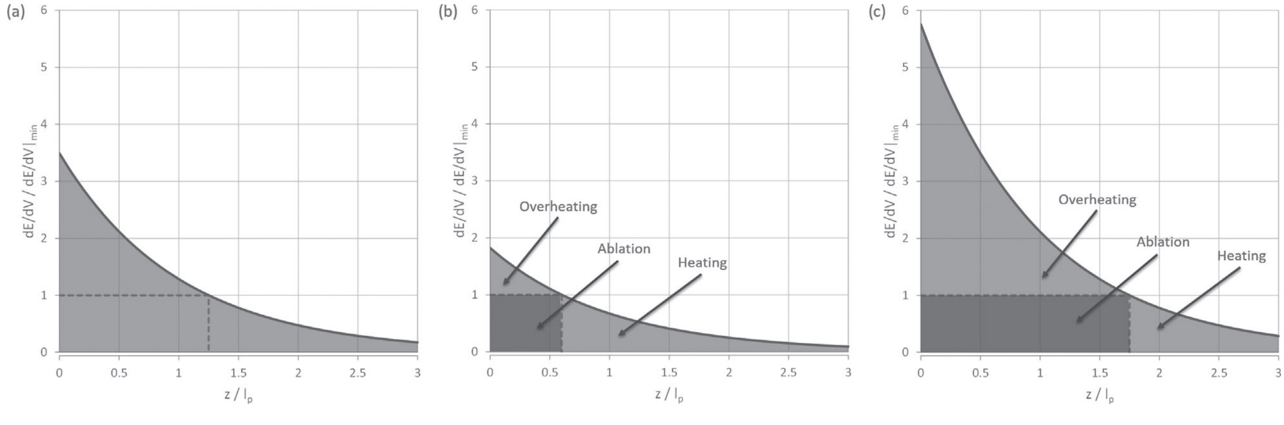

FIGURE 5.9 Absorbed energy per unit volume (in units of the minimum energy per unit volume needed for ablation) as a function of the depth (in units of the energy penetration depth). The light gray area in (a) corresponds to the total absorbed energy per unit area, and the dark gray area in (b) and (c) corresponds to the energy per unit area really needed for the ablation process. The red tail in (b) and (c) represents the part of the energy heating but not ablating material, whereas the part which is overheating the ablated material is represented in the upper red part of the graphs.

penetration depth l_p, and the ablated volume per pulse reads $\Delta V_{\max,1D} = A \cdot l_p$, with A being the area of the top hat beam.

5.3.2.2 Gaussian Beam

Most laser beams for micromachining don't have a top hat intensity profile but nearly a Gaussian one with a varying local fluence:

$$\phi_G(r) = \phi_0 \cdot e^{-2\cdot\frac{r^2}{w^2}} \quad \text{with} \quad \phi_0 = \frac{2 \cdot E_p}{\pi \cdot w^2} \tag{5.24}$$

The peak fluence ϕ_0 in the beam centre therefore amounts to two times the mean fluence of the pulse. Introducing (5.24) this into (5.20) leads to the ablation depth of a Gaussian pulse:

$$z_{\text{abl}}(r) = \begin{cases} l_p \cdot \left(\ln\left(\dfrac{\phi_0}{\phi_{\text{th}}} \right) - 2\dfrac{r^2}{w^2} \right) & r \le R \\ 0 & r > R \end{cases} \tag{5.25}$$

With the ablation radius:

$$R = w \cdot \sqrt{\frac{1}{2} \ln\left(\frac{\phi_0}{\phi_{\text{th}}} \right)} \tag{5.26}$$

From this, the ablated volume per pulse can be calculated by (Raciukaitis et al. 2009; Neuenschwander 2010)

$$\Delta V = \int_0^R \int_0^{2\pi} z_{\text{abl}}(r) \cdot d\varphi \cdot r \cdot dr = \frac{\pi \cdot w^2}{4} \cdot l_p \cdot \ln^2\left(\frac{\phi_0}{\phi_{\text{th}}} \right) \tag{5.27}$$

The energy really needed to ablate this volume amounts following (5.19) $E_{\min} = \Delta V \cdot \rho \cdot \Omega = \Delta V \cdot \dfrac{\phi_{\text{th}}}{l_p}$, whereas the energy in the pulse is (5.24) $E_p = \dfrac{\phi_0 \cdot \pi \cdot w^2}{2}$. The efficiency of the ablation process is then given by:

$$\eta_G = \frac{E_{\min}}{E_{\text{in}}} = \frac{1}{2} \cdot \ln^2\left(\frac{\phi_0}{\phi_{\text{th}}} \right) \cdot \frac{\phi_{\text{th}}}{\phi_0} \tag{5.28}$$

Also for a Gaussian beam the efficiency of the ablation process shows a maximum value. A short calculation leads to:

$$\eta_{\max,\text{G}} = \frac{2}{e^2} \quad \text{when} \quad \phi_{0,\text{opt}} = e^2 \cdot \phi_{\text{th}} \tag{5.29}$$

which is only 27.1%. The maximum depth in the centre is then (5.20), (5.25) $2l_p$, and the ablated volume per pulse amounts to (5.27) $\Delta V_{\max,G} = \pi \cdot w^2 \cdot l_p$.

For a top hat intensity distribution as well as for a Gaussian beam, the ablation process shows a maximum efficiency obtained at a certain fluence. Please note that the optimum fluences going with the highest efficiencies only depend on the threshold fluence, whereas the energy penetration depth linearly scales with the volume ablated per pulse. But even in this optimum case, about two-thirds or more of the energy is lost in heating of not evaporated and overheating of evaporated material. Different intensity distributions would lead to slightly different results but the existence of an optimum fluence with highest efficiency of the ablation process will still hold. Therefore, one can conclude that the efficiency of the ablation process is physically limited and is not really high indeed even at the optimum point.

5.3.3 Specific Removal Rate

For the daily use, the specific removal rate – which means the removed volume per energy or the removal rate per average power – is much more convenient compared to the efficiency. The efficiency of the ablation process in the previous section is given by the energy $dE_{\min}$ really needed to ablate a certain volume dV per pulse divided by the energy dE in the pulse. Following (5.19) the needed energy can be expressed by $dE_{\min} = dV \cdot \dfrac{\phi_{\text{th}}}{l_p}$ and we obtain:

$$\eta = \frac{dE_{\min}}{dE} = \frac{dV \cdot \dfrac{\phi_{\text{th}}}{l_p}}{dE}. \tag{5.30}$$

And from this, the specific removal rate is given by:

$$\frac{dV}{dE} = \frac{{}^{dV}\!/_{dt}}{P_{\text{av}}} = \eta \cdot \frac{l_p}{\phi_{\text{th}}}, \tag{5.31}$$

where η is the efficiency of the corresponding beam profile. The fluences for the highest obtainable specific removal rate then read $\phi_{\text{opt}} = e \cdot \phi_{\text{th}}$ and $\phi_{0,\text{opt}} = e^2 \cdot \phi_{\text{th}}$ for a top hat and a Gaussian beam, respectively. The specific removal rates and their maximum values then read:

$$\frac{dV}{dE} = \frac{l_p}{\phi} \cdot \ln\left(\frac{\phi}{\phi_{\text{th}}} \right) \qquad \left. \frac{dV}{dE} \right|_{\max} = \frac{1}{e} \cdot \frac{l_p}{\phi_{\text{th}}}. \tag{5.32}$$

$$\frac{dV}{dE} = \frac{1}{2} \cdot \frac{l_p}{\phi_0} \cdot \ln^2\left(\frac{\phi_0}{\phi_{\text{th}}} \right) \qquad \left. \frac{dV}{dE} \right|_{\max} = \frac{2}{e^2} \cdot \frac{l_p}{\phi_{\text{th}}} \tag{5.33}$$

for a Gaussian beam. Figure 5.10 shows the very good agreement of the model function (5.33) for a top hat (5.32) respectively a Gaussian (5.33) beam with the measured values for copper C12200 (in the following only called copper), steel AISI 304 (in the following only called steel), nickel, brass, silver and gold.

As discussed in a previous section, especially for fs pulses, a material can show 2 or even 3 different ablation regimes. This should in principal be considered for the efficiency (5.28) and the specific removal rate (5.33). The calculation for the two-regime situation is presented in Jaeggi et al. (2017a) and leads to a rather long formula not shown here. Figure 5.11 illustrates that for copper and 350 fs pulses at 1030 nm, the two-regime model fits the measured values significantly better but the deviations of the one-regime model are still acceptable.

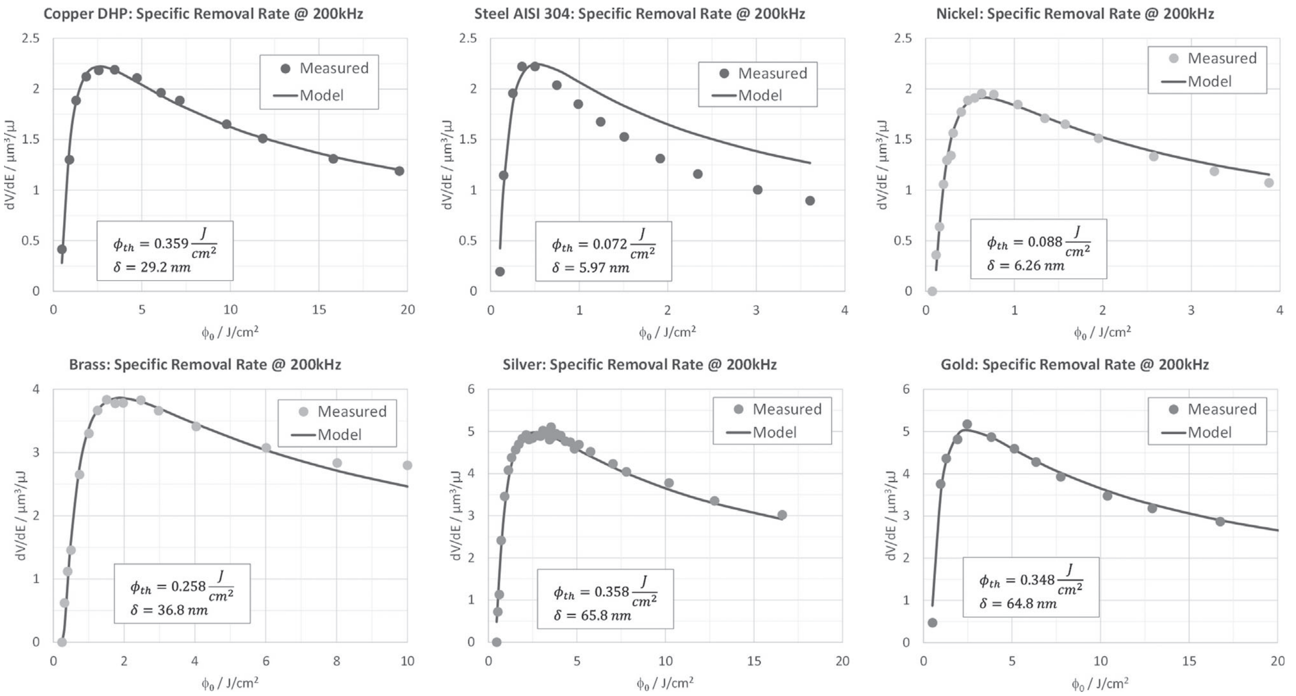

FIGURE 5.10 Measured specific removal rates for 10 ps pulses at a wavelength of 1064 nm for copper, steel AISI 304, nickel, brass, silver and gold and corresponding least-square fits to the model function for a Gaussian beam. The rates were measured by ablating squares of a side length of 1.6 mm with a spot radius of 16 µm.

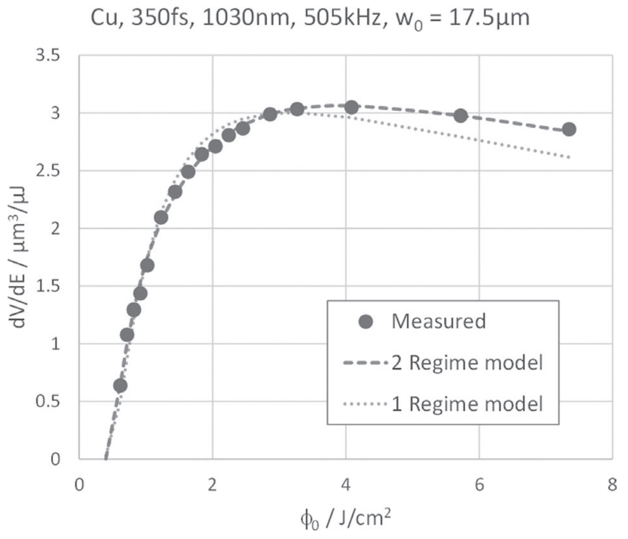

FIGURE 5.11 Specific removal rate for copper and 350 fs pulses at 1030 nm as well as corresponding least-square fits for a two-regime and a one-regime model.

5.3.4 Consequences from the Model

The last subsections showed that for a Gaussian beam the ablation process shows a maximum efficiency with highest specific removal rate (5.33) at an optimum fluence (5.29), but have in mind that applying a fluence of twice the optimum value in fact will lead to a reduced efficiency, but not to a drop in the removal rate as illustrated in Figure 5.12a. The light grey line represents the specific removal rate as a function of the average power P_{av} for 10 ps pulses on copper, a repetition rate of 200 kHz and a spot size of $w_0 = 16\,\mu\text{m}$ is plotted with the optimum point denoted by the light grey dotted lines. Following (5.31), the removal rate *dV/dt* is directly obtained by multiplying the specific removal rate with the average power. The corresponding removal rate in mm³min⁻¹ (dark grey full line) increases indeed with the average power but with decreasing slope. In contrast, a linear increase in the removal rate (orange dotted line) would be achieved if the fluence would be kept at its optimum value by adapting the repetition rate accordingly.

Many USP laser systems offer the possibility to vary the repetition rate at an almost constant average power. The corresponding removal rate as a function of the repetition rate can easily be deduced from (5.32) and (5.33). For a Gaussian beam, it reads:

$$\frac{dV}{dt} = \frac{\pi \cdot w^2}{4} \cdot l_p \cdot f \cdot \ln^2\left(\frac{2 \cdot P_{\text{av}}}{f \cdot \pi \cdot w^2 \cdot \phi_{\text{th}}}\right) \tag{5.34}$$

Figure 5.12b shows the corresponding curve for a fixed average power of 10 W. A maximum removal rate is obtained at the repetition rate where the pulses have the optimum peak fluence (5.29). This optimum repetition rate and the maximum removal rate as well directly scale with the average power:

$$f_{\text{opt}} = \frac{2}{e^2} \cdot \frac{1}{\phi_{\text{th}} \cdot \pi \cdot w^2} \cdot P_{\text{av}} \tag{5.35}$$

Thus, working at the optimum point leads to highest throughput for a given average power and power scale-up should be realized by keeping the optimum fluence and increasing the repetition rate whenever this is possible.

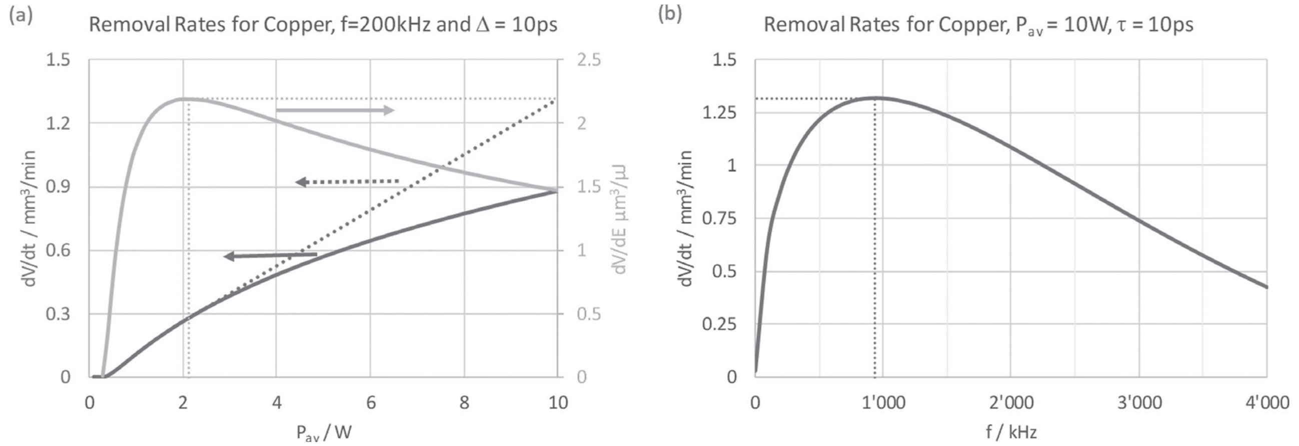

FIGURE 5.12 (a) Specific removal rate (light grey solid line) and removal rate (orange solid line) when the average power is raised by raising the pulse energy. The dark grey dotted line represents the removal rate which would be achieved when the pulse energy would be at its optimum point (light grey dotted lines), and the average power is changed by increasing the repetition rate. It can clearly be seen that this scale-up process is preferable. (b) Removal rate as a function of the repetition rate for a constant average power. The maximum removal rate is obtained at the optimum repetition rate going with optimum peak fluence.

5.3.5 Incubation

The specific removal rate (5.31)–(5.33) depends on the material parameters threshold fluence ϕ_{th} and energy penetration depth l_p. An often applied method to deduce the threshold fluence is the one of Liu (1982), where the squared radius or diameter of the area ablated by a circular laser pulse is plotted versus the fluence. Following (5.26), this leads to a logarithmic dependence on the fluence for a Gaussian beam (5.26) and the spot radius can be calculated from the corresponding slope. For a non-Gaussian beam, the logarithmic dependence often still holds and the intersection can be used to deduce the threshold fluence. However, the Liu method does not provide any information about the energy penetration depth. The energy penetration depth can be obtained by machining craters with a given number of pulses but varying pulse energies with a top hat or a Gaussian beam, and the measurement of its depth is a function of the applied fluence. At least for metals, the ablation depth per pulse should then follow the logarithmic ablation law (5.20), and the threshold fluence and the energy penetration depth can be deduced by a least-square fit as illustrated in Figures 5.5 and 5.7b and c.

Even for ns pulses, it was found that the threshold fluence depends on the number of pulses N which are applied (Jee et al. 1988) following:

$$\phi_{\text{th}}(N) = \phi_1 \cdot N^{S-1} \tag{5.36}$$

where S is a parameter denoting if the material is hardening ($S > 1$) or softening ($S < 1$) from pulse to pulse. In Jee et al. (1988), the incubation is related to the storage cycle of thermal stress–strain energy, i.e. accumulation of plastic deformations induced by the laser pulses. This model was confirmed also for ultra-short pulses in the fs regime for metals (Byskov-Nielsen et al. 2010), semiconductors (Bonse et al. 2001) and transparent materials (Rosenfeld et al. 1999). For ultra-short pulses, it is not clear if the explanation with the thermal stress–strain energy is still applicable. Increased absorption arising from a rougher surface, increased surface damage on microscale, etc. are alternative approaches to explain the nature of the incubation. Further, Neuenschwander et al. (2013) show that also the energy penetration depth underlies an incubation effect as illustrated in Figure 5.13. As the ablated depth per pulse is low, all measurements with less than 10 pulses show a big measurement error leading to deviations in the plots. For higher pulse numbers, it can be seen from Figure 5.13 that neither the ablation threshold nor the energy penetration depth strongly depends on the surrounding gas. Additionally, equation (5.36) would lead to a vanishing threshold for a high number of pulses, which is finally not possible. Therefore, an alternative model to describe the dependence on the number of pulses is proposed:

$$\phi_{\text{th}}(N) = \phi_{\text{th},\infty} + \Delta\phi_{\text{th}} \cdot N^{S-1} \quad \text{and} \quad l_p(N) = l_{p,\infty} + \Delta l_p \cdot N^{S-1} \tag{5.37}$$

The dotted lines in Figure 5.13 represent the least-square fits with this model.

Considering Equations (5.32) and (5.33), the maximum values depend on l_p/ϕ_{th}, and as both material parameters show the identical trend, their influence on the specific removal rate is significantly reduced as also described in Neuenschwander et al. (2013), and the incubation effect becomes finally only significant when a low number of pulses is applied.

5.3.6 Influence of the Pulse Duration

Many investigations concerning the pulse duration have been done. Generally, shorter pulses lead to higher removal rates, but care must be taken when different situations are compared. As illustrated in Figure 5.12b, the removal rate strongly changes with the applied fluence respectively average power which optimum values depend on the threshold fluence. Thus, comparing two situations at the same fluence can lead to misinterpretation as the removal rate for situation 1 can be lower or higher than for situation 2, whereas for the maximum values, it

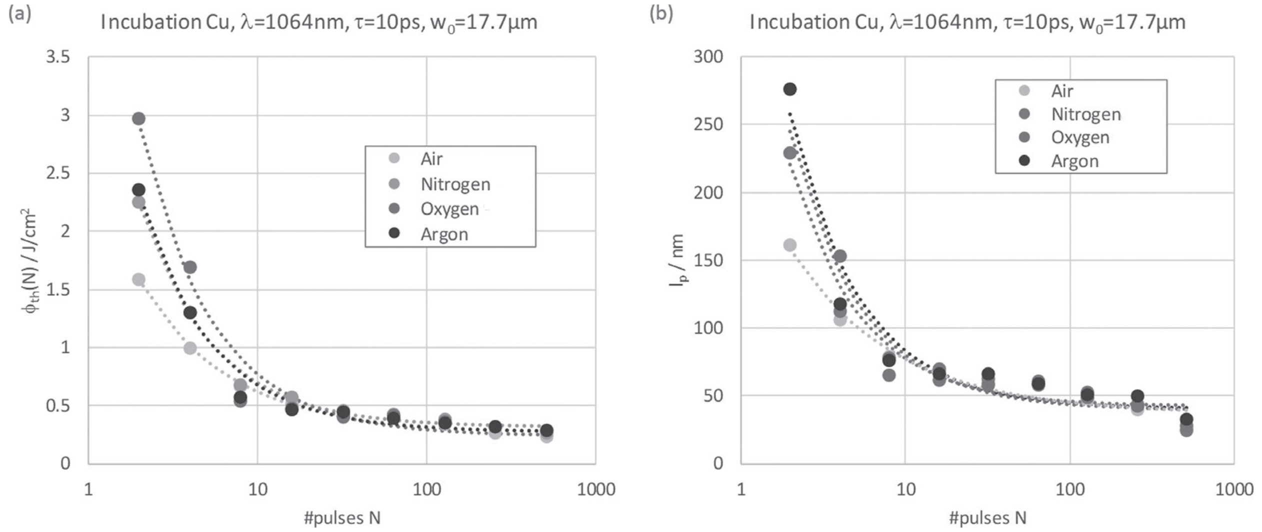

FIGURE 5.13 Threshold fluence (a) and energy penetration depth (b) for copper as a function of the number of applied pulses with different surrounding gases under a pressure of 500 mbar. Both material parameters show a similar incubation effect. The dotted lines represent guides to the eye following an alternative model (Neuenschwander et al. 2013).

could be vice versa. For a fair comparison, the specific removal rate should be measured as a function of the peak fluence as done for different metals in Figure 5.10 and its maximum values should then be compared. This comparison is shown in Figure 5.14a for copper and steel for a wavelength of 1030 nm/1064 nm and pulse durations ranging from 350 fs up to 4 ns. Both metals show a huge decrease of about one magnitude in the maximum specific removal rate when the pulse duration is raised from 10 to 50 ps. For longer pulses up to 4 ns, the maximum specific removal rate rests low. For pulses down to 350 fs the maximum specific removal rate increases up by a factor of about 2 and 1.25 for steel and copper compared to 10 ps. The explanation of this dependence on the pulse duration can partially be found in the behaviour of the threshold fluence and the energy penetration depth shown in Figure 5.14 b and c. The threshold fluence stays almost unchanged for pulse durations of 10 ps and less, and starts to increase for longer pulses as expected from (5.14). For the energy penetration depth, the situation is different. For copper it seems to be almost constant for pulse durations up to 3 ps followed by the decreases for longer pulses up to a duration of 50 ps, whereas the constant phase for steel is observed for pulses shorter than 1 ps followed by the strong decrease up to 30 ps. Thus, having (5.33) in mind, the decrease in the maximum specific removal rate for pulses up to a pulse duration of 10 ps is mainly caused by the decreasing energy penetration depth, and for longer pulses, this effect is even enhanced by an increasing threshold fluence. Also non-metals show a similar trend for the maximum specific removal rate as shown for pulse durations between 10 and 50 ps for silicon, PCD, PEEK and zirconium oxide (ZrO_2) as illustrated in Figure 5.14d.

Glasses can show a completely different behaviour as illustrated in Figure 5.15a for soda–lime glass (So-Li) and UV fused silica (UVFS). For So-Li, a very low specific removal rate is observed for the shortest pulse durations followed by a rapid changeover to a second regime at a specific pulse duration (depending on the peak fluence) and a drop when the pulse duration is further raised. Figure 5.15b shows the difference between the two observed regimes: For the short pulse durations going with low specific removal rates, a very flat surface with a low roughness but melt splatters is obtained, whereas for the longer pulses, the specific removal rate is much higher but the surface becomes rough and scattering. It has to be said that the presented experiments were performed with a fs-laser system based on bulk technology and could not be reproduced with another fs system based on fibre technology. A long discussion with the manufacturers revealed that the dispersion, which is better compensable in a bulk system, might be responsible for this strange behaviour.

For UVFS the obtained specific removal rates do not significantly depend on the pulse duration and the values between 5 and 7.5 $\mu m^3\ \mu J^{-1}$ were obtained. At the investigated wavelength of about 1030 nm and for 2 *ps* at $\phi_0 = 3.1\ J\ cm^{-2}$ or 5 *ps* at $\phi_0 = 4.2\ J\ cm^{-2}$, the location of the ablation process moved from the front side to the back side due to self-focusing via the Kerr effect as an only 1-mm-thick target was used for the presented experiments. The scanning electron microscope (SEM) picture pictures in Figure 5.15b show a rough and scattering surface for the 223 fs pulses as well as for the 2 ps pulses but the structure size increases with the pulse duration.

5.3.7 Influence on the Machining Quality

5.3.7.1 Metals

The applied peak fluence does not only define the specific removal rate, but also has an influence on the machining quality. This is illustrated in Figure 5.16 for gold and steel, machined with 10 ps pulses, a spot radius of $w_0 = 16\ \mu m$, a spot-to-spot distance (pitch) of 8 µm and 96 repetitions for gold, and 192 for steel. For both metals, a very good surface quality

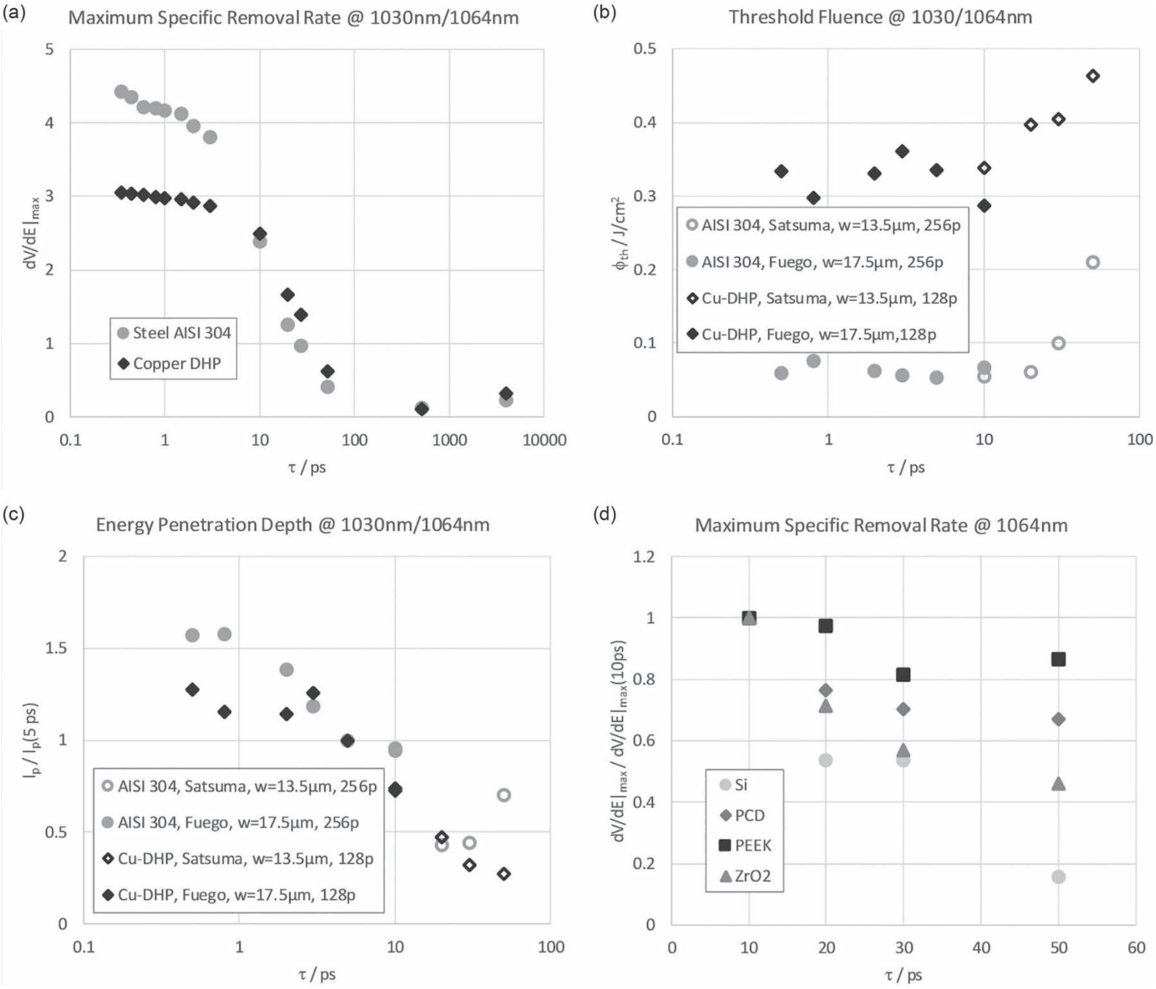

FIGURE 5.14 (a) Maximum specific removal rate, (b) threshold fluence and (c) energy penetration depth of copper and steel as a function of the pulse duration. The energy penetration depth is given in units of the one measured for a pulse duration of 5 ps, which amounts to 9.5 and 54.3 nm for steel and copper, respectively. (d) Maximum specific removal rates as a function of the pulse duration for silicon, PCD, PEEK and ZrO_2 in units of the one obtained at a pulse duration of 10 ps amounting to 1.29, 0.75, 27.2 and 7.7 $\mu m^3\ \mu J^{-1}$ for silicon, PCD, PEEK and ZrO_2, respectively.

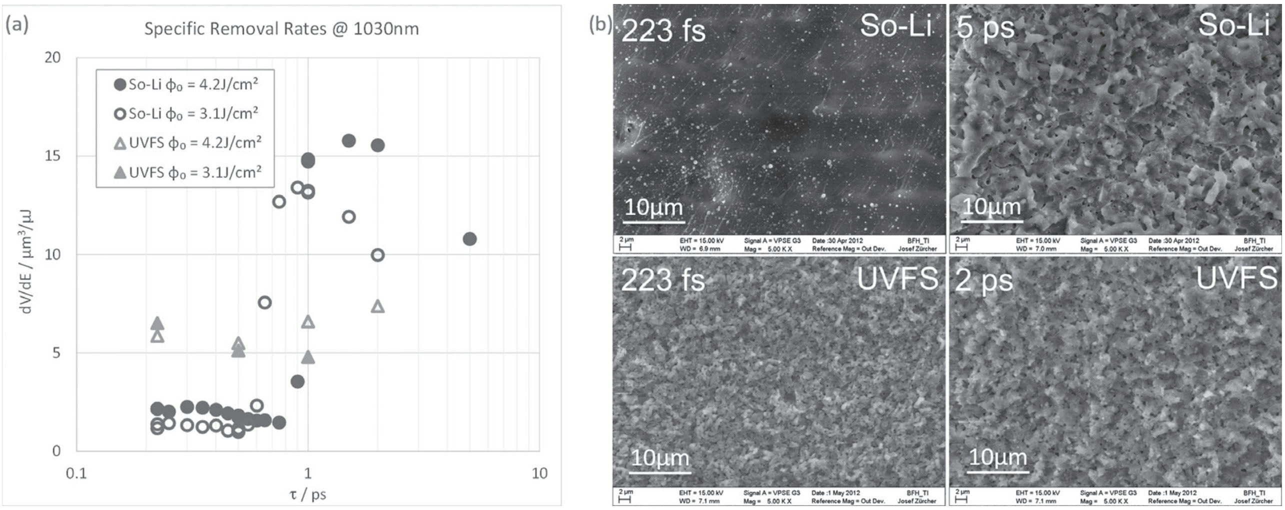

FIGURE 5.15 (a) Specific removal rate as a function of the pulse duration of soda–lime glass and fused silica for the two peak fluences of 4.2 and 3.1 J cm^{-2} and a spot size of 19.5 µm. The laser repetition rate was 200 kHz, and the line-to-line as well as the spot-to-spot distance amounted to 8 µm. (b) SEM micrographs of the surfaces machined with the shortest and the longest investigated pulse duration and a peak fluence of 4.2 J cm^{-2}.

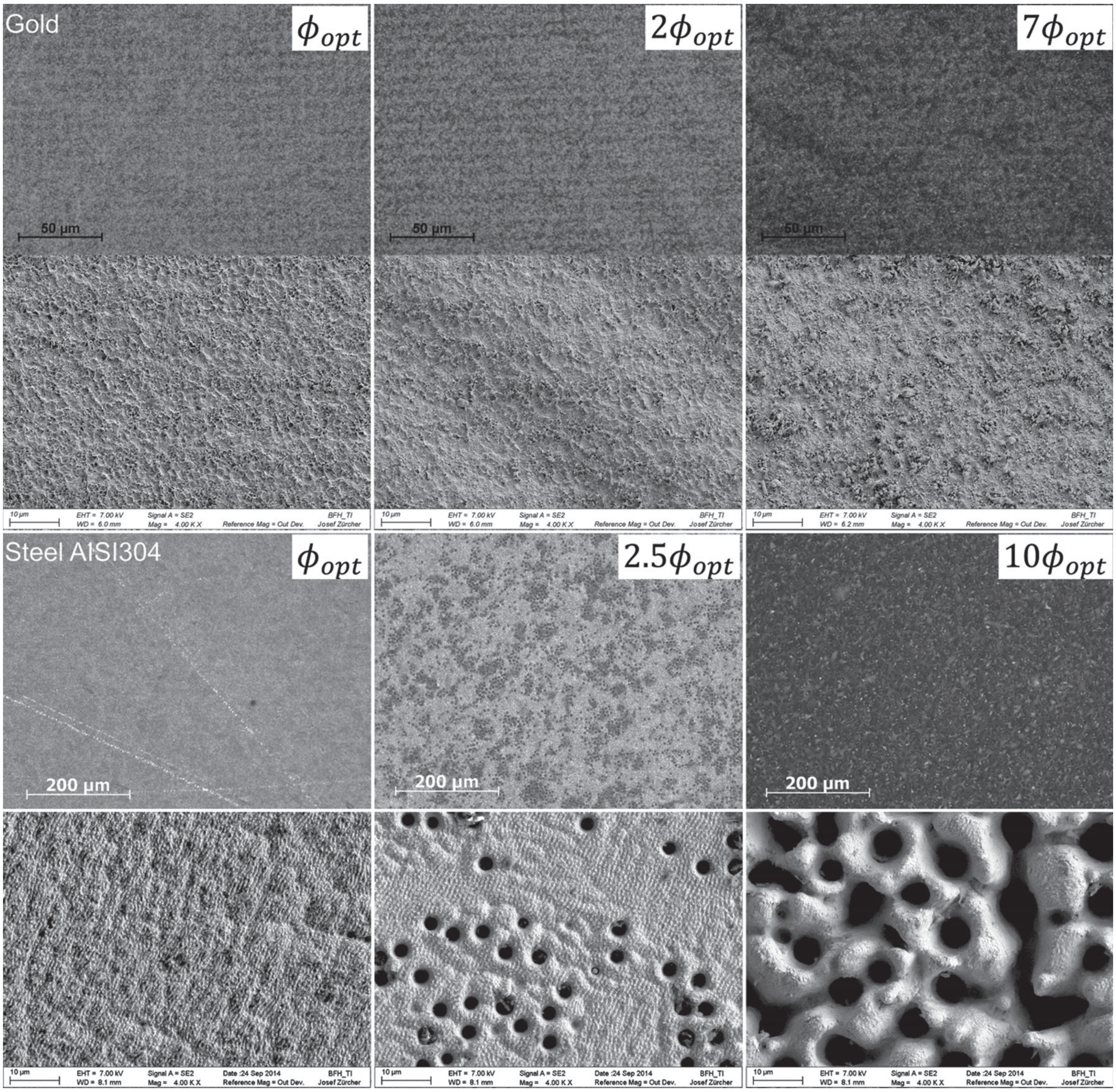
Gold
ϕ_{opt}
50 µm
$2\phi_{opt}$
50 µm
$7\phi_{opt}$
50 µm
10 µm EHT = 7.00 kV WD = 6.0 mm Signal A = SE2 Mag = 4.00 K X Reference Mag = Out Dev. BFH_TI Josef Zürcher
10 µm EHT = 7.00 kV WD = 6.0 mm Signal A = SE2 Mag = 4.00 K X Reference Mag = Out Dev. BFH_TI Josef Zürcher
10 µm EHT = 7.00 kV WD = 6.2 mm Signal A = SE2 Mag = 4.00 K X Reference Mag = Out Dev. BFH_TI Josef Zürcher
Steel AISI304
ϕ_{opt}
200 µm
$2.5\phi_{opt}$
200 µm
$10\phi_{opt}$
200 µm
10 µm EHT = 7.00 kV WD = 8.1 mm Signal A = SE2 Mag = 4.00 K X Date :24 Sep 2014 Reference Mag = Out Dev. BFH_TI Josef Zürcher
10 µm EHT = 7.00 kV WD = 8.1 mm Signal A = SE2 Mag = 4.00 K X Date :24 Sep 2014 Reference Mag = Out Dev. BFH_TI Josef Zürcher
10 µm EHT = 7.00 kV WD = 8.1 mm Signal A = SE2 Mag = 4.00 K X Date :24 Sep 2014 Reference Mag = Out Dev. BFH_TI Josef Zürcher

FIGURE 5.16 Micrographs from optical microscope and SEM of machined surfaces of gold (upper part) and steel (lower part) at the optimum fluence (left), roughly doubled fluence (middle) and high fluence (right). The corresponding studies concerning the specific removal rates are shown in Figure 5.10.

is obtained at the optimum peak fluence (see Figure 5.10) for both metals. For gold, the machining quality remains high when the applied peak fluence is doubled or tripled and can be still acceptable for higher fluences. This is also valid for metals like copper, brass, silver and nickel. But the situation completely changes for steel and titanium (Tsukumoto et al. 2017). In case of steel, a peak fluence of roughly the doubled value of the optimum one leads to the formation of small cavities on the surface, and this effect becomes stronger when the applied peak fluence is further increased and finally the surface will be fully covered by the so-called cone-like protrusions (CLPs). The formation of CLP may also explain the deviation from the measured specific removal rates from the model function for steel, as shown in Figure 5.10, and occurs also for other steel grades (Lauer et al. 2014). The exact formation mechanism of the CLPs is still unclear and subject of actual investigations.

Thus, the process window for most metals is quite large, and the applied peak fluence may amount to multiples of the optimum value by still obtaining an acceptable machining quality. Even the efficiency is lower, one will still benefit from an increased effective removal rate as illustrated in Figure 5.12a. But for steels, the process window is narrow and limited to an area around the optimum peak fluence to avoid CLP formation.

5.3.7.2 Semiconductors: Silicon and Germanium

CLP formation also occurs for silicon and germanium when the materials are machined with fs pulses at 1030 nm as illustrated in Figure 5.17 for 223 fs and 350 fs on [100] – oriented silicon and [111] – oriented germanium, respectively. For both materials, the CLP dimension increases with the applied peak fluence, whereas it is larger for germanium, which also shows CLP formation for 10 ps pulses at 1064 nm.

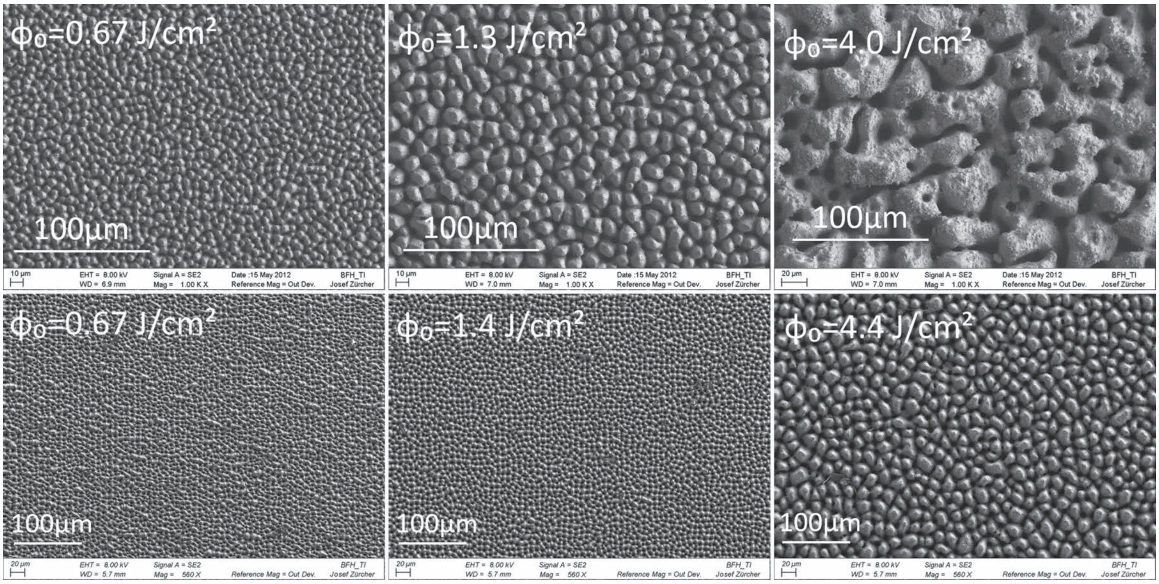
ϕ₀=0.67 J/cm²
100µm
10 µm EHT = 8.00 kV WD = 6.9 mm Signal A = SE2 Mag = 1.00 K X Date :15 May 2012 Reference Mag = Out Dev. BFH_TI Josef Zürcher
ϕ₀=1.3 J/cm²
100µm
10 µm EHT = 8.00 kV WD = 7.0 mm Signal A = SE2 Mag = 1.00 K X Date :15 May 2012 Reference Mag = Out Dev. BFH_TI Josef Zürcher
ϕ₀=4.0 J/cm²
100µm
20 µm EHT = 8.00 kV WD = 7.0 mm Signal A = SE2 Mag = 1.00 K X Date :15 May 2012 Reference Mag = Out Dev. BFH_TI Josef Zürcher
ϕ₀=0.67 J/cm²
100µm
20 µm EHT = 8.00 kV WD = 5.7 mm Signal A = SE2 Mag = 560 X Reference Mag = Out Dev. BFH_TI Josef Zürcher
ϕ₀=1.4 J/cm²
100µm
20 µm EHT = 8.00 kV WD = 5.7 mm Signal A = SE2 Mag = 560 X Reference Mag = Out Dev. BFH_TI Josef Zürcher
ϕ₀=4.4 J/cm²
100µm
20 µm EHT = 8.00 kV WD = 5.7 mm Signal A = SE2 Mag = 560 X Reference Mag = Out Dev. BFH_TI Josef Zürcher

FIGURE 5.17 SEM micrographs from surfaces of germanium (upper row) and silicon (lower row) machined with fs pulses (223 fs for germanium and 350 fs for silicon) at 1030 nm.

For silicon and 10 ps pulses at 1064 nm wavelength, a rapid changeover in the surface roughness can be observed. The surface roughness drops down from a maximum value of $s_a = 2.1\,\mu\text{m}$ at $\phi_0 = 1.05\ \text{J cm}^{-2}$ to $s_a = 0.5\ \mu\text{m}$ at $\phi_0 = 1.3\ \text{J cm}^{-2}$ and finally, $s_a = 0.1\ \mu\text{m}$ for $\phi_0 = 1.55\ \text{J cm}^{-2}$. For higher fluences, the roughness slightly increases but remains below $s_a = 0.3\ \mu\text{m}$, as illustrated in Figure 5.18a. SEM micrographs of the corresponding machined surface are shown in Figure 5.19. The increase in the surface roughness up to $\phi_0 = 1.05\ \text{J cm}^{-2}$ is caused by increasing CLPs analogous to Figure 5.17. Then, a melting effect occurs which starts to prevent the CLP formation until a completely flattened but molten surface is obtained for $\phi_0 = 1.55\ \text{J cm}^{-2}$. This rapid changeover goes with a transition from one ablation regime to another as can be seen from the specific removal rate as shown in Figure 5.17b. The melted silicon has another reflectivity and energy penetration depth l_p, leading to a different threshold fluence ϕ_{th} and finally the specific removal rate (5.33). In this case, silicon shows two different regimes as illustrated by the solid and the dashed line in Figure 5.18b. The values for the corresponding material parameters are deduced by least-square fits and amount to $\phi_{\text{th},1} = 0.09\ \text{J cm}^{-2}$ and $l_{p,1} = 18.7\ \text{nm}$ in the first, respectively, $\phi_{\text{th},2} = 0.29\ \text{J cm}^{-2}$ and $l_{p,2} = 44\ \text{nm}$ in the second regime.

A similar changeover in the surface roughness caused by the melting effect is also obtained for the wavelength of 532 nm and 10 ps pulses. It changes from $s_a = 1.5\ \mu\text{m}$ to $\text{s}_\text{a} =$

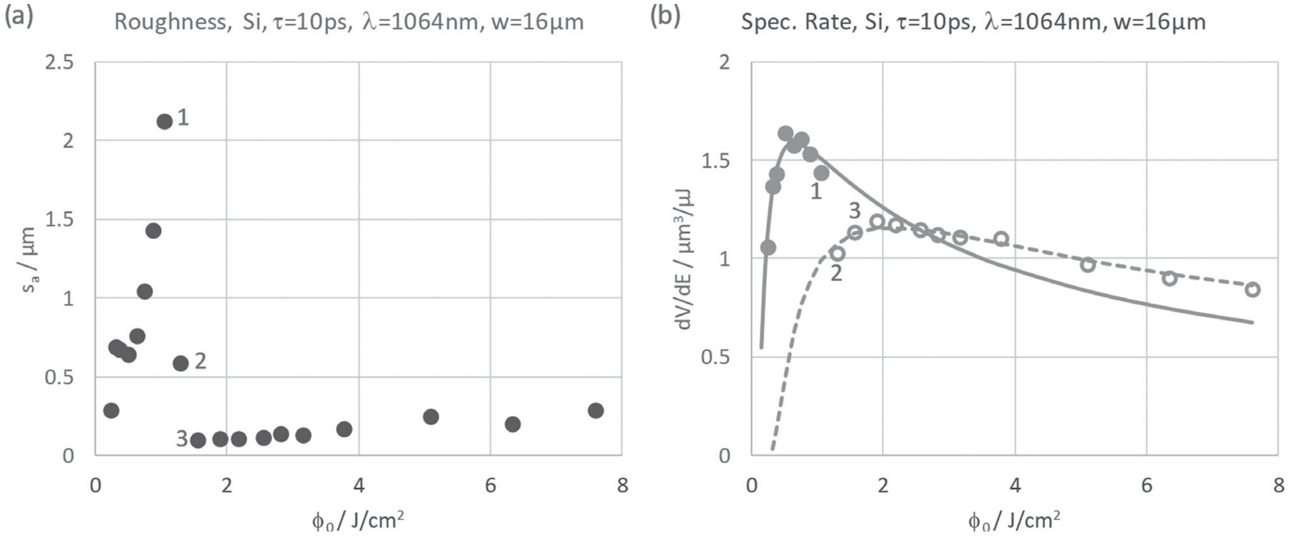

FIGURE 5.18 (a) Surface roughness and (b) specific removal rate of silicon machined with 10 ps pulses at a wavelength of 1064 nm with a focus radius of 16 µm, a pitch of 8 µm and 96 repetitions. The rapid changeover in the surface roughness is denoted with the numbers 1–3, which can also be found in the specific removal rate. The changeover goes with the transition between two regimes having different threshold fluences and energy penetration depths.

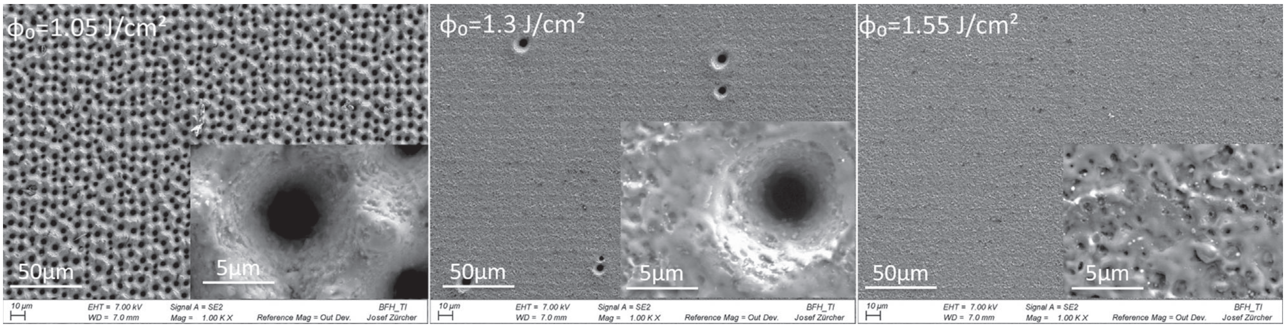
ϕ₀=1.05 J/cm²
50µm
5µm
ϕ₀=1.3 J/cm²
50µm
5µm
ϕ₀=1.55 J/cm²
50µm
5µm
10 µm EHT = 7.00 kV WD = 7.0 mm Signal A = SE2 Mag = 1.00 K X Reference Mag = Out Dev. BFH_TI Josef Zürcher

FIGURE 5.19 SEM micrographs of the machined surface in the changeover (1–3 in Figure 5.17). It can clearly be seen that the enormous drop in the surface roughness is caused by a melting which is flattening the surface.

0.2 µm when the peak fluence is raised from $\phi_0 = 1.2\ \mathrm{J\,cm^{-2}}$ to $\phi_0 = 1.67\ \mathrm{J\,cm^{-2}}$. But this one does not lead to different regimes in the specific removal rate; i.e., the threshold fluence and the energy penetration depth are not significantly affected by melting for the wavelength of 532 nm.

5.4 Power Scale-up for Surface Structuring: Demands, Solutions and Limiting Factors

5.4.1 Surface Structuring

Machining structures into a surface is generally done in a 2.5D process where the desired pattern is sliced, and for each slice, the areas which must be removed are filled with a hatch pattern. The different layers with their hatch patterns are then machined in order, and the desired structure is obtained. The whole process is illustrated in Figure 5.20. Thus, in principal straight lines are marked with a scanning system, usually a galvo scanner. With the findings from the previous section, one is now able to design and optimize the corresponding processes.

The removed depth per layer d is given by the specific removal rate, the spot-to-spot distance p_x, the line-to-line distance p_y – called pitch in scan and cross-scan direction, respectively – and the pulse energy E_p by:

$$d = \frac{E_p}{p_x . p_y} \cdot \frac{dV}{dE} \tag{5.38}$$

Thus, for a Gaussian beam, one obtains with (5.33):

$$d = \frac{1}{4} \cdot \underbrace{\frac{\pi \cdot w^2}{p_x \cdot p_y}}_{=d_{opt}} \cdot l_p \cdot ln^2\left(\frac{\phi_0}{\phi_{\mathrm{th}}}\right) \tag{5.39}$$

where d_{opt} is the depth per layer for the optimum point. With this, it becomes now possible either to deduce the right number of layers for the slicing process or to adapt the layer thickness by adjusting the pulse energy and/or the pitches. From the quality and efficiency aspects, the pulse energies, i.e. the peak fluence, should be chosen near their optimum value, and following Jaeggi et al. (2012), both pitches should amount between ¾ and ¼ of the spot radius. The parameter window allows therefore an adaption of the removed depth per layer but not in one order of magnitude.

5.4.2 Marking Speed and Power Scale-up

For a given repetition rate f, the marking speed to achieve the pitch p_x in scan direction is given by:

$$v_{\mathrm{mark}} = p_x \cdot f \tag{5.40}$$

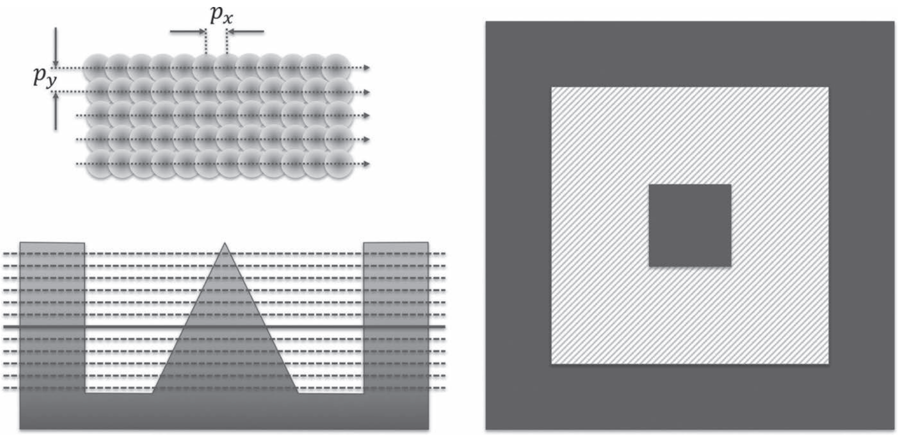

FIGURE 5.20 Sketch of a standard 2.5D process for surface structuring: The desired structure is sliced in n layers with distance d (lower left), and for each layer, the area to be removed is filled with a hatch (right). Important to deduce the removed depth per layer is the pitch p_x in scan direction and the pitch p_y in cross-scan direction (upper left).

Together with the optimum repetition rate for a Gaussian beam (5.35) and a pitch in scan direction of half of a spot radius one obtains:

$$v_{\mathrm{mark,opt}} = \frac{1}{e^2} \cdot \frac{P_{\mathrm{av}}}{\phi_{\mathrm{th}} \cdot w \cdot \pi} \tag{5.41}$$

The desired marking speed therefore linearly scales with the average power and is inversely proportional to the threshold fluence and the spot radius. The result for copper with a spot radius of 16 µm (typical for a $f = 160$ mm objective) and steel with a spot radius of 25 µm (typical for a 250 mm objective) is shown in Figure 5.21. Today high-end galvano scanners achieve a maximum marking speed of about 32 m s^{-1} with a $f = 160$ mm objective and 50 m s^{-1} with a $f = 250$ mm objective.

For copper, this speed is reached at an average power of 42 W and a repetition rate of 3 MHz. Having in mind that for copper, also a higher peak fluence by keeping an acceptable machining quality can be applied, up to 100 W average power could be used for a machining process with a galvano scanner.

For steel, the situation changes dramatically, due to the low threshold fluence. Even for the bigger spot radius, the maximum marking speed of 50 m s^{-1} is already reached at an average power of about 21 W with a repetition rate of 9.6 MHz. Due to the CLP formation discussed in the previous section, working at higher peak fluences is not preferable and the average power which can be used with a galvano scanner is therefore limited to about 20 W.

Higher marking speeds are offered by polygon line scanners as, for example, shown in Jaeggi et al. (2014). In this work, a polygon line scanner with a maximum speed of 100 m s^{-1}, 400 lines s^{-1}, a line length of 170 mm and a spot radius of 29 µm for 1064 nm was used. Steel could be machined up to an average power of 43 W at a repetition rate of 6.83 MHz. Figure 5.22 shows SEM micrographs of the steel surface machined with repetition rates from 200 kHz up to 6.83 MHz. For the first three repetition rates, a galvano scanner and a beam with a spot radius of 16 µm were used. All experiments were done at the optimum peak fluence, and almost no difference in the surface quality can be observed for all investigated repetition rates and average powers. Thus, the power scale-up process on steel was successful up to an average power of about 43 W.

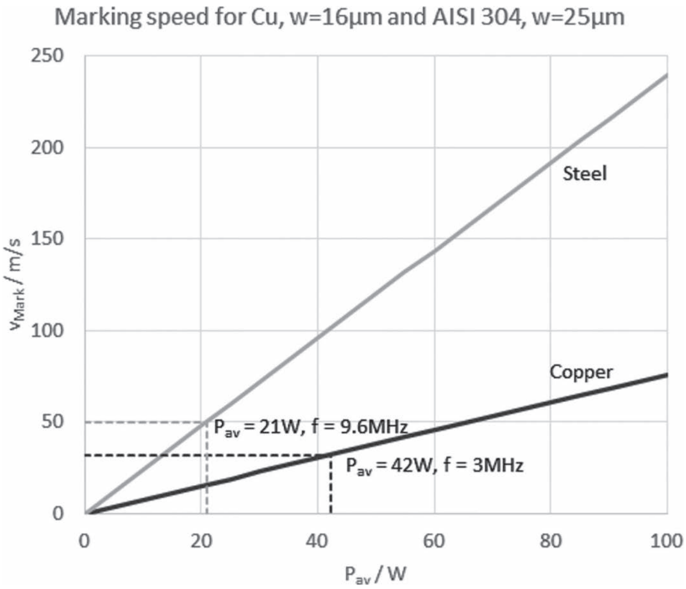

FIGURE 5.21 Demanded marking speed at the optimum point for 10 ps pulses and a wavelength of 1064 nm as a function of the average power for copper and a spot radius of 16 µm, respectively, for steel and a spot radius of 25 µm.

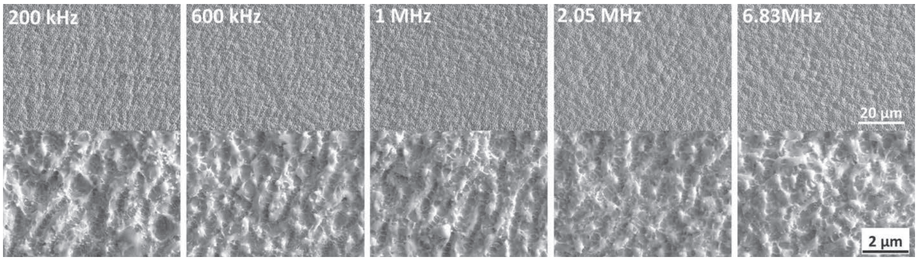

FIGURE 5.22 SEM micrographs of steel surfaces machined with 10 ps pulses at a wavelength of 1064 nm and different repetition rates. For the first three repetition rates up to 1 MHz, a galvano-scanner set-up with a spot radius of 16 µm and a pitch of 8 µm was used, whereas the surfaces for the two high repetition rates were realized with a polygon line scanner having a spot radius of 29 µm and a pitch of 14.5 µm. (Reprinted by permission from: Jaeggi, B., Neuenschwander, B., Zimmermann, M. et al. 2014. High Throughput and High Precision Laser Micromachining with ps-Pulses in Synchronized Mode with a fast Polygon Line Scanner. Proc. of SPIE 8967: 89670Q.)

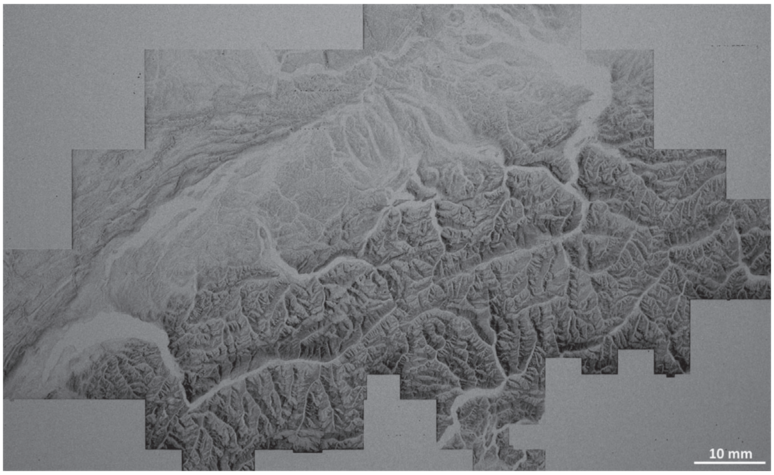

FIGURE 5.23 Topography of Switzerland machined in steel with a polygon line scanner and 10 ps pulses at 1064 nm. The laser average power was 26 W, and the repetition rate amounted to 4.1 MHz. (Reprinted by permission from: Jaeggi, B., Neuenschwander, B., Zimmermann, M. et al. 2014. High Throughput and High Precision Laser Micromachining with ps-Pulses in Synchronized Mode with a fast Polygon Line Scanner. Proc. of SPIE 8967: 89670Q.)

To demonstrate the applicability of a polygon line scanner for surface structuring, the topography of Switzerland was machined into steel with 2233 layers, 26 W of average power, a repetition rate of 4.1 MHz and a marking speed of 60 m s^{-1}. The maximum average power of 43 W could not be used due to the laser system, which was not able to switch single pulses at the high repetition rate of 6.83 MHz. The high number of pre- and post-pulses would have led to a bad machining quality (Figure 5.23).

5.4.3 Limiting Factors

5.4.3.1 Heat Accumulation

A further power scale-up into the multi-100 W regime for steel, copper and brass is presented in Jaeggi et al. (2017b). These experiments were performed with a pulse duration of 3 ps at a wavelength of 1030 nm; repetition rates of 2.065, 5.063, 8.1, 10.13 and 40.5 MHz; and average powers up to 300 W. The polygon line scanner had a maximum speed of 480 m s^{-1} with a duty cycle of 62.5%. Figure 5.24 shows the obtained specific removal rates for steel as (i) a function of the repetition rate and (ii) a function of the overlap $o = 1 - {}^{p_x}\!/_{2w}$. As expected, the maximum specific removal rates are higher for 3 ps than for 10 ps but a drop of about 10% is observed when the repetition rate is raised from 10.13 MHz up to 40.5 MHz. For the latter, the maximum specific removal rate is obtained already at a peak fluence of about 0.3 J cm^{-2}, whereas for the repetition rate of 10.13 MHz, the optimum peak fluence amounts to 0.433 J cm^{-2}. The corresponding points are highlighted by circles, and the SEM micrographs of the obtained surfaces are shown in Figure 5.25a. Compared to the result for the optimum fluence for the 10 ps pulses at a repetition rate of 200 kHz, shown in Figure 5.16 lower left, the surfaces for 10.13 and 40.5 MHz are covered with bumps. Bauer et al. (2015a) showed that these bumps appear on steel surfaces if the maximum temperature due to heat accumulation just before the next pulse impinges on the surface exceeds a threshold value of about 610°C. Therefore, it is assumed that the bumps, as shown in Figure 5.25a, are caused by heat accumulation. For the repetition rate of 10.13 MHz, the overlap

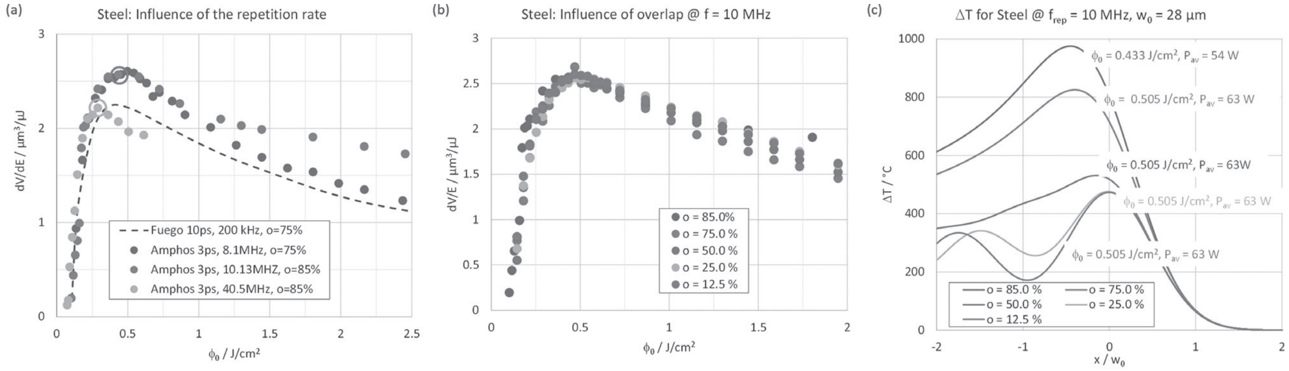

FIGURE 5.24 Specific removal rate for steel as a function of the applied peak fluence for different repetition rates (a) and different overlaps at a repetition rate of 10.13 MHz. (c) shows the calculated temperature raises at the optimum peak fluences due to heat accumulation for the situations shown in (b). The two rings in (a) denote the parameters for which the surfaces are shown in Figure 5.25a.

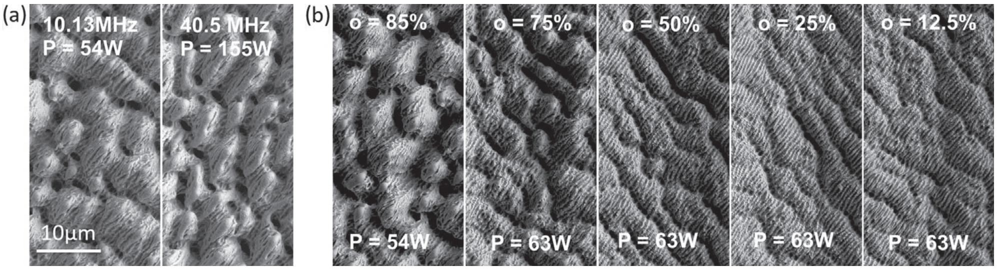

FIGURE 5.25 SEM micrographs of the machined surfaces at the optimum peak fluences (a) for the repetition rates of 10.13 and 40.5 MHz, as shown in Figure 5.24a, and (b) for different overlaps at a repetition rate of 10.13 MHz, as shown in Figure 5.24b. For the overlap of 0.85, the peak fluence amounted to 0.433 J cm^{-2}, whereas it was 0.505 J cm^{-2} for all other situations.

was constantly decreased from 0.85 to 0.125 by increasing the marking speed up to the limit of 480 m s^{-1}. The corresponding specific removal rates are shown in Figure 5.24b, and the SEM micrographs of the surfaces in Fig. 5.25 (for the overlap of 0.85, the peak fluence amounted to 0.433 J cm^{-2}, whereas it was 0.505 J cm^{-2} for all other overlaps). Although the specific removal rates do not significantly differ, the formation of bumps disappears between an overlap of 0.75 and 0.5. Figure 5.24c shows the temperature raise, for a pulsed Gaussian heat source moving along a straight line, just before the next pulse will impinge onto the surface. The calculations were done following the analytic expression presented in Bauer et al. (2015a) deduced with a longer calculation following (5.10). These calculations clearly show that the maximum temperature raise decreases from about 820°C to about 550°C and therefore below the threshold temperature when the overlap is reduced from 0.75 to 0.5, which corresponds to the surfaces as shown in Figure 5.25.

Thus, heat accumulation is a serious issue for steel. Based on the analytical model and the threshold temperature of about 610°C, Neuenschwander et al. (2015a) discuss several strategies to scale up to 100 W average power for steel without bump formation. Following (5.41), the marking speed can be reduced by increasing the spot size *w*. For an average power of 100 W, the maximum temperature raise would stay below 600°C for a spot radius of 50 µm, which may be not well suited for micromachining. For a given spot radius of 22.6 µm going with a repetition rate of 26 MHz, a marking speed of >800 m s^{-1} going with an overlap <0.3 would be demanded leading to a separation of the single spots and an uneven surface. In the same work, it is shown that this drawback can be overcome by an "interlaced" mode, i.e. a given pattern can be divided into *n* subpatterns having *n* times the distance between two spots as illustrated in Figure 5.26. In this mode, the appearance of bumps can be avoided by finally keeping the overlap and resolution. However, this mode demands very high marking speeds, repetition rates and a full synchronization (Jaeggi et al. 2012) between the scanning device and the laser source, and power scale-up for steel remains a demanding task.

5.4.3.2 Plasma and Particle Shielding

By pump-probe experiments, Koenig et al. (2005) have shown that the transmission perpendicular to the direction of the incoming ultra-short pulse is affected by shielding effects. Within the first 30 ns after the pulse, the transmission almost vanishes due to absorption in the generated plasma followed by a weaker absorption in the expanding particle plume as illustrated in Figure 5.27. As a repetition rate of 1 MHz already corresponds to a time interval of 10^{-6}s between two pulses, particle shielding could become evident for higher repetition rates. For steel with a fluence of 0.4 J cm^{-2}, a reduction of the transmission to 90% within the first few tens of ns was measured, which corresponds well with the drop in the specific removal rate observed for 40.5 MHz on steel, as shown in Figure 5.24a. However, most applied fluences in the experiments in Koenig et al. (2005) were much higher than the ones that are used for surface structuring, and a direct transformation of the results is not possible.

Figure 5.28a shows the specific removal rate for copper as a function of the applied peak fluence for different repetition rates ranging from 2 to 40 MHz. It can clearly be seen that the maximum specific peak fluence decreases with increasing repetition rate. For 40 MHz, it amounts less than half of the value obtained for 2 MHz; thus, plasma/particle shielding becomes dominating for repetition rates of a few MHz and higher. SEM micrographs of the obtained surfaces machined at 5.06, 10.13 and 40.5 MHz with an average power of 305 W, i.e. at the highest peak fluence, are shown in Figure 5.18b. In contrast to steel, the surface quality for the repetition rate of 40.5 MHz is still high although more melting effects can be observed. But the increased shielding affects the removal rate, which amounted to 40, 32 and 13 mm^{3}min^{-1} for 5.06, 10.13 and 40.5 MHz, respectively.

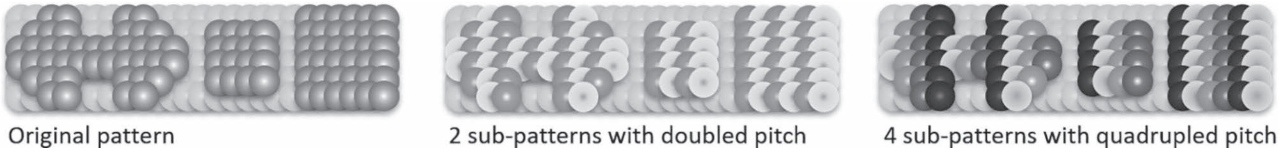
Original pattern
2 sub-patterns with doubled pitch
4 sub-patterns with quadrupled pitch

FIGURE 5.26 Interlaced mode by dividing one pattern in *n*-sup patterns having *n* times the distance between two spots.

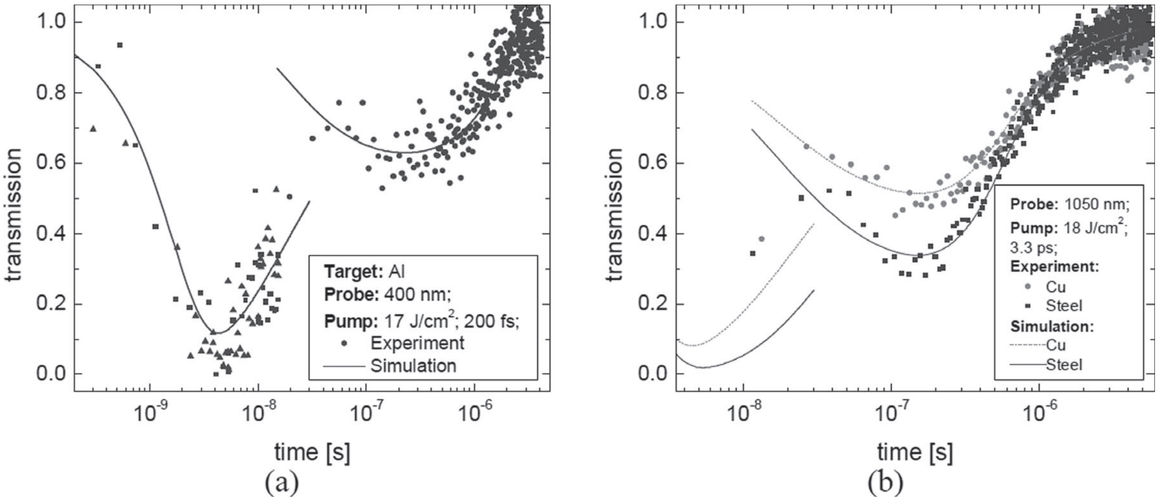

FIGURE 5.27 (a) Temporal transition of probe pulses with a wavelength of $\lambda_{\text{probe}}=400\,\text{nm}$ for the ablation of aluminum with $\tau_H=200\,\text{fs}$ pulses at a peak fluence of $\phi_0=17\,\text{J cm}^{-2}$; (b) temporal transmission of probe pulses with a wavelength of $\lambda_{\text{probe}}=1050\,\text{nm}$ for ablation of $\tau_H=3.3$ ps pulses at $\phi_0=18\,\text{J cm}^{-2}$ (Reprinted by permission from: The Optical Society of America, Optics Express Vol. 13, Issue 26, pp. 10597–10607 (2005): "Plasma evolution during metal ablation with ultra-short laser pulses", J. König, S. Nolte, and A. Tünnermann, doi.org/10.1364/ OPEX.13.010597.)

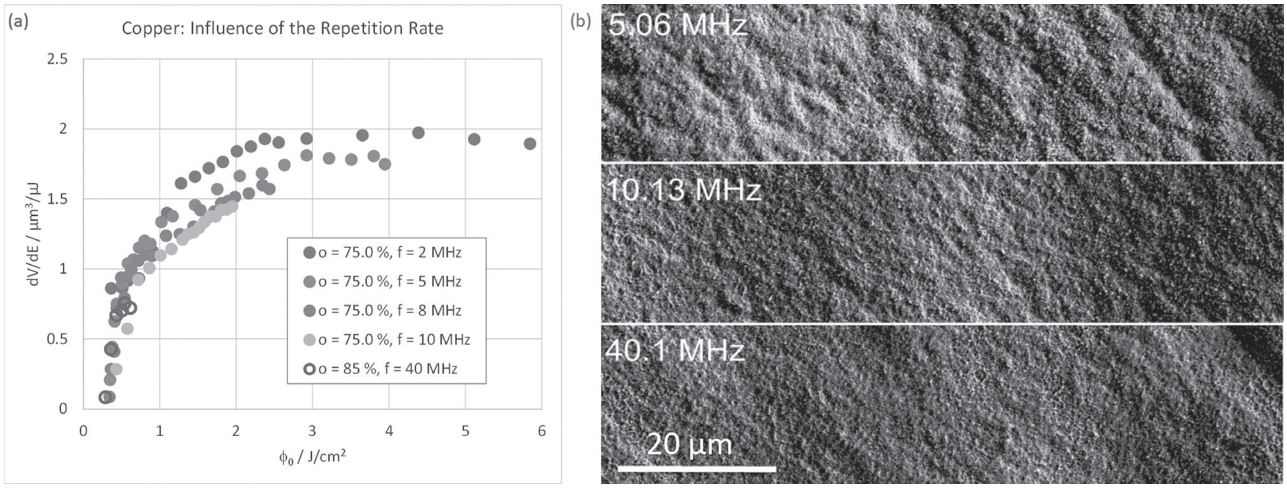

FIGURE 5.28 (a) Specific removal rate for copper as a function of the peak fluence for different repetition rates and overlaps. (b) SEM micrographs of the surfaces machined with 305 W average power but different repetition rates.

Thus, for copper (and many other nonferrous metals), plasma/particle shielding strongly limits the scale-up process for repetition rates exceeding a few MHz. In principal, the "interlaced" mode discussed in the previous subsection should also help to significantly reduce the influence of these shielding effects. Anyway, by working at fluences above the optimum value, removal rates of up to $40\,\text{mm}^3\text{min}^{-1}$ with acceptable surface quality were achieved, and removal rates up to $1\,\text{mm}^3\text{s}^{-1}$ should be achievable with a few 100 W of average power. However, a scale-up into the 1 kW regime is considered as unrealistic with today's technical equipment.

5.4.4 Pulse Bursts

The previous subsections clearly showed that the power scale-up process is often limited by the high repetition rates and marking speeds which should be used. One often discussed method to reduce the demands on the repetition rate is the use of pulse bursts (Knappe et al. 2010). A burst denotes a sequence of consecutive pulses with a short intra-burst time separation from 1 ns up to a few tens of ns, corresponding to the repetition rate of the seed laser. The bursts itself are then emitted by the laser system with their repetition rate. In general, the advantage of the burst mode is the reduction of the peak fluence for the single sub-pulses in the burst: If the lasers system runs at a given repetition rate and average power, the sub-pulses in a burst with *n* pulses have a *n* times reduced peak fluence (and energy) compared to single pulses at identical repetition rate and average power. With this, the peak fluence of the sub-pulses can be near the optimum value (5.29) although the whole burst sequence contains a high energy.

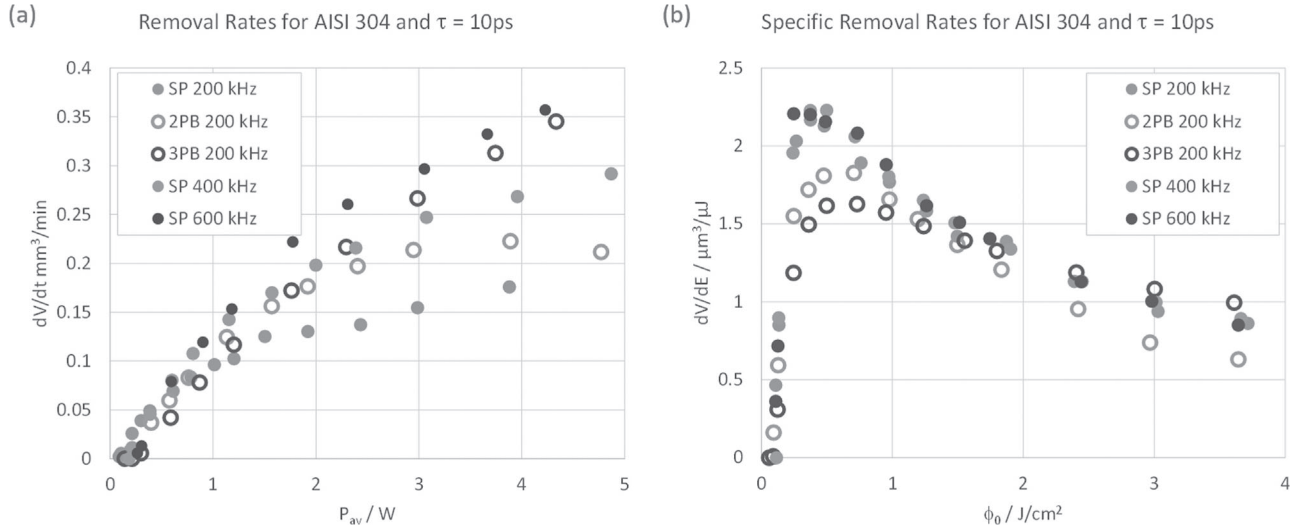

FIGURE 5.29 (a) Removal rate as a function of the average power and (b) specific removal rate as a function of the peak fluence for steel and for single pulses at 200, 400 and 600 kHz as well as a two-pulse and a three-pulse burst at 200 kHz.

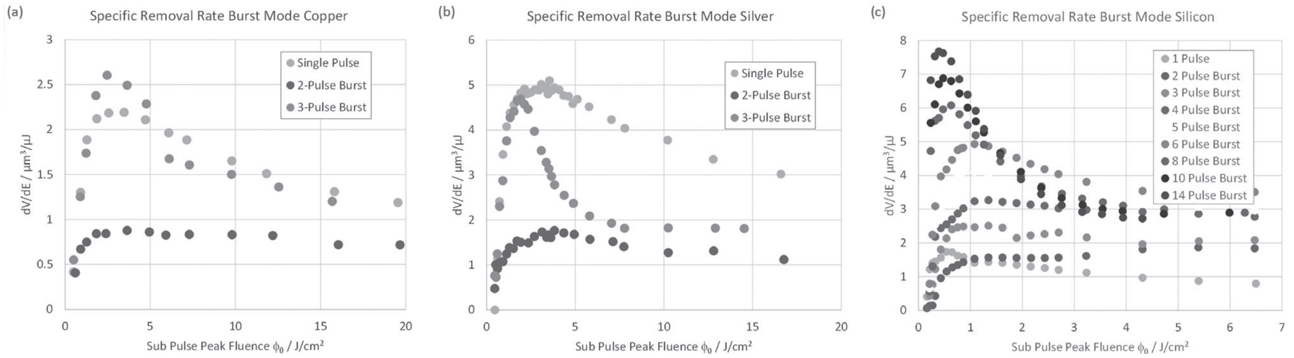

FIGURE 5.30 Specific removal rate for single pulses, a two-pulse burst and a three-pulse burst for (a) copper and (b) silver for 10 ps pulses at 1064 nm with an intra-burst time separation of 12 ns. (c) Specific removal rate for silicon with the same laser parameters but up to a 14-pulse burst.

But in general bursts are not more efficient than single pulses because a burst with *n* pulses should be compared with single pulses at an *n* times higher repetition rate to have the same average power and sub-pulse peak fluence. If the energies of the *n* sub-pulses can be adjusted so that they equal each other, the specific removal rate can be given in terms of the sub-pulses and a direct comparison becomes possible. This is illustrated for steel in Figure 5.29: In (a), the removal rate for single-pulse, a two-pulse and a three-pulse burst at a repetition rate of 200 kHz is shown as a function of the average power. Indeed, the removal rate increases with the number of pulses per burst, but compared to single pulses at 400 kHz, the removal rate for two-pulse burst is lower and the same effect is observed for the three-pulse burst and single-pulse burst at a repetition rate of 600 kHz. This fact is reflected in the specific removal rate, which is identical for all single-pulse situations. For the two-pulse and the three-pulse burst, the maximum specific removal rate is reduced compared to single pulses. But for steel pulse bursts can have other advantages compared to single pulses. If the number of pulses in the burst and its peak fluence are chosen in proper way, a melting effect on the surface can be induced as shown in Neuenschwander (et al. 2015b). This will in fact flatten the surface and prevent CLP formation, and together with an additional cleaning step at significantly lower fluence, a polishing of the surface can be obtained.

Therefore, in general, using a pulse burst will not lead to higher efficiencies but can show further advantages like surface melting and reduces the demands on the repetition rate and marking speed to work near the optimum points. But there exist situations where the burst mode can lead to a higher efficiency indeed.

A surprising behaviour is observed for copper and silver or gold; the results for 10 ps pulses at 1064 nm with an intra-burst time separation of 12 ns for copper and silver are shown in Figure 5.30 a and b. For all three metals, the specific removal rate for a two-pulse burst drops below half of the value for single pulses; i.e., material has to be re-deposited on the surface (Kramer 2017; Foerster et al. 2018) by the second pulse. If a third pulse is added to the burst, the specific removal rate significantly increases up to the values of single pulses for silver and even higher for copper, i.e. the third pulse for itself seems

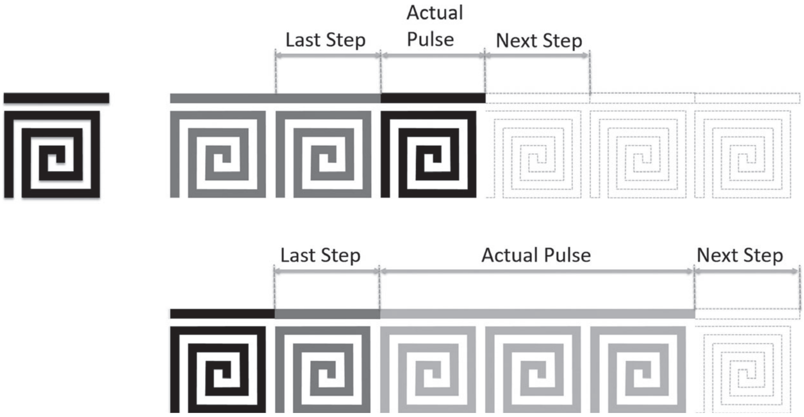

FIGURE 5.31 Sketch of "stamping" with a DOE; upper row with one elementary cell and lower row with 3×1 elementary cells both moved forward by 1 period between two pulses.

to be significantly more efficient than the first one. Omitting the second pulse would lead to a two-pulse burst with twice intra-burst time separation, again leading to a specific removal rate below half of the one of single pulses (Neuenschwander et al. 2015a, 2017). Thus, the inefficient second pulse is needed so that the third can be efficient. Foerster et al. (2018) showed for copper that the second pulse is re-depositing material but also almost completely removes the particle plume and the third pulse will then be undisturbed. Jaeggi et al. (2018) and Neuenschwander et al. (2019) have further shown that the absorptance of a copper surface increases from 13% to 16% and 26% when it is machined with a two-pulse burst and a three-pulse burst, respectively. This means that for a three-pulse burst at least the first pulse in the burst is absorbed twice as much compared to single pulses. This effect can finally explain the surprising behaviour observed for two- and three-pulse bursts for copper, silver and gold. Due to the lower threshold fluence and the smaller amount of ablated material per pulse at the optimum point, it is expected that steel would show a similar behaviour when the intra-burst time separation could be reduced down to 1 or 2 ns.

An even more pronounced effect is observed for silicon and 10 ps pulses at 1064 nm with an intra-burst time separation of 12 ns. About a five times higher maximum specific removal rate is obtained by applying a 14-pulse burst compared to single pulses as illustrated in Figure 5.30c. Non-linear absorption effects (5.4) and not changes in the absorptance are expected to be responsible for this observed gain in the specific removal rate.

5.4.5 Alternative Approaches

Another possibility to overcome the bottleneck of missing fast-beam guiding systems is multisport processing. Bursts as discussed in the previous subsection can be considered as temporal multisport processing. A spatial multisport processing can be realized with a corresponding diffractive optical element (DOE) with an adapted optics in front of the scanning device. This method, for example, allows the generation of a pattern with $N = m \cdot n$ equally spaced spots. In a first approximation the average power in (5.41) can then be divided by the number of used spots N. An application in structuring of solar cells is, for example, described in Schuetz et al. (2012), and first multi-beam scanners are already available on the market. However, this technology is limited to parallel processing of identical structures.

Spatial light modulators (SLMs) are variable DOEs and offer more flexibility. They, for example, offer the possibility to dynamically change the spot pattern and the number of spots (Paivasaari et al. 2014) or to generate specific intensity distributions like triangles (Beck et al. 2010). In this case, one benefits from the higher spot area and therefore pulse energy, i.e. reduced repetition rate to work at the optimum fluence. As SLMs are phase-only devices, they suffer from speckles which can significantly be reduced by averaging different holograms for the same pattern (Haefner et al. 2018). But today, the available SLMs are still limited in speed with about 50–100 Hz refresh rate and also maximum average power of about 200 W. However, SLMs are a very promising approach for future applications.

If a pattern has to be periodically reproduced, it can also be generated by a DOE, which has a significantly bigger resolution than an SLM. This pattern can then be stamped by moving exactly one elementary cell forward between two pulses but would demand a fully synchronized scanning device (Jaeggi et al. 2012). The pulse energy needed per pulse can further be increased by generating a pattern with multiples of the elementary cell but still moving only one forward between two pulses as illustrated in Figure 5.31.

Some regular and repetitive patterns can also be produced by multi-beam interference leading to the technology of direct laser interference pattering (DLIP), which allows to generate periodic patterns on metal surfaces as embossing cylinders with very high throughput (Bieda et al. 2016).

5.5 Summary and Future Challenges

The previous sections clearly showed that USP laser systems are very well suited for high-quality laser micromachining. Process efficiency and process quality can be optimized by choosing the right fluence, wavelength and pulse duration. But the needed energy per pulse is often only small, making the use of high-power lasers a demanding task as high marking speeds and repetition rates will be needed. High-speed polygon scanners can offer marking speeds up to several 100 m s^{-1}, but the scale-up process is limited, on the one hand, by heat accumulation and shielding effects and, on the other hand, by the demand for single pulse switching and synchronization at very high repetition rates. Pulse bursts offer a possibility to reduce the demands on the repetition rate but still many open questions have to be solved to understand the light–matter interaction in more detail to take an optimum benefit of pulse bursts.

The development of USP laser system continues, 100–200 W is becoming industrial standard, and systems in the kW regime are under development in the laboratories of different research institutions. Thus, missing average power will not be the future problem; the bottleneck is the system technology which is able to deal with these powers and is able to make laser micromachining even more economic. Multi-beam and direct patterning combined with today's standard scanning technologies are promising approaches on the way to kW laser micromachining.

REFERENCES

Bauer, F., Michalowski, A., Nolte, S. 2015a. Residual heat in ultra-short pulsed laser ablation of metals. *JLMN J. Laser Micro Nanoeng.* 10: 325–328.

Bauer, F., Michalowski, A., Kiedrowski, T., Nolte, S. 2015b. Heat accumulation in ultra-short pulsed scanning laser ablation of Metals. *Opt. Expr.* 23: 1035–1043.

Bäuerle, D. 2000. *Laser Processing and Chemistry*, pp. 101–143. Springer – Verlag, Berlin.

Beck, R.J., Parry, J.P., McPherson, W.N., et al. 2010. Application of cooled spatial light modulator for high power nanosecond laser micromachining. *Opt. Expr.* 18: 17059–17067.

Bieda, M., Siebold, M., Lasagni, A.F. 2016. Fabrication of submicron surface structures on copper, stainless steel and titanium using picosecond laser interference patterning. *Appl. Surf. Sci.* 387: 175–182

Bonse, J., Wrobel, J.N., Krüger, J., Kautek, W. 2001. Ultrashort-pulse laser ablation of indium phosphide in air. *Appl. Phys. A* 72: 89–94

Byskov-Nielsen, J., Savolainen, J.M., Christensen, M.S., Balling, P. 2010. Ultra-short pulse laser ablation of metals: threshold fluence, incubation and ablation rates. *Appl. Phys. A* 101: 97–101

Chichkov, B.N., Momma, C., Nolte, S., Alvensleben, F., Tünnermann, A. 1996. Femtosecond, picosecond and nanosecond laser ablation of solids. *Appl. Phys. A* 63: 109–115

Derrien, T.J.Y., Sarnet, T., Sentis, M., Itina, T.E. 2010. Application of a two-temperature model for the investigation of the periodic structure formation on Si surface in femtosecond laser interactions. *J. Optoelectr. Adv. Mater.* 12: 610–615.

Foerster, D., Faas, S., Groeninger, S., et al. 2018. Shielding effects and re-deposition of material during processing of metals with bursts of ultra-short laser pulses. *Appl. Surf. Sci.* 440: 926–931.

Gafner, M., Remund, M.S., Chaja, M., Maehne, T., Neuenschwander, B. 2020. Ultrafast stamping by combination of synchronized galvanometer scanning with DOE's or SLM. *Procedia CIRP* 94: 802 – 806.

Grehn, M., Seuthe, T., Höfner, M., et al. 2014. Femtosecond-laser induced ablation of silicate glasses and the intrinsic dissociation energy. *Opt. Mat. Expr.* 4: 689–700.

Haefner, T., Strauss, J., Roider, C., Heberle, J., Schmidt, M. 2018. Tailored laser beam shaping for efficient and accurate microstructuring. *Appl. Phys. A* 124: 111.

Jaeggi, B., Foerster, D., Weber, R., Neuenschwander, B. 2018. Residual heat during laser ablation of metals with bursts of ultra-short pulses. *Adv. Opt. Technol.* 7: 175–182.

Jaeggi, B., Neuenschwander, B., Hunziker, U. et al. 2012. Ultra high precision surface structuring by synchronizing a galvo scanner with an ultra short pulsed laser system in MOPA arrangement. *Proc. SPIE* 8243: 82430K.

Jaeggi, B., Neuenschwander, B., Remund, S., Kramer, T. 2017a. Influence of the pulse duration and the experimental approach onto the specific removal rate for ultra-short-pulses. *Proc. SPIE* 10091: 100910J.

Jaeggi, B., Neuenschwander, B., Zimmermann, M., et al. 2014. High throughput and high precision laser micromachining with ps-pulses in synchronized mode with a fast polygon line scanner. *Proc. SPIE* 8967: 89670Q.

Jaeggi, B., Remund, S., Streubel, R., Goekce, B., Barcikowski, S., Neuenschwander, B. 2017b. Laser micromachining of metals with ultra-short pulses: Factors limiting the scale-up process. *JLMN J. Laser Micro Nanoeng.* 12: 267–273.

Jee, Y., Becker, M.F., Walser, R.M. 1988. Laser induced damage on single-crystal metal surfaces. *J. Soc. Am. B* 5: 648–549.

Klett, I., Rethfeld, B. 2018. Relaxation of a nonequilibrium phonon distribution induced by femtosecond laser irradiation. *Phys. Rev. B* 98: 144306.

Knappe, R., Haloui, A., Seifert, A., Weis, A., Nebel, A. 2010. Scaling ablation rates for picosecond lasers using burst micromachining. *Proc. SPIE* 7585: 75850H.

Koenig, J., Nolte, S., Tünnerman, J. 2005. Plasma evolution during metal ablation with ultrashort laser pulses. *Opt. Expr.* 13: 10597–10607.

Kramer, T., Zhang, Y., Remund, S., et al. 2017. Increasing the specific removal rate for ultra short pulsed laser-micromachining by using pulse bursts. *JLMN J. Laser Micro/Nanoeng.* 12: 107–114.

Lauer, B., Jaeggi, B., Neuenschwander, B. 2014. Influence of the pulse duration onto the material removal rate and machining quality for different types of Steel. *Phys. Proceedia* 56: 963–972.

Liu, J.M. 1982. Simple technique for measurements of pulsed Gaussian-beam spot sizes. *Opt. Lett.* 7: 196–198.

Momma, C., Cichkov, B.N., Nolte, S., et al. 1996. Short-pulse laser ablation of solid targets. *Opt. Commun.* 129: 134–142.

Neuenschwander, B., Bucher, G.F., Nussbaum, C. et al. 2010. Processing of metals and dielectric materials with ps-laserpulses: Results, strategies, limitations and needs. *Proc. SPIE* 7584: 75840R.

Neuenschwander, B., Jaeggi, B., Foerster, D., Kramer, T., Remund, S. 2019. Influence of the burst mode onto the specific removal rate for metals and semiconductors. *J. Laser Appl.* 31: 022203.

Neuenschwander, B., Jaeggi, B., Schmid, M., et al. 2013. Factors controlling the incubation in the application of ps laser-pulses on copper and iron surfaces. *Proc. SPIE* 8707: 86070D.

Neuenschwander, B., Jaeggi, B., Zimmermann, M., Markovic, V., Resan, B., Weingarten, K. 2015a. Laser surface structuring with 100 W of average power and sub-ps pulses. *J. Laser Appl.* 28: 022506.

Neuenschwander, B., Kramer, T., Lauer, B., Jaeggi, B. 2015b. Burst mode with ps- and fs-pulses: Influence on the removal rate, surface quality and heat accumulation. *Proc. SPIE* 9350: 93500U.

Nolte, S., Momma, C., Jacobs, H., et al. 1997. Ablation of metals by ultrashort laser pulses. *J. Opt. Soc. Am. B* 14: 2716–2722.

Paivasaari, K., Silvennoinen, M., Kaakkunen, J., Vahimaa, P. 2014. Femtosecond laser processing and spatial light modulator. *Proc. SPIE* 8967: 89670F.

Preuss, S. Demchuk, A., Stuke, M. 1995. Sub-picosecond UV laser ablation of metals. *Appl. Phys. A* 61: 33–37.

Preuss, S., Späth M., Zhang, Y., Stuke, M. 1993. Time resolved dynamics of subpicosecond laser ablation. *Appl. Phys. Lett.* 62: 3049–3051.

Raciukaitis, G., Brikas, M., Gecys, P., Voisiat, B., Gedvilas, M. 2009. Use of high repetition rate and high power lasers in microfabrication: How to keep the efficiency high? *JLMN J. Laser Micro/Nanoeng.* 4: 186–191.

Ready, J.F. 2001. *LIA Handbook of Laser Materials Processing.* ed. D.F. Farson, pp. 184–201, Orlando, FL: Laser Institute of America.

Rosenfeld, A., Lorenz, M., Stoian, R. 1999. Ultrashort-laser-pulse damage threshold of transparent materials and the role of incubation. *Appl. Phys. A* 69(suppl): 373–376.

Schille, J., Schneider, L., Loeschner, U. 2015. Process optimization in high-average-power ultrashort pulse laser microfabrication: How laser process parameters influence efficiency, throughput and quality. *Appl. Phys. A* 120: 847–855.

Schuetz, V., Horn, A., Stute, U. 2012. High-throughput process parallelization for laser surface modification on Si-Solar cells: determination of the process window. *Proc. SPIE* 8244: 82440X.

Stuart, B.C., Feit, M.D., Herman, S., Rubenchik, A.M. Shore, B.W., Perry, M.D. 1996. Optical ablation by high-power short-pulse lasers. *J. Opt. Soc. Am. B* 13: 459–468.

Tsukumoto, M., Kayahara, T., Nakano, H., et al. 2007. Microstructures formation on titanium plate by femtosecond ablation. *J. Phys. Conf. Ser.* 59: 666–669.

van Driel, H.M. 1987. Kinetics of high-density plasmas generated in Si by 1.06- and 0.53-μm picosecond laser pulses. *Phys. Rev. B* 35: 8166–8176.

Von Allmen, M., Blatter, A. 1995. *Laser–Beam Interactions with Materials.* Springer Series in Material Sciences, eds. U. Gonser, M.B. Panish, pp. 41–54. Springer-Verlag, Berlin.

Weber, R., Graf, T., Berger, P., et al. 2014, Heat accumulation during pulsed laser processing. *Opt. Expr.* 22: 11312–11324.

Weber, R., Graf, T., Freitag, Ch., Feuer, A., Kononenko, T., Konov, V.I. 2017. Processing constraints resulting from heat accumulation during pulsed and repetitive laser materials processing. *Opt. Expr.* 25: 3966–3979.

6

Rapid Manufacturing

Gary K. Lewis

CONTENTS

6.1 Basic Principles 71
6.2 Main Technologies and System Requirements 72
    6.2.1 Control of Material Composition Changes 74
6.3 Case Study 75
6.4 Future Trends 77
References 78

6.1 Basic Principles

The term ‘rapid prototyping’ is used to describe the fabrication technology that has advanced primarily since the 1980s for building models, prototypes or components directly from a computer component design [1–8]. Such processing is also referred to generally as ‘solid free-form fabrication’, ‘direct deposition’, ‘layered manufacturing’ and ‘automated fabrication’. With this technology, component shapes are formed in a single step from a three-dimensional computer model by additively stacking planar layers of deposited material. In contrast, subtractive processes, such as computer numerical control (CNC) machining, remove material to form a component. Rapid prototyping requires only a motion path or deposition control code, developed from a solid model, to deposit material where desired to reproduce the design in solid form. Comparatively, conventional processing requires moulds, dies or exterior fixtures combined with pressing, extrusion, rolling, stamping, casting or forging equipment to force material into a desired shape for a particular application.

Additive processing techniques are applied to polymer, metal, ceramic, intermetallic and composite material systems [9–14]. The first additive technologies introduced in the 1980s used ultraviolet light to solidify the top surface of a liquid polymer into a planar cross-sectional layer of a desired component. The light source is either a laser beam that scans the desired area producing overlapping lines of solidified material, or a lamp that shines through a mask producing an entire layer in one exposure. After the planar cross section is exposed and solidified it is indexed down into the liquid by a distance equal to the layer thickness and the next layer is built on top. Thermoplastic powders are processed into components by rolling out a planar layer of powder and scanning a laser across the powder bed, line by line, to fuse the powders together where desired. Additional layers are built on top until the entire part is produced. Wax components are fabricated by heating and extruding wax through a deposition head to produce lines of material that are placed side by side to form planar layers. Similarly, ceramics are deposited in lines as a slurry, to form cross-sectional layers that are dried and fired to form solid parts. Ink-jet-like printing machines are used to accurately inject liquid binders onto powder beds that dry to form a planar cross-sectional layer. Deposition heads that carry laser-focusing optics are used to melt metal powder feed to produce line deposits and build planar layers into components. Other processes use lasers to cut out planar layers from paper or metal sheet stock, which are bonded together for additive build-up of components.

The primary advantages of using rapid prototyping technology are (i) reduced fabrication cost; (ii) reduced time to market; and (iii) enhanced fabrication capability for component features that cannot be made, or are too complicated by conventional fabrication methods. As the technology has developed, the applications have spread from fabrication of models and prototypes to patterns and functional components [15–17]. For example, photopolymer, thermoplastic, wax and paper patterns made from various rapid prototyping processes are used to produce investment casting moulds for metallic parts, such as gas turbine engine blades or golf club heads. Higher accuracy, repeatability, lower costs and less time in producing patterns are realized. Fabrication of injection moulding dies and moulds using direct metal deposition rapid prototyping technology can reduce time to market by reducing conventional mould making time by one-tenth. Use of the enhanced fabrication capability of rapid prototyping allows placement of cooling channels in injection moulding dies for optimal cooling rate, resulting in reduced cycle time for high production volume manufacturing. Optimized placement may otherwise be impossible by conventional machining or require complex welded assemblies. Fabrication of materials that are difficult to form conventionally, such as tungsten, which requires many metal processing steps, is processed similarly in one step using the additive deposition approach of rapid prototyping.

6.2 Main Technologies and System Requirements

Direct deposition of metal to additively build a functional component [18–26] is the subject of ongoing research and development efforts. The directed light fabrication (DLF) process [27] is shown in Figure 6.1. A three-dimensional part is defined by a solid model on a computer, and a motion path is created to control a five-axis motion system. The motion control program moves the focal zone of an Nd–YAG laser beam, which melts metal powder into a liquid pool, to form a bead of solidified material as it cools. Beads are placed adjacent to one another with their length defined by the part boundaries so that a cross-sectional layer is formed. Layers are added sequentially until the entire part volume is produced. Five axes of motion provide deposition in any plane, not just the horizontal. Multiple powder feeders can provide different powders to be fed into the laser beam to produce sharp composition changes or gradients within the part. Processing is performed in an argon, inert-gas box with oxygen controlled to 1 ppm levels to prevent oxidation. Control of the bead overlap, layer thickness, laser power, velocity and powder feed can produce fully dense metal parts to high accuracy.

For the DLF process, motion commands are developed much the same as CNC commands are used for milling away of metal in a conventional machining process relative to the solid boundaries of the part. However, commands are created to add metal to build the part rather than subtracting it. The milling tool radius specified for machining is equivalent to the molten pool radius specified for deposition, and the depth of cut specified for machining is equivalent to the layer thickness for deposition. Using this approach allows for flexibility in the motion control system to optimize the deposition process based on the complexities of the desired part. Beads are laid down along any desired contour in any planar orientation, not only in a straight line.

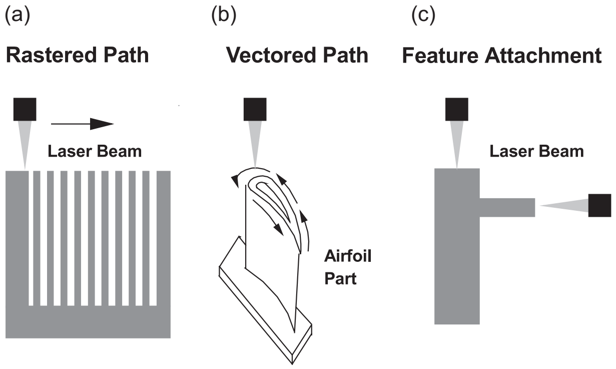

FIGURE 6.2 A CNC programming approach to developing motion commands allows flexibility in depositing a part. Raster mode (left), vector mode (centre) and feature attachment mode (right) are chosen depending on the part complexities for build optimization.

Figure 6.2 shows three primary modes of depositing metal components. A rastered path, shown in the left-hand drawing, simply rasters across the plane containing the part cross section, turning the laser shutter on and off at the part boundaries to start and stop the deposit. In this example, multiple features are built up at the same time instead of individually. A vectored path, shown in the centre drawing, follows around the part boundaries and fills in while the beam remains on the part continuously. The third mode, in the right-hand drawing, is the feature attachment to a main body performed by reorienting the focusing head or part. Motion paths for specific feature attachments can be programmed independently and placed as a subroutine in the deposition motion control program. For example, an aircraft fuselage structure, built vertically along a *z*-axis by adding cross-sectional layers oriented within the

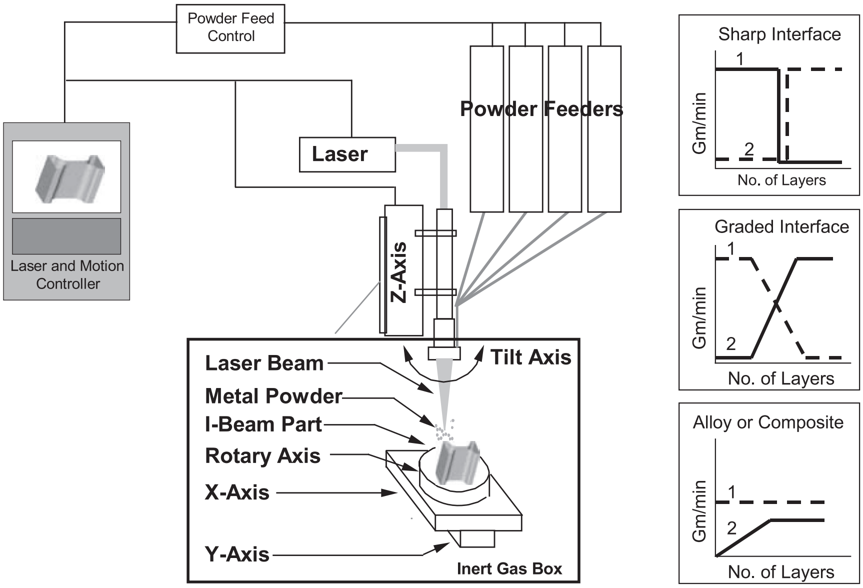

FIGURE 6.1 Schematic diagram of the DLF process. A five-axis motion system moves a laser beam, which fuses metal powder particles a layer at a time to produce the entire part volume. Multiple powder compositions can be fed simultaneously or sequentially.

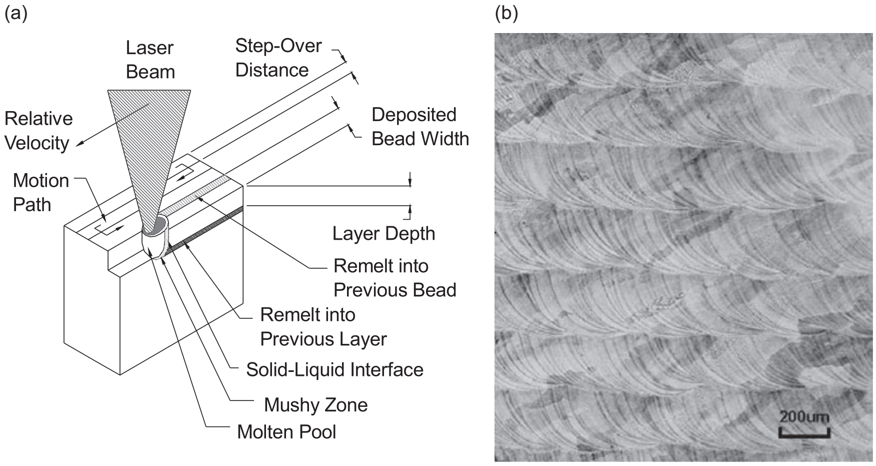

FIGURE 6.3 A plate is made by overlapping beads of metal that are equal to the width of the molten pool created at the laser focal point (left). The microstructure of a type 316 stainless steel deposited plate is shown in the right-hand photograph. Layers were deposited in the horizontal plane at a power of 175 W, a traverse speed of 0.015 m s^{-1}, a bead overlap of 0.3 mm and a layer thickness of 0.25 mm. Each new bead is bonded to the previous layer by re-melting into the top surface of that layer.

x–y horizontal plane, can have wings attached by swinging the deposition head 90° from vertical and building the wing layers oriented in the *z–y* plane additively in the *x*-axis direction.

Many rapid prototyping systems require the development of the motion commands through the use of stereolithography files (.stl file format) [1,2] although new methods are also being developed and interfaced with more advanced solid modelling technology [28]. Stereolithography file generation involves tessellation of the solid model to break it into a system of triangular facets, with each facet defined mathematically by the three corner vertices and a unit normal. A slicing algorithm is used to define the cross-sectional layers to be built to form the part. These types of motion control files are used for deposition in the horizontal, *x–y* plane, making it difficult to build unsupported attachments at varying angles.

Figure 6.3 (a) shows a plate being fabricated using the DLF process. The plate thickness can be equivalent to the diameter of the molten pool produced, or a multiple of that thickness by overlapping beads of deposited material, forming a planar cross-sectional layer. The molten pool can be varied within the size range of 0.5–2.5 mm depending on laser power, velocity and powder feed parameters. High traverse speeds and low powers produce beam widths at the low end of the range, and low traverse speeds and high powers produce beam widths at the high end of the range. The laser focal spot diameter is 0.5 mm and has a power range up to 2000 W continuous wave average power producing a maximum power density of 106 W cm^{-2}. Traverse speeds are typically 25–200 cm min^{-1} (10–80 in min^{-1}), and powder feed is 10–20 g min^{-1}. Layer thickness corresponds to the amount the focal zone is moved to start the next layer and is chosen to provide a small amount of remelting into the top surface of the previous layer to produce complete bonding between layers. Material thermal properties (thermal diffusivity, melting point and enthalpy) and material reflectivity at the 1.06 μm Nd–YAG wavelength determine the laser power required to produce the desired molten pool width and depth. Aluminium and copper, having high thermal diffusivity and high reflectivity, require significantly more power for deposition than a stainless steel alloy (Fe–18Cr–8Ni) having low thermal diffusivity and low reflectivity. The layered microstructure of a deposited-type 316 stainless steel plate is shown in Figure 6.3 (c). Layers are delineated by the horizontal boundaries in the photograph that represent the bottom boundary of the molten pool as a layer is deposited. Each new layer melts into the previous layer to produce a continuous microstructure upon solidification, assuring full density and structural integrity.

Extension of the process to a more complex shape is shown in Figure 6.4, where a hemisphere is being deposited onto a stem, requiring four axes of motion. As the shape is built with successive layers, the laser beam axis is kept perpendicular to the direction of the bead being deposited to form the boundary

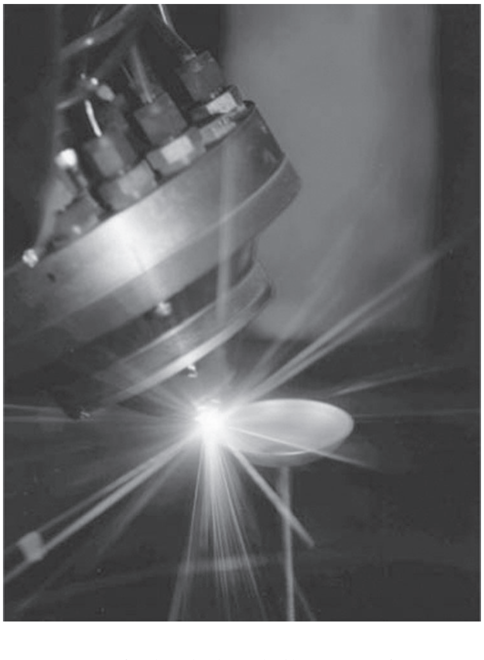

FIGURE 6.4 DLF of a hemisphere built on top of a stem using four axes of motion.

of the hemisphere. The laser head is horizontally tilted at first attachment to the stem and its orientation is changed for each layer added until it becomes perpendicular at the equator of the hemisphere. This requires four axes positioning commands plus a traverse speed command to maintain a constant surface speed for each change in radius, for each new layer. Every layer is deposited in a different planar orientation. If a wall thickness greater than the width of the molten pool is required, additional circumferential overlapping beads are deposited. Each circumferential path requires a new four-axis coordinate command to place the laser focal zone along a radial direction from the centre of the hemisphere.

6.2.1 Control of Material Composition Changes

The DLF technology offers the designer new flexibility to tailor composition and properties within a component. Materials that exhibit inhomogeneous microstructures and properties, and that are placed to respond to specific functional and performance requirements of an intended application, are classed as functionally gradient or functionally graded materials, FGMs [29–32]. FGMs can be applied to design problems involving thermal expansion mismatch between materials, overstress conditions at stress concentrations in components and thermal barrier coatings that require grading from high-temperature oxidation or corrosion resistance to high-temperature strength and toughness. Processing methods to produce FGMs include thermal spray [33], powder processing [34], chemical vapour deposition (CVD) [35], self-propagating high-temperature synthesis [36], physical vapour deposition (PVD) and diffusion treatments. These methods provide the means to change composition in a graded fashion over thickness but are nondirectional, are often limited by symmetry and consequently do not provide the capability to selectively place discrete volumes of material where desired within a component.

The DLF process provides a fabrication method to design material changes into the solid model of a desired component and place materials with different properties where required. By controlling multiple powder feed inputs, metal alloys can be produced at the laser focal zone by inputting two or more materials simultaneously; sharp changes in composition can be created by stopping one powder feed and starting another, and compositional gradients are produced by ramping powder feed rates simultaneously. Control of the metallurgy and chemistry is possible over the entire part at a resolution based on the size of the molten pool created. In contrast, control of properties in conventionally processed metal parts is limited because the entire part is cast into a forming mould, or plastically deformed into a die, resulting in uncontrolled variations in properties with little capability to alter or tailor properties locally.

Figure 6.5 shows an example of compositional control used for functional grading in the fabrication of a four-point-bend specimen. Plastic zone boundaries were calculated using an Abacus finite element code for a specific load applied to a commercially pure nickel 200 bend specimen. The plastic zone boundary coordinates were transferred to the solid model to define the plastic volume to be replaced by the higher strength Ni-30 wt% Cu, Monel K500 alloy, which would not plastically deform under the same applied load. A motion path was then developed that recognized the part boundary and commanded material powder feeders to alter the composition. The desired compositional gradient or sharp interface is produced by ramping two feeders across a region near the boundary, or stopping the feed of one and starting the second at the boundary.

Hardness and composition are shown relative to the boundary in Figure 6.4. The materials were chosen because they represent a simple binary solid solution material system, Ni–Cu, which can be age-hardened when Al and Ti are added to form a gamma prime precipitate (Monel K500). Commercially processed Ni 200 has a yield strength up to 276 MPa (40 KSI) depending on processing. Monel K500 has a yield strength from 276 to 689 MPa (40–100 KSI) as processed and 689–958 MPa (100–135 KSI) when solution-treated and aged providing two different strength options from 'as-deposited' and 'as-deposited plus aged material'.

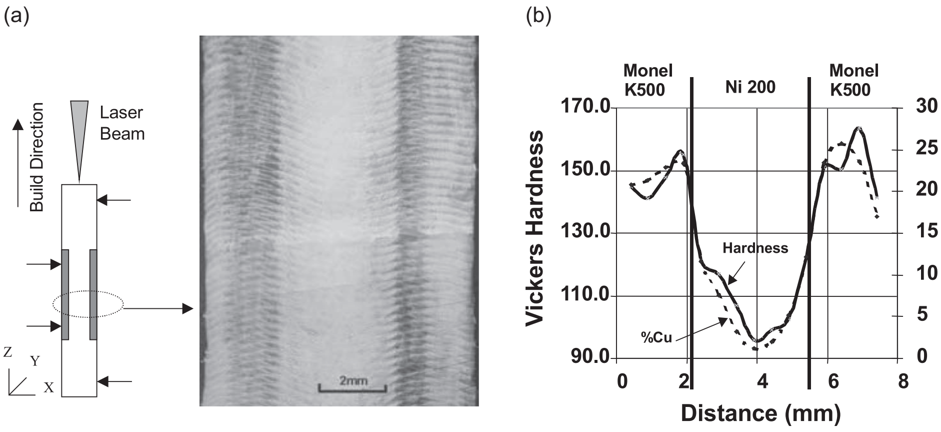

FIGURE 6.5 The shaded areas in the four-point-bend, nickel test specimen were replaced with Monel K500 alloy, having four times the strength of nickel indicated by the hardness and compositional profile (right). The microstructure (centre) shows the transition in composition for the yield volumes that were calculated using finite element analysis. A sharp interface or graded interface can be deposited by control of the powder feed for the two materials during deposition of each planar layer.

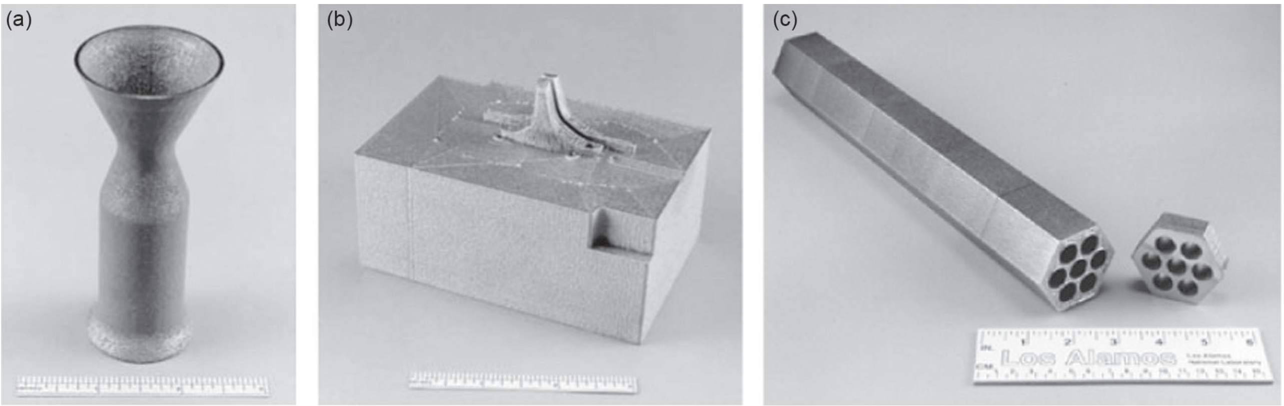

FIGURE 6.6 Examples of components fabricated by the DLF process are a Ti–6Al–4V alloy, 25 mm diameter × 75 mm high, rocket thruster (a), a type 316 stainless steel injection moulding die insert (b) and an Inconel 690 nominal 50 mm × 355 mm high hexagonal conduit (c).

TABLE 6.1

Processing Rates

Component	Material	Deposition Time (h)	Deposition Rate		Powder Flow Rate (g h^{-1})	Powder Efficiency (%)
			(cm^{3}h^{-1})	(gh^{-1})		
Rocket thruster	Ti–6Al–4V	0.75	12	55	431	13
	316 SS	0.87	9.8	77	822	6
Die insert	316 SS	57.7	7.2	59	822	7
Hexagonal conduit	Inconel 690	172	2.1	18	454	4
Plate (2.6 × 0.14″)	Haynes 188	6.3	10.7	95	794	12
Rod (0.75″ diameter)	Inconel 690	15.6	7.2	59	277	21

6.3 Case Study

Figure 6.6 shows a rocket thruster component, an injection moulding die insert and a hexagonal conduit made by the DLF process from three different metal alloys. Build times for each component were 0.8, 58 and 172 h, all unattended operation. Fabrication of each component required a development phase of work and a final build cycle. The development involves establishing process parameter data to achieve full fusion and thereby full density by optimizing process parameters for the alloy and for the motion path chosen for the part. Laser power, velocity, powder feed rate, bead overlap and layer thickness must be optimized based on prior data for the same material or by the evaluation of deposits produced from a parameter matrix. Microstructural evaluation of deposited material is typically used for characterization. Motion path parameters must be optimized based on feature complexity and local thermal diffusivity to maintain a constant width and depth of the molten pool created so that bead overlap and layer thickness remain constant. With process parameters held constant, deposition over a large bulk volume of a block or plate having high thermal diffusivity will produce a small molten pool, whereas deposition over a thin section having low thermal diffusivity will produce a larger molten pool. Typically, trial deposits are used to adjust these parameters prior to a final build of the entire part. Once a knowledge base is established for particular types of features and specific materials, development cycle time is minimized, which reduces the total cost.

Deposition efficiencies are shown in Table 6.1. Total build time, the rate of build in volume and mass per unit time, and the powder efficiency, which is the per cent of powder that actually goes into the built part relative to the total powder fed during the build, are shown. In addition to the three parts shown in Figure 6.6, a plate and rod built from Haynes 188 and Inconel 690 are shown for comparison. Efficiencies and build rates are lowest for the most complex parts – the die insert and the hexagonal conduit – and higher for the less complex parts – the rocket thruster, plate and rod. Powder efficiency depends on the ability to focus the feed powder stream into the molten pool created and can be increased by enlarging the pool with a trade-off in accuracy and fineness of detail.

Material properties of deposits for several materials are compared to conventionally processed material in Table 6.2. As-deposited tensile yield strength of DLF-processed type 316 stainless steel and Inconel 690 exceeded that of conventionally processed wrought material. Tensile elongation was 41% and 49% for the two materials. Tensile yield strength for Ti–6Al–4V, produced by DLF, fell in the equivalent range for wrought material; however, elongation was only 6% compared to 10% and higher for conventionally cast and wrought products.

Tensile data show that properties equivalent to wrought material can be achieved for some materials. This eliminates the need for multiple thermomechanical processing treatments in conventional processing. Chemical segregation in cast ingots, which makes homogenization heat treatments and plastic deformation processing for grain refinement necessary

TABLE 6.2

Tensile Properties of DLF Material Compared to Conventionally Processed Material

Material	0.2 YS MPa (KSI)	UTS MPa (KSI)	Elong (%)
Type 316 Stainless Steel			
DLF (as-deposited)	296 (43)	579 (84)	41
Wrought annealed	262 (38)	572 (83)	63
Investment cast 316	269 (39)	517 (75)	39
Inconel 690 (58Ni–29Cr–9Fe)			
DLF (as-deposited)	450 (65.2)	666 (96.6)	48.8
Hot rolled rod	372 (54)	738 (107)	50
Ti–6Al–4V			
DLF with mill anneal	958 (139)	1027 (149)	6.2
Wrought bar (annealed)	827–1000 (120–145)	931–1069 (135–155)	15–20
Cast + anneal	889 (129)	1014 (147)	10

in ingot metallurgy, is eliminated by using the direct deposition technology to fuse and shape metal powders. Chemical homogenization is achieved through randomization of composition by using powders as input material and by limiting chemical diffusion in the liquid state to the boundaries of the small molten pool that is used to deposit the entire component.

The hexagonal conduit, seven-hole-array structure as shown in Figure 6.6, was built to 356 mm in height from Inconel 690, a difficult-to-process high-temperature, nickel-based alloy. The nominal composition of Inconel 690 in wt% is 58Ni, 29Cr and 9Fe. The part was deposited at a laser power of 160 W, a speed of 12.7 mm s^{-1}, a vertical layer increment of 0.25 mm and a bead overlap of 0.27 mm, and the powder feed rate was approximately 9 g min^{-1}. Oxygen was controlled to less than 10 ppm in an argon atmosphere. Deposition time was 172 h at a rate of 18 g h^{-1} in one continuous, unattended operation. Dimensional inspection of the part features indicated that hole diameters were produced within ±0.05 mm of the specified diameter for six out of the seven holes and were centred to within ±0.13 mm of the specified location. Radial distance from the centre of the cross section to the centre of the hexagonal faces was within ±0.076 mm. Surface roughness was 12 µm, arithmetic average, which is similar to investment cast surfaces. However, one hole was smaller because of an extra deposition pass inserted into the inside radius of the hole motion path, making it 12.62 mm in diameter, and two extra passes were inserted for motion outside the desired hexagon boundary, making it 24.33 mm instead of the specified 23.8 mm. These extra passes could easily be removed from the motion path but a second part was not made.

Cost advantage lies in the single-step processing for metals from powders. Conventional processing requires a method of forming metal into the desired shape, such as using a forging process to force metal into the shape of a die. These processes require large investments in capital equipment (e.g. a forging press or stamping mill), die design and fabrication for each new component, and space. Additionally, preconditioning of metal stock for chemical homogeneity and grain size refinement can require multiple thermomechanical processing steps from the time the metal is cast into billet from raw materials to when it is ready to be placed in the forging press. Some materials that cannot be cast because of chemical segregation are formed by powder metallurgy processes, which also require multiple consolidation and deformation steps. Polymer and other non-metal rapid prototyping processes have helped improve the fabrication of metals by enhancing and reducing the conventional pattern-making processes used for investment casting. However, depositing metals directly with a rapid prototyping process reduces the steps to one, saving time and money, and also eliminates handling and contamination from die lubricants, mould materials and cleaning solvents.

For illustration, Figure 6.7 shows a comparison of some modern metal fabrication process steps divided between pattern-dependent and pattern-independent processing. Shown are electric discharge machining (EDM), investment casting and non-directional processes, e.g. plasma spray, liquid spray, electrodeposition and vapour deposition, which require patterns to produce electrodes, moulds and mandrels in multistep processes. In comparison, CNC machining, subtractive processing and direct deposition of metals, and additive processing produce a part without patterns, moulds and dies direct from a computer solid model. CNC machining produces parts to high accuracy and surface finish compared to direct metal deposition, which would require a finishing polish to achieve a comparable surface finish. However, direct metal deposition processes such as DLF have demonstrated the flexibility to form nearly any metal, or material, that can be made into powder and melted by the laser beam, and the selectivity to deposit mixed materials to take advantage of selected properties in local areas of a part. Additionally, entire assemblies can be made, eliminating the need for weld fixtures and chucks for precision weld processes.

Other cost and time considerations are defined by the production volume requirements. For high production volume, the costs for equipment, space, die design and fabrication are offset by the capability of a stamping process to deliver a part or more per second or minute, compared to a direct deposition process to deliver of the order of a few thousand parts per year. The aircraft industry may have requirements for 100–2000 parts per year but the automotive industry may require the same numbers per day or per hour.

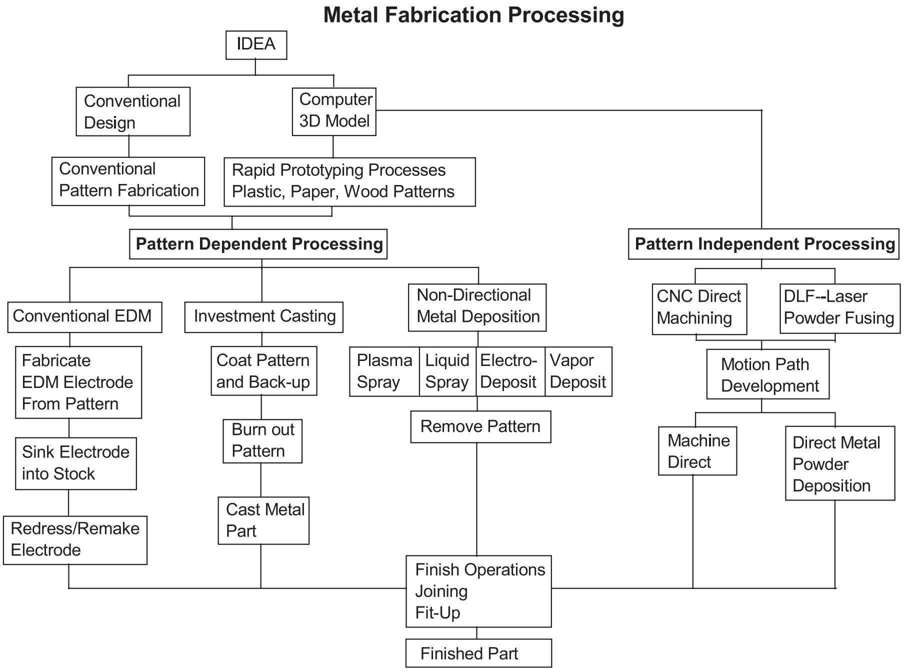
Metal Fabrication Processing
IDEA
Conventional Design
Computer 3D Model
Conventional Pattern Fabrication
Rapid Prototyping Processes Plastic, Paper, Wood Patterns
Pattern Dependent Processing
Pattern Independent Processing
Conventional EDM
Investment Casting
Non-Directional Metal Deposition
CNC Direct Machining
DLF--Laser Powder Fusing
Fabricate EDM Electrode From Pattern
Coat Pattern and Back-up
Plasma Spray
Liquid Spray
Electro-Deposit
Vapor Deposit
Motion Path Development
Remove Pattern
Burn out Pattern
Sink Electrode into Stock
Machine Direct
Direct Metal Powder Deposition
Cast Metal Part
Redress/Remake Electrode
Finish Operations Joining Fit-Up
Finished Part

FIGURE 6.7 A comparison of conventional *versus* rapid prototyping fabrication is divided between pattern-dependent and pattern-independent technologies.

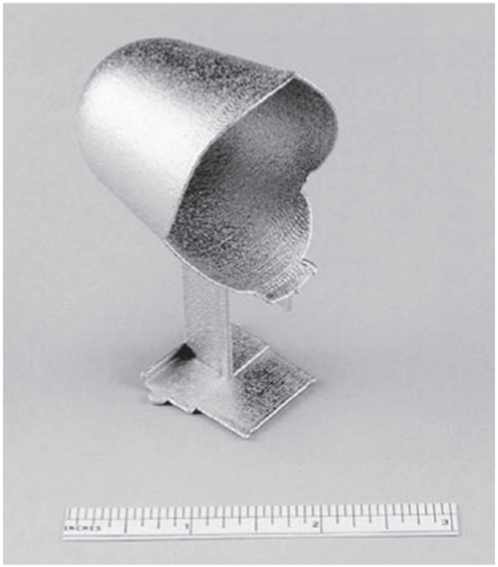

FIGURE 6.8 A headlight bulb holder assembly produced in a single deposition run of approximately 1 h. Conventional processing requires die design and fabrication for stamping and welding of components at 25 times the cost of direct deposition.

However, rapid prototyping processes can be applied indirectly to high production volume manufacturing in the form of prototyping and die fabrication. Figure 6.8 shows a light bulb holder made for an automobile headlight produced by DLF. The part was generated from a computer solid model and deposited using five axes of motion. The 'ears' on the cup portion of the part are computer-generated from models that predict light intensity distribution onto the highway. The cup is typically stamped requiring die design, fabrication and stamping machine. The support leg is cut, rolled and formed from sheet metal and resistance welded to the cup portion requiring additional forming and welding fixtures to be designed and fabricated. Process development is required to develop production forming, assembly and welding parameters. For conventional processing, prototype tooling and process development costs approximately $50 000, and production tooling and process development costs approximately $100 000. DLF processing of a first single part, taking 1 h of deposition and process development, costs approximately $20 000. Although DLF would not be considered for the production of the light holder because volumes are too high, many different prototype models are required for the many different automobile designs. Additional prototypes, once DLF processing is developed and a knowledge base established for the original model, can be made for approximately $2000 development cost and 1 h machine time for approximately a 25 times decrease compared to conventional processing requiring separate tooling design and fabrication for each prototype.

6.4 Future Trends

Rapid prototyping technology offers a new fabrication capability that saves costs by reducing processing steps. The capability to process any material that can be melted and fused by a laser beam into a useful component in a single step, by layered build-up, makes these processes more flexible and applicable than any other metal working process at a cheaper cost. By adjusting the process parameters of laser power, velocity, powder feed rate, bead overlap and layer thickness, tungsten can be processed by the same machine as steel, instead of requiring an entirely different set of processes and related equipment. Where required, different materials or gradients in material composition can be placed within components where required for local property enhancement for design optimization. Component features that are impossible to machine, or require joined assemblies of subcomponents, are made in a single step.

Rapid prototyping has been accepted and used to build models that establish fit and form for polymer applications and as patterns for building investment casting moulds, but worldwide acceptance as a direct metal fabrication process by industry is dependent on additional development. Improvements in surface finish, deposition rate and motion path development technologies are necessary to overcome the resistance to change from developed metal shaping processes of casting and forging and to compete with single-step CNC processing. Additionally, broad acceptance of solid modelling must occur.

The flexibility of the processing must also be recognized and applied by designers and engineers who base current designs on conventional manufacturing and fabrication process technology. Hollow geodesic-type structures can support the same loads as massive solid metal components but are too expensive and complex to fabricate by conventional shaping and joining processes. Layered deposition technology provides the tool to build and vary such structures to efficiently accommodate the design requirements while saving weight, reducing size and controlling properties such as load, thermal transfer and fluid flow. The integration of the design analysis with the solid modelling and deposition process makes the fabrication and use of these structures possible in a single processing step.

REFERENCES

1. Burns M. 1993 *Automated Fabrication-Improving Productivity in Manufacturing* (Englewood Cliffs, NJ: Prentice-Hall).
2. Johnson J. L. 1994 *Principles of Computer Automated Fabrication* (Irvine, CA: Palatino).
3. Wohlers T. 1999 *Rapid Prototyping and Tooling, State of the Industry* (Fort Collins, CO: Wohlers Associates).
4. Pham D. T. and Gault R. S. 1998 A comparison of rapid prototyping technologies, *Int. J. Mach. Tools Manuf.* **38** 1257–87.
5. Conley J. G. and Marcus H. L. 1997 Rapid prototyping and solid free-form fabrication, *J. Manuf. Sci. Eng. Trans. ASME* **119** 811–16.
6. Chua C. K., Chou S. M. and Wong T. S. 1998 A study of the state-of-the-art rapid prototyping technologies, *Int. J. Adv. Manuf. Technol.* **14** 146–52.
7. Grant E. 1997 Rapid prototyping, *IEEE Robot. Autom. Mag.* **4** 17–20.
8. Kochan D., Kai C. C. and Ahaohui D. 1999 Rapid prototyping issues in the 21st century, *Comput. Indust.* **39** 3–10.
9. Pham D. T., Dimov S. and Lacan F. 1999 Selective laser sintering: applications and technological capabilities, *Proc. Inst. Mech. Eng. Part B—J. Eng. Manuf.* **213** 435–49.
10. Spencer J. D., Dickens P. M. and Wykes C. M. 1998 Rapid prototyping of metal parts by 3-dimensional welding, *Proc. Inst. Mech. Eng. Part B—J. Eng. Manuf.* **212** 175–82.
11. Klosterman D., Chartoff R., Graves G., Osborne N. and Priore B. 1998 Interfacial characteristics of composites fabricated by laminated object manufacturing, *Compos. Part A—Appl. Sci. Manuf.* **29** 1165–74.
12. Heschel M., Mullenborn M. and Bouwstra S. 1997 Fabrication and characterization of truly 3–D diffuser/nozzle microstructures in silicon, *J. Microelectromech. Syst.* **6** 41–7.
13. Wang G. and Krstic V. D. 1998 Rapid prototyping of ceramic components, *Can. Ceram.* **67** 52–8.
14. Young J. S., Fox S. R. and Anseth K. S. 1999 A novel device for producing three-dimensional objects, *J. Manuf. Sci. Eng. Trans. ASME* **121** 474–7.
15. Sriraman V., Winek G. and Habingreither R. 1999 Tooling applications of rapid prototyping, *J. Eng. Technol.* **16** 34–8.
16. Springer A. 1998 Evaluating aerodynamic characteristics of wind-tunnel models produced by rapid prototyping methods, *J. Spacecraft Rockets* **35** 755–9.
17. Bocking C., Jacobson D. M., Sangha S. P. S., Dickens P. M. and Soar R. 1997 The production of large rapid prototype tools using layer manufacturing technology, *GEC J. Technol.* **14** 110–14.
18. Bourell D. L., Beaman J. J., Crawford R. H., Marcus H. L. and Barlow J. W. 1997 *Proceedings of the Eighth Solid Free-Form Fabrication Symposium* (Austin, TX: University of Texas).
19. Lewis G. K., Nemec R. B., Milewski J. O., Thoma D. J., Barbe M. R. and Cremers D. A. 1994 Directed light fabrication *Proc. ICALEO'94* (Orlando, FL: Laser Institute of America).
20. Lewis G. K., Thoma D. J., Milewski J. O. and Nemec R. B. 1996 Directed light fabrication of near-net shape metal components. In *World Congress on Powder Metallurgy and Particulate Materials (Washington, DC)* (Princeton, NJ: Metal Powder Industries Federation) pp 15–76.
21. Lewis G. K., Thoma D. J., Milewski J. O. and Nemec R. B. 1997 Directed light fabrication of refractory metals. In 1997 *International Conference on Powder Metallurgy and Particulate Materials (Chicago, IL)* (Princeton, NJ: Metal Powder Industries Federation).
22. Lewis G. K., Milewski J. O., Thoma D. B. and Nemec R. B. 1997 Properties of near-net shape metallic components made by the directed light fabrication process. In *The Eighth solid Free-Form Fabrication Symposium* (Austin, TX: University of Texas).
23. Griffith M. L., Schlienger M. E., Harwell L. D., Oliver M. S., Baldwin M. D., Ensz M. T., Smugeresky J. E., Essien M., Brooks J., Robino C. V., Hofmeister W. H., Wert M. J. and Nelson D. V. 1998 Thermal behaviour in the LENS process. In *Proceedings of the Solid Free-Form Fabrication Symposium* (Austin, TX: University of Texas) p 89.
24. Schlienger M. E., Griffith M. L., Oliver M., Romero J. A., Smugeresky J. 1998 Sacrificial materials for complex geometry fabrication. In *Proceedings Solid Free-Form Fabrication Symposium* (Austin, TX: University of Texas) p 205.
25. Romero J. A., Griffith M. L., Atwood C. L., Smugeresky J. E., Jeantette F. P., Harwell L. D. and Greene D. L. 1996 Laser engineered net shaping (LENSTM) for additive component processing. In *Proceedings of Rapid Prototyping and Manufacturing Conference (Dearborn, MI)* (Albuquerque, NM: SNL).

26. Mazumder J., Choi J., Nagarathnam K., Koch J. and Hetzner D. 1997 The direct metal–deposition of H13 tool steel For 3-D components, *J. Minerals Metals Mater. Soc.* **49** 55–60.
27. Lewis G. K., Milewski J. O., Cremers D. A., Nemec R. B. and Barbe M. R. US Patent 5,837,960, Laser production of articles from powders.
28. Chandru V. and Monohar S. 1997 Volume modelling for emerging manufacturing technologies, *Sadhana—Academy Proc. Eng. Sci.* **22** 199–216.
29. Ghosh A., Miyamoto Y., Reimanis I. and Lannutti J. 1997 *Functionally Graded Materials: Manufacture, Properties, and Applications, 76 Ceramic Transactions* (Westerville, OH: The American Ceramic Society).
30. Rabin B. H. and Shiota I. 1995 Functionally gradient materials, *MRS Bull.* **20** 14–15.
31. Koizumi M. and Niino M. 1995 Overview of FGM research in Japan, *MRS Bull.* **20** 19–21
32. Kaysser W. A. and Iischner B. 1995 FGM research activities in Europe, *MRS Bull.* **20** 22–6.
33. Sampath S., Herman H., Shimoda N. and Saito T. 1995 Thermal spray processing of FGMs, *MRS Bull.* **20** 27–31.
34. Watanabe R. 1995 Powder processing of functionally gradient materials, *MRS Bull.* **20** 32–4.
35. Hirai T. 1995 CVD processing, *MRS Bull.* **20** 45–7.
36. Stangle G. C. and Miyamoto Y. 1995 FGM fabrication by combustion synthesis, *MRS Bull.* **20** 52–3.

Taylor & Francis
Taylor & Francis Group
http://taylorandfrancis.com

7

Laser Printing

Zacharias Vangelatos and Costas P. Grigoropoulos

CONTENTS

7.1 Introduction 81
7.2 Multiphoton Polymerization 81
7.3 Stimulated Emission Depletion for Multiphoton Lithography (STED) 83
7.4 Laser-induced Forward Transfer 85
7.5 Conclusions 86
References 86

7.1 Introduction

The inexorable advance in printing technologies through the past decades is a consequence of the establishment of the laser on this field. Utilizing a beam instead of a deposition tip or nozzle to modify the shape of a material provides an auspicious advantage to create complex structures and devices with extremely high resolution. Laser printing techniques are defined as all of the technologies that modify the material to create a new structure in an additive manner with a laser source. Even though technologies such as digital light processing or dynamic optical projection stereolithography utilize the same physical principles for fabrication, they employ light sources or projectors, which will not be discussed in this chapter. Among the plethora of various techniques encompassing both high resolution and malleability, some of the most remarkable ones are the multiphoton polymerization techniques for fabrication and the laser-induced forward transfer (LIFT) for controlled deposition. This chapter will focus on the fundamental mechanisms dictating these techniques. Moreover, the corollary of increasing the resolution with stimulated emission depletion will be addressed along with its contemporary scientific challenges. All of these techniques are considered direct laser writing (DLW) techniques, because they do not require pre-existing patterns, such as lithographic masking or stamping. Even though the aforementioned techniques are imperative due to their low cost in mass production, DLW techniques can provide significant advantages, such as resource footprint for device fabrication, allowing rapid prototyping, simple modifications, and microelectromechanical systems (MEMS) device fabrication and repair.

7.2 Multiphoton Polymerization

3D fabrication utilizing photoresists was initially developed as a form of stereolithography [1]. In conventional stereolithography, thin layers of photoresist are irradiated by ultraviolet (UV) light, depending on the specific geometry splitting it into subsequent layers and utilizing projecting micromirror devices [2], converting a monomer material into a polymer. Utilizing this technique, 2D lines of 1 μm thickness can be fabricated [3]. However, the depth resolution of this technique is still restricted to several micrometres due to the layer-by-layer nature of the technique. To overcome the limitations of single-photon polymerization (1PP), two-photon absorption polymerization (2PP) was employed for producing 3D microstructures [4,5]. An alternative name for the commercialized apparatuses utilizing 2PP is DLW. The physical mechanism of 2PP is delineated in Figure 7.1. During this procedure, a photoresist absorbs two near-infrared (IR) photons concurrently in a single quantum event. The coalesced energy of these photons must correspond to the UV region of the spectrum. The rate of two-photon absorption is proportional to the square of the light intensity, such that the near-IR light is primarily absorbed only at the focal point within the photoresist. This quadratic intensity dependence enables to confine the writing to submicron dimensions, even beyond the diffraction limit of light as it will be discussed later. The above effect of the multiphoton polymerization provides the fabrication of 3D microstructures by scanning the laser focus inside a photoresist [6]. Figure 7.1c juxtaposes the excitation regions in the case of 1PP and 2PP.

The probability of 2PP is extremely low as its cross section is approximately 31 orders of magnitude lower than the cross section of the single-photon process [6]. Hence, 2PP requires a substantially high density of photons to be effective, by spatially and temporally restraining the photons. This can be accomplished by coupling high numerical aperture objectives to ultra-short pulsed lasers such as titanium-sapphire lasers emitting in the near-IR region [7]. Approaching the focal point of the objective lens, the photon density will sharply increase, as it is depicted in Figure 7.1. Therefore, the low probability of the 2PP process will be automatically confined around this focal point in an area defined in the literature as "voxel". If the sample is transparent to the IR radiation of the laser and absorptive to the UV irradiation, the voxel around the focal

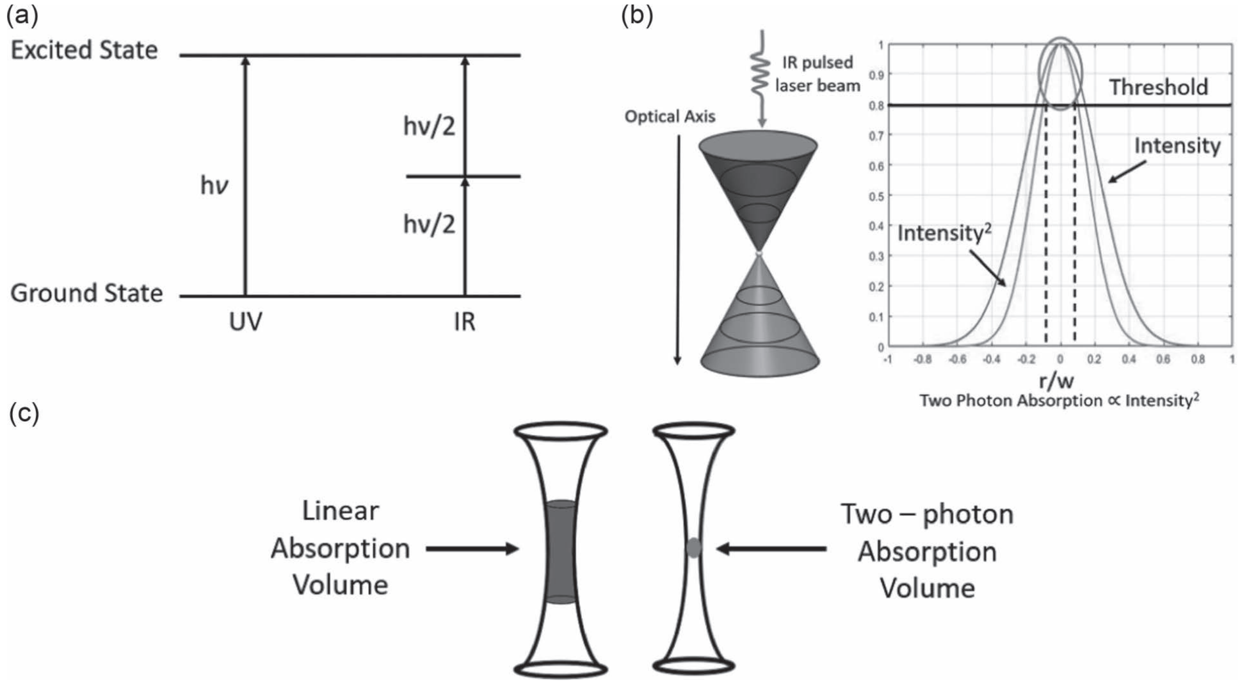
(a)
Excited State
hν
hν/2
hν/2
Ground State
UV
IR
(b)
IR pulsed laser beam
Optical Axis
Threshold
Intensity
Intensity²
1
0.9
0.8
0.7
0.6
0.5
0.4
0.3
0.2
0.1
0
-1
-0.8
-0.6
-0.4
-0.2
0
0.2
0.4
0.6
0.8
1
r/w
Two Photon Absorption ∝ Intensity²
(c)
Linear Absorption Volume
Two – photon Absorption Volume

FIGURE 7.1 Fundamentals of multiphoton polymerization generated by a focused laser beam. (a) The excitation process for single-photon and two-photon absorption. (b) Comparison of the intensity and the squared intensity (which is proportional to the two-photon absorption, as a function of the beam radius). (c) Comparison of the polymerized volume for the case of the single-photon absorption and the two-photon absorption.

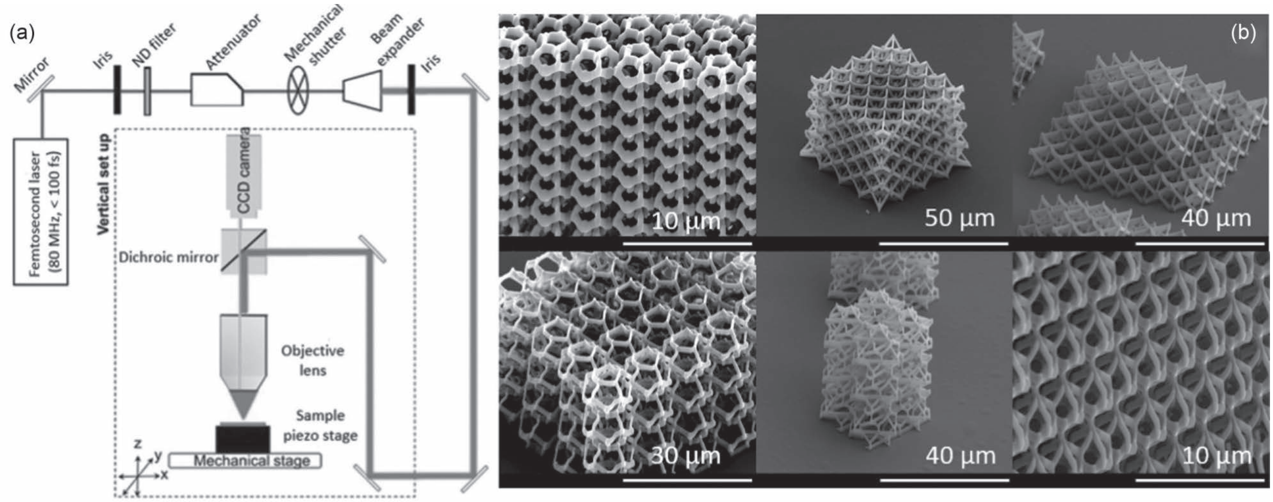
(a)
Mirror
Iris
ND filter
Attenuator
Mechanical shutter
Beam expander
Iris
Femtosecond laser (80 MHz, < 100 fs)
Vertical set up
CCD camera
Dichroic mirror
Objective lens
Sample piezo stage
Mechanical stage
z
y
x
(b)
10 µm
50 µm
40 µm
30 µm
40 µm
10 µm

FIGURE 7.2 (a) Schematic of the 2PP experimental set-up. (b) Fabricated structures by 2PP.

point will be excited, while the adjacent regions of the sample will remain transparent and unaffected by the incident radiation. A characteristic experimental set-up for the 2PP is demonstrated in Figure 7.2a. The system includes a FemtoFiber pro NIR laser with a wavelength of 780 nm, a pulse width of 100 fs and a repetition rate of 80 MHz. At this repetition rate and wavelength, the desired localized polymerization can be achieved. The beam is focused by a 100 × microscope objective lens (Plan-ApoChromat 100×/1.40 Oil M27, Zeiss). By tightly focusing the laser in the photosensitive material, the material was locally polymerized. The stage is then translated so that the focused beam can "write" inside the material and fabricate the desired 3D structure. In this fabrication method, the beams of the structure were designed as lines in a 3D space. This geometry was then converted to a g-code, whose coordinates defined the edges of the structure to be fabricated [8,9]. Utilizing this set-up, highly complex architected geometries can be fabricated in microscale, as the ones presented in Figure 7.2b. For the case of 1PP, the same set-up can be utilized, but instead of a Ti:sapphire laser, a UV wavelength laser must be utilized, such as an argon ion (Ar^+) laser with a wavelength of 365 nm.

Even though these polymerization techniques enable the fabrication in the regime of a few micrometres, they are still substantially inadequate to reach the nm length scale.

To overcome this barrier, there are two main techniques. One is the surpassing of Abbe's diffraction limit with multi-wavelength mechanisms that will be addressed later. The other one is to tailor the photochemistry of the photoresist to mitigate the effective area of the voxels via the so-called diffusion-assisted high-resolution direct femtosecond laser writing [10]. This method utilizes an inhibiting molecule, such as a quencher, into the photoresist [11]. Regarding the photochemical procedure during the 2PP, the photoresist consists of three main components: (i) the monomer chains that will crosslink creating the polymer hybrid, (ii) the ceramic core that provides stability to the crosslinked network and (iii) the photoinitiator that initiates the photon excitation process. As the photoinitiator becomes excited, it starts producing radicals that "attack" the monomer molecules to create the macroradicals of the polymer. Finally, the radicals are terminated to provide the final polymer. Radical termination can also be substantiated by oxygen and various other molecules into the system, defined as scavengers. The quenching is competitive with the photopolymerization and is initially detrimental to the process. Nevertheless, in multiphoton photopolymerization, it can be utilized to fabricate structures of very high resolution. This can be accomplished by modulating the light intensity at the focal point such that the produced radicals, whose spatial concentration is proportional to the square of the light intensity, supersede the quenchers and initiate polymerization in the region where the exposure energy is larger than the upper threshold. This is determined by the nexus between a mobile quenching molecule and a slow laser scanning speed, enabling the diffusion of the quencher in the polymerized area, the depletion of the radicals and the regeneration of the consumed quencher. This technique has enabled the fabrication of woodpile structures, used as photonic crystals, with approximately 100 nm thickness, as illustrated in Figure 7.3 [10]. However, there are also other means to improve the resolution of these laser printing processes, by introducing multiple laser sources hitting the sample, which will be presented next.

7.3 Stimulated Emission Depletion for Multiphoton Lithography (STED)

One of the major reasons that limit the resolution of the fabrication process is the diffraction limit. Diffraction prohibits light to be focused to a volume smaller than approximately one and a half of the light wavelength along the lateral directions and three times larger along the optical axis (around 200 and 600 nm, for the case of visible light, respectively) based on the following equations [12]:

$$\text{Abbe Resolution}_{x,y} = \frac{\lambda}{2NA} \tag{7.1}$$

$$\text{Abbe Resolution}_{z} = \frac{2\lambda}{NA^2}, \tag{7.2}$$

where λ is the wavelength of the source and NA is the numerical aperture of the lens. STED microscopy surpasses this diffraction limit by reversibly depleting fluorophores at the predetermined locations of the diffraction-limited excitation regions [13]. Therefore, only the nondepleted fluorophores in the complementary areas emit light, providing the threshold for features indistinguishable by the diffraction limit to be separated. In the most typical STED microscopy implementation, the fluorescent confinement is accomplished by aligning the Gaussian excitation beam of a scanning microscope with a second beam, defined as the STED beam, whose wavelength is tailored to de-excite fluorophores by stimulated emission and is modulated in phase and polarization to form a doughnut-shaped focal intensity distribution without any intensity at the centre. Even though the distribution of the STED beam focal intensity is also limited by Abbe's criterion, high intensities saturate the stimulated emission transition and preserve the fluorophores in the ground state, except those positioned in a region with no intensity, whose size reaches subdiffraction values and diminishes with the rise of the STED beam intensity.

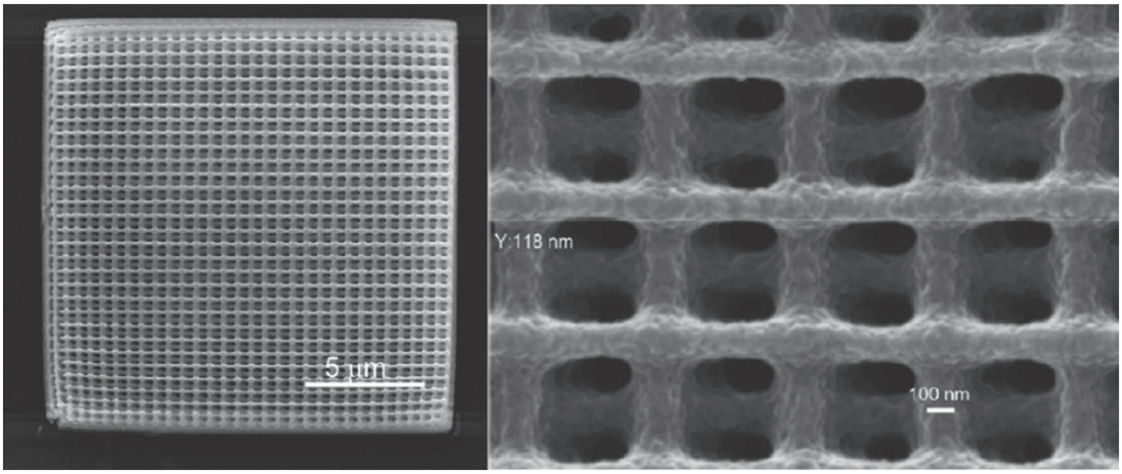

FIGURE 7.3 3D woodpile structure with 600 nm interlayer periodicity fabricated utilizing diffusion-assisted high-resolution direct femtosecond laser writing [10]. (Reprinted with permission from ACS.)

Theoretically, the resolution of STED microscopy can reach the size of a molecule, which is the absolute limit of a fluorescent microscope. In practice, it is hindered by the signal-to-noise ratio. To obtain the desired resolution enhancement, it is imperative to synergistically generate subdiffraction fluorescent regions across the whole specimen (according to the Nyquist sampling condition) and to attain, from all these regions, ample fluorescent photons to facilitate an adequate signal-to-noise ratio. With the profound advance in STED microscopy, the direct consequence was to transfer this technology to a field that required high resolution as well, that of microstereolithography [14]. For the coupled multiphoton polymerization and STED, the schematic of the electron states and how the physical mechanism is manifested is delineated in Figure 7.4.

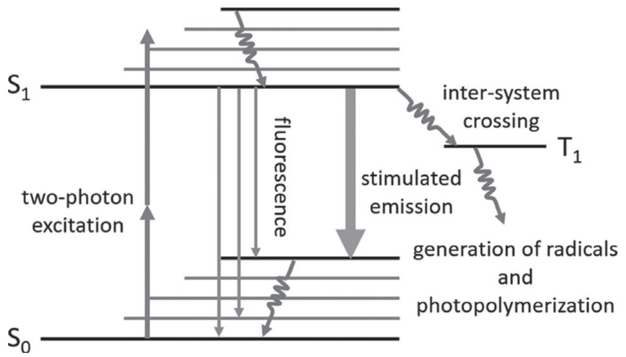
S_1
inter-system crossing
T_1
two-photon excitation
fluorescence
stimulated emission
generation of radicals and photopolymerization
S_0

FIGURE 7.4 Schematic Jablonski diagram of a photoinitiator molecule and illustration of the relevant optical transitions and processes.

Two photons mediate the optical transition from the ground state into an electronically excited state. Rapid non-radiative relaxation occurs afterwards. Under normal circumstances, the "virtual" intermediate state should be occupied for a very short period of time such that the photo-induced excitation is efficiently transcended into a chemical reaction resulting in cross-linking. Spontaneous emission of light (fluorescence) from the intermediate S1 state is not desired, as the fluorescence quantum efficiency is low and the inter-system crossing efficiency is substantial. Nevertheless, without spontaneous emission, the required stimulated emission would not be efficient. In particular, the STED rate is unlikely to overcome the inter-system crossing rate. Efficient stimulated emission demands an electric-dipole-allowed optical S0–S1 transition. A large oscillation strength requires a sufficient spatial overlap of the involved orbitals. Hence, a π–π* transition is preferred instead of a *n*–π * transition. In addition, the inter-system crossing rate must not be too large. The set-up required to perform coupled multiphoton lithography (MPL) with STED is depicted in Figure 7.5 [15].

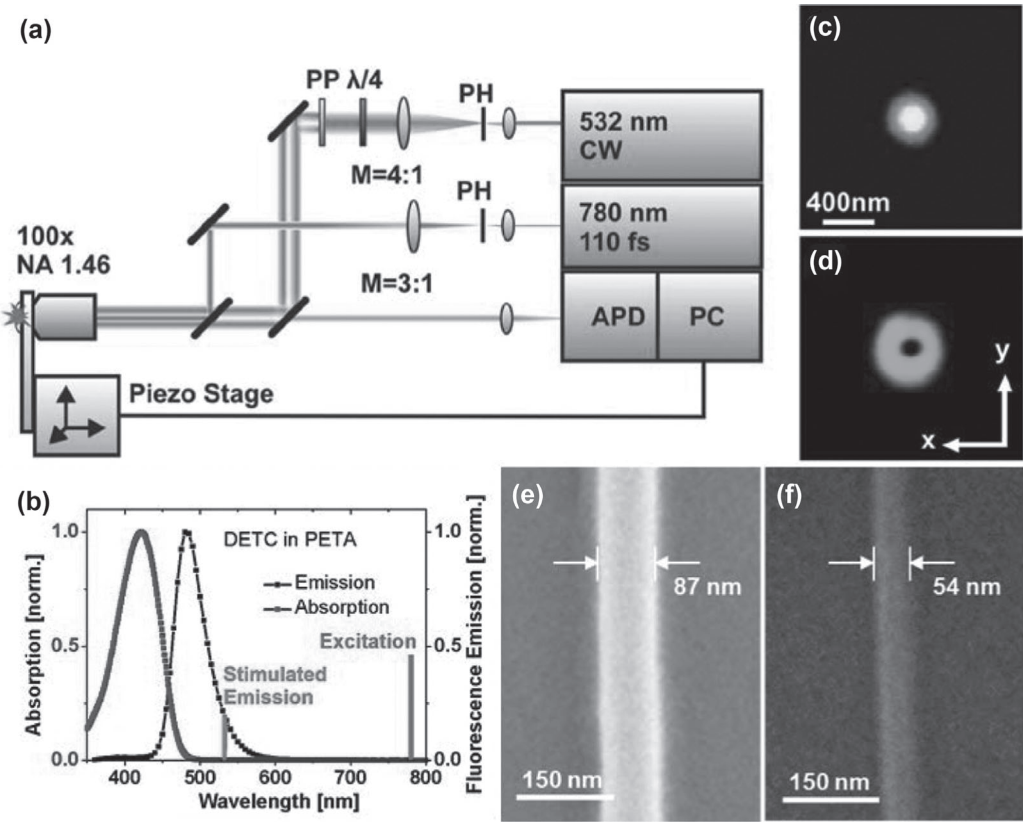
(a)
PP λ/4
PH
532 nm CW
M=4:1
PH
780 nm 110 fs
100x NA 1.46
M=3:1
APD
PC
Piezo Stage
(b)
DETC in PETA
Emission
Absorption
Excitation
Stimulated Emission
Absorption [norm.]
Fluorescence Emission [norm.]
1.0
0.5
0.0
400
500
600
700
800
Wavelength [nm]
(c)
400nm
(d)
y
x
(e)
87 nm
150 nm
(f)
54 nm
150 nm

FIGURE 7.5 (a) Scheme of a characteristic 2PP/STED lithography set-up. Red depicts the excitation beam for 2PP (780 nm, 100 fs pulse duration), and green depicts the optional depletion beam (532 nm continuous wave [CW]). The depletion beam is shaped into a donut using a 2π spiral phase plate (PP) or into a 3D STED beam using an annular PP rotating the centre by π, (b) measured spectra of the photoinitiator used, (c,d) measured cross sections at the focal plane of the 2PP and the depletion beams, respectively, upon back-reflection from a 50 nm gold nanoparticle, (e) polymerized line by 2PP, (f) polymerized line by STED+2PP manifesting the higher resolution [15]. (Reprinted with permission from OSA.)

The two-photon polymerization initiator is excited with 780 nm ultra-short laser pulses, which are locally depleted in the outer volume of the voxel with a depletion beam (532 nm, continuous wave (CW)). The depletion beam is shaped into a donut shape function for 2D structuring utilizing a 2π spiral phase mask and a $\lambda/4$ wave plate [15]. For 3D fabrication, an annular phase mask combined with a $\lambda/4$ wave plate can be used to create a bottle beam shape function. Both beams have to be focused through an oil immersion objective lens, with the same NA as the substrate of the photoresist. Excitation and depletion powers are measured in front of the objective lens. Nevertheless, even though STED seems a promising technique to improve the resolution of the fabricated geometries, understanding and optimizing of the photochemistry is likely the key factor for further resolution improvement. Under this scope, it can be stated that photochemistry and polymer chemistry are limiting the attainable resolution in STED-DLW and not the optics of the system. This is evidenced by the fact that the field has not advanced in the fabrication of highly complex structures such as plasmonic or mechanical metamaterials. The main challenge lies in creating a material that utilizes the monomer, the ceramic, the photoinitiator (for multiphoton absorption) and for STED the coinitiator (for depletion) to create a stable and rigid hybrid material. Therefore, this is the objective that must be accomplished for the STED MPL to be utilized efficiently in the fabrication procedure.

7.4 Laser-induced Forward Transfer

The laser-induced forward transfer (LIFT) technique can be utilized for direct writing for a vast range of materials with a resolution that can reach 300 nm [16]. It has gained the interest of the research community due to its ability to pattern materials in ambient conditions onto any substrate [17]. Typical materials that can be deposited include metals, oxides, superconductors, DNA, proteins, fungal spores and polycrystalline Si [18]. To employ LIFT, a pulsed laser beam is focused on a thin film of the donor material (i.e. the material that will be deposited) through its supporting substrate. The substrate must be transparent to the laser irradiation. Because of the laser pulse, a miniscule portion of the donor material is ejected towards the receiving substrate. However, this mechanism occurs for thicker films and high laser fluence; for thin films and fluence above the threshold for material transfer, LIFT can occur by melting through of the source film [16–18]. The process is illustrated in Figure 7.6. Through this process, a voxel is formed on the substrate. Repeating this process for multiple voxels can lead to the fabrication of a patterned surface [19]. For the case of depositing liquids, the deposition process begins with the absorption of the laser irradiation that initiates a swift vaporization of the absorbing agent. Hence, a vapour bubble is generated, expanding against the surrounding fluid. The dynamic response of both bubble and displaced fluid has been unravelled utilizing time-resolved imaging for different fluids and irradiation conditions [18]. The extreme pressure inside the bubble promotes its rapid propagation during the first microseconds after the laser pulse. Simultaneously with the expansion of the bubble, a protrusion is formed in the fluid layer as the vapour pressure pushes the liquid surrounding the bubble. When the bubble starts collapsing, it creates a thin needle-like jet. During the bubble collapse, the jet continues advancing in the axial direction towards the receiving substrate. The contact of the jet with the receiving substrate results in the deposition of the droplet, even for high aspect ratios (width of a few micrometres over a length of few millimetres).

LIFT has been conducted utilizing short pulses (ns) or ultrashort pulses (ps or fs). Nevertheless, there are some LIFT variants using long pulses (from μs to cw) [20]. Shorter pulses are preferred as the thermal effects are diminished and smaller voxels can be obtained [16]. The wavelength is selected based on the intermediate layer or the transferred material but the most common is UV. The pulse energy and the laser beam size are the key parameters for LIFT to be efficient. However, laser fluence is actually another major factor [21]. Typical deposited droplets are shown in Figure 7.7 using a Ti:sapphire laser (800 nm, 110 fs) [16]. The centre of the 4 mm diameter full width at half-maximum Gaussian laser output illuminated a 120 μm diameter circular aperture to give an approximately uniform profile. The aperture was transferred onto the carrier–film interface using a 100× microscope objective lens with NA equal to 0.8, resulting in a spot diameter of approximately 4 μm at the film surface.

Regarding the alignment of the donor and the receiver, a minimum gap between the donor film and the receiving substrate must be preserved to avoid any contact between them, which might cause the volatile massive transfer of fluid. Since jets generated in LIFT are stable during several millimetres of travel, transfer in the jetting regime allows some tolerance

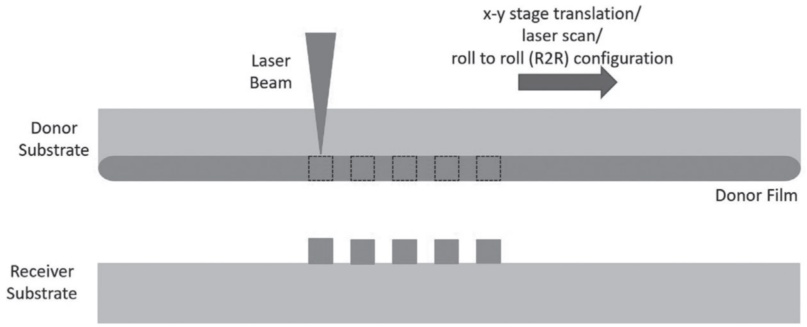

FIGURE 7.6 The principle of operation of the LIFT technique for solid films.

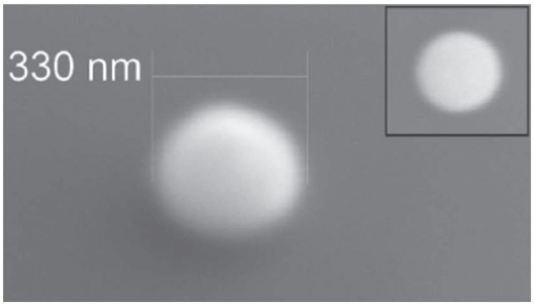

FIGURE 7.7 SEM image of a deposit produced using fluence equal to 325 mJ cm^{-2}. The image was taken at an angle of 45° to the receiver surface normal. Inset: same deposit from directly above [16]. (Reprinted with permission from AIP.)

between the donor film and the receiver substrate. Thus, it can vary from a few tens of micrometres up to a few millimetres. This degree of tolerance is beneficial taking into account the potential industrial implementation of the technique in a production line. However, in the case of small gaps and under certain operating conditions, the jet when impacting the receiving substrate can be faster compared to large gaps, thus leading to the modification of the contact angle [22,23], resulting in different droplet diameters. In that case, even though the deposition mechanism is manifested differently, the transferred volume is like that even for larger gaps. However, the final diameter of the droplets is different due to the different contact angles. Consequently, the gap between the donor and the receiver can affect the wetting of the fluid on the receiving surface [22]. There are many instantiations of the LIFT mechanism, with the main difference laying on how the laser power is absorbed and converted into the mechanical energy required for ejection [20]. Characteristic examples include the (i) indirect interaction – LIFT [24]; (ii) the matrix-assisted pulsed laser evaporation – direct write (MAPLE-DW) [25]; (iii) the laser molecular implantation [26]; (iv) the long-pulsed lift (LP-LIFT) [27]; and (v) the BLAST (ballistic laser-assisted solid transfer)-LIFT [28]. Indirect interaction – LIFT – involves the implementation of an intermediate layer, which absorbs the laser radiation and protects the donor material from direct laser irradiation. This obstructs photolytic and pyrolytic damage to the transferred material and enables the use of sensitive materials as receiver substrates. MAPLE-DW is an alternative process to the standard pulsed laser deposition (PLD), in which the material to be deposited is dissolved into a solvent matrix material with a lower evaporation point. The laser pulse evaporates the matrix and the material is released with ample energy to be deposited in the receiver substrate without an egregious result, allowing the deposition of complex undamaged molecules. In the laser molecular implantation, the molecules are deposited into a thin polymer film applied to a glass substrate. For this case, the receiver substrate, which can be another polymer film, and the donor are kept in contact. The laser pulse heats the polymer, thus expanding it and subsequently increasing the contact between the films. The molecules are then transferred and deposited into the receiver film through diffusion process. As both the donor and the receiver are polymers, backward transfer is also possible. LP-LIFT is conducted using laser pulses in the order of μs or longer. The LP-LIFT experimental apparatus is similar to the common LIFT, but the donor and the receiver are preserved in close contact. The donor is heated, resulting in its thermal expansion overcoming the small gap. The donor is annealed to the acceptor without melting and is bounded to the receiver. The physical mechanism of this process is different from the conventional LIFT. BLAST is utilized for solid materials. With multiple, subthreshold energy femtosecond laser pulses, the adhesion of the solid film to the transparent substrate is reduced until a solid block of material is ejected towards the receiver substrate. As BLAST-LIFT is functional for low fluences, it can be utilized to deposit more delicate materials than with the other variations of LIFT. The major advantage of LIFT as a laser printing technique is the potential of depositing a vast range of materials, both inorganic and organic, solid or liquid [29], rendering LIFT a versatile tool to be employed in various crucial fields. For example, time-resolved imaging of LFT of copper nanoparticle (NP) inks in conjunction with computational imaging revealed the dynamics of the jetting process, whose understanding is crucial towards optimizing the deposition process [30]. Firstly, a potential application is the electronics industry, to print the circuit itself and various active and passive elements such as diodes, transistors and sensors. Secondly, LIFT can be utilized as an additive manufacturing technique for microfabrication of arbitrary 3D structures. Finally, the third major area of LIFT is the bioprinting [20,31].

7.5 Conclusions

DLW processes have rapidly expanded. The extremely high resolution of new materials that can be incorporated has mediated into industrial applications, paving the way to design and fabricate structures for a plethora of applications. Characteristic examples are electromagnetic, acoustical and mechanical metamaterials; scaffolds for tissue engineering; and bioprinting. Even though this vast and imperative range of applications has advanced these techniques, there are still scientific challenges regarding the photochemistry of the utilized materials and the physical mechanism dictating these phenomena. Nevertheless, the utility and perpetual advance and research of these processes facilitate them as the spearhead of additive manufacturing and laser printing.

REFERENCES

1. Kodama H. 1998 Automatic method for fabricating a three dimensional plastic model with photohardening polymer, *Review of Scientific Instruments* **52** 1770.
2. Warner J. J., Gilles A. R., Hwang H. H., Zhang H., Lieber R. L. and Chen S. 2017 3D-printed biomaterials with regional auxetic properties, *Journal of the Mechanical Behavior of Biomedical Materials* **76** 145–152.
3. Maruo S. and Ikuta K. 2002 Submicron stereolithography for the production of freely movable mechanisms by using single-photon polymerization, *Sensors and Actuators A* **100** 70–76.

4. Ovsianikov A., Viertl J., Chichkov B., Oubaha M., MacCraith B., Sakellari I., Giakoumaki A., Gray D., Vamvakaki M., Farsari M. and Fotakis C. 2008 Ultra-low shrinkage hybrid photosensitive material for two-photon polymerization microfabrication, *ACS Nano* **2** 2257–2262.
5. Maruo S. and Fourkas J. T. 2008 Recent progress in multiphoton microfabrication, *Laser & Photonics Reviews* **2** 100–111.
6. Dorkenoo K. D. (H.), Sungur E., Bulou H., Taupier G. and Boeglin A. 2012 Monitoring the contractile properties of optically patterned liquid crystal based elastomers, *Advanced Elastomers-Technology, Properties and Applications* 37–60.
7. Choi J., Koo S., Sakellari I., Kim H., Su Z., Carter K. R., Farsari M., Grigoropoulos C. P. and Russell T. P. 2018 Guided assembly of block copolymers in three-dimensional woodpile scaffolds, *ACS Applied Materials & Interfaces* **10** 42933–42940.
8. Vangelatos Z., Melissinaki V., Farsari M., Komvopoulos K. and Grigoropoulos C. 2019 Intertwined microlattices greatly enhance the performance of mechanical metamaterials, *Mathematics and Mechanics of Solids*. doi:10.1177/1081286519848041.
9. Vangelatos Z., Komvopoulos K. and Grigoropoulos C. 2018 Vacancies for controlling the behavior of microstructured three-dimensional mechanical metamaterials, *Mathematics and Mechanics of Solids* **24** 511–524.
10. Sakellari I., Kabouraki E., Gray D., Purlys V., Fotakis C., Pikulin A., Bityurin N., Vamvakaki M. and Farsari M. 2012 Diffusion-assisted high-resolution direct femtosecond laser writing, *ACS Nano* **6** 2302–2311.
11. Park S. H., Lim T. W., Yang D. Y., Kim R. H. and Lee K. S. 2006 Improvement of spatial resolution in nano-stereolithography using radical quencher, *Macromolecular Research* **14** 559–564.
12. Vicidomini G., Bianchini P. and Alberto D. 2018 STED super-resolved microscopy, *Nature Methods* **15** 173–182.
13. Sivankuttya S., Hernándeza I. C., Bourga N., Dupuisb G. and Forta S. L. 2019 Supercritical angle fluorescence for enhanced axial sectioning in STED microscopy, *Methods* doi:10.1016/j.ymeth.2019.03.027.
14. Fischer J. and Wegener M. 2011 Three-dimensional direct laser writing inspired by stimulated-emission-depletion microscopy, *Optical Materials Express* **1** 614–624.
15. Wollhofen R., Katzmann J., Hrelescu C., Jacak J. and Klar T. A. 2013 120 nm resolution and 55 nm structure size in STED-lithography, *Optics Express* **21** 10831–10840.
16. Banks D. P., Grivas C., Mills J. D. and Eason R. W. 2006 Nanodroplets deposited in microarrays by femtosecond Ti:sapphire laser-induced forward transfer, *Applied Physics Letters* **89** 193107.
17. Papakonstantinou P., Vainos N. A. and Fotakis C. 1999 Microfabrication by UV femtosecond laser ablation of Pt, Cr and indium oxide thin films, *Applied Surface Science* **151** 159–170.
18. Piqué A. and Serra P. 2018 *Laser Printing of Functional Materials: 3D Microfabrication, Electronics and Biomedicine* (Wiley – VCH - Weinheim, Germany).
19. Zergioti I., Mailis S., Vainos N. A., Papakonstantinou P., Kalpouzos C., Grigoropoulos C. P. and Fotakis C. 1998 Microdeposition of metal and oxide structures using ultrashort laser pulses, *Applied Physics A* **66** 579–582.
20. Morales M., Munoz-Martin D., Marquez A., Lauzurica S. and Molpeceres C. 2018 Chapter 13- Laser-induced forward transfer techniques and applications. In: Lawrence, J. (ed.) *Advances in Laser Materials Processing*, pp. 339–379. Woodhead Publishing, Cambridge.
21. Colina M., Duocastella M., Fernández-Pradas J. M., Serra P. and Morenza J. L. 2006 Laser-induced forward transfer of liquids: Study of the droplet ejection process, *Journal of Applied Physics* **99** 084909.
22. Boutopoulos C., Papageorgiou D. P., Zergioti I. and Papathanasiou A. G. 2013 Sticking of droplets on slippery superhydrophobic surfaces by laser induced forward transfer, *Applied Physics Letters* **103** 024104.
23. Rapp L., Ailuno J., Alloncle A. P. and Delaporte P. 2011 Pulsed-laser printing of silver nanoparticles ink: control of morphological properties, *Optics Express* **19** 21563–21574.
24. Kattamis N. T., McDaniel N. D., Bernhard S., and Arnold C. B. 2009 Laser direct write printing of sensitive and robust light emitting organic molecules, *Applied Physics Letters* **94** 103306.
25. Piqué A., Chrisey D. B., Auyeung R. C. Y., Fitz-Gerald J., Wu H. D., McGill R. A., Lakeou S., Wu P. K., Nguyen V. and Duignan M. 1999 A novel laser transfer process for direct writing of electronic and sensor materials, *Applied Physics A* **69** S279–S284.
26. Goto M., Hobley J., Oishi T., Kasahara A., Tosa M., Yoshihara K., Kishimoto M. and Fukumura H. 2004 Micropatterning of multiple organic molecules by laser implantation, *Applied Physics A* **79** 157–160.
27. Kantor Z., Toth Z. and Szorenyi T. 1995 Metal pattern deposition by laser-induced forward transfer, *Applied Surface Science* **86** 196–201.
28. Kantor Z. and Szorenyi T. 1995 Dynamics of long-pulse laser transfer of micrometer-sized metal patterns as followed by time-resolved measurements of reflectivity and transmittance, *Journal of Applied Physics* **78** 2775.
29. Piqué A., Auyeung R. C. Y., Kim H., Charipar N. A. and Mathews S. A. 2016 Laser 3D micro-manufacturing, *Journal of Physics D: Applied Physics* **49** 223001.
30. Kalaitzis A., Makrygianni M., Theodorakos I., Hatziapostolou A., Melamed S., Kabla A., de la Vega F. and Zergioti I. 2019 Jetting dynamics of Newtonian and non-Newtonian fluids via laser-induced forward transfer: Experimental and simulation studies, *Applied Surface Science*. **465** 136–142.
31. Chatzipetrou M., Massaouti M., Tsekenis G., Trilling A. K., van Andel E., Scheres L., Smulders M. M. J., Zuilhof H. and Zergioti I. 2016 Direct creation of biopatterns via a combination of laser-based techniques and click chemistry, *Langmuir*, **33** 848–853.

Taylor & Francis
Taylor & Francis Group
http://taylorandfrancis.com

8

3D Printing and Additive Manufacturing

V. Melissinaki and M. Farsari

CONTENTS

8.1 Introduction 89
8.2 Stereolithography 90
8.3 Selective Laser Sintering (SLS) Technology 91
8.4 Microscale 3D Printing Techniques 91
  8.4.1 Projection Micro-stereolithography 92
  8.4.2 Multiphoton Lithography 92
    8.4.2.1 Multiphoton Polymerization Technique 94
    8.4.2.2 Sequential and Simultaneous Two-photon Absorption (TPA) 94
    8.4.2.3 Experimental Set-up 94
    8.4.2.4 Materials for Laser Polymerization 95
    8.4.2.5 Applications 96
References 97

8.1 Introduction

There are a number of methods that can be used to manufacture a solid object. One of these methods is subtractive manufacturing. In this method, material is cut away from a starting block. Subtractive manufacturing has many drawbacks. The process generates waste and is time- and cost-intensive. Also, the number of shapes/configurations that can be created is limited.

Another technology used to generate objects is formative manufacturing. In formative manufacturing, a resin, polymer, or metal is forced into a mould and subsequently cured or allowed to cool. Examples of this include investment casting, injection moulding, and compressive moulding. This technology also has a number of drawbacks, including requiring a labour force that has a broad range of expertise. The process can also be time- and cost-intensive.

Additive manufacturing (AM) technology was developed to alleviate some of the problems of the aforementioned technologies. AM technology builds 3D objects in a layer-by-layer fashion, significantly reducing manufacturing time and costs without limiting shape configuration. It emerged during the past three decades as a game-changing technology for the rapid prototyping industry. AM contains a series of different technological processes, including stereolithography (SLA), selective laser sintering (SLS), three-dimensional printing (3DP), fused deposition modelling (FDM), and laminated object manufacturing (LOM).

As it is already mentioned, 3D printing is an AM technique for fabricating a wide range of three-dimensional structures and complex geometries from digital model data. The process consists of printing successive layers by depositing or fusing materials, such as polymers, liquids, plastic, powders, and metal, in layers that are formed on top of each other.

Like most solid free-form fabrication techniques, 3D printing allows the fabrication of objects from a computer-aided design (CAD) file. The geometry of the structure that is to be built can either be designed using 3D modelling computer software such as AutoCad® or Solidworks®, be described using mathematical equations [1,2], or be derived from scanning data of clinical imaging technologies such as magnetic resonance imaging (MRI) or tomography techniques [3]. The 3D model is sliced into horizontal layers by using appropriate software such as VisCAM RP® or 3D Slicer®, and loaded to the 3D printer.

Nowadays, 3D printing has evolved using various methods, materials, and equipment. New applications are emerging as novel materials, and AM methods are continuously being developed. Particularly, laser-based techniques became very popular among other 3D printing techniques, as the laser beam can be focused and directed in very accurately manner, resulting in high-resolution structures in micro- and nano-metre scales.

In this chapter, we will present and compare the most popular laser-based 3D printing techniques. In Sections 8.2 and 8.3 we will describe the most industrial laser-based 3D printing techniques, SLA, and SLS. Finally, in Section 8.4, we will concentrate on the most popular and widely used microscale 3D printing techniques, projection stereolithography (PSL, Section 8.4.1), and multiphoton lithography (MPL, Section 8.4.2), and we will describe extensively their principles and applications.

8.2 Stereolithography

Stereolithography, or "SLA" printing, is an early and widely used AM 3D printing technology. Chuck (Charles W.) Hull coined the term "stereolithography" in his U.S. Patent entitled "Apparatus for Production of Three-Dimensional Objects by Stereolithography" issued on March 11, 1986 [4]. He defined stereolithography as a method and apparatus for making solid objects by successively "printing" thin layers of the ultraviolet (UV) curable material, one on top of the other, starting from the bottom layer to the top layer. After the patent was granted, Hull co-founded the world's first 3D printing company, 3D systems in Valencia, California, to commercialize rapid prototyping [5]. Hull realized that his concept was not limited to liquids and therefore gave it the generic name "stereolithography" (3D printing), and filed broad patent claims covering any "material capable of solidification" or "material capable of altering its physical state".

In a SLA machine, an UV laser is focusing on a vat of photopolymer resin (see Figure 8.1). With the help of computer-aided manufacturing or computer-aided design (CAM/CAD) software, the UV laser is used to draw a pre-programmed design or shape on to the surface of the photopolymer vat. Photopolymers are sensitive to UV light, so the resin is photochemically solidified and forms a single layer of the desired 3D object. Then, the build platform lowers one layer and a blade (sweeper) re-coats the top of the tank with resin. This process is repeated for each layer of the design until the 3D object is complete. After the completion of the laser writing, the unexposed photopolymer must be washed off with the immersion of the sample in an appropriate solvent that dissolves the liquid monomer. SLA requires the use of supporting structures that are attached to the elevator platform to prevent deflection due to gravity and resist lateral pressure from the resin-filled blade. Supports are typically created automatically during the preparation of CAD models and can also be made manually. In either situation, the supports must be removed manually after printing.

A variety of liquid photopolymers are available for SLA. Epoxy-based systems and hybrids have replaced previously used acrylates because of higher strength, higher temperature resistance, lower moisture absorption, and lower shrinkage of the former. Prominent examples of the materials used in the stereolithographic procedures are silicone rubber, urethane, epoxy, or any type of medical-grade FDA-approved material. Photopolymer resins with mechanical properties similar to engineering plastics such as ABS (acrylonitrile butadiene styrene), nylon, and polycarbonate are also used for prototype production. Moreover, metal powder and ceramic powder are also used nowadays [6].

SLA can produce functional prototypes in a time length from a few hours to more than a day [7]. The overall size depends on the type of the machine and the size of the elevator platform. Typically, an SLA machine will be capable of producing components of maximum size $60 \times 60 \times 50\,\text{cm}^3$ [7,8]. However, nowadays there are SLA machines, such as the Mammoth [9], that can produce sizes up to two metres. On the downside, both photosensitive resins and SLA machines can be very expensive.

SLA is particularly versatile with respect to the freedom of designing structures and the scales at which these can be built.

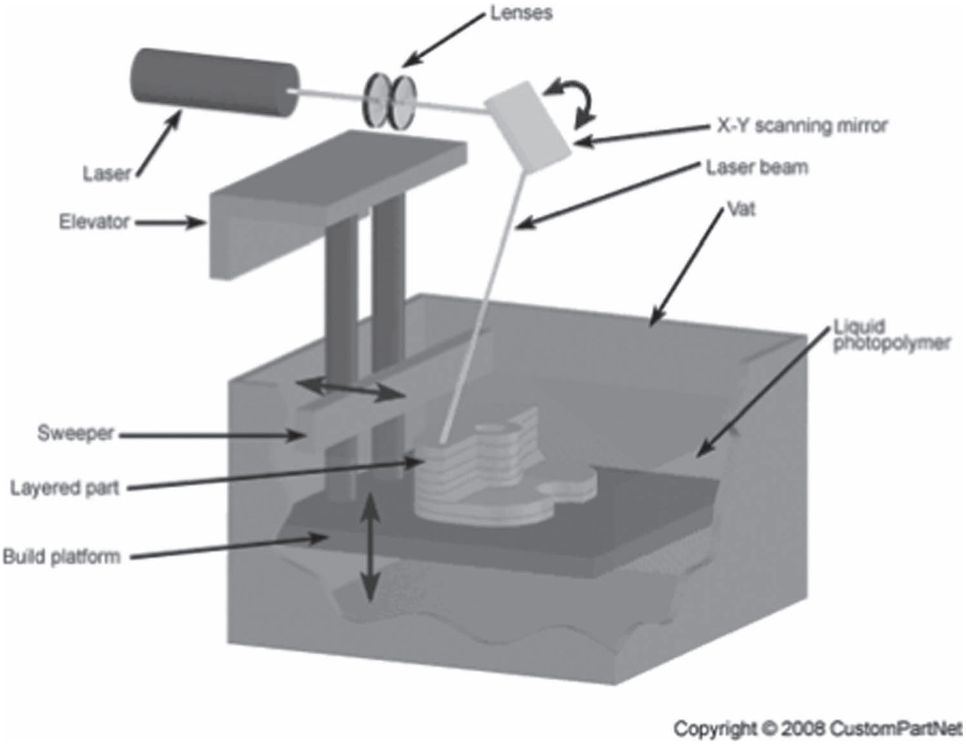

Copyright © 2008 CustomPartNet

FIGURE 8.1 SLA set-up.

This technique has been employed in industries for different applications, for example from medical prototyping [10] to the car [11,12] and aerospace industries [13].

In the biomedical field, these developments have led to the fabrication of patient-specific models for mould-assisted implants and scaffolds fabrication for bone and cartilage tissue engineering [14–19], aid for complex surgery [20], guide for tumour identification and surgery guidance [21] and tailor-made parts such as hearing aids. More recently, biodegradable materials have been developed for the preparation of medical implants, such as tissue engineering scaffolds, by SLA.

8.3 Selective Laser Sintering (SLS) Technology

SLS is a technique that uses high-power lasers (usually CO_2 lasers) to sinter powdered materials. This technique was developed and patented by Carl Deckar and Joe Beaman in 1989 at the University of Texas in Austin. Later on, they took part in foundation of Desk Top Manufacturing (DTM) Corp. that was sold to its big competitor 3D Systems in 2001. As was stated previously, 3D systems Inc. developed SLA, which in some way is very similar to SLS. SLS produces durable, high precision parts, and it can use a wide range of materials. It's a perfect technology for fully-functional, end-use parts and prototypes. SLS is quite similar to SLA technology with regard to speed and quality. The main difference is with the materials, as SLS uses powdered substances, whereas SLA uses liquid resins.

In SLS technique, a laser beam is moving to produce the 3D prototype, and it is selectively fusing powdered materials. This fusing is achieved by scanning cross sections, which are generated from CAD data. As in all rapid prototyping processes, the parts are built upon a platform that adjusts in height equal to the thickness of the layer being built (see Figure 8.2). After each section has been scanned, the base of the machine is lowered in order additional powder to be deposited on the top of the solidified layer and sintered. This powder is rolled onto the platform from a bin. The powder is maintained at an elevated temperature so that it fuses easily upon exposure to the laser. In SLS there is no requirement of special support structures. The excess powder in each layer acts as a support to the part being built [22].

A wide variety of materials in powder form can be used in SLS technique. Metals such as titanium [23–31], steel [32–40], and alloys [28,41–45], plastic, ceramics [46] or glass materials are used in order to form solid 3D objects. Moreover, a great selection of polymers such as polystyrene [47–56] and nylon [55,57–62] are also available for rapid 3D prototype. Finally, mixtures of the aforementioned materials with other biopolymers could also be used [63–90].

While SLS was initially used for prototyping, nowadays it is used in custom or limited-run manufacturing to produce complex end-use parts. SLS has been extensively used to create hard scaffolds for bone [46,75,91] and cartilage tissue engineering [92,93] or even dental implants (see Figure 8.3a) [94,95]. SLS technique is also proposed today in engineering applications [96] and lattice structure design optimization framework of various industrial applications for lightweight purposes in future (see Figure 8.3f) [97].

8.4 Microscale 3D Printing Techniques

Nowadays, the demand of high-resolution micro- and nanostructures for the development of new micro-electromechanical system (MEMS) and nano-electromechanical system (NEMS), as well as the present tendency towards miniaturization of products in many industries comprising medical, automotive, optics, electronics, and biotechnology sectors, leads to the progress of 3D printing technologies. In the following paragraphs, two laser-based 3D microfabrication printing techniques will be described: projection micro-stereolithography (μSLA) and MPL.

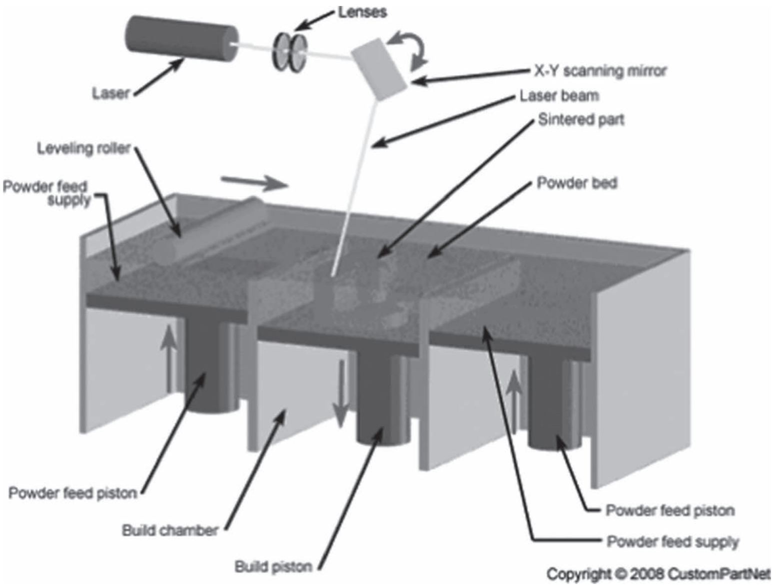

FIGURE 8.2 SLS set-up.

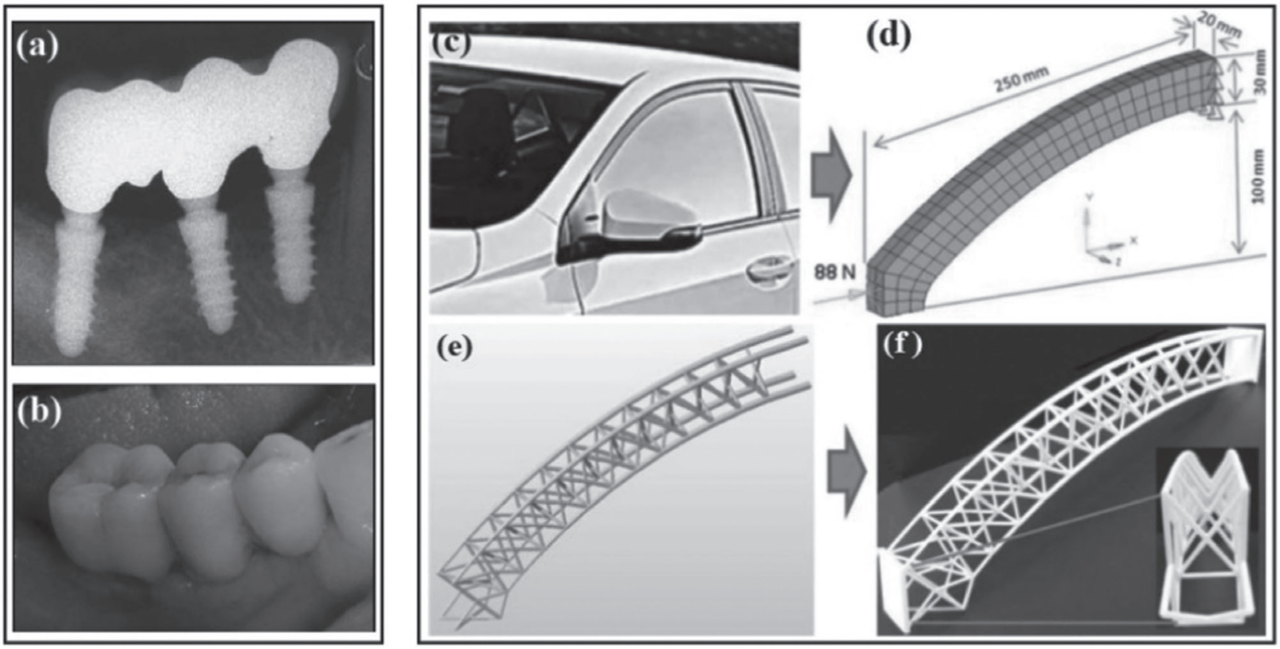

FIGURE 8.3 Fixed partial prostheses (FPP) supported by three, 1-piece, narrow-diameter, SLS implants in the posterior right mandible: (a) 2-year radiographic follow-up and (b) 2-year clinical control [95]. (c) A-pillar of an automobile, (d) the simplified geometry of the A-pillar used in lattice-based optimization, (e) the 3D geometry of the optimized lattice-based A-pillar design using MFD algorithm and (f) the A-pillar design fabricated by SLS process [97].

8.4.1 Projection Micro-stereolithography

μSLA is derived from the conventional SLA process and is used to fabricating complex high-resolution 3D structures in micrometre scale [98,99]. This technology can be divided into scanning and projection methods, which have different levels of precision and fabrication speeds. Scanning μSLA fabricates very fine 3D microstructures by controlling the position of the laser beam on the resin surface. Projection μSLA quickly fabricates one layer with one exposure using a mask (Figure 8.4).

The first paper presenting an integral μSLA machine was published in 1995 by Alain Bertsch et al., who proposed a new system, where a liquid crystal display (LCD) was used to project a dynamic mask pattern on the liquid resin surface. Every pixel of such LCD panels is a small cell that can be set either to its transparent state or to its opaque state, by changing the orientation of the molecules it contains. By this way, each layer of the pattern was photopolymerized in one shot [101,102]. When the first experiments were started on the use of LCDs as spatial light modulators (SLMs) in μSLA, this component was not compatible with UV light. Therefore, the beam of a green laser source (515 nm) was required in the apparatus to project the image on a platform immersed into the photosensitive resist. The problem that came up by that time was that any of the commercially available photosensitive resins that were designed for classic SLA could be used and new photoresins that could react with visible wavelengths had to be developed.

Chatwin et al. presented in 1998 an integral μSLA process where the LCD was replaced with a custom-made SLM [103], transparent to UV, while at the same time several materials were synthesized and were available to be used [103–106].

By replacing the LCDs with SLMs, the material availability problem was solved but low contrast and transmittance problems were observed. These problems were associated with the low switching speed and the low optical density of the refractive elements of the SLMs. To overcome these problems, a digital micromirror device (DMD), which was developed by Texas Instruments, has been used as the dynamic pattern generator due to its high contrast and resolution [99,107]. The DMD is an array of micromirrors actuated by electrostatic forces, and they can successfully be used as pattern generator for μSLA. This component is a fast MEMS working as a digital light switch. C. Sun et al. replaced the SLM with a DMD projection system and succeed high-quality, seamless, all-digital images with exceptional stability and minimal power loss [108]. The quality and resolution of the structures fabricated using this technique were superior to anything presented before.

Today, most research has focused on improving the process of the projection μSLA rather than developing applications [109–112]. However, the main area of research applications has been developing microstructures for cell growth and bio-applications [113–117] or more recently in mechanical metamaterials field [118] (Figure 8.5).

8.4.2 Multiphoton Lithography

MPL is a powerful 3D printing technique which enables the “direct writing” of computer-designed structures within the volume of a photosensitive material [120,121]. This technique is based on the phenomenon of multiphoton polymerization. When the beam of an ultrafast infrared laser is tightly focused into the volume of a photosensitive material, the

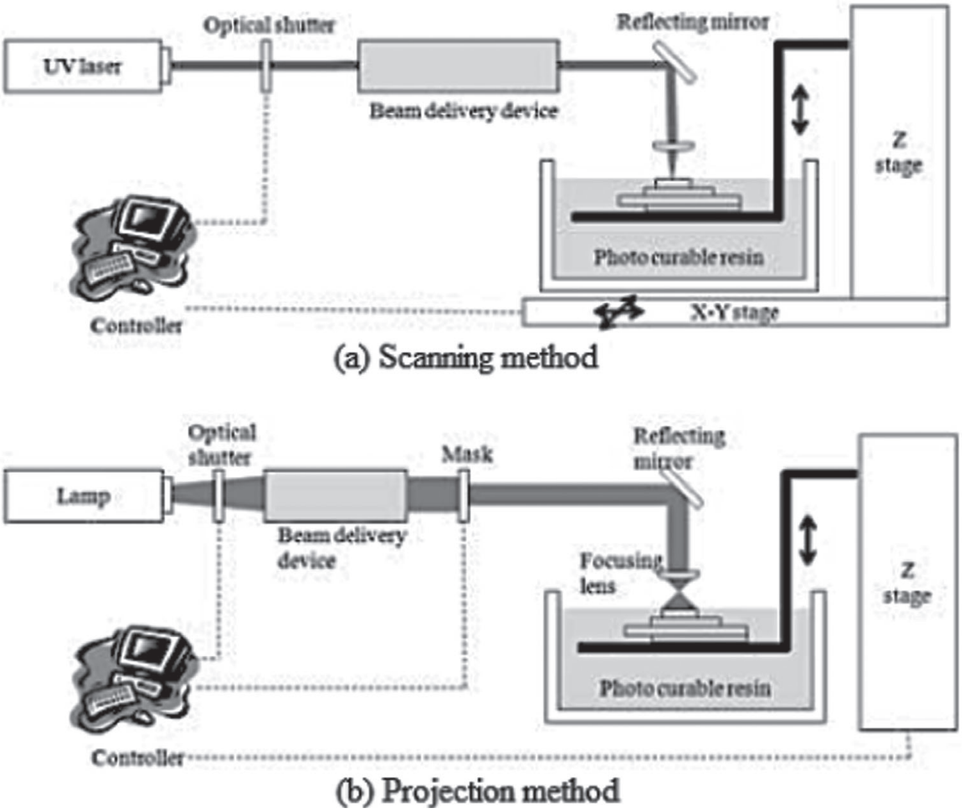
Optical shutter
Reflecting mirror
UV laser
Beam delivery device
Z stage
Photo curable resin
Controller
X-Y stage
(a) Scanning method
Optical shutter
Mask
Reflecting mirror
Lamp
Beam delivery device
Focusing lens
Z stage
Photo curable resin
Controller
(b) Projection method

FIGURE 8.4 Schematics of the µSLA [100].

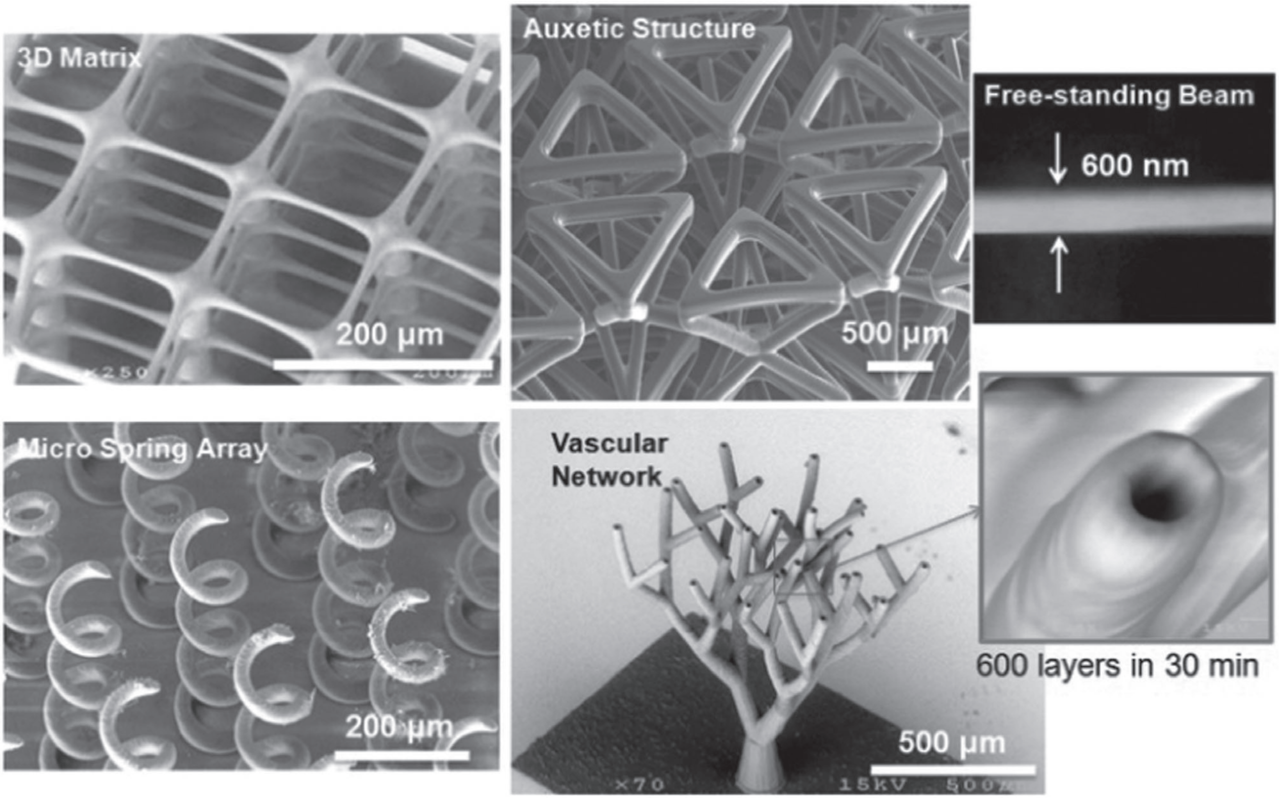
3D Matrix
200 µm
Auxetic Structure
500 µm
Free-standing Beam
600 nm
Micro Spring Array
200 µm
Vascular Network
500 µm
600 layers in 30 min

FIGURE 8.5 3D complex microstructures fabricated employing projection µSLA [119].

polymerization process can be initiated by non-linear absorption within the focal volume. By moving the laser focus three dimensionally through the photosensitive material, 3D structures can be fabricated. MPL was first demonstrated in 1997 [122], and it was used by the photonics community for the fabrication of 3D photonic crystals and nano-photonic devices [123–126]. Today, it is used in many different fields such as microfluidics [127], biomedical implants [128,129], complex 3D scaffolds for tissue engineering [130–135], micro-optical components [136–140], and optical fibre sensors [141–143]. Resolution below 100 nm has been achieved using this technique [144].

No other competing technology offers this resolution. Classic 3D prototyping techniques such as UV laser SLA, 3D inkjet printing, and laser sintering can also produce fully three-dimensional structures; however, they cannot provide resolution better than a few microns. On the other hand, lithographic techniques with superior resolution, such as e-beam lithography, cannot produce anything more complicated than high-aspect ratio two-dimensional structures.

8.4.2.1 Multiphoton Polymerization Technique

Although two-photon absorption (TPA) was originally predicted by Maria Göppert-Mayer in 1931 in her doctoral dissertation, the first experimental verification came thirty years later by Isaac Abella, after the invention of the laser [145]. Initially, this principle found limited applications, for example as a spectroscopic tool, due to the extremely small TPA cross section of most materials. In 1965, two-photon polymerization (TPP) was experimentally reported for the first time by Pao and Rentzepis, as the first example of multiphoton excitation-induced photochemical reactions. After that work, no particular efforts were devoted to two-photon photopolymerization until this technology found value as a microfabrication tool with the use of femtosecond lasers.

8.4.2.2 Sequential and Simultaneous Two-photon Absorption (TPA)

TPA is a popular multiple-photon excitation approach to the initiation of photochemical changes. There are two different mechanisms of TPA: sequential and simultaneous two-photon excitation [120,145,146]. The sequential excitation involves the excitation of the absorbing species to a real intermediate state (S_1) (see Figure 8.6b). This first excited state becomes populated by the first absorbed photon and has a well-defined lifetime, typically 10^{-4} to 10^{-9} s. Then a second photon is absorbed, as illustrated in Figure 8.6b. The other mechanism is shown in Figure 8.6c. In this case, there is no real intermediate state, but a virtual intermediate state is created by the interaction of the absorbing species with the first photon. Only if the second photon arrives within the virtual state lifetime, about 10^{-15} s, it can be absorbed. Therefore, in the second case, higher intensities are required.

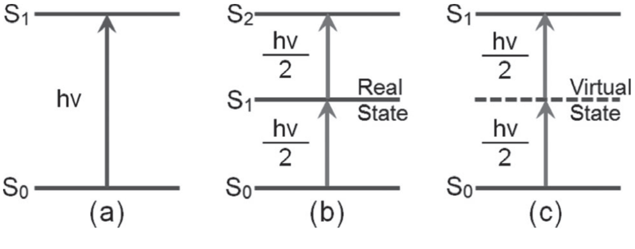

FIGURE 8.6 (a) Single-photon excitation, (b) two-photon sequential excitation, and (c) two-photon simultaneous excitation.

In TPA, two photons, each with half energy of the gap between the two energy levels, namely hv/2, induce the electron transition. Ti:sapphire lasers are widely used for the inducing TPA because they produce ultrahigh peak power with a very short pulse width of approximately 100 femtoseconds (fs) or less. Furthermore, these lasers are very useful for TPP because of their central wavelength of approximately 800 nm, which is close to half of the wavelength of the polymerization. This enables easy control of the polymerization threshold energy.

When the laser is focused tightly with a high NA objective lens into a volume of photocurable resin, the photoinitiator used to initiate the polymerization will absorb two or more photons and produce radicals. As the material response is proportional to the square of the intensity, this will only happen at the focal point. The two-photon transition rate is extremely small in general, so a very high spatial resolution can be obtained [121].

8.4.2.3 Experimental Set-up

A typical experimental set-up for the fabrication of 3D microstructures by MPL is shown in Figure 8.7. Typically, a Ti:sapphire femtosecond oscillator operating at 800 nm is used as the laser source. The laser will typically have a pulse length of less than 200 fs and a repetition rate of 50–80 MHz.

The photopolymerized structure is usually generated in a layer-by-layer fashion. To avoid the distortion of the focused laser beam by the built structure, the layers are fabricated bottom up with the last layer attached to the glass coverslip. Each layer is formed either using a *x–y* galvanometric mirror scanner or *x–y* piezoelectric stages. The main difference between the two cases being that in the first case, the structure is generated by the laser beam moving while the sample remains immobile, whereas in the second case, the *x–y* stages move the sample and the laser beam remains immobile. Movement on the *z*-axis can be achieved using a piezoelectric or a high-resolution linear stage.

To achieve the tight focusing conditions required for TPP process to occur, a microscope objective needs to be used. Beam control can be achieved by either using a fast mechanical shutter or using an acousto-optic modulator, while beam intensity control can be achieved using neutral density filters, a variable attenuator, or a combination of a polarizer and a waveplate.

For the online monitoring of the photopolymerization process, a CCD camera can be mounted behind a dichroic mirror, as shown in Figure 8.7. This is possible as the refractive index of most photopolymers changes during polymerization, so that the illuminated structures become visible during the building process.

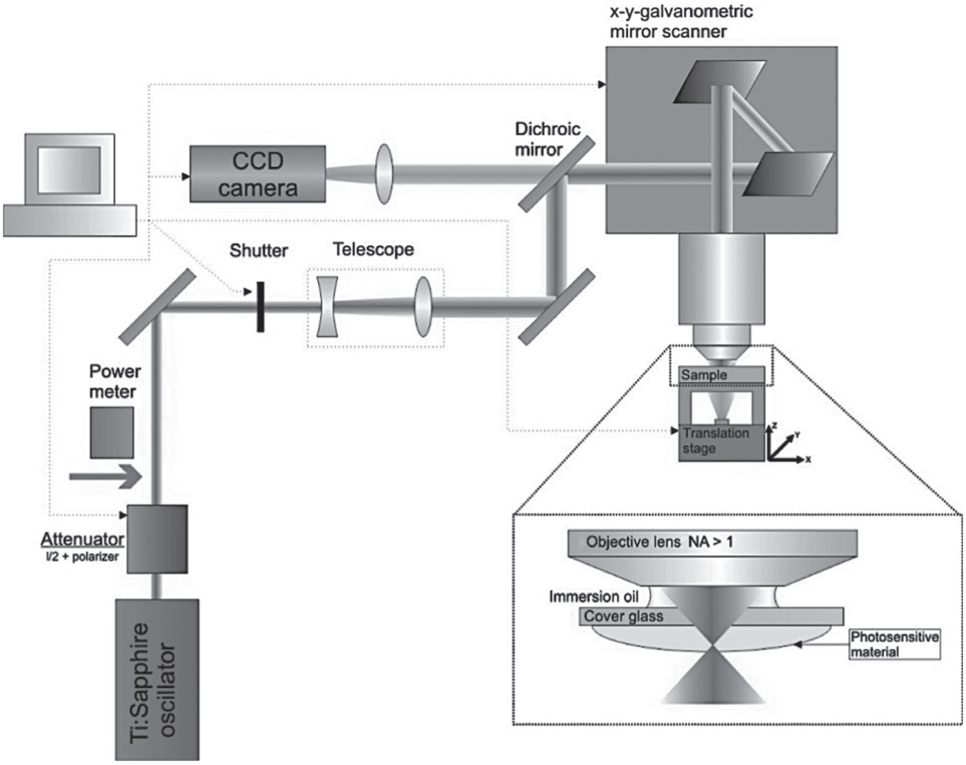
x-y-galvanometric
mirror scanner
Dichroic
mirror
CCD
camera
Shutter
Telescope
Power
meter
Attenuator
l/2 + polarizer
Ti:Sapphire
oscillator
Sample
Translation
stage
z
y
x
Objective lens NA > 1
Immersion oil
Cover glass
Photosensitive
material

FIGURE 8.7 A typical set-up for multiphoton polymerizations.

After the completion of the photopolymerization process, the samples need to be developed in order to remove the unphotopolymerized resin. The developer used and the time for development will depend on the material.

The experimental procedure for fabricating a 3D structure by MPL is shown in Figure 8.8. (i) The laser beam is tightly focused onto the volume of the material; (ii) either the focused beam or the sample moves following a computer-generated layer-by-layer pattern; (iii) after the laser writing of the structure, the sample is immersed into the appropriate developer; and (iv) the freestanding structure is revealed.

8.4.2.4 Materials for Laser Polymerization

In general, a material suitable for structuring with MPL includes at least two components: (i) a monomer, or a mixture of monomers/oligomers, which will provide the final polymer, and (ii) a photoinitiator which will absorb the laser light and provide the active species that will cause this polymerization. Several monomer/oligomer and photoinitiator combinations have been used for this purpose. These are mostly negative photoresists such as hydrogels, acrylate materials [147,148], the epoxy-based photoresist SU-8 [149], and hybrid materials

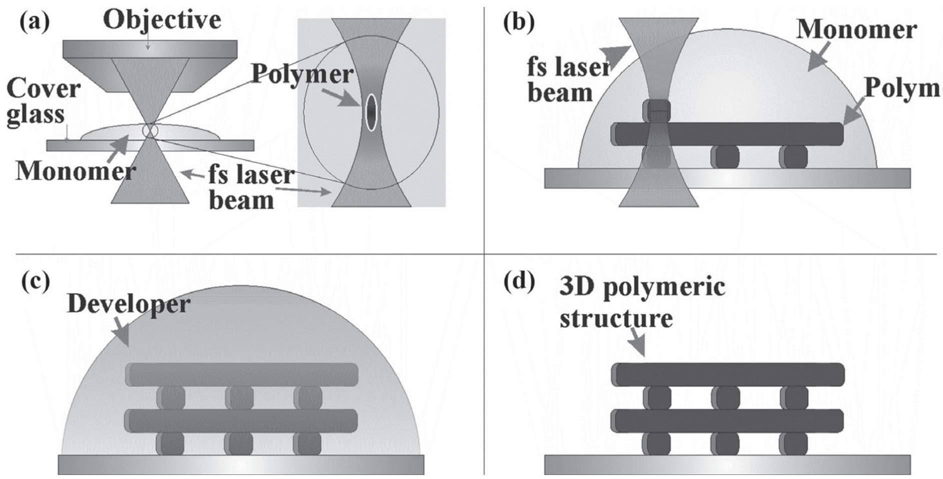
(a)
Objective
Cover
glass
Polymer
Monomer
fs laser
beam
(b)
fs laser
beam
Monomer
Polymer
(c)
Developer
(d)
3D polymeric
structure

FIGURE 8.8 MPL experimental procedure: (I) beam focusing, (II) laser writing, (III) development and (IV) completed structure.

[150,151]. Recently, redox and Diels–Alder photopolymerization have also been reported [126,152].

8.4.2.5 Applications

8.4.2.5.1 Biomedical Applications

The biomedical applications of MPL can be divided into two categories: biomedical microdevices and scaffolds for cell culture. The first category, biomedical microdevices, includes devices such as microneedles for drug delivery, and micromechanics, microfluidic, or optofluidic functional devices [153,154]. Most of these structures are free-standing and have not been integrated into a functional device [155–162]. The second category, MPL scaffolds for cell culture studies and tissue engineering, has seen an enormous growth over the last few years. An important part of the development of artificial tissue is the choice of scaffold as it can influence the attachment, migration, and proliferation of cells. 3D cell cultures offer a realistic environment where the functional properties of cells can be observed and manipulated [163–165]. Recent reviews by Raimondi et al. [166], Ovsianikov et al. [167], and Selimis et al. [168] describe in great detail the use of lasers in tissue engineering applications. In this field, most research groups have used permanent scaffolds for hard tissue engineering or investigating cell (including stem cell) growth [133,169–182]. More recently, there has been a lot of active research into the synthesis of new, biocompatible, and biodegradable materials [183–186] (Figure 8.9).

8.4.2.5.2 Metamaterials

Metamaterials are artificial materials with properties that don't exist in nature; these properties are due to structure and not material composition. Photonic metamaterials consist of nanostructured metal-dielectric subwavelength building components, and allow the realization of many new and unusual optical properties, such as negative refractive index, magnetism at optical frequencies, perfect absorption, and enhanced optical non-linearities. The realization of these applications requires the fabrication of large-scale metal-dielectric structures, a very challenging task.

MPL is the only inherently 3D fabrication technique, with the potential to fabricate 3D structures, but the majority of the materials structurable by MPL are dielectrics. A popular approach is to use MPL to make dielectric structures, and subsequently metallize them. The most successful approaches are (i) MPL of positive photoresists and filling with gold using electroplating [187,188], (ii) MPL of dielectric structures and non-selective metallization with electroless plating [189–192], (iii) MPL of dielectric structures and selective metallization with electroless plating [193–195], and (iv) MPL of dielectric structures and metallization with chemical vapour deposition (CVD) [196].

8.4.2.5.3 MPL onto Optical Fibres

Over the last decade, MPL had been also used in order 3D micro-optical elements to be fabricated directly onto the endface of optical fibres, while exploiting the specific optical interface.

More specifically, photonic elements, including microprisms, woodpile and chiral photonic crystals [138,197,198], micro-lenses (spherical, cylindrical, conical, toric lenses) [138,139,198–200], parabolic micro-reflectors [201], spherical surface-enhanced Raman scattering (SERS) radar configurations [202], phase masks [203], axicons [140,204,205],

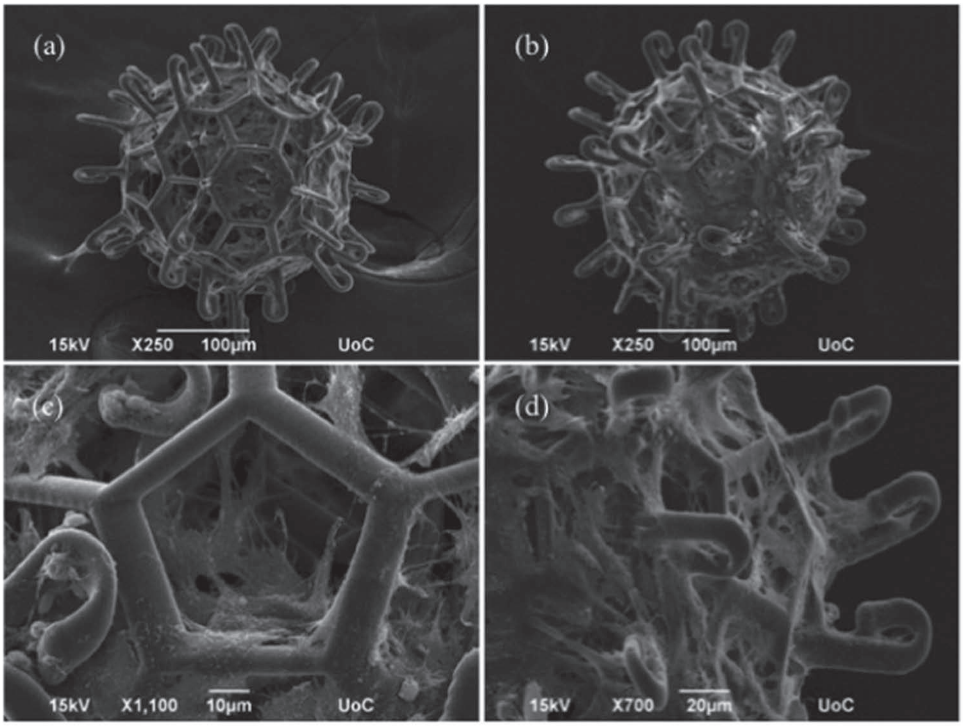

FIGURE 8.9 SEM images of preosteoblastic cells seeded in concentric microscaffold [177].

gradient index anti-reflective coatings [206], and polarization filtering [198], have been fabricated on the end-face of optical fibres in recent years by several groups.

The fabricated elements are being used in a variety of applications such as beam shaping or focusing [198,200], gas or liquid sensors [141–143,207], SERS sensors [202], or even in bioimaging [139] and biomedical applications [140].

REFERENCES

1. Zheng, X.; Fu, Z.; Du, K.; Wang, C.; Yi, Y. Minimal surface designs for porous materials: From microstructures to mechanical properties. *Journal of Materials Science* **2018**, *53*, 10194–10208.
2. Gabbrielli, R.; Turner, I.; Bowen, C. Development of modelling methods for materials to be used as bone substitutes. *Key Engineering Materials* **2008**; *361–363*, 903–906.
3. Mankovich, N.J.; Samson, D.; Pratt, W.; Lew, D.; Beumer, J. Surgical planning use three dimensional imaging and computer modeling. *Otolaryngologic Clinics of North America* **1994**; *27*, 875–889.
4. Hull, C.W. Apparatus for production of three-dimensional objects by stereolithography **1986**.
5. http://www.3dsystems.com.
6. Chavan Shekhar, S.; Ahire Satishkumar, S.; Ghongade Harshvardhan, P.; Jadhav Mahesh, C.; Joshi Bhagyashri A. A review on stereo-lithography. *Global Research and Development Journal for Engineering* **2016**, *1*, 16–19.
7. https://studiofathom.com/rapid-prototyping/3d-printing-stereolithography-sla/.
8. https://www.arrk.com/newsroom/blog/4-reasons-why-stereolithography-sla-is-perfect-for-prototyping/.
9. http://manufacturing.materialise.com/mammoth-stereolithography.
10. Melchels, F.P.W.; Feijen, J.; Grijpma, D.W. A review on stereolithography and its applications in biomedical engineering. *Biomaterials* **2010**, *31*, 6121–6130.
11. https://www.3dhubs.com/knowledge-base/automotive-3d-printing-applications.
12. http://en.shining3d.com/support_detail-4307.html.
13. Vashishtha, V.K.; Makade, R.; Mehla, N. Advancement of rapid prototyping in aerospace industry -a review. *International Journal of Engineering Science and Technology* **2011**, *3*, 2486–2493.
14. D‘Urso, P.; John Earwaker, W.; Barker, T.; Redmond, M.; Thompson, R. G.; Effeney, D.J.; Tomlinson, F. H. Custom cranioplasty using stereolithography and acrylic. *British Journal of Plastic Surgery* **2000**; *53*, 200–204.
15. Chu, T.M.G.; Halloran, J.W.; Hollister, S.J.; Feinberg, S.E. Hydroxyapatite implants with designed internal architecture. *Journal of Materials Science-Materials in Medicine* **2001**, *12*, 471–478.
16. Fisher, J.P.; Vehof, J.W.M.; Dean, D.; van der Waerden, J.; Holland, T.A.; Mikos, A.G.; Jansen, J.A. Soft and hard tissue response to photocrosslinked poly(propylene fumarate) scaffolds in a rabbit model. *Journal of Biomedical Materials Research* **2002**, *59*, 547–556.
17. Hollister, S.J. Porous scaffold design for tissue engineering. *Nature Materials* **2005**, *4*, 518–524.
18. Hutmacher, D.W.; Sittinger, M.; Risbud, M.V. Scaffold-based tissue engineering: Rationale for computer-aided design and solid free-form fabrication systems. *Trends in Biotechnology* **2004**, *22*, 354–362.
19. Chang, P.S.H.; Parker, T.H.; Patrick, C.W.; Miller, M.J. The accuracy of stereolithography in planning craniofacial bone replacement. *Journal of Craniofacial Surgery* **2003**, *14*, 164–170.
20. Sarment, D.; Sukovic, P.; Clinthorne, N. Accuracy of implant placement with stereolithographic surgical guide. *The International Journal of Oral & Maxillofacial Implants* **2002**; *18*, 571–577.
21. Kermer, C.; Rasse, M.; Lagogiannis, G.; Undt, G.; Wagner, A.; Millesi, W. Colour stereolithography for planning complex maxillofacial tumour surgery. *Journal of Cranio-Maxillofacial Surgery* **1998**, *26*, 360–362.
22. https://www.laserproto.com/services/selective-laser-sintering/selective-laser-sintering-process.
23. Das, S.; Wohlert, M.; Beaman, J.J.; Bourell, D.L. Processing of titanium net shapes by sls hip. *Materials & Design* **1999**, *20*, 115–121.
24. Engel, B.; Bourell, D.L. Titanium alloy powder preparation for selective laser sintering. *Rapid Prototyping Journal* **2000**, *6*, 97–106.
25. Fischer, P.; Romano, V.; Blatter, A.; Weber, H.P. Highly precise pulsed selective laser sintering of metallic powders. *Laser Physics Letters* **2005**, *2*, 48–55.
26. Hayashi, T.; Maekawa, K.; Tamura, M.; Hanyu, K. Selective laser sintering method using titanium powder sheet toward fabrication of porous bone substitutes. *JSME International Journal Series a-Solid Mechanics and Material Engineering* **2005**, *48*, 369–375.
27. Tolochko, N.K.; Savich, V.V.; Laoui, T.; Froyen, L.; Onofrio, G.; Signorelli, E.; Titov, V.I. Dental root implants produced by the combined selective laser sintering/melting of titanium powders. *Proceedings of the Institution of Mechanical Engineers Part L-Journal of Materials-Design and Applications* **2002**, *216*, 267–270.
28. Shishkovsky, I.V.; Volova, L.T.; Kuznetsov, M.V.; Morozov, Y.G.; Parkin, I.P. Porous biocompatible implants and tissue scaffolds synthesized by selective laser sintering from ti and niti. *Journal of Materials Chemistry* **2008**, *18*, 1309–1317.
29. Shishkovsky, I.V.; Yadroitsev, I.A.; Smurov, I.Y. Manufacturing three-dimensional nickel titanium articles using layer-by-layer laser-melting technology. *Technical Physics Letters* **2013**, *39*, 1081–1084.
30. Traini, T.; Mangano, C.; Sammons, R.L.; Mangano, F.; Macchi, A.; Piattelli, A. Direct laser metal sintering as a new approach to fabrication of an isoelastic functionally graded material for manufacture of porous titanium dental implants. *Dental Materials* **2008**, *24*, 1525–1533.
31. Williams, J.V.; Revington, P.J. Novel use of an aerospace selective laser sintering machine for rapid prototyping of an orbital blowout fracture. *International Journal of Oral and Maxillofacial Surgery* **2010**, *39*, 182–184.
32. Chatterjee, A.N.; Kumar, S.; Saha, P.; Mishra, P.K.; Choudhury, A.R. An experimental design approach to selective laser sintering of low carbon steel. *Journal of Materials Processing Technology* **2003**, *136*, 151–157.

33. Childs, T.H.C.; Hauser, C.; Badrossamay, M. Selective laser sintering (melting) of stainless and tool steel powders: Experiments and modelling. *Proceedings of the Institution of Mechanical Engineers Part B-Journal of Engineering Manufacture* **2005**, *219*, 339–357.
34. Dewidar, M.M.; Dalgarno, K.W.; Wright, C.S. Processing conditions and mechanical properties of high-speed steel parts fabricated using direct selective laser sintering. *Proceedings of the Institution of Mechanical Engineers Part B-Journal of Engineering Manufacture* **2003**, *217*, 1651–1663.
35. Dewidar, M.M.; Khalil, K.A.; Lim, J.K. Processing and mechanical properties of porous 316l stainless steel for biomedical applications. *Transactions of Nonferrous Metals Society of China* **2007**, *17*, 468–473.
36. Morgan, R.; Sutcliffe, C.J.; O'Neill, W. Density analysis of direct metal laser re-melted 316l stainless steel cubic primitives. *Journal of Materials Science* **2004**, *39*, 1195–1205.
37. Murali, K.; Chatterjee, A.N.; Saha, P.; Palai, R.; Kumar, S.; Roy, S.K.; Mishra, P.K.; Choudhury, A.R. Direct selective laser sintering of iron-graphite powder mixture. *Journal of Materials Processing Technology* **2003**, *136*, 179–185.
38. Niu, H.J.; Chang, I.T.H. Instability of scan tracks of selective laser sintering of high speed steel powder. *Scripta Materialia* **1999**, *41*, 1229–1234.
39. Niu, H.J.; Chang, I.T.H. Selective laser sintering of gas and water atomized high speed steel powders. *Scripta Materialia* **1999**, *41*, 25–30.
40. Niu, H.J.; Chang, I.T.H. Selective laser sintering of gas atomized M2 high speed steel powder. *Journal of Materials Science* **2000**, *35*, 31–38.
41. Agarwala, M.; Bourell, D.; Beaman, J.; Marcus, H.; Barlow, J. Direct selective laser sintering of metals. *Rapid Prototyping Journal* **1995**, *1*, 26–36.
42. Hunt, J.A.; Callaghan, J.T.; Sutcliffe, C.J.; Morgan, R.H.; Halford, B.; Black, R.A. The design and production of Co-Cr alloy implants with controlled surface topography by cad-cam method and their effects on osseointegration. *Biomaterials* **2005**, *26*, 5890–5897.
43. Ju, Y.-W.; Eto, H.; Inagaki, T.; Ida, S.; Ishihara, T. Preparation of Ni-Fe bimetallic porous anode support for solid oxide fuel cells using $LaGaO_3$ based electrolyte film with high power density. *Journal of Power Sources* **2010**, *195*, 6294–6300.
44. Tolochko, N.; Mozzharov, S.; Laoui, T.; Froyen, L. Selective laser sintering of single- and two-component metal powders. *Rapid Prototyping Journal* **2003**, *9*, 68–78.
45. Zhang, J.; Shi, Y.S.; Liu, J.H.; Chen, K.H.; Huang, S.H. Investigation into manufacturing fe-cu-c alloy parts through indirect selective laser sintering. *Materials Science and Technology* **2007**, *23*, 333–337.
46. Seyed Farid Seyed, S.; Samira, G.; Mehdi, M.; Hooman, Y.; Hendrik Simon Cornelis, M.; Nahrizul Adib, K.; Noor Azuan Abu, O. A review on powder-based additive manufacturing for tissue engineering: Selective laser sintering and inkjet 3D printing. *Science and Technology of Advanced Materials* **2015**, *16*, 033502.
47. Leite, J.L.; Salmoria, G.V.; Paggi, R.A.; Ahrens, C.H.; Pouzada, A.S. A study on morphological properties of laser sintered functionally graded blends of amorphous thermoplastics. *International Journal of Materials & Product Technology* **2010**, *39*, 205–221.
48. Schmidt, M.; Pohle, D.; Rechtenwald, T. Selective laser sintering of peek. *Cirp Annals-Manufacturing Technology* **2007**, *56*, 205–208.
49. Shi, Y.; Wang, Y.; Chen, J.; Huang, S. Experimental investigation into the selective laser sintering of high-impact polystyrene. *Journal of Applied Polymer Science* **2008**, *108*, 535–540.
50. Shi, Y.S.; Li, Z.C.; Sun, H.X.; Huang, S.H.; Zeng, F.D. Development of a polymer alloy of polystyrene (PS) and polyamide (PA) for building functional part based on selective laser sintering (SLS). *Proceedings of the Institution of Mechanical Engineers Part L-Journal of Materials-Design and Applications* **2004**, *218*, 299–306.
51. Soe, S.P. Improving dimensional accuracy in the production of a castform (TM) polystyrene pattern for investment casting. *Proceedings of the Institution of Mechanical Engineers Part B-Journal of Engineering Manufacture* **2010**, *224*, 1663–1670.
52. Soe, S.P.; Eyers, D.R. Fea support structure generation for the additive manufacture of castform (TM) polystyrene patterns. *Polymer Testing* **2014**, *33*, 187–197.
53. Xu, Z.F.; Zhang, J.; Zheng, H.Z.; Cai, C.C.; Huang, Y.H. Morphology and mechanical properties of PS/Al_2O_3 nanocomposites based on selective laser sintering. *Journal of Materials Science & Technology* **2005**, *21*, 866–870.
54. Yan, C.; Shi, Y.; Yang, J.; Liu, J. Investigation into the selective laser sintering of styrene-acrylonitrile copolymer and postprocessing. *International Journal of Advanced Manufacturing Technology* **2010**, *51*, 973–982.
55. Yan, C.; Shi, Y.; Yang, J.; Liu, J. Multiphase polymeric materials for rapid prototyping and tooling technologies and their applications. *Composite Interfaces* **2010**, *17*, 257–271.
56. Zheng, H.Z.; Zhang, J.; Lu, S.Q.; Wang, G.C.; Xu, Z.F. Effect of core-shell composite particles on the sintering behavior and properties of nano-Al_2O_3/polystyrene composite prepared by SLS. *Materials Letters* **2006**, *60*, 1219–1223.
57. Berry, E.; Brown, J.M.; Connell, M.; Craven, C.M.; Efford, N.D.; Radjenovic, A.; Smith, M.A. Preliminary experience with medical applications of rapid prototyping by selective laser sintering. *Medical Engineering & Physics* **1997**, *19*, 90–96.
58. Chung, H.; Das, S. Processing and properties of glass bead particulate-filled functionally graded nylon-11 composites produced by selective laser sintering. *Materials Science and Engineering a-Structural Materials Properties Microstructure and Processing* **2006**, *437*, 226–234.
59. Kim, J.; Creasy, T.S. Selective laser sintering characteristics of nylon 6/clay-reinforced nanocomposite. *Polymer Testing* **2004**, *23*, 629–636.
60. Yan, C.; Shi, Y.; Yang, J.; Liu, J. Preparation and selective laser sintering of nylon-12 coated metal powders and post processing. *Journal of Materials Processing Technology* **2009**, *209*, 5785–5792.
61. Yan, C.Z.; Shi, Y.S.; Yang, J.S.; Liu, J.H. Preparation and selective laser sintering of nylon-coated metal powders for the indirect SLS process. *Rapid Prototyping Journal* **2009**, *15*, 355–360.
62. Zarringhalam, H.; Hopkinson, N.; Kamperman, N.F.; de Vlieger, J.J. Effects of processing on microstructure and properties of SLS nylon 12. *Materials Science and Engineering a-Structural Materials Properties Microstructure and Processing* **2006**, *435*, 172–180.

63. Chua, C.K.; Leong, K.F.; Tan, K.H.; Wiria, F.E.; Cheah, C.M. Development of tissue scaffolds using selective laser sintering of polyvinyl alcohol/hydroxyapatite biocomposite for craniofacial and joint defects. *Journal of Materials Science-Materials in Medicine* **2004**, *15*, 1113–1121.
64. Duan, B.; Wang, M.; Zhou, W.Y.; Cheung, W.L. Synthesis of Ca-P nanoparticles and fabrication of Ca-P/PHBV nanocomposite microspheres for bone tissue engineering applications. *Applied Surface Science* **2008**, *255*, 529–533.
65. Dyson, J.A.; Genever, P.G.; Dalgarno, K.W.; Wood, D.J. Development of custom-built bone scaffolds using mesenchymal stem cells and apatite-wollastonite glass-ceramics. *Tissue Engineering* **2007**, *13*, 2891–2901.
66. Hao, L.; Savalani, M.M.; Zhang, Y.; Tanner, K.E.; Harris, R.A. Effects of material morphology and processing conditions on the characteristics of hydroxyapatite and high-density polyethylene biocomposites by selective laser sintering. *Proceedings of the Institution of Mechanical Engineers Part L-Journal of Materials-Design and Applications* **2006**, *220*, 125–137.
67. Hao, L.; Savalani, M.M.; Zhang, Y.; Tanner, K.E.; Harris, R.A. Selective laser sintering of hydroxyapatite reinforced polyethylene composites for bioactive implants and tissue scaffold development. *Proceedings of the Institution of Mechanical Engineers Part H-Journal of Engineering in Medicine* **2006**, *220*, 521–531.
68. Kanczler, J.M.; Mirmalek-Sani, S.-H.; Hanley, N.A.; Ivanov, A.L.; Barry, J.J.A.; Upton, C.; Shakesheff, K.M.; Howdle, S.M.; Antonov, E.N.; Bagratashvili, V.N., et al. Biocompatibility and osteogenic potential of human fetal femur-derived cells on surface selective laser sintered scaffolds. *Acta Biomaterialia* **2009**, *5*, 2063–2071.
69. Lorrison, J.C.; Dalgarno, K.W.; Wood, D.J. Processing of an apatite-mullite glass-ceramic and an hydroxyapatite/phosphate glass composite by selective laser sintering. *Journal of Materials Science-Materials in Medicine* **2005**, *16*, 775–781.
70. Peltola, S.M.; Melchels, F.P.W.; Grijpma, D.W.; Kellomaki, M. A review of rapid prototyping techniques for tissue engineering purposes. *Annals of Medicine* **2008**, *40*, 268–280.
71. Shishkovsky, I.V.; Tarasova, E.Y.; Zhuravel, L.V.; Petrov, A.L. The synthesis of a biocomposite based on nickel titanium and hydroxyapatite under selective laser sintering conditions. *Technical Physics Letters* **2001**, *27*, 211–213.
72. Tan, K.H.; Chua, C.K.; Leong, K.F.; Cheah, C.M.; Cheang, P.; Abu Bakar, M.S.; Cha, S.W. Scaffold development using selective laser sintering of polyetheretherketone-hydroxyapatite biocomposite blends. *Biomaterials* **2003**, *24*, 3115–3123.
73. Tan, K.H.; Chua, C.K.; Leong, K.F.; Cheah, C.M.; Gui, W.S.; Tan, W.S.; Wiria, F.E. Selective laser sintering of biocompatible polymers for applications in tissue engineering. *Bio-Medical Materials and Engineering* **2005**, *15*, 113–124.
74. Tan, K.H.; Chua, C.K.; Leong, K.F.; Naing, M.W.; Cheah, C.M. Fabrication and characterization of three-dimensional poly(ether-ether-ketone)/-hydroxyapatite biocomposite scaffolds using laser sintering. *Proceedings of the Institution of Mechanical Engineers Part H-Journal of Engineering in Medicine* **2005**, *219*, 183–194.
75. Williams, J.M.; Adewunmi, A.; Schek, R.M.; Flanagan, C.L.; Krebsbach, P.H.; Feinberg, S.E.; Hollister, S.J.; Das, S. Bone tissue engineering using polycaprolactone scaffolds fabricated via selective laser sintering. *Biomaterials* **2005**, *26*, 4817–4827.
76. Wiria, F.E.; Leong, K.F.; Chua, C.K.; Liu, Y. Poly-epsilon-caprolactone/hydroxyapatite for tissue engineering scaffold fabrication via selective laser sintering. *Acta Biomaterialia* **2007**, *3*, 1–12.
77. Zhang, Y.; Hao, L.; Savalani, M.M.; Harris, R.A.; Tanner, K.E. Characterization and dynamic mechanical analysis of selective laser sintered hydroxyapatite-filled polymeric composites. *Journal of Biomedical Materials Research Part A* **2008**, *86A*, 607–616.
78. Zhou, W.Y.; Duan, B.; Wang, M.; Cheung, W.L. Crystallization kinetics of poly(l-lactide)/carbonated hydroxyapatite nanocomposite microspheres. *Journal of Applied Polymer Science* **2009**, *113*, 4100–4115.
79. Zhou, W.Y.; Lee, S.H.; Wang, M.; Cheung, W.L.; Ip, W.Y. Selective laser sintering of porous tissue engineering scaffolds from poly(l)/carbonated hydroxyapatite nanocomposite microspheres. *Journal of Materials Science-Materials in Medicine* **2008**, *19*, 2535–2540.
80. Zhou, W.Y.; Wang, M.; Cheung, W.L.; Guo, B.C.; Jia, D.M. Synthesis of carbonated hydroxyapatite nanospheres through nanoemulsion. *Journal of Materials Science-Materials in Medicine* **2008**, *19*, 103–110.
81. Chua, C.K.; Leong, K.F.; Sudarmadji, N.; Liu, M.J.J.; Chou, S.M. Selective laser sintering of functionally graded tissue scaffolds. *MRS Bulletin* **2011**, *36*, 1006–1014.
82. Duan, B.; Cheung, W.L.; Wang, M. Optimized fabrication of Ca-P/PHBV nanocomposite scaffolds via selective laser sintering for bone tissue engineering. *Biofabrication* **2011**, *3*, 015001.
83. Duan, B.; Wang, M.; Zhou, W.Y.; Cheung, W.L.; Li, Z.Y.; Lu, W.W. Three-dimensional nanocomposite scaffolds fabricated via selective laser sintering for bone tissue engineering. *Acta Biomaterialia* **2010**, *6*, 4495–4505.
84. Eshraghi, S.; Das, S. Micromechanical finite-element modeling and experimental characterization of the compressive mechanical properties of polycaprolactone-hydroxyapatite composite scaffolds prepared by selective laser sintering for bone tissue engineering. *Acta Biomaterialia* **2012**, *8*, 3138–3143.
85. Kolan, K.C.R.; Leu, M.C.; Hilmas, G.E.; Brown, R.F.; Velez, M. Fabrication of 13–93 bioactive glass scaffolds for bone tissue engineering using indirect selective laser sintering. *Biofabrication* **2011**, *3*, 025004.
86. Shuai, C.; Gao, C.; Nie, Y.; Hu, H.; Qu, H.; Peng, S. Structural design and experimental analysis of a selective laser sintering system with nano-hydroxyapatite powder. *Journal of Biomedical Nanotechnology* **2010**, *6*, 370–374.
87. Shuai, C.; Gao, C.; Nie, Y.; Hu, H.; Zhou, Y.; Peng, S. Structure and properties of nano-hydroxypatite scaffolds for bone tissue engineering with a selective laser sintering system. *Nanotechnology* **2011**, *22*.
88. Shuai, C.; Li, P.; Liu, J.; Peng, S. Optimization of TCP/HAP ratio for better properties of calcium phosphate scaffold via selective laser sintering. *Materials Characterization* **2013**, *77*, 23–31.

89. Xia, Y.; Zhou, P.; Cheng, X.; Xie, Y.; Liang, C.; Li, C.; Xu, S. Selective laser sintering fabrication of nano-hydroxyapatite/poly-epsilon-caprolactone scaffolds for bone tissue engineering applications. *International Journal of Nanomedicine* **2013**, *8*, 4197–4213.
90. Zhang, Y.; Hao, L.; Savalani, M.M.; Harris, R.A.; Di Silvio, L.; Tanner, K.E. In vitro biocompatibility of hydroxyapatite-reinforced polymeric composites manufactured by selective laser sintering. *Journal of Biomedical Materials Research Part A* **2009**, *91A*, 1018–1027.
91. Lohfeld, S.; Barron, V.; McHugh, P. Biomodels of bone: A review. *Annals of Biomedical Engineering* **2005**, *33*, 1295–1311.
92. Lee, M.Y.; Tsai, W.W.; Chen, H.J.; Chen, J.P.; Chen, C.H.; Yeh, W.L.; An, J. Laser sintered porous polycaprolacone scaffolds loaded with hyaluronic acid and gelatin-grafted thermoresponsive hydrogel for cartilage tissue engineering. *Bio-Medical Materials and Engineering* **2013**, *23*, 533–543.
93. Yeong, W.Y.; Sudarmadji, N.; Yu, H.Y.; Chua, C.K.; Leong, K.F.; Venkatraman, S.S.; Boey, Y.C.F.; Tan, L.P. Porous polycaprolactone scaffold for cardiac tissue engineering fabricated by selective laser sintering. *Acta Biomaterialia* **2010**, *6*, 2028–2034.
94. Ho, B.; Ng, S.H.; Yoon, Y.-J. A review on 3D printed bioimplants. *International Journal of Precision Engineering and Manufacturing* **2015**, *16*, 1035–1046.
95. Mangano, F.; Pozzi Taubert, S.; Zecca, P.A.; Luongo, G.; Sammons, R.; Mangano, C. Immediate restoration of fixed partial prostheses supported by one-piece narrow-diameter selective laser sintering implants: A 2-year prospective study in the posterior jaws of 16 patients. *Implant Dentistry* 2013; *22*, 388–393.
96. Yuan, S.; Shen, F.; Bai, J.; Chua, C.K.; Wei, J.; Zhou, K. 3D soft auxetic lattice structures fabricated by selective laser sintering: TPU powder evaluation and process optimization. *Materials & Design* **2017**, *120*, 317–327.
97. Gorguluarslan, R.M.; Gandhi, U.N.; Song, Y.; Choi, S.-K. An improved lattice structure design optimization framework considering additive manufacturing constraints. *Rapid Prototyping Journal* **2017**, *23*, 305–319.
98. Zhang, X.; Jiang, X.N.; Sun, C. Micro-stereolithography of polymeric and ceramic microstructures. *Sensors and Actuators a-Physical* **1999**, *77*, 149–156.
99. Bertsch, A.; Jiguet, S.; Bernhard, P.; Renaud, P. Microstereolithography: A review. *MRS Proceedings* **2011**, *758*, LL1.1.
100. Ha, Y.M.; Choi, J.W.; Lee, S.H. Mass production of 3-D microstructures using projection microstereolithography. *Journal of Mechanical Science and Technology* **2008**, *22*, 514.
101. Bertsch, A.; Zissi, S.; Jezequel, J.Y.; Corbel, S.; Andre, J.C. Microstereophotolithography using a liquid crystal display as dynamic mask-generator. *Microsystem Technologies* **1997**, *3*, 42–47.
102. Bertsch, A.; Yezequel, J.Y.; Andre, J.C. Study of the spatial resolution of a new 3D microfabrication process: The microstereophotolithography using a dynamic mask-generator technique. *Journal of Photochemistry and Photobiology A: Chemistry* **1997**, *107*, 275–281.
103. Chatwin, C.; Farsari, M.; Huang, S.P.; Heywood, M.; Birch, P.; Young, R.; Richardson, J. UV microstereolithography system that uses spatial light modulator technology. *Applied Optics* **1998**, *37*, 7514–7522.
104. Farsari, M.; Huang, S.; Birch, P.; Claret-Tournier, F.; Young, R.; Budgett, D.; Bradfield, C.; Chatwin, C. Microfabrication by use of a spatial light modulator in the ultraviolet: Experimental results. *Optics Letters* **1999**, *24*, 549–550.
105. Farsari, M.; Claret-Tournier, F.; Huang, S.; Chatwin, C.R.; Budgett, D.M.; Birch, P.M.; Young, R.C.D.; Richardson, J.D. A novel high-accuracy microstereolithography method employing an adaptive electro-optic mask. *Journal of Materials Processing Technology* **2000**, *107*, 167–172.
106. Bertsch, A.; Jiguet, S.; Renaud, P. Microfabrication of ceramic components by microstereolithography. *Journal of Micromechanics and Microengineering* **2004**, *14*, 197–203.
107. Hornbeck, L.J. Digital light processing for high-brightness high-resolution applications. In: Electronic Imaging'97, **1997**; International Society for Optics and Photonics: pp. 27–40.
108. Sun, C.; Fang, N.; Wu, D.M.; Zhang, X. Projection micro-stereolithography using digital micro-mirror dynamic mask. *Sensors and Actuators a-Physical* **2005**, *121*, 113–120.
109. Emami, M.M.; Barazandeh, F.; Yaghmaie, F. An analytical model for scanning-projection based stereolithography. *Journal of Materials Processing Technology* **2015**, *219*, 17–27.
110. Lee, M.P.; Cooper, G.J.T.; Hinkley, T.; Gibson, G.M.; Padgett, M.J.; Cronin, L. Development of a 3D printer using scanning projection stereolithography. *Scientific Reports* **2015**, *5*, 9875.
111. Luo, N.; Gao, Y.; Zhang, Z.; Xiao, M.; Wu, H. Three-dimensional microstructures of photoresist formed by gradual gray-scale lithography approach. *Optica Applicata* **2012**, *42*, 853–864.
112. Xu, K.; Chen, Y. Mask image planning for deformation control in projection-based stereolithography process. *Journal of Manufacturing Science and Engineering-Transactions of the Asme* **2015**, *137*, 425–437.
113. Choi, J.-W.; Wicker, R.; Lee, S.-H.; Choi, K.-H.; Ha, C.-S.; Chung, I. Fabrication of 3D biocompatible/biodegradable micro-scaffolds using dynamic mask projection microstereolithography. *Journal of Materials Processing Technology* **2009**, *209*, 5494–5503.
114. Han, L.-H.; Mapili, G.; Chen, S.; Roy, K. Projection microfabrication of three-dimensional scaffolds for tissue engineering. *Journal of Manufacturing Science and Engineering-Transactions of the ASME* **2008**, *130*, 021005.
115. Wang, S.; Foo, C.W.P.; Warrier, A.; Poo, M.; Heilshorn, S.C.; Zhang, X. Gradient lithography of engineered proteins to fabricate 2D and 3D cell culture micro environments. *Biomedical Microdevices* **2009**, *11*, 1127–1134.
116. Zhang, A.P.; Qu, X.; Soman, P.; Hribar, K.C.; Lee, J.W.; Chen, S.; He, S. Rapid fabrication of complex 3D extracellular microenvironments by dynamic optical projection stereolithography. *Advanced Materials* **2012**, *24*, 4266–4270.

117. Gauvin, R.; Chen, Y.-C.; Lee, J.W.; Soman, P.; Zorlutuna, P.; Nichol, J.W.; Bae, H.; Chen, S.; Khademhosseini, A. Microfabrication of complex porous tissue engineering scaffolds using 3D projection stereolithography. *Biomaterials* **2012**, *33*, 3824–3834.
118. Zheng, X.; Lee, H.; Weisgraber, T.H.; Shusteff, M.; DeOtte, J.; Duoss, E.B.; Kuntz, J.D.; Biener, M.M.; Ge, Q.; Jackson, J.A., et al. Ultralight, ultrastiff mechanical metamaterials. *Science* **2014**, *344*, 1373.
119. http://zhoufan.weebly.com/microstereolithography.html.
120. Maria, F.; Maria, V.; Chichkov Boris, N. Multiphoton polymerization of hybrid materials. *Journal of Optics* **2010**, *12*, 124001.
121. Lee, K.S.; Yang, D.Y.; Park, S.H.; Kim, R.H. Recent developments in the use of two-photon polymerization in precise 2D and 3D microfabrications. *Polymers for Advanced Technologies* **2006**, *17*, 72–82.
122. Maruo, S.; Nakamura, O.; Kawata, S. Three-dimensional microfabrication with two-photon-absorbed photopolymerization. *Optics Letters* **1997**, *22*, 132–134.
123. Juodkazis, S.; Mizeikis, V.; Misawa, H. Three-dimensional microfabrication of materials by femtosecond lasers for photonics applications. *Journal of Applied Physics* **2009**, *106*, 051101.
124. Sakellari, I.; Kabouraki, E.; Gray, D.; Purlys, V.; Fotakis, C.; Pikulin, A.; Bityurin, N.; Vamvakaki, M.; Farsari, M. Diffusion-assisted high-resolution direct femtosecond laser writing. *ACS Nano* **2012**, *6*, 2302–2311.
125. Sakellari, I.; Gaidukeviciute, A.; Giakoumaki, A.; Gray, D.; Fotakis, C.; Farsari, M.; Vamvakaki, M.; Reinhardt, C.; Ovsianikov, A.; Chichkov, B.N. Two-photon polymerization of titanium-containing sol-gel composites for three-dimensional structure fabrication. *Applied Physics a-Materials Science & Processing* **2010**, *100*, 359–364.
126. Kabouraki, E.; Giakoumaki, A.N.; Danilevicius, P.; Gray, D.; Vamvakaki, M.; Farsari, M. Redox multiphoton polymerization for 3d nanofabrication. *Nano Letters* **2013**, *13*, 3831–3835.
127. Amato, L.; Gu, Y.; Bellini, N.; Eaton, S.M.; Cerullo, G.; Osellame, R. Integrated three-dimensional filter separates nanoscale from microscale elements in a microfluidic chip. *Lab Chip* **2012**, *12*, 1135–1142.
128. Schizas, C.; Melissinaki, V.; Gaidukeviciute, A.; Reinhardt, C.; Ohrt, C.; Dedoussis, V.; Chichkov, B.N.; Fotakis, C.; Farsari, M.; Karalekas, D. On the design and fabrication by two-photon polymerization of a readily assembled microvalve. *International Journal of Advanced Manufacturing Technology* **2010**, *48*, 435–441.
129. Galanopoulos, S.; Chatzidai, N.; Melissinaki, V.; Selimis, A.; Schizas, C.; Farsari, M.; Karalekas, D. Design, fabrication and computational characterization of a 3D microvalve built by multi-photon polymerization. *Micromachines* **2014**, *5*, 505–514.
130. Melissinaki, V.; Gill, A.A.; Ortega, I.; Vamvakaki, M.; Ranella, A.; Haycock, J.W.; Fotakis, C.; Farsari, M.; Claeyssens, F. Direct laser writing of 3D scaffolds for neural tissue engineering applications. *Biofabrication* **2011**, *3*, 045005.
131. Raimondi, M.T.; Eaton, S.M.; Nava, M.M.; Lagana, M.; Cerullo, G.; Osellame, R. Two-photon laser polymerization: From fundamentals to biomedical application in tissue engineering and regenerative medicine. *Journal of Applied Biomaterials & Functional Materials*. **2012**, *10*, 56–66.
132. Ovsianikov, A.; Deiwick, A.; Van Vlierberghe, S.; Dubruel, P.; Moller, L.; Drager, G.; Chichkov, B. Laser fabrication of three-dimensional cad scaffolds from photosensitive gelatin for applications in tissue engineering. *Biomacromolecules* **2011**, *12*, 851–858.
133. Danilevicius, P.; Georgiadi, L.; Pateman, C.J.; Claeyssens, F.; Chatzinikolaidou, M.; Farsari, M. The effect of porosity on cell ingrowth into accurately defined, laser-made, polylactide-based 3D scaffolds. *Applied Surface Science* **2015**, *336*, 2–10.
134. Malinauskas, M.; Danilevicius, P.; Baltriukiene, D.; Rutkauskas, M.; Zukauskas, A.; Kairyte, Z.; Bickauskaite, G.; Purlys, V.; Paipulas, D.; Bukelskiene, V., et al. 3D artificial polymeric scaffolds for stem cell growth fabricated by femtosecond laser. *Lithuanian Journal of Physics* **2010**, *50*, 75–82.
135. Torgersen, J.; Ovsianikov, A.; Mironov, V.; Pucher, N.; Qin, X.H.; Li, Z.Q.; Cicha, K.; Machacek, T.; Liska, R.; Jantsch, V., et al. Photo-sensitive hydrogels for three-dimensional laser microfabrication in the presence of whole organisms. *Journal of Biomedical Optics* **2012**, *17*, 10.
136. Harnisch, E.; Russew, M.; Klein, J.; Konig, N.; Crailsheim, H.; Schmitt, R. Optimization of hybrid polymer materials for 2PP and fabrication of individually designed hybrid microoptical elements thereof. *Optical Materials Express* **2015**, *5*, 456–461.
137. Reinhardt, C.; Passinger, S.; Chichkov, B.N.; Marquart, C.; Radko, I.P.; Bozhevolnyi, S.I. Laser-fabricated dielectric optical components for surface plasmon polaritons. *Optics Letters* **2006**, *31*, 1307–1309.
138. Williams, H.E.; Freppon, D.J.; Kuebler, S.M.; Rumpf, R.C.; Melino, M.A. Fabrication of three-dimensional microphotonic structures on the tip of optical fibers using su-8. *Optics Express* **2011**, *19*, 22910–22922.
139. Gissibl, T.; Thiele, S.; Herkommer, A.; Giessen, H. Two-photon direct laser writing of ultracompact multi-lens objectives. *Nature Photonics* **2016**, *10*, 554–560.
140. Sokolovskii, G.S.; Dudelev, V.V.; Melissinaki, V.; Losev, S.N.; Soboleva, K.K.; Deryagin, A.G.; Kuchinskii, V.I.; Farsari, M.; Sibbett, W.; Rafailov, E.U. Optical trapping with superfocused high-m^2 laser diode beam. In: SPIE LASE, **2015**; SPIE: p. 7.
141. Melissinaki, V.; Farsari, M.; Pissadakis, S. A fiber-endface, fabry-perot vapor microsensor fabricated by multiphoton polymerization. *IEEE Journal of Selected Topics in Quantum Electronics* **2015**, *21*, 10.
142. Melissinaki, V.; Konidakis, I.; Farsari, M.; Pissadakis, S. Fiber endface fabry-perot microsensor with distinct response to vapors of different chlorinated organic solvents. *IEEE Sensors Journal* **2016**, *16*, 7094–7100.
143. Melissinaki, V.; Farsari, M.; Pissadakis, S. A fiber optic fabry–perot cavity sensor for the probing of oily samples. *Fibers* **2017**, *5*, 1.

144. Haske, W.; Chen, V.W.; Hales, J.M.; Dong, W.T.; Barlow, S.; Marder, S.R.; Perry, J.W. 65 nm feature sizes using visible wavelength 3-D multiphoton lithography. *Optics Express* **2007**, *15*, 3426–3436.
145. Sun, H.-B.; Kawata, S. Two-photon photopolymerization and 3D lithographic microfabrication. In: Fatkullin, N.; Ikehara, T.; Jinnai, H.; Kawata, S.; Kimmich, R.; Nishi, T.; Nishikawa, Y.; Sun, H.B., (Eds.) *NMR • 3D Analysis • Photopolymerization*. Springer, Berlin, **2004**; pp. 169–273.
146. Misawa, H.; Juodkazis, S., (Eds.) *3D Laser Microfabrication: Principles and Applications*. Wiley-VCH Verlag GmbH & Co, Weinheim, **2006**.
147. LaFratta, C.N.; Fourkas, J.T.; Baldacchini, T.; Farrer, R.A. Multiphoton fabrication. *Angewandte Chemie International Edition* **2007**, *46*, 6238–6258.
148. Farsari, M.; Filippidis, G.; Sambani, K.; Drakakis, T.S.; Fotakis, C. Two-photon polymerization of an eosin y-sensitized acrylate composite. *Journal of Photochemistry and Photobiology A: Chemistry* **2006**, *181*, 132–135.
149. Juodkazis, S.; Mizeikis, V.; Misawa, H. Three-dimensional microfabrication of materials by femtosecond lasers for photonics applications. *Journal of Applied Physics* **2009**, *106*, 051101.
150. Farsari, M.; Chichkov, B.N. Two-photon fabrication. *Nature Photonics* **2009**, *3*, 450–452.
151. Farsari, M.; Vamvakaki, M.; Chichkov, B.N. Multiphoton polymerization of hybrid materials. *Journal of Optics* **2010**, *12*.
152. Quick, A.S.; Rothfuss, H.; Welle, A.; Richter, B.; Fischer, J.; Wegener, M.; Barner-Kowollik, C. Fabrication and spatially resolved functionalization of 3D microstructures via multiphoton-induced diels–alder chemistry. *Advanced Functional Materials* **2014**. doi:10.1002/adfm.201304030.
153. Narayan, R.; Goering, P. Laser micro-and nanofabrication of biomaterials. *MRS Bulletin* **2011**, *36*, 973–982.
154. Waldbaur, A.; Rapp, H.; Lange, K.; Rapp, B.E. Let there be chip-towards rapid prototyping of microfluidic devices: One-step manufacturing processes. *Analytical Methods* **2011**, *3*, 2681–2716.
155. Schizas, C.; Melissinaki, V.; Gaidukeviciute, A.; Reinhardt, C.; Ohrt, C.; Dedoussis, V.; Chichkov, B.N.; Fotakis, C.; Farsari, M.; Karalekas, D. On the design and fabrication by two-photon polymerization of a readily assembled micro-valve. *The International Journal of Advanced Manufacturing Technology* **2010**, *48*, 435–441.
156. Lin, C.L.; Wang, I.; Dollet, B.; Baldeck, P.L. Velocimetry microsensors driven by linearly polarized optical tweezers. *Optics Letters* **2006**, *31*, 329–331.
157. Maruo, S.; Hasegawa, T.; Yoshimura, N. Replication of three-dimensional rotary micromechanism by membrane-assisted transfer molding. *Japanese Journal of Applied Physics* **2009**, *48*, 06FH05.
158. Lee, J.T.; George, M.C.; Moore, J.S.; Braun, P.V. Multiphoton writing of three-dimensional fluidic channels within a porous matrix. *Journal of the American Chemical Society.* **2009**, *131*, 11294–11295.
159. Lin, C.L.; Vitrant, G.; Bouriau, M.; Casalegno, R.; Baldeck, P.L. Optically driven archimedes micro-screws for micropump application. *Optics Express* **2011**, *19*, 8267–8276.
160. Gittard, S.D.; Miller, P.R.; Boehm, R.D.; Ovsianikov, A.; Chichkov, B.N.; Heiser, J.; Gordon, J.; Monteiro-Riviere, N.A.; Narayan, R.J. Multiphoton microscopy of transdermal quantum dot delivery using two photon polymerization-fabricated polymer microneedles. *Faraday Discussions* **2011**, *149*, 171–185.
161. Gittard, S.D.; Narayan, R.J.; Jin, C.; Ovsianikov, A.; Chichkov, B.N.; Monteiro-Riviere, N.A.; Stafslien, S.; Chisholm, B. Pulsed laser deposition of antimicrobial silver coating on ormocer (r) microneedles. *Biofabrication* **2009**, *1*, 041001.
162. Gittard, S.D.; Ovsianikov, A.; Akar, H.; Chichkov, B.; Monteiro-Riviere, N.A.; Stafslien, S.; Chisholm, B.; Shin, C.C.; Shih, C.M.; Lin, S.J., et al. Two photon polymerization-micromolding of polyethylene glycol-gentamicin sulfate microneedles. *Advanced Engineering Materials* **2010**, *12*, B77–B82.
163. Zhang, S.G.; Gelain, F.; Zhao, X.J. Designer self-assembling peptide nanofiber scaffolds for 3D tissue cell cultures. *Seminars in Cancer Biology* **2005**, *15*, 413–420.
164. Abbott, A. Cell culture: Biology's new dimension. *Nature* **2003**, *424*, 870–872.
165. Stratakis, E.; Ranella, A.; Farsari, M.; Fotakis, C. Laser-based micro/nanoengineering for biological applications. *Progress in Quantum Electronics* **2009**, *33*, 127–163.
166. Raimondi, M.T.; Eaton, S.M.; Nava, M.M.; Laganà, M.; Cerullo, G.; Osellame, R. Two-photon laser polymerization: From fundamentals to biomedical application in tissue engineering and regenerative medicine. *Journal of Applied Biomaterials and Fundamental Materials* **2012**, *10*, 56–66.
167. Ovsianikov, A.; Mironov, V.; Stampfl, J.; Liska, R. Engineering 3d cell-culture matrices: Multiphoton processing technologies for biological and tissue engineering applications. *Expert Review of Medical Devices* **2012**, *9*, 613–633.
168. Selimis, A.; Mironov, V.; Farsari, M. Direct laser writing: Principles and materials for scaffold 3D printing. *Microelectronic Engineering* **2015**, *132*, 83–89.
169. Ovsianikov, A.; Schlie, S.; Ngezahayo, A.; Haverich, A.; Chichkov, B.N. Two-photon polymerization technique for microfabrication of cad-designed 3D scaffolds from commercially available photosensitive materials. *Journal of Tissue Engineering and Regenerative Medicine* **2007**, *1*, 443–449.
170. Psycharakis, S.; Tosca, A.; Melissinaki, V.; Giakoumaki, A.; Ranella, A. Tailor-made three-dimensional hybrid scaffolds for cell cultures. *Biomedical Materials* **2011**, *6*, 16.
171. Malinauskas, M.; Danilevicius, P.; Baltriukiene, D.; Rutkauskas, M.; Zukauskas, A.; Kairyte, Z.; Bickauskaite, G.; Purlys, V.; Paipulas, D.; Bukelskiene, V., et al. 3D artificial polymeric scaffolds for stem cell growth fabricated by femtosecond laser. *Lithuanian Journal of Physics* **2010**, *50*, 75–82.
172. Klein, F.; Richter, B.; Striebel, T.; Franz, C.M.; von Freymann, G.; Wegener, M.; Bastmeyer, M. Two-component polymer scaffolds for controlled three-dimensional cell culture. *Advanced Materials* **2011**, *23*, 1341–1345.

173. Correa, D.S.; Tayalia, P.; Cosendey, G.; dos Santos, D.S.; Aroca, R.F.; Mazur, E.; Mendonca, C.R. Two-photon polymerization for fabricating structures containing the biopolymer chitosan. *Journal of Nanoscience and Nanotechnology* **2009**, *9*, 5845–5849.
174. Tayalia, P.; Mendonca, C.R.; Baldacchini, T.; Mooney, D.J.; Mazur, E. 3D cell-migration studies using two-photon engineered polymer scaffolds. *Advanced Materials* **2008**, *20*, 4494–4498.
175. Raimondi, M.T.; Eaton, S.M.; Laganà, M.; Aprile, V.; Nava, M.M.; Cerullo, G.; Osellame, R. Three-dimensional structural niches engineered via two-photon laser polymerization promote stem cell homing. *Acta Biomaterialia* **2013**, *9*, 4579–4584.
176. Terzaki, K.; Kissamitaki, M.; Skarmoutsou, A.; Fotakis, C.; Charitidis, C.; Farsari, M.; Vamvakaki, M.; Chatzinikolaidou, M. Pre-osteoblastic cell response on three-dimensional, organic-inorganic hybrid material scaffolds for bone tissue engineering. *Journal of Biomedical Materials Research Part A* **2013**. doi:10.1002/jbm.a.34516.
177. Danilevicius, P.; Rezende, R.A.; Pereira, F.; Selimis, A.; Kasyanov, V.; Noritomi, P.Y.; da Silva, J.V.L.; Chatzinikolaidou, M.; Farsari, M.; Mironov, V. Burr-like, laser-made 3D microscaffolds for tissue spheroid encagement. *Biointerphases* **2015**, *10*, 021011.
178. Chatzinikolaidou, M.; Rekstyte, S.; Danilevicius, P.; Pontikoglou, C.; Papadaki, H.; Farsari, M.; Vamvakaki, M. Adhesion and growth of human bone marrow mesenchymal stem cells on precise-geometry 3D organic–inorganic composite scaffolds for bone repair. *Materials Science and Engineering: C* **2015**, *48*, 301–309.
179. Terzaki, K.; Kissamitaki, M.; Skarmoutsou, A.; Fotakis, C.; Charitidis, C.A.; Farsari, M.; Vamvakaki, M.; Chatzinikolaidou, M. Pre-osteoblastic cell response on three-dimensional, organic-inorganic hybrid material scaffolds for bone tissue engineering. *Journal of Biomedical Materials Research Part A* **2013**, *101A*, 2283–2294.
180. Terzaki, K.; Kalloudi, E.; Mossou, E.; Mitchell, E.P.; Forsyth, V.T.; Rosseeva, E.; Simon, P.; Vamvakaki, M.; Chatzinikolaidou, M.; Mitraki, A., et al. Mineralized self-assembled peptides on 3D laser-made scaffolds: A new route toward 'scaffold on scaffold' hard tissue engineering. *Biofabrication* **2013**, *5*, 045002.
181. Skarmoutsou, A.; Lolas, G.; Charitidis, C.A.; Chatzinikolaidou, M.; Vamvakaki, M.; Farsari, M. Nanomechanical properties of hybrid coatings for bone tissue engineering. *Journal of the Mechanical Behavior of Biomedical Materials* **2013**, *25*, 48–62.
182. Mačiulaitis, J.; Deveikytė, M.; Rekštytė, S.; Bratchikov, M.; Darinskas, A.; Šimbelytė, A.; Daunoras, G.; Laurinavičienė, A.; Laurinavičius, A.; Gudas, R. Preclinical study of SZ2080 material 3D microstructured scaffolds for cartilage tissue engineering made by femtosecond direct laser writing lithography. *Biofabrication* **2015**, *7*, 015015.
183. Claeyssens, F.; Hasan, E.A.; Gaidukeviciute, A.; Achilleos, D.S.; Ranella, A.; Reinhardt, C.; Ovsianikov, A.; Xiao, S.; Fotakis, C.; Vamvakaki, M., et al. Three-dimensional biodegradable structures fabricated by two-photon polymerization. *Langmuir* **2009**, *25*, 3219–3223.
184. Engelhardt, S.; Hoch, E.; Borchers, K.; Meyer, W.; Kruger, H.; Tovar, G.; Gillner, A. Fabrication of 2D protein microstructures and 3D polymer–protein hybrid microstructures by two-photon polymerization. *Biofabrication* **2011**, *3*, 3025003.
185. Turunen, S.; Käpylä, E.; Terzaki, K.; Viitanen, J.; Fotakis, C.; Kellomäki, M.; Farsari, M. Pico- and femtosecond laser-induced crosslinking of protein microstructures: Evaluation of processability and bioactivity. *Biofabrication* **2011**, *3*, 045002.
186. Ovsianikov, A.; Malinauskas, M.; Schlie, S.; Chichkov, B.; Gittard, S.; Narayan, R.; Lobler, M.; Sternberg, K.; Schmitz, K.P.; Haverich, A. Three-dimensional laser micro- and nano-structuring of acrylated poly(ethylene glycol) materials and evaluation of their cytoxicity for tissue engineering applications. *Acta Biomaterialia* **2011**, *7*, 967–974.
187. Gansel, J.K.; Latzel, M.; Frolich, A.; Kaschke, J.; Thiel, M.; Wegener, M. Tapered gold-helix metamaterials as improved circular polarizers. *Applied Physics Letters* **2012**, *100*, 101109.
188. Gansel, J.K.; Thiel, M.; Rill, M.S.; Decker, M.; Bade, K.; Saile, V.; von Freymann, G.; Linden, S.; Wegener, M. Gold helix photonic metamaterial as broadband circular polarizer. *Science* **2009**, *325*, 1513–1515.
189. Chen, Y.-S.; Tal, A.; Torrance, D.B.; Kuebler, S.M. Fabrication and characterization of three-dimensional silver-coated polymeric microstructures. *Advanced Functional Materials* **2006**, *16*, 1739–1744.
190. Radke, A.; Gissibl, T.; Klotzbücher, T.; Braun, P.V.; Giessen, H. Three-dimensional bichiral plasmonic crystals fabricated by direct laser writing and electroless silver plating. *Advanced Materials* **2011**, *23*, 3018–3021.
191. Hrapovic, S.; Liu, Y.L.; Enright, G.; Bensebaa, F.; Luong, J.H.T. New strategy for preparing thin gold films on modified glass surfaces by electroless deposition. *Langmuir* **2003**, *19*, 3958–3965.
192. Mallory, G.O.; Hajdu, J.B. (Eds.) *Electroless Plating: Fundamentals and Applications*. American Electroplaters and Surface Finishers Society, Orlando, FL, **1990**; pp. 29–33.
193. Terzaki, K.; Vasilantonakis, N.; Gaidukeviciute, A.; Reinhardt, C.; Fotakis, C.; Vamvakaki, M.; Farsari, M. 3D conducting nanostructures fabricated using direct laser writing. *Optical Materials Express* **2011**, *1*, 586–597.
194. Vasilantonakis, N.; Terzaki, K.; Sakellari, I.; Purlys, V.; Gray, D.; Soukoulis, C.M.; Vamvakaki, M.; Kafesaki, M.; Farsari, M. Three-dimensional metallic photonic crystals with optical bandgaps. *Advanced Materials* **2012**, *24*, 1101–1105.
195. Takeyasu, N.; Tanaka, T.; Kawata, S. Fabrication of 3D metal/polymer microstructures by site-selective metal coating. *Applied Physics A: Materials Science and Processing* **2008**, *90*, 205–209.
196. Rill, M.S.; Plet, C.; Thiel, M.; Staude, I.; Von Freymann, G.; Linden, S.; Wegener, M. Photonic metamaterials by direct laser writing and silver chemical vapour deposition. *Nature Materials* **2008**, *7*, 543–546.
197. Malinauskas, M.; Zukauskas, A.; Purlys, V.; Gaidukeviciute, A.; Balevicius, Z.; Piskarskas, A.; Fotakis, C.; Pissadakis, S.; Gray, D.; Gadonas, R., et al. 3D microoptical elements

formed in a photostructurable germanium silicate by direct laser writing. *Optics and Lasers in Engineering* **2012**, *50*, 1785–1788.

198. Gissibl, T.; Thiele, S.; Herkommer, A.; Giessen, H. Submicrometre accurate free-form optics by three-dimensional printing on single-mode fibres. *Nature Communications* **2016**, *7*, 9.
199. Malinauskas, M.; Zukauskas, A.; Purlys, V.; Belazaras, K.; Momot, A.; Paipulas, D.; Gadonas, R.; Piskarskas, A.; Gilbergs, H.; Gaidukeviciute, A., et al. Femtosecond laser polymerization of hybrid/integrated micro-optical elements and their characterization. *Journal of Optics* **2010**, *12*, 124010.
200. Žukauskas, A. Improvement of the fabrication accuracy of fiber tip microoptical components via mode field expansion. *Journal of Laser Micro/Nanoengineering* **2014**, *9*, 68–72.
201. Bianchi, S.; Rajamanickam, V.P.; Ferrara, L.; Di Fabrizio, E.; Liberale, C.; Di Leonardo, R. Focusing and imaging with increased numerical apertures through multimode fibers with micro-fabricated optics. *Optics Letters* **2013**, *38*, 4935–4938.
202. Xie, Z.W.; Feng, S.F.; Wang, P.J.; Zhang, L.S.; Ren, X.; Cui, L.; Zhai, T.R.; Chen, J.; Wang, Y.L.; Wang, X.K., et al. Demonstration of a 3D radar-like sers sensor micro- and nanofabricated on an optical fiber. *Advanced Optical Materials* **2015**, *3*, 1232–1239.
203. Gissibl, T.; Schmid, M.; Giessen, H. Spatial beam intensity shaping using phase masks on single-mode optical fibers fabricated by femtosecond direct laser writing. *Optica* **2016**, *3*, 448–451.
204. Cojoc, G.; Liberale, C.; Candeloro, P.; Gentile, F.; Das, G.; De Angelis, F.; Di Fabrizio, E. Optical micro-structures fabricated on top of optical fibers by means of two-photon photopolymerization. *Microelectronic Engineering* **2010**, *87*, 876–879.
205. Sokolovskii, G.S.; Melissinaki, V.; Dudelev, V.V.; Losev, S.N.; Soboleva, K.K.; Kolykhalova, E.D.; Deryagin, A.G.; Kuchinskii, V.I.; Viktorov, E.A.; Farsari, M., et al. In Superfocusing of high-m^2 semiconductor laser beams: Experimental demonstration. SPIE Photonics Europe, **2014**; SPIE: p. 7.
206. Kowalczyk, M.; Haberko, J.; Wasylczyk, P. Microstructured gradient-index antireflective coating fabricated on a fiber tip with direct laser writing. *Optics Express* **2014**, *22*, 12545–12550.
207. Melissinaki, V.; Konidakis, I.; Farsari, M.; Pissadakis, S. In Fiber endface fabry-perot vapor microsensors fabricated by multiphoton polymerization technique. SPIE OPTO, **2015**; SPIE: p. 8.

9

Photolithography

Shinji Okazaki

CONTENTS

9.1 Basic Principles 105
9.2 System Requirements 106
9.3 Case Study (KrF Excimer Laser Lithography) 107
9.4 Future Trends 108
Bibliography 109

9.1 Basic Principles

Photolithography is widely used in the semiconductor industry to delineate ultra-large-scale integration (ULSI) patterns on a Si wafer. Advanced photolithography employs an excimer laser as a light source in the exposure tools. The principle of photolithography is similar to that of photography: the exposure of mask images through an optical system produces latent images in a photosensitive resist material (photoresist), which is then developed in a developer solution to form resist patterns. Photolithography is a system composed of various subsystems such as light sources, exposure tools (optics and exposure systems), masks, pellicles and photoresist materials. There are two types of photoresist: positive and negative tones. As shown in Figure 9.1, in a positive-tone photoresist material, the area exposed to light becomes soluble in the developer, producing positive-tone patterns in the photoresist layer. In contrast, in a negative-tone photoresist, the area exposed to light becomes insoluble in the developer, producing negative-tone patterns in the photoresist layer. In the industrial world, positive-tone photoresists are widely used because they provide better resolution. However, due to the development of high-resolution negative-tone photoresist materials and the fact that various resolution-enhancement techniques require a negative-tone resist, these resists are starting to see greater use in specific fields.

There are several types of photoresist materials for use at specific exposure wavelengths. For example, polyvinylphenol resin-based photoresists with chemical amplification systems

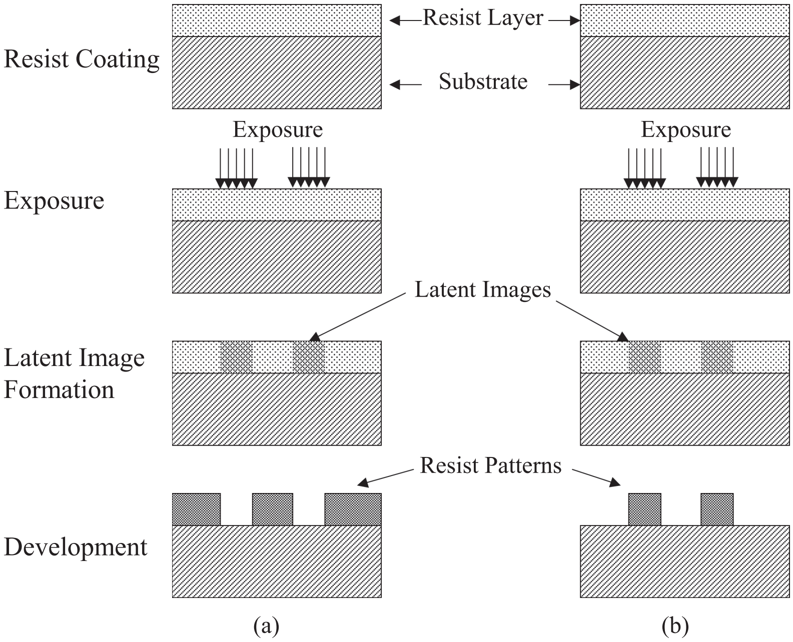

FIGURE 9.1 Resist pattern formation process.

are widely used for KrF excimer laser light (248 nm). The resolution capability of reduction-projection exposure is given by Rayleigh's equation:

$$R = k_1\lambda/NA$$

where λ is the exposure wavelength, *NA* is the numerical aperture of the projection optics, and k_1 is a constant that depends on the resist process and exposure method. The depth of focus is given by

$$\text{DOF} = k_2\lambda/NA^2$$

where k_2 is a constant that depends on the resist process and exposure method. According to this expression, a small increase in the numerical aperture greatly reduces the depth of focus.

The resolution limit of the optical lithography was thought to be around the exposure wavelength itself if using a relatively thick resist layer. However, development of resolution-enhancement and chemical–mechanical polishing (CMP) technologies makes it possible to use a thinner resist layer and to delineate patterns with wavelengths smaller than the exposure wavelength. These technological revolutions are revealed in a reduction in the k_1 factor and, in some cases, in the enlargement of the k_2 factor.

In conventional optical lithography, the k_1 factor was thought to be around 0.8–0.6; however, by the use of resolution-enhancement technologies and thinner resist layers, the k_1 factor can be as low as 0.4–0.5.

However, the use of resolution-enhancement technology puts various limitations on the pattern arrangements and shapes. The delay in the development of a photolithography system with shorter wavelengths is pushing the development of such a technological innovation.

9.2 System Requirements

Resolution is the most critical issue in photolithography, and the best ways to improve it are to use a shorter wavelength, a higher numerical aperture or a smaller k_1 factor. However, a higher numerical aperture results in a smaller depth of focus, and the use of resolution enhancement to obtain a smaller k_1 factor limits the pattern arrangements as previously mentioned. Accordingly, the use of a shorter wavelength is the most practical way to obtain higher resolutions. The minimum feature size of current ULSI devices is 0.18 µm or less. To make such small patterns, assuming an NA of 0.7 and a k_1 factor of 0.5, we need an exposure wavelength of 0.25 µm or less. However, there are few light sources with a wavelength below 0.3 µm. In fact, the only suitable candidate is excimer laser light.

Table 9.1 lists various kinds of excimer lasers. The KrF excimer laser was selected from among the possible candidates for feature sizes of 0.25 µm and below because its fabrication is a mature technology and because quartz—a very stable and readily available material—is transparent at the wavelength of KrF excimer laser light.

There are three types of reduction-projection optical systems: a dioptric system, which consists of refractive optical components; a cataoptric system, which consists of reflective optical components; and a catadioptric system, which comprises both refractive and reflective optical components. Dioptric systems can be further broken down into two categories: monochromatic ones, which employ just a single optical material, and achromatic ones, which use at least two different optical materials to compensate for the chromatic aberration of the reduction-projection optical system. Since several refractive materials are available for the longer-wavelength region, such as the g-line (436 nm) and i-line (365 nm) exposure wavelengths of a mercury lamp, achromatic systems are widely used. However, at the wavelength of KrF excimer laser light (248 nm) or shorter, few optical materials can be used for refractive optics. As previously mentioned, quartz is the most appropriate material for a refractive optical system using this wavelength. To build a monochromatic dioptric system using quartz requires a very narrow spectral bandwidth. Several line-narrowing systems have been developed for advanced KrF stepper and scanner systems, with the most common one being a combination of a grating and a prism.

Catadioptric systems were devised to eliminate the need for special line narrowing. The use of both refractive and reflective optics allows the spectral bandwidth to be rather wide. Commercial catadioptric systems are built with lenses, mirrors and a big quartz corner cube, as shown in Figure 9.2. The required spectral bandwidths for both systems are listed in Table 9.2. Since a catadioptric system allows the use of a spectral bandwidth several times larger than a dioptric system does, no line-narrowing system is needed in the excimer laser source.

TABLE 9.1

Various Candidates for the Light Source of Exposure System

Excimer laser	Wavelength (nm)	Remarks
XeCl	308	Insufficient resolution
KrF	248	Chemically amplified resist with phenolic resin, quartz for the optic materials.
KrCl	222	New resist materials will be required.
ArF	193	Chemically amplified resist with cyclo-polymer or acrylic polymer, quartz and CaF_2 for the optical materials.
F2	157	CaF_2 for the optic materials, chemically amplified resist with fluorine-containing polymer, fluorine-containing quartz for mask substrate.

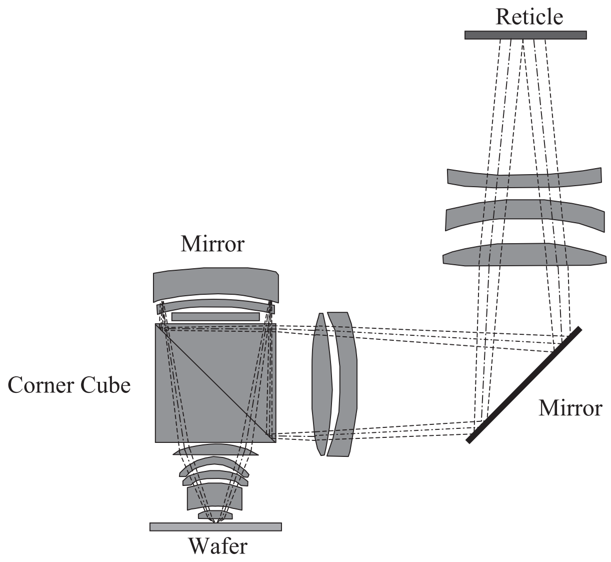

FIGURE 9.2 An example of a catadioptric optical system.

TABLE 9.2

Requirements for the Spectral Bandwidth of a KrF Exposure System

Exposure System	Required Spectral Bandwidth (pm)
Monochromatic dioptric	<1.0
Achromatic dioptric	<10.0
Catadioptric	<3.0

Cataoptric systems also need no line-narrowing systems in the light source. In the case of an extreme ultraviolet (EUV) lithography system, there are no materials that are transparent to EUV light, so cataoptric systems use all-reflective optical systems. In this case, the exposure wavelength is selected by the reflection bandwidth of the reflective mirrors. Mirrors with a multilayer structure can reflect EUV light, and several structures have been proposed—typically Mo/Si and Mo/Be. An Mo/Si multilayer structure reflects light at wavelengths in the range 13–14 nm. In contrast, an Mo/Be multilayer reflects light at around 11 nm. Accordingly, the light source must be selected to adapt to the bandwidth of the multilayer mirrors.

There are two types of exposure systems: steppers and scanners. In a stepper system, the exposure field is square or rectangular in shape and covers an area of one or more chips, as shown in Figure 9.3a. The stage moves in a step-and-repeat fashion, which gives rise to the name 'stepper'. The exposure area of the reduction-projection system is limited to 20–25 mm square, and the step-and-repeat process enables an entire wafer to be covered. In contrast, in a scanner system, the exposure field is a strip or crescent and covers only part of a chip or chips, as shown in Figure 9.3b. Scanning the exposure field enables several chips to be covered at the same time. The stage moves continuously in one direction to the end of a scan and then steps down perpendicular to the scanning direction and begins the next scan. In this way, it can cover an entire wafer.

9.3 Case Study (KrF Excimer Laser Lithography)

KrF excimer laser lithography is widely used for the delineation of 0.25 and 0.18 μm patterns. It is also expected to be used for 0.13 μm patterns. As previously mentioned, one of the two types of reduction-projection optical systems employing quartz for the optical material is a monochromatic dioptric system. The majority of the commercially available KrF exposure systems are of this type. Since it requires a very narrow spectral bandwidth, an excimer laser must be equipped with a line-narrowing system.

The other one is a catadioptric optical system, which also employs quartz for the optical material. This type of system has a big corner cube, and there is no need for line narrowing.

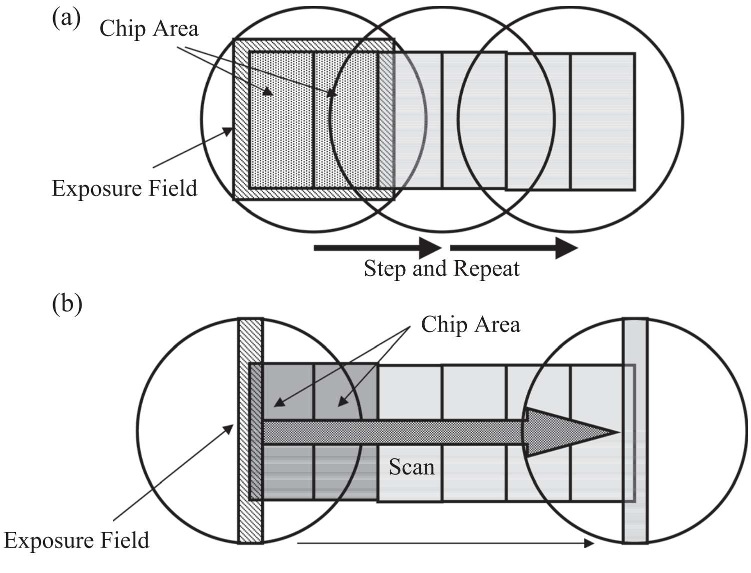

FIGURE 9.3 Comparison of the exposure procedure of (a) stepper and (b) scanner.

TABLE 9.3

Specifications for an Excimer Laser Light Source for a Dioptric System

Manufacturer Model	Cymer ELS-7000	Lambda Physik K2000	Giga-Photon G21
Wavelength (nm)	248	248	248
Pulse energy (mJ)	7.5		10
Average output power (W)	30	8	20
Pulse frequency (Hz)	4000	2000	2000
Spectral bandwidth (pm)	<0.5	<0.4	<0.5

TABLE 9.4

Specifications for KrF Excimer Laser Exposure Systems

Manufacturer Model	MicrascanIII	Nikon NSR2205	Canon FPA3000	ASML PAS5500	Nikon NSRS206D	Canon FPA6000ES5	ASML SVGL PAS500/850B
NA	0.45–0.60	0.50–0.65	0.50–0.70	0.82	050–0.80	0.55–0.80	0.50 (variable)
Scanner/stepper	Stepper	Stepper	Stepper	Scanner	Scanner	Scanner	Scanner
Optical system	Dioptric	Dioptric	Dioptric	Dioptric	Dioptric	Dioptric	Catadioptric
Magnification	5×	5×	4×	4×	4×	4×	4×
Field size (mm)	22 × 22	22 × 22	22 × 22	25 × 33	26 × 33	26 × 32	26 × 32.5
Overlay (nm)	<40	<25	<45	<35	<18	<20	<45
Light source	KrF	KrF	KrF	KrF	KrF	KrF	KrF

Accordingly, the specifications for the light source for a dioptric system are much stricter than those for a catadioptric system. They are listed in Table 9.3.

Table 9.4 gives the specifications for KrF excimer laser exposure systems. Almost all the developed exposure systems for ULSI fabrication are scanner systems. For the same size of optical system, a scanner system provides a larger field than a stepper system.

9.4 Future Trends

There remains a strong demand for a reduction in the minimum feature size in ULSI devices, which has been progressing at the rapid pace of 30% every 2–3 years. This trend is expected to continue into the foreseeable future. To meet the demand, the exposure wavelength must be reduced accordingly. This has spurred intensive investigations into shorter-wavelength light sources. Currently, ArF excimer laser sources are now ready for industrial use, and leading-edge ULSI manufacturers have started to use them in their exposure systems. At the ArF exposure wavelength (193 nm), there are several problems with using quartz, for instance compaction (reduction in the volume of the quartz). To avoid such problems, the new optical material CaF_2 will be employed in the reduction optical system for ArF exposure systems. Table 9.5 gives the specifications for future laser systems.

Table 9.6 gives the specifications for modern ArF excimer laser exposure systems. The numerical aperture value is above 0.75 to obtain higher resolution.

Further reduction in the exposure wavelength has also been pursued. F_2 lasers (157 nm) are now under development. At this wavelength, quartz will no longer be useful and CaF_2 is being considered as a suitable material. To use CaF_2, we have to overcome its intrinsic birefringence and this problem has been investigated. The maximum difference in the optical path along the different crystal axes exceeds 12 nm. To overcome this problem, averaging the light path by using various axes of the crystal will be necessary. However, as the annealing effects of the birefringence phenomenon in CaF_2 crystal still remain, further work will be necessary before CaF_2 is ready for industrial use. There is still some discussion about what type of projection optical system will give the best results.

There are two candidates—a monochromatic dioptric system using CaF_2 and a catadioptric system—and an achromatic dioptric system is also under consideration. However, the

TABLE 9.5

Specifications for Modern Laser Sources

Manufacturer Model	Cymer XLA 100	Gigaphoton G40A	Lambda Physik Experiment	A4000	F2020
Wavelength (nm)	193	193	157	193	157
Pulse energy (mJ)	10	5			
Average output power (W)	40	20	15	40	20
Pulse frequency (Hz)	4000	4000	2000	4000	2000
Spectral bandwidth (pm)	<0.2	<0.35	<1.5	<0.35	1

TABLE 9.6

Specifications for Modern ArF Excimer Laser Exposure Systems

Manufacturer Model	Nikon NSR-S306C	Canon FPA-6000AS4	ASML TWINSCAN AT1:1100B
NA	0.78	0.55–0.85	0.50–0.75
Scanner/stepper	Scanner	Scanner	Scanner
Optical system	Dioptric	Dioptric	Dioptric
Magnification	4×	4×	4×
Field size (mm)	25 × 33	26 × 33	26 × 32
Overlay (nm)	<23	<18	<20
Light source	ArF	ArF	ArF

development of an achromatic system requires a new optical material, with one possibility being BaF_2. As even the use of CaF_2 is still under development as previously mentioned, other materials need a lot of work before they can be of practical use. As shown in Table 9.5, several F_2 laser systems have also been developed with output powers of 15–20 W with a repetition rate of 2000 Hz. The spectral bandwidth is still relatively wide around 1–1.5 pm level. To utilize such laser systems, either a catadioptric or an achromatic dioptric system must be used. However, as mentioned earlier, as the range of lens materials is limited, the catadioptric system will be the best solution for the first industrial implementation of an F_2 exposure system. There are also several other problems with the use of F_2 laser light. Conventional resist materials are not transparent at 157 nm, so new resist materials will need to be developed. Currently, fluorine-containing materials are found to be transparent at 157 nm. Several candidates for resist materials have been proposed and developed, and relatively good patterns have been reported. However, the practical characteristics of the resist materials, such as dry-etching durability, line-edge roughness and resist out-gas, have not yet been investigated. In addition, pellicle materials have not yet been developed. Soft pellicles made from organic thin films are widely used. However, there are no good soft pellicle materials suitable for 157 nm light. We are investigating hard pellicle materials made of quartz. However, the uniformity of their thickness does not meet the optical design parameters. Purging is another issue. Oxygen and H_2O absorb 157 nm light significantly. So we have to eliminate O_2 and H_2O to below the several ppb level. To realize such conditions, the light path from the light source to the wafer must be purged by N_2 or equivalent gases. The adsorbed water vapour on the surface of the reticle also absorbs 157 nm light, so the reticle must be kept in dry air or an N_2 atmosphere. As mentioned earlier, there are still many issues to be resolved before the practical use of 157 nm light is possible. However, as the resolution capability is also limited, early introduction is strongly desired. Otherwise, there will be no practical chance for this technology to be introduced into semiconductor fabrication. However, a gradual reduction in the exposure wavelength will not reduce the resolution capability. Hence, to obtain much higher resolution, abrupt reduction in the exposure wavelength has also been investigated. The use of EUV is the choice. The exposure wavelength is 13–14 nm. In this wavelength region, only multilayer mirrors can be used for the exposure optical system. The exposure wavelength is chosen with respect to the band range of the reflection wavelength of the multilayer mirror. Multilayers of Mo and Si have been selected, and the mirror has a reflectivity maximum at around 13.5 nm with a bandwidth of about 1 nm.

There are several major light sources for EUV light: a laser-produced plasma source, a discharge-produced plasma source or a synchrotron radiation ring can be used. The laser-produced plasma source is one of the most promising candidates for EUV light. A YAG laser was selected as the exciting laser and Xe for the target material. Other target materials such as Sn and SnO_2 are suitable for generating EUV light with wavelengths of 13–14 nm; however, such solid targets usually generate much debris which damages the illumination optics significantly. Hence, a gas-phase target was thought to be the best choice for an EUV light source. A Xe gas target has been intensively investigated. A Xe laser-produced plasma source emits EUV light with a high peak at 11 nm and a strongly reduced intensity level compared to the peak intensity in 13–14 nm wavelength range. In fact, this source has been fitted to an Mo/Be multilayer mirror, which gave a high reflectance peak at 11 nm. However, as Be is very toxic, semiconductor and semiconductor-equipment manufacturers have not found Mo/Be multilayers acceptable for mirror materials. Requirements for an output power of EUV light exceeding 100 W at the intermediate focus have meant that liquid-phase Xe and solid-phase Xe have been intensively investigated. Other solid targets, such as Sn and SnO_2, have also been reconsidered as candidates for target materials. As can be seen, selecting the EUV source and selecting the target material in laser-produced plasmas are both hot topics in the development of an EUV source.

BIBLIOGRAPHY

1. Lin B. J. 1987 *Microelectron. Eng.* **9** 31.
2. Okazaki S. 1991 *J. Vac. Sci. Technol. B* **9** 2829.
3. Pol V. et al. 1986 *Proc. SPIE* **633** 6.
4. Nakase M. et al. 1987 *Proc. SPIE* **773** 226.
5. Sasago M. et al. 1986 *IEDM Tech. Digest* 316.
6. Reiser A. 1989 *Photo-Reactive Polymers* (New York: Wiley).
7. Nonogaki S. et al. (ed.) 1998 *Microlithography Fundamentals in Semiconductor Devices and Fabrication Technology* (New York: Marcel Decker).
8. Levenson M. D. et al. 1991 *IEEE Trans.* **ED-29** 1828.
9. Ueno T. et al. 1990 *Proc. SPIE* **1262** 26.
10. Ito H. and Wilson C. G. 1983 *Polymer Eng.* **23** 1012.

11. Thackeray J. W. et al. 1992 *Proc. SPIE* **1672** 15.
12. Kline M. V. 1970 *Optics*(New York: Wiley).
13. Buckley J. D. et al. 1989 *J. Vac. Sci. Technol. B* **7** 1607.
14. Cote D. R. et al. 1999 *Proc. SPIE* **3679** 473.
15. Ozaki Y. et al. 1990 *Japan. J. Appl. Phys.* **29** 707.
16. Sandstrom R. 1991 *Proc. SPIE* **1463** 610.
17. Williamson D. et al. 1993 US Patent 5,212,593
18. International Technology Roadmap for Semiconductors 1999 (ed International SEMATECH) http://www.itrs.net/ntrs/publntrs.nsf/.
19. Chatterjee P. K. and Doering R. R. 1998 *Proc. IEEE* **86** 176.
20. Taur Y. 1999 *IEEE Spectr.* **36** 25.
21. Rothchild M. and Ehrlich D. J. 1987 *J. Vac. Sci. Technol. B* **5** 389.
22. Rothchild M. et al. 1996 *J. Vac. Sci. Technol. B* **14** 4157.
23. Hofmann T. et al. 2000 *Proc. SPIE* **4000** 511.
24. Rothchild M. and Sedlacek J. H. C. 1992 *Proc. SPIE* **1848** 537.
25. Liberman V. et al. 1999 *J. Vac. Sci. Technol. B* **17** 3273.
26. Rothchild M. et al. 1999 *J. Vac. Sci. Technol. B* **17** 3262.
27. Kunz R. R. et al. 2000 *Proc. SPIE* **4000** 474.
28. Liberman V. et al. 2000 *Proc. SPIE* **4000** 488.
29. Miller R. E. et al. 2000 *Proc. SPIE* **4000** 567.
30. Kunz R. R. et al. 1999 *J. Vac. Sci. Technol. B* **17** 3267.

10

Pulsed Laser Deposition of Thin Films

Binod Subedi, Venkata S. Puli, Ian W. Boyd, and Douglas B. Chrisey

CONTENTS

10.1 History and Background 111
10.2 Operation of PLD and Process Steps 112
  10.2.1 Laser–Material Interaction 112
  10.2.2 Material Transport 113
  10.2.3 Nucleation and Growth 113
10.3 Materials Grown by Using PLD 114
  10.3.1 Metals and Alloys 114
  10.3.2 Oxides 115
    10.3.2.1 Ferroelectric, Multiferroics, and Piezoelectric Oxides 115
    10.3.2.2 Superconducting Oxides 117
    10.3.2.3 Transparent Conducting Oxides 118
  10.3.3 Nitrides 118
  10.3.4 Transition Metal Dichalcogenides 119
  10.3.5 Diamond-like Carbon 119
  10.3.6 Polymers 120
  10.3.7 Biomaterials 120
  10.3.8 Other Materials 121
10.4 Advantages and Disadvantages of PLD 121
10.5 Summary 121
References 121

10.1 History and Background

The attempts to understand the interaction of lasers with material systems began shortly after the invention of laser in 1960. In 1964 Smith and Turner provided the first ever proof of concept for the pulsed laser deposition (PLD) of thin films [1]. They used a pulsed ruby laser to ablate different materials and deposited the contents of the ablated plume in the form of thin films. However, these layers were not uniform and the materials ejected from the target did not readily adhere to the substrate. As sputtering and other conventional physical vapour deposition techniques were already known to provide good-quality thin films, further development of PLD was hampered. In the late 1980s, high-quality epitaxial thin films of high-temperature superconducting $YBa_2Cu_3O_{(7-x)}$ were successfully deposited using PLD at extreme non-equilibrium conditions, and the difficult, but necessary attributes were found to be easily reproducible [2]. The ability of PLD to deposit multi-component oxide materials with complex stoichiometry as thin films in a controlled manner quickly evolved PLD into a valuable tool for thin-film ceramic material research. Now it is widely used as a method in academic research and has aided the development of many new materials with disparate applications. This chapter provides a brief review of the PLD technique along with some highly cited examples to highlight the broad range of materials that can be deposited.

A pulsed laser has both spatial and temporal coherence and the short-duration pulses produced can be focused to a small area on the target material with extremely high peak power densities. Under optimal conditions, the intense energy reaching the surface is strongly absorbed by the target material and the temperature at the surface becomes very high, exceeding the cohesive energy. This results in rapid vaporization of the surface material, thereby creating very small particles which interact with the remainder of the incoming laser pulse and subsequently dissociate into neutral atoms, molecules, high-energy ions, and electrons. In this way, a dense plume of plasma forms and is propelled with a distribution mostly perpendicular to the surface. This dense plasma plume impacts the substrate, and the material in the plume adheres to form a thin film [3].

Since the plume is highly forward directed, the distribution of atoms that hit the substrate is nearly equal to that of the original target material, even when the target is made up of multiple components [4]. If the substrate is heated to a favourable temperature and the sticking fraction is close to unity, the material that grows on the substrate can have the same stoichiometry as that of the target. Crystalline thin films with highly preferred orientation, or in many cases epitaxial to the substrate, can be readily deposited. Besides the principle advantage of stoichiometric transfer from a bulk material to thin films, PLD has an edge over other physical vapour deposition techniques because of the position of the laser source. In PLD, the laser source remains outside the chamber that allows a dynamic range of operating pressure (10^{-10}–100 Torr) inside the vacuum chamber. Reactive gases like oxygen can be filled in the vacuum chamber, and the stoichiometry in the films can be varied in a controlled manner without further processing [5]. A PLD system provides highly reproducible results and has a simple set-up as compared to other methods of physical vapour deposition.

10.2 Operation of PLD and Process Steps

As shown in the schematic diagram (Figure 10.1), a PLD system consists of a laser whose wavelength is strongly absorbed by the target material (usually an excimer laser) and a chamber with vacuum pumps to control the pressure. The vacuum chamber is equipped with one or more solid targets attached to rotation motors, an inlet for reactive gases, a substrate attached to a heater, and pressure gauges/controllers to regulate the gas pressure inside the chamber. By utilizing external optics, including attenuators, apertures, mirrors, and lenses, the laser beam with desired energy density is directed into the chamber and focused on the surface of the target material. KrF (248 nm, 5.0 eV), ArF (193 nm, 6.4 eV), and the fourth harmonic of Nd:YAG (266 nm, 4.6 eV) are some of the lasers widely used for PLD of thin films. When the laser pulse enters the chamber, the photons are efficiently absorbed by the outermost electrons of the atoms in the surface region of the target material and their energy is then transferred to the lattice to induce intense heat that leads to rapid evaporation. The vaporized target material then passes through the gas in the chamber in the form of the aforementioned plasma plume. For a UV excimer laser with a pulse duration of 10 ns, power densities of the order 10–500 MW cm^{-2} are required [6].

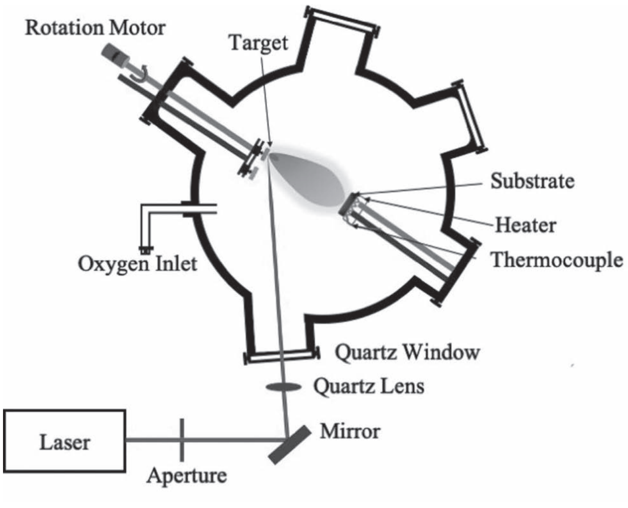

FIGURE 10.1 Schematic diagram of the PLD system.

The quality of the thin layers deposited by PLD depends on a number of different parameters such as laser wavelength, fluence, pulse duration, target material, ambient gas choice and its pressure, target-to-substrate distance, substrate type, and temperature. All of these parameters need to be optimized to achieve good-quality thin films. Generally, lasers having a wavelength of 248 and 308 nm with a pulse duration of ~20 ns are used, and the laser fluence, the optimized choice of substrate, its temperature, ambient gas pressure, and gas choice depend upon the material to be deposited.

The target is rotated using an external motor to obtain more uniform ablation and prevent the formation of a laser pit or hole in the irradiated zone. A good target should be dense and have a high absorption coefficient at least above $10^5 cm^{-1}$, to ensure substantial surface heating and extensive evaporation rather than just volume boiling. Depending upon the target material and the laser type, there is a threshold at which the ablation of a material starts. The optimum fluence is usually considered to be two to three times the value of the threshold fluence. At fluences close to threshold, vaporization is similar to thermal evaporation, whereas at very high fluences, highly energetic ions are formed which have detrimental effects in the film quality. The optimized background substrate temperature is about half of the melting point of the target material.

The pressure in the vacuum chamber is also an important parameter. Generally, the chamber is pumped down to 7.5×10^{-4} mTorr before introducing the gas of choice. The gas in the chamber helps to reduce the energy of the excited species and prevents the re-sputtering and other damage to the deposited film [7]. Also, in some cases the gas helps to supply some of the constituent of the film itself like in oxides and nitride deposition. The interaction of the laser with the target material, the transport of the plasma plume towards the substrate, and the nucleation and film growth are the main steps in a PLD process. The mechanism of each of the process steps is discussed below.

10.2.1 Laser–Material Interaction

The process of thin-film deposition starts with the interaction of the laser beam with the target material. Radiation from the IR to the UV mostly interacts with the outermost electrons of a material and sometimes with atomic or molecular vibrations (phonons). The outer, or conduction band electrons in metals, and the valence band electrons in semiconductors and dielectrics readily absorb the energy from the photons. If the energy of the incident photons is lower than the material band gap of semiconductor or dielectric material, then the energy can be absorbed by impurities, defects, surface states, and any free carriers. The energy absorbed by the electrons is then transferred into the lattice within a few picoseconds.

For stoichiometric transfer of the material from bulk to a high-quality thin film, the target should be heated only on the surface and volume heating should be avoided. The absorption length $1/\alpha$ where α is the optical absorption coefficient, and the thermal diffusion length $l_{th} = 2\,(D\tau)^{1/2}$, where D is thermal diffusivity and τ is the laser pulse duration, determine the type of heating that takes place at the target. If $\alpha l_{th} \ll 1$, volume boiling occurs and the ejected material contains large particulates which degrades the film quality. If $\alpha l_{th} \gg 1$, the surface of the target heats up only up to a depth of ~l_{th} and vaporization of the surface material takes place ensuring the stoichiometric transfer. A rapid heating rate of the order of 10^3 K ns^{-1} occurs when energy densities of 1–10 J cm^{-2} impact the target surface to ensure melting and vaporization. Thermionic emission, photo-excitation, photo-ionization, and their consequential effects result in the emission of ions and electrons. The coupling of electrons with the laser photons results in inverse Bremsstrahlung that further increases the electron density and their excitation leading to a rapid cascade ionization. An extremely high temperature is generated by the interaction of the electrons with the incoming laser pulses that turns the ejected material into dense plasma. The energy of the laser pulses is rapidly shared throughout the particles in the dense plasma [8]. Different models of laser ablation have been proffered, but the processes of laser ablation is a complex phenomenon, and since the properties of many materials at high temperatures are still poorly known, the predictions made by these models of ablation have a limited applicability.

10.2.2 Material Transport

Regardless of the direction of the incoming laser pulses, the centroid of ejected material is generally perpendicular to the target surface. When the laser pulses evaporate multiple monolayers of material per pulse, a layer of vaporized material called Knudsen layer is formed adjacent to the surface. The vapour in this layer has absence of translational equilibrium, and there are temperature, pressure, and density discontinuities across this layer. Collisions among the species allow them to reach a full Maxwellian distribution with a high centre of mass velocity (~10^4 m s^{-1}) and they propagate forward [9] (Figure 10.2).

The plasma extends over the area of the surface exposed to the laser pulse, and consists of electrons, ions, atoms, molecules, clusters, and particulates of varying sizes. After irradiation, the amount of material enlarging the plasma will drop considerably. The plasma plume will then expand favourably away from the target directed towards greatest density gradients, accelerating the species to top speeds that are 1000 times the usual speeds encountered during thermal evaporation. Ambient pressure and the energy contained within each incoming laser pulse determine the speed of the plume.

10.2.3 Nucleation and Growth

The deposition of the thin film on the substrate starts with the plume hitting on the substrate. As the plasma moves forward, recombination of the ions and electrons takes place and the degree of ionization decreases. The material in the plume that is relatively cool impinges on the substrate and a thin film starts to grow. Before a continuous film is formed, the material goes through various steps, including sticking onto the surface, diffusion, re-evaporation or interaction with other adatoms, nucleation, clustering, island formation, coalescence of islands, and filling of the empty spaces [4] (Figure 10.3).

The nucleation of first few monolayers plays an important role in determining the final structure of the film. The flux and state of the components in the plasma plume and the ambient gas, and substrate properties like crystallinity, orientation, and cleanliness can heavily influence the nucleation of these first monolayers. According to theoretical calculations based on the simple capillarity model, $r = -2WG/kT$ gives the radius of the critical cluster size, where W is the volume of an adatom, G is the surface free energy, k is Boltzmann's constant, T is the temperature, and $x = p/p_e$ is the supersaturation ratio (where p is the actual pressure and p_e is the equilibrium pressure of the condensing vapour). PLD film growth is a highly non-equilibrium process, and models based only on thermodynamic considerations do not apply well but experimentally the condition for nucleation and growth of epitaxial or dense crystalline

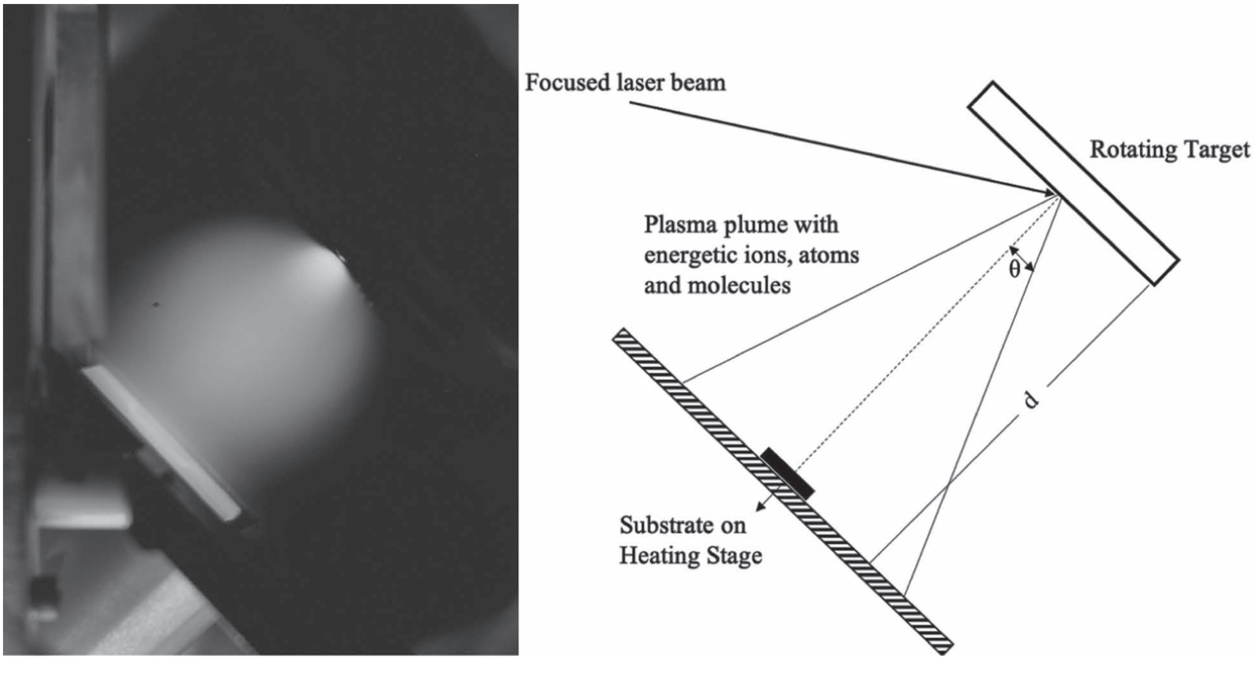
Focused laser beam
Rotating Target
Plasma plume with energetic ions, atoms and molecules
θ
d
Substrate on Heating Stage

FIGURE 10.2 Plasma plume in PLD and its schematic representation.

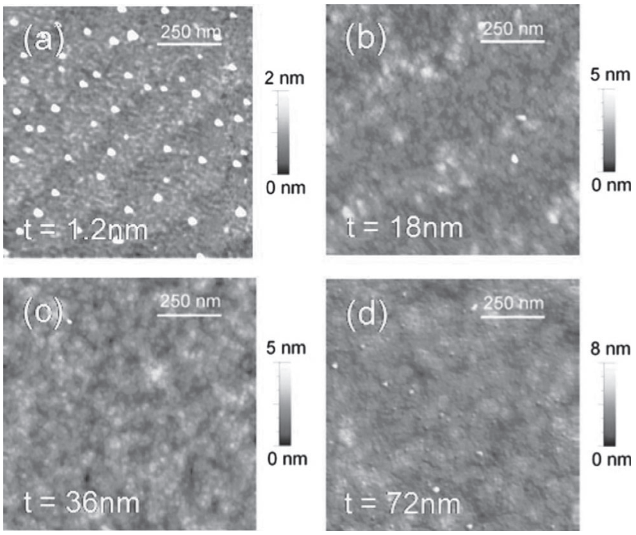

FIGURE 10.3 Atomic force microscope (AFM) images of different stages of film growth in Fe(Se,Te) superconducting thin film on LAO substrate. (a) Small islands form, (b) concentration of islands occurs at the edges, (c) islands coalesce, and (d) film with uniform coverage is formed [10].

films with highly preferred orientation has been found to be easily fulfilled during PLD.

The surface morphology and crystallinity of the films grown also depend on the deposition rate in addition to other parameters. When the deposition rate is increased, the relative flux of impurities decreases in the film and an improvement in the surface morphology and the crystallinity of the thin film will be observed. The bombardment of the substrate with ions having energy of the order of 10–100 eV in the plasma is considered to be helpful for improving the crystallinity due to the formation of nucleation sites, activation of the ambient gas, removal of impurity from substrate, and increase in the mobility of the surface adatoms as a result of collision with these ions. This has been confirmed by removing the ions using an electric field. The removal of ions with this energy range from the plasma plume was found to decrease the crystallinity in the films. However, ions having higher energy than 100 eV were seen to be harmful and have unwanted consequences like re-sputtering of the deposited material, chemical alteration, and appearance of defects in the films [11] (Figure 10.4).

To achieve films with excellent quality, understanding of the processes relative to the specific material, laser, and the deposition parameters is crucial. In the following section, examples of different materials deposited by using PLD are presented.

10.3 Materials Grown by Using PLD

10.3.1 Metals and Alloys

Surface heating of the target material is favoured when the thermal diffusion length is shorter than the optical absorption depth, but in case of metals, the reverse is true. By their inherent nature, metals have high reflectivity, high density, and high thermal conductivity. Because of these reasons, in metals, the laser energy is absorbed and then transported to the level of thermal diffusion length and that significantly reduces the efficiency of photons to ablate the material. Higher laser fluence is required for ablating metals as compared to other materials. The ablation threshold for a particular metal depends on the cohesive energy and thermal conductivity. Despite their

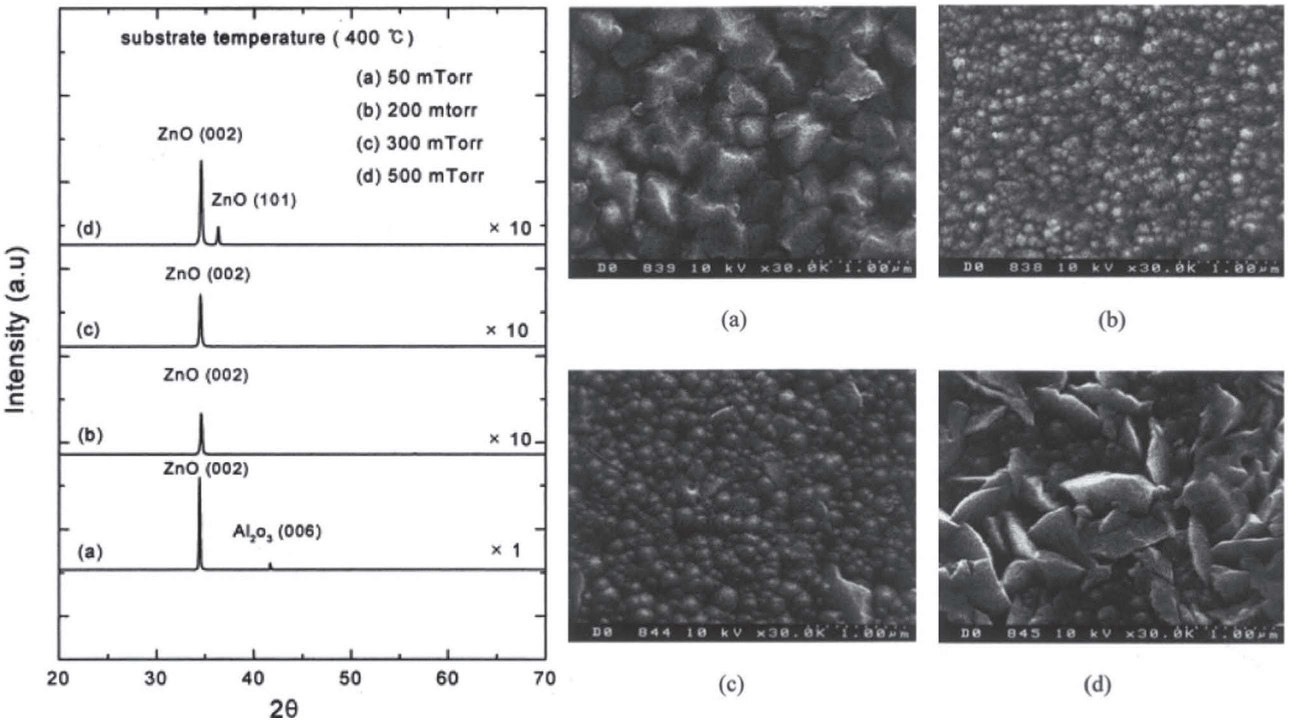

FIGURE 10.4 XRD spectra (left) and SEM images (right) of ZnO films prepared by PLD at different chamber pressure. (a) 50 mTorr, (b) 200 mTorr, (c) 300 mTorr, and (d) 500 mTorr [12].

reflective nature, metals were some of the first materials to be deposited in the form of thin film using PLD [13]. It has been seen that the deposition rate and the crystalline structure of the films deposited depend on the morphology of the target.

Depending on the temperature of the substrate, two different types of film formation have been seen in metallic films. For low-temperature substrates, continuous films with low crystalline quality were formed, and as the temperature of the substrate was increased, improved crystalline quality films with island growth were observed. Any islands formed coalesced and continuous films were established after a critical thickness was reached. This critical thickness was found to be dependent on temperature. Copper films with highly preferred orientation have been deposited on silicon substrate, while tungsten films grown on sapphire substrate were seen to have 3D epitaxy [14].

The growth of metastable structured films has been achieved using PLD. Fcc γ-Fe has been deposited on Cu (100) and Cu (111) to study magnetic properties [15,16]. Similarly, growth and magnetism of fcc Co has been studied. Fe and Co-based amorphous alloys were also deposited using PLD [17] and are known to have superior magnetic properties, including giant magnetoimpedance. PLD-grown thin films of amorphous Fe-Co-Ni-Si-B on glass and silicon were reported to have controllable magnetic properties [18]. PLD has also been used to deposit multilayered superlattices of material with alternating values of low-Z and high-Z like molybdenum–silicon multilayer for application in soft X-ray mirrors [19].

10.3.2 Oxides

PLD is widely used to grow thin films of oxide materials for different applications. PLD-deposited oxide materials have polycrystalline, oriented, or epitaxial structure. Optimized sets of process parameters are required for obtaining precise stoichiometry, good crystalline structure, and electrical properties on appropriate substrates for potential electrical and microelectronics applications.

10.3.2.1 Ferroelectric, Multiferroics, and Piezoelectric Oxides

Ferroelectric and multiferroic oxide thin films are important classes of materials that have been widely studied by film growth using PLD. In 1969, Helmut Schwarz and H. A. Tourtellotte made the first attempt to utilize PLD to deposit thin film of ferroelectric $BaTiO_3$ (BTO) [20]. They used fine grain powder of BTO for film deposition on glass substrate. Single-phase stoichiometric BTO films on crystalline Si substrate were pulsed laser-deposited by Ogale et al., at low temperature (450°C) at various temperatures and oxygen partial pressures [21]. They reported the dependence of the film properties on laser energy density, oxygen partial pressure during deposition, and substrate bias. The structural quality of their films was improved using high energy density (15 J cm^{-2}) at an oxygen partial pressure of 0.1 Torr. Still further improved quality BTO films were achieved at similar energy densities (15 J cm^{-2}) at an oxygen partial pressure of 10^{-6} Torr, when a bias field (330 V cm^{-1}) was applied between substrate (+ve) and the target (ground).

The synthesis of ferroelectric lead zirconate titanate (PZT) films was realized by using PLD at 248 nm [22]. This study focused on producing thin ($\lesssim 0.6\,\mu m$) PZT films on bare and platinum-coated MgO <100> substrates. Deposition was in an oxygen gas ambient (30 mTorr) at temperatures typically ~525°C. Electrical measurements were made on the films before and after annealing to determine the dielectric constant and polarization. Properties after annealing were substantially improved, with dielectric permittivity values comparable to bulk PZT. Various materials, $BaTiO_3$-BTO, Pb(Zr, Ti) O_3-PZT, (Pb, La)(Zr, Ti)O_3-PLZT, $Bi_4Ti_3O_{12}$, $Ba_{1-x}Ca_xTiO_3$, $(Ba_{0.955}Ca_{0.045})(Zr_{0.17}Ti_{0.83})O_3$, $Bi_{0.9}Sm_{0.1}Fe_{0.95}Co_{0.05}O_3$ (BSFCO) were tested for ferroelectric stability [23–32]. Both oxygen ambient and heat treatment play a crucial role in ferroelectric stability and long-term reliability, including fatigue, retention, and imprint behaviour. Intrinsic properties of the materials such as oxygen vacancies, alignment of defect dipole complexes, and trapping of the free charges can induce the imprint behaviour in ferroelectric materials. The crystalline quality is also another important factor for asymmetric ferroelectric polarization switching and imprints behaviour in thin films [26]. The imprint effect is also observed in spite of the symmetric electrode configuration of an epitaxial Pt/ $Bi_4Ti_3O_{12}$/ Pt films. Single-crystal $Bi_4Ti_3O_{12}$ exhibits two polarization axes, the major one with spontaneous polarization $Ps = 50\ \mu C\ cm^{-2}$, along the *a*-axis of the (pseudo-)orthorhombic structure, while the minor polarization axis along the *c*-axis with $Ps = 4\ \mu C\ cm^{-2}$. The coercive fields were 50 and 3–5 kV cm^{-1} for *c* and *a* axes, respectively. Stoichiometric $Bi_4Ti_3O_{12}$ films were also grown using pulsed excimer laser deposition on various substrates [Si(100), MgO(110), and Pt-coated Si(100)] at temperatures as low as 500°C by Buhay et al. [33]. They reported stable ferroelectric $Bi_4Ti_3O_{12}$ films at or above 675°C growth temperature and films deposited at or below 500°C growth temperature displayed bulk-type ferroelectric behaviour.

The effect of Ca-doped $BaTiO_3$ polycrystalline thin films deposited on Pt-coated Si substrates using pulsed excimer laser ablation technique is reported by Victor et al. [34]. The pulsed laser-ablated Ca-doped $BaTiO_3$ thin films deposited at 100 mTorr exhibited a higher dielectric constant and lower dielectric loss as well as an anomalous decrease in phase transition from 140°C to 110°C. This was attributed to the oxygen vacancy motion, which could have been created due to Ca^{2+} occupying the Ti^{4+} in $BaTiO_3$ lattice, thereby introducing compressional stress in the lattice.

There has been considerable amount of research on perovskite ferroelectric $(Ba_{1-x}Sr_x)TiO_3$ (BST) thin films for active microwave device applications [35–37]. BST thin films offer a significant advantage over bulk materials for active microwave device applications because they can achieve the required fields (<200 kV cm^{-1}) from low (0–10 V) bias voltages. Qadri et al. reported high-quality epitaxial $Ba_{0.5}Sr_{0.5}TiO_3$ thin films for these applications on various substrates, including MgO (100), $SrTiO_3$ (100), and $LaAlO_3$ (012) using PLD at 0.35 Torr of oxygen partial pressure (5–10 standard $cm^3\,min^{-1}$) and substrate temperature to 750°C–850°C [35]. $Ba(Zr_xTi_{1-x}O_3)$ (BZT) is a possible alternative to BST in the fabrication of tunable dielectric materials because Zr^{4+} is chemically more stable than Ti^{4+}. Even though BST thin films are well studied, they have a

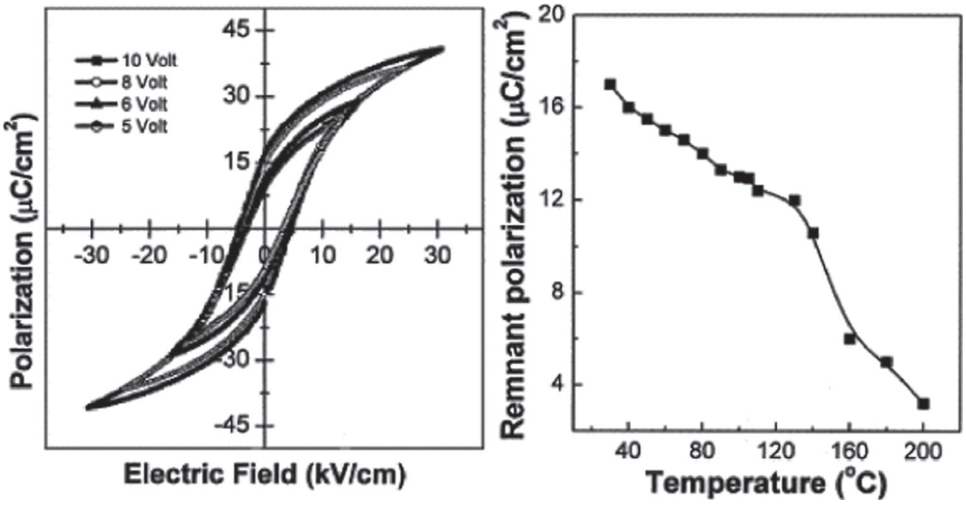

FIGURE 10.5 Hysteresis loop of PMN-PT films at room temperature showing remnant and saturation polarization of 16.9 and 40.8 μC cm^{-2}, respectively, with a coercive field of 4.5 kV cm^{-1} (left). Remnant polarization (P_r) was seen to drop gradually with an increase in temperature (right). (Adapted from [41].)

very high leakage current at low electric field. Zr^{4+} substitution at Ti^{4+} site in $BaTiO_3$ lattice has also been found to be an effective way to decrease the Curie temperature, and exhibits several interesting features in the dielectric behaviour of $BaTiO_3$ ceramics. Paraelectric BZT thin films are also attractive candidate materials for DRAMs and tunable dielectric devices. Ferroelectric $Ba(Zr_{0.15}Ti_{0.85})O_3$ thin films were successfully grown on Pt/Ti/SiO_2/Si(111) using PLD, and they were crystallized *in situ* at several different oxygen background pressures and temperatures. Smooth film surface with good electrical properties were found at an optimal deposition temperature of 675°C and oxygen partial pressure of 300 mTorr [38]. The remnant polarization (P_r) and coercive field (E_c) for samples deposited at 300 mTorr were 3.31 μC cm^{-2} and 93.56 kV cm^{-1}, respectively. The ferroelectric properties of these films were comparatively lower than those of their bulk counterparts; typically, this is attributed to several effects such as the clamping effect of the substrate on the films and strains [39].

PLD-grown lanthanum-substituted bismuth titanate ($Bi_{3.25}La_{0.75}Ti_3O_{12}$-BLT) is one more suitable material for non-volatile ferroelectric random access memory (FeRAM) applications with its excellent structural and ferroelectric properties with high excellent fatigue endurance up to 10^{10} switching cycles on metal electrodes. The PLD processing temperature (650°C) for the BLT films is lower than that reported for strontium bismuth tantalate (SBT) films by 100°C–200°C [40].

High-performance electrostrictive $Pb(Nb_{2/3}Mg_{1/3})O_3$-$PbTiO_3$ (PMN–PT) films were grown on Pt/TiO_2/SiO_2/Si in the presence of high-purity oxygen in the range of 150–350 mTorr with the substrate temperature during deposition varying from 600°C to 850°C, and using a $La_{0.5}Sr_{0.5}CoO_3$ (LSCO) template buffer layer [41] (Figure 10.5).

Paraelectric lanthanum-doped lead titanate (PLT) thin films were grown by PLD on Pt-coated Si-substrates for DRAM applications [42]. A rapid thermal annealing process (600°C) was adopted to induce polycrystallization with fine microstructure in the films. Temperature and pressure dependence of PLD-grown antiferroelectric lead zirconate ($PbZrO_3$-PZO) thin films is shown by Bharadwaja et al. [43,44]. Antiferroelectric materials are found to be good alternative material compositions for high charge storage devices and micromechanical transducer applications. As stated earlier, the oxygen partial pressure during film growth process plays a responsive role in obtaining the good crystalline perovskite thin films. It is clear from their studies that the films deposited at low pressure (10 mTorr) with a deposition temperature of 300°C and post-annealing temperature of 650°C for 10 min were very poor in crystalline quality. However, films deposited at a higher pressure of 50 mTorr with the same deposition and annealing temperatures for 10 min as stated above resulted in better crystallinity. The perovskite phase formation was gradually increased with the increase in annealing temperature. Preferential growth of the films also decides the ferroelectric nature of the films. PLD deposition and annealing temperatures have a profound effect on both the microstructure and crystalline perovskite phase in PMN-PT thin films [45].

Multiferroic materials have coupled electric, magnetic, and structural order parameters that result in ferroelectricity, ferromagnetism, and ferroelasticity. The multiferroic coupling allows switching of the ferroelectric state with a magnetic field, and vice versa, and they lead to a new generation of memory devices that can be electrically written and magnetically read [46]. They also offer the possibility of combining the best qualities of FeRAMs and magnetic random access memories (MRAMs): fast low-power electrical write operation and non-destructive magnetic read operation. Over the past 20 years or so, there has been considerable research based on single-phase multiferroics, composite multiferroics, and magnetoelectrics (antiferroelectric and/or antiferromagnetic) in various forms, such as ceramic, single crystal, and thin film using various preparation methods (Figure 10.6).

The perovskite single-phase $BiFeO_3$ (BFO) with ferroelectric and antiferromagnetic (weak magnetic) properties is one among the most studied materials towards multiferroic

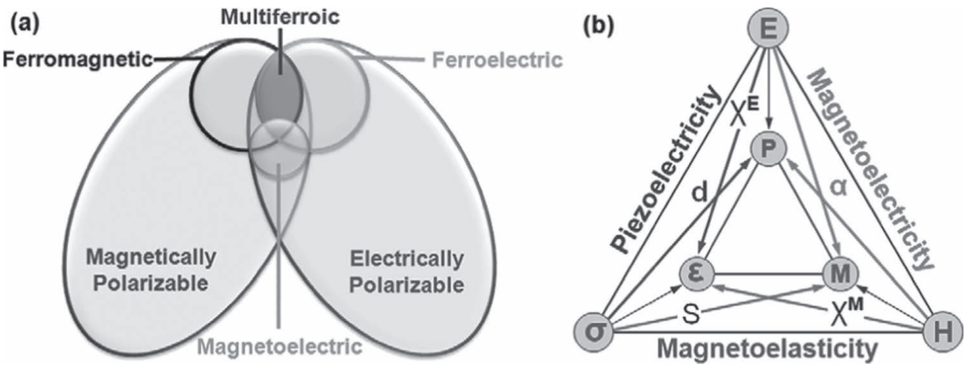

FIGURE 10.6 Schematics showing properties required for a material to be multiferroic material and illustration of different types of coupling present in materials. (a) Adapted from [47] and (b) from [48].)

magnetoelectric (ME) applications. Wang et al. reported PLD growth of high-quality heteroepitaxial BFO thin films on $SrRuO_3$ (SRO) bottom electrode onto $SrTiO_3$ (100) substrate [49] exhibiting enhanced remnant polarization ~50–60 μC cm^{-2} with an out-of-plane piezoelectric coefficient (d_{33}) of 70 pm V^{-1}. In-plane compressive stress (heteroepitaxial constraint) imposed due to SRO substrate might be the reason for these enhanced ferroelectric and piezoelectric properties.

Earlier in 1999, Kenji Ueda et al. reported multiferroic properties (coexistence of ferroelectricity and ferromagnetism) in $(Bi_{0.7}Ba_{0.3})(Fe_{0.7}Ti_{0.3})O_3$ thin films grown on Nb-doped $SrTiO_3$(100) by PLD [50]. They claimed that the low ferroelectric properties were due to the effect of lattice stress. Yun et al. have claimed giant ferroelectric polarization values of ~110 μC cm^{-2} at room temperature and ~166 μC cm^{-2} at 80 K, respectively, for the polycrystalline BFO films grown on $Pt/TiO_2/SiO_2/Si$ substrates [51]. While some speculate that this polarization maximum is probably an artefact due to leakage and charge injection [52], some experimental results [49] and theoretical reports [53,54] suggest that epitaxial strain might be the cause of such high values of remnant polarization (P_r) and remnant magnetization (M_r). Studies by Eerenstein [55] showed that epitaxial strain does not enhance M_r in BFO thin films. However, they believed that the heteroepitaxy induces significant and important structural changes in BFO thin films, which may lead to higher values for Pr. Bea et al. [56] explored the influence of deposition temperature and oxygen pressure on the growth of $BiFeO_3$ thin films by PLD onto (001)-oriented $SrTiO_3$ substrates. They reported that the higher oxygen partial pressure or lower temperature results in excess Bi_2O_3, while the opposite conditions, i.e. lower pressure or higher temperature, lead to iron oxide (Fe_2O_3) formation. These impurity phases were detrimental to the physical properties of BFO films.

However, the pure $BiFeO_3$ phase is formed closed to an oxygen partial pressure of 10^{-2}mbar and a deposition temperature of 580°C. Both single-layered $BiFeO_3$ and multilayered $BaTiO_3/BiFeO_3$ epitaxial thin films were deposited using PLD and studied by means of nuclear resonant scattering of synchrotron radiation [57]. A spin reorientation is observed in the multilayered films when compared to the single-phase $BiFeO_3$ layers and this spin reorientation indicates that strain and interfaces play a considerable role in tuning the magnetic spin order. Saturation magnetization of these multilayered films is substantially larger than that of the single-phase $BiFeO_3$ and $BaTiO_3$, and this can be attributed to the suppression of the spiral spin magnetic structure due to high epitaxial strain in the $BiFeO_3$ layers [58]. Multiferroic ($BaTiO_3$–$BiFeO_3$) multilayer heterostructures have shown high ME coefficients α_{ME} up to 24 V cm^{-1} Oe at 300 K. This value is much higher than that of a single-phase $BiFeO_3$ reference film ($\alpha_{ME} = 4.2$ V cm^{-1} Oe), which is correlated with increasing oxygen partial pressure during growth [59].

10.3.2.2 Superconducting Oxides

Thin films have been deposited on different substrates to study high-temperature superconductivity. Yttrium barium copper oxide (YBCO), one of the most prevalent high-temperature superconductors, was one of the first complex materials to be successfully deposited as a thin film by using PLD. The deposition of YBCO thin films worked as a relatively simple proof that the stoichiometric transfer of a complex material from target to a thin film was possible. This also encouraged the dramatic development of PLD as an easy and reliable method for thin-film deposition of complex materials.

Dijkkamp et al. were the first to deposit superconducting thin films of YBCO by pulsed laser ablation of a single bulk target [60]. After annealing the layers of YBCO deposited on $SrTiO_3$ substrates at a temperature of 900°C for an hour, the films showed a critical temperature of 85 K. Similar layers on sapphire substrates had a T_c of 75 K. They attributed the difference in critical temperature to the difference in grain size, among other reasons. The grain size was found to be 500 and 150 nm for $SrTiO_3$ and sapphire substrates, respectively. The similarity in composition of the thin films with that of the target was assigned to the highly non-equilibrium heating by the pulsed laser.

While studying the distribution of composition and the thickness, T. Venkatesan et al. found that there were two distinct types of components in the deposited YBCO films [61]. They detected that there was one forward peaked component and a slowly varying component. In the forward peaked component, the stoichiometric composition was found to be close to that of the target, and in the slowly varying component, the composition was different. They explained these two different compositions with two different type of ablation mechanisms of the target: thermal evaporation of the target responsible for the slowly varying component which had a slight change in the stoichiometry and an evaporation-initiated secondary process responsible for the forward peaked distribution. This was supported by the fact that the forward directed component decreased with a decrease in laser energy. Models to explain the secondary process include the formation of a shock-wave, explosion of the subsurface due to its high temperature and rapid surface cooling [62], the formation of Knudsen layer in a system with a large number of collisions leading to the re-condensation and emission in a forward peaked distribution [63], and superheating of the surface due to recoiling of the evaporated material [64]. To achieve good-quality films, post-processing of the deposit was considered necessary. Later, by using the optimized parameters and using an oxygen supply within the chamber, A. Inam et al. deposited superconducting YBCO thin films without post-deposition annealing [2]. They reported a high current density (J_c) of ~10^6 A cm^{-2} and a high T_c of up to 89K in as-deposited films. This showed that PLD could deposit thin films with excellent electrical and morphological properties in a simple and repeatable way.

Matsumoto et al. increased the current density in PLD-deposited YBCO films by introducing artificial defects in the form of Y_2O_3 nano-islands that extended to the c-axis of the film. They reported high increase in J_c at 77 K due to strong vortex pinning [65]. Studies of $BaZrO_3$ doping on YBCO films at a concentration from 0.9 to 9 wt% were done by Peurla et al. [66], who showed that the critical temperature decreased almost linearly with increasing concentration of $BaZrO_3$, and at a concentration of 3.9 wt%, the critical current density was found to be maximum. Also, the accommodation field B^* was found to be enhanced by the doping. YBCO-coated conductors were similarly manufactured by high-rate PLD [67], suggesting that together with quasi-equilibrium heating, this method could make these coated conductors on an industrial scale.

10.3.2.3 *Transparent Conducting Oxides*

A number of candidates have been studied for their possible use as transparent conducting oxides (TCOs) in optoelectronic applications. Indium tin oxide (ITO) is the most widely used TCO but since indium metal is not abundant, ITO is expensive. ZnO doped with different elements has been studied as an alternative. Al-doped ZnO thin films of different thickness having high optical transmittance in visible region and excellent electrical properties were deposited on glass substrates by Kaur et al. using PLD [68]. The films were reported to have *c*-axis, plane (002) orientation with uniform grain morphology. However, compressive stress was reported in the films, which was attributed to Al doping and thickness of the film.

Similarly, F-doped SnO_2 films were deposited on glass and their performance with different levels of F doping was studied [69]. Electrical resistivity of 5×10^{-4} Ω-cm, average optical transmittance of 87% in the visible range, and optical band gap of 4.25 eV were reported for 400-nm-thick films with optimum value of F-doping level. Cao et al. also deposited fluorine-doped ZnO films with high transmittance and electrical conductivity [70]. Resistivity was as low as 4.83×10^{-4} Ω cm with a carrier concentration of $5.43 \times 10^{20} cm^{-3}$ for the film deposited at optimum oxygen pressure that was 0.1 Pa. The Hall mobility was found to be 23.8 $cm^2 V^{-1} s^{-1}$, and higher than 90% average optical transmittance was seen for the visible wavelength region. These TCOs have applications in thin-film solar cells, sensors, light-emitting diodes, and flat panel displays.

10.3.3 Nitrides

PLD is also used to deposit Group III nitride thin films on sapphire, SiC, Si, oxides, and metals substrates for light-emitting diodes, laser diodes, and other optoelectronic applications. Sapphire has been one of the conventional substrates for nitride films because it is thermally stable and can be used in high-temperature processes like CVD and MBE. However, high-density dislocations exist in nitride films deposited on sapphire due to the large lattice mismatch. It also has low thermal conductivity that leads to a decrease in the efficiency of devices [71]. A wide range of thermally active oxide substrates and even conductive metals are therefore being explored as alternative substrates. Since using thermally active substrates in high-temperature processes like CVD and MBE can have different unwanted consequences, PLD has a clear advantage over these processes.

Epitaxial AlN layers were deposited on sapphire substrates by pulsed laser ablation of a solid AlN target using a KrF excimer laser [72]. At a deposition temperature of 800°C, base pressure of 5×10^7 Torr, and fluence range of 2–3 J cm^{-2}, the films were found to have good crystallinity and they were epitaxial with the *c*-axis normal to the Al_2O_3 (0001) surface. The films had a resistivity of more than 10^{13} Ω cm. In the same deposition study, using higher laser fluence >10 J cm^{-2} and lower temperatures <650°C, the films were deficient of nitrogen and the presence of free metallic aluminium was detected. The films prepared at high fluence also had a low resistivity of 7–25 Ω cm. AlN, GaN, and InN thin films were deposited on sapphire by Feiler et al. in an ultra-high vacuum with a base pressure of 10^{-9} Torr and also in nitrogen ambient atmosphere [73]. It was found that both AlN and GaN film grown in nitrogen ambient environment yielded higher rms roughness value than the AlN and GaN films grown in vacuum.

Si has large thermal conductivity of 130 W mK^{-1}, which is advantageous over sapphire with a thermal conductivity of 22 W mK^{-1} [74]. Jagannadham et al. deposited AlN films on Si(111) substrates at different temperatures using PLD. They reported an increase in grain size of AlN from 18 to 30 nm when the temperature was increased from 500°C to 750°C. There was large residual compressive stress in the AlN film grown at 600°C as compared to the films grown at 750°C [75]. Ohta et al. deposited GaN thin films on Si(111) and characterized the crystallinity with reflection high-energy electron diffraction (RHEED). GaN films directly grown on Si(111) had poor crystalline quality as suggested by faint pattern in RHEED. So an AlN buffer layer was deposited before GaN growth. When the thickness of the AlN layer increased to 27 nm, the RHEED pattern changed to clear streaks, showing a flat layer of AlN film. The AlN buffer layer was thus found to be helpful in improving the crystalline quality of GaN grown on Si [76].

Oxide substrates have many advantages over Si and sapphire, including lower lattice mismatch with nitride thin films, less difference in coefficient of thermal expansion, ability to grow non-polar nitride films, and higher reactivity of oxides providing easy peeling of nitride films to obtain freestanding nitride thin films. $LiGaO_2$ substrate with a tiny lattice mismatch of 0.9% with GaN was used to grow high-quality GaN directly without any buffer layer [77]. RHEED showed a sharp pattern implying high quality of GaN. AFM (atomic force microscopy) of these films showed low rms roughness of 2.0 nm in 200-nm-thick GaN films. Diffusion of Li atoms in nitride films was reduced by the optimized deposition using PLD. Another oxide substrate used for the deposition of nitride thin films is $MgAl_2O_4$. Good-quality AlN thin films were grown on $MgAl_2O_4$ at room temperature [78]. In addition to a uniform AlN layer with sharp RHEED pattern and no Mg atoms, these films were seen to have no interfacial layer. Even when annealed at 800°C, the films were very stable and no changes were seen at the interface. GaN films deposited on $MgAl_2O_4$ at various temperature revealed that the interface layer thickness decreases from 8.1 to 0 nm when the deposition temperature decreases from 600°C to RT. High crystalline quality and low rms roughness showed RT as the optimum temperature to deposit GaN films on $MgAl_2O_4$. MgO substrates were also used to deposit nitride thin films [79]. Metal polar films are often more flat. Using MgO as substrate, nitride films were deposited where they were Al polar as compared to N-polar in sapphire [80]. It was found that the rms roughness of AlN was better on MgO than on sapphire. TiN was used as a buffer layer to grow GaN on MgO. Rawat et al. reported that cubic GaN is obtained in the TiN (4.3 nm)/GaN (1.2 nm) multilayer on MgO (100), while GaN with hexagonal and cubic mixed phases is formed in a TiN (12.2 nm)/GaN (6.2 nm) multilayer [42]. TiN thickness plays an important role in determining the structure of GaN [81]. Hexagonal boron nitride (BN) films with epitaxial-like growth on highly oriented pyrolytic graphite substrate, and amorphous BN (*a*-BN) on the sapphire substrates, were also deposited using PLD [82].

Besides oxide substrates, nitride films were also deposited on electrically conductive substrates like ZnO [83], and metals like Ta, Mo, nitrided Al, and Cu substrates [84–87]. On Ag, AlN was deposited as a blocking layer to prevent the diffusion of Ag atoms. High-quality films with a surface roughness of 3.8 nm were deposited, and the interface was found to be stable at temperatures up to 700°C. It was seen that reduced growth temperature is required to deposit nitride films using PLD as compared to other methods of AlN [88].

10.3.4 Transition Metal Dichalcogenides

PLD-grown molybdenum disulphide (MoS_2) thin films were studied for field electron emission applications. Late et al. deposited MoS_2 thin films on tungsten tip and silicon substrates [89]. They reported the growth of films with dense nanostructured morphology in both the tungsten tip and silicon substrates. For MoS_2 film on Si substrate, a turn-on field of $2.8\,V\,\mu m^{-1}$ was required to achieve an emission current density of $10\,\mu A\,cm^{-2}$. Also, a large emission current density of $\sim 30\,mA\,cm^{-2}$ was emitted by the MoS_2 film-deposited tungsten tip emitter at a relatively lower applied voltage of ~3.8 kV. Kapton substrates were used to show good photoresponse and recovery of the MoS_2 thin films in flexible substrates (Figure 10.7).

WS_2 films were also deposited using PLD to study the photodetection properties. It was reported that PLD-deposited WS_2-based photoresistor demonstrated the broadest range of all WS_2-based photodetectors (370–1064 nm) and surpassed the performance of CVD-grown WS_2 [90]. The responsivity of the device approached a high value of $0.51\,AW^{-1}$ in an ambient environment because of the large optical absorbance of 40%–85% and high carrier mobility of $31\,cm^2 V^{-1} s^{-1}$ in the PLD films.

For use as tribological coatings, PbO-MoS_2 composite films were grown on stainless steel substrates. KrF excimer laser with a wavelength of 248 nm was used to deposit these films [91]. By varying the ratio of PbO:MoS_2 and substrate temperature, lubricious and long-lasting coatings could be achieved. It was seen that the composite films perform better at higher-temperature applications.

10.3.5 Diamond-like Carbon

Diamond-like carbon (DLC) coatings have a low coefficient of friction of about 0.2. So they can be used as tribological coatings. Both hydrogenated and hydrogen-free DLC films have been considered for these applications. In a PLD system, a broad range of particle energies can be achieved without using external bias to accelerate ions. This advantage along with the capability of PLD to produce both hydrogen free and hydrogenated DLC makes PLD a useful technique for the deposition of DLC thin films.

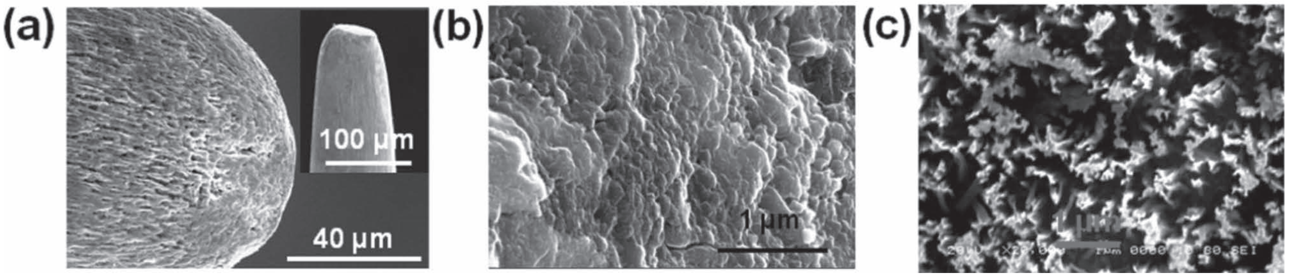

FIGURE 10.7 SEM images of PLD-grown MoS_2 thin film: on W-tip substrate (a and b) and on Si substrate (c). Inset of panel a shows an image of the bare W-tip. (Adapted from [89].)

Hydrogen-free diamond-like amorphous carbon thin films were deposited by using 193 nm ArF laser. At a laser power density of 5×10^8 W cm^{-2}, the films were obtained by pulsed laser ablation of graphite at room temperature. The deposited films were thermally stable and had hardness of up to 38 GPa and optical energy band gap of 2.6 eV [92]. Voevodin et al. deposited both hydrogen-free and hydrogenated DLC coatings using graphite and polycarbonate targets. Coatings grown from graphite targets were found to be amorphous DLC (a-C), and the ones from polycarbonate targets were found to be amorphous hydrogenated carbon (a-C:H). Hardness of 55–70 GPa for a-C coatings and the hardness of 12–20 GPa for a-C:H coatings were observed depending on the substrate bias. Friction coefficients were found below 0.1 for a-C coatings and were as low as 0.03 in dry nitrogen [93].

PLD-deposited DLC coatings were studied for tribological and scratch resistance properties with metal interlayers of Cr, Ag, Ti, and Ni. It was reported that remarkably high scratch resistance property can be achieved in DLC deposited with Ni and Ti as transition metal interlayers. Formation of graphitized/amorphized tribofilm during sliding was noticed, and an easy in-plane sliding provided low friction coefficient for these systems [94].

10.3.6 Polymers

The laser ablation and deposition of polymers as thin film is relatively different from PLD of inorganic materials. In the plasma plume formed by polymer, there are atoms and small molecular entities. In some cases, deposition of organic polymer with similar structure to original material is possible but generally these atoms and molecules do not self-assemble into original molecular structure on the target. Unzipping of volatile monomers from the polymer target by laser energy and recombination at the substrate may take place in some polymers at optimum conditions.

Smith and Turner grew thin films of fuchsine (an organic dye) and Ni-dimethylglyoxime (a pigment used in paints and cosmetics) in the early stage of development of PLD [1]. For almost two decades after that, there was very little work done on organics and polymers by using PLD. Then, Hansen and Robitaille used UV pulsed lasers to deposit a variety of polymer systems, including polymethylmethacrylate (PMMA), polyethylene, polyimide, and polycarbonate [95,96]. Their study showed that the ablation of the target material and the morphology of the resulting film both improve with a decrease in laser wavelength. Hansen and Robitaille further observed that the film quality was enhanced by using laser fluences near the ablation threshold for the polymers. A decrease in molecular weight of the polymer was observed for all films.

Blanchet et al. studied PLD of polytetrafluoroethylene (Teflon) an important polymer because of its role in electronics industry and also as a tribological coating, and explained the mechanism of ablation in terms of the thermal effect generated by the laser energy [97,98]. The deposition of chemically intact and high-quality PTFE thin films by PLD was demonstrated in their study. However, there was no evidence as to whether photolytic and/or pyrolytic processes were responsible for the dissociation of the bonds in the ablation of PTFE. For the ablation of PMMA, Srinivasan et al. found that the photolytic process of bond dissociation was important [99,100]. With the exception of PMMA, most of the other works showed that thermal processes play a dominant role but depending upon the type of polymers and processing parameters such as laser wavelength, laser fluence, and laser pulse duration, photolytic effects can also have an effect in the ablation behaviour. Jiang and coworkers also demonstrated the growth of crystalline PTFE films, and it was seen that crystallinity depends on substrate temperature [101]. Ueno et al. and coworkers deposited crystalline PTFE films using an excimer laser in an Ar background [102] and were able to make smooth PTFE films by heating the substrate to 97°C. Li et al. *also* reported crystalline PTFE thin-film growth by using 248 nm laser, at a substrate temperature of 300°C under an Ar background pressure of 75–750 mTorr [103]. High deposition rates of PTFE as compared to other methods were achieved with PLD (up to 16 nm s^{-1}). Katoh and Zhang deposited PTFE thin films with smooth surface morphologies and identical chemical composition to that of the target by PLD using synchrotron radiation etching [104,105]. They found that the polymer chains in PTFE films deposited by synchrotron radiation were aligned perpendicular to the substrate surface and the PTFE films deposited by UV-PLD had molecular axis oriented parallel to the substrate surface. Highly oriented PTFE films generated by PLD were used for aligning liquid crystals for display applications.

Other polymers deposited by using PLD include PMMA [99], polyvinylidene fluoride (PVDF), polyphenylene sulphide (PPS) [106], polythiophene [107], and polyacrylonitrile (PAN) [108]. In most of the studies, it was found that the morphology of the films depended upon the substrate temperature. Some polymers like PVDF deposited using PLD were found to be amorphous in nature, while in some other polymers like PPS, crystalline features were observed.

10.3.7 Biomaterials

Thin films of biomaterials like enzymes, proteins, and bioceramics were also deposited using PLD. Hydroxyapatite (HAp) bioceramic thin films were deposited on Ti, alpha-Al2O$_3$, SiO$_2$/Si(100), and SrTiO$_3$(100) substrates using an ArF laser [109]. The electrical properties of the HAp films were measured using Au/HAp/Nb-doped SrTiO$_3$(100) structures for biocompatible coating for implants and dielectric material in bioelectronic devices. Dielectric constant and breakdown voltage were found to be 5.7 (at 1 MHz) and 10^4 V cm^{-1}, respectively, at room temperature.

Active protein thin films were deposited by using matrix-assisted pulsed laser evaporation (MAPLE) method [110]. It was confirmed that the mass of protein in the deposited films was not modified due to the deposition process. Fourier transform infrared (FTIR) spectroscopy showed that the chemical functionality and secondary structure in the deposited thin films of horseradish peroxidase were nearly identical to those of the native protein. HAp thin films with different extents of strontium doping (0, 1, 3, or 7 at.%) were successfully deposited by using PLD [111]. Films with granular surface and a good degree of crystallinity were reported. The crystallinity was diminished with an increase in the amount of strontium.

10.3.8 Other Materials

In addition to the above listed materials, PLD has also been used to deposit iron-based superconductors like $FeSe_{1-x}$ [112], $FeTe_{1-x}$ [113], $Fe_{1+x}Te{:}O_y$ [114], $FeSe_{1-x}Te_x$ [115,116], and $BaFe_{2-x}Co_xAs_2$ [117], quasicrystals like Al-Cu-Fe [118], carbon nanotubes [119] for anode of lithium ion batteries, Cu_2ZnSnS_4 (CZTS) thin films for solar cells [120], etc.

10.4 Advantages and Disadvantages of PLD

PLD can deposit a wide range of thin-film materials. Stoichiometric transfer of target material even for complex compounds makes PLD a valuable tool. The kinetic energy of the ejected species can be optimized in such a way that it is high enough to promote uniform growth but low enough to avoid damage in the already-deposited film. Material evaporation is limited to the laser irradiated area, while the plasma plume generated is highly forward directed and this prevents the loss of material during the process and makes the stoichiometric transfer possible. The deposition can take place in UHV or high pressure of reactive gases, while the ability to deposit material on substrates at room temperature or an elevated temperature makes PLD a flexible technique.

However, stoichiometric transfer is not easy for large-chain materials like polymers. Good-quality thin films of polymers and biomaterials can be achieved but some modifications should be incorporated in the conventional PLD process. Difficulty in scaling up the process to large areas is another considerable impediment to the development of PLD.

10.5 Summary

PLD has emerged as one of the versatile methods for the deposition of thin films for materials research. By careful optimization of the process parameters, excellent-quality thin films can be achieved. The scalability of PLD for large-scale commercial applications is a challenging issue but for the purpose of thin-film material research, PLD is an easy, efficient, and cost-effective method of film deposition.

REFERENCES

1. Smith, H. M., and A. F. Turner. “Vacuum deposited thin films using a ruby laser.” *Applied Optics* 4.1 (1965): 147–148.
2. Inam, A., et al. “As-deposited high T_c and J_c superconducting thin films made at low temperatures.” *Applied Physics Letters* 53.10 (1988): 908–910.
3. Geohegan, D. B., D. B. Chrisey, and G. K. Hubler. *“Pulsed Laser Deposition of Thin Films.”* D. B. Chrisey and G.K. Hubler (eds.), Wiley, New York (1994): 59–69.
4. Boyd, I. W, and D. B. Chrisey. “Pulsed laser deposition of thin films.” *Handbook of Laser Technology and Applications (Three-Volume Set).* C. Webb and J. D. C. Jones (eds.), CRC Press, Boca Raton, FL (2003): 1675–1689.
5. Suresh, A., et al. “Transparent, high mobility InGaZnO thin films deposited by PLD.” *Thin Solid Films* 516.7 (2008): 1326–1329.
6. Willmott, P. R., and J. R. Huber. “Pulsed laser vaporization and deposition.” *Reviews of Modern Physics* 72.1 (2000): 315.
7. Horwitz, J. S., et al. “In situ deposition of epitaxial $PbZr_xTi_{(1-x)}$O3 thin films by pulsed laser deposition.” *Applied Physics Letters* 59.13 (1991): 1565–1567.
8. Fa, S., and H.-U. Krebs. “Calculations and experiments of material removal and kinetic energy during pulsed laser ablation of metals.” *Applied Surface Science* 96 (1996): 61–65.
9. Kelly, R., and R. W. Dreyfus. “Reconsidering the mechanisms of laser sputtering with Knudsen-layer formation taken into account.” *Nuclear Instruments and Methods in Physics Research Section B: Beam Interactions with Materials and Atoms* 32.1–4 (1988): 341–348.
10. Bellingeri, E., I. Pallecchi, R. Buzio, A. Gerbi, D. Marrè, M. R. Cimberle, … and C. Ferdeghini. $T_c = 21$ K in epitaxial $FeSe_{0.5}Te_{0.5}$ thin films with biaxial compressive strain. *Applied Physics Letters*, 96.10 (2010): 102512.
11. Sturm, K., and H.-U. Krebs. “Quantification of resputtering during pulsed laser deposition.” *Journal of Applied Physics* 90.2 (2001): 1061–1063.
12. Jin, B. J., S. Bae, S. Y. Lee, and S. Im. “Effects of native defects on optical and electrical properties of ZnO prepared by pulsed laser deposition.” *Materials Science and Engineering: B*, 71.1–3 (2000): 301–305.
13. Schwarz, H., and H. A. Tourtellotte. “Vacuum deposition by high-energy laser with emphasis on barium titanate films.” *Journal of Vacuum Science and Technology* 6.3 (1969): 373–378.
14. Lunney, J.G. “Pulsed laser deposition of metal and metal multilayer films.” *Applied Surface Science* 86.1–4 (1995): 79–85.
15. Shen, J., et al. “In-plane anisotropy and reversed spin reorientation of fcc Fe ultrathin films on Cu (100) by pulsed-laser deposition.” *EPL (Europhysics Letters)* 43.3 (1998): 349.
16. Shen, J., et al. “The effect of spatial confinement on magnetism: Films, stripes and dots of Fe on Cu (111).” *Journal of Physics: Condensed Matter* 15.2 (2002): R1.
17. Giergiel, J., et al. “Stages of structural transformation in iron thin film growth on copper (100).” *Surface Science* 310.1–3 (1994): 1–15.
18. Nikitin, P. I., et al. “Amorphous magnetic films produced by pulsed laser deposition.” *Journal of Applied Physics* 82.3 (1997): 1408–1415.
19. Weaver, I., et al. “PLD fabrication of a soft X-ray multilayer mirror and LPP reflectance test.” *Applied Surface Science* 127(1998): 915–921.
20. Schwarz, H., and H. A. Tourtellotte. “Vacuum deposition by high-energy laser with emphasis on barium titanate films.” *Journal of Vacuum Science and Technology* 6.3 (1969): 373–378.
21. Nawathey, R., et al. “Pulsed laser deposition of barium titanate films on silicon.” *Solid State Communications* 71.1 (1989): 9–12.
22. Saenger, K. L., et al. “Lead zirconate titanate films produced by pulsed laser deposition.” *MRS Online Proceedings Library Archive* 200 (1990): 115.
23. Warren, W. L., D. Dimos, and R. M. Waser. “Degradation mechanisms in ferroelectric and high-permittivity perovskites.” *MRS Bulletin* 21.7 (1996): 40–45.

24. Lee, J., et al. "Imprint and oxygen deficiency in (Pb, La)(Zr, Ti)O_3 thin-film capacitors with La-Sr-Co-O electrodes." *Applied Physics Letters* 66.11 (1995): 1337–1339.
25. Warren, W. L., et al. "Voltage shifts and imprint in ferroelectric capacitors." *Applied Physics Letters* 67.6 (1995): 866–868.
26. Lee, J., and R. Ramesh. "Imprint of (Pb, La)(Zr, Ti)O_3 thin films with various crystalline qualities." *Applied Physics Letters* 68.4 (1996): 484–486.
27. Park, B.H., et al. "Pulsed laser deposition of $Bi_4Ti_3O_{12}$ thin films and their anomalous imprint characteristics." *Integrated Ferroelectrics* 14.1–4 (1997): 181–191.
28. Victor, P., R. Ranjith, and S. B. Krupanidhi. "Normal ferroelectric to relaxor behavior in laser ablated Ca-doped barium titanate thin films." *Journal of Applied Physics* 94.12 (2003): 7702–7709.
29. Cheng, B. L., et al. "Dielectric properties of $(Ba_{0.8}Sr_{0.2})(Zr_xTi_{1-x})O_3$ thin films grown by pulsed-laser deposition." *Journal of the European Ceramic Society* 25.12 (2005): 2295–2298.
30. Chan, N. Y., et al. "The structural and in-plane dielectric/ferroelectric properties of the epitaxial (Ba, Sr)(Zr, Ti)O_3 thin films." *Journal of Applied Physics* 115.23 (2014): 234102.
31. Puli, V. S., et al. "Nanoscale polarisation switching and leakage currents in $(Ba_{0.955}Ca_{0.045})(Zr_{0.17}Ti_{0\cdot 83})O_3$ epitaxial thin films." *Journal of Physics D: Applied Physics* 48.35 (2015): 355502.
32. Puli, V. S., et al. "Photovoltaic effect in transition metal modified polycrystalline $BiFeO_3$ thin films." *Journal of Physics D: Applied Physics* 47.7 (2014): 075502.
33. Buhay, H., et al. "Pulsed laser deposition and ferroelectric characterization of bismuth titanate films." *Applied Physics Letters* 58.14 (1991): 1470–1472.
34. Victor, P., R. Ranjith, and S. B. Krupanidhi. "Normal ferroelectric to relaxor behavior in laser ablated Ca-doped barium titanate thin films." *Journal of Applied Physics* 94.12 (2003): 7702–7709.
35. Qadri, S. B., et al. "X-ray characterization of extremely high quality (Sr, Ba) TiO_3 films grown by pulsed laser deposition." *Applied Physics Letters* 66.13 (1995): 1605–1607.
36. Knauss, L. A., et al. "The effect of annealing on the structure and dielectric properties of $Ba_xSr_{1-x}TiO_3$ ferroelectric thin films." *Applied Physics Letters* 69.1 (1996): 25–27.
37. Horwitz, J. S., et al. "The effect of stress on the microwave dielectric properties of $Ba_{0.5}Sr_{0.5}TiO_3$ thin films." *Journal of Electroceramics* 4.2–3 (2000): 357–363.
38. James, A. R., and C. Prakash. "Ferroelectric properties of pulsed laser deposited $Ba(Zr_{0.15}Ti_{0.85})O_3$ thin films." *Applied Physics Letters* 84.7 (2004): 1165–1167.
39. Yu, Z., R. Guo, and A. S. Bhalla. "Dielectric behavior of $Ba(Ti_{1-x}Zr_x)O_3$ single crystals." *Journal of Applied Physics* 88.1 (2000): 410–415.
40. Park, B. H., et al. "Lanthanum-substituted bismuth titanate for use in non-volatile memories." *Nature* 401.6754 (1999): 682.
41. Laha, A., S. Saha, and S. B. Krupanidhi. "Role of $La_{0.5}Sr_{0.5}CoO_3$ template layers on dielectric and electrical properties of pulsed-laser ablated $Pb(Nb_{2/3}Mg_{1/3})O_3$–$PbTiO_3$ thin films." *Thin Solid Films* 424.2 (2003): 274–282.
42. Venkateswarlu, P., S. S. N. Bharadwaja, and S. B. Krupanidhi. "Study of pulsed laser deposited lead lanthanum titanate thin films." *Thin Solid Films* 389.1–2 (2001): 84–90.
43. Bharadwaja, S. S. N., and S. B. Krupanidhi. "Antiferroelectric lead zirconate thin films by pulsed laser ablation." *Materials Science and Engineering: B* 64.1 (1999): 54–59.
44. Bharadwaja, S. S. N., and S. B. Krupanidhi. "Dielectric and dc electrical studies of antiferroelectric lead zirconate thin films." *Materials Science and Engineering: B* 78.1 (2000): 1–10.
45. Laha, A., S. Bhattacharyya, and S. B. Krupanidhi. "Impact of microstructure on dielectric properties of $Pb(Mg_{1/3}Nb_{2/3})O_3$–$PbTiO_3$ thin films." *Materials Science and Engineering: B* 106.2 (2004): 111–119.
46. Scott, J. F. "Data storage: Multiferroic memories." *Nature Materials* 6.4 (2007): 256.
47. Eerenstein, W., Mathur, N. D., and Scott, J. F. Multiferroic and magnetoelectric materials. *Nature* 442.7104 (2006): 759.
48. Martin, L. W., Crane, S. P., Chu, Y. H., Holcomb, M. B., Gajek, M., Huijben, M., … and Ramesh, R. Multiferroics and magnetoelectrics: Thin films and nanostructures. *Journal of Physics: Condensed Matter*, 20.43 (2008): 434220.
49. Wang, J. B. N. J., et al. "Epitaxial $BiFeO_3$ multiferroic thin film heterostructures." *Science* 299.5613 (2003): 1719–1722.
50. Ueda, K., H. Tabata, and T. Kawai. "Coexistence of ferroelectricity and ferromagnetism in $BiFeO_3$–$BaTiO_3$ thin films at room temperature." *Applied Physics Letters* 75.4 (1999): 555–557.
51. Yun, K.Y., et al. "Enhancement of electrical properties in polycrystalline $BiFeO_3$ thin films." *Applied Physics Letters* 89.19 (2006): 192902.
52. Palai, R., et al. "β phase and γ− β metal-insulator transition in multiferroic $BiFeO_3$." *Physical Review B* 77.1 (2008): 014110.
53. Li, J., et al. "Dramatically enhanced polarization in (001), (101), and (111) $BiFeO_3$ thin films due to epitiaxial-induced transitions." *Applied Physics Letters* 84.25 (2004): 5261–5263.
54. Ederer, C., and N. A. Spaldin. "Weak ferromagnetism and magnetoelectric coupling in bismuth ferrite." *Physical Review B* 71.6 (2005): 060401.
55. Eerenstein, W., et al. "Comment on "Epitaxial $BiFeO_3$ multiferroic thin film heterostructures"." *Science* 307.5713 (2005): 1203–1203.
56. Béa, H., et al. "Influence of parasitic phases on the properties of $BiFeO_3$ epitaxial thin films." *Applied Physics Letters* 87.7 (2005): 072508.
57. Lazenka, V., et al. "Magnetic spin structure and magnetoelectric coupling in $BiFeO_3$-$BaTiO_3$ multilayer." *Applied Physics Letters* 106.8 (2015): 082904.
58. Lorenz, M., et al. "Multiferroic $BaTiO_3$–$BiFeO_3$ composite thin films and multilayers: Strain engineering and magnetoelectric coupling." *Journal of Physics D: Applied Physics* 47.13 (2014): 135303.
59. Lorenz, M., et al. "Correlation of magnetoelectric coupling in multiferroic $BaTiO_3$-$BiFeO_3$ superlattices with oxygen vacancies and antiphase octahedral rotations." *Applied Physics Letters* 106.1 (2015): 012905.

60. Dijkkamp, D., et al. "Preparation of Y-Ba-Cu oxide superconductor thin films using pulsed laser evaporation from high T_c bulk material." *Applied Physics Letters* 51.8 (1987): 619–621.
61. Venkatesan, T., et al. "Observation of two distinct components during pulsed laser deposition of high T_c superconducting films." *Applied Physics Letters* 52.14 (1988): 1193–1195.
62. Gagliano, F. P., and U. C. Paek. "Observation of laser-induced explosion of solid materials and correlation with theory." *Applied Optics* 13.2 (1974): 274–279.
63. Kelly, R., and R. W. Dreyfus. "On the effect of Knudsen-layer formation on studies of vaporization, sputtering, and desorption." *Surface Science* 198.1–2 (1988): 263–276.
64. Ready, J. F. "Effects due to absorption of laser radiation." *Journal of Applied Physics* 36.2 (1965): 462–468.
65. Matsumoto, K., et al. "Critical current control in $YBa_2Cu_3O_{7-\delta}$ films using artificial pinning centers." *Japanese Journal of Applied Physics* 44.1L (2005): L246.
66. Peurla, M., et al. "Optimization of the $BaZrO_3$ concentration in YBCO films prepared by pulsed laser deposition." *Superconductor Science and Technology* 19.8 (2006): 767.
67. Usoskin, A., and H. C. Freyhardt. "YBCO-coated conductors manufactured by high-rate pulsed laser deposition." *MRS Bulletin* 29.8 (2004): 583–589.
68. Kaur, G., A. Mitra, and K. L. Yadav. "Pulsed laser deposited Al-doped ZnO thin films for optical applications." *Progress in Natural Science: Materials International* 25.1 (2015): 12–21.
69. Kim, H., R. C. Y. Auyeung, and A. Piqué. "Transparent conducting F-doped SnO_2 thin films grown by pulsed laser deposition." *Thin Solid Films* 516.15 (2008): 5052–5056.
70. Cao, L., et al. "Highly transparent and conducting fluorine-doped ZnO thin films prepared by pulsed laser deposition." *Solar Energy Materials and Solar Cells* 95.3 (2011): 894–898.
71. Liu, L., and J. H. Edgar. "Substrates for gallium nitride epitaxy." *Materials Science and Engineering: R: Reports* 37.3 (2002): 61–127.
72. Vispute, R. D., H. Wu, and J. Narayan. "High quality epitaxial aluminum nitride layers on sapphire by pulsed laser deposition." *Applied Physics Letters* 67.11 (1995): 1549–1551.
73. Feiler, D., et al. "Pulsed laser deposition of epitaxial AlN, GaN, and InN thin films on sapphire (0001)." *Journal of Crystal Growth* 171.1–2 (1997): 12–20.
74. Horng, R.-H., et al. "Performance of GaN-based light-emitting diodes fabricated using GaN epilayers grown on silicon substrates." *Optics Express* 22.101 (2014): A179–A187.
75. Jagannadham, K., et al. "Structural characteristics of AlN films deposited by pulsed laser deposition and reactive magnetron sputtering: A comparative study." *Journal of Vacuum Science & Technology A: Vacuum, Surfaces, and Films* 16.5 (1998): 2804–2815.
76. Ohta, J., et al. "RHEED and XPS study of GaN on Si (1 1 1) grown by pulsed laser deposition." *Journal of Crystal Growth* 233.4 (2001): 779–784.
77. Takahashi, H., et al. "Structural properties of GaN grown on $LiGaO_2$ by PLD." *Journal of Crystal Growth* 259.1–2 (2003): 36–39.
78. Li, G., et al. "Room-temperature epitaxial growth of AlN on atomically flat $MgAl_2O_4$ substrates." *Applied Physics Letters* 89.18 (2006): 182104.
79. Kakuda, M., et al. "RF-MBE growth of cubic AlN on MgO (001) substrates via 2-step c-GaN buffer layer." *Journal of Crystal Growth* 378 (2013): 307–309.
80. Chen, X. W., et al. "Epitaxial growth and optical properties of Al-and N-polar AlN films by laser molecular beam epitaxy." *Journal of Physics D: Applied Physics* 47.12 (2014): 125303.
81. Rawat, V., and T. Sands. "Growth of Ti N/ Ga N metal/semiconductor multilayers by reactive pulsed laser deposition." *Journal of Applied Physics* 100.6 (2006): 064901.
82. Glavin, N. R., et al. "Synthesis of few-layer, large area hexagonal-boron nitride by pulsed laser deposition." *Thin Solid Films* 572 (2014): 245–250.
83. Ueno, K., et al. "Epitaxial growth of nonpolar AlN films on ZnO substrates using room temperature grown GaN buffer layers." *Applied Physics Letters* 91.8 (2007): 081915.
84. Hirata, S., et al. "Epitaxial growth of AlN films on single-crystalline Ta substrates." *Journal of Solid State Chemistry* 180.8 (2007): 2335–2339.
85. Okamoto, K., et al. "Epitaxial growth of AlN on single crystal Mo substrates." *Thin Solid Films* 516.15 (2008): 4809–4812.
86. Wang, W., et al. "Epitaxial growth of high quality AlN films on metallic aluminum substrates." *CrystEngComm* 16.20 (2014): 4100–4107.
87. Inoue, S., et al. "Epitaxial growth of AlN on Cu (1 1 1) substrates using pulsed laser deposition." *Journal of Crystal Growth* 289.2 (2006): 574–577.
88. Inoue, S., et al. "Growth of single crystalline GaN on silver mirrors." *Applied Physics Letters* 91.20 (2007): 201920.
89. Late, D.J., et al. "Pulsed laser-deposited MoS_2 thin films on W and Si: Field emission and photoresponse studies." *ACS Applied Materials & Interfaces* 6.18 (2014): 15881–15888.
90. Yao, J. D., et al. "Stable, highly-responsive and broadband photodetection based on large-area multilayered WS_2 films grown by pulsed-laser deposition." *Nanoscale* 7.36 (2015): 14974–14981.
91. Zabinski, J. S., et al. "Chemical and tribological characterization of PbO-MoS_2 films grown by pulsed laser deposition." *Thin Solid Films* 214.2 (1992): 156–163.
92. Xiong, F., et al. "Pulsed laser deposition of amorphous diamond-like carbon films with ArF (193 nm) excimer laser." *Journal of Materials Research* 8.9 (1993): 2265–2272.
93. Voevodin, A. A., et al. "Mechanical and tribological properties of diamond-like carbon coatings prepared by pulsed laser deposition." *Surface and Coatings Technology* 76(1995): 534–539.
94. Gayathri, S., et al. "Tribological properties of pulsed laser deposited DLC/TM (TM= Cr, Ag, Ti and Ni) multilayers." *Tribology International* 53 (2012): 87–97.
95. Hansen, S. G., and T. E. Robitaille. "Formation of polymer films by pulsed laser evaporation." *Applied Physics Letters* 52.1 (1988): 81–83.
96. Hansen, S. G., and T. E. Robitaille. "Arrival time measurements of films formed by pulsed laser evaporation of polycarbonate and selenium." *Journal of Applied Physics* 64.4 (1988): 2122–2129.
97. Blanchet, G. B. "Deposition of amorphous fluoropolymers thin films by laser ablation." *Applied Physics Letters* 62.5 (1993): 479–481.

98. Blanchet, G.B., and S. Ismat Shah. “Deposition of polytetrafluoroethylene films by laser ablation.” *Applied Physics Letters* 62.9 (1993): 1026–1028.
99. Srinivasan, R., et al. “Photochemical cleavage of a polymeric solid: Details of the ultraviolet laser ablation of poly (methyl methacrylate) at 193 nm and 248 nm.” *Macromolecules* 19.3 (1986): 916–921.
100. Srinivasan, R., and B. Braren. “Ultraviolet laser ablation of organic polymers.” *Chemical Reviews* 89.6 (1989): 1303–1316.
101. Jiang, W., et al. “Pulsed-laser deposition of polytetrafluoroethylene.” *Journal of Materials Research* 10.4 (1995): 1038–1043.
102. Ueno, Y., T. Fujii, and F. Kannari. “Deposition of fluoropolymer thin films by vacuum-ultraviolet laser ablation.” *Applied Physics Letters* 65.11 (1994): 1370–1372.
103. Li, S. T., et al. “Pulsed-laser deposition of crystalline Teflon (PTFE) films.” *Applied Surface Science* 125.1 (1998): 17–22.
104. Zhang, Y., T. Katoh, and A. Endo. “Changing molecular orientation in fluorocarbon thin films deposited by different photo-processing: Synchrotron radiation etching vs laser ablation.” *The Journal of Physical Chemistry B* 104.26 (2000): 6212–6217.
105. Zhang, Y., T. Katoh, and A. Endo. “Deposition of highly oriented Teflon thin films by synchrotron radiation etching.” *Journal of Electron Spectroscopy and Related Phenomena* 119.2–3 (2001): 247–253.
106. Kale, S., et al. “Deposition of polyphenylene sulphide (PPS) polymer by pulsed excimer laser ablation.” *Materials Letters* 15.4 (1992): 260–263.
107. Nishio, S., et al. “Preparation of polythiophene thin films by UV laser-assisted deposition of 2, 5-dichlorothiophene with a 248 nm excimer laser beam.” *Journal of Photochemistry and Photobiology A: Chemistry* 116.3 (1998): 245–249.
108. Nishio, S., et al. “Preparation of polymer films by laser ablation of polyacrylonitrile: Significant dependence on ablation wavelengths.” *Applied Surface Science* 106(1996): 132–136.
109. Hontsu, S., et al. “Electrical properties of hydroxyapatite thin films grown by pulsed laser deposition.” *Thin Solid Films* 295.1–2 (1997): 214–217.
110. Ringeisen, B. R., et al. “Novel laser-based deposition of active protein thin films.” *Langmuir* 17.11 (2001): 3472–3479.
111. Capuccini, C., et al. “Strontium-substituted hydroxyapatite coatings synthesized by pulsed-laser deposition: In vitro osteoblast and osteoclast response.” *Acta Biomaterialia* 4.6 (2008): 1885–1893.
112. Wu, M. K., et al. “The development of the superconducting PbO-type β-FeSe and related compounds.” *Physica C: Superconductivity* 469.9–12 (2009): 340–349.
113. Han, Y., et al. “Superconductivity in iron telluride thin films under tensile stress.” *Physical Review Letters* 104.1 (2010): 017003.
114. Si, W., et al. “Superconductivity in epitaxial thin films of $Fe_{1.08}Te:O_x$.” *Physical Review B* 81.9 (2010): 092506.
115. Kumary, T. G., et al. “Superconducting $Fe_{1+\delta}Se_{1-x}Te_x$ thin films: Growth, characterization and properties.” *Superconductor Science and Technology* 22.9 (2009): 095018.
116. Hanawa, M., et al. “Empirical selection rule of substrate materials for iron chalcogenide superconducting thin films.” *Japanese Journal of Applied Physics* 51.1R (2011): 010104.
117. Katase, T., et al. “Atomically-flat, chemically-stable, superconducting epitaxial thin film of iron-based superconductor, cobalt-doped $BaFe_2As_2$.” *Solid State Communications* 149.47–48 (2009): 2121–2124.
118. Teghil, R., et al. “Picosecond and femtosecond pulsed laser ablation and deposition of quasicrystals.” *Applied Surface Science* 210.3–4 (2003): 307–317.
119. Chou, S.-L., et al. “Silicon/single-walled carbon nanotube composite paper as a flexible anode material for lithium ion batteries.” *The Journal of Physical Chemistry C* 114.37 (2010): 15862–15867.
120. Moholkar, A. V., Shinde, S. S., Babar, A. R., Sim, K. U., Kwon, Y. B., Rajpure, K. Y., … and Kim, J. H. “Development of CZTS thin films solar cells by pulsed laser deposition: Influence of pulse repetition rate”. *Solar Energy*, 85.7 (2011): 1354–1363.

11

Surface Micro- and Nano-structuring on Metals with Femtosecond Lasers

Jianjun Yang and Chunlei Guo

CONTENTS

11.1 Introduction 125
11.2 Basic Principles 125
11.3 Femtosecond Laser Nano-/Microstructuring 126
  11.3.1 Irregular Nanostructures 127
  11.3.2 Femtosecond Laser-induced 1D Periodic Subwavelength Structures 128
  11.3.3 Femtosecond Laser-Induced 2D Periodic Subwavelength Structures 131
11.4 Conclusion 134
References 134

11.1 Introduction

Micro-/nanostructuring of materials has attracted a significant attention in recent years, because it can be used for engineering material properties and has found a wide range of applications in optics, optoelectronics, photonics, plasmonics, optical biosensing, microfluidics, optofluidics, and biomedicine, to name a few, see the Chapter 1 “Laser Material Processing” and the references therein [4]. Conventionally, nano- and microfabrication were carried out via mature technology of lithography [1]. However, this kind of top-down approach often requires complex procedures under controlled conditions by requiring mask designs and photoresists. With the advent of femtosecond lasers, the potential for femtosecond lasers in ablation-based micro- and nanoprocessing has been demonstrated [2–5]. Initially, a number of techniques using femtosecond lasers assisted by other techniques were developed for surface nanostructuring and nanopatterning of solids, such as near-field nanomachining [6], laser-assisted chemical etching [7], and deposition from femtosecond laser-ablated plumes [8]. It was also found that laser-induced periodic surface structures (LIPSS) that had previously been generated using long-pulsed lasers can also be produced by femtosecond laser pulses on nearly all types of materials, including semiconductors [9–12], dielectrics [13,14], and metals [15–17]. More recently, direct femtosecond laser processing stood out as a new field for surface nanostructuring and nanopatterning due to its flexibility, simplicity, and capability of producing a large variety of surface structures suitable for a wide range of applications [4,5]. Compared to various other methods – for example, electron beam photolithography, fast atom beam or ion etching, and interference lithography – the processing of femtosecond laser pulses represents a novel, simple, and versatile technology for producing micro- and nanostructures, and their advantages are as follows [4]: (i) various structures containing both micro- and nanoscale structures can be created without any masks, thus making the process more efficient; (ii) a single-step processing at a high speed under ambient air environment, thus avoiding expensive and time-consuming vacuum facilities or additional chemical procedures; (iii) ability to produce nanostructures on a surface over the area from microscale to macroscale. In this chapter, we will focus on a review of surface structuring of metals with the direct femtosecond laser irradiation on metal surfaces.

11.2 Basic Principles

In general, micro- and nanoprocessing of materials by a femtosecond laser is based on pulse ablation i.e. material ejection from the irradiated sample. Physical processes underlying femtosecond laser ablation are complex because of various effects take place over a short duration of time, which have been discussed in numerous works [2,4,18–22]. Figure 11.1 shows the interaction dynamics of a femtosecond laser pulse with metals that lead to the ablation and the formation of surface structures [4]. When a femtosecond laser pulse strikes a metal surface, the pulse energy will be absorbed by the electrons first through the inverse bremsstrahlung mechanism over a skin layer on the order of 10 nm thickness. In most cases, the thermalization of the excited electrons can be assumed to occur instantaneously (on a time scale of 100 fs) due to the short electron–electron scattering time, which leads to an elevated electron temperature. Therefore, the overall picture of a nonequilibrium system in metals is normally described as constituting two subequilibrium systems, the hot electrons and the cold lattice [23,24]. This transient two-temperature

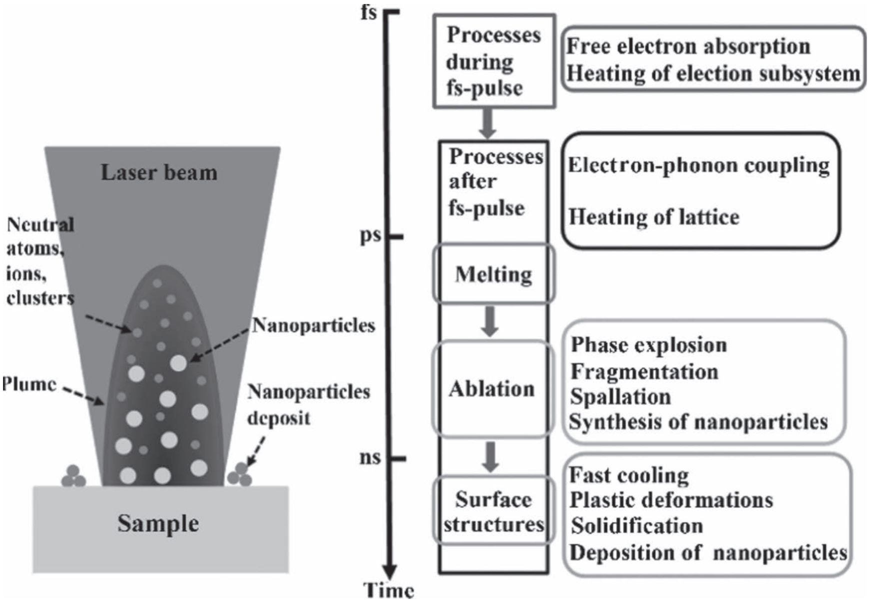
fs
ps
ns
Time
Laser beam
Neutral atoms, ions, clusters
Nanoparticles
Plume
Nanoparticles deposit
Sample
Processes during fs-pulse
Free electron absorption
Heating of election subsystem
Processes after fs-pulse
Electron-phonon coupling
Heating of lattice
Melting
Ablation
Phase explosion
Fragmentation
Spallation
Synthesis of nanoparticles
Surface structures
Fast cooling
Plastic deformations
Solidification
Deposition of nanoparticles

FIGURE 11.1 Physical processes of femtosecond laser processing of metals via ablation [4].

system will tend to reach equilibrium within a few picoseconds through electron–phonon (*e-ph*) coupling as well as electron diffusion out of the excited region [24–26]. This dynamic process is described by the so-called two-temperature model [27]. The interaction between electrons and phonons is very important for micro- and nanostructuring. For metals with a large *e-ph* coupling factor, the absorbed laser energy is transferred faster from the electrons to the lattice than for metals with low *e-ph* coupling factor, and thus, no significant amount of heat transfers to the inside of materials.

When the lattice temperature is elevated high enough, melting and ablation may occur. Laser–material interaction before a few picoseconds is considered a nonthermal process, whereas events occurring afterwards are considered thermal process. Melting occurs on the picosecond time scale – between a few and a few hundred picoseconds. Ablation, the removal of material, usually begins a few hundreds of picoseconds (~100 ps) following the femtosecond laser pulse and can last up to several nanoseconds [28,29]. The plume of the ablated material is composed of neutral atoms, ions, clusters, and nanoparticles, depending on the laser irradiation parameters. Following ablation, the sample surface cools down at a very high rate of about 10^{13}–10^{15} K s^{-1} [30] and rapidly re-solidifies to give rise to surface structures. The morphology of the laser-induced surface structures depends on the laser parameters. Some of the nanoparticles generated in ablation are deposited back onto the sample and form a nanostructured film [8,15]. The redeposition of nanoparticles depends on ambient gas pressure [31–34].

11.3 Femtosecond Laser Nano-/Microstructuring

A typical set-up used for surface micro- and nanostructuring through direct femtosecond laser ablation is shown in Figure 11.2 [4]. Pulses from a femtosecond laser system are focused by a lens onto a sample mounted on a computer-controlled *X–Y* translation stage. One can also use a cylindrical lens to focus the laser beam into a focused line [35]. A beamsplitter and joulemeter are used for monitoring the energy of femtosecond laser pulse. An electro-mechanical shutter is used to control the number of applied laser pulses or to block the laser beam in raster scanning. A variable attenuator is used to vary the incident laser fluence on the sample. A polarizer is used to control the laser light polarization in producing polarization-sensitive surface structures. The femtosecond laser set-up shown in Figure 11.2 is suitable for structuring a single spot on the sample when the translation stage sits still, and a single line when a sample is translated along the *X*- or *Y*-axis, or a large area when the sample is raster-scanned in both *X*- and *Y*-directions. During the latter two cases, the number of laser pulses partially overlapped on per spot area can also be controlled by varying the scanning velocity. By varying the parameters of the laser pulses incident upon the treated

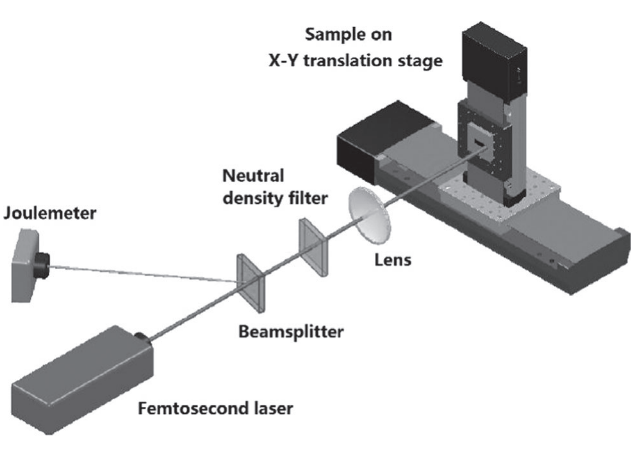
Sample on
X-Y translation stage
Neutral
density filter
Joulemeter
Lens
Beamsplitter
Femtosecond laser

FIGURE 11.2 A typical experimental set-up for femtosecond laser structuring of material surfaces [4].

metal, a large variety of controlled surface structures can be produced.

Micro- and nanoscale surface structures produced by direct femtosecond laser ablation can be classified into the following categories: (i) irregular nanostructures (nanocavities, nanospheres, nanoprotrusions, nanowires); (ii) laser-induced one-dimensional (1D) periodic and quasi-periodic subwavelength structures; and (iii) laser-induced two-dimensional (2D) periodic subwavelength structures. Below, we will discuss these types of surface structures in detail.

11.3.1 Irregular Nanostructures

It has been identified that the fabrication of irregular nanostructures on metals can be performed with direct femtosecond laser ablation in air [4,5] and in liquids [36]. The nanostructured surface contains one or more following entities: nanocavities, nanoholes, nanospheres, nanoprotrusions, and nanowires [5]. A systematic study of irregular nanostructure formation by femtosecond laser following ablation of a bulk copper sample in air has been reported in Ref. [5]. The evolution of surface nanostructuring with increasing number of laser shots is shown by the scanning electron microscope (SEM) images in Figure 11.3. The typical structures include circular nanopores with a diameter in the range of 40–100 nm, nanoprotrusions with a diameter in the range of 20–70 nm and a length of 20–80 nm, nanocavities of arbitrary form, and nanorims around nanocavities. From Figure 11.3a, one can see that when the incident laser fluence is close to the laser ablation threshold, the spatial variations in deposited laser energy can produce a melt at the localized nanoscale sites even for a single laser shot irradiation. The random distribution of nanoscale dips and protrusions suggests an initial nonuniform laser energy deposition due to enhanced plasmonic absorption by initial surface nanostructural defects present on the real sample. Figure 11.3b shows that a nanopore or nanocavity is immediately accompanied by a nanorim or nanoprotrusion, indicating a nanoscale material relocation to an adjacent site. It is also found in Figure 11.3d that at a larger number of laser shots, the nanostructures still continue to form; however, their density becomes significantly smaller. Studies on nanostructuring of other metals have been also performed for gold [15], titanium [37], and copper, gold, and silver [38].

Hwang et al. have performed a comparative study of femtosecond laser-induced nanostructures on three noble metals (Cu, Ag, and Au) under identical experimental conditions [38]. It was found that the surface nanostructuring directly relates to the competition of two ultrafast processes, electron–phonon coupling and hot electron diffusion, following the femtosecond laser irradiation of the metals. The former plays the dominant role in nanostructuring, while the effects of thermal conductivity and heat capacity are relatively unimportant. Dou et al. have demonstrated that the surface nanostructuring of alloys can involve a change of the surface chemical composition due to preferential ablation of some alloy components [39]. Li et al. have found that femtosecond laser nanostructuring of Al in air increases the thickness of oxide film and the content of alpha crystalline aluminium oxide (αAl_2O_3) [40]. Furthermore, X-ray photoelectron spectroscopy and X-ray diffraction analysis showed the formation of crystalline anorthic

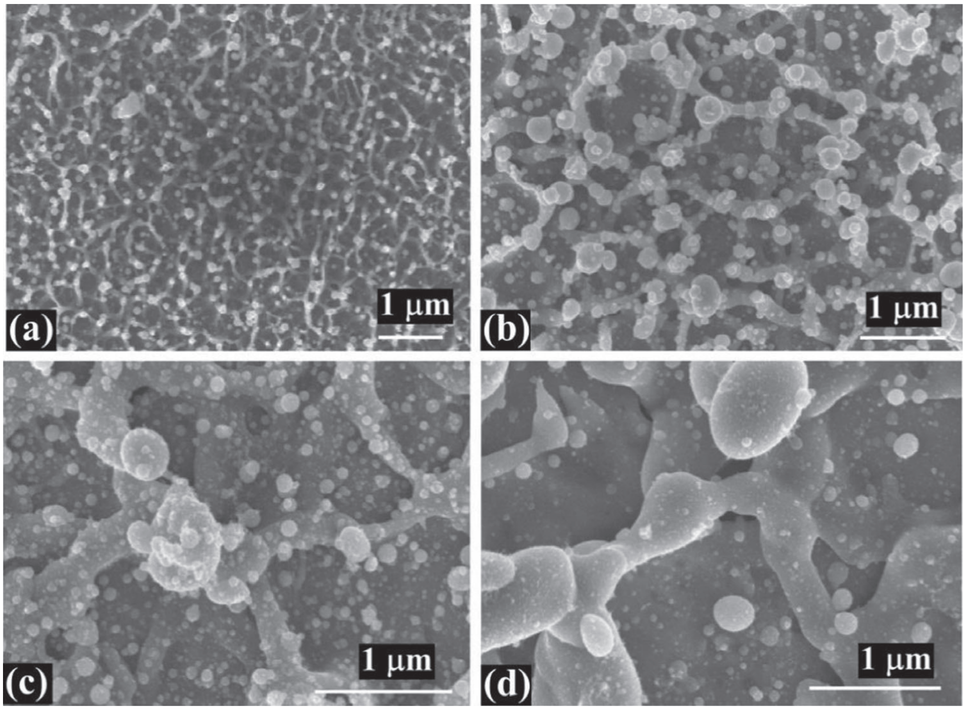

FIGURE 11.3 SEM images of the central part of the irradiated spot on copper following ablation at $F = 1.52\,\text{J cm}^{-2}$ (a) surface after 1 shot featuring only random nanostructures in the form of nanoprotrusions and nanocavities, (b) surface after 2 shots featuring only random nanostructures in the form of spherical nanoprotrusions and nanocavities, (c) surface after 10 shots featuring both nano- and microstructures, (d) surface after 1000 shots showing microstructures being dominating [5].

$Al(OH)_3$. Although most studies on laser nanostructuring were carried out in air, interesting results on nanostructuring were also obtained for ablation in liquids [41,42]. Stratakis et al. have studied surface nanostructures on Al following ablation in liquids (water and ethanol) [41]. The authors found that the surface nanostructures are not produced on an optically polished sample; however, they easily form when the surface is roughened with sandpaper prior to the laser ablation.

The formation of nano- and microstructures is attributed to the following mechanisms [5]: (i) femtosecond laser-induced melt dynamics, (ii) cavitation nanospallation, and (iii) redeposition of ablated species back to the irradiated sample. The first mechanism of nanostructuring occurs due to localized nanoscale melts, where a high radial temperature gradient in a nanomelt induces a radial surface tension gradient (Marangoni force) that expels the liquid to the periphery of the nanomelt [5]. This melt flow leads to the formation of nanocavities, nanoprotrusions, and nanorims due to fast freezing of the expelled liquid as discussed above. This regime of nanostructuring occurs at low laser fluence and a low number of laser shots. With increasing the laser fluence or the number of laser shots, the surface nanomelts grow and then merge in a large melt pool, and the ejection of liquid nanoparticles from the melt pool begins to occur [5]. In this regime, those of liquid nanoparticles that are frozen at a moment of their detachment process will form surface nanoprotrusions of various shapes [5,41]. The second mechanism explains the formation of surface nanostructures by deformation of the spallation layer by cavitation bubbles. The superfast cooling of the surface melt “roughened” by the cavitation bubbles results in surface nanocavities. The third mechanism of the surface structure formation depends on ambient gas pressure. It is known that ablated species are intensively deposited back onto the irradiated sample and form aggregates of nanoparticles when ablation occurs in an ambient gas of atmospheric pressure [8,15,34]. However, the back deposition significantly diminishes when the ambient gas pressure decreases [33]. Although most studies on laser nanostructuring were carried out in air, some promising results were also obtained when sample ablation is performed in liquids [36]. More recently, progresses have been made to control nanostructures and the surface functionalities [43].

11.3.2 Femtosecond Laser-induced 1D Periodic Subwavelength Structures

1D laser-induced periodic surface structures (1D-LIPSS) were first observed on polished germanium single crystal using a focused ruby laser beam by Birnbaum in 1965 [44]. Since then, LIPSS were extensively studied using both relatively long-pulsed and ultrashort-pulsed lasers [4,9–17,44–52]. Usually, the 1D-LIPSS, or termed ripples, emerge as a surface relief composed of (quasi-)periodic lines [4,9–17,44–52]. As a universal phenomenon that occurs on solids upon irradiation of femtosecond laser, the formation of such surface structures is strongly dependent on material properties, laser parameters (wavelength, energy/fluence, dose/scanning speed, angle of incidence, and polarization), and ambient environments [52]. For bulk metal materials, the femtosecond 1D-LIPSS are most often oriented perpendicular to the incident laser beam polarization (for a linearly polarized beam), and they are called the LIPSS-I [52]. However, in some cases, for example, on thin metal films, the femtosecond 1D-LIPSS can be oriented parallel to the laser beam.

The formation of type LIPSS-I has been reported on metals of W, Mo, and Ti, when the femtosecond laser was operated at the repetition rate of 1 kHz with the central wavelength of 800 nm or 400 nm [52–55], and the typical results are shown in Figure 11.4. It was observed that with increasing the laser fluence, the structure period was enlarged. The effect of the number of laser pulses on the LIPSS-I formation was investigated on Pt and TiNi alloys by 800 nm femtosecond laser [17,56], and the decreasing LIPSS periods were seen for a large number of pulses. The influence of surface roughness on the period of LIPSS-I has been observed in Ref. [57,58]. The effects of laser light polarization were studied in Ref. [59,60], where it was found that the LIPSS orientation was perpendicular to the polarization direction for the linearly polarized laser light, while −45° for the left circularly polarized light and +45° for the right circularly polarized light relative to the incident plane. Other laser factors affecting the LIPSS-I generation on metals and alloys have also been studied in the literature [61–65]. Roles of both electron–phonon coupling and electron diffusion in LIPSS-I formation were investigated in Ref. [16,66]. Another approach to control the LIPSS period is using femtosecond laser ablation in liquids, which shows a significant reduction in the structure period as compared with ablation in air. For example, the LIPSS period was observed to be 400–450 nm and 370–390 nm following ablation of Ni/Cu foils in air and distilled water ($\varepsilon_d \approx 1.75$), respectively [67].

Recently, Cruz et.al. compared the LIPSS-I formation with different scanning directions [68]. It was found that the structure regularity can be improved if the scanning direction of the laser beam is perpendicular to its linear polarization. In addition, the LIPSS-I formation was also reported on nickel surface irradiated by radially polarized femtosecond laser beams, which demonstrates that the LIPSS strictly follow the orientation of the local (linear) polarization direction (being perpendicular to it) [69]. Moreover, by using femtosecond laser irradiations operating at the high repetition rate of 600 kHz with the central wavelength of $\lambda = 1030$ nm, Iaroslav et al. have demonstrated the highly regular LIPSS-I on the surfaces of Mo, steel alloy, and Ti materials at a competitive throughput of about 1 cm^2 per 10 s based on a galvoscanner and a translation stage [70], wherein the samples of Ti and Mo consist of 300-nm-thick coatings deposited on glass (quartz) substrates.

The underlying mechanisms for the formation of type LIPSS-I on metals are often explained by interference of the incident laser light with surface electromagnetic waves generated by scattering of the laser light on the surface roughness relief and may involve the excitation of surface plasmon polaritons (SPP) [52], which results in spatially periodic energy distribution on the surface. In particular, this excitation channel is of very importance for femtosecond laser irradiation because initially non-active plasmonic materials can transiently be switched into a state of supporting plasmons [71], which allows a direct excitation of SPPs. For the type of LIPSS-I, when a

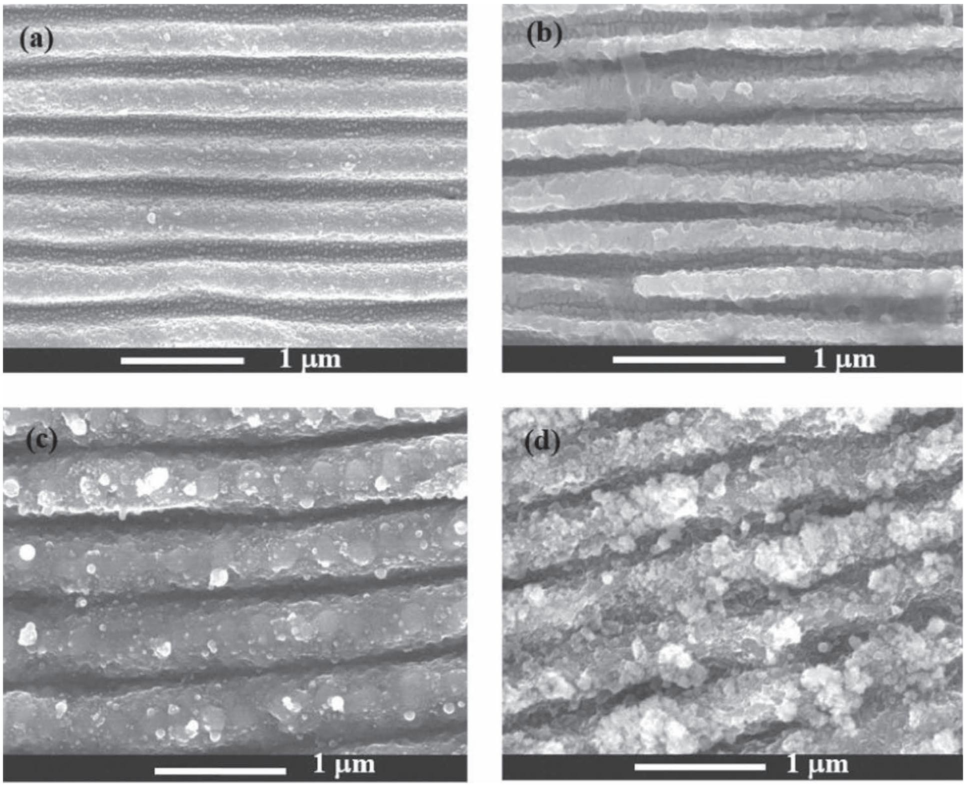

FIGURE 11.4 Formation of LIPSS-I on the surfaces of different bulk metals by the single-beam irradiation of femtosecond laser pulses (800 nm, 1 kHz). (a) Tungsten, (b) molybdenum, (c) copper, (d) aluminium [53].

linearly polarized laser light is incident on the metal surface, the SPP spatial period Λ_{spp} can be given by [72]

$$\Lambda_{\text{spp}} = \lambda/(\eta \pm \sin\theta), \tag{11.1}$$

where θ is the angle of the incident light, $\eta = \text{Re}\left[\varepsilon/(\varepsilon+1)\right]^{1/2}$ is the real part of the effective refractive index of the air–metal interface, and ε is the dielectric constant of the metal. For a small number of laser pulses to make the surface corrugation with shallow depth, the LIPSS period, Λ_{LIPSS}, may coincide with Λ_{spp}. However, optical interference between the laser light and the excited SPP can be imprinted into the surface morphology. The generation of pronounced and well-aligned LIPSS usually takes place after irradiation by multiple laser pulses. During repetitive irradiation, specific spatial frequencies of the surface roughness can have better optical absorption to favour the formation of the LIPSS pattern. Such positive feedback processes can occur during the time duration of a laser pulse and between successive pulses.

Figure 11.5 shows a diagram of the basic physical processes involved in the LIPSS-I formation and its physical evolution on titanium [73]. Usually, the first few laser shots produce sparsely and randomly distributed nanostructures (Figure 11.5b). It is known that surface nanoroughness on a metal surface can couple free-space light to SPPs due to diffraction [74]. Therefore, the next laser pulses couple to SPPs via previously produced nanostructures. The interference between the linearly polarized laser light and SPPs causes a periodic spatial modulation of the energy deposited into the irradiated sample [53,73]. This leads to spatially modulated heating of the surface (after the termination of the femtosecond laser pulse) and formation of the periodic structures. At the initial stage, only small patches of nascent periodic structures are observed in various isolated locations within the irradiated spot. An example of the nascent periodic structure is demonstrated in Figure 11.5c [73]. With the formation of the nascent periodic structures, the coupling of laser light to SPPs begins switching from non-resonant to resonant, which results in much more efficient coupling. In this process, deepening of the grooves provides a positive feedback. With a further increase in the number of laser shots, the nascent periodic structures become sharper, grow, and coalesce into a clear extended LIPSS [4,73]. An example of the clear extended LIPSS-I is demonstrated in Figure 11.5d.

Despite the evident role of self-assembly in the LIPSS process, both uniformity and long-range order of the surface structures usually remain poor. To solve these problems, Lei et al. recently fabricated the extremely uniform subwavelength grating structures on a bulk Fe-based metallic glass ($Fe_{82}Si_{11}C_7$), by employing two femtosecond laser beams with different linear polarizations and certain temporal delays, which is in contrast to the conventional method of the single-beam laser irradiation, and the result are shown in Figure 11.6 [91]. Clearly, the laser-exposed surface is modified into the 1D-LIPSS with the spatial period of 635 nm. There are two striking features in this case: one is the extraordinarily uniform distribution on the whole laser-scanned surface, without disintegrated irregularities such as bending, breaking, and bifurcation; the other is the structure

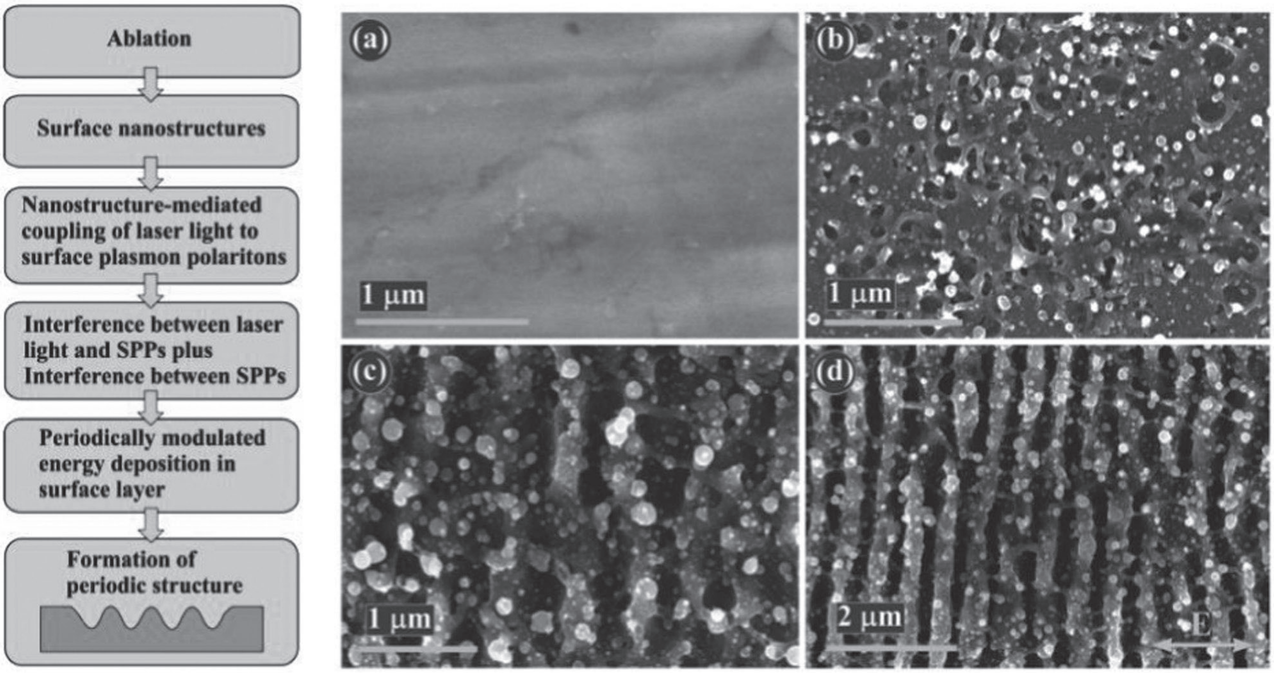
Ablation
Surface nanostructures
Nanostructure-mediated coupling of laser light to surface plasmon polaritons
Interference between laser light and SPPs plus Interference between SPPs
Periodically modulated energy deposition in surface layer
Formation of periodic structure
(a)
1 μm
(b)
1 μm
(c)
1 μm
(d)
2 μm
E

FIGURE 11.5 Mechanisms of the LIPSS formation on metals and an example of LIPSS-I formation on titanium irradiated in air. (a) Sample surface prior to laser treatment. (b–d) Sample surface after the application of 2, 10, and 40 laser shots, respectively [73].

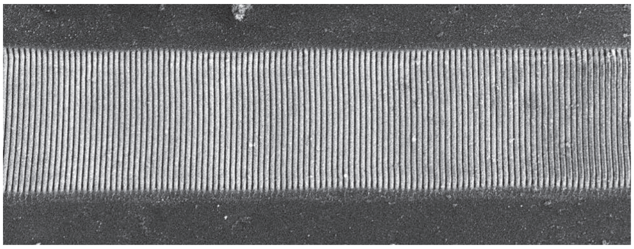

FIGURE 11.6 Fabrication of the uniform subwavelength structures on the surface of Fe-based metallic glass, using two temporally delayed femtosecond laser beams with different linear polarizations [91].

orientation perpendicular to the linear polarization direction of the delayed incident laser beam. Remarkably, through comparing the centre and the lateral edges of the laser-scanned areas, we can find that the structure uniformity can take place across the whole areas of the laser beam spot.

On the other hand, Bonse et al. reported that the semi-periodic 1D surface structures with an orientation parallel to the polarization can be seen in the centre of the irradiated spot [75], when the linearly polarized femtosecond laser pulses (30 fs, 790 nm, 1 kHz) were employed as the light source to focus on the mechanically polished sample pieces of titanium sheet metal (with dimensions of $10 \times 10 \times 1\,\text{mm}^3$) by a spherical dielectric mirror (500 mm focal length). The Fourier transform analysis revealed that the structures have the spatial periods between 65 and 95 nm, much smaller than the incident laser wavelength. Evidently, such kind of surface structures belong to the type LIPSS-II [52]. More interestingly, when the thin metal films were adopted as the sample material, for example, TiO_2 or tungsten films deposited by DC magnetron sputtering onto cleaned glass substrates (the thicknesses of the films used in this study ranged from 50 to 400 nm as confirmed by using optical interferometry), an excellent regularity of metal-oxide nanostructures can be fabricated with the spatial orientation parallel to the direction of the laser polarization [76], as shown in Figure 11.7. During this study, the used laser source was a Yb-doped fibre laser, operating at the repetition rate of 1 MHz with a central wavelength of 1060 nm, and the pulse duration was compressed to 100 fs. The pulses were focused by an objective lens into a spot size of about 12 μm (full-width at half-maximum intensity). Noticeably, the formed 1D grating-like surface structures exhibit the non-ablative features, i.e. the laser-induced structures exhibit the spatially periodic arrangement of the bumpy lines above the initial surface, instead of the commonly ablated pit of lines below the initial surface.

The formation process of the aforementioned surface structures can be explained in three steps, which is depicted in Figure 11.8. (i) The laser beam, with a peak intensity close to the ablation threshold for titanium, is focused on a titanium surface, where it is scattered by an existing nanostructures or any surface defects. Interference of the scattered and incident fields leads to the intensity variations in the immediate neighbourhood of the scattering point. (ii) At points where the threshold intensity for ablation is exceeded, titanium reacts rapidly with O_2 from the air, forming titanium dioxide (TiO_2). The use of ultrashort pulses is necessary to ensure this process occurs faster than heat diffusion, as this can smear out the nanometre-scale localization of the deposited laser energy. The first two steps constitute a positive feedback loop (Figure 11.8a) [76]. As the nanostructure grows, so does its

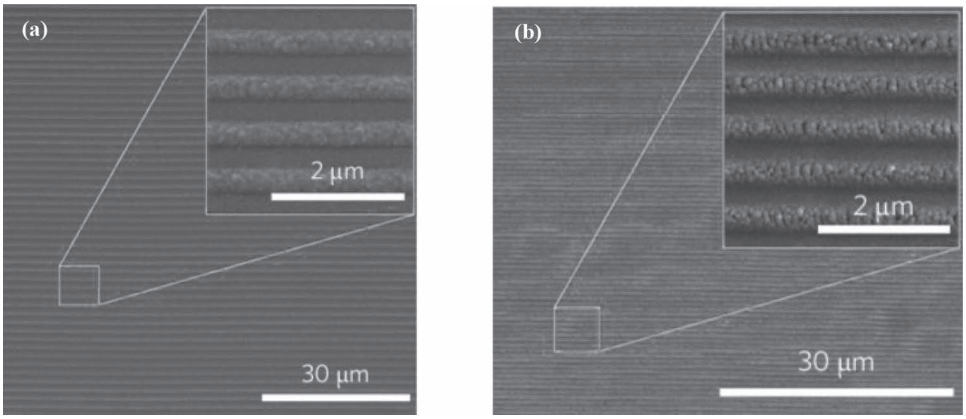

FIGURE 11.7 Formation of type LIPSS-II on two different thin metal films by incident femtosecond laser pulses with the central wavelength of 1060 nm at the repetition rate of 1 MHz. (a) TiO_2. (b) Tungsten [76].

scattering power. (iii) The growth mechanism also has an imbedded negative feedback loop. As TiO_2 grows on top of the titanium, penetration of O_2 through the oxide layer decreases exponentially, decelerating and eventually halting the growth process (Figure 11.8b).

11.3.3 Femtosecond Laser-Induced 2D Periodic Subwavelength Structures

By applying two-colour femtosecond laser pulses after the frequency doubling of Ti:sapphire femtosecond laser (800 nm, 50 fs, 1 kHz) via a beta barium borate (BBO) crystal, which includes two beams (with the central wavelengths of 800 and 400 nm, respectively) propagating in a spatial collinear way and then focused by the same objective lens (4×, N.A = 0.1), J. Cong et al. have successfully produced 2D periodic matrix of nanodot structures on bulk molybdenum (Mo) surfaces in a single-step process [77]. A typical result is shown in Figure 11.9a. It was found that the structural alignment in two dimensions can be effectively tuned via changing of the laser polarization. In particular, their experimental results demonstrated that the structure periods can be varied with different temporal delays of the two laser beams, as shown in Figure 11.9b, which indicates the formation of dot-matrix

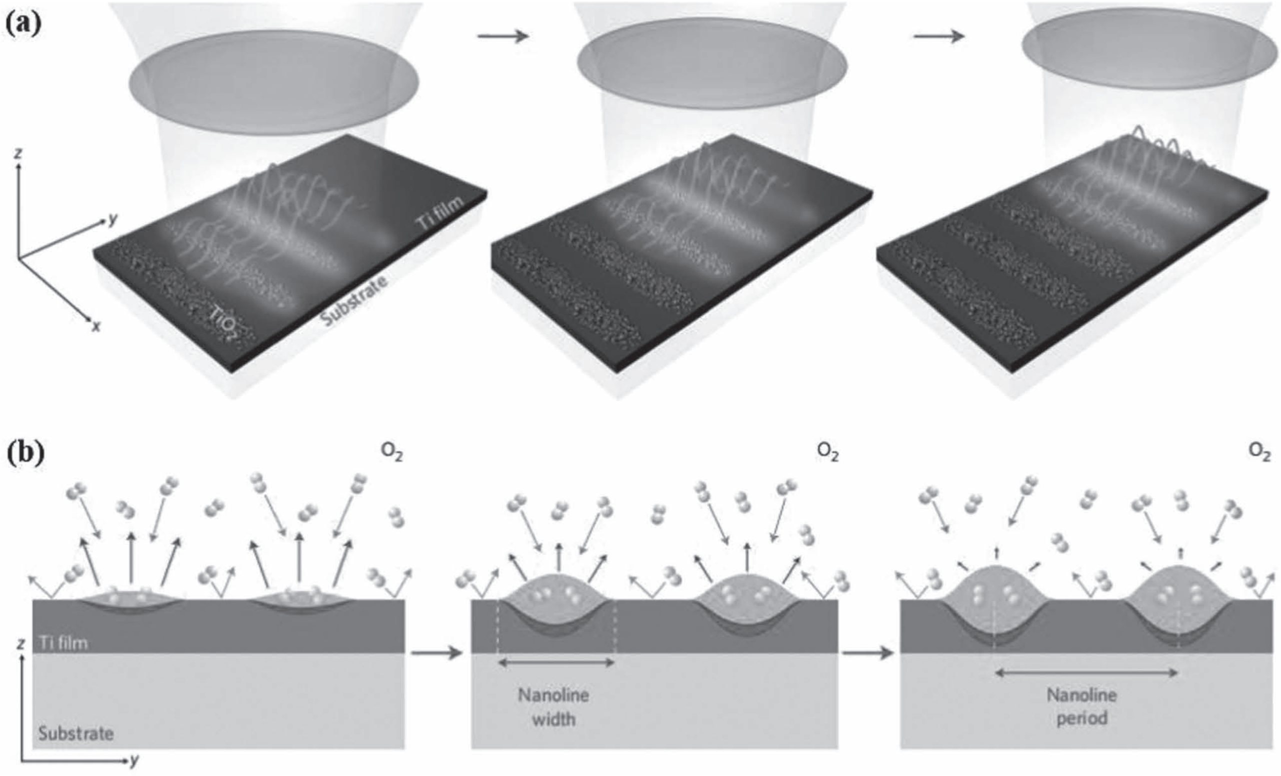

FIGURE 11.8 (a) Schematic of the nanostructure formation process as a laser beam is scanned over the surface. (b) Schematic showing a cross-sectional view of the surface, depicting the deceleration of the growth process due to negative feedback [76].

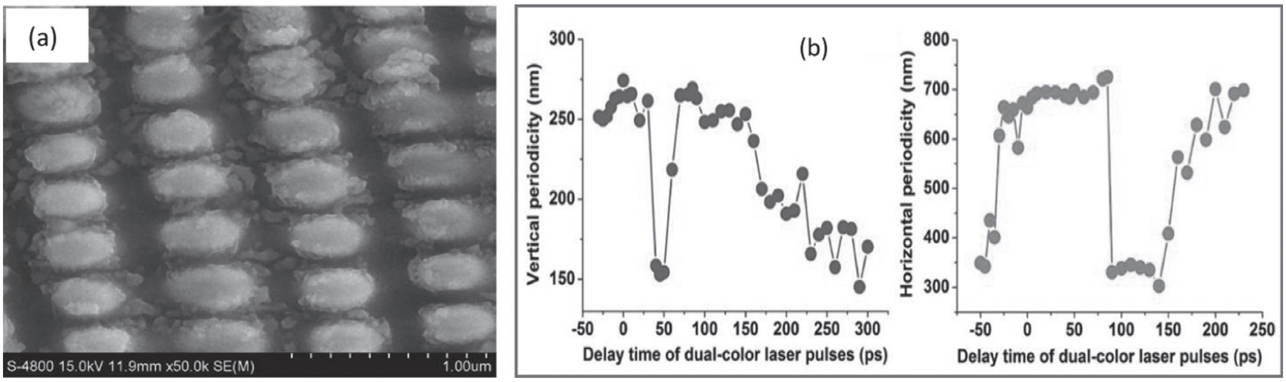

FIGURE 11.9 (a) SEM images of 2D subwavelength dot-matrix structures on Mo surfaces upon irradiation of two-colour femtosecond laser beams propagated in a collinear way. (b) Measured variations of the structure period in two dimensions as a function of the time delay between two-colour laser beams [77].

structures is physically based on the transient correlation of the dual laser–matter interactions through modifying their ultrafast surface dynamics, rather than a simple overlapping of two orthogonal LIPSS that are individually obtained from two-colour laser beams. Moreover, with the help of the transient correlated actions, the dot-matrix structures can be transformed into different types, even with a great reduction of the periods by half at certain time delays.

In order to improve the efficiency of producing 2D periodic subwavelength surface structures, Qiao et al. have proposed a method to directly fabricate the metallic photonic crystal-like (MPC) structures on the surfaces of hard material of tungsten [78], through the cylindrical focusing of two femtosecond laser beams. In this case, the two laser beams were obtained by using a birefringent crystal of YVO4 (1.26 mm thickness) to make the incident laser beam split into two parts with the temporal delay of 1.2 ps and orthogonal linear polarizations. The focusing optics was a fused silica-based plano-convex cylindrical lens with a focal length of $f = 50$ mm, resulting in a line-shaped focal spot with a length of approximately 4.5 mm. Figure 11.10 shows a schematic diagram of the experimental set-up. The microscopic examination of the surface morphology suggested the formation of regular 2D arrays of truncated cone-like bumps with a diameter of 320 nm, a depth of 150 nm, and a spatial period of approximately 560 nm. It was also observed that the structural characteristics and homogeneity can be engineered by varying the laser parameters such as the ratio of pulse energy, the scanning speed, and the directions of the laser polarization. In addition, their further experiments also revealed that such 2D surface structures began to disappear when the time delay of double laser pulses increased up to several hundred picoseconds, which confirms the physical contributions of the two laser-induced transient temperature gratings. More recently, Jalil et al. have also reported the formation of uniform 2D subwavelength structures using temporally delayed triple femtosecond laser beams [79], wherein the period of the subwavelength structures can be controlled by only changing the time delay of femtosecond laser pulses.

More interestingly, in the above experimental configuration, if the incident laser energy before the birefringent crystal was reduced, the generation of 2D periodic surface structures began to change in geometry, resulting in evident triangular-shaped structures [80,81], as shown in Figure 11.11. The detailed inspections revealed that the triangular structure units are spatially interlocked by three ablated grooves, or the 2D periodic triangular structure arrays are developed by the spatial crossing of three 1D-LIPSS with several different orientations, wherein each group of 1D-LIPSS has the spatial period of about 610 nm. Three side lengths of the structure unit were measured almost equivalent to about 480 nm. From another viewpoint, we can consider that the spatial arrangements of the surface structures constitute the hexagonal patterns, each of which is composed of six adjacent triangular units. The width of each groove was measured 130 nm. The modulation depth of the subwavelength

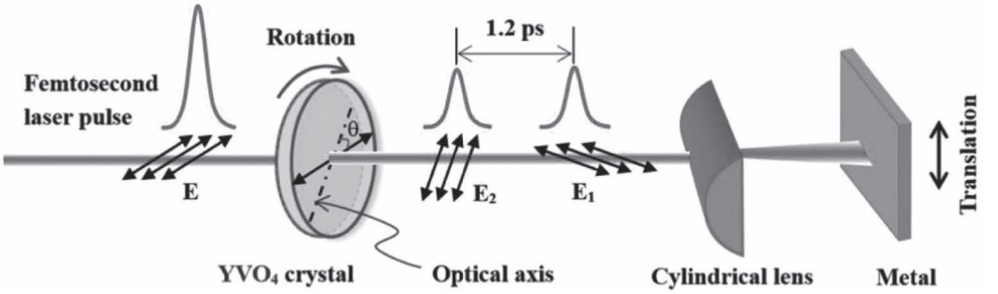

FIGURE 11.10 Schematic of the experimental set-up for direct fabricating large-area 2D structures on tungsten surface by two cross-polarization femtosecond lasers. The double arrows represent the directions of the linear polarization of femtosecond lasers, and θ for the azimuth angle of the birefringent crystal with respect to the incident laser polarization [78].

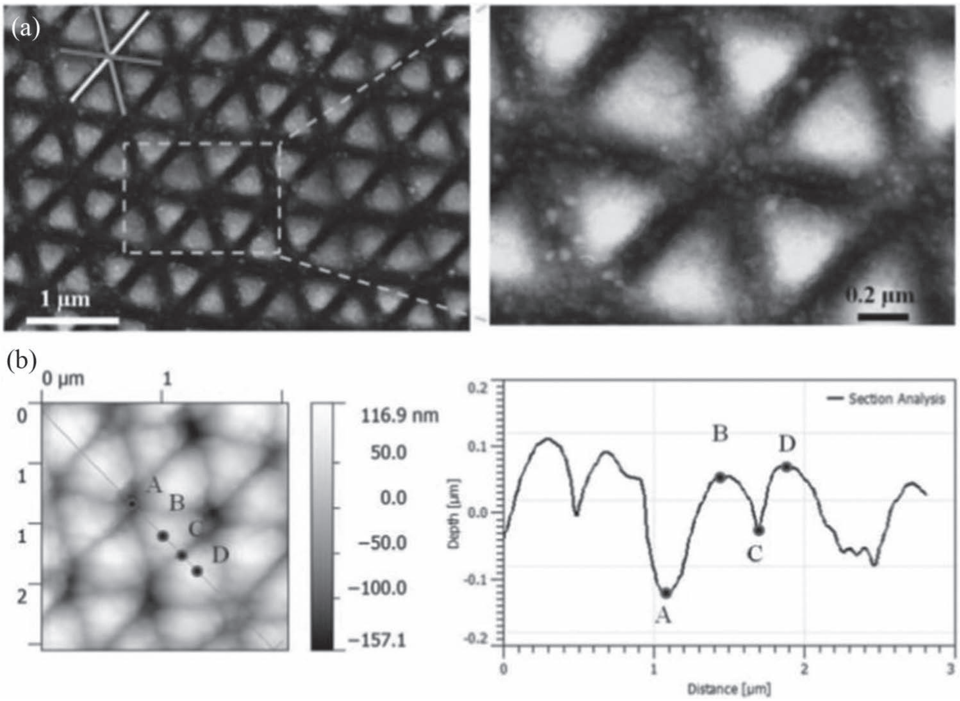

FIGURE 11.11 (a) SEM images of 2D periodic subwavelength triangular structures on tungsten surfaces induced by two collinear propagating time-delayed femtosecond laser beams with orthogonal polarizations. (b) Atomic force microscopic measurement of the triangular surface structures, where A, B, C, and D represent different positions on the structured surface [80].

triangular structures is approximately 100 nm. Such kind of 2D triangular structure arrays have also been reported on the bulk material surface of cobalt [82]. More importantly, they control the geometry and organization of the formed structures demonstrating spherical, triangular, rhombic, and high spatial frequency LIPSS using two temporally delayed orthogonally polarized femtosecond laser beams. Recently, Romano et al. reported the formation of the subwavelength triangular structures on the steel surfaces with irradiation of circularly polarized femtosecond laser pulses [83]. Similarly, Fraggelakia et al. also observed the triangular and square structures on the stainless steel surfaces [84], through employing double time-delayed femtosecond lasers with crossed either linear polarization or circular polarization.

Furthermore, based on the configuration of two time-delayed femtosecond laser beams, Qin et al., have recently introduced the one-step maskless method to fabricate the groove–particle composite subwavelength periodic structures on a single-crystal Cu surface [85], by using the linearly polarized femtosecond laser at the central wavelength of 400 nm after pre-irradiation with a circularly polarized infrared femtosecond laser at the central wavelength of 800 nm. The achieved composite surface structures, as shown in Figure 11.12, consist of nanoscale-spaced ablative 1D-LIPSS and the nanoparticle chains distributed in the groove valleys. The available groove period is about 275 nm, much smaller than the incident laser wavelength of 400 nm. The measured particle diameter and the groove width approximate 111 and 95 nm, respectively. The average particle spacing is about 181 nm. With increasing the energy fluence of the infrared laser pulse, both the groove width and particle diameter were observed to reduce, while the measured spacing-to-diameter ratio of the nanoparticles tended to present an increasing tendency. A physical scenario is proposed to elucidate the underlying mechanisms [85]: as the infrared femtosecond laser pulse pre-irradiates the target, the copper surface is triggered to display anomalous transient physical properties, on which the subsequently incident Gaussian blue laser pulse is spatially modulated into

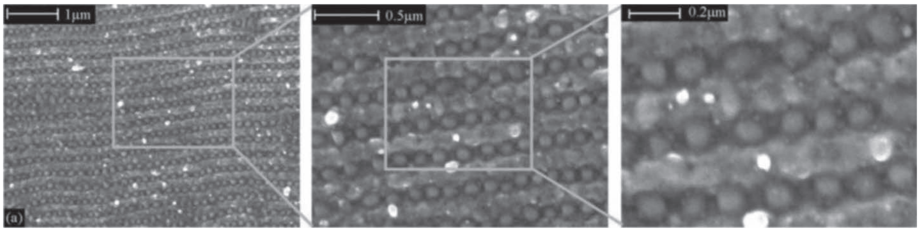

FIGURE 11.12 A typical result of generating groove–particle composite periodic structures on the bulk copper surfaces with linearly polarized 400 nm femtosecond laser after 28 ps time delay irradiation of the circularly polarized 800 nm infrared femtosecond laser [85].

fringe-like energy depositions via the excitation of ultrafast surface plasmons. During the following relaxation processes, the periodically heated thin-layer regions can be transferred into the metastable liquid rivulets, and then, they break up into nanodroplet arrays owing to the modified Rayleigh-like instability.

11.4 Conclusion

In this chapter, we reviewed the current state of direct femtosecond laser nano-/microstructuring on metal surfaces, which emerges recently as a new research area in laser–material interactions [4]. Through varying the laser parameters, such as the energy, the wavelength, the repetition rate, and utilizing double-pulsed beams, the induced periodic surface structures can be controlled in many aspects, including the transition from 1D to 2D dimensions, spatial alignment, distribution uniformity, structure accuracy, and the geometric profiles. This technique also demonstrates a substantial degree of non-linear physical effects occurring in the femtosecond laser nano-/microstructuring, for example, in the triangular structure formation process. Moreover, it has been found that different metals and different forms, such as bulk or thin films, can yield different results. Some future studies in this area include further understanding of the structural formation mechanisms, controlling ultrafast dynamics for modifying structure fabrications, and utilizing temporally and spatially shaping femtosecond pulses for processing. Surface nano-/microstructuring on metals can functionalize the surfaces and renders them with dramatically altered optical, thermal, and wetting properties [4,15,86–90], which can find a wide range of applications in photonics, plasmonics, optoelectronics, solar energy absorbers, thermophotovoltaics, microfluidics, cooling, and biomedicine.

REFERENCES

1. Tennant D. M. 1998 *Nanotechnology* (G. Timp Springer Verlag, Berlin).
2. Pronko P. P., Dutta S. K., Squier J., Rudd J. V., Du D. and Mourou G. 1995 Machining of submicron holes using a femtosecond laser at 800-nm *Opt. Commun.* **114** 106–110.
3. Korte F., Serbin J., Koch J., Egbert A., Fallnich C., Ostendorf A. and Chichkov B. N. 2003 Towards nanostructuring with femtosecond laser pulses *Appl. Phys. A* **77** 229–235.
4. Vorobyev A. and Guo C. 2013 Direct femtosecond laser surface nano/microstructuring and its applications *Laser Photon. Rev.* **7** 385–407.
5. Vorobyev A. Y. and Guo C. 2006 Femtosecond laser nanostructuring of metals *Opt. Express* **14** 2164–2169.
6. Nolte S., Chichkov B. N., Welling H., Shani Y., Liebermann K. and Terkel H. 1999 Nanostructuring with spatially localized femtosecond laser pulses *Opt. Lett.* **24** 914–916.
7. Wu C., Crouch C. H., Zhao L., Carey J. E., Younkin R., Levinson J. A., Mazur E., Farrell R. M., Gothoskar P. and Karger A. 2001 Near-unity below-band-gap absorption by microstructured silicon *Appl. Phys. Lett.* **78** 1850–1852.
8. Pereira A., Cros A., Delaporte P., Georgiou S., Manousaki A., Marine W. and Sentis M. 2004 Surface nanostructuring of metals by laser irradiation: effects of pulse duration, wavelength and gas atmosphere *Appl. Phys. A* **79** 1433–1437.
9. Borowiec A. and Haugen H. K. 2003 Subwavelength ripple formation on the surfaces of compound semiconductors irradiated with femtosecond laser pulses *Appl. Phys. Lett.* **82** 4462–4464.
10. Costache F., Kouteva Arguirova S. and Reif J. 2004 Sub–damage–threshold femtosecond laser ablation from crystalline Si: Surface nanostructures and phase transformation *Appl. Phys. A* **79** 1429–1432.
11. Bonse J., Munz M. and Sturm H. 2005 Structure formation on the surface of indium phosphide irradiated by femtosecond laser pulses *J. Appl. Phys.* **97** 013538.
12. Vorobyev A. Y. and Guo C. 2011 Direct creation of black silicon using femtosecond laser pulses *Appl. Surf. Sci.* **257**(16) 7291–7294.
13. Hnatovsky C., Taylor J. R., Rajeev P. P., Simova E., Bhardwaj V. R., Rayner D. M. and Corkum P. B. 2005 Pulse duration dependence of femtosecond-laser-fabricated nanogratings in fused silica *Appl. Phys. Lett.* **87** 14104–14106.
14. Reif J., Costache F., Eckert S. and Henyk M. 2004 Ripples revisited - non-classical morphology at the bottom of femtosecond laser ablation craters in transparent dielectrics *Appl. Phys. A* **79** 1229.
15. Vorobyev A. Y. and Guo C. 2005 Enhanced absorptance of gold following multi-pulse femtosecond laser ablation *Phys. Rev. B* **72** 195422.
16. Wang J. and Guo C. 2005 Ultrafast dynamics of femtosecond laser-induced periodic surface pattern formation on metals *Appl. Phys. Lett.* **87** 251914.
17. Yang Y., Yang J. J., Liang C. Y., Wang H. S., Zhu X. N., Kuang D. F. and Yang Y. 2008 Sub-wavelength surface structuring of NiTi alloy by femtosecond laser pulses *Appl. Phys. A* **92** 635.
18. Nilson R. H., Tchikanda S. W., Griffiths S. K. and Martinez M. J. 2006 Steady evaporating flow in rectangular microchannels *Int. J. Heat Mass Transfer* **49** 1603–1618.
19. Zorba V., Persano L., Pisignano D., Athanassiou A., Stratakis E., Cingolani R., Tzanetakis P. and Fotakis C. 2006 Making silicon hydrophobic: Wettability control by two-lengthscale simultaneous patterning with femtosecond laser irradiation *Nanotechnology* **17** 3234–3238.
20. Baldacchini T., Carey J. E., Zhou M. and Mazur E. 2006 Superhydrophobic surfaces prepared by microstructuring of silicon using a femtosecond laser *Langmuir*, **22** 4917–4919.
21. Zhigilei L. V., Lin Z., and Ivanov D. S. 2009 Atomistic modeling of short pulse laser ablation of metals: Connections between melting, spallation, and phase explosion *J. Phys. Chem. C* 113, 11892.
22. Yang J., Zhao Y. and Zhu X. 2006 Transition between non-thermal and thermal ablation of metallic targets under the strike of high-fluence ultrashort laser pulses *Appl. Phy. Lett.* **88** 094101.
23. Rethfeld B., Kaiser A., Vicanek M. and Simon G. 2002 Ultrafast dynamics of nonequilibrium electrons in metals under femtosecond laser irradiation *Phy. Rev. B* **65** 214303.

24. Fujimoto J. G., Liu J. M., Ippen E. P. and Bloembergen N. 1984 Femtosecond laser interaction with metallic tungsten and nonequilibrium electron and lattice temperatures *Phys. Rev. Lett.* 53, 1837.
25. Eesley G. L. 1983 Observation of nonequilibrium electron heating in copper *Phys. Rev. Lett.* **51** 2140–2143.
26. Elsayedali H. E., Norris T. B., Pessot M. A. and Mourou G. A. 1987 Time-resolved observation of electron-phonon relaxation in copper *Phys. Rev. Lett.* **58** 1212–1215.
27. Anisimov S. I., Kapeliovich B. L. and Perel'man T. L. 1974 Electron emission from metal surfaces exposed to ultrashort laser pulses *Sov. Phys. JETP* **39** 375–377.
28. Oguri K., Okano Y., Nishikawa T. and Nakano H. 2009 Dynamics of femtosecond laser ablation studied with time-resolved x-ray absorption fine structure imaging *Phys. Rev. B* **79**, 144106.
29. Glover T. E., Ackerman G. D., Lee R. W., Padmore H. A. and Young D. A. 2004 Metal–insulator transitions in an expanding metallic fluid: Particle formation during femtosecond laser ablation *Chem. Phys.* **299** 171–181.
30. Zavestovskaya I. N., Kanavin A. P. and Men'kova N. A. 2008 Crystallization of metals under conditions of superfast cooling when materials are processed with ultrashort laser pulses *J. Opt. Technol.* **75** 353–358.
31. Vorobyev A. Y. and Guo C. 2006 Enhanced energy coupling in femtosecond laser-metal interactions at high intensities *Opt. Express* **14**, 13113.
32. Amoruso S., Bruzzese R., Wang X. and Xia J. 2008 Propagation of a femtosecond pulsed laser ablation plume into a background atmosphere *Appl. Phys. Lett.* 92 041503.
33. Vorobyev A. Y. and Guo C. 2007 Shot-to-shot correlation of residual energy and optical absorptance in femtosecond laser ablation *Appl. Phys. A* **86** 235–241
34. Pereira A., Delaporte P., Sentis M., Marine W., Thomann A. L. and Boulmer-Leborgne C. 2005 *J. Appl. Phys.* 98, 064902.
35. Das S. K., Dasari K., Rosenfeld A. and Grunwald R. 2010 Extended-area nanostructuring of TiO_2 with femtosecond laser pulses at 400 nm using a line focus *Nanotechnology* **21** 155302.
36. Stratakis E., Zorba V., Barberoglou M., Fotakis C. and Shafeev G. 2009 Laser writing of nanostructures on bulk Al via its ablation in liquids *Nanotechnology* **20** 105303.
37. Vorobyev A. Y. and Guo C. 2007 Femtosecond laser structuring of titanium implants, *Appl. Surf. Sci.* **253** 7272–7280.
38. Hwang T. Y., Vorobyev A. Y. and Guo C. 2009 Ultrafast dynamics of femtosecond laser-induced nanostructure formation on metals *Appl. Phys. Lett.* **95** 123111.
39. Dou K., Knobbe E. T. and Parkhill R. L. 2003 Femtosecond study of surface structure and composition and time-resolved spectroscopy in metals *Appl. Phys. A.* **76** 303–307.
40. Li X., Yuan C., Yang H., Li J., Huang W., Tang D. and Xu Q. 2010 Morphology and composition on Al surface irradiated by femtosecond laser pulses *Appl. Surf. Sci.* **256** 4344–4349.
41. Stratakis E., Zorba V., Barberoglou M., Fotakis C. and Shafeev G. 2009 Laser writing of nanostructures on bulk Al via its ablation in liquids *Nanotechnology* **20** 105303.
42. Barmina E. V., Barberoglu M., Zorba V., Simakin A. V., Stratakis E., Fotakis C. and Shafeev G. A. 2009 Surface nanotexturing of tantalum by laser ablation in *water Quantum Electron.* **39** 89–93.
43. Jalil S. A., Lai B., ElKabbash M., Zhang J., Singh S. C. and Guo C. 2020 Spectral absorption control of femtosecond laser-treated metals and application in solar-thermal devices *Light Sci. & Appl.* **9**:14.
44. Birnbaum M. 1965 Semiconductor surface damage produced by ruby lasers *J. Appl. Phys.* **36** 3688–3689.
45. Guosheng Z., Fauchet P. M. and Siegman A. E. 1982 Growth of spontaneous periodic surface structures on solids during laser illumination *Phys. Rev. B* **26**, 5366.
46. Sipe J. E., Young J. F., Preston J. S. and van Driel H. M. 1983 Laser-induced periodic surface structure. I. Theory *Phys. Rev. B* **27**, 1141.
47. Clark S. E. and Emmony D. C. 1989 Ultraviolet-laser-induced periodic surface structures *Phys. Rev. B* **40**, 2031.
48. Bonse J., Baudach S., Krüger J., Kautek W. and Lenzner M. 2002 Femtosecond laser ablation of silicon–modification thresholds and morphology *Appl. Phys. A: Mater. Sci. Process.* **74**, 19–25.
49. Shimotsuma Y., Kazansky P. G., Qiu J. and Hirao K. 2003 Self-organized nanogratings in glass irradiated by ultrashort light pulses *Phys. Rev. Lett.* **91**, 247405.
50. Jia T. Q., Chen H. X., Huang M., Zhao F. L., Qiu J. R., Li R. X., Xu Z. Z., He X. K., Zhang J. and Kuroda H. 2005 Formation of nanogratings on the surface of a ZnSe crystal irradiated by femtosecond laser pulses *Phys. Rev. B* **72**, 125429.
51. Buividas R., Mikutis M. and Juodkazis S. 2014 Surface and bulk structuring of materials by ripples with long and short laser pulses: Recent advances. *Prog. Quantum Electron. **38*** 119–156.
52. Bonse J., Höhm S., Kirner S. V., Rosenfeld A., Krüger J. 2017 Laser-induced periodic surface structures—A scientific evergreen. *IEEE J. Sel. Top. Quantum Electron.* 23:3.
53. Xue L., Yang J., Yang Y., Wang Y. and Zhu X. 2012 Creation of periodic subwavelength ripples on tungsten surface by ultrashort laser pulses *Appl. Phys. A* **109** 357–365.
54. Hashida M., Ikuta Y., Miyasaka Y., Tokita S. and Sakabe S. 2019 Simple formula for the interspaces of periodic grating structure self-organized on metal surfaces by femtosecond laser ablation *Appl. Phys. Lett.* **102** 174106.
55. Okamuro K., Hashida M., Miyasaka Y., Ikuta Y., Tokita S. and Sakabe S. 2010 Laser flfluence dependence of periodic grating structures formed on metal surfaces under femtosecond laser pulse irradiation *Phys. Rev. B* **82** 165417.
56. Vorobyev A. Y. and Guo C. 2007 Effects of nanostructure-covered femtosecond laser-induced periodic surface structures on optical absorptance of metals *Appl. Phys. A* **86** 321–324.
57. Tomita T., Kinoshita K., Matsuo S. and Hashimoto S. 2007 Effect of surface roughening on femtosecond laser-induced ripple structures. *Appl. Phy. Lett.* **90** 153115.
58. Yang Y., Yang J., Xue L. and Guo Y. 2010 Surface patterning on periodicity of femtosecond laser-induced ripples *App. Phys. Lett.* **97** 141101.
59. Wang J. and Guo C. 2006 Permanent recording of light helicity on optically inactive metal surfaces *Opt. Lett.* **31** 3641.
60. Tang Y., Yang J., Zhao B., Wang M. and Zhu X. 2012 Control of periodic ripples growth on metals by femtosecond laser ellipticity *Opt. Express* **20** 25826–25833.

61. Zhao Q. Z., Malzer S. and Wang L. J. 2007 Self-organized tungsten nanospikes grown on subwavelength ripples induced by femtosecond laser pulses *Opt. Express* **15** 15741–15746.
62. Li Z., Li P., Fan J., Fang R. and Zhang D. 2010 Energy accumulation effect and parameter optimization for fabricating of high-uniform and large-area period surface structures induced by femtosecond pulsed laser *Opt. Lasers Eng.* **48** 64–68.
63. Golosov E. V., Emel'yanov V. I., Ionin A. A., Kolobov Yu. R., Kudryashov S. I., Ligachev A. E., Novoselov Yu. N., Seleznev L. V. and Sinitsyn D. V. 2009 Femtosecond laser writing of subwave one-dimensional quasiperiodic nanostructures on a titanium surface *JETP Lett.* **90** 107–110.
64. Vorobyev A. Y. and Guo C. 2008 Femtosecond laser-induced periodic surface structure formation on tungsten *J. Appl. Phys.* **104** 063523.
65. Hwang T. Y. and Guo C. 2010 Angular effects of nanostructure-covered femtosecond laser induced periodic surface structures on metals *J. Appl. Phys.* **108** 073523.
66. Colombier J. P., Garrelie F., Faure N., Reynaud S., Bounhalli M., Audouard E., Stoian R. and Pigeon F. 2012 Effects of electron-phonon coupling and electron diffusion on ripples growth on ultrafast-laser-irradiated metals *J. Appl. Phys.* **111** 024902.
67. Korolkov V. P., Ionin A. A., Kudryashov S. I., Seleznev L. V., Sinitsyn D. V., Samsonov R. V., Masliy A. I., Medvedev A. Zh. and Goldenberg B. G. 2011 Surface nanostructuring of Ni/Cu foilsby femtosecond laser pulses *Quantum Electron.* **41** 387–392.
68. Ruiz de la Cruz A., Lahoz R., Siegel J., de la Fuente G. F. and Solis J. 2014 High speed inscription of uniform, large-area laser-induced periodic surface structures in Cr films using a high repetition rate fs-laser *Opt. Lett.* **39** 2491.
69. Tsibidis G., Skoulas E. and Stratakis E. 2015 Ripple formation on nickel irradiated with radially polarized femtosecond beams *Opt. Lett.* **40** 5172.
70. Gnilitskyi I., Derrien T., Levy Y., Bulgakova N., Mocek T. and Orazi L. 2017 High-speed manufacturing of highly regular femtosecond laser-induced periodic surface structures: Physical origin of regularity *Sci. Rep.* **7** 8485.
71. Bevillon E., Colombier J. P., Recoules V., Zhang H., Li C. and Stoian R. 2016 Ultrafast switching of surface plasmonic conditions in nonplasmonic metals *Phys. Rev. B* **93** 165416.
72. Bonch-Bruevich A. M., Libenson M. N., Makin V. S. and Trubaev V. V. 1992 Surface electromagnetic waves in optics *Opt. Eng.* **31** 718–730.
73. Vorobyev A. Y., Makin V. S. and Guo C. 2007 Periodic ordering of random surface nanostructures induced by femtosecond laser pulses on metals *J. Appl. Phys.* **101** 034903.
74. Zayats A. V. and Smolyaninov I. I. 2003 Near-field photonics: Surface plasmon polaritons and localized surface plasmons *J. Opt. A* **5** S16–S50.
75. Bonse J., Kruger J., Hohm S. and Rosenfeld A. 2012 Femtosecond laser-induced periodic surface structures *J. Laser Appl.* **24** 042006.
76. Öktem B. O., Pavlov I., Ilday S., Kalaycıoglu H., Rybak A., Yavas S., Erdogan M. and Ilday F. 2013 Nonlinear laser lithography for indefinitely large-area nanostructuring with femtosecond pulses *Nat. Photonics* **7** 897–901.
77. Cong J., Yang J., Zhao B. and Xu X. 2015 Fabricating subwavelength dot-matrix surface structures of Molybdenum by transient correlated actions of two-color femtosecond laser beams *Opt. Express* **23** 5357–5367.
78. Qiao H., Yang J., Wang F., Yang Y. and Sun J. 2015 Femtosecond laser direct writing of large-area two-dimensional metallic photonic crystal structures on tungsten surfaces *Opt. Express* **23** 26617–26627.
79. Jalil S., Yang J., Elkabbash M., Lei Y., He W. and Guo C. 2019 Formation of uniform two-dimensional subwavelength structures by delayed triple femtosecond laser pulse irradiation", *Opt. Lett.* **44** 2278.
80. Qiao H., Yang J., Li J., Liu Q., Liu J. and Guo C. 2018 Formation of subwavelength periodic triangular arrays on tungsten through double-pulsed femtosecond laser irradiation *Materials* **11** 2380.
81. Liu Q., Zhang N., Yang J., Qiao H. and Guo C. 2018 Direct fabricating large-area nanotriangle structure arrays on tungsten surface by nonlinear lithography of two femtosecond laser beams *Opt. Express* **26** 11718–11727.
82. Jalil S., Yang J., Elkabbash M., Cong C. and Guo C. 2019 Formation of controllable 1D and 2D periodic surface structures on cobalt by femtosecond double pulse laser irradiation *Appl. Phys. Lett.* **115** 031601.
83. Romano J. M., Garcia-Giron A., Penchev P. and Dimov S. 2018 Triangular laser-induced submicron textures for functionalising stainless steel surfaces *Appl. Surf. Sci.* **440** 162–169.
84. Fraggelakisa F., Mincuzzia G., Lopez J., Manek-Hönninger I. and Kling R. 2019 Controlling 2D laser nano structuring over large area with double femtosecond pulses *Appl. Surf. Sci.* **470** 677–686.
85. Qin W. and Yang J. 2017 Controlled assembly of high-order nanoarray metal structures on bulk copper surface by femtosecond laser pulses *Surf. Sci.* **661** 28–33.
86. Vorobyev A. Y. and Guo C. 2008 Colorizing metals with femtosecond laser pulses, *Appl. Phys. Lett.* **92** 041914.
87. Vorobyev A. Y. and Guo C. 2009 Metal pumps liquid uphill, *Appl. Phys. Lett.* **94** 24102.
88. Fadeeva E., Schlie S., Koch J., Chichkov B. N., Vorobyev A. Y. and Guo C. 2009 Femtosecond laser-induced surface structures on platinum and their effects on surface wettability and fibroblast cell prolifereation. In *Contact Angle, Wettability and Adhesion*, edited by K. L. Mittal (VSP/Brill, Leiden), Vol. 6, pp. 163–171.
89. Kietzig A. M., Hatzikiriakos S. G. and Englezos P. 2009 Patterned superhydrophobic metallic surfaces, *Langmuir* **25** 4821.
90. Vorobyev A. Y. and Guo C., 2015,Multifunctional surfaces produced by femtosecond laser pulses *J. App. Phys.* **117** 033103.
91. Lei Y., Yang J., Cong C., and Guo C. 2020 Fabrication of homogenous subwavelength grating structures on metallic glass using double-pulsed femtosecond lasers, *Opt. & Lasers in Eng.*, 134, 106273.

12

Laser Ablation in Liquids for Nanoparticle Generation and Modification

Subhash C. Singh and Chunlei Guo

CONTENTS

12.1 Introduction 137
12.2 Background of LP-PLA of a Solid Target at the Solid–Liquid Interface 138
  12.2.1 Nucleation and Growth of NPs from Laser-produced Plasmas Confined in Liquid 138
    12.2.1.1 Early Stage 138
    12.2.1.2 Intermediate Stage 138
    12.2.1.3 Later Stage 139
12.3 Effects of Different Experimental Parameters on the Dynamics of Laser Ablation 139
12.4 Cavitation Bubble Formation and Related Effects 141
12.5 Non-reactive LP-PLA of Solids for the Generation of Elemental Nanoparticles 142
12.6 Reactive Pulsed Laser Ablation for the Generation of Metal Compound Nanoparticles 142
12.7 Laser Ablation of Suspended Particles in Liquids 144
12.8 Conclusions 146
References 146

12.1 Introduction

Nanoparticles (NPs @) are playing an increasingly important role in emerging sectors such as photonics, energy, medicine, and biotechnology [1–5]. These materials have an enhanced surface activity due to their larger surface-to-volume ratios and a larger number of free dangling bonds [6,7]. They have fascinating electronic, catalytic, and optical properties, he global nanomaterials market was $8.5 billion in 2019 and is expected to grow at a compound annual growth rate of 13.1% from 2020 to 2027 [8]. However, most of the applications of NPs require specific surface properties, which depend on the processes used in their preparation. NPs with surfaces free from residual chemical precursors and without the addition of any stabilizing ligands have much higher efficiencies for applications in medical technology, catalysis, biotechnology, and other areas where pure surfaces are necessary.

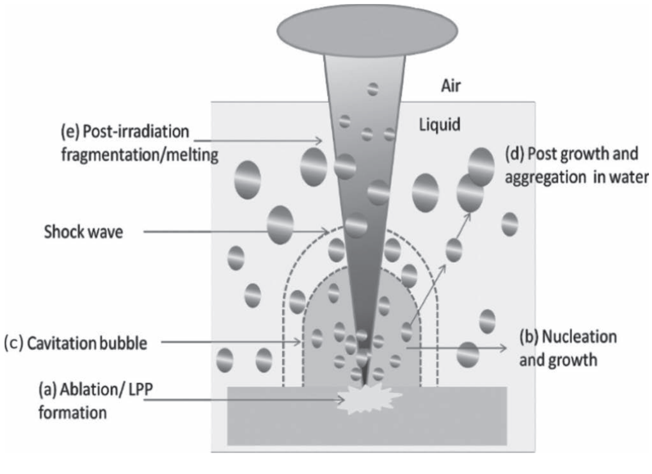
Air
Liquid
(e) Post-irradiation fragmentation/melting
(d) Post growth and aggregation in water
Shock wave
(c) Cavitation bubble
(b) Nucleation and growth
(a) Ablation/ LPP formation

FIGURE 12.1 Mechanisms of LP-PLA synthesis of NPs with different steps like (a) ablation/evaporation of target surface for LPP formation, (b) nucleation and growth of particles inside cavitation bubble, (c) mixing of particle into water after collapse of cavitation, (d) growth/aggregation of particles in solution, and (e) post-irradiation, melting/fragmentation of particle in laser path.

Pulsed laser ablation in liquids (PLAL) also termed as *liquid-assisted pulsed laser ablation* or *liquid-phase pulsed laser ablation* (*LP-PLA*) exhibits much simpler and low-cost experimental arrangements as compared to gas-phase laser ablations. LP-PLA where a pulsed laser beam ablates a solid target or suspended NPs at solid–liquid or particle–liquid interface (Figure 12.1), is a topical and fast-growing field of research with proven applications in photoablation therapy [9], microinjection for painless drug delivery [10], and synthesis and modifications of nano-/microparticles [11,12]. Compared to a wet-chemical approach, LP-PLA is a clean, one-step, and non-equilibrium method that yields pure, electrostatically stabilized colloidal solution of NPs with high conjugation efficiency [13,14] and surface coverage [15] for a wealth of applications. The NPs produced via this green route have charged surfaces, which facilitate *in situ* [16,17] or *ex situ* [18,19] electrostatic transportation leading to efficient Surface assisted laser desorption ionization (SALDI) substrates [20], thin films for devices [21,22], and surface decoration by NPs

[23]. LP-PLA has potential to deliver two products at the same time: (i) NPs suspended in the solution and (ii) nano-/micro-structures produced on the target surface.

12.2 Background of LP-PLA of a Solid Target at the Solid–Liquid Interface

Laser ablation of a solid target creates a plasma plume that expands normally to the target surface. The rate and mechanism of removal of the target material depend on laser irradiance on the target surface. The plasma produced in the vacuum expands freely and follows a linear relationship, $R(t) =$ a.t, for the position of the plume front with time, where a is a positive constant [24,25]. The plasma plume becomes confined under the ambient gas where the degree of confinement depends on the background gas pressure. For example, expansion of the plume follows the shock wave model, $R(t) = a.t^b$, at low ambient pressures and the drag model, $R(t) = a(1-e^{-b.t})$, at high ambient pressures, where a and b are the constants with $a>0$ and $0<b<1$ [24]. An increase in the ambient pressure causes an increase in the spatial confinement of the plasma plume. Therefore, there would be better reactions among the plasma species inside the plasma plume and between the plasma species and ambient at the plasma–ambient interface. At extremely low pressures, such as in a vacuum, PLA generates supersonically expanding plasma where the species do not have enough time to form clusters and consequently are deposited on the substrate in the form of atomic layers, i.e. a thin film [26,27]. In contrast to this, PLA in a high-pressure environment causes spatial confinement of the plasma plume and its condensation to nanoclusters or NPs [28,29]. The spatial confinement of the plasma plume transfers it to the thermodynamic state of high temperature, high pressure, and high density (HTHPHD), where special reactions can take place to generate unique, metal-stable phases of nanostructures, such as BN (boron nitride) and diamond particles that cannot be synthesized in normal conditions [30,31]. Liquids have higher densities as compared to gases; therefore, PLA in liquids generates a plasma plume under a higher degree of confinement and induces a higher level of HTHPHD conditions. Unlike a chemical processing, which possesses slow processes under thermodynamic equilibrium, the reactions in LP-PLA occur in ns and ps durations that are fast and ultrafast process that occur under non-equilibrium conditions. The NPs produced under non-equilibrium conditions have surfaces with a greater number of defects [32] and voids that provide a larger number of active sites for functionalization, bioconjugation, and catalytic applications [15].

12.2.1 Nucleation and Growth of NPs from Laser-produced Plasmas Confined in Liquid

Processes for short and ultrashort laser ablation of solid target in liquids are divided into three stages, namely (i) early stage: absorption of laser energy by target surface (photon–electron and, electron–phonon interactions; ultrafast processes), ejection of material, and plume formation; (ii) intermediate stage, which includes expansion of the plume under liquid confinement; nucleation and growth of particles (fast: ns-µs); (iii) last stage in which the plume will mix with the liquid and a number of slow processes (several µs to days) take places, such as coalescence, prolonged growth, and aggregation/agglomeration of particles [13,33].

12.2.1.1 Early Stage

Assuming a laser pulse having a peak intensity I_0 and a pulse duration τ generates plasma at a solid target surface. Then initial pressure (P_0) inside the plume and its initial length (L_0) are given by the following expressions:

$$P_0 = 0.01\sqrt{Z^* I_0\left(\frac{\alpha}{2\alpha+3}\right)}$$

$$\text{(i)} \quad \text{and} \quad L_0 = L(\tau) = \frac{4\tau}{3}\sqrt{\frac{\alpha}{2\alpha+4}\frac{I_0}{Z}}, \qquad (12.1)$$

where $Z^* = {2Z_1Z_2}/{Z_1 + Z_2}$ is effective impedance with Z_1 and Z_2 being shock impedances of target and liquid, respectively, and α the ratio of thermal energy to the ionization energy of the plasma, which is very small for ultrashort pulses. Therefore, the plasmas produced by short laser pulses have higher pressure and a shorter plume length, i.e. better confinement of the plasma species [18,41]. This early stage is described by Step 1 in Figure 12.2.

12.2.1.2 Intermediate Stage

In the intermediate stage, plasma plume expands adiabatically behind the shock wave and the cavitation bubble. The pressure and length of the Lase Produced Plasma (LPP) are described by the following expressions:

$$P(t) = P_0\left[1+\frac{\gamma+1}{\tau}(t-\tau)\right]^{-\gamma/\gamma+1}$$

$$\text{(iii)} \quad \text{and} \quad L(t) = L_0\left[1+\frac{\gamma+1}{\tau}(t-\tau)\right]^{1/\gamma+1}, \qquad (12.2)$$

where $\gamma = 1+2\alpha/3$ is the adiabatic parameter.

Here, we can see that the final pressure and length of the plume depend on their corresponding initial values and adiabatic parameter. Therefore, at this stage, the plume number density is higher, while the plume temperature is lower for shorter laser pulses. These conditions favour the formation of smaller-sized NPs, which is controlled by free energy as follows:

$$\Delta G(n,c) = -nkT\ln\left(\frac{c}{c_0}\right) + 4\pi a^2 n^{2/3}\sigma, \qquad (12.3)$$

where T is the temperature in Kelvin, n is the number of monomers/atoms in the nucleus, a is the effective radius of plume species, c and c_0 are the concentration and equilibrium concentration respectively, k is the Boltzmann constant, and σ is

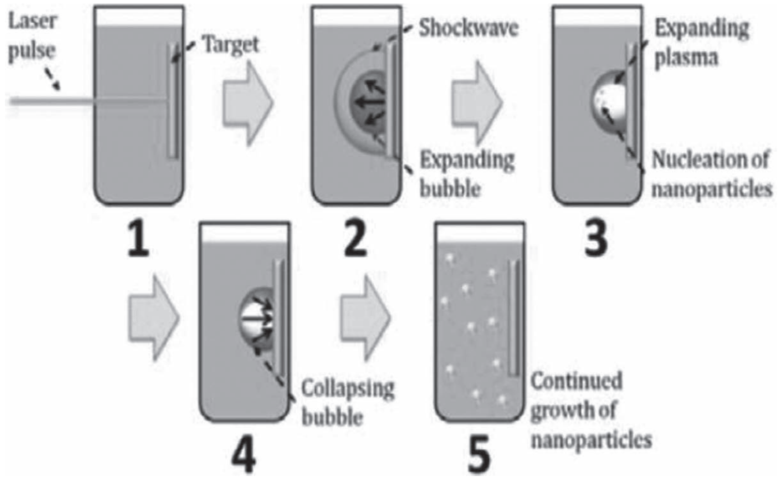

FIGURE 12.2 Steps representing different stages of LP-PLA in NPs generation: early phase (step 1), intermediate phase (steps 2–4), and later phase (step 5).

the effective surface tension. The peak of the nucleation barrier corresponds to the critical cluster size as follows:

$$n_c = \left[\frac{8\pi a^2\sigma}{3kT\ln(S)}\right]^3 ; S > 1 \text{ is supersaturation parameter}. \quad (12.4)$$

The nuclei generated at this stage can grow due to the addition of both monomer and cluster, and can evaporate due to the interaction with succeeding laser pulses. The size of the nuclei continues to grow inside the plasma plume until the density of the plasma plume drops and collision stops. The growth process dominates over the evaporation if the temperature of the cluster and plasma is low. In the short-pulse laser ablation (fs and ps lasers), laser pulses do not reheat the expanding plasma; therefore, cluster growth is more favourable in fs-laser ablation over ns and ms laser ablation. These nuclei, grown in the intermediate stage, act as seeds for the prolonged growth of particles in the later stage [13,33]. The intermediate stage is represented by steps 2–4 in Figure D.11.2.

12.2.1.3 Later Stage

At this stage, species from the plasma plume, such as atoms and clusters, get mixed in the liquid to form a solution. The processes of nucleation and growth of clusters in the solution depend on the initial conditions, such as solute concentration, temperature, particle size, and density of the solution. For example, if the solution is supersaturated, then a new nucleus can be formed in the solution, while if the solution concentration is not high, then growth of the particles produced in the intermediate stage would occur. The rate of formation of critical clusters at this stage is given by

$$\rho(t) = 4\pi a n_c^{1/3} D c^2 \exp\left[\frac{-\Delta G(n,c)}{kT}\right], \quad (12.5)$$

where D is the diffusion coefficient of target atoms in the liquid. If the number density of nuclei is sufficiently high for collisions, then the processes of coalescence and aggregation occur, resulting in an increase in the particle size. Etina [33] described growth processes using the following three equations:

$$\frac{dN_1}{dt} = \rho(t) - \sum_{j=2}^{\infty} j\frac{dN_j}{dt}\left(\text{Here } N_1 \text{ is primary particle}\right) \quad (12.6)$$

$$\frac{dN_2}{dt} = fk_1N_1^2 - k_2N_1N_2$$

$$\left(\text{Here } N_2 \text{ is secondary particles with 2 primary particles}\right) \quad (12.7)$$

$$\frac{dN}{dt} = k_{s-1}N_1N_{s-1} - K_sN_1N_s$$

$$\left(\text{Here } N \text{ is particles with } s \geq 3 \text{ primary particles}\right) \quad (12.8)$$

where N_s (t) is the time-dependent number density of secondary particles having s number of primary particles; $K_s = 4\pi (R_1+R_s)(D_1+D_s)$ is the attachment rate constant; $R_s = 1.2rs^{1/3}$; r is the average radius of primary particle; $D_s = D_1s^{-1/3}$ is the diffusion constant of secondary particles having s number of primary particles. Here, diffusion coefficient of the primary particle is given by Stokes–Einstein relation, $D_1 = kT/6\pi\eta\sigma$, which depends on the viscosity and temperature of the liquid medium.

12.3 Effects of Different Experimental Parameters on the Dynamics of Laser Ablation

The rate of material removal from the solid surfaces in the course of laser irradiation depends on the wavelength, pulse width, laser irradiance at the target surface, and on the ablation environment. At a given laser parameter, higher absorption coefficient, i.e. lower reflectance, $R = \left[(n_T - n_m)/(n_T + n_m)\right]^2$, where n_T and n_m are the refractive indices of target and ablation medium, respectively, of the laser beam from target surface causes a higher rate of ablation. For a given target material, the absorption coefficient of laser light at the target–medium interface depends on the wavelength of laser and ablation media. Since liquids have higher refractive indices than air/gases, therefore ablation of solids in liquids has higher absorption coefficients as compared to ablation in vacuum or gases. For the same laser parameters, the crater formed on the surface of silicon by PLA in water has almost twice depth and diameter as compared to that obtained in the air [34]. The rate of ablation of Si in water is always higher as compared to ablation in air in the fluence range of 2–5 J cm^{-2}, but the difference in the ablation rate decreases at higher fluence due to the breakdown of water, i.e. water hammer effect [35]. Liquids have higher light absorption coefficients as compared to vacuum or gases; therefore, PLA of solid targets in liquids possesses a significant absorption of laser light by liquids, resulting in a reduced rate of ablation. Lower reflectivity of laser light at a solid–liquid interface favours a higher rate of ablation, on the one hand, while absorption of laser light by liquid layers reduces the ablation rate, on the other hand. Therefore, optimization of the thickness of the liquid layer is another key experimental parameter to optimize the rate of ablation. Zhu et al. [36] studied the effect of water-layer thickness on the ablation rate. They observed an increase in the rate of ablation with the increase in the liquid-layer thickness in the range of 1.0–1.1 mm with a maximum ablation for 1.1 mm thick water layer. The ablation rate decreases from 62 nm/pulse to 0.5 nm/pulse with an increase in the water-layer thickness from 1.1 to 2.2 mm. For a given liquid medium and laser parameters, the rate of material removal depends on the refractive index of the target material and its physical properties such as specific heat, melting, and boiling temperatures. Similarly, for a given target material and laser parameters, the rate of ablation and particle generation depends on the transmission coefficient and refractive index of the liquid medium at a given laser wavelength. It is reported that the ablation threshold in acetone is minimum for copper and maximum for ZrO_2 among the studied samples [37].

The effective focal length of the lens decreases if the distance between the lens and the target is partially or fully filled by any liquid having a refractive index higher than air. Therefore, for an optimal rate of ablation, the distance of the target surface from the lens should be lesser than its actual focal length. Due to the differences in the refractive indices of liquid media, the position of the target for optimal ablation also differs for different liquids. For example, acetone ($n \sim 1.36$) has a higher refractive index than water (~1.33); therefore for the same focusing lens and laser wavelength, the target distance for optimal ablation should be smaller for PLA in acetone as compared to PLA in water (Figure 12.3). In addition to this linear effect, at higher laser irradiances, *self-focusing*, a non-linear phenomenon, takes place which focuses the laser beam at shorter distances than that of the actual focal length [38]. Self-focusing of laser light is the consequence of an increase in the refractive index of propagation medium with the laser field intensity as follows:

$$n = n_0 + \Delta n = n_0 + \gamma I = n_0 + n_2 {E^2}\!/_{2}, \qquad \text{(D1.9.9)}$$

where n_0 is the linear refractive index of the medium, Δn is the refractive index change, n_2 is the non-linear refractive index, I is the intensity of the light, and E is the amplitude of the electric field. The distance at which the beam shrinkage due to self-focusing effect is given by $d = \left(\frac{D}{2}\right)\sqrt{n_{0/2n_2I_0}}$, where D is the maximum diameter of the laser beam and I_0 is the laser intensity [38].

For a given liquid medium, the longer wavelength of the laser beam possesses a lower refractive index ($n = A + B/\lambda^2$); therefore, it needs a lesser shift in the position of target surface for optimal ablation as compared to the corresponding position in the air. Tsuji et al. [39,40] demonstrated the influence of laser wavelength and focusing conditions on the ablation efficiency of Ag and Cu targets in the water. For PLA of Ag, they observed that for an unfocussed beam, the rate of ablation was higher for shorter wavelength (355 > 532 > 1064), while in the case of PLA of Cu under the unfocused beam,

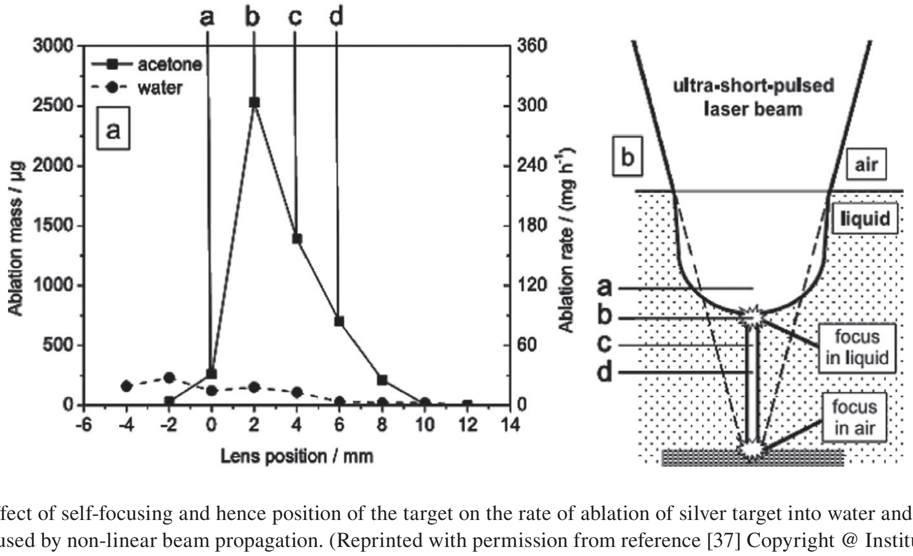

FIGURE 12.3 (a) Effect of self-focusing and hence position of the target on the rate of ablation of silver target into water and acetone, (b) sketch of focal displacement caused by non-linear beam propagation. (Reprinted with permission from reference [37] Copyright @ Institute of Physics.)

the maximum ablation was registered for 532 nm wavelength (532 >355 >1064). Under the focussed beam conditions, higher wavelength results in a larger rate of ablation for both targets (1064 nm> 532 nm>355 nm).

The pulse duration of the laser has also a significant influence on the rate of ablation and hence the size, shape, and morphology of the produced nanomaterials. Longer pulses have comparatively larger thermal effects and absorption in liquids; therefore, a comparatively smaller fraction of energy reaches the target surface. Longer pulse length laser shows a higher ablation rate for PLA of the target at the air–target interface, while shorter laser pulses exhibit faster materials removal for PLA at the target–water interface. Sakka et al. [41] investigated the influences of pulse width on the ablation rate of copper target in water using optical emission spectroscopy, time-resolved plume imaging, shadowgraph of cavitation bubble, and measurement of pit volume at the target surface. A higher proportion of energy from a longer laser pulse reheats the plasma rather than the removal of material from the target surface, while a larger fraction of a shorter laser pulse is used to remove material from the target surface. The rate of material removal by PLA of a solid target in liquid and hence nucleation/growth of NPs depend on the temperature of liquid medium. Hong et al. [42] reported that colder liquids result in a higher ablation rate. In their investigation, they used 20% aqueous solution of KOH or distilled water as ablation media for the ablation/etching of silicon in the temperature range of 4°C–30°C and observed ~37 nm/pulse rate of ablation at 10°C temperature. It changes slightly as the liquid temperature increases, with a variation of 5nm/pulse. However, the rate of ablation for PLA of Si in the KOH solution varied greatly with the variation in temperature. The ablation rate was ~75 nm/pulse at a liquid temperature of 6°C, which reduces to ~22 nm/pulse at a liquid temperature of 30°C.

12.4 Cavitation Bubble Formation and Related Effects

Cavitation is a dynamic phenomenon that occurs in the flowing liquid, where the local pressure is less than the saturated vapour pressure at ambient temperature. Cavitation bubbles have several destructive as well as constructive effects in laser material processing. When a laser pulse is focussed onto a solid target surface at the target–liquid interface, it generates a shock wave, cavitation bubbles, and high-pressure plasma plume. A cavitation bubble is produced by the high-pressure plasma plume, and its radial motion is governed by the pressure gradient between outside and inside of the bubble. Rayleigh has theoretically developed a relationship between the maximum radius $R_{\max}$ of the spherical-shaped cavitation bubble in an infinite liquid and its collapse time T_c, as follows:

$$R_{\max} = \frac{T_c}{0.915\sqrt{\rho/\left(P_\infty - P_0\right)}}, \qquad (12.10)$$

where $R_{\max}$ is the maximum radius of a spherical bubble, T_c is the collapsing time of the bubble, ρ is the density of the fluid, P_∞ is the static pressure, and P_0 is the vapour pressure inside the bubble. There are two pathways for the formation of the cavitation bubble in the PLA of solid targets under liquids. The first one is associated with the laser-induced photothermal effect that causes an increase in the target surface temperature above the boiling point of the liquid, resulting in the generation of bubbles near the solid surface. The second phenomenon involves laser-induced optical breakdown of liquid at the target surface to generate liquid plasmas. The liquid plasma heats nearby liquid above its boiling point to form vapour bubbles. Time-dependent shadowgraphs for the growth, decay, and collapse of cavitation bubble and shock wave during PLA of titanium metal in distilled water are shown in Figure 12.4. Surfaces of long-lived cavitation bubbles support smaller-sized NPs to fabricate larger-sized hollow spheres [43]. The change in the surface energy for the adsorption of a nanocluster at the surface of a bubble is given by the following equation:

$$\Delta G = -\pi r^2 \left(1 - \cos\theta\right)^2, \qquad (12.11)$$

where r is the radius of the NP, γ is the surface tension of bubble interface, and θ is the contact angle of the liquid on the particle. Reduction in the free energy provides a driving force for the adsorption of NPs; once a particle is adsorbed at the bubble interface, the energy barrier $|\Delta G|$ will obstruct its escape. Yan et al. [44] numerically calculated that for a 2 nm-sized ZnO particles in the water–ethanol mixture at 20°C ($\gamma \approx 30 \times 10^3$ N m^{-1}, θ≈ 30°), $|\Delta G| = 12.5 \times K_B T$, where K_B is the Boltzmann constant and $T = 293$ K, which is much larger than the thermal energy of the NP. This makes irreversible trapping of NPs by the bubble. During the shrinkage of the bubble, the areal density of clusters increases, which could cause formation of a network of NPs bounded by capillary action. This bonding generates a steric barrier sticking the interface motion to assemble NPs into a hollow nanosphere (NS).

For a given experimental condition, the ability of cavitation bubble-assisted fabrication of hollow NPs from the assembly of smaller-sized solid NPs depends on the target–liquid system. Yan et al. fabricated hollow nanostructures of ZnO, Si, Ag, Fe-Ni alloy, and Al with the assistance of *LP-PLA*-induced cavitation bubbles [44]. Figure 12.5a and b shows hollow NS of Ni-Fe alloy fabricated by PLA of bulk Ni-Fe alloy target material in the ethanol–water mixture. Hollow NPs of Si

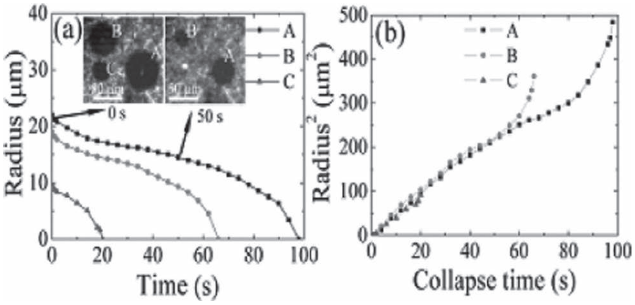

FIGURE 12.4 (a) Time variation in the sizes of three different laser-induced cavitation bubbles in water–ethanol mixture with the insets showing optical images of bubbles and (b) square of the cavitation bubble radius *versus* time of their collapse. (Reprinted with the permission from Yan et al. [66] copyright @ American Institute of Physics.)

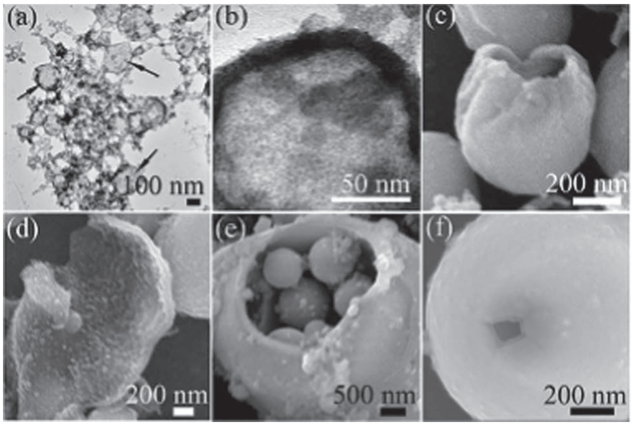

FIGURE 12.5 Transmission Electron Microscopic (TEM) images of NPs produced fabricated by PLA of Fe-Ni alloy in the ethanol–water mixture. Scanning Electron Microscopic (SEM) images of (c,d) hollow NS produced by PLA of (c,d) Si in water and (e,f) Ag in ethanol–water mixture with Triton X-100. (Reprinted with the permission from Yan et al. [66] copyright @ American Institute of Physics.)

were produced by PLA in pure water as shown in Figure 12.5c and d, while it needs addition of ethanol in water to prepare zinc oxide NS under almost the same experimental conditions. The authors felt difficulty in the preparation of hollow Ag NS even in the ethanol–water mixture, which was not so difficult for the preparation of hollow NS of ZnO, Si, and Fe-Ni alloy. In order to solve this issue, they added Triton X-100 (0.06% v/v) in the ethanol–water mixture and successfully prepared Ag NS. The addition of Triton X-100 probably further elongated the lifetime of the cavitation bubble by increasing the viscosity of the liquid medium.

12.5 Non-reactive LP-PLA of Solids for the Generation of Elemental Nanoparticles

In non-reactive LP-PLA, the species of target material do not react with the surrounding liquid medium; thus, the formed NPs have the same composition as their mother targets. Noble metals such as silver, gold, and platinum are non-reactive with most of the liquids; therefore, PLA of these metal targets in liquid media produces their corresponding NPs and assemblies. In other words, depending on the stoichiometry of the target, the non-reactive laser ablation produces particles of a single element or alloy. Non-reactive laser ablation illustrates a set of experimental parameters such as laser parameters, liquid media composition, and target parameters, which prevent any reaction between laser-produced plasmas and liquid molecules at plasma–liquid interface, inside the plasma, and inside the liquid. For a particular target material and liquid medium, a set of laser parameters may exhibit reactive conditions, while others may possess non-reactive situations. In most of the cases, PLA of Ag [45–51], Au [52–59], and Pt [60–62] in most of the liquids produces their corresponding elemental metal NPs by non-reactive PLA, but in certain conditions, depending on laser and liquid media parameters, metal compounds are also produced on the surface of noble metal NPs through reactive PLA to synthesize core @ shell nanostructures. For example, Zn core @ ZnO shell NPs were produced by nanosecond PLA of Zn target in water [63]. Reactivity of the laser-produced metal plasma with surrounding liquid molecules depends on its thermodynamics, which is monitored by laser parameters.

Šišková et al. [45] have ablated Ag metal target in the aqueous media of some strongly adsorbing ions, which resulted in the formation of chemically modified Ag NPs. Yang et al. have fabricated Ag-nanostructured films through electrophoretic deposition (EPD) in the PLA-synthesized colloidal solution of Ag NPs [47]. It is reported that the morphology of produced film is tunable and controllable with the EPD parameters. PLA of Ag targets in water or aqueous media of electrolyte solutions (HCl, NaCl, NaOH, $AgNO_3$, and/or Na_2SO_3) using fundamental wavelength of Nd:YAG laser, produced spherical Ag NPs with different surface morphologies [49]. Amendola et al. [50] used acetonitrile (AN), *N*, *N*-dimethyl formamide (DMF), tetrahydrofuran (THF), or dimethyl sulphoxide (DMSO) as ablation media for the PLA of Ag target using 1064 nm wavelength, 9 ns pulse width, and 10 Hz repetition rate. They reported that the NPs produced in AN have an average radius of 3.5 nm and a spheroid contribution of only 2%, while Ag NPs with 5 nm average size and 100% spheroidal contribution were produced in DMF.

Petersen et al. [52] ablated Au target in the aqueous media of 1 or 5 µM for *in situ* bioconjugation of Au NPs for a rapid design of cell-penetrating nano-markers for intracellular bioimaging. Significantly enhanced penetrating conjugation efficiencies were observed at higher pH values, whereas the size and morphology of bioconjugates depend on the peptide concentration during ablation. Ana Menendez-Manjon et al. [54] studied the effect of water temperature on the hydrodynamic diameter of Au NPs produced by LAL. The temperature of liquid media affects its physical properties such as viscosity, surface tension, and compressibility, which drive volume, expansion velocity, and lifetime of cavitation bubbles. Saitow et al. [59] studied the effect of the density of fluid on the size of the produced Au NPs. They used supercritical CO_2 in high-pressure (up to 20 MPa) cell as ablation medium for LAL and synthesized Au nanonecklaces and NS.

12.6 Reactive Pulsed Laser Ablation for the Generation of Metal Compound Nanoparticles

The laser-induced plasmas (LIPs) ionizes surrounding liquids to produced plasma-induced plasmas (PIPs) at the plasma–liquid interface. The LIPs have ionic species from the target material, while PIPs contain species from the liquid medium. In the case of PLA of active metals and active metal ions, cations of the LIPs rapidly react with anions of the PIPs to synthesize metal compound NPs. For example, PLA of zinc in water or in alcohol produces zinc oxide [64] or $ZnO/Zn(OH)_2$ nanocomposites [65], or ZnO/ZnOOH nanocomposite [66,67] NPs. Similarly, PLA of Ti produces TiO_x, including TiO, TiO_2, and Ti_2O_3 NPs in water [68,69], TiN in liquid nitrogen [70], TiO and TiC in 2-propanol [71,72], and TiH NPs in *n*-hexane [73].

The ratio of cation to anion in the NPs and their phase depend on the laser and liquid media parameters. PLA of Ti in water produces different phases of titanium oxide NPs at different laser irradiances [72,73]. At lower laser irradiances (130 and 150 MW cm^{-2}), amorphous TiO, Ti_2O_3, and TiO_2 NPs with 5.2 and 5.5 GPa internal strains, respectively, were produced, while at higher laser irradiance (110 GW cm^{-2}), multiwall nanotube (MWNT) of TiO, Ti_2O_3, and TiO_2 with 4.2 GPa internal stress and at 140GW cm^{-2} MWNT of only TiO_2 with 4.5 GPa internal strain were produced. It is observed that the content of elements from liquids (anions) is higher in the smaller-sized NPs [73].

Golghtly and Castleman [72] reported ablation of Ti in 2-propanol, water, ethanol, and *n*-hexane, and produced TiC, TiO_x, and TiH NPs. They observed that higher laser fluences produce larger-sized particles with wider size distribution in all the three liquid media. The PLA in water gives a higher number of larger-sized (>70nm) particles as compared to 2-propanol, while the PLA in *n*-hexane produces particles <70nm. In all the liquids, smaller-sized particles have a higher ratio of anion to cation. Singh and Gopal reported PLA of zinc in methanol [64] using 1064 nm wavelength from a nanosecond Nd: YAG laser and produced drop-shaped zinc oxide QDs and their electrostatic self-assembly into various dendritic nanostructures. Figure 12.6 presents assemblies of drop-shaped zinc oxide NPs into various dendritic nanostructures and schemes for their branching with the axis. In another study, Singh and Gopal reported LP-PLA of a cadmium rod placed on the bottom of a glass vessel containing aqueous media of Sodium Dodecyl Sulfate (SDS) at different concentrations to produce a variety of cadmium hydroxide nanostructures from NPs to nanorods (NRs), nanotetrapods, nanoflower buds, and 2D and 3D nanoflowers [74,75]. It is suggested that initially produced spherical NPs get self-assembled into 1D NRs, which themselves also get assembled into their successor complex 3D nanoarchitectures. An aqueous medium of 20 mM SDS was found most suitable for the growth of such nanostructures.

Simultaneous flow of oxygen in the close vicinity of laser-produced plasma plume during PLA has the ability to increase oxygen content in the NPs, increase oxide/hydroxide ratio in nanocomposite, increase crystallinity of the particles, and decrease their size and distribution [66]. PLA of active metals in water or alcohols produces first their hydroxides NPs. These hydroxide NPs either get dehydrated into their oxides by losing water through hydrothermal reaction process or get clusterized to form hydroxide NPs. In some cases, oxide/hydroxide nanocomposites are produced [65–67]. PLA of zinc in water [65] or low concentration of surfactant [66,67] produces pure zinc oxide or zinc oxide/hydroxide nanocomposite, while PLA of Cd under almost the same experimental conditions produces $Cd(OH)_2$ nanostructures [74,75]. These $Cd(OH)_2$ nanostructures can be converted into CdO nanostructures through the post-annealing process [74].

Concentration of surfactant in the liquid media controls the rate of reaction at the plasma–liquid interface before the particle synthesis or at the particle–liquid interface after the production of NPs in solutions, as well as colloidal stability of NPs. PLA in liquid without any surfactant or low concentration (<Critical Micelle Concentration (CMC)) allows dominance of reactions between plasma species and species from the liquid media over the reaction among the plasma species that results in the synthesis of metal compound NPs instead of metal NPs [76]. At the concentration of surfactant near their CMC, the rate of reaction among the plasma species becomes higher than the rate of reaction between the plasma species and species from the liquid media, which results in the formation of metallic core with metal compound shell NPs. With the ageing of NPs in the solution, the thickness of shell layer increases. PLA in the liquid media having concentrations of surfactant higher than the CMC supports the formation of metal NPs with strong protecting layer of surfactant molecules. Capping with surfactant molecules prevents the reaction between surface atoms of NPs with the species of liquid media at the particle–liquid interface, as well as disperses NPs in the solution to enhance their colloidal stability. The effects

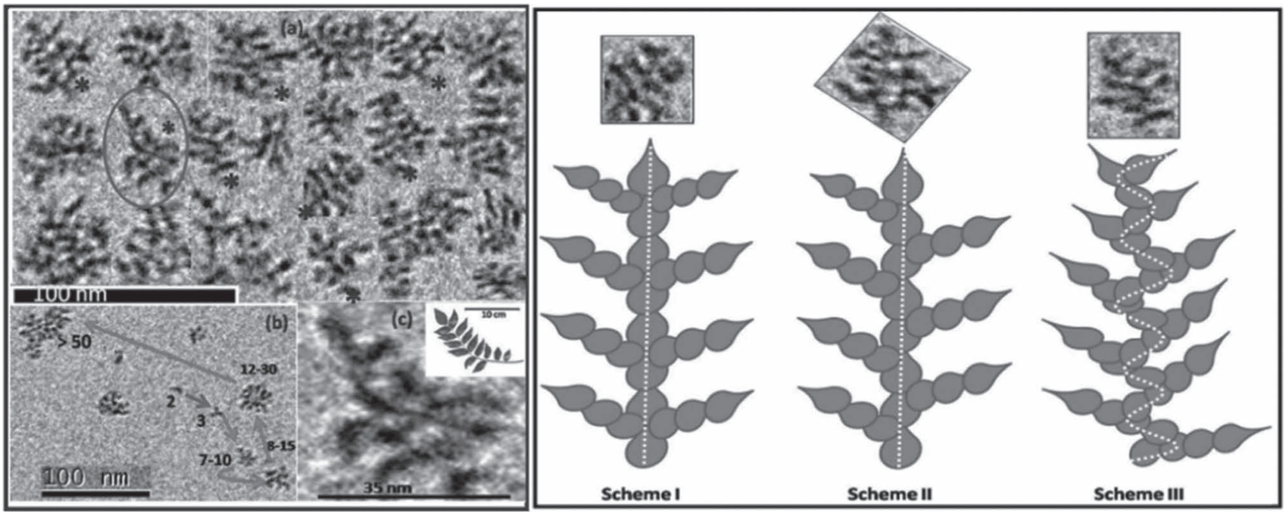

FIGURE 12.6 Assemblies of drop-shaped zinc oxide quantum dots into various dendritic nanostructures, three possible branching schemes. (Reprinted with the permission from Singh and Gopal [64] copyright @ Elsevier.)

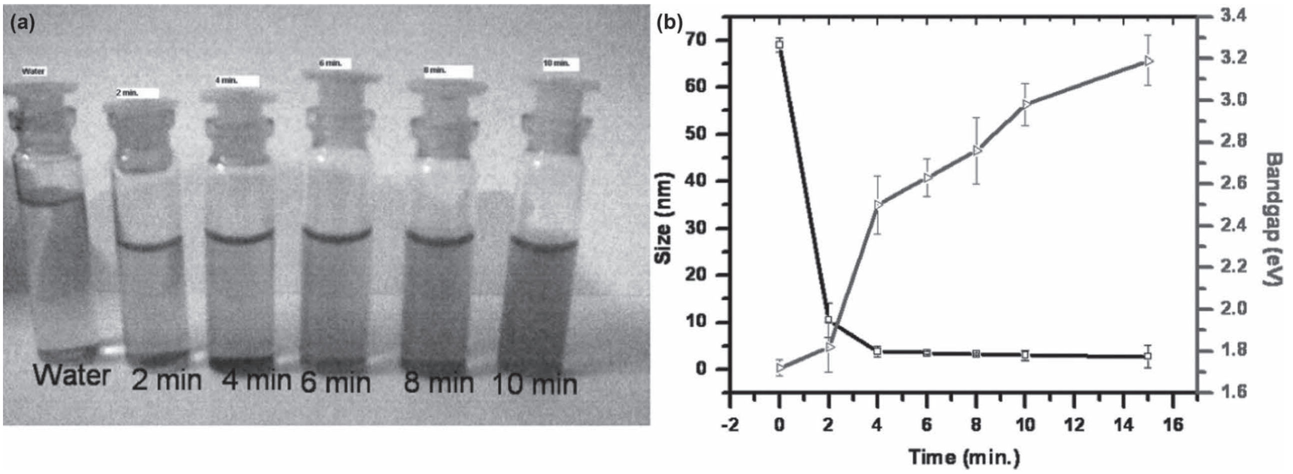

FIGURE 12.7 (a) Photographs, (b) sizes and corresponding band gap energies of colloidal solution of Se QDs obtained after different times of laser irradiation (Reprinted with the permission from Singh et al. [94] copyright @ American Chemical Society.)

of surfactant concentration on the size and shape of NPs and the stability of colloidal solution produced by LAL depend on the nature of charge on the NPs' surface and nature of surfactant. For example, an increase in the concentration of SDS decreases the size and distribution, increases the colloidal stability of negatively surface-charged particles such as Zn or ZnO [76], and increases the size and rate of aggregation of positively surface-charged particles such as $Cd(OH)_2$ NPs [75].

Liang et al. reported reaction between laser-produced zinc plasma and water molecules for the synthesis of zinc hydroxide/dodecyl sulfate inorganic/organic hybrid nanostructures. A layered zinc hydroxide/surfactant composite (ZnDS) was produced by PLA of Zn in the aqueous media of SDS at the concentration of 1, 10, and 100 mM [77]. The ZnDS products were octagonal platelets with a single crystalline form in hexagonal symmetry. In the composite formation process, the charged zinc hydroxide molecules were produced through the strong reaction between zinc species and water molecules, which are assembled into a layered structure through step-by-step by surfactant molecules. Usui et al. [78,79] reported that an increase in the length of alkyl chain in sodium alkyl sulphate increases inter-planer spacing and angle of tilt between two planes in layered $Zn(OH)_2$/DS nanocomposite. Yan et al. [80] controlled the morphology of zinc hydroxide/DS nanostructures through varying the composition of ethanol/water in liquid media. PLA of zinc in pure water produces ZnO, while in water/H_2O_2 mixture, it generates ZnO_2 NPs [81]. PLA of Al in aqueous media of NaOH produces β-$NaAlO_2$ and γ-Al_2O_3 spherical NPs. At higher concentrations of NaOH, the amount of $NaAlO_2$.4/2 H_2O and β-$NaAlO_2$ NPs dominates over γ-Al_2O_3 NPs [82]. Ablation of Al in hydrogen-saturated liquid ethanol produces core–shell NPs with multiple shell layers [83]. NPs have fcc Al single crystalline as core, amorphous Al as middle layer, and Al_2O_3 as outer shell layer. Zhang et al. studied the effects of laser pulse duration and wavelength on the oxidation, hydrolysis, and ageing of Al NPs in water, and reported the synthesis of Al_2O_3 and $Al(OH)_3$ NPs [84].

12.7 Laser Ablation of Suspended Particles in Liquids

Small size NPs with a narrow size distribution are required in several scientific and technological applications such as in sensing, catalysis, high density data storage etc., due to their larger surface to volume ratio. Most of the physical and chemical processes result in larger-sized particles with a wide dispersion and, therefore, need resizing and size narrowing of produced NPs. Photoinduced resizing and/or reshaping of NPs has been a subject of recent interest with a range of results favouring either thermal ablation [93–102], or a nonthermal pathway involving charging of the NPs [85–88,91–92] or the creation of strong fields [90]. If colloidal solutions of nano-/ microparticles, or powders/flakes dispersed in the solution, are used as a target in place of the usual solid target placed at the bottom of liquid container, some very interesting phenomena would occur. Nano-/microparticles or powder/flakes could undergo in the process of melting/vaporization or fragmentation to synthesize smaller-sized particles of same or different shapes, phase, and composition. As a remarkable function, this method can be used to re-produce or modify size, shape, composition, and phase of NPs. Through a careful selection of colloidal solution of NPs produced by LAL or chemical methods, and laser parameters, two different effects are generally observed. Firstly, the laser irradiation of mixture of two different colloids of NPs could lead to alloy or core/shell particle formation [93]. Secondly, laser irradiation of a single kind of colloid could lead to melting /vaporization or fragmentation of larger-sized NPs into smaller. Melting/vaporization or fragmentation of NPs, produced by preceding laser pulses in LP-PLA of solid target, may also take place by succeeding laser pulses to modify their size and shapes.

Three mechanisms are proposed for the resizing and/or reshaping of the nanostructures and/or their surface modification using laser irradiation. First is the laser-induced melting and/or vaporization of larger-sized particles and rearrangements of atomic species into smaller-sized clusters or larger-sized nanostructures with the same or different shapes depending on the experimental conditions. Second and third routes are based on the non-thermal excitation of the particles using ultrashort laser pulses and take place below the melting point of the particles. Second mechanism is laser-induced Columbic explosion, which involves ejection of photo- or thermal electrons from the surface of particles that leave positive charges behind them. These induced surface charges drive electrostatic repulsion between different parts of the surfaces, and consequently fragmentation of a single larger-sized particle into several smaller ones with different shapes than their mother particles, which may finally become spherical to minimize their surface energy. Kamat et al. [85] adopted this model in order to interpret 355 nm picoseconds laser-induced fragmentation of silver NPs on the basis of observed hydrated electrons in the transient absorption measurements. Afterwards, Mafune and co-workers [86,87] observed hydrated electrons in the nanosecond laser irradiation of SDS-suspended gold NPs and reported higher size reduction efficiencies for 355 nm irradiation as compared to 532 nm the Surface Plasmon Resonance (SPR) band excitation of gold NPs. The higher rate of size reduction was explained on the basis of inter-band electronic excitation–relaxation that provides higher absorption cross section for incident photons than the SPR absorption cross section. Moreover, they observed gold ions in the mass spectroscopy and suggested that the thermionic emission of electrons, which is a consequence of inter-band excitation, is responsible for the faster rate of fragmentation of gold NPs. Koda and co-workers proposed photothermal evaporation concept for the size reduction of chemically prepared gold NPs [88].

Inasawa and co-workers performed a schematic and detailed investigation in the support of Koda's work and proposed that the size reduction in the picoseconds irradiation of water-suspended gold NPs takes place by a layer-by-layer mechanism on the basis of observed bimodal distribution of particles [89]. Third mechanism of size reduction is quietly different from photothermal ablation and Coulombic explosion, and is based on the field enhancement near curved surfaces [90]. Experimental conditions to follow these mechanisms are quite different. First requires a laser irradiance that can make the temperature of the mother target higher than its boiling point to vaporize the surface atoms/molecules, second needs either laser photon energy higher than the sum of work function of target material and ionization potential or needs much higher laser irradiance for multiphoton ionization for the ejection of photoelectrons, while the third mechanism takes place with ultrashort laser pulses. Laser-induced fragmentation may also be achieved with the laser wavelength having photon energy much less than the work function, through multiphoton ionization, which is a non-linear process and requires very high, ~10^{17}–10^{18} W cm^{-2}, laser intensity. Such high intensity can be achieved from shorter pulses such as pulses from picosecond or femtosecond laser systems.

Recent theoretical investigations by Werner and Hashimoto [91] suggested that the fragmentation is a dominating process for fs irradiation, while purely thermal evaporation occurs for ns irradiation even at 355 nm wavelength excitation. They proposed an improved working model for the size reduction of Au NPs through the processes of heat dissipation, bubble formation, and electron–phonon dynamics. Pyatenko et al. [92] also supported a similar phenomenon. They demonstrated that electron ejection from the surface of NPs can be practically neglected for all possible parameters of a nanosecond laser used under unfocussed condition. Different strategies of laser treatment of liquid-suspended particles can also increase their dimension larger than their mother particles. For example, ultrafast laser irradiation of ethanol-suspended copper flakes converted them into copper nanowires and copper NS [93]. The diameter of nanowires (NWs) increases with the rate of 10.2–54.2 nm min^{-1} with the increase in the time of laser irradiation. After 10 min of irradiation, all NWs were converted into copper NS.

Singh et al. [94] proposed that the rate of particle size reduction strongly depends on the size of particles and has different values above and below the critical size (R_c) (size at which strong quantum confinement occurs) of the particle. For the selenium NPs

$$\frac{dR}{dt} = \alpha R \qquad \text{for} \quad R > R_c \tag{12.12}$$

$$\frac{dR}{dt} = \beta R \qquad \text{for} \quad R < R_c. \tag{12.13}$$

From Equations (12.13) and (12.14), we have

$$R(t) = R_0 e^{-\alpha t} \qquad \text{for} \quad R > R_c \tag{12.14}$$

$$R(t) = R_0 e^{-t} \qquad \text{for} \quad R > R_c, \tag{12.15}$$

where R_0 is the radius of particle before laser irradiation. They irradiated 69.0 nm size of Se particles dispersed in double-distilled water using fundamental wavelength of pulsed Nd:YAG laser and reported 0.44, 0.12, and 3.75 nm values for α, β, and R_c, respectively. They obtained size reduction constants ($\tau = 1/\alpha$ or $1/\beta$) of 2.27, 8.33 s, $T_{1/2}$ (time at which size becomes half of its initial value) of 1.57 and 5.57 min for particles above and below the critical size Fig. 12.7 shows photographs of colloidal solutions of Se NPs produced after different times of laser irradiation (Fig. 12.7 a) and size of NPs produced with the time of ablation.

Link et al. [95] reported shape transformation of Au NRs in micellar solution through laser photothermal melting and fragmentation of liquid-suspended Au NRs, and studied their dependence on laser fluence (µJ to mJ) and pulsed width (911 fs and 7 ns). They had observed that at a particular laser wavelength ($\lambda = 800$ nm) and fluence (40 µJ/pulse), femtosecond laser (100 fs, 400 MW) converted all the NRs into NS, while nanosecond (7 ns, 6 kW) laser converted them into NRs of shorter aspect ratios whose length decreases with the increase in irradiation time. In another set of experiments using 20 mJ/pulse (3 MW) energy from 7 ns pulse width laser system and 200 nJ/pulse

(2 MW) energy for femtosecond system, they had observed that nanosecond laser converted all the NRs into NS, while femtosecond laser converted NRs of longer aspect ratio into that of shorter one. Hodak et al. [93] used nanosecond and picosecond laser irradiation of water-suspended Au core/Ag shell or Ag core/Au shell NPs to produce Au:Ag alloy NPs. Similarly, Chen and Yeh [96] irradiated a mixture of colloidal solution of gold and silver NPs, while Zhang et al. [97] irradiated a mixture of gold and silver powders for the synthesis of alloy particles.

Mafune et al. [98] observed the formation of Au nanonetworks and small Au NPs through 532 nm laser irradiation of LAL-synthesized water or aqueous medium of SDS-suspended ~20 nm Au NPs. Irradiation of water or low concentration of SDS solution-suspended Au NPs undergone a network formation where the size of network increases with the irradiation time. However, irradiation of particles suspended in higher concentration of SDS solutions resulted in Au NPs of smaller sizes. Kawasaki and Masuda [99] irradiated water-suspended Au flakes of >10 μm sizes using 1 J cm^{-2} energy of nanosecond 532 nm laser light to attain fine Au NPs through the intermediate stage of submicron-sized spherical Au particles. Geleski et al. [100] have irradiated 1-*n*-butyl-3-methylimidazolium (BMI.PF6) ionic liquid-suspended Pd or Rh NPs using nanosecond laser having 532 nm wavelength, 8 ns pulse width, and 200 mJ/pulse energy to produce corresponding fine NPs. Usui et al. [101] irradiated water-suspended ITO (indium-doped SnO_2) NPs using different irradiances from nanosecond laser working at 355 nm wavelength and 7 ns pulse width, and studied the optical properties of the obtained colloidal solution.

Zeng et al. [102] produced zinc oxide QDs of 1–8 nm sizes through laser irradiation of colloidal solution of zinc oxide hollow spheres. They have reported that the size of NPs decreases rapidly with the increase in irradiation time in the range of 0–10 min and starts increasing in the time range of 15–30 min. Three steps, namely fragmentation in the irradiation time range of 0–10 min, growth in the range of 10–20 min, and ripening in the duration of 20–30 min, were proposed. The residual thermal effect facilitated Ostwald ripening through incorporating small nanocrystals into large ones.

12.8 Conclusions

In this chapter, we presented a detailed review on the current state of art on laser ablation of NP generation, their resizing, and reshaping. Fundamentals of pulsed laser ablation of solid target at solid–liquid interface for non-reactive and reactive laser ablation for the generation of elemental/alloy and compound NPs are presented in detail. Recent advances on laser-induced melting/vaporization of liquid-suspended particles for their resizing and reshaping are also presented in detail. LP-PLA can generate NPs from elemental, binary, ternary as well as complex multi-elemental targets or powders in desired chemical compositions for their applications in various fields of science and technology. Therefore, this method of nanomaterials processing can be used as a green, simple, and quick process of nanomaterial sampling in future.

REFERENCES

1. M. Salvador, B.A. MacLeod, A. Hess, A.P. Kulkarni, K. Munechika, J.I.L. Chen, D.S. Ginger, *ACS Nano* 6 (2012) 10024.
2. S.C. Singh, H. Li, C. Yao, Z. Zhan, W. Yu, Z. Yu, C. Guo, *Nano Energy* 51 (2018) 774.
3. A.S. Thakor, J. Jokerst, C. Zavaleta, T.F. Massoud, S.S. Gambhir, *Nano Lett.*, 11 (2011), 4029.
4. M.D. Baaske, M.R. Foreman, F. Vollmer, *Nature Nanotech.*, 9 (2014) 933.
5. B. Lai, S.C Singh, J.K. Bindra, C.S. Saraj, A. Shukla, T.P. Yadav, W. Wu, S.A. McGill, N.S. Dalal, A. Srivastava, C. Guo, *Mater. Today Chem.*, 14 (2019) 100207.
6. J.L. Pitters, I.A. Dogel, R.A. Wolkow, *ACS Nano* 5 (2011) 1984.
7. K.-H. Hong, J. Kim, J.H. Lee, J. Shin, U.I. Chung, *Nano Lett.*, 10 (2010) 1671.
8. Nanomaterials Market Size, Share & Trends Analysis Report By Product (Carbon Nanotubes, Titanium Dioxide), By Application (Medical, Electronics, Paints & Coatings), By Region, And Segment Forecasts, 2020-2027, https://www.grandviewresearch.com/
9. Y.F. Huang, K.S. Huang, S. Bamrungsap, H.-T. Chang, W. Tan, *Langmuir* 24 (2008) 11860.
10. Commercialized Er:YAG laser based painless laser epidermal system (PLEASE) of Pantec Biosolutions.
11. H. Zeng, X. Du, S.C. Singh, S. Kulinich, S. Yang, J. He, W. Cai, *Adv. Func. Mater.* 22 (2012), 1333.
12. S. Petersen and S. Barcikowski, *Adv. Funct. Mater.* 19 (2009) 1167.
13. S.C. Singh, H. Zeng, C. Guo, W. Kai (Ed.), *Nanomaterials: Processing and Characterizations with Lasers*, Wiley-VCH, Germany, ISBN: 978-3-527-32715-7, Aug. 2012.
14. W. Qian, M. Murakami, Y. Ichikawa and Y. Che, *J. Phys. Chem. C*, 115 (2011) 23293.
15. S. Petersen and S. Barcikowski, *J. Phys. Chem. C*, 113 (2009) 9830.
16. P. Wagener, A. Schwenke and S. Barcikowski, *Langmuir*, 28 (2012) 6132.
17. P. Liu, Y. Liang, X. Lin, C. Wang and G. Yang, *ACS Nano*, 5 (2011) 4748.
18. G. Compagnini, M. Sinatra, P. Russo, G.C. Messina, O. Puglisi and S. Scalese, *Carbon*, 50 (2012) 2362.
19. A.M. Manjon, J. Jakobi, K. Schwabe, J.K. Krauss and S. Barcikowski, *J. Laser Micro/Nanoeng.*, 4 (2009) 95.
20. T. Tsuji, T. Mikuzi, M. Yasutomo, M. Tsuji, H. Kawasaki, T. Yonezawa and F. Mafune, *Appl. Surf. Sci.*, 257 (2011) 2046.
21. J. Jakobi, A.M. Manjon, V.S.K. Chakravadhanula, L. Kienle, P. Wagener and S. Barcikowski, *Nanotechnology*, 22 (2011) 145601.
22. W. Guo and B. Liu, *ACS Appl. Mater. Interfaces*, 4 (2012) 7036.
23. H. He, W. Cai, Y. Lin and B. Chen, *Langmuir*, 26 (2010) 8925.
24. S.S. Harilal, C.V. Bindhu, M.S. Tillack, F. Najmabadi, A.C. Gaeris, *J. Appl. Phys.*, 93 (2003) 2380.
25. S.C. Singh, C. Fallon, P. Hayden, M. Mujawar, P. Yeates, J.T. Costello, *Phys. Plasmas* 21 (2014), 093113.
26. J. Perriere, C. Boulmer-Leborgne, R. Benzerga, S. Tricot, *J. Phys. D: Appl. Phys.*, 40 (2007) 7069.

27. A. Leitner, C.T. Rogers, J.C. Price, D.A. Rudman, D.R. Herman, *Appl. Phys. Lett.*, 72 (1998) 3065.
28. C. N. Huang, S. Y. Chen, P. Shen, *J. Phys. Chem. C*, 111 (2007) 3322.
29. L. Zbroniec, T. Sasaki, N. Koshizaki, *Appl. Phys. A*, 79 (2004) 1783.
30. T. Sakka, S. Iwanage, Y.H. Ogata, A. Matsunawa, T.J. Takemoto, *Chem. Phys.*, 112 (2000) 112.
31. T. Sakka, K. Takatani, Y.H. Ogata, M. Mabuchi, *J. Phys. D Appl. Phys.*, 35 (2002) 35.
32. S.C. Singh, R.K. Kotnala, R Gopal, *J. Appl. Phys.*, 118 (2015) 064305.
33. T.E. Etina, *J. Phys. Chem. C*, 115 (2011) 5044.
34. S. Zhu, Y.F. Lu, M.H. Hong, X.Y. Chen, *J. Appl. Phys.*, 89 (2001) 2400–2403.
35. J.C. Isselin, A.P. Alloncle, M. Autric, *J. Appl. Phys.*, 84 (1998) 5766.
36. S. Zhu, Y.F. Lu, M. H. Hong, *Appl. Phys. Lett.*, 79 (2001) 1396–1398.
37. N. Barsch, J. Jakobi, S. Weiler, S. Barcikowski, *Nanotechnol.*, 20 (2009) 445603–445611.
38. P. Lallemand, N. Bloembergen, *Phys. Rev. Lett.*, 15 (1965) 1010–1012.
39. T. Tsuji, K. Iryo, Y. Nishimura, M. Tsuji, *J. Photochem. Photobiol. A: Chem.*, 145 (2001) 201–207.
40. T. Tsuji, K. Iryo, H. Ohta, Y. Nishimura, *Jpn. J. Appl. Phys.*, 39 (2000) L981–L983.
41. T. Sakka, S. Masai, K. Fukami, *Spectrochim. Acta B*, 64 (2009) 981–985.
42. Y.H. Ogata, M.H. Hong, K.Y. Ng, Q. Xie, L.P. Shi, T.C. Chong, *Appl. Phys. A*, 93 (2008) 153.
43. W. Soliman, N. Takada, K. Sasaki, *Appl. Phys. Express*, 3 (2010) 035201–035203.
44. Z. Yan, R. Bao, R.N. Wright, D.B. Chrisey, *Appl. Phys. Lett.*, 97 (2010) 124106–124108.
45. K. Siskova, B. Vlckova, P.-Y. Turpin, A. Thorel, M. Prochazka, *J. Phys. Chem. C*, 115 (2011) 5404.
46. R. Zamiri, B.Z. Azmi, A.R. Sadrolhosseini, H.A. Ahangar, A.W. Zaidan, M.A. Mahdi, *Int. J. Nanomed.*, 6 (2011) 71–75.
47. S. Yang, W. Cai, G. Liu, H. Zeng, *J. Phys. Chem. C*, 113 (2009) 7692–7696.
48. K. Siskova, B. Vlckova, P.-Y. Turpin, C. Fayet, *J. Phys. Chem. C*, 112 (2008) 4435–4443.
49. T.X. Phuoc, Y. Soong, M.K. Chyu, *Opt. Lasers Eng.*, 45 (2007) 1099–1106.
50. V. Amendola, S. Polizzi, M. Meneghetti, *Langmuir*, 23 (2007) 6766–6770.
51. T. Tsuji, Y. Okazaki, T. Higuchi, M. Tsuji, *J. Photochem. Photob. A*, 183 (2006) 297–303.
52. S. Petersen, A. Barchanski, U. Taylor, S. Klein, D. Rath, S. Barcikowski, *J. Phys. Chem. C*, 115 (2011) 5152–5159.
53. E. Messina, E. Cavallaro, A. Cacciola, M.A. Iati, P.G. Gucciardi, F. Borghese, P. Denti, R. Saija, G. Compagnini, M. Meneghetti, V. Amendola, O.M. Marago, *ACS Nano*, 5 (2011) 905–913.
54. A. Menendez-Manjon, B.N. Chichkov, S. Barcikowski, *J. Phys. Chem. C*, 114 (2010) 2499–2504.
55. M. Kalyva, G. Bertoni, A.Milionis, R. Cingolani, A. Athanassiou, *Microsc. Res.Tech.*, 73 (2010) 937–943.
56. E. Axente, M. Barberoglou, P.G. Kuzmin, E. Magoulakis, P. A. Loukakos, E. Stratakis, G.A. Shafeev, C. Fotakis, 2010, http://arxiv.org/abs/1008.0374.
57. S. Besner, A.V. Kabashin, F.M. Winnik, M. Meunier, *J. Phys. Chem. C*, 113 (2009) 9526–9531.
58. S. Petersen, S. Barcikowski, *J. Phys. Chem. C*, 113 (2009) 19830–19835.
59. K. Saitow, T. Yamamura, T. Minami, *J. Phys. Chem. C*, 112 (2008) 18340–18349.
60. M. Maaza, H. Chambalo, S. Ekambaram, O. Nemraoui, B.D. Ngom, N. Manyala, *Int. J. Nanopart.*, 1 (2008) 212–223.
61. W.T. Nichols, T. Sasaki, N. Koshizaki, *J. Appl. Phys.*, 100 (2006) 114911–114913.
62. F. Mafune, J. Kohno, Y. Takeda, T. Kondow, *J. Phys. Chem. B*, 107 (2003) 4218.
63. S.C. Singh, R.K. Swarnkar and R. Gopal, *Bull. Mater. Sci.*, 33 (2010) 21–26.
64. S.C. Singh and R. Gopal, *Appl. Surf. Sci.* (2010). doi:10.1016/j.apsusc.2011.05.018.
65. S.C. Singh, *J. Nanopart. Res.* (2011). doi:10.1007/s11051-011-0359-2.
66. S.C. Singh and R. Gopal, *J. Phys. Chem. C*, 112 (2008) 2812.
67. S.C. Singh and R. Gopal, *Phys. E*, 40 (2008) 724.
68. A.S. Nikolov, P.A. Atanasov, D.R. Milev, T.R. Stoyanchov, A.D. Deleva, Z.Y. Peshev, *Appl. Surf. Sci.*, 255 (2009) 5351.
69. S.C. Singh, R.K. Swarnkar and R. Gopal, *J. Nanosci. Nanotech.*, 9 (2009) 5367.
70. N. Takada, T. Sasaki, K. Sasaki, *Appl. Phys. A: Mater. Sci. Process., Appl. Phys. A*, 93 (2008) 833.
71. S.I. Dolgaev, A.V. Simakin, V.V. Voronov, G.A. Safeev, F. Bozon-Verduraz, *Appl. Surf. Sci.*, 186 (2002) 546.
72. J.S. Golightly and A.W. Castleman, *J. Phys. Chem. B*, 110 (2006) 19979.
73. C.-N. Huang, J.-S. Bow, Y. Zheng, S.-Y. Chen, N. J. Ho, P. Shen, *Nanoscale Res. Lett.*, 5 (2010) 972.
74. S.C. Singh, R.K. Swarnkar and R. Gopal, *J. Nanopart. Res.*, 11 (2009) 1831.
75. S.C. Singh and R. Gopal, *J. Phys. Chem. C*, 114 (2010) 9277.
76. H. Zeng, W. Cai, Y. Li, J. Hu, P. Liu, *J. Phys. Chem. B*, 109 (2005) 18260.
77. C. Liang, Y. Shimizu, M. Masuda, T. Sasaki, N. Koshizaki, *Chem. Mater.*, 16 (2004) 963.
78. H. Usui, T. Sasaki, N. Koshizaki, *Chem. Lett.*, 34 (2005) 700.
79. H. Usui, T. Sasaki, N. Koshizaki, *Chem. Lett.*, 35 (2006) 752.
80. Z. Yan, R. Bao, D.B. Chrisey, *Chem. Phys. Lett.*, 497 (2010) 205.
81. M.A. Gondal, Q.A. Drmosh, Z.H. Yamani, T.A. Saleh, *Appl. Surf. Sci.*, 256 (2009) 298–304.
82. I.L. Liu, B.C. Lin, S.Y. Chen, P. Shen, *J. Phys. Chem. C*, 115 (2011) 4994–5002.
83. G. Viau, V. Collière, L.-M. Lacroix, G.A. Shafeev, *Chem. Phys. Lett.*, 501 (2011) 419–422.
84. K. Zhang, D.S Ivanov, R.A Ganeev, G.S. Boltaev, P.S. Krishnendu, S.C. Singh, M.E. Garcia, I.N. Zavestovskaya and C. Guo, *Nanomaterials*, 9 (2019) 767.

85. P.V. Kamat, M. Flumiani, G. V. Hartland, *J. Phys. Chem. B*, 102 (1998) 3123–3128.
86. K. Yamada, Y. Tokumoto, T. Nagata, F. Mafune, *J. Phys. Chem. B*, 110 (2006) 11751–11756.
87. K. Yamada, K. Miyajima, F. Mafune, *J. Phys. Chem. C*, 111 (2007) 11246–11251.
88. A. Takami, H. Kurita, S. Koda, *J. Phys. Chem. B*, 103 (1999) 1226–1232.
89. S. Inasawa, M. Sugiyama, Y. Yamaguchi, *J. Phys. Chem. B*, 109 (2005) 9404–9410.
90. H, Reiss, I.B. Wilson, *J. Coll. Sci.*, 3 (1948) 551–561.
91. D. Werner and S. Hashimoto, *J. Phys. Chem. C*, 115 (2011) 5063–5072.
92. A. Pyatenko, M. Yamaguchi, M. Suzuki, *J. Phys. Chem. C*, 113 (2009) 9078–9085.
93. J.H. Hodak, A. Henglein, M. Giersig, G.V. Hartland, *J. Phys. Chem, B*, 104 (2000) 11708–11718.
94. S.C. Singh, S.K. Mishra, R.K. Srivastava, R. Gopal, *J. Phys. Chem. C*, 114 (2010) 17374–17384.
95. S. Link, C. Burda, B. Nikoobakht, M.A. El-Sayed, *J. Phys. Chem. B*, 104 (2000) 6152–6163.
96. Y.-H. Chen and C.-S. Yeh, *Chem. Comm.*, 4 (2001) 371.
97. J. Zhang, J. Worley, S. Denommee, C. Kingston, Z.J. Jakubek, Y. Deslandes, M. Post, B. Simard, *J. Phys. Chem. B*, 107 (2003) 6920.
98. F. Mafune, J. Kohno, Y. Takeda, T. Kondow, *J. Phys. Chem. B*, 107 (2003) 12589.
99. M. Kawasaki, K. Masuda, *J. Phys. Chem. B*, 109 (2005) 9379.
100. M.A. Gelesky, A.P. Umpierre, G. Machado, R.R.B. Correia, W.C. Magno, J. Morais, G. Ebeling, J. Dupont, *J. Am. Chem. Soc.*, 127 (2005) 4588.
101. H. Usui, T. Sasaki, N. Koshizaki, *J. Phys. Chem. B*, 110 (2006) 12890–12895.
102. H. Zeng, S. Yang, W. Cai, *J. Phys. Chem. C*, 115 (2011) 5038–5043.

13

Laser-Induced Forward Transfer

Alexandra Palla Papavlu and Thomas Lippert

CONTENTS

13.1 Introduction 149
  13.1.1 LIFT with a Sacrificial Layer 150
  13.1.2 LIFT of Liquids 152
13.2 LIFT in Science: Examples of Materials and Devices Transferred by LIFT 153
13.3 LIFT in Industry 156
13.4 Conclusions and Future Directions 157
Acknowledgements 157
References 157

13.1 Introduction

Nowadays the field of electronics, in particular the fabrication of integrated circuits, micro- and nanodevices, is dominated by various microfabrication processes, in particular by lithography technologies. These technologies are used to fabricate different-sized patterns, from the nanoscale, i.e. from few nanometres, to the mesoscale, i.e. micrometres to millimetres, which ultimately may be arranged in various architectures to create complex structures.

Depending on the fabrication technology source type, i.e. applications envisioned, the majority of the lithography techniques fall into two categories: techniques that require masks or moulds (such as photolithography, [1] soft lithography [2], and nanoimprint lithography (NIL) [3]) and direct write techniques (such as electron beam and focused ion beam lithography [4,5], scanning probe lithography [6], screen printing, inkjet printing) or laser direct write techniques (such as laser-induced forward transfer (LIFT)) [7].

The use of laser direct writing methods, in particular LIFT for printing various materials and its ability to integrate dissimilar materials into devices, is the fulcrum of this chapter. Therefore, first, we will briefly introduce the conventional printing techniques, showing their advantages and limitations, followed by a brief history of the laser direct writing methods, i.e. LIFT, ultimately showing few examples of its variations and some of the most successful applications.

Photolithography is the main technique used in industry for pattern transfer and microdevice fabrication. Depending on the working principle, photolithography may be divided into contact, proximity, and projection lithography. Contact and proximity photolithography relies on the exposure of a polymer, i.e. a photoresist to UV light, through a photomask which allows the definition of the desired pattern. Photolithography is a multistep process – i.e. firstly, a thin film of photoresist is coated onto a substrate, and then the photomask with the desired pattern is positioned above the photoresist (in contact, close proximity, or projection). The photoresist that is not covered by the photomask is illuminated with UV light and becomes soluble or insoluble, and the photoresist that is covered by the photomask may be removed (or remains) in a subsequent dissolving step.

Projection photolithography is a technique in which a system of optical lenses is used which focus the UV light onto the photoresist, thus allowing the reduction of the patterns to few nanometres [8].

Soft lithography is a class of techniques applied for rapid prototyping micro- and nanoscale structures and devices. There is a large number of techniques, e.g. microcontact printing [9], replica moulding [10], microtransfer moulding [11], and nanotransfer printing [12], just to name a few, which fall into the soft lithography category. All these techniques are basically based on printing, moulding, and embossing with an elastomeric stamp.

Similar to soft lithography, NIL utilizes a stamp, mould, master, template, or shim to physically deform a polymer for nanoscale patterning [13]. In order to achieve high throughput and high resolution at a relatively low cost, nowadays different versions of NIL, i.e. thermal wafer-scale NIL, UV wafer-scale NIL, UV step, and repeat NIL and roll-to-roll printing, have emerged.

Electron beam and focused ion beam lithography complement the main fabrication techniques for nanoscale patterns. These techniques use either an electron beam or a focused ion beam (e.g. gallium ions) to scan the surface of a sample. The high resolution of the techniques, i.e. 2–20 nm, makes them appealing for applications in microelectromechanical systems (MEMS) or protein engineering.

Scanning probe lithography utilizes a sharp scanning probe (most of the techniques use the tip of an atomic force microscope (AFM)) to heat, scratch, oxidize, or transfer material to a surface for patterning nanoscale features [14]. The most common of the scanning probe lithography methods is the dip-pen nanolithography technique, which relies on coating the probe of an AFM with the material to be transferred, i.e. ink, polymer, and upon contact with a surface, deposits the material. This approach is used in a variety of applications, including surface assembly, nanoelectronics, and cell–surface interactions [15].

These techniques, although allowing patterning with ultrahigh resolution, i.e. down to few nanometres, are limited in industrial applications, for mass production. In contrast, direct write techniques such as screen printing and inkjet printing are widely used for mass production; however, their lateral resolution lies in the micrometre range, e.g. around 70 µm in the case of screen printing.

Screen printing is a low-cost technique in which a paste or a precursor of the material to be transferred is applied onto a steel mesh (i.e. the screen) which is pre-patterned with the desired feature. The paste or precursor is pressed with force through the screen, thus transferring the pattern onto the substrate. This technique has the advantage that thick layers can be realized.

To date, *inkjet printing* is the most popular printing technology. This technique relies on the production of droplets containing the material of interest, which are propelled through a nozzle onto a substrate. Depending on the mechanism of transfer, there are two categories of inkjet printing technologies: continuous inkjet and drop-on-demand. Continuous inkjet printing is based on the continuous generation of droplets, which makes it a rather wasteful process and thus is not widely used. In contrast, drop-on-demand inkjet printing is simpler than continuous inkjet printing, and droplets are ejected on demand.

Despite the advancements in classical printing technologies, there are still many challenges to surmount. For example, most of these techniques are not flexible as they use cylinder, masks, and screens. In addition, the use of solvents is also an issue for applications which require the fabrication of multilayers. Finally, there is a stringent need for new materials with tailored properties, and alternative sintering and curing techniques so that heat addition to the printed flexible substrates can be kept minimal.

Since the invention of the first laser in 1960, laser-based techniques and related applications have developed rapidly. Nowadays, lasers are standard tools in different fields, i.e. in industrial processes like cutting or welding, in medicine for eye surgeries, or tattoo removals. Moreover, recently, the laser-based techniques used in microfabrication and microstructuring applications [16] are close to the transition from the research laboratories to industry.

One of the laser-based techniques used for microfabrication applications, which has drawn a lot of attention over the years, is laser-induced forward transfer (LIFT). LIFT is a direct write method, initially developed for the graphics industry, to write inks to glass substrates [17,18]. In 1986, Bohandy et al. were the first to use LIFT to transfer Cu metal films from a quartz substrate with an excimer laser working at 193 nm, first in vacuum and one year later in air [19].

The basic principle of LIFT is rather simple; i.e., the material to be printed is spread as a thin film (named the donor film) onto a substrate which is transparent to the laser radiation (also known as the donor substrate). The laser beam is either focused or imaged through the donor substrate onto the donor film (see Figure 13.1a). Each laser pulse interacts with the donor film material, and with a high enough laser energy per pulse, the material is delaminated from the donor substrate and is transferred onto the receiver substrate placed parallel and in close proximity to the donor. The shape and dimension of the transferred material is determined by the shape of the laser beam. The entire donor–receiver system is placed onto a *xyz* stage, thus allowing the transfer of arbitrary patterns onto the receiver substrate. In addition, another advantage of LIFT is that the process is carried out in air and at ambient temperature, without any additional photolithography step.

Conventional LIFT, i.e. with the material to transfer directly deposited onto a transparent donor support, works well for inorganic materials such as metals or ceramics, e.g. Al_2O_3 [20]. However, soft materials, e.g. polymers, proteins, cells, and tissues, or more complex materials such as superconductors can be transferred using different variations of LIFT, in which an additional layer is added to the donor system between the material to transfer and the transparent support. This is due to the fact that soft materials may be damaged by the laser beam during transfer due to thermal or photochemical decomposition. In addition, an interlayer that absorbs the laser radiation is needed in case of none or weakly absorbing materials, where standard LIFT proves to be difficult. Therefore, in the literature, there are various reports on LIFT with an additional light-absorbing layer. This layer, on the one hand, absorbs the laser radiation and at the same time shields the material of interest from the laser light. Various names have been given to LIFT with an interlayer between the material to transfer and the transparent support, e.g. blister actuated LIFT [21], dynamic release layer (DRL) LIFT [22], and absorbing film-assisted (AFA) LIFT [23], just to name a few. A sketch of LIFT with an interlayer in the donor system is shown in Figure 13.1b.

13.1.1 LIFT with a Sacrificial Layer

The first LIFT experiments using an additional interlayer were carried out in 1993 [24]. The authors of the study used an aluminium thin film as an interlayer, which they named light-to-heat conversion layer due to the transfer mechanism which was purely thermal [25]. Later studies showed the successful transfer of different materials with metal interlayers, also known as sacrificial layers. The basic principle relies on superheating the metal interlayer with the laser beam, generating a plasma which expands, and thus, the material on top is ejected.

Another variation of LIFT is using polymer thin films as a sacrificial layer. One class of polymers used as DRL or sacrificial layers is represented by photodegradable polymers, e.g. polymers that incorporate the triazene unit into the backbone. The chemical structure of the triazene polymers is shown in Figure 13.2.

In the case of the TP used as a DRL, the photons break specific chemical bonds and thus decompose the polymer completely into gaseous products initiating the forward

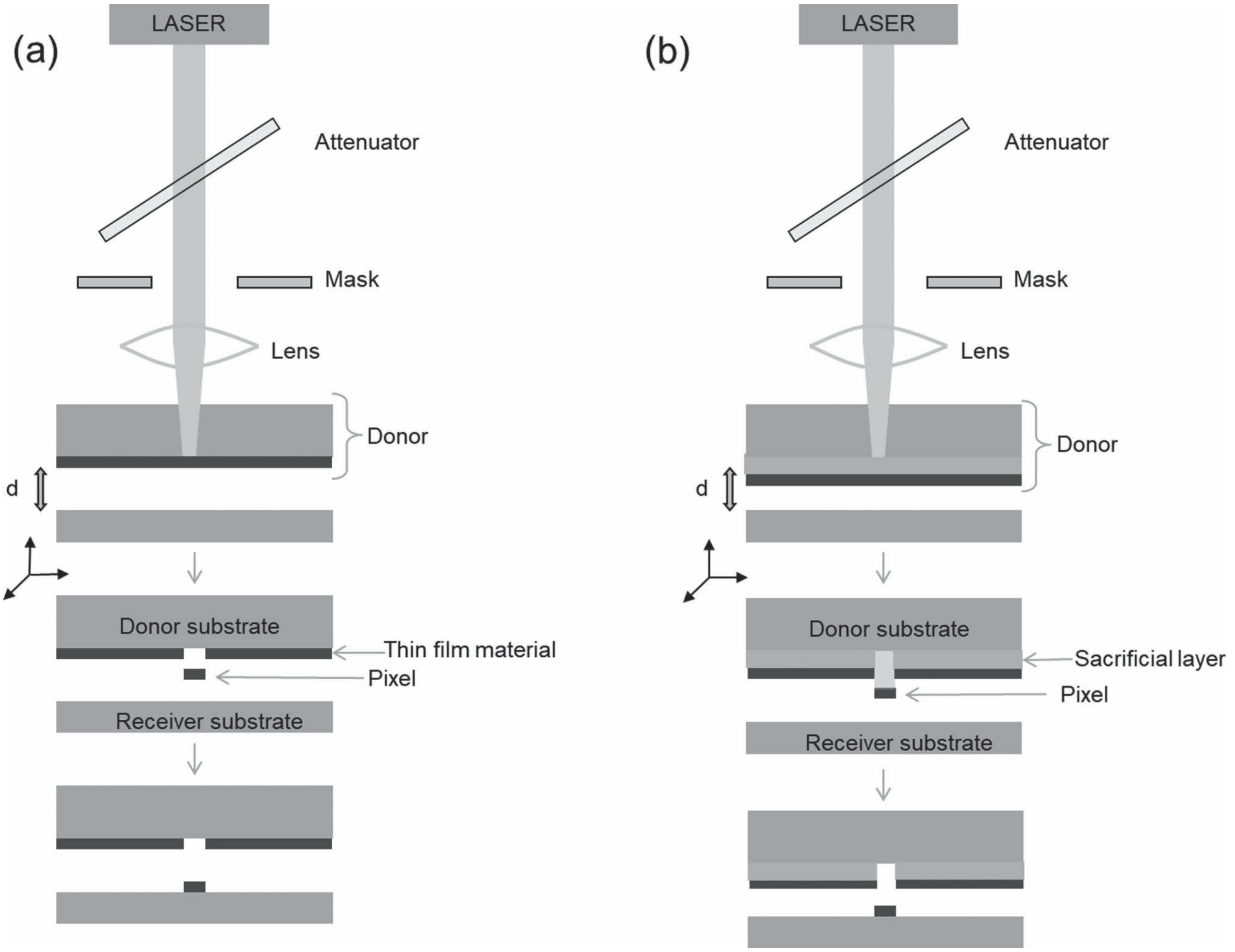
(a)
LASER
Attenuator
Mask
Lens
Donor
d
Donor substrate
Thin film material
Pixel
Receiver substrate
(b)
LASER
Attenuator
Mask
Lens
Donor
d
Donor substrate
Sacrificial layer
Pixel
Receiver substrate

FIGURE 13.1 The basic principle of LIFT (of solid thin films). (a) The laser is focused at the interface transparent donor substrate – material to be transferred. The material is heated by the laser light, and due to the heat expansion, a flyer is ejected. (b) The laser is focused at the interface transparent donor substrate – sacrificial layer. The sacrificial layer absorbs the laser radiation, at the same time shielding the material of interest from the laser light, and transfers the material on top onto the nearby receiver substrate.

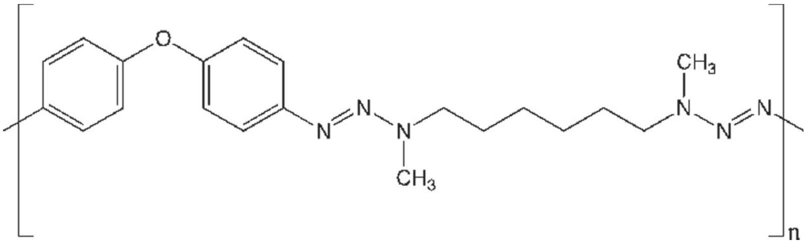
O
N
N
N
CH3
CH3
N
N
N
n

FIGURE 13.2 Chemical structure of the triazene polymer used as a DRL in most of the LIFT experiments.

transfer of the material of interest. One of the advantages of the TP is the fact that they absorb and decompose between 150 and 360 nm, making them well suited for irradiation with different wavelengths of laser [26]. Two absorption maxima can be distinguished in the UV-VIS absorption spectrum of a typical triazene polymer thin film, one around 200 nm which can be assigned to the aromatic system and one around 330 nm which corresponds to the triazene unit, as shown in Figure 13.3 [27].

Adjusting the TP thickness to achieve a well-defined transfer made it possible to transfer a wide range of materials and functional devices, from polymers for sensors [28], biomaterials [29], cells in a polymer matrix [30], and organic light-emitting diodes (OLEDs) [31].

Following the works on LIFT with an intermediate layer, a new approach was developed, based on chemically unstable materials that decompose upon absorption of UV radiation. This technique was named reactive LIFT [32], and it was

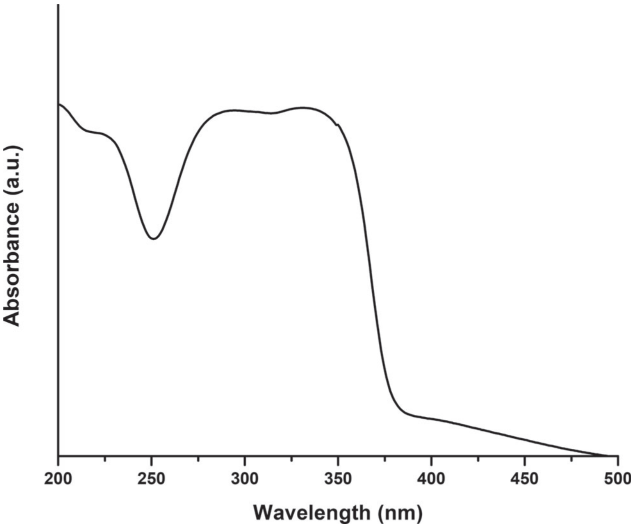

FIGURE 13.3 UV-VIS spectra of the triazene polymer thin film spin-coated onto a fused silica plate.

used for the transfer of metal oxide semiconductor materials aiming at sensor applications [33]. Tin oxide was transferred by an irradiation of a metal complex precursor material, i.e. acetylacetonate $SnCl_2(acac)_2$, with a 308 nm laser beam. Upon irradiation, the $SnCl_2(acac)_2$ acts as a DRL and partially decomposes to SnO_2. These materials are particularly appealing due to fact that they are cheap, have low deposition temperatures, are ideal for implementation onto flexible substrates, and present an excellent potential for scaling-up.

13.1.2 LIFT of Liquids

The implementation of LIFT that can compete on an equal basis with the more conventional direct writing techniques is expected to advance the state of the art within the fields of microelectronics for the fabrication of devices (sensors or OLEDs) and also biology for microarray fabrication or tissue engineering. The possibility of LIFT to print directly not only solid materials but also fluids from thin liquid films can direct the future industrial implementation of the technique as a realistic goal. In addition to this, in this section we will show that with LIFT, it is possible to print liquid materials with a resolution in the order of one or several micrometer(s). Thus, with liquid-phase LIFT, it is possible to obtain comparable levels of integration to the usual photolithography, with consequent advantages in terms of speed and flexibility. While the latter is at a higher stage of development, LIFT has significant advantages for the fabrication of microarrays: no problems related to printing head (nozzle) clogging or tips cleaning, only minor limitations on the rheological properties of solutions to deposit, and the ability to work with lower sample volumes.

Demonstrations of LIFT using liquid donor films with different DRLs are reported in the literature. A large number of functional materials have been transferred by LIFT aiming at applications in chemical sensors [34], biosensors, or tissue engineering, e.g. proteins [35,36], DNA [37], cells [30], and even tissue [38].

In addition to the works presented above, studies on the ejection mechanism in the case of LIFT of liquids have been carried out and a completely different behaviour to the case of solids has been found. The principle of LIFT for material transfer in a liquid phase is shown in Figure 13.4a. In the case of LIFT of liquids, both with polymers and with metal DRL layers, the transfer mechanism is dominated by the formation of long needle-like jets (see Figure 13.4b), which upon contact with the receiver substrate form sessile droplets. Liquid-phase LIFT is driven by the formation and expansion of a high-pressure vapour bubble. This bubble is attributed to the plasma formed after laser ablation of the metal DRL layer. The bubble expansion process can result in three different situations depending on the applied laser fluence. At low fluences, a needle-like jet is developed; however, this jet has not enough energy to overcome the surface tension forces, and thus, the jet does not reach the receptor and no material is transferred. At intermediate fluences, the same jet is formed, but in this case, it advances at a constant velocity while getting thinner. At high fluences, the bubble expansion is so violent that it overcomes the surface tension, resulting in bubble bursting. This is a situation which generates splashing on the receptor substrate [39,40]. A series of time-resolved images of liquid jets is presented in Figure 13.4b.

Conventional LIFT for liquids has emerged over the last years as a powerful technique for printing a wide class of biomaterials in particular for the fabrication of microarrays (see Figure 13.4c), being an interesting alternative to other printing techniques, since it is free from the clogging problems characteristic of inkjet printing, and also from the contamination issues usually associated with the incorrect cleaning of pins in dip-pen printing. In addition, LIFT allows achieving higher degrees of resolution. However, it presents the drawback of requiring the preparation of the liquid to be printed in thin film form, which limits its possibilities towards industrialization.

In the studies reported in Ref. [41] a new idea for a laser-based technique allowing the direct printing of biological solutions without the need for preparing the liquid in thin film form has been developed. Thus, the main drawback of conventional liquid LIFT can be overcome. The new technique allows a significant improvement in micropatterning in terms of control, reproducibility, and resolution.

The operating principle of this new technique relies on strongly focusing a femtosecond pulsed laser beam inside the liquid to be printed just below the free surface, so that the laser pulse energy is absorbed in a tiny volume around the focal point. This generates a cavitation bubble that projects a small fraction of the liquid beyond the free surface, and the liquid is deposited on a substrate as a printed droplet. The displacement of the substrate with respect to the free surface allows the realization of micropatterns. In order to obtain the proper absorption, two conditions are mandatory: (i) The liquid must be either transparent to or weakly absorbing of the laser radiation; otherwise, the absorption would take place right at the surface and not below. This condition is fulfilled by almost any biomolecule solution. (ii) The laser beam must be tightly focused, so that absorption occurs in the beam waist and not in the rest of the beam path.

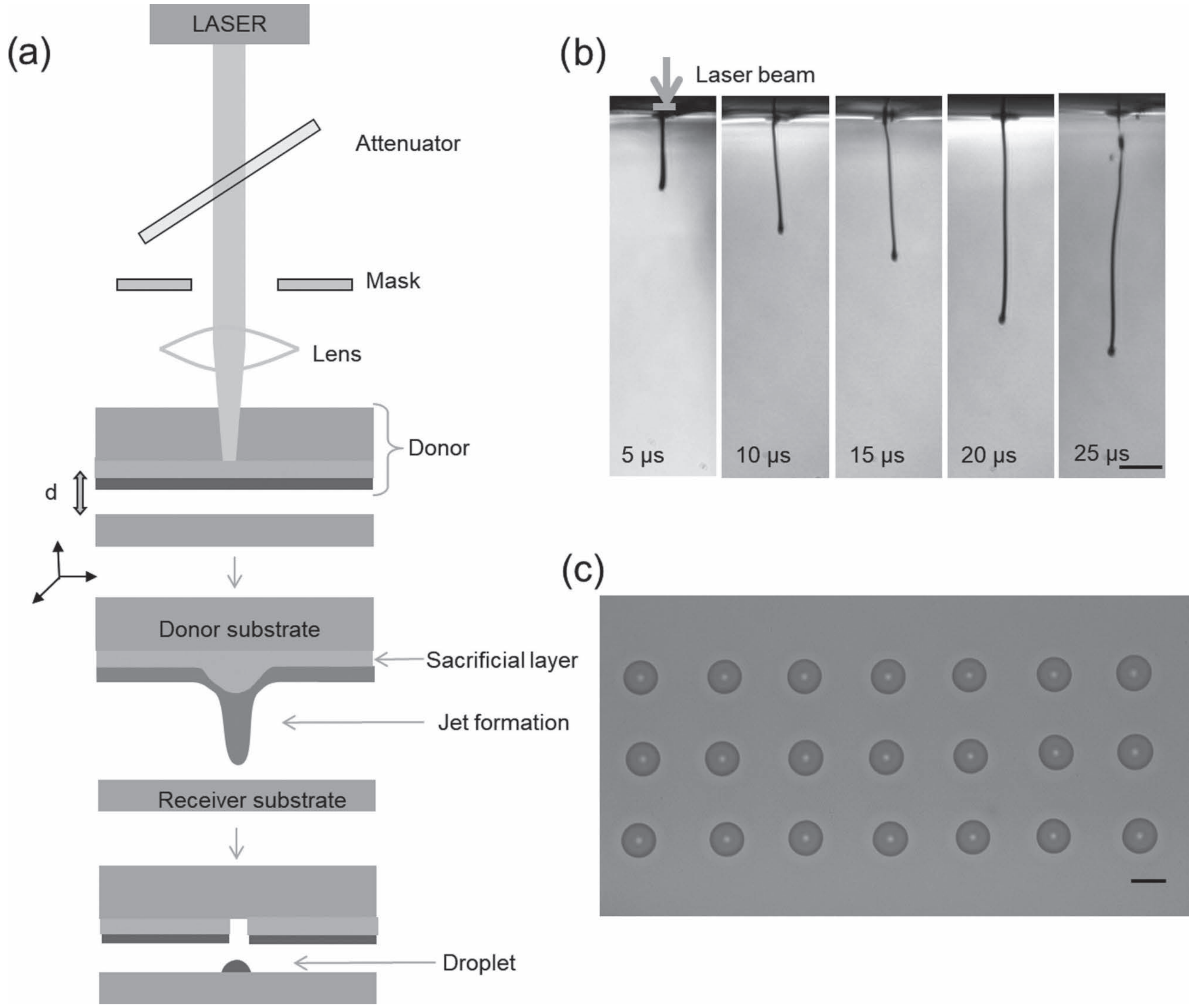

FIGURE 13.4 (a) The principle of LIFT (the material of transfer is in the form of a liquid layer). (b) Time-resolved images of TP-LIFT. The laser used for irradiation is the XeCl (308 nm), the TP layer is 60 nm, and the laser fluence is 25 mJ cm^{-2}. Scale bar is 500 µm. (c) Optical microscopy image of a microarray printed by TP-LIFT (TP thickness is 60 nm) on glass at 25 mJ cm^{-2}. Scale bar is 50 µm.

However, one of the main disadvantages of this technique is the use of femtosecond laser, which, at present, makes it a rather expensive alternative.

13.2 LIFT in Science: Examples of Materials and Devices Transferred by LIFT

Since the first experiments of LIFT, this technique was successfully applied for the transfer of various materials both in solid and in liquid phase as well as complex materials which were ultimately integrated into functional devices. Below we will show a few examples of some of the materials transferred by LIFT and several other variations of the technique and also a few examples of functional devices fabricated with this method.

One of the most popular variations to LIFT is matrix-assisted pulsed laser evaporation – direct write (MAPLE-DW), a process similar to the matrix-assisted pulsed laser evaporation (MAPLE), which in turn is derived from the classical pulsed laser deposition (PLD) [42]. MAPLE is an organic thin film deposition technique, where the material of interest, a biological compound, or polymer is suspended into a solvent and the resulting solution is flash-frozen in liquid nitrogen in order to obtain a solid target [43]. This target is then irradiated with a laser beam, as in the case of PLD. MAPLE-DW has the advantage of MAPLE; i.e., it can be applied to most soft materials, combined with the lateral resolution of LIFT. MAPLE-DW has been mostly used for the transfer of polymers and organic compounds, including also some devices, such as batteries and sensors [44].

More recently, a technique similar to MAPLE-DW has been reported, namely laser decal transfer (LDT), which has been used to transfer custom metallic nanoinks [45] aiming at applications such as microbridges and microcantilevers [46,47]. With LDT, mostly high-viscosity nanoparticle suspensions

(1000–100 000 cP) were used as inks for the fabrication of the donors, unlike most of the works by other groups [48], where the nanoinks used in laser transfers have viscosities lower than 100 cP. In addition, this technique has been successfully proven for the fabrication of three-dimensional stacked structures [49].

A first example of successful solid material transfer with LIFT using a polymer intermediate layer, i.e. a triazene polymer, is the fabrication of polystyrene microbeads (PS-μbeads) microarrays on Thermanox coverslips, which can ultimately be applied in biochip applications. TP layers of 100 nm were used to propel close-packed monolayers of PS-μbeads, which do not suffer any chemical decomposition during transfer [50,51]. In the same study, an investigation of the transfer dynamics is shown; i.e. the authors use shadowgraphy imaging to get an insight into the transfer mechanism following the laser pulse. A scheme of the set-up for time-resolved imaging experiments for LIFT is shown in Figure 13.5a, while in Figure 13.5b and c, two pictures taken for back-side ablation of a PS-μbeads pixel on top of a 100-nm-thick triazene polymer layer together with the corresponding optical microscopy images of the pixels transferred are shown.

Another important field of application for LIFT and its variations is printing of different inks and pastes for the printed electronics industry. LIFT comes as a direct competitor of inkjet printing, which despite being a leader in the field, still presents some limitations mainly related to printing head clogging, resolution, and customized inks, just to name a few. Several studies have focused on the potential of LIFT for printing lines from different donor materials. One of the first examples where the possibility of printing long lines from liquid-phase donor materials by varying the distance between successive droplets is presented in Ref. [52] (see Figure 13.6a–c). Other studies focused on demonstrating the successful printing of silver lines narrower than 20 μm, which have a resistivity lower than 20 μΩ cm [53,54].

More recently, a number of studies from the group of P. Delaporte [55,56] have been focused on printing silver lines by LIFT and also on the investigation of the dynamics of the process in LIFT of silver inks. First, in Ref. [57], they showed the successful transfer by LIFT of conductive 20 μm-width silver lines at a velocity up to 4 m s^{-1} in three passes. Then, they demonstrated that they could print a continuous line in a single-step process by reaching velocities up to 17 m s^{-1}. Moreover, they carried out fundamental studies on the laser transfer process and found that below a minimum distance between two successive laser spots, it is not possible to print features with a high resolution, and in addition, high printing velocities do not allow the overlapping of the droplets and the single-step printing of a continuous line.

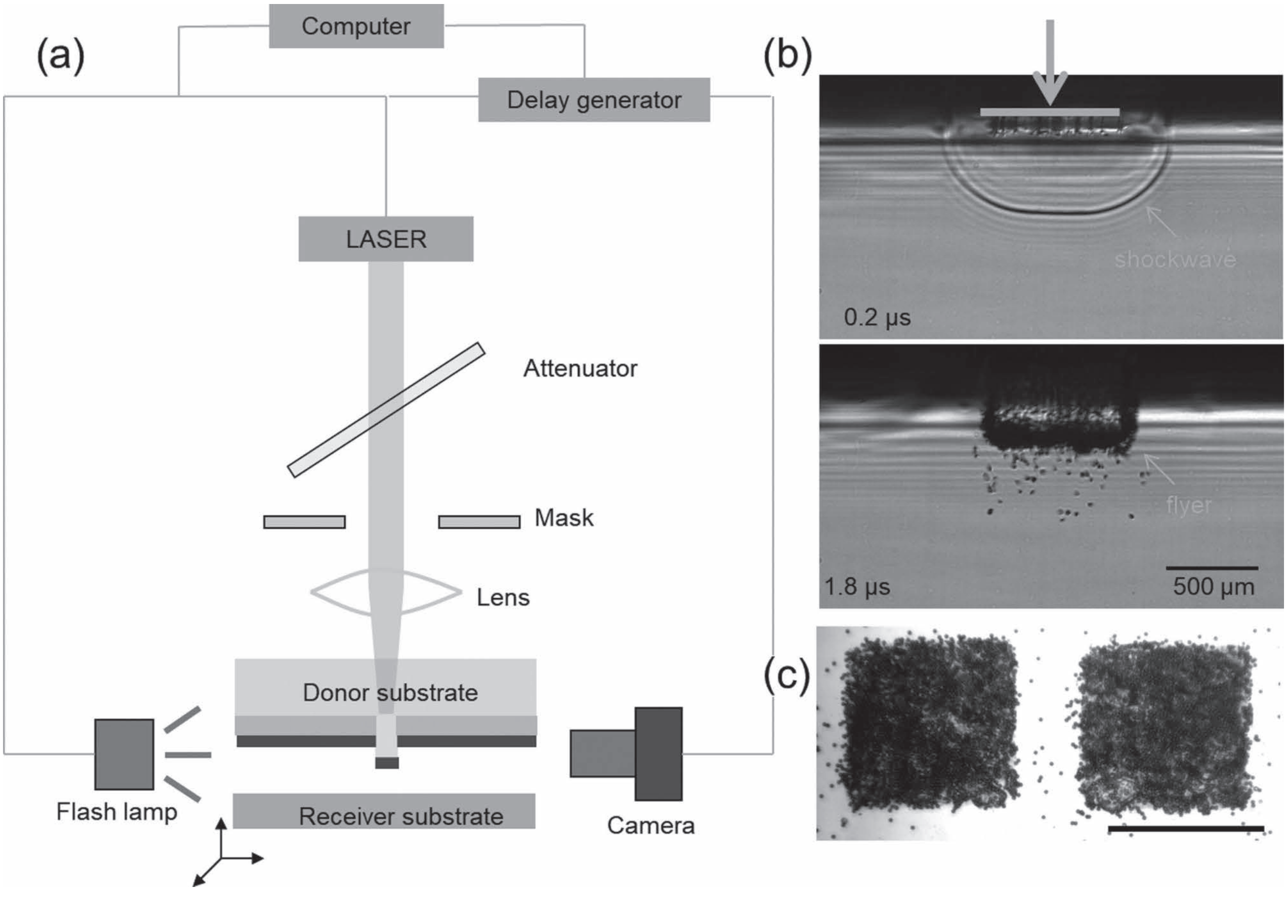

FIGURE 13.5 (a) Set-up for time-resolved imaging experiments for LIFT of solid donors. (b) Sequence of photographs taken for back-side ablation of a microbeads array on top of a 100 nm triazene polymer film at 1.5 J cm^{-2} laser fluence. (c) Two microbead pixels printed by LIFT at 2 J cm^{-2} (left-hand side image) and 1 J cm^{-2} (right-hand side image) laser fluence. Scale bar is 200 μm.

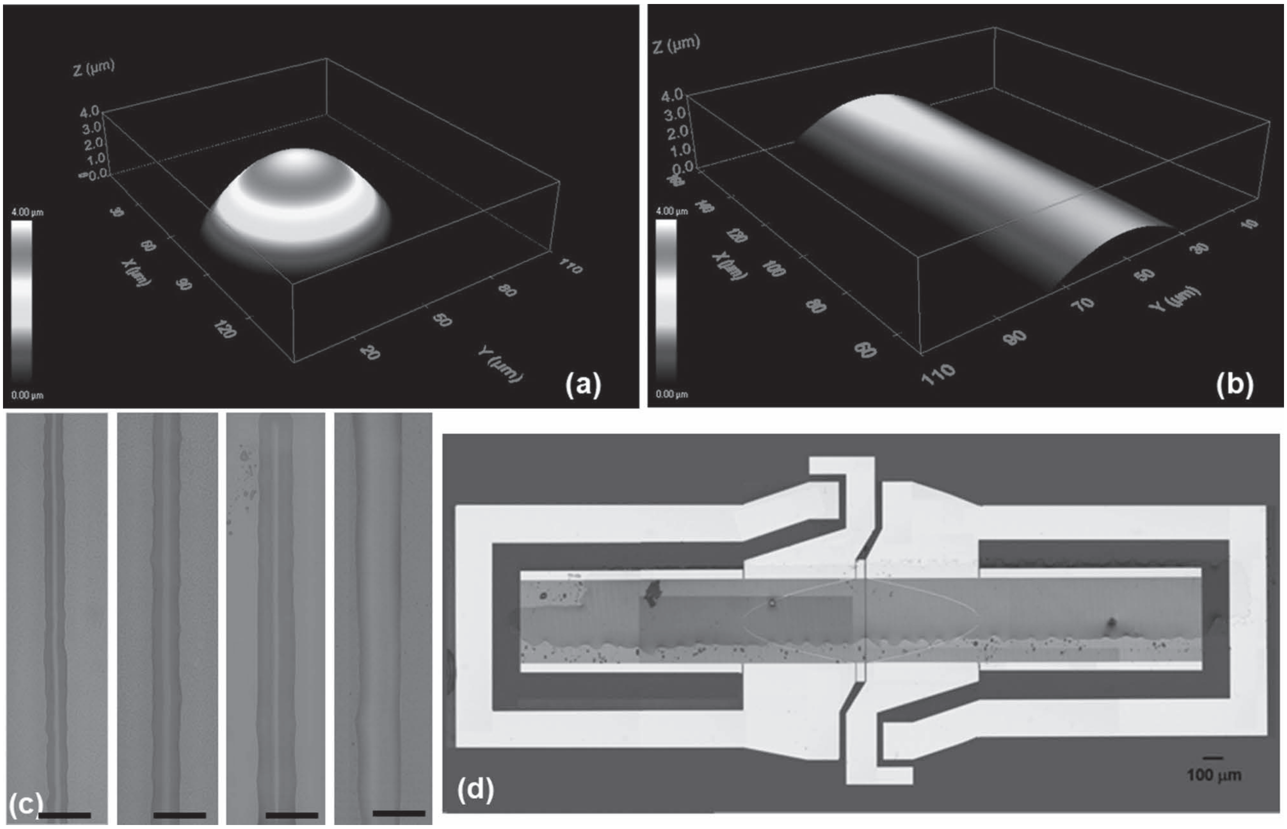

FIGURE 13.6 Confocal microscopy images of (a) a water:glycerol (50% v/v) droplet printed by LIFT, (b) a uniform water:glycerol (50% v/v) line obtained by printing successive individual droplets, (c) optical microscopy image of uniform lines. Printing direction is from top to bottom, and scale bar is 100 µm. (d) Optical microscopy images of a SAW device coated by overlapping droplets (20% v/v OBP solution) printed by LIFT at 700 mJ cm^{-2} laser fluence.

Further on, LIFT has been extensively used for the fabrication of sensors, and the following paragraphs briefly present few examples of the achievements.

A surface acoustic wave e-nose has been fabricated by printing different polymers, i.e. polyethylenimine, polyepichlorohydrin, polyisobutylene, hydroxypropylmethyl cellulose, and poly(styrene-co-maleic acid), partial isobutyl/methyl mixed ester on the interdigitated transducers of SAW devices. The functionality of the SAW e-nose was demonstrated by its ability to detect low concentrations of analytes (dichloromethane, dichloropentane, dimethyl methylphosphonate, ethyl acetate, and water) and also to discriminate between the tested analytes. The results obtained in Ref. [58,59] indicated that laser deposition of polymers onto SAW resonators is possible without significant modifications of their functionality and with a good reliability and reproducibility.

Not only sensors in solid phase, but also biosensors may be fabricated by LIFT, as it has been shown by Touloupakis et al. [60] and Palla Papavlu et al. [61]. Touloupakis et al. have demonstrated the successful fabrication of electrochemical-based biosensors for the detection of diuron and linuron herbicides. They used thylakoid proteins as active materials which were directly immobilized (taking advantage of the high pressures achieved during LIFT) onto the metal electrodes of the biosensors, thus eliminating an addition functionalization step.

In Ref. [62] a SAW biosensor array composed of SAW devices coated by LIFT with different odorant-binding proteins (OBPs) (see Figure 13.6d for an example of a SAW biosensor printed with a solution containing OBPs) has been described. The biosensor system was tested in N$_2$ atmosphere upon exposure to vapours of octenol (also called mushroom alcohol, is an enantiomer produced by several plants and fungi) and carvone (an enantiomer that smell like spearmint).

A last example of successful material printing by LIFT aiming at applications in the microelectronics field is presented below. Most of the applications envisioned target the domain of organic electronics, specifically the fabrication of OLEDs and organic thin film transistors (OTFTs). Different materials have been printed, e.g. organic semiconductors (CuPc, poly(3,3‴-didodecylquaterthiophene) (PQT-12), poly(3-hexylthiophene-2,5-diyl) (P3HT), distyryl-quaterthiophene (DS4T), bis(2-phenylthynyl) end-substituted terthiophene (diPhAc-3T), pentacene), and different metal nanoparticle inks or polymers such as poly(3,4-ethylenedioxythiophene)/poly(styrenesulfonate) (PEDOT: PSS) for the fabrication of the source and drain electrodes in OTFTs. Although OTFTs have been realized using other printing techniques, their laser printing has so far proven to be the only digital technique that works well with a wide range of materials. In our particular case, the OTFTs obtained by laser printing exhibited good electrical performances, with mobilities of few 0.01 cm^{2}V s^{-1}

and I_{on}/I_{off} of the order of 10^5. However, the laser printing process can also come with some drawbacks, such as the induction of mechanical stress or the structural reorganization of the material. In this context, the LIFT technique can be particularly attractive for the printing of organic materials having high structural cohesion.

The laser printing process has been successfully applied also for the fabrication of OLEDs, in particular polymer light-emitting diodes (PLEDs). Two main approaches have been considered to this end: (i) the single-step transfer of a solid multilayered stack [31,63] and (ii) the printing of an active organo-metallic material in liquid phase between two electrodes, as reported by the group of C. Arnold. In both of these instances, the use of a sacrificial DRL has proven to be mandatory in order to avoid the thermal or photochemical degradation of the luminescent material. As such, red-green-blue (RGB) pixels of PLEDs have been successfully achieved through the single-step transfer of a multilayered structure, without the loss of device performance. The functional properties of the obtained PLEDs (e.g. luminance, efficiency) are comparable to those of conventionally fabricated devices, while in the case of blue pixels, it was found to surpass them. For the electroluminescent devices printed in liquid phase, their testing in air revealed that the emission spectra, luminous efficiencies, and lifetimes are similar to those of devices fabricated in nitrogen environment. Multi-colour luminophore patterns with diameters down to 10 µm have also been printed with laser direct write, thus demonstrating the versatility of the technique [56,64].

To conclude, laser printing has been successfully applied to obtain organic devices exhibiting similar, or even superior, performances as compared to those obtained through conventional techniques. The technique allows for the downsizing of both pixel size and resolution. The simplicity of the procedure stems from its potential to transfer multilayer stacks of solid materials in a single step, without the need of subsequent thermal treatments. On the other hand, solid-state laser printing can lead to the formation of debris on the receiver and is not always easy to integrate in current industrial manufacturing production chains for organic electronic devices.

13.3 LIFT in Industry

For the past decade, LIFT technology has contributed to the direct writing of various materials, from simple metals to complex oxides and liquid-phase materials like biological compounds and living cells. LIFT and its modifications could be the technology that is used to create patterns with a feature size ranging from a few micrometres up to few millimetres which can ultimately be implemented into complex microscale structures. Unlike photolithography, LIFT doesn't require to be combined with special optics or other fabrication processes, like etching, being therefore well suited for transfer to industry.

Currently, in addition to the few patents that exist on LIFT, there are also a few companies which use LIFT and different variations of LIFT, adapted to the specific applications envisioned.

In this section, we will present some of the patents that exist on LIFT together with a couple of examples where LIFT has taken the next step forward and made it to industry.

The first patent on a technique used to transfer inks with a laser beam, named laser thermal printing, was submitted in 1993 [65]. The laser is absorbed in a heat-converting layer, and the ink is ejected due to the heat expansion. With this process, digital printing of images with high resolution can be achieved. The process got further developed and patented such that transfers from donor ribbons can be achieved [66,67].

Kodak improved the process further getting the capability of a roll-to-roll printing process where four-colour printing is possible in consecutive production steps [68]. Aurentum GmbH, which was taken over by LPKF Laser and Electronics AG in March 2015, has worked on the development (and obtained a patent) of a laser-based method for digital printing of viscous pastes [69–71].

Furthermore, Daetwyler Graphics AG from Switzerland has built a LIFT prototype for writing inks onto different substrates with a CW pulse-modulated laser working at 1070 nm wavelength [72]. The main idea is to develop a cheap alternative for small-scale rotogravure, i.e. for the production of individual packaging. They can achieve a printing speed of $5\,\mathrm{m\,s^{-1}}$ on for 1.2-m-wide foils. The operating principle of the LIFT prototype is based on a laser beam which passes through a transparent substrate and heats up the ink. The solvent vaporizes and the ink is transferred onto a substrate in proximity. In case of transparent inks, the donor substrate is coated with an absorbing layer. The laser light passes through the ink from the front and is absorbed in the layer below on the printing cylinder. The energy of the light is converted to heat and the solvent in the ink on top of it is vaporized leading to an ejection and a transfer.

Based on the same patents, the German company BASF has developed LTP technology [73] to write electrical connections on solar cells by using metal inks. In LTP, the transparent donor, named belt, is coated with the ink in a continuous process using an inking station. The substrate and the guide roll substrate are moved parallel with respect to the laser beam. The donor is moved circularly, and therefore, the unused ink can be recycled as the ink station controls the viscosity of the ink and can replace evaporated solvent if necessary.

This process already fulfils the main requirements for the commercial market as it has a similar speed to screen printing and it is contact-free, digital, and can achieve a line width of ≤60 µm. The ink contains silver or aluminium powders which are already well established in photovoltaic industry, and the printing process is capable with continuous wafer transportation.

Another process similar to LIFT, named LITI (laser-induced thermal imaging), has been patented by Samsung, and it is used for OLED fabrication [74]. In LITI, a light-to-heat conversion layer is used, which absorbs the infrared light, thus heating up the exposed area. This leads in turn to the delamination of the material from the donor which is pressed towards the close-contact receiver substrate. The three different colours for an OLED display are sub-sequentially transferred [75,76]. To overcome the possible damage of the OLEDs due to the separation of the donor and receiver – e.g. device degradation and the release of gases (e.g. O_2, H_2O etc.) from a polyimide film donor – Sony has developed an improved version named laser-induced pattern-wise sublimation (LIPS) [77,78]. In their process, the polymer foil is replaced with a rigid glass substrate, which is easier to align and use. The glass substrate is transferred into vacuum, and the deposition of different layers (hole injection layer, hole transport layer, and bottom electrodes) can be carried out by conventional evaporation. The donor substrate holding the emission layer is placed on top of it holding a small gap. Special clamping equipment holds up the gap in atmospheric pressure where the laser transfer takes place. The patterning of the individual pixel is carried out separately for each emission layer by the process. Other common layers such as an electron transport layer and a top electrode are formed on the patterned substrate after removing the donor glass in inert gas. In contrast to LITI, polymer transfer by LIPS is not possible.

13.4 Conclusions and Future Directions

In this chapter, we have reviewed the state of the art and applications of laser-based direct write techniques, in particular LIFT. LIFT, although a relatively new technology, as compared to conventional microfabrication techniques, such as lithography, has contributed to the advancement in the direct printing and patterning industry as well as the success of commercial ink printed for the graphics industry.

For the past 10 years, LIFT has come a long way, from printing different materials, from solids to liquids and customized inks, to their integration into devices, e.g. OLEDs, OTFTs, DNA and protein microarrays, and sensor devices. Modifications to LIFT have been extensively developed for specific applications: blister actuated LIFT for a wide range of bioapplications, LIFT with a metallic interlayer for bioelectronics, biosensors, and gas sensors, reactive LIFT for functional metal oxide semiconductor gas sensors. However, the amount of real sensors printed to this point is still low, and printing sensors is a time-consuming task and improvements of the process are absolutely essential.

Among them, triazene polymers have sturdily emerged as it is able to circumvent the issues in conventional LIFT technology, thereby allowing a high-throughput and high-resolution method with a relatively low cost. This emerging discipline provides alternative routes to overcome current technical barriers in many areas, including electronics, medicine, electromechanical systems, and biosensors. Such a dramatic advancement in science and technology is leading to technology revolutions in a broad range from the next-generation electronic devices to healthcare systems, from cosmetics to textiles, and from agriculture to high-tech businesses.

Up to this point only small amounts of sensors could be printed and the sensors have to be placed individually onto supporting substrates. The sensor microstructures are produced in wafer scale, and it would be desirable to coat the sensors directly on the wafer. Thus, large amounts of samples could be produced leading to a reduced amount of handling. This would in turn reduce the production time as well as the failures due to handling errors.

Moving towards large-scale production a set-up only for LIFT printing of sensors needs to be built. Printing under better controllable conditions is then possible, and faster production can be achieved with improved equipment and without the time required for set-up changes. Ideas about such a prototype were developed within the European e-LIFT project, and possible costs are in the range of 800 000 Euro.

Acknowledgements

Financial support from the Paul Scherrer Institute, the Romanian National Program 4N/2016, the Commission for Technology and Innovation CTI (Project No. 16713.1 PFNM-NM), and the Romanian National Authority for Scientific Research and Innovation, CNCS – UEFISCDI, Project Number PN-II-RU-TE-2014-4-2311 (Flex-SENS) is gratefully acknowledged.

REFERENCES

1. Pimpin A. and Srituravanich W. 2012 Review on micro- and nanolithography techniques and their applications, *Eng. J.* **16** (1) 37–55
2. Gates B. D., Xu Q., Stewart M., Ryan D., Willson C. G. and Whitesides G. M. 2005, New approaches to nanofabrication: Molding, printing, and other techniques, *Chem. Rev.* **105** 1171–96.
3. Chou S. Y., Krauss P. R. and Renstrom P. J. 1996 Imprint lithography with 25-nanometer resolution, *Science* **272** 85–87.
4. Grigorescu A. E. and Hagen C. W. 2009 Resists for sub-20-nm electron beam lithography with a focus on HSQ: state of the art, *Nanotechnol.* **20** 292001.
5. Tseng A. A. 2004 Recent developments in micromilling using focused ion beam technology, *J. Micromech. Microeng.* **14** R15–R34.
6. Shim W., Braunschweig A. B., Liao X., Chai J., Lim J. K., Zheng G. F. and Mirkin C. A. 2011 Hard-tip, soft-spring lithography, *Nature* **469** 516–520.
7. Arnold C., Serra P. and Pique A. 2007 Laser direct-write techniques for printing of complex materials, *MRS Bull.* **32** 23–31.
8. Rothschild M. 2005 Projection optical lithography, *Mater. Today* **8** 18–24.
9. Kumar A. and Whitesides G. M. 1993 Features of gold having micrometer to centimeter dimensions can be formed through a combination of stamping with an elastomeric stamp and an alkanethiol ink followed by chemical etching, *Appl. Phys. Lett.* **63** 2002–2004.
10. Xia Y. et al. 1997 Replica molding using polymeric materials: A practical step toward nanomanufacturing. *Adv. Mater.* **9** 147–149.
11. Zhao X. M., Xia Y. and Whitesides G. M. 1996 Fabrication of three-dimensional microstructures: Microtransfer molding, *Adv. Mater.* **8** 837–840.
12. Jeon S. et al. 2004 Three-dimensional nanofabrication with rubber stamps and conformable photomasks, *Adv. Mater.* **16** 1369–1371.

13. Schift H. 2015 Nanoimprint lithography: 2D or not 2D? A review, *Appl. Phys. A* **121** 415–435.
14. Garcia R., Knoll A. W. and Riedo E. 2014 Advanced scanning probe lithography, *Nature Nanotechnology* **9** 577–587.
15. Rosi N. L. and Mirkin C. A. 2005 Nanostructures in Biodiagnostics, *Chem. Rev.* **105** (4) 1547–1562.
16. Kopitkovas G., Lippert T., David C., Sulcas R., Hobley J., Wokaun A., and Gobrecht J. 2004 Laser micromachining of optical devices, *Proc. SPIE* **5662** 515.
17. Braudy R. S. 1969 Laser writing, *Proc. IEEE* **57** (10) 1771–1772.
18. Levene M. L., Scott R. D. and Siryj B. W. 1970 Material transfer recording, *Appl. Opt.* **9** (10) 2260–2265.
19. Bohandy J., Kim B. F. and Adrian F. J. 1986 Metal deposition from a supported metal film using an excimer laser, *J. Appl. Phys.* **60** (4) 1538–1539.
20. Greer J. A. and Parker T. E. 1988 Laser induced forward transfer of metal oxides to trim the frequency of surface acoustic wave resonator devices, *Proc. SPIE* **998** 113–125.
21. Kattamis N. T., Brown M. S., Arnold C. B. 2011 Finite element analysis of blister formation in laser-induced forward transfer, *J. Mater. Res.* **26** (18) 2438–2449.
22. Nagel M., Hany R., Lippert T., Molberg M., Nuesch F. A. and Rentsch D. 2007 Aryltriazene photopolymers for UV-laser applications: Improved synthesis and photodecomposition study, *Macromol. Chem. Phys.* **208** (3) 277–286.
23. Hopp B., Smausz T., Barna N., Vass C., Antal Z., Kredics L. and Chrisey D. B. (2005) Time-resolved study of absorbing film assisted laser induced forward transfer of Trichoderma longibrachiatum conidia, *J. Phys. D: Appl. Phys.* **38** 833–837.
24. Tolbert W. A., Sandy Lee I. Y., Doxtader M. M., Ellis E. W. and Dlott D. D. 1993 High-speed color imaging by laser ablation transfer with a dynamic release layer: fundamental mechanisms, *J. Imaging Sci. Technol.* **37** 411–421.
25. Lee S. T., Lee J. Y., Kim M. H., Suh M. C., Kang T. M., Choi Y. J., Park J. Y., Kwon J. H., Chung H. K., Baetzold J., Bellmann E., Savvateev V., Wolk M. and Webster S. 2002 A new patterning method for full-color polymer light-emitting devices: Laser induced thermal imaging (LITI), *SID Symp. Dig. Tech. Pap.* **33**(1) 784–787.
26. Palla Papavlu A. and Lippert T. (2017) Chapter 3: LIFT with a dynamic release layer. In *Laser Printing of Functional Materials: Electronics, 3D Microfabrication and Biomedicine* First Edition, A. Pique and P. Serra (eds.), Wiley-VCH Verlag GmbH & Co. KGaA, Weinheim.
27. Lippert T. 2009 UV Laser ablation of polymers: From structuring to thin film deposition. In *Laser-Surface Interactions for New Materials Production Tailoring Structure and Properties*, A. Miotello, P. M. Ossi (eds.), Springer Series in Materials Chemistry Vol. 130, Springer, Berlin, pp. 141–175.
28. Dinca V., Palla-Papavlu A., Dinescu M., Shaw-Stewart J., Lippert T., Di Pietrantonio F., Cannata D., Benetti M. and Verona E. 2010 Polymer pixel enhancement by laser-induced forward transfer for sensor applications, *Appl. Phys. A* **101**(3) 559–565.
29. Palla-Papavlu A., Paraico I., Shaw-Stewart J., Dinca V., Savopol T., Kovacs E., Lippert T., Wokaun A. and Dinescu M. 2011 Liposome micropatterning based on laser induced forward transfer, *Appl. Phys. A* **102**(3) 651–659.
30. Doraiswamy A., Narayan R., Lippert T., Urech L., Wokaun A., Nagel M., Hopp B., Dinescu M., Modi R., Auyeung R. and Chrisey D. 2006 Excimer laser forward transfer of mammalian cells using a novel triazene absorbing layer, *Appl. Surf. Sci.* **252** 4743–4747.
31. Fardel R., Nagel M., Nuesch F., Lippert T. and Wokaun A. 2007 Fabrication of organic light-emitting diode pixels by laser-assisted forward transfer, *Appl. Phys. Lett.* **91** 061103.
32. Mattle T., Hintennach A., Lippert T. and Wokaun A. 2013 Laser induced forward transfer of SnO_2 for sensing applications using different precursors systems, *Appl. Phys. A* **110** 309–316.
33. Palla Papavlu A., Mattle T., Temmel S., Lehmann U., Hintennach A., Grisel A., Wokaun A. and Lippert T. 2016 Highly sensitive SnO_2 sensor via reactive laser-induced transfer, *Sci. Rep.* **6** 25144.
34. Boutopoulos C., Touloupakis E., Pezzotti I., Giardi M. T. and Zergioti I. 2011 Direct laser immobilization of photosynthetic material on screen printed electrodes for amperometric biosensor, *Appl. Phys. Lett.* **98**(9) 093703-1–093703-3.
35. Dinca V., Ranella A., Farsari M., Kafetzopoulos D., Dinescu M., Popescu A. and Fotakis C. 2008 Quantification of the activity of biomolecules in microarrays obtained by direct laser transfer, *Biomed. Microdevices* **10**(5) 719–25.
36. Fernandez-Pradas J. M., Colina M., Serra P., Dominguez J. and Morenza J. L. 2004 Laser-induced forward transfer of biomolecules, *Thin Solid Films* **453–454** 27–30.
37. Karaiskou A., Zergioti I., Fotakis C., Kapsetaki M. and Kafetzopoulos D. 2003 Micro fabrication of biomaterials by the sub-ps laser-induced forward transfer process, *Appl. Surf. Sci.* **208** 245–249.
38. Chrisey D., Pique A., McGill R., Horwitz J., Ringeisen B., Bubb D. and Wu P. 2003 Laser deposition of polymer and biomaterial films, *Chem. Rev.* **103** 553–576.
39. Duocastella M., Fernandez-Pradas J., Dominguez J., Serra P. and Morenza J. 2008 Printing biological solutions through laser-induced forward transfer, *Appl. Phys. A* **93**(4) 941–945.
40. Duocastella M., Fernandez-Pradas J. M., Morenza J. and Serra P. 2009 Time-resolved imaging of the laser forward transfer of liquids, *J. Appl. Phys.* **106**(8) 084907-1–084907-7.
41. Patrascioiu A., Duocastella M., Fernández-Pradas J. M., Morenza J. L. and Serra P. 2011 Liquids microprinting through a novel film-free femtosecond laser based technique, *Appl. Surf. Sci.* **257** 5190–5194.
42. Eason R. (ed.) 2006 *Pulsed Laser Deposition of Thin Films: Applications – LED Growth of Functional Materials.* Wiley. ISBN: 978-0-471-44709-2.
43. Palla Papavlu A., Dinca V., Filipescu M. and Dinescu M. 2017 Matrix assisted pulsed laser evaporation of organic thin films: Applications in biology and chemical sensors. In *Laser Ablation – From Science to Applications*, T. E. Itina (ed.), Intech. ISBN 978-953-51-5565-2.
44. Ringeisen B. R., Chrisey D. B., Pique A., Young H. D., Modi R., Bucaro M., Jones Meehan J. and Spargo B. J. 2002 Generation of mesoscopic patterns of viable *Escherichia coli* by ambient laser transfer, *Biomaterials* **23** 161.
45. Piqué A., Auyeung R. C. Y., Metkus K. M., Kim H., Mathews S. A., Bailey T., Chen X. and Young L. J. 2008 Laser decal transfer of electronic materials with thin film characteristics, *Proc. SPIE* 6879, 687911-1–687911-8.

46. Auyeung R. C. Y., Kim H., Birnbaum A. J., Zalalutdinov M. K., Mathews S. A. and Piqué A. 2009 Laser decal transfer of freestanding microcantilevers and microbridges, *Appl. Phys. A*. **97** 513519.
47. Birnbaum A. J., Auyeung R. C. Y., Wahl K. J., Zalalutdinov M. K., Laracuente A. R. and Piqué A. 2010 Laser printed micron-scale free standing laminate composites: Process and properties, *J. Appl. Phys.* **108** 83526-1–83526-7.
48. Puerto D., Biver E., Alloncle A. P. and Delaporte P. 2016 Single step high-printing of continuous silver lines by laser-induced forward transfer, *Appl. Surf. Sci.* **374** 183–189.
49. Wang J., Auyeung R. C. Y., Kim H., Charipar N. A. and Piqué A. 2010 Three-dimensional printing of interconnects by laser direct-write of silver nanopastes, *Adv. Mater.* **22** 4462.
50. Palla-Papavlu A., Dinca V., Paraico I., Moldovan A., Shaw-Stewart J., Schneider C. W., Kovacs E., Lippert T. and Dinescu M. 2010 Microfabrication of polystyrene microbead arrays by laser induced forward transfer, *J. Appl. Phys.* **108** 033111-1–033111-6.
51. Palla Papavlu A., Dinca V., Luculescu C., Shaw-Stewart J., Nagel M. and Dinescu M. 2010 Laser induced forward transfer of soft materials, *J. Opt.* **12** 124114-1–124114-9.
52. Palla-Papavlu A., Córdoba C., Patrascioiu A., Fernández-Pradas J. M., Morenza J. L. and Serra P 2013 Deposition and characterization of lines printed through laser-induced forward transfer, *Appl. Phys. A* **110** 751.
53. Kim H., Auyeung R. C. Y., Lee S. H., Huston A. L. and Piqué A. 2009 Laser forward transfer of silver electrodes for organic thin-film transistors, *Appl. Phys. A* **96** 441–445.
54. Boutopoulos C., Kalpyris I., Serpetzoglou E. and Zergioti I. 2014 Laser-induced forward transfer of silver nanoparticle ink: time-resolved imaging of the jetting dynamics and correlation with the printing quality, *Microfluid. Nanofluid.* **16** (3) 493–500.
55. Biver E., Rapp L., Alloncle A. P., Serra P. and Delaporte P. 2014 High-speed multi-jets printing using laser forward transfer: Time-resolved study of the ejection dynamics, *Opt. Express* **22** (14) 17122–17134.
56. Delaporte P. and Alloncle A. P. 2016 Laser-induced forward transfer: A high resolution additive manufacturing technology, *Opt. Laser Technol.* **78** 33–41.
57. Rapp L., Biver E., Alloncle A. P. and Delaporte P. 2014 High-speed laser printing of silver nanoparticles ink, *J. Laser MicroNanoEng.* **9** (1) 5–9.
58. Cannatà D., Benetti M., Di Pietrantonio F., Verona E., Palla-Papavlu A., Dinca V., Dinescu M. and Lippert T. 2012 Nerve agent simulant detection by solidly mounted resonators (SMRs) polymer coated using laser induced forward transfer (LIFT) technique, *Sens. Actuators B* **173** 32–39.
59. Di Pietrantonio F., Benetti M., Cannatà D., Verona E., Palla-Papavlu A., Dinca V., Dinescu M., Mattle T. and Lippert T. 2012 Volatile toxic compound detection by surface acoustic wave sensor array coated with chemoselective polymers deposited by laser induced forward transfer: Application to sarin, *Sens. Actuators B* **174** 158–167.
60. Touloupakis E., Boutopoulos C., Buonasera K., Zergioti I. and Giardi M. T. 2012 A photosynthetic biosensor with enhanced electron transfer generation realized by laser printing technology, *Anal. Bioanal. Chem.* **402** (10) 3237–3244.
61. Palla-Papavlu A., Patrascioiu A., Di Pietrantonio F., Fernández-Pradas J. M., Cannatà D., Benetti M., D'Auria S., Verona E. and Serra P. 2014 Preparation of surface acoustic wave odor sensors by laser-induced forward transfer, *Sens. Actuators B* **192** 369–377.
62. Di Pietrantonio F., Benetti M., Cannatà D., Verona E., Palla-Papavlu A., Fernández-Pradas J. M., Serra P., Staiano M., Varriale A. and D'Auria S. 2015 A surface acoustic wave bio-electronic nose for detection of volatile odorant molecules, *Biosens. Bioelectron.* **67** 516–523.
63. Shaw-Stewart J., Mattle T., Lippert T., Nagel M., Nuesch F. A. and Wokaun A. 2013 The fabrication of small molecule organic light-emitting diode pixels by laser-induced forward transfer, *J. Appl. Phys.* **113** 043104.
64. Kattamis N. T., McDaniel N. D., Bernhard S. and Arnold C. B. 2011 Ambient laser direct-write printing of a patterned organo-metallic electroluminescent device, *Org. Electron.* **12** 1152–1158.
65. Kaneko A., Hitomi C. and Hoshikawa J. 1993 Laser printer and thermal transfer printing method. European Patent EP0542544.
66. Hutt K. W., Hann R. A. and Tran H. C. V. 1999 Laser dye thermal transfer printing, United State Patent 5864356
67. Chang S. 2002 Transfer printing, United State Patent 6476842.
68. Moulin M. and Huang J. 2005 Method and apparatus for laser-induced thermal transfer printing, United State Patent 6894713.
69. Lehmann U. and Meyer D. 2009 Quality printing method and printing machine, European Patent EP1485255
70. Lehmann U. 2011 Printing machine and printing method therefore, European Patent EP2155499.
71. Lehmann U. 2007 Method of printing and corresponding print machine, European Patent EP1268211.
72. Hennig G., Baldermann T., Nussbaum C., Rossier M., Brockelt A., Schuler L. and Hochstein G. 2012 Lasersonic lift process for large area digital printing, *J. Laser Micro/Nanoeng.* **7** (3) 299–305.
73. Jager F. K., Kaczun J. and Lehmann U. 2011 Printing machine and methode for printing a substrate, United State Patent 20110310205.
74. Sun J. W., Kang T. M., Noh S. W. and Suh M. C. 2012 Laser induced thermal imaging mask, laser irradiation apparatus including the same, and method of manufacturing organic light emitting device by using the same, United State Patent 20120099615.
75. Wolk M., Potts J., Li Y. and Huynh K. 2010 Donor films with pattern-directing layers, United State Patent 12/557675.
76. Wolk M. B., Lamansky S. and Tolbert W. A. 2008 Progress in laser induced thermal imaging of oleds, *SID Symp. Dig. Tech. Pap.* **39**(1) 511–514.
77. Hirano T., Matsuo K., Kohinata K., Hanawa K., Matsumi T., Matsuda E., Matsuura R., Ishibashi T., Yoshida A and Sasaoka T 2007 53.2: Distinguished paper: Novel laser transfer technology for manufacturing large-sized oled displays, *SID Symp. Dige. Tech. Pap.* **38**(1) 1592–1595.
78. Blanchet G. B., Loo Y.-L., Rogers J., Gao F. and Fincher C. 2003 Large area printing of organic transistors via a high throughput dry process. In Materials Research Society Symposium Proceedings, vol. 736. Cambridge Univ Press, 283–288.

Taylor & Francis
Taylor & Francis Group
http://taylorandfrancis.com

14

Laser Pyrolysis

Mohammad Malekzadeh, Parham Rohani, and Mark T. Swihart

CONTENTS

14.1 Introduction 161
14.2 Experimental Set-up 161
14.3 Control Parameters 163
14.4 Typical Operating Procedures for Laser Pyrolysis 164
14.5 Examples of NPs Synthesized by Laser Pyrolysis 165
  14.5.1 Elemental NPs 165
  14.5.2 Compound Non-oxide NPs 165
  14.5.3 Compound Oxide NPs 166
14.6 Challenges and Future Work 167
14.7 Conclusions 167
References 168

14.1 Introduction

Nanoparticle (NP) synthesis methods can be classified in several ways. The most general categories are based on the precursors from which NPs are synthesized and the change in particle size that leads to their production. These categories are (i) top-down methods, in which the primary substances are larger bulk materials that are reduced in size to produce NPs (Gao 2007), and (ii) bottom-up methods, in which the primary substances are atoms and molecules from which NPs are built up. Bottom-up methods can be further classified into solution-phase and vapour-phase processes based upon the phase of the medium in which the NPs grow (Mijatovic, Eijkel, and Van Den Berg 2005).

In vapour-phase methods, precursors must be delivered as a vapour, small droplets, or particles that can be vaporized in the process. An energy source such as a flame, plasma, or laser initiates and sustains chemical reactions in the vapour phase. Through chemical reactions and/or quenching of vaporized precursors, the vapour phase becomes supersaturated, initiating the formation of a solid phase. At a certain supersaturation level, nucleation occurs homogeneously. Once particles have nucleated, the system should be quenched rapidly to stop particle growth and sintering and to limit the particle size (Haggerty 1981; Swihart 2003; Kortshagen 2009).

Laser pyrolysis is one of the important vapour-phase NP synthesis methods. After Cannon's pioneering laser pyrolysis synthesis of silicon and silicon-based ceramic NPs, in the early 1980s (Cannon, Danforth, Flint, et al. 1982), iron pentacarbonyl $Fe(CO)_5$ and metal hexacarbonyl complexes $M(CO)_6$ (M: Cr, Mo, and W) were decomposed thermally by this technique in the mid-1980s (Duncan, Dietz, and Smalley 1981; Lewis, Golden, and Smith 1984). These early studies demonstrated the potential of this synthesis method. In laser pyrolysis, a focused continuous wave CO_2 laser beam at a wavelength of 10.6 µm is employed to heat a gas mixture. The laser pyrolysis method relies upon a resonance between the CO_2 laser beam and a vibrational mode of a precursor or a photosensitizer. Laser energy deposited in this vibrational mode is then transferred to non-absorbing molecules via collisions. The resulting rapid heating of the gas mixture leads to precursor decomposition, which produces reactive species and/or a supersaturated vapour from which NPs nucleate. After nucleation, the remaining superstation can be relieved via condensation and fast particle growth. Further growth can occur by coagulation and coalescence. When the particles and gas stream leave the laser beam, they are rapidly cooled by mixing with unheated gases that did not absorb the laser energy. This includes both gases that did not pass through the laser beam and those that passed through the laser beam but did not contain a species that absorbs at the laser wavelength. At a sufficiently high temperature, coalescence of particles is faster than their coagulation, leading to spherical NP formation. At a low temperature, coalescence is negligible, which leads to loose agglomerate formation. Rapid transition between these conditions prevents the formation of hard agglomerates of partially sintered NPs, which are produced by partial coalescence (Li et al. 2011; Rice and Woodin 1989; Martínez, Sebastián, and Hueso 2014).

14.2 Experimental Set-up

Figure 14.1a shows a schematic of an experimental set-up to synthesize NPs by laser pyrolysis. The precursors can be solid, liquid, or vapour. Precursors that are gases or vapours at ambient temperature, such as silane, acetylene, germane,

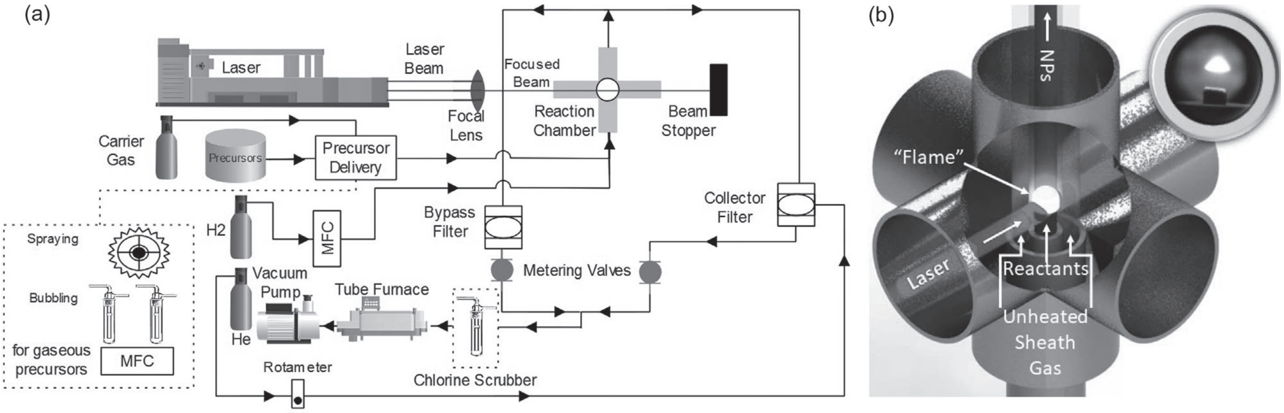

FIGURE 14.1 (a) Schematic of a complete experimental set-up for laser pyrolysis synthesis of NPs. (b) Schematic of the reaction zone in laser pyrolysis synthesis, with an inset showing a photograph of the reaction zone during synthesis (Rohani, Kim, and Swihart 2016).

or diborane, can be directly fed into the reaction zone from compressed gas cylinders, via mass flow controllers (MFCs). If more than one precursor is needed, they must be mixed thoroughly before entering the reaction zone. Likewise, if a photosensitizer is needed, it must be added before the precursors reach the reaction zone. Because of safety and availability issues, use of precursors that are solid or liquid at ambient conditions is often preferred or required. Liquid precursors with sufficiently high vapour pressure can be delivered as vapours using a bubbler in which a carrier gas, delivered through an MFC, is saturated with the precursor vapour before entering the reactor. For some elements, no sufficiently volatile precursor is available and vapour-phase delivery is either impractical or impossible. In such cases, a general spray-based precursor delivery method, using an atomizer to generate aerosol droplets, is needed. If at least one of the precursors is a low-viscosity liquid at ambient conditions, and other precursors are soluble in it, then the precursors may be delivered as a spray from an atomizer, without using a solvent. Otherwise, one or more precursors can be dissolved in an appropriate solvent for delivery by an atomizer. These precursors enter the reaction zone as small droplets that rapidly evaporate upon laser heating.

Figure 14.2 shows a schematic of a commonly used ultrasonic atomizer. An ultrasound transducer in a water bath generates an ultrasonic wave, which is coupled through a thin membrane into a chamber containing a small amount of a precursor solution. Ultrasonic atomization produces aerosol droplets from the precursor solution, which is continuously replenished using a syringe pump (Fu et al. 2016). A carrier gas, which can be inert or contains a precursor, is used to deliver aerosol droplets to the reaction zone. Moderate heating can be applied to the tubing between the atomizer and the reaction zone to avoid aerosol droplet deposition and condensation on the tube walls.

A continuous wave CO_2 laser beam at a wavelength of $10.6\,\mu m$ is employed to decompose the precursor mixture in the reaction zone directly above the inlet nozzle. The laser power can range from 27 W (Kim et al. 2015) to 1200 W (D'Amato et al. 2013) or more depending on the desired scale of NP production, the temperature required for the synthesis, and the efficiency of absorbing the laser energy. Figure 14.1b shows a schematic of the reaction zone in a typical laboratory-scale laser pyrolysis reactor. The reaction zone is defined by the intersection of the reactant stream, which enters through a nozzle and usually exits along a vertical flow path, with the horizontal axis through which the laser beam passes. The third axis of the reactor typically contains windows to observe the reaction zone (Rohani, Kim, and Swihart 2016). Many variations in this reactor geometry are possible. Designs for larger-scale synthesis are described in the patent literature. For example, researchers at NanoGram Corporation have patented a design for an elongated length rectangular channel within their gas delivery system (Bi and Kambe 2001). The width of reactant gas stream is approximately the width of the radiation beam, which minimizes the waste of either radiation beam or reactant gas stream. They have optimized the length of the reactant gas inlet to find the maximum length over which the

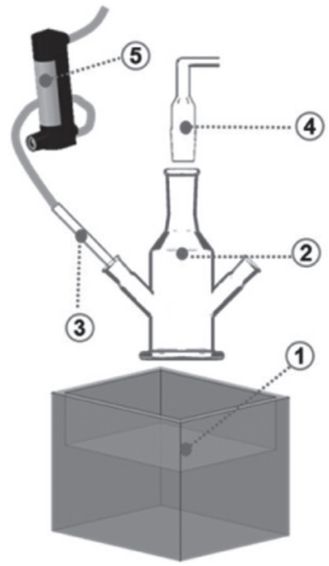

FIGURE 14.2 Atomization system. 1 Water bath in which an ultrasonic transducer is submerged. 2 Nebulization (atomization) chamber. 3 Carrier gas delivery to the nebulization chamber. 4 Aerosol droplet delivery to the reaction zone. 5 Gas flow meter (Fu et al. 2016).

laser beam has a sufficient energy to initiate and continue the chemical reaction. The preferred width and length of the reactant gas inlet were specified in their patent as about 0.5 mm to about 30 mm and about 5 mm to about 1 m, respectively. They also used two elongated sheath gas channels (one channel on each side of the reactant gas channel) leading into the reaction chamber. They reported that designing sheath gas channels at an angle provided more confinement of the reactant gas stream. Greater angle between sheath gas channels and reactant gas channel can be used for lighter reactant molecules. The preferable width for each sheath gas channel was given as about 2 mm to about 10 mm with these channels slightly longer than the reactant gas inlet. In another interesting variation, to coat the synthesized NPs with another element in the same process, two reaction chambers were used in series. The core NPs form in the first reaction chamber. Then, they are transferred to the second reaction chamber, where they mix with the coating precursor. Laser-driven decomposition of the second precursor coats the core particles (Sourice et al. 2016).

The distance between the inlet and the laser beam is typically 2–5 mm, adjusted to avoid any deposition onto the nozzle, but minimized to limit the diffusion of precursors out of the beam. The continuous wave CO_2 laser beam is often focused at the centre of the reaction zone to increase its local intensity. Kim et al. (2015) fully described a nozzle design. The waist of the laser beam at the focal point can be calculated according to the following equation:

$$w_0 = \frac{4\lambda M^2 f}{\pi D} + k\frac{D^3}{f^2} \tag{14.1}$$

where w_0 is the waist of a laser beam at the focal point, λ is the laser wavelength, M^2 is the laser beam divergence, f is the focal length, D is the expanded beam aperture, and k is the index of refraction. The beam diameter at any point after the focal length can be calculated using the following equation:

$$w(z) = w_0\sqrt{\left(1+\frac{1}{f^2}\left(\frac{D^2}{w_0^2}-1\right)z^2\right)} \tag{14.2}$$

where z-axis refers to the beam path direction, the origin of which is the focal point, and $w(z)$ is the diameter of the laser beam at any point in the direction. By changing the lens position, the focal point moves relative to the reaction zone. As a result, the beam diameter can typically be adjusted down to about 0.5 mm, by changing the lens position to move the focal point relative to the reaction zone. Use of a semi-elliptical nozzle, rather than a circular one, is often preferable in order to increase the laser–precursor interaction and thereby maximize product yield and avoid wasting the precursor. The inner tube is centred within another tube through which a sheath flow enters the reactor, confining the precursor stream to a region near the reactor centreline. The sheath gas can be inert (*e.g.* argon, nitrogen, or helium) or a gas that participates in the particle formation reaction (*e.g.* hydrogen). For the effective decomposition of precursor molecules in the reaction zone, the reactant stream must contain a species that can absorb the laser energy at 10.6 µm. There are three types of precursors with this characteristic: (i) photosensitive precursors, such as silane (SiH_4), that directly produce the NPs; (ii) photosensitizers, such as sulphur hexafluoride (SF_6), that only absorb the laser and transfer energy to reactants, without participation in the reaction; and (iii) Species that absorb laser energy, decompose, and react to cause the decomposition of other precursors, like ethylene (C_2H_4) used to produce vanadium oxide (Martínez, Sebastián, and Hueso 2014). The gaseous stream containing NPs mixes with the unheated gas immediately after the reaction zone. This quenches the as-synthesized particles and stops their further growth. An inert gas stream is typically used near all windows to keep them cool and prevent particle deposition. An inert gas must also be used to purge the system several times before and after each synthesis run if the precursors are hazardous (toxic or pyrophoric) or the precursors or NPs are oxygen sensitive. The flow rates of all gaseous streams are typically set using MFCs. The typical flow rates of gaseous streams in the laser pyrolysis reactor are in the range of 200 sccm (standard cubic centimetres per minute) to 10 slm (standard litres be minute) (Herlin-Boime, Mayne-L'Hermite, and Reynaud 2006). A vacuum pump is required to control the reactor pressure below the ambient pressure. Typically, the pressure of the reaction chamber is in the range of 6.7–80 kPa (D'Amato et al. 2013). Most often, products are collected on filters, as shown in Figure 14.1a, but other approaches such as electrostatic precipitation or direct collection into liquid are also possible. A needle valve or back-pressure regulator between the collection filter and vacuum pump controls the system pressure, which is measured before the collection filter. In the set-up shown in Figure 14.1a, the collection filters are configured to allow a pulse of reverse flow of an inert gas to remove particles from the filter paper when the pressure drop due to particle loading on the filter becomes too high. The system can also be configured with multiple collection filters, each with isolation valves, so that one can switch between multiple collection filters in each run. In addition, a bypass collection filter set-up in parallel with the main collection filter is used during start-up, shutdown, or whenever the reactor is not running at the desired conditions. Before the gas flow exhausts, a tube furnace, placed after the collection filters, decomposes any unreacted precursor, followed by another filter to collect any produced particles. If chlorinated precursors are used, the production of corrosive and toxic hydrochloric acid (HCl) as a by-product is problematic. Thus, a bubbler of base solution must be used before the tube furnace to absorb the hydrochloric acid. It is important to mention that there are other components in the system such as a chiller to provide cooling water to the laser (if it is water-cooled), a laser power supply, power supplies and interfaces for the MFCs, additional valves, and pressure transducers that have been excluded from the schematic for simplicity.

14.3 Control Parameters

The most important factors to control the NP synthesis by laser pyrolysis method are residence time in the reaction zone, reaction temperature, and precursor flow rate. The operating parameters that affect these factors are laser power, reactor pressure, gas flow rates, diameter of the nozzle, and the width of the laser beam (Kim et al. 2015; Bi and Kambe 2001). Decreasing the reactor pressure, at fixed mass flow rates, decreases the residence time due to the proportional decrease in gas density (increase in gas volume). Increasing the flow rate of precursors and decreasing the diameter of the nozzle will also reduce the residence time. These changes will also usually reduce the reaction temperature. When the pressure is reduced, both the residence time during which the gases absorb the laser energy and the concentration of the absorbing species are reduced. When flow rates are increased or the nozzle diameter is decreased, the concentration of absorbing species remains the same, but the time available for absorbing the laser energy is still reduced. Thus, all of these changes tend to reduce both particle size and production yield. Kim and coworkers (2015) studied the effect of laser power on the size and yield of germanium NPs. They increased the laser power in their system from 27 to 57 W, which led to an increase in yield from 12.0% to 31.1% as more energy was absorbed to drive the decomposition of precursor molecules. This increase in the laser energy simultaneously increased the mean diameter of the NPs from 32.8 to 41.4 nm due to aggregation followed by sintering. Increasing the concentration of the photosensitizer, or using a more strongly absorbing photosensitizer, increases the amount of laser energy that will be transferred to the precursor molecules and thus also increases the yield and size of NPs. Other factors that produce an increase in the temperature will have effects similar to an increase in the laser power. Increasing the temperature can lead to the formation of higher-temperature phases of the products (Bi and Kambe 2001). The shape of the nozzle should be designed in a way which maximizes the interaction of laser beam and precursor molecules. This increase in the interaction will increase yield and reduce waste of precursors. Therefore, semi-elliptical shape will be more preferable than circular shape. Another way to increase laser intensity in addition to increasing the laser power is focusing the laser beam more tightly. Although this approach will increase the peak laser power density, it will lead to less volume of interaction between laser beam and precursors and therefore a decrease in yield. A strategy to decrease this loss will be to change the shape of the nozzle to maximize the interaction between the laser beam and precursors. The main problem with this approach can be a decrease in the residence time which can go below the minimum required residence time for particle nucleation and growth to the desired size. For the synthesis of alloys in nanoparticulate form by laser pyrolysis, we can change the concentration of precursors in the precursor mixture to vary the composition. In general, because the conversion from precursors to products is not 100%, and some precursors are more reactive than others, the ratio of elements in the multicomponent product particles will differ from their ratio in the precursor stream.

14.4 Typical Operating Procedures for Laser Pyrolysis

This section presents a typical operating procedure for a laser pyrolysis reactor system. Of course, the details of the procedure will depend on the specific configuration of the reactor system, the materials to be synthesized, and the precursors that are being used. More detailed standard operating procedures (SOPs) should be developed for any particular laser pyrolysis system. However, many of these points will be common to different reactor configurations, and this outline of a typical operating procedure can give an idea of what is involved in operating such a system. Note that this section does not attempt to address the many possible hazards associated with any particular laser pyrolysis synthesis process. Toxic and pyrophoric gases that have often been used as precursors in laser pyrolysis should be handled according to best safety practices. Laser burn hazards vary greatly depending on laser power and whether the beam path is open or enclosed.

Before the reactor can be started, one must ensure that the laser path is correctly aligned and that the reactor windows are clean. Unintended reflections of the CO_2 laser beam can be quite hazardous. Debris or contamination on the reactor windows can absorb laser energy, heating the window and causing it to fail. To purge the reactor for start-up, the downstream furnace or other gas scrubbing equipment should be turned on to ensure a complete decomposition of any reaction by-products. When working with air-reactive precursors, the system must be evacuated and refilled with an inert gas to a pressure above atmospheric pressure. This process should be repeated as appropriate to ensure residual air has been removed from the system. Leak tests, which can include both a positive pressure test and a negative pressure test, should then be performed.

To run the reactor, gas supply cylinders, including inert gas, sheath gas, photosensitizer (if used), and gaseous precursors (if used), should be opened and the flow rates should be adjusted. If spray-based precursor delivery is being used, the pump should be turned on to transfer the precursor to the atomizer and correct precursor delivery rate should be set. If delivery from a bubbler is being used, the bubbler temperature should be at the desired value, and the valves should be opened to direct flow through the bubbler. Then, the bypass metering valve or other backpressure regulating device is adjusted until the desired system pressure is achieved. During start-up, the reactor effluent is typically sent to a bypass filter so that particles produced before the reactor has stabilized are collected separately from the product. Thereafter, the laser should be turned on and the "flame" should be checked at the point where the laser and precursor gas stream meet. The laser must not hit the inlet nozzle. Once the flame appearance is correct, and the process is stable, the effluent can be directed to the collection filter.

Finally, to shut down the reactor, the laser should be turned off. Then, the delivery systems for the precursors and photosensitizer should be shut down. Inert gas flow should continue for a few minutes, or the appropriate time, to purge the particular system. All collection filters must be purged, even if not in use at the end of the run. Isolation valves for all collection filters should be closed after purging. Evacuation and purge cycles should be repeated to remove all residual precursors and by-products from the system. Finally, the vacuum pump and tube furnace or scrubber system can be turned off, and the collection filters should be removed and transferred to an inert atmosphere glovebox, if appropriate (for air-sensitive NPs).

14.5 Examples of NPs Synthesized by Laser Pyrolysis

Clearly, a great number of materials have been prepared by laser pyrolysis with various applications which cannot be covered in detail here. Thus, here we describe a few important types of NPs that have been synthesized by laser pyrolysis. We present these in three subsections: elements, non-oxide compounds, and oxide compounds.

14.5.1 Elemental NPs

Silicon is the most widely used elemental semiconductor because of its abundance, its effective and economical manufacturing, its chemical properties, its structure, and its moderate bandgap, which is 1.12 eV at 0 K (Abstreiter and Lockwood 1998). The strong absorbance of silane, a precursor for silicon NP synthesis, at a wavelength of 10.6 µm facilitates the synthesis of silicon NPs by laser pyrolysis (Herlin-Boime, Mayne-L'ermite, and Reynaud 2006). Conventional vapour-phase synthesis methods like furnace-heated, rf-heated, and arc-plasma methods do not achieve ideal thermal profiles and reaction zone, which leads to broad particle size distributions as a result of the distribution in nucleation and growth times. Laser pyrolysis is among the best methods to synthesize silicon NPs, because its small reaction volume and steep temperature gradients allow short residence times and high throughput, lack of contact with reactor walls provides high purity, and the atmosphere and conditions can be controlled to achieve efficient use of reactants and to prevent oxidation (Cannon, Danforth, Flint, et al. 1982; Cannon, Danforth, Haggerty, et al. 1982).

Silicon NPs were the first NPs synthesized by Cannon and coworkers, the pioneers of the laser pyrolysis method. Because SiH_4 has a strong absorption near 10.6 µm, they chose it as the precursor rather than $SiCl_4$ or other chlorosilanes. They used a 150 W CO_2 laser with unfocused power intensities of 270–1020 W cm^{-2}, and focused power intensities of up to 10^5 W cm^{-2} to decompose silane at a flow rate of 11 sccm and a total pressure of 0.08–1.0 atm. A coaxial argon stream (400 sccm) was used to confine the particles. The temperature of the reaction zone was estimated to be 1030°C based on pyrometer measurements. They produced very fine, uniform, spherical, nonporous, and loosely agglomerated silicon NPs from 10 to 100 nm in diameter, with high purity and crystallinity (Cannon, Danforth, Flint, et al. 1982; Cannon, Danforth, Haggerty, et al. 1982).

In order to exhibit bright photoluminescence, silicon NPs should be much smaller than those produced in Cannon's work. Li et al. synthesized silicon NPs below 5 nm in diameter in macroscopic quantities (20–200 mg h^{-1}) with intense visible photoluminescence. They used silane as the main precursor at a flow rate of 24 sccm and SF_6 at a flow rate of 2 sccm as a photosensitizer for more effective decomposition of silane molecules. To reduce the particle size and passivate the particle surface, the NPs were dispersed in methanol and then etched with a mixture of HF and HNO_3 in water. The NPs are oxidized by HNO_3, and then the oxide is dissolved by HF. As a result, the size of NPs decreased in a controllable manner. The as-synthesized NPs showed little or no visible photoluminescence, but after etching they exhibited intense visible photoluminescence. Figure 14.3 shows visually the effect of etching time on the photoluminescence. As presented in the figure, increasing the etching time led to brighter and shorter-wavelength visible photoluminescence under UV illumination, which is the result of decreasing size with increasing etching time (Li et al. 2003).

14.5.2 Compound Non-oxide NPs

High electron mobility and high optical absorbance of germanium make germanium-containing NPs very valuable for optoelectronic applications. Additionally, germanium-containing NPs, which have high lithium diffusivity and high charge capacity, are interesting NPs for use in batteries. Besides, low toxicity of them makes them useful NPs for biomedical applications. Germanium NPs can be easily dispersed in many polar solvents, which is an advantage for biomedical applications. Laser pyrolysis allows scalable and controllable synthesis of germanium-containing NPs that cannot be readily prepared by other means. Because germanium-containing precursors do not significantly absorb at a wavelength of 10.6 µm, the use of a photosensitizer is necessary (Kim et al. 2015).

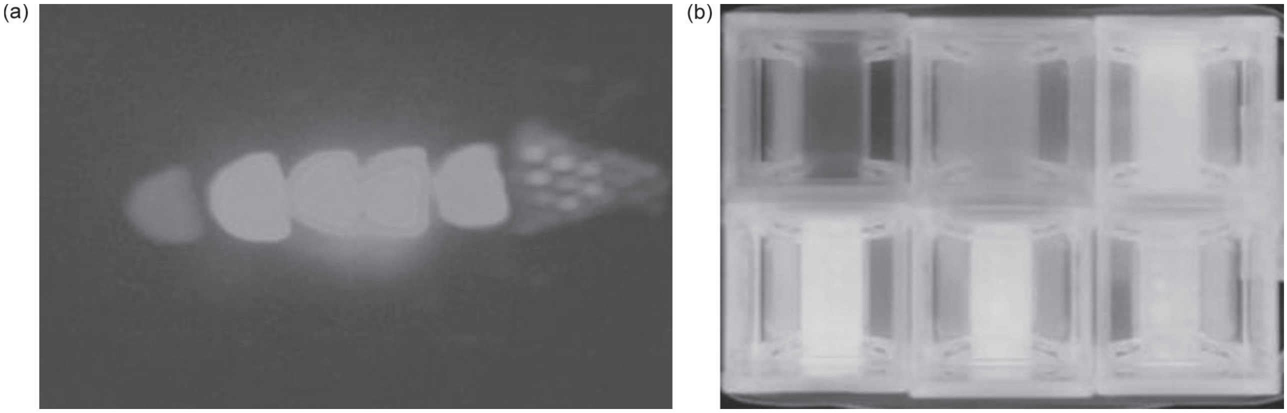

FIGURE 14.3 (a) Powder samples and (b) particles dispersed in methanol, both from the same experiment, and both with bright visible photoluminescence under UV illumination. The etching time increases for samples from left to right in (a) and from upper left to lower right in (b) (Li et al. 2003) (see the original paper for a color version of this figure).

Kim et al. used laser pyrolysis of germane (50 sccm) and SF_6 (25 sccm) to synthesize pristine germanium NPs. They used a mixture of GeH_4 and SF_6 with higher SF_6 flow rate to synthesize sulphur-coated germanium, through decomposition of SF_6 at higher temperature. The thin sulphur layer can prevent oxidation, which is useful for various applications. This sulphur coating via SF_6 decomposition is possible for Ge, but not for Si, because the Si-F bond is much stronger than the Ge-F bond. Thus, SF_6 decomposition during silicon NP synthesis leads to the formation of SiF_4, suppressing particle formation, but this does not occur for germanium (Kim et al. 2015).

Interest in alloying group (IV) semiconductors, especially silicon and germanium, is due to their optoelectronic properties. Alloys of silicon and germanium can absorb a large range of the solar spectrum by tuning the bandgap between 0.66 and 1.12 eV by changing the composition (Erogbogbo et al. 2011). There are some studies on the synthesis of silicon–germanium alloys in liquid phase, but these processes are very time-consuming and produced low material yields and a broad range of sizes and shapes (Lew et al. 2003; Wu, Fan, and Yang 2002). Non-thermal plasma is another demonstrated method to synthesize silicon–germanium alloys, but it synthesizes just small quantities of the NPs (Ren, Cheng, and Peter 2004).

Kim et al. also used simultaneous laser pyrolysis of silane as the photosensitizer and the source of silicon and germane as the source of germanium to synthesize silicon germanium alloy NPs. They combined a constant flow of silane (25 sccm) with varying flows of germane (2.5, 5, 20, and 40 sccm) to tune the composition. The NPs produced with the four different flow rates of germane were similar in shape and size. The compositions of the alloy NPs were $Si_{0.92}Ge_{0.08}$, $Si_{0.61}Ge_{0.39}$, $Si_{0.54}Ge_{0.46}$, and $Si_{0.23}Ge_{0.77}$ for the germane flow rates of 2.5, 5, 20, and 40 sccm, respectively, which confirmed the increase in the atomic fraction of germanium with increasing flow rate of germane. TEM images of silicon–germanium alloys with different compositions synthesized by Kim and coworkers are shown in Figure 14.4 (Kim et al. 2015).

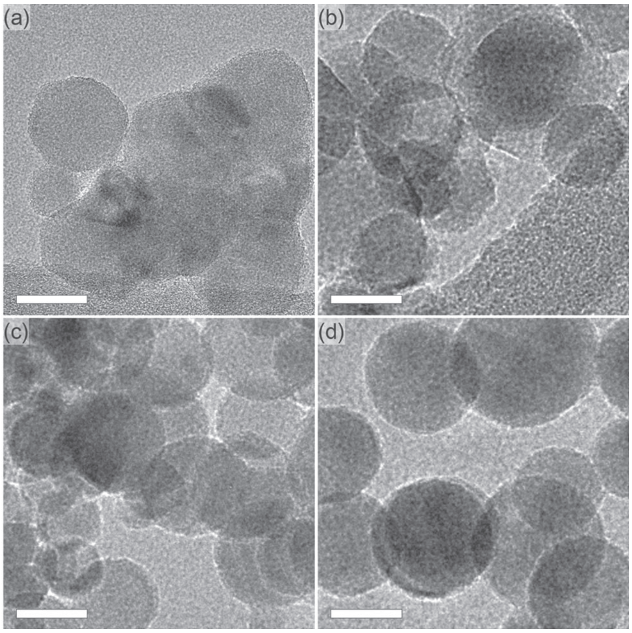

FIGURE 14.4 TEM image of silicon–germanium alloy NPs synthesized by a constant flow rate of silane and different flow rates of germane (a: 2.5 sccm, b: 5 sccm, c: 20 sccm, d: 40 sccm). Scale bar: 20 nm (Kim et al. 2015).

14.5.3 Compound Oxide NPs

Titania NPs exhibit high refractive index and dielectric constant, high physical and chemical stabilities, and photocatalytic activity that make them useful in industrial processes, including photocatalysis, catalysis, solar cells, microelectronics, chemical sensors, and electrochemistry. As a result, they are the most important metal oxide NPs, and many different methods have been developed to prepare them, including ion beam-enhanced deposition, sol–gel, liquid-phase deposition, pulsed laser ablation, chemical vapour synthesis, gas condensation processing, flame-based synthesis methods, and laser pyrolysis. Rutile, anatase, and brookite are crystalline phases of titania NPs. Due to the difficulty of synthesizing brookite titania NPs in pure microcrystalline form, their properties are less known. Anatase is more applicable in photocatalysis, but less stable than rutile and transforms to rutile at temperatures between 700°C and 1000°C. The efficiency of titania NPs in specific applications depends on their phase composition and microstructure, including particle size, morphology, and porosity. Although flame-based processes provide efficient low-cost methods to synthesize titania NPs, laser pyrolysis allows more accurate control of particle size, size distribution, and chemical composition as well as control of the anatase/rutile ratio, which make the method very advantageous to produce titania NPs for specific high-value applications (Alexandrescu et al. 2004; Pignon et al. 2008).

Alexandrescu et al. used the laser pyrolysis of $TiCl_4$ as the main precursor, C_2H_4 as the photosensitizer, and N_2O and air as the oxygen precursors to synthesize titania NPs. The chemical reaction that leads to the oxidation of $TiCl_4$ is exothermic, but requires increasing the temperature to about 1000 K to initiate reaction. They used four sets of precursor flow rates to synthesize the NPs: 500 sccm ethylene flow through the $TiCl_4$ bubbler and 40 sccm air (ST2), 250 sccm ethylene flow through the $TiCl_4$ bubbler and 40 sccm N_2O (ST5), 250 sccm ethylene flow through the $TiCl_4$ bubbler and 70 sccm N_2O (ST6), and 250 sccm ethylene flow through the $TiCl_4$ bubbler and 40 sccm air (ST7). The resulting titania NPs were ultrafine, and their colour varied from white to grey (pure grey by using N_2O as the oxygen precursor). By increasing N_2O flow rate, very thin dark grey spots distributed non-homogeneously appeared on the surface of NPs, which is related to trace carbon from ethylene decomposition. The range of mean particle size was 15–28, 18–28, 20–27, and 12–27 for ST2, ST5, ST6, and ST7 samples, respectively (Alexandrescu et al. 2004).

Another advantage of the synthesis of titania by laser pyrolysis is the possibility of doping the NPs in a single step. Doped titania NPs have better photocatalytic activity than pristine titania NPs and are therefore useful for the destruction of pollutants in air and water. Bouhadoun et al. used laser pyrolysis to synthesize TiO_2, $N\text{-}TiO_2$, $X\text{-}Au\text{-}TiO_2$ (X is wt%), and $Au/N\text{-}TiO_2$ in a single step. They used titanium tetraisopropoxide ($Ti[OCH(CH_4)_2]_4$) as the titanium precursor, hydrogen tetrachloroaurate (III) ($HAuCl_4.3H_2O$) as the gold precursor, and ammonia (NH_3) as the nitrogen precursor. The precursors were delivered to the reactor as small aerosol droplets using an ultrasonic atomizer and argon as the carrier gas. They successfully synthesized TiO_2 (10.0 nm), 0.04-Au-TiO_2 (9.0 nm), 0.09-Au-TiO_2 (9.5 nm), 0.12-Au-TiO_2, 0.16-Au-TiO_2, N-TiO_2, and Au/N-TiO_2 with specific surface areas of 155, 177, 167, 163, 161, 162, and 210 $m^2 g^{-1}$ and average sizes of 10.0, 9.0, 9.5, 10.0, 9.5, 9.5, and 7.5 nm, respectively. Figure 14.5 presents the colour evolution of typical NPs synthesized in that study. Based on their results, all the synthesized NPs showed higher efficiency in photocatalytic activity than commercial P25 TiO_2, and among them, Au/N-TiO_2 NPs had the best efficiency (Bouhadoun et al. 2015).

14.6 Challenges and Future Work

Although many researchers have investigated the chemical mechanisms that lead to particle formation in laser pyrolysis, and the overall process is generally understood, a detailed understanding and the ability to predictively model the process remain lacking. Generally, particle nucleation in laser pyrolysis cannot be described well as classical nucleation of a supersaturated vapour, but in most cases will involve complex chemical reactions. Moreover, direct measurement of temperature, species concentrations, particle size and concentration, and other properties within the small reaction zone formed by the intersection of the laser beam and precursor gas stream, is exceedingly difficult. *In situ* spectroscopic measurements of temperature and composition in the reaction zone, *e.g.* by tunable diode laser absorbance spectroscopy, could provide valuable insights into the fundamental mechanisms of precursor decomposition and particle formation in laser pyrolysis, but will be extremely challenging measurements and will require significant investments in dedicated spectroscopic equipment.

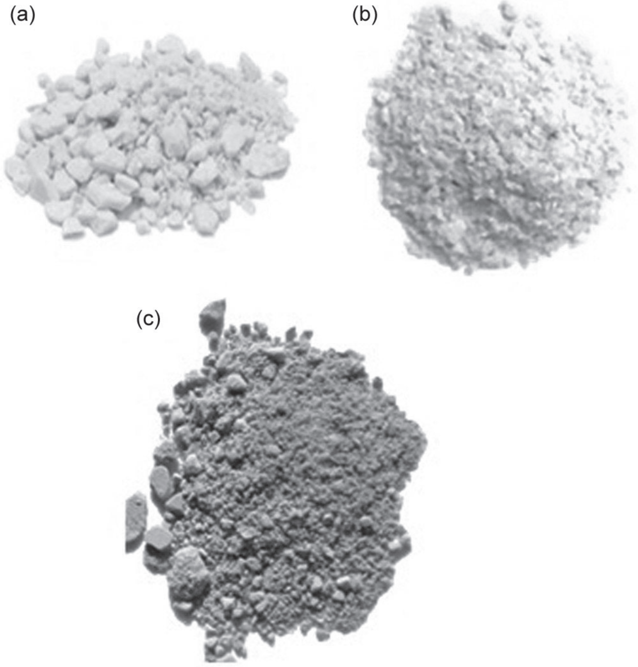

FIGURE 14.5 (a) TiO_2, (b) N-TiO_2, and (c) 0.16-Au-TiO_2 laser pyrolysis synthesized NPs (Bouhadoun et al. 2015) (see the original paper for a color version of this figure).

Identification and adoption of appropriate precursors are another key challenge in laser pyrolysis. Current precursors for silicon, germanium, boron, and multicomponent materials containing them are toxic and/or pyrophoric gases. The need for volatile precursors and sensitivity to the oxidation of product particles limits precursor selection. Spray-based delivery of precursors may provide more flexibility. Additionally, chemistry developed for chemical vapour deposition of films can be adapted for laser pyrolysis. Process modifications such as spray delivery of precursors may help to replace current toxic pyrophoric compressed gas precursors for the most commonly produced NPs with safer alternatives. Also, although many materials have been prepared by laser pyrolysis, new opportunities exist in applications like catalysis and optical materials, for which the production of high-purity NPs of new materials with well-controlled size and composition will be valuable. Thus, continued exploration of new precursors and materials will remain a fruitful area of research.

At reasonably high production rates, collision of newly formed particles is inevitable, leading to at least soft agglomeration via van der Waals attractions between particles (Saidur, Leong, and Mohammad 2011). Rapid quenching can limit the formation of hard agglomerates (partially sintered aggregates). *In situ* capping of newly formed NPs with ligands might enable direct production of dispersible primary particles, but can also potentially introduce contamination into the product particles. *In situ* functionalization of particles with other ligands immediately after production may allow direct production of stable colloidal dispersions for subsequent applications. Development of *in situ* functionalization of NPs from laser pyrolysis is thus a potential area of further research.

Other future directions for research are application specific. For hydrogen generation using water splitting by reaction with boron NPs (Rohani, Kim, and Swihart 2016), silicon NPs (Erogbogbo et al. 2013), or similar materials, we would like to incorporate hydrogen into the NPs during synthesis. For biological applications (Erogbogbo et al. 2010), particles must be produced with high reproducibility (sufficient to meet regulatory approval standards) and must be modified to be dispersible in biological (aqueous) systems using biocompatible agents. For the production of solar cells and other optoelectronic devices from NPs (Sublemontier et al. 2009), we must be able to disperse the NPs in stable “nano-inks” that can be used for low-cost patterning of devices, and must do so without introducing contaminants in the final devices that degrade the semiconductor properties. Each of these challenges presents opportunities for refinement and extension of the laser pyrolysis process technology to improve product performance.

14.7 Conclusions

The main goal of this chapter has been to present the application of laser pyrolysis to synthesize NPs. Laser pyrolysis is one of the most powerful methods to synthesise various NPs with high purity and control of composition and size, features that are important in numerous applications. Among the advantages of laser pyrolysis, the synthesis of NPs with narrow size distribution and high specific surface area can be considered the most important. The major difficulty in this method is difficulty in the identification and adoption of efficient and safe precursors, because the precursors for some common materials synthesized by laser pyrolysis are dangerous and alternative precursors for them are not as efficient as previous ones. We outlined some of the most important remaining challenges to the broader application of laser pyrolysis and some future research paths that may address these challenges which will improve the technology of laser pyrolysis to synthesize NPs.

REFERENCES

Abstreiter, G., and D. Lockwood. 1998. Light emission in silicon: From physics to devices. *Semiconductors and Semimetals* 49:38–39.

Alexandrescu, R., F. Dumitrache, I. Morjan, et al. 2004. TiO_2 nanosized powders by $TiCl_4$ laser pyrolysis. *Nanotechnology* 15 (5):537.

Bi, X., and N. Kambe. 2001. Efficient production of particles by chemical reaction. Google Patents.

Bouhadoun, S., C. Guillard, F. Dapozze, et al. 2015. One step synthesis of N-doped and Au-loaded TiO2 nanoparticles by laser pyrolysis: Application in photocatalysis. *Applied Catalysis B: Environmental* 174–175:367–375.

Cannon, W.R., S.C. Danforth, J.H. Flint, J.S. Haggerty, and R.A. Marra. 1982. Sinterable ceramic powders from laser-driven reactions: I, process description and modeling. *Journal of the American Ceramic Society* 65 (7):324–330.

Cannon, W.R., S.C. Danforth, J.S. Haggerty, and R.A. Marra. 1982. Sinterable ceramic powders from laser-driven reactions: II, powder characteristics and process variables. *Journal of the American Ceramic Society* 65 (7):330–335.

D'Amato, R., M. Falconieri, S. Gagliardi, et al. 2013. Synthesis of ceramic nanoparticles by laser pyrolysis: From research to applications. *Journal of Analytical and Applied Pyrolysis* 104:461–469.

Duncan, M.A., T.G. Dietz, and R.E. Smalley. 1981. Laser synthesis of metal-clusters from metal-carbonyl microcrystals. *Journal of the American Chemical Society* 103 (17):5245–5246.

Erogbogbo, F., T. Lin, P.M. Tucciarone, et al. 2013. On-demand hydrogen generation using nanosilicon: Splitting water without light, heat, or electricity. *Nano Letters* 13 (2):451–456.

Erogbogbo, F., T. Liu, N. Ramadurai, et al. 2011. Creating ligand-free silicon germanium alloy nanocrystal inks. *ACS Nano* 5 (10):7950–7959.

Erogbogbo, F., K.-T. Yong, I. Roy, et al. 2010. In vivo targeted cancer imaging, sentinel lymph node mapping and multi-channel imaging with biocompatible silicon nanocrystals. *ACS Nano* 5 (1):413–423.

Fu, J., N.N. Daanen, E.E. Rugen, D.P. Chen, and S.E. Skrabalak. 2016. Simple reactor for ultrasonic spray synthesis of nanostructured materials. *Chemistry of Materials* 29 (1):62–68.

Gao, B. 2007. Fabrication and activation processes for nanostructure composite field emission cathodes. Google Patents.

Haggerty, J.S. 1981. Sinterable powders from laser driven reactions: final report.

Herlin-Boime, N., M. Mayne-L'Hermite, and C. Reynaud. 2006. Advances in the laser pyrolysis synthesis of nanoparticles. Paper read at Annales de chimie.

Kim, S., S.Y. Park, J. Jeong, et al. 2015. Production of pristine, sulfur-coated and silicon-alloyed germanium nanoparticles via laser pyrolysis. *Nanotechnology* 26 (30):305703.

Kortshagen, U. 2009. Nonthermal plasma synthesis of semiconductor nanocrystals. *Journal of Physics D: Applied Physics* 42 (11):113001.

Lew, K.-K., L. Pan, E.C. Dickey, and J.M. Redwing. 2003. Vapor–liquid–solid growth of silicon–germanium nanowires. *Advanced Materials* 15 (24):2073–2076.

Lewis, K. E., D. M. Golden, and G. P. Smith. 1984. Organomettalic bond-dissociation energies - laser pyrolysis of $Fe(CO)_5$, $Cr(CO)_6$, $Mo(CO)_6$, and $W(CO)_6$. *Journal of the American Chemical Society* 106 (14):3905–3912.

Li, L., M. Hong, M. Schmidt, et al. 2011. Laser nano-manufacturing–state of the art and challenges. *CIRP Annals-Manufacturing Technology* 60 (2):735–755.

Li, X., Y. He, S.S. Talukdar, and M.T. Swihart. 2003. Process for preparing macroscopic quantities of brightly photoluminescent silicon nanoparticles with emission spanning the visible spectrum. *Langmuir* 19 (20):8490–8496.

Martínez, G., V. Sebastián, and J.L. Hueso. 2014. Alternative methodologies for the production of nanomaterials based on microfluidics and laser pyrolysis technologies. *Manufacturing Nanostructures*:417–448.

Mijatovic, D., J.C.T. Eijkel, and A. Van Den Berg. 2005. Technologies for nanofluidic systems: top-down vs. bottom-up—a review. *Lab on a Chip* 5 (5):492–500.

Pignon, B., H. Maskrot, V.G. Ferreol, et al. 2008. Versatility of laser pyrolysis applied to the synthesis of TiO_2 nanoparticles–Application to UV attenuation. *European Journal of Inorganic Chemistry* 2008 (6):883–889.

Ren, S.-F., C. Wei, and P.Y. Yu. 2004. Microscopic investigation of phonon modes in SiGe alloy nanocrystals. *Physical Review B* 69 (23):235327.

Rice, G.W., and R.L. Woodin. 1989. Kinetics and mechanism of laser-driven powder synthesis from organosilane precursors. *Journal of Materials Research* 4 (06):1538–1548.

Rohani, P., S. Kim, and Swihart, M.T. 2016. Boron nanoparticles for room-temperature hydrogen generation from water. *Advanced Energy Materials* 6 (12).

Saidur, R., K.Y. Leong, and H.A. Mohammad. 2011. A review on applications and challenges of nanofluids. *Renewable and Sustainable Energy Reviews* 15 (3):1646–1668.

Sourice, J., A. Bordes, A. Boulineau, et al. 2016. Core-shell amorphous silicon-carbon nanoparticles for high performance anodes in lithium ion batteries. *Journal of Power Sources* 328:527–535.

Sublemontier, O., F. Lacour, Y. Leconte, N. Herlin-Boime, and C. Reynaud. 2009. CO_2 laser-driven pyrolysis synthesis of silicon nanocrystals and applications. *Journal of Alloys and Compounds* 483 (1):499–502.

Swihart, M.T. 2003. Vapor-phase synthesis of nanoparticles. *Current Opinion in Colloid & Interface Science* 8 (1):127–133.

Wu, Y., R. Fan, and P. Yang. 2002. Block-by-block growth of single-crystalline Si/SiGe superlattice nanowires. *Nano Letters* 2 (2):83–86.

15

Laser Spectroscopy: Section Introduction

Subhash C. Singh, Pavel Redkin, and Chunlei Guo

This section discusses various types of laser spectroscopy techniques. Raman scattering is inelastic scattering of light with excitation or de-excitation of matter. Typically, only a small fraction of photons scatters inelastically. Therefore, before the advent of lasers, Raman scattering had far less practical relevance. Today, Raman spectroscopy has a wide range of applications, including biology, medicine, temperature sensing in optical fibres, analyses of artworks, and the detection of explosives. In Chapter 16, a detailed review of modern state of laser Raman spectroscopy and its applications is presented.

On the other hand, Rayleigh scattering is an elastic process. Chapter 17 describes the application of Rayleigh scattering of laser radiation for the determination of particle sizes with a complicated statistical technique of dynamic light scattering (DLS).

High-intensity laser beam can induce optical breakdown, which can be used for spectral characterization of materials, leading to the so-called laser-induced breakdown spectroscopy to be reviewed in Chapter 18.

Rapid detection and classification is important in biotechnology and medicine. Most complex molecules have characteristic fluorescence bands, which are so narrow that only laser sources can provide a required spectral power. This property of lasers is widely used in the detection of molecular systems. Recent advances in laser-induced fluorescence in the detection of vegetation and microbes is the subject of Chapter 19.

The last three chapters discuss the importance and applications of non-linear optics in laser spectroscopy. Indeed, the advent of the laser enables strong non-linear optical processes, which further revolutionize optical spectroscopy.

Chapter 20 describes different non-linear processes. Recently, novel nanomaterials were used for generating strong optical non-linearities. Chapter 21 reviews the creation of nanomaterials for non-linear optics and describes their non-linear optical properties.

Taylor & Francis
Taylor & Francis Group
http://taylorandfrancis.com

16

Laser Raman Spectroscopy: Fundamentals to Applications

Siva Umapathy Deepak Ranjan Nayak, Khokan Roy, and Sanchita Sil

CONTENTS

16.1 Raman Scattering ... 171
16.2 Theory of Raman Scattering ... 172
  16.2.1 Classical Description of Raman Effect ... 173
  16.2.2 Quantum Mechanical Description of Raman Effect ... 175
  16.2.3 Instrumentation ... 176
16.3 Other Raman Spectroscopic Techniques ... 178
  16.3.1 Surface-Enhanced Raman Scattering ... 178
    16.3.1.1 Origin of Enhancement ... 178
  16.3.2 Non-linear Raman and Ultrafast Spectroscopy ... 180
    16.3.2.1 Theory and Instrumentation of Non-linear Third-Order Processes ... 181
    16.3.2.2 Experimental Method ... 181
16.4 Applications of Raman Spectroscopy ... 182
  16.4.1 Carbon Characterization Using Raman Spectroscopy ... 182
  16.4.2 Applications of SERS ... 183
  16.4.3 Raman Spectroscopy in Semiconductors ... 183
  16.4.4 Raman Spectroscopy for Pharmaceutical Analysis ... 184
16.5 Raman Spectroscopic Techniques for Non-invasive Depth-Resolved Studies ... 186
    16.5.1.1 Spatially Offset Raman Spectroscopy ... 186
    16.5.1.2 Universal Multiple-Angle Raman Spectroscopy ... 186
    16.5.1.3 Transmission Raman Spectroscopy (TRS) ... 186
16.6 Raman Imaging: From 2D Mapping Towards 3D Imaging ... 187
16.7 Non-linear Spectroscopic Applications ... 188
  16.7.1 Photoisomerization of Optically Excited Solvated *Trans*-stilbene ... 189
  16.7.2 Ultrafast Structural Dynamics ... 190
  16.7.3 Excited-state Planarization Dynamics of Bis(phenylethnyl)benzene ... 191
16.8 Conclusion and Future Directions ... 192
References ... 193

16.1 Raman Scattering

When an electromagnetic (EM) radiation is incident on a particle, a multitude of processes can occur. First, the energy can be re-radiated by the particle at the same wavelength. The secondary radiation by the particle may take place in all directions with different intensities. Secondly, the radiant energy may be transformed to other forms of energy such as heat or is expended to drive a chemical reaction. This process is termed as absorption. For some molecules, the electron absorbs a high-energy photon and the system gets excited electronically and vibrationally. The system eventually relaxes vibrationally (internal conversion) and fluoresces at a longer wavelength. These processes are summarized in Figure 16.1. When light is scattered from a molecule, most photons are elastically scattered. The scattered photons have the same energy (and therefore same frequency and wavelength) as the incident photons. However, when the incident photons exchange energy with the matter, a small fraction of the scattered light (approximately 1 in 10^7 photons) is at optical frequencies different from, and usually lower than, the frequency of the incident photons. The process leading to this inelastic scattering is termed the Raman effect. The frequency of the scattered photon can be shifted upwards or downwards from the original incident photon. The downshifted scattered frequency is known as Stokes Raman scattering, and the upshifted scattered frequency is known as anti-Stokes Raman scattering (Figure 16.1b). The energy absorbed by the molecules is utilized for rotational or vibrational transitions of Raman active modes. Such transitions are governed by the quantum mechanical selection rules.

It is a widely used spectroscopic technique to study molecular properties of matter as rotational and vibrational energy levels of molecules can be easily probed using visible laser

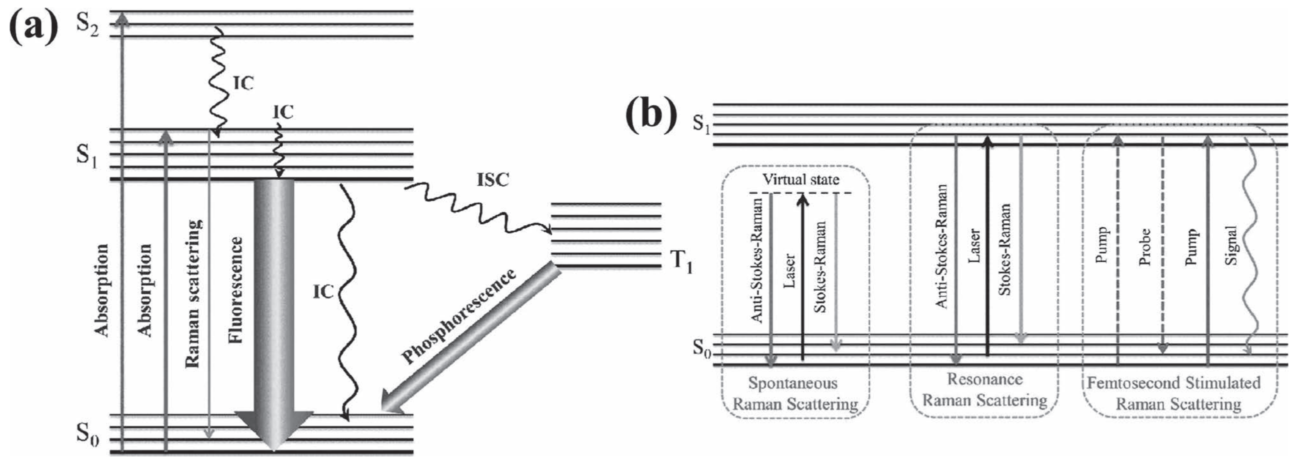

FIGURE 16.1 Jablonski diagram for various linear and non-linear processes.

sources. Generally, spatially coherent lasers are the best monochromatic light sources for Raman scattering.

16.2 Theory of Raman Scattering

When an electric field is applied to a molecule, it induces a dipole moment. This induced dipole moment is linearly proportional to the applied electric field. Alternatively, susceptibility or polarizability (α) is a measure of the ease with which the electron cloud in the oscillator can be deformed. The deformation is dependent (directly proportional) on the extent of the external force or the applied electric field. The displaced electrons and the nucleus form a dipole, and the magnitude (the direction points towards the applied electric field) of the induced dipole moment is expressed as follows:

$$\begin{gathered}\vec{P}=\varepsilon_0\chi_e\vec{E}\\ \text{or, }\vec{P}=\alpha\vec{E}\end{gathered}\tag{16.1}$$

where ε_0 is the electric permittivity of free space and χ_e is the electric susceptibility. Equation (16.1) does not hold for higher magnitude of electric field ($>10^{10}\,\text{V m}^{-1}$) but for the current discussion pertaining to Rayleigh (elastic scattering) and Raman (inelastic scattering) satisfies a linear relation between the induced dipole moment and the applied electric field. In case of non-linear spectroscopic technique such as stimulated Raman scattering (SRS), higher-order terms of Equation (16.1) have to be considered as explained in Section 16.1.3.2.

The expression above is necessary in deriving the atomic polarizability but not sufficient when applied to molecular polarizability. To define molecular polarizability, the vectorial nature of P and E along with the tensor α needs to be evoked. The induced dipole moment may not be along the applied electric field due to the symmetry of the molecule. For example, linear molecule CO_2 has a polarizability of $4.5 \times 10^{-40}\,\text{C}^2\text{m N}^{-1}$ ($\alpha_\parallel$) when the applied electric field is along the axis of the molecule but $2 \times 10^{-40}\,\text{C}^2\text{m N}^{-1}$ ($\alpha_\perp$) when the field is perpendicular. If the field is applied at a certain angle to the molecular axis, the induced dipole moment may not be along the applied field. To find out the direction, the electric field needs to be resolved along and perpendicular to the molecular axis. This is well explained by fixing a two-axis coordinate system with the molecule as shown in Figure 16.2.

As discussed earlier, the polarizability for the system can be expressed in the form of matrix as follows:

$$\begin{gathered}\vec{P}=\alpha\vec{E}\\ \Rightarrow\begin{pmatrix}P_\perp\\ P_\parallel\end{pmatrix}=\begin{pmatrix}\alpha_{\perp,\perp} & \alpha_{\perp,\parallel}\\ \alpha_{\parallel,\perp} & \alpha_{\parallel,\parallel}\end{pmatrix}\begin{pmatrix}E_\perp\\ E_\parallel\end{pmatrix}\end{gathered}\tag{16.2}$$

The perpendicular component of the polarizability is zero when the electric field is applied along the parallel axis, and vice versa. This makes both the off-diagonal components zero. Thus, Equation (16.2) reduces to the expression given below:

$$\begin{gathered}\begin{pmatrix}P_\perp\\ P_\parallel\end{pmatrix}=\begin{pmatrix}\alpha_{\perp,\perp} & 0\\ 0 & \alpha_{\parallel,\parallel}\end{pmatrix}\begin{pmatrix}E_\perp\\ E_\parallel\end{pmatrix}\\ \Rightarrow\vec{P}=\alpha_\perp E_\perp+\alpha_\parallel E_\parallel\end{gathered}\tag{16.3}$$

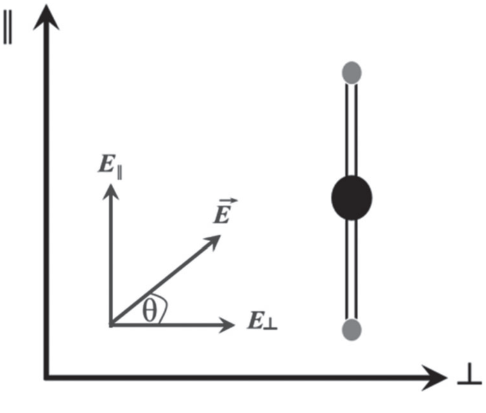

FIGURE 16.2 Vector analysis of the incident electric field w.r.t. CO_2 molecule's coordinate system.

The previous example is simple enough to comprehend due to the symmetry of the molecule. Describing the polarizability for an asymmetric molecule would require considering all the components along the three axes, which can be written as follows:

$$\begin{bmatrix} P_x \\ P_y \\ P_z \end{bmatrix} = \begin{bmatrix} \alpha_{xx} & \alpha_{xy} & \alpha_{xz} \\ \alpha_{yx} & \alpha_{yy} & \alpha_{yz} \\ \alpha_{zx} & \alpha_{zy} & \alpha_{zz} \end{bmatrix} \begin{bmatrix} E_x \\ E_y \\ E_z \end{bmatrix} \tag{16.4}$$

The polarizability matrix thus described is a second rank tensor – tensor whose elements have two indices connecting two vectors $\left(\vec{P} \text{ and } \vec{E}\right)$. Choosing a proper coordinate system in the case of CO_2 reduced the number of elements in the polarizability matrix. The same theory can be applied to any asymmetric molecule to reduce the number of components (α_{ij}, $i, j=x, y$ or z) in the matrix to three diagonal components (α_{ii}) by choosing a proper axis transformation (Long 2002). The polarizability tensor can be further simplified by representing it in terms of an ellipsoid where the principal components, α_{ii}, represent the semi-minor axes of the ellipsoid. These axes have values of $\alpha_{ii}^{-1/2}$, implying a small ellipsoid in graphical representation to a large polarizability. The relation will be recalled in the Raman polarizability ellipsoid discussion.

The polarizability discussed above is the intrinsic polarizability of the molecule. Incident EM radiation causes the electronic distribution of the molecule to deform, thereby inducing a dipole. The dipole in turn oscillates in phase (phase difference arises if α is complex) with the applied electric field of the EM wave and re-emits EM wave at the same frequency. But the incident EM wave does not induce the same amount of dipole moment all the time; i.e., the molecule does not exhibit the same polarizability due to the molecular vibrations.

Molecule with N atoms ($N \geq 2$) has $3N$ internal degrees of freedom (i.e., three coordinates for each atom). A total of six motions correspond to translation and rotation along three axes of the molecule as a whole. The rest $3N$-6 ($3N$-5 for linear molecules) correspond to discrete vibrational motions in the molecule. The chemical bonds between the atoms restrict moving far away from the equilibrium position. The vibrations are considered to be small with a specific frequency from the molecular equilibrium. Molecules vibrate even in the ground state, and the vibrations of small amplitude perturb the electronic structure. This causes a slight change in the intrinsic polarizability of the molecule, which is observed from the scattered radiation. The derivation of the expression for the total polarizability and subjecting it to Taylor series expansion is essential to depict these molecular vibrations.

The change in the polarizability depends on the vibration, and for each vibrational mode, the molecular arrangement changes from its equilibrium position. There are a total of $3N$-6 normal vibrational modes ($3N$-5 for linear molecules). These are called normal mode k (k=1, 2, … $3N$-6), and each k corresponds to the specific vibrational pattern for which all the atoms in the molecule oscillate at the same frequency ω_k. An ideal quantum harmonic oscillator can be used to define the small vibration around the equilibrium position, where the y-axis denotes the energy and the x-axis denotes the normal mode coordinate with vibrational energy levels spaced at $\hbar\omega_k$ (Figure 16.3). The following section will provide the characteristic requirement of the molecule to exhibit vibrational information in the scattered light and Raman scattering in general.

16.2.1 Classical Description of Raman Effect

The weakly perturbed polarizability due to kth vibrational mode can be expressed using a Taylor series expansion, which is given as follows:

$$\alpha_{ij} = \left(\alpha_{ij}\right)_0 + \sum_k \left(\frac{\partial \alpha_{ij}}{\partial Q_k}\right)_0 Q_k + \frac{1}{2!}\sum_{k,l}\left(\frac{\partial^2 \alpha_{ij}}{\partial Q_k \, \partial Q_l}\right)_0 Q_k Q_l + \dots \tag{16.5}$$

where $(\alpha_{ij})_0$ is the value of polarizability at the equilibrium position or the intrinsic polarizability. The summations are over all the normal modes, and the higher-order terms contain combination and overtones. The first-order approximation to the polarizability of kth normal mode would contain only the first two terms of Equation (16.5). The total induced dipole moment in the first-order approximation due to kth normal mode is derived by using the following equation:

$$\alpha_{ij} = \left(\alpha_{ij}\right)_0 + \left(\frac{\partial \alpha_{ij}}{\partial Q_k}\right)_0 Q_k$$

$$\text{or, } P_k^1 = \left(\alpha_{ij}\right)_0 \vec{E} + \left(\frac{\partial \alpha_{ij}}{\partial Q_k}\right)_0 Q_k \vec{E} \tag{16.6}$$

The first term of Equation (16.6) represents the Rayleigh scattering involving the intrinsic polarizability of the molecule. As explained earlier, the vibration along the normal mode coordinate can be expressed as a harmonic oscillator with assumed amplitudes (Q_{k0} along Q_k). Rewriting the second term due to oscillatory nature of vibration as well as the electric field (with E_0 amplitude and ω frequency) describing the Raman dipole $\left(P_R^1\right)$ would result in the following expression:

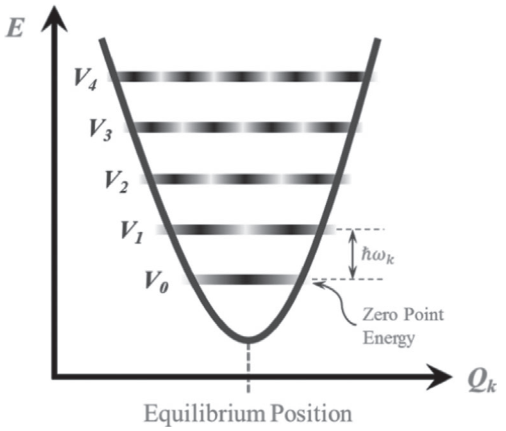

FIGURE 16.3 Simple harmonic oscillator with vibrational levels. The darker shaded region represents higher probability density.

$$P_R^1 = \left(\frac{\partial \alpha_{ij}}{\partial Q_k}\right)_0 Q_{k0} \cos\omega_k t E_0 \cos\omega t$$

$$\Rightarrow P_R^1 = \left(\frac{\partial \alpha_{ij}}{\partial Q_k}\right)_0 Q_{k0} E_0 \frac{1}{2}\left[\cos(\omega - \omega_k)t + \cos(\omega + \omega_k)t\right] \tag{16.7}$$

The Raman dipole radiates at two frequencies: frequency less than that of the incident EM wave $(\omega - \omega_k)$ called as Stokes and frequency higher than that of the incident wave $(\omega + \omega_k)$ called as anti-Stokes.

This phenomenon can be pictorially represented by taking only stretching vibration of a diatomic molecule (A-B). The explanation given below should be looked at discretely as there are some fundamental assumptions in the picture to keep the description simple. The assumptions are as follows: the phase of the oscillating dipole and the incident electric field of the EM wave are the same, the amplitude of the dipole moment with respect to the electric field is exaggeratedly plotted for visualization, and the figures are not to be scaled; hence, the phase and frequency information should not be retrieved. The picture (Figure16.4) depicts only Raman Stokes shift.

The vibration happens at a relatively smaller frequency than at the frequency of the incident EM wave, and the EM wave interacts with this oscillating molecule (Figure 16.4a). When the molecule is stretched, the electric field causes the electron cloud of the bond to deviate farther away from the equilibrium position and creates a large dipole moment; in other words, the polarizability increases. The dipole moment is small when the molecule is contracted. This vibrational mode modulates the induced dipole moment in the molecule with the frequency at which the stretching and contraction happen (Figure 16.4b). Thus, there are two (actually three, the other one for anti-Stokes, which is omitted for clarity in the schematic) oscillating dipoles radiating EM wave (Figure 16.5). One has the same frequency as that of the incident EM wave depicting Rayleigh scattering. The other dipole radiates at the frequency modulated by the vibrational frequency of the molecule, which is called Stokes Raman scattering.

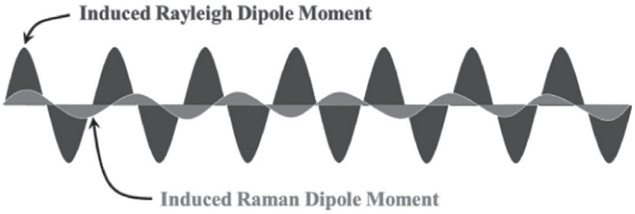

FIGURE 16.5 Different frequency components of the oscillating dipole.

It is obvious from Equation (16.7) that a molecule will emit Raman signal for kth vibrational mode only if the condition mentioned below is satisfied.

$$\left(\frac{\partial \alpha_{ij}}{\partial Q_k}\right)_0 \neq 0 \tag{16.8}$$

Equation (16.8) states that the change in the polarizability caused by the kth vibration at the equilibrium value should not be zero. The following discussion pertains to the vibrational modes of CO_2 molecule and their agreement with the above-mentioned condition.

The polarizability is plotted against the normal mode of vibrations of CO_2 molecule in Figure 16.6. CO_2 is a linear molecule and hence has four vibrational modes: asymmetric C-O stretch, symmetric C-O stretch, and two degenerate bending vibrations (in-plane and out-of-plane). The polarizability ellipsoid and induced dipole moment are related, as discussed earlier. In the stretching mode, the charges get separated during oscillation in an electric field as the atoms move far apart, thus increasing the tendency of being more polarizable. This is represented by decreasing the semi-axis lying along (as well all parallel) the bond. As the molecules contract, the axes have to be increased in size to represent the decrease in polarizability. These polarizability values have been plotted against the normal mode coordinate.

When the polarizability plot is observed for different vibrational modes, Equation (16.7) results in a nonzero value only for the symmetric stretching mode (kth vibration), whereas other modes yield zero slope at the equilibrium value. This becomes a general condition for Raman activity. The quantum

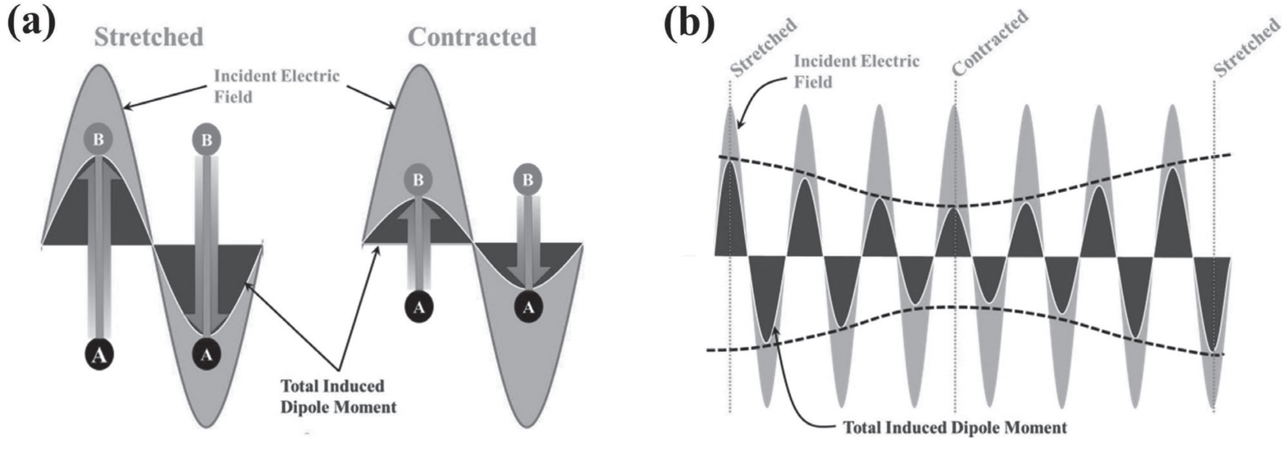

FIGURE 16.4 Induced dipole moment during stretching and compression of the molecule. Oscillating dipole due to stretching vibrational mode of the molecule.

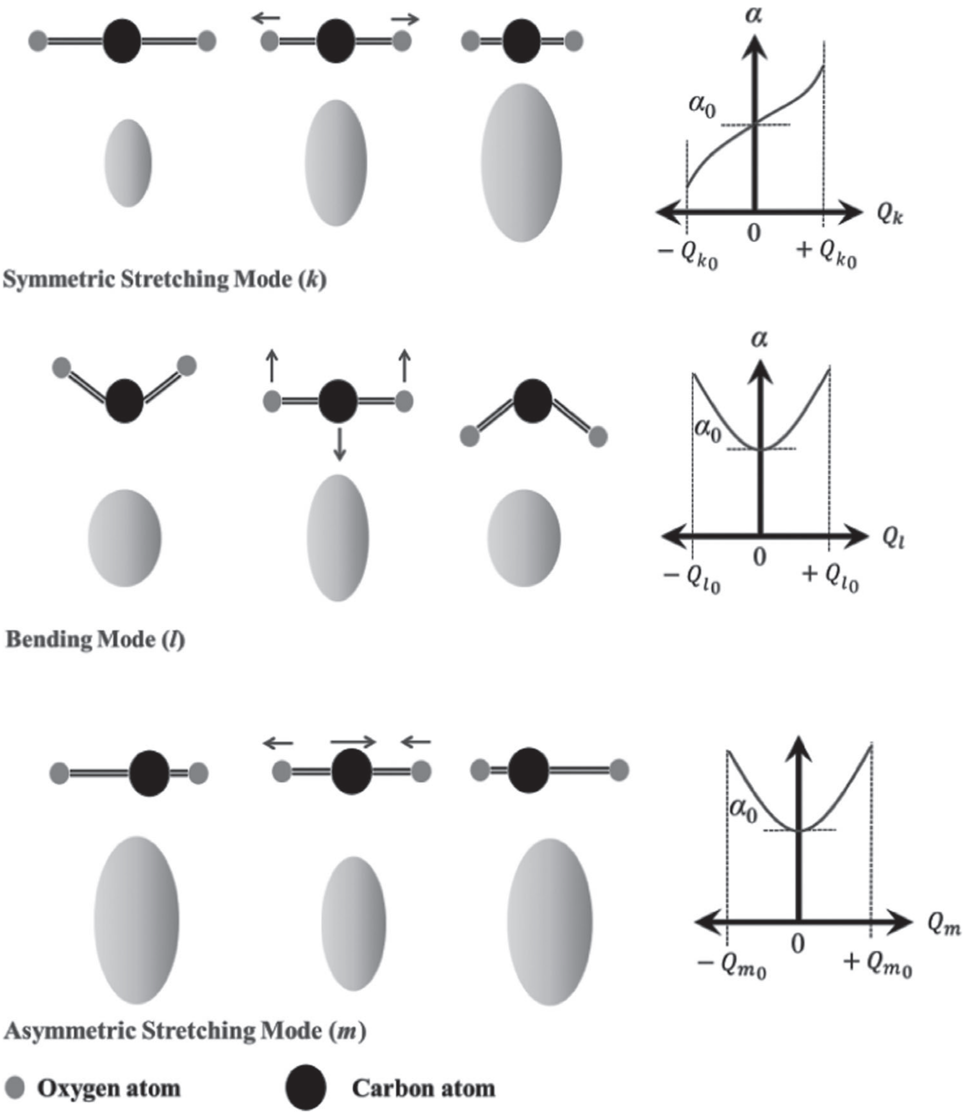

FIGURE 16.6 Different modes of vibrations, corresponding polarizability ellipsoid, and plot of change in the induced polarization.

mechanical description as well as the higher-order terms will be looked at more carefully in the next section.

16.2.2 Quantum Mechanical Description of Raman Effect

Excitation of a molecule should result in a nonzero transition dipole moment, which is defined in Dirac bracket notation as follows:

$$P_{fi} = \left\langle \psi_f | \hat{P} | \psi_i \right\rangle \tag{16.9}$$

The operator $\hat{P}$ is an induced dipole moment operator, and ψ_i and ψ_f are the initial and final vibrational state wave functions of the molecule. All the terms are a function of the nuclear coordinate. The assumption in Equation (16.9) requires the incident frequency to be greater than the vibrational transition frequency but less than the electronic transition frequency and the molecule's ground state to be non-degenerate. The dipole moment operator takes the same expression as in Equation (16.2) with an exception of the polarizability tensor, which acts as an operator $\left(\hat{P} = \hat{\alpha} E_0\right)$. The dimensions of the molecules are in the order of Angstroms; hence, it is quite reasonable to take a constant electric field over the entire molecule at a given instant of time. Thus, the modified Equation (16.9) in matrix and bracket notation is expressed as follows:

$$\begin{bmatrix} (P_x)_{fi} \\ (P_y)_{fi} \\ (P_z)_{fi} \end{bmatrix} = \begin{bmatrix} (\alpha_{xx})_{fi} & (\alpha_{xy})_{fi} & (\alpha_{xz})_{fi} \\ (\alpha_{yx})_{fi} & (\alpha_{yy})_{fi} & (\alpha_{yz})_{fi} \\ (\alpha_{zx})_{fi} & (\alpha_{zy})_{fi} & (\alpha_{zz})_{fi} \end{bmatrix} \begin{bmatrix} E_x \\ E_y \\ E_z \end{bmatrix}$$

$$\text{where, } (\alpha_{xx})_{fi} = \left\langle \psi_f | \alpha_{xx} | \psi_i \right\rangle \text{and so on} \tag{16.10}$$

Equation (16.11) should consider all the nine components of the polarizability tensor. However, the subscript is dropped for simplicity.

From Equations (16.9) and (16.10), the following expression can be written within the first-order approximation.

$$(\alpha)_{fi} = \langle \psi_f | (\alpha)_0 | \psi_i \rangle + \sum_k \left(\frac{\partial \alpha}{\partial Q_k} \right)_0 \langle \psi_f | \hat{Q}_k | \psi_i \rangle \tag{16.11}$$

In the harmonic oscillator, the total vibrational wave function for a particular state is the product of all the vibrational wave functions of each normal mode of vibration. Thus, the vibrational states are expressed as follows:

$$\begin{aligned} \psi_f &= \prod_k \psi_f^k (Q_k) \\ \text{and } \psi_i &= \prod_k \psi_i^k (Q_k) \end{aligned} \tag{16.12}$$

where $\psi_f^k(Q_k)$ and $\psi_i^k(Q_k)$ are the wave functions associated with the normal mode Q_k and have vibrational quantum numbers v_f^k and v_i^k corresponding to the final and the initial state of the *k*th mode. Hence, Equation (16.11) is rewritten as

$$\begin{aligned} (\alpha)_{fi} = &\left\langle \prod_k \psi_f^k (Q_k) | (\alpha)_0 | \prod_k \psi_i^k (Q_k) \right\rangle \\ &+ \sum_k \left(\frac{\partial \alpha_{ij}}{\partial Q_k} \right)_0 \left\langle \prod_k \psi_f^k (Q_k) | \hat{Q}_k | \prod_k \psi_i^k (Q_k) \right\rangle \end{aligned} \tag{16.13}$$

The first term in the equation has the intrinsic polarizability, which is a constant, in the inner product. As the constant is taken out of the inner product, the term is nonzero when both the wave functions have the same quantum number (due to orthogonality). Hence,

$$\left\langle \prod_k \psi_f^k (Q_k) | \prod_k \psi_i^k (Q_k) \right\rangle = \left\{ \begin{array}{l} 0 \text{ for } v_f^k \neq v_i^k \\ 1 \text{ for } v_f^k = v_i^k \end{array} \right\} \tag{16.14}$$

This is the basis of Rayleigh scattering where the molecule ends up in the same initial state for any normal mode.

The second term has the operator $\hat{Q}_k$ similar to the displacement operator. The solution to the inner product (McHale 1999) is given as follows:

$$\left\langle \prod_k \psi_f^k (Q_k) | \hat{Q}_k | \prod_k \psi_i^k (Q_k) \right\rangle = \left\{ \begin{array}{c} \sqrt{\dfrac{\hbar \left(v_i^k + 1 \right)}{2\omega_k}} \delta_{v_f^k,\ v_i^k + 1} \\ \sqrt{\dfrac{\hbar v_i^k}{2\omega_k}} \delta_{v_f^k,\ v_i^k - 1} \end{array} \right\} \tag{16.15}$$

The Kronecker delta function becomes the selection rule for the Raman scattering. The rule $v_f^k = v_i^k \pm 1$ suggests that the vibrations are allowed where the quantum number changes by 1 or to the adjacent vibration level. The −1 and +1 changes indicate a decrease and an increase in the vibrational level, respectively, corresponding to anti-Stokes and Stokes. These are the fundamental transitions. The value $\sqrt{\dfrac{\hbar}{2\omega_k}}$ is the amplitude of oscillation similar to that described in Equation (16.7).

The higher-order terms in Equations (16.5) and (16.11) relate to the anharmonicity in the oscillator. These are operators in the quantum treatment and can be expressed as follows:

$$\begin{aligned} &\sum_k \left(\frac{\partial^2 \alpha}{\partial {Q_k}^2} \right)_0 {\hat{Q}_k}^2 \\ &\text{and, } \sum_{k,l} \left(\frac{\partial^2 \alpha}{\partial Q_k \, \partial Q_l} \right)_0 \hat{Q}_k \hat{Q}_l \end{aligned} \tag{16.16}$$

The operators described in Equation (16.16) operate on the total vibrational state of the molecule (Equation 16.12). Nonzero terms for *k*th mode are as follows:

$$\left(\frac{\partial^2 \alpha}{\partial {Q_k}^2} \right)_0 \psi_f^k (Q_k) | {\hat{Q}_k}^2 | \psi_i^k (Q_k) \tag{16.17}$$

$$\text{and, } \sum_{k,l} \left(\frac{\partial^2 \alpha}{\partial Q_k \, \partial Q_l} \right)_0 \psi_f^k (Q_k) | \hat{Q}_k | \psi_i^k (Q_k) \psi_f^l (Q_l) | \hat{Q}_l | \psi_i^l (Q_l) \tag{16.18}$$

Equation (16.17) is nonzero for vibrational quantum number change $v_f^k = v_i^k \pm 2$, which relates to the vibrational overtone. The conditions for Equation (16.18) are the same as those in Equation (16.15); i.e., quantum number should change by ±1 for both *k*th and *l*th modes. These are combination bands of two different vibrations which are allowed only if the second derivative is nonzero. The elaborate quantum mechanical treatment for Raman scattering can be found in textbooks (McHale 1999) using KHD (Kramers–Heisenberg–Dirac) expression. The KHD formalism suggests a transition dipole moment operator, which causes a transition from an initial vibrational state to a virtual state, and another operator which causes a transition from the virtual to the final state.

16.2.3 Instrumentation

A generic dispersive Raman spectroscopic instrument consists of the following components: a laser source, a spectrometer (consisting of gratings and mirrors), and a detector (such as a charge-coupled device) (Figure 16.7). Most of the modern-day Raman systems are equipped with a microscope to provide a better spatial resolution. Typically, light from a laser source is directed towards a sample either using conventional optics or through a microscope. In many cases, optical fibres are used to deliver light and collect Raman signals. The scattered light carrying the molecule-specific signatures is guided through suitable optics into a spectrometer, which consists of a grating that disperses the light into individual wavelength. The dispersed photons are collected by the detector and viewed on a computer. A Raman spectrum contains information of the scattered light intensity, which is plotted against energy (Raman shift, cm^{-1}). Raman microspectrometers in general have a 180° backscattering geometry. However, other

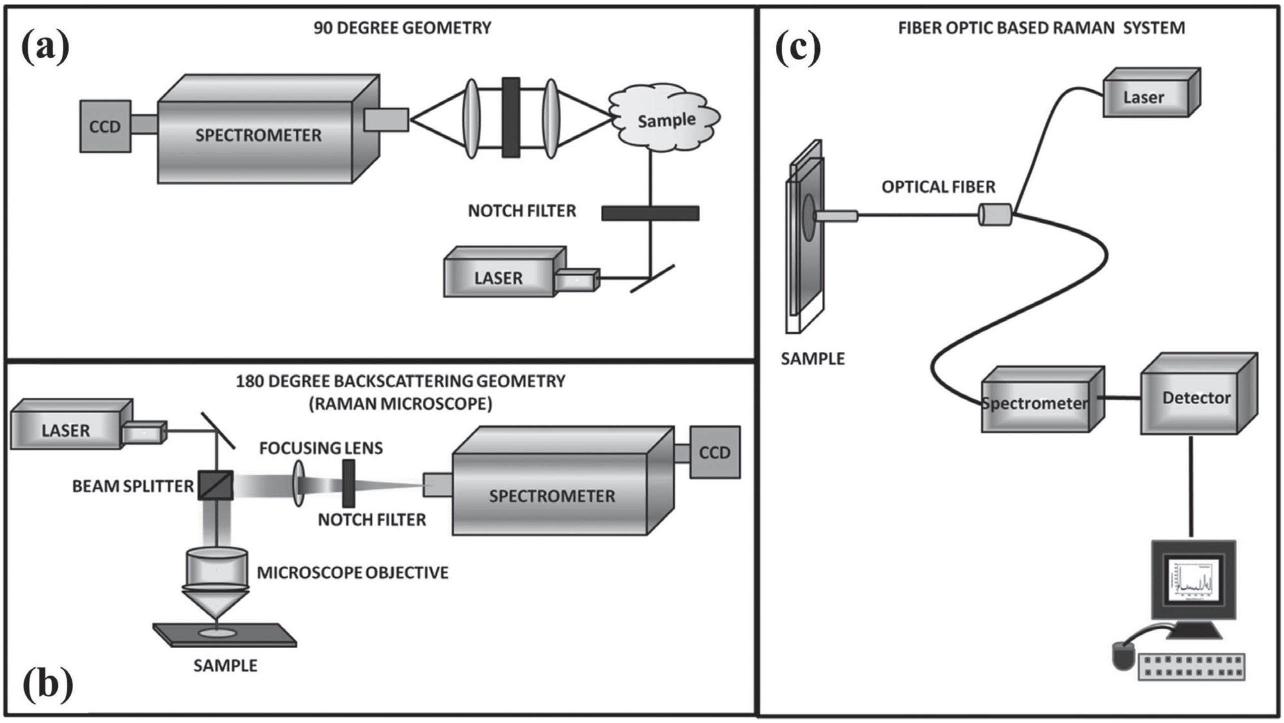
(a)
90 DEGREE GEOMETRY
CCD
SPECTROMETER
Sample
NOTCH FILTER
LASER
(b)
180 DEGREE BACKSCATTERING GEOMETRY
(RAMAN MICROSCOPE)
LASER
FOCUSING LENS
BEAM SPLITTER
NOTCH FILTER
SPECTROMETER
CCD
MICROSCOPE OBJECTIVE
SAMPLE
(c)
FIBER OPTIC BASED RAMAN SYSTEM
Laser
OPTICAL FIBER
SAMPLE
Spectrometer
Detector

FIGURE 16.7 Schematic representation of commonly used configurations for Raman spectroscopic studies. (a) 90° geometry, (b) 180° geometry, and (c) fibre optics-based Raman system. The figures are merely representation and are not to scale. In the Raman microscopic system, the microscope is not shown for brevity.

configurations including 90° and 0° (transmission) are also employed for Raman analysis (Figure 16.8). These configurations have a profound effect on the signal magnitude, reproducibility, and the signal-to-noise ratio. Therefore, one must critically review the applications before designing the Raman spectrometer.

The incident laser photon gets scattered by the molecule, and one in a million photon either loses or gains energy equivalent to the energy gap of molecular vibrations. The energy is expressed in the unit of wavenumber [cm^{-1}]. This difference is plotted in the Raman spectrum with respect to intensity. The relationship between Raman (λ_R) and incident radiation (λ_I) is as follows:

$$\bar{\nu}\left[\text{cm}^{-1}\right] = \frac{10^7}{\lambda_I\,[\text{nm}]} - \frac{10^7}{\lambda_R\,[\text{nm}]} \tag{16.19}$$

The energy gap and hence the shift always remain the same irrespective of the excitation. In the previous example, CO_2 symmetric stretch has ~1390 cm^{-1} Raman shift, which means the Raman wavelength is 554 nm for 514 nm laser excitation and 694 nm for 633 nm laser excitation.

Raman spectrum gives three important information: frequency (Raman shift), intensity, and bandwidth. Molecular structure dictates Raman shift. The bandwidth is affected by homogeneous and inhomogeneous broadening. As the word suggests, homogenous broadening is caused by certain effects experienced by all the molecules under study. The laser bandwidth ($\Delta\lambda$) adds energy ($\Delta\lambda/\ \lambda^2$[cm^{-1}]) to the actual spectral width of a Raman peak, which contributes to homogenous broadening. Another instance of such broadening is observed in vibrational state fluctuation due to environmental, for example, increase in temperature. Inhomogeneous broadening is caused by few molecules under experiment, and it is observed in a different environment than others. For example, molecules near to a surface resulting in physisorption or chemisorption would result in certain energy shift compared to free molecules. Thus, the overall statistics will result in a broadened peak.

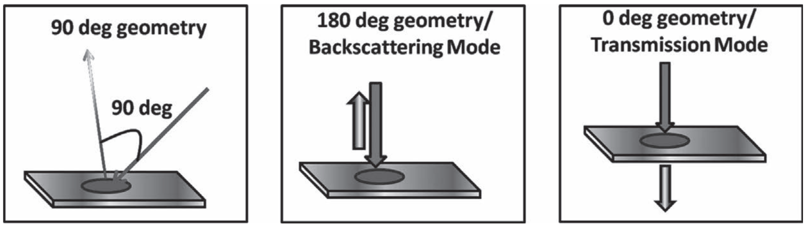
90 deg geometry
90 deg
180 deg geometry/
Backscattering Mode
0 deg geometry/
Transmission Mode

FIGURE 16.8 Schematic representation of sampling geometries in Raman spectroscopic studies. The selection of a particular geometry is dictated by the specific applications.

Doppler effect also causes such type of broadening. This effect is governed by statistics and therefore results in a Gaussian distribution of spectral intensity. The homogeneous broadening, however, is a Lorentzian function. Hence, spectral analysis by curve fitting should be carried out carefully with a well-chosen line shape function. Mostly used Voigt profile takes both the broadening types into account as it is a convolution of Gaussian and Lorentzian functions (McHale 1999).

The Raman intensity (I_R) can be expressed as follows:

$$I_R \propto I_{\text{Laser}} C_{\text{volume}} \sigma_{\text{Raman}} g$$

$$\text{or, } I_R \propto I_{\text{Laser}} C_{\text{volume}} \frac{\alpha_{\text{raman}}{}^2}{\lambda_{\text{Laser}}{}^4} g \tag{16.20}$$

The Raman intensity depends on the incident laser intensity (I_{Laser}), which is the square of the electric field of the EM wave. The number of molecules (C_{volume}) probed in the volume relates to the number of Raman photons scattered. Hence, an analyte solution with high concentration would provide a better Raman spectrum. The intensity depends on the Raman cross section (σ_{Raman}) of the molecule, which inherently has the polarizability $(\alpha_{\text{raman}}{}^2)$ and wavelength $(\lambda_{\text{Laser}}{}^4)$ dependency. However, in many cases such as in biological samples, fluorescence masks the Raman signal. Therefore, longer-wavelength laser is desirable albeit with low scattering. The above expression gives the intensity for Stokes shift, whereas the intensity of anti-Stokes is obtained by multiplying the Boltzmann factor. The molecule should be in a vibrationally excited state to exhibit anti-Stokes shift.

These are some fundamental and inherent properties of the whole process but essentially the collection profile of the instrumentation (g) is a crucial parameter in deciding the sensitivity and resolution of Raman spectrum. Most Raman microscopes are designed to collect at 180° scattering geometry. The objectives in such instruments majorly contribute to the collection efficiency.

The collection efficiency and the illumination of the sample depend on the numerical aperture (NA) of the objective. Half of the angular aperture (θ) decides the beam profile as given in Figure 16.9. The beam waist (ω_0) and Rayleigh range (z_R) depend on the NA of the objective and the medium refractive index (n) as given in Equation (16.21) (Álvarez-Puebla 2012). The waist size and the incident laser power (P_{inc}) decide the power density of the sample, which is a crucial factor to be controlled during experiment in order to avoid sample degradation.

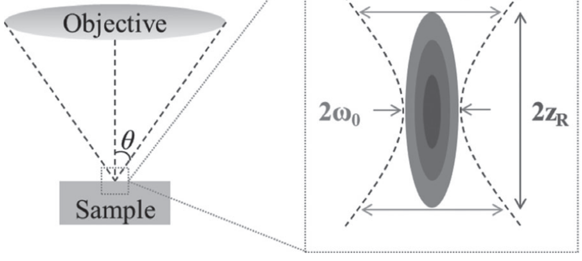

FIGURE 16.9 Depiction of focal volume and the electric field intensity profile in the focal volume.

$$NA = n \sin\theta$$

$$2\omega_0 = 1.22 \frac{\lambda_{\text{Laser}}}{NA}, \; z_R = \frac{\pi n \omega_0{}^2}{\lambda_{\text{Laser}}} \tag{16.21}$$

$$\text{Power Density} \left[W\!\big/_{m^2} \right] = \frac{2P_{\text{inc}}}{\pi \omega_0{}^2}$$

The collection efficiency and spot size decide the quality of spectra obtained from sample. Spot size controls the spatial resolution as well as power density of the sample. Biological samples, for example, cells and tissues, require a precise spatial information for which objective with high NA should be used with optimum power to avoid photodegradation. Raman spectra are typically obtained with low NA objective for liquid samples.

16.3 Other Raman Spectroscopic Techniques

Historically, low sensitivity and fluorescence interference were considered deterrents for Raman spectroscopy measurements as compared to Fourier transform infrared spectroscopy. However, these impediments have been overcome by technological innovations in Raman instrumentation. Resonance Raman spectroscopy and surface-enhanced Raman scattering (SERS) have an increased sensitivity. These technological breakthroughs have enabled Raman spectroscopy to be applied in myriad analytical problems. Compatibility of fibre optic probe with Raman spectrometer has increased the popularity of Raman for remote monitoring, for process control, and in field applications. Some of these variants of Raman spectroscopy have been discussed in the subsequent sections.

16.3.1 Surface-Enhanced Raman Scattering

Raman spectroscopy has garnered a profound attention in analytical measurements but lacks sensitivity resulting from low-scattering cross section. SERS has brought both specificity and sensitivity on the same platform. The specificity in SERS technique is largely attributable to the unique vibrations in the molecules giving rise to finger print-like spectra. Sensitivity, however, is tailored from the electric field enhancement in plasmonic nanostructure and fabrication of nanostructure for a specific wavelength.

16.3.1.1 Origin of Enhancement

16.3.1.1.1 Electromagnetic Enhancement

SERS was first observed by Fleischman et al. in 1974 for pyridine absorbed on electrochemically roughened Ag electrode (Fleischmann, Hendra, and McQuillan 1974). In 1978, Van Duyne et al. attributed the significant increase in the Raman intensity to the excitation of the surface plasmons (King, Van Duyne, and Schatz 1978).

Localised Surface Plamon Resonance (LSPR) is non-propagating excitation of the free electrons of metallic nanostructures coupled to EM field. The basic mathematical expression for such type of interaction is obtained by considering the radius a of particle much smaller than the incident wavelength. The polarizability (α) of a sphere in the approximation is given as follows:

$$\alpha = 4\pi a^3 \frac{\varepsilon - \varepsilon_m}{\varepsilon + 2\varepsilon_m} \tag{16.22}$$

where ε and ε_m are the permittivity of metal and that of adjacent medium, respectively.

Resonant enhancement in the vicinity of the sphere is observed at the wavelength for which ε is equal to $-2\varepsilon_m$. Large local field enhancement due to LSPR couples with incident and Raman EM field, which causes a remarkable enhancement in the Raman intensity. This effect is termed as EM enhancement mechanism.

The local electric field (E_{loc}) on the surface of metallic structure is tens of order of magnitude more than the incident electric field (E_{inc}). The local field hence induces a Raman dipole, whose magnitude is enhanced by a factor equal to the ratio of the electric field, which is expressed as follows:

$$EF_{\text{loc}}(\lambda_{\text{Laser}}) = \frac{\left|E_{\text{loc}}(\lambda_{\text{Laser}})\right|^2}{\left|E_{\text{inc}}\right|^2} \tag{16.23}$$

Signal enhancement takes place where Raman dipole radiation is enhanced due to the presence of the dipole near the metallic surface. The Raman radiation from the molecule is largely affected by the environment; in this case it is a metallic nanostructure. This can be obtained by solving a problem with a dipole near a metal surface (Le Ru et al. 2006). Therefore, a proper mathematical representation would require the incorporation of complex directional vectors to define the radiation reaching the detector (Le Ru et al. 2006). But it can be simplified as follows:

$$EF_{\text{loc}}(\lambda_{\text{Raman}}) = \frac{\left|E_{\text{loc}}(\lambda_{\text{Raman}})\right|^2}{\left|E_{\text{inc}}\right|^2} \tag{16.24}$$

The local field enhancement and the Raman radiation enhancement have the same origin of incident EM field coupling to the LSPR. The coupling is not identical but it can be qualitatively similar. Raman shift is small and hence can be approximated as $\lambda_{\text{Raman}} \approx \lambda_{\text{Laser}}$. In this approximation, the total enhancement factor (EF) due to LSPR is expressed as E^4 enhancement approximation (Le Ru and Etchegoin 2006).

$$EF = EF_{\text{loc}}(\lambda_{\text{Laser}})EF_{\text{loc}}(\lambda_{\text{Raman}}) = \frac{\left|E_{\text{loc}}(\lambda_{\text{Laser}})\right|^2}{\left|E_{\text{inc}}\right|^2}\frac{\left|E_{\text{loc}}(\lambda_{\text{Raman}})\right|^2}{\left|E_{\text{inc}}\right|^2}$$

$$= \frac{\left|E_{\text{loc}}(\lambda_{\text{Laser}})\right|^4}{\left|E_{\text{inc}}\right|^4} \tag{16.25}$$

The SERS EM enhancement factor of the nanoparticle, described in Figure 16.10, can be calculated to be approximately 7×10^5. EF varies from 4 to 6 orders of magnitude for SERS substrate with 2D array of metallic nanostructures. The nanostructures, when close to each other, can exhibit higher local electric field than individual. This is due to the coupling of individual LSPRs. In this case, the EF can be estimated to be more than 10^{10} (Xu et al. 2000).

The E^4 assumption fails as the Raman shift (or radiated wavelength) moves father away from the incident wavelength. Hence, it is reasonable to assume that different modes in the Raman spectra undergo EM enhancement of ${E_{\text{loc}}}^4$ to ${E_{\text{loc}}}^2$ from lower wavenumber to higher wavenumber. Since Raman radiation wavelength lies farther for longer excitation wavelength, the enhancement for the scenario is $\sim{E_{\text{loc}}}^2$.

High field enhancement is achieved by either matching the LSPR peak of the metal nanostructure to the excitation wavelength by design (size, shape, or arrangements of clusters) or choosing excitation wavelength according to the position of LSPR. This is a good practice to obtain the maximum sensitivity; however, the exact picture is slightly different. Experimental reports suggest that the maximum enhancement is obtained when the LSPR falls between the excitation and Raman wavelength $\left(\lambda_{\text{LSPR}} = \frac{\lambda_{\text{Laser}} + \lambda_{\text{Raman}}}{2}\right)$ (Felidj et al. 2003; Haynes and Van Duyne 2003).

16.3.1.1.2 Chemical Enhancement

Although the EM enhancement theory is widely accepted and successfully explains the large enhancement in the intensity,

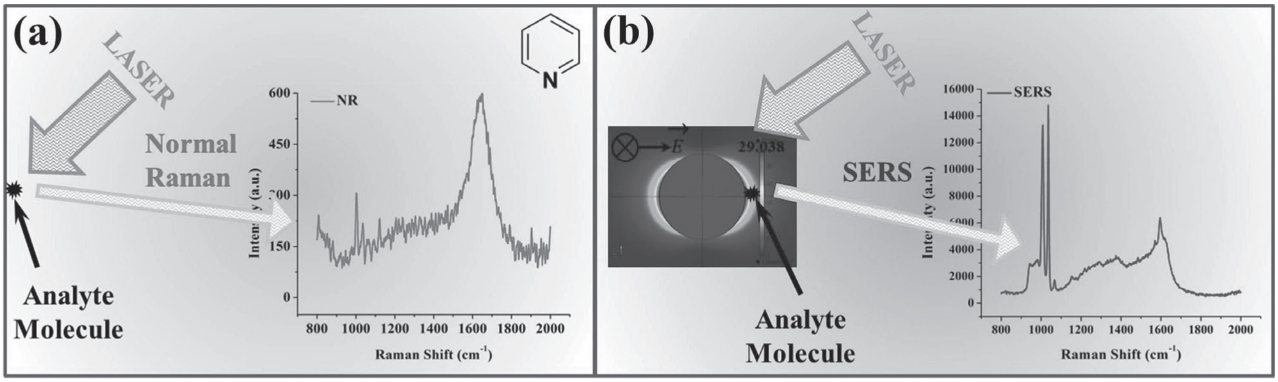

FIGURE 16.10 Schematic of (a) normal Raman and (b) SERS process.

chemical enhancement (CE) factor also contributes to the enhancement. As the effect of CE is not established thoroughly, it can be viewed as (i) modification of electronic polarizability of the adsorbed molecules and (ii) charge transfer (CT) mechanism (Creighton 1986; Wu et al. 2005). There is a probability that the molecule is physisorbed on the metal, which does not cause any significant change to the molecular structure but causes a small perturbation to the electronic structure. The other interaction can be a formation of chemical bond (chemisorption) with the metal, which forms a complex creating states which are resonant or near resonant to the laser (Gersten, Birke, and Lombardi 1979; Xie et al. 2003). The difference between the states of the molecule and the Fermi level of the metal falls in the visible region. This was experimentally observed by applying potential to the metal, thereby changing the band gap and tuning to different laser frequencies (Osawa et al. 1994; Xie et al. 2003). The maximum contribution of the CE mechanism can be up to 1–2 orders of magnitude.

16.3.1.1.3 SERS Spectrum

SERS spectrum is orders of magnitude enhanced compared to the NR (near-infrared) spectrum; hence, it is important to define a standard parameter which expresses the enhancement in a quantitative manner. This quantitation is done by calculating the SERS enhancement factor (EF). The EF can be of two types from the experimental point of view (Le Ru et al. 2007). Average EF is independent of spatial hotspots and gives an average enhancement of the SERS system. SMEF (single-molecule EF) is related to specific positions and hotspots. It is mostly used in SERS substrates with localized hotspots due to lithographically created nanostructures.

Average EF has mainly two types of calculation: SERS substrate EF (SSEF) and analytical EF (AEF). In all the calculations, the intensity of SERS (I_{SERS}) and NR (I_{NR}) is obtained with fixed instrument parameters. Suitable baseline correction is required in order to avoid EF estimation error due to background fluctuation.

SSEF is calculated as follows:

$$\mathrm{SSEF} = \frac{I_{\mathrm{SERS}} / N_{\mathrm{surf}}}{I_{\mathrm{NR}} / N_{\mathrm{vol}}} \tag{16.26}$$

The above-mentioned expression denotes the average number of molecules adsorbed on the surface (N_{surf}) of the metal nanostructure. The surface coverage must be in monolayer to calculate the actual number of molecules in the focal volume. The calculation becomes uncertain for complex nanoparticle structures. The probed number of molecules (N_{vol}) for NR is calculated from the concentration and the focal volume of the NR measurement.

The other simple method is AEF as given by the following equation:

$$\mathrm{SSEF} = \frac{I_{\mathrm{SERS}} / C_{\mathrm{SERS}}}{I_{\mathrm{NR}} / C_{\mathrm{NR}}} \tag{16.27}$$

It depends on the concentration of analyte used for SERS and NR rather than on the number of molecules. Although the calculation is simple, it relies on the adsorption of analyte on the metal nanostructure as well as sample preparation methods. This results in a sample-to-sample variability in EF if the analyte is not adsorbed. This is most suited for colloidal solution but presents a better picture from an analytical point of view.

The method of measuring SERS intensity is mainly by dropping the analyte solution on the SERS substrate. The main reason for choosing this method is to avoid the calculation error and compare the EF based on the detection of a specific analyte on the same type of substrates (e.g. Ag nanostructures created by PVD of Ag). This brings out the efficacy of nanostructures from an analytical point of view.

SERS EF of all Raman bands is not identical (Yamamoto and Itoh 2016). Adsorption mechanism (Tanaka et al. 2004; Wu et al. 2008), electric field variation (Aikens, Madison, and Schatz 2013; Ayars, Hallen, and Jahncke 2000), and surface selection rules (Moskovits and Suh 1984; Le Ru et al. 2011) are few of the aspects that contribute to a dissimilar enhancement among bands of an analyte. SERS spectrum is not always identical to the NR spectrum. The main variations observed are peak shift, relative peak intensity, and appearance of new peaks. The peaks may exhibit an increased bandwidth. Adsorption mechanism modifies the polarizability of the molecule and may give rise to new modes due to symmetry breaking. The new modes can also arise due to gradient of the intense electric field near to the metal surface. The adsorption mechanism of pyridine on silver and gold results in a change in the relative peak intensity between the ring breathing mode and asymmetric ring deformation mode. Based on the reports available, it is difficult to point out a specific reason for the change in the spectral feature. Broadly, the changes are due to all the above reasons. Hence, it is imperative to compare NR spectrum and SERS spectrum carefully and assign bands as well as reasons for variations.

16.3.2 Non-linear Raman and Ultrafast Spectroscopy

Understanding the properties of intermediate species is one of the important aspects in the area of chemistry and biology. This will help us to decode the reaction mechanism of chemical or biological processes with better clarity and thus may help in the advancement of the field. In general, the lifetimes of the intermediate species is very short for most of the chemical and biological transformations. The typical lifetime of such intermediates ranges from millisecond (10^{-3} s) to femtosecond (10^{-15} s) depending upon the reaction involved. In case of biological transformation like protein folding, dynamics occurs in microsecond to millisecond timescale. However, bond making and bond breaking, electron transfer, proton transfer, photo-induced ring opening, and *cis–trans* isomerization of retinal chromophore occur in picosecond to femtosecond timescales. All of these reactions go through some very short-lived intermediates. The notion of freezing the motion of such short-lived intermediate was introduced as "femto chemistry" by Dr. Ahmed Zewail for which he received the Nobel Prize in chemistry in 1999.

16.3.2.1 Theory and Instrumentation of Non-linear Third-Order Processes

The foregoing sections considered the linear regime of spectroscopy pertaining to the first-order expansion of polarizability (16.1). The description of non-linear spectroscopy is based on the time-dependent induced polarization $\vec{P}(t)$ considering higher-order terms as given in the following equation:

$$\vec{P}(t) = \varepsilon_0 \left[\chi^{(1)}\vec{E}(t) + \chi^{(2)}\overline{\vec{E^2}}(t) + \chi^{(3)}\overline{\vec{E^3}}(t) + \ldots\right] \qquad (16.28)$$

where the proportionality constants $\chi^{(1)}$ or χ_e, $\chi^{(2)}$, and $\chi^{(3)}$ are linear, second-order, and third-order susceptibility, respectively. For strong fields, the electronic displacement is no longer linear with respect to the applied field; therefore, the driving electric field and the induced polarization are no longer linearly related. Due to the symmetric nature of $\chi^{(2)}$, it vanishes for centrosymmetric molecules. As there is a symmetry requirement which is involved for third-order response, almost all molecular systems show third-order susceptibilities. Third-order spectroscopic techniques based on $\chi^{(3)}$ (referred as four-wave mixing processes) are more widely applied to molecular systems in the condensed phase. SRS, ultrafast Raman loss scattering (URLS), and coherent anti-Stokes Raman scattering (CARS) are typical examples of third-order non-linear optical methods. In this book, we have discussed the URLS (which is analogous to SRS with better signal-to-noise ratio), which is a third-order non-linear optical technique extensively, and its utilization in deciphering the chemical reaction dynamics as well as photophysical processes. URLS/SRS involves an interaction of three input electric fields with the molecular system. Two fields from two optical pulses are used to drive a molecular vibration in a coherent manner followed by the interaction of another field from either of the beams that leads to SRS. The two optical pulses are called Raman pump (ω_p) and Raman probe (ω_{probe}) as depicted for the ground-state URLS technique, as shown in Figure 16.11. It is a self-phase-matched process where URLS/SRS signal comes in the probe direction. So signal appears on top of the white light broadband probe. The phase matching condition of SRS is $k_{\text{sig}} = -k_1 + k_2 + k_1$, where k_1 is Raman pump and k_2 is Raman probe. So, $k_{\text{sig}} = k_2$, which implies that stimulated Raman signal always comes in the white light probe direction (Kukura et al. 2005; Mallick, Lakhsmanna, and Umapathy 2011; Umapathy, Lakshmanna, and Mallick 2009). However, for a time-resolved experiment, one photo-pump (PP) needs to be implemented to create non-stationary state. During the evolution of the non-stationary state, molecular structure is probed using the combination of Raman pump and Raman probe.

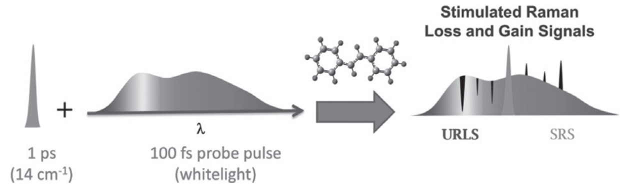

FIGURE 16.11 A schematic illustration of ground-state URLS technique implemented on the molecular system.

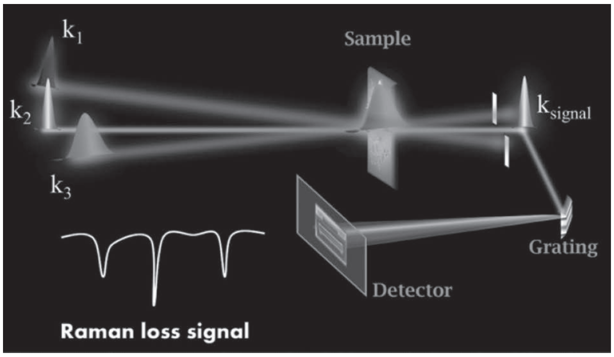

FIGURE 16.12 A schematic illustration of excited-state URLS experimental procedure with three pulses.

A simplified schematic for the excited-state ultrafast Raman measurements is given in Figure 16.12. A PP of 100 fs, resonance with an electronic transition, initiates photochemistry. The transient population subsequently evolves in the excited state. A pair of ps Raman (RP) and fs probe pulse white light (WL) interacts with the system at a later time Δt, resulting in stimulated Raman process from non-stationary excited state of the evolving molecular system.

16.3.2.2 Experimental Method

A short description of experimental set-up typically employed for time-resolved stimulated Raman experiments has been provided. FSRS (femtosecond stimulated Raman spectroscopy) / URLS requires a synchronization of multiple pulses in both space and time with two broadband fs pulses, the PP, and the probe pulse for transient absorption measurement. By delaying the PP with respect to the pair of Raman and probe pulses, time-resolved spectral dynamics are measured. Broadband detection requires a large spectral window (~ 1500 cm^{-1}) for the probe pulse. The most efficient way for producing broadband fs probe pulses is based on supercontinuum generation from a suitable non-linear crystal. This can be achieved by focusing a small fraction of laser fundamental into a sapphire or rotating CaF_2 plate. The supercontinuum generation is a highly non-linear phenomenon based on self-phase modulation and self-focusing, which can create a modulation in the spectral profile. The second or third harmonic (SHG/THG) signal of fundamental Ti: sapphire amplifier output is regularly used as a PP in time-resolved experiments. Optical parametric amplifier (OPA) output can be used as tunable excitation wavelengths from UV to the visible region. The actinic pump should have a sufficient energy (~ µJ/pulse) to produce enough molecules in the excited state. The time resolution depends on the cross-correlation between actinic and probe pulse. Fundamental pulses with 100 fs time duration can provide a time resolution of ~ 200 fs. Suitable prism compressor can be employed to increase the time resolution up to 100 fs. A schematic of the experimental set-up is shown in Figure 16.13 (Roy et al. 2017).

The spectral resolution and spectral line shapes critically depend on the shape and temporal width of the Raman pulse. Tuning the Raman pump pulse into the resonance of an electronic transition significantly improves Raman signal and specificity.

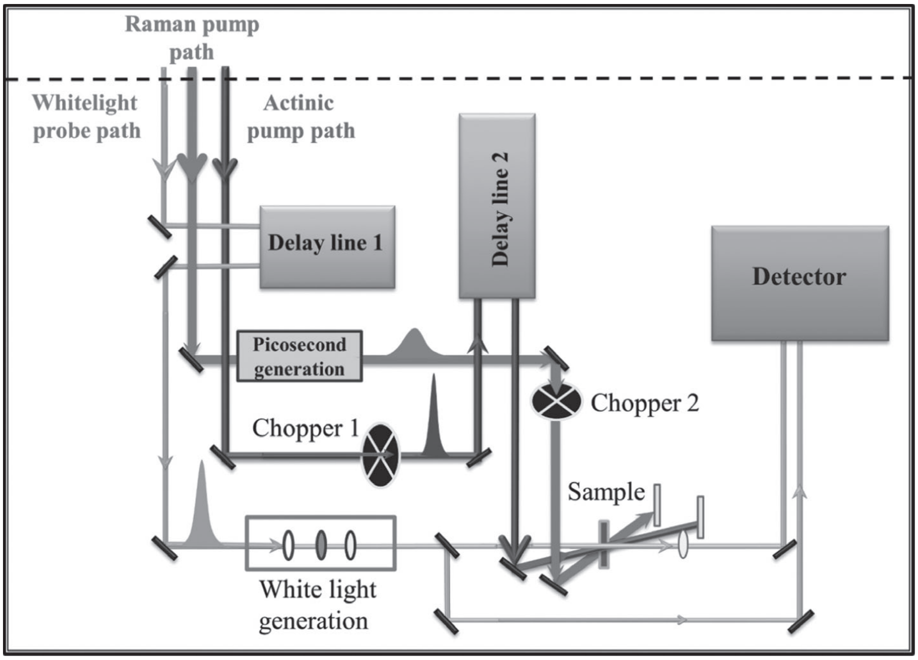

FIGURE 16.13 A schematic of experimental set-up for femtosecond transient absorption and ultrafast Raman loss spectroscopic techniques.

Several methods have been employed to produce narrowband ps Raman pulses from fs laser. Spectral filtering of the fundamental/frequency-doubled output remains the simplest way to generate ps pulses. The concept is known as spectral compression. This is different from the pulse stretcher (used in amplifiers), which simply increases the delay between the frequency components of the pulse while leaving the pulse spectrum unaltered. The spectral compression of the broadband fs pulses is done by using a grating pair. It involves spectral filtering of the broadband fs pulses by a slit in the Fourier plane of a 4*f* pulse shaper. This ensures zero dispersion in the output ps pulse. The set-up consists of two grating pair and two lenses. This specific arrangement is known as a zero-dispersion spectral compressor. The tunability of the Raman pump wavelength is achieved through the use of fs OPA as an input to the spectral filter set-up. This process is extremely inefficient (<0.5%) as most of the fs pulses are rejected in order to obtain narrowband pulse.

16.4 Applications of Raman Spectroscopy

The preceding sections provide a foundation on the basic aspects of Raman spectroscopy, including surface-enhanced Raman spectroscopic technique and non-linear Raman spectroscopic methods. The proliferation of Raman spectroscopic methods in materials and biology in the last few decades has been remarkable owing to the technological development towards robust instrumentation, particularly in the laser sources, spectrometers, detectors, and other optical components. Few applications where Raman spectroscopy or its variants have been extensively used shall be briefly discussed to provide the prospective researchers an idea about the strength of this technique.

16.4.1 Carbon Characterization Using Raman Spectroscopy

Raman spectroscopy has been the technique of choice for solid-state physicists towards the characterization of sp^2 carbon ranging from three-dimensional graphitic carbons to 2D carbon materials like graphene and 1D nanotubes and 0D fullerenes. Raman spectra of such carbon materials are rich with information pertaining to their state of hybridization, presence of chemical impurities, elastic constants, crystal disorder, number of layers (for graphene), etc. Figure 16.14 shows the Raman spectra of some bulk and sp^2 carbon materials.

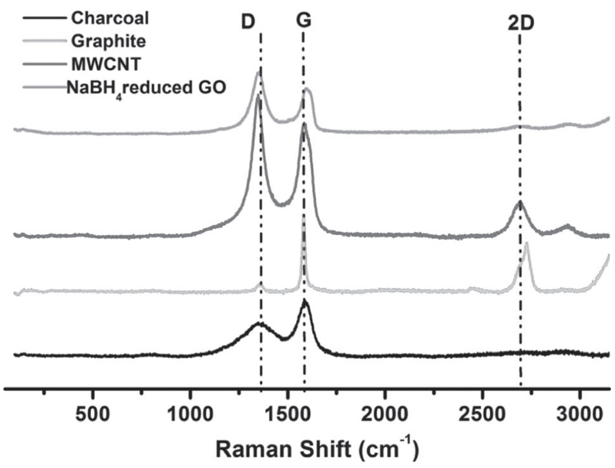

FIGURE 16.14 Raman spectra of bulk and sp^2 carbon materials such as charcoal, graphite, MWCNT, and sodium borohydride reduced graphene oxide.

The Raman spectra of such carbon materials have a characteristic peak at around 1580 cm^{-1}, known as the G (graphitic) band. This represents the in-plane vibrational mode of C-C of the sp^2-hybridized carbon atom. This mode generally shifts to higher wavenumber as the number of layers decreases from graphite to graphene. The position of the G band is also indicative of the number of layers in graphene. A pristine single layer of sp^2 carbon, *i.e.*, graphene, shows two Raman peaks: the first-order G band and the second-order G′ band (or 2D band). This band which appears around 2700 cm^{-1} arises due to the two-phonon lattice vibrational process. However, another Raman feature which is most rampant is the defect-activated (disorder) peak called the D-band, which is usually observed around 1350 cm^{-1} for almost all carbon materials. This band is weak in high-quality graphene. The D-band is attributed to the ring breathing mode of the sp^2 carbon rings. In most of the practical cases, carbon materials are never defect-free and have the D-band. Therefore, the intensity ratio of the D and the G peaks (I_D/I_G) provides an idea about the extent of disorder nature of the sp^2 carbon materials, which indicates the quality of bulk samples. Raman spectrum of single-walled carbon nanotube (SWCNT), as shown in Figure 16.15, shows an intensity ratio of 0.28, thus reflecting high-quality SWCNT. Comparable intensities of these bands imply the presence of large quantities (as in multi-walled carbon nanotube (MWCNT) in Figure 16.14) of structural defects.

Another interesting feature of SWCNT Raman spectra is that the modes are dependent on the energy of the laser. In such a case, the density of states matches with the wavelength of the excitation exhibiting a resonance Raman spectrum. This would allow one to find the presence of various species of CNTs (carbon nanotubes) in the sample.

The characteristic low-frequency Raman peaks in SWCNT, known as the radial breathing modes (RBM, between 100 and 250 cm^{-1}), are observed, which can be used as an identifier for the presence of SWCNT in any sample. The RBM correspond to the atomic vibration of the carbon atoms in the radial direction akin to breathing of the tube. They are characteristic features used to determine the diameter of the nanotube through the relationship,

$$w\text{RBM}\left(\text{cm}^{-1}\right) = \frac{A}{d} + B$$

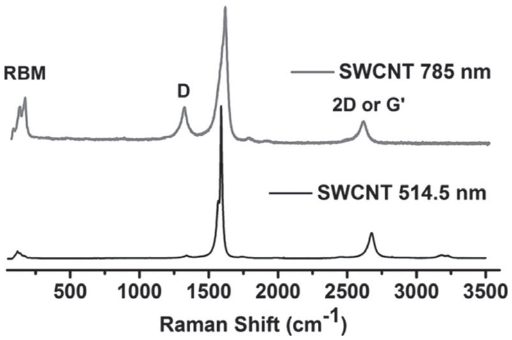

FIGURE 16.15 Raman spectra of SWCNT acquired at different laser wavelengths.

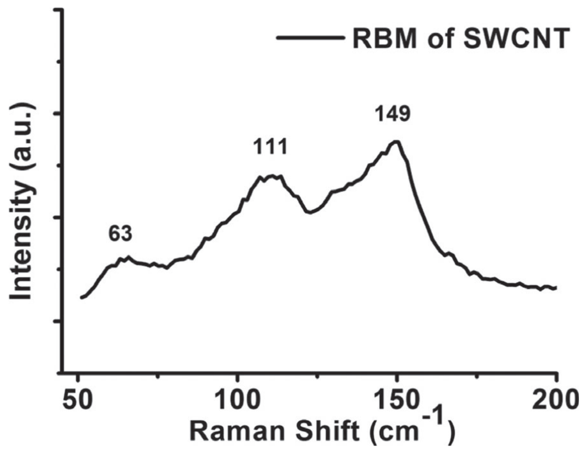

FIGURE 16.16 Expanded version of the RBM of the Raman spectra of SWCNT acquired at 785 nm.

where A and B are the experimentally determined parameters and d is the diameter of the nanotube. Considering the 149 cm^{-1} peak in Figure 16.16, and taking the value of $A = 234\,\text{cm}^{-1}\text{nm}$ and $B = 10\,\text{cm}^{-1}$ from the literature, the diameter of nanotube is ~1.68 nm (Dresselhaus et al. 2002; Costa et al. 2008).

16.4.2 Applications of SERS

Raman has a potential application in the field of chemistry, which can be further extended to trace analyte detection in chemical mixtures and reactions (Schlücker 2014; McNay et al. 2011). Unique spectral signature of chemicals in Raman makes it an ideal tool for forensic application, and SERS further improves the applicability (Muehlethaler, Leona, and Lombardi 2015). SERS has been successfully employed in the field of biology for various applications (Kneipp et al. 2002). SERS-based microfluidic device has a wide range of applications. Microfluidics implements the fluidic phenomena due to scaling, which in turn enables it to achieve faster and controlled analysis with low usage of reagents/sample. It can handle all preprocesses regarding sample, which would aid in the detection and sensing at the SERS site. SERS can provide molecular-specific information from these preprocessed samples, which includes molecular profiling of biological samples, chemical analysis, and detection of trace analytes in fluids (Li, Li, and Wang 2013; Huang et al. 2015; Zhou and Kim 2016).

16.4.3 Raman Spectroscopy in Semiconductors

Raman spectroscopy has garnered a profound attention in the modern electronics era. There is a vast research in developing and employing new materials to feed the need for ever-evolving semiconductor devices. Guidelines from ITRS (International Technology Roadmap for Semiconductors) emphasize transformation to unconventional MOSFET (Metal Oxide Field Effect Transistor) designs with FinFETs and 2D materials from classical MOSFETs. The most attractive materials for the applications are CNT and graphene owing to their electrical properties. Raman spectroscopy has established itself as a superior technique to above all in order to characterize the materials starting from identification to quality (Cantarero 2015; Zhang et al. 2016). It has been widely used for the characterization of purity and contamination, alloy composition and lattice structure, stress/strain with defects, and doping (De Wolf 1996). Innovations in III-V compound semiconductor for applications in photonic device technology and high electron mobility transistors require essential characterization pertaining to composition, lattice structure, and film stress.

The capability of Raman spectroscopy in the identification of material is evident from the following studies. Figure 16.17 presents a classical MOSFET with a poly-Si gate width of 10 μm. The lightly doped source, drain region, and underneath p-type Si substrate show almost the same Raman spectra. But heavily doped poly-Si loses its crystallinity and shows a different spectrum as shown in Figure 16.17b. Intensity has been normalized, and the area under the curve has been used to differentiate between the crystallinities (Figure 16.17c).

Graphene-like 2D materials play a key role in miniaturizing Field Effect Transistors (FETs). Figure 16.18a shows the layout of a typical graphene transistor. The map in Figure 16.18b shows graphene, p-type Si, and metal contacts on a graphene transistor. Raman spectroscopy not only precisely locates graphene but also reveals information about its layers (Figure 16.18c). The absence of a band around 1350 cm^{-1} is suggestive of a high-quality graphene.

16.4.4 Raman Spectroscopy for Pharmaceutical Analysis

Raman spectroscopy is an attractive technique for the analysis of pharmaceutical samples (Li and Church 2014; Ember et al. 2017). The active pharmaceutical ingredients (APIs) are organic molecules composed of aromatic moieties often with extended conjugation that render these molecules high Raman cross sections. Therefore, these APIs have a strong Raman signal. As mentioned in Section 16.1.2.3, Raman microscopy provide high spatial resolution (diffraction-limited) and can map the distribution of APIs spatially. Additionally, individual components can be identified, and a quantitative analysis is possible. Apart from chemical identification, the polymorphism of the drug molecules, hydrate formation, and crystallinity can also be characterized using Raman spectroscopy. In the early days, quantitative studies of pharmaceutical formulations using Raman spectroscopy could be carried out with simple powder mixtures. However, it has been applied to complex mixtures such as tablets, capsules, and microspheres. These studies have been achieved using Raman spectroscopy combined with multivariate analysis. With the development of depth-sensitive techniques such as spatially offset Raman spectroscopy (SORS), transmission Raman spectroscopy (TRS), and universal multiple-angle Raman spectroscopy

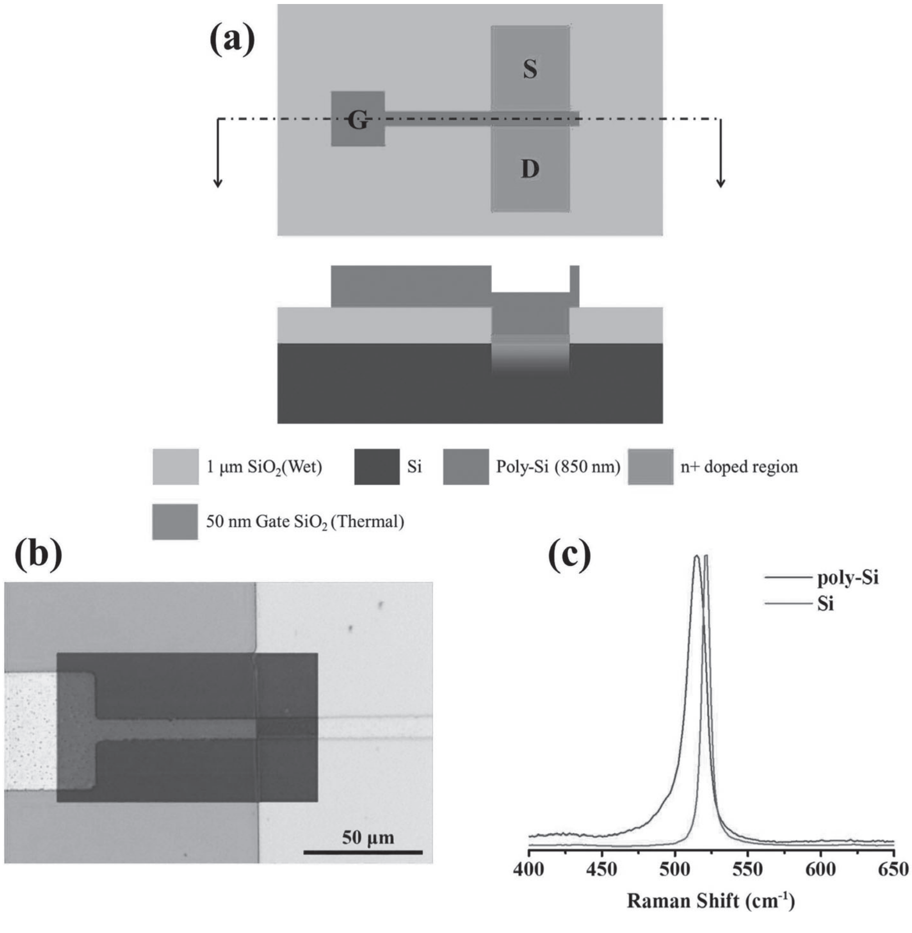

FIGURE 16.17 (a) Schematic of a MOFET. (b) Area mapping of a fabricated MOSFET with area under the band of Si peak. (c) Comparison of Raman spectrum obtained from poly-Si gate and crystalline Si substrate.

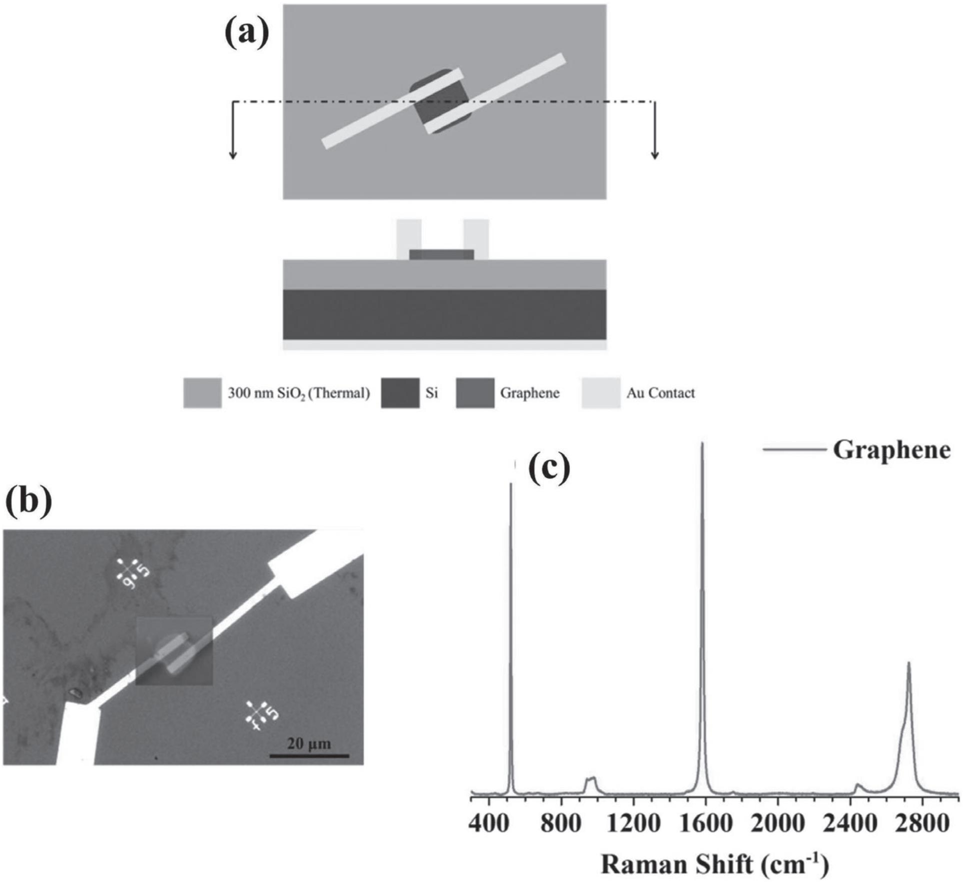

FIGURE 16.18 (a) Schematic of a graphene transistor. (b) Area mapping of a fabricated graphene transistor with Si and graphene band. (c) Spectrum of graphene on Si substrate in the mapped region.

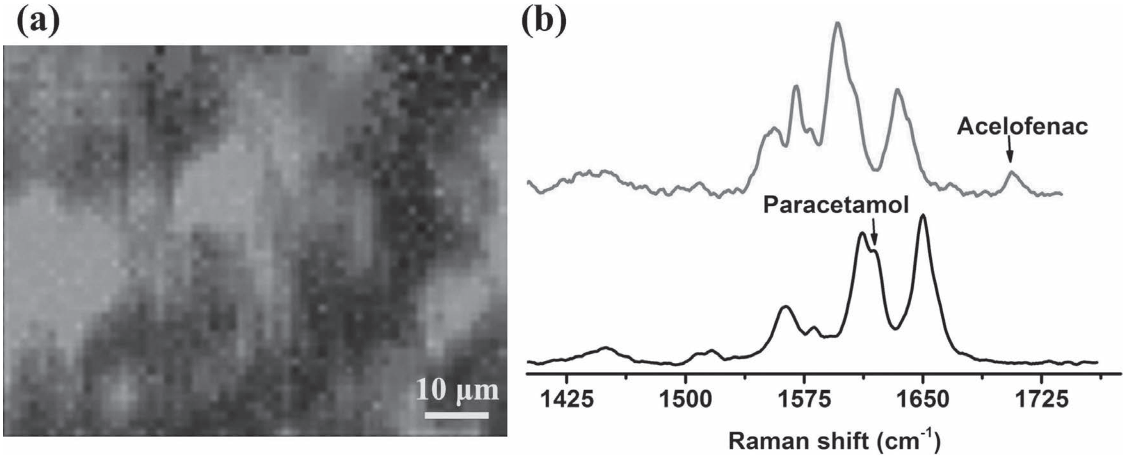

FIGURE 16.19 (a) Raman image of a tablet composed of paracetamol (250 mg, shown in red) and aceclofenac (150 mg, shown in green). (b) Raman spectra of the tablet showing the presence of paracetamol and aceclofenac.

(UMARS), pharmaceutical tablets can be studied directly through packaging. A simple illustration of application of Raman spectroscopy in pharmaceutical analysis is shown here. Figure 16.19 shows a 2D Raman image of a tablet composed of paracetamol (250 mg, shown in red) and aceclofenac (150 mg, shown in green). The Raman image was acquired using 785 nm laser, and a 50× objective lens was employed for the mapping with a step size of 1.5 µm. Frequency-specific mapping was performed using 1619 cm^{-1} peak of paracetamol and 1726 cm^{-1} peak of aceclofenac. Although this is a homogeneous mixture, we can see the distribution of both the APIs clearly on the Raman image.

16.5 Raman Spectroscopic Techniques for Non-invasive Depth-Resolved Studies

It has been recognized that in the case of optical fibres where the excitation and collection fibres are placed adjacent to each other or separated by a distance in the case of n-around-1 configuration, this technique can retrieve subsurface information of materials. This was first demonstrated by McCreery's group and later theoretically demonstrated by Plaza's group (Schwab and McCreery 1984; Plaza et al. 1986). In the initial days of development, the interrogated samples were mostly pure solvents and bulk materials; therefore, a maximum overlap of the excitation and collection cones was desirable. However, Shim et al. obtained a depth-resolved Raman signal from intralipid suspension phantom using a 7-around-1 FO probe with beveled tips (Shim et al. 1999). They demonstrated that when tips with increasing bevel angles were used, the distance between the collection regions moved closer to the sample. In a later study by Feld's group, 15 collection fibres were used to obtain Raman signal from highly scattering sample. In some initial studies, bone signal was obtained underneath adipose tissue (Shim and Wilson 1997; Shim et al. 1999). This idea was extended in the later years for obtaining a depth-resolved information from layered materials (Matousek, Clark, et al. 2005). The technique was termed as spatially offset Raman spectroscopy (SORS).

16.5.1.1 Spatially Offset Raman Spectroscopy

In the case of turbid media, where light undergoes multiple scattering, the locus of the photon inside such a medium may be one or two orders longer than the paths of the unscattered photons (Sasic and Ozaki 2011). Multiple scattering leads to depolarization of light, and the photon gets randomized. There is a finite probability of such a photon to be either reflected back or transmitted from the material. A general observation of the imaging fraternity is that the image quality is degraded due to multiple scattering. One of the ways to minimize the degradation is by observing the most probable light paths through a highly scattering material, which forms a semi-circular-shaped volume connecting the entry and exit points of the photons in the material.

As the separation between the point of illumination and the point of collection of the photons is increased, the depth of the material being probed by the EM radiation is also increased. This methodology is commonly used in NR spectroscopy for depth discrimination (Das, Liu, and Alfano 1997; Jobsis 1977; Strangman, Boas, and Sutton 2002). A similar approach may be adopted for Raman spectroscopic-based techniques for non-invasive depth-sensitive detection of concealed objects (Matousek 2007; Matousek, Clark, et al. 2005; Matousek, Morris, et al. 2005). In an initial study, millimetre depth penetration was shown by spatially offsetting the collection fibre from the excitation fibre using a two-fibre probe. In its rudimentary form, SORS does not provide details on spatial distribution of subsurface components. The n-around-1 geometries can retrieve certain amount of information. Morris et al. have reported that the Raman spectra from bone tissue could be obtained transcutaneously through 1–4 cm of overlying tissue (Okagbare et al. 2010). In one such measurement, transcutaneous Raman spectra of bone tissue using an annulus arrangement (laser light surrounding the field of view of a circular array of collection fibres) of fibre optic probes were demonstrated in rat and chicken tibia with overlying tissue thicknesses of 1 and 4 mm, respectively (Schulmerich et al. 2006). SORS has been applied for retrieving subsurface information of objects. Various applications of SORS include the detection of hazardous liquids concealed in plastic bottles (few mm), analysis of coated pharmaceutical tablets, and contraband items.

16.5.1.2 Universal Multiple-Angle Raman Spectroscopy

In an endeavour to obtain the depth-resolved signals at depths beyond a couple of centimetres, a new technique was proposed which is independent of the geometry of the incident and the collection geometry. This technique has been termed as universal multiple-angle Raman spectroscopy (UMARS) (Sil and Umapathy 2014; Periyasamy et al. 2015). It has the capability to detect and identify materials such as explosives and hazardous chemicals concealed inside non-metallic containers such as commercial polyethylene bottles, coloured glass bottles, envelopes, and parcels Schematic representation of the UMARS method where Raman signals are collected from multiple angles and multiple sides independent of the illumination geometry is demonstrated in Figure 16.20 (a). Figure 16.20 (b) shows an experimental demonstration of UMARS to detect a hidden object (t-stilbene concealed in chicken) non-invasively and the collected TS spectrum is shown in Figure 16.20 (c).

UMARS technique exploits the multiple scattering phenomena where the Raman scattered light from strongly scattering media undergoing multiple scattering events is recorded from multiple angles and sides. Since the photon direction is randomized, Raman photons collected from any angle or geometry carry molecular and spatial information of substances lying deep within such media. UMARS technique is independent of geometry of excitation and collection. Therefore, it can be used for depth-sensitive detection of layered compounds non-invasively at depths beyond 10 mm. The depth of penetration can be improved by optimizing the experimental parameters and can be as deep as 80 mm. This technique would be ideal for field applications such as airport screening and screening at public places at check points for inspection items; this technique can also be extended in the field of biomedical diagnostics as well as in pharmaceutical industry. This technique has the potential to be used for frequency-specific 3D imaging studies of layered compounds to understand the shape, size, and spatial distribution of chemicals that are concealed at the particular depth.

16.5.1.3 Transmission Raman Spectroscopy (TRS)

Another technique for depth profiling is transmission Raman spectroscopy (TRS). This was first reported as early as 1967 by Schrader and Bergmann (1967). In this case, the Raman photons are collected from the opposite face of the bulk material, as shown in Figure D1.2.8. One of the ways to reduce the overwhelming surface signals for layered substances is the adoption of transmission Raman geometry. Samples comprising low absorption coefficient can be studied using this method where the Raman photons can migrate through thick samples. Therefore, TRS can be useful for the bulk analysis of mixtures

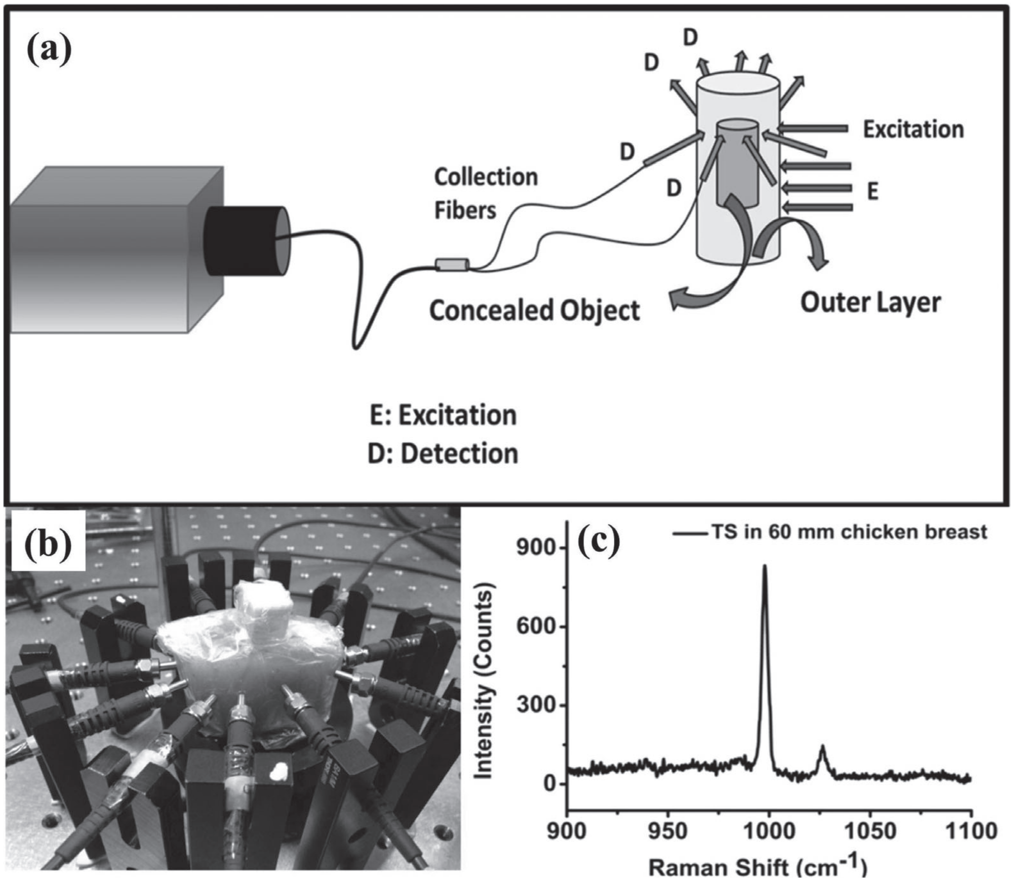

FIGURE 16.20 (a) Schematic representation of the UMARS method where Raman signals are collected from multiple angles and multiple sides independent of the illumination geometry. The panels below are depiction of the (b) experimental demonstration of UMARS to detect hidden object (*t*-stilbene concealed in chicken) non-invasively and the collected (c) TS spectrum.

with less contribution from the top layer and in pharmaceutical industry for quality checks for tablets.

TRS saw a revival in the last decade when Matousek and Parker reported the use of this technique for the bulk analysis of pharmaceutical drugs (Matousek and Parker 2006). In addition, TRS has also been explored to study calcification in breast, such as in breast cancer, non-invasively (Ellis et al. 2013; Matousek and Stone 2007). Figure 16.21a shows the Raman spectrum of trinitrotoluene concealed in high density polyethylene (HDPE) container in transmission mode.

Figure 16.21b shows the line image of a 7-mm-thick pharmaceutical tablet (Hostaflam, an analgesic) obtained in a transmission Raman geometry with an acquisition time of 100 s. With suitable modifications to the transmission set-up, such as in a transmission-type Raman microscope or inverted microscope, it is possible to image thick solid mixtures or hazardous liquids and chemicals. Retrieval of Raman photons from different depths in a given sample can be achieved using TRS.

Techniques such as SORS, UMARS, and TRS have the ability to percolate in all the areas of science from materials to medicine. A miniaturized version of these techniques can be developed for specific applications such as assessment of gems, pharmaceutical tablets, and food quality.

16.6 Raman Imaging: From 2D Mapping Towards 3D Imaging

Although microscopy was in use since the 14th century, the first confocal microscopy on brain tissue was used only in 1955 (Minsky 1988, 1961). The conjunction of microscopy with Raman spectroscopy happened only in the 1970s by Dhamelincourt and Delhaye (1975). Raman microscopy enabled a high spatial resolution of samples, thereby allowing the detection of micron-sized objects. Since Raman microscopy employs backscattering geometry, the NA of the objective lens determines the spatial resolution of the microscope. In the case of measurements in air medium, the maximum NA is limited to the refractive index of air and the half cone angle of light cannot exceed 72° (NA= $\eta \sin\theta$). Spatial resolution has been increased by using water or oil immersion objectives (Gautam et al. 2015). Raman microscopy has been useful for applications requiring high lateral resolution with good image quality (2D imaging). Three-dimensional imaging of micrometre resolution (lateral and depth) through any medium such as biological samples has been performed using confocal Raman microscopy (Brenan and Hunter 1996; Esposito et al. 2003; Chan et al. 2004; Sasic and Ozaki 2011). Since the laser spot size determines the spatial resolution, confocal Raman

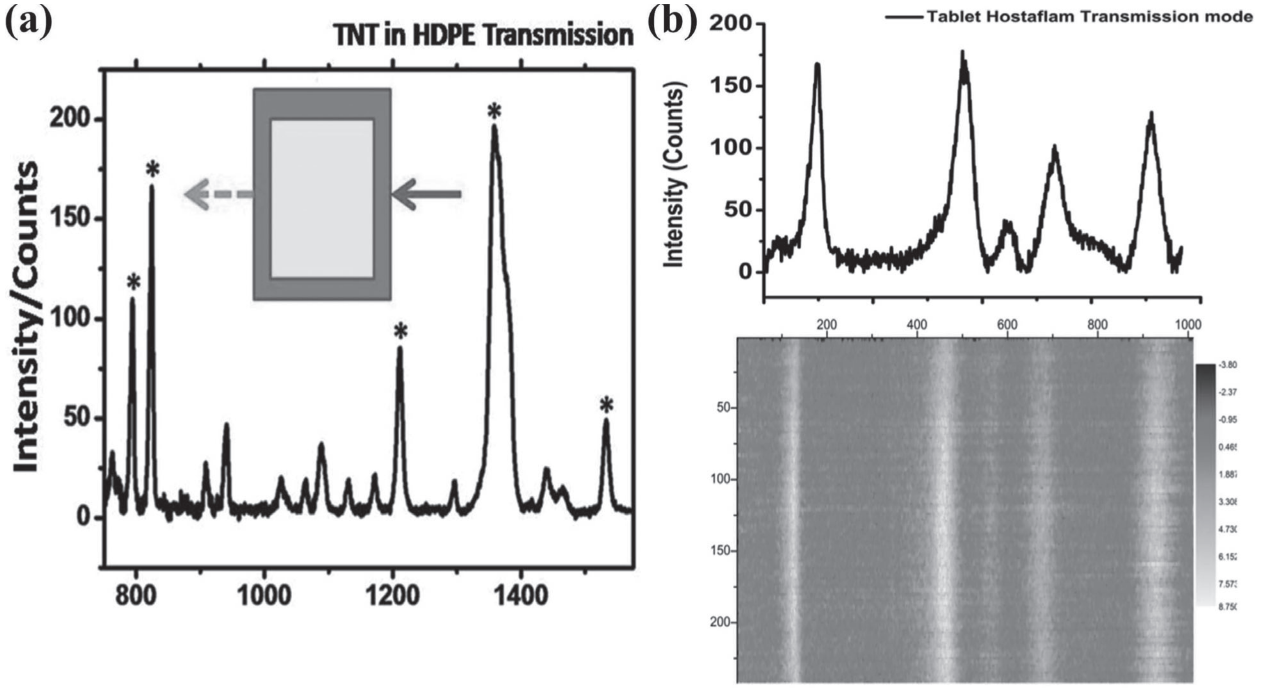

FIGURE 16.21 (a) Raman spectrum of trinitrotoluene concealed in HDPE container in transmission mode. (b) Transmission Raman line image of a 7-mm-thick tablet Hostaflam.

microscopy can achieve up to 300 nm spatial resolution for visible light (diffraction-limited). Although efforts are made to improve the resolution even further for applications in the field of nanotechnology, the depth penetration in the case of confocal microscopy is limited to a few hundred microns. Therefore, for medical diagnostics, confocal microscopy may not be a desirable option for reconstructing 3D images of bone defects or cancer tissues, *etc*. Techniques such as SORS, TRS, and UMARS can be effectively used for 3D imaging albeit with spatial resolutions limited to few tens of microns. However, the limitation is overcome by probing depths beyond few millimetres, which is not possible with confocal microscopy.

3D Raman imaging for biomedical diagnostics has been elusive so far, due to the constraint imposed for illumination and collection optics geometry. Raman tomographic studies on canine hind limb were conducted by Morris's group in both transmission geometry and backscattering mode (Schulmerich et al. 2008). In another report by Srinivasan et al., high-contrast molecular and structural information was obtained where both reflectance and transmission geometries were used (Srinivasan et al. 2008). In this case, image-guided Raman spectroscopy was employed where X-ray CT images of the tissue were used to recover the signal. The authors reported a thickness range of 24–45 mm for the canine limb. In the discussion, the authors have, however, mentioned obtaining Raman signals at a depth of 10 mm in the reflectance mode. In a recent study conducted by Morris's group, micro-CT was coupled with Raman imaging towards developing next-generation Raman tomography instrument for non-invasive *in vivo* bone imaging (Demers et al. 2015). In their study, they used tissue phantoms, cadavers, and live rat systems to validate the efficiency of the system. For tomographic reconstruction, they employed NIRFAST software.

UMARS technique has also been employed for 3D imaging and image reconstruction of objects embedded/concealed at depths beyond 10 mm. In a feasibility demonstration, UMARS has been effectively used to obtain shapes of the hidden object. Imaging experiments using the UMARS technique were conducted for bilayer solid compounds, in this case ammonium nitrate (AN, top layer) and *trans*-stilbene (TS, concealed layer) (Figure 16.22a–e). TS was packed in a glass container which was custom-made in the shape of a dumb bell, as shown in Figure 16.22a–e. The experimental set-up uses four illumination fibres (core diameter 400 μm) to irradiate the sample at different location as shown in Figure 16.22. Nine collection fibres with the same core diameter were placed around the sample in the same plane at known angles (Figure 16.22). Signals were collected from the top position of the container, and the collection fibres were shifted down by 1 mm after each collection. In this case, 40 images were obtained to cover the entire length of the container. 3D image reconstruction was carried out using MATLAB 2009. The final 3D surface plot for TS as well as AN is shown in Figure 16.22c–e.

UMARS 3D imaging provides information on the shape, size, location, and chemical identification of a concealed material. The group envisages the future application of Raman tomography for clinical applications such as diagnosing bone-related disorder and tumour.

16.7 Non-linear Spectroscopic Applications

Femto chemistry deals with optical spectroscopy using ultrashort pulses, which is known as pump probe technique. In pump probe technique, a strong PP initiates the photochemistry

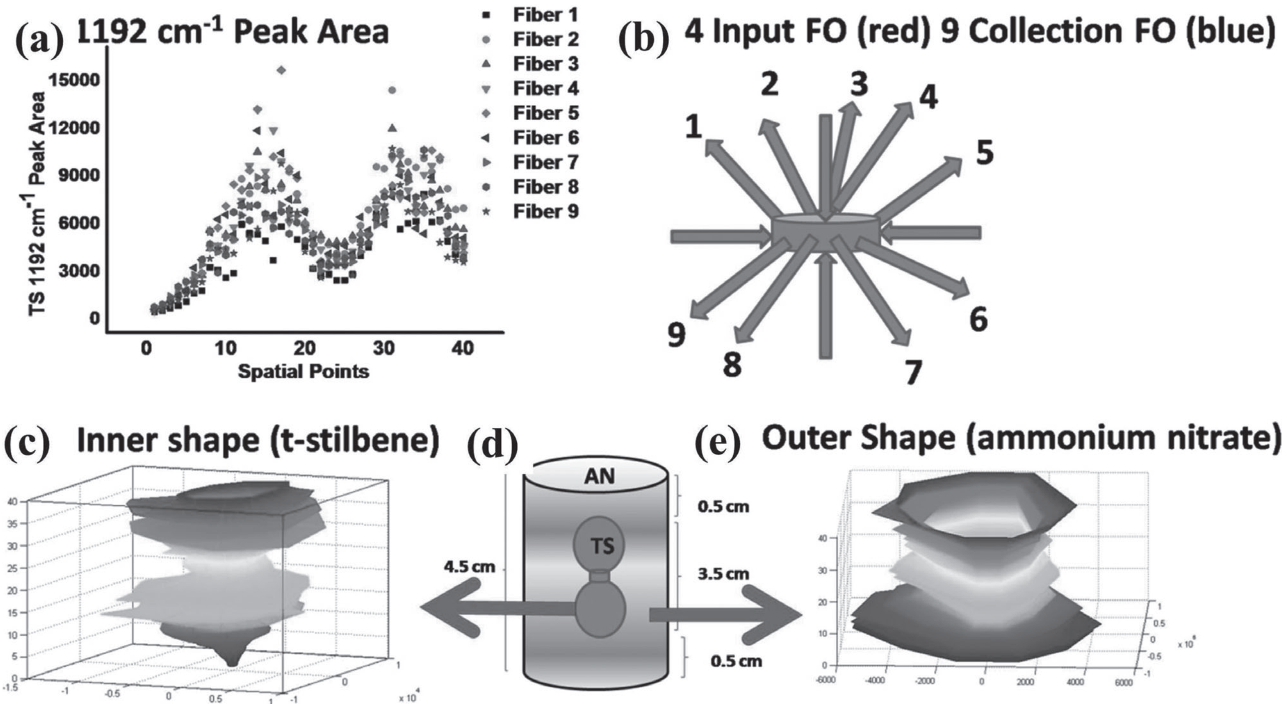

FIGURE 16.22 A demonstration of 3D shape reconstruction using UMARS. Here, *t*-stilbene was concealed inside ammonium nitrate, and the experiments were conducted using four illumination fibres and nine collection fibres. The images below correspond to the reconstructed shape (3D surface plots using MATLAB program).

or photophysics, and a weak ultrashort probe pulse (typically ~100 fs) captures the dynamics during the time evolution of the non-stationary excited state. Electronic spectroscopy, like fluorescence up-conversion and transient absorption, was utilized during the initial stage of femto chemistry to reveal the reaction dynamics of many elementary reactions. However, those techniques suffer from poor spectral resolution. Most of the time, all the dynamical information gets buried under the broad envelope of electronic absorption or emission band, which makes it difficult to understand the dynamical aspect of underlying photochemistry or photophysics. Fortunately, a rapid development in the field led to the invention of femtosecond Raman technique; particularly, FSRS offers the scope of transient detection of short-lived species with excellent time (10–100 fs) and spectral resolution (10 cm^{-1}). In the next section, the applications of femto chemistry in photochemical and photophysical processes have been discussed.

16.7.1 Photoisomerization of Optically Excited Solvated *Trans*-stilbene

Photoisomerization reaction is well known for its implication in nature, biology, and optoelectronics applications. Such kind of reactions involves a rearrangement of atoms or group from one part of the molecule to the other part at femtosecond or picosecond timescales, which produces configurational isomer. One of the very fascinating examples of such isomerization reaction is the photochemistry of vision where retinal chromophore of rhodopsin protein in human eyes undergoes structural changes from 11-*cis* to all-*trans* retinal in 50–100 fs timescales (Figure 16.23). Innumerable research work has been published by many groups regarding this system. This ultrafast photoisomerization reaction is the elementary step, which triggers the vision process. It has been reported that the reaction involves a rotation around the C=C bond from the excited-state potential energy surface (Kukura et al. 2005). It is also reported that the transformation is barrier less in the excited state. However, the intermediate state for this reaction is not known so far, and hence, it has been ascribed to "phantom state" in the literature. An FSRS study by Mathies group has revealed some interesting results regarding the global nuclear motions during isomerization process. The characteristic vibrational frequencies of rhodopsin chromophore are 1548 cm^{-1} (symmetric C=C ethylenic stretch), 1100–1300 cm^{-1} (C-C single bond stretch + C-H rocking mode), and 969 cm^{-1} (which belongs to the hydrogen out-of-plane wagging motion of C_{11} and C_{12} hydrogens (HOOP)). In the photoproduct bathorhodopsin, the 969 cm^{-1} band shows a quite interesting behaviour. It undergoes a substantial redshift and splits into three distinct modes (920, 875, and 850 cm^{-1}). Such a dramatic spectral change of the HOOP motion arises due to the distortion of the conjugated backbone of the retinal chromophore. Additionally, the corresponding blue shift in frequency is due to the strengthening of C=C bond in the less sterically congested form all-*trans* retinal.

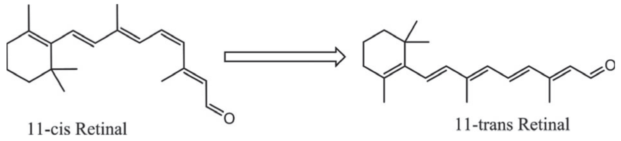

FIGURE 16.23 Structural change associated with 11-*cis*-retinal.

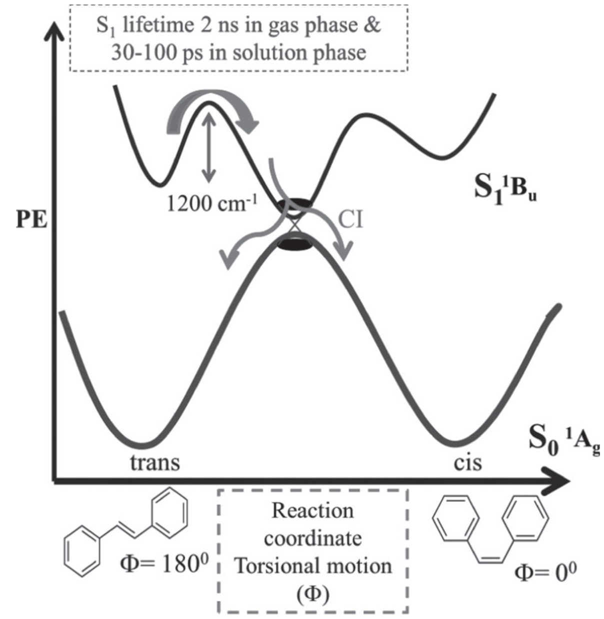

FIGURE 16.24 Ground- and excited-state potential energy surface of *trans*- and *cis*-stilbene along with their reaction coordinate and molecular structures.

Another very well-known example of the photo-switching reaction is the *trans*- to *cis*- photoisomerization of optically excited stilbene. This unimolecular reaction is studied by many groups to develop more understanding from the mechanistic point of view as depicted in Figure 16.24. The reaction is known to happen from the excited electronic potential energy surface, and the reaction barrier is ~1200 cm^{-1}. It is reported that in the gas phase, the rate constant of photoisomerization is ~ 2 ns^{-1}; however, this rate constant is dependent on excess vibrational energy. The rate constant increases to 100 ps^{-1} at sufficiently high vibrational energy (4500 cm^{-1}).

Interestingly, in the solution phase, the rate increases from 100 ps^{-1} to 25 ps^{-1} depending upon the polarity of the solvent environments. A fascinating fact about the reaction is that it shows non-Rice–Ramsperger–Kassel–Marcus (RRKM) behaviour where theoretical prediction always overestimates the actual experimentally determined rate. Various Raman spectroscopic techniques have been applied to understand the solute–solvent interaction and vibrational energy flow in this system after optical excitation. Vibrational cooling time of optically excited TS is ~10 ps in solution phase. FSRS was employed by Ernstings group to understand the vibrational signature of the TS molecule (Syage et al. 1982; Weigel and Ernsting 2010).

An investigation using URLS technique reveals time-dependent changes in peak intensity and peak position for different solvents after 285 nm photoexcitation. Transient URLS spectra for different time delays are given in Figure 16.25. Vibrational energy flow in both short and long timescales has been captured by following the time-dependent changes in intensity and peak position of transient Raman bands ranging from low-frequency to high-frequency vibrations. The ethylenic CC double-bond stretch is the reporter mode which is established as Franck–Condon active mode of optically excited TS as given in Figure 16.26. Photoexcitation by actinic pump pulse deposits excess vibrational energy to this normal mode. It is reported that anharmonic coupling could exist between reaction coordinate and high-frequency C=C double bond, which is responsible for vibrational energy flow from FC active mode to reaction coordinate.

16.7.2 Ultrafast Structural Dynamics

Excited electronic states play a vital role in controlling the photochemical and photophysical properties of molecules. The pathways and the final outcome of such processes merely

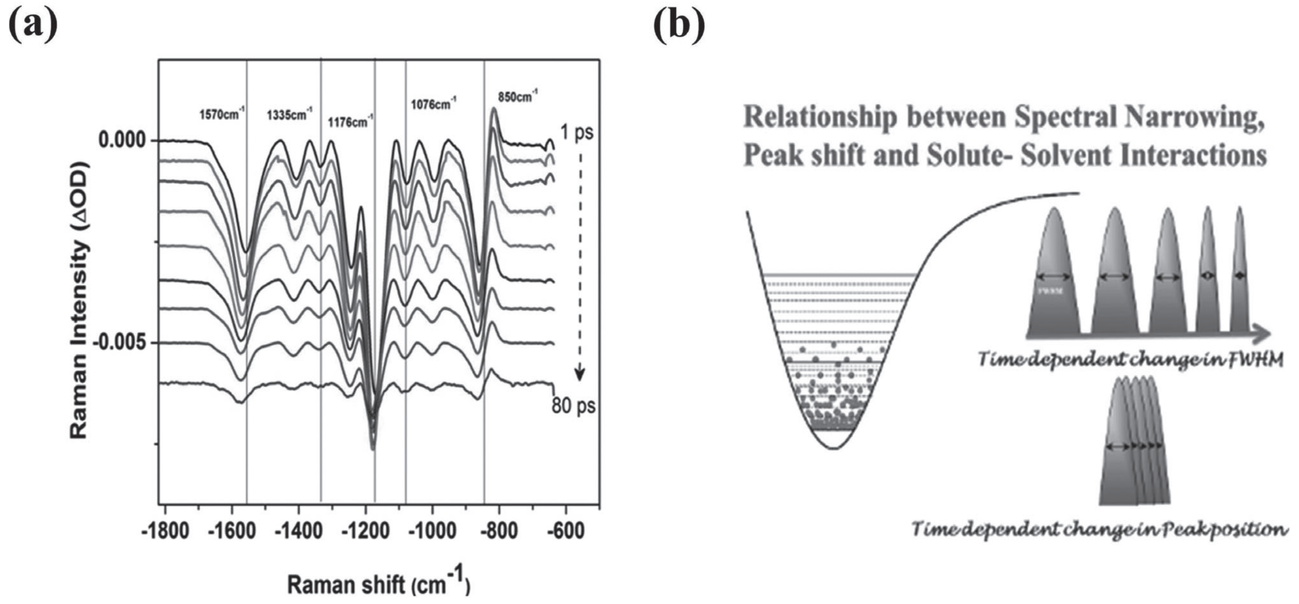

FIGURE 16.25 (a) Representative URLS spectra of *trans*-stilbene after 285 nm photoexcitation in butyronitrile. (b) Effect of vibrational cooling on the peak width and peak position is schematically presented. Cooling leads to a decrease in peak bandwidth as well as peak position.

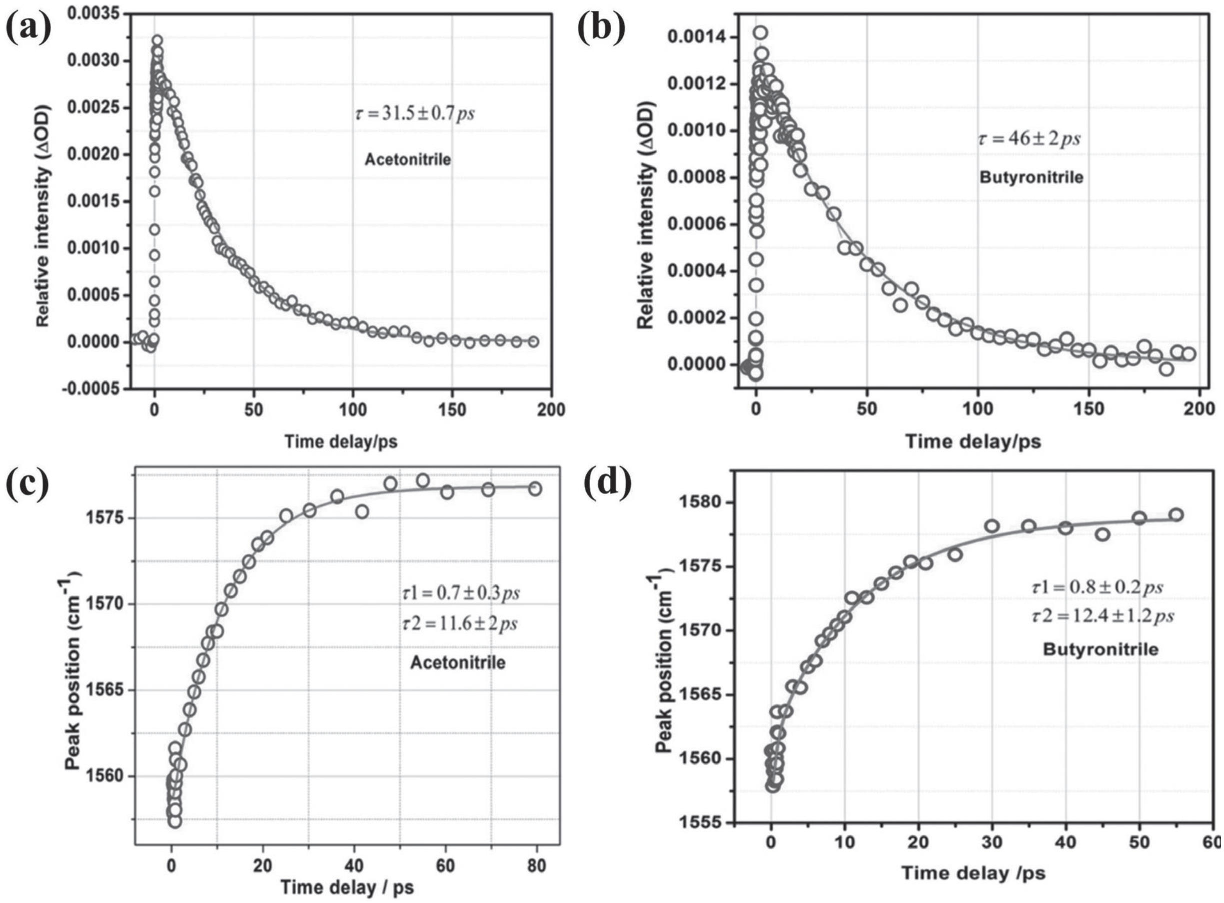

FIGURE 16.26 Transient URLS kinetics of CC double-bond stretching with exponential fit is shown as (a) and (b). The time evolution of peak positions is represented in figure c and d along with their double exponential fitting in two different solvents.

depend on the structural dynamics of a particular electronic state and its coupling with other electronic states as well. The electronic state is composed of 3N-6 normal modes, which are basically vibrational degrees of freedom of a polyatomic non-linear molecule. So the nature of the potential energy hypersurface is dependent on the vibrations of the molecule. Force constant of different vibrations is different, and this difference gives rise to hills and valley in potential energy hypersurface. The potential energy of the electronic state is maximum (global maxima) in the hill and minimum (global minima) in the valley. These ups and downs in potential energy landscape have a major contribution in affecting the outcomes of photo-induced processes.

16.7.3 Excited-state Planarization Dynamics of Bis(phenylethnyl)benzene

One of the important aspects of excited-state structural dynamics is ultrafast planarization of pi-conjugated systems where aromatic bridges are involved in pi-conjugation. A well-studied example includes bis(phenylethnyl)benzene (BPEB), an acetylene pi-conjugated system, where the torsional motion of phenyl rings plays a vital role in the excited-state planarization dynamics.

Such kinds of systems are important in the field of optoelectronics because of their excellent optical properties and extended linear pi-conjugation which run along their long molecular axis. It is reported that the ground state of BPEB contains a mixture of different conformers as shown in Figure 16.27.

Torsional degrees of freedom of terminal and middle phenyl rings introduce a different kind of conformer because of low rotational barrier (<*k*T), and the effects of middle and terminal phenyl rings are different on the electronic structure of BPEB, in both ground and excited states. This system has very good fluorescence quantum yield, and it is claimed that the excited state of the molecule is planar and the rotational barrier in the excited state is very high. Investigation of ultrafast excited-state dynamics of BPEB shows multiple kinetic components revealing the microscopic origin of planarization of different conformers. Femtosecond transient absorption shows an increase in absorption cross section with time till 50–60 ps as evident from the spectra in Figure 16.28a. The blue part of the spectrum shows an ultrafast decay component within one picosecond timescale. The origin of such component could be due to the torsional relaxation of highly twisted conformers. The kinetics obtained from longer wavelength doesn't carry such ultrafast component, indicating the conformational relaxation of the slightly twisted conformer. The kinetic plot in a

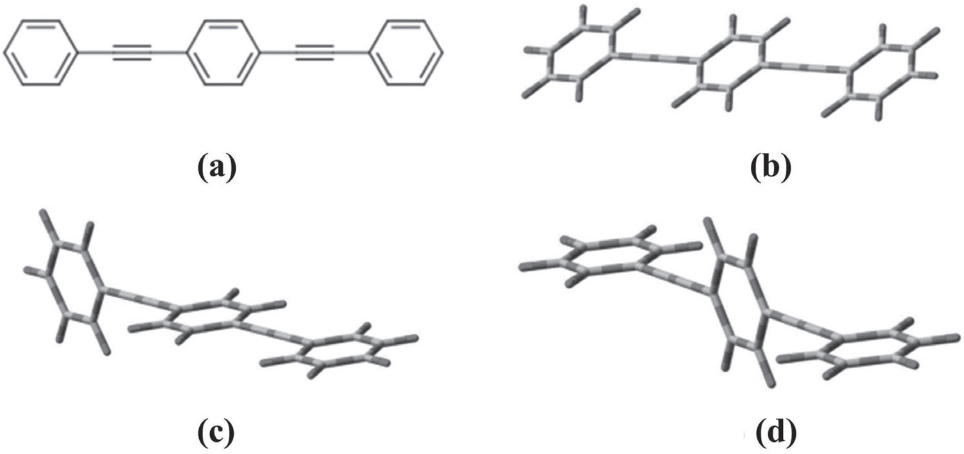

FIGURE 16.27 Molecular structure of BPEB in planar form (a, b) and its different conformational isomers (c, d).

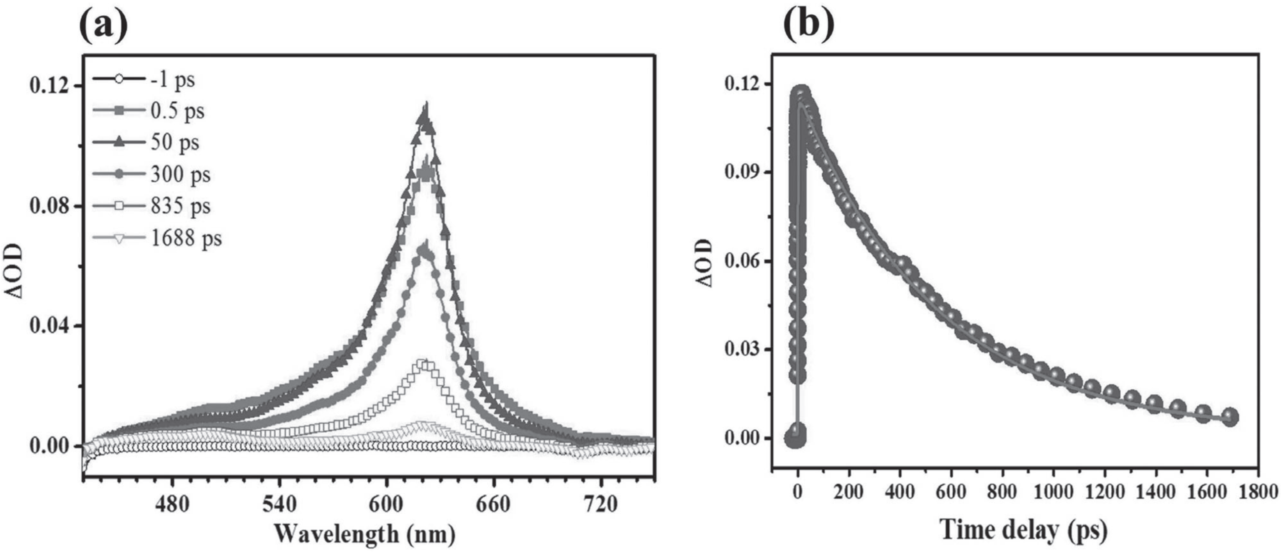

FIGURE 16.28 Transient kinetics of excited BPEB for different time delays along with its single exponential decay in both linear and logarithmic scales is shown.

linear scale is shown in Figure 16.28b, along with multiexponential fitting.

Excited-state photochemistry and photophysics of small organic molecules in solution phase from femtosecond transient absorption and ultrafast Raman loss spectroscopy have been demonstrated. Vibrational energy relaxation is portrayed through vibrational cooling of high-frequency vibration of excited TS from URLS peak positions at picosecond timescales. Dynamics of different conformational isomers of BPEB has been observed from the ultrafast study. Till to date, an enormous number of fundamental photophysics and photochemistry have been studied using time-resolved spectroscopic techniques both in solution and in gas phase. Most of the studies discuss about the structure and dynamics of molecular system. Both structure and dynamics are important for any molecular system to perform work, which is the ultimate goal of scientific community. It will be really fascinating to study the function of molecule along with structure and dynamics. Recent trend is moving towards combining ultrafast spectroscopy with other advanced techniques like X-ray and ultra-bright electron pulse, which could be very useful in understanding ultrafast dynamics in device during its performance.

16.8 Conclusion and Future Directions

This chapter presented a brief overview of Raman spectroscopy and its variants. The basics were discussed in the first part of this chapter, while the second half was dedicated for the latest developments in the field over the last few decades. SERS has become popular due to its high sensitivity. Brief background on SERS along with its application in microfluidics/LOC has been presented. The field of Raman spectroscopy has expanded due to the development in instrumentation such as pulsed lasers. It has opened up avenues to understand molecular dynamics in sub-picosecond timescale. A background on ultrafast stimulated Raman spectroscopy along with a few applications was therefore necessary to provide interested readers an introduction to the field of time-resolved Raman spectroscopic techniques. Few applications of Raman spectroscopy spanning over materials and biology have also been discussed. Demand of Raman spectroscopy in the pharmaceutical industry has grown over the last decade, and therefore, it was befitting to give an example of Raman spectroscopic methods in drug analysis. Additionally, fibre optic-based Raman spectroscopic application was also briefly discussed. Subsurface analysis using different types of Raman spectroscopic methods has been discussed with examples. Ninety years after its discovery, Raman spectroscopy still holds the appeal within the spectroscopy community due to its capability. Novel methods are being researched upon to increase the resolution, portability, and for the development of point-of-care Raman instruments for disease diagnosis.

REFERENCES

Aikens, C.M., L.R. Madison, and G.C. Schatz. 2013. Raman spectroscopy: The effect of field gradient on SERS. *Nature Photonics* 7 (7):508–510.

Álvarez-Puebla, R.A. 2012. Effects of the excitation wavelength on the SERS spectrum. *The Journal of Physical Chemistry Letters* 3 (7):857–866.

Ayars, E.J., H.D. Hallen, and C.L. Jahncke. 2000. Electric field gradient effects in Raman spectroscopy. *Physical Review Letters* 85 (19):4180.

Brenan, C.J.H., and I.W. Hunter. 1996. Volumetric Raman microscopy through a turbid medium. *Journal of Raman Spectroscopy* 27 (8):561–570.

Cantarero, A. 2015. Raman scattering applied to materials science. *Procedia Materials Science* 9:113–122.

Chan, J.W., A.P. Esposito, C.E. Talley, C.W. Hollars, S.M. Lane, and T. Huser. 2004. Reagentless identification of single bacterial spores in aqueous solution by confocal laser tweezers Raman spectroscopy. *Analytical Chemistry* 76 (3):599–603.

Costa, S., E. Borowiak-Palen, M. Kruszynska, A. Bachmatiuk, and R.J. Kalenczuk. 2008. Characterization of carbon nanotubes by Raman spectroscopy. *Materials Science-Poland* 26 (2):433–441.

Creighton, J.A. 1986. The resonance Raman contribution to SERS: Pyridine on copper or silver in aqueous media. *Surface Science* 173 (2–3):665–672.

Das, B.B., F. Liu, and R.R. Alfano. 1997. Time-resolved fluorescence and photon migration studies in biomedical and model random media. *Reports on Progress in Physics* 60 (2):227.

De Wolf, I. 1996. Micro-Raman spectroscopy to study local mechanical stress in silicon integrated circuits. *Semiconductor Science and Technology* 11 (2):139.

Delhaye, M., and P. Dhamelincourt. 1975. Raman microprobe and microscope with laser excitation. *Journal of Raman Spectroscopy* 3 (1):33–43.

Demers, J.-L.H., F.W.L. Esmonde-White, K.A. Esmonde-White, M.D. Morris, and B.W. Pogue. 2015. Next-generation Raman tomography instrument for non-invasive in vivo bone imaging. *Biomedical Optics Express* 6 (3):793–806.

Dresselhaus, M.S., G. Dresselhaus, A. Jorio, A.G. Souza Filho, M.A. Pimenta, and R. Saito. 2002. Single nanotube Raman spectroscopy. *Accounts of Chemical Research* 35 (12):1070–1078.

Ellis, D.I., D.P. Cowcher, L. Ashton, S. O'Hagan, and R. Goodacre. 2013. Illuminating disease and enlightening biomedicine: Raman spectroscopy as a diagnostic tool. *Analyst* 138 (14):3871–3884.

Ember, K.J.I., M.A. Hoeve, S.L. McAughtrie, et al. 2017. Raman spectroscopy and regenerative medicine: A review. *NPJ Regenerative Medicine* 2 (1):12.

Esposito, A.P., C.E. Talley, T. Huser, C.W. Hollars, C.M. Schaldach, and S.M. Lane. 2003. Analysis of single bacterial spores by micro-Raman spectroscopy. *Applied Spectroscopy* 57 (7):868–871.

Felidj, N., J. Aubard, G. Levi, et al. 2003. Optimized surface-enhanced Raman scattering on gold nanoparticle arrays. *Applied Physics Letters* 82 (18):3095–3097.

Fleischmann, M., P.J. Hendra, and A.J. McQuillan. 1974. Raman spectra of pyridine adsorbed at a silver electrode. *Chemical Physics Letters* 26 (2):163–166.

Gautam, R., A. Samuel, S. Sil, et al. 2015. Raman and mid-infrared spectroscopic imaging: applications and advancements. *Current Science* 108 (3):341.

Gersten, J.I., R.L. Birke, and J.R. Lombardi. 1979. Theory of enhance i light scattering from molecules adsorbed at the metal-solution interface. *Physical Review Letters* 43 (2):147.

Haynes, C.L., and R.P. Van Duyne. 2003. Plasmon-sampled surface-enhanced Raman excitation spectroscopy. *The Journal of Physical Chemistry B* 107 (30):7426–7433.

Huang, J.-A., Y.-L. Zhang, H. Ding, and H.-B. Sun. 2015. SERS-enabled lab-on-a-chip systems. *Advanced Optical Materials* 3 (5):618–633.

Jobsis, F.F. 1977. Noninvasive, infrared monitoring of cerebral and myocardial oxygen sufficiency and circulatory parameters. *Science* 198 (4323):1264–1267.

King, F.W., R.P. Van Duyne, and G.C. Schatz. 1978. Theory of Raman scattering by molecules adsorbed on electrode surfaces. *The Journal of Chemical Physics* 69 (10):4472–4481.

Kneipp, K, H. Kneipp, I. Itzkan, R.R. Dasari, and M.S. Feld. 2002. Surface-enhanced Raman scattering and biophysics. *Journal of Physics: Condensed Matter* 14 (18):R597.

Kukura, P., D.W. McCamant, S. Yoon, D.B. Wandschneider, and R.A. Mathies. 2005. Structural observation of the primary isomerization in vision with femtosecond-stimulated Raman. *Science* 310 (5750):1006–1009.

Le Ru, E.C., E. Blackie, M. Meyer, and P.G. Etchegoin. 2007. Surface enhanced Raman scattering enhancement factors: a comprehensive study. *The Journal of Physical Chemistry C* 111 (37):13794–13803.

Le Ru, E.C., and P.G. Etchegoin. 2006. Rigorous justification of the| E| 4 enhancement factor in surface enhanced Raman spectroscopy. *Chemical Physics Letters* 423 (1):63–66.

Le Ru, E.C., S.A. Meyer, C. Artur, et al. 2011. Experimental demonstration of surface selection rules for SERS on flat metallic surfaces. *Chemical Communications* 47 (13):3903–3905.

Li, Q., B. Li, and Y. Wang. 2013. Surface-enhanced Raman scattering microfluidic sensor. *RSC Advances* 3 (32):13015–13026.

Li, Y.-S., and J.S. Church. 2014. Raman spectroscopy in the analysis of food and pharmaceutical nanomaterials. *Journal of Food and Drug Analysis* 22 (1):29–48.

Long, D.A. 2002. Classical Theory of Rayleigh and Raman Scattering. In *The Raman Effect: A Unified Treatment of the Theory of Raman Scattering by Molecules*. John Wiley & Sons, Ltd., Hoboken, NJ.

Mallick, B., A. Lakhsmanna, and S. Umapathy. 2011. Ultrafast Raman loss spectroscopy (URLS): Instrumentation and principle. *Journal of Raman Spectroscopy* 42 (10):1883–1890.

Matousek, P., I.P. Clark, E.R.C. Draper, et al. 2005. Subsurface probing in diffusely scattering media using spatially offset Raman spectroscopy. *Applied Spectroscopy* 59 (4):393–400.

Matousek, P., and A.W. Parker. 2006. Bulk Raman analysis of pharmaceutical tablets. *Applied Spectroscopy* 60 (12):1353–1357.

Matousek, P. 2007. Deep non-invasive Raman spectroscopy of living tissue and powders. *Chemical Society Reviews* 36 (8):1292–1304.

Matousek, P., M.D. Morris, N. Everall, et al. 2005. Numerical simulations of subsurface probing in diffusely scattering media using spatially offset Raman spectroscopy. *Applied Spectroscopy* 59 (12):1485–1492.

Matousek, P., and N. Stone. 2007. Prospects for the diagnosis of breast cancer by noninvasive probing of calcifications using transmission Raman spectroscopy. *Journal of Biomedical Optics* 12 (2):024008-1–024008-8.

McHale, J.L. 1999. *Molecular spectroscopy*: Pearson College Division.

McNay, G., D. Eustace, W.E. Smith, K. Faulds, and D. Graham. 2011. Surface-enhanced Raman scattering (SERS) and surface-enhanced resonance Raman scattering (SERRS): A review of applications. *Applied Spectroscopy* 65 (8):825–837.

Minsky, M. 1961. Microscopy apparatus. US3013467 A.

Minsky, M. 1988. Memoir on inventing the confocal scanning microscope. *Scanning* 10 (4):128–138.

Moskovits, M., and J.S. Suh. 1984. Surface selection rules for surface-enhanced Raman spectroscopy: Calculations and application to the surface-enhanced Raman spectrum of phthalazine on silver. *The Journal of Physical Chemistry* 88 (23):5526–5530.

Muehlethaler, C., M. Leona, and J.R. Lombardi. 2015. Review of surface enhanced Raman scattering applications in forensic science. *Analytical Chemistry* 88 (1):152–169.

Okagbare, P.I., F.W.L. Esmonde-White, S.A. Goldstein, and M.D. Morris. 2010. Development of non-invasive Raman spectroscopy for in vivo evaluation of bone graft osseointegration in a rat model. *Analyst* 135 (12):3142–3146.

Osawa, M., N. Matsuda, K. Yoshii, and I. Uchida. 1994. Charge transfer resonance Raman process in surface-enhanced Raman scattering from p-aminothiophenol adsorbed on silver: Herzberg-Teller contribution. *The Journal of Physical Chemistry* 98 (48):12702–12707.

Periyasamy, V., S. Sil, G. Dhal, F. Ariese, S. Umapathy, and M. Pramanik. 2015. Experimentally validated Raman Monte Carlo simulation for a cuboid object to obtain Raman spectroscopic signatures for hidden material. *Journal of Raman Spectroscopy* 46: 669–676.

Plaza, P., N.Q. Dao, M. Jouan, H. Fevrier, and H. Saisse. 1986. Simulation et optimisation des capteurs a fibres optiques adjacentes. *Applied Optics* 25 (19):3448–3454.

Roy, K., S. Kayal, F. Ariese, A. Beeby, and S. Umapathy. 2017. Mode specific excited state dynamics study of bis (phenylethynyl) benzene from ultrafast Raman loss spectroscopy. *The Journal of Chemical Physics* 146 (6):064303.

Sasic, S., and Y. Ozaki. 2011. *Raman, Infrared, and Near-Infrared Chemical Imaging*: John Wiley & Sons, Hoboken, NJ.

Schlücker, S. 2014. Surface-Enhanced Raman spectroscopy: Concepts and chemical applications. *Angewandte Chemie International Edition* 53 (19):4756–4795.

Schrader, B., and G. Bergmann. 1967. Die Intensität des Ramanspektrums polykristalliner Substanzen. *Fresenius' Zeitschrift für Analytische Chemie* 225 (2):230–247.

Schulmerich, M.V., J.H. Cole, K.A. Dooley, et al. 2008. Noninvasive Raman tomographic imaging of canine bone tissue. *Journal of Biomedical Optics* 13 (2):020506-1–020506-3.

Schulmerich, M.V., K.A. Dooley, M.D. Morris, T.M. Vanasse, and S.A. Goldstein. 2006. Transcutaneous fiber optic Raman spectroscopy of bone using annular illumination and a circular array of collection fibers. *Journal of Biomedical Optics* 11 (6):060502-1–060502-3.

Schwab, S.D., and R.L. McCreery. 1984. Versatile, efficient Raman sampling with fiber optics. *Analytical Chemistry* 56 (12):2199–2204.

Shim, M.G., and B.C. Wilson. 1997. Development of an in vivo Raman spectroscopic system for diagnostic applications. *Journal of Raman Spectroscopy* 28 (2-3):131–142.

Shim, M.G., B.C. Wilson, E. Marple, and M. Wach. 1999. Study of fiber-optic probes for in vivo medical Raman spectroscopy. *Applied Spectroscopy* 53 (6):619–627.

Sil, S., and S. Umapathy. 2014. Raman spectroscopy explores molecular structural signatures of hidden materials in depth: Universal multiple angle Raman spectroscopy. *Scientific Reports* 4: 5308.

Srinivasan, S., M. Schulmerich, J.H. Cole, et al. 2008. Image-guided Raman spectroscopic recovery of canine cortical bone contrast in situ. *Optics Express* 16 (16):12190–12200.

Strangman, G., D.A. Boas, and J.P. Sutton. 2002. Non-invasive neuroimaging using near-infrared light. *Biological Psychiatry* 52 (7):679–693.

Syage, J.A., W.R. Lambert, P.M. Felker, A.H. Zewail, and R.M. Hochstrasser. 1982. Picosecond excitation and trans-cis isomerization of stilbene in a supersonic jet: dynamics and spectra. *Chemical Physics Letters* 88 (3):266–270.

Tanaka, T., A. Nakajima, A. Watanabe, T. Ohno, and Y. Ozaki. 2004. Surface-enhanced Raman scattering of pyridine and p-nitrophenol studied by density functional theory calculations. *Vibrational Spectroscopy* 34 (1):157–167.

Umapathy, S., A. Lakshmanna, and B. Mallick. 2009. Ultrafast Raman loss spectroscopy. *Journal of Raman Spectroscopy* 40 (3):235–237.

Weigel, A., and N.P. Ernsting. 2010. Excited stilbene: Intramolecular vibrational redistribution and solvation studied by femtosecond stimulated Raman spectroscopy. *The Journal of Physical Chemistry B* 114 (23):7879–7893.

Wu, D.-Y., X.-M. Liu, S. Duan, et al. 2008. Chemical enhancement effects in SERS spectra: A quantum chemical study of pyridine interacting with copper, silver, gold and platinum metals. *The Journal of Physical Chemistry C* 112 (11):4195–4204.

Wu, D.-Y., S. Duan, B. Ren, and Z.-Q. Tian. 2005. Density functional theory study of surface-enhanced Raman scattering spectra of pyridine adsorbed on noble and transition metal surfaces. *Journal of Raman Spectroscopy* 36 (6-7):533–540.

Xie, Y., D.Y. Wu, G.K. Liu, et al. 2003. Adsorption and photon-driven charge transfer of pyridine on a cobalt electrode analyzed by surface enhanced Raman spectroscopy and relevant theories. *Journal of Electroanalytical Chemistry* 554:417–425.

Xu, H., J. Aizpurua, M. Käll, and P. Apell. 2000. Electromagnetic contributions to single-molecule sensitivity in surface-enhanced Raman scattering. *Physical Review E* 62 (3):4318.

Yamamoto, Y.S., and T. Itoh. 2016. Why and how do the shapes of surface-enhanced Raman scattering spectra change? Recent progress from mechanistic studies. *Journal of Raman Spectroscopy* 47 (1):78–88.

Zhang, X., Q.-H. Tan, J.-B. Wu, W. Shi, and P.-H. Tan. 2016. Review on the Raman spectroscopy of different types of layered materials. *Nanoscale* 8 (12):6435–6450.

Zhou, Q., and T. Kim. 2016. Review of microfluidic approaches for surface-enhanced Raman scattering. *Sensors and Actuators B: Chemical* 227:504–514.

Taylor & Francis
Taylor & Francis Group
http://taylorandfrancis.com

17

Laser Scattering Spectroscopy: Rayleigh Scattering and Dynamic Light Scattering

Haruhisa Kato

CONTENTS

17.1 Introduction 197
17.2 General Principles of DLS (Photon Correlation Spectroscopy) 198
17.3 Consideration of Angular and Concentration Effect on the DLS Measurement 200
17.4 Consideration of Uncertainty Sources of the DLS Measurement 202
17.5 Consideration of the Size Distribution of Particles Determined by DLS 202
17.6 Conclusion 203
References 204

17.1 Introduction

Characterization methods for the reliable particle size determination in colloidal materials in liquid phase is one of the important keys to the development of novel nano- and biotechnological materials, as their physical and chemical properties depend on the size of the suspended particles [1–10]. As the potential usefulness of nanomaterials can increase with the decrease in the size of their structural elements, the number of studies on the reduction of the size of units of nanoscale materials is growing. For example, good photocatalyst requires a large catalytic surface area available for adsorption and decomposition of the target molecules, which is defined by the size of the primary catalyst nanoparticles.

In the past few decades, dynamic light scattering (DLS) has been widely used for determining the size of Brownian nanoparticles in nano- and submicron-scale colloidal suspensions [11–16]. Because of the convenience and usability of DLS instruments, a large number of commercial devices based on various principles underlying the DLS method are available. In contrast to electron microscopic method, DLS can be applied to characterize the size of structural elements of materials in liquid phase without any special treatments such as drying of liquid samples; thus, one can observe *in situ* colloidal structure of particles suspension. Indeed, primary nanoparticles that are generally observed by electron microscope tend to aggregate easily when dispersed nanoparticles in various liquid phases are prepared, as high ionic strength of the liquid, along with electrostatic and van der Waals particle interactions, results in the production of larger, aggregated secondary particles [17,18]. In this case, secondary particle size is important because van der Waals interaction is approximately proportional to the particle size, attributing to the stability of such commercial nanoparticle dispersions. Therefore, the characterization by DLS gives a meaningful information. In addition, secondary particle size is related to the amount of the uptake by cell in nanotoxicology assessment *in vitro* [19]. Hence, DLS is an essential characterization method for obtaining important information in nanosuspension.

DLS is widely used to determine the size of Brownian nanoparticles in colloidal suspensions in nanoscale and submicron ranges [11–16]. Particles dispersed in liquid are in incessant random motion, that is, Brownian motion, in which a given particle undergoes random position changes in time. Assuming the distribution for the displacement of a particle undergoing Brownian motion in aqueous solution is a Gaussian function, the average root mean square (RMS) displacement in two dimensions can be calculated using the concentration of the particles as

$$\left\langle (r - r_0)^2 \right\rangle = 2Dt \tag{17.1}$$

where t is the diffusion time (see Figure 17.1). The diffusion of spherical particles can be described by the Stokes–Einstein equation:

$$D = \frac{k_B T}{3\pi\eta d} \tag{17.2}$$

where k_B is the Boltzmann constant, T is the absolute temperature, η is the viscosity of the solvent, D is the diffusion coefficient of the particles, and d is the diameter of the particles. According to the Stokes–Einstein assumption, small particles move quickly by diffusion.

Using DLS, the diffusion phenomena and the Stokes–Einstein assumption are utilized in the determination of Brownian nanoparticle size in solution. In this method, the diffusion coefficient of the nanoparticles is determined first, and then, the size of the particles is calculated from the diffusion

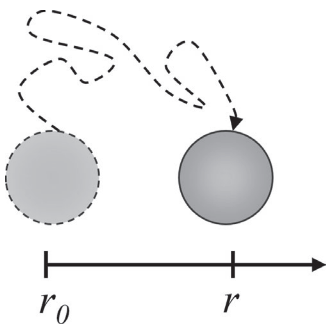

FIGURE 17.1 Illustration of Brownian motion of a nanoparticle in two dimensions. The RMS displacement is defined in Equation (17.1).

coefficient using the Stokes–Einstein assumption (Equation 17.2). The practical upper limit of the particle size determined using the DLS method is ~1–3 μm because of the dependence on Brownian motion and relaxation time. Typically, the upper limit can be probed with the available laser power and detector. The observed size range corresponds well with a large number of commercial nanoparticle dispersion applications. In addition, an advantage of using the DLS method compared with, for example, electron microscopy is the possibility of *in situ* size determination of secondary nanoparticles in the suspension. The DLS method is therefore one of the most powerful and useful tools to determine colloidal secondary particle size in suspension.

17.2 General Principles of DLS (Photon Correlation Spectroscopy)

In DLS, coherent light from an incident laser beam illuminates liquid medium in which small particles are suspended. When the particle size is much smaller (e.g., <10%) than the wavelength of light, the scattered radiation from the particles is in phase. If the incident light is unpolarized with irradiance I_0, the scattered irradiance I_s at an angle θ to the incident light source can be described by Rayleigh light scattering theory [20–22]. The Rayleigh light scattering intensity I_s observed for a uniform size distribution of nanoparticles is given by

$$I_s = I_0 \frac{c}{2r^2}\left(\frac{2\pi}{\lambda}\right)^4\left(\frac{d}{2}\right)^6\left|\frac{m^2-1}{m^2+2}\right|^2\left(1+\cos^2\theta\right) \qquad (17.3)$$

where c is the number of nanoparticles, d is the diameter of the spherical nanoparticles, m is the refractive index of the particle relative to that of the medium, r is the distance to the particles, and λ is the wavelength of the polarized laser. The scattered light intensity follows an inverse square law ($1/r^2$) and is proportional to $1/\lambda^4$. Scattered light is partially polarized perpendicular to the incident beam even if the incident light is unpolarized, with the last term, ($1+\cos^2\theta$), in Equation (17.3), representing the vertical (1) and horizontal ($\cos^2\theta$) components of the scattering relative to the incident light source, as shown in Figure 17.2. Vertically polarized light has equal intensity at all scattering angles, while the intensity of the horizontal component depends on the scattering angle and is zero at 90°.

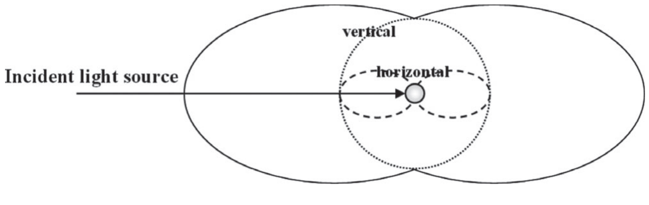

FIGURE 17.2 Angular distribution of Rayleigh light scattering by a spherical nanoparticle. The solid line represents the total light scattering, the dotted line represents the vertically polarized light, and the dashed line represents the horizontally polarized light.

As a result, when sufficiently small spherical particles are illuminated by an unpolarized light source, the scattered light is completely polarized at a scattering angle of 90°.

While using DLS, information about the dynamics of a particle in suspension is extracted from Rayleigh light scattering spectrum. Consequently, measurement of the variation in intensity and frequency of scattered light from particles can be correlated with the Brownian motion and dynamics of the particles. DLS is ideally suited for particles smaller than 1 μm and requires dilute particle dispersion, due to the dependence on random Brownian motion and relaxation time. DLS uses the phenomenon by which light scattered from a moving particle will have a slightly different frequency compared to the incident light source, known as the Doppler effect. When the particle suspension is illuminated by a laser source, random Brownian motion of the suspended particles induces the scattered light to vary randomly in frequency, resulting in random fluctuations in the scattered light intensity, as shown in Figure 17.3.

In order to detect the scattered light, optical mixing techniques (i.e., homodyning and heterodyning) are commonly used. In these methods, no filter is inserted between the

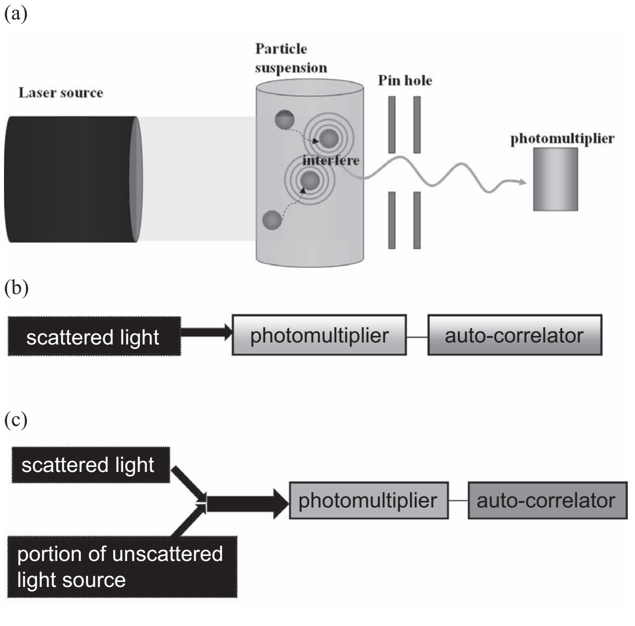

FIGURE 17.3 Schematic of a DLS system. (a) Scattered intensity in a typical DLS set-up, (b) illustration of the homodyne (or self-beat) detection technique, (c) illustration of the heterodyne detection technique.

scattering medium and the photomultiplier; therefore, the scattered light profile impinges directly onto the photomultiplier, as shown in Figure 17.3a. The scattered light intensity is then analysed by autocorrelation, measured via pulses from a photomultiplier tube, or an avalanche-photodiode detector, which has higher sensitivity. In the homodyne (or self-beat) detection method, only scattered light reaches the photocathode. In the heterodyne method, a local oscillator (i.e., a portion of the unscattered laser source) is mixed with the scattered light at the photocathode surface. These two detection methods are illustrated in Figure 17.3b and c, respectively. The homodyne method is more convenient and the widely used detection scheme for DLS apparatus because of the difficulty in stabilizing two light sources in the heterodyne method.

In light scattering experiments, the incident light source field is sufficiently weak that the system can be assumed to respond linearly to it. The change of the light field caused by the scattering of light by particles and the response of the equilibrium system to this weak incident field can be described accurately. The resultant scattering pattern is comprised of scattering by individual particles and scattering by the wider many-particle system, which changes in time due to the Brownian motion of particles. Time-dependent correlation functions are therefore used in DLS measurements to provide a concise method for expressing the degree to which two dynamical properties are correlated over a period of time. Illustration of the intensity of scattered light from nanoparticle dispersion as a function of time is shown in Figure 17.4a. The measured scattered intensity of the light field can be simply time-averaged as shown in Equation (17.4).

$$\bar{I}(t_0,\tau)=\frac{1}{\tau}\int_{t_0}^{t_0+\tau} dt\,I(t), \tag{17.4}$$

where t_0 is the time at which the measurement is initiated and τ is the time over which it is averaged. The average becomes meaningful only if τ is sufficiently large compared to the period of fluctuation, indicating that the ideal experimental time tends to infinity and that this infinite-time average of intensity is independent of t_0. Because of its independence of t_0, the noise signal of light scattered intensity, $I(t)$, can be expressed as

$$\langle I\rangle=\lim_{\tau\to\infty}\frac{1}{\tau}\int_{0}^{\tau} dt\;I(t) \tag{17.5}$$

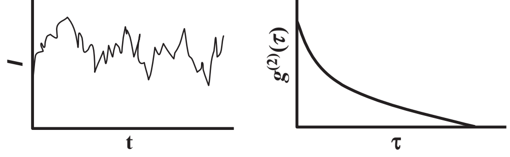

FIGURE 17.4 (a) Illustration of the intensity of light scattered from a dispersion of different-sized nanoparticles (I) as a function of time (t). (b) Illustration of the time-averaged autocorrelation function of scattered light as described by Equation (17.6).

In light scattering experiments, $I(t)$ and $I(t+\tau)$ have quite different values. However, when τ is sufficiently small compared to the observation time, $I(t)$ and $I(t+\tau)$ can take fairly similar values. The correlation between the two values can be defined as

$$g_2(\tau)=\frac{\langle I(t)I(t+\tau)\rangle_t}{\langle I(t)\rangle_t^2} \tag{17.6}$$

where $g_2(\tau)$ is known as the light scattering intensity autocorrelation function. In homodyne detection, $g_2(\tau)$ is related to the electric field autocorrelation function, assuming that its instantaneous current output is proportional to the square of the incident electric field. It is defined as

$$g_2(\tau)=1+\beta\left|g_1(\tau)\right|^2 \tag{17.7}$$

where β is a fundamental constant having a maximum value of 1 [23], and $g_1(\tau)$ is known as the homodyne correlation function.

However, in the heterodyne method, the autocorrelation function of scattered light can be defined as

$$g_2(\tau)=1+\frac{2\beta\langle I_s\rangle g_1(\tau)}{I_{\mathrm{LO}}} \tag{17.8}$$

where $\langle I_s\rangle$ is the average scattered light intensity, I_{LO} is the scattered light intensity of a constant local oscillator, and $g_1(\tau)$ is the heterodyne correlation function. In this case, it is assumed that fluctuations of the local oscillator field are negligible and that the local oscillator field and the scattered field are statistically independent. When the local oscillator intensity lies between the extremes $I_{\mathrm{LO}}=0$ in the homodyne case and $I_{\mathrm{LO}}>>\langle I_s\rangle$ in the heterodyne case, $g_2(\tau)$ will be a weighted sum of $g_1(\tau)$ and $\left|g_1(\tau)\right|^2$.

Assuming that particle suspension is *monodisperse* and dilute (i.e., all the particles have the same size and shape) and that there is no interaction between particles, $g_1(\tau)$ can be represented by

$$\ln(g_1(\tau))=-\Gamma\tau \tag{17.9}$$

$$\Gamma=DQ^2 \tag{17.10}$$

and

$$Q=\frac{4\pi n_0}{\lambda_0\sin\left(\frac{\theta}{2}\right)} \tag{17.11}$$

where θ is the observed angle, λ_0 is the wavelength of the laser source in vacuum, n_0 is the refractive index of the medium solvent, and D is the diffusion coefficient of particles in the medium. The delay rate, Γ, is related to the translational diffusion coefficient of the particles. Q is the modulus of the scattering vector and is given by Equation (17.11). According to the Stokes–Einstein relation (Equation 17.2), the hydrodynamic diameter, *d,* of the particles can then be calculated from *D* via DLS, assuming there is no size distribution.

When the particle suspension is polydisperse, that is, the particles have some finite size distribution, the correlation function is represented as

$$g_1(\tau) = \int_0^\infty G(\Gamma)\exp(-\Gamma\tau)d\Gamma \tag{17.12}$$

and

$$\int_0^\infty g_1(\Gamma)d\Gamma = 1 \tag{17.13}$$

For DLS analysis of polydisperse particles, the cumulant method is readily used if the particle distribution is narrow and monodisperse. In this method, the light scattering intensity correlation function is expanded around the averaged value, $\overline{\Gamma}$, in polynomial series, which is normally truncated after the quadratic term in the series for the sake of simplicity, yielding

$$g_2(\tau) \approx 1 + \beta\exp\left(-2\overline{\Gamma}\tau + \mu_2\tau^2\right) \tag{17.14}$$

In the cumulant method [24, 25], the electric field autocorrelation function is described by

$$\ln\left|g_1(\tau)\right| = \sum_{m=1}^{\infty} K_m \frac{(-\tau)^m}{m!} \tag{17.15}$$

$$K_1 = \overline{\Gamma} \tag{17.16}$$

$$K_2 = \overline{\left(\Gamma - \overline{\Gamma}\right)^2} \tag{17.17}$$

where K_1 is the slope of the plot of $\ln|g_2(\tau)|$ vs τ, and K_1/Q_2 is related to the diameter of particles in the dispersion. The polydispersity index [16], *PI*, is defined as

$$PI = \frac{2K_2}{\overline{\Gamma}^2} \tag{17.18}$$

This value represents the size distribution of particles measured by DLS analysis of *monomodal* disperse particle solution. However, the interpretation of the *PI* is not important; therefore, this value is used only to monitor the qualitative change of the size distribution of particles.

For *multimodal* size-distributed particle dispersion, Laplace inversion analytical method is generally used to determine the size distribution by DLS [26–28]. The outline of this method is only briefly described here, because, unfortunately, there is no standardized algorithm and the method is strongly dependent on the specific DLS equipment used. However, the outline of the method is simple. Equation (17.11) is fixed by a particle size range and divided into a discrete set of respective fixed particle sizes, after which the light scattering intensity-weighted fraction of particles can be determined. In this method, the size distribution is, therefore, calculated as a discrete set of particle diameters with corresponding light scattering intensity-weighted fractions. Such a stepped analysis is mathematically unstable, producing incoherent analytical results in some cases.

In principle, the concentration of the particle suspension in DLS measurements must be sufficiently low so that a multiple scattering effect is avoided. Unless the concentration is low, any scattered photon has a nonzero probability of being rescattered on its continued path through the suspension. The autocorrelation function of such multiple light scattering decays faster, resulting in the estimated particle size being smaller than the true particle size. Because of this, in theory, the concentration of the particles should be low, and the optical path must be sufficiently short to avoid multiple scattering. However, sufficiently low concentration of particles induces unstable scattering, and the DLS measurement results can easily be affected by small amounts of dust. One of the solutions to this problem is the extrapolation of apparent diffusion coefficients (observed in sufficient numbers for different concentrations) to infinite dilution, yielding more reliable values than those obtained for just one concentration [14]. To consider the effect of the multiple light scattering on the determination of the size by DLS, the photon cross-correlation spectroscopy (PCCS) is utilized [29–34]. In the PCCS method, two different lasers are focused on the same sample scattering volume, resulting in two separate respective scattering patterns. The experimental layout of the PCCS system is illustrated in Figure 17.5. It is important to note that cross-correlation method can in principle completely eliminate any contribution from multiple light scattering from highly concentrated particle dispersions. In theory, two separated light scattering signals in this system are the same. However, in practice, they differ to varying degree due to the different noise level and the extent of multiple scattering. Therefore, under ideal and well-controlled conditions, the cross-correlation of two scattering signals works to remove the influence of noise and multiple scattering, making it possible to extract information about the particles even in highly concentrated particle dispersions. However, this method does not consider the interaction between particles in such high-concentration measurement systems; it just reduces the effect of multiple light scattering on sizing.

17.3 Consideration of Angular and Concentration Effect on the DLS Measurement

In principle, the particle concentration in the suspension and the optical path length must be sufficiently low to prevent multiple scattering. For a higher-concentration suspension, scattered photon has non-negligible probability of being rescattered when passing through the suspension. The autocorrelation function for such multiple scattering decays faster than the one for single scattering, resulting in the underestimation

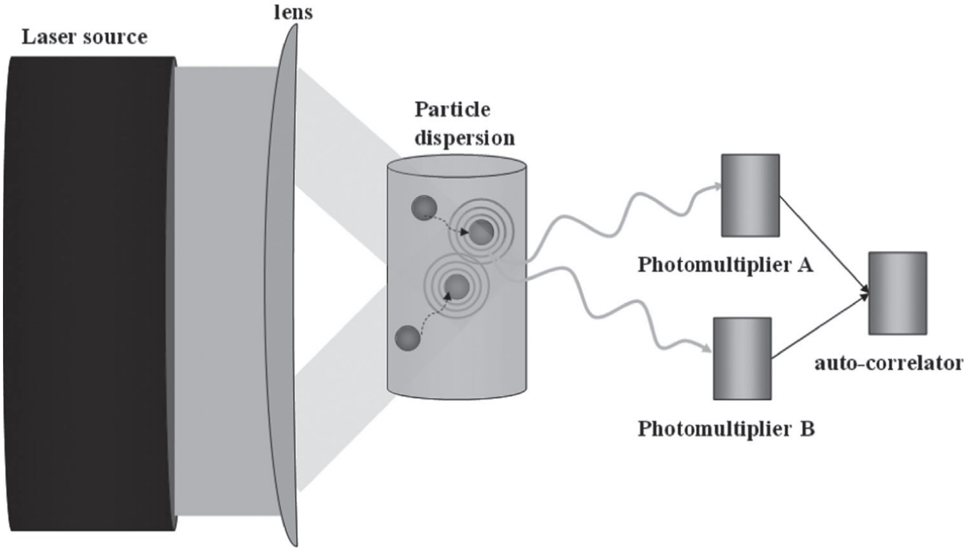

FIGURE 17.5 Schematic of the photon cross-correlation spectroscopic (PCCS) DLS system.

of particle size. However, if the particle concentration is too low, the scattering is unstable. DLS measurements can also be easily affected by traces of dust. As described before, one of the solutions to this problem is to extrapolate the apparent diffusion coefficients observed at a large number of concentrations to infinite dilution. Doing so yields more reliable results than those obtained by measurements at only one concentration. The measured apparent intensity-averaged hydrodynamic diameter is therefore extrapolated to infinite dilution and to zero angle in order to determine the true hydrodynamic size in an aqueous medium, being referred to the double extrapolation plot as a Zimm plot [14]. Figure 17.6a shows an example of the plot of the raw photon correlation function of polystyrene latex (PSL) determined by DLS measurement. The concentration of the aqueous suspension of PSL was 0.009 mg mL^{-1}. Light scattering was observed at a scattering angle of 90°. Filled circles in Figure 17.6a indicate the raw data, and the red line is the linear least-squares fit with the observed photon correlation function according to Equation (17.9).

A typical example of plots of apparent diameter $d_{\text{l, app}}$ calculated from the first cumulant of PSL against the PSL concentration and observed scattering angles is presented in Figure 17.6b. For the aqueous suspension of PSL, 40 independent DLS measurements were taken in the concentration range from 0.009 to 0.044 mg mL^{-1}. Light scattering was observed at 8 scattering angles from 45° to 150°. In all of the measurements, the observed raw photon correlation function showed a linear decay similarly to the result in Figure 17.6a, but the slopes were different for corresponding angles and concentrations of PSL suspensions. There was almost a linear dependence of $d_{\text{l, app}}$ on concentration for each investigated concentration and scattering angle.

The observed behaviour in Figure 17.6b can be quantitatively represented by the following equation:

$$d_{l,\text{app}} = d_l\left(1 + k_c c + k_Q Q^2 + \cdots\right) \tag{17.19}$$

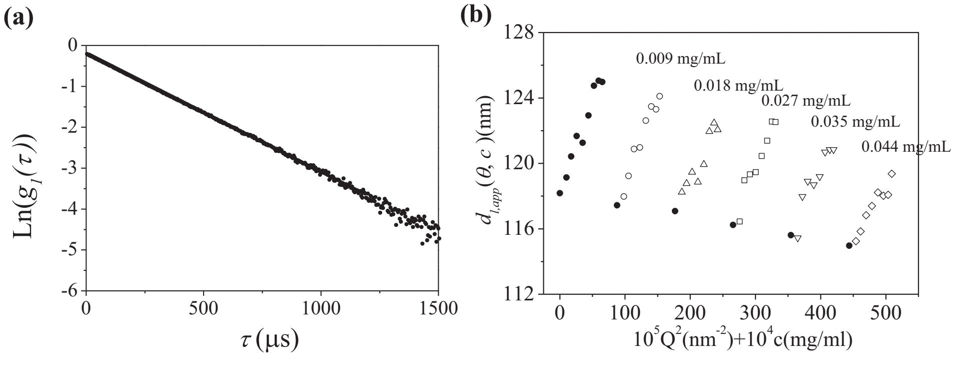

FIGURE 17.6 (a) Example of observed homodyne photon correlation function for PSL analysed by DLS (filled circle plots). The concentration of the aqueous PSL suspension was 0.009 mg mL^{-1}, and light scattering was observed at a scattering angle of 90°. The solid line is the linear least-squares fit of the experimental results. (b) Example of the constructed Zimm plots for PSL analysed by DLS at a concentration range from 0.009 to 0.044 mg mL^{-1}. Light scattering was observed at eight different scattering angles from 45° to 150°. The true d_{l} was calculated to be 118.2 nm [14].

where d_l is the true diameter, k_c and k_Q are the constants, and c is the concentration of PSL nanoparticles in the suspension. The d_l, k_c, and k_Q values for specific PSL concentration and observed scattering angle in Equation (17.8) are determined by extrapolating the corresponding PSL concentration and observed scattering angle to zero in Figure 17.6b. Cichocki et al. [35] described the relationship between diffusion coefficients and interactions between nanoparticles by using the "effective radius," which represents not only hydrodynamic interaction but also electrostatic repulsion and attraction at longer distances. Figure 17.6b clearly shows that the dynamics of PSL in aqueous suspension are dominated by long-range electrostatic interactions between PSL nanoparticles since $d_{\mathrm{l,\ app}}$ shows clear dependence on angle and concentration. The particle scattering factor determined by static light scattering and the existence of electrostatic interactions between particles suggest a large angular distribution, as shown in Figure 17.6b. The effects of polydispersity of PSL and multiple scattering are not responsible for these dependences because (i) higher polydispersity makes the observed particle sizes larger at lower angles and (ii) the most concentrated sample with the largest particle size did not exhibit multiple scattering effects at various intensities of the incident beam. Therefore, the double extrapolation of concentration and angular dependences in the DLS results can be used to determine d_l in Equation (17.19). For example, in the Zimm plot analysis in Figure 17.6b, the d_l value is estimated to be 118.2 nm [14]. This result indicated that the careful consideration of apparent DLS measurement result is important.

17.4 Consideration of Uncertainty Sources of the DLS Measurement

The consideration of the uncertainty sources of DLS is important to estimate the reliability of the measurement results. In addition, in the interlaboratory comparison process, not only the measured values of particles size are matched, but also the uncertainty of these values. In order to estimate the uncertainty sources, a standard of the uncertainty estimation, often called GUM and published by the standard bodies such as the Bureau International des Poids et Mesures (BIPM) and the International Organization for Standardization (ISO), was employed. The individual uncertainty sources of light scattering intensity-averaged diameter (d_l) of the materials in aqueous solution were determined as described in the supporting information. The Boltzmann constant $\left(u(k_B)\right)$ [36], the estimated value of temperature variation $\left(u(T)\right)$, the viscosity of the solvent $\left(u(\eta)\right)$ [37], the delay rate $\left(u(\Gamma)\right)$, the refractive index of solvent $\left(u(n)\right)$ [38,39], the value of wavelength $\left(u(\lambda)\right)$, the observed scattering angle $\left(u(\theta)\right)$, the repeatability of DLS measurements $\left(u_{\mathrm{rep}}(d_l)\right)$, and the extrapolation to infinite dilution and to zero angles in Zimm plot $\left(u_{\mathrm{Zimm}}(d_l)\right)$ should be considered as the uncertainty sources [14]. The calculation of the combined standard uncertainty of light scattering intensity-averaged diameter by DLS was made as follows. According to Stokes–Einstein assumption (Equation 17.2), the light scattering intensity-averaged diameter determined by DLS can be calculated as follows:

$$d_l = \frac{k_B T Q^2}{3\pi\eta\Gamma} = \frac{16\pi k_B T n^2}{3\eta\lambda^2\Gamma}\sin^2\left(\frac{\theta}{2}\right) \tag{17.20}$$

The standard uncertainty of d_l is then expressed as

$$\begin{aligned} u^2(d_l) = {} & \left(\frac{\partial d_l}{\partial k_B}\right)^2 u^2(k_B) + \left(\frac{\partial d_l}{\partial T}\right)^2 u^2(T) + \left(\frac{\partial d_l}{\partial \eta}\right)^2 u^2(\eta) \\ & + \left(\frac{\partial d_l}{\partial \Gamma}\right)^2 u^2(\Gamma) + \left(\frac{\partial d_l}{\partial n}\right)^2 u^2(n) \\ & + \left(\frac{\partial d_l}{\partial \lambda}\right)^2 u^2(\lambda) + \left(\frac{\partial d_l}{\partial \theta}\right)^2 u^2(\theta) + u_{\mathrm{rep}}^2(d_l) \\ & + u_{\mathrm{Zimm}}^2(d_l) + u_{\mathrm{homo}}^2(d_l) \end{aligned} \tag{17.21}$$

which, when expanded, becomes:

$$\begin{aligned} u^2(d_l) = {} & \left(\frac{16\pi T n^2}{3\eta\lambda^2\Gamma}\sin^2\left(\frac{\theta}{2}\right)\right)^2 u^2(k_B) + \left(\frac{16\pi k_B n^2}{3\eta\lambda^2\Gamma}\sin^2\left(\frac{\theta}{2}\right)\right)^2 u^2(T) \\ & + \left(-\frac{16\pi k_B T n^2}{3\eta^2\lambda^2\Gamma}\sin^2\left(\frac{\theta}{2}\right)\right)^2 u^2(\eta) \\ & + \left(-\frac{16\pi k_B T n^2}{3\eta\lambda^2\Gamma^2}\sin^2\left(\frac{\theta}{2}\right)\right)^2 u^2(\Gamma) \\ & + \left(\frac{32\pi k_B T n}{3\eta\lambda^2\Gamma}\sin^2\left(\frac{\theta}{2}\right)\right)^2 u^2(n) \\ & + \left(-\frac{32\pi k_B T n^2}{3\eta\lambda^3\Gamma}\sin^2\left(\frac{\theta}{2}\right)\right)^2 u^2(\lambda) \\ & + \left(\frac{8\pi k_B T n^2}{3\eta\lambda^2\Gamma}\sin(\theta)\right)^2 u^2(\theta) \\ & + u_{\mathrm{rep}}^2(d_l) + u_{\mathrm{Zimm}}^2(d_l) \end{aligned} \tag{17.22}$$

17.5 Consideration of the Size Distribution of Particles Determined by DLS

The apparent diameters of particles with a wide size distribution obtained by DLS depend on the analytical algorithm [17,40]. The light scattering from larger particles masks that of smaller particles, and thus, the mean size and size distribution obtained by DLS only reflect the sizes of larger materials. In addition, the calculated size distribution of particles by DLS is strongly dependent on the calculation algorithm, analytical method, and instrument manufacturer. Commercial materials often have a wide size distribution; therefore, it is important to examine whether DLS can be used for determining not only the mean size but also the size distribution of a colloidal sample with a wide size distribution. In contrast to the DLS method, asymmetric flow field flow fractionation (AF4) is an elution technique in which particles and macromolecules are separated by flow control in an aqueous medium [41,42]. Therefore, AF4 is a reliable and quantitative method to determine the size distributions of particles in liquid phase [42]. In order to establish the reliability of the determination of the size distribution of particles in liquid by DLS, the hyphenated AF4 and multiangle light scattering (MALS) methods are applied to distinguish the differences in the size distributions of PSL aqueous suspensions as follows.

Figure 17.7 shows the example of establishing the reliability of the size distribution determined by AF4-MALS and DLS methods. Figure 17.7a and b shows the size distribution of PSL suspensions (PSL-A: mean diameter is 107 nm and CV value calculated from the standard deviation of the size distribution is 3.1%; PSL-B: mean diameter is 118 nm and CV value calculated from the standard deviation of the size distribution is 10%) characterized by AF4-MALS. Figure 17.7c and d shows the size distribution of PSL suspensions (PSL-A and PSL-B, respectively) characterized by DLS.

The size distributions of the two PSL suspensions determined by DLS were found to be similar (Figures 17.7c and d). However, the size distributions of the same two PSL nanoparticles determined by AF4-MALS were found to be markedly different (Figures 17.7a and b), with PSL-B showing a wider size distribution. These results indicate that the size distribution determined by DLS is not reliable. This also implies that the weight- and number-averaged diameters obtained by DLS are quite unreliable, since those values calculated from the intensity-averaged diameter by DLS are strongly dependent on the light scattering intensity size distribution. It was also examined the coverage and accuracy of using experimental DLS method and theoretical approach to determine a submicron bimodal size distribution [42]. For a mixture of two different sizes of submicron-sized particles with a size difference of more than sixfold, the model of simple summation of two different photon correlation functions between the non-interacting particles agreed well with the experimental DLS homodyne photon correlation function. However, for a mixture of particles with a size difference 2- or 3.3-fold, the homodyne correlation functions were approximately linear and DLS could not give a stable and accurate bimodal size distribution.

17.6 Conclusion

Accurate determination of the size of units of materials is a key to the development of bio- and nanotechnologies, as the size determines many of the physical and chemical properties of the functional materials. The DLS method is widely used as an effective technique to determine the average size of Brownian nanoparticles in colloidal suspensions. In this chapter, the fundamental principles of DLS based on the PCCS method are presented first; then, more practical aspects such as angular and concentration effects on the DLS measurement,

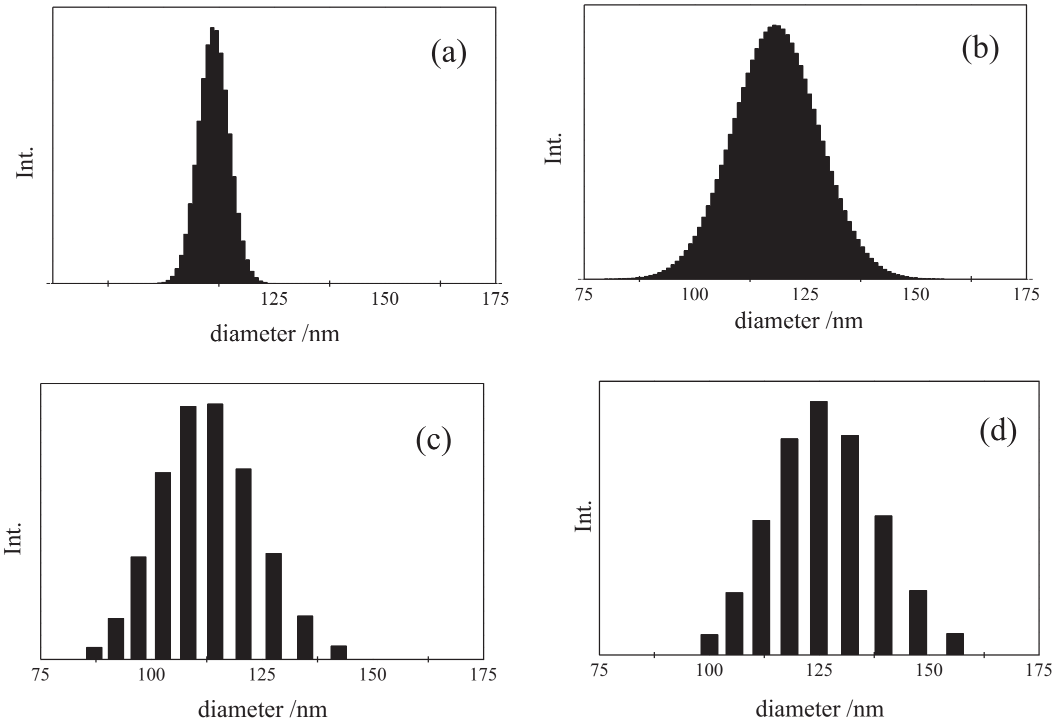

FIGURE 17.7 Examples of size distribution of PSL suspensions determined by AF4-MALS and DLS using a cumulant analytical method. Two PSLs were used; PSL-A: mean diameter is 107 nm and CV value calculated from the standard deviation of the size distribution is 3.1%, PSL-B: mean diameter is 118 nm and CV value calculated from the standard deviation of the size distribution is 10%. (a) Calculated size distribution of PSL-A by AF4-MALS, (b) calculated size distribution of PSL-B by AF4-MALS, (c) calculated size distribution of PSL-A by DLS, and (d) calculated size distribution of PSL-B by DLS.

determination of the uncertainty of DLS results, and limitations of the practical usage of DLS are contained in the latter part. The European Commission has declared that a nanomaterial is "a natural, incidental, or manufactured material containing particles, in an unbound state or as an aggregate or as an agglomerate and where, for 50% or more of the particles in the number size distribution, one or more external dimensions is in the size range of 1–100 nm." According to this definition, not only the size but also the size distribution of materials is an important factor in the fields of nanotechnology and biotechnology. While more convenient DLS apparatuses are desired in the nanotechnological field, the precise size distribution and determination of materials using DLS or other metrological techniques are necessary for considering the recently established regulation of the nanomaterial import/export in all over the world and consideration of the nanotoxicity problem. Because of the limitations of the ability of the sizing by DLS, the DLS metrology is expected to be utilized as a qualitative screening method for these aspects.

REFERENCES

1. A. Kasuy, G. Milczarek, I. Dmitruk, et al. 2002. Size- and shape-controls and electronic functions of nanometer-scale semiconductors and oxides. *Colloids Surf. A* 202: 291–296.
2. N. T. Tran, C. G. Campbell, F. G. Shi 2006. Study of particle size effects on an optical fiber sensor response examined with Monte Carlo simulation. *Appl. Opt.* 45: 7557–7566.
3. A. J. Maira, K. L. Yeung, C. Y. Lee, et al. 2000. Size effects in gas-phase photo-oxidation of trichloroethylene using nanometer-sized TiO_2 catalysts. *J. Catal.* 192: 185–196.
4. S. Kambe, S. Nakade, Y. Wada, et al. 2002. Effects of crystal structure, size, shape and surface structural differences on photo-induced electron transport in TiO_2 mesoporous electrodes. *J. Mater. Chem.* 12: 723–728.
5. H. Yano, J. Inukai, H. Uchida, et al. 2006. Particle-size effect of nanoscale platinum catalysts in oxygen reduction reaction: an electrochemical and^{195}Pt EC-NMR study. *Phys. Chem. Chem. Phys.* 8: 4932–4939.
6. B. Chen, D. Penwell, L. R. Benedetti, et al. 2002. Particle-size effect on the compressibility of nanocrystalline alumina. *Phys. Rev. B.* 66: 144101-1.
7. A. M. Doyle, S. K. Shaikhutdinov, H. Freund, 2005. Surface-bonded precursor determines particle size effects for alkene hydrogenation on palladium. *Angew. Chem. Int. Ed.* 44: 629–631.
8. A. A. Gribb, J. F. Banfield, 1997. Particle size effects on transformation kinetics and phase stability in nanocrystalline TiO_2. *Am. Mineral.* 82: 717–728.
9. J. Duran, J. Rajchenbach, E. Clément, 1993. Arching effect model for particle size segregation. *Phys. Rev. Lett.* 70: 2431–2434.
10. J. Sarkar, P. Pal, G. B. Talapatra, 2005. Self-assembly of silver nano-particles on stearic acid Langmuir–Blodgett film: Evidence of fractal growth. *Chem. Phys. Lett.* 401: 400–404.
11. B. J. Berne and R. Pecora 2000. *Dynamic Light Scattering: With Applications to Chemistry, Biology, and Physics*; Dover Pubns., Mineola, NY.
12. B. Chu 2007. *Laser Light Scattering: Basic Principles and Practice*, 2nd edition; Dover Pubns., Mineola, NY.
13. R. Pecora 1985. *Dynamic Light Scattering: Applications of Photon Correlation Spectroscopy*; Plenum, New York.
14. H. Kato, A. Nakamura, K. Takahashi, et al. 2012. Accurate size and size-distribution determination of polystyrene latex nanoparticles in aqueous medium using dynamic light scattering and asymmetrical flow field flow fractionation with multi-angle light scattering. *Nanomaterials* 2: 15–30.
15. ISO 13321:1996, Particle size analysis-Photon correlation spectroscopy (diluted suspensions).
16. ISO 22412:2008, Particle size analysis -Dynamic light scattering.
17. H. Kato, M. Suzuki, K. Fujita, et al. 2009. Reliable size determination of nanoparticles using dynamic light scattering method for in vitro toxicology assessment. *Toxicol. Vitro* 23: 927–934.
18. H. Kato, K. Fujita, M. Horie, et al. 2010. Dispersion characteristics of various metal oxide secondary nanoparticles in culture medium for in vitro toxicology assessment. *Toxicol. Vitro* 24: 1009–1018.
19. M. Horie, K. Nishio, K. Fujita, et al., 2010. Cellular responses by stable and uniform ultrafine titanium dioxide particles in culture-medium dispersions when secondary particle size was 100 nm or less. *Toxicol. Vitro* 24: 1629–1638.
20. L. Rayleigh, 1881. On the electromagnetic theory of light. *Philos. Mag.* 12: 81–101.
21. L. Rayleigh, 1914. On the diffraction of light by spheres of small relative index. *Proc. Roy. Soc. A* 90: 219–225.
22. L. Rayleigh, 1918. On the scattering of light by spherical shells, and by complete spheres of periodic structure, when the refractivity is small. *Proc. Roy. Soc. A* 94, 296–300.
23. R. J. Glauber, 1963. Coherent and Inconherent states of the radiation field. *Phys. Rev.* 131: 2766–2788.
24. D. E. Kopperl, 1972. Analysis of macromolecular polydispersity in intensity correlation spectroscopy: The method of cumulants. *J. Chem. Phys.* 57: 4814–4820.
25. J. C. Brown, P. N. Pusey, R. J. Dietz, 1975. Photon correlation study of polydisperse samples of polystyrene in cyclohexane. *J. Chem. Phys.* 62: 1136–1144.
26. S. W. Provencher, 1982. A constrained regularization method for inverting data represented by linear algebraic or integral equations. *Comput. Phys. Commun.* 27: 213–227.
27. S. W. Provencher, J. Hendrix, L. D. Maeyer, et al. 1978. Direct determination of molecular weight distributions of polystyrene in cyclohexane with photon correlation spectroscopy. *Chem. Phys.* 69: 4273–4276.
28. S. W. Provencher, 1979. Inverse problems in polymer characterization: Direct analysis of polydispersity with photon correlation spectroscopy. *Macromol. Chem.* 180: 201–209.
29. K. J. Schåtzel, 1991. Suppression of multiple scattering by photon cross-correlation techniques. *J. Mod. Optics* 38: 1849–1865.
30. L. B. Aberle, W. Staude, O.-D. Hennemann, 1999. Three-dimensional cross correlation technique: influence of multiply scattered light in the Rayleigh–Gans regime. *Phys. Chem. Chem. Phys.* 1: 3917–3921.
31. E. Overbeck, C. Sinn, 1999. Three-dimensional dynamic light scattering. *J. Modern Opt.* 46: 303–326.

32. L. B. Aberle, P. Hülstede, S. Wiegand, et al. 1998. Effective suppression of multiply scattered light in static and dynamic light scattering. *Appl. Opt.* 37: 6511–6524.
33. L. B. Aberle, M. Kleemeier, P. Hülstede, et al. 1999. A comparison of 3D static light-scattering experiments with Monte Carlo simulations. *J. Phys. D. Appl. Phys.* 32: 22–28.
34. P. N. Pusey, 1999. Suppression of multiple scattering by photon cross-correlation techniques. *Curr. Opin. Colloid Interface Sci.* 4: 177–185.
35. B. Cichocki, B. U. Felderhof, 1991. Diffusion of Brownian particles with hydrodynamic interaction and hard core repulsion. *J. Chem. Phys.* 94: 556–562.
36. PAC, 1996, 68, 957. Glossary of terms in quantities and units in Clinical Chemistry (IUPAC-IFCC Recommendations 1996).
37. J. A. Riddick, W. B. Bunger, T. K. Sakano, 1986. *Organic Solvents: Physical Properties and Methods of Purification*, 4th edition, Wiley-Interscience, New York.
38. M. B. Huglin, S. J. O'Donohue, M. A. Radwan, 1989. Refractometric and light scattering parameters at 633 nm for polystyrene solutions. *Eur. Polym. J.* 25: 543–547.
39. E. Moreels, C. de Greef, R. Finsy, 1984. Laser light refractometer. *Appl. Opt.* 23: 3010–3013.
40. H. Kato, A. Nakamura, N. Ouchi, et al., 2016. Determination of bimodal size distribution using dynamic light scattering methods in the submicrometer size range. *Mat. Express*, 6: 175–182.
41. M. Schimpf, K. Caldwell, J. C. Giddings 2000. *A Field-Flow Fractionation Handbook*, John Wiley & Sons, Inc., Hoboken, NJ.
42. H. Kato and A. Nakamura, 2014. Separation of nano- and micro-sized materials by hyphenated flow and centrifugal field-flow fractionation. *Anal. Meth.* 6: 3215–3218.

Taylor & Francis
Taylor & Francis Group
http://taylorandfrancis.com

18

Laser-Induced Breakdown Spectroscopy

Parviz Parvin and Seyedeh Zahra Mortazavi

CONTENTS

18.1 Introduction 207
18.2 Application of LIBS 208
  18.2.1 Determination of Gold Fineness by Laser-induced Breakdown Spectroscopy 208
  18.2.2 Laser-induced Plasma to Decompose Hydrocarbon Molecules 210
    18.2.2.1 Medical Application 214
References 217

18.1 Introduction

Among the many spectroscopic methods, laser-induced breakdown spectroscopy (LIBS) is well known as an efficient and popular technique with attractive applications in many areas. In fact, LIBS has been aggressively investigated for environmental, industrial, geological, planetary, art, and medical applications. The success of the technique mainly arises from its multielemental capability, low cost, and the simplicity of working in atmospheric or low-pressure environments, as well as its ability to detect various components in a great variety of matrices. LIBS is also utilized in monitoring alloy elements during metal processing [1–4].

Despite its prominent superiority among the alternation techniques, the sensitivity is relatively low with respect to some traditional analytical techniques such as inductively coupled plasma atomic emission spectrometry (ICP-AES) and inductively coupled plasma mass spectroscopy (ICP-MS) [5]. Furthermore, there are several disadvantages of LIBS such as minimum detection level ranging from ppm to ppb. The accuracy limits to the laser instability, and this technique is minimally invasive not to be recommended to inspect the precious stone, archaeological articles, and valuable paintings [6].

This method is based on laser beam focusing to deliver sufficient energy density on the sample in order to create a fast-expanding plume above the surface. It is enough to result in plasma formation through the subsequent process of vaporization, atomization, and ionization in a single step. It leads to a high-temperature dense plasma that can be spectrally resolved and detected, which contains the characteristic peaks with a significant information on the nature and concentration of the elements. The integrated emission of the individual spectral lines, in principle, is associated with the number density of the corresponding emitting species in the plume. However, this, in turn, can be correlated with the concentration of element in the sample via the various calibration methods leading to the quantitative analysis.

In general, it is desirable to increase the signal-to-noise (S/N) ratio by scaling the strength of the signal, which can be achieved using several techniques. A number of works have previously reported using dual pulse techniques to enhance the emission spectra, mainly due to the pre- and reheating process, using dual laser arrangements. The effects of heated samples have been studied in terms of the spectral features as well as the morphology of the ablated craters at ambient atmospheric pressures. A notable dependence of signal emission intensity on temperature was reported. The presence of oxygen and other oxidizing gases causes the target surface to oxidize, while the high bulk temperature rise also leads to phase changes. In a research work [4], the traditional LIBS technique was carried out on Cu samples using a Nd:YAG laser. In order to avoid the distortion of the samples, the focal point of the laser was located approximately 1 mm away from the surface to create the microplasma in air rather than on the solid surface. This reduces the amount of distortion due to mass ablation, which, in turn, results in a noticeable reduction in the emission lines. In fact, while the emission lines due to nitrogen in air remain invariant, some of the characteristic peaks disappear due to the lack of sufficient Cu components ablated from the surface. In order to enhance the emission lines, a dual beam arrangement was employed, such that irradiation from a CW CO_2 laser preheats the sample, leading to a local temperature rise. This changes the thermal and optical properties of the sample surface, leading to greater energy coupling. This means that there is a significant addition of sensible energy to the system, which does not then have to be supplied by the pulsed laser. This makes more of the energy available to heat the plasma, which is perfectly consistent with the plasma temperature measurements. The plasma electronic temperature was measured to increase up to ~10 000 K, subsequently. Moreover, the IB (inverse Bremsstrahlung) reaction rate increases due to the strong absorption cross section at longer wavelengths, which reheats the plasma with better excitation, contributing to heating as a subsidiary effect [4].

In fact, LIBS introduces a number of potential applications involving high electron density and temperature. The transient characteristics of the plasma motivate the optical emission spectroscopy (OES) technique with time and space resolution, which is appropriate to study the plasma dynamics.

The plasma temperature differs substantially at early time delays after the formation of the plasma that is clearly supported by the line-to-continuum approach. In this framework, researchers have mainly focused either on the understanding of physical phenomena involved in the laser-induced plasma, or on the analytical achievements of the technique [6].

There are several reports on the time-resolved measurements in the early stages of the plasma expansion, i.e. in the first nanoseconds after the laser pulse [7–9]. The plasma acts as if it were in Local Thermal Equilibrium (LTE), at least after 1 μs, and the LIBS plasma behaves very close to the condition of LTE. The most popular criterion used in the literatures for checking LTE condition is the so-called McWhirter criterion [10], which is a necessary but not sufficient condition for LTE to hold. Two more criteria to check the existence of LTE have been introduced based on the experimental measurement of the plasma temperature. One of them is the comparison of the excitation and ionization temperatures, deduced from the Boltzmann and Saha–Boltzmann equations, respectively. The other is the agreement between the Boltzmann distribution and the experimentally measured line intensities, which is reflected in the linearity of the Boltzmann plot. Moreover, Moon et al. [9] have proposed two diagnostic approaches, aimed at evaluating the departure from LTE in laser-induced plasma. The first approach is based upon the observed temporal behaviour of the ratio between selected atomic transitions and the nearby spectral continuum, while the second approach makes use of the plot of the ion fraction of different elements as a function of their respective ionization potentials. It is shown that the experimental results obtained with both methods agree with those reported in the literature using more conventional approaches. As a result, a combination of different diagnostic approaches is essential to determine LTE condition. Several of these methods have been discussed in the literature [6,9]. Despite the versatility of LIBS in the analytical applications, the physical processes of laser ablation and laser-induced plasma formation are not yet fully understood. In fact, the initial phenomena involved in the establishment of the breakdown plasma differ as a function of the nature of the target sample, and its further evolution apparently occurs in a similar way. Hence, the plasma radiation characteristics are related to the thermal and electronic properties of the sample, laser parameters, and the ambient conditions accordingly. Therefore, it is essential to perform a systematic study on the laser-induced plasma of different metals and the corresponding physical properties. The temporal evolution of the palladium plasma induced by IR (1064 nm) and UV (193 nm) lasers was characterized independently by varying the time delays from 1.2 up to 32 μs [6]. Differences in the plasma dynamics were probed using the ratio of typical peak intensity to the background emission. In general, both the characteristic line and the corresponding background always reduced as a function of time delay. It was shown that the peak-to-background (P/B) ratio increased with time delay to reach a maximum at a definite characteristic time and then gradually decreased afterwards. Hence, a characteristic time delay was suggested whose value matched with maximum P/B ratio to ensure the existence of LTE for time interval shorter than that definite value, whereas the likelihood of the departure from LTE significantly enhanced at the longer time delays. An attempt was made to correlate the P/B ratio with the corresponding plasma temperature based on the Boltzmann plot. It demonstrates a situation where the deviation from LTE occurs. In fact, the P/B ratio was considered as a complementary indicator to evaluate LTE condition accompanying McWhirter criterion. Furthermore, it was shown that IR laser creates more energetic plasma on the metal targets with respect to UV exposure mainly due to IB process investigating the plasma properties such as characteristic line amplitude, quenching rate, and the temperature. Moreover, the IR pulse repetition rate thermally affects the induced plasma regarding the sensible residual energy deposition on the metal target, while there is no similar effect during UV laser exposure. The lack of characteristic peaks corresponding to ambient air, i.e. atomic and ionic nitrogen and oxygen species, within the spectra due to UV laser exposure attests the creation of less energetic (colder) plasma. The plasma temperature is in the same order of magnitude, ranging from 4500 to 7000 K; however, the P/B ratio shows a drastic difference between IR/UV exposures. The maximum P/B ratio takes place at relatively longer characteristic time delay for IR exposure with respect to UV. Hence, it is believed that more energetic plasma corresponds to the greater P/B ratio at longer time delays [6]. On the other hand, various metal targets such as Au, Pd, Co, Cu, Ni, and Mo were examined to investigate the effect of matrix on the plasma characteristics. It was found that the plasma temperature is inversely related to the ionization energy of the metal target, whereas the electron density is remarkably high for the metals having low threshold fluence (Fth). It is concluded that the plasma temperature is strongly dependent on electronic property of metals, while the electron density mainly arises from the thermal characteristics such as latent heat of vaporization, thermal diffusivity, and density [6].

18.2 Application of LIBS

18.2.1 Determination of Gold Fineness by Laser-induced Breakdown Spectroscopy

The determination of gold fineness is always an attractive subject in gold industry as well as exploration and mining. Several techniques for the identification of the elemental compositions have been currently used, such as atomic absorption spectroscopy (AAS), ICP-AES, neutron activation analysis (NAA), X-ray fluorescence spectroscopy (XRF), and particle-induced X-ray emission (PIXE). None of these techniques can be considered as a valid alternative to the traditional cupellation method. According to the performance guideline, the accuracy and precision of the standardized cupellation method ranges from 0.1% to 0.5% under ideal conditions [11]. In jewellery manufacturing, a fast and accurate method was recently employed to evaluate the cartage of precious alloys using LIBS [12]. Those techniques require a system calibration with a reference sample of similar composition. Unfortunately, the composition of precious alloys may greatly vary in function. Paradoxically, the spectroscopic techniques usually need a preliminary knowledge of the composition itself, in order to determine the alloy compositions. XRF – a nondestructive test – and LIBS – a technique with microscopic damage – are fast, easy to use, and sample preparation-free analyses. As the limits of detection, XRF requires a relatively flat and sufficiently large surface of the jewellery. Furthermore, for small or ball-shaped samples, practical analysis of all elements in the periodic table and feasibility of remote analysis can be done using the latter method. These features demonstrate significant practical advantages for LIBS over XRF industrial setting. In LIBS, a Q-switched Nd:YAG laser with GW cm^2 power density is focused on the sample to be high enough to generate dense and high-temperature microplasma. Subsequently, the de-excitation of the atoms and ions within plasma leads to the emission of light at characteristic lines. The integrated emission of the individual spectral lines, in principle, is associated with the number density of the corresponding emitting species in the plume. However, this, in turn, can be correlated with the concentration of sample elements, via the various calibration methods for the quantitative analysis. Although LIBS possesses inherently microanalysis capabilities, induced crater would be created with a diameter up to few hundred microns and depth of 10mm or more. The size of crater diameter and the corresponding depth are dependent on the quality of the laser beam, focusing optics, and the energy applied to the sample. Furthermore, the thermal and mechanical responses of the surface as well as the absorption cross section of the material play an important role in the quantity of material extracted for specific laser energy. By using LIBS in Q-switched regime, it is possible to control the process in real time and to check the cleaning results online without visible damage to the substrate [11].

Shoursheini et al. [11] precisely reported the determination of gold fineness by using the dual beam arrangement, including simultaneous irradiation of CW-CO$_2$ and Q-SW Nd:YAG lasers. It was shown that the enhancement of the characteristic emission lines occurs at higher temperatures with a minimal surface distortion of the target with respect to that of single beam exposure. The accuracy of gold concentration was determined to be as low as 0.7% using calibration-free (CF) method.

Experimental set-up consists of IR coherent sources, conducting and focusing optics, laser pulse diagnostics, delay generator, spectrometer, and the microprocessor as shown in Figure 18.1. A Q-switched Nd:YAG laser model Brilliant made by Quantel system has been used as the coherent source delivering maximum 360 mJ/pulse at 1064 nm with 5 ns duration and 1–10 Hz repetition rate to generate the microplasma on the target. The output pulsed energy was decreased by adjusting the time delay between flash lamp and the Q-switched fire order as well as situating Neutral Density Filter (NDF) in front of the output beam. A home-made sealed CW-CO$_2$ laser at 10.6 mm with 1 mm diameter on the target was employed with the mean power up to 20 W in order to create 200–500 1C mm^{-1} temperature gradients. A couple of ZnSe and quartz lenses with 75 and 150 mm focal length were situated in front of the beams to increase the power density. A couple of ternary alloy samples (Au, Ag, and Cu), i.e. standard one gold coin (Iranian Azady Bahar) and a gold foil with 900/1000 and 750/1000 in weight, respectively, were used to be analysed by LIBS. The samples were irradiated by a couple of cross beams of CW-CO$_2$ laser (20 W) and a pulsed Nd:YAG laser with 95 mJ/pulse energy, 5 ns duration, and 1 Hz pulse repetition rate, as shown in Figure 18.1. In order to estimate the element concentration, the plasma electron density Ne during the time gate of detection is determined based on the Stark effect. The fineness of precious alloys is straightforwardly estimated. The CF analyses for single and dual beam techniques as well as competitive PIXE method of ternary alloys are carried out. It was shown that the data from standard gold coin taken from X-ray characteristic emission of the material using PIXE analysis gives us a greater deviation from the nominal value with respect to the optical emission characteristics of plasma due to dual beam CF-LIBS. It likely arises from the energy spread of the proton beam (700 KeV) and the lower accuracy in the detection of X-ray emissions. The difference between measured and nominal values offers the measurement accuracy of the analysis technique. It was shown that the relative error was reduced from 2% (PIXE) to 0.67% (dual beam), which implies better accuracy in the detection of plasma characteristic emission than that of X-ray emission. In dual beam arrangement, the increase of S/N ratio enables us to use this technique for the quantitative assessment of alloy compositions such that the target endures smaller damage [11].

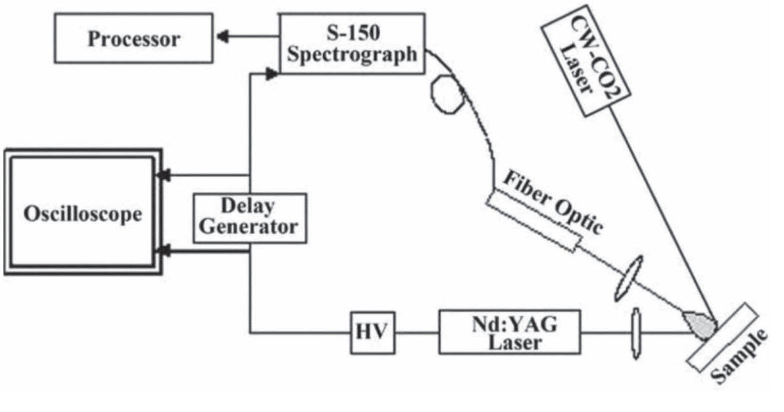

FIGURE 18.1 Schematic diagram of the experimental apparatus for LIBS dual beam arrangement. (Taken from Ref. [11].)

18.2.2 Laser-induced Plasma to Decompose Hydrocarbon Molecules

A variety of applications are reported for LIBS. One of them is to apply metal-assisted laser-induced plasma to decompose hydrocarbon molecules, which is an active field in plasma chemistry [13–17]. The decomposition of hydrocarbon molecules using the metal-assisted laser-induced plasma is an embryonic field in the plasma chemistry. The metal target-assisted laser-induced plasma with various hydrocarbon molecules is used for the purpose of the molecular decomposition and the conversion to the other hydrocarbons. The idea of combining the two worlds of plasma chemistry and catalysis has since quite some time spurred a considerable research interest, and several reviews were published. There are, however, two fundamentally different notations of what plasma catalysis can refer to: (i) the use of plasma-excited species to initiate a chemical reaction: the plasma contributes only a small amount to the total energy input needed for the reaction, but leads, similar to a catalyst, to a considerable increase in conversion. (ii) The plasma is applied to initiate a gas-phase reaction, either in the presence of or followed by a solid (heterogeneous) catalyst bed, which controls the product distribution and yield. A review of the possible interactions of plasma-excited species and solid catalyst surfaces in plasma-catalytic hydrocarbon conversion was recently published.

It takes it for granted that the laser applications in the decomposition process exhibit its ability to decompose methane without producing any CO_2 and combustion. It can help to solve the global issues such as air pollution and greenhouse effects.

Wang et al. [18] investigated the dissociation of methane in the intense laser field experimentally and theoretically using an amplified ultrafast Ti:sapphire laser at ~ 800 nm coupled to a Time of Flight (TOF) mass spectrometer with the laser intensities ranging from 10^{13} to 10^{14} W cm^{-2}. This gives rise to the dissociation of methane, which proceeds via a stepwise mechanism by gradually increasing the laser intensity.

Reyhani et al. [13] have reported the methane decomposition during Pd-assisted laser-induced plasma in the controlled chamber at various pressures using nanosecond pulsed Q-switched Nd:YAG laser at 1064 nm. Real-time LIBS monitoring has revealed the mechanisms involved in methane decomposition by inspecting the plasma parameters at manometric pressures of 1–10 mbar. The dependence of the electron density and the plasma temperature with pressure is also studied. It is shown that the plasma recreates higher hydrocarbons during the methane decomposition. In addition, Fourier transform infrared spectroscopy, gas chromatography, scanning electron microscopy, and transmission electron microscopy are employed to support the findings. Furthermore, there are several researches to irradiate methane, propane, and ethane molecules in the control chamber using the Q-SW Nd:YAG laser at 1064 nm in the presence of various catalyst targets, i.e. Ni, Pd, Fe, and Cu. The decomposition takes place during the plasma formation where the electron impact processes are dominant. Obviously, the Nd:YAG laser shots at 1064 nm are unable to ignite photodissociation because the photon energy does not match with the vibrational or the electronic transitions of the hydrocarbon molecules. However, the dissociation is mainly based on the electron impact process during the induced plasma formation. The electron density of the induced plasma formed on the catalyst surface is usually sufficiently high because of the abundance of the free electron available in the target. There is an initial electron energy distribution in the plasma plume. In this case, the plasma is heated via IB absorption leading to the sensible shift to the harder energies to give out relatively more energetic species. Regarding the multiphoton absorption and dissociation as well as the tunnel ionization, the electron is being accelerated via IB to collide more energetically with the nearby molecules. In general, the kinetic energy of the excited species and the electrons in the laser-induced plasma is usually low to induce

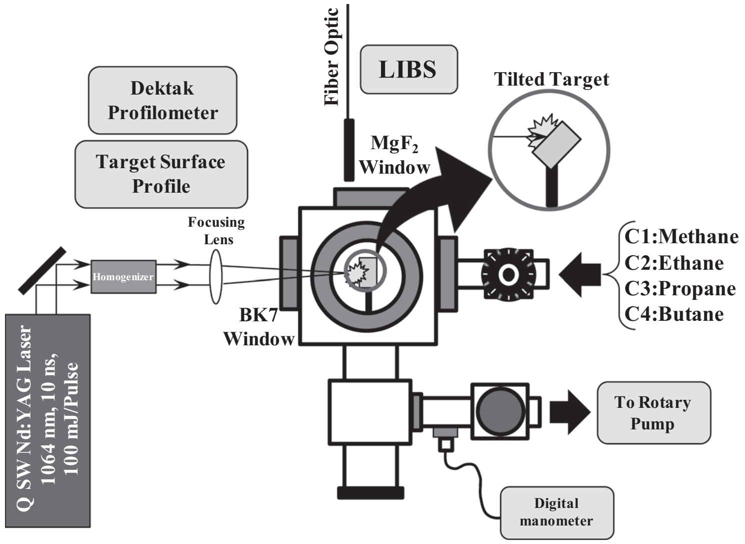

FIGURE 18.2 Experimental arrangement for hydrocarbon decomposition using metal target-assisted Q-SW Nd:YAG laser-induced plasma within the controlled chamber for the assessment of microplasma formation, i.e. the electron density and the plasma temperature in various hydrocarbon environments: methane, ethane, propane, and butane. (Taken from Ref. [14].)

the decomposition reactions according to the concept of plasma chemistry. Nevertheless, the conditions drastically change once the catalysts attend in the plasma region. Those are realized as the active species generated in the plasma in order to reduce the activation energy, giving rise to enhancement of the catalytic reactions. These gain the excessive electrons through the successive collisions. In fact, the hydrocarbon molecules are absorbed on the metal Nanoparticle (NP) surface mainly due to low chemisorption energy. It emphasizes that the catalytic aspect of the metal targets resembles to be more effective than the competitive electron impact process. OES of plasma reveals the real-time formation of the dissociative compounds and the carbon nanostructures, following the decomposition and recombination events leading to the generation of a wide distribution of C1–C5 species.

The experimental set-up is shown in Figure 18.2 that consists of an irradiation chamber, high vacuum systems, conducting and focusing optics, and laser pulse diagnostics. The home-made cross-type chamber was made up of stainless steel with six outlets – four of them are allocated for the windows. An AR (acoustic response)-coated BK_7 window with 5 cm diameter was employed to traverse laser beam into the chamber. In order to monitor the dominant characteristic absorption peaks using Fourier-transform infrared spectroscopy (FTIR), two broadband (500–20 000 cm^{-1}) AR-coated ZnSe windows were situated perpendicular to the axis along the BK_7 window [14]. Furthermore, an AR-coated BK_7 window was situated at the top of the chamber in order to observe the plasma plume location. Ni, Cu, Fe, and Pd targets were inserted in the holder inside the chamber, which is situated in front of laser beam.

The microplasma takes place when an Nd:YAG laser with sufficient power density ($\geq 10^8$ W cm^{-2}) is focused on the target. Figure 18.3 illustrates the plasma emissions at various pressures (1, 2, 5, and 10 mbar) in the controlled chamber. As mentioned before, each spectrum is obtained from the accumulation of the signals averaging over 50 successive laser shots so that laser power density (fluence) is determined to be 5×108 W cm^{-2} (50 mJ/pulse focused at 1 mm^2 with 10 ns duration). The characteristic lines of C and H as well as Pd emission lines for four distinct pressures (i.e. 1, 2, 5, and 10 mbar) are shown particularly in UV and visible spectral regions. It obviously indicates the methane dissociation into the elemental species. Increasing the manometric methane pressure, the intensity of the plasma emission in the UV region noticeably decreases due to the dominant Rayleigh scattering, which is proportional to λ^{-4} [13].

Figure 18.4 illustrates the emission spectra of palladium in the methane, ethane, propane, and butane molecular environments, as well as in the synthetic air at several pressures (10, 100, and 500 mbar). Each spectrum is obtained by averaging the signals from 50 successive laser shots. The characteristic lines due to the excited C and H species, as well as the emission peaks from Pd species, are shown over UV and visible spectral regions. A number of diatomic species are also identified such as C_2 and CH compounds. The corresponding lines due to C_2 bonds are identified throughout the visible range. The C_2 emissions in the spectra (known as the Swan bonds) are the oldest lines observed in the molecular electronic spectra. These lines are observed at 516.5 and 473.7 nm. Two CH compounds are observed around 430 and 390 nm, and the CH bonds are readily seen within the laser-induced plasma as a consequence of hydrocarbon decompositions. Moreover, alpha-hydrogen H_α and beta-hydrogen H_β lines, respectively, at 656 and 486 nm are clearly identified during the laser irradiation [14].

While hydrogen transitions are expected to form in hydrocarbon environments, it does not appear in the air spectra due to hydrogen's low density. Moreover, the notable N(I) characteristic emissions at 742.4, 744.2, and 746.8 nm as well as the O(I) line at 777.2 nm are clearly detected in the air spectra as expected, whereas these characteristic emissions do not appear in the hydrocarbon gases. It is worth noting that the synthetic air (99.999%) is free of CO_2 and methane (impurities grade 5) containing 20% oxygen and 80% nitrogen normally with ppm content of CO_2 and methane. Therefore, no C is available to be identified based on detector threshold. Furthermore, the air components, including nitrogen and oxygen, are not available in LIBS analysis of hydrocarbons because the control chamber is filled with dominant hydrocarbon molecules at 500 mbar. Therefore, CN characteristic emissions are not detected in the LIBS spectra. If the nitrogen and carbon atoms simultaneously exist in the control chamber, the CN component may appear in the spectra. Otherwise, the plasma may be short-lived as there is not adequate time for the recombination reactions to occur [14].

On the other hand, the emission spectra of the hydrocarbon molecules in the vicinity of palladium target are almost identical, especially at the pressure of 500 mbar, because of the similarity of the species, i.e. carbon and hydrogen atoms. Moreover,

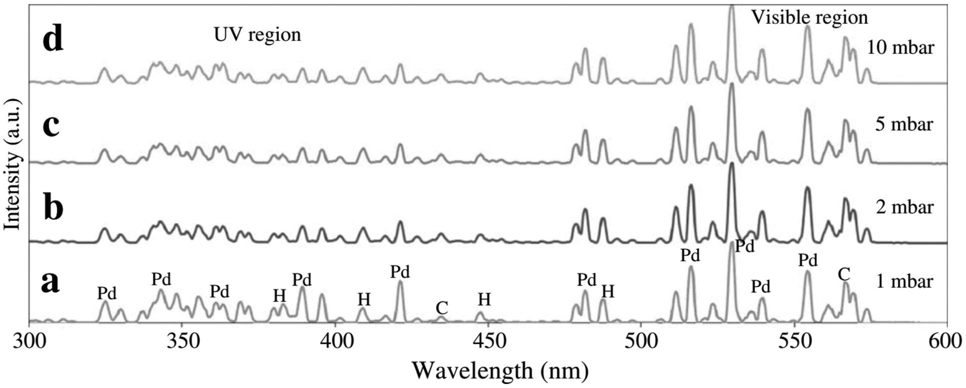

FIGURE 18.3 Emission lines taken from Nd:YAG laser (50 mJ/pulse, 10 ns pulse width, 5 Hz repetition rate, 1064 nm)-induced plasma due to the Pd-assisted decomposition of methane at manometric pressures of (a) 1, (b) 2, (c) 5, and (d) 10 mbar. (Taken from Ref. [13].)

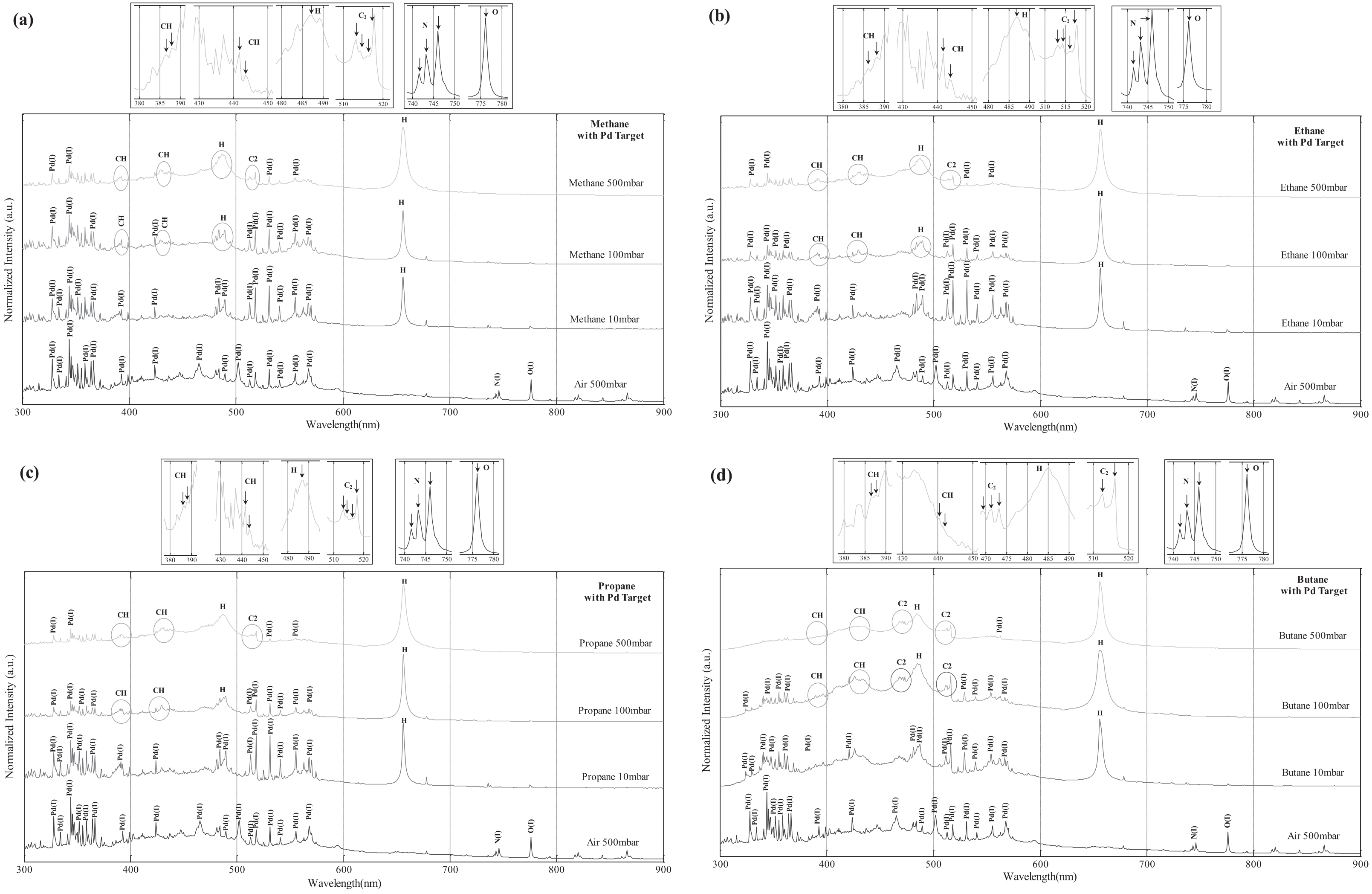

FIGURE 18.4 Characteristic optical emission spectra of (a) methane, (b) ethane, (c) propane [15], and (d) butane during the time-integrated spectroscopy of laser-induced plasma at the surface of Pd target. (Taken from Ref. [14].)

the characteristic emission lines of palladium species disappear at higher pressure, as seen in Figure 18.4, mainly due to the photon scattering by the adjacent hydrocarbon molecules. The strong Pd emission lines are identified at lower pressures mostly in the range of 330–370 nm. Furthermore, a certain C2 band is lucidly detected only in the butane spectra at 437.7 nm possibly due to the abundance of more carbon atoms in butane molecules as compared to the hydrocarbons of interest.

The plasma temperature (Te) is usually determined using the slope of the Boltzmann plot [19]:

$$\ln\left(\frac{I\lambda}{gA}\right) = -\frac{1}{kT_e}E + \ln\left(\frac{hcN_0}{4\pi Z}\right) \tag{18.1}$$

where I, A, E, g, k, h, c, N_0, and Z ascertain the line intensity, the transition probability, the level excitation energy, the statistical weight for the upper level, the Boltzmann constant, Planck's constant, speed of light, total species population, and the partition function usually taken as the statistical weight of the ground state, respectively. The slope (inverse of kT_e) is determined by using a linear regression fit among the data points of the left-hand side of the equation versus E. The plasma temperatures are determined by using five characteristic neutral lines of Pd(I) at 300.2, 311.4, 369.0, 379.9, and 421.3 nm. These spectral parameters are taken from the database of the National Institute for Standards and Technology (NIST).

In addition, the electron density is known as a significant plasma parameter that is determined using the LTE criteria. According to McWhirter criterion, the LTE condition remains valid as long as $N_e \geq 6 \times 10^{12} T^{1/2} \Delta E^3$, where N_e(cm^{-3}) is the electron density, T(K) denotes the plasma temperature, and ΔE(eV) ascertains the largest energy transition. For instance, this criterion is valid ($N_e = 1.11 \times 10^{18} \geq 5.02 \times 10^{16}$) for the propane plasma at 4533 K temperature and 1.11×10^{18} cm^{-3} electron density using the largest energy transition of Pd ($\Delta E = 5.06$ eV) to show that this is an adequately collisional plasma. Since the McWhirter is necessary but not sufficient, two more criteria are examined for validating LTE condition in the inhomogeneous plasma, namely relaxation time (τ_{rel}) and diffusion length of atoms/ions given by $\lambda = (D.\tau_{\text{rel}})^{1/2}$. The relaxation time τ_{rel} of the plasma is the time needed for the establishment of excitation and ionization equilibrium, which is much shorter than the time of thermodynamic parameters variation. The variation in the plasma temperature and the electron density is usually in the range of 10^{-6}–10^{-5} s. The relaxation time is roughly estimated by equation 18.2 [20] as follows:

$$\tau_{\text{rel}} \approx \frac{6.3\times 10^4}{N_e f_{12}\langle \bar{g}\rangle}\Delta E_{21}(kT)^{1/2}\exp\left(\frac{\Delta E_{21}}{kT}\right) \tag{18.2}$$

where f_{12} is the oscillator strength. Here, the relaxation time for the various plasma environments is larger than 10^{-8} s, which is much lower than the usual variation of plasma parameters. Furthermore, in the case of strong gradients, the diffusion of atoms and ions is not negligible and should be considered for assessing LTE. Hence, the diffusion length of atoms/ions must be shorter than the variation length of plasma temperature and electron number density during relaxation time order. In fact, the condition for the validity of LTE in inhomogeneous plasma is that plasma diameter (d) is at least ten times larger than λ, i.e. $d > 10\lambda$. The diffusion length is expressed by taking some assumptions given by [20]:

$$\lambda \approx 1.4\times 10^{12}\frac{(kT)^{3/4}}{n_e}\left(\frac{\Delta E}{M_A f_{12}\langle \bar{g}\rangle}\right)^{1/2}\exp\left(\frac{\Delta E}{2kT}\right) \tag{18.3}$$

where M_A is the relative mass of the species. Here, this criterion is also valid such that the diffusion length is 5.11×10^{-4} for the propane plasma using palladium target, which is lower with respect to the plasma diameter (0.1 mm). Stark line width, due to the atomic or ionic lines, is a routine method to estimate N_e, where the contribution of ion broadening is presumed to be negligible. Hence, the Stark broadening $\Delta\lambda_s$ of the desired non-hydrogen-like species as the full width at half maximum (FWHM) in nanometres is given [11] as follows:

$$N_e = 10^{16}\left(\frac{\Delta\lambda_s}{2W}\right) \tag{18.4}$$

where W is the electron impact parameter. The expression for the electron density in terms of the line width of hydrogen lines is given by:

$$N_e = 8.02\times 10^{12}\left(\frac{\Delta\lambda_s}{\alpha_{1/2}}\right)^{\frac{3}{2}} \tag{18.5}$$

where $\Delta\lambda_s$ is expressed in angstroms.

Moreover, the electron density of the induced plasma in the presence of palladium target in C1-C4 hydrocarbons and air environments is determined. Accordingly, the electron density of the air and hydrocarbon-induced plasma is determined using the nitrogen and H$_\alpha$ lines at 742.36 and 656.28 nm, respectively. It is worth noting to mention that the LTE is not affected by a longer time gate due to the rapid decay of atomic emission lines (within microseconds). On the other hand, when the plasma chemistry is happening, it can take place on a much longer timescale (tens of microseconds). Regarding the additional LTE tests, it can be concluded that the calculated plasma parameters are at least qualitatively valid. The dominantly qualitative characteristics of the measurements of plasma thermodynamic parameters are carried out using long gate widths. In fact, the spatially and temporally integrated spectroscopy leads to the qualitative measurements of both N_e and T_e. The discrepancies among various plasma environments indicate the statistically significant comparative values. Conversely, the absolute parameters usually require the calibration based on the other spectroscopy methods. Therefore, it is focused entirely on the qualitative measurements. The electron density and plasma temperature are elevated in C1-C4 hydrocarbon atmospheres compared to those in the air. The discrepancies arise mainly from the thermal diffusivity, mass density variations, and formation of the molecular bonds during decomposition/recombination of hydrocarbon molecules plus the effect of atomized carbon, carbon clusters, and the soot which are generated during laser pulse and recombination events, respectively. The plasma temperature is lower in the air compared to the hydrocarbon environments, mainly due to the higher thermal diffusivity of the air. The energy that is released via the exothermic reactions during catalytic decomposition of the hydrocarbons is certainly an indicative parameter, especially in the case of methane [14].

It is worth noting that the heat of formation, i.e. energy released during decomposition/recombination processes, slightly changes over hydrocarbon molecules of interest due to the formation of a distribution of product species from C1 to C5. In fact, the carbon particles are more generated for the heavier hydrocarbons mainly due to the larger carbon content in the heavier hydrocarbon molecules (i.e. propane and butane), while no further decomposition events take place in comparison. While the conversion ratio is smaller, the decomposition events for heavier hydrocarbons lead to the generation of a larger amount of carbon fragments with respect to lighter one. In fact, the production rates of the carbon particles are non-linearly increased in case of heavier hydrocarbons [14].

18.2.2.1 Medical Application

Invasive breast carcinoma IBC is the most common cancer that infects female population all over the world. There are some risk factors such as family history, age, genetic defects, breast density, oestrogen fluctuation, and radiation exposure. However, it is not exactly known how these factors induce the cell malfunction. Currently, the death rates from mammal neoplasia have been declining due to the recent diagnostic improvements and early detection through screening, as well as the progress in cancer treatment [21]. Mammography is a well-known screening technique and a common tool for detecting the non-tangible breast cancers. However, this method utilizes X-ray as an ionizing radiation, which is harmful for the live organs. Moreover, it is prone to the false signal phenomenon that may lead to an unnecessary biopsy. The ultrasound, CT scan, and MRI imaging techniques are also employed as secondary diagnostic procedures. The high cost of MRI and relatively low sensitivity of ultrasound seriously limit their applications. Positron emission tomography (PET) may be advisable in some cases at the expense of a very high cost. When a lesion is found through various clinical breast examinations, the biopsy is routinely administered. Then, the biopsied tissue is fixed and stained by a pathologist for analysis. This can be quite time-consuming due to a multistage process which is prone to errors. On the other hand, the laser spectroscopic techniques are proven to be a minimally invasive protocol. Recently, progress has been made to improve the spectroscopic effects for a more reliable identification of cancerous tissues in various organs [21].

LIBS identifies trace elements up to ppm level. It is an effective method for the identification of major biomaterial constituents in a short timescale, without need for a lengthy sample preparation. In this method, the laser shot is focused on a sample through an appropriate lens. The intense peak power induces the microplasma. The optical emission of the microplasma includes the atomic/ionic characteristic spectra of the species. This gives a valuable information pertaining to the biomaterial structures and the abundance of trace elements. Alternatively, the inductive coupled plasma–optical emission spectroscopy (ICP-OES), quadrupole–mass spectroscopy (QP-MS) – driven by the nanosecond (or femtosecond) laser shots – and the gas chromatography–mass spectroscopy (GC-MS) methods usually support the LIBS data [21].

Kumar et al. [22] observed that Ca and Al emission lines at 394.4 and 396.15 nm are stronger in malignant liver tissues of a dog with respect to the normal ones. Nasiadek et al. [23] have found a significant increase in Ca and Mg abundance in uterine cancerous tissues against the non-neoplastic tissues. They report a significant rise in Mg and Mg/Ca ratio of uterine myoma. El-Hussein et al. [24] have also shown a distinct difference of calcium and magnesium traces in LIB spectra of the malignant breast and colorectal tissue samples.

Ghasemi et al. [21] employed LIBS and subsequent AR during microplasma formation to identify cancerous human breast tissues. The characteristic optical emissions identify Ca-, Na-, and Mg-rich species in cancerous tissues compared to those of healthy ones. Furthermore, they reported that the characteristic parameters of the microplasma, generated on the unhealthy tissues, are elevated. It is shown higher-decibel (dB) audio signals emanate from laser-induced microplasma and a subsequent audio blue-shift for malignant tissues. The higher abundance of trace elements in cancerous tissues as well as higher plasma temperature and electron density in laser-induced microplasma (leading to a stronger shockwave) intensifies the acoustic signals.

It is believed that the rise of intracellular calcium, sodium, and magnesium concentrations in tissues arises from the neoplastic tumoral growth. These trace elemental concentrations within the tissues are assessed by virtue of the laser-induced microplasma data of the normal and cancerous tissues. Figure 18.5a sketches the empirical arrangement for the LIBS accompanying the acoustic analyses. Figure 18.5b–d illustrates the optical emission spectra of the normal and malignant breast samples, including the characteristic emissions of trace elements and air components. The prominent peaks found in the microplasma emission spectra are attributed to the atomic and ionic emissions of calcium, sodium, and magnesium species as well as molecular C–C and C–N bonds recorded in the atomic database in the NIST. The spectra can roughly be segmented into three major spectral regions, i.e. UV (260–450 nm), visible (450–750 nm), and IR (750–950 nm). This helps identify the desired transitions in the congested spectral regions of the characteristic emission lines [21].

These results emphasize a noticeable difference between LIBS data taken from the healthy and unhealthy tissues. Table 18.1 gives the mean concentration ratios of Na, Ca, and Mg trace elements available in the cancerous tissues compared to those in the normal samples. The findings are supported by the alternative methods such as ICP-OES, QP-MS, and GC-MS. The data given by GC-MS, QP-MS, and ICP-OES are also in good agreement with LIBS, indicating a consistent analysis. The slight differences in the given values of Table 18.1 may arise from various small instrumental errors and mass values when ICP-OES and GC-MS analyses are applied [21].

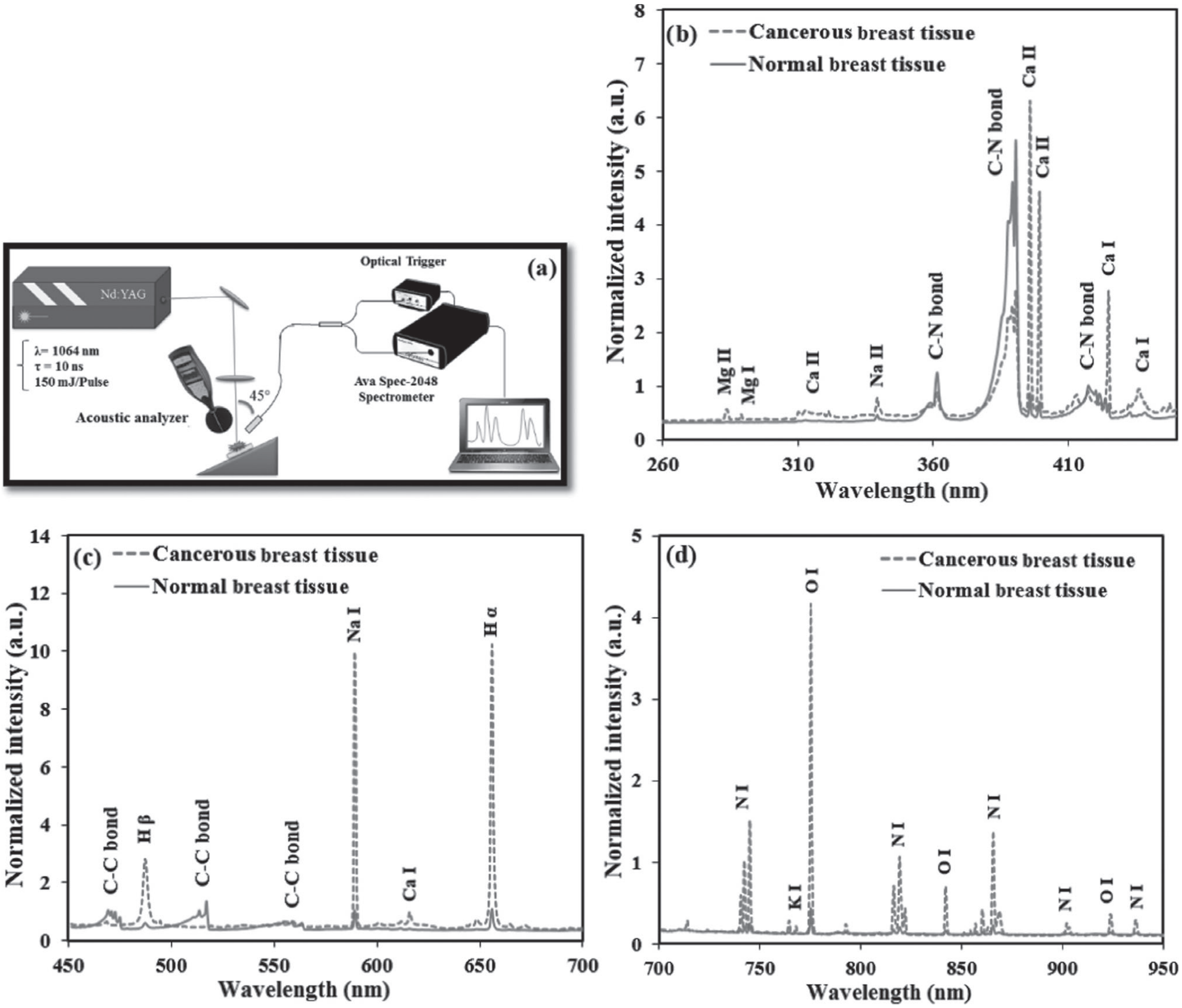

FIGURE 18.5 (a) Schematic arrangement for the LIBS accompanying the acoustic analyses. (b) Mean spectra taken by LIBS of the normal and cancerous breast tissues, over UV, (c) visible, and d) NIR spectral regions. The major characteristics emissions are attributed to the following species: Mg II (280.27 nm), Mg I (285.213 nm), Ca II (317.933, 393.366, and 396.847nm), Ca I (422.67, 435.5, and 616.217nm), Na I (589.59nm), Na II (339.92), and K I (766.48 and 769.89 nm). (Taken from ref.21).

The microplasma temperature is usually determined using the Boltzmann plot given by Ln ($I_{i\,j}\lambda/g_i\ A_{ij}$) = Ln ($n^s/U^s\ (T_e)$) − ($E_i/kT_e$), where I_{ij}, A_{ij}, g_i, T_e, and E_i are the intensity, the transition probability, the atomic-level degeneracy, plasma temperature, and the excitation energy of an *i*th level, respectively. Furthermore, n^s and k denote the total number density of the species in the microplasma and the Boltzmann constant, respectively. U^s (T_e) ascertains the internal partition function of the s species at temperature T_e. The laser-induced microplasma is generally assumed to be optically thin due to LTE, consistent with the fact that the collisional processes are dominant relative to the radiative ones. The above equation

TABLE 18.1

Mean Ratios of Na, Ca, and Mg Species Concentration in the Cancerous Tissue to the Normal Ones Given by Various Techniques: LIBS, ICP-OES, GC-MS, and QP-MS (taken from Ref. [21])

	Elemental Concentration Ratio (Cancerous/Normal Tissues)		
Techniques	**Na**	**Ca**	**Mg**
LIBS	4.81 ± 0.06	4.47 ± 0.09	2.32 ± 0.05
ICP-OES	4.68 ± 0.17	4.12 ± 0.09	2.24 ± 0.12
GC-MS	4.96 ± 0.21	-	-
QP-MS	-	3.97 ± 0.08	-

exhibits a linear dependence for the signal as a function of excitation energy with a slope of $-1/kT_e$ in LTE condition. LTE presumes the identical temperature for ionic and atomic species. Here, the relative emissions of the ionic Ca II species are used to determine the microplasma temperature by applying a linear fit to the experimental data. Figure 18.6a illustrates the Boltzmann plot to extract the microplasma temperature from the slope of the best linear fit. Those temperatures are measured to be ~9100 ± 100 K and ~10 600 ± 80 K for the normal and cancerous tissues, respectively. The same temperatures are also estimated based on the relative emission of the Ca I and N I species. A clear difference of ~1500 K is measured between the plasma temperatures of the normal and cancerous tissues, indicating a more energetic microplasma in the case of malignancy. Similar to the spectrum intensity tests, these temperature data are also analysed via the standard SPSS v19 statistical package to reveal that the unhealthy tissue temperatures are larger than the healthy ones at the 99% confidence level. However, the plasma temperature is not sufficiently hot to excite the ionized N II and O II species – as expected due to their higher ionization energies.

On the other hand, the Stark broadened line width of the plasma emission of certain species, such as hydrogen Balmer line H_α, is usually used to estimate the electron density. The electron density is given by $n_e\ (\mathrm{cm}^{-3}) = 8.02 \times 10^{12}\ (\Delta\lambda_{1/2}/\alpha_{1/2})^{1.5}$, where $\alpha_{1/2}$ is a coefficient indicating a weak dependence on the microplasma temperature and pressure, and $\Delta\lambda_{1/2}$ denotes the FWHM of the spectral line in A°. Furthermore, the electron density satisfies the LTE condition given by McWhirter criterion $n_e \geq 1.6\times10^{12} T_e^{1/2} (\Delta E)^3$, where ΔE is the largest interval between adjacent energy levels of the atoms and ions in the microplasma in eV. Figure 18.6b depicts the emissive line width at 656.3 nm due to H_α after microplasma ignition. In practice, a broader FWHM of the H_α line appears for the generated microplasma for the cancerous tissues. The mean electron density in our samples is determined to be $\sim3.5 \times 10^{17}\,\mathrm{cm}^{-3}$ for the unhealthy tissue, significantly higher than that for the normal tissues ($n_e \sim 3.1 \times 10^{17}\,\mathrm{cm}^{-3}$). The calculated electron density is well compatible with the McWhirter criterion $\left(n_e \geq 0.11\times10^{16}\ \mathrm{cm}^{-3}\right)$, to assure the validity of the LTE. The electron densities data are also analysed by means of the standard SPSS v19 statistical package to reveal that the cancerous electron densities are larger than the normal ones at the 99% confidence level [21].

All empirical conditions during the tissue examination are nearly identical, so that any difference in the microplasma parameters arises from the structure and the composition of the samples. The intense peaks of the trace elements attest to the higher plasma temperatures for the cancerous tissues. Due to the malignant tissues' higher abundance of the trace elements, an excessive initial electron density appears, which, in turn, facilitates the microplasma formation and the ablation of cancerous tissues. Therefore, more energy imparts to the plasma due to the IB absorption that gives rise to a more energetic microplasma leading to a higher plasma temperature. Conversely, in the case of the healthy tissues, most of the laser shot energy is imparted to the ablation process. As a result, a relatively smaller electron density appears in the microplasma [21].

In summary, the health of a large population of women prone to the breast cancer is globally at risk. This lethal rise may be mitigated by a diagnosis with laser-induced multispectral emissions of tumours according to the breakdown and acoustic effects. Lengthy systematic experiments are carried out based on LIBS and AR to discriminate between the normal and cancerous breast tissues. LIBS reveals a notable rise in trace elements such as calcium, sodium, and magnesium in the malignant tissues determined by the characteristic emissions of Mg I, Mg II, Ca I, Ca II, Na I, and Na II species within the laser-induced microplasma. The findings are supported by GC-MS, ICP-OES, and QP-MS analyses. In addition, more energetic microplasmas are created on cancerous tissues accompanying yet an elevated acoustic level due to the intense atomic/ionic characteristic emissions of species. Furthermore, in LTE condition, the microplasma parameters

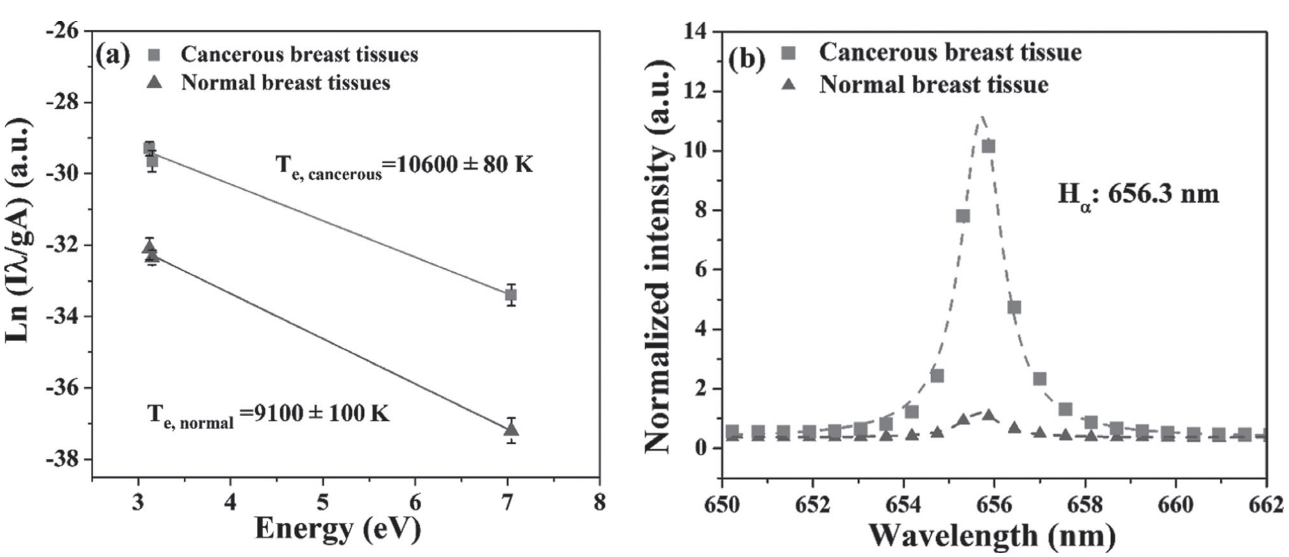

FIGURE 18.6 (a) Boltzmann plots for Ca II species used in a linear fit (based on least-squares method), to reveal the plasma temperatures, (b) Stark broadened line H_α at 656.3 nm, due to large electron densities. (Taken from Ref. [21].)

such as the temperature and electron density are increased, giving rise to a measurable audio intensity caused by an energetic microplasma formation on the cancerous tissues. It is shown that the emitter species within the plasma on the unhealthy tissues moves towards the detector slightly faster leading to an audio blue-shift difference. Unlike the healthy ones, the cancerous breast tissues are characteristically denser media accompanied by a large number of the microcavities, affecting their spectroscopic features. Eventually, the findings taken from LIBS are in good accordance with AR experiment data [21].

REFERENCES

1. L. J. Radziemski, Review of selected analytical applications of laser plasmas and laser ablation, 1987-1994. *Microchem. J* 50, 218–234 (1994).
2. K. Knight, N.L. Scherbarth, D.A. Cremers, M.J. Ferris, Characterization of laser-induced breakdown spectroscopy (LIBS) for application to space exploration. *Appl. Spectrosc* 54, 331 (2000).
3. P. Lucena and J. J. Laserna, Three-dimensional distribution analysis of platinum, palladium and rhodium in auto catalytic converters using imaging-mode laser-induced breakdown spectrometry. *Spectrochim. Acta Part* B 56, 177-185 (2001).
4. S. Z. Shoursheini, P. Parvin, B. Sajad, M.A. Bassam, Dual-laser-beam-induced breakdown spectroscopy of copper using simultaneous continuous wave CO_2 and Q-Switched Nd:YAG lasers. *Appl Spectrosc* 63, 423–9 (2009).
5. C. Sánchez-Aké, M. Bolaños, C.Z. Ramírez, Emission enhancement using two orthogonal targets in double pulse laser-induced breakdown spectroscopy. *Spectrochim Acta Part B* 64, 857–62 (2009).
6. S.Z. Mortazavi, P. Parvin, M.R. Mousavi Pour, A. Reyhani, A. Moosakhani, Sh. Moradkhani, Time-resolved evolution of metal plasma induced by Q-switched Nd: YAG and ArF-excimer lasers. *Opt Laser Technol* 62, 32–39 (2014).
7. J.J. Camacho, L. Diaz, J.M.L. Poyato, Time-resolved spectroscopic diagnostic of laser-induced plasma on germanium targets. *J Appl Phys* 109, 103304 (2011).
8. J.J. Camacho, L. Díaz, J.P. Cid, J.M.L. Poyato, Time-resolved spectroscopic diagnostic of the CO_2 plasma induced by a high-power CO_2 pulsed laser. *Spectrochim Acta Part B* 66, 698–705 (2011).
9. H.Y. Moon, B.W. Smith, N. Omenetto, Temporal behavior of line-to-continuum ratios and ion fractions as a means of assessing thermodynamic equilibrium in laser-induced breakdown spectroscopy. *Chem Phys* 398, 221–7 (2012).
10. R.W.P. McWhirter. In: Huddlestone R.H., Leonard S.L., (eds.), *Plasma Diagnostic Techniques*. New York: Academic Press (1965). pp. 201–64 (chapter 5).
11. S.Z. Shoursheini, B. Sajad, P. Parvin, Determination of gold fineness by laser induced breakdown spectroscopy with the simultaneous use of CW-CO_2 and Q-SW Nd:YAG lasers. *Opt Lasers Eng* 48, 89–95 (2010).
12. M. Corsi, G. Cristoforetti, V. Palleschi, A. Salvetti, E. Tognoni, A fast and accurate method for the determination of precious alloys caratage by laser induced plasma spectroscopy. *Eur Phys J D* 13, 373–7 (2001).
13. A. Reyhani, S.Z. Mortazavi, P. Parvin, Z. Mahmoudi, Simultaneous laser induced breakdown spectroscopy and Pd-assisted methane decomposition at different pressures. *Spectrochim Acta Part B: Atomic Spectrosc* 74, 124–30 (2012).
14. A. Moosakhani, P. Parvin, S.Z. Mortazavi, A. Reyhani, S. Abachi, Effect of hydrocarbon molecular decomposition on palladium-assisted laser-induced plasma ablation. *Appl Opt* 56 (11), E64–E71 (2017).
15. A. Moosakhani, P. Parvin, A. Reyhani, S.Z. Mortazavi, Propane decomposition and conversion into other hydrocarbons using metal target assisted laser induced plasma. *Phys Plasmas* 24 (1), 013505 (2017).
16. Z. Ghorbani, P. Parvin, A. Reyhani, S.Z. Mortazavi, A. Moosakhani, M. Maleki, S. Kiani, Methane decomposition using metal-assisted nanosecond laser-induced plasma at atmospheric pressure. *J Phys Chem* C 118 (51), 29822–29835 (2014).
17. M. Maleki, P. Parvin, A. Reyhani, S.Z. Mortazavi, A. Moosakhani, Z. Ghorbani, S. Kiani, Decomposition of ethane molecules at atmospheric pressure using metal assisted laser induced plasma. *JOSA B* 32 (4), 493–505 (2015).
18. S. Wang, X. Tang, L. Gao, M.E. Elshakre, F. Kong, Dissociation of methane in intense laser fields. *Inst Chem* 107 (32), 6123–6129 (2003).
19. L.J. Radziemski, D.A. Cremers, *Handbook of Laser-Induced Breakdown Spectroscopy*. John Wiley and Sons, New York (2006).
20. G. Cristoforetti, A. De Giacomo, M. Dell'Aglio, S. Legnaioli, E. Tognoni, V. Palleschi, N. Omenetto, Local thermodynamic equilibrium in laser-induced breakdown spectroscopy: beyond the McWhirter criterion. *Spectrochim Acta Part B At Spectrosc* 65, 86–95 (2010).
21. F. Ghasemi, P. Parvin, N.S.H. Motlagh, A. Amjadi, S. Abachi, Laser induced breakdown spectroscopy and acoustic response techniques to discriminate healthy and cancerous breast tissues. *Appl Opt* 55 (29), 8227–8235.
22. A. Kumar, F.-Y. Yueh, J. P. Singh, S. Burgess, Characterization of malignant tissue cells by laser-induced breakdown spectroscopy. *Appl Opt* 43, 5399 (2004).
23. M. Nasiadek, T. Krawczyk, A. Sapota, Tissue levels of cadmium and trace elements in patients with myoma and uterine cancer. *Hum Exp Toxicol* 24, 623 (2005).
24. A. El-Husseina, A.K. Kassema, H. Ismailb, M. Har, Exploiting LIBS as a spectrochemical analytical technique in diagnosis of some types of human malignancies. *Talanta* 82, 495 (2010).

Taylor & Francis
Taylor & Francis Group
http://taylorandfrancis.com

19

Laser-Induced Fluorescence (LIF) for the Detection of Microbes

Frank Duschek, Lea Fellner, and Karin Grünewald

CONTENTS

19.1 Introduction 219
19.2 Principles of Fluorescence and LIF from Microbes 220
  19.2.1 Physical Principles and Special Properties in Biological Samples 220
  19.2.2 Biological Fluorophores 220
  19.2.3 Basic Fluorescence Behaviour of Microbes 223
19.3 Equipment for Laser-Induced Fluorescence 225
19.4 Data Analysis 226
  19.4.1 Classification, Discrimination, Identification 226
  19.4.2 LIDAR Equation: Application for LIF Stand-off Detection 226
19.5 Fields of Application 227
  19.5.1 Single-Particle Detection (Short Distances) 227
  19.5.2 Bulk Detection (Short and Long Distances) 228
    19.5.2.1 LIF Stand-Off Detection of Diluted Microbes 228
    19.5.2.2 LIF Stand-Off Detection of Atmospheric Aerosols (Fluorescence LIDAR) 229
19.6 Summary 230
References 230

19.1 Introduction

Laser-induced fluorescence (LIF) is a spectroscopic technique that involves the excitation of molecular targets by laser radiation followed by the detection of subsequent spontaneous emission of radiation from the target molecules. LIF is a mature technique that has been reported first in 1968, exactly half a century ago by Zare [1]. Since then, LIF has proven to provide excellent detection capabilities: samples can be excited with high spatial resolution given by the spot of the exciting laser beam allowing for imaging. In addition, fluorescence detection is highly sensitive, and since signals can be detected from different angles, it allows for imaging. From the delay between the excitation and detection events, it is also possible to learn about processes during that time. Pioneering LIF work was focused on small molecules, the detailed description of electronic states, and their kinetics from excitation to emission. The progress in understanding fluorescence processes and the availability of equipment such as laser sources with wavelengths down to the deep ultraviolet lead to applications of LIF in wide areas like online process monitoring and life sciences. Living matter in vegetation and microbes is complex: firstly, this matter consists of various different (and complex) molecular substances which all influence fluorescence emission, and secondly, living organisms change their morphology and chemical composition.

Sizes of microbes are typically in the micrometre range (0.5–5 μm). LIF spectroscopic studies can be distinguished between two different categories depending on the size of the laser focus: firstly, microscopic investigations with the diameter of the laser focus below the size of bacteria cells, and secondly, the size of the laser beam being larger than the size of a single specimen. The first method is able to resolve details of a cell, while the latter is unable to resolve the cell structure covering a single cell, a colony forming unit (CFU), or a bulk of microbes.

All optical microscopes are limited in the resolution that they can achieve by a series of fundamental physical factors. In a perfect optical system, resolution is restricted by the numerical aperture of optical components and by the wavelength of excited and emitted light. The concept of resolution is inseparable from contrast. Resolution is defined as the minimum separation between two points that results in a certain level of contrast between them. In a conventional fluorescence microscope, contrast is dependent on the number of photons collected from the sample, the dynamic range of the signal, optical aberrations of the imaging system, and the number of pixels per unit area in acquired images. For confocal laser microscopes, the resolution is in the range of a few hundred nanometres. With specific fluorescence probes, a detection of a single bacterial cell is possible. The physical limit for these configurations, which is described by the Abbe limit, can be bypassed by advanced concepts such as photoactivatable localization microscopy (PALM), stochastic optical reconstruction microscopy (STORM), and stimulated emission depletion (STED) microscopy [2]. Here, the exciting beam can be focused onto the sample with high spatial resolution, which allows for 3D imaging of cellular substructures. In addition, higher pulse energies allow to exploit non-linear effects such as the possibility for two-photon absorption and fluorescence excitation into higher electronic states.

In this chapter, a brief introduction to LIF is given with special emphasis on living organisms, e.g. bacteria. Typical instrumentation for LIF and data analysis tools and finally selected applications of LIF diagnostics are presented. Fluorescence microscopy has experienced a huge interest in research and in many successful applications. Hence, microscopic techniques deserve an own chapter and will not be covered in this chapter.

19.2 Principles of Fluorescence and LIF from Microbes

19.2.1 Physical Principles and Special Properties in Biological Samples

The relevant mechanisms of fluorescence processes in small molecules are well described in the literature [3]. Commonly, the Jablonski scheme can be used to understand the kinetics of fluorescence emission even for larger molecules. Figure 19.1 represents a simplified scheme for a fluorescent molecule with its potential energy as a function of the nuclear distance. Potential energy curves are given for the ground state and the excited electronic state with corresponding vibrational levels (horizontal lines).

Absorption of ultraviolet or visible laser light with the wavelength λ_{exc} transfers the molecule from its electronic ground state S_0 into a vibrational level of excited electronic states (S_1, S_2). Intramolecular energy transfer processes like radiationless vibrational relaxation (VR) occur in timescales competitive to fluorescence, while intersystem crossing (ISC) between singlet and triplet states leads to a slow phosphorescence emission (Table 19.1). If the wavelength λ_{exc} is small enough, the molecule is excited into a repulsive state and photo-dissociated (i.e. following probing of the sample might result in different spectra).

The right panel of Figure 19.2 shows a transformation scheme for the resulting fluorescence emission from the S_1 and S_2 transition into the ground state. Transitions presented by red and green arrows in the Jablonski scheme transform to the enveloping curve.

TABLE 19.1

Typical Timescales During Fluorescence Process

Process	Time Scale (s)
Absorption	$10^{-}15$
Internal conversion	$10^{-}11$–$10^{-}14$
Intersystem crossing	10^{-8}–10^{-3}
Phosphorescence	10^{-4}–10^{-1}
Fluorescence	10^{-9}–10^{-7}
Static and dynamic quenching	$10^{-}10$–$10^{-}9$

Biological samples are complex systems consisting of a variety of fluorophores (see section "Biological fluorophores") and of a larger number of non-fluorescent components which are able to interact with fluorophores in static and dynamic quenching, i.e. the strong reduction of fluorescence. Quenching processes are reviewed in Ref. [3]. Since quenching happens on timescales similar to fluorescence, a strong dependency of the measured fluorescence signal on the fluorophore's environment can be observed due to resonance energy transfer between neighboured molecules.

Due to this complexity, the resulting spectra are typically broad and – compared to fluorescence emission from small molecules – less specific. Complementary information can be extracted from polarization and lifetime measurements of the fluorescence emission.

Many fluorophores respond to environmental changes with lifetime variations of fluorescence signals. Hence, lifetime measurements can also be used to distinguish dynamic and static quenching mechanisms.

Fluorescence polarization measures the rotational orientation and diffusion rate of macromolecules. Rotational diffusion contains information related to protein structure and also biological macrostructures (e.g. bacteria).

Comprehensive information from fluorescence emission can be acquired by choosing proper and multiple excitation wavelengths.

19.2.2 Biological Fluorophores

Living organisms including bacteria are complex structures built up of many different molecules in a more or less specific spatial order. Some of these biological molecules are fluorescent.

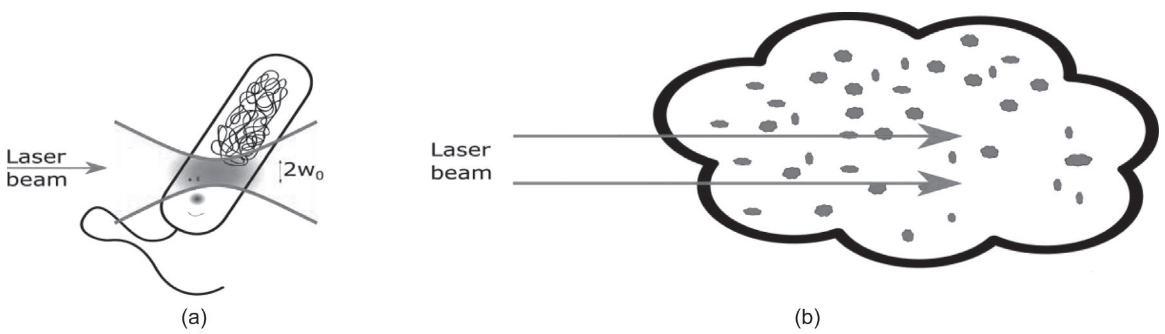

FIGURE 19.1 Illustration of a laser beam exciting a cell in a microscope (a) and *in situ* application on an assembly of cells (bulk) material with a freely propagating laser beam (b).

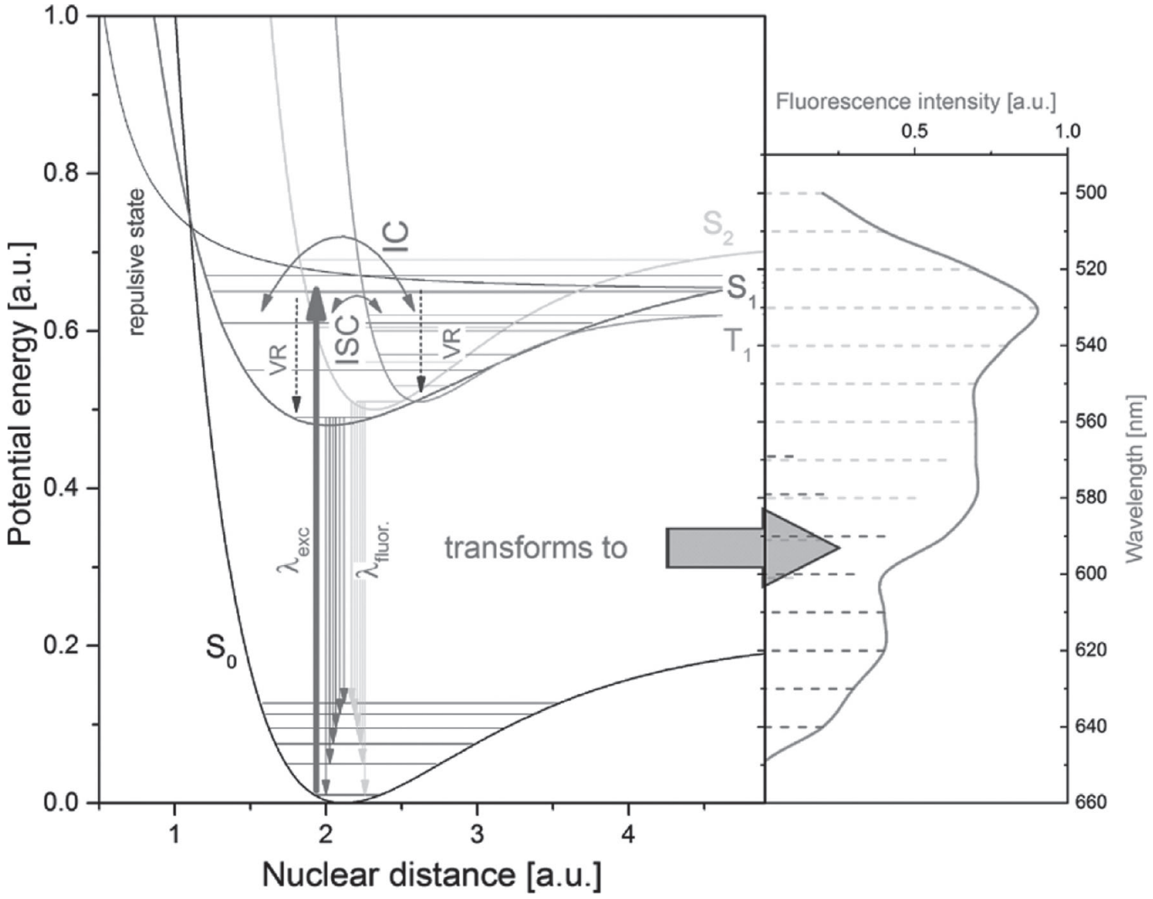

FIGURE 19.2 Jablonski scheme for singlet ground states S_0, excited singlet states S_1 and S_2, and triplet state T_1 (ISC: intersystem crossing; IC: internal conversion; λ_{exc}: excitation wavelength; λ_{fluor}: wavelength of fluorescence).

There are a few primary metabolites which are fluorescent and abundant in almost all living organisms. These are amino acids with aromatic side chain (tryptophan, phenylalanine, and tyrosine) and the coenzymes NAD(P)H, flavins, and vitamin B6. Some of these fluorophores occurring in living organisms are listed in Table 19.2. Examples of absorption spectra of biological fluorophores are given in Figure 19.3.

Plants synthesize pigments like chlorophyll and beta-carotene, which give them their green or orange colour and are essential for photosynthesis. In pollen, beta-carotenes are more abundant than chlorophylls and serve here as protection against UV radiation. The so-called secondary metabolites in pollen (plants) are often fluorescent. Secondary metabolites have phenolic components and are synthesized from phenylalanine as precursor. Secondary metabolites play a role as antibiotics, natural pesticides, signalling substances for symbiosis with fungi, attractants for pollinators, protectors from UV light, and insulating material, and for stabilization purposes. Pollen contains hydroxylated cinnamic acid derivatives, flavonoid, and anthocyanins.

Bacteria are usually single-celled organisms, and their cell wall and membrane are transparent enough to measure fluorescence of NAD(P)H, vitamin B6, and flavins, which are usually located in the cytoplasm. Plants are often multicellular organisms and usually synthesize several pigments, and thus, fluorescence usually originates from fluorophores on the surface of the plant. Algae can be unicellular or multicellular organisms and are usually located in the water. Pollen grains are small (6–100 µm) reproductive units of plants and can be released by plants in the air. In a pollen grain, 95% of the light does not reach the cytoplasm, and thus, fluorescence is dominated by pigments in the pollen sporoderm because of reflection, fluorescence, and absorption of the sporoderm. Here, the fluorescence originates from the cell wall-associated fluorophores [4].

Fluorescence intensity can be decreased by different mechanisms, e.g. by collision with another molecule. Fluorescence characteristics of intrinsic biological fluorophores of an organism are dependent on the microenvironment in which they are located. For instance, amino acids are the building blocks of proteins. The indole group of tryptophan is responsible for its fluorescence. The fluorescence of the indole group is dependent on the polarity of the solvent. When protein in an aqueous solution is unfolded, fluorescence of tryptophan is blue-shifted compared to fluorescence of tryptophan buried in a protein. NAD(P)H, flavins, vitamin B6, chlorophylls, and other light-absorbing molecules of plants can be bound to proteins or occur unbound in the bacterial or plant cell, which influences their absorption or fluorescence properties. For instance, when NADH is bound to proteins, the fluorescence is often increased. When NADH is bound to a protein, it is usually in

TABLE 19.2

Biological Fluorophores with Main Fluorescence Excitation and Emission Wavelengths (A: Animals, B: Bacteria, F: Fungus, P: Plants)

Fluorophore	Excitation (nm)	Emission (nm)	Lifetime (ns)	Occurrence/Remark	% Dry weight Bacteria [6]
Primary Metabolites					
Phenylalanine	260	260–282	6.8	A, B, F, P	*E. coli:* 2.9% Bacillus : 4%
Tryptophan	280	340	3.6	A, B, F, P	*E. coli:* 1.1% Bacillus: 4%
Tyrosine	275	304	3.6	A, B, F, P	*E. coli:* 2.4% Bacillus: 3.5%
Cysteine	350–366	700–740		A, B, F, P	*E. coli:* 1% Bacillus: 3%
DNA	260	415		A, B, F, P	*E. coli:* 3.1% Bacillus: 3%
RNA	260			A, B, F, P	*E. coli:* 20.5% Bacillus: 16%
Nicotinamide adenine dinucleotide (NADH)	340	460	0.4 (aqueous) 1.2 (bound to proteins)	A, B, F, P (important for the energy metabolism)	*E. coli:* 0.57% Bacillus: 0.15%
Nicotinamide adenine dinucleotide phosphate (NADPH)	340	460		A, B, F, P (important for anabolic reactions in metabolism)	*E. coli:* 0.048% Bacillus: 0.058%
Flavins:	450	525	A, B, F, P	*E. coli:* 0.056%	Flavins:
Riboflavin					Bacillus: 0.055%
Flavin adenine dinucleotide (FAD)			2.3 (FAD)		
Flavin adenine mononucleotide (FMN)			4.7 (FMN)		
Vitamin B6: pyridoxine, pyridoxal, Pyridoxamine, and their phosphates	330–390	400–500		A, B, F, P	*E. coli:* 0.012% Bacillus: 0.012%
Ubiquinone/ubiquinol	300–360	> 400		A, B, F, P (electron transport chain, respiration)	*E. coli:* 0.027% Bacillus: 0.0%
Vitamin K2 menaquinone / menaquinol	250	425		A, B, F, P (electron transport chain, respiration)	*E. coli:* 0.012% Bacillus: 0.026 %
Other Fluorophores in Bacteria and Bacterial Endospores					
Calcium dipicolinate	300	400-500		Bacterial endospores	5%–10% (dry weight) of Bacillus endospores
Porphyrin (pyoverdine, siderophore)	407	600–700		Pseudomonas fluorescence	
Molecules Involved in Photosynthesis					
Chlorophyll a	350, 650	675		P, some B, e.g. cyanobacteria (photosynthesis)	
Chlorophyll b	450	640		P (photosynthesis)	
Phycoerythrin	400–550	580		Cyanobacteria, red algae	
Phycocyanin	420–620	630		Cyanobacteria, red algae	
Carotenoids	460	520		P	
Phenolic Components as Secondary Metabolites in Pollen (Plants)					
Cinnamic acid derivatives, flavonoids, anthocyanin	280, 360	450		P	

its extended conformation. The binding of NADH to the protein prevents the reduction of nicotinamide group of NADH, which is quenched by its adenine group [5].

The influence of the excitation wavelength on fluorescence spectra and intensities is demonstrated in Figure 19.4. The spectra are depicted for 280 and 355 nm excitation wavelengths, respectively. The most salient differences between the two excitation wavelengths are strong changes in the relative fluorescence intensities, the width of the broadband spectral emission, and the peak values of the fluorescence. These differences stem from the different absorption values of the cells as well as different relaxation channels towards final states in the molecules.

The environment in which the living organism is located can influence the overall fluorescence. Fluorophores on the surface like the pigments of pollen might be quenched when

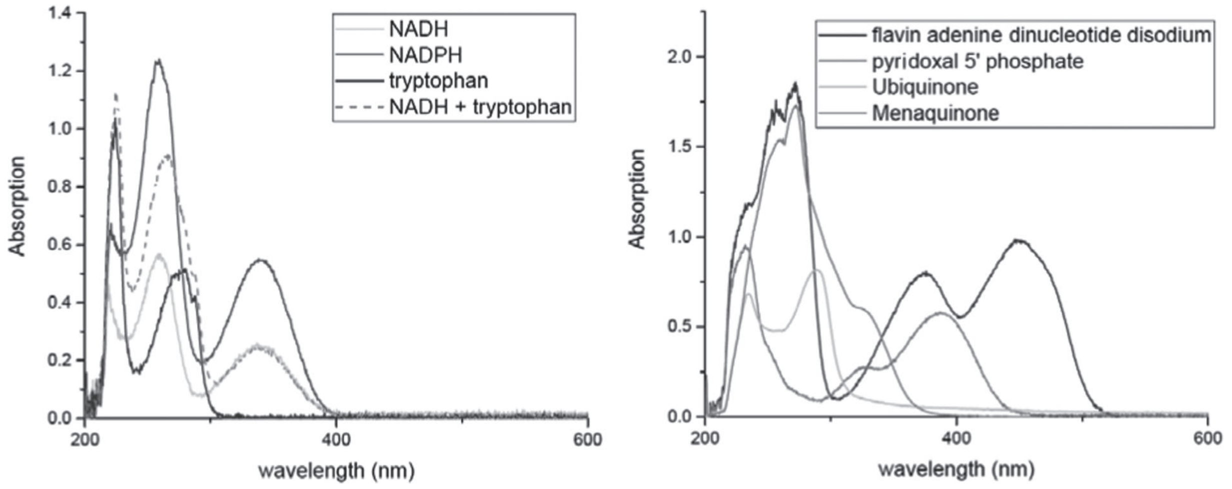

FIGURE 19.3 Absorption spectra of biological fluorophores NADH, NADPH, tryptophan, flavin adenine dinucleotide (FAD), and pyridoxal 5'phosphate which were all dissolved in phosphate-buffered saline. Ubiquinone and menaquinone were dissolved in diethyl ether. The concentration of solutions was 10^{-4}M.

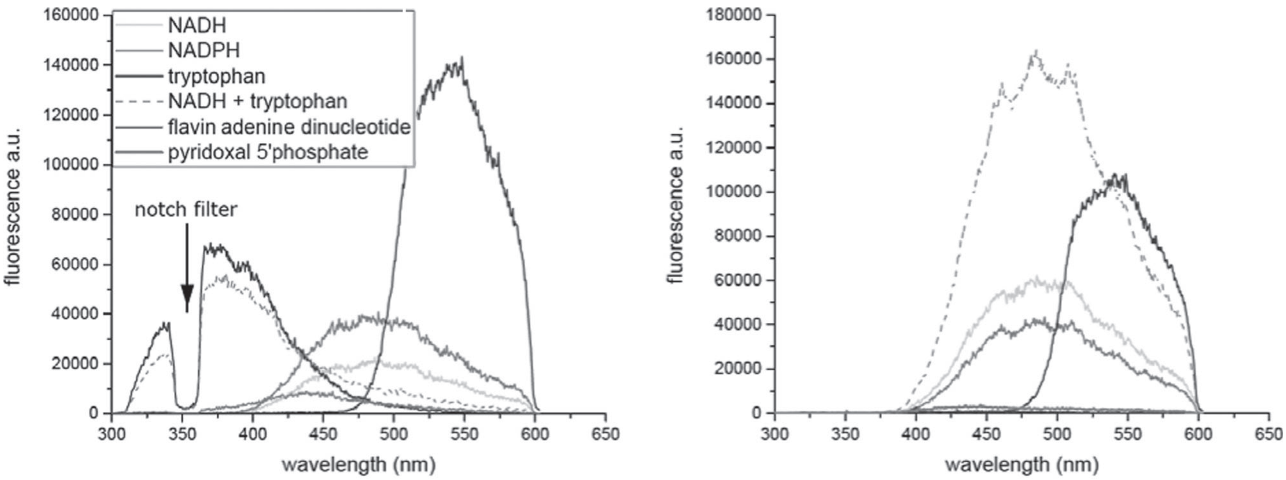

280nm excitation

355nm excitation

FIGURE 19.4 Fluorescence spectra of biological fluorophores (primary metabolites) excited with laser pulses at 280 and 355 nm wavelength. Substances are dissolved in phosphate-buffered saline at 10^{-4} M.

they come in contact with watery solutions. Dried bacteria in aerosols can have different fluorescence spectra compared to bacteria in aqueous suspension.

19.2.3 Basic Fluorescence Behaviour of Microbes

Living organisms adapt to their environment and change their metabolism and thus the concentration of their metabolites accordingly. Old organism can have a different chemical composition than younger organism [7]. Plants infected by bacteria and fungi often have a different metabolic composition than healthy plants.

For instance, NADH is important for the energy metabolism of living organisms. NADH and NADPH are found in living organisms. NADH and NADPH are converted in metabolism between the reduced form (NAD(P)H) and oxidized form (NAD(P)). Only the reduced forms of these molecules are fluorescent. The concentration and the redox status of NAD(P)/NAD(P)H can vary in the same organism depending on its living condition.

To evaluate the variation in fluorescence spectra caused by different metabolic states of bacteria, the fluorescence of a bacterial population during different growth phases in a batch culture was investigated [7]. During the so-called exponential growth phase (Figure 19.5, 0–5 h), bacteria had sufficient nutrients and the bacterial population was growing. In the exponential growth phase, optical density ($OD_{565\,nm}$) and the number of colony forming units/ml (cfu/ml) were increasing. When nutrients are depleting, the bacterial population attains the stationary phase. In this phase, the total bacterial count does not change. After 1–2 days, cfu/ml is decreasing due to the death of bacteria. After 6 days, the endospore content of the bacterial population has increased significantly. When excited at 280 nm, the fluorescence spectra without a significant

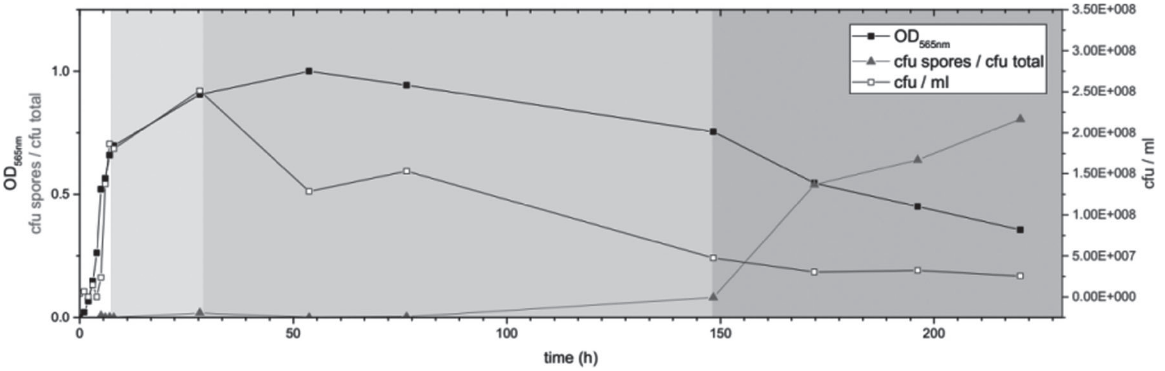

FIGURE 19.5 Growth curve of a *Bacillus thuringiensis* population. Total bacteria were quantified by measuring the optical density at 565 nm (black curve). Maximum was normalized to one. The number of viable bacteria was quantified by colony forming units/ml (blue curve). The ratio of endospores in the population is shown by the blue curve.

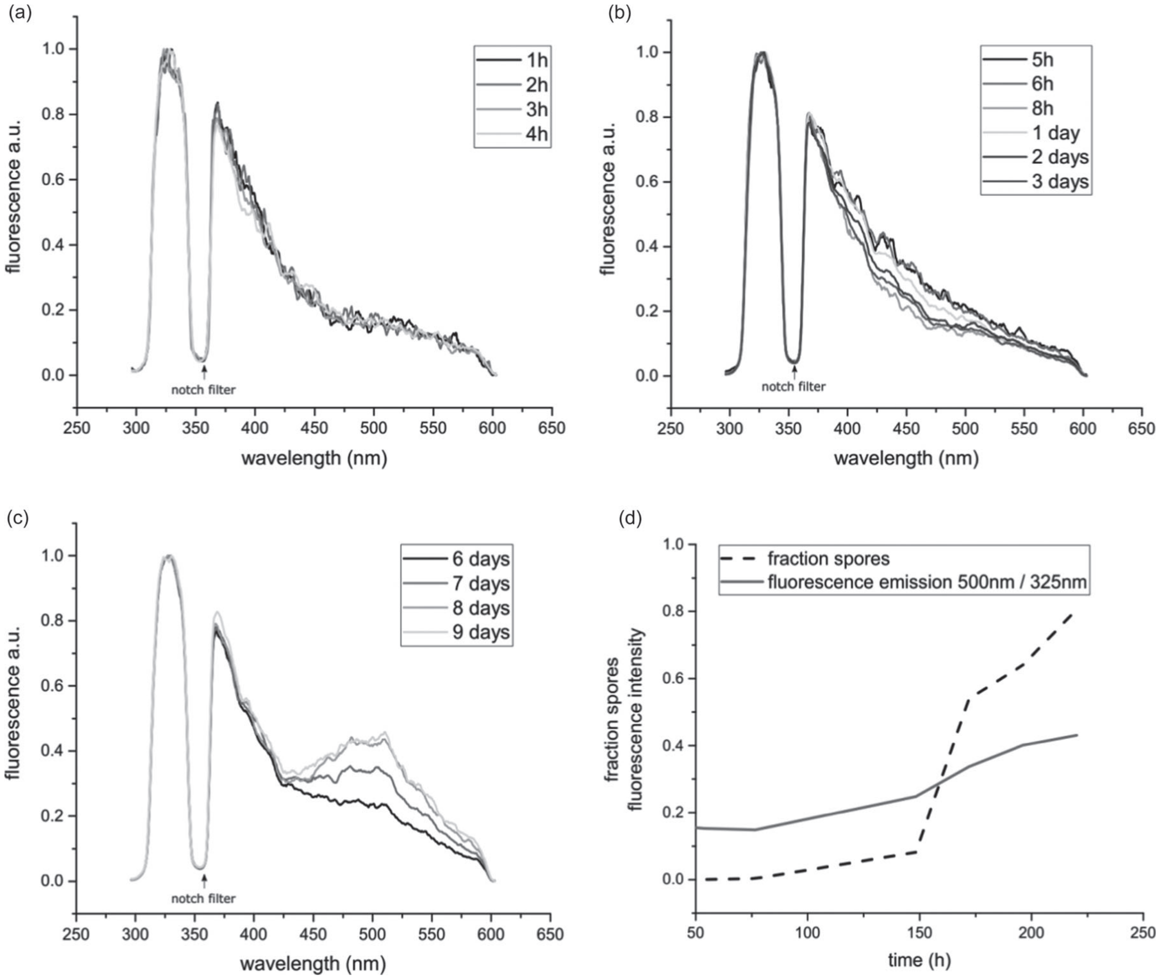

FIGURE 19.6 Fluorescence spectra of a bacterial population in different metabolic states for excitation with 280 nm. (a) Exponential growth phase, (b) stationary phase, (c) ageing population with increasing endospore content. (d) The graph shows an increase in fluorescence at 500 nm in the ageing bacterial population.

endospore content are very similar for different cultivation times with the most fluorescence observed between 300 and 450 nm (Figure 19.6). Fluorescence spectra of a bacterial population containing spores show an additional peak at about 500 nm. When excited at 355 nm, fluorescence of bacteria from the exponential growth phase differs slightly from that of ageing bacteria and samples containing endospores (Figure 19.7).

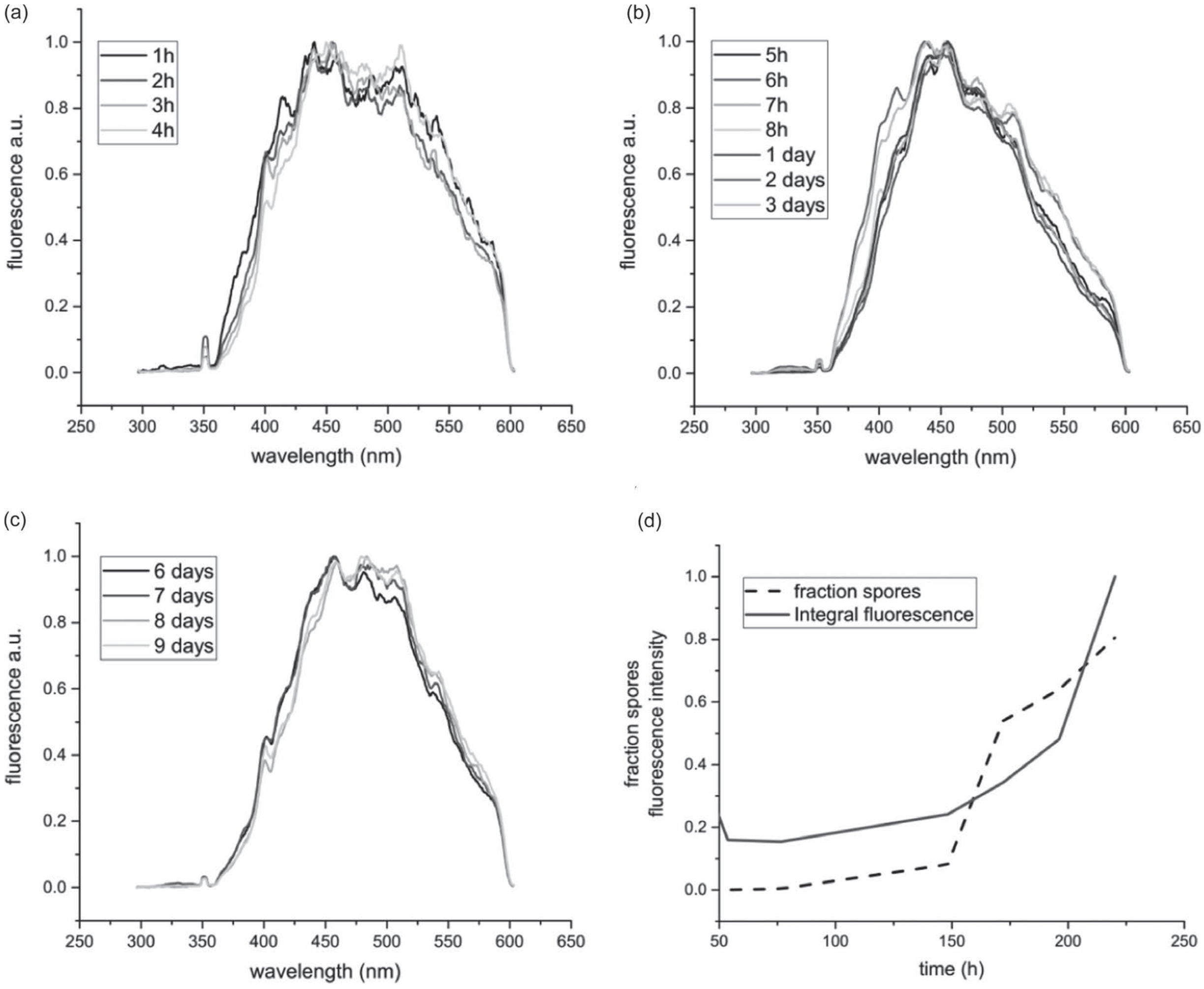

FIGURE 19.7 Fluorescence spectra of a bacterial population in different metabolic states for excitation with 355 nm. (a) Exponential growth phase, (b) stationary phase, (c) ageing population with increasing endospore content. (d) The graph shows an increase in overall fluorescence intensity in the ageing bacterial population.

19.3 Equipment for Laser-Induced Fluorescence

Requirements with respect to the laser excitation wavelength and line width are compared to other spectroscopic techniques remarkably relaxed as long as the fluorophores in microbes can be probed. Absorption bands of fluorophores as shown in Figure 19.3 are broad within a range of tens of nanometres. Typically, the fluorophores absorb in the ultraviolet region, and an intrinsic fluorescence is emitted. For LIF applications, continuous wave (cw) and – preferably – pulsed lasers are used. The major advantages of pulsed UV lasers are as follows:

- Suppressing background light by optimizing the time gate of the recorded signal
- Retrieving local information from laser ranging and mapping of fluorescence signals according to the run-time of the light
- Obtaining information on the fluorescence lifetime and the kinetics of the fluorescent process.

Fluorescence lifetimes are in the range up to several nanoseconds; hence, pulsed picosecond laser sources are needed for a proper measurement. Early LIF biological particle sensors used harmonic generation of UV in solid-state lasers to excite fluorescence. UV diode lasers have advantages compared to the traditional lasers: a greater selection of wavelengths for efficient and selective excitation of specific fluorophores. Another advantage is the ability to combine several UV diode lasers and to use them as a compact multiple-wavelength source for simultaneous or alternating excitation of several biological fluorophores. The detection of multiple bio-fluorophores is expected to markedly improve the discrimination of airborne pathogens from non-biological background aerosols. UV laser developments have been leading to commercially available compact sources with pulse compression down to a few picoseconds [8]. Fluorescence lifetimes have been shown to provide valuable features for the classification of bacteria even for stand-off applications [9].

The selection of detection equipment for LIF is designed for the intended application and strongly influenced by the properties of the laser source. Detectors for spectral and

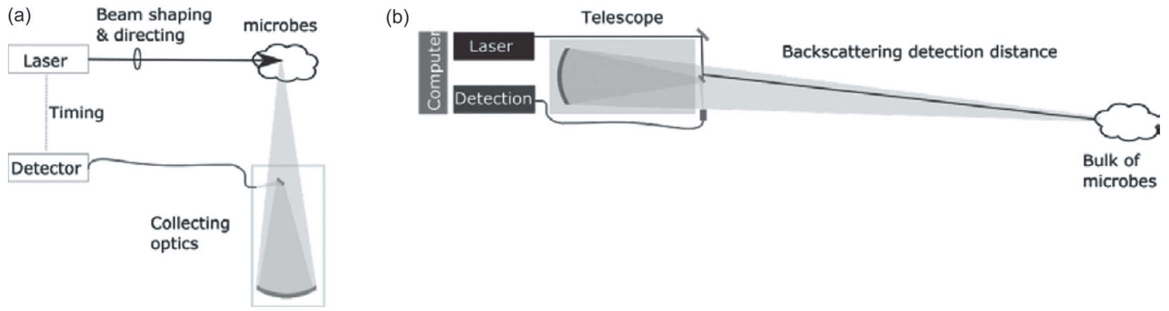

FIGURE 19.8 Schemes for a LIF set-up in 90° (a) and backscattering geometry (b).

time-resolved measurements can be selected from their wide varieties. For a short range (and for strong signal returns), spectral and hyperspectral imaging techniques with CCD or intensified CCD cameras can be used to spatially resolve and acquire data. In combination with wavelength-selective elements such as (tunable) optical filters and spectrometers, these detectors are often applied for the spectral detection of fluorescence signatures in the UV to VIS. For biological agents, a spectral resolution of a few nanometres is mostly sufficient. Therefore, photomultiplier tubes (PMT) are employed for fast detection with high sensitivities. The short response times of PMT allow for gated, time-resolved operation. Arranged in an array and attached to a spectrometer, it is possible to get both spectral and temporal information from fluorescence channels. LIF PMT detectors are often integrated in a simplified configuration into compact, sensitive LIDAR (light detection and ranging) systems for long-range detection.

Additional criteria have to be taken into account for the design of a LIF-based system:

- Sensitivity (time to acquire data, detection distance)
- Number of substances to be detected, classified, or identified
- Number of interfering substances to be discriminated from.

The main advantages of lasers in LIF are the possibility to direct the beam onto the sample even from large distances and the strong intensity of the signal (e.g. compared to Raman scattering), which allows for a fast retrieval of information on the sample.

Typical LIF set-ups (Figure 19.8) consist of an exciting laser with a beam shaping unit, which directs the laser onto the sample. Since LIF can be detected from any angle, it is preferably collected from 90° in order to minimize specular or diffuse elastic scattering (left). Backscattering geometry allows for detection from a single position. This configuration is chosen as default for stand-off LIF detection (right). Detectors are electronically linked to the lasers for timing purposes.

19.4 Data Analysis

For LIF on complete cells or even on bulk samples with many cells, return signals contain integrated signatures for all substances participating in the fluorescence process. Furthermore, the fluorescence signature for biological samples is not as specific as for other spectroscopic technologies (e.g. like in vibrational spectroscopy). Combining all the information which might be delivered by the experimental set-up, i.e. from LIDAR, yields comprehensive results even for LIF detection from large distances. This approach is generally supported by the state-of-the-art statistical methods.

19.4.1 Classification, Discrimination, Identification

The terms classification, discrimination, and identification name the process of increasing specification. For LIF application, the terms are used in the following meanings. The aim of *classification* is the ability to predict the group to which an object belongs based on a set of features. *Discriminations* are made within a preselected, limited group of species. In biology, *identification* is the exact determination of the species with the pre-existing name.

Fluorescence spectra of (bulk) biological material are not specific enough to allow for direct identification. For stand-off applications, it is not required to identify substances, but to find abnormal occurrences. False negatives yield a loss of information, and false positives cause unnecessary effort and expenditure. The accuracy of classifications or discriminations is enhanced by additional experimental features like elastic scattering information and fluorescence cross sections.

A classification of fluorescent substances [10–13] up to a discrimination between individual samples of bacteria [14] can be achieved by trained statistical algorithms. Common techniques for the statistical evaluation of the fluorescence returns are the decision tree method or other machine learning algorithms like neural networks. The numerical routines have to be trained by acquired data with the specific detection device and the species of interest before being applied for in the detection.

19.4.2 LIDAR Equation: Application for LIF Stand-off Detection

Elastic backscattering of a polychromatic laser-based LIDAR by aerosol[1] particles provides information on the location of aerosol clouds, the aerosol concentration, the aerosol size distribution, and the shapes of the particles.

A short laser pulse propagating through the atmosphere evokes elastic scattering by air molecules (Rayleigh scattering) and aerosols (Mie scattering). A simplified description of the elastically backscattered intensity $I(z, \lambda)$ received from a distance z at the laser wavelength λ is given by

$$I(z,\lambda) = E_0(\lambda) \cdot \eta(\lambda) \cdot v_{\mathrm{GK}}(z) \cdot \frac{A \cdot c}{2 \cdot z^2} \cdot \beta(z,\lambda) \cdot e^{-2 \cdot \int_0^z \alpha(z',\lambda)dz'} .$$

Multiple scattering [15] and absorption are neglected in this approach. The energy of the laser pulse is given by E_0, the efficiency of the receiving/detecting unit by $\eta(\lambda)$, and the receiver area by A. The geometric compression v_{GK} describes the overlap of the fields of view of the laser beam and the telescope. The backscattering coefficient $\beta(z, \lambda)$ as well as the extinction coefficient $\alpha(z, \lambda)$ comprises contributions from Rayleigh scattering and Mie scattering. Both coefficients are proportional to the particle density and the scattering cross sections of the irradiated aerosols. The distance z between the stand-off detector and the scattering cloud follows from the delay time t between the laser pulse emission and the signal return. Together with the speed of light in the air c, the distance is $z = t \cdot c/2$ with the increment z'.

1 In this chapter, the expression "aerosol" is used to name the airborne particle not *stricto sensu* for the designation of the suspension of the particles.

The aerosol particle size distribution can be derived from the evaluation of backscattering and extinction coefficients. The Mie theory allows for relating the coefficients to the radii r of the scattering particles, as shown by Fredholm integral equations of the first kind [16,17]

$$\beta(\lambda,z) = \int_{r_a}^{r_b} \pi \cdot r^2(r,\lambda,m) \cdot n(r,z)dr, \quad \alpha(\lambda,z)$$

$$= \int_{r_a}^{r_b} \pi \cdot r^2 Q_{\mathrm{ext}}(r,\lambda,m) \cdot n(r,z)dr \qquad .$$

The refractive index is given by m and the particle size distribution by $n(r, z)$. The efficiencies Q_{bs} for backscatter and Q_{ext} for extinction follow from Mie theory [18] The range of particle sizes has the lower limit r_a and the upper limit r_b. The values of $\beta(z, \lambda)$ and $\alpha(z, \lambda)$ result from LIDAR measurements [19]. Contributions from Rayleigh scattering can be unfolded by atmospheric modelling [20,21] or true atmospheric profiles of the specific location. With this information, the aerosol particle size distribution can be calculated by solving the inverse problem in a multistep numerical retrieval [22,23].

The shape of a particle can be derived from depolarization effects. Here, a parallel polarized laser beam is emitted, and the backscattering signal is split into two orthogonal polarization planes: one plane parallel and the other plane orthogonally to the polarization plane of the laser pulse. The relation between the backscatter coefficients of both polarization planes delivers information on the shape of the scattering particles. The evaluation can follow several numerical approaches [24–26].

Further detailed information towards the discrimination between different types of aerosols can be gained from evaluating the inelastic processes like Raman scattering or LIF.

19.5 Fields of Application

LIF is helpful to detect allergenic material like pollen or hazardous material like pathogenic bacteria in the environment. It is used to monitor drinking water, wastewater, or natural water bodies [27].

Fluorescence of phytoplankton (e.g. cyanobacteria and algae) is dominated by pigments which are relevant for photosynthesis: chlorophyll, phycoerythrin, and phycocyanin [28]. It has been shown that the health state of plants, e.g. agricultural crops, can be monitored by LIF, even from airborne devices.

When plants are infected by pathogens, they change their metabolism, which leads to different fluorescence spectra [29]. Microorganisms on food, e.g. on meat, can be detected by fluorescence spectroscopy [11,30].

Airborne aerosols interfere with modern information transfer [31] and air traffic [32], and affect the development of the earth climate [33,34]. Being respirable, they are also a risk for human health [35,36]. Aerosols can also be produced and misused as warfare agents [37]. For all these reasons, the aerosol distribution, their location, and direction of propagation are investigated by different means [38–40].

For security stand-off applications, prototypes of UV LIF LIDAR systems have demonstrated their capability to detect bioaerosols on distances between several hundreds of metres up to the kilometre range [41–43]. UV LIDAR method was assessed in comparison with results derived from elastic scatter depolarization and differential scattering. The UV LIF LIDAR systems are transportable and can be incorporated into robust systems. The LIF LIDAR principle has proven to be no longer on a laboratory state but is applicable to even-demanding tasks in the open environment.

Besides bulk measurement of airborne aerosols by UV LIF LIDAR in the atmosphere, real-time UV LIF of single particles is also applied for atmospheric monitoring [44]. A high-speed (1 µs of the laser pulse), real-time, *in situ*, single-shot, single-particle fluorescence spectrometer is suitable for bioaerosol particle discrimination; sorting and collecting is deployed for the preselection of possible biothread in air traffic control. In the case of suspicious result, the selected particle is aerodynamically deflected to a sampler. An enriched sample of targeted particles is captured for the subsequent microbiological identification [45,46].

19.5.1 Single-Particle Detection (Short Distances)

Excitation–emission fluorescence spectra of single particles are recorded in order to discriminate between biological and non-biological aerosols and as far as possible between different biological species up to the discrimination between different species of bacteria.

For this reason, biological aerosol in size ranges around 1 µm can be generated from diluted suspensions or aspirated from the environment, dried, and fed into an optical chamber. This chamber is equipped with light sources for fluorescence excitation and efficient fluorescent-collecting and measuring instrumentation. Since particle fluorescence is by several orders of magnitudes weaker than the fluorescence excitation [45],

$$I_{\text{flu}} = k \cdot I_0 \cdot Q \cdot \sigma_{\text{absorp}}$$

elastically scattered light from the light source and the optical components has to be blocked. In the above equation, I_{flu} is the measured fluorescence, k the instrumental optical loss parameter, Q the quantum efficiency, σ_{absorb} the absorption cross section, and I_0 the excitation flux.

The excitation wavelengths are chosen according to the absorption capabilities of the biological agent and should meet a high fluorescence quantum yield. But for the discrimination between different species, the excitation wavelengths can also yield differences in the fluorescence spectra of the particular species. Exceeding the S/N threshold of the instrumentation and allowing for discrimination are partially contradicting prerequisites and require a multiwavelength excitation of the fluorescence for satisfactory results [47]. The excitation energy has to generate sufficiently high fluorescence signal in the particle without changing its properties by the energy deposit. The allowed range for the initial flux depends on the associated wavelength, the operation mode of the light source (cw/ pulse), and the acquired dispersion of the spectrum. The minimum value for Nd:YAG lasers, e.g., is given by above 1 mJ cm^{-2} [45] up to a maximum of about 10 mJ cm^{-2} [48].

Single-particle spectrometers allow for the detection of the fluorescence cross sections of particles to provide a device-independent database for LIF LIDAR applications. For this purpose, an absolute calibration of the spectrometer is necessary. The calibration is performed by scattering measurements of substances with renowned absorption and emission coefficients. The information of fluorescence cross sections is used as a support for classification and discrimination together with information from elastic scatter [49] and classification codes.

Comprehensive work was performed by many groups over the last years in designing and evaluating single-particle fluorescence spectrometers [45,50]. The approaches differ by the choice of light sources, detector systems, pursued spectral dispersion, aerosol generation, and aerosol singling processes. For the investigation of particles of the same species, a diluted particle flow can be fed through a particle counter or the particles are gathered on a filter tape after the fluorescence measurement. The number of particles can be counted online or offline, depending on the method. The fluorescence cross section is then derived from the fluorescence intensity of the flow and the particle number density. Multiple excitations have to be avoided painstakingly to achieve reliable results. If the sample contains different species, the particle fluorescence measurement can be triggered by a single particle passing an elastic scattering measurement before it enters the fluorescence excitation [51].

When the signal of the elastic scattering exceeds a preset threshold on the provided detector, the fluorescence excitation and measurement is started.

19.5.2 Bulk Detection (Short and Long Distances)

For long-range applications, the classical LIF spectroscopic system is often replaced by most important LIF wavelength channels and integrated into LIDAR systems in order to enhance the signal-to-noise ratio of the fluorescence return. For short or medium distances with sufficient fluorescence returns, hyperspectral LIF imaging or spectrally resolved detection can be used [30].

19.5.2.1 LIF Stand-Off Detection of Diluted Microbes

When detecting bacteria in the environment, e.g. as aerosols or in water, differentiation of bacteria from other particles in the environment is of primary interest. Fluorescence spectra of dry particles or particles in liquid can be different [4]. There might be even a mixed fluorescence signal of different materials, like bacteria in nutrient broth. For the bulk detection of bacteria, interferents might be, e.g., pollen, dust, rain drops, herbicides, or insecticides.

As shown in Figure 19.9, bacteria can be distinguished from the possible background material like diesel and pollen by fluorescence spectroscopy. The diagrams show that a

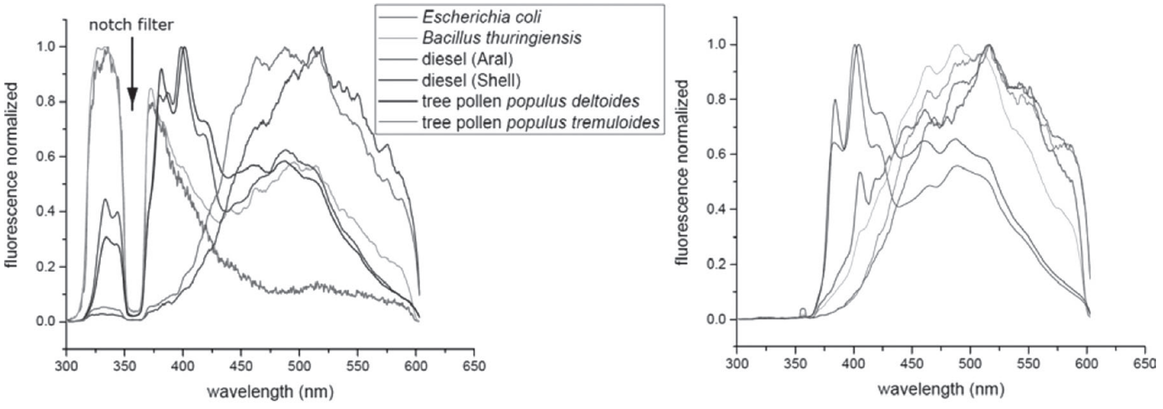

280nm excitation

355nm excitation

FIGURE 19.9 Fluorescence spectra of bacteria (*Escherichia coli* and *Bacillus thuringiensis*), diesel from two different gas stations (Aral and Shell), and pollen of two different aspen species (*Populus deltoides* and *Populus tremuloides*) excited at two different wavelengths.

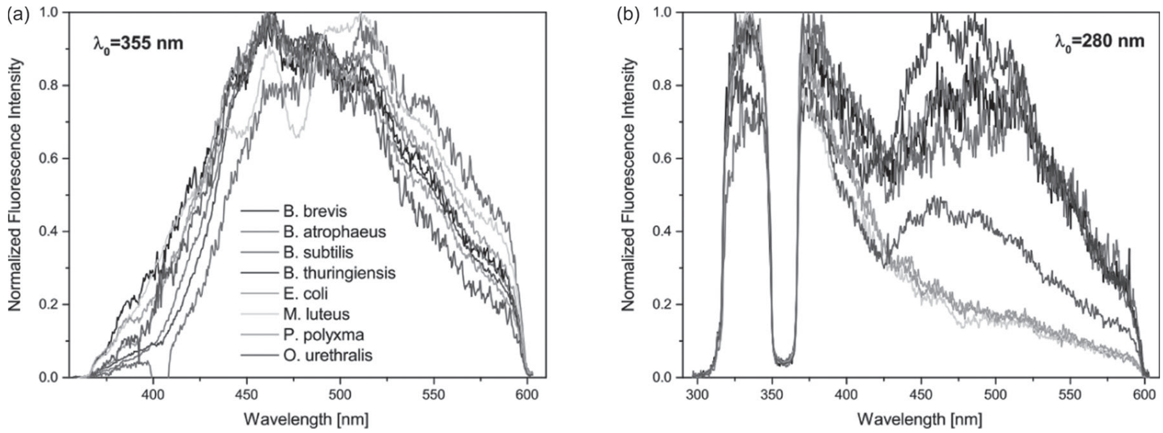

FIGURE 19.10 Normalized LIF spectra of bacterial samples in watery suspension excited at 355 nm (a) and 280 nm (b) [14].

multiwavelength excitation is helpful for a reliable distinction between the agents. For instance, the spectra of diesel and *Bacillus thuringiensis* (endospores) are quite similar at 280 nm excitation, but there is more difference in spectra at 355 nm excitation (Figure 19.10).

The discrimination of single bacterial strains from a set of more or less closely related bacterial strains is investigated for the excitation wavelengths at 280 and 355 nm, respectively. Figure 19.7 presents the corresponding fluorescence spectra. A decision tree algorithm is applied to the data set, and 91% of these spectra are correctly assigned to their species in spite of the similar and less specific spectra. Despite the successful and fast discrimination between known bacterial species, the identification of bacterial species requires a verification with biological methods (e.g. polymerase chain reaction or DNA sequencing) in a second step (Table 19.3).

The result promises a considerable benefit of the algorithms in the stand-off detection, classification, and discrimination. The challenge will be the classification of or discrimination between species out of mixtures or out of an aerosol bulk [14].

19.5.2.2 LIF Stand-Off Detection of Atmospheric Aerosols (Fluorescence LIDAR)

Biological, organic, and non-organic chemical aerosols are the components of any natural environment. Aerosols are also permanently released by local industry and traffic. The airborne solid and liquid particles change in composition, size distributions, and floating times depending on the specific area, climate, seasons, and weather conditions. In the troposphere, the size of the particles varies generally between 10^{-9} and 10^{-4} m in diameter with the predominant chemical components such as sulphate, nitrate, ammonium, sea salt, mineral dust, organic compounds, and black or elemental carbon [52].

Natural biological aerosols like pollen, bacteria, virus, or fungi as well as some carbon-based particles fluoresce when excited in the ultraviolet spectrum. Further, fluorescent material like chlorophyll from leaves can be released into the air, and fluorescent algae [45,53] can be aerosolized with the sea mist [54–56]. In the context of a biological threat, harmful biological particles – bacteria or biological toxins – can be deliberately applied to the air. For the specific detection and ranging of such biological clouds, laser-based LIDAR systems have been developed working in the UV spectral range.

This type of LIDAR takes advantage of the fluorescent capabilities of the biological material, when excited in the UV spectrum. Advanced IR LIDAR technology using simultaneous broadband differential scattering (DISC) or depolarization can be a valuable support for reliably distinguishing between biological components and background material [57]. On shorter distances, the UV Raman LIDAR will also contribute to the detection and recognition of biological aerosols [58] as well as polarized LIDAR technique [59].

UV LIF LIDAR wavelengths are chosen primarily for a proper excitation of the fluorophores in biological material. Main fluorophores in a biological cell are listed in Table 19.2.

TABLE 19.3

Correlation Matrix of the C5.0 Algorithm for Classification of Bacteria

	Predicted							
Actual	**B. atroph.**	**B. brevis**	**B. subt.**	**B. thur.**	**E. coli**	**M. lutelus**	**O. ureth.**	**P. poly.**
B. atroph.	42							
B. brevis		25		1				
B. subt.		1	22		1	1		1
B. thur.		1		31			1	
E. coli			1		20		4	
M. lutelus				1		26		2
O. ureth.		1					28	
P. poly.			1			4	1	24

The absorption wavelengths can slightly differ for solvents or aerosols [3,60]. As a consequence of the necessary spectral range for LIF of biological aerosols, the demand for large detection ranges of a UV LIF LIDAR has to meet the requirements of the fluorescence excitation. The short laser wavelength suffers from the strong atmospheric absorption band in the ultraviolet. Day-light performance and ranging of UV LIF LIDAR is furthermore limited by the regulations of the eye-safety directive. Once the system is operated in the open environment, the intensity of the laser beam has to be adapted to the permitted value for the chosen wavelength [61]. This adaptation is handled by expanding the beam width, before the beam is leaving the protective housing. Therefore, the range of a UV LIDAR is a compromise of safe laser operation and optimum signal level. LIDAR systems have to deal with the real, less predictable, complex, and continuously changing situation in the atmosphere. Unspecific aerosol bulks challenge the discrimination efforts. Direct sunlight, absorption by increased ozone concentrations, and diffusively scattered or reflected natural radiation in the band of the excitation and fluorescence wavelengths reduce the stand-off range during daytime.

UV LIF LIDAR is able to find, detect, and range a cloud of biological aerosols but it is not yet able to identify one single biological particle out of the atmospheric bulk, a bulk that provides a variety of different fluorescing aerosols. To meet this challenge, the specificity of the UV LIDAR can be improved by multiwavelengths (excitation and detection) operation [14,24] and the application of trained classification algorithms. Modern approaches prefer such multiwavelength excitation in the UV spectrum [62–65] to enhance the information for classification algorithms.

A combined technology of UV LIF and long-range IR LIDAR allows for long-range scanning of the atmosphere in the IR spectrum with on-time precise detection of biological aerosols by the LIF technique. This combination delivers punctual information on the fluorescence as well as cloud mapping and particle sizing. As a consequence, the present LIF LIDAR systems use at least three excitation wavelengths (two in the UV and one in the IR) provided by an arrangement of different lasers or using OPO (optical parametric oscillation) techniques.

19.6 Summary

Since its invention in 1968, LIF technique has been established in many fields of application. Among them, the detection of microbes is more challenging task. LIF from bacterial cells in a bulk is by far more complex than LIF from uniform substances due to many involved fluorophores and quenchers and changing constitution. The technology is capable of providing important features for the characterization of living and nonliving matter. In addition to spectral signatures, the knowledge of fluorescence lifetimes of complete bacterial cells increases the information content for online classification of data with high hit rates.

LIF allows for scanning of surfaces or the atmosphere and for distinguishing biological material from natural background. Therefore, it is suited for screening and monitoring applications. Though a classification with a trained data set yields high performance, LIF technology does not generally claim for an identification of biomaterial. Besides social, scientific, and ecological challenges, early detection and identification of biological specimen (and threats) motivates a fusion of the best present technologies [66] for the protection of the environment and the population. The requirements are the fast localization and inspection of suspicious species by remotely controlled stand-off procedures and a targeted and reliable identification by microbiological means. LIF and Raman technologies are used in search for life on extraterrestrial planets. A detailed knowledge of fluorescence from bioorganic compounds as well as from minerals is necessary for the interpretation of LIF spectra and Raman spectra with fluorescent background.

LIF combined with information from elastic and further inelastic backscattering is already successfully combined in LIF LIDAR systems. The evaluation of additive information, e.g. anisotropic behaviour and analysis of elastic scattering, will extend the accuracy of LIF substance classification. Especially, anisotropy data represent another important feature for the characterization of bulk biological material for stand-off detection purposes.

Innovations in the development of laser sources like compact UV laser sources with pulsed picosecond lasers enable the measurement of fluorescence anisotropy. Together with the progresses in the detector technology, robust, efficient, and small-sized lasers enable the compaction of the overall system and will lead to portable devices. Ongoing rapid digitalization efforts allow for easy-to-use design specially shaped for end-users' demands. These developments will widen field applications: environmental and health protection, e.g. in contaminated buildings, food production, air-conditioning and ventilation plants, supply chains for drinking water, to name just a few.

REFERENCES

1. W. J. Tango, J. K. Link, R. N. Zare. Spectroscopy of K2 using laser-induced fluorescence. *The Journal of Chemical Physics*. 49, 1968, pp. 4264–4268.
2. S. W. Hell. Far-field optical nanoscopy. *Science*. 5828, 2007, p. 1153.
3. J. R. Lakowicz. *Principles of Fluorescence Spektroscopy*. New York: SpringerScience+Business Media, LLC3, 2006.
4. J. Kunnil, B. Swartz, L. Reinisch. Changes in the luminescence between dried and wet bacillus spores. *Applied Optics*. 43 (28), 2004, p. 5404.
5. M. Kraus, L. Fellner, F. Gebert, K. Grünewald, C. Pargmann, A. Walter, F. Duschek Comparison of classification models of spectral data of laser induced fluorescence. Rome, Italy: *1st Scientific International Conference on CBRNE*, 2017.
6. M. Gelfusa, A. Murari, M. Lungaroni, A. Malizia, S. Parracinoa, E. Peluso, O. Cenciarelli, M. Carestia, R. Pizzoferrato, P. Gaudio. A support vector machine approach to the automatic identification of fluorescence spectra emitted by biological agents. *Proc. SPIE*. 2016, Vol. 9455.
7. L. Fellner, F. Gebert, A. Walter, K. Grünewald, F. Duschek. Variations in fluorescence spectra of a bacterial population during different growth phases. Rome, Italy: *1st Scientific International Conference on CBRNE*, 2017.

8. F. Finkenwirth, O. Neubauer, J. Gunzenhäuser, J. Schoknecht, S. Scolari, M. Stöckl, T. Korte, A. Herrmann, T. Eitinger. Subunit composition of an ECF-type biotin transporter analyzed in living bacteria. *Biochemical Journal*. 2010, Vol. 431, p. 373.
9. F. Gebert, M. Kraus, L. Fellner, A. Walter, C. Pargmann, K. Grünewald, F. Duschek. Novel standoff detection system for the classification of chemical and biological hazardous substances combining temporal and spectral laser induced fluorescence techniques. Rome, Italy: s.n., 2017.
10. A. Hausmann, F. Duschek, T. Fischbach, C. Pargmann, V. Aleksejev, L. Poryvkina, I. Sobolev, S. Babichenko, J. Handke. Standoff detection: classification of biological aerosols using laser induced fluorescence (LIF) technique. Baltimore, USA: s.n., 2014. SPIE.DSS 2014 Defense and Security, 5–9 May 2014.
11. T. Fischbach, V.I. Aleksejev, F. Duschek, A. Hausmann, C. Pargmann, L. Poryvkina, I. Sobolev, S. Babichenko, J. Handke. Standoff detection of chemical and biological substances using laser induced fluorescence technique. Fraunhofer Verlag, Berlin, Germany: *9th Future Security, Security Research Conference, Proceedings*, 16–18 Sep. 2014, pp. 327–334.
12. F. Duschek, T. Fischbach, A. Hausmann, C. Pargmann, J. Thieser, S. Julich, V. Aleksejev, L. Poryvkina, I. Sobolev, H. Tomaso, S. Babichenko, J. Handke (eds.). A fast hyperspectral laser induced fluorescence application for standoff detection and online classification of biological hazardous materials. Stuttgart Fraunhofer Verlag. Berlin: s.n., *Security Research Conference Proceedings*, 15–17 Sep. 2015, pp. 97–104.
13. T. Fischbach, F. Duschek, A. Hausmann, C. Pargmann, V. Aleksejev, L. Poryvkina, I. Sobolev, S. Babichenko, J. Handke. Standoff detection and classification procedure for bioorganic compounds by hyperspectral laser- induced fluorescence. In *Proc. SPIE*, 2015, 9455. p. 945508.
14. F. Duschek, L. Fellner, F. Gebert, K. Grünewald, A. Köhntopp, M. Kraus, P. Mahnke, C. Pargmann, H. Tomaso, and A. Walter. Standoff detection and classification of bacteria by multispectral laser-induced fluorescence. *Advances in Optics*. 6 (2), 2017, pp. 75–83.
15. R.L. Bissonnette. Multiple-scattering lidar equation. *Applied Optics*. 35 (33), 1996, pp. 6449–6465.
16. W. Rudin. *Functional Analysis*. New York: McGraw-Hill, 1973.
17. A.M. Wazwaz. The regularization method of Fredholm integral equations of the first kind. *Computer and Mathematics with Applications*. 61, 2011, pp. 2981–2986.
18. W.J. Wiscombe. Improved Mie scattering algorithms. *Applied Optics*. 19 (9), 1980, pp. 1505–1509.
19. R.M. Measures. *Laser Remote Sensing: Fundamentals and Applications*. New York: Krieger Publishing Company, 1992.
20. A.T. Young. Revised depolarization corrections for atmospheric extinction. *Applied Optics*. 19, 1980, p. 20.
21. B. Bodhaine, N.B. Wood, E.G. Dutton, J.R. Slusser. On Rayleigh optical depth calculations. *Journal of Atmospheric and Oceanic Technology*. 16, 1999, pp. 1854–1861.
22. J.D. Klett. Lidar inversion with variable backscatter/extinction ratios. *Applied Optics*. 24 (11), 1985, pp. 1638–1643.
23. W.J. Lentz, A.W. Cooper, M.M. Regush (eds.). Improved Klett lidar inversion techniques. SPIE. Orlando, Florida, USA: s.n., *Proceedings of SPIE*, 1994.
24. M. Mishchenko, J. Hovenier. Depolarization of light backscattered by randomly oriented non- spherical particles. *Optics Letters*. 20, 1995, pp. 1356–1358.
25. J.A. Bravo-Aranda, G. de Arruda Moreira, F. Navas-Gusman, M.J. Granados-Munoz, J.L. Guerrero-Rascado, D. Pozo-Vazquez, C. Arbizu-Barrena, F.J. Olmo Reyes, M. Mallet, L.A. Aroledas. A new methodology for PBL height estimations based on lidar depolarization measurements: Analysis and comparison against MWR and WRF model-based results. *Atmospheric Chemistry and Physics*. 17, 2017, pp. 6839–6851.
26. B. Liu, Z. Wang. Improved calibration method for depolarization lidar measurement. *Optics Express*. 21 (12), 2013, pp. 14583–14590.
27. S. Buteau, L. Stadnyk, S. Rowsell, J.-R. Simard, J. Ho, B. Déry, J. McFee, Spectrally resolved laser-induced fluorescence for bioaerosols standoff detection. *Proc. SPIE*. 6756, 2007, pp. 675608-1–675608-10.
28. S. Buteau, J.-R. Simard, B. Déry, G. Roy, P. Lahaie, P. Mathieu, J. Ho, J. McFee. Bioaerosols laser-induced fluorescence provides specific robust signatures for standoff detection. *Proc. SPIE*. 6378, 2006, pp. 637813-1–637813-12.
29. P. Jonsson, M. Elmqvist, O. Gustafsson, F. Kullander, R. Persson, G. Olofsson, T. Tjärnhage, Ø. Farsund, T.V. Haavardsholm, G. Rustad. Evaluation of biological aerosol stand-off detection at a field trial. *Proc. SPIE*. 7484, 2009, p. 74840I.
30. B. Park, R. Lu. *Hyperspectral Imaging Technology in Food and Agriculture* (Food Engineering Series). Heidelberg: Springer, 2015.
31. Chen, C.C. *Attenuation of Electromagnetic Radiation By Haze, Fog, Clouds, and Rain*. s.l.: National Technical Information Service, U.S. Department of Commerce, 1975.
32. Eurocontrol Statistics and Forecast Service. *Ash-cloud of April and May 2010: Impact on Air Traffic*. European Organisation for the Safety of air Navigation. Brussels: Eurocontrol, 2010, pp. 1–45. STATFOR/Doc 394 V.1.
33. V. Ramanathan, P.J. Crutzen, J.T. Kiehl, D. Rosenfeld. Aerosols, climate, and the hydrological cycle. *Science*. 294, 2001, pp. 2119–2124.
34. J. Fan, Y. Wang, D. Rosenfeld, X. Liu. Review of aerosol-cloud interactions: Mechanisms, significance, and challenges. *Journal of the Atmospheric Sciences*. 73, 2016, pp. 4221–4251.
35. J.H. Seinfeld, S.N. Pandis. *Atmospheric Chemistry and Physics: from Air Pollution in Climate Change*. Hoboken, NJ: Wiley, 2016.
36. C.I. Davidson, R.F. Phalen, P.A. Solomon. Airborne particulate matter and human health: A review. *Aerosol Science and Technology*. 39, 2005, pp. 737–749.
37. Stockholm International Peace Research Institute. The rise of CB weapons. *The Problem of Chemical and Biological Weapons*. 1, 1971, pp. 111–124.
38. P. Kulkarni, P.A. Baron, K. Willeke, (eds.). *Aerosol Measurement: Principles, Techniques, and Applications*. Hoboken, NJ: Wiley & Sons, Inc., 2011.
39. P.F. DeCarlo, J.R. Kimmel, A. Trimborn, M.J. Northway, J.T. Jayne, A.C. Aiken, et al. Field-deployable, high-resolution, time-of-flight, aerosol mass spectrometer. *Analytical Chemistry*. 78 (24), 2006, pp. 8281–8289.

40. M.A. Zawadowicz, K.D. Froyd, D.M. Murphy, D.J. Cziczo. Improved identification of primary biological aerosol particles using single-particle mass spectrometry. *Atmospheric Chemistry and Physics*. 17, 2017, pp. 7193–7212.
41. Task Group SET-98/RTG-55. *Laser Based Stand-Off Detection of Biological Agents*. s.l.: NATO-OTAN - Research and Technology Organisation, 2010. RTO-TR-SET-098.
42. K. Pfeilstricker, H. Bäsch, C. Camy-Peyret, R. Fitzenberger, H. Harder, H. Osterkamp. First atmospheric profile measurements of UV/Visible O_4 absorption band intensities: Implications for the spectroscopy, and the formation enthalpy of the O_2-O_2 dimer. *Geophysical Research Letters*. 28 (24), 2001, pp. 4595–4598.
43. C. Nitschelm. Theoretical transmittance in the near UV, visible and near IR through the atmosphere for several observatories. *Astronomy & Astrophysics Supplement Series*. 74, 1988, pp. 67–72.
44. Y.-L. Pan. Detection and characterization of biological and other organic-carbon aerosol particles in atmosphere using fluorescence. *Journal of Quantitative Spectroscopy & Radiative Transfer*. 150, 2015, pp. 12–35.
45. Y.-L. Pan, J.D. Eversole, P.H. Kaye, V. Foot, R.G. Pinnick, S.C. Hill, M.W. Mayo, J.R. Bottiger, A. Huston, V. Sivaprakasam, R.K. Chang. Bio-aerosol fluorescence. In V. Maltsev, G. Videen, A. Hoekstra. *Optics of Biological Particles, Nato Science Series, II. Mathematics, Physics and Chemistry*. Dordrecht: Springer, 2007, Vol. 238, pp. 63–165.
46. Y.-L. Pan, V.E. Boutou, J.R. Bottinger, S.S. Zahng, J.P. Wolf, et al. A puff of air sorts bioaerosols for pathogen identification. *Aerosol Science & Technology*. 38, 2014, pp. 598–602.
47. R.G. Pinnick, S.C. Hill, P. Nachman, J.D. Pendleton, G.L. Fernande, M.W. Mayo, J.G. Bruno. Fluorescence particle counter for detecting airborne bacteria and other biological particles. 2007. doi:10.1080/02786829508965345.
48. G.W. Faris, R.A. Copeland, K. Mortelmans, B.V. Bronk. Spectrally resolved absolute fluorescence cross sections for bacillus spores. *Applied Optics*. 36, 1997, pp. 2686–2688.
49. P.H. Kaye, J.E. Barton, F.E. Hirst, J.M. Clark. Simultaneous light scattering and intrinsic fluorescence measurement for the classification of airborne particles. *Applied Optics*. 39 (21), 2000, pp. 3738–3745.
50. R. Weichert, W. Klemm, K. Legenhausen, C. Pawellek. Determination of fluorescence cross- sections of biological aerosols. *Particle & Particle Systems Characterization*. 19, 2002, pp. 216–222.
51. Y.-L. Pan, R.G. Pinnick, S.C. Hill, R.K. Chang. Particle-fluorescence spectrometer for real-time single-particle measurements of atmospheric organic carbon and biological aerosol. *Environmental Science & Technolgy*. 43 (2), 2009, pp. 429–434.
52. U. Poeschl. Atmospheric aerosols: Composition, transformation, climate and health effects. *Angewandte Chemie International Edition*. 44, 2005, pp. 7520–7540.
53. A. Palucci. Optical and morphological characterization of selected phytoplanktonic communities application for remote sensing. *Optics of Biological Particles*. Dordrecht: Springer, 2017, pp. 165–193.
54. R. Doerffer, J. Fischer. Concentrations of chlorophyll, suspended matter, and gelbstoff in case II waters derived from satellite coastal zone color scanner data with inverse modeling methods. *Journal of Geophysical Research*. 9 (C4), 1994, pp. 7457–7466.
55. D. Diouf, A. Niang, J. Brajard, M. Crepon, S. Thiria. Retrieving aerosol characteristics and sea- surface chlorophyll from satellite ocean color multi-spectral sensors using a neural-variational method. *Remote Sensing of Envieronment*.130, 2013, pp. 74–86.
56. C. Shi, T. Nakajima, M. Haschimoto. Simultaneous retrieval of aerosol optical thickness and chlorophyll concentrations from multiwavelength measurement over East China Sea. *Journal of Geophysical Research: Atmospheres*. 121, 2016, pp. 14084–14101.
57. S. Lampbert-Girard, N. Ho, B. Bourliaguet, P.-F. Paradis, M. Piche, F. Babin. Proposal for a standoff bio-agent detection SWIR/MWIR differential scattering lidar. Baltimore: SPIE, *Proceedings of SPIE*, 2012. Vol. 8358.
58. V. Amiridis, D.S. Balis, E. Giannakaki, A. Stohl, S. Kazadzis, M.E. Koudouli, P. Zanis. Optical characteristics of biomass burning aerosols over Southeastern Europe determined from UV- Raman lidar measurements. *Atmospheric Chemistry and Physics*. 9, 2009, pp. 2431–2440.
59. Z. Yang, C. Li, F. Chen, J. Mao, T. Wu. *Ultraviolet Polarized LiDAR System for Biological Aerosols*. s.l.: United Kingdom Simulation Society. ISSN: 1473-804x online. doi:10.5013/IJSSST.a.17.36.26.
60. F.W.J. Teale, G. Weber. Ultraviolet fluorescence of the aromatic amino acids. *Biochemical Journal*. 65 (3), 1957, pp. 476–482.
61. Counsel of the European Parliament. Directive 2006/25/EC of the European Parliament and of the Counsel on the minimum health and safety requirements regarding the exposure of workers to risks arising from physical agents (artificial optical radiation). *Official Journal of the European Union*. 49, 2006, Amendments 2007, 2008, 2013, L114.
62. J. Wojtanowski, M. Zygmunt, M. Muzal, P. Knysak, A. Mlodzianko, A. Gawlikowski, et al. Performance verification of a LIF-LIDAR technique for stand-off detection and classification of biological agents. *Optics & Laser Technol*. 67, 2015, pp. 25–37.
63. S. Frey, H. Willea, F. Wilsenack. Mobile Demonstrator for Biological Aerosol Standoff Detection. *Proc. SPIE*. 7484, 2009, p. 748407.
64. O. Farsund, G. Rustad, G. Skogan. Standoff detection of biological agents using laser induced fluorescence – a comparison of 294 nm and 355 nm excitation wavelength. *Biomedical Optics Express*. 3, 2012, p. 11.
65. Z. Mierczyk, K. Kopczynski, M. Zygmunt, J. Wojtanowski, J. Mlynczak, et al. (ed.) Fluorescence/depolarization lidar for mid-range stand-off detection of biological agents. SPIE, *Proceedings of SPIE*, 2018. Vol. 8037.
66. S. Buteau, S. Rowsell. Biological material detection identification and monitoring: combining point and standoff sensors technologies. *Proc. SPIE*, 9995, 2016, pp. 99950B-1–99950B-10.

20

Harmonic Generation—Materials and Methods

David J Binks

CONTENTS

20.1 Introduction ... 233
20.2 Second-harmonic Generation ... 233
  20.2.1 Effective Non-linear Coefficient ... 234
  20.2.2 Conversion Efficiency ... 235
  20.2.3 Phase-matching ... 237
  20.2.4 Phase-matching Bandwidth ... 240
  20.2.5 Intra-cavity and Resonant Cavity Second-harmonic Generation ... 241
20.3 Sum and Difference Frequency Mixing ... 243
  20.3.1 Theory ... 244
  20.3.2 Sum Frequency Mixing ... 244
  20.3.3 Difference Frequency Mixing ... 245
20.4 Third- and Higher-harmonic Generation ... 245
20.5 Non-linear Materials for Frequency Conversion ... 246
  20.5.1 Birefringent Materials ... 247
  20.5.2 Quasi-Phase-matched Materials ... 248
  20.5.3 Self-doubling and Summing Materials ... 249
20.6 Frequency Conversion of Particular Lasers ... 249
  20.6.1 Nd Lasers ... 249
  20.6.2 Ti:sapphire Lasers ... 250
  20.6.3 Carbon Dioxide Lasers ... 250
20.7 Developing and Growth Areas ... 250
References ... 251
Further reading ... 252

20.1 Introduction

The fundamental output wavelength of a laser is limited by the linewidth of the atomic transition involved; this linewidth may be very narrow, giving essentially a fixed frequency output as in the case of Nd:YAG, or it may be relatively broad allowing some degree of tunability. Even for Ti:sapphire, however, the most widely tunable visible/near infrared laser gain medium, this tuning range is limited to ~700–1100 nm, and for most other laser sources, it is significantly less.

The wavelength range of laser radiation can be greatly extended by utilizing the non-linear optical properties of birefringent crystals to *frequency convert* the output of a laser to other wavelengths. Perhaps, the most common example of frequency conversion is second-harmonic generation, in which part or all of the laser output is converted to a beam of double the frequency. This process can be thought of as being equivalent to adding together two photons from the original beam to produce a single photon of twice the energy. Second-harmonic generation is a special case of the more general process of sum frequency mixing (SFM) which adds together photons of different energies from separate sources. Difference frequency mixing is the related process by which a wave is produced at a frequency equal to the difference between the frequencies of the beams interacting within the crystal.

In this chapter, the frequency conversion techniques of second-harmonic generation, SFM and difference frequency mixing will be described. (The closely related effects of parametric amplification and oscillation will be discussed in the next chapter.) The theoretical analysis of each of these three phenomena will be outlined initially, followed by a discussion of the non-linear materials commonly used in this type of process. Finally, the design considerations pertinent to the frequency conversion of some common laser systems will be discussed.

20.2 Second-harmonic Generation

The optics of anisotropic crystals plays an important part in frequency conversion processes such as second-harmonic generation. The subject of crystal optics is covered very thoroughly in Born and Wolf (see further reading); a brief outline will be given here, however, to allow the discussion to proceed directly. Light passing through an anisotropic crystal is in general resolved into two beams of orthogonal polarizations, each of which experiences a different refractive index; this is the phenomenon known as birefringence or double refraction. Generally, the value of these two refractive indices will vary in different ways with the direction of light propagation through a crystal, and there will be certain directions in which the two values happen to be equal. These special directions are termed the *optic axes* and anisotropic crystals are either uniaxial or biaxial, having one or two of these axes, respectively. In the case of uniaxial crystals, beams with polarization directions perpendicular to the optic axis experience a refractive index, n_o, that is independent of propagation direction, and are called ordinary or o-rays. In contrast, the beams with a polarization orthogonal to that of the ordinary rays are subject to a direction-dependent refractive index and are hence named extraordinary or e-rays. The refractive index experienced by an e-ray ranges from n_e, when its polarization is parallel to the optic axis, to n_o, when it is perpendicular to the axis. Crystals are termed positive if $n_e > n_o$ and negative if $n_o > n_e$.

This formalism is useful both for the calculation of effective non-linear coefficients (see the next section) and of *phase-matching* conditions. The phase-evolution of a wave is determined by the refractive index to which it is subject as it propagates through a medium. Moreover, material dispersion usually ensures that the different wavelengths involved in a frequency conversion process experience different refractive indices and therefore become out of phase as they propagate. This generally results in destructive interference between waves generated by the non-linear process in one part of the crystal and another because the generated wave is produced with the same relationship to the incident wave at each point. However, the birefringent properties of non-linear crystals can be used to ensure that the refractive index for each wave is equal and hence they remain in-phase and interference is constructive. This important technique of phase-matching will be detailed in Section 20.2.3.

20.2.1 Effective Non-linear Coefficient

The amplitude of the non-linear polarization of the material depends on the product of the interacting fields and on the second-order non-linear susceptibility, $\chi^{(2)}$, which in general is a tensor quantity. Each tensor element, $\chi^{(2)}_{ijk} = 2d_{ijk}$, contributes differently to the non-linear material polarization depending on the directions that the fundamental and second-harmonic beams take through the crystal relative to the crystal axes and whether they are ordinary or extraordinary rays. It is a usual practice to collect together all the relevant contributions for a particular experimental arrangement and hence calculate an *effective non-linear coefficient*, d_{eff}, for that case. The value of d_{eff} indicates the strength of the non-linear interaction that can be expected from a $\chi^{(2)}$ material for a given situation and is useful in selecting appropriate materials for an application and predicting the efficiency of the non-linear process. This section shows how the effective non-linear coefficient can be calculated from the experimental geometry and the tensor components. The analysis will be for the particular case of second-harmonic generation but can be readily extended to sum and difference mixing by allowing the interacting fields to have different frequencies, i.e. ω_1 and ω_2, and the resulting non-linear polarization to be at the sum, $\omega_1+\omega_2$, or difference, $\omega_1-\omega_2$, frequency.

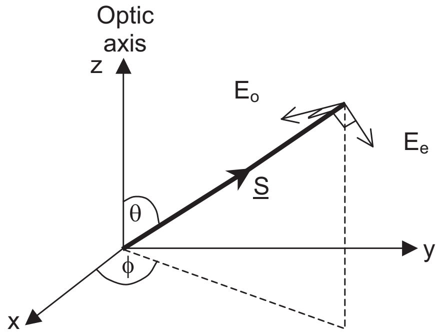

FIGURE 20.1 Orientation of the Poynting vector, S, and the ordinary (E_o) and extraordinary (E_e) polarizations relative to the crystal axis.

The effective non-linear coefficient for second-harmonic generation is defined by the following equation:

$$P(2\omega) = d_{\text{eff}} E(\omega) E(\omega). \tag{20.1}$$

Figure 20.1 shows a general geometric arrangement: the Poynting vector, $\boldsymbol{S} = \boldsymbol{E} \times \boldsymbol{H}$, corresponding to the fundamental beam is shown relative to Cartesian axes. The Poynting vector represents the direction of energy transfer (see [1], appendix 5), i.e. the direction in which a beam travels, and in birefringent materials, such as $\chi^{(2)}$ non-linear crystals, is not in general parallel to the wave propagation vector, k. To ensure that the non-linear interaction is birefringently phase-matched, the second-harmonic electric field, $E(2\omega)$, must be of orthogonal polarization to at least one of the fundamental electric fields, $E(\omega)$. (A non-orthogonal fundamental field can be resolved into parallel and orthogonal component fields.) For the purposes of the following example, it will be assumed that the non-linear medium is a negative uniaxial crystal (i.e. $n_o > n_e$) with the optic axis parallel to the z-axis and that the fundamental wave corresponds to an ordinary ray and the second harmonic to an extraordinary (e-) ray.

Hence, in this case, the components of the fundamental electric field along the crystal axes are

$$\begin{aligned} E_x &= E\cos\left(\phi - \frac{\pi}{2}\right) = E\sin(\phi) \\ E_y &= E\sin\left(\phi - \frac{\pi}{2}\right) = -E\cos(\phi) \\ E_z &= 0 \end{aligned} \tag{20.2}$$

As a third-rank tensor, $\chi^{(2)}$ has in principle 27 independent components but because no physical significance is attached to the order of the interacting fields, i.e. $E_i E_j \equiv E_j E_i$, then this number can be reduced to 18 and the non-linear polarization, $P(2\omega)$, is found by evaluating:

$$\begin{pmatrix} P_x \\ P_y \\ P_z \end{pmatrix} = \begin{pmatrix} d_{11} & d_{12} & d_{13} & d_{14} & d_{15} & d_{16} \\ d_{21} & d_{22} & d_{23} & d_{24} & d_{25} & d_{26} \\ d_{31} & d_{32} & d_{33} & d_{34} & d_{35} & d_{36} \end{pmatrix} \begin{pmatrix} E_x^2 \\ E_y^2 \\ E_z^2 \\ 2E_xE_y \\ 2E_xE_z \\ 2E_xE_y \end{pmatrix}. \tag{20.3}$$

Furthermore, if for the particular interaction the polarization is due only to electron displacement, rather than including a component from ion displacement, and if there is negligible loss, then the Kleinman conjecture [2] is valid and the following symmetries apply: $d_{21} = d_{16}$, $d_{24} = d_{32}$, $d_{31} = d_{15}$, $d_{13} = d_{35}$, $d_{14} = d_{36} = d_{25}$, $d_{12} = d_{26}$ and $d_{32} = d_{24}$. These conditions apply to most practical cases and so the Kleinman conjecture constitutes a powerful way of simplifying the calculation of the effective non-linear coefficient. Non-linear crystals are usually classified according to their point-group and each of these groups has further symmetries, which further reduces the number of independent tensor components (see [3,p. 382] for a useful table of crystal symmetries). For a particular non-linear material, some of the tensor components, whilst non-zero and independent, will be very small in magnitude compared with other components and can be safely neglected. For most materials then, the effective non-linear coefficient will typically depend between 1 and 3 of the tensor components only; the relative importance of each of these remaining components is determined by the geometrical arrangement of the second-harmonic scheme.

For example, β-barium borate (BBO) is a negative uniaxial crystal and has $d_{22} = -d_{21} = -d_{16}$, $d_{31} = d_{32}$ and $d_{15} = d_{24}$ with all other components zero except d_{35}, therefore

$$\begin{aligned} P_x &= -2d_{16}\sin(\phi)\cos(\phi)E^2 = d_{22}E^2\sin(2\phi) \\ P_y &= \left[d_{21}\sin^2(\phi) + d_{22}\cos^2(\phi)\right]E^2 = d_{22}E^2\cos(2\phi) \\ P_z &= \left[d_{31}\sin^2(\phi) + d_{32}\cos^2(\phi)\right]E^2 = d_{32}E^2. \end{aligned} \tag{20.4}$$

Since the second-harmonic beam corresponds to an e-ray,

$$\begin{aligned} P(2\omega) &= \sin\left(\theta + \frac{\pi}{2}\right)\left[P_x\cos(\phi) + P_y\sin(\phi)\right] + \cos\left(\theta + \frac{\pi}{2}\right)P_z \\ &= \left[d_{22}\cos(\theta)\sin(3\phi) - d_{31}\sin(\theta)\right]E^2 \end{aligned} \tag{20.5}$$

Hence, in this case, $|d_{\text{eff}}| = d_{22}\cos(\theta)\sin(3\phi) - d_{31}\sin(\theta)$.

20.2.2 Conversion Efficiency

In this section, the general solution to the coupled wave equations that describe second-harmonic generation for plane waves will be presented. This general solution represents the conversion efficiency achievable for any degree of fundamental wave depletion and for arbitrary phase-mismatch between the waves. The limits of non-depletion of the pump beam (i.e. fundamental wave) and of zero phase-mismatch will then be examined individually. Note that the field strengths, E, and intensities, I, that are used to describe the interacting waves in the following analysis are *instantaneous* quantities, and hence, the results that follow apply equally well to both continuous wave and pulsed systems. Total pulse energies can be found by simply integrating over the corresponding instantaneous powers.

General solution. In general, all three-wave mixing phenomena (i.e. second-harmonic generation, SFM and difference frequency mixing) can be described by the following coupled wave equations, which relate the Fourier components of the three electric fields propagating collinearly along the z-axis:

$$\begin{aligned} \frac{\partial E_1}{\partial z} &= -i\frac{\omega_1 d_{\text{eff}}}{n_1 c}E_2^* E_3\exp(-i\Delta kz) \\ \frac{\partial E_2}{\partial z} &= -i\frac{\omega_2 d_{\text{eff}}}{n_2 c}E_1^* E_3\exp(-i\Delta kz) \\ \frac{\partial E_3}{\partial z} &= -i\frac{\omega_3 d_{\text{eff}}}{n_3 c}E_1 E_2\exp(-i\Delta kz) \end{aligned} \tag{20.6}$$

where Δk is the phase-mismatch defined by

$$\Delta k = k_3 - k_2 - k_1. \tag{20.7}$$

For frequency-doubling, the subscript 3 corresponds to the second harmonic and subscripts 1 and 2 both correspond to the fundamental wave, hence, $\omega_1 = \omega_2$ and $\omega_3 = 2\omega_1$.

The following assumptions are now made:

1. The waves are infinite, unbounded, plane and monochromatic.
2. The non-linear material is non-magnetic and lossless.
3. The slowly varying envelope approximation is valid [4].
4. The group and phase velocities are equal [5].
5. Any higher-order non-linear processes are negligible [6].

Under these assumptions, Milton [7] showed that the second-harmonic conversion efficiency, η, is given by

$$\eta = \frac{I_3}{I_1} = 2B \times sn^2\left(\sqrt{\frac{K L^2 I_1 A}{\hbar\omega_1}}, \gamma\right) \tag{20.8}$$

where L is the interaction length, I_1 is the fundamental intensity, I_3 is the second-harmonic intensity and sn is a Jacobian elliptic function [8]. The coupling coefficient, K, is given by

$$K = \frac{2\hbar\omega_1\omega_2\omega_3}{n_1 n_2 n_3 \varepsilon_0 c^3}d_{\text{eff}}^2 \tag{20.9}$$

and the parameters A, B and γ are

$$\begin{aligned} A, B &= \tfrac{1}{2}\left[(1 + \sigma + \delta) \pm \sqrt{(1 + \sigma + \delta)^2 - 4\sigma^2}\right] \\ \gamma &= \left|\frac{A}{B}\right| \end{aligned} \tag{20.10}$$

where

$$\sigma = \frac{I_2\omega_2}{I_1\omega_2}$$
$$\delta = \frac{\hbar\omega_1}{KI_1}\left(\frac{\Delta k}{2}\right)^2 \tag{20.11}$$

σ is the *photon balance* parameter, i.e. it is unity if the number of photons in the two interacting beams is equal. This is always true for type I phase-matching but only true for types II and III if the angle between the fundamental polarization and the optic axis is exactly 45°. (See section 20.2.2 for a definition of phase-matching type.) The parameter δ is the normalized phase error and is equal to zero for a phase-matched interaction.

Non-depleted pump beam and arbitrary phase mismatch. To illustrate the importance of phase-matching, the non-phase-matched case will now be considered but, for simplicity, in the limit of non-depletion of the fundamental intensity, i.e. $I_\omega(z) = I_\omega(0)$. Now, the rate of change of the second-harmonic amplitude depends on a constant intensity of the fundamental wave and its z-dependence is only through the phase-matching term $\exp(i\Delta kz)$:

$$\frac{\mathrm{d}A_3}{\mathrm{d}z} = I_\omega \exp(i\Delta kz). \tag{20.12}$$

The total second-harmonic conversion efficiency over the interaction length, L (which may be simply limited to the physical length of the non-linear crystal involved or maybe less than that due to effects such as 'walk-off'—this will be discussed later), may be found by integrating the above expression between the limits of 0 and L to give, in terms of intensity,

$$\eta = \frac{I_3(L)}{I_1} = \frac{A_3^*A_3}{2Z_3I_1} = 2\frac{K\,L^2I_1}{\hbar\omega_3}\mathrm{sinc}^2\left(\frac{\Delta kL}{2}\right) \tag{20.13}$$

where Z_3 is the plane wave impedance for the second-harmonic wavelength. A plot of efficiency as a function of phase-mismatch is shown in Figure 20.2 and shows that a failure to ensure phase-matching, i.e. $\Delta k = 0$, results in a much reduced second-harmonic efficiency. Physically, if the fundamental wave gets out-of-phase with the second-harmonic wave as it progresses through the crystal then the subsequent second-harmonic wavelets it produces interfere destructively with the existing second-harmonic wave, resulting in a reduced amplitude and the oscillatory behaviour shown in Figure 20.2. The characteristic length over which the fundamental and second-harmonic waves stay in phase is known as the coherence length, l_c, and for a particular interaction in a material, it is given by

$$l_c = \frac{\pi}{\Delta k}. \tag{20.14}$$

Such is the benefit of ensuring good phase-matching that applications of the second harmonic that require efficient conversion generally employ a phase-matching technique; these will be described in Section 20.2.2. Unless otherwise indicated, all analyses from now on will assume that such a technique has been used and therefore that $\Delta k = 0$.

Depleted pump. For a phase-matched second-harmonic scheme involving plane waves in which the fractional conversion of the fundamental wave is non-negligible, the coupled wave equations can be solved exactly to give, in terms of intensity, the following expressions for the fundamental and second-harmonic waves [9]:

$$\frac{I_1(z)}{I_1(0)} = \mathrm{sech}^2\left(\frac{z}{l}\right) = 1 - \eta$$
$$\eta = \frac{I_3(z)}{I_1(0)} = 2\tanh^2\left(\frac{z}{l}\right) \tag{20.15}$$

where l is a characteristic length for the interaction and is given here again

$$l = \left(Kz\sqrt{\frac{I_1}{\hbar\omega_1}}\right)^{-1}. \tag{20.16}$$

The evolution of the fundamental and second-harmonic intensities is shown in Figure 20.3. Hence, given a sufficiently large effective non-linear coefficient or sufficiently intense fundamental wave or a long enough interaction length, complete conversion of the fundamental wave to the second harmonic is possible. Furthermore, note that the non-linear conversion efficiency function is monotonic with z and so, if the assumptions listed here are valid, then there is no back conversion

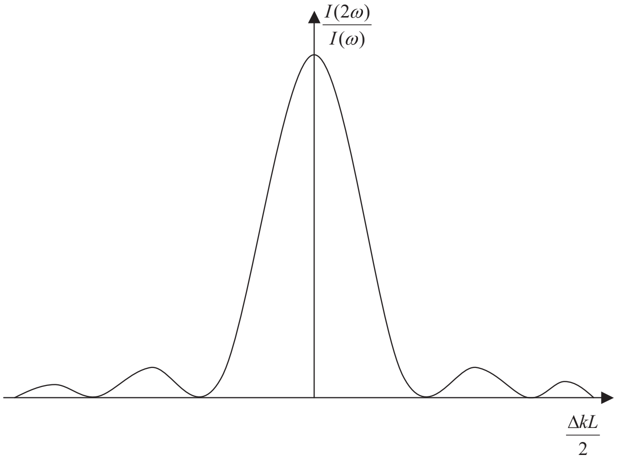

FIGURE 20.2 Second-harmonic conversion efficiency as a function of phase mismatch, Δk.

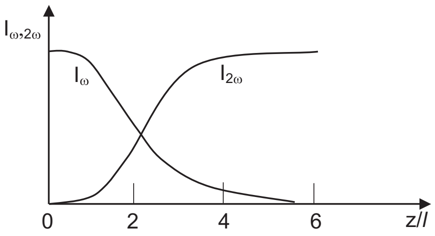

FIGURE 20.3 Evolution of fundamental and second-harmonic intensities as a function of the distance normalized to l.

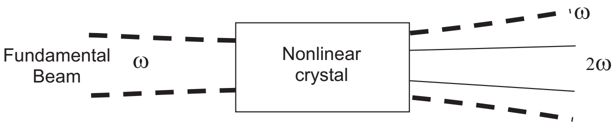

FIGURE 20.4 Second-harmonic generation with Gaussian beams. In general, the fundamental and second harmonic have different beam diameters and divergences.

from the second harmonic to the fundamental. We shall see later that this is a special case for second-harmonic generation when the fundamental is either a pure e-ray or o-ray; it does not necessarily hold for the more general case of SFM or for frequency doubling when the fundamental has both e- and o-ray components. In other words, there will be the possibility of back conversion whenever the interacting fields are distinguishable either by their frequency or polarization direction.

Gaussian beams. Due to the weakness of second-order interactions at intensities anything less than those typical of lasers, in general, the waves that interact within a non-linear crystal are usually best described not by plane waves but by Gaussian beams. Therefore, for a more accurate description of the second-harmonic process, the finite spot size and divergence of the fundamental and second-harmonic beams must be considered, which in general will be different from one another, as in Figure 20.4.

The plane wave analysis described shows that the second-harmonic efficiency is proportional to the fundamental intensity and so one would expect that greater efficiency could be had from a Gaussian fundamental beam that is tightly focused into the non-linear crystal. However, two factors mitigate this advantage: the reduced Rayleigh length and increased divergence of the focused beam. If the Rayleigh length, z_0, of the fundamental beam is much shorter than the interaction length (the crystal length in a well-designed scheme) then, even though the peak fundamental intensity is increased by tighter focusing, the average intensity over the interaction length is less and the overall conversion efficiency is reduced. An in-depth analysis by Boyd and Kleinman [10] shows that the optimum conversion efficiency results when the interaction length is $5.68z_0$. Moreover, under these conditions, the conversion efficiency increases linearly with interaction length, L, rather than with L^2 as in the plane wave analysis. The greater beam divergence brought about by tight focusing can also have a deleterious effect on efficiency depending on how it compares to the phase-matching acceptance angle for the particular non-linear material and experimental arrangement, a subject that will be discussed in the next section.

20.2.3 Phase-matching

As was illustrated in the previous section, the conversion efficiency of second-harmonic generation, and indeed, all three-wave mixing processes depend crucially on the phase-matching condition being satisfied, i.e.

$$\Delta k = k_3 - k_2 - k_1 = 0 \tag{20.17}$$

where k_i represents the magnitude of the propagation vectors of, for $i = 1,2$, the two waves that interact to produce the third, $i = 3$. Since the momentum of a photon is given by $p = \hbar k$ then this statement is equivalent to requiring that momentum is conserved. (Similarly, energy is conserved if $\hbar\omega_3 = \hbar\omega_1 + \hbar\omega_2$.) Dielectric media such as non-linear crystals are generally dispersive and hence $k = n(\lambda)/\lambda$, where $n(\lambda)$ is the wavelength-dependent refractive index for that material. Hence, the phase-matching condition becomes:

$$\frac{n_3(\lambda_3)}{\lambda_1} = \frac{n_1(\lambda_1)}{\lambda_1} + \frac{n_2(\lambda_2)}{\lambda_2} \tag{20.18}$$

which, for the case of second-harmonic generation, i.e. $\lambda_1 = \lambda_2 = \lambda$ and $2\lambda_3 = \lambda$, means that for exact phase-matching, $\Delta k = 0$, the refractive experienced by the second-harmonic wave should be equal to that experienced by the fundamental.

The wavelength dependence of refractive index is usually described by a semi-empirical dispersion relation, called a Sellmeier equation, which would typically be of the form (although other forms are common)

$$n^2 = a + \sum_k \frac{b_k}{\lambda^2 - \lambda_k^2} \tag{20.19}$$

where a and b are constants and the summation is over the k absorption resonances that contribute to dispersion in a particular spectral region; usually dispersion is well described by including only one or two of these resonances. There will be a separate Sellmeier equation for both ordinary and extraordinary refractive indices for uniaxial (i.e. having a single optic axis) crystals, whilst three Sellmeier equations are required to describe refractive index dispersion in biaxial crystals (i.e. having two optic axes), one corresponding to each crystal axis (X, Y, Z). For example, the ordinary and extraordinary refractive index (n_o and n_e, respectively) of BBO is well described over its transparency range (~0.2–2.6 μm) by

$$\begin{aligned} n_0^2 &= 2.7405 + \frac{0.0184}{\lambda^2 - 0.0179} - 0.00155\lambda^2 \\ n_e^2 &= 2.3730 + \frac{0.0128}{\lambda^2 - 0.0156} - 0.0044\lambda^2 \end{aligned} \tag{C31.20}$$

where λ is in units of microns; this is shown in Figure 20.5.

The refractive index for a second-harmonic and a fundamental wave of the same polarization will in general be different because of this wavelength dispersion. Hence, to achieve phase-matching during frequency-doubling, the second-harmonic polarization must be orthogonal to at least one of the fundamental waves. (A single fundamental beam can be regarded as two different waves, one with a polarization parallel and the other with a polarization perpendicular to that of the second harmonic.) Whether the second-harmonic ray should be ordinary or extraordinary to achieve phase-matching depends on whether the crystal involved is positive uniaxial ($n_e > n_o$) or negative uniaxial ($n_o > n_e$). The various permutations of possible polarization combinations of the three waves involved determine, by convention, the *type* of phase-matching scheme, as outlined in Table 20.1. A non-linear

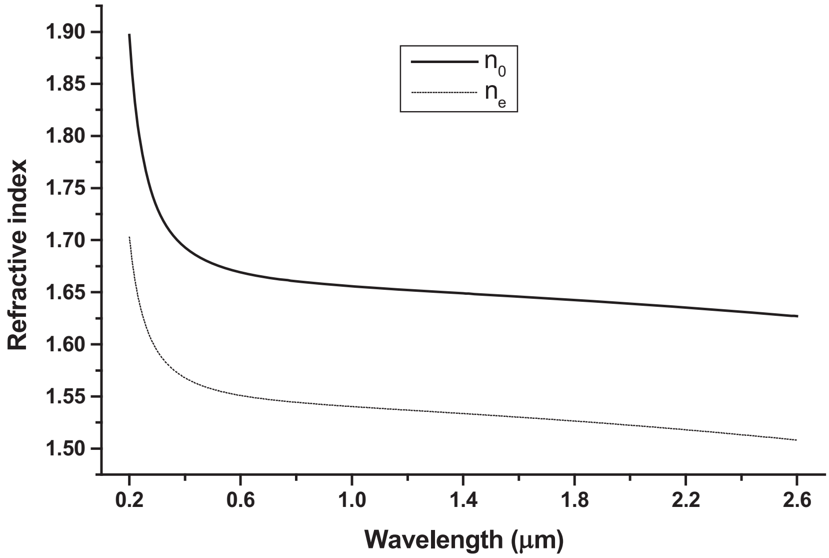

FIGURE 20.5 Ordinary (n_o) and extraordinary (n_e) refractive index change with wavelength for BBO.

TABLE 20.1

Phase-Matching Types. The Notation $s_1s_2 \rightarrow s_3$ Indicates the Polarization States s_i = o, e (i = 1, 2, 3) of Each of the Three Waves Involved in the Interaction

Phase-Matching Type	Positive Crystal	Negative Crystal
I	ee → o	oo → e
II	eo → o	oe → e
III	oe → o	eo → e

interaction between three waves, E_i (i = 1, 2, 3), of polarization states s_i = o, e is often described by the notation, $s_1s_2 \rightarrow s_3$, to indicate which of the waves involved are ordinary (o) or extraordinary (e). For type I phase-matching, waves 1 and 2 are of the same polarization state which is orthogonal to that of 3 (i.e. ee → o or oo → e). Similarly, the polarization of waves 1 and 3 is the same and orthogonal to that of 2 for type II phase-matching (i.e. oe → o or eo → e); for type III, 2 and 3 are the same polarization and the state of 1 is orthogonal to the others (i.e. eo → o or oe → e).

Birefringent phase-matching. In uniaxial crystals, the extraordinary refractive index depends not only on wavelength but only also on the angle that the e-ray makes with the optic axis (see Figure 20.6). Calculation of the refractive index experienced by a wave passing through a biaxial crystal at an arbitrary angle is much more complex than for the uniaxial case, and there is not an e-ray and an o-ray component for propagation at this arbitrary angle. If, however, the ray is restricted to one of the principal planes (i.e. *XZ*, *XY* or *YZ*) then the calculation of the refractive indices for two orthogonally polarized waves reduces to be the same as for a uniaxial case. For instance, if propagation is restricted to the *XY* plane then the wave polarized normal to this plane is constant (i.e. becomes the effective o-ray) and has a value of $n_o = n_Z$, where n_X, n_Y and n_Z are the principal refractive indices (see Figure 20.7). On the other hand, the refractive index experienced by the wave polarized in the *XY* plane depends on the angle it makes with

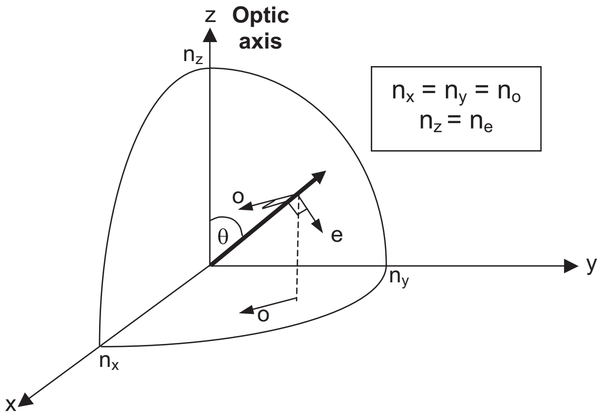

FIGURE 20.6 Index ellipsoid for a uniaxial crystal showing the o- and e-rays.

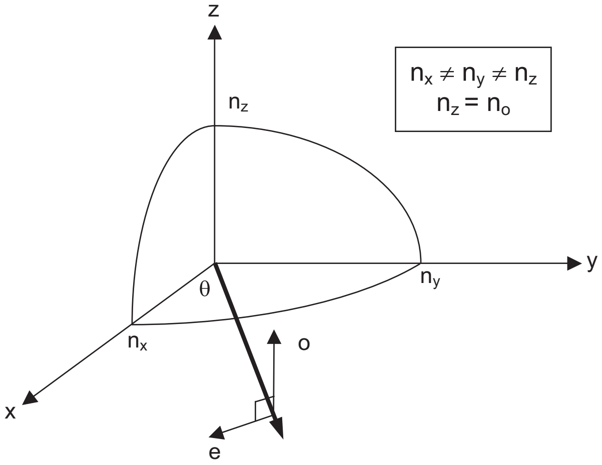

FIGURE 20.7 Index ellipsoid for a biaxial crystal showing the o- and e-rays.

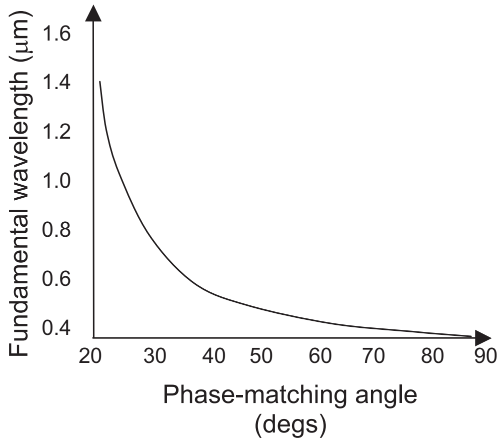

FIGURE 20.8 Phase-matching curve for type I second-harmonic generation in BBO.

the *X*-axis and hence can be regarded as the extraordinary ray for this plane with $n_e = n_X$. In both cases, the loci of n_e values trace out an ellipse as the propagation direction varies between $\theta = 0°$ and 90° (relative to the optic axis for uniaxial crystals and relative to the appropriate principal axis for biaxial crystals). Hence, the refractive index of the extraordinary ray, $n(\theta)$, can be calculated from the expression

$$\frac{1}{n^2(\theta)} = \frac{\sin^2(\theta)}{n_e^2} + \frac{\cos^2(\theta)}{n_o^2} \tag{20.21}$$

The combination of Equations (20.18), (20.20) and (20.21) allows the angle required for phase-matching to be calculated as a function of fundamental wavelength for a particular crystal and phase-matching type. As an example, Figure 20.8 shows the phase-matching curve for second-harmonic generation using a BBO crystal.

Quasi-phase-matching. Quasi-phase-matching (QPM) is an alternative method to birefringent phase-matching (BPM) of ensuring that the phase-mismatch of a particular non-linear interaction is zero, i.e. $\Delta k = 0$, and thus frequency conversion efficiency is maximized. In contrast to the birefringent technique, which utilizes the natural properties of non-linear crystals, QPM works by artificially imposing a periodicity onto the non-linear coefficient at twice the coherence length, l_c; this resets the accumulated phase difference between the fundamental and second-harmonic wave before destructive interference can cause energy to flow back to the fundamental from the second harmonic (see Figure 20.9).

This periodic variation of the non-linear coefficient can be achieved by reversing its sign every l_c to form domains. There are several ways in which such domains can be created, including the stacking of thin plates of the material in alternating orientations [11] and carefully controlled crystal growth [12,13]. However, over the last decade or so, the technique of imposing a domain structure onto bulk samples of ferroelectric crystals by electric field poling has emerged and proved to be a practical way of producing useful materials for non-linear optics. The chief benefit of QPM over BPM is that it can be used to ensure that any non-linear interaction within the transparency range of the material can be phase-matched irrespective of angle; hence, the propagation direction is now free to be chosen so that walk-off and angular bandwidth are optimized (see next subsection). Further, given this freedom of phase-matching, the beam directions and polarization can be chosen so that the largest component of the non-linear coefficient tensor can be used for coupling the fields together. This can bring about a considerable improvement in the effective non-linear

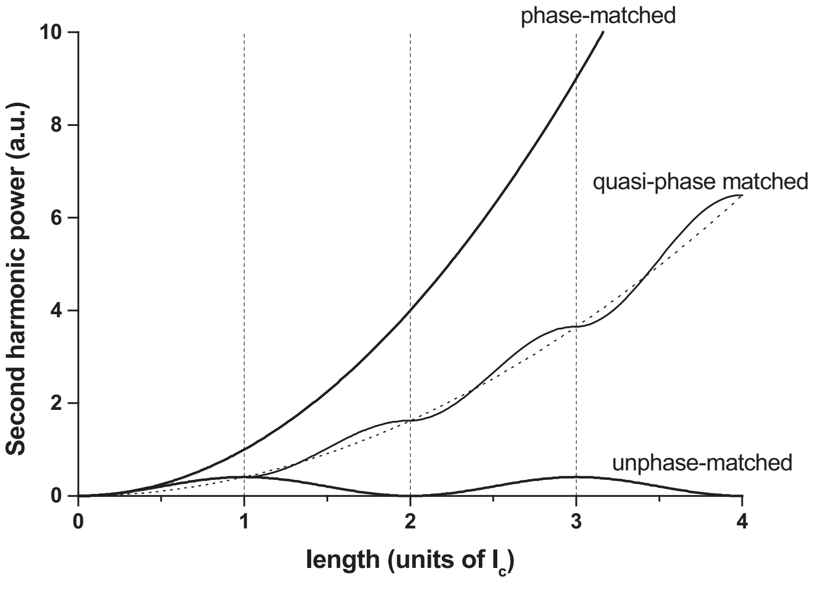

FIGURE 20.9 Second-harmonic power as a function of distance (normalized to coherence length, l_c) for phase-matched, quasi-phase-matched and unphase-matched interactions. The phase-matched interaction experiences monotonic growth, whilst, for the unphase-matched situation, energy continuously flows back and forth between the fundamental and second-harmonic waves. For the quasi-phase-matched interaction, the solid line represents the second-harmonic power variation as the poling direction is alternated every l_c, thereby preventing the onset of power transfer back to the fundamental; the dotted line is the phase-matched growth for an effective non-linear coefficient of d_Q (see Equation 20.23).

coefficient for an interaction; for example, if lithium niobate (LNB) is used to frequency-double the fundamental wavelength of a Nd:YAG laser, λ = 1064 nm, then the interaction for BPM has d_{31} = 4.1 pm V^{-1}, whereas the equivalent QPM interaction has d_{eff} = 21.6 pm V^{-1}. This translates to more than an order of magnitude improvement in conversion efficiency in the non-depleted pump limit (see Equation 20.13).

The concept of QPM was in fact suggested as long ago as the early 1960s by Armstrong et al. [14] and independently by Franken and Ward [15], and the analysis of this effect [16] proceeds largely along the same lines as BPM, except that now the phase-mismatch is given by

$$\Delta k = k_3 - k_1 - k_2 - \frac{2m\pi}{\Lambda} \tag{20.22}$$

where Λ is the repeat length of the non-linear coefficient variation and m is an integer and represents the order of the process. The non-linear coefficient of the QPM interaction, d_Q, is related to the effective non-linear coefficient, d_{eff}, of the equivalent birefringently phase-matched interaction, i.e. the same wavelength, polarization and propagation direction relative to the crystal axes, *if it could be phase-matched*, is given by

$$d_Q = \frac{2}{m\pi} d_{\mathrm{eff}} \sin(m\pi D). \tag{20.23}$$

D is the duty cycle, defined as $D = l_p/\Lambda$, where l_p is the length of the positive sections of the non-linear coefficient modulation.

A full analysis of QPM, including tuning, bandwidths and the effects of deviations away from the ideal modulation of the non-linear coefficient is presented in [16]; the broadening of the QPM second-harmonic bandwidth has been analysed [17].

20.2.4 Phase-matching Bandwidth

In the previous section, the propagation direction through a particular non-linear crystal required to phase-match a *monochromatic plane wave* was calculated. In practice, however, the fundamental wave will have some finite spectral bandwidth and some finite divergence, and these deviations from the perfect phase-matching condition will reduce the efficiency of non-linear conversion because $\Delta k \neq 0$ for all the energy in the fundamental wave. Indeed, effectively no non-linear conversion will take place for frequencies and angles far from the $\Delta k = 0$ condition, and an *angular* and *spectral phase-matching bandwidth* (PMB) can be defined. Similarly, because refractive index in non-linear crystals depends on temperature then a *temperature PMB* can also be defined. The phase mismatch, that is the deviation from $\Delta k = 0$, as a function of angle, θ, temperature, T, and frequency, v, can be written to the first approximation as

$$\Delta k \approx \frac{\partial(\Delta k)}{\partial \theta}\Delta\theta + \frac{\partial(\Delta k)}{\partial T}\Delta T + \frac{\partial(\Delta k)}{\partial v}\Delta v \tag{20.24}$$

where Δv, $\Delta\theta$ and ΔT are the spectral, angular and temperature bandwidths, respectively. If the bandwidths are defined as deviation from the $\Delta k = 0$ value that produces a 50% reduction in output power, i.e. when sinc$^2(\Delta kL) = 0.5$, then they can be written as

$$\Delta\theta = \frac{1.772\pi}{L\left[\dfrac{\partial(\Delta k)}{\partial\theta}\right]_{\theta=\theta_{pm}}} \qquad \Delta T = \frac{1.772\pi}{L\left[\dfrac{\partial(\Delta k)}{\partial T}\right]_{T=T_{pm}}}$$

$$\Delta v = \frac{1.772\pi}{L\left[\dfrac{\partial(\Delta k)}{\partial v}\right]_{v=v_{pm}}} \tag{20.25}$$

where the subscript pm indicates the value at $\Delta k = 0$.

The values of these bandwidths will depend upon which phase-matching type is employed (i.e. either I, II or III) and whether the crystals is uniaxial or biaxial because the $n_e = f(\theta)$ but $n_o \neq f(\theta)$ and also because the rate of change with temperature and frequency is different for n_e and n_0. Reference [18 conveniently tabulates the expressions for these bandwidths for the full range of phase-matching schemes.

For a phase-matching angle of θ = 90°, the first derivative $\partial(\Delta k)/\partial\theta = 0$ and the angular bandwidth now depend on the second derivative

$$\Delta\theta_{90} = 2\sqrt{\frac{0.886\pi}{L\left[\dfrac{\partial^2(\Delta k)}{\partial\theta^2}\right]}} \tag{20.26}$$

and is generally much broader than the bandwidth for phase-matching at angles significantly different from 90°; in other words, there is an enhanced angular tolerance at this angle. For this reason, phase-matching is said to be *non-critical* at θ = 90° in contrast to *critical phase-matching* otherwise. Restricting beam propagation to the θ = 90° direction of course prevents phase-matching being achieved by careful selection of crystal orientation. Hence, second-harmonic generation is usually phase-matched at this angle by QPM or by control of crystal temperature; for example, LNB will frequency-double 1064 nm radiation from a Nd:YAG with θ = 90° at a temperature of 120°C [19].

Walk-off. Another advantage of non-critical phase-matching is that at θ = 90°, there is no 'walk-off' between ordinary and extraordinary beams. What is intuitively thought of as the beam direction is the direction of energy transport which is determined by the Poynting vector, $\boldsymbol{S} = \boldsymbol{E}\times\boldsymbol{H}$. In free space and isotropic media, the propagation wavevector, $\boldsymbol{k}$, is parallel to $\boldsymbol{S}$, but in anisotropic media, this is not generally true because of the tensor nature of the dielectric constant. This means that for collinear phase-matching schemes, i.e. when $\boldsymbol{k}_1$, $\boldsymbol{k}_2$ and $\boldsymbol{k}_3$ are all parallel, the corresponding Poynting vectors, $\boldsymbol{S}_1$, $\boldsymbol{S}_2$ and $\boldsymbol{S}_3$, will not be parallel. For finite beam diameters, this results in any extraordinary beams 'walking-off' or separating from the unaffected ordinary beams, as illustrated in Figure 20.10. For an extraordinary ray propagating through an anisotropic crystal such that its k-vector makes an angle, θ, with the optic axis then the S-vector will be at an angle ρ to the k-vector, where

$$\rho = \pm\tan^{-1}\left[\left(\frac{n_0}{n_e}\right)^2 \tan\theta\right] \mp \theta \tag{20.27}$$

and the upper signs correspond to a negative ($n_o > n_e$) crystal and the lower signs to a positive ($n_e > n_o$) crystal (see [20],

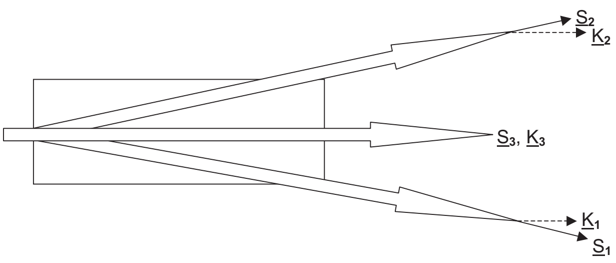

FIGURE 20.10 'Walk-off' of the Poynting vectors of the phase-matched waves in a non-linear crystal.

Section 20.2.3). The deleterious effects of walk-off can be largely avoided by the use of large beam diameters; however, if small diameters are necessary then the resulting Poynting vector walk-off length, l_a, can act as the effective interaction length and limit conversion efficiency, where

$$l_a = \frac{w0\sqrt{\pi}}{\rho} \tag{20.28}$$

where w_0 is the beam waist radius.

20.2.5 Intra-cavity and Resonant Cavity Second-harmonic Generation

As was seen in Section 20.2.2, the conversion efficiency of second-harmonic generation depends linearly on the intensity of the fundamental beam. For most gain-switched, Q-switched or mode-locked lasers, the high peak intensities obtained during the pulse (usually kW cm^{-2} or greater) are sufficient to achieve efficient frequency conversion from the non-linear crystals available. In these cases, simply directing the output beam through an appropriately phase-matched non-linear crystal is usually adequate. However, the output powers typically available from most continuous wave (cw) lasers are several orders of magnitude less (usually ~1 W or less), and consequently, low intensity becomes a limiting factor to the conversion efficiency. Furthermore, as described in Section 20.2.2, there is a limit to the efficiency gains to be had from the tight focusing of a cw laser beam because of the associated reduction in Rayleigh length and increase in divergence. One solution is to increase the intensity of the fundamental beam not by focusing but by resonating it inside an optical cavity and the obvious choice for that is the laser cavity itself.

Non-linear output coupling. A laser cavity consisting of a mirror that is ~100% reflecting at the laser wavelength and an output coupling mirror which transmits a certain fraction, T, at the same wavelength will have a circulating power that is approximately T^{-1} times larger than the output power available to pump a second-harmonic crystal external to the cavity. This enhancement factor is increased even further if the transmission of the output coupling mirror is made highly reflecting at the laser wavelength as well, i.e. the finesse of the cavity is made as high as possible at this wavelength. In this case, energy escapes the cavity not through transmission at a partially reflecting mirror, as is the case for most laser designs, but by conversion to the second harmonic because the mirror reflectivities have been chosen to be highly transmitting at the doubled frequency as well as highly reflecting at the fundamental wavelength. The frequency-doubling crystal now acts as a non-linear output coupler because the fraction of light that it couples out of the cavity depends on the circulating intensity. An interesting consequence of this non-linear coupling is that the threshold power for the laser is significantly reduced because the losses due to transmission at the mirrors have been virtually eliminated, and these are usually the chief source of loss in a well-designed laser. There is also a minimal output coupling *via* the non-linear crystal because at threshold the circulating intensities are very low. This arrangement is sometimes called a 'threshold-less' laser even though, of course, there will also be some residual losses and therefore a small but finite threshold. Another benefit of an intra-cavity scheme is that, whilst for extra-cavity frequency-doubling, the coupling between the fundamental and second-harmonic fields should be as large as possible to maximize conversion; the non-linear coupling at the operating power should be equivalent to the optimum output coupling for the laser. In other words, an extra-cavity-doubling crystal should have a conversion efficiency as near to 100% as possible for a single pass whilst for a laser cavity with an optimum output coupling of, say, 10% then the non-linear conversion efficiency needs only be at this lower level. In this situation, an effective conversion efficiency of 100% has been achieved in the sense that as much second-harmonic power is produced as would have been produced at the fundamental wavelength from a similar laser with a coupling mirror of optimum transmittance.

Disadvantages. Even though there are clear benefits to be had from an intra-cavity frequency doubling scheme, it is not always the best frequency-doubling technique because there are a number of disadvantages with the method. The introduction of any additional optical component into a laser cavity inevitably introduces extra loss, whether it be by absorption in the non-linear crystal or by reflection from its surfaces, and thereby reduces the efficiency of the system. Also, if the laser normally operates on a number of longitudinal modes, the action of the non-linear crystal and the gain medium can effectively couple them together resulting in chaotic power fluctuations—often called the 'green problem'. These power fluctuations are most problematic for lasers that operate on a few mode axial modes because if there are a large number of modes then fluctuations tend to average out. Ensuring single-mode operation completely obviates the green problem but this can involve introducing lossy optical components into the cavity or finding and securing the resonance of a suitable seed laser. A third disadvantage of intra-cavity second-harmonic generation is that in a standing wave cavity the fundamental circulates into two directions, and therefore, the second harmonic is also generated into two directions at once. For many laser designs, only the second harmonic generated in one of the two directions is readily extractable, and at the very least, the second-harmonic power is split between two beams. A travelling wave cavity solves this problem but usually at the expense of the introduction into the cavity of some component that ensures unidirectional oscillation, such as an optical diode, which inevitably increases the losses.

Resonant cavity second-harmonic generation. All of the problems with intra-cavity frequency doubling can be avoided

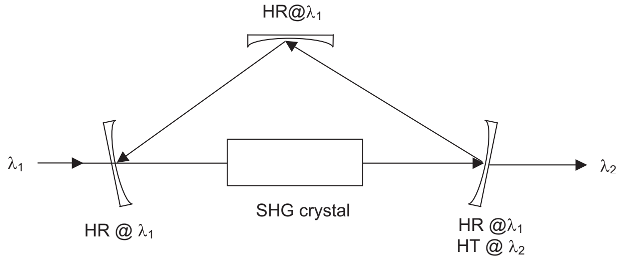

FIGURE 20.11 Optical cavity for resonant second-harmonic generation. (HR = highly reflecting; HT = highly transmitting; SHG = second harmonic generating.)

by putting the non-linear crystal in a separate optical cavity. Nothing has been introduced into the fundamental laser cavity and so clearly its threshold and slope efficiency have not been compromised. Similarly, separating the laser gain medium and the non-linear crystal prevents the laser modes from coupling together and producing chaotic power fluctuations. Finally, a ring resonator geometry, such as the one shown in Figure 20.11, produces a second-harmonic wave only in one direction because the fundamental passes through the non-linear crystal in that direction only. However, the resonant cavity technique has a drawback in that it requires that the fundamental wave is kept resonant within the cavity containing the frequency-doubling crystal. At resonance, the optical impedance of the cavity is well matched to that of the beam path from the laser source, and hence, back reflection is suppressed. Moreover, resonance maximizes the fundamental intensity within the cavity. To achieve resonance, precision control of the cavity length is required, usually by a rapid electronic feedback system and vibration isolation and thermal stabilization. Without these measures, fluctuations in the second-harmonic power will result as the fundamental power inside the resonant cavity varies as the cavity length moves in and out of resonance with the fundamental frequency. These control requirements make for a considerably more complicated and less robust frequency doubling system than the simpler intra-cavity or external second-harmonic generation schemes.

Theory of intra-cavity second-harmonic generation

i. *Steady state*. The steady-state operation of an intra-cavity frequency-doubled cw laser can be analyzed by including a non-linear loss term into the oscillation condition, i.e. loss = gain, which represents the fraction of light intensity that is lost from the oscillating fundamental wave by conversion to the second harmonic. Hence, the round-trip saturated gain is equated to the combined linear and non-linear losses per round trip (i.e. twice the single-pass second-harmonic conversion efficiency, η):

$$\frac{2g_0 L_1 I_s}{I_s + I} = F + 2\kappa\eta \tag{20.29}$$

where g_0 is the unsaturated gain coefficient, I is the intensity of the fundamental wave inside the cavity, I_s is the saturation intensity of the laser gain medium, L_1 is the length of the gain medium, F is the fractional linear loss per round trip and $\kappa = I_{\text{non-linear}}/I_{\text{gain}}$ is the ratio of the fundamental intensity in the non-linear crystal, $I_{\text{non-linear}}$, and the fundamental intensity in the laser gain medium, I_{gain}. The value of this ratio is typically significantly greater than 1 because the non-linear crystal is usually placed at the beam waist of the cavity, where the fundamental intensity is highest, and the gain medium is usually placed elsewhere in the cavity where the cavity mode has a larger diameter, as illustrated in Figure 20.12. It is advantageous to place the gain medium where the diameter is large because then higher powers can be extracted from the laser before gain saturation.

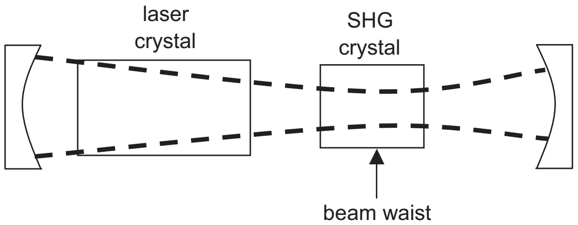

FIGURE 20.12 Intra-cavity second-harmonic generation configuration, showing the SHG crystal placed at the beam waist and the laser crystal placed where the beam diameter is larger.

It can be shown [21,22] that, in the steady-state case, the output-coupling through the non-linear crystal will be optimum, and therefore, the second-harmonic power output will be greatest when

$$\kappa K L^2 = \frac{F}{I_s}. \tag{20.30}$$

Thus, the non-linear coupling required for maximum second-harmonic power depends only on the cavity losses and the saturation intensity of the gain medium and is independent of the gain. Hence, optimum coupling is achieved for all gain values and consequently all power levels of a given system. This is in contrast to linear output-coupling, typically through the partially reflecting mirror, where the optimum value of the coupling is gain-and, therefore, power-dependent [23]. Moreover, if the frequency-doubling crystal can be inserted into the laser cavity with minimal additional loss then the maximum second-harmonic power achieved equals the maximum fundamental power obtainable from the same system, i.e. there is an effective conversion efficiency of 100%.

ii. *Pulsed lasers*. The analysis of pulsed intra-cavity frequency-doubled lasers is achieved by the addition of an extra term to the rate equations that represents the energy flow from the fundamental field to the second-harmonic field [24]:

$$\begin{aligned} \frac{\mathrm{d}N}{\mathrm{d}t} &= R - \sigma c\phi N - \frac{n}{\tau} \\ \frac{\mathrm{d}\phi}{\mathrm{d}t} &= \frac{-\phi}{\tau_c} + \sigma cN\phi - KL^2\phi^2 \end{aligned} \tag{20.31}$$

where N is the population inversion density, ϕ is the photon density, R is the rate at which the laser is pumped, τ is the upper laser level lifetime and τ_c is the lifetime of fundamental photons in the cavity.

These equations cannot be solved analytically, but numerical integration is straightforward and can be used to predict second-harmonic pulse energy, peak power and pulse durations; it also reveals that these quantities have an interesting dependence on the magnitude of the non-linear coupling coefficient. At low non-linear coupling levels, much less than optimum coupling, the laser can be said to be *undercoupled* in that the second-harmonic pulse energy extracted is less than the maximum possible value and is improved if the coupling coefficient is increased. In this regime, the pulse duration is approximately constant, and hence, the peak power scales with the pulse energy. Once optimum coupling is achieved, however, this behaviour changes. The pulse energy becomes essentially fixed and is unaffected by a further increase in the coupling coefficient. In contrast, additional non-linear coupling in this regime extends the pulse duration, and consequently, the peak power decreases; in this situation, the laser can be said to be *overcoupled*. Reduced peak powers caused by overcoupling can be problematic if high powers are required, for a subsequent frequency conversion step, for instance [25]. Since the non-linear coupling coefficient can be readily reduced by introducing some degree of phase mismatch, by de-tuning a non-linear crystal away from the optimum phase-matching angle for example, then this effect can be used to tune the duration and peak power of the second-harmonic pulse whilst maintaining a constant pulse energy. This can be useful for applications such as SFM between two pulsed lasers because a good temporal overlap between the two pulses is required for high-conversion efficiency [25].

If the bandwidth of the intra-cavity fundamental wave is much broader than the PMB of the non-linear crystal for intra-cavity second-harmonic generation, then a form of spectral hole-burning can be observed for pulsed lasers even though they might have a homogeneously broadened gain medium. For instance, this type of behaviour has been reported [26] for a gain-switched Ti:sapphire laser, which is pumped by the frequency-doubled output of a Q-switched Nd:YAG laser, and includes a BBO non-linear crystal for intra-cavity frequency-doubling. The bandwidth of the fundamental wave in this free-running laser was ~90 nm whilst the PMB of the BBO crystal in this particular configuration was ~3 nm. A 3 nm spectral hole is 'burnt' into the fundamental spectrum by the doubling effect; the frequency conversion process is effectively suppressing the fundamental intensity with the PMB. In this case, if the BBO crystal is rotated in the cavity, changing the phase-matching angle, then this spectral hole can be tuned to different parts of the oscillating fundamental bandwidth. This example also illustrates the importance for conversion efficiency of matching the fundamental bandwidth to the PMB: only the radiation within the PMB is converted. This was demonstrated for the present example by introducing a seeding beam from a single-mode diode laser into the Ti:sapphire cavity which, when resonant, resulted in a narrowing of the fundamental bandwidth to less than the PMB and a consequent improvement in the second-harmonic conversion efficiency from <3% to 17% [26].

20.3 Sum and Difference Frequency Mixing

Second-harmonic generation is a special case of the more general phenomenon of SFM (sometimes called 'up-conversion'), in which the two waves that mix together *via* a second-order non-linear susceptibility to produce a third are at the same frequency. The analysis of the SFM process essentially proceeds along the same lines as that of second-harmonic generation presented in the previous section but with the two initially present waves allowed to be of different frequencies, i.e. $\omega_1 \neq \omega_2$.

SFM and second-harmonic generation both obey the general phase-matching relations for frequency and propagation vector (corresponding to photon energy and momentum conservation, respectively):

$$\begin{aligned} \omega_3 &= \omega_1 + \omega_2 \\ \boldsymbol{k}_3 &= \boldsymbol{k}_1 + \boldsymbol{k}_2 \end{aligned} \tag{20.32}$$

with ω_3 and $\boldsymbol{k}_3$ representing the frequency and propagation vector, respectively.

However, two waves interacting in a non-linear material also produce a wave corresponding to the difference in their energy and momentum. This process is called difference frequency mixing or 'down-conversion'. That both sum and difference waves are produced concurrently can be seen by considering two plane waves, with entirely real amplitudes A_1 and A_2, interacting *via* an effective non-linear coefficient, d_{eff}, to produce a plane polarization wave also with an entirely real amplitude, P_3, where

$$\begin{aligned} P_3 \cos(\boldsymbol{k}_3 \cdot \boldsymbol{r} - \omega_3 t) &= d_{\text{eff}} E_1 \cos(\boldsymbol{k}_1 \cdot \boldsymbol{r} - \omega_1 t) E_2 \cos(\boldsymbol{k}_2 \cdot \boldsymbol{r} - \omega_2 t) \\ &= \frac{d_{\text{eff}}}{2} E_1 E_2 \left\{ \cos\left([\boldsymbol{k}_1 + \boldsymbol{k}_2] \cdot \boldsymbol{r} - [\omega_1 + \omega_2] t \right) \right. \\ &\quad \left. + \cos\left([\boldsymbol{k}_1 - \boldsymbol{k}_2] \cdot \boldsymbol{r} - [\omega_1 - \omega_2] t \right) \right\}. \end{aligned} \tag{20.33}$$

Which of the sum or difference frequency light waves actually develops depends on which of them is phase-matched; only the phase-matched wave will have significant conversion efficiency. Hence, equating the space and time-varying components yields the phase-matching equation for difference frequency mixing:

$$\begin{aligned} \omega_3 &= \omega_1 - \omega_2 \\ \boldsymbol{k}_3 &= \boldsymbol{k}_1 - \boldsymbol{k}_2 \end{aligned} \tag{20.34}$$

where $\omega_1 > \omega_2 > \omega_3$ and $k_1 > k_2 > k_3$. Photon energy and momentum are conserved in this case, because physically, a ω_2 photon stimulates a ω_3 photon to decompose into a ω_3 photon and a further ω_2 photon.

As for SFM, the field strengths, E, and intensities, I, used in the analysis of difference frequency mixing are instantaneous quantities and apply equally to both pulsed and steady-state interactions. Again, pulse energies can be simply retrieved by integrating the appropriate instantaneous power function. In contrast to second-harmonic generation, however, pulsed sum and difference frequency mixing is further complicated because the two interacting pulses are not necessarily synchronized or of the same duration. Any temporal mismatch between the pulses will reduce the overall conversion efficiency because the magnitude of the generated non-linear polarization is proportional to the product of the fields corresponding to each pulse. For maximum conversion efficiency, care has to be taken then to maximize the pulse overlap integral:

$$\int_{-\infty}^{\infty} E_1(t)E_2(t-\tau)\,\mathrm{d}t \tag{20.35}$$

where E_1 and E_2 are independent fields corresponding to the interacting pulses of generally different functional forms and durations and τ is the delay time between the pulses. It is usually straightforward to ensure that the pulses are synchronized, i.e. $\tau = 0$, by suitable electronic triggering of two separate laser pulses [25]. The pulse durations of the two laser sources are determined by such factors as the gain media used (usually different if two distinct wavelengths are being mixed), the pumping rate and the cavity design. Hence, there is typically less control over the relative durations of the interacting pulses.

20.3.1 Theory

In this section, the general theories of the sum and difference frequency mixing of plane waves will be described and some special cases examined including: perfect phase-matching (i.e. $\Delta k = 0$), exact photon balance between the interacting waves (i.e. $\sigma = 1$), one interacting field of much larger intensity than the other ($\sigma = 0$ or $\sigma = \infty$) and low total conversion efficiency ($D_{1,2} \rightarrow 0$).

20.3.2 Sum Frequency Mixing

The analysis developed by Milton for the mixing of three plane waves and presented in section 20.2.2 for the case of second-harmonic generation can be generalized for SFM simply by allowing $\omega_1 \neq \omega_2$, and hence, the efficiency of converting wave 1 to wave 3, η_{13}, is

$$\eta_{13} = \frac{I_3}{I_1} = \frac{\omega_3}{\omega_1} B \times sn^2\left(A\sqrt{D_1}, \gamma\right) \tag{20.36}$$

and similarly, the efficiency of converting wave 2 to wave 3, η_{23}, is

$$\eta_{23} = \frac{I_3}{I_2} = \frac{\omega_3}{\omega_2} B \times sn^2\left(A\sqrt{D_2}, \gamma\right) \tag{20.37}$$

where D_i is the dimensionless 'non-linear drive' parameter for wave i and is defined as

$$D_i = K L^2 \frac{I_i}{\hbar\omega_i} \tag{20.38}$$

D_i is equivalent to the *photon number* conversion efficiency from wave i as $D_i \rightarrow 0$. Note that whilst for the special case of second-harmonic generation by type *I* phase-matching, the photon balance parameter, σ, was equal to unity, for SFM $\sigma \neq 1$, in general.

Perfect phase-matching. For the case of $\Delta k = 0$, the conversion efficiency for the ith wave is considerably simplified and becomes

$$\eta_{i3} = \frac{\omega_3}{\omega_i} \sigma \times sn^2\left(A\sqrt{D_i}, \sqrt{\sigma}\right). \tag{20.39}$$

From now on, it will be assumed that the SFM interactions described are all phase-matched.

Perfect photon balance. Under the condition that both the interacting fields, $i = 1,2$, are equal in photon number, that is $I_1/\omega_1 = I_2/\omega_2$, then the parameter $\sigma = 1$ and the conversion efficiencies become

$$\begin{aligned} \eta_{13} &= \frac{\omega_3}{\omega_1} \frac{I_2}{\hbar\omega_2} \tanh^2\left(\sqrt{D_1}\right) \\ \eta_{23} &= \frac{\omega_3}{\omega_2} \frac{I_2}{\hbar\omega_2} \tanh^2\left(\sqrt{D_2}\right) \end{aligned} \tag{20.40}$$

which is the same result as for second harmonic if $\omega_1 = \omega_2$. It can be shown that the elliptic function *sn* reduces to a monotonically growing function (i.e. tanh) only when the condition $\sigma = 1$ is met. In other words, there is no back-conversion from the generated wave ($i = 3$) to the initially interacting waves ($i = 1,2$) only when there is photon number parity between the two initial fields. This is clearly not necessarily true for general SFM between waves of different frequencies; it is also not always achieved for second-harmonic generation when a type II or III phase-matching scheme is used. In those cases, the polarization of the fundamental wave is usually orientated at some angle to the optic axis of the non-linear crystal so that it can be regarded as consisting of two component fields, one parallel to the optic axis and one orthogonal. Only if this angle is exactly 45° will the magnitude of the two component fields be equal and the photon number parity condition be met. Hence, in general, sum frequency mixed interactions can suffer from back-conversion of the generated wave.

Large intensity ratio, $I_1 \gg I_2$. If the intensity of one of the interacting fields is much larger than the other, and we can choose $I_1 \gg I_2$ and still retain generality, the conversion efficiency becomes

$$\eta_{23} = \frac{\omega_3}{\omega_2} \sin^2\left(\sqrt{D_1}\right). \tag{20.41}$$

However, caution must be exercised when using this approximate form because its domain of validity is difficult to estimate [7].

Weak non-linear interaction, $D_1 \rightarrow 0$. In the limit of only a weak interaction between the fields, the conversion efficiency becomes

$$\begin{aligned} \eta_{23} &\rightarrow \frac{\omega_3}{\omega_2} D_1 \\ \eta_{23} &= \frac{\omega_3}{\omega_1} D_2. \end{aligned} \tag{20.42}$$

20.3.3 Difference Frequency Mixing

The general solution to the coupled wave equations for the difference frequency mixing of plane waves yields the following result for non-linear conversion efficiency

$$\eta_{13} = \frac{I_3}{I_1} = \frac{\omega_3}{\omega_1} B' \left[\frac{\gamma' sn^2\left(\Lambda, \sqrt{\gamma'}\right)}{1 - \gamma' sn^2\left(\Lambda, \sqrt{\gamma'}\right)} \right] \qquad (20.43)$$

where

$$\begin{aligned} \gamma &= \frac{A'}{A' + B'} \\ \Lambda &= \sqrt{D} \times \sqrt{(\sigma - 1 - \varepsilon)^2 + 4\sigma} \\ A', B' &= \tfrac{1}{2}\left[\pm(\sigma - 1 - \varepsilon) + \sqrt{(\sigma - 1 - \varepsilon)^2 + 4\sigma} \right] \\ \sigma &= \frac{I_2}{I_1}\frac{\omega_1}{\omega_2}. \end{aligned} \qquad (20.44)$$

This expression has been derived under the same assumptions as for the SFM analysis.

As for SFM, approximations can be made to the above expression under different conditions:

Perfect phase-matching, $\Delta k = 0$.

$$\eta_{13} = \frac{\omega_3}{\omega_1} \left[\frac{\gamma' sn^2\left(\sqrt{D_1(1+\sigma)}, \sqrt{\gamma'}\right)}{1 - \gamma' sn^2\left(\sqrt{D_1(1+\sigma)}, \sqrt{\gamma'}\right)} \right] \qquad (20.45)$$

where now

$$\gamma' = \frac{\sigma}{1+\sigma}. \qquad (20.46)$$

Large intensity ratio, $I_1 \gg I_2$. If there is a large ratio between the intensities of the two interacting waves, then the photon balance parameter $\sigma \to 0$ and the conversion efficiency to the difference frequency becomes:

$$\eta_{13} = \frac{\omega_3}{\omega_2}\frac{I_2}{I_1} \sin^2\left(\sqrt{D_1}\right). \qquad (20.47)$$

Weak non-linear interaction, $D_1 \to 0$. When the mixing between the waves is weak due either to weak beam intensities, small effective non-linear coefficient, short interaction length or poor phase-matching then the conversion efficiency tends to the following expression:

$$\eta_{13} = \frac{\omega_3}{\omega_2}\frac{I_2}{I_1} D_1. \qquad (20.48)$$

Gaussian beams. The analyses presented before for sum and difference mixing assume that the interacting waves were all plane, which implies that they are infinite in transverse extent (see the first assumption in Section 20.2.2). As for second-harmonic generation, experimentally, beams of finite cross section will be used and these will be most likely a TEM_{00} Gaussian mode, and hence, consideration of the effect of this deviation from the plane wave approximation has to be considered. A comprehensive analysis of three-wave mixing between Gaussian modes has been carried out by Boyd and Kleinman [10]. This analysis reveals that for maximum conversion, the *confocal parameter, b*, of all three waves must be equal; the confocal parameter for the *i*th wave is given by

$$b_i = k_i w_0^2 \qquad (20.49)$$

where w_0 is the radius of Gaussian beam waist and hence b is twice the Rayleigh length, z_0. Therefore, for optimally efficient sum and difference frequency mixing, the two interacting beams must be focused such that they are collinear and the position of their beam waists overlaps, and furthermore, their spot sizes (i.e. $\text{beam waist area} = \pi w_{0,i}^2$) must be in the same ratio as their respective wavelengths, λ_i, i.e.

$$\frac{w_{0,1}^2}{w_{0,2}^2} = \frac{\lambda_1}{\lambda_2}. \qquad (20.50)$$

Further to this, for maximum conversion efficiency from a non-linear crystal of length, l (assuming crystal length limits the interaction length in this case, i.e. $l = L$), then the same optimum focusing condition as was described for second-harmonic generation in Section 20.2.2 applies: $2.84 \times b = 5.68 \times z_0 = l$.

20.4 Third- and Higher-harmonic Generation

Third- and higher-order non-linear effects are generally very much weaker than the second-order phenomena. This is because the magnitude of the third-order non-linear susceptibility, $\chi^{(3)}$, is approximately seven orders of magnitude smaller than $\chi^{(2)}$, and the higher-order non-linear susceptibilities, $n > 3$, are much smaller than that. Hence, the efficient generation of third- and higher-order harmonics is not done by utilizing the corresponding order of non-linear response of the material but rather by using a sequence of second-order processes. For instance, laser radiation can be converted to its third harmonic by initially frequency-doubling part of the output and then SFM this second-harmonic wave with the residual fundamental wave, as illustrated in Figure 20.13.

Each individual second-order frequency conversion step of an overall high-order harmonic generation scheme can be treated separately, and hence, the analyses presented in the previous section can be used to describe the whole process. One step interacts with the next simply by determining the photon balance parameter, σ, of the radiation incident on the subsequent step. As noted in the previous section, the conversion efficiency is only a monotonic function of distance through the crystal for a perfect photon balance, i.e. $\sigma = 1$, and hence, only in this case is the mixing process free from the possibility of back conversion. For perfect photon balance, complete conversion of the fundamental to the desired harmonic can be achieved, in principle. In all other cases, there will be an optimum distance into the crystal up to which the generated wave grows steadily in amplitude and after which the amplitude decreases or oscillates. Efficient high-harmonic

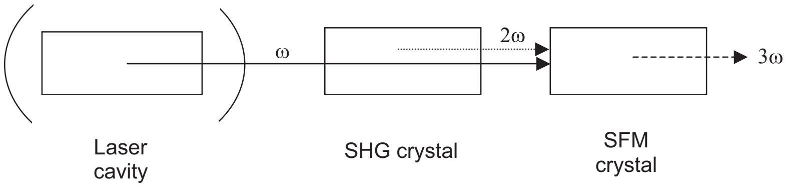

FIGURE 20.13 Third-harmonic generation by cascaded SHG and SFM.

generation schemes, therefore, ensure that there is a perfect photon balance before each constituent frequency conversion step.

For the third-harmonic generation, Craxton [27,28] demonstrated that the requirement of perfect photon balance can be achieved automatically by an appropriate choice of polarization angle in the frequency-doubling crystal (the first step). In fact, it was shown that there are several possible ways of achieving this, depending on the type of phase-matching used in both steps and the polarization angle. In each case, however, exactly 2 out of 3 of the fundamental photons are converted into second-harmonic photons after the first step, leaving an equal number of second-harmonic and residual fundamental photons for the final SFM step, thus ensuring a theoretical 100% conversion to the third harmonic. In practice, the use of each of these schemes has resulted in up to 80% conversion efficiency to the third harmonic [29], but for simplicity, those schemes that obviate the need for rotation of the fundamental polarization by wave plates in-between stages are preferred. The need for a wave plate is removed by careful choice of the polarization angle of the fundamental beam relative to the optic axis of the first crystal. For a negative uniaxial crystal, for example, a polarization angle of 55° results in two-thirds of the photons contributing to the o-ray and one-third to the e-ray. After the frequency-doubling stage, maximum conversion efficiency produces equal numbers of second-harmonic and fundamental photons, with the polarization angle for the residual fundamental being either 0° or 90° depending on the phase-matching type. This perfect photon balance and the alignment of the residual fundamental polarization so that it is entirely an o- or e-ray allows complete conversion to the third harmonic. In contrast, at other initial polarization angles, the fundamental after the first stage is neither purely an o- nor an e-ray. Hence, even though the photon numbers may be balanced, complete conversion to the third harmonic is not possible.

A notable example of multiple harmonic generations is Zayhowski's work using microchip lasers [30]. In that case, a passively Q-switched, microchip laser (a 1 mm^3 dielectrically coated Nd:YAG crystal) was used to produce 8.0, 3.5, 0.3, 0.7 and 0.01 μJ of pulse energy at the first to fifth harmonic, respectively; KTP and BBO were used as the non-linear crystals (see the next section for a description of these materials). The excellent beam quality and short (~200 ps) pulse duration obtained from microchip lasers make them well suited to non-linear frequency conversion at such modest pulse energies.

Very high harmonic generation that produces light in the extreme ultraviolet (XUV) or X-ray regions of the spectrum can be achieved at very high intensities (typically in the terawatt range or higher) in, usually, a noble gas medium. In this process, atoms are ionized by the laser field and the resulting free electrons accelerated by the same field before recombination. The high-energy photons produced in this way can interfere constructively to produce a coherent XUV or X-ray beam. Further details can be found in a review [31].

20.5 Non-linear Materials for Frequency Conversion

Since the first demonstration of harmonic generation in the early sixties just after the invention of the laser, a great number of non-linear crystals have been studied. This section will not attempt a comprehensive survey of these materials; such reviews already exist. For instance, the book by Dmitriev et al. [20] provides an extensive review of over 50 non-linear crystals and lists all the parameters necessary to calculate the phase-matching angles and conversion efficiencies for each material. Yariv [3] provides a useful table on non-linear coefficients for over 20 materials. In contrast, Koechner [32] provides a more selective survey of non-linear materials but with more commentary on each (see further reading for details of these books). Similarly, this section will concentrate on those few materials whose superior characteristics have meant that they have come to prominence. These materials can be divided into two classes: *birefringent*, for which phase-matching is ensured by using the natural properties of the crystal, and *quasi-phase-matched*, which rely on an imposed periodic poling of the crystal domains to achieve phase-matching. Self-doubling and self-summing crystals will also be described, which are an interesting, though not yet commonplace, class of materials.

There are many questions regarding the properties of non-linear crystals that can have a bearing on their selection for a particular application; some important ones are listed below:

1. Is it possible to phase-match the interaction in question?
2. What will the effective non-linear coefficient be?
3. Do all the wavelengths concerned lie within the transparency range of the crystal?
4. Will the peak intensity damage the crystal?
5. What are the absorption coefficients at the relevant wavelengths?
6. Is the divergence of the pump laser larger than the angular bandwidth?

7. Is the spectral width of the pump laser larger than the frequency bandwidth?
8. If the interaction has a small temperature bandwidth, will temperature stabilization of the crystal be required?
9. What crystal sizes are available?
10. What is the optical quality of the crystal?
11. Is the crystal chemically stable?
12. Is the crystal mechanically stable?

The relative importance of these questions will depend on the details of the application. For instance, for cw interactions, a large effective non-linear coefficient and a low absorption coefficient are usually desirable, whilst for the frequency conversion of high-energy pulses, a high damage threshold and good optical quality are likely to be more important. Moreover, if the beam path within the material limits the interaction length then large crystal size can compensate for a lower effective non-linear coefficient.

20.5.1 Birefringent Materials

The phase-matching of three-wave mixing interactions in this class of materials relies on the natural angle, polarization, temperature or field dependence of the refractive indices experienced by the interacting waves as they pass through the medium. The materials used for three-wave mixing in the UV, visible and near- and mid-infrared are described in this section. Direct comparisons of some of the crystals described here have been reported elsewhere [33,34]. In this work, the properties of the materials discussed are compared in Table 20.2. Since many of the important material performance parameters, such as effective non-linear coefficient and absorption coefficient, are determined by the particular non-linear interaction and the wavelengths of the beams involved; the relative merit of each type of crystal depends on the application. Nevertheless, a comparison based on a particular application does indicate relative performance; the parameters listed in Table 20.2 are based, where possible, on perhaps the most common application of non-linear crystals: the second-harmonic generation of the fundamental wavelength of an Nd:YAG laser (1064 nm); the other two materials listed are compared on the basis of their performance in frequency-doubling the fundamental of a CO_2 laser.

KDP, *KD*P*, *ADP and CDA*. Good optical quality crystals of potassium dihydrogen phosphate, KH_2PO_4, and its deuterated analogue KD*P can be grown from aqueous solution at room temperature up to diameters of 27 cm, the largest size for any non-linear crystal [35]. However, as well as being water-soluble, these crystals must be used below 100°C and heated at a rate no greater than 5°C min^{-1}. The non-linear coefficients of KDP are rather low compared to other leading non-linear materials ($d_{36} = 0.44$ pm V^{-1}; $d_{36} = 0.40$ pm V^{-1} for KD*P); however, this is largely compensated for by the large size and good optical quality of the crystals, and high conversion efficiencies have been achieved. Since KDP and another of its analogues, ammonium dihydrogen phosphate (ADP), were the crystals used in the first demonstration of phase-matched second-harmonic generation [36], the non-linear coefficients of other materials are often given relative to that of KDP. A comprehensive calculation of the properties of KDP relevant to the generation of harmonics of 1 μm radiation has been reported [37]. Two further analogues of KDP, caesium dihydrogen phosphate (CDA) and caesium dideuterium phosphate (CD* A), have also been studied and are interesting because they can non-critically phase-match the fundamental wavelength of both Nd:YAG and Nd:glass [38,39].

KTP and KTA. Potassium titanyl phosphate, $KTiOPO_4$, (KTP) has a very favourable set of characteristics when compared with other birefringent materials; other materials might score more highly in particular categories but KTP has superior overall properties. It has large non-linear coefficients ($d_{31} = 6.5$ pm V^{-1} and $d_{32} \sim 5.0$ pm V^{-1}), phase-matches over

TABLE 20.2

Properties of Some Non-linear Crystals Pertinent to SHG

Material	Phase-Matching Type[a]	Phase-Matching Angle[a]	d_{eff} (pm V^{-1})[a]	Transparency Range (μm)	Damage Threshold (GW cm^{-2})[b]	Absorption Coefficient (cm^{-1})[a]	Angular Bandwidth (mrad)[c]	Temperature Bandwidth (°C)[c]	Spectral Bandwidth (nm)[c]
KD*P	II	53.5°	0.38	0.2–2.0	0.5	0.005	5.0	13	6.5
KTP	II	25°	5.27	0.35–4.5	1.0	0.05	15–68	25	0.56
$LiNbO_3$	I	78°	5.89	0.33–5.5	0.06	0.08	3.1	1.1	0.3
BBO	I	21°	2.01	0.2–2.6	23	0.005[d]	1.8[e]	50[e]	0.66[d]
LBO	I	90°	1.17	0.16–2.6	19	0.000 35[f]	70[f]	5.8[f]	4.37[g]
Te†	I	14.5°	629	3.8–32	0.045	0.96	0.7	—	0.001
$ZnGeP_2$†	I	76°	35.4	0.74–12	0.06	0.9	24.5	44[h]	0.05

Notes: All the data in the table have been taken from Dmitriev et al. (see further reading), unless otherwise indicated:

[a] for 1064 nm radiation, except for † which are for 10 μm radiation;

[b] for 1064 nm, ~10 ns pulses, except for† which are for 10 μm and ~200 ns;

[c] for a 1 cm interaction length;

[d] [32, Table 10.1];

[e] [43];

[f] [45];

[g] Velsko S. P., Webb M., Davis L. and Huang C. 1991 *IEEE J. Quantum Electron*. **27** 2182;

[h] Kato K. 1997 *Appl. Opt*. **36** 2506.

a wide wavelength range (for type II) and has broad angular and temperature bandwidths; its thermal properties are also good and it has a high damage threshold. These properties often make it the non-linear crystal of choice for the important application of the frequency-doubling of Nd:lasers. However, growing KTP is a difficult process, which limits the crystal size and availability makes it an expensive material. Even with the relatively small size of crystals available, the high non-linear coefficients of KTP mean that the high-frequency doubling efficiencies can be readily achieved. KTP is also susceptible to photochemical degradation or 'grey tracking', which is a cumulative effect dependent on total exposure; it leads to increased absorption and eventual crystal-cracking. Fortunately, operation at high temperature (>65°C) prevents and reverses the degradation process. Potassium titanyl arsenate (KTA) is an isomorph of KTP that has largely similar properties. It differs from KTP in that it cannot phase-match SHG for a Nd:YAG laser, although it will phase-match 1053 nm radiation and so can be used to frequency-double Nd:YLF lasers and, for this application, exhibits a 1.6×higher effective non-linear coefficient [40]. It also absorbs less than KTP in the 3–5 µm part of the infrared spectrum and has found use as a material for optical parametric oscillators.

LNB. Lithium niobate, $LiNbO_3$, has favourable chemical and mechanical properties, being non-hygroscopic and hard, thus making the processing and polishing of these crystals straightforward. It also has relatively large non-linear coefficients ($d_{31} = -5.4$ pm V^{-1} and $d_{22} = 2.8$ pm V^{-1};) and can be temperature-tuned when non-critically phase-matched. However, a low damage threshold and a particular susceptibility to degradation by photorefractive damage offset these advantageous properties. As with KTP, this degradation is reversed by increasing the temperature but, for the LNB, the temperatures required are much higher, at ~170°C. The susceptibility to damage is reduced by doping LNB with magnesium oxide, MgO, to a typical level of 5%. Due to these damage problems and emergence of newer materials without these limitations, LNB had been receiving less attention until the invention of the QPM technique. It was the first material to be successfully periodically poled and, hence, once again became the focus of much interest. Quasi-phase-matched materials will be covered in more detail in the next section.

BBO. Barium borate, BaB_2O_4 (BBO), was discovered in 1984 by Chen et al. [41] and has two crystalline phases, α and β, with the β-phase being non-centrosymmetric. BBO has non-linear coefficients ($d_{22} = 2.2$ pm V^{-1} and $d_{31} = 0.16$ pm V^{-1}) that are somewhat smaller than some of the other materials discussed but it is its other properties that make it interesting. It has a wide temperature PMB, low absorption (~0.01 cm^{-1} at $\lambda = 532$ nm [42]) and a very high damage threshold. Of particular note is that the transparency range of BBO extends down to wavelengths of just 189 nm, thus allowing second-harmonic generation and sum-frequency mixing into the ultraviolet. The only major weakness of BBO as a non-linear material is that it has a small angular PMB. A comprehensive review of the properties and applications of BBO has been published [43].

LBO. Lithium triborate, LiB_3O_5 (LBO), was discovered in 1988 by the same group who had earlier developed BBO [44]. At 155 nm, the short-wavelength limit of its transparency range extends even further into the important UV part of the spectrum than does that of BBO. It is a hard, chemically stable, non-hygroscopic crystal making it easy to handle and able to take a good polish. It can also be non-critically phase-matched and temperature-tuned. However, it has non-linear coefficients that are even smaller than those of BBO ($d_{31} = 1.1$ pm V^{-1} and $d_{32} = 1.2$ pm V^{-1}) but does not suffer from the same narrow angular bandwidth. Its properties and applications have been comprehensively reviewed [45].

20.5.2 Quasi-Phase-matched Materials

The physical properties of quasi-phase-matched materials are identical to their birefringently phase-matched counterparts except with regard to their phase-matching behaviour and the effective non-linear coefficients. Nowadays, the domain structure is imposed onto bulk ferroelectric materials by lithographically writing a pattern of electrodes onto the crystals and then applying large electric fields (typically 25 kV mm^{-1} for lithium niobate); hence, these materials are often termed 'periodically poled'. A more detailed description of poling process is given in [46]. Another advantage of the poling technique is that domain structures other than the simple periodic grating can be implemented and these can determine, for example, the spectral dependence of the conversion [47], the tuning range [48] and the beam profile [49].

Periodically poled lithium niobate. Periodically poled lithium niobate (PPLN) was the subject of much of the initial development of QPM materials fabricated by this technique because it is ferroelectric and because of its favourable chemical and mechanical properties, making it available in large, easily processable samples. The PPLN crystal is usually poled so that phase-matching occurs for all three waves polarized parallel to the crystal z-axis. This enables the largest non-linear coefficient component, $d_{33} = 34$ pm V^{-1}, to be utilized; hence, theoretically $d_Q = 2d_{33}/\pi = 21.6$ pm V^{-1} but imperfections in the domain grating lead to a reduction in the effective value of d_Q to typically [50] 15–17pm V^{-1}. Experimentally, QPM typically leads to a factor ~10–20 improvement in the conversion efficiency over the birefrigent phase-matched case (which can only use the smaller d_{31} component) [51]. This high non-linearity enables cw and low-energy pulses to be efficiently converted to the second harmonic, even for an extra-cavity, single-pass arrangement. For example, approximately 40% frequency-doubling conversion efficiency has been obtained in such an arrangement both for a 6.5 W cw 1064 nm Nd:YAG laser [52] and a 7 nJ $pulse^{-1}$, 946 nm Nd:YAG laser [53]. A poling period could be chosen such that NCPM occurred at room temperature but generally PPLN is operated at an elevated temperature, typically ~150°C, to mitigate the photorefractive effect.

Periodically poled KTP. The periodic poling of KTP was first demonstrated in 1994 and has developed rapidly since. Periodically poled KTP (PPKTP) has a number of advantages over PPLN: the field required for poling is approximately an order of magnitude less, the higher crystal anisotropy prevents lateral domain growth and so allows smaller domain sizes to be fabricated more consistently, its transparency extends further into the UV and, finally, KTP is less susceptible to photorefractive damage allowing room-temperature operation [54]. On the other hand, the value of the non-linear coefficient tensor component used in PPKTP interactions, also d_{33}, is at 16.9 pm V^{-1} less than half that of PPLN. Nevertheless, conversion efficiencies of approximately 65% have been reported for the extra-cavity frequency-doubling of sub-millijoule pulses in both the picosecond and nanosecond [55] regimes for Nd:YAG (twice that for BPM KTP). For a cw Ti:sapphire laser, a doubling efficiency of 10% has been reported [56] for a 1 cm long crystal. The greater UV transparency of KTP compared with LNB has been utilized to generate 390 nm radiation from a mode-locked femtosecond Ti:sapphire laser [56] and 460 nm light from a mode-locked diode laser [57].

Periodically poled lithium tantalate. Periodically poled lithium tantalate (PPLT) has a smaller non-linear coefficient than either PPLN or PPKTP: $d_{33} = 13.8$ pm V^{-1} for a wavelength of 1064 nm, corresponding to a theoretical, and experimentally observed, effective non-linear coefficient for first-order QPM of $d_Q =$ pm V^{-1} [58]. However, it does have a photorefractive damage threshold nearly twice that of PPLN [59] and is transparent to wavelengths as low as 280 nm [60]. For pumping with low-power cw diodes, conversion efficiencies of 1.2% $W^{-1}cm^{-1}$ have been demonstrated [61]. For higher peak powers, conversion efficiencies of 13% and 35% have been reported for pulsed diode [62] and fibre lasers [63]. For doubling into the UV region, however, the effective d_Q achievable drops to ~2 pm V^{-1} because of the difficulty in fabricating grating periods of ~2 μm and the necessity of using second-order ($m = 2$) QPM in some cases [62,63].

Periodically poled rubidium titanyl arsenate. Periodically poled rubidium titanyl arsenate, $RbTiOAsO_4$, or PPRTA is an isomorph of KTP and shares many of its advantageous properties such as large non-linear coefficients (e.g. $d_{33} = 15.6$ pm V^{-1} [64]) and a high-photorefractive damage threshold permitting room-temperature operation; like KTP, RTA requires poling fields approximately one order of magnitude less than LNB. Furthermore, the absorption coefficient for RTA is smaller than that for KTP in the mid-infrared region [65,66], which is advantageous for DFM; RTA is flux grown, a technique that often allows crystals to be produced more cheaply and in larger sizes than the hydrothermal technique used for KTP. A normalized conversion efficiency of 6.5% $W^{-1}cm^{-1}$ for the frequency-doubling of cw laser diode at a wavelength of 875 nm has been reported [64].

20.5.3 Self-doubling and Summing Materials

Certain non-linear materials can be doped with laser active ions to produce crystals that act as both a laser gain medium and an intra-cavity frequency doubler or summer. The requirement that the crystal must both accept the dopant ion and also be phase-matchable for the laser emission wavelength in practice restricts this phenomenon to only a few possible combinations of ions and crystals. A thorough review of self-doubling and self-summing lasers, including a survey of materials and performance results, has been published [67]; it also contains a theoretical analysis of the self-doubling and self-processes.

The first demonstration of a self-doubled laser [68] utilized Tm doped in LNB (doped also with MgO to reduce photorefractive damage), although Nd and Yb have been the more common dopant ions. Apart from LNB, other non-linear crystals that are successfully doped with laser active ions include $LaBeGeO_5$ (LBG), $Ba_2NaNb_5O_{15}$ (BNN), $Gd_2(MoO_4)_3$, $YAl_3(BO_3)_4$ (YAB), $CaY_4(BO_3)_3O$ (YCOB) and $CaGd_4(BO_3)_3O$ (GdCOB). Of the Nd-doped crystals, YAB has produced the best results so far [69,70], and the best reported efficiency for a Yb-doped laser has been for a LNB:MgO crystal [71]. Self-frequency doubling has also been reported in some quasi-phase-matched materials: periodically poled Nd-doped lithium tantalate [72] and periodically poled Ti-doped LN [73].

20.6 Frequency Conversion of Particular Lasers

This section surveys the materials and techniques used in the frequency conversion of a few common laser types. Each laser will be examined in turn and the non-linear techniques utilized for different relevant regimes of operation, such as cw, Q-switched or mode-locked and high- or low-energy/power. Further information of this type can be found in the books listed in further reading; in particular, Koechner [32] describes a variety of laser cavity designs for the intra-cavity frequency-doubling of Nd:YAG lasers, and Dmitriev et al. [20] have produced a very comprehensive survey of the techniques used for harmonic generation and sum and difference mixing of a wide range of important lasers, including all the major solid-state and gas types.

20.6.1 Nd Lasers

KTP is probably the most important non-linear material for the SHG of Nd lasers in both the cw regime (see [74], for example) and the pulsed regime up to high powers [75] and for pulse durations greater than a few hundred picoseconds [76]. Its large non-linearity and large angular and temperature PMBs for the SHG of 1.06 μm radiation (~0.5° and 20°C, respectively, for a 1 cm long crystal [77]) are a compelling combination for most applications; it also has a high damage threshold and is non-hygroscopic. In the pulsed regime, extra-cavity conversion efficiencies of 55%–60% have been obtained [75,76].

However, for very high-energy picosecond Nd lasers, such as the ones used in thermonuclear fusion research, KDP may be a more appropriate material. KDP has a number of advantageous properties in this regime: it is resistant to optical damage by sub-nanosecond pulses of intensities up to 10 GW cm^{-2}, it exhibits low one- and two-photon absorption at the harmonics of Nd lasers and both picosecond continuum generation and stimulated Raman scattering do not occur in this material for intensities less than 100 GW cm^{-2}. Moreover, high-quality KDP crystals can be grown to large sizes, which enable the large beam cross sections necessary to prevent damage to optical components to be accommodated. The lower value of the effective non-linear coefficient for KDP compared with KTP is not an issue in this high peak power regime, and second-harmonic conversion efficiencies of 90% have been reported [78].

Higher-harmonic generation for Nd lasers has been achieved for a number of different non-linear materials including KDP, ADP and BBO. For instance, KDP has been used to convert 0.15 ns pulses at the fundamental wavelength of Nd:YAG to the third harmonic with 32% efficiency [79], and a 85% second- to fourth-harmonic efficiency has been achieved for 30 ps pulses in ADP [80]. For very high-intensity lasers, the overall conversion efficiency (fundamental to harmonic) rises to 80% for the third [78] and 70% for the fourth harmonic [81]. A combination of BBO and KTP has also been used to produce tunable UV radiation (230–330 nm) from a Q-switched Nd:YAG by a combination of harmonic generation and sum-frequency mixing [82] with an overall efficiency of 5%.

20.6.2 Ti:sapphire Lasers

Ti:sapphire (i.e. the Ti^{3+} ion doped into Al_2O_3) has the widest tunability of any gain medium in the visible and near-infrared optical region; lasing having been demonstrated from 645 nm to 1178 nm [83]. This impressive tunability can be extended even further, however, by the use of non-linear frequency conversion techniques, to cover the range from ~200 nm to 3000 nm. Given the wide range of possible fundamental wavelengths from a Ti:sapphire laser, it is not surprising that there are a number of non-linear crystals that will phase-match over at least part of its tuning range. In fact, three of the leading non-linear materials described in the previous section will frequency-double the output of a Ti:sapphire laser over its full tuning range and have low absorption at the second-harmonic wavelength. These three are LBO, BBO and KDP, and a comparison of the relative performance of these materials for frequency conversion applications (second-, third- and fourth-harmonic generation, and both sum and difference frequency mixing) is reported in [72]. The use of NCPM, temperature tuned LBO for the frequency-doubling of Ti:sapphire output has also been studied elsewhere [84] and includes details of temperature-tuning curves and PMBs. For SHG, LBO proved to have the lowest threshold of the three materials for both type I and type II phase-matching, with the latter being significantly the lowest. However, LBO will only phase-match for the entire Ti:sapphire tuning range in a type I arrangement; for type II, there is a short wavelength cut-off at 792 nm. Of the other two materials, BBO demonstrated the lowest threshold and highest conversion efficiency, and importantly, because of its sensitivity to change in phase-matching angle, a single crystal could be used to frequency-double the entire tuning range of Ti:sapphire. (Other materials need to have several crystals, each cut at different angles to the crystal axes, to cover the entire range.) The disadvantage of this angular sensitivity, however, is small phase-matching tolerance angles, necessitating low divergence pump beams for efficient frequency conversion. On the other hand, the phase-matching temperature for BBO was the greatest of the three at ~20°C.

20.6.3 Carbon Dioxide Lasers

The long fundamental wavelength, $\lambda = 10\,\mu m$, of the CO_2 laser lies outside the transparency range of all of the major non-linear crystals described in the previous section. Frequency conversion of CO_2 laser output is achieved by using one of a number of semiconductor materials that are non-centrosymmetric and are transparent deep into the infrared; these include proustite (Ag_3AsS_3), pyrargyrite (Ag_3SbS_3), silver thiogallate ($AgGaS_2$), $AgGaSe_2$, $ZnGeP_2$, $CdGeAs_2$, gallium selenide (GaSe), mercury sulphide (HgS), selenium and tellurium. The important properties of these for frequency conversion can be found in Dmitriev et al. [20], and the properties of $ZnGeP_2$ and tellurium are compared in Table 20.2. The non-linear coefficients for these materials can be very large compared with those of the crystals used for frequency conversion in the UV, visible and near-infrared, e.g. at 10 μm, tellerium has d_{11} = 650 pm V^{-1}. However, the advantage of the consequent factor of ~10^4 increase in $(d_{eff})^2$ is offset by the factor of ~10 decrease in the frequency of all three of the interacting waves and the rise in the values of refractive index experienced by each wave (e.g. at 10 μm $n_0 \approx 5$ and $n_e \approx 6.5$ for tellurium). Hence, despite the very large non-linear coefficients of this type of material, the coupling coefficient, K (see Equation (20.9)), achievable in the 10 μm region is comparable to that obtained at shorter wavelengths.

For SHG, conversion efficiencies as high as 80% inside a 3 mm long crystal of zinc germanium phosphide ($ZnGeP_2$; d_{36} = 75.4 pm V^{-1}) have been reported [85] for 10 mJ, 2 ns pulses. The high refractive index of these materials means that Fresnel reflection losses are high and so the corresponding conversion efficiency outside the crystal was ~50%.

SFM between CO_2 and near-infrared and visible lasers has also been reported. For instance, in the nanosecond pulse regime, conversion efficiencies between 30% and 40% have been obtained by mixing 10 μm radiation with the output from a Nd:YAG laser in proustite [86] and silver thiogallate [87] and a dye laser in silver thiogallate [88] to obtain 976 and 564 nm radiation, respectively.

20.7 Developing and Growth Areas

Current research into the frequency conversion of laser sources is continuing across a broad range of topics covering basic physics, new materials and applications. In this section, a few of the areas that are presently receiving attention will be briefly discussed. The success of the quasi-phase-matching technique over the past decade has encouraged further investigations into structured non-linear materials. This structuring can take the form of variations from the simple periodically poled grating used for QPM such as fanning and chirping of the grating [89,90] to produce, for instance, near-transform limited SHG pulses. The formation of QPM materials into waveguide structures is also being actively studied [91–93], and highlights include the observation of 99% single-pass conversion efficiency to the second harmonic of a quasi-cw beam in a PPLN waveguide [94]. The use of the periodic structure of photonic bandgap materials for harmonic generation has also been investigated [95,96].

Some of the physical phenomena associated with frequency conversion that have lately attracted interest are the vortices and singularities that can form in the optical field [97,98]. Other processes investigated include quantum noise and squeezing of light in SHG [99,100], and optical pattern formation [101]. Finally, the increasingly powerful diode lasers coupled with the emergence of QPM materials with high effective non-linearities in the same period has made the combination of these two technologies a practical prospect. Diode lasers have the benefits of being compact and efficient but are only generally available (at the moment) economically and at high powers for emission in the red and near-infrared part of the spectrum. Combination with an efficient non-linear material extends this wavelength range to the blue and near-UV part of the spectrum, which is an important region for various sensing applications. For instance, several groups have used PPKTP to double the frequency of picosecond pulses from a diode laser [102,103].

REFERENCES

1. Davis C. 1996 *Lasers and Electro-Optics* (Cambridge: Cambridge University Press).
2. Kleinman D. A. 1962 Nonlinear dielectric polarization in optical media *Phys. Rev.* **126** 1977.
3. Yariv A. *Quantum Electronics* 3rd edn (New York: Wiley) p. 387.
4. Byer R. L. and Herbst R. L. 1977 *Parametric oscillation and mixing Nonlinear Infrared Generation ed Y R Shen* (Berlin: Springer)
5. Armstrong J. A., Jha S. S. and Shiren N. S. 1970 *IEEE J. Quantum Electron.* **6** 123.
6. Harter D. J. and Brown D. C. 1982 *IEEE J. Quantum Electron.* **18** 1146.
7. Milton M. J. 1992 *IEEE J. Quantum Electron.* **28** 739.
8. Byrd P. F. and Friedman M. D. 1954 *Handbook of Elliptic Integrals for Engineers and Scientists* (Berlin: Springer)
9. Boyd G. D., Ashkin A., Dziedzic J. M. and Kleinman D. A. 1965 *Phys. Rev.* **137** 1305.
10. Boyd G. D. and Kleinman D. A. 1968 Parametric interaction of focused Gaussian light beams *J. Appl Phys.* **39** 3597.
11. Okada M. Takizawa K. and Ieiri S. 1976 *Opt. Commun.* **18** 331.
12. Feisst A. and Koidl P. 1985 *Appl. Phys. Lett.* **47** 1125.
13. Wang W. S., Zhou Q., Geng Z. H. and Feng D. 1986 *J. Cryst. Growth* **79** 706.
14. Armstrong J. A., Bloembergen N., Ducuing J. and Pershan P. S. 1962 *Phys. Rev.* **127** 1918.
15. Franken P. A. and Ward J. F. 1963 *Rev. Mod. Phys.* **35** 23.
16. Fejer M. M., Magel G. A., Jundt D. H. and Byer R. L. 1992 *IEEE J. Quantum Electron.* **28** 2631.
17. Mizuuchi K., Yamamoto K., Kato M. and Sato H. 1994 *IEEE J. Quantum Electron.* **30** 1596.
18. Dmitriev V. G., Gurzadyan G. G. and Nikogosyan D. N. 1991 *Handbook of Nonlinear Optical Crystals* (Berlin: Springer) section 2.10, p. 33.
19. Byer R. L., Park Y. K., Feigelson R. S. and Kway W.L. 1981 *Appl. Phys. Lett.* **39** 17.
20. Dmitriev V. G., Gurzadyan G. G. and Nikogosyan D. N. 1991 *Handbook of Nonlinear Optical Crystals* (Berlin: Springer).
21. Guesic J. E., Levinson H. J., Singh S., Smith R. G. and van Uitert L. G. 1968 *Appl. Phys. Lett.* **12** 306.
22. Smith R. G. 1970 *IEEE J. Quantum Electron.* **6** 215.
23. Degnan J. J. 1989 *IEEE J. Quantum Electron.* **25** 214.
24. Murray J. E. and Harris S. E. 1970 *J. Appl. Phys.* **41** 609.
25. Binks D. J., Golding P. S. and King T. A. 2000 *J. Mod. Opt.* **47** 1899.
26. Mohammed A. K., Pruvost J.-A., Ribet I., Lefebvre M., Rosencher E. and Binks D. J. 2001 *IEEE J. Quantum Electron.* **37** 290.
27. Craxton R. S. 1981 *IEEE J. Quantum Electron.* **17** 1771.
28. Craxton R. S. 1980 *Opt. Comm.* **34** 474.
29. Seka W., Jacobs S. D., Rizzo J. E., Boni R. and Craxton R. S. 1980 *Opt. Commun.* **34** 469.
30. Zayhowski J. J. 1996 *Opt. Lett.* **21** 588. Zayhowski J. J. 1996 *Opt. Lett.* 21 1618.
31. Balcou P. et al. 2002 *Appl. Phys. B* **74** 509.
32. Koechner W. 1996 *Solid State Laser Engineering* (Berlin: Springer) section 10.1.3.
33. Eckardt R. C., Masuda H., Fan Y. X. and Byer R. L. 1990 *IEEE J. Quantum Electron.* **26** 921.
34. Borsutzky A., Brünger R., Huang Ch. and Wallenstein R. 1991 *Appl. Phys. B* **52** 52.
35. Koechner W. 1996 *Solid State Laser Engineering* (Berlin: Springer) p. 580.
36. Ashkin A., Boyd G. D. and Dziedzic J. M. 1963 *Phys. Rev. Lett.* **11** 14.
37. Craxton R. S., Jacobs S. D., Rizzo J. E. and Boni R. 1981 *IEEE J. Quantum Electron.* **17** 1782.
38. Kato K. 1973 *IEEE J. Quantum Electron.* **10** 616.
39. Kato K. 1973 *Opt. Commun.* **9** 249.
40. Bierlein J. O., Vanherzeele H. and Ballman A. A. 1989 *Appl. Phys. Lett.* **54** 783.
41. Chen C., Wu B., Jiang A. and You G. 1985 *Sci. Sin. B* **28** 235.
42. Fan Y. X., Eckardt R. C., Byer R. L., Chen C. and Jiang A. D. 1989 *IEEE J. Quantum Electron.* **25** 1196.
43. Nikogosyan D. N. 1991 *Appl. Phys. A* **52** 359.
44. Chen C., Wu Y., Jiang A., Wu B., You G., Li R. and Lin S. 1989 *J. Opt. Soc. Am. B* **6** 616.
45. Nikogosyan D. N. 1994 *Appl. Phys. A* **58** 181.
46. Myers L. E., Miller G. D., Eckhardt R. C., Fejer M. M., Byer R. L. and Bosenberg W. R. 1995 *Opt. Lett.* **20** 52.
47. Bortz M. L., Fujimara M. and Mejer M. M. 1997 *Opt. Lett.* **22** 1341.
48. Ishigame Y., Suhara T. and Ishihara H. 1991 *Opt. Lett.* **3** 3597.
49. Imeshev G., Proctor M. and Fejer M. M. 1998 *Opt. Lett.* **23** 673.
50. Myers L. E., Eckardt R. C., Fejer M. M., Byer R. L., Bosenberg W. R. and Pierce J. W. 1995 *J. Opt. Soc. Am. B* **12** 2102.
51. Myers L. E., Miller G. D., Eckardt R. C., Fejer M. M., Byer R. L. and Bosenberg W. R. 1995 *Opt. Lett.* **20** 52.
52. Miller G. D., Batchko R. G., Tulloch W. M., Weise D. R., Fejer M. M. and Byer R. L. 1997 *Opt. Lett.* **22** 1834.
53. Ross G. W., Pollnau M., Smith P. G. R., Clarkson W. A., Britton P. E. and Hanna D. C. 1998 *Opt. Lett.* **23** 171.
54. Pasiskevicius V., Wang S., Tellefsen J. A., Laurell F. and Karlsson H. 1998 *Appl. Opt.* **37** 7116.
55. Englander A., Lavi R., Katz M., Oron M., Eger D., Lebiush E., Rosenman G. and Sklair A. 1997 *Opt. Lett.* **22** 1598.
56. Wang S., Pasiskevicius V., Laurell F. and Karlsson H. 1998 *Opt. Lett.* **23** 1883.

57. Woll D., Schumacher J., Robertson A., Tremont M. A., Wallenstein R., Katz M., Eger D. and Englander A. 2002 *Opt. Lett.* **27** 1055.
58. Meyn J.-P. and Fejer M. M. 1997 *Opt. Lett.* **22** 1214.
59. Skvortsov L. A. and Stepantsov E. S. 1993 *Kvantovaya Electron.* **20** 1127.
60. Kase S. and Ohi K. 1974 *Ferroelectrics* **8** 1201.
61. Mizuuchi K., Yamamoto K. and Kato M. 1997 *Appl. Phys. Lett.* **70** 1201.
62. Yamamoto K., Mizuuchi K., Litaoka Y. and Kato M. 1995 *Opt. Lett.* **20** 273.
63. Champert P. A., Popov S. V., Taylor J. R. and Meyn J. P. 2000 *Opt. Lett.* **25** 1252.
64. Risk W. P. and Loiacono G. M. 1996 *Appl. Phys. Lett.* **69** 311.
65. Scheidt M., Beier B., Boller K.-J. and Wallenstein R. 1997 *Opt. Lett.* **22** 1287.
66. Karlsson H., Olson M., Arvidsson G., Laurell F., Bader U., Botsuzky A., Wallenstein R., Wickstrom S. and Gustafsson M. 1999 *Opt. Lett.* **24** 330.
67. Brenier A. 2000 *J. Lumin.* **91** 121.
68. Johnson L. F. and Ballman A. A. 1969 *J. Appl. Phys.* **40** 297.
69. Amano S. and Mochizuki T. 1991 *Nonlinear Opt.* **1** 297.
70. Hemmati H 1992 *IEEE J. Quantum Electron.* **28** 1169.
71. Montoya E., Capmany J., Bausa L. E., Kellner T., Diener A. and Huber G. 1999 *Appl. Phys. Lett.* **74** 3113.
72. Adedin K. S., Tsuritani T., Sato M. and Ito H. 1997 *Appl. Phys. Lett.* **70** 10.
73. Amin J., Pruneri V., Webjorn J., Russell P. S., Hanna D. C. and Wilkinson J. S. 1997 *Opt. Commun.* **135** 41.
74. Jiangrui G., Hai W., Maoquan H., Changde X., Kunchi P., Zhenggang Y., Changqin M. and Xuning W. 1995 *Appl. Opt.* **34** 1519.
75. Driscoll T. A., Hoffman H. J., Stone R. E. and Perkins P. E. 1986 *J. Opt. Soc. Am. B* **3** 683.
76. Moody S. E., Eggleston J. M. and Seamans J. F. 1987 *IEEE J. Quantum Electron.* **23** 335.
77. Lavorovskaya O. I., Pavlova N. I. and Tarasov A. V. 1986 *Sov. Phys. Crystallogr.* **31** 678.
78. Gulamov A. A., Ibragimov E. A., Redkorechev V. I. and Usmanov T. 1983 *Sov. J. Quantum Electron.* **13** 1054.
79. Attwood D., Pierce E. L. and Coleman L. W. 1975 *Opt. Commun.* **15** 10.
80. Reintjes J. J. and Eckhardt R. C. 1977 *Appl. Phys. Lett.* **30** 91.
81. Linford G. J., Johnson B. C., Hildum J. S., Martin W. E., Snyder K., Boyd R. D., Smith W. L., Vercimak C. L., Eimerl D. and Hunt J. T. 1982 *Appl. Opt.* **21** 3633.
82. Fix A. and Ehret G. 1998 *Appl. Phys. B* **67** 331.
83. Rines G. A., Zenzie H. H., Schwarz R. A., Isyanova Y. and Moulton P. F. 1995 *IEEE J. Sel. Top. Quantum Electron.* **1** 50.
84. Chen D. W. and Lin J. T. 1992 *IEEE J. Quantum Electron.* **29** 307.
85. Andreev Y. M., Baranov V. Yu., Voevodin V. G., Geiko P. P., Gribenyukov A. A., Izyumov S. V., Kozochkin S. M., Pismenny V. D., Sato Yu. A. and Streltsov A. P. 1987 *Sov. J. Quantum Electron.* **17** 1435.
86. Jaanimagi P. A., Richardson M. C. and Isenor N. R. 1979 *Opt. Lett.* **4** 45.
87. Voronin E. S., Solomatin V. S., Cherepov N. I., Shuvalov Y. V., Badikov V. V. and Pivovarov O. N. 1975 *Sov. J. Quantum Electron.* **2** 597.
88. Jantz W. and Koidl P. 1977 *Appl. Phys. Lett.* **31** 99.
89. Zimmermann J., Struckmeier J., Hofmann M. R. and Meyn J. P. 2002 *Opt. Lett.* **27** 604.
90. Schober A. M., Imeshev G. and Fejer M. M. 2002 *Opt. Lett.* **27** 1129.
91. Rafailov E. U., Birkin D. J. L., Sibbett W., Battle P., Fry T. and Mohatt D. 2002 *Opt. Lett.* **26** 1961.
92. Parameswaran K. R., Route R. K., Kurz J. R., Roussev R. V., Fejer M. M. and Fujimura M. 2002 *Opt. Lett.* **27** 179.
93. Rafailov E. U., Loza-Alvarez P., Brown C. T. A., Sibbett W., De La Rue R. M., Millar P., Yanson D. A., Roberts J. S. and Houston P. A. 2001 *Opt. Lett.* **26** 1984.
94. Parameswaran K. R., Kurz J. R., Roussev R. V. and Fejer M. M. 2002 *Opt. Lett.* **27** 43.
95. Shin K. C., Hoshi H., Chung D. H., Ishikawa K. and Takezoe H. 2002 *Opt. Lett.* **27** 128.
96. Norton A. H. and de Sterke C. M. 2003 *Opt. Lett.* **28** 188.
97. Frend I. 2002 *Opt. Lett.* **27** 1640.
98. Loina-Terriza G., Petrov D. V., Recolons J. and Torner L. 2002 *Opt. Lett.* **27** 625.
99. Lodahl P. and Saffman M. 2002 *Opt. Lett.* **27** 110.
100. Lodahl P. and Saffman M. 2002 *Opt. Lett.* **27** 551.
101. Mamaev A. V., Lodahl P. and Saffman M. 2003 *Opt. Lett.* **28** 31.
102. Rafailov E. U., Birkin D. J. L., Sibbett W., Battle P., Fry T. and Mohatt D. 2001 *Opt. Lett.* **26** 1961.
103. Woll D., Schumacher J., Robertson A., Tremont M. A., Wallenstein R., Katz M., Eger D. and Englander A. 2002 *Opt. Lett.* **27** 1055.

FURTHER READING

Dmitriev V. G., Gurzadyan G. G. and Nikogosyan D. N. 1991 *Handbook of Nonlinear Optical Crystals* (Berlin: Springer).

A very thorough survey of over 50 non-linear crystals; it also includes a detailed description of the theory of three-wave mixing interactions and describes the results of harmonic-generation experiments performed on a wide range of different lasers.

Yariv A. 1989 *Quantum Electronics* 3rd edn (New York: Wiley).

First published in 1967, this is an introduction to general laser physics that includes chapters on second-harmonic generation and other frequency-conversion techniques. This work approaches the subject from a rigorous theoretical standpoint, often returning to the quantum mechanical basis of many phenomena.

Koechner W. 1996 *Solid State Laser Engineering* (New York: Springer).

A detailed and practical-minded overview of modern techniques in laser engineering, which includes descriptions of many actual laser systems and comprehensively references the literature.

Davis C. 1996 *Lasers and Electro-optics* (Cambridge: Cambridge University Press).

This is a wide-ranging text that covers many areas of laser physics, non-linear optics and photonics at a level suitable for senior undergraduate or graduate students.

Saleh B. E. A. and Teich M. C. 1991 *Fundamentals of Photonics* (New York: Wiley).

This book covers a broad of topics that includes lasers; the principles of non-linear optics are described.

Born M. and Wolf E. 1999 *Principles of Optics* 7th edn (Cambridge: Cambridge University Press).

This book describes classical optics in a very thorough and authoritative way. Although it does not cover the physics of lasers or their applications, it does describe the optics of crystals in great detail.

Taylor & Francis
Taylor & Francis Group
http://taylorandfrancis.com

21

Non-linear Optical Properties of Novel Nanomaterials

Soma Venugopal Rao, K. Naga Krishnakanth, C. Indumathi, and T.C. Sabari Girisun

CONTENTS

21.1 Introduction 255
  21.1.1 Origin of NLO: Master-Slave Flip Flop 256
  21.1.2 Maxwell's Equations and Non-linear Polarization 256
21.2 Second-order NLO Properties 258
  21.2.1 Second Harmonic Generation 258
  21.2.2 Sum Frequency Generation 259
  21.2.3 Difference Frequency Generation 259
  21.2.4 Nanomaterials for Second-Order Non-linear Optics 259
21.3 Third-Order Optical Non-linearities 260
  21.3.1 Non-linear Absorption 260
    21.3.1.1 Saturable Absorption and Reverse Saturable Absorption 260
    21.3.1.2 Genuine Multi-photon Absorption 263
    21.3.1.3 Excited-state Absorption and Free Carrier Absorption 265
  21.3.2 Non-linear Refraction 266
    21.3.2.1 Electronic Polarization 266
    21.3.2.2 Raman-induced Kerr Effect and Photorefractive Effect 266
    21.3.2.3 Molecular Orientational Effects and Population Redistribution 267
    21.3.2.4 Electrostriction 267
    21.3.2.5 Thermo-optic Effects 267
  21.3.3 Optical Limiting 268
  21.3.4 Z-scan Experimental Technique 269
    21.3.4.1 Theory of Open Aperture Z-scan 271
    21.3.4.2 Wavelength-dependent Non-linear Absorption Coefficient 271
    21.3.4.3 Theory of Closed Aperture Z-scan 272
  21.3.5 Third-order NLO Susceptibility and Optical Limiting 273
  21.3.6 Third-order NLO Materials: Brief Survey 273
    21.3.6.1 Metal Nanoparticles 274
    21.3.6.2 Metal Nanocomposites 278
    21.3.6.3 Perovskite Materials 279
21.4 Conclusions 281
21.5 Future Scope 281
References 282

21.1 Introduction

The study of energy of vision called as optics is a venerable division of Physics as it reveals the unravelling mysteries of nature and offers universal application towards the improvement in quality of the humankind (Sutherland, 2003; Wake and Brady, 1993). All needs from energy generation to detection and communication to information processing have been successfully extended as the domain of photonics that emerge from trough to peak. In the journey of exploring the unseen, the year 1960 records one of the greatest inventions in the history of Science. The curiosity-driven research has combined the sparking ideas of Fabry–Perot interferometer-based optical resonator by Charles Fabry and Alfred Perot in the year 1897, the prediction of stimulated emission of light by Albert Einstein in the year 1916, optical pumping by Alfred Kastler in 1950, MASER and its extension towards optical range by Arthur Schawlow and Charles Townes in the year 1958 as one optical source called as LASER (Light Amplification by Stimulated Emission of Radiation) by Maiman in 1960. It is a source, which emits a kind of light of unrivalled purity and intensity not found in any of the previously known sources of electromagnetic radiation. The great diversity of their range of applications makes them unique, and here, lasers are being used to weld thick metals as well as delicate layers of retina. The laser industry is surging briskly not only in terms of technological advances but also in terms of implementation in new application sectors. The arrival of laser nearly 60 years ago created many fascinating new fields, among which non-linear optics (NLO) undoubtedly has opened the biggest unexplored domain of optics (Shen, 1984; Laud, 2011). As a consequence of intensity dependence of the optical parameters, many exciting NLO effects such as photon-photon interaction (exchange of energy among light beams), generation of new frequencies (harmonic generation), modulation and control of light beam properties (optical limiting (OL)), etc. were observed. At present NLO has now burgeoned into the mature field of Science that has enhanced our fundamental light-matter interactions as well as provided the means for rejuvenation of optical technology (Saravanan et al., 2017). Among the NLO processes that have been studied, one of the most technologically important phenomena is optical-limiting. This is because sudden exposure to intense laser beam can cause damage to human eyes, optical sensors and sensitive optical components. Therefore, worldwide there is a search for effective optical protectors called as optical limiters that can protect human eye and photo-sensitive components from the damage by intense laser beam. The phenomenon used for the operation of optical limiters can be mainly achieved by non-linear absorption (NLA) and/or non-linear refraction. This chapter presents the origin of NLO, Maxwell's equations and non-linear polarization, different NLO processes (second and third order), various classes of NLA and non-linear refraction, OL phenomenon, experimental techniques to measure/evaluate NLO coefficients (Z-scan) and brief review of recently reported NLO materials (Boyd, 2003).

21.1.1 Origin of NLO: Master-Slave Flip Flop

Theodore Maiman (1960), developer of the first laser, was of the opinion that laser was a solution-seeking problem, and even 60 years later, the phrase remains unrevoked. Lasers are not only ruling the technological world but also stand as a special vision to explore the uncharted domains in optics. Earlier in the pre-laser era, the study on the energy of vision revealed the most beautiful optical phenomena that exist in nature with periodicity and linearization, while the vision through laser revealed the most exciting non-linearity of optics in nature. The transformation of beauty in linearity to excitement with non-linearity in optics is analogy to the travel of a person in giant wheel and roller coaster. The dynamics involved in giant wheel is purely linear and periodic and thus avails the beauty of thrill through its predictable events. At the same time, the kinetics of roller coaster that involves anharmonicity is the journey of excitement comprising the unpredictable events. This transformation of explored linear optics to unexplored NLO revealed the most fascinating optical phenomenon, and interestingly, all the materials in this universe are non-linear. Thus, NLO is the study of interaction of highly intense electromagnetic radiation with matter in which optical properties of a material are intensity-dependent. It is an interesting Boson interaction in a material medium in which the intense Bosons first induce a non-linear response in a medium and then the medium modifies the optical field in a non-linear way.

The dependence of optical properties on the incident input intensity of radiation was not realized in the pre-laser era. And the evolution of NLO happened soon after the invention of laser and its origin can be simply explained by a "Master-Slave Flip Flop". It is known that the conventional light sources that function on spontaneous emission lack coherence and thus possess a weak electric field strength in the order of ~$10^3\,\mathrm{V\,cm^{-1}}$. Under light-matter interaction, the Boson field strength (~$10^3\,\mathrm{V\,cm^{-1}}$) is much smaller than the atomic and inter-atomic field strengths $\left(E_{\mathrm{at}} = e/a_0^2 \sim 10^7\,\mathrm{V\,cm^{-1}}\right)$. This allows an atom to behave as master and the interacting photons as slave. However, the laser through its stimulated emission avails high degree of coherence and thus possesses extremely high spatial concentration of light power, with a field strength varying from 10^5 to $10^9\,\mathrm{V\,cm^{-1}}$. This creates a change in situation, and as a result, there occurs a master-slave flip flop in which photons act as master and material as slave. Thus, under intense field, the optical behaviour no longer remains linear, and this induced non-linearity brings intensity-dependent optical parameters (Laud, 2011; Boyd, 2003). The well-established theory of linear optics about the interaction of light and matter inculcates the basic ideas in the theory of NLO. To get a clear insight, consider a dielectric matter that consists of a collection of positively charged cores (of atoms or molecules) with surrounding negatively charged electrons. When a dielectric medium is placed in an external dc electric field ($\boldsymbol{E}$ being a constant), the medium undergoes the following transformations: (i) molecules form themselves as dipoles, (ii) dipoles align themselves parallel to applied electric field and (iii) dipole moment per unit volume gives polarization and is directly proportional to the applied electric field. When dc field is replaced by ac electric field, additionally, the medium undergoes oscillation at a frequency in resonance with the frequency of the applied electric field. It is known that the electric field in light interacts primarily with matter by exerting force on the valence electrons. These pull the optical electrons from its equilibrium position, and thus, the oscillating charge radiates at its frequency of oscillation (light energy converted into mechanical energy and vice versa). When the interacting light is sufficiently intense to turn the medium non-linear, electrons are pulled with higher force. So, instead of charges being pulled back smoothly, they are jerked back roughly that instigate charge to oscillate with new frequencies due to non-linear restoring force. Accordingly, all the optical parameters turn light intensity-dependent and no more remain constant. Hence, the deviation from linear behaviour (Polarization vs Electric field) implants such interactions in this regime and provokes the field "NLO" as defined by the laws of classical optics (Boyd, 2003).

21.1.2 Maxwell's Equations and Non-linear Polarization

As light is an electromagnetic wave with rapidly time-varying electric and magnetic field, Maxwell's equations can be utilized to explain the light-matter interaction. To get started out understanding of NLO, Maxwell's equations for the optical fields and a specification of the dependence on the induced polarizations are essential. For a non-magnetic material without free charges and free current, the wave equation using Maxwell's equations (Boyd, 2003) is

$$\nabla \ X \ \nabla \ X \ \boldsymbol{E} + \mu_0 \varepsilon_0 \frac{\partial^2}{\partial t^2} \ \boldsymbol{E} = 0 \tag{21.1}$$

where *E(r, t)* is the electric field and *D(r, t)* is the displacement current. With unidirectional property of laser, the equation of the electric field propagating primarily in one direction is written as

$$\boldsymbol{E} \ (\boldsymbol{r}, t) = \hat{\boldsymbol{e}} \ A(\boldsymbol{r}, t) e^{[i(kz - \omega t)]} \tag{21.2}$$

where $\hat{\boldsymbol{e}}$ is the unit vector, A is the wave amplitude as function of space and time, $\boldsymbol{k}$ is the wave vector and ω is a circular frequency of the rapidly oscillating wave. Treating the finite beam as the TEM$_{00}$ mode of a circular Gaussian beam,

$$\boldsymbol{E} \ (\boldsymbol{r}, t) = \hat{\boldsymbol{e}} \ A(Z, t) \frac{\omega_0}{\omega(Z)} e^{\left[i \left(\frac{kr^2}{2q(Z)} kz - \tan\left(\frac{Z}{Z_0} \right) \omega t \right) \right]} \tag{21.3}$$

The radius has a minimum, defined by ω_o, at the plane $Z = 0$ and $\omega(Z)$ is given by

$$\omega(Z) = \omega_0 \left[1 + \left(\frac{Z}{Z_0} \right)^2 \right]^{\frac{1}{2}} \ ; \ Z_0 = \frac{n_0 \pi \omega_0^2}{\lambda} \tag{21.4}$$

Here, z_0 is the Rayleigh range, n_0 is the refractive index of the material and λ is the optical wavelength in free space (Sutherland, 2003). The material can be non-linear under laser interaction, and the fields $\boldsymbol{D}$ and $\boldsymbol{E}$ are related by

$$\boldsymbol{D} = \varepsilon_0 \boldsymbol{E} + \boldsymbol{P} \tag{21.5}$$

Interestingly the dependence of polarization $\boldsymbol{P}$ upon the electric field strength $\boldsymbol{E}$ is non-linear under non-linear interaction. Total polarization $\boldsymbol{P}$ is thus the sum of linear polarization ($\boldsymbol{P}^{(\mathrm{L})}$) and non-linear polarization ($\boldsymbol{P}^{(\mathrm{NL})}$) given as

$$\boldsymbol{P} = \boldsymbol{P}^{(\mathrm{L})} + \boldsymbol{P}^{(\mathrm{NL})} \tag{21.6}$$

Thus, the wave equation describing the electric field in the medium generated by the driving polarization can be expressed as (Boyd, 2003)

$$\begin{aligned} -\nabla^2 \boldsymbol{E} + \frac{1}{c^2} \frac{\partial^2}{\partial t^2} \boldsymbol{E} &= -\frac{1}{\varepsilon_0 c^2} \frac{\partial^2 \boldsymbol{P_L}}{\partial t^2} \\ -\nabla^2 \boldsymbol{E} + \frac{\varepsilon}{c^2} \frac{\partial^2}{\partial t^2} \boldsymbol{E} &= -\frac{1}{\varepsilon_0 c^2} \frac{\partial^2 \boldsymbol{P_{NL}}}{\partial t^2} \end{aligned} \tag{21.7}$$

At low intensity levels of natural light sources, the relation of the polarization with the applied field is linear. If L signifies a linear polarization, ε_0 is electric permittivity of free space and $\chi^{(1)}(r - r', t - t')$ is the linear dielectric response tensor, then electric polarization is

$$P_L(r,t) = \varepsilon_0 \int_{-\infty}^{\infty} \int_{-\infty}^{\infty} \chi^{(1)}(r - r', t - t') \ \boldsymbol{E} \left(r', t' \right) dr' \ dt' \tag{21.8}$$

When the intensity of the light is sufficiently high, a small additional non-linear polarization will appear and is written as $\mathbf{P}_{\mathrm{NL}} = \mathbf{P}^{(2)} + \mathbf{P}^{(3)} + \ldots.$ that signifies the non-linear polarization and here

$$P^{(2)}(r,t) = \varepsilon_0 \int_{-\infty}^{\infty} \int_{-\infty}^{\infty} \chi^{(2)}(t - t', t - t'') \ \boldsymbol{E} \ (r, t') \ \boldsymbol{E} \ (r, t'') \ dt' \ dt''$$

$$\begin{aligned} P^{(3)}(r,t) = \varepsilon_0 \int_{-\infty}^{\infty} \int_{-\infty}^{\infty} \int_{-\infty}^{\infty} \chi^{(3)}(t - t', t - t'', t - t''') \ \boldsymbol{E} \ (r, t') \ \boldsymbol{E} \ (r, t'') \\ \boldsymbol{E} \ (r, t''') dt' \ dt'' \ dt''' \end{aligned} \tag{21.9}$$

This assimilates the origin of NLO through the discussion on non-linear polarization. The above equation takes the form of inhomogeneous wave equation, and the right-hand side represents the non-linear response of the medium that acts as a driving term. This non-linear wave equation imparts a framework for relating all the non-linear light-matter interactions. However, it is to be noted that Maxwell's equations describe only the generation of a new wave by non-linear polarization but failed to address how electric field is generated by non-linear polarization. The description of the interaction of light with a bulk medium can be considered within the framework of a dielectric material subjected to an electric field. With linear restoring force and small fields, the system behaves like a classical simple harmonic oscillator, and the strength of the applied field is proportional to the displacement of charge from the equilibrium position. When a conventional light source interacts with matter, the medium gets polarized and the linear polarization is written as follows:

$$\boldsymbol{P}^{(\mathrm{L})} = \varepsilon_0 \chi^{(1)} \boldsymbol{E} \tag{21.10}$$

where ε_0 is the permittivity of the free space ($8.85 \times 10^{-12} \mathrm{C}^2 \mathrm{N}^{-1} \mathrm{m}^{-2}$) and $\chi^{(1)}$ is the linear susceptibility of a collection of molecules.

When laser sources are considered, the nature of the response turns non-linear as the intensity of the optical field is greater than the order of atomic field. The displacement of the electron is not directly proportional to the field and higher order non-linear terms in the restoring force become more relevant. In the non-linear regime, there is no direct proportionality between the polarization of the medium and the electric field. Here, the polarization can be expanded as power series in the electric field $\boldsymbol{E}$ as

$$\boldsymbol{P} = \varepsilon_0 \left(P_0 + \chi^{(1)} \mathrm{E} + \chi^{(2)} \boldsymbol{EE} + \chi^{(3)} \boldsymbol{EEE} + \ldots \right) \tag{21.11}$$

where $\boldsymbol{P}_0$ is the dc polarization of the sample (static dipole moment per unit volume), $\chi^{(1)}$ is the linear susceptibility, $\chi^{(2)}$ and $\chi^{(3)}$ are the second- and third-order NLO susceptibilities of the material, respectively (parameters that determine the magnitude of the second- and third-order NLO responses). The order of $\chi^{(n)}$ is determined by the number of photons or waves involved in an interaction, i.e. $\chi^{(1)}$ involves the two-wave interaction, $\chi^{(2)}$ indicates the three-wave interaction, $\chi^{(3)}$ represents the four-wave interaction, *etc*. With increasing field strength, non-linear effects become more important due to the inclusion of higher powers of the field $\boldsymbol{E}$. During this interaction, both energy and momentum must be conserved and the waves must be combination of any frequencies. Second-order NLO effects can be conceptualized when the interaction of two waves at frequencies ω_1 and ω_2 generate a new frequency ω_3, i.e. simply a three-wave mixing process. Here, the NLO susceptibility $\chi^{(2)}$ being three-wave interaction is expressed as $\chi^{(2)}(-\omega_3;\omega_1,\omega_2)$ and is responsible for SHG, sum and difference frequency generation (DFG), optical rectification and the electro-optic effect. The component of $\chi^{(2)}$ is restricted by a symmetry condition as it is three-wave interaction process and is non-zero only if the material lacks centre of symmetry. Similarly, the third-order NLO effects can be described as four-wave mixing process, which makes $\chi^{(3)}$ independent of symmetry restrictions (Zernike and Midwinter, 2006; Zhang et al., 2009). Third harmonic generation, wave mixing, self-focusing and self-defocusing are some of the important third-order NLO phenomena (Zhang et al., 2009; Liu et al., 2009; Li et al., 2011). The description of non-linear polarization and the domain of entire NLO can be understood by considering the power series of the polarization equation (substitute $\boldsymbol{E}=\boldsymbol{E_0}$ cos(wt) in Equation 1.11) (Laud, 2011)

$$\boldsymbol{P} = \frac{1}{2}\varepsilon_0\chi^{(2)}E_0^2 + \varepsilon_0\left(\chi^{(1)} + \frac{3}{4}\chi^{(3)}E_0^2\right)E_0\cos(\omega t) + \frac{1}{2}\varepsilon_0\chi^{(2)}E_0^2\cos(2\omega t) + \frac{1}{4}\varepsilon_0\chi^{(3)}E_0^3\cos(3\omega t)\ldots \qquad (21.12)$$

The first term in the above expression is an unvarying term that gives a dc field across the medium which corresponds to the phenomenon called optical rectification. The second follows the external polarization and is called the first harmonic of polarization, the third is called the second harmonic of polarization that oscillates at frequency 2ω, the fourth is called the third harmonic of polarization, and so on. In addition to photons, other types of excitations like optical and molecular vibrational waves (Stimulated Raman and Stimulated Brillouin process) can also spawn the medium to be non-linear. Plenty of researches have been made to understand the origin of NLO. Although the domain of investigation is restricted earlier with second-order NLO effects, the advent of intense laser provided the opportunity to explore the higher-order NLO phenomena. This in turns imposed the essentiality to extend the understanding beyond non-linear polarization like NLA, non-linear refraction, etc.

21.2 Second-order NLO Properties

21.2.1 Second Harmonic Generation

Let us consider a laser beam whose electric field $\tilde{E}(t) = Ee^{-i\omega t} + c.c.$ interacting with a second-order NLO material. The generated non-linear polarization is then given by

$$\tilde{\boldsymbol{P}}^{(2)}(t) = \varepsilon_0\chi^{(2)}\tilde{E}^{(2)}(t).$$

$$\tilde{\boldsymbol{P}}^{(2)}(t) = 2\varepsilon_0\chi^{(2)}EE^* + \left(\varepsilon_0\chi^{(2)}E^2e^{-2i\omega t} + c.c.\right). \qquad (21.13)$$

The second-order non-linear polarization has contribution from optical rectification (first term) and second harmonic at frequency 2ω (second term) as depicted in Figure 21.1. Under proper experimental conditions, efficient second harmonic generation (SHG) is possible. One use of the SHG is to generate the SHG from fixed frequency laser, for example Ti:sapphire laser output at 800 nm can be brought down to 400 nm by using a BBO crystal. In general, the different interacting fields with the second-order NLO material are

$$\tilde{\mathbf{E}}(t) = E_1e^{-i\omega_1 t} + E_2e^{-i\omega_2 t} + c.c. \qquad (21.14)$$

From Equation 21..13, the second-order polarization has terms such as

$$\tilde{\boldsymbol{P}}^{(2)}(t) = \varepsilon_0\chi^{(2)} \times\left[E_1^2e^{-2i\omega_1 t} + E_2^2e^{-2i\omega_2 t} + 2E_1E_2e^{-i(\omega_1+\omega_2)t} + 2E_1E_2^*e^{-i(\omega_1-\omega_2)t} + c.c.\right] + 2\varepsilon_0\chi^{(2)}\left[E_1E_1^* + E_2E_2^*\right] \qquad (21.15)$$

In terms of frequency the second-order non-linear polarization individual components can be represented as

$$P(2\omega_1) = \varepsilon_0\chi^{(2)}E_1^2 \quad (\textbf{SHG}) \qquad (21.16)$$

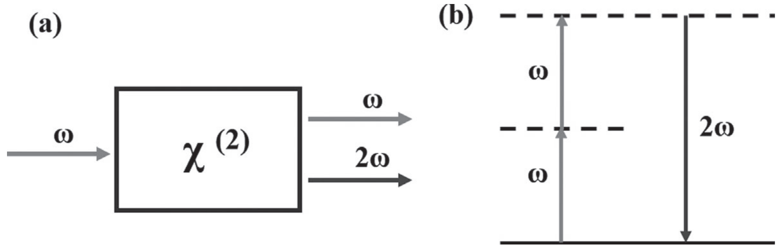

FIGURE 21.1 Second harmonic generation (a) geometry of the interaction; (b) energy-level representation.

$$P(2\omega_2) = \varepsilon_0 \chi^{(2)} E_2^2 \quad (\textbf{SHG}) \tag{21.17}$$

$$P(\omega_1 + \omega_2) = 2\varepsilon_0 \chi^{(2)} E_1 E_2 \quad (\textbf{SFG}) \tag{21.18}$$

$$P(\omega_1 - \omega_2) = 2\varepsilon_0 \chi^{(2)} E_1 E_2^* \quad (\textbf{DFG}) \tag{21.19}$$

$$P(0) = 2\varepsilon_0 \chi^{(2)} \left[E_1 E_1^* + E_2 E_2^* \right] \quad (\textbf{Optical Rectification}) \tag{21. 20}$$

21.2.2 Sum Frequency Generation

The process of sum frequency generation (SFG) is illustrated in Figure 21.2. The non-linear polarization for the SFG process according to Equation (21.18) is

$$P(\omega_1 + \omega_2) = 2\varepsilon_0 \chi^{(2)} E_1 E_2 \quad (\text{SFG})$$

which is mostly considered as SHG; the main difference in SFG is involving two input fields at different frequencies. The use of SFG is to generate tunable radiation from a fixed input laser beam. In SFG generation usually one of the input lasers is tunable, and the other laser is fixed at visible frequency.

21.2.3 Difference Frequency Generation

The process of difference frequency generation (DFG) also known as optical parametric amplification is illustrated in Figure 21.3. According to Equation 21.19, the non-linear polarization at DFG is

$$P(\omega_1 - \omega_2) = 2\varepsilon_0 \chi^{(2)} E_1 E_2^*$$

Here, the generated non-linear polarization is at the difference frequency of the two input beams. One application of DFG is generation of tunable infrared radiation by mixing a tunable wavelength visible laser with a fixed wavelength visible laser. The main difference between the SFG and DFG processes can be described using the energy-level diagrams (Figures 21.2 and 21.3). In DFG process an input laser at higher frequency photon ω_1 is destroyed to generate photon at lower frequency ω_2. Thus, the lower input filed frequency is amplified by the DFG.

21.2.4 Nanomaterials for Second-Order Non-linear Optics

There have been several studies in recent literature highlighting the advantages of nanomaterials for second-order NLO processes. We limit our discussion to a selected few reports from the literature. Kole's group studied the SHG properties of ZnS QDs by using the Kurtz powder method and compared with KDP crystal (Kole et al., 2014). They have shown that the sample with larger particle size was less efficient. They have also reported the synthesis of ZnS/PMMA nanocomposites (NCs) and found that the NCs are thermally more stable than pure PMMA. Ozga and team have established a substantial enhancement of the photo-induced second- and third-order NLO susceptibilities of the nanostructured zinc sulphide (ZnS) crystallites (Ozga et al., 2016). The effect of dielectric nanoparticle shape on the second-harmonic signal was studied recently and the work presented a method for finding the selection rules for particles of arbitrary shapes from any non-centrosymmetric material (Frizyuk, 2019). A recent demonstration comprised of the SHG enhancement in a metal-dielectric nanodimer of $BaTiO_3$-Au, where the surface plasmon resonance (SPR) of a gold nanoparticle enhanced the linear scattering of $BaTiO_3$ nanoparticles (NPs) and drove the efficient harmonic generation from the bulk of the same $BaTiO_3$ NPs (Timpu et al., 2017). They have, using numerical simulations, shown that the efficiency of the SHG enhancement is determined by the crystal orientation of $BaTiO_3$ and size.

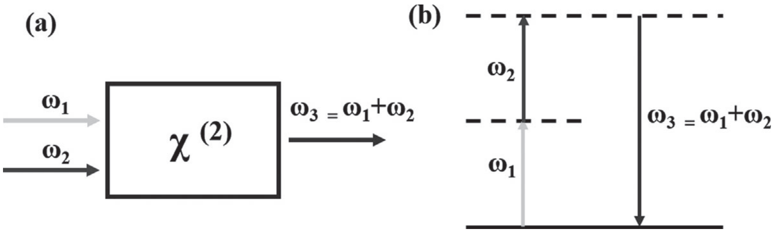

FIGURE 21.2 Sum frequency generation (a) geometry of the interaction; (b) energy-level representation.

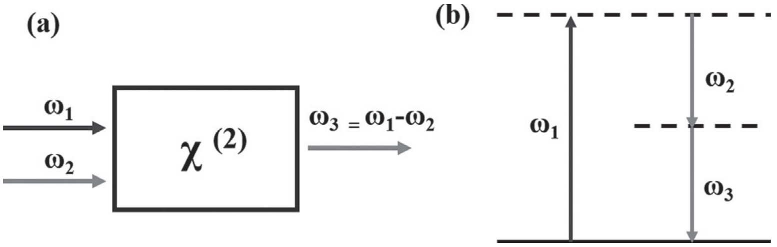

FIGURE 21.3 Difference frequency generation (a) geometry of the interaction; (b) energy-level representation.

Similarly, the same group (Timpu et al., 2016) has measured the linear scattering spectra of individual $BaTiO_3$ NPs, wavelength-dependent measurement of the SHG signal generated by the same NPs. SHG enhancement of more than four orders of magnitude compared with the bulk $BaTiO_3$ crystal was measured for a 200 nm $BaTiO_3$ NPs. They have also extended the field of all-dielectric NPs to second-order non-linearities by using a perovskite non-centrosymmetric material that is transparent in a broad range of wavelengths. Murugan et al. demonstrated nano-crystallization via controlled crystallization of the $Li_2B_4O_{7-x}SrBi_2Ta_2O_9$ glassy system (Murugan and Varma, 2002). They observed an increase in crystallite size of SBT on the nanometre scale has been with increase in both the composition and the heat-treatment temperature. They have also shown relative permittivity of the glasses as well as glass NCs increase with increase in SBT content, whereas the dielectric loss decreases. Butet et al. summarized the basic principles of SHG emphasizing the role played by symmetry in both the origin of the non-linearity (local surface versus non-local bulk contributions) and the shape dependence of the scattered SH wave. The relationship between the specific properties of SHG from plasmonic nanostructures and some advanced applications has been outlined (Butet et al., 2015). Another group (Nelson et al., 2017) presented a synergistic combination of tight binding theory and SHG spectroscopy to characterize the surface structure and the NLO properties of ZnO NPs dispersed in a liquid medium. The second-order susceptibilities of these sources have been determined. They reported that there is no significant change in the crystal symmetry of the ZnO NP surface upon adsorption of the coumarin dye and a modification of the overall SHG polarization. Ali et al. have successfully prepared single-crystalline $LiNbO_3$ NPs. Furthermore, they have reported that second-harmonic response of the nanocrystals could be further tuned by choosing a suitable wavelength for the incident laser (Ali et al., 2019). Frizyuk and co-workers have analysed the SHG from crystalline non-centrosymmetric NPs, possessing second-order bulk non-linearity. They have calculated the dependence of the SH intensity on the orientation of the crystalline axes with respect to the incident light polarization (Frizyuk et al., 2018). Another team has shown that the SHG generated in the far-field is 26 times higher than that from X-cut unpatterned $LiNbO_3$ (Barakat et al., 2013). While the metal constituents lead to a strong localized field, non-linearity was provided by the embedded $LiNbO_3$. They have also performed comparative studies of SH signal in metamaterials with different parameters and established the largest non-linear response in the embedded Ag–$LiNbO_3$ (Barakat et al., 2013). Frizyuk et al. have studied the effect of the nanoparticle shape on the second-harmonic signal and present the same method for finding the selection rules for particles of arbitrary shapes from any non-centrosymmetric material (Frizyuk, 2019). Kulyk and co-workers have demonstrated the properties of the ZnO/PMMA nanocomposite films for second and THG of picosecond optical pulses. Further, they have also demonstrated that the SHG as well as THG signal increased with ZnO NCs concentration (Kulyk et al., 2009). Ren et al. proposed novel NCs of Ag-coated non-linear nanocuboid and demonstrated as an efficient sub-wavelength coherent light source through SHG. Their study was based on numerical simulation using non-linear DDA method NPs (Ren et al., 2014). Frizyuk et al. have theoretically analysed the SHG by spherical dielectric NPs made of materials with non-zero bulk second-order non-linear susceptibility tensor $\chi^{(2)}$ (Frizyuk et al., 2019). Considering two typical crystalline solids, $BaTiO_3$ and AlGaAs, Pan and his research group have designed a high-efficiency nanostructure to enhance the SHG and revealed a significant approach to take advantage of the mode-matched plasmon at SH frequency for the SHG enhancement in the centrosymmetric nanostructures (Pan et al., 2017). Finally, Zolotovskaya et al. shown that both SHG and multiphoton-absorption-induced luminescence are present for ellipsoidal Ag NPs embedded in soda-lime glass. It was shown that SHG is prominent for NPs with higher aspect ratios. Both mechanical stretching and laser-assisted reshaping of the Ag NPs provide a simple and yet effective tool for spectral manipulation of the SPRs. Laser reshaping (unlike mechanical stretching) provides spectral selectivity and, more importantly, the much-needed spatial selectivity (Zolotovskaya et al., 2016). Table 21.1 summarizes the various second-order NLO studies on different nanomaterials.

21.3 Third-Order Optical Non-linearities

21.3.1 Non-linear Absorption

NLA refers to the profound change in transmittance of a material as a function of intensity or fluence. Under the excitation of intense monochromatic radiation from a laser, the probability of absorbing multi-photon by a material can be greatly enhanced. As early before the invention of laser, Goppert-Mayer (1931) derived the two-photon transition probability in a system using second-order quantum perturbation theory (Göppert-Mayer, 1931). Experimental evidences on NLA involving two and more photons were soon realized after the invention of the laser. Correspondingly, laser-induced population redistribution leads to interesting complicated energy transitions and free carrier generation. These phenomena are manifested optically as a reduced (saturable) or increased (reverse saturable) absorption. Several mechanisms are proposed to understand the intensity dependence of NLA.

21.3.1.1 Saturable Absorption and Reverse Saturable Absorption

Dependence of transmittance of a material with intensity or fluence is generally called as NLA which can be broadly classified into saturable and reverse saturable absorption (RSA). Saturable absorption (SA) is the process in which the absorption of light by a material decreases with increase in light intensity, i.e., high transmittance at high intensities. Here, the absorption is saturated at high intensity as the rate at which atoms get excited to higher energy states is sufficiently higher than the time taken to decay back to ground state, which is generally termed as ground-state depletion. Thus, non-linear process that can be associated with real (rather than virtual) energy levels and population changes in those levels is known as SA. Major factors influencing SA includes (i) absorbing

TABLE 21.1

Summary of the Second-Order NLO Studies Using Various Nanomaterials

S. No.	Samples Investigated	Laser Used	NLO Parameters Measured	Studies	Ref. No.
1	ZnS quantum dots, ZnS/PMMA nanocomposites	Q-switched Nd:YAG laser radiation of 1064 nm	The standard KDP crystal showed a value of 17.5 mV whereas nanocomposite S1 sample exhibited a value of 7 mV and nanocomposite S2 sample depicted a value of 3.5 mV in a digital oscilloscope	SHG and observation on optical properties	Kole et al. (2014)
2	ZnS/PVA nanocomposites	18 ns, 1064 nm Nd:YAG laser	Increase of the effective SHG signal obtained from the dc-electric field >0.8 kV cm^{-1}	SHG	Ozga et al. (2016)
3	Dielectric nanoparticles	Theoretical studies at 1480 nm	–	Theoretical study of SHG in a monocrystalline nanoparticle with a non-centrosymmetric crystalline lattice	Frizyuk (2019)
4	Hybrid metal-dielectric nanodimer consisting of an inorganic perovskite nanoparticle of barium titanate ($BaTiO_3$) coupled to a metallic gold (Au) nanoparticle	A femtosecond (fs) laser beam	SHG signal at the position of the linear resonance of the $BaTiO_3$–Au nanodimer (580 nm) is enhanced compared to the off-resonance SHG signal (570 and 640 nm). SHG signal (570 and 640 nm). For instance, at 15 mW, the SHG signal at the resonance was 4 times higher than the SHG signal off the resonance	Enhanced SHG	Timpu et al. (2017)
5	Perovskite nanoparticles	Ti:sapphire 100 fs laser wavelengths between 700 and 1040 nm	The SHG is measured for incident beam wavelengths between 710 and 950 nm with a step of 5 nm, giving an SHG signal in the range from 355 to 425 nm. In the home-built set-up, the same ratio of 17 between the highest and the lowest SHG signal is found	Linear scattering spectra of individual $BaTiO_3$ nanoparticles. SHG enhancement with Mie resonances	Timpu et al. (2016)
6	Lithium borate–strontium bismuth tantalate glass nanocomposite	Nd:YAG laser radiation of 1064 nm	The d_{eff} of the glass nanocomposites corresponding to the compositions x ~5, 15 and 20 were computed to be 0.255, 0.264 and 0.373 pm/V, respectively, with reference to quartz (d11 of Quartz ~0.5 pm/V)	Linear and NLO properties.	Murugan and Varma (2002)
7	Plasmonic nanostructures	Ultrashort femtosecond pulses (~30 fs and shorter).	The case of 60 nm silver nanoparticles is a good illustration of the benefit provided by this approach since the quadrupolar LSPR has a figure of merit = 9.5, while the Dipolar LSPR has a figure of merit = 3.8 only. A figure of merit twice as large can be obtained by switching from the linear to the non-linear response.	SHG from plasmonic nanoparticles.	Butet et al. (2015)
8	Zinc oxide (ZnO) in the form of nanoparticles	Theoretical Studies		Calculations of second-order susceptibility values of ZnO NPs	Nelson et al. (2017)
9	Sub-10 nm $LiNbO_3$ nanocrystals	Femtosecond laser (tunable from 680 to 1080)	Successfully prepared single-crystalline $LiNbO_3$ nanoparticles with average diameters of 7 nm.	Generation of optical SHG with a tunable response from 400 to 500 nm.	Ali et al. (2019)

(*Continued*)

TABLE 21.1 (*Continued*)

Summary of the Second-Order NLO Studies Using Various Nanomaterials

S. No.	Samples Investigated	Laser Used	NLO Parameters Measured	Studies	Ref. No.
10	AlGaAs (*Td* crystalline symmetry) and $BaTiO_3$ (C4*v* symmetry) nanoparticles were assumed to be monocrystalline	Theoretical studies	–	Second harmonic generation in nanoparticles with Mie resonances.	Frizyuk et al. (2018)
11	Coaxial nanopatterned lithium niobate embedded in Ag	OSICSECL external cavity laser module with a 1500–1600 nm wavelength range	SHG enhancement factor of 26 compared to unpatterned X-cut lithium niobate wafer	Second-harmonic generation (SHG) enhancement	Barakat et al. (2013)
12	ZnO nanocrystals and Nanocomposite films	Nd:YAG; 1064 nm, picosecond optical pulses	At the ZnO NCs concentration of 5% wt. and less, the values effective for second-order NLO susceptibilities are higher than that of ZnO bulk	Theoretical SHG and THG	Kulyk et al. (2009)
13	Ag-coated $LiNbO_3$ (LN) core-shell nanocuboids	Fundamental wavelength of 900 nm	Enhancement of SHG by 3×10^5 in comparison to a bare LN	SHG	Ren et al. (2014)
14	Dielectric nanoparticles made of non-centrosymmetric materials with bulk quadratic non-linearity	At the fundamental wavelength of 1050 nm	–	SHG cross-section for $BaTiO_3$ nanoparticle without and with account for the anisotropy of material parameters	Frizyuk et al. (2019)
15	Silver-dielectric-gold-dielectric (SDGD) nanostructure	Theoretical studies	The second-harmonic field is enhanced by 1.21×10^5 times with the super-resonance at the fundamental frequency, 4.43×10^2 times with the super-resonance at the SH frequency and 6.55×10^7 times with the double super-resonances at both the fundamental and SH frequencies	Gain-assisted double plasmonic resonances to enhance SHG in a centrosymmetric multi-layered silver-dielectric-gold-dielectric	Pan et al. (2017)
16	Spherical silver nanoparticles of 30 nm diameter embedded in soda-lime glass	10 ps pulse laser at 1064 nm	–	SHG and multiphoton-absorption-induced luminescence in the embedded laser-reshaped NPs	Zolotovskaya et al. (2016)

wavelength range, (ii) its dynamic response (how fast it recovers) and (iii) its saturation intensity/fluence (where it saturates) (Boyd, 2003). To understand SA, consider a system with three vibronically broadened electronic energy level in which the absorptive transition of interest takes place between Level 1 and Level 3. The normalized rate equations for the energy level as shown in Figure 21.4 define $n = (n_1 - n_3)$, and the steady-state solution is (Hercher, 1967)

$$n_s = \left(1 + W_{13}\left[\left(2 + {}^{A_{32}}\!/_{A_{21}}\right)/\left(A_{31} + A_{32}\right)\right]\right)^{-1} \quad (21.21)$$

where A_{ij} is transition probabilities with associated lifetime of τ_{ij} and W_{13} is the absorption rate.

Treating the effective lifetime as

$$\tau = \left(2\tau_{31}\tau_{32} + \tau_{31}\tau_{21}\right)/\left(\tau_{32} + \tau_{31}\right) \quad (21.22)$$

The steady-state solution can be rewritten as

$$n_s = \left(1 + I\sigma_{13}\tau\right)^{-1} \quad (21.23)$$

And, defining saturation intensity as

$$I_s = \left(\sigma_{13}\tau\right)^{-1} \quad (21.24)$$

Thus,

$$n_s = \left(1 + I/I_s\right)^{-1} \quad (21.25)$$

Thus, the SA coefficient α_{SA}, of a saturable absorber, is related to intensity I of the applied field by the relation (Boyd, 2003)

$$\alpha_{\text{SA}} = \alpha_{\circ} n_s = \frac{\alpha_{\circ}}{1 + I / I_s} \quad (\text{D2.26})$$

where α_0 is the low-intensity absorption coefficient and $\boldsymbol{I_s}$ is a parameter known as the saturation intensity. Most materials show SA and are used for generating giant pulses by passive Q-switching, optical isolator in laser amplifiers and mode-locking (Kafalas et al., 1964; Soffer, 1964; DeMaria et al., 1966).

RSA generally arises in a molecular system when the excited state absorption cross section is larger than the ground-state cross section. In contrast with SA, in which the absorption properties fade with increasing intensity due to the ground-state depletion, RSA can result in large absorption at high intensity. To understand the RSA mechanism, consider a system modelled with three vibronically broadened electronic energy levels having lifetime τ_1, τ_2 and τ_3 (seconds) as shown in Figure 21.4b. Let σ_1 and σ_2 be the absorption cross section for Level 1 to Level 2 and Level 2 to Level 3. As light is absorbed by the material, the first excited state begins to become populated and contributes to the total absorption cross section. Here, when $\sigma_2 \gg \sigma_1$, the total absorption increases, and the material is known as a reverse saturable absorber (Tutt and Boggess, 1993). The three-level diagram describes the simplest case for RSA materials but can generally be applied under circumstances in which transitions from the second excited state are negligible. The change in the intensity of a beam as it propagates ('Z' direction) through the medium is

$$\frac{dI}{dZ} = -\left[N_T\sigma_1 + N_2\left(\sigma_2 - \sigma_1\right)\right]I \quad (21.27)$$

Here, N_T is the total number of active molecules per area in the slice dZ. Thus, transparency at low input energy (level 2 is unpopulated) and high absorption at high input energy (level 2 is substantially populated and level 1 is depleted) leading to OL can be achieved with multi-photon absorbers.

21.3.1.2 Genuine Multi-photon Absorption

Genuine multi-photon absorption (MPA) involves transition from the ground state to an excited state via the simultaneous absorption of 'n' photons. This process can happen either through the absorption of photons that have the same frequency (degeneracy) or that have different frequencies (non-degeneracy) (Liaros and Fourkas, 2017). A single optical field travelling through a medium (along the z-axis) gives rise to degenerate MPA whose optical loss is given by

$$\frac{dI(z,t)}{dz} = -\alpha I(z,t) - \beta I^2(z,t) - \gamma I^3(z,t) - \ldots, \quad (21.28)$$

where $I(z, t)$ is the instantaneous irradiance of the optical beam at position z at time t (the time displacement is to account for the fact that a pulsed laser may be used) and $\alpha^{(n)}$ is the n-photon absorption coefficient.

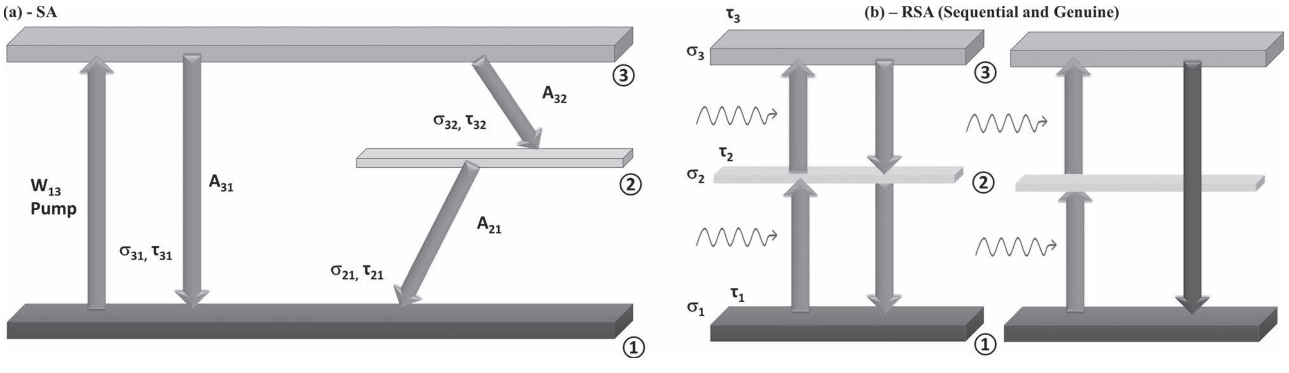

FIGURE 21.4 Three-level energy diagram for (a) SA and (b) RSA.

Two-photon absorption (2PA) involves a transition from the ground state of a system to high-lying state by the simultaneous absorption of two photons from an incident radiation field as shown in Figure 21.5a. This process involves different selection rules than those of single-photon absorption. Hence 2PA spectroscopy compliments linear absorption spectroscopy in studying the excited states of systems. Either two photons from the same optical field oscillating at frequency ω are absorbed to make a transition at 2ω or two optical fields at frequencies ω_e (pump) and ω_p (probe) are absorbed to have a transition at $\omega_e+\omega_p$. In both the cases, the intermediate states are not real (virtual), and hence, two photons are absorbed simultaneously. For a single beam, the 2PA is obtained by the relation,

$$\frac{dI}{dz} = -\alpha I - \beta I^2 \tag{21.29}$$

where dI/dz is optical loss, α is the linear absorption coefficient and β is the 2PA coefficient, which is a macroscopic property characterizing the material.

Three-photon absorption (3PA) involves the transition to excited state by simultaneous absorption of three photons from incident radiation as displayed in Figure 21.5b. These cases are shown involving one, two and three fields. For 3PA, the attenuation of a beam is given by

$$\frac{dI}{dz} = -\alpha I - \gamma I^3 \tag{21.30}$$

where γ is the 3PA coefficient. 3PA is a fifth-order non-linear process and is related to fifth-order susceptibility. In a similar fashion, NLA can be extended to an arbitrary number of absorbed photons. MPA (nPA) refers to the simultaneous absorption of '*n*' photons from a laser beam. The optical loss associated with this mechanism is

$$\frac{dI}{dz} = -\left(\alpha + \gamma^{(n+1)} I^n\right) I \tag{21.31}$$

where $\gamma^{(n+1)}$ is the $(n+1)$ photon absorption coefficient.

Interaction of light with matter can be explained by time-dependent perturbation theory. For conventional light sources with weak field, the first-order perturbation is sufficient to explain the single-photon interaction with atoms or molecules. However, under laser excitation, atoms or molecules interact with more than one photon at the same time. Such NLO processes can be explained with second- and higher-order approximations of the perturbation theory (Laud, 2011). The Schrodinger equation of a quantum system described by time-dependent Hamiltonian $\boldsymbol{H_0}$ under the influence of perturbation represented by $\boldsymbol{H'(t)}$ operator is (Göppert-Mayer, 1931)

$$\left(\hat{H}_0 + \hat{H}'(t)\right)\left|\psi, t\right\rangle = i\hbar \frac{\partial}{\partial t}\left|\psi, t\right\rangle \tag{21.32}$$

whose solution with linear combination of basic states $\left|u_n\right\rangle$ representing the lower state n is

$$\left|\psi, t\right\rangle = \sum C_n(t)\exp\left(-iE_n t/\hbar\right)\left|u_n\right\rangle \tag{21.33}$$

Under light interaction, single-photon absorption results in perturbation of the system to move from energy state '*n*' (Level 1) to energy state 'm' (Level 2) (Figure 21.5b) whose first-order solution is given as

$$C_m^{(1)}(t) = \frac{eE_0\left\langle u_m|\chi|u_n\right\rangle}{2\hbar} \times \left\{\frac{1+\exp\left(\left(i\ \omega_{mn}+\omega\right)t\right)}{\omega_{mn}+\omega} + \frac{1-\exp\left(\left(i\ \omega_{mn}-\omega\right)t\right)}{\omega_{mn}-\omega}\right\} \tag{21.34}$$

When one more photon is absorbed to perturb the system to move from energy state '*m*' (Level 2) to energy state 'l' (Level 3) whose second-order solution is given as

$$C_l^{(2)}(t) = \frac{1}{4\hbar^2}\sum_m e^2 E_0{}^2 \left\langle u_l|\chi|u_m\right\rangle\left\langle u_m|\chi|u_n\right\rangle \times \left\{\frac{1-\exp\left(\left(i\ \omega_{lm}-\omega\right)t\right)}{(\omega_{mn}-\omega)(\omega_{lm}-\omega)} - \frac{1-\exp\left(\left(i\ \omega_{ln}-2\omega\right)t\right)}{(\omega_{mn}-\omega)(\omega_{ln}-2\omega)}\right\} \tag{21.35}$$

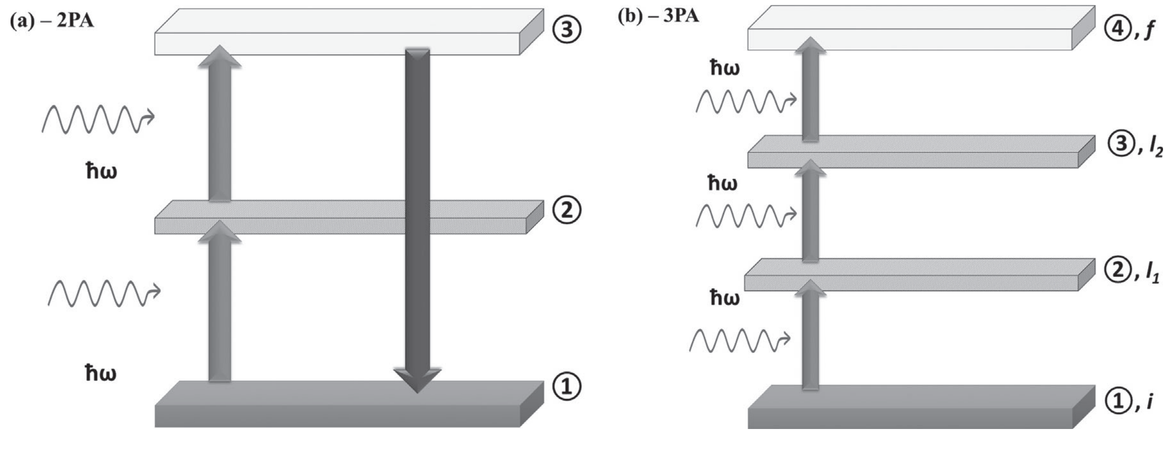

FIGURE 21.5 Energy-level diagram: (a) 2PA and (b) 3PA ($n = 3$).

In the second-order approximation, the presence of two-photon absorption process is observed and the rate of two-photon absorption is (Göppert-Mayer, 1931)

$$P_{n\to l}^{(t)} = \left|C_l^{(2)}(t)\right|^2 = \sum_m \frac{e^4 E_0{}^4}{16\hbar^4} \frac{\left|\langle u_l|\chi|u_m\rangle\langle u_m|\chi|u_n\rangle\right|^2}{(\omega_{mn}-\omega)^2} \times \left\{ \frac{4t\,\sin^2(\,\omega_{ln}-2\omega\,)t/2}{(\omega_{ln}-2\omega)^2\,t} \right\} \tag{21.36}$$

The wave equation for 2PA process driven by single-beam excitation can be described as

$$\frac{dI(z,t)}{dz} = -\alpha^{(1)} I(z,t) - \beta I^2(z,t) \tag{21.37}$$

It is to be mentioned that the macroscopic parameter 2PA coefficient (β) depends on molar concentration. The relation between β (in cm/GW) and molecular 2PA cross section σ_2 (in cm^4/GW) is

$$\beta = \sigma_2\,N_0 = \sigma_2\,N_A C \times 10^{-3}\,(\text{cm/GW}) \tag{21.38}$$

where N_0 is the molecular density of the compound (in cm^{-3}), N_A is the Avogadro's number and C is the molar concentration. The cross section is also often given in units of Göppert-Mayer (GM) in honour of Noble Laureate Maria Göppert-Mayer. 1 GM is equal to 10^{-50}cm^{4}s (Göppert-Mayer, 1931).

Generalizing the expression for the transition from initial state $|i\rangle$ to final state $|f\rangle$ gives the rate equation for MPA as (Laud, 2011)

$$P_{i\to f}^{(t)(t)} = \left| \frac{2\pi}{\hbar^2}\langle f|\hat{H}'|i\rangle + \frac{1}{\hbar}\sum_l \frac{\langle f|\hat{H}'|l\rangle\langle l|\hat{H}'|i\rangle}{(\omega_i-\omega_l)} + \ldots + \frac{1}{\hbar^{n-1}}\sum_{l_1}\sum_{l_2}\ldots\sum_{l_{n-1}} \frac{\langle f|\hat{H}'|l_1\rangle\langle l_1|\hat{H}'|l_2\rangle\ldots\langle l_{n-1}|\hat{H}'|i\rangle}{(\omega_i-\omega_{l_1})(\omega_i-\omega_{l_2})\ldots(\omega_i-\omega_{l_{n-1}})}\ldots \right|^2 X\ \delta(\omega_i-\omega_f) \tag{21.39}$$

Thus, n-photon absorption process can be recast as

$$\frac{dI(z,t)}{dz} = -\alpha^{(1)} I(z,t) - \alpha^{(n)} I^{(n)}(z,t) \tag{21.40}$$

The n^{th} order absorption coefficient $\alpha^{(n)}$ has units of cm$^{(2n-3)}$/GW^{n-1} and the n-photon absorption cross section is given by

$$\sigma_n = \frac{\alpha^{(n)}(\hbar\omega)^{n-1}}{N} \tag{21.41}$$

21.3.1.3 Excited-state Absorption and Free Carrier Absorption

Unlike MPA which involves virtual or bound intermediate excited states, some NLO processes involve population redistribution among real states. One such RSA process is excited-state absorption (ESA) which involves sequential absorption of photons through real states. ESA process can be frequently observed in systems that possess near-resonant electronic states close to the excitation wavelength. Consider a three-level system in which a photon absorption transits a molecule to the first excited state from its ground state (Figure 21.6a). If this molecules can also absorb another photon at the excitation wavelength, to transit to the second excited state before it decays back to the ground state, the involved RSA process is generally termed as ESA (Sutherland et al., 2005; Wang et al., 1990; Aloukos et al., 2011). The light attenuation in this situation can be described by

$$\frac{\partial I(z,t)}{\partial z} = -\sigma_{12}(N_1-N_2)I(z,t) - \sigma_{23}N_2 I(z,t) \tag{21.42}$$

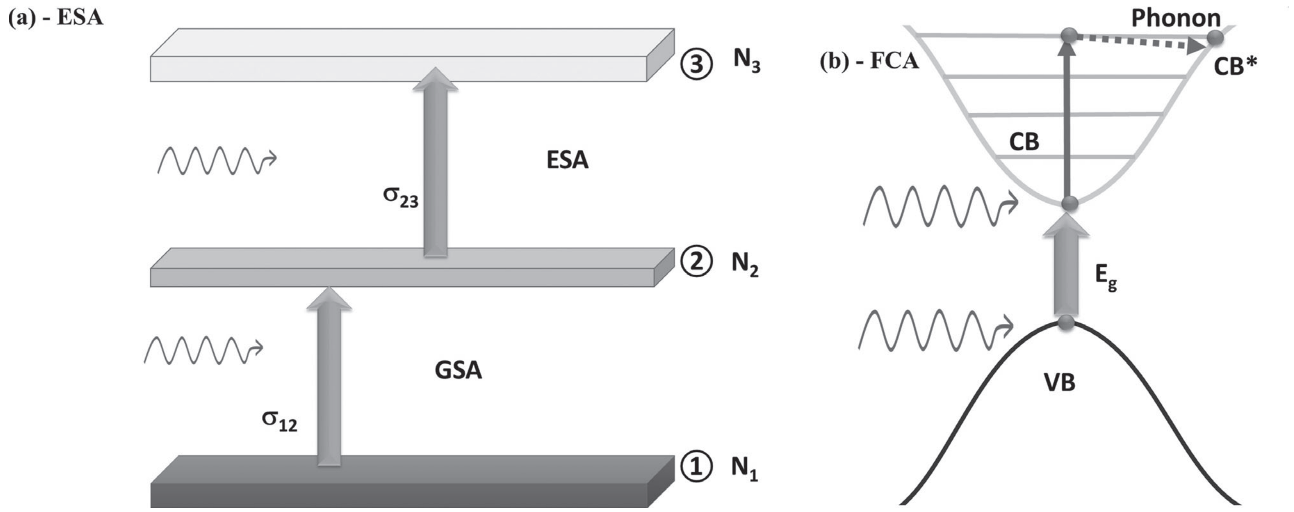

FIGURE 21.6 Energy diagram demonstrating (a) ESA and (b) FCA process.

Here $N_1 \gg N_2$ and $N_3 = 0$, where N_T is the number of absorbing molecules, then

$$\frac{\partial I(z,t)}{\partial z} = -\sigma_{12} N_T I(z,t) - b\sigma_{12}\sigma_{23} N_T I^2(z,t) = -\alpha I(z) - \beta I^2(z) \tag{21.43}$$

Although this equation is analogous in form to equation for 2PA, the quantity β which is constant in 2PA is replaced by the quantity $b\sigma_{12}\sigma_{23}N_T$. This latter quantity is not constant, but rather depends on the irradiance/fluence through the N_T term. When the irradiance/fluence is increased, ground-state depletion becomes important. For these reasons, it is common to use an effective NLA coefficient, β_{eff}, to describe two-step ESA that involves population redistribution (Xia et al., 1997; McLean et al., 1993; Henari et al., 1992).

The free-carrier absorption (Figure 21.6b) is a phenomenon that is analogous to the excited state absorption commonly observed in semiconductors and organic molecules. In semiconductors, during absorption of a photon (equalling the energy band gap of the material), an electron is transferred from maxima of valence band to minima of conduction band. In linear optics, these excited electrons will relax back to the conduction band to recombine with an excited hole after a recombination time. Under sufficiently high intensities with laser, non-linearity promotes the electron in the conduction band to absorb another photon. This process is called free-carrier absorption (FCA) and is mostly phonon-assisted (Tutt and Boggess, 1993). Thus, the attenuation due to free-carrier absorption can be described by

$$\frac{\partial I(z,t)}{\partial z} = -\sigma_0 I(z,t) - \sigma_c \; N_c(I) I(z,t) \tag{21.44}$$

where $\sigma_c = {e^2}\big/{\varepsilon_0 n_0 C m^* \omega^2 \tau}$ is free-carrier cross-section, ω is optical frequency and τ is free-carrier decay time (Wolfe et al., 1989). The free-carrier density is governed by rate equation that is given by

$$\frac{\partial N_c}{\partial t} = \frac{\sigma_0 I}{\hbar\omega} - \frac{N_c}{\tau_c} \tag{21.45}$$

where τ_c is the free-carrier relaxation time due to electron-hole recombination and carrier diffusion. Solving the above equation gives the fluence attenuation as

$$\frac{\partial F}{\partial Z} = \left(1 + \frac{F}{2F_S}\right) F \tag{21.46}$$

where $F_s = \hbar\omega/\sigma_c$ is the saturation fluence.

21.3.2 Non-linear Refraction

Many of the interesting phenomena of NLO such as optical Kerr effect, non-local effects, saturation and changes in physical properties of medium and cascading effects derive their behaviour from non-linear refraction. In general, non-linear index of refraction can be defined as a change in the refractive index or the spatial distribution of the refractive index of a medium due to the presence of intense optical waves. The non-linear index of refraction can also produce detrimental effects, such as unwanted phase aberrations or even optical damage. Thus, it becomes an important consideration in any experiment or application employing the manipulation of intense optical beams (Sutherland, 2003; Boyd, 2003). Consider a laser beam with intensity of optical field I is interacting with material whose refractive index can be given as

$$n = n_0 + \Delta n = n_0 + n_2 I \tag{21.47}$$

where n is the total refractive index, n_0 is the linear refractive index, n_2 is the non-linear refractive index and I is the intensity of light given by (Verma et al., 2007)

$$I = \frac{n_0 C}{2\pi} \left|E(\omega)\right|^2 \tag{21.48}$$

where $E(\omega)$ is the amplitude of the incident light. The non-linear refractive index is related to the third-order NLO susceptibility by the relation

$$n_2 = \frac{12\,\pi^2}{{n_0}^2 C} \chi^{(3)} \tag{21.49}$$

A small change in the non-linear refractive index can lead to dramatic NLO effects. Different physical phenomena responsible for non-linear refraction are summarized as follows.

21.3.2.1 Electronic Polarization

It involves the electric dipole interaction between the electrons in atoms and molecules and an electromagnetic field. Here, a distortion of the electron cloud about an atom or molecule by the optical field takes place and the polarization induced by the field has a non-linear component. If the atom or molecule is highly polarizable, then it can exhibit a significant electronic non-linearity. The proportionality is calculated from the first-order perturbation theory, and in the condensed matter limit pertinent to NLO, the interactions are described by the sum of three different third-order susceptibilities $\chi^{(3)}_{ijkl}$ derived from the molecular susceptibilities. The non-linear refractive index associated with the electronic polarization is (Sutherland, 2003)

$$n_2 = \frac{3}{4n_0} \chi^{(3)}_{ijkl} \tag{21.50}$$

21.3.2.2 Raman-induced Kerr Effect and Photorefractive Effect

Bound electronic Kerr effect is dominant in the transparency range of semiconductors and dielectrics. Here, the non-linearity is instantaneous and is due to anharmonic motion of bound electrons. This effect is related to stimulated Raman scattering and is an example of a strong beam inducing a refractive index change for a weak probe beam. It is a third-order non-linear polarization process, and the polarization at the Stokes frequency is directly proportional to the real part of NLO susceptibility. It is a four-photon process wherein a Stokes beam incident on a Raman active medium is amplified. If g_s is Raman gain coefficient and λ_s is Stokes wavelength, then the non-linear refractive index associated with Raman-induced Kerr effect is (Sutherland, 2003)

$$n_2 = \frac{C\varepsilon_0 n_0 \lambda_s}{8\pi} g_s \tag{21.51}$$

Unlike the previous examples, in Photorefractive effect the change in non-linear refractive index does not depend on the magnitude of the intensity. Rather, it depends on the spatial variation of intensity which induces a non-local change in refractive index. The formation of this space charge density leads to the build-up of an internal space charge field. This field forms an index grating by the linear electro-optic (Pockel's) effect.

21.3.2.3 Molecular Orientational Effects and Population Redistribution

Under the influence of a strong electric field, the molecules tend to orient themselves parallel to the applied electric field to minimize the free energy. When a strong optical wave like laser is applied to a system, the permanent and induced dipole moments of the molecules experience a torque attempting to align the most polarizable axis with the applied field. This will experience a change in the local index of refraction and thus the molecular non-linear polarization. In fact, these molecular orientational polarizations are responsible for the thermal energy-dependent contribution to the NLO effects. Here when the applied field is dc and the system responds to time-averaged field squared, it is called as optical Kerr effect (Sutherland, 2003; Laud, 2011). Real transitions are induced in molecule if the frequency of excitation is near a resonant energy transition. This is called as population redistribution as the electrons can occupy real excited states for a finite period of time. At low intensity of the excitation, the total number of atoms or molecules in the ground electronic state determines the optical polarization, and thus, population redistribution produces a change in the index of refraction. Population redistribution-induced non-linear refraction commonly occurs in transparent metal-doped dielectric solids, organic liquids and molecular vapours and, most importantly, in semiconductors.

21.3.2.4 Electrostriction

It is a property of all insulators and dielectrics, in which under the applied electric field, the system by itself manifests a relatively slight change of shape, or mechanical deformation. However, reversal of the electric field does not reverse the direction of the deformation. This phenomenon occurs due to the superposition of coherent waves and it depends on the presence of an inhomogeneous (spatially varying time-averaged electric field) intensity. An interference pattern of bright and dark fringes along the propagation creates an inhomogeneous field-induced force. This field-induced stress called as electrostrictive force leads to an increase in the material density. Increase in the density of molecules increases the electromagnetic energy density and thus an increase in the refractive index. For an electrostrictive medium having density ρ with ν_a as the acoustic velocity, non-linear refractive index is given as (Sutherland, 2003)

$$n_2 = \frac{\varepsilon_0}{36\nu_a^2\rho}\frac{\left[\left(n_0^2+2\right)\left(n_0^2-1\right)\right]^2}{n_0} \tag{21.52}$$

21.3.2.5 Thermo-optic Effects

Thermo-optic non-linearity arises mainly due to partial absorption of laser power as it propagates through medium. Absorption leads to a temperature change δT, which in turn also leads to a change in local density. A change in density leads to the generation of sound waves, which effectively relieve the stresses induced by the density changes. Both δT and $\delta\rho$ lead to changes in refractive index (Christodoulides et al., 2010)

$$\delta n = \left(\frac{\delta n}{\delta\rho}\right)_T \delta\rho + \left(\frac{\delta n}{\delta T}\right)_\rho \delta T \tag{21.53}$$

Since the effect on index of density changes is usually much smaller than temperature changes, density changes in the first approximation are neglected.

The change in index due to a temperature rise ΔT can be expressed by

$$n_2 = \frac{\alpha\tau}{\rho C}\frac{dn}{dT} \tag{21.54}$$

where α is the linear absorption coefficient, τ is the thermal diffusion time and $\frac{dn}{dT}$ is called the thermo-optic coefficient. Under laser interaction, most of the liquids and solids expand with decrease in density, and the change in refractive index represented as $\frac{dn}{dT}$ is generally negative. However, in some semiconductors, due to Franz–Keldysh effect the absorption band edges are red-shifted with temperature and it produces a positive thermo-optic coefficient (Christodoulides et al., 2010; Sutherland, 2003). Among the different modes of laser excitation, continuous wave mode laser excitation generally induces thermo-optic non-linearity. And, also in pulsed laser, short-pulse (millisecond-nanosecond) and high-repetition laser shows thermal effects. If $I^{\max}$ is the laser intensity at the centre of the laser beam with radius R and k is the thermal conductivity of the medium, then maximum temperature at the centre of the laser beam is

$$T_1^{\max} = \frac{\alpha I^{\max} R^2}{K} \tag{21.55}$$

And for pulsed laser, the maximum temperature is related to the pulse duration (t_τ) and heat capacity per unit volume ($\rho_o C$) as

$$T_1^{\max} = \frac{\alpha I^{\max} t_\tau}{\rho_0 C} \tag{21.56}$$

Consequently, it is interesting to note that the pulse duration is an important factor that decides the nature of non-linear response. For laser pulses that are short ($t_p \ll 30$ ps) thermal effects make the contribution (Boyd, 2003). In the thermo-optic non-linearity, one of the fascinating concepts that can be explained in non-linear refraction is self-focusing and self-defocusing. Under laser excitation, the medium by itself acts as thermal lens to self-focus or self-defocus the laser beam due to non-linear refraction.

Since the laser possesses intensity distribution in the form of a Gaussian profile, refractive index gradient (change in refractive index as a function of position) also follows the shape of the beam. This makes the medium to behave equivalent like a large number of glasses placed with refractive index gradient from the centre of the beam. This avails the medium to act like a positive or negative lens to converge or diverge the laser beam due to the contribution of non-linear refractive index. For a positive non-linear refractive index ($n_2 > 0$), larger phase retardation occurs at on-axis than in the wings of the beam. This has the effect of creating a positive lens that tends to focus the beam. For medium with negative non-linear refractive index ($n_2 < 0$), the phase retardation at on-axis is smaller than that in the wings, and the beam thus diverges as illustrated in Figure 21.7 (Sutherland, 2003).

21.3.3 Optical Limiting

Although plenty of NLO phenomena are identified in the past 60 years, current research is mainly focused on OL. This is because the field of laser has shown a large overwhelming advance and it is now easy to attain power flux densities of the ultrashort light pulses in the range 10^{12}–10^{19} W cm^{-2}. Thus, the need for the protection of optical components and human eyes from laser inflicted damages has increased enormously. An OL is an NLO effect in which the transmitted energy/fluence/power/irradiance by an optical system is limited below the maximum value, irrespective of the magnitude of the input, while maintaining high transmittance at low input powers (Tutt and Boggess, 1993; Fakhri et al., 2015). A graph drawn between the input intensity versus output intensity (see Figure 21.8) with non-linear interaction can be divided into three regions. Region I is designated as the linear regime (input increases linear with output) which obeys Beer's law; Region II is limiting regime (output gets saturated) that originates due to non-linearity and Region III is damage regime (input increases with output) due to catastrophic breakdown of materials. Here, the terms I_{th}, I_c and I_d represent the limiting threshold, clamping amplitude and damage threshold, respectively. In an ideal optical limiter, the transmittance changes abruptly at some critical input intensity or threshold and therefore exhibits an inverse dependence on the intensity; the output is thus clamped at a certain value. If this value is below the minimum that can damage the particular equipment, the optical limiter becomes an efficient safety device. The limiting threshold ($I_{1/2}$) of the material is defined as the input intensity/fluence at which the transmittance reduces to half of the linear transmittance (Fakhri et al., 2015). Clamping threshold of the material is defined as the input intensity/fluence at which the transmittance starts clamping. An optical limiter can clamp the output intensity/fluence over a wide range of input intensity/fluence but may breakdown after certain value and exhibit high transmittance again. The threshold up to which the material can provide effective limiting is called the damage threshold, and the ratio of damage threshold to the limiting threshold is called the dynamic range of the optical limiter. Desirable attributes of an effective optical limiter are (i) low limiting threshold and high optical damage threshold and stability, leading to a large dynamic range; (ii) sensitive broadband response to long and short pulses; (iii) fast response time and (iv) high linear

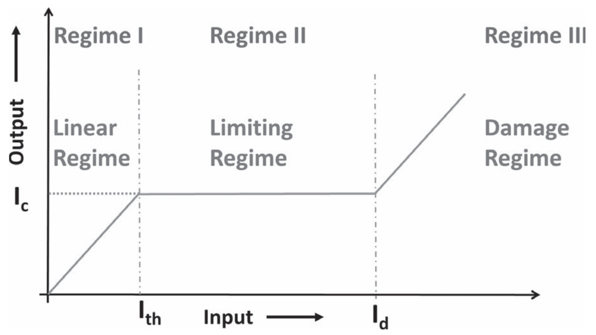

FIGURE 21.8 Schematic representation of the behaviour of an ideal optical limiter.

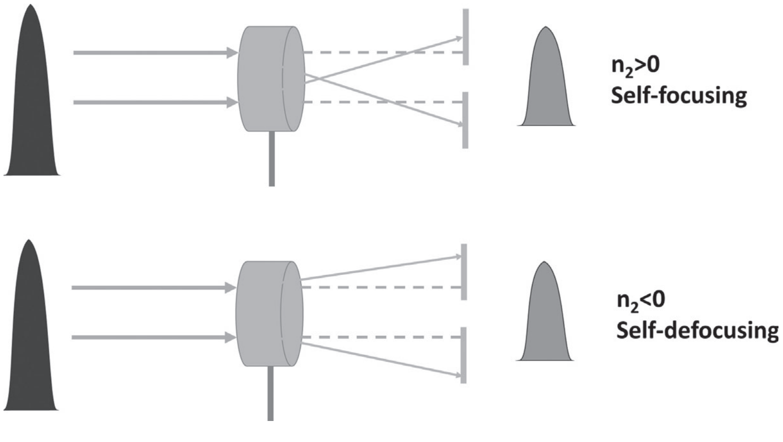

FIGURE 21.7 Schematic illustrations of self-focusing and defocusing: (a) $n_2 > 0$; (b) $n_2 < 0$.

transmittance, optical clarity and robustness (i.e., resistance to damage/degradation with time due to humidity, temperature, etc.) (Sutherland, 2003; Khoo et al., 1988).

A variety of NLO phenomena used to demonstrate OL include non-linear absorptive processes such as RSA, multi-photon absorption and FCA, non-linear refractive processes such as self-focusing, self-defocusing, photo-refraction and optically induced scattering. However, the OL effect can be broadly classified as (i) energy-spreading and (ii) energy-absorbing optical limiters. Figure 21.9 shows the classification of the various NLO phenomena that can lead to OL action (Henari et al., 1992). The mechanism involved in energy-spreading optical limiters is non-linear refraction and non-linear scattering in NLO media. The key requirement of these optical limiters is to place an aperture in front of a detector to utilize the spatial energy distribution of transmitted beam. With increase in the input laser intensity, major portion of the incident laser spreads to wider angle range, and the portion passing through a small aperture will decrease accordingly resulting in OL effect. The energy-absorbing optical limiters do not require any aperture or pinhole, and the OL effect relies on NLA in which the transmissivity decreases with increase in input laser intensity. Here at sufficiently high intensities, the probability of absorbing more than one photon by the medium can be greatly enhanced. Thus, the non-linear medium behaves like a smart material to be highly transparent for lower intensity and turns opaque for higher intensity of input light as depicted in Figure 21.10 (Perry 1997; Lepkowicz et al., 2002).

21.3.4 Z-scan Experimental Technique

Optical non-linearities in materials that arise due to laser interaction can be measured by several techniques. Among them ellipse rotation and beam-distortion measurements are although frequently used, they are insensitive and require precise beam scans followed by detailed wave-propagation analysis. Further, non-linear interferometry, degenerate four-wave and three-wave mixing are meant for their sensitivity but involve complex experimental set-up. Overcoming the limitations of existing experiments to measure the intensity-dependent NLO coefficients of materials, a simple experimental technique called as Z-scan technique was developed by Sheik Bahae et al. (1989). This method works on the principle of spatial beam distortion which involves the transformation of phase-to-amplitude distortion. It minimizes the parasitic effects due to the presence of linear sample inhomogeneities and allows a direct measurement of both the sign and magnitude of real and imaginary parts of the third-order NLO susceptibility ($\chi^{(3)}$) of materials. In this single-beam Z-scan configuration, the far-field intensity as a function of position is measured by subjecting the sample to undergo translational motion along the axis of a focused Gaussian laser beam (generally treated as the Z-direction). This allows the sample to suffer increase and decrease in maximum intensity incident on the sample which produce wavefront distortions with both amplitude and phase variations due to NLO effects (Sheik-Bahae et al., 1990). Z-scan can be performed in two modes, viz., (i) open aperture (OA) and (ii) closed aperture (CA). In the CA mode Z-scan experiment, the far-field transmittance is measured through an aperture placed with respect to the focal region. The collected central part of the transmitted light contains information about both NLA and non-linear refraction. Since the phase distortion is converted into corresponding amplitude variation, the real part of the NLO susceptibility tensor can be calculated.

On the other hand, in OA mode Z-scan experiment, the far-field transmittance is measured without an aperture. As the output intensity is sensitive only to the NLA of the sample, the imaginary part of the NLO susceptibility tensor can be calculated. The ratio of CA Z-scan data by the OA Z-scan data gives information on pure non-linear

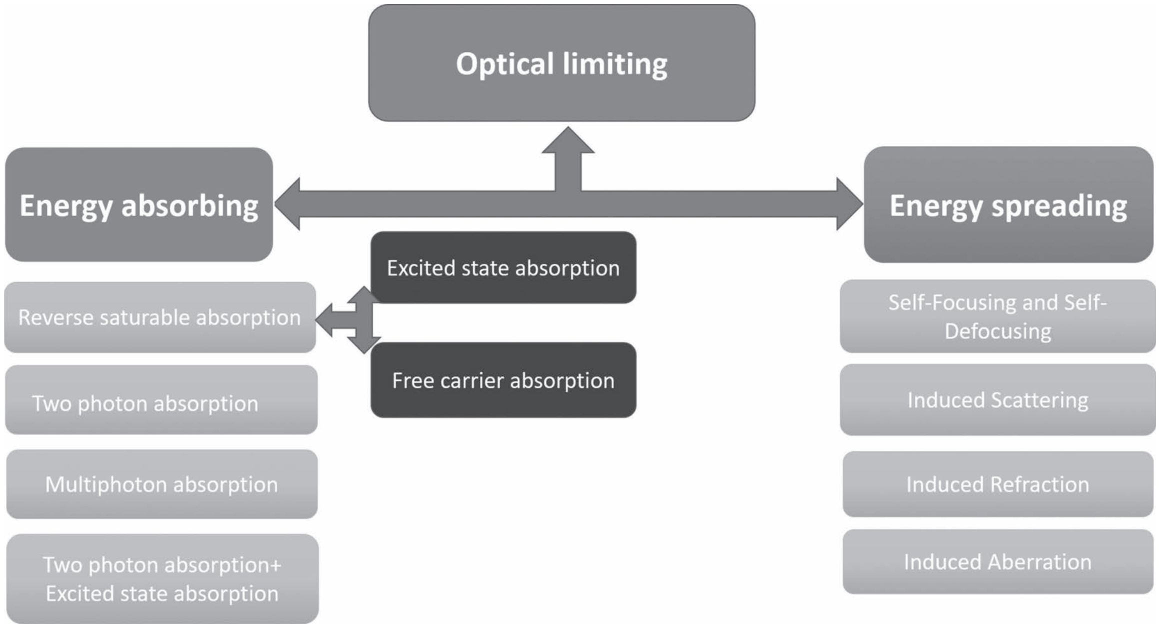

FIGURE 21.9 Classification of optical limiting behaviour.

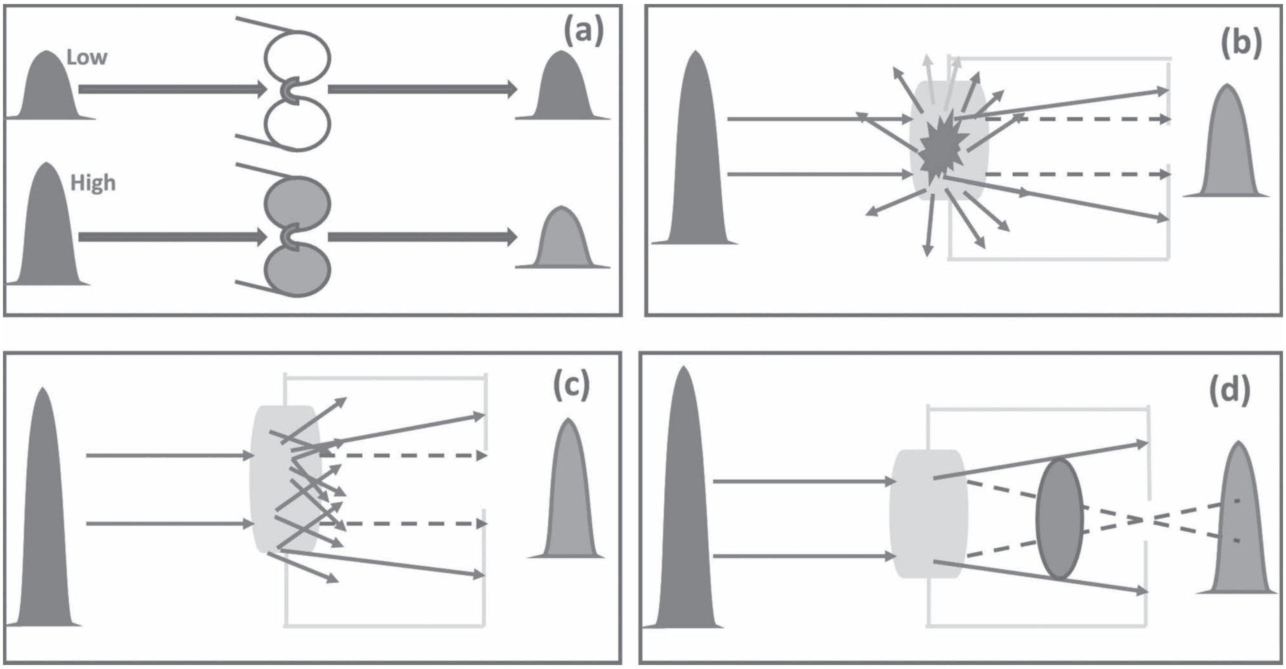

FIGURE 21.10 Schematic of optical limiting device based on (a) non-linear absorption in which material acts as transparent medium at low intensity and turn opaque medium at high intensity, and energy-spreading-type optical limiting device based on (b) induced aberration, (c) induced scattering and (d) induced refraction.

refraction, and the method is known as "divided Z-scan graph" (Sheik-Bahae et al., 1989, 1990). The simple schematic arrangement of Z-scan is shown in Figure 21.11, and it uses a Gaussian laser beam in a tight-focusing geometry. The focused beam possesses maximum intensity at the focus of the lens (termed as $Z = 0$), and as it moves towards (+Z direction) and away (–Z direction) from laser source, it suffers an intensity variation in both directions. Thus, the measurement of transmittance as a function of position is equivalent to the measurement of non-linear transmittance as a function of intensity.

Z-scan measurement functions on "thin medium" approximation and slowly varying envelope approximation. Here the Rayleigh's range Z_0 is maintained to be always greater than sample thickness, and thus, the beam profile does not vary appreciably inside the sample. This technique is highly sensitive to the thickness of the samples and Gaussian profile of the beam, and any deviation gives rise to erroneous results.

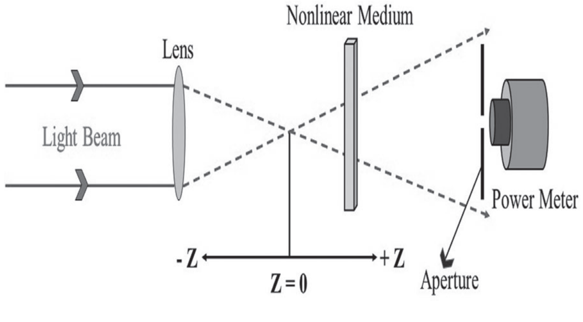

FIGURE 21.11 Schematic diagram of Z-Scan experiment.

Thus, Rayleigh range Z_0 is an important parameter in *Z*-scan and is defined by the expression (Justus et al., 1993),

$$Z_0 = \frac{k\omega_0^2}{2} \tag{21.57}$$

where k is the wave vector and $2\omega_0$ is the beam waist (diameter) and is given by

$$2\omega_0 = \frac{4f\lambda}{\rho D} \tag{21.58}$$

In this expression, 'f' is the focal length of the lens used, 'λ' is the wavelength of the radiation used and 'D' is the beam diameter. Apart from the single-beam Z-scan method, extensions have been added to enhance its sensitivity and applicability (Chapple et al., 1997). EZ-scan (eclipsed Z-scan) utilizes the fact that the wings of a circular Gaussian beam are much more sensitive to the far-field beam distortion (Bridges et al., 1995). A reflection Z-scan technique has been introduced to study the optical non-linearities of surfaces. Z-scan with top-hat beams and elliptical Gaussian beams avails better sensitivity (Huang and Sun, 2000). Two-colour Z-scan can measure the non-degenerate non-linearities and time-resolve the dynamics of the non-linear process by introducing a delay between the pump and probe beams (Chapple et al., 1994). Astigmatic Gaussian beams can also be employed for Z-scan measurements in which a slit is used instead of a (circular) aperture. The Z-scan technique is used extensively to study different materials like semiconductors, nanocrystals, semiconductor-doped glasses, liquid crystals, organic materials, biomaterials, etc.

21.3.4.1 Theory of Open Aperture Z-scan

Under "thin medium approximation", far-field transmittance measurement without aperture is insensitive to non-linear refraction, and thus, NLA is manifested in the OA Z-scan measurements. As samples are moved with respect to focus, Z-scan traces are symmetric with minimum or maximum at $Z = 0$. For NLA like MPA (nPA), a transmission minimum is observed at the focal point (Saravanan et al., 2016, 2018). On the other hand, saturation of absorption, transmission increases with increase in incident intensity and results in a transmission maximum at the focal region. And further for linear absorption, a straight-line Z-scan graph is obtained. Typical OA Z-scan curves for RSA, SA and linear absorption are illustrated in Figure 21.12.

The intensity-dependent NLA coefficient $\propto(I)$ can be written in terms of linear absorption coefficient, $\propto$, and 2PA coefficient, β, as follows (Sheik-Bahae et al., 1989, 1990):

$$\propto(I) = \propto + \beta I \tag{21.59}$$

The irradiance distribution at the exit surface of the sample can be written as

$$I_r(z,r,t) = \frac{I_r(z,r,t)e^{-\alpha l}}{1+q(z,r,t)} \tag{21.60}$$

where

$$q(z,r,t) = \beta I(z,r,t)L_{\text{eff}} \tag{21.61}$$

Here, L_{eff} is the effective length and is given in terms of sample length l and α by the relation

$$L_{eff} = \left(\frac{1-e^{-\alpha l}}{\alpha}\right) \tag{21.62}$$

The total transmitted power $P(z,t)$ is obtained by integrating Equation 21.50 over z and r and is given by

$$P(z,t) = P_i(t)e^{-\alpha l}\frac{ln\left[1+q_0(z,t)\right]}{q_0(z,t)} \tag{21.63}$$

$P_1(t)$ and $q_0(z, t)$ are given by Equation 21.52 and 21.53, respectively, as

$$P_1(t) = \frac{\pi\omega_0^2 I_0(t)}{2} \tag{21.64}$$

$$q_0(z,t) = \frac{\beta I_{0L_{\text{eff}}} z_0^2}{Z^2+z_0^2} \tag{21.65}$$

For a pulse of Gaussian temporal profile, Equation 21.47 can be integrated to give the transmission as

$$T(z) = \frac{C}{q_0\sqrt{\pi}}\int_{-\infty}^{\infty}\ln\left(1+q_0 e^{-t^2}\right)dt \tag{21.66}$$

By fitting the experimental results to Equation 21.54, the NLA coefficient is obtained. If $|q_0| < 1$, then it can be simplified as

$$T_{OA} = \sum_{m=0}^{\infty}\frac{[-q_0(z,0)]^m}{(m+1)^{\frac{3}{2}}} \tag{21.67}$$

Once an OA Z-scan is performed, NLA coefficient (β) can be unambiguously deduced. Estimation of NLA coefficient can be made by theoretically fitting the normalized transmittance with experiment OA data.

21.3.4.2 Wavelength-dependent Non-linear Absorption Coefficient

Employing the Sheik-Bahae formalism (Sheik-Bahae et al., 1989, 1990), the nature of non-linearity and the magnitude of NLA coefficient can be estimated from the recorded OA Z-scan using the normalized transmittance equation as

$$T_{\text{OA}} = \frac{1}{1+\beta L_{\text{eff}}\left[\dfrac{I_0}{\left(1+\left(\dfrac{Z}{Z_0}\right)^2\right)}\right]} \tag{21.68}$$

where $q_0(z,o) = \beta I_0 L_{\text{eff}}, \mathrm{I}_0 = \frac{2\,\mathrm{P}}{\pi\omega_0{}^2}$ is the on-axis peak intensity at the focus ($Z = 0$), $L_{\text{eff}} = \frac{\left[1-\exp(-\alpha l)\right]}{\alpha}$ is the effective

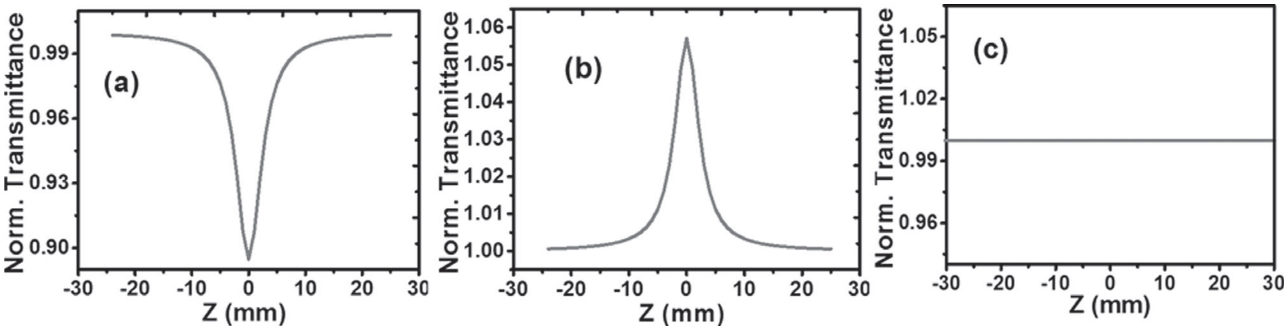

FIGURE 21.12 Typical OA Z-Scan curve of sample with (a) RSA, (b) SA and (c) linear absorption.

thickness of the sample, α is the linear absorption co-efficient and L is the sample thickness. To understand the relation between wavelength and NLA coefficient (Muruganandi et al., 2018), the above equation can be rewritten in terms of wavelength by putting, $Z_0 = \frac{\pi\omega_0^2}{\lambda}$

$$T_{\mathrm{OA}} = \frac{1}{1+\beta L_{\mathrm{eff}}\left[\dfrac{I_0}{1+\left(\dfrac{Z}{\pi\omega_0{}^2/\lambda}\right)^2}\right]} \tag{21.69}$$

Rearranging Equation 21.57 gives,

$$\beta = \frac{1}{L_{\mathrm{eff}} I_0}\left\{\frac{1+\dfrac{Z^2\lambda^2}{\pi^2\omega_0{}^4}}{T_{\mathrm{OA}}} - 1 - \frac{Z^2\lambda^2}{\pi^2\omega_0{}^4}\right\} \tag{21.70}$$

$$\beta = \frac{1}{L_{\mathrm{eff}} I_0}\left\{\frac{1}{T_{\mathrm{OA}}} + \frac{Z^2\lambda^2}{\pi^2\omega_0{}^4 T_{\mathrm{OA}}} - 1 - \frac{Z^2\lambda^2}{\pi^2\omega_0{}^4}\right\} \tag{21.71}$$

$$\beta = \frac{1}{L_{\mathrm{eff}} I_0 T_{\mathrm{OA}}} + \frac{Z^2}{L_{\mathrm{eff}} I_0 \pi^2\omega_0{}^4 T_{\mathrm{OA}}}\lambda^2 - \frac{1}{L_{\mathrm{eff}} I_0} - \frac{Z^2}{L_{\mathrm{eff}} I_0 \pi^2\omega_0{}^4}\lambda^2 \tag{21.72}$$

$$\beta = \frac{1}{L_{\mathrm{eff}} I_0 T_{\mathrm{OA}}} - \frac{1}{L_{\mathrm{eff}} I_0} + \frac{Z^2}{L_{\mathrm{eff}} I_0 \pi^2\omega_0{}^4}\left\{\frac{1}{T_{\mathrm{OA}}} - 1\right\}\lambda^2 \tag{21.73}$$

$$\beta = A' - B' + C'\lambda^2 \tag{21.74}$$

Generalizing Equation 21.62 establishes the relation between NLA coefficient and wavelength as (Sabari Girisun et al., 2018a, b),

$$\beta \ \alpha \ \mathrm{A}\lambda^2 \pm C \tag{21.75}$$

The equation resembles the equation of a parabola, and it clearly emphasizes that NLA coefficient varies as square of the wavelength. Considering the positive quadrant of the curve, it can be observed that NLA coefficient increases with increase in wavelength. However, it is to be admitted that variation of NLA coefficient with respect to wavelength is material-dependent (Sabari Girisun et al., 2018a, b),

21.3.4.3 Theory of Closed Aperture Z-scan

The transmittance characteristics of the sample measured at far-field with a finite aperture depend on the non-linear refractive index of the sample. During Z-scan experiment, as the sample is positioned at various points along the Z-scan axis, the sample behaves like a self-lens of variable focal length due to the change in the refractive index at each position ($n = n_o + n_2 I$). When the sample is far from the focus and closer to the lens, the irradiance is low and the transmittances are linear. Hence, the transmittance through the aperture is fairly constant in this region. As the sample is moved closer to focus, the irradiance increases inducing a lensing effect. A negative lens before the focus tends to collimate the beam leading to an increase in the measured transmittance at the aperture. And after the focus it tends to diverge the beam resulting in the decrease of transmittance. Thus, the curve for Z versus transmittance has a peak followed by a valley for a negative refractive non-linearity (Figure 21.13a). The curve for a positive refractive non-linearity gives rise to the opposite effect (Figure 21.13b), i.e., a valley followed by a peak (Sheik-bahae et al., 1989, 1990).

Following the approach of Sheik-Bahae et al. (1989, 1990) based on the "Gaussian decomposition" method, the normalized Z-scan transmittance $T(z)$ for CA mode can be calculated as

$$T_{\mathrm{CA}}(z) = \frac{\int_{-\infty}^{\infty} P_r\left(\Delta\Phi_0(t)\right)dt}{S\int_{-\infty}^{\infty} P_i(t)\,dt} \tag{21.76}$$

where $P_i(t) = \pi\omega_0^2 I_0(t)/2$ is the instantaneous input power, ω_0 is the beam waist of the laser, P_r is the transmitted power through the aperture of radius r_a, $S = 1 - \exp\left(-2r_a^2/\omega_a^2(z)\right)$ is the aperture's linear transmittance, with ω_a denoting the beam radius at the aperture, and $\Delta\Phi_0 = k\gamma' I_0(t) L_{\mathrm{eff}}$ is the on-axis

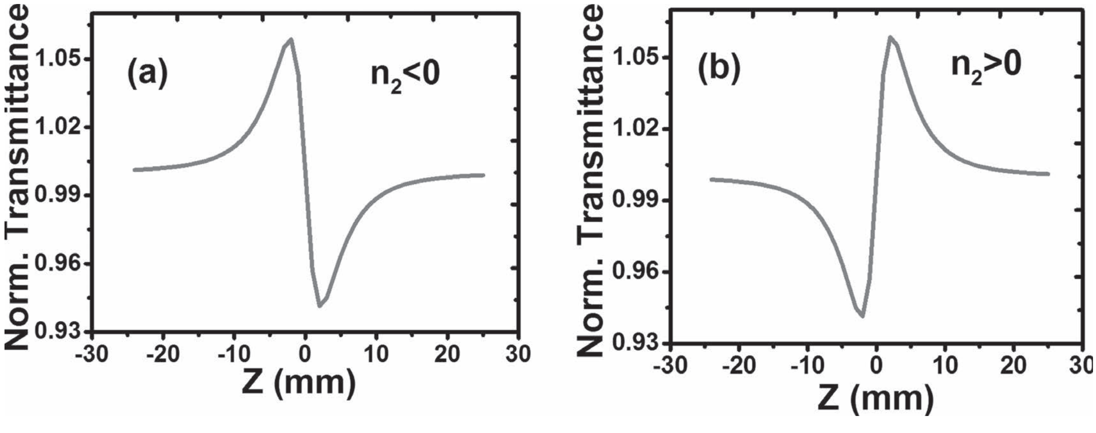

FIGURE 21.13 Typical closed aperture Z-scan curve of samples having (a) negative and (b) positive non-linear refractive index.

phase shift at the focus, with $k = 2\pi/\lambda$ being the wave vector and γ' being the non-linear refraction parameter. Assuming cubic non-linearity (i.e., a $\chi^{(3)}$ effect) and square pulses, for small phase distortions $\left(|\Delta\Phi_0| < 1\right)$ and small aperture $(S \cong 0)$ placed in the far-field, the expression for the transmittance simplifies to

$$T_{\text{CA}}(x) \cong 1 - \frac{4\Delta\Phi_0 x}{\left(x^2+9\right)\left(x^2+1\right)} \tag{21.77}$$

where $x = Z/Z_0$ and Z_0 is the Rayleigh length. For the positive $\Delta\Phi_0$ value, the normalized transmittance shows a "valley-peak" feature, indicating positive refractive non-linearity. In other words, the sample in this case acts as positive lens. On the other hand, for the negative $\Delta\Phi_0$ value, the obtained curve exhibits a peak-valley trace, indicating negative refractive non-linearity (i.e. a defocusing lens). Also, the *Z*-axis separation between the two extremes (peak and valley) is constant and is given by

$$\Delta Z_{p-v} \cong 1.7 Z_0 \tag{21.78}$$

For small phase distortion and a small aperture ($S \cong 0$)

$$\Delta T_{p-v} \cong 0.406|\Delta\Phi_0| \tag{21.79}$$

Therefore, by substituting $\Delta\Phi_0 = k\gamma' I_0(t) L_{\text{eff}}$ in Equation 21.67, the non-linear refractive index parameter n_2 or γ' can be deduced from the "closed-aperture" curve. Here, it is to be mentioned that the non-linear refractive index can also be obtained directly from $\Delta T_{\text{pv}}^{\text{CA}}$ (NLA coefficient from $\Delta T_{p\ (\text{or})\ v}^{\text{OA}}$ value of experimental data).

21.3.5 Third-order NLO Susceptibility and Optical Limiting

In both modes of Z-scan experiment, NLA coefficient and non-linear refractive index calculated from the theoretical fit will always be slightly lower than those from the experimental data. The non-linear curve fitting tends to be more accurate in the theoretical fit which depends on the whole range of values rather than just the maximum and minimum. The real and imaginary parts of the third-order NLO susceptibility can be obtained using the relations (Sutherland, 2003),

$$\text{Re}\chi^{(3)} = \frac{10^{-4}\ \varepsilon_{\circ} C^2\ n_{\circ}^2 n_2 \left(\text{cm}^2\ \text{W}^{-1}\right)}{\pi} \tag{21.80}$$

$$\text{Im}\,\chi^{(3)} = \frac{10^{-2}\ \varepsilon_{\circ} C^2\ n_{\circ}^2\ \lambda\beta\left(\text{cm}\,\text{W}^{-1}\right)}{4\pi^2} \tag{21.81}$$

where ε_0 is the permittivity of the vacuum, n_0 is the linear refractive index of the sample and C is the velocity of light in vacuum. When the real part of the third-order non-linear susceptibility is larger than the imaginary part, it indicates that the non-linearity is dominated by the non-linear refraction behaviour. Thus, the third-order NLO susceptibility is

$$\chi^{(3)} = \sqrt{\left[\text{Re}\left(\chi^{(3)}\right)\right]^2 + \left[\text{Im}\left(\chi^{(3)}\right)\right]^2} \tag{21.82}$$

OL is the non-linear process in which beyond a particular fluence (called as onset limiting threshold), the transmittance gets attenuated by a non-linear process providing the possibility to avoid induced laser damage. From the Z-scan curve, it is possible to plot the OL curve (Figure 21.14) in which sample transmission against input laser fluence can be drawn (Sutherland, 2003). The input fluence $F_{\text{in}}(z)$ at any position Z can be calculated from the corresponding beam radius $\omega(z)$ and the input laser pulse energy E_{in} using the relation,

$$\omega(z) = \omega(0)\left[1 + (z/z_0)^2\right]^{1/2} \tag{21.83}$$

The position-dependent fluence is given by (Saravanan et al., 2017)

$$F(z) = 4\sqrt{\ln 2}\left(\frac{E_{\text{in}}}{\pi^{3/2}}\right) \Big/ \omega(Z)^2 \tag{21.84}$$

where $\omega(0)$ is the focal spot radius and Z_0 is the Rayleigh range.

As the equation emphasize, position-dependent input fluence also depends upon wavelength and change in wavelength of excitation has a direct impact on fluence, even though input pulse energy (E_{in}) is maintained to be the same. Thus, wavelength-dependent non-linearity can induce different range of OL fluence domain, which is very important to be explored for the realization of broadband optical limiter. The OL curve can also be directly drawn by performing Z-scan experiment at single position (preferably peak or valley position of CA Z-scan mode). Here, the input is varied and the corresponding output is measured.

21.3.6 Third-order NLO Materials: Brief Survey

Materials are probably deeper seated and advancement of societies has been intimately tied to the ability to produce and manipulate materials. With tremendous development in the molecular engineering, numerous materials have evolved with specialized characteristics to meet the needs of humankind

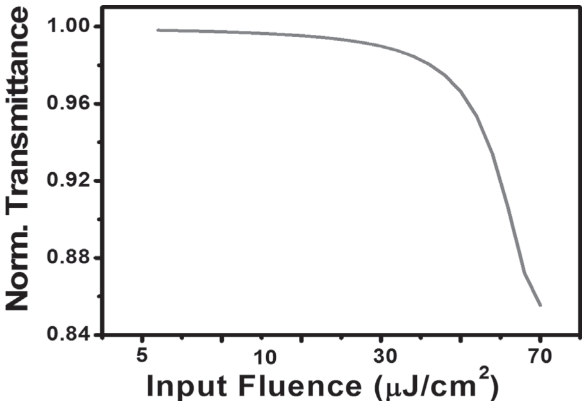

FIGURE 21.14 Typical optical limiting curve obtained from the OA Z-scan data.

(Callister and Rethwisch, 2007). Basically, all nanomaterials exhibit NLO phenomenon, and they are broadly classified as metal NPs, metal NCs, perovskites and metal dichalcogenides. Apart from the focus on second-order NLO materials which have been exclusively used for frequency conversion process, it is also necessary to understand the third-order NLO materials due to their recent demand in the OL applications. In this short review, non-linearity of some of the known nanomaterials is briefly discussed. Tables 21.2 and 21.3 summarize the estimated third-order NLO properties of metal NPs and metal NCs by Z-scan method under different lasers like CW laser, nanosecond pulsed laser, picosecond laser and femtosecond laser. It is known that non-linearity is an intensity-dependent phenomenon and thus very sensitive to experimental parameters. Thus, direct comparison of NLO coefficients is not appropriate, and data summarized are to inculcate the basic ideas of relating structural and NLO behaviour.

21.3.6.1 Metal Nanoparticles

Among the pure metal NPs, NLO properties of Group IB elements, particularly Gold (Au) metal NPs, were exhaustively investigated because of its interesting optoelectronic properties arising from SPR. A good recent review article by Zhang

TABLE 21.2

NLO Coefficients of Metal Nanoparticles Estimated by Z-scan Experiments Using Different Laser Excitations (CW – continuous wave; NS – nanosecond, PS – picosecond and FS – femtosecond mode)

S. No.	Compound	Laser Parameters	NLO Coefficients	Ref.
	Au NPs	CW, $\lambda = 632.8\,\text{nm}$	$n_2 = 1.82 \times 10^{-7}\,\text{cm}^2\,\text{W}^{-1}$ $\beta = 4.9 \times 10^{-1}\,\text{cm W}^{-1}$	Majles Ara et al. (2012)
	Au NPs (spherical)	CW, $\lambda = 633\,\text{nm}$	$n_2 = -2.33 \times 10^{-8}\,\text{cm}^2\,\text{W}^{-1}$	Jia et al. (2008)
	Au NPs	NS, $\lambda = 532\,\text{nm}$	$\beta = 0.152$ cm/GW	Li et al. (2009)
	Au NPs (microwave)	NS, $\lambda = 532\,\text{nm}$	OLT = 0.243 GW cm^{-2}	Augustine et al. (2014)
	Au nanorods and nanospheres	PS, $\lambda = 1064\,\text{nm}$	$\beta = 0.1 - 0.7$ cm/GW	De Boni et al. (2008)
	Au NPs	PS, $\lambda = 1064\,\text{nm}$	$\beta = -1.52 \times 10^{-10}\,\text{m W}^{-1}$	Zhan et al. (2004)
	Au NPs (biosynthesis with coriander leaves)	PS, $\lambda = 800\,\text{nm}$	$n_{2=}\, 7 \times 10^{-15}\,\text{cm}^2\,\text{W}^{-1}$ $\beta = 0.14$ cm/GW	Rao (2011)
	Au NPs	PS, $\lambda = 532\,\text{nm}$	$n_2 = 1.7 \times 10^{-11}$ esu	Philip et al. (2000)
	Au nanocubes	FS, $\lambda = 800\,\text{nm}$	$\beta = 0.16\,\text{cm W}^{-1}$	Lee et al. (2009)
	Au nanooctahedra	FS, $\lambda = 800\,\text{nm}$	$\beta = 0.24\,\text{cm W}^{-1}$	Lee et al. (2009)
	Au nanorods	FS, $\lambda = 800\,\text{nm}$	$\beta = 1.5$ cm/GW	Elim et al. (2006)
	Ag NPs (laser-ablated)	CW, $\lambda = 532\,\text{nm}$	$\beta = 3.29 \times 10^{-3}\,\text{cm W}^{-1}$	Zulina et al. (2017)
	Ag NPs (green synthesis)	CW, $\lambda = 532\,\text{nm}$	$\beta = 3.103 \times 10^{-3}\,\text{cm W}^{-1}$	Pugazhendhi et al. (2018)
	Ag NPs (chemical reaction)	CW, $\lambda = 633\,\text{nm}$	$n_2 = -1.60 \times 10^{-8}\,\text{cm}^2\,\text{W}^{-1}$	Jia et al. (2008)
	Ag NPs (hydrogen reduction)	CW, $\lambda = 632.8\,\text{nm}$	$n_2 = 2.53$ to $4.04 \times 10^{-7}\,\text{cm}^2\,\text{W}^{-1}$	Sathyavathi et al. (2010)
	Ag NPs (biosynthesized)	NS, $\lambda = 532\,\text{nm}$	$\beta = 72.5$ cm/GW	Majles Ara et al. (2010)
	Polymer Ag NPs	NS, $\lambda = 532\,\text{nm}$	$\beta = 27.2$ to $116 \times 10^{-11}\,\text{m W}^{-1}$	George et al. (2017)
	Ag NPs	NS, $\lambda = 532\,\text{nm}$	$\Delta\text{T}_{\text{max}} = 0.4–1.2$	Zvyagin et al. (2018)
	Ag NPs (curcumin reduction)	NS, $\lambda = 532\,\text{nm}$	$\beta = 1$ to $4.75 \times 10^{-10}\,\text{m W}^{-1}$	Dhanya (2017)
	Ag nanorods	FS, $\lambda = 800\,\text{nm}$	$\beta = 1.73$ cm/GW (2PA) $\gamma = -0.08\,\text{cm}^3/\text{GW}^2$ (3PA)	Kyoung and Lee (1999)
	Cu NPs (green synthesized)	CW, $\lambda = 532\,\text{nm}$	$\beta = 33.7$ cm/GW	John et al. (2019)
	Laser-ablated Ni NPs	CW, $\lambda = 632\,\text{nm}$ NS, $\lambda = 532\,\text{nm}$	$\beta = 1.5 \times 10^{-3}\,\text{cm W}^{-1}$ $\beta = 7 \times 10^{-5}\,\text{cm W}^{-1}$	Alikhani et al. (2013)
	Pt NPs	NS, $\lambda = 532\,\text{nm}$	$\beta = 3.2 \times 10^{-10}\,\text{m W}^{-1}$	Gao et al. (2005)
	Ni, Ti and Co NPs	FS, $\lambda = 800\text{nm}$	$\beta = 8.9 \times 10^{-11}\,\text{cm W}^{-1}$(Ni) $n_2 = 1.6 \times 10^{-15}\,\text{cm}^2\,\text{W}^{-1}$ (Ni) $\beta = 7.8 \times 10^{-11}\,\text{cm W}^{-1}$ (Ti), $\beta = 8 \times 10^{-12}\,\text{cm W}^{-1}$ (Co), $n_2 = 5 \times 10^{-16}\,\text{cm W}^{-1}$ (Ti), $n_2 = 1.5 \times 10^{-16}\,\text{cm W}^{-1}$ (Co),	Ganeev (2018)
	Au, Ag, Pt and Cu, colloids	PS, $\lambda = 1064\,\text{nm}$	$n_2 = -1.82 \times 10^{-14}$e.s.u. (Au) $n_2 = 3.39 \times 10^{-14}$e.s.u. (Ag) $n_2 = 4.2 \times 10^{-14}$e.s.u. (Cu) $n_2 = 1.13 \times 10^{-14}$e.s.u. (Pt)	Ganeev et al. (2001)

TABLE 21.3

NLO Coefficients of Metal Nanocomposites Estimated by Z-scan Experiments Using Different Laser Excitation (CW – continuous wave; NS – nanosecond, PS – picosecond and FS – femtosecond mode)

S. No.	Compound	Laser Parameter	NLO Coefficients	Ref.
	Fullerene-functionalized AuNPs	CW, $\lambda = 514\,\text{nm}$	$\beta = 1.2 \times 10^{-2}\,\text{cm W}^{-1}$	Frare et al. (2019)
	Au:TiO_2	CW, $\lambda = 532\,\text{nm}$	$\beta = 2.15$ to $3.19 \times 10^{-3}\,\text{cm W}^{-1}$	Kumar et al. (2019)
	Graphene oxide: Au composite	CW, $\lambda = 442\,\text{nm}$	$\beta = 4.4 \times 10^{-3}\,\text{cm W}^{-1}$ (DMF) $\beta = 1.2 \times 10^{-3}\,\text{cm W}^{-1}$ (Water) $\beta = 6.2 \times 10^{-3}$ cm/GW (NMP)	Fakhri et al. (2015)
	Au-doped phenylhydrazone	NS, $\lambda = 532\,\text{nm}$	$\beta = 23.8 \times 10^{-11}\,\text{m W}^{-1}$	Sudheesh et al. (2013)
	Au-doped TiO_2	NS, $\lambda = 532\,\text{nm}$	$\gamma = 10.79 \times 10^{-24}\,\text{m}^3\,\text{W}^{-2}$	Rahulan et al. (2011)
	Au:$BaTiO_3$	NS, $\lambda = 532\,\text{nm}$	$\beta = 2.22 \times 10^{-6}\,\text{m W}^{-1}$	Wang et al. (2003)
	Au in SiO_2	NS, $\lambda = 532\,\text{nm}$	$\beta = -0.23$ to $-22 \times 10^{-3}\,\text{cm W}^{-1}$	Pinçon-Roetzinger et al. (2002)
	Au in graphene	NS, $\lambda = 532\,\text{nm}$	$\beta = 4.6 \times 10^{-10}\,\text{m W}^{-1}$	Pradhan et al. (2015)
	Au:Al_2O_3	NS, $\lambda = 1064\,\text{nm}$	$n_2 = -9.4–14.6 \times 10^{-11}\,\text{cm}^2\,\text{W}^{-1}$	Ganeev et al. (2005)
	Au embedded in lead lanthanum borate glass	NS, $\lambda = 532\,\text{nm}$	$\beta = 2 \times 10^{-11}\,\text{m W}^{-1}$	Rajaramakrishna et al. (2014)
	Au:PVP films	NS, $\lambda = 532\,\text{nm}$	$\beta = 3.56 \times 10^{-6}\,\text{cm W}^{-1}$	He et al. (2009)
	Au NP's-doped sodium zinc borate glass	FS, $\lambda = 750\,\text{nm}$ $\lambda = 800\,\text{nm}$ $\lambda = 850\,\text{nm}$	$\beta = 3.6$ to $4.6 \times 10^{-14}\,\text{m W}^{-1}$ $\beta = 8.1$ to $5.2 \times 10^{-14}\,\text{m W}^{-1}$ $\beta = 10.12$ to $7.2 \times 10^{-14}\,\text{m W}^{-1}$	Kolavekar et al. (2018)
	Ag-doped phenylhydrazone	NS, $\lambda = 532\,\text{nm}$	$\beta = 20.4 \times 10^{-11}\,\text{m W}^{-1}$	Sudheesh et al. (2013)
	Ag:SiO_2 and Ag:ZrO_2	NS, $\lambda = 532\,\text{nm}$	RSA with laser damage threshold higher than ~ 20 J cm^{-2}	Anija et al. (2003)
	Ag:Al_2O_3	NS, $\lambda = 1064\,\text{nm}$	$n_2 = 1.1$ to $1.8 \times 10^{-11}\,\text{cm}^2\,\text{W}^{-1}$	Ganeev et al. (2005)
	Ag:PVP films	NS, $\lambda = 532\,\text{nm}$	$\beta = 6.19 \times 10^{-7}\,\text{cm W}^{-1}$	Sakho et al. (2016)
	Nitrogen sulphur co-doped rGO Ag nanohybrids	NS, $\lambda = 532\,\text{nm}$ FS, $\lambda = 800\,\text{nm}$	$\beta_{532\,\text{nm}} \times 10^{-10}\,\text{m W}^{-1}$; $\beta_{800\,\text{nm}} \times 10^{-15}\,\text{m W}^{-1}$ Sphere 5.6–10 ; 6.2–7.3 Cube 2.8–3.9 ; 4.5–5.0 Wire 2.5–2.9 ; 4.1–5.0	Nair et al. (2018)
	Glutamic acid functionalized Ag NP's	NS, $\lambda = 532\,\text{nm}$ FS, $\lambda = 800\,\text{nm}$	$\beta_{532\,\text{nm}} = 5.5 \times 10^{-11}\,\text{m W}^{-1}$ $\beta_{800\,\text{nm}} = 1.60 \times 10^{-14}\,\text{m W}^{-1}$	Nidya et al. (2015b)
	L-phenylalanine-functionalized Ag NP's	NS, $\lambda = 532\,\text{nm}$ FS, $\lambda = 800\,\text{nm}$	$\beta_{532\,\text{nm}} = 3.6 \times 10^{-11}\,\text{m W}^{-1}$ $\gamma_{800\,\text{nm}} = 1.95 \times 10^{-25}\,\text{m}^3\,\text{W}^{-2}$	Nidya et al. (2015a)
	Non-covalent-functionalized rGO/Ag NP's	FS, $\lambda = 800\,\text{nm}$ NS, $\lambda = 532\,\text{nm}$	$\beta_{532\,\text{nm}} = 4.8–6.7 \times 10^{-15}\,\text{m W}^{-1}$ $\beta_{800\,\text{nm}} = 7.9–13.9 \times 10^{-10}\,\text{m W}^{-1}$	Sakho et al. (2016)
	Ag NP's decorated rGO	FS, $\lambda = 800\,\text{nm}$	$n_2 = -1.1 \times 10^{-12}\,\text{m}^2\,\text{W}^{-1}$	Yue et al. (2018)
	Ag-glass composite	FS, $\lambda = 800\,\text{nm}$	$\beta = -1.9 \times 10^{-5}\,\text{cm W}^{-1}$	Karvonen et al. (2013)
	Ag-doped GeO_2-Bi_2O_3	FS, $\lambda = 500–580\,\text{nm}$	$\beta_{500\,\text{nm}} = 0.11$ cm/GW $\beta_{520\,\text{nm}} = 0.11$ cm/GW $\beta_{540\,\text{nm}} = 0.11$ cm/GW $\beta_{560\,\text{nm}} = 0.05$ cm/GW $\beta_{580\,\text{nm}} = 0.05$ cm/GW	Almeida et al. (2014)
	Cu NP's in indium tin oxide matrix	CW, $\lambda = 532\,\text{nm}$	$\beta = (-3.45$ to $-3.61) \times 10^{-3}\,\text{cm W}^{-1}$	Ryasnyansky et al. (2006)
	Cu:Al_2O_3	NS, $\lambda = 1064\,\text{nm}$	$n_2 = (-1.3$ to $-1.7) \times 10^{-11}\,\text{cm}^2\,\text{W}^{-1}$	Ganeev et al. (2005)
	Copper silica metal glass composites	PS, $\lambda = 527\,\text{nm}$	$\beta = (3.1–8.5) \times 10^{-7}\,\text{cm W}^{-1}$	Polloni et al. (2003)
	Cu:SiO_2	PS, $\lambda = 1064\,\text{nm}$	$n_2 = -13.7 \times 10^{-8}$ esu	Karmakar et al. (2016)
	Ag:SiO_2	PS, $\lambda = 1064\,\text{nm}$	$n_2 = 1.5 \times 10^{-8}$ esu	Karmakar et al. (2016)
	Cu:SLSG	PS, $\lambda = 1064\,\text{nm}$	$n_2 = 3.6 \times 10^{-8}$ esu	(Karmakar et al., 2016)

(*Continued*)

TABLE 21.3 (*Continued*)

NLO Coefficients of Metal Nanocomposites Estimated by Z-scan Experiments Using Different Laser Excitation (CW – continuous wave; NS – nanosecond, PS – picosecond and FS – femtosecond mode)

S. No.	Compound	Laser Parameter	NLO Coefficients	Ref.
	Ag:SLSG	PS, $\lambda = 1064$ nm	$n_2 = 3.5 \times 10^{-8}$ esu	Karmakar et al. (2016)
	Cu:Bi_2O_3	FS, $\lambda = 800$ nm	$\beta_{deposited} = 0.11 \times 10^{-6}$cm W^{-1} $\beta_{annealed} = -1.82 \times 10^{-6}$cm W^{-1}	You et al. (2007)
	Cu-In-Na_2O-B_2O_3-SiO_2 glass	FS, $\lambda = 800$ nm	High non-linear Susceptibility	Zhong et al. (2013)
	GO:Pt	NS, $\lambda = 532$ nm	$\beta = 0.53$ cm/GW	Zhong et al. (2013)
	GO:Pt-Cu	NS, $\lambda = 532$ nm	$\beta = 0.62$ cm/GW	Zheng et al. (2016)
	GO:triangular Pd	NS, $\lambda = 532$ nm	$\beta = 0.59$ cm/GW	Zheng et al. (2014)
	GO:Pd composite	CW, $\lambda = 442$ nm	$\beta = (1.13 \pm 0.05) \times 10^{-2}$cm W^{-1}	Omidvar et al. (2018)
	$ZnFe_2O_4$-(15 wt%)rGO	FS, $\lambda = 800$ nm	$\beta = -0.04 \times 10^{-10}$m W^{-1}	Saravanan et al. (2017)
	$CdFe_2O_4$-(15 wt%)rGO	FS, $\lambda = 800$ nm	$\beta = -0.21 \times 10^{-10}$m W^{-1}	Saravanan et al. (2017)
	$CuFe_2O_4$-(40 wt%)rGO	FS, $\lambda = 800$ nm	$\beta = -1.30 \times 10^{-10}$m W^{-1}	Sabari Girisun et al. (2019)
	Au-Fe_2O_3-(15 wt%)rGO	FS, $\lambda = 800$ nm	$\beta = -9.30 \times 10^{-10}$m W^{-1}	Sabari Girisun et al. (2018a)
	Ag-Fe_2O_3-(25 wt%)rGO	FS, $\lambda = 800$ nm	$\beta = -3.80 \times 10^{-10}$m W^{-1}	Sabari Girisun et al. (2018b)
	rGO-BBO	CW, $\lambda = 532$ nm	$\beta = 605 \times 10^{-3}$cm W^{-1}	Muruganandi et al. (2018)
	Ni:NiO	NS, $\lambda = 532$ nm	$\beta = 1.5 \times 10^{-10}$m W^{-1}	Rahulan et al. (2013)
	Ni:$Ni_2Co_2O_4$ (1:2)	NS, $\lambda = 532$ nm	$\beta = 5.2 \times 10^{-10}$m W^{-1}	Rahulan et al. (2013)
	Ni:$Ni_2Co_2O_4$ (2:1)	NS, $\lambda = 532$ nm	$\beta = 3 \times 10^{-10}$m W^{-1}	Rahulan et al. (2013)
	Yb:YAG	CW, $\lambda = 532$ nm	$n_2 = 8.36$ to 8.64×10^{-8}cm^2 W^{-1}	Agrawal et al. (2015)
	Mg-doped ZnO	CW, $\lambda = 632$ nm	$\beta = (44.80–45.50) \times 10^{-2}$m W^{-1}	Agrawal et al. (2015)
	$CdFe_2O_4$-(40 wt%)rGO	CW, $\lambda = 532$ nm	$\beta = 6 \times 10^{-3}$m W^{-1}	M et al. (2018)
	Sb:Sodium borosilicate glass	FS, $\lambda = 1064$ nm	$\beta = -1.71 \times 10^{-10}$m W^{-1}	Zhong et al. (2014)
	Bimetallic Au-Cu embedded in glass	FS, $\lambda = 800$ nm	$\beta = 4.7$ to 6.0×10^{-12}m W^{-1}	Zhang et al. (2018)
	Pb NP's in Na_2O-B_2O_3-SiO_2 glass	FS, $\lambda = 800$ nm	$\beta = 7.02 \times 10^{-11}$m W^{-1}	Zhang et al. (2014)
	Te-Bi_2Te_3	FS, $\lambda = 775$ nm	$\beta = 0.16$ to 4.75×10^3 cm/GW	He et al. (2017)
	Cu:$SrTiO_3$	FS, $\lambda = 775$ nm	$\beta = 1.78$ to 6.15×10^{-12}cm W^{-1}	Cetin et al. (2010)
	Tb:$SrTiO_3$	FS, $\lambda = 800$ nm	$\beta = 5.53$ to 13.4×10^{-12}cm W^{-1}	Cetin et al. (2010)
	PbO-GeO_2 containing Au NP's	PS, $\lambda = 532$ nm FS, $\lambda = 800$ nm	$\beta = 1.7 \times 10^4$ cm/GW $\beta = < 60$cm W^{-1}	de Araújo et al. (2013)
	Mixtures of dye molecules-DEC, erythrozine, thionine and ZnS NPs	PS, $\lambda = 1064$ nm	$\beta = 5 \times 10^{-11}$cm W^{-1} $n_2 = 4 \times 10^{-16}$cm^2 W^{-1}	Boltaev et al. (2017)
	Ag2S QDs	FS, $\lambda = 1064$ nm	$\beta = 8 \times 10^{-11}$cm W^{-1}	Boltaev et al. (2016)
	Mg-doped $LiNbO_3$ single crystals	NS, $\lambda = 1064$ nm	$\beta = 2.811 \times 10^{-8}$cm W^{-1} $n_2 = 8.2 \times 10^{-12}$cm^2 W^{-1}	Choubey et al. (2009)
	As_2S_3 and CdS NPs.	NS, $\lambda = 1064$ nm	$\beta = 6 \times 10^{-10}$cm W^{-1}. $\beta = 2.9 \times 10^{-10}$cm W^{-1}. $n_2 = 2.21 \times 10^{-12}$ e.s.u. $n_2 = 1.72 \times 10^{-12}$ e.s.u.	Ganeev et al. (2003)
	Sapphire-doped Ag, Cu, and Au NPs	PS, $\lambda = 1064$ nm,	Ag:Al_2O_3 $n_2 = 1.8 \times 10^{-11}$cm^2 W^{-1} Cu:Al_2O_3 $n_2 = -1.3 \times 10^{-11}$cm^2 W^{-1} Au:Al_2O_3 $n_2 = -9.4 \times 10^{-11}$cm^2 W^{-1}	Ganeev et al. (2005)
	Cu- and Ag NPs-doped silica glasses	PS, $\lambda = 1064$ nm	$\beta = 9 \times 10^{-6}$ (SG: Cu), $n_2 = -13.7 \times 10^{-8}$ e.s.u. (SG: Cu), $n_2 = 1.5 \times 10^{-8}$ e.s.u. (SG: Ag),	Ganeev et al. (2004b)

(*Continued*)

TABLE 21.3 (*Continued*)

NLO Coefficients of Metal Nanocomposites Estimated by Z-scan Experiments Using Different Laser Excitation (CW – continuous wave; NS – nanosecond, PS – picosecond and FS – femtosecond mode)

S. No.	Compound	Laser Parameter	NLO Coefficients	Ref.
	CdS and ZnS nanoparticlesimplanted into zirconium oxide thin films	FS, λ = 795 nm	ZrO_2: CdS (Cr) $n_2 = (1 \pm 0.3) \times 10^{-9}$ ZrO2: ZnS (Mn) film $n_2 = -(5 \pm 1) \times 10^{-11} cm^2 W^{-1}$	Ganeev et al. (2004a)
	Ge and GaAs nanoparticle suspensions	NS, $\lambda = 1053$ nm	$\beta = 3.2 \times 10^{-10} cm\ W^{-1}$ (GaAs) $\beta = 1.9 \times 10^{-10} cm\ W^{-1}$ (Ge) $n_2 = 6.8 \times 10^{-15} cm^2 W^{-1}$ (GaAs) $n_2 = 7.9 \times 10^{-15} cm^2 W^{-1}$ (Ge)	Ganeev et al. (2007)
	Silicate glasses doped with silver nanoparticles	PS, $\lambda =$ 532 nm	$\beta = 6.7 \times 10^{-5}$ Ag: SLSG $\beta = 3.6 \times 10^{-5}$ Ag: SG $n_2 = 4.1 \times 10^{-10} cm^2 W^{-1}$ Ag: SLSG $n_2 = -6.2 \times 10^{-10} cm^2 W^{-1}$ Ag: SG	Ganeev et al. (2004c)
	Fe- and Zn-doped PVP	PS, $\lambda = 1064$ nm	$n_2 = -6.7 \times 10^{-13}$ e.s.u (PVP: Fe)	Ganeev et al. (2002)

et al. has summarized the numerous methods for the preparation of nanocomposite materials and their NLO coefficients obtained using different techniques (Zhang and Wang, 2017). Gold metal NPs with different morphologies under excitation of various lasers exhibit variety of NLO phenomena. Z-scan experiment using CW laser with wavelength 632.8 nm was performed on stable Au metal NPs prepared by the simple reduction of Au^{3-} ions in aqueous starch dispersion. Au metal nanoparticle with spherical structure exhibited self-defocusing phenomena, and the OA Z-scan technique exposed the two-photon absorption (2PA) effect (Majles Ara et al., 2012). A similar observation of metal Au colloidal solution prepared by chemical reaction method exhibiting self-defocusing effect under CW 633 nm excitation was reported. Non-linear refractive index and thermo-optic coefficient were calculated to be $-2.23 \times 10^{-8} cm^2\ W^{-1}$ and $1.23 \times 10^{-4}\ K^{-1}$, respectively (Jia et al., 2008). Gold NPs protected by a novel π-conjugated polymer (poly(p-phenylene ethynylene)) exhibit SPR at 530 nm. Interestingly, under pulsed laser excitation (532 nm, 4 ns), samples show a peculiar NLA with simultaneous presence of weak SA and strong RSA resulting from third-order and fifth-order NLA, respectively. Estimated absorption coefficients $\alpha_2 = -1.52 \times 10^{-10} mW^{-1}$ and $\alpha_4 = -2.7 \times 10^{-21} m^3 W^{-2}$. Polymer-capped Au NPs possess higher NLO coefficient than bare gold NPs. Unlike CW excitation, polymer-capped Au exhibits self-focusing effect due to involved strong NLA and SPR effect (Li et al., 2009).

At the same time, spherical and mono-dispersed Au NPs synthesized by microwave irradiation method having a particle size of 8 nm exhibit RSA behaviour under Z-scan technique with 532 nm nanosecond pulsed laser. The observed strong RSA behaviour due to longitudinal SPR made Au as good optical limiters at high laser fluence (Augustine et al., 2014). The NLA of gold nanospheres and nanorods was investigated under picosecond white-light supercontinuum open-aperture Z-scan method. The work reported the peculiar SA at low-input pulse (oscillation within plasmonic bands) and RSA at high-input energies (photodegradation of NPs). Applications of Au nanoparticle-based optical switches in the low-energy regime and optical limiters in the high-energy range were demonstrated by Leonardo De Boni's group (De Boni et al., 2008). The near-IR picosecond (1064 nm, 35 ps) optical non-linearity of 1-dodecanethiol protected gold NPs showed peak-valley configuration, a self-defocusing with a negative non-linear refractive index of $-1.55 \times 10^{-18} m^2\ W^{-1}$. 1-Dodecanethiol-protected Au in tetrahydrofuran solution showed a high ESA and a strong OL performance with a very low OL threshold (Zhan et al., 2004). Biosynthesized Au NPs using coriander leaf extract with an average size of 30 nm were subjected to Z-scan technique using 2 ps pulses near 800 nm. Open-aperture data suggested the presence of saturation absorption and closed-aperture data suggested the availability of self-focusing refraction. The magnitude of the third-order non-linearity of gold NPs was estimated to be 3.3×10^{-13} esu (Rao, 2011).

Optical non-linearity in octanethiol- and octadecanethiol-capped gold nanoclusters was investigated under 532 nm, 35 ps pulses. The peak-valley-type CA Z-scan revealed that thiol-capped Au displayed negative refractive (self-defocusing) non-linearity. At lower pump intensity, the ground-state plasmon bleach leads to saturated absorption, and at higher intensities, RSA was observed due to free-carrier absorption. Also, octanethiol capping with Au with good photostability yields a better limiting compared with octadecanethiol capping Au (Philip et al., 2000). Peculiar observation of SA and self-focusing arises due to the excess of organic molecules left as by-products left in biosynthesis procedure. Nanocubes and nano-octahedra of gold NPs were prepared, and their NLA properties were investigated using femtosecond laser pulses at 800 nm. Both exhibited a shift from SA to RSA at higher excitation intensities. Both Au nanocubes and nano-octahedra showed strong two-photon excitation emission which made them useful in many applications like OL devices, optical switches, two-photon imaging, etc. (Lee et al., 2009). Saturable (lower intensity) and reverse saturable (higher intensity) absorption due to longitudinal SPR in gold nanorods was observed using Z-scan and transient absorption techniques with 220 fs laser pulses at 1 kHz repetition rate (Elim et al., 2006). Thus, in consolidation, Au NPs suffered a shift in nonlinearity (SA to RSA) with increase in input fluence, and morphology played a major role in varying NLO coefficient.

Similar to gold NPs, investigations on silver metal NPs are also well carried out. Ag NPs' stable colloid solution with size in the range of 27–120 nm was formed by laser ablation of chemically pure silver rod in liquid monometer isodecyl acrylate. CW 532 nm laser-based NLA and refraction studies depicted strong third-order NLO response with real and imaginary parts of the coefficients as Re $\chi^{(3)} = 1.31 \times 10^{-5}$ esu and Im $\chi^{(3)} = 7.64 \times 10^{-5}$ esu which is comparable with that of single-walled carbon nanotube (Zulina et al., 2017). Highly stable silver NPs prepared by a novel green method using *Mirabilis jalap*a exhibit SPR peak at 420 nm and negative non-linearity-based OL under 532 nm, CW laser beam (Pugazhendhi et al., 2018). Metal Ag colloidal solutions prepared by the chemical reaction method exhibited thermo-optic-based negative non-linear self-defocusing refraction under CW 633 nm excitation (Jia et al., 2008). Poly(vinyl pyrrolidone)-capped silver NPs prepared by the reduction method exhibited self-defocusing effect under He-Ne 632.8 nm CW laser (Sathyavathi et al., 2010). Biosynthesis of silver NPs using *Coriandrum sativum* leaf extract with an average size of 26 nm was made, and their NLO properties were studied by Z-scan technique with 532 nm laser having 6 ns pulse duration. The non-linear refractive index and magnitude of the third-order non-linearity were measured to be 6×10^{-13} cm^2 W^{-1} and 1.38×10^{-9} esu, respectively. Ag NPs were found to exhibit strong RSA with high third-order NLO susceptibility that was responsible for OL (Majles Ara et al., 2010).

Plasmon-enhanced two-photon absorption in modified Styrene–Maleic anhydride silver NPs was observed in OA non-linear Z-scan experiments with 532 nm, 5 ns laser pulses. On incorporation of silver NPs in SMA, the NLA coefficient was found to be increasing to 0.1×10^{-8} m W^{-1} which can be attributed to local field effects induced by Ag nanoparticle (George et al., 2017). Silver NPs with spherical and triangular shapes were synthesized by citrate-borohydride approach. Morphology-dependent NLA was observed by Z-scan using 532 nm, 10 ns laser pulses. Changing the geometry of Ag NPs shifted the NLA as RSA (spherical), dominating RSA with minor SA (mixed spherical and triangular) and dominating SA with traces of RSA (triangular) (Zvyagin et al., 2018). Intensity-dependent NLO investigations of uniform sized, spherical silver NPs synthesized by curcumin reduction showed the presence of excited state absorption involved sequential 2PA process under 532 nm, 5 ns laser pulse excitation (Dhanya, 2017). The first measurement of NLO coefficients of ellipsoidal silver NPs in the longitudinal surface plasmon absorption region (800 nm) using Z-scan technique with fs laser pulse excitation was reported by Kyoung's group. Silver nanorods exhibited a self-focusing effect with a positive refractive index due to the longitudinal SPR effect caused by the inter-band transition (Kyoung and Lee, 1999). In a similar manner, investigation of NLO properties of other metal NPs like Cu, Ni and Pt was also carried out which demonstrated higher NLO coefficients. In metal NPs, the contribution of longitudinal SPR effect is unique, and enhanced NLO performance with improved OL action makes Au and Ag metal NPs an important entity.

21.3.6.2 Metal Nanocomposites

Emergence of nanostructured materials as NCs has evolved quickly as wink as it combines the advantages of many materials as one. In recent years, investigations of NLO properties of NCs particularly for OL applications have increased tremendously. Consolidating all metal NCs is difficult, and thus, focus is made on widely known transition metal-based NCs. Apart from metal NPs, a large number of alloys and composites were also investigated and varieties of NLO phenomena were demonstrated. Gold NCs under different CW laser excitation exhibit SA, and the role of solvent in altering the absorption coefficient was reported (Frare et al., 2019; Kumar et al., 2019; Fakhri et al., 2015). A new class phenylhydrazones with gold NPs showed the material to be well suited for optical devices (Sudheesh et al., 2013). OL action of Au-doped TiO$_2$ NPs due to effective 3PA mechanisms under 532 nm, 5 ns laser pulse excitation was demonstrated by Mani Rahulan et al. (2011). Composites films consisting of nanoscale Au particles uniformly embedded in barium titanate (BaTiO$_3$) matrices were prepared by pulsed laser deposition technique. Au:BaTiO$_3$ composite films showed self-defocusing effect with enhanced non-linear refractive index (Wang et al., 2003). Third-order NLO properties of thin films of Au/SiO$_2$ cermets synthesized using a radio-frequency sputtering technique were studied by Z-scan using 532 nm, 7 ns pulse laser. Large enhancement in the imaginary part of optical Kerr with increase in Au metal due to large enhancement of the local field factor in cermet was observed (Pinçon-Roetzinger et al., 2002). Prabahan et al. reported that low-dimensional gold-decorated graphene NCs can synergistically combine the NLO properties of metallic/inorganic nanostructures for enhancing the OL performance. Prolific decrease in the limiting threshold for gold-graphene (0.4 J cm^{-2}) compared with the bare gold NPs (9 J cm^{-2}) and many other metal-decorated graphene, carbon nanotube composites and metal NPs reported earlier in literature was observed (Pradhan et al., 2015). The investigation of sapphire doped with Au NPs using reflection Z-scan technique exposed the self-defocusing property with strong mechanism on non-linear refraction (Ganeev et al., 2005). Au NPs embedded in lead lanthanum borate glass were prepared by melt-quenching technique. NLO measurement showed RSA behaviour at higher intensities, indicating its potential use in OL devices (Rajaramakrishna et al., 2014). Phenylhydrazone derivatives and metal nanocolloids exhibited negative non-linear effect (RSA) due to excited state absorption at 532 nm, 7 ns (Sudheesh et al., 2013). Au and Ag doped with polyvinylpyrrolidone (PVP) thin films exhibited RSA and self-defocusing effect. It reports that pulse width has a large influence on non-linear refractive index and longer pulse duration will result in larger non-linear refraction (He et al., 2009). Wavelength-dependent Au NP's doped sodium zinc borate glass shows increase in NLA coefficient with increase in IR wavelength under femtosecond excitation due to the quantum confinement and SPR effects (Kolavekar et al., 2018). Stable Ag NPs with TiO$_2$, ZrO$_2$

and SiO_2 shells show SA at low input pulses and RSA at high input pulses of 532 nm ns laser which was explained through electronic Kerr non-linearity. This core-shell structure renders a high laser damage threshold to these materials and made them promising candidates for high-energy OL applications (Anija et al., 2003).

Non-linear refraction studies with 1064 nm, 55 ps laser of $Ag:Al_2O_3$ NPs showed that the sample possesses self-focusing properties with a positive refractive index, $n_2 = 1.8\times10^{-11}\,cm^2\,W^{-1}$ (Ganeev et al., 2005). Both colloidal Ag- and Ag-doped PVP composite films exhibited RSA with 532 nm, 38 ps laser pulses (Ganeev et al., 2005). A novel class of nitrogen and sulphur co-doped graphene/Ag nanomorphotypes (sphere, cube and wire) synthesized by hydrothermal method was found to exhibit RSA ascribed to be excited state absorption process (Nair et al., 2018). L-glutamic acid functionalized silver (Glu-Ag) NPs exhibited a weak 2PA process and strong ESA under 800 nm, 100 fs and 532 nm, 5 ns respectively. The NLA coefficient was three orders of magnitude smaller for fs excitation compared with ns excitation (Nidya et al., 2015a). Similarly, L-phenylalanine-capped silver NPs (Phe-Ag NPs) in a sol-gel thin film showed interesting 2PA with traces of SA process and 3PA under 532 nm, 5 ns and 800 nm, 100 fs respectively (Nidya et al., 2015a). Improved NLO limiting properties due to 2PA in combination with SA in the femtosecond regime and RSA along with SA in the nanosecond regime in non-covalent functionalized reduced graphene oxide (rGO)/silver NPs were demonstrated recently (Sakho et al., 2016). Ag-glass nanocomposite fabricated by a two-step ion exchange method possessed high positive non-linear refractive index and SA coefficient (Karvonen et al., 2013). Sapphire doped with Cu NPs exhibited self-defocusing effect with non-linear refractive index $-1.7 \times 10^{-11}\,cm^2\,W^{-1}$ under 1064 nm, 55 ps laser pulses (Ganeev et al., 2005). Implantation of Cu and Ag nanoparticle ions into amorphous SiO_2 and soda-lime silicate glasses (SLSG) was made, and their IR picosecond laser non-linearity was studied. It showed that the NLA could be associated with two-photon absorption at a wavelength of 1064 nm, and the non-linear refraction was associated with Kerr effect. The OL was analyzed for the composite materials, and it was shown that the $Cu:SiO_2$ composite is characterized by a 15-fold limiting (Karmakar et al., 2016). Under fs pulses excitation, both real and imaginary parts of the third-order NLO susceptibility of $Cu:Bi_2O_3$ were enhanced due to photo-induced hot electrons (You et al., 2007). $Na_2O\text{-}B_2O_3\text{-}SiO_2$ glass doped with Cu_2In NPs exhibited NLO SA and refraction with self-defocusing effect (Zhong et al., 2013). NCs of Ni/NiO and $Ni/NiCO_2O_4$ synthesized by a chemical reduction technique reported ESA and 2PA with enhanced OL properties under 7 ns laser pulses at 532 nm (Rahulan et al., 2013). Although variety of NCs were explored, recent literature clearly showcases the dominance of graphene and its derivatives as host matrix. Numerous graphene-based NCs were identified as excellent NLO materials for OL applications. With fs laser pulse excitation, rGO decorated with silver NPs demonstrated an enhanced SA caused by bleaching of the valence band due to the transfer of light-excited carriers from graphene to metal state (Yue et al., 2018). Bimetallic Cu NPs were homogenously deposited on graphene oxide (GO) sheets and their NLO properties were studied with 532 nm, 4 ns pulse excitation, which revealed two-photon absorption and non-linear scattering. Inter-band transition of Cu NPs and charge transfer between GO and metal contributed towards enhanced NLO and OL properties (Zheng et al., 2016). Novel GO nanocrystal composites were prepared by the reduction of palladium acetate on the surface of GO, and two-photon absorption was revealed from OA Z-scan technique (Zheng et al., 2014). Enhancement of the NLO properties of GO by repairing with palladium NPs was reported with CW laser (Rahulan et al., 2013).

The NLA induced with femtosecond laser excitation is found to be strongly material-dependent, i.e., GO exhibit SA while rGO possesses RSA behaviour. In the composite, interaction between metal ferrites-rGO altered the band structure and thus exhibit different NLA. Interesting NLA mechanisms observed are (i) $ZnFe_2O_4$-decorated rGO exhibits 2PA/3PA (Saravanan et al., 2016), (ii) unusual switching of RSA at low intensity to SA at high intensities in $CdFe_2O_4$-rGO (Saravanan et al., 2017), (iii) peculiar W-pattern at low intensity and 2PA (1PA+ESA) at high intensity in $CuFe_2O_4$-rGO (Sabari Girisun et al., 2019), (iv) transition of SA to RSA with change in wavelength in $Ag\text{-}Fe_2O_3$-rGO (Sabari Girisun et al., 2018a) and (v) strong broadband limiting in $Au\text{-}Fe_2O_3$-rGO (Sabari Girisun et al., 2018b). Higher NLO coefficients of the NCs can be attributed to various factors such as (i) larger extent of conjugation, for higher chance of electron/energy transfers, (ii) tailoring the proportion of oxygen-containing groups in the graphene layers, (iii) metal ferrites loading on the graphene sheets, (iv) size, morphology and defect state of composite and (v) the formation of complex energy state due to interaction of metal NPs and rGO. Particularly, the ability to deliver ultrafast pulses with controlled micro-joules of energy through flexible fibres can open up a host of possibilities towards developing robust ultrafast laser microsurgery systems. Appealing enhancement in the NLO performance of NCs when compared with the individual unit of complexes gives the wide scope of extending the investigation of a greater number of metal complexes-decorated rGO.

21.3.6.3 Perovskite Materials

Semiconductor QDs with dimensions close to the Bohr radius of electron-hole pair have gained tremendous attention in the past decades due to their unique physical and chemical properties. Some of the widely studied materials are listed in Table 21.4. The rich chemical and structural diversity of perovskites nanocrystals along with their tunable bandgap, large oscillator strength (Schmitt-Rink et al., 1987; Wei et al., 2016) and moderate exciton binding energy enables their applications in NLO materials; the chemical and optical stabilities restrict their device applications. The quantum confinement and dielectric confinement effects make the perovskite QDs a promising class of materials with large third-order non-linear susceptibilities (Gao et al., 2004; Krishnakanth et al., 2019). In recent years, different types of organic and organic-inorganic perovskite QDs have been studied because of potential applications in optoelectronic and photonic devices from optical non-linearity. Compared with semiconductor quantum dots, perovskite quantum dots showed superior NLO properties. The non-linear refractive indexes and two-photon absorption

TABLE 21.4

NLO Coefficients of Perovskite Nanocrystals Estimated by Z-scan Experiment Under Different Laser Excitation

S. No.	Compound	Laser Parameter	NLO Coefficients	Ref.
	$CH_3NH_3PbI_3$ (Film)	PS, $\lambda = 1064\,nm$	$\beta = -2.25\,cm\,MW^{-1}$ $n_2 = 3.74 \times 10^{-15} m^2\,W^{-1}$	Schmitt-Rink et al. (1987)
	(QDs) $CsPbBr_3$	FS, $\lambda = 800\,nm$	$\beta = 8.5 \times 10^{-11}$	Wei et al. (2016)
	(NCs) $CsPbCl_3$	FS, $\lambda = 787\,nm$	$\beta = 1.4 \times 10^{-11}$ $n_2 = 5.3 \times 10^{-15}$	Gao et al. (2004)
	Cs_4PbBr_6 Non-fluorescent film	FS, $\lambda = 500–800\,nm$	$\beta = 4–46 \times 10^{-8} cm\,W^{-1}$ $n_2 = 4–6 \times 10^{-9} cm^2\,W^{-1}$	Krishnakanth et al. (2019)
	Cs_4PbBr_6 fluorescent film	FS, $\lambda = 500–800\,nm$	$\beta = 1–1.29 \times 10^{-8} cm\,W^{-1}$ $n_2 = 0.7–2.7 \times 10^{-9} cm^2\,W^{-1}$	Krishnakanth et al. (2019)
	$CsPbI_3$ (NCs)	FS, $\lambda = 787\,nm$	$\beta = 3.2 \times 10^{-11}$ $n_2 = 6.8 \times 10^{-15}$	Zhang et al. (2016)
	$CH_3NH_3PbBr_3$ films	PS, λ = mid-IR	$n_2 \sim 10^{-12} m^2\,W^{-1}$	Yi et al. (2017)
	$CH_3NH_3Pb_{0.75}Sn_{0.25}I_3$ (thin film)	FS, $\lambda = 1535\,nm$	$\beta = 1.15\,cm\,kW^{-1}$	Xie et al. (2018)
	$CH_3NH_3PbCl_3$	PS, $\lambda = 532\,nm$	$\beta = 13 \times 10^{-3}\,mMW^{-1}$	Saouma et al. (2017)
	$CH_3NH_3PbI_3$ film	PS, $\lambda = 1064\,nm$	$\beta = 23 \times 10^{-3}\,cmMW^{-1}$ $n_2 = 1.37 \times 10^{-14} cm^2\,W^{-1}$	Saouma et al. (2017)
	$CsPbBr_3$ NRs	FS, $\lambda = 800\,nm$	$\beta = 7.1 \times 10^{-6} cm\,MW^{-1}$ $n_2 = -2.09 \times 10^{-11} cm^2\,W^{-1}$	Krishnakanth et al. (2018)
	PbS/n-hexane	FS, $\lambda = 800\,nm$	$n_2 = -0.02377 \times 10^{-17} m^2\,W^{-1}$	Cheng et al. (2015)
	CdSe/toluene	FS, $\lambda = 680\,nm$	$n_2 = -5 \times 10^{-17} m^2\,W^{-1}$	Gerdova and Haché (2005)
	CdTe/water	FS, $\lambda = 800\,nm$	$\beta = 0.015 \times 10^{-11} mW^{-1}$ $n_2 = 0.25 \times 10^{-17} m^2\,W^{-1}$	Jin et al. (2009)
	$MAPbBr_3/(OA)_2PbBr_4$	FS, $\lambda = 2050–2300\,nm$	$\eta\delta_5 = (0.29 \pm 0.04–20 \pm 3) \times 10^{-136} cm^{10} s^4$ photon^{-4}	Chen et al. (2017)

of a few colloidal perovskite nanocrystals are estimated to be several orders of magnitude larger than those of bulk materials. Many others have investigated the ultrafast non-linear refractive index and two-photon absorption at different laser pulse excitation of perovskite QDs at a moderate quantum confinement regime. They have found several orders of magnitude enhancement in the NLO coefficients (Li et al., 2018; Xu et al., 2019).

Organic/inorganic hybrid halide perovskites have emerged recently as extremely promising semiconducting materials because of their tunable architecture, which allows engineering the perovskite NCs as optimized NLO performers. Snaith (Zhang et al., 2016) and Tischler (Kalanoor et al., 2016) and their co-workers reported the third-order NLO properties of $CH_3NH_3PbI_3$ perovskite thin films. The non-linear refractive index obtained by Z-scan technique is three orders of magnitude larger than Silicon. A comprehensive study of $CH_3NH_3PbX_3$ ($X = Br_3$, Cl_3, I_3) perovskite films shows the $CH_3NH_3PbI_3$ stronger NLA in the order of ~10^{-7} cmW^{-1} (at 40fs 800nm wavelength) compared with $CH_3NH_3PbCl_3$ and $CH_3NH_3PbBr_3$ halide perovskites (Ganeev et al., 2018). The CA Z scan measurements of $CH_3NH_3PbI_3$ show the positive refractive index (self-focusing) with an NRI of ~10^{-12}m^{2}W^{-1} pumped at IR range (1560–1930nm). By slightly tuning the band gap by replacing Pb with Sn ions ($CH_3NH_3Pb_{0.75}Sn_{0.25}I_3$), Zhang and co-workers (Xie et al., 2018) have shown an ultra-large NLA coefficient 1.15cm kW^{-1} at 1535nm, which is comparable to optical communication wavelength. So they have realized direct IR photo detection device. Another research group (Walters et al., 2015) studied a high-quality single crystals of $CH_3NH_3PbBr_3$ and measured their two-photon absorption (2PA) coefficient to be 8.6±0.5cm GW^{-1} with ultrashort pulses of 100fs at 800nm wavelength. The obtained values are comparable to that of epitaxial single-crystal semiconductors with similar band-gaps. They also observed a sharp and narrow two-photon excited photoluminescence (PL) peak at 572nm from $CH_3NH_3PbBr_3$ single crystals.

Inorganic caesium lead halide perovskites ($CsPbX_3$, X = Cl, Br, I) have gained much attention in recent years as a type of popular optoelectronic material having broad applications ranging from high-efficiency solar cells, photodetectors, LED to lasers. Caesium lead halide perovskites crystallize possesses centrosymmetry, so the second-order NLO properties are not expected to be by themselves. However, the tunability of perovskite composition and structure helps to synthesize diverse $(CsGe(BrxCl1{-}x)_3$, where x = 0, 1/6, 2/6, 3/6, 4/6, 5/6, 1) caesium lead halide perovskite derivatives for NLO materials. They demonstrated a striking SHG response 28.3 times larger than KDP. By altering the composition x linearly which increases the lattice constant and second-order NLO susceptibility with decreasing band gap values. In this way, one can modulate the perovskite NCs properties such as susceptibility, band gap, laser damage threshold and transparency range. Remarkably, Sum and co-workers demonstrated efficient five-photon absorption cross sections from core-shell

$CsPbBr_3$/$MAPbBr_3$ colloidal halide perovskite nanocrystals to be $\eta\delta_5 \approx 10^{-136}\,cm^{10} s^4$ photon^{-4}, about nine orders of magnitude larger than the state-of-the-art designed NLO organic molecules (Chen et al., 2017). The MPA capabilities of all-perovskite nanocrystals offer significant advantages of greater spatial confinement, increased penetration depth, reduced auto fluorescence, enhanced sensitivity and improved resolution over lower orders in bio-imaging and in OL. In nanocrystals, the non-linearities are primarily due to state-filling and Coulomb multi-particle interactions. State-filling leads to the bleaching of the inter-band optical transitions; the changes of absorption resulting from this are proportional to sum of electron-hole occupation numbers. In single-crystal $CsPbX_3$, the NLO properties are highly anisotropic (Clark et al., 2016). There have been studies on the polarization-selective MPA on a Bridgman-grown single crystal of $CsPbBr_3$ (Clark et al., 2016). They have observed the absence of three photon-excited fluorescence emission when the polarization is changed from orthogonal to parallel.

Zero-dimensional perovskite-related materials (0-D PRMs) are a new class of materials having high exciton binding energy ($E_g \geq 180$ meV) with a strong PL quantum yield. By considering the structure and electronic confinement in all three dimensions, these materials are often called as zero-dimensional perovskite material (0-D PRM). The rhombohedra Cs_4PbBr_6 crystals are made of electronically decoupled ($PbBr_6$) octahedral units and caesium ions bridge between them. Since photo-excitation generates excitons in ($PbBr_6$) units, excitons are confined within the individual octahedron and feature a higher binding energy. Our group (Krishnakanth et al., 2019) has studied the MPA properties of Cs_4PbBr_6 NCs and have found a strong two- and three-photon absorption cross-section values compared with recent perovskite NCs which also demonstrated a large third-order NLO susceptibility $\chi^{(3)}$ (~10^{-7}esu). The strong quantum confinement arising from the spatially isolated, exciton containing individual $(PbBr6)^{4-}$octahedron which can give the local-field enhancement, such effects significantly enhance the NLO properties. The processing of perovskite class of materials can replace the existing photonic materials.

There have been plenty of NLO studies on different nanomaterials with cw, ns, ps and fs laser pulses. Nanomaterials in pure and in composite forms have been investigated. The various applications of the third-order NLO materials can be summarized as follows:

- Materials with strong n_2 values and small linear absorption can be used for optical switching applications. Of course, the response time of n_2 has to be fast (few femtoseconds to few hundreds of femtoseconds) enough (electronic in nature).
- Materials with strong 2PA/3PA can be used for microscopy and imaging applications (especially for biological molecules).
- Materials with ESA/RSA can be used as OL materials. This is true especially for nanosecond laser pulses.
- Materials with strong SA properties are finding applications in ultrafast fibre lasers (for mode-locking) leading to compact and economic lasers.

Though several applications have been envisaged through numerous studies, there are actually quite few studies on the actual device preparation and testing. A concerted effort is required from physicists, chemists and material scientists to prepare robust, cost-effective nanomaterials, test their efficacy and find practical applications in photonics by preparing the requisite devices comprising these nanomaterials.

21.4 Conclusions

Nanomaterials play an important role in the field of NLO and photonics. In this chapter, we have reviewed some of the novel nanomaterials synthesized recently and their relevance to NLO. Starting with the basics of NLO (second order and third order), we have explained the techniques used for evaluating the NLO materials. Some of the metal NPs and NCs prepared during the last decade have been evaluated and their NLO coefficients are summarized. A new class of materials called perovskites have also been evaluated for their NLO performance. All these nanomaterials have significant NLO properties (both real and imaginary parts of the third-order NLO susceptibility). Materials with strong n_2 find applications in optical switching and limiting. Materials with strong 2PA/3PA/4PA find applications in OL and biological imaging applications. Materials possessing strong SA are useful for mode-locking applications in ultrafast lasers.

21.5 Future Scope

Apart from metal NPs, metal NCs, and very recently perovskite materials, there has been interest in other novel nanomaterials, for instance, 2D materials (hexagonal boron nitride (h-BN), black phosphorous (BP) and transition metal dichalcogenides (TMDs) such as MoS_2, $MoSe_2$ and WS_2). See for example, a nice review article on the NLO properties of two-dimensional materials by Liu et al. 2019. TMDs are a set of layered materials and have the chemical structure MX_2, where M is the transition metal atoms (Mo, W) and X is the chalcogen atom (S, Se). Depending on the number of layers, the band gap of these materials can be engineered easily. Several reports till date reported SA in these few-layer TMDs at near-infrared wavelengths. This corresponds to photon energies lower than the expected material bandgap for most TMDs. Based on the observed SA, several applications have been envisaged and demonstrated recently, including the fabrication of ultrafast fibre lasers (See, for example, a review of such applications in Woodward and Kelleher, 2015). Another review article, particularly devoted to MoS_2-based saturable absorbers for ultrafast laser technologies (Woodward et al., 2015), summarized recent progress in processing and integration of these materials into saturable absorber devices. It has been recently understood that composites comprising metal NPs embedded in dielectric media present large NLO response owing to electronic transitions in the NPs (Reyna and De Araújo, 2017). They highlight the numerous studies undertaken recently and conclude that "metal nanocolloids are versatile platforms for NLO studies and the recent results may stimulate the synthesis of novel metal–dielectric nanocomposites (based on inorganic glasses/polymers) with optimized characteristics for specific photonic device applications" (Reyna and De Araújo, 2017). Another class of materials which have shown promise recently are the nanoscale antennas (Suh et al., 2013). These are capable of localizing and concentrating the EM fields into subwavelength volumes at their localized surface plasmon frequencies. The huge local-field concentration reinforced by metal nanoantennas can induce strong optical non-linearities, which makes them promising for NLO applications such as (i) frequency conversion, (ii) four-wave mixing and (iii) Q-switching.

In the field of second-order NLO, molecular nanoparticles (which are assembled from small molecules through non-covalent interactions) are relatively less explored but equally captivating materials (Patra et al., 2012). The significance of molecular materials is the ability to modify their assembly, structure and function. This can be realized easily through the refinement of the intermolecular interactions, which are relatively weak. Several studies are underway to achieve efficient and robust molecular nanoparticles for practical applications in photonics.

REFERENCES

Agrawal, A., Ahmad Dar, T., Solanki, R., Phase, D. M. and Sen, P. 2015. Study of nonlinear optical properties of pure and Mg-doped ZnO films. *Physica Status Solidi (b),* 252: 1848–1853.

Ali, R.F., Bilton, M, Gates, B.D. 2019. One-pot synthesis of sub-10 nm $LiNbo_3$ nanocrystals exhibiting a tunable optical second harmonic response†. *Nanoscale Adv.* 1: 2268-2275.

Alikhani, S., Tajalli, H. and Koushki, E. 2013. Third order optical nonlinearity and diffraction pattern of Ni nanoparticles prepared by laser ablation. *Optics Communications,* 286: 318–321.

Almeida, J. M. P., Da Silva, D. S., Kassab, L. R. P., Zilio, S. C., Mendonca, C. R. and De Boni, L. 2014. Ultrafast third-order optical nonlinearities of heavy metal oxide glasses containing gold nanoparticles. *Optical Materials,* 36: 829–832.

Aloukos, P., Iliopoulos, K., Couris, S., Guldi, D. M., Sooambar, C., Mateo-Aloonso, A., Nagaswaran, P. G., Bonifazi, D. and Prato, M. 2011. Photophysics and transient nonlinear optical response of donor–(60)fullerene hybrids. *Journal of Materials Chemistry,* 21: 2524–2534.

Anija, M., Thomas, J., Singh, N., Sreekumaran Nair, A., Tom, R. T., Pradeep, T. and Philip, R. 2003. Nonlinear light transmission through oxide-protected Au and Ag nanoparticles: an investigation in the nanosecond domain. *Chemical Physics Letters,* 380: 223–229.

Augustine, A. K., Nampoori, V. P. N. and Kailasnath, M. 2014. Rapid synthesize of gold nanoparticles by microwave irradiation method and its application as an optical limiting material. *Optik,* 125: 6696–6699.

Barakat, E., Bernal, M. P. and Baida, F. I. 2013. Doubly resonant Ag–$LiNbO_3$ embedded coaxial nanostructure for high second-order nonlinear conversion. *JOSA B,* 30(7): 1975–1980.

Boltaev, G. S., Sobirov, B. R., Reyimbaev, S., Sherniyozov, H., Usmanov, T., Smirnov, M. S., Ovchinnikov, O. V., Grevtseva, I. G., Kondratenko, T. S., Shihaliev, H. S. and Ganeev, R. A. 2016. Nonlinear optical characterization of colloidal solutions containing dye and Ag_2S quantum dot associates. *Applied Physics A,* 122: 999.

Boltaev, G. S., Sobirov, B. R., Usmanov, T., Smirnov, M. S., Ovchinnikov, O. V., Zvyagin, A. I., Klyuev, V. G., Volykhin, D. V. and Ganeev, R. A. 2017. Nonlinear optical absorption in mixtures of dye molecules and ZnS nanoparticles. *Journal of Nonlinear Optical Physics and Materials,* 26: 1750045.

Boyd, R. W. 2003. *Nonlinear Optics*, Elsevier, New York.

Bridges, R. E., Fischer, G. L. and Boyd, R. W. 1995. Z-scan measurement technique for non-Gaussian beams and arbitrary sample thicknesses. *Optics Letters,* 20: 1821–23.

Butet, J., Brevet, P. F. and Martin, O. J. 2015. Optical second harmonic generation in plasmonic nanostructures: from fundamental principles to advanced applications. *ACS Nano,* 9(11): 10545–10562.

Callister, W. D. and Rethwisch, D. G. 2007. *Materials Science and Engineering: An Introduction*, John Wiley and Sons, New York.

Cetin, A., Kibar, R., Hatipoglu, M., Karabulut, Y. and Can, N. 2010. Third-order optical nonlinearities of Cu and Tb nanoparticles in $SrTiO_3$. *Physica B: Condensed Matter,* 405: 2323–2325.

Chen, W., Bhaumik, S., Veldhuis, S. A., Xing, G., Xu, Q., Gratzel, M., Mhaisalkar, S., Mathews, N. and Sum, T. C. 2017. Giant five-photon absorption from multidimensional core-shell halide perovskite colloidal nanocrystals. *Nature Communications,* 8: 15198.

Chapple, P.B. Staromlynska, J., Hermann, J.A., McKay, T.J. and McDuff, R. G. 1997. Single-beam Z-scan: measurement techniques and analysis *J. Nonlinear Opt. Phys. Mater.* 6: 51–293.

Chapple, P.B. Staromlynska, J. and McDuff, R.G. 1994. Z-scan studies in the thin- and the thick-sample limits. *J. Opt. Soc. Am. B* 11: 975-982.

Cheng, H., Wang, Y., Dai, H., Han, J.-B. and Li, X. 2015. Nonlinear Optical Properties of PbS Colloidal Quantum Dots Fabricated via Solvothermal Method. *The Journal of Physical Chemistry C,* 119: 3288–3292.

Choubey, R. K., Trivedi, R., Das, M., Sen, P. K., Sen, P., Kar, S., Bartwal, K. S. and Ganeev, R. A. 2009. Growth and study of nonlinear refraction and absorption in Mg doped single crystals. *Journal of Crystal Growth,* 311: 2597–2601.

Christodoulides, D. N., Khoo, I. C., Salamo, G. J., Stegeman, G. I. and Van Stryland, E. W. 2010. Nonlinear refraction and absorption: mechanisms and magnitudes. *Advances in Optics and Photonics,* 2: 60–200.

Clark, D. J., Stoumpos, C. C., Saouma, F. O., Kanatzidis, M. G. and Jang, J. I. 2016. Polarization-selective three-photon absorption and subsequent photoluminescence in $CsPbBr_3$ single crystal at room temperature. *Physical Review B,* 93: 195202.

De Araújo, C. B., Oliveira, T. R., Falcao-Filho, E. L., Silva, D. M. and Kassab, L. R. P. 2013. Nonlinear optical properties of $PbO–GeO_2$ films containing gold nanoparticles. *Journal of Luminescence,* 133: 180–183.

De Boni, L., Wood, E. L., Toro, C. and Hernandez, F. E. 2008. Optical Saturable Absorption in Gold Nanoparticles. *Plasmonics,* 3: 171–176.

Demaria, A. J., Stetser, D. A. and Heynau, H. 1966. Self Mode-locking of lasers with saturable absorbers. *Applied Physics Letters,* 8, 174–176.

Dhanya, N. P. 2017. Nonlinear optical investigations of silver nanoparticles synthesised by curcumin reduction. *Optical Materials,* 73: 384–387.

Elim, H. I., Yang, J., Lee, J.-Y., Mi, J. and Ji, W. 2006. Observation of saturable and reverse-saturable absorption at longitudinal surface plasmon resonance in gold nanorods. *Applied Physics Letters,* 88: 083107.

Fakhri, P., Vaziri, M. R. R., Jaleh, B. and Shabestari, N. P. 2015. Nonlocal nonlinear optical response of graphene oxide-Au nanoparticles dispersed in different solvents. *Journal of Optics,* 18: 015502.

Frare, M. C., Pilot, R., De Filippo, C. C., Weber, V., Signorinin, R., Maggini, M. and Bozio, R. 2019. Fullerene functionalized gold nanoparticles for optical limiting of continuous wave lasers. *Applied Physics B,* 125: 47.

Frizyuk, K. S., Smirnova, D. A., Poddubny, A. N. and Petrov, M. I. 2018. Second harmonic generation in nanoparticles with Mie resonances. *Journal of Physics: Conference Series,* 1092(1), 012037.

Frizyuk, K. 2019. Second-harmonic generation in dielectric nanoparticles with different symmetries. *JOSA B,* 36(8): F32–F37.

Frizyuk, K., Volkovskaya, I., Smirnova, D., Poddubny, A. and Petrov, M. 2019. Second-harmonic generation in Mie-resonant dielectric nanoparticles made of noncentrosymmetric materials. *Physical Review B,* 99(7): 075425.

Ganeev, R. 2018. Strong third-order optical nonlinearities of the Ag, Ni, Ti, and Co nanoparticles synthesized during laser ablation of bulk metals in liquids. *Optics and Spectroscopy,* 125: 982–996.

Ganeev, R. A., Morita, M., Ryasyanskii, A. I., Baba, M., Rau, D., Fujii, H., Suzuki, M., Turu, M. and Kuroda, H. 2004a. Nonlinear optical characteristics of CdS and ZnS nanoparticles implanted into zirconium oxide thin films. *Optics and Spectroscopy,* 97: 580–587.

Ganeev, R. A., Rao, K. S., Yu, Z., Yu, W., Yao, C., Fu, Y., Zhang, K. and Guo, C. 2018. Strong nonlinear absorption in perovskite films. *Optical Materials Express,* 8: 1472.

Ganeev, R. A., Ryasnyansky, A. I. and Usmanov, T. 2007. Optical and nonlinear optical characteristics of the Ge and GaAs nanoparticle suspensions prepared by laser ablation. *Optics Communications,* 272: 242–246.

Ganeev, R. A., Ryasnyansky, A. I., Kamalov, S. R., Kodirov, M. K. and Usmanov, T. 2001. Nonlinear susceptibilities, absorption coefficients and refractive indices of colloidal metals. *Journal of Physics D: Applied Physics,* 34: 1602–1611.

Ganeev, R. A., Ryasnyansky, A. I., Kodirov, M. K., Kamalov, S. R., Li, V. A., Tugushev, R. I. and Usmanov, T. 2002. Third harmonic generation of laser radiation in Fe- and Zn-doped polyvinylpyrrolidone. *The European Physical Journal D - Atomic, Molecular and Optical Physics,* 20: 129–131.

Ganeev, R. A., Ryasnyansky, A. I., Stepanov, A. L., Marques, C., Da Silva, R. C. and Alves, E. 2005. Application of RZ-scan technique for investigation of nonlinear refraction of sapphire doped with Ag, Cu, and Au nanoparticles. *Optics Communications,* 253: 205–213.

Ganeev, R. A., Ryasnyansky, A. I., Stepanov, A. L. and Usmanov, T. 2004b. Characterization of nonlinear optical parameters of copper- and silver-doped silica glasses at $\lambda = 1064\,\text{nm}$. *Physica Status Solidi (b),* 241: 935–944.

Ganeev, R. A., Ryasnyansky, A. I., Stepanov, A. L. and Usmanov, T. 2004c. Saturated absorption and nonlinear refraction of silicate glasses doped with silver nanoparticles at 532 nm. *Optical and Quantum Electronics,* 36, 949–960.

Ganeev, R. A., Ryasnyansky, A. I., Tugushev, R. I. and Usmanov, T. 2003. Investigation of nonlinear refraction and nonlinear absorption of semiconductor nanoparticle solutions prepared by laser ablation. *Journal of Optics A: Pure and Applied Optics,* 5: 409–417.

Gao, Y., Huong, N. Q., Birman, J. L. and Potasek, M. J. 2004. Large nonlinear optical properties of semiconductor quantum dot arrays embedded in an organic medium. *Journal of Applied Physics,* 96: 4839–4842.

Gao, Y., Zhang, X., Li, Y., Liu, H., Wang, Y., Chang, Q., Jiao, W. and Song, Y. 2005. Saturable absorption and reverse saturable absorption in platinum nanoparticles. *Optics Communications,* 251: 429–433.

George, N., Subha, R., Thomas, A. R. and Mary, N. L. 2017. Plasmon enhanced two-photon absorption in modified Styrene–Maleic Anhydride Silver nanocomposites. *Nano-Structures and Nano-Objects,* 11: 32–38.

Gerdova, I. and Hache, A. 2005. Third-order non-linear spectroscopy of CdSe and CdSe/ZnS core shell quantum dots. *Optics Communications,* 246: 205–212.

Göppert-Mayer, M. 1931. Über Elementarakte mit zwei Quantensprüngen. *Annalen der Physik,* 401: 273–294.

He, T., Wang, C., Pan, X. and Wang, Y. 2009. Nonlinear optical response of Au and Ag nanoparticles doped polyvinylpyrrolidone thin films. *Physics Letters A,* 373: 592–595.

He, X., Wei, R., Tian, X., Qiu, J., Zhang, M., Zeng, Q. and Liu, J. 2017. Thermal evaporated $Te-Bi_2Te_3$ alloy thin film and its nonlinear optical properties. *Journal of Alloys and Compounds,* 714: 363–369.

Henari, F., Callaghan, J., Stiel, H., Blau, W. and Cardin, D. J. 1992. Intensity-dependent absorption and resonant optical nonlinearity of C_{60} and C_{70} solutions. *Chemical Physics Letters,* 199: 144–148.

Hercher, M. 1967. An Analysis of Saturable Absorbers. *Applied Optics,* 6: 947–954.

Huang, Y.-L. and Sun, C.-K. 2000. Z-scan measurement with an astigmatic Gaussian beam. *Journal of the Optical Society of America B,* 17: 43–47.

Jia, T., He, T., Li, P., Mo, Y. and Cui, Y. 2008. A study of the thermal-induced nonlinearity of Au and Ag colloids prepared by the chemical reaction method. *Optics and Laser Technology,* 40: 936–940.

Jin, Q., Wu, W., Zheng, Z., Yan, Y., Liu, W., Li, A., Yang, Y. and Su, W. 2009. The third-order optical nonlinearity and upconversion luminescence of CdTe quantum dots under femtosecond laser excitation. *Journal of Nanoparticle Research,* 11: 665–670.

John, J., Mathew, R. M., Rejeena, I., Jayakrishnan, R., Mathew, S., Thomas, V. and Mujeeb, A. 2019. Nonlinear optical limiting and dual beam mode matched thermal lensing of nano fluids containing green synthesized copper nanoparticles. *Journal of Molecular Liquids,* 279: 63–66.

Justus, B. L., Huston, A. L. and Campillo, A. J. 1993. Broadband thermal optical limiter. *Applied Physics Letters,* 63: 1483–1485.

Kafalas, P., Masters, J. I. and Murray, E. M. E. 1964. Photosensitive liquid used as a nondestructive passive Q-switch in a ruby laser. *Journal of Applied Physics,* 35: 2349–2350.

Kalanoor, B. S., Gouda, L., Gottesman, R., Tiroshi, S., Haltzi, E., Zaban, A. and Tischler, Y. R. 2016. Third-order optical nonlinearities in organometallic methylammonium lead iodide perovskite thin films. *ACS Photonics,* 3: 361–370.

Karmakar, B., Rademann, K. and Stepanov, A. L. 2016. *Preface: Glass Nanocomposites*. Elsevier, Amsterdam.

Karvonen, L., Rönn, J., Kujala, S., Chen, Y., Saynatjoki, A., Tervonen, A., Svirko, Y. and Honkanen, S. 2013. High non-resonant third-order optical nonlinearity of Ag–glass nanocomposite fabricated by two-step ion exchange. *Optical Materials,* 36: 328–332.

Khoo, I.C., Micheal, R. and Finn, G. 1988. Self-phase modulation and optical limiting of a low-power CO_2 laser with a nematic liquid-crystal film. *Applied Physics Letters,* 52: 2108–2110.

Kolavekar, S. B., Ayachit, N. H., Jagannath, G., Nagakrishnakanth, K. and Venugopal Rao, S. 2018. Optical, structural and Near-IR NLO properties of gold nanoparticles doped sodium zinc borate glasses. *Optical Materials,* 83: 34–42.

Kole, A. K., Gupta, S., Kumbhakar, P. and Ramamurthy, P. C. 2014. Nonlinear optical second harmonic generation in ZnS quantum dots and observation on optical properties of ZnS/PMMA nanocomposites. *Optics Communications,* 313: 231–237.

Krishnakanth, K. N., Seth, S., Samanta, A. and Rao, S.V. 2018. Broadband femtosecond nonlinear optical properties of CsPbBr_3 perovskite nanocrystals. *Optics Letters,* 43: 603–606.

Krishnakanth, K. N., Seth, S., Samanta, A. and Venugopal Rao, S. 2019. Broadband ultrafast nonlinear optical studies revealing exciting multi-photon absorption coefficients in phase pure zero-dimensional Cs4PbBr6 perovskite films. *Nanoscale,* 11: 945–954.

Kulyk, B., Sahraoui, B., Krupka, O., Kapustianyk, V., et al. (2009). Linear and nonlinear optical properties of ZnO/PMMA nanocomposite films. *Journal of Applied Physics,* 106(9): 093102.

Kumar, A., Singh, R., Mohanty, T. and Taneja, A. 2019. Tunable optical nonlinearity of Au-TiO2 nanocomposites. *Photonics and Nanostructures-Fundamentals and Applications,* 33: 1–9.

Kyoung, M. and Lee, M. 1999. Nonlinear absorption and refractive index measurements of silver nanorods by the Z-scan technique. *Optics Communications,* 171: 145–148.

Laud, B. B. 2011. *Lasers and Non-linear Optics* (Online). New Age International Publishers, New Delhi. Available: http://site.ebrary.com/id/10594271.

Lee, Y. H., Yan, Y., Polavarapu, L. and Xu, Q.-H. 2009. Nonlinear optical switching behavior of Au nanocubes and nano-octahedra investigated by femtosecond Z-scan measurements. *Applied Physics Letters,* 95: 023105.

Lepkowicz, R. Kobyakov, A. Hagan, D.J. and Van Stryland, E.W. 2002. Picosecond optical limiting in reverse saturable absorbers: a theoretical and *experimental study. J. Opt. Soc.* Am. B 19: 94-101.

Li, C., Jiang, L., Liu, H., Li, Y. and Song, Y. 2009. Stabilization and large nonlinearity of gold nanoparticles functionalized with a π-conjugated polymer. *ChemPhysChem,* 10: 2058–2065.

Li, P. P., Chen, Y., Zhu, J., Feng, M., Zhuang, X., Lin, Y. and Zhan, H. 2011. Charm-bracelet-type poly (N-vinylcarbazole) functionalized with reduced graphene oxide for broadband optical limiting. *Chemistry–A European Journal,* 17: 780–785.

Li, R., Wei, Z., Zhao, H., Yu, H., Fang, X., Fang, D., Li, J., He, T., Chen, R. and Wang, X. 2018. Linear and nonlinear optical characteristics of all-inorganic perovskite $CsPbBr_3$ quantum dots modified by hydrophobic zeolites. *Nanoscale,* 10: 22766–22774.

Liaros, N. and Fourkas, J. T. 2017. The characterization of absorptive nonlinearities. *Laser and Photonics Reviews,* 11: 1700106.

Liu, Y., Zhou, J., Zhang, X., Liu, Z., Wan, X., Tian, J., Wang, T. and Chen, Y. 2009. Synthesis, characterization and optical limiting property of covalently oligothiophene-functionalized graphene material. *Carbon,* 47: 3113–3121.

Liu, Z., Zhang, B. and Chen, Y. 2019. Recent progress in two-dimensional nanomaterials for laser protection, *Chemistry,* 1: 17–43.

Majles Ara, M. H., Dehghani, Z., Sahraei, R., Daneshfar, A., Javadi, Z. and Divsar, F. 2012. Diffraction patterns and nonlinear optical properties of gold nanoparticles. *Journal of Quantitative Spectroscopy and Radiative Transfer,* 113: 366–372.

Majles Ara, M. H., Dehghani, Z., Sahraei, R. and Nabiyouni, G. 2010. Non-linear optical properties of silver nanoparticles prepared by hydrogen reduction method. *Optics Communications,* 283: 1650–1653.

Mclean, D. G., Fleitz, P. A., Pottenger, T., Sutherland, R. L., Brant, M. C. and Brandelik, D. M. 1993. Nonlinear absorption study of a C_{60}–toluene solution. *Optics Letters,* 18: 858–860.

Murugan, G. S. and Varma, K. B. R. (2002). Lithium borate–strontium bismuth tantalate glass nanocomposite: a novel material for nonlinear optic and ferroelectric applications. *Journal of Materials Chemistry,* 12(5): 1426–1436.

Muruganandi, G., Saravanan, M., Vinitha, G., Jessie Raj, M. B. and Sabari Girisiun, T. C. 2018. Barium borate nanorod decorated reduced graphene oxide for optical power limiting applications. *Optical Materials,* 75: 612–618.

Nair, A. K., Bhavitha, K. B., Perumbilavil, S., Sankar, P., Rouxel, D., Kala, M. S., Thomas, S. and Kalarikkal, N. 2018. Multifunctional nitrogen sulfur co-doped reduced graphene oxide – Ag nano hybrids (sphere, cube and wire) for nonlinear optical and SERS applications. *Carbon,* 132: 380–393.

Nelson, C. B., Zubkov, T., Adair, J. D. and Subir, M. 2017. A synergistic combination of local tight binding theory and second harmonic generation elucidating surface properties of ZnO nanoparticles. *Physical Chemistry Chemical Physics,* 19(44): 29991–29997.

New, G. 2011. *Introduction: Introduction to Nonlinear Optics*. Cambridge University Press, Cambridge.

Nidya, M., Umadevi, M., Sankar, P., Philip, R. and Rajkumar, B. J. M. 2015a. l-Phenylalanine functionalized silver nanoparticles: Photocatalytic and nonlinear optical applications. *Optical Materials,* 42: 152–159.

Nidya, M., Umadevi, M., Sankar, P. and Rajkumar, B. J. M. 2015b. l-Glutamic acid functionalized silver nanoparticles and its nonlinear optical applications. *Journal of Materials Science: Materials in Electronics,* 26: 4124–4131.

Omidvar, A., Rashidianvaziri, M. R. and Jaleh, B. 2018. Enhancing the nonlinear optical properties of graphene oxide by repairing with palladium nanoparticles. *Physica E: Low-Dimensional Systems and Nanostructures,* 103: 239–245.

Ozga, K., Michel, J., Nechyporuk, B. D., Ebothé, J., Kityk, I. V., Albassam, A. A., … and Fedorchuk, A. O. 2016. ZnS/PVA nanocomposites for nonlinear optical applications. *Physica E: Low-Dimensional Systems and Nanostructures,* 81: 281–289.

Pan, G. M., Yang, D. J., Zhou, L., Hao, Z. H. and Wang, Q. Q. 2017. Enhanced second harmonic generation by mode matching in gain-assisted double-plasmonic resonance nanostructure. *Scientific Reports,* 7(1): 9776.

Patra, A., Chandaluri, Ch. G. and Radhakrishnan, T. P. 2012, Optical materials based on molecular nanoparticles, *Nanoscale*, 4: 343–359.

Philip, R., Kumar, G. R., Sandhyarani, N. and Pradeep, T. 2000. Picosecond optical nonlinearity in monolayer-protected gold, silver, and gold-silver alloy nanoclusters. *Physical Review B,* 62: 13160–13166.

Pinçon-Roetzinger, N., Prot, D., Palpant, B., Charron, E. and Debrus, S. 2002. Large optical Kerr effect in matrix-embedded metal nanoparticles. *Materials Science and Engineering: C,* 19: 51–54.

Perry, J.W., mansour, K., Marder, S.R., Perry, K.J., Alvarez, D.,Choong, I. 1997. Enhanced reverse saturable absorption and optical limiting in heavy-atom-substituted phthalocyanines. *Opt. Lett.* 19: 625-627.

Polloni, R., Scremin, B. F., Calvelli, P., Cattaruzza, E., Battaglin, G. and Mattei, G. 2003. Metal nanoparticles–silica composites: Z-scan determination of non-linear refractive index. *Journal of Non-Crystalline Solids,* 322: 300–305.

Pradhan, P., Podila, R., Molli, M., Kaniyoor, A., Sai Muthukumar, V., Siva Sankara Sai, S., Ramaprabhu, S. and Rao, A. M. 2015. Optical limiting and nonlinear optical properties of gold-decorated graphene nanocomposites. *Optical Materials,* 39: 182–187.

Pugazhendhi, S., Palanisamy, P. K. and Jayavel, R. 2018. Synthesis of highly stable silver nanoparticles through a novel green method using Mirabillis jalapa for antibacterial, nonlinear optical applications. *Optical Materials,* 79: 457–463.

Rahulan, K. M., Ganesan, S. and Aruna, P. 2011. Synthesis and optical limiting studies of Au-doped TiO2nanoparticles. *Advances in Natural Sciences: Nanoscience and Nanotechnology,* 2: 025012.

Rahulan, K. M., Padmanathan, N., Philip, R., Balamurugan, S. and Kanakam, C. C. 2013. Structural evaluation and nonlinear optical properties of Ni/NiO, Ni/NiCo_2O_4 and Co/Co_3O_4 nanocomposites. *Applied Surface Science,* 282: 656–661.

Rajaramakrishna, R., Saiyasombat, C., Aanvekar, R. V. and Jain, H. 2014. Structure and nonlinear optical studies of Au nanoparticles embedded in lead lanthanum borate glass. *Journal of Non-Crystalline Solids,* 406: 107–110.

Rao, S. V. 2011. Picosecond nonlinear optical studies of gold nanoparticles synthesised using coriander leaves (Coriandrum sativum). *Journal of Modern Optics,* 58: 1024–1029.

Ren, M. L., Liu, S. Y., Wang, B. L., Chen, B. Q., Li, J. and Li, Z. Y. 2014. Giant enhancement of second harmonic generation by engineering double plasmonic resonances at nanoscale. *Optics Express,* 22(23): 28653–28661.

Reyna, A.S., De Araújo, C.B. 2017. High-order optical nonlinearities in plasmonic nanocomposites—a review. *Advances in Optics and Photonics,* 9(4): 720–774.

Ryasnyansky, A. I., Palpant, B., Debrus, S., Khaibullin, R. I. and Stepanov, A. L. 2006. Nonlinear optical properties of copper nanoparticles synthesized in indium tin oxide matrix by ion implantation. *Journal of the Optical Society of America B,* 23: 1348–1353.

Sabari Girisun, T. C., Saravanan, M. and Soma, V. R. 2018a. Wavelength-dependent nonlinear optical absorption and broadband optical limiting in Au-Fe_2O_3-rGO nanocomposites. *ACS Applied Nano Materials,* 1: 6337–6348.

Sabari Girisun, T. C., Saravanan, M. and Venugopal Rao, S. 2018b. Enhanced broadband optical limiting and switching of nonlinear absorption in functionalized solar exfoliated reduced graphene oxide–Ag-Fe_2O_3 nanocomposites. *Journal of Applied Physics,* 124: 193101.

Sabari Girisun, T. C., Saravanan, M. and Venugopal Rao, S. 2019. Femtosecond nonlinear absorption and optical limiting action in nanoplatelet CuFe2O4 decorated rGO nanocomposites. *SN Applied Science* 1: 400.

Sakho, E. H. M., Oluwafemi, O. S., Sreekanth, P., Philip, R., Thomas, S. and Kalarikkal, N. 2016. Improved nonlinear optical and optical limiting properties in non-covalent functionalized reduced graphene oxide/silver nanoparticle (NF-RGO/Ag-NPs) hybrid. *Optical Materials,* 58: 476–483.

Saouma, F. O., Park, D. Y., Kim, S. H., Jeong, M. S. and Jang, J. I. 2017. Multiphoton absorption coefficients of organic–inorganic lead halide perovskites $CH_3NH_3PbX_3$ (X = Cl, Br, I) Single Crystals. *Chemistry of Materials,* 29: 6876–6882.

Saravanan, M., Girisun, T. C. S. and Venugopal Rao, S. 2017. Super-paramagnetic and unusual nonlinear absorption switching behavior of an in situ decorated $CdFe_2O_4$–rGO nanocomposite. *Journal of Materials Chemistry C,* 5: 9929–9942.

Saravanan, M. and Sabari Girisun, T. C., 2017. Enhanced nonlinear optical absorption and optical limiting properties of superparamagnetic spinel zinc ferrite decorated reduced graphene oxide nanostructures. *Applied Surface Science,* 392: 904–911.

Saravanan, M, Sabari Girisun, T.C. and Vinitha, G. 2018. Facile hydrothermal synthesis of $CdFe_2O_4$-reduced graphene oxide nanocomposites and their third-order nonlinear optical properties under CW excitation. *Journal of Molecular Liquids,* 256: 519–526.

Saravanan, M., Sabari Girisun, T. C., Vinitha, G. and Venugopal Rao, S. 2016. Improved third-order optical nonlinearity and optical limiting behaviour of (nanospindle and nanosphere) zinc ferrite decorated reduced graphene oxide under continuous and ultrafast laser excitation. *RSC Advances,* 6: 91083–91092.

Sathyavathi, R., Krishna, M. B., Rao, S. V., Saritha, R. and Rao, D. N. 2010. Biosynthesis of silver nanoparticles using *Coriandrum Sativum* leaf extract and their application in nonlinear optics. *Advanced Science Letters,* 3: 138–143.

Schmitt-Rink, S., Miller, D. A. B. and Chemla, D. S. 1987. Theory of the linear and nonlinear optical properties of semiconductor microcrystallites. *Physical Review B,* 35: 8113–8125.

Sheik-Bahae, M., Said, A. A. and Van Stryland, E. W. 1989. High-sensitivity, single-beam n_2 measurements. *Optics Letters,* 14: 955–57.

Sheik-Bahae, M., Said, A. A., Wei, T. H., Hagan, D. J. and Van Stryland, E. W. 1990. Sensitive measurement of optical nonlinearities using a single beam. *IEEE Journal of Quantum Electronics*, 26: 760–769.

Shen, Y. R. 1984. *The Principles of Nonlinear Optics*, Wiley, New York.

Soffer, B. H. 1964. Giant pulse laser operation by a passisve, reversibly bleachable absorber. *Journal of Applied Physics,* 35: 2551–2551.

Sudheesh, P., Siji Narendran, N. K. and Chandrasekharan, K. 2013. Third-order nonlinear optical responses in derivatives of phenylhydrazone by Z-scan and optical limiting studies-influence of noble metal nanoparticles. *Optical Materials,* 36: 304–309.

Suh, J. Y. and Odom, T. W. 2013, Nonlinear properties of nanoscale antennas, *Nano Today,* 8: 469–479.

Sutherland, R. L. 2003. *Handbook of Nonlinear Optics*, CRC Press, Boca Raton, FL.

Sutherland, R. L., Brant, M. C., Heinrichs, J., Rogers, J. E., Slagle, J. E., Mclean, D. G. and Fleitz, P. A. 2005. Excited-state characterization and effective three-photon absorption model of two-photon-induced excited-state absorption in organic push-pull charge-transfer chromophores. *Journal of the Optical Society of America B,* 22: 1939–1948.

Timpu, F., Sergeyev, A., Hendricks, N. R. and Grange, R. 2016. Second-harmonic enhancement with Mie resonances in perovskite nanoparticles. *ACS Photonics,* 4(1): 76–84.

Timpu, F., Hendricks, N. R., Petrov, M., Ni, S., Renaut, C., Wolf, H. and Grange, R. 2017. Enhanced second-harmonic generation from sequential capillarity-assisted particle assembly of hybrid nanodimers. *Nano Letters,* 17(9): 5381–5388.

Tutt, L. W. and Boggess, T. F. 1993. A review of optical limiting mechanisms and devices using organics, fullerenes, semiconductors and other materials. *Progress in Quantum Electronics,* 17: 299–338.

Verma, Y., Divakar Rao, K., Mohanty, S. K. and Gupta, P. K. 2007. Optical coherence tomography using a tapered single mode fiber tip. *Laser Physics Letters,* 4: 686–689.

Wake, L.V. and Brady, R. 1993. Formulating infrared coatings for defence applications. Materials Research Labs Ascot Vale (AUSTRALIA). https://apps.dtic.mil/dtic/tr/fulltext/u2/a267555.pdf.

Walters, G., Sutherland, B. R., Hoogland, S., Shi, D., Comin, R., Sellan, D. P., Bakr, O. M. and Sargent, E. H. 2015. Two-photon absorption in organometallic bromide perovskites. *ACS Nano,* 9: 9340–9346.

Wang, W., Qu, L., Yang, G. and Chen, Z. 2003. Large third-order optical nonlinearity in BaTiO3 matrix-embedded metal nanoparticles. *Applied Surface Science,* 218: 24–28.

Wang, Y., Suna, A., Mchugh, J., Hilinski, E. F., Lucas, P. A. and Johnson, R. D. 1990. Optical transient bleaching of quantum-confined CdS clusters: The effects of surface-trapped electron–hole pairs. *The Journal of Chemical Physics,* 92: 6927–6939.

Wei, K., Xu, Z., Chen, R., Zheng, X., Cheng, X. and Jiang, T. 2016. Temperature-dependent excitonic photoluminescence excited by two-photon absorption in perovskite $CsPbBr_3$ quantum dots. *Optics Letters,* 41: 3821–3824.

Wolfe, C. M., Holonyak, N. and Stillman, G. E. 1989. *Physical Properties of Semiconductors*, Prentice Hall, Upper Saddle River, NJ.

Woodward, R. I. and Kelleher, E. J. R. 2015a, 2D saturable absorbers for fibre lasers, *Applied Science,* 5: 1440–1456.

Woodward, R. I., Howe, R. C. T., Hu, G., Torrisi, F., Zhang, M., Hasan, T. and Kelleher, E. J. R. 2015b, Few-layer MoS_2 saturable absorbers for short-pulse laser technology: Current status and future perspectives, *Photonics Research Journal,* 3(2): A30–A42.

Xia, T., Hagan, D. J., Dogariu, A., Said, A. A. and Van Stryland, E. W. 1997. Optimization of optical limiting devices based on excited-state absorption. *Applied Optics,* 36: 4110–4122.

Xie, Y., Fan, J., Liu, C., Chi, S., Wang, Z., Yu, H., Zhang, H., Mai, Y. and Wang, J. 2018. Giant two-photon absorption in mixed halide perovskite $CH_3NH_3Pb_{0.75}Sn_{0.25}I_3$ thin films and application to photodetection at optical communication wavelengths. *Advanced Optical Materials,* 6: 1700819.

Xu, J., Li, X., Xiong, J., Yuan, C., Semin, S., Rasing, T. and Bu, X. H. 2019. Halide Perovskites for Nonlinear Optics. *Advanced Materials,* 32: 1806736. https://onlinelibrary.wiley.com/doi/abs/10.1002/adma.201806736.

Yi, J., Miao, L., Li, J., Hu, W., Zhao, C. and Wen, S. 2017. Third-order nonlinear optical response of $CH_3NH_3PbI_3$ perovskite in the mid-infrared regime. *Optical Materials Express,* 7: 3894–3901.

You, G., Zhou, P., Dong, Z., Zhang, C., Chen, L. and Qian, S. 2007. Ultrafast third-order nonlinear optical response of $Cu:Bi_2O_3$ nanocomposite films. *Physica B: Condensed Matter,* 393: 188–194.

Yue, M., Si, J., Yan, L., Yu, Y. and Hou, X. 2018. Enhanced nonlinear optical properties of reduced graphene oxide decorated with silver nanoparticles. *Optical Materials Express,* 8: 698–703.

Zernike, F. and Midwinter, J. E. 2006. *Applied Nonlinear Optics*, Courier Corporation, Chelmsford, MA.

Zhan, C., Li, D., Zhang, D., Xu, W., Nie, Y. and Zhu, D. 2004. The excited-state absorption and third-order optical nonlinearity from 1-dodecanethiol protected gold nanoparticles: Application for optical limiting. *Optical Materials,* 26: 11–15.

Zhang, Y.-X. and Wang, Y.-H. 2017, Nonlinear optical properties of metal nanoparticles: A review, *RSC Advances,* 7: 45129–45144.

Zhang, C., Xiang, W., Luo, H., Liu, H., Liang, X., Ma, X., Pei, L., Chen, Z., Li, J., Gao, H. and Ma, L. 2014. Third-order optical nonlinearity of Na2O–B2O3–SiO2 glass doped with lead nanoparticles prepared by sol–gel method. *Journal of Alloys and Compounds,* 602: 221–227.

Zhang, R., Fan, J., Zhang, X., Yu, H., Zhang, H., Mai, Y., Xu, T., Wang, J. and Snaith, H. J. 2016. Nonlinear optical response of organic–inorganic halide perovskites. *ACS Photonics,* 3: 371–377.

Zhang, X.-L., Zhao, X., Liu, Z.-B., Liu, Y.-S., Chen, Y.-S. and Tian, J.-G. 2009. Enhanced nonlinear optical properties of graphene-oligothiophene hybrid material. *Optics Express,* 17: 23959.

Zhang, Y., Jin, Y., He, M., Zhou, L., Xu, T., Yuan, R., Lin, S., Xiang, W. and Liang, X. 2018. Optical properties of bimetallic Au-Cu nanocrystals embedded in glass. *Materials Research Bulletin,* 98: 94–102.

Zheng, C., Chen, W., Cai, S., Xiao, X. and Ye, X. 2014. Enhanced optical limiting properties of graphene oxide/triangular Pd nanocrystal composites. *Materials Letters,* 131: 284–287.

Zheng, C., Li, W., Xiao, X., Ye, X. and Chen, W. 2016. Synthesis and optical limiting properties of graphene oxide/bimetallic nanoparticles. *Optik,* 127: 1792–1796.

Zhong, J., Ma, X., Lu, H., Wang, X., Zhang, S. and Xinag, W. 2014. Preparation and optical properties of sodium borosilicate glasses containing Sb nanoparticles. *Journal of Alloys and Compounds,* 607: 177–182.

Zhong, J., Xiang, W., Liang, X., Chen, Z. and Zhao, W. 2013. Na_2O-B_2O_3-SiO_2 glass doped with In and Cu2In nanoparticles prepared by sol–gel method. *Journal of Non-Crystalline Solids,* 361: 124–129.

Zolotovskaya, S. A., Tyrk, M. A., Stalmashonak, A., Gillespie, W. A. and Abdolvand, A. 2016. On second harmonic generation and multiphoton-absorption induced luminescence from laser-reshaped silver nanoparticles embedded in glass. *Nanotechnology,* 27(43): 435703.

Zulina, N. A., Pavlovetc, I. M., Baranov, M. A. and Denisyuk, I. Y. 2017. Optical, structural and nonlinear optical properties of laser ablation synthesized Ag nanoparticles and photopolymer nanocomposites based on them. *Optics and Laser Technology,* 89: 41–45.

Zvyagin, A. I., Perepelista, A. S., Lavlinskaya, M. S., Ovshinniokv, O. V., Smirnov, M. S. and Ganeev, R. A. 2018. Demonstration of variation of the nonlinear optical absorption of non-spherical silver nanoparticles. *Optik,* 175: 93–98.

Taylor & Francis
Taylor & Francis Group
http://taylorandfrancis.com

22

Lasers in Imaging: Section Introduction

Pavel Redkin, Subhash C. Singh, and Chunlei Guo

Lasers can deliver high power and coherent radiation. These features make them ideal for applications in different types of optical microscopy. This section starts with Chapter 23 that provides a review of laser microscopy.

The coherence of laser radiation enables coherent diffraction imaging (CDI), which is also called 'lensless microscopy'. When the object is illuminated by the coherent radiation, scattered light produces a diffraction pattern containing information of the object. The principles of CDI are discussed in Chapter 24.

Chapter 25 describes the usage of laser pulses to image high-speed dynamics of objects. Many ultrafast events occur at femtosecond time scale, and the technology of such ultrafast optical imaging is discussed in Chapter 26.

Many imaging techniques suffer from problems of background noise. Transient absorption is the secondary absorption of specific molecules that are already excited by the primary absorption. In contrast to the primary absorption, which is often concealed in a high background, secondary absorption is performed with little environmental interference. The differences between transient absorption microscopy and classical imaging and microscopy lie in their high temporal resolution and in their ability to study non-fluorescent molecular species. Therefore, this method belongs to the group of label-free imaging methods. Chapter 27 describes the methodology of transient absorption and its application to low-noise ultrafast imaging of nanostructures.

Taylor & Francis
Taylor & Francis Group
http://taylorandfrancis.com

23

Lasers in Microscopy

Peng Xi

CONTENTS

23.1 Introduction 291
23.2 Basic Principles of Microscopy 291
  23.2.1 Wide-field and Laser Scanning Microscopy 291
  23.2.2 Fluorescence Excitation and Emission 292
  23.2.3 Resolution 293
  23.2.4 Scattering and Absorption of the Specimen 294
23.3 Advanced Techniques in Microscopy 295
  23.3.1 Two-photon Excitation 295
  23.3.2 Raman Microscopy 295
  23.3.3 Coherent Anti-Stokes Raman Scattering (CARS) and Stimulated Raman Scattering (SRS) Microscopy 296
  23.3.4 Super-resolution Microscopy 297
    23.3.4.1 Stimulated Emission Depletion (STED) 297
    23.3.4.2 Single-molecule Localization Microscopy (SMLM) 297
23.4 Conclusion and Discussion 297
References 298

23.1 Introduction

The history of optical microscopy can be traced back to Antoni van Leeuwenhoek (1632–1723) [1], who invented single lens microscope to observe the tiny living creatures hidden inside the tartar, later named "bacteria". It is extended by British scientist Robert Hooke [2], who invented the compound microscope – a combination of objective and eyepiece. He also observed the fine structure of a piece of soft wood and found grid-like structures like rooms in prison – hence comes the name "cell". Benefitted from microscopic techniques, biologists have two major research domains to work on.

When laser was invented in the 1960s, it installed its wings to optical microscopy. Many novel microscopic techniques such as confocal, two-photon, Raman, coherent anti-Stokes Raman scattering (CARS), stimulated Raman scattering (SRS), and the recent stimulated emission depletion (STED) are all directly developed from laser technology.

23.2 Basic Principles of Microscopy

23.2.1 Wide-field and Laser Scanning Microscopy

The layout of a conventional wide-field microscopy is relatively simple: as shown in Figure 23.1, the entire field of view (FOV) of the specimen is illuminated, and an objective lens is used to form a real image of the specimen. A CCD sensor can be used to capture the image, store it in a computer, or display it either real time or later on.

In a conventional microscope, the entire FOV is illuminated, whereas in a laser scanning microscope, usually only one point is illuminated and data from this point is collected. This sampling procedure scans across the specimen to form a 2D or 3D image. Confocal laser scanning microscopy (CLSM), or confocal microscopy, has been widely applied in the cutting-edge biological research for its three-dimensional, high-resolution imaging capability [3]. It is the simplest version of laser scanning microscopy.

The principle of confocal microscopy is illustrated in Figure 23.1. In confocal microscopy, only one point is illuminated. Then, it is magnified by objective, just like other forms of microscopes. Then, instead of using a two-dimensional detector, a point detector is employed. In addition, a pinhole is employed in front of the point detector to further reject the out-of-focus noise. The relative movement between the target and the laser focal spot forms an image.

When looking a specimen under a microscope, the image represents a form of contrast within the FOV. A homogenous sample, such as a drop of pure water, cannot form a high-quality image. Because water accounts for 80% of biological cells, it is quite transparent and can only form very weak contrast when viewing directly under a microscope. Therefore, fluorescent staining or labelling must be performed to enhance the contrast.

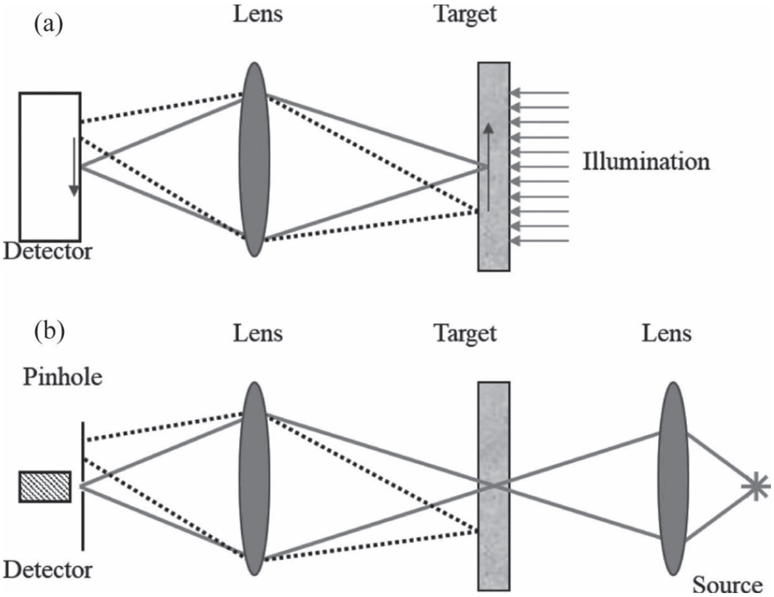

FIGURE 23.1 Different types of microscopy: (a) wide-field microscopy; (b) confocal microscopy. (Adapted from Ref. [4].)

23.2.2 Fluorescence Excitation and Emission

Confocal microscopy is popularly used together with fluorescence microscopy. Fluorescence is preferable because the fluorophore molecules can be uniquely labelled on the subcellular organelles, making them glow under fluorescent excitation. Hence, the fluorescence microscopic image reflects the structure and dynamics of the respective subcellular organelles.

In fact, the physical process of fluorescence is very common to laser scientists. As described in Chapter 2, the generation of laser has three states: (i) the excitation, in which the electron on the ground state is excited to high energy state by a photon; (ii) the non-radiative decay, in which the electron relaxes to a sub-stable state; and (iii) at the sub-stable state, it has two destinations, namely (i) spontaneous emission, in which the electron goes back to the ground state and emits a photon, and (ii) stimulated emission, which happens when an incident photon energy matches the energy difference, and the electron at upper level will instantly go back to the ground state and release a very same photon as the incident photon. Fluorescence is a result of spontaneous emission.

Fluorescence is also convenient technique because it absorbs high-energy photon and emits lower-energy photon; therefore, a very little fluorescent dye can even tag the organelle and hence is used for visualization purpose. The fluorescent dye is far superior to the chromatic dyes, because sufficient concentration of chromatic dyes is necessary for visualization.

Fluorescence absorption describes the relative possibility of a photon in different wavelength being absorbed by a fluorophore. Figure 23.2 illustrates the absorption and emission diagrams of FITC. As can be seen, for 488 nm, the excitation efficiency is 88% relative to its absorption maximum (495 nm); for 514 nm, the excitation efficiency is only 30%.

Conventional bright-field microscopy illuminates the specimen with a white light source through the condenser, whereas in fluorescence microscopy, the illumination passes through the same objective for imaging, which is termed epi-illumination. As shown in Figure 23.3, the mercury lamp

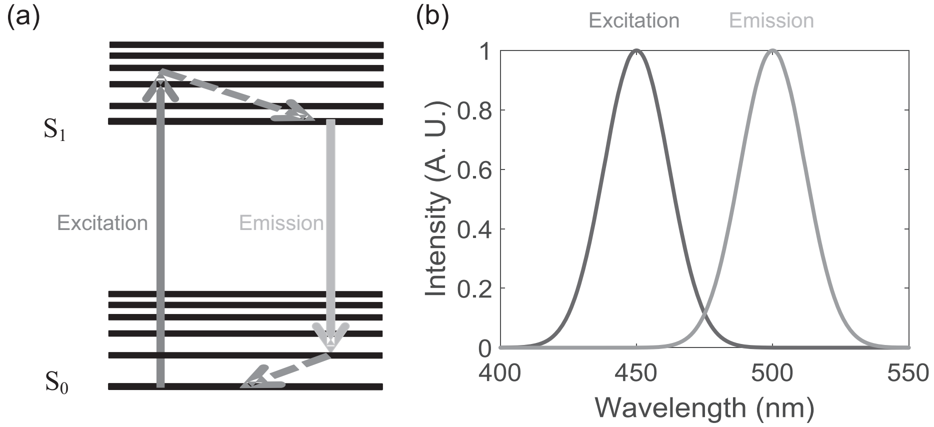

FIGURE 23.2 (a) The Jablonski diagrams of fluorescence excitation and emission. (b) The fluorescence excitation and emission spectra.

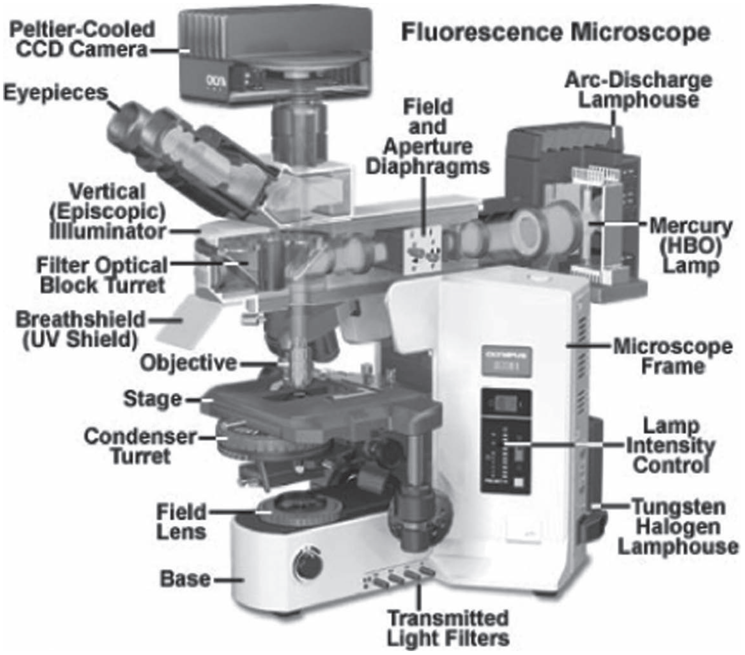

FIGURE 23.3 Anatomy of a fluorescence microscope. (Adapted from: https://micro.magnet.fsu.edu/primer/techniques/fluorescence/anatomy/fluoromicroanatomy.html.)

(shown as magenta) is used for excitation, and it is reflected downwards to the objective and the sample. The back-propagated fluorescence from the sample (shown as green) is then collected by the objective, passed through the filter cube, and then collected by either the CCD camera (on top) or the eyepiece for direct view. The purpose of epi-illumination is to ensure that only the sample in the FOV is excited, as overexposing the fluorophore to the excitation can cause unnecessary photobleaching if not in the FOV.

When using a laser in optical microscopy, the proper choice of a filter is essential, because the laser line can be 3–4 orders-of-magnitude stronger than the fluorescence. Typically, a filter cube is employed, which consists of an excitation filter, a dichroic filter in 45°, and an emission filter.

In addition, because the laser line may contain more than one single emission, it is critical to have a bandpass filter that effectively blocks the “ghost lines” from lasers. An easy way to check this is to put a blank sample onto the sample holder, and see what is presented at the detector. If the detector detects no noise while using blank sample, then the filter set is fine. Otherwise, the detector can detect excessive noise.

A comprehensive list of the dyes that can be used for fluorescence microscopy, together with their excitation and emission spectra, can be found in a variety of websites of fluorescent molecule vendors, such as BD Bioscience (Figure 23.3) and Thermal Fisher (Figure 23.4).

23.2.3 Resolution

The resolution of an optical microscopy is often determined by the most essential element of the microscopic system: the objective. However, it is identified by a different approach for wide-field or confocal microscopy. Hence, it derives different techniques to surpass the resolution limit defined by the respective diffraction barrier.

In a wide-field microscopy, the specimen is evenly illuminated, so we can assume that the specimen is composed of “point cloud”, in which each molecule (point source) sheds its light onto the detector. Physically, each point has an infinitely small size, with a certain intensity and spatial coordinate, which can be described as $I_{\text{dot}}(x,y,z) = I_{\text{dot}} \cdot \delta(x,y,z)$. When such point passes through the objective, because of the border of the lens, the diffraction effect makes it no longer a dot, which has an infinitely small size, but with a fixed size of distribution. This distribution is often called the Airy pattern, to describe the shape of the imaged spot. It is also termed point spread function (PSF).

Now, the resolution is to resolve two close-by dots, at the detector. Naturally, the digitization process, or the CCD camera’s pixel size, can also influence the resolution, which is called digital resolution. Here to simplify the problem, we assume that the detector has very small pixel size. Of course, we will find that the PSFs of the two points may overlap, with different degrees related to their distance. As the objective magnifies the sample and the PSFs, we can discuss this in the sample plane, which is to project (shrink) the real PSFs back to each point which illuminates light.

Mathematically, this approach is called convolution, in which each point is replaced with a PSF, and then, we sum all the PSFs together. This type of image formation can be expressed as:

$$\begin{aligned} I(x,y,z) &= I_{\text{dot}} \cdot \delta(x,y,z) \otimes PSF \\ &= I_{\text{dot}} \cdot PSF(x,y,z). \end{aligned} \tag{23.1}$$

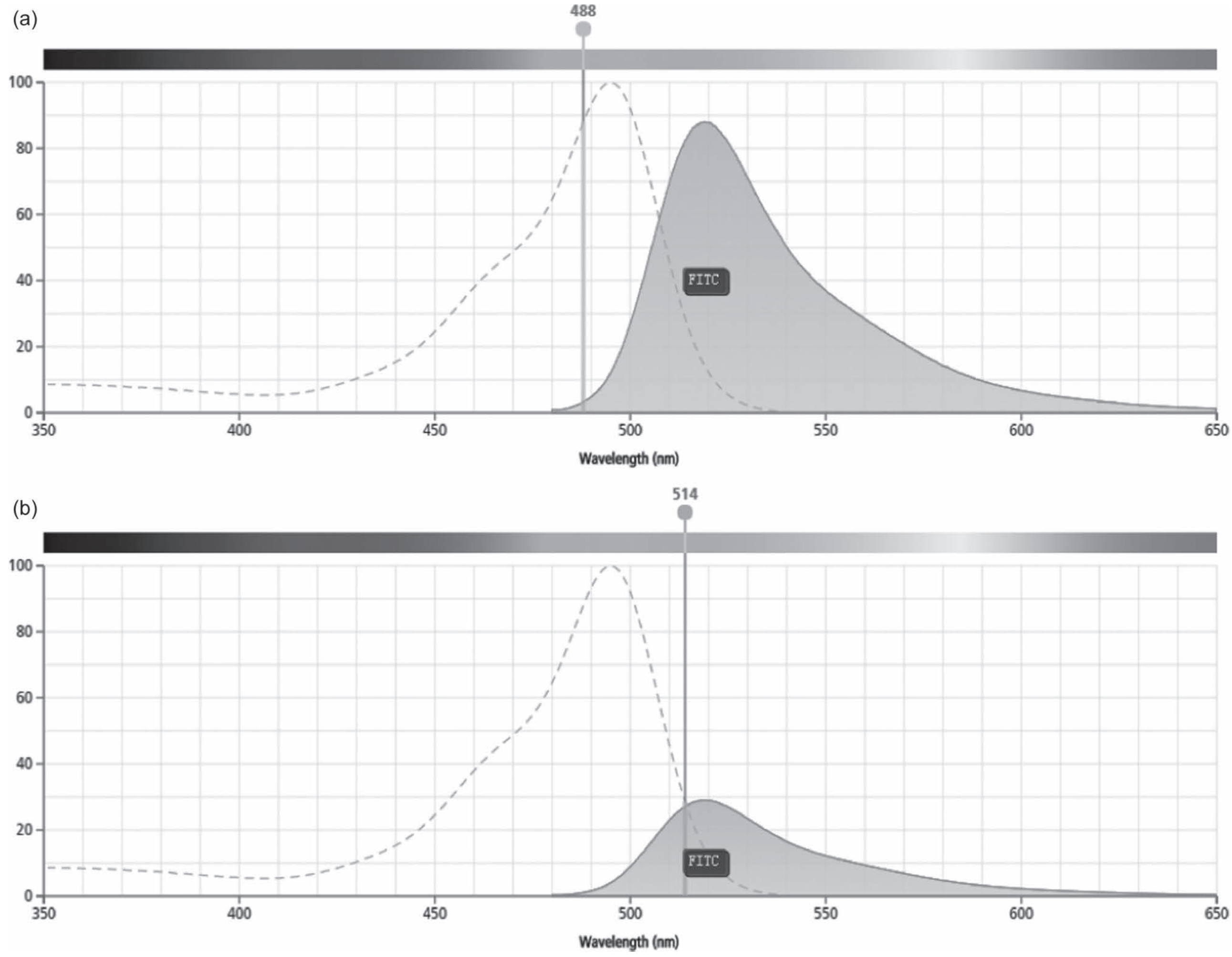

FIGURE 23.4 The absorption and emission spectra of FITC at (a) 488 nm excitation; (b) 514 nm excitation. (Adapted from BD Bioscience SpectrumViewer.)

The full-width-at-half-maximum of the PSF at the sample plane can be expressed as

$$d_{\text{FWHM}} = 0.5\frac{\lambda}{NA}, \tag{23.2}$$

in which the numerical aperture (NA) of the objective is defined as $NA = n\sin\alpha$, where n is the refraction index of the medium and α is the half-angle of the focusing cone angle.

In CLSM, the approach is very different. Now, the sample is being illuminated, and scanned, by a laser spot. Taking advantage of the high spatial coherence of laser, the excitation can be focused to a tight spot, determined by the wavelength and the lens's collection power only. The full-width-at-half-maximum of the focal spot size, or PSF, can be expressed as $d_{\text{FWHM}} = 0.5\frac{\lambda}{NA}$.

This type of image formation can be expressed as:

$$\begin{aligned} I(x,y,z) &= PSF \otimes I_{\text{dot}} \cdot \delta(x,y,z) \\ &= I_{\text{dot}} \cdot PSF(x,y,z), \end{aligned} \tag{23.3}$$

where the PSF results from the excitation. According to the commutative law, the image will be the same as the wide-field microscopy, if the confocal pinhole is large enough. Reducing the confocal pinhole can improve the resolution and brings optical sectioning capability.

23.2.4 Scattering and Absorption of the Specimen

In laser microscopy, the biological tissue can have a strong scattering and absorption capacity to the laser light. Because the tissue has different scattering and absorption coefficients, the 700–1300 nm is often regarded as biological window for the optimal penetration depth, if one wishes to image deep into the tissue [5]. And since the resolution is generally better at shorter wavelength, 600–800 nm lasers are often used (Figure 23.5).

Confocal microscopy can not only detect the fluorescence, but also detect the reflection [6]. On a tiny focal spot inside a biological specimen, the reflection signal is generated from the mismatch of the refractive index. For example, the refractive index for water is ~1.33, and for melanin,

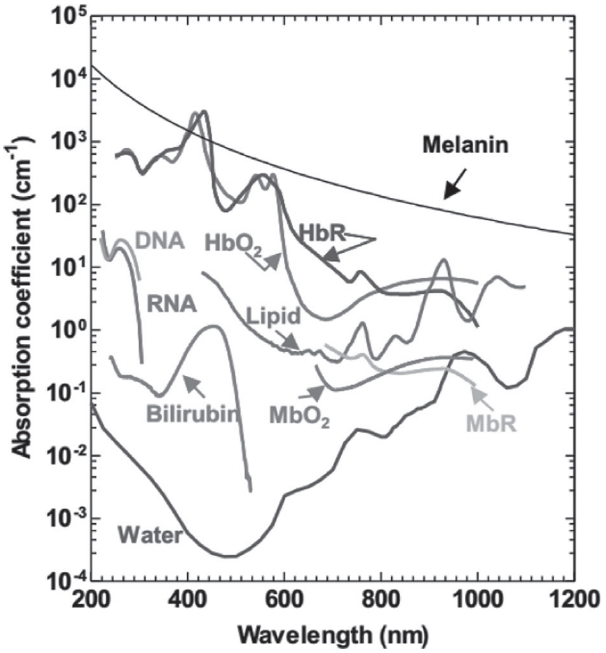

FIGURE 23.5 The absorption spectrum of major endogenous chromophores in biological tissue at normal concentrations. (Adapted from Ref. [5].)

it is 1.7. So the reflectivity can be calculated using the formula $R = \frac{n_0 - n_1}{n_0 + n_1}$. Hence, about 12% of the incident beam can be reflected. This technique has been applied in confocal dermatology and ophthalmology [7].

23.3 Advanced Techniques in Microscopy

23.3.1 Two-photon Excitation

In two-photon excitation (TPE) microscopy, the fluorescent molecules are excited with two photons simultaneously [8]. As shown in Figure 23.6, there is no middle-energy level for the electron to stay. Hence, the electron receiving the first photon stays at a "virtual state" with lifetime in attosecond level, until the second photon arrives and continues going up to S_1 level (Figure 23.6).

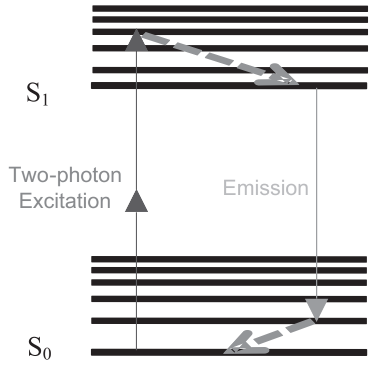

FIGURE 23.6 Jablonski diagram of two-photon excitation process.

Due to the quantum theory of electron orbit, the virtual state is forbidden so it has to be very short. This leads to two facts: (i) the two photons have to be coherent and synchronized and (ii) the cross section is very small. The unit of TPA cross section is Goeppert Mayer (GM), in memory of the woman scientist, Nobel laureate Maria Goeppert Mayer who predicted TPA in 1931. $1\text{GM} = 10^{-50}\,\text{cm}^4 \cdot \text{s} \cdot \text{photon}^{-1}$.

Because TPE requires high photon density for excitation, two factors are essential: (i) condensed photon in spatial domain, or using a high NA objective, and (ii) condensed photon in time domain, or using a pulsed laser.

The TPEF intensity can be calculated as [9]:

$$I_{\text{em}} \approx \frac{p_0^2 \delta}{\tau_p f_p^2}\left(\frac{NA^2}{2\hbar c \lambda}\right)^2, \tag{23.4}$$

where p_0: average incident intensity
δ: two-photon cross section
τ_p: pulse width
f_p: pulse repetition rate.

We can see that, as its name suggests, TPEF signal is proportional to the square of the average intensity. It is also inversely proportional to the pulse duration, which means that short pulse is preferred. However, due to the time-bandwidth product of an ultrashort pulse, the pulse can be largely chirped by the chromatic dispersion of the glass material of the microscope [10,11]. This has to be precompensated, so that one can get the optimal TPEF signal.

In TPEF microscopy, femtosecond laser is commonly used. Moreover, because the biological tissue cannot tolerate high peak power, usually the Ti:sapphire oscillator with an output of 500 mW, 100 MHz (5 nJ), and a pulse width of ~100 fs is sufficient for effective TPEF generation. Taking advantage of its wide tuning range, Ti:Sa becomes the most popular laser system in TPEF microscopy. Other pulsed lasers in this ballpark are also applicable for TPEF microscopy (Figure 23.7).

Although using pulses shorter than 100 fs can generate a stronger non-linear effect, in practice they are not widely used, because of the time-bandwidth product of non-linear pulses. For example, a 100 fs pulse has a spectral width of ~10 nm, but a 10 fs ultrashort pulse has a spectral width of 100 nm, which causes much larger dispersion if not corrected properly. After high-order dispersion adaptive correction, Xi et al. have demonstrated many advantages of using 10 fs ultrashort pulses in multiphoton microscopy [10,11].

23.3.2 Raman Microscopy

Different from fluorescence that requires extragenous fluorophores, Raman signal can reflect the vibration spectrum of a molecule itself; hence, it is called label-free imaging. Similar to Raman spectroscopy, all kinds of lasers can be used in Raman microscopy. As the Raman signal is generously very weak, the data acquisition time is much longer than that of fluorescence or reflective confocal microscopy. Figure 23.8 illustrates the Jablonski diagram of Raman scattering. Note that after interaction with the molecule, the frequency of Raman signal ω_s is generally shorter than the incident frequency ω_p,

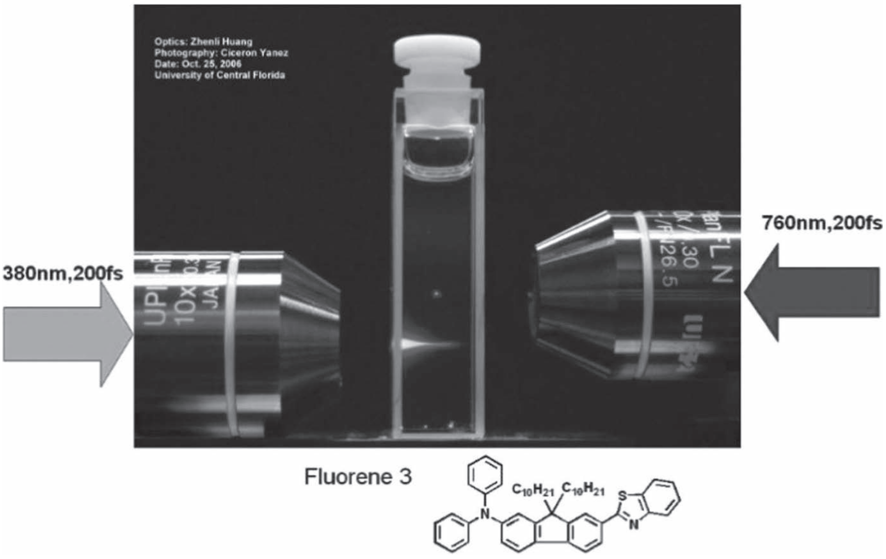
Optics: Zhenli Huang
Photography: Ciceron Yanez
Date: Oct. 25, 2006
University of Central Florida
380nm,200fs
760nm,200fs
Fluorene 3
$C_{10}H_{21}$ $C_{10}H_{21}$

FIGURE 23.7 Comparison of the fluorescence emission of fullerene 3 with the single-photon excitation (left) at 380 nm, and two-photon excitation (right) at 760 nm. Image courtesy Prof. Zhenli Huang.

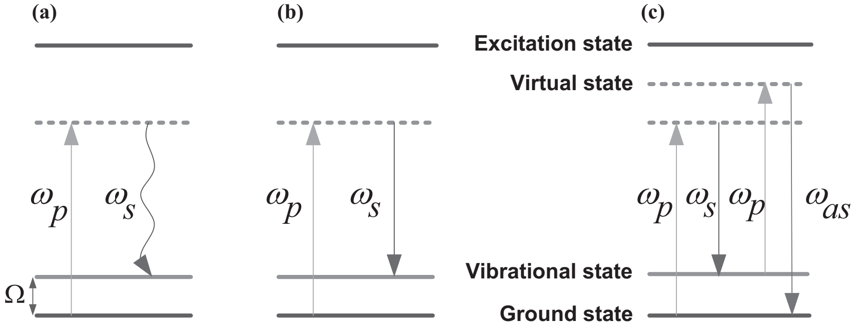

FIGURE 23.8 Jablonski diagrams of (a) Raman scattering, (b) SRS, and (c) CARS.

and the energy loss $\Omega = \omega_p - \omega_s$ reflects the vibration of the molecule. The frequency of Ω is at the infrared region. For this reason, Raman spectrum is often complementary to the infrared absorption spectrum.

In practice, the lasers used in Raman scattering or Raman microscopy should have a very narrow frequency spectrum; otherwise, the Raman spectral width will be expanded. When choosing a Raman laser, two rules should be considered: (i) just like Rayleigh scattering, Raman scattering signal is also inversely proportional to λ^4; therefore, the shorter the wavelength, the stronger the Raman scattering, and (ii) the shorter wavelength incidence may also excite the autofluorescence signal of the specimen. Because fluorescence signal is much stronger than Raman scattering, this factor should be considered; otherwise, the Raman signal can be buried.

23.3.3 Coherent Anti-Stokes Raman Scattering (CARS) and Stimulated Raman Scattering (SRS) Microscopy

Because Raman signal is generally very weak, it is very challenging or time-consuming to apply Raman to microscopy imaging. Yet, as fluorescent labelling may interrupt the biological system, it is often desired to image the specimen at its native state. CARS and SRS are two kinds of imaging techniques to boost the Raman signal for imaging without extrinsic labelling introduced [12].

In Raman process, the pump laser will excite the electron to a virtual energy level (Figure 23.8a). When the electron returns to the ground level, because of the vibration of the molecule, there exist multiple sublevels. This corresponds to the peaks at the Raman spectrum.

In SRS, a second laser is employed, which has the same wavelength as one of the Raman peak of interest. Then, the stimulated emission can enhance the Raman process at this energy level (Figure 23.8b). This enhanced Raman signal can report the concentration of the molecule. Combining this process with CLSM, one can obtain an SRS image of the sample.

In CARS, two pulsed lasers are employed: the pump laser and the Stokes laser. The two lasers are synchronized picosecond lasers. When the resonant frequency meets the difference between the pump laser and the Stokes laser, the vibrational state can be populated (Figure 23.8c); it is then further pumped by the pump laser to a higher energy level, resulting in the great enhancement of the anti-Stokes signal. CARS is also referred to as a four-wave-mixing process.

The most commonly used laser system for CARS and SRS is picosecond Nd:YVO_4 or Ti:sapphire oscillator as Stokes beam, and optical parameter oscillator (OPO) is pumped by the same pump laser to generate the Raman pump beam, so that the pump and Stokes beams are synchronized. Taking advantage of the wavelength tunability of the OPO, different components of the specimen can be imaged.

23.3.4 Super-resolution Microscopy

23.3.4.1 Stimulated Emission Depletion (STED)

As described in confocal fluorescence microscopy, the resolution is determined by the PSF size of excitation, which forms an Airy pattern at the specimen. Naturally, if one can shrink the size of the Airy pattern, then super-resolution breaking the diffraction barrier can be obtained [13].

Because of its efficient photon conversion capability, fluorescence is also the fundamental of laser material: before lasing, the laser has to fluoresce first. As fluorescence is a spontaneous emission, it has a broad emission spectrum. Then, through continual popping the electron to upper state, one can maintain a situation that there are always electrons at higher energy level, which is called population inversion. At this point, if a photon with energy $h\nu = E_1 - E_0$ is presented, then stimulated emission can happen, which generates an identical photon. This means that its energy (spectrum), polarization, propagation direction, and phase are all identical.

With this, we can actually modulate the PSF of fluorescence emission (spontaneous emission) with stimulated emission. For example, if one can generate a "donut" PSF with wavelength matching the stimulated emission, then with sufficient intensity, the donut area will be forced to generate stimulated emission (Figure 23.9).

Now, with a simple dichroic filter, we can block the stimulated emission from spontaneous emission. Or we can "switch off" the fluorescence with stimulated emission. Consequently, the spontaneous emission can be suppressed, resulting in a narrower PSF, or super-resolution.

In STED, the excitation laser is the same as a confocal fluorescent microscope. But because STED employs stimulated emission to supress the spontaneous emission, the laser for STED process has to be of high intensity, which means that it is either pulsed or high-power CW laser. In practice, this laser should be chosen at the tail of the emission, far from the excitation cut-off, to minimize the "re-excitation" process.

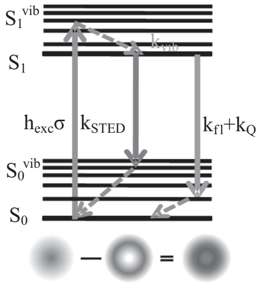

FIGURE 23.9 Diagram of the STED process: an organic fluorophore is first excited by a Gaussian PSF; then, a donut STED beam is applied, so that the fluorescence is depleted from the S_1 energy level.

23.3.4.2 Single-molecule Localization Microscopy (SMLM)

As described earlier, the imaging process is a group of points convolutes a PSF. Therefore, when the size of the PSF is large, two close-by points cannot be discerned. In STED, the fluorescence (spontaneous emission) PSF is modulated/suppressed with a strong "donut" EM field, so that the PSF is narrowed.

SMLM techniques such as photoactivated localization microscopy (PALM)/stochastic optical reconstruction microscopy (STORM) take a different approach. Instead of modulating the PSF, SMLM approach employs photochemical reactions to modulate the On/Off of the fluorescent molecules. Firstly, most of the fluorophores are switched "off", and only very scattered molecules are at "On" state. Because these molecules are randomly distributed, one can safely assume that there is at most one molecule at "On" state within one focal spot. Then, one can find the location of this molecule accurately. These molecules can be switched off afterwards. Next, through photoactivation/photon conversion/photoswitching processes, a new batch of molecules can be switched on for localization. After a certain iterations, a sufficient number of fluorophores can be localized to obtain the super-resolution image [14].

In SMLM, the key is to design the molecule that attributes a long Off state, so that the single-molecule state can be easily obtained; the molecule should be photoswitchable through light. Because it is often employed at the wide field, a stronger (100–200 mW) CW laser is often required.

23.4 Conclusion and Discussion

In Chapter 22, we have learnt that the laser is generally categorized by its gain medium, and it can provide discrete and narrow wavelength, high power, and excellent coherency. These features make it ideal for applications in optical microscopy.

The fluorescence is a very important branch in optical microscopy in life science, because we can label the transparent subcellular organelle with the fluorophores. The excitation process of a fluorophore is exactly the same as the laser: the electron gets energy and jumps to upper energy level, and it then releases the energy as a photon and returns to the ground level. This is a typical spontaneous emission process, which emits a relatively broad spectrum. Of course, in laser, we then add laser cavity to amplify one certain wavelength; thus, the stimulated emission overwhelms the spontaneous ones. This process has been used in STED (Chapter 3.5.1).

When choosing laser for optical microscopy, the wavelength and power are the first two parameters to be considered. And since laser is only the light source of an entire microscopic system, its size, cost, and stability are also the important

TABLE 23.1

List of the Typical Lasers Used in Microscopy

Type	Wavelength (nm)	Output Power level	Mode	Application
Diode-pumped solid-state (DPSS)	355, 405, 445, 473, 488, 515, 532, 553, 561, 633, 638, 647, 660	50–200 mW	CW	WF, confocal, SMLM
Laser diode	405	mW	CW	WF, confocal, SMLM
Argon	488,514	10 mW	CW	WF, confocal
Nd:YAG	532 (frequency doubled)	10 mW	CW	WF, confocal
DPSS	561	10 mW	CW	WF, confocal
HeNe	543, 594, 633	10 mW	CW	WF, confocal, STED
Ti:sapphire	680–1030	500 mW	Pulsed/femto-second	Two-photon
Ti:sapphire	680–1030	500 mW	Pulsed/pico-second	CARS, SRS, STED
Ti:sapphire	720–780 nm	W	CW	STED
Nd:YVO4	1064 nm/532 nm	W	Pulsed/pico-second	CARS, SRS
OPO	660–960 nm	W	Pulsed/pico-second	CARS, SRS, STED
Laser diode	800 nm	10 mW	CW	Reflective confocal
White-light laser	400–2000 nm		Pulsed/MHz level tunable	
Rare earth element-doped fibre lasers	1040 nm (Yb-doped) 1550 nm (Er-doped) 2000 nm (thulium-doped)	10 mW ~ 10 W	CW Pulsed/MHz~KHz Picosecond/femtosecond	CARS, SRS, SHG, STED, THG, multiphoton fluorescence

factors for choosing a proper laser in microscopy. In addition, the spatial mode of a laser (the M^2) describes the focal spot size, which is very important in laser scanning microscopy. Table 23.1 lists the typical lasers used in optical microscopy. It is for reference only and by no means an exhaustive one. With the constant development of both laser and microscopic techniques, we anticipate that laser will play more and more roles in microscopy.

REFERENCES

1. Zuylen, J.V., The microscopes of Antoni van Leeuwenhoek. *Journal of Microscopy*, 1981. 121(3): pp. 309–328.
2. Gest, H., The discovery of microorganisms by Robert Hooke and Antoni Van Leeuwenhoek, fellows of the Royal Society. *Notes and Records*, 2004. 58(2): pp. 187–201.
3. Pawley, J., *Handbook of Biological Confocal Microscopy*. 2nd edition. 1995, New York: Plenum Press.
4. Xi, P., et al., The design and construction of a cost-efficient confocal laser scanning microscope. *American Journal of Physics*, 2007. 75: pp. 203–207.
5. Yao, J. and L.V. Wang, Sensitivity of photoacoustic microscopy. *Photoacoustics*, 2014. 2(2): pp. 87–101.
6. Langley, R.G., et al., Confocal scanning laser microscopy of benign and malignant melanocytic skin lesions in vivo. *Journal of the American Academy of Dermatology*, 2001. 45(3): pp. 365–376.
7. Chen, W.L., et al., Combination of multiphoton and reflective confocal imaging of cornea. *Microscopy Research and Technique*, 2008. 71(2): pp. 83–85.
8. Zipfel, W.R., R.M. Williams, and W.W. Webb, Nonlinear magic: Multiphoton microscopy in the biosciences. *Nature Biotechnology*, 2003. 21(11): pp. 1369.
9. Denk, W., J.H. Strickler, and W.W. Webb, Two-photon laser scanning fluorescence microscopy. *Science*, 1990. 248(4951): pp. 73–76.
10. Xi, P., et al., Two-photon imaging using adaptive phase compensated ultrashort laser pulses. *Journal of Biomedical Optics*, 2009. 14(1): p. 014002.
11. Xi, P., et al., Greater signal, increased depth, and less photobleaching in two-photon microscopy with 10 fs pulses. *Optics Communications*, 2008. 281(7): pp. 1841–1849.
12. Folick, A., W. Min, and M.C. Wang, Label-free imaging of lipid dynamics using Coherent Anti-stokes Raman Scattering (CARS) and Stimulated Raman Scattering (SRS) microscopy. *Current Opinion in Genetics & Development*, 2011. 21(5): p. 585–590.
13. Hell, S.W., Toward fluorescence nanoscopy. *Nature Biotechnology*, 2003. 21(11): pp. 1347–1355.
14. Huang, B., H. Babcock, and X. Zhuang, Breaking the diffraction barrier: Super-resolution imaging of cells. *Cell*, 2010. 143(7): pp. 1047–1058.

24

Laser-based Coherent Diffractive Imaging

Garth J. Williams

CONTENTS

24.1 Introduction 299
24.2 Methods 299
  24.2.1 Plane-Wave CDI 301
  24.2.2 Fresnel CDI 301
  24.2.3 Ptychography 301
24.3 Algorithms 302
  24.3.1 Error Reduction 302
  24.3.2 HIO 303
  24.3.3 Projector Notation 303
24.4 Applications 303
24.5 Perspective 304
References 304

24.1 Introduction

Coherent diffractive imaging (CDI) is a kind of microscopy, originally developed to circumvent the limitations of traditional imaging optics, i.e., lenses. Alternately referred to in the literature as "coherent diffraction imaging" or "coherent diffraction microscopy," CDI provides images from the intensity measurement of a field scattered by a sample. CDI originated from an information theoretical question: can the phase of a field be retrieved from an adequately sampled measurement of its intensity? [1] As such, the image recovery in CDI is an ill-posed inverse problem whose solution is normally found through the application of an iterative algorithm. Phase information is particularly powerful in microscopy. In X-ray crystallography, phase is integral to the determination of structure and can reveal lattice deformation, i.e., strain. In microscopy, the phase contrast channel provides invaluable information concerning weakly scattering components of the sample. Here, CDI is capable of providing a unique insight: the complex amplitude of the wave emerging from a sample of interest can be manipulated to display contrast in ways that an intensity-only measurement cannot.

It was in the field of microscopy that CDI first found an experimental application. The original implementation of modern CDI – see, for example, Miao et al. [2] and Robinson et al. [3] – illuminated a sample of interest with a highly coherent, nearly planar X-ray field, in these cases provided by a synchrotron source. The normal coherence requirements for the illumination are set out in Spence et al. [4]. The resulting diffraction was measured in the far-field of the sample, and this signal was sampled above the Nyquist frequency. The far-field signal was assumed to be band-limited: i.e., the diffracting object was of finite extent. The sequential application of these constraints – the measured intensity was used as the magnitude of the field in the far-field and the known, finite extent of the sample was used as a "support" constraint in the exit plane of the sample – to an estimate of the field emerging from the sample in an iterative algorithm provides the complex field as it emerges from the exit surface of the sample. This exit-surface field can then be used to calculate an intensity or phase contrast image of the sample. A 3D image can be developed by borrowing tomographic imaging techniques [5].

There are three fundamental assumptions made in a typical CDI application that: the scattering process obeys the first Born approximation – i.e., the once-diffracted field does not further interact with the sample; the propagation to the detector occurs within the paraxial approximation; and the illuminating field does not appreciably change under propagation through the sample. It is important to note that any of these assumptions can be contravened when the underlying physics is well understood or when sufficient prior knowledge exists to solve the additional inverse problem.

Below, we will briefly review a selection of CDI experimental geometries, present the algorithms used to find a solution to the CDI inverse problem, and present a few representative results that highlight the benefit of laser-like illumination in CDI.

24.2 Methods

To fully understand the range of applicability and the potential of CDI, it is valuable to consider the propagation of a monochromatic field. Without a significant loss of generality, we will treat the illumination as being composed of photons. We assume a monochromatic field of wavelength $\lambda, \psi(\mathbf{r}_n, z_n)$, where z denotes the direction of propagation and $\mathbf{r}_n$ is a 2D vector in the plane at z_n. Under the paraxial approximation, the propagation of this field from a plane at z_n to one at z_m is given by

$$\begin{aligned}\psi(\mathbf{r}_n, z_m) &= \frac{-i}{\lambda z_{nm}} \exp\left(\frac{i2\pi z_{nm}}{\lambda}\right) \exp\left(\frac{i\pi r_m^2}{\lambda z_{nm}}\right) \\ &\quad \times \int d\mathbf{r}_n \psi(r_n, z_n) \exp\left(\frac{i\pi r_n^2}{\lambda z_{nm}}\right) \exp\left(\frac{-2\pi i \mathbf{r}_n \cdot \mathbf{r}_m}{\lambda z_{nm}}\right) \\ &= \Theta(\mathbf{r}_m, z_n m) \times \widehat{f}\left[\Xi(\mathbf{r}_n, z_{nm}) \psi(\mathbf{r}_n, z_n)\right] \end{aligned} \tag{24.1}$$

where we have introduced $\Theta(\mathbf{r}_m, z_n m)$ the prefactor term outside of the integral; $\Xi(\mathbf{r}_n, z_{nm})$, the spherical phase term inside the integral; and the operator $\widehat{f}$, representing the Fourier transform. We will be principally concerned with three planes: the entrance surface plane of the sample at z_e, the exit-surface plane of the sample at z_s, and the detector plane at z_d. Further, we will denote the distance between two planes with double subscripts, for example, the distance $\|z_s - z_d\| = z_{sd}$. The inverse problem of CDI is therefore the recovery of the complex-valued exit-surface wave $\psi(\mathbf{r}_s, z_s)$ from the measurement of the diffracted intensity

$$I(\mathbf{r}_d, z_d) = \psi(\mathbf{r}_d, z_d) \psi^*(\mathbf{r}_d, z_d) \tag{24.2}$$

where $\psi^*(.)$ is the complex conjugate of $\psi(.)$.

What then is the relationship between $\psi(\mathbf{r}_s, z_s)$ and the properties of the sample? Mathematically, it is generally assumed that the projection approximation holds; in other words, it is assumed that the thickness of the sample $\tau(\mathbf{r}_s)$ is negligible (for the purposes of the propagation integral, $z_e = z_s$). The thickness must then satisfy

$$\tau(\mathbf{r}_s) \ll \frac{2}{k\theta_{\max}^2} = \frac{4\delta^2}{\pi\lambda} \tag{24.3}$$

where $\theta_{\max}$ is the largest angle to which a significant scattering can be measured, k is the wavenumber, and δ is the length scale of the smallest resolvable detail in the CDI-provided image. The relationship between the complex-valued exit-surface waves is generally expressed within the projection approximation, which asserts that there is a linear relationship between the illumination and the sample surface exit plane:

$$\psi(\mathbf{r}_s, z_s) = T(\mathbf{r}_s, z_s) \times \psi(\mathbf{r}_e, z_s) \tag{24.4}$$

The transfer function $T(\mathbf{r})$ is related to the index of refraction by

$$T(\mathbf{r}) = \exp\left[\frac{i2\pi}{\lambda} \int_{\text{sample}} dz n(\mathbf{r}, z)\right] \tag{24.5}$$

$$\simeq \exp\left[\frac{i2\pi}{\lambda} n(\mathbf{r}) \tau(\mathbf{r})\right] \qquad \text{for visible light, or} \tag{24.6}$$

$$\simeq \exp\left\{\frac{i2\pi}{\lambda} [1 - \delta(\mathbf{r}) + i\beta(\mathbf{r})] \tau(\mathbf{r})\right\} \qquad \text{for } X\text{-rays.} \tag{24.7}$$

In this way, many 2D measurements may be combined to recover a 3D index of refraction map using tomographic reconstruction techniques.

In planning a CDI experiment, the field of view, the resolution of the resulting images, and the experimental parameters are, to a good approximation (the approximation in question is that the maximal scattering angle is $\theta_{\max} \simeq \tan(\theta_{\max})$), related by the properties of the discrete Fourier transform. The relevant quantities are as follows:

$D_{x,y}$	the linear dimension of the detector
$d_{x,y}$	the pixel pitch of the detector
$N_{x,y}$	the linear number of pixels
σ	the sample size
z_{sd}	the distance between the exit surface and the detector
λ	the wavelength of the illumination
δ	the desired image resolution.

Typically, the properties of the detection apparatus are fixed and the experiment design relates to the choice of wavelength and detector distance for a sample of a given extent and the desired image resolution. An upper bound on the size of the sample can be acquired by means of traditional microscopy when needed.

In calculating the sampling requirement, we recall that Equation (24.2) represents the physical observable that is relevant to the CDI inverse problem. Applying the Fourier convolution theorem to Equation (24.2), we note that the Fourier transform of the intensity is the autocorrelation of our image-forming quantity $\psi(\mathbf{r}_s, z_s)$. As a result, the Nyquist rate of the diffracted intensity is twice that of the desired exit-surface wave. A critical sampling of the intensity is equivalent to a sampling rate that is twice as fine as

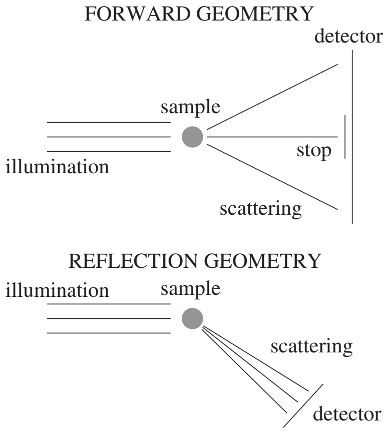

FIGURE 24.1 Schematic of the most common CDI scattering geometries. The forward-scattering, small-angle case is depicted above: a plane-wave illumination is incident upon a sample of interest, and the intensity of the diffracted illumination is collected on a detector far away, while a beam stop blocks the incident illumination from overpowering the detector. Below, the reflection geometry shares the illumination condition, but the scattered intensity is measured from a reflection and no beam stop is required to block the illumination.

would be required were we be able to measure the complex field in the detector plane. This is often referred to as "oversampling" in the literature. Confusingly, CDI experiments are often designed to sample the intensity at a rate higher than the Nyquist rate to accommodate detector deficiencies; hence, care must be taken when studying the literature. The rule-of-thumb for determining $\lambda$and $z_{sd}$is

$$\lambda z_{sd} = 2\sigma D \tag{24.8}$$

The pixel resolution of the image determined by CDI is

$$\delta = \frac{\lambda z_{sd}}{D}. \tag{24.9}$$

However, the image resolution may be less than this value, depending on the scattering strength and contrast within the sample.

24.2.1 Plane-Wave CDI

In traditional CDI implementations, the incoming illumination is assumed to be planar and the detector is in the far-field, giving $\Xi(\mathbf{r}_n, z_{nm}) = 1$, and reducing the propagation, in practice, to a computationally inexpensive fast Fourier transform routine.24 The two original CDI experimental geometries are sketched in In Figure 24.1. Figure 24.1 (top) shows the small-angle forward-scattering experiment that is most similar to conventional microscopy. A carefully prepared, coherent illumination is incident upon a sample. The intensity of the diffracted field is measured a long distance away. In this experiment, the best possible image resolution is given by the numerical aperture of the detection apparatus and the wavelength of the probing radiation.

When conducting CDI experiments in a reflection – both Bragg and Laue – geometry (we will call this Bragg CDI for clarity and it is sketched in Fig. 1(bottom)), the recovered diffraction plane complex amplitude is related to the sample by

$$\psi(r_s, z_s) \simeq \rho(\mathbf{r}_s)\exp\left(i\mathbf{q}_{hkl}\cdot\mathbf{u}(\mathbf{r})\right) \tag{24.10}$$

where $\rho(\mathbf{r}_s)$ is proportional to the electron density of the sample, $\mathbf{q}_{hkl}$ is the momentum transfer associated with the reflection (hkl), and $\mathbf{u}(\mathbf{r})$ is the displacement of the lattice within the sample. The quantity $\mathbf{u}(\mathbf{r})$ is often referred to as "the deformation field" within the sample and is related to the strain by the Young's modulus of the material.

In either case, a 3D image is acquired by discretely rotating the sample and collecting 2D images at each step. To understand this, consider the Ewald construction as shown in Figure 24.2. In case of low-angle, forward-scattering CDI, the intensity distribution measured is centred around $\mathbf{q}_{000}$, and one must rotate the sample by 180° to sample the entire distribution. To sample the distribution around any other $\mathbf{q}_{hkl}$, one must measure a smaller total angular range with smaller steps. Similarly, the exit-surface wave in Bragg CDI can be written in analogy to Equation (24.4) as:

$$\psi(\mathbf{r}_s, z_s) = \int_{\text{sample}} d\mathbf{k}n(\mathbf{r},z)s(\mathbf{r},z)\exp\left[i\mathbf{q}_{hkl}\cdot\mathbf{u}(\mathbf{r})\right]\times\psi(\mathbf{r}_e, z_s) \tag{24.11}$$

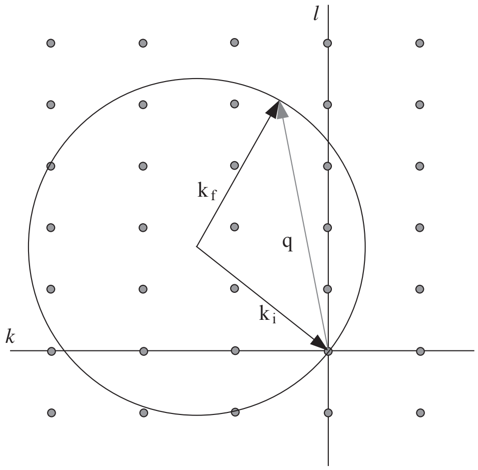

FIGURE 24.2 A demonstration of the Ewald construction on a hypothetical 2D simple cubic lattice with reciprocal axes (*kl*). $\mathbf{k_i}$ indicates the incident beam direction, while $\mathbf{k_f}$ is the scattering beam direction and $\mathbf{q}$ is the momentum transfer. A reflection is excited when the sphere intersects its representation, the blue spheres. A 3D data set is collected by rocking the sphere, i.e., changing $\mathbf{k_i}$, through a reflection. In the case of forward-scattering CDI, $\mathbf{k_i}$ and $\mathbf{k_f}$ point in the same direction and the sample must be rotated by 180°.

where the integral through the sample follows the trajectory of each ray, and we have substituted $n(\mathbf{r},z)s(\mathbf{r},z)$ for the electron density in Equation (24.10). Here, we can see explicitly that the small-angle, forward-scattering geometry is a special case where $\|\mathbf{q}_{hkl}\| = 0$ and the measurement is insensitive to strain within the sample.

In practice, plane-wave CDI experiments are conducted on isolated samples to fulfil the underlying assumptions of a band-limited diffraction signal. Two notable variations, whose development was largely motivated by expanding the applicability of CDI beyond isolated samples, will be discussed in the following sections.

24.2.2 Fresnel CDI

Fresnel CDI differs from plane-wave CDI in that the diffraction pattern measured is no longer assumed to be Fraunhofer diffraction ($\Xi(.)$ in Equation (24.1) differs from unity). By illuminating the sample with a diverging beam, Fresnel CDI substitutes the finite extent of the probing beam on a large sample for the requirement of an isolated sample. Additionally, the presence of a known, non-trivial phase in the illuminating beam is beneficial for the convergence behaviour of the algorithms discussed below [6]. In Fresnel CDI, it is necessary to separate the probe, i.e., illumination function, from the transfer function before imposing constraints on the exit-surface wave, which is accomplished by means of the reconstruction of a "white-field" image taken with the same geometry as the Fresnel CDI measurement with the sample removed.

24.2.3 Ptychography

The traditional method is useful in overcoming the limitations of imperfect optics, which is often the case when imaging with X-rays. Visible-light CDI is most commonly used in a scanning geometry, where the method is often referred to as "ptychography" [7,8]. In particular, ptychography exploits the concept of "diversity" by solving the inverse problem using a 2D image at each scan point to ensure that a sufficient unique information is available in the data set to uniquely determine a solution. Generally, the scan step in ptychography is much smaller than the probing beam size, and the probe is reconstructed in parallel to the desired sample exit-surface wave. Ptychography requires a special reconstruction algorithm, called the ptychographic iterative engine [9]. Like Fresnel CDI, the transfer function and the probe function are separated in the reconstruction algorithm; however, unlike Fresnel CDI, the probe is recovered from the data set rather than from a separate measurement.

24.3 Algorithms

CDI relies on the solution of an ill-posed inverse problem. All current CDI implementations use one or several variations of a family of iterative algorithms. The traditional error reduction (ER) [10] and hybrid input/output (HIO) [11] algorithms are graphically displayed in Figures 24.3 and 24.4. These algorithms search a high-dimensional Hilbert space for a solution that is consistent with both the detector plane – sometimes called reciprocal-space, measurement – and the prior knowledge that we provide in the sample plane, the so-called real-space. When the algorithms converge, they provide the best estimate of the solution that can be determined with the data and prior knowledge that has been provided. See Marchesini [12] for a comprehensive review of CDI algorithms.

24.3.1 Error Reduction

Figure 24.3 is a graphical demonstration of the ER algorithm. The starting guess at the solution to a given CDI problem is $g_0(x)$, where x is a pixel in the computational array. The usual starting guess is a function that has unit amplitude over the domain of the object's support, i.e., its real-space extent, denoted S with randomly assigned phase values, creating a complex function to act as a trial exit-surface wave. The fast Fourier transform is used to propagate $g_k(x)$ to the detector plane, where it becomes $G_0(q)$. The measured amplitude data is applied to $G_0(q)$, preserving the phase of the complex object, but replacing its magnitude – the so-called Fourier modulus constraint. The new quantity $G'_0(q)$ is the new reciprocal-space estimate of the solution. This is propagated back to the exit-surface plane, where $g'_0(x)$ becomes the best estimate of the

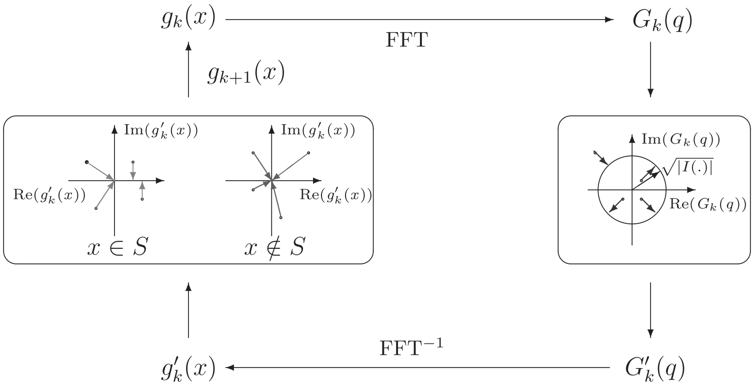

FIGURE 24.3 A graphical depiction of the error reduction algorithm. An iterate is propagated between the exit-surface plane of the sample and detector. In each plane, a constraint is applied to the iterate to establish convergence. In the exit sample plane, the amplitude of the exiting field is set to zero, while in the detector plane, the magnitude of the field is replaced by the measured one.

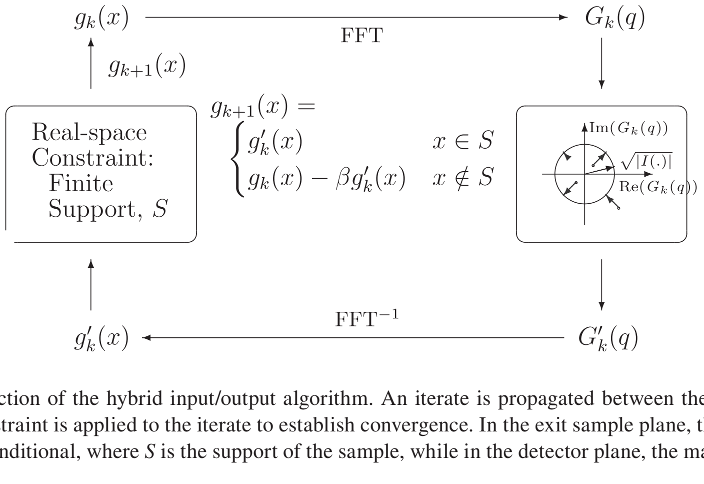
$g_k(x)$
FFT
$G_k(q)$
$g_{k+1}(x)$
Real-space Constraint: Finite Support, S
$g_{k+1}(x) = \begin{cases} g'_k(x) & x \in S \\ g_k(x) - \beta g'_k(x) & x \notin S \end{cases}$
$\mathrm{Im}(G_k(q))$
$\sqrt{|I(.)|}$
$\mathrm{Re}(G_k(q))$
FFT^{-1}
$g'_k(x)$
$G'_k(q)$

FIGURE 24.4 A graphical depiction of the hybrid input/output algorithm. An iterate is propagated between the exit-surface plane of the sample and detector. In each plane, a constraint is applied to the iterate to establish convergence. In the exit sample plane, the amplitude of the exiting field is modified according to the inset conditional, where S is the support of the sample, while in the detector plane, the magnitude of the field is replaced by the measured one.

solution to the exit-surface wave. The $k+1$th iterate is created by setting the values of all points outside of S to 0. This process is repeated until the algorithm converges. The error is estimated on the k iteration in the exit-surface plane by

$$E^2_{\mathrm{ESW},k} = \sum_{x=1}^{N} \left| gk+1(x) - g'_k(x) \right|^2 \tag{24.12}$$

and in the detector plane by

$$E^2_{\mathrm{det},k} = \sum_{q=1}^{N} \left| G_k(q) - G'_k(q) \right|^2 \tag{24.13}$$

ER is prone to stagnation at near-solutions to the CDI inverse problem. Often, this process will be repeated with different random starting guesses to ensure that all such estimates agree.

24.3.2 HIO

The HIO algorithm was developed to overcome the stagnation of ER. It does this by introducing a mixing between the iterate on the kth and $k+1$th iteration, with the contribution being weighed by a scalar β. Since the iterate $g_k(x)$ is not intended to have the form of the solution in HIO, the error is often evaluated by the total energy and the estimate that falls outside of the support constraint:

$$E^2_{\mathrm{HIO},k} = \sum_{x \notin S} \left| g'_k(x) \right|^2 \tag{24.14}$$

24.3.3 Projector Notation

Most recently, the iterative algorithms used for CDI have been expressed in a projector notation that helps to generalize the action of the various constraints upon the iterate [13]. We define the iterate to be $\rho_k = g_k(x)$. The Fourier modulus constraint is now $\pi_m = \widehat{\mathcal{F}}^{-1}\tilde{\pi}_m\widehat{\mathcal{F}}$, and the support constraint is π_s. One iteration of ER is now expressed by $\rho k+1 = (\pi_s\pi_m)\rho k$. Similarly, one application of HIO is $\rho k+1 = \left[1+(1+\beta)\pi_s\pi_m - \pi_s - \beta\pi_m\right]\rho k$.

24.4 Applications

Microscopy has been a widely applied enabling technique for the study of both hard and biological materials. The desire for ever-higher-resolution images of structure, which are used to deduce function, has driven the diversification of microscopy from visible light to its application with extreme ultraviolet light (EUV) and X-rays. As we have seen, the methods underlying CDI rely heavily upon providing a coherent illumination to the sample, although some variation from this condition is allowed. As we observed in Equation (24.9), the image resolution in a CDI system is limited by the wavelength of the probe and the angular acceptance of the detector. An additional benefit is that this method provides a complex wave as a solution to the imaging problem. When the interaction of the photons with the sample falls within the first Born approximation, the recovered exit-surface wave can be propagated "within" the sample, providing some degree of freedom from the depth-of-field limitations of traditional microscopy. This independence from the limitations of objective lenses can be an important strength in visible light, EUV, and X-ray microscopy.

An example of the application of CDI-related methods to optical microscopy can be found in the so-called Fourier ptychographic microscopy. Here, a low-numerical-aperture lens is combined with a novel illumination: one data frame is collected while each element of an array is used as an illuminator. This is, obviously, a variation of the ptychographic method [7] described above where the sample is moved under a fixed illumination. Such a data set can be treated, through iterative algorithms, to recover the complex field leaving the sample quantitatively at a resolution higher than that allowed by the numerical aperture of the lens alone [14]. This is particularly powerful for the imaging of biological systems. When this method is applied with laser illumination, it is possible to benefit from these improvements in a time-resolved measurement [15].

Because the resolution of a CDI system primarily depends on the wavelength of the radiation, its application with EUV light was one of the first practical demonstrations [16]. In that experiment, a high-harmonic generation (HHG) source was used to provide a coherent illumination to the sample at $\lambda = 29\,\mathrm{nm}$, with multilayer mirrors used to select only the desired harmonic. In a separate experiment, it was demonstrated that a larger bandwidth of the comb-like EUV spectrum from a HHG source could be accommodated [17,18] by treating each bandwidth element in parallel. Compared to visible microscopy, this application could provide images with resolution that is improved by more than an order of magnitude. For an overview of related developments, see Witte et al. [19].

CDI was first demonstrated and popularized as an X-ray imaging technique. Here, this method promises to overcome the strong limitations of X-ray lenses, which are famously difficult to manufacture due to the short wavelength of the radiation. Since its original demonstration [2], this method has been extended to image large samples [8,20], limited regions within large samples [21], and deformation of crystalline materials [3,22]. Although storage ring X-ray sources are very bright, they are not fully coherent and the plane-wave approximation is not entirely valid, thus leading to the extension of the technique to structured and partially coherent illumination [6,18,23]. In large part, the motivation for the latter enhancement is an attempt to compensate for the insufficient photon flux in the illumination at X-ray sources.

X-ray-free electron lasers (XFELs) [24] are advanced X-ray sources that generate coherent X-ray photons from a carefully prepared electron pulse. A pulse of electrons is ejected from a cathode and carefully shaped before being accelerated through a LINAC to several to tens of GeV. The electrons are subjected to a periodic magnetic structure and undergo a phenomenon referred to as "micro-bunching," wherein they behave as a macroparticle and coherently emit X-ray photons. X-ray pulses generated in this way are highly coherent and typically have a duration of tens of femtoseconds – characteristics that make them ideal for time-resolved and highly sensitive CDI experiments.

One of the original motivating science cases for the construction of XFELs was the possibility to image bioparticles through CDI. The scientific need derives from the difficulty in obtaining atomic-scale structural information from single molecules of interest for human health. A typical XFEL pulse is sufficiently powerful to destroy such a molecule during a single X-ray pulse, and they must be delivered to the X-ray beam as isolated samples, most often in an aerosol. Such experiments by Martin et al. [25], Ekeberg et al. [26], and Munke et al. [27] require a method like CDI, whose "dose efficiency" – the magnitude of the usable signal to the energy deposited – is limited by the scattering power of the sample and the efficiency of detection, which is very high for X-ray photons in the energy range of 1 to 15 keV. Likewise, a laser-like source is well suited to the problem due to the highly coherent and pulsed nature of the generated illumination. The extremely short pulse durations allow for significant scattering from the sample before its electron density is disturbed by the incident field. For materials that are not prone to radiation damage, for example, metals, the pulsed nature of an XFEL can be used to probe the dynamics of structure. For example, by exciting phonon modes in gold crystals with an optical laser, it is possible to use the pulsed XFEL radiation to map acoustic modes in crystalline materials [28,29].

24.5 Perspective

CDI is a powerful technique with particular strengths when applied to weakly scattering objects or in overcoming the limitations of available optics. The method provides an imaging channel with resolution limited, in principle, by the wavelength and scattering properties of the object under investigation. It requires a carefully prepared experiment and some prior knowledge concerning one's sample. Nevertheless, when combined with laser-like illumination, the strengths of this method are apparent: by providing a coherent illumination, CDI can deliver the complex wave exiting the sample and allow for sophisticated data analysis that can reveal, for example, phase contrast and structural deformation, and overcome the difficulties introduced into optical microscopy by the use of high-numerical-aperture lenses; a pulsed illumination allows CDI to reveal dynamics on timescales limited by the pulse duration and scattering power of the sample; and the combination of a short-pulse and coherent illumination can reveal "freeze-frame" images of weakly scattering systems like single molecules.

REFERENCES

1. D. Sayre. Some implications of a theorem due to Shan non. *Acta Crystallographica*, 5(6):843–843, November 1952. ISSN 0365-110X. doi:10.1107/S0365110X52002276. URL http://scripts.iucr.org/cgi-bin/paper?S0365110X52002276.
2. J. Miao, P. Charalambous, J. Kirz, and D. Sayre. Extending the methodology of X-ray crystallography to allow imaging of micrometer-sized non-crystalline specimens. *Nature*, 400(6742):342, 1999. doi:10.1038/22498. URL https://www.nature.com/articles/22498.
3. I. K. Robinson, I. A. Vartanyants, G. J. Williams, M. A. Pfeifer, and J. A. Pitney. Reconstruction of the shapes of gold nanocrystals using coherent X-ray diffraction. *Physical Review Letters*, 87(19), October 2001. ISSN 0031-9007, 1079-7114. doi:10.1103/PhysRevLett.87.195505. URL https://link.aps.org/doi/10.1103/PhysRevLett.87.195505.
4. J. C. H. Spence, U. Weierstall, and M. Howells. Coherence and sampling requirements for diffractive imaging. *Ultramicroscopy*, 101(2–4):149–152, November 2004. ISSN 03043991. doi:10.1016/j.ultramic.2004.05.005. URL http://linkinghub.elsevier.com/retrieve/pii/S0304399104000956.
5. H. N. Chapman, and K. A. Nugent. Coherent lensless X- ray imaging. *Nature Photonics*, 4:833, November 2010. URL https://doi.org/10.1038/nphoton.2010.240.
6. G. J. Williams, H. M. Quiney, B. B. Dhal, C. Q. Tran, K. A. Nugent, A. G. Peele, D. Paterson, and M. D. de Jonge. Fresnel coherent diffractive imaging. *Physical Review Letters*, 97(2), July 2006. ISSN 0031-9007, 1079-7114. doi:10.1103/PhysRevLett.97.025506. URL https://link.aps.org/doi/10.1103/PhysRevLett.97.025506.
7. H. M. L. Faulkner, and J. M. Rodenburg. Movable aperture lens- less transmission microscopy: A novel phase retrieval algorithm. *Physical Review Letters*, 93(2), July 2004. ISSN 0031-9007, 1079-7114. doi:10.1103/PhysRevLett.93.023903. URL https://link.aps.org/doi/10.1103/PhysRevLett.93.023903.
8. P. Thibault, M. Dierolf, A. Menzel, O. Bunk, C. David, and F. Pfeiffer. High-resolution scanning X-ray diffraction microscopy. *Science*, 321(5887):379–382, July 2008. ISSN 0036-8075, 1095-9203. doi:10.1126/science.1158573. URL http://www.sciencemag.org/cgi/doi/10.1126/science.1158573.
9. A. M. Maiden, and J. M. Rodenburg. An improved ptychographical phase retrieval algorithm for diffractive imaging. *Ultramicroscopy*, 109(10):1256–1262, September 2009. ISSN 03043991. doi:10.1016/j.ultramic.2009.05.012. URL https://linkinghub.elsevier.com/retrieve/pii/S0304399109001284.
10. J. R. Fienup. Reconstruction of an object from the modulus of its Fourier transform. *Optics Letters*, 3(1):27, July 1978. ISSN 0146-9592, 1539-4794. doi:10.1364/OL.3.000027. URL https://www.osapublishing.org/abstract.cfm?URI=ol-3-1-27.
11. J. R. Fienup. Phase retrieval algorithms: A comparison. *Applied Optics*, 21(15):2758, August 1982. ISSN 0003-6935, 1539-4522. doi:10.1364/AO.21.002758. URL https://www.osapublishing.org/abstract.cfm?URI=ao-21-15-2758.
12. S. Marchesini. Invited article: A unified evaluation of iterative projection algorithms for phase retrieval. *Review of Scientific Instruments*, 78(1):011301, January 2007. ISSN 0034-6748, 1089-7623. doi:10.1063/1.2403783. URL http://aip.scitation.org/doi/10.1063/1.2403783.
13. V. Elser. Phase retrieval by iterated projections. *Journal of the Optical Society of America*, 20(1):40–55, Jan 2003. doi:10.1364/JOSAA.20.000040. URL http://josaa.osa.org/abstract.cfm?URI=josaa-20-1-40.
14. X. Ou, R. Horstmeyer, C. Yang, and G. Zheng. Quantitative phase imaging via Fourier ptychographic microscopy. *Optics Letters*, 38(22):4845, November 2013. ISSN 0146-9592, 1539-4794. doi:10.1364/OL.38.004845. URL https://www.osapublishing.org/abstract.cfm?URI=ol-38-22-4845.

15. J. Chung, H. Lu, X. Ou, H. Zhou, and C. Yang. Wide-field Fourier ptychographic microscopy using laser illumination source. *Biomedical Optics Express*, 7(11):4787, November 2016. ISSN 2156-7085, 2156-7085. doi:10.1364/BOE.7.004787. URL https://www.osapublishing.org/abstract.cfm?URI=boe-7-11-4787.
16. R. L. Sandberg, A. Paul, D. A. Raymondson, S. Hädrich, D. M. Gaudiosi, J. Holtsnider, R. I. Tobey, O. Cohen, M. M. Murnane, H. C. Kapteyn, C. Song, J. Miao, Y. Liu, and F. Salmassi. Lensless diffractive imaging using tabletop coherent high-harmonic soft- X-ray beams. *Physical Review Letters*, 99(9), August 2007. ISSN 0031-9007, 1079-7114. doi:10.1103/PhysRevLett.99.098103. URL https://link.aps.org/doi/10.1103/PhysRevLett.99.098103.
17. B. Chen, R. A. Dilanian, S. Teichmann, B. Abbey, A. G. Peele, G. J. Williams, P. Hannaford, L. V. Dao, H. M. Quiney, and K. A. Nugent. Multiple wavelength diffractive imaging. *Physical Review A*, 79(2), February 2009. ISSN 1050-2947, 1094-1622. doi:10.1103/PhysRevA.79.023809. URL https://link.aps.org/doi/10.1103/PhysRevA.79.023809.
18. R. A. Dilanian, B. Chen, G. J. Williams, H. M. Quiney, K. A. Nugent, S. Teichmann, P. Hannaford, L. V. Dao, and A. G. Peele. Diffractive imaging using a polychromatic high-harmonic generation soft-x-ray source. *Journal of Applied Physics*, 106(2):023110, July 2009. ISSN 0021-8979, 1089-7550. doi:10.1063/1.3176976. URL http://aip.scitation.org/doi/10.1063/1.3176976.
19. S. Witte, V. T. Tenner, D. W. E. Noom, and K. S. E. Eikema. Lens-less diffractive imaging with ultra-broadband tabletop sources: from infrared to extreme-ultraviolet wavelengths. *Light: Science & Applications*, 3(3): e163–e163, March 2014. ISSN 2047-7538. doi:10.1038/lsa.2014.44. URL http://www.nature.com/articles/lsa201444.
20. D. J. Vine, G. J. Williams, B. Abbey, M. A. Pfeifer, J. N. Clark, M. D. de Jonge, I. McNulty, A. G. Peele, and K. A. Nugent. Ptychographic Fresnel coherent diffractive imaging. *Physical Review A*, 80(6), December 2009. ISSN 1050-2947, 1094-1622. doi:10.1103/PhysRevA.80.063823. URL https://link.aps.org/doi/10.1103/PhysRevA.80.063823.
21. B. Abbey, K. A. Nugent, G. J. Williams, J. N. Clark, A. G. Peele, M. A. Pfeifer, M. de Jonge, and I. McNulty. Keyhole coherent diffractive imaging. *Nature Physics*, 4(5):394–398, May 2008. ISSN 1745-2473, 1745-2481. doi:10.1038/nphys896. URL http://www.nature.com/doifinder/10.1038/nphys896.
22. M. C. Newton, S. J. Leake, R. Harder, and I. K. Robinson. Three-dimensional imaging of strain in a single ZnO nanorod. *Nature Materials*, 9(2): 120–124, February 2010. ISSN 1476-1122, 1476-4660. doi:10.1038/nmat2607. URL http://www.nature.com/doifinder/10.1038/nmat2607.
23. L. W. Whitehead, G. J. Williams, H. M. Quiney, D. J. Vine, R. A. Dilanian, S. Flewett, K. A. Nugent, A. G. Peele, E. Balaur, and I. McNulty. Diffractive imaging using partially coherent X-rays. *Physical Review Letters*, 103(24), December 2009. ISSN 0031-9007, 1079-7114. doi:10.1103/PhysRevLett.103.243902. URL https://link.aps.org/doi/10.1103/PhysRevLett.103.243902.
24. C. Bostedt, S. Boutet, D. M. Fritz, Z. Huang, H. J. Lee, H. T. Lemke, A. Robert, W. F. Schlotter, J. J. Turner, and G. J. Williams. Linac coherent light source: The first five years. *Reviews of Modern Physics*, 88(1):015007, March 2016. doi:10.1103/RevModPhys.88.015007. URL https://link.aps.org/doi/10.1103/RevModPhys.88.015007.
25. A. V. Martin, et al. Single particle imaging with soft x-rays at the linac coherent light source. In *Advances in X-ray Free-Electron Lasers: Radiation Schemes, X-ray Optics, and Instrumentation*, *Proceedings of the SPIE*, vol. 8078, p. 807809, 2011.
26. T. Ekeberg, M. Svenda, C. Abergel, F. R. N. C. Maia, V. Seltzer, J.-M. Claverie, M. Hantke, O. Jönsson, C. Nettelblad, G. van der Schot, M. Liang, D. P. DePonte, A. Barty, M. Marvin Seibert, B. Iwan, I. Andersson, N. Duane Loh, A. V. Martin, H. Chapman, C. Bostedt, J. D. Bozek, K. R. Ferguson, J. Krzywinski, S. W. Epp, D. Rolles, A. Rudenko, R. Hartmann, N. Kimmel, and J. Hajdu. Three-dimensional reconstruction of the giant mimivirus particle with an X-ray free-electron laser. *Physical Review Letters*, 114(9), March 2015. ISSN 0031-9007, 1079-7114. doi:10.1103/PhysRevLett.114.098102. URL https://link.aps.org/doi/10.1103/PhysRevLett.114.098102.
27. A. Munke, J. Andreasson, A. Aquila, S. Awel, K. Ayyer, A. Barty, R. J. Bean, P. Berntsen, J. Bielecki, S. Boutet, M. Bucher, H. N. Chapman, B. J. Daurer, H. DeMirci, V. Elser, P. Fromme, J. Hajdu, M. F. Hantke, A. Hi-gashiura, B. G. Hogue, A. Hosseinizadeh, Y. Kim, R. A. Kirian, H. K. N. Reddy, T.-Y. Lan, D. S. D. Larsson, H. Liu, N. Duane Loh, F. R. N. C. Maia, A. P. Mancuso, K. Mühlig, A. Nakagawa, D. Nam, G. Nelson, C. Nettelblad, K. Okamoto, A. Ourmazd, M. Rose, G. van der Schot, P. Schwander, M. Marvin Seibert, J. A. Sellberg, R. G. Sierra, C. Song, M. Svenda, N. Timneanu, I. A. Vartanyants, D. Westphal, M. O. Wiedorn, G. J. Williams, P. L. Xavier, C. H. Yoon, and J. Zook. Coherent diffraction of single Rice Dwarf virus particles using hard X-rays at the Linac Coherent Light Source. *Scientific Data*, 3, August 2016. ISSN 2052-4463. doi:10.1038/sdata.2016.64. URL http://www.ncbi.nlm.nih.gov/pmc/articles/PMC4968191/.
28. J. N. Clark, L. Beitra, G. Xiong, A. Higginbotham, D. M. Fritz, H. T. Lemke, D. Zhu, M. Chollet, G. J. Williams, M. Messerschmidt, B. Abbey, R. J. Harder, A. M. Korsunsky, J. S. Wark, and I. K. Robinson. Ultrafast three-dimensional imaging of lattice dynamics in individual gold nanocrystals. *Science*, 341(6141):56–59, July 2013. ISSN 0036-8075, 1095-9203. doi:10.1126/science.1236034. URL http://science.sciencemag.org/content/341/6141/56.
29. J. N. Clark, L. Beitra, G. Xiong, D. M. Fritz, H. T. Lemke, D. Zhu, M. Chollet, G. J. Williams, M. M. Messerschmidt, B. Abbey, R. J. Harder, A. M. Korsunsky, J. S. Wark, D. A. Reis, and I. K. Robinson. Imaging transient melting of a nanocrystal using an X-ray laser. *PNAS*, 112(24):7444–7448, June 2015. ISSN 0027-8424, 1091-6490. doi:10.1073/pnas.1417678112. URL http://www.pnas.org/content/112/24/7444.

Taylor & Francis
Taylor & Francis Group
http://taylorandfrancis.com

25

High-Speed Imaging

Adam Whybrew

CONTENTS

25.1 Properties of Laser Radiation Which Make It Useful for High-speed Imaging 307
  25.1.1 Short-duration Pulses 307
  25.1.2 Low Divergence....308
  25.1.3 Fibre Delivery....308
  25.1.4 Lightsheets....309
  25.1.5 Laser Speckle 309
  25.1.6 High-Brightness Imaging 309
25.2 High-speed Camera Technology....310
  25.2.1 High-speed Film....310
  25.2.2 Electronic Cameras 310
25.3 Choice of Laser 311
  25.3.1 Illumination Techniques....312
25.4 Application Examples 312
  25.4.1 Time-resolved PIV in Engines 312
  25.4.2 Agricultural Spray Characterization 312
  25.4.3 Drug Delivery Sprays....313
25.5 Summary....313
References....313
Further Reading 314

25.1 Properties of Laser Radiation Which Make It Useful for High-speed Imaging

The first high-speed movie was taken by William Henry Fox Talbot (1852) [1]. He showed that after photographing a rapidly rotating page of *The Times* newspaper illuminated by a short spark, the text was clear in the resulting negative. It was not obvious, when the laser was invented more than a century later [2], that this new technology might offer some new capabilities to the high-speed photographer. However, the fundamental properties of the laser which make it a useful tool for high-speed imaging were known then and are discussed in this chapter.

Most high-speed imaging is possible without lasers. For example, two of the most important industrial applications of high-speed imaging—machine vision and car crash testing—rarely employ laser illumination. Fuller [3,4] has reviewed conventional lighting techniques for high-speed imaging, and also touched on laser illumination. Fuller's review is found in an excellent introduction to the technology, techniques and applications of high-speed photography [5] in a book, which also includes a contribution from Errey [6] on the use of laser illumination. There have also been a series of high-speed photography conferences in San Diego, USA, covering a variety of topics both with and without laser illumination (see, e.g., [7]).

25.1.1 Short-duration Pulses

Lasers offer a fast but controllable way to extract energy rapidly from a storage medium. Pulse compression techniques can be used to squeeze the duration of a single pulse of laser light to a few femtoseconds.

The short duration of the laser pulses can be used to illuminate and so 'freeze' the motion of fast-moving objects in the camera image. The laser pulse duration required to freeze motion depends on the size of the object in question and its velocity. If we assume a characteristic linear dimension, d, and a speed, v, then the laser pulse should have a duration, t, short enough for the object to move less than 10% of its characteristic dimension during the pulse. The choice of 10% is arbitrary, but is sufficient blurring to degrade even qualitative measurements. In other words, we require that

$$t \leq \frac{d}{10v} \tag{25.1}$$

Therefore, the shortest pulses are required for the smallest and fastest objects. The smallest particles we can resolve optically are about 1 μm, and the fastest velocities available on Earth are about 10 km s^{-1}, suggesting that we require minimum laser pulse durations of around 10 ps. This means that

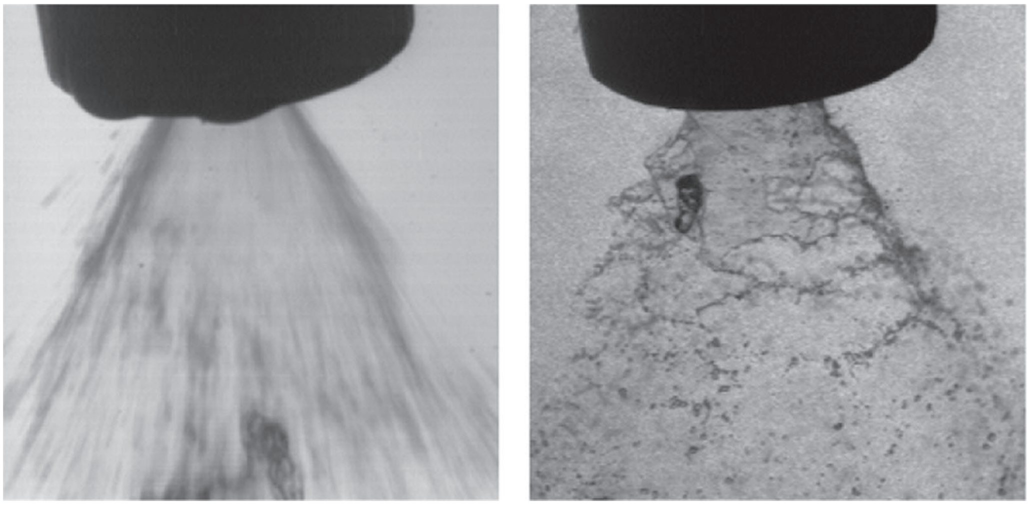

FIGURE 25.1 Effect of laser illumination to freeze motion. Both images are of an agricultural sprayer, taken at 4 500 frames per second. In the image on the left-hand side, continuous illumination is used, while for the image on the right-hand side, 25 ns pulses from a copper vapour laser have been used to freeze the motion. (Courtesy of Oxford Lasers.)

femtosecond lasers are never required for high-speed imaging, but this is an extreme example and, for the overwhelming majority of applications, laser pulses in the 1–1000 ns range are sufficient.

It is very important to realize that when using pulsed lasers with high-speed cameras, the duration of the flash from the laser determines the exposure time—the camera exposure time is not relevant. This is illustrated in Figure 25.1, which shows images of the same spray, taken by the same camera at the same speed, illuminated in one case by continuous lighting (direct current halogen lamp) and in the other case by 25 ns pulses from a copper vapour laser. From these images, it is clear that the laser-illuminated image is qualitatively better than the continuously illuminated one—notably because the short pulse duration has frozen the motion, revealing the continuous-sheet region of the spray, as well as the break-up region and the individual droplets.

25.1.2 Low Divergence

The low divergence of lasers can be useful for high-speed imaging if the light source must be situated far from the subject to be imaged (e.g. when imaging explosions). However, it is usually a secondary property of the low-divergence nature that is most useful—namely that a laser beam can be brought to a very tight focus. This lends itself to two experimental configurations: fibre beam delivery and lightsheets.

25.1.3 Fibre Delivery

Delivery of laser light through optical fibres can be extremely useful in order to illuminate inaccessible subjects [8]. For example, Rao et al. [9] used an optical fibre to deliver light in order to study combustion processes within a firing diesel engine cylinder. An illustration of their work is shown in Figure 25.2.

The most common approach to coupling light into optical fibres is to focus a beam onto the core of an optical fibre, after the beam has emerged from the laser cavity. There are conflicting considerations that influence the choice of fibre to be used, namely:

- The output of light from a well-scrambled multimode optical fibre is well described as a planar source of size equal to the core section at the output end of the fibre, and emitting into an angle equal to the acceptance angle of the fibre. If this light must be refocused (for example to form a lightsheet), then the smallest focus that can be achieved is typically around one half of the core diameter. Therefore, for a fine focus or a thin lightsheet, a narrow core is desirable.
- A laser focus is associated with a high fluence and peak intensity—indeed, this can be exploited to drill hard materials. However, for an efficient coupling into the fibre, the focus must be no larger than the fibre core, and so, to avoid damage to the fibre,

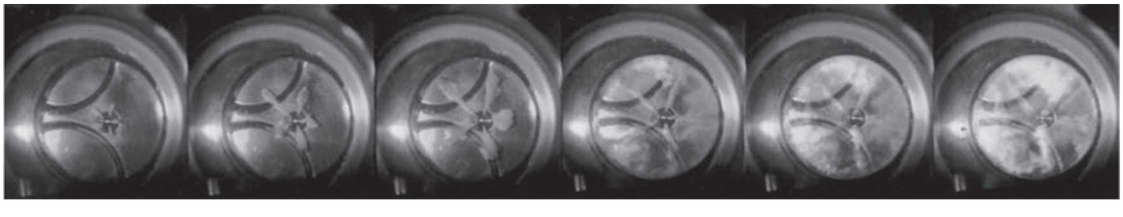

FIGURE 25.2 A sequence of stills from a high-speed movie of diesel fuel injection. Taken with a film camera and copper vapour laser illumination. (Courtesy of Koteswara Rao Kunkulagunta, FIE Technical specialist, Ford Motor Company, Dunton, UK.)

a large core is desirable. This means that the smallest fibres that can be used with high-power lasers have core diameters ranging from about 400 µm upwards, and 600–1000 µm is typical.

25.1.4 Lightsheets

A sheet of light can be formed from a laser by focusing the beam with astigmatic optics, such as cylindrical lenses [10]. Lightsheets are used to illuminate complex flow structures, e.g. in sprays, and are essential for the particle image velocimetry (PIV) technique. Sheet lighting is often the only way to simplify the structure of a turbulent flow sufficiently to gain insight into its behaviour. Generally, the thinner the lightsheet, the better the illumination. Figure 25.6 shows an example of lightsheet illumination—used to visualize the spray from a metered dose inhaler (MDI).

25.1.5 Laser Speckle

Lasers are well known for emitting light into a very narrow range of wavelengths, which gives rise to two considerations in high-speed imaging—laser speckle and high-brightness imaging. Laser speckle [11] is usually undesirable, introducing an intrusive random background into the image intensity, although it can be exploited in the electronic speckle pattern interferometry (ESPI) technique [12].

Speckle can be reduced by using fibre-optic light delivery (which scrambles the spatial coherence of the beam) and by using two or more spatially separated diffusers [13]. Speckle is exacerbated by narrow wavelength distribution and the use of small apertures in imaging lenses. The use of small apertures in imaging lenses is often unavoidable but the wavelength distribution can be broadened (and speckle avoided) by judicious choice of laser (e.g. a diode laser, as used by Murphy in Ref. [14]) or by using the laser to illuminate a fluorescent material which re-emits over a broad spectrum, provided that it does not lase [15].

25.1.6 High-Brightness Imaging

It is often desirable to apply high-speed imaging techniques to bright (incandescent) subjects. For example, type approval of novel aircraft jet engines requires a blade-off test in which one of the turbine blades is explosively fractured from a running engine. The manufacturer must demonstrate that no part of the engine escapes its outer protective canopy in the resulting explosion. The massive cost of such experiments means that the event is invariably surrounded by high-speed cameras in order to establish the cause of any failure. However, a ball of fire is produced, and this dazzles the cameras. Although it is possible to use filters to prevent this, it then becomes impossible to see the event before the fireball, as there is insufficient light to expose the camera. Oxford Lasers and General Electric have shown (in work which cannot be published for reasons of commercial sensitivity) that laser illumination techniques described in this section can eliminate this problem. Indeed, they can be essential in any imaging application in which both incandescent and dark objects must be imaged.

Bright objects emit light over a range of wavelengths, which is dependent on the temperature of the objects and their chemical composition. Laser illumination is over a much narrower range of wavelengths. This is illustrated in Figure 25.3, which shows how the light from a laser light source might be compared with the light from a bright object. If we illuminate the bright object with the laser and place a filter in front of the camera which only allows the laser light to pass, then we make the bright object much darker, but there is a little effect on the laser illumination. By using widely available multilayer interference filters, having a passband of 1–2 nm, we can achieve a reduction in intensity of a factor of ~125, or seven photographic stops, by using this spectral filtering technique.

Even more contrast between the laser illumination and the bright subject can be achieved by using temporal filtering in addition to spectral filtering. A camera exposure time of 100 µs may be used, which is the shortest time typically available on electronic cameras. On the other hand, a copper vapour laser that offers 30 ns FWHM pulses may be used. Section 25.3 discusses the range of lasers available for high-speed imaging. For high-brightness applications, the copper vapour laser is usually the most suitable because it offers the shortest possible pulses of any laser type at a rate suitable for use with high-speed cameras (a few kilohertz) and with sufficient pulse energy to be useful (a few millijoules) illumination. If a very high-speed optoelectronic shutter is placed in front of the camera, the exposure time of each frame can be reduced to 100 ns, with all of the laser pulse still captured, and without the need for very critical

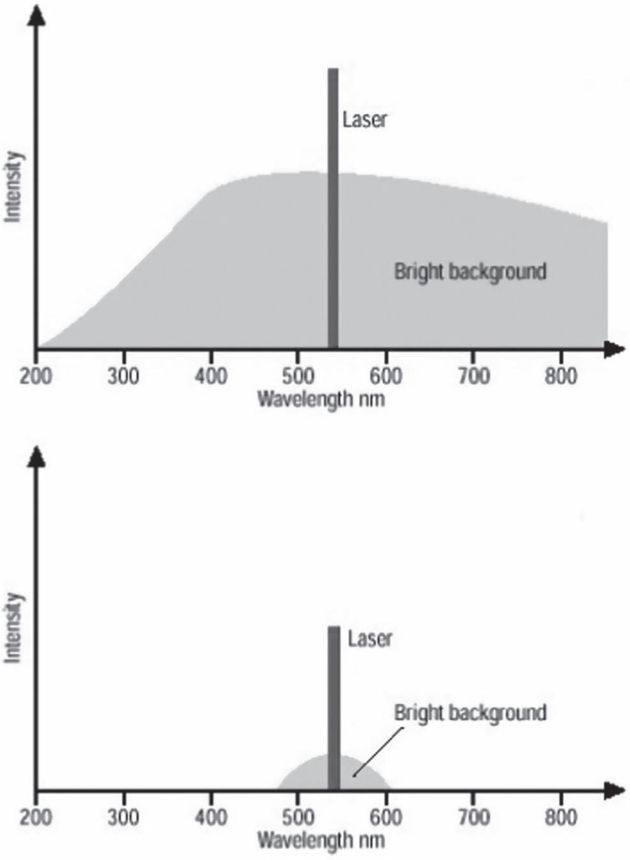

FIGURE 25.3 Wavelength spectrum emitted by a bright object, and by a laser, under normal conditions (upper) and as viewed through a narrowband interference filter (lower). (Courtesy of Oxford Lasers.)

adjustment of the timing window (with great care, shorter times are possible). In this case, the brightness of the bright subject has been reduced by a factor of 1000 (the ratio of the 100 μs camera exposure time to the 100 ns shutter time), or 10 photographic stops, with no reduction in the apparent brightness of the laser.

Krishnaswami et al. [16] have described an experimental arrangement for such a system, based on a copper vapour laser. A different illustration of the technique applied to a firework is shown in Figure 25.4. These techniques have been applied to a range of applications, including research into welding, metal sprays, explosives, high-current electromechanical devices and destructive testing of aircraft jet engines already described.

25.2 High-speed Camera Technology

The technology of electronic cameras is moving spectacularly fast at the time of writing. The reader may well find that the camera-company web sites listed in the references are the best source of current information [17–27].

25.2.1 High-speed Film

The first high-speed cameras all used photographic film as the recording medium. Film is comparatively expensive and is tedious to use, typically taking anything from 15 min to 1 h to develop, and with only limited opportunity to preview the experiment. Nevertheless, it is still used widely, mainly because it offers much greater sustained data rates than even the fastest electronic cameras.

Film cameras for use with lasers fall into several categories, and the most common types are as follows:

- *Conventional intermittent-action cine cameras.* These are based on the conventional movie-camera design, in which the film comes to a complete stop during the film exposure, which limits the maximum exposure speeds to 500 images per second [22].
- *High-speed cine cameras with rotating prisms.* These cameras use a rotating multifaceted prism, synchronized with the film motion, to project a moving image onto the moving film. This means that there is no net relative movement of image and film. With short enough laser pulses, the prism is not actually needed since the laser defines the exposure time. Frame rates are up to 10 000 frames per second in full format, while those are up to 20 000 frames per second at half-height. It takes about a second for the film to accelerate to full speed, typically leaving about 2 s of full-speed recording time [18,19,21,22].
- *Rotating drum cameras.* In rotating drum cameras, a length of 35 mm format film (typically 1 m) is laid around the inside perimeter of an evacuated drum. The drum is rotated at high speed (typically 300 revolutions per second), and the image from the lens is projected onto the film. In streak cameras, the image is stationary, and the film moves underneath it, so short laser pulses (e.g. from a copper vapour laser) prevent blurring. Full-frame recording rates of a little more than 10 000 frames per second are achieved, with faster frame rates possible simply by means of a suitable aperture limiting the height of the image on the film, giving a typical maximum frame rate of around 50 000 frames per second [17].
- *Rotating mirror cameras.* These can give framing rates up to 25 000 000 frames per second, but lasers having enough pulse energy to be useful cannot keep pace with these rates. These cameras have been reviewed by Rendell and Honour [28] and are made by Cordin [17].

25.2.2 Electronic Cameras

Electronic cameras currently dominate the high-speed imaging arena. This is due almost entirely to their ease of use, since their capabilities (especially the sensitivity and the information storage rate, which is the product of the recording speed and the number of independent elements, or pixels, forming each image) generally do not yet match those of film cameras. Various technologies are in use, often in combination with each other:

- *Charge-coupled device* (*CCD*) *sensors.* In these devices, incident light is converted to electrons which are stored in capacitors. The readout of one pixel at a time limits the total speed of the camera, but the total speed can be improved by multiple readout taps [29].
- *Complementary metal oxide semiconductor* (*CMOS*) *technology.* This uses phototransistors, rather than

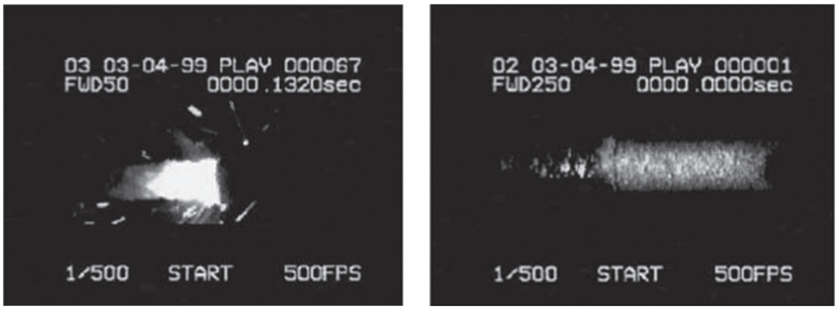

FIGURE 25.4 Both images show a burning firework, used to demonstrate the high-brightness imaging technique. On the left-hand side under normal illumination, the hot region is overexposed and the cold region is underexposed. On the right-hand side, the high-brightness imaging technique is employed, and both regions can be seen clearly. (Courtesy of Oxford Lasers.)

photocapacitors [30]. Compared with CCDs, CMOS devices generally offer lower sensitivity (because more of the area which would be available to light-sensitive components is needed for ancillary electronics), but higher speed for a given cost since the production processes used to make integrated circuits can be used to make CMOS sensors almost without modification.

- *On-chip pixel storage*. Many electronic sensors have multiple sets of pixels on the same chip. Generally, only one set is light sensitive, and the others may have a physical barrier to the light reaching them. The image is shifted from the light-sensitive to the non-light-sensitive pixels after each exposure, for all the pixels at the same time. This can be done very fast—typical times are in the 200 ns–1 µs range. This is useful since it allows a technique known as frame-straddling. This involves firing a laser at the end of one camera exposure, and then the beginning of the next, so that the time between subject exposures is much less than the framing time. Some cameras have many sets of pixels on chip, such as the SMD cameras described by Ref. [31], and these cameras are used to allow a limited number of frames to be captured in quick succession. Etoh [32] has reviewed the current state of the art.
- *Image splitting*. Some cameras take the incoming image and split it using a beamsplitter into two to eight independent sensors [33]. Each camera requires a high-speed opto-electronic shutter, so that it is light sensitive only at the correct time. These shutters generally take the form of third-generation image intensifiers, using microchannel plate (MCP) technology. These cameras provide the fastest possible frame rates (1 000 000–100 000 000 frames per second), but the two main disadvantages of this type of camera are cost (expensive components must be duplicated) and the limited number of frames that can be stored.

Table 25.1 lists (in order of increasing storage bandwidth) some high-speed cameras. Note that many cameras can be made to run faster (often ten times faster) by reducing the image resolution.

25.3 Choice of Laser

A number of lasers are available for high-speed imaging. Generally, the user has a choice between pulse energy, pulse duration, repetition rate and cost. Some commonly used lasers are given in Table 25.2.

TABLE 25.1

List of some high-speed cameras

Camera Type	Example (and Non-exhaustive List of Other Suppliers of a Similar Specification	Maximum Resolution (Pixels)	Speed at Maximum Resolution (Frames per Second)	Number of Frames Stored	Pixels per Second (million)
High-speed CCD	Roper Motionscope (also: NAC, Weinberger, Photron)	512 × 512	250	2048	65
Low-cost CMOS	Vosskuhler HCC 1000	1000 × 1000	462	512	462
State of the art (Oct 02)	Vision Research	1024 × 1024	1000	4096	1048
High-speed CMOS	Phantom 5 (also: NAC, Roper, Photron)				
Near-launch high speed CMOS (Oct 02)	Vision Research Phantom 7	800 × 600	6000	8400	2880
Film, rotating drum, streak	Cordin 317	2400 × 1800	13 500	52	58 000
Two-image PIV camera (uses on-chip storage)	PCO Sensicam (also: Roper, Hamamatsu)	1280 × 1024	5 000 000	2	6 600 000
Split image, multisensor (also uses on-chip storage)	Cordin 220 (also:PCO, Hadland)	1300 × 1030	100 000 000	8	134000 000

TABLE 25.2

List of some commonly used lasers.

Laser Type	Example	Wavelength (nm)	Pulse Length (ns)	Maximum Pulse Repetition Rate (Hz)	Pulse Energy (mJ)
Copper vapour	Oxford Lasers LS 20–50	511 + 578	10–30	50 000	0.5–5
CW-pumped Q-switched YAG	Lee Laser LDP-50- MQG	532	120–450	50 000	0.5–5
Flash-pumped Q-switched YAGs	New Wave Solo PIV, quantel twins	532	10–20	5–50 and 20 000 000 (burst)	10–500
Argon ion (CW), with chopper	Coherent Innova	488 + 514		Depends on how chopper/ scanning is used. Laser power typically 5–10 W	
Diode laser	Oxford Lasers HSI 5000	808	500–100 000	5000 and 400 000 (burst)	0.09–17.5

From this, we can see that the copper vapour laser [7] offers high repetition rates, short pulses and moderate pulse energy. CW-pumped Q-switched YAG lasers offer similar features, in a smaller package, but with pulse durations 5–10 times greater. Flash-pumped Q-switched YAG laser pairs comprise two lasers, from which the beams are combined. They are used almost exclusively for PIV since they can only provide two exposures in short succession.

Argon ion lasers give a continuous output, and this can be chopped into shorter-duration bursts, or the beam can be scanned in order to generate a lightsheet. Although in widespread use, their low power, very high electricity and cooling requirements, and short service interval mean that they are now generally being replaced by solid-state (diode laser) alternatives, offering 20 times the power for short pulse applications, in a much smaller and easier-to-use package [34].

25.3.1 Illumination Techniques

Various illumination techniques are used for high-speed photography.

- Backlighting involves providing a bright screen behind a subject, which appears dark against it. It is particularly suitable for sprays and is required for image-based sizing.
- Sheet lighting is used to slice through complicated three-dimensional fluid flows, and is used for sprays and liquid flows. It is much the most common form of lighting employed for PIV. Of the lighting techniques described here, it is the only one that can only be well performed with a laser rather than a conventional light source.
- Front lighting consists of illuminating the subject from the front and viewing light reflected or scattered by the subject. It is suitable for applications where there is optical access from one side only (e.g. for use with endoscopes) or for looking at the motion of machines or manufacturing processes. Front lighting is the type of lighting used in most conventional photography, such as landscapes and portraits of people.
- Shadowgraphy and Schlieren photography visualize the variations in fluid density or refractive index, e.g. shock waves behind projectiles, convection currents, combustion processes [35], explosive gas flows [36]. This makes these techniques fundamentally different from the others described because the contrast they produce could otherwise be invisible to the human eye. Shadowgraphy is simple to set up. Schlieren photography is more sensitive, since it measures the first derivative of the density, but is more difficult to set up. Practical and theoretical details are given in Ref. [4].

25.4 Application Examples

25.4.1 Time-resolved PIV in Engines

Airflows in automotive engines are vital to the performance of the engine—affecting fuel mixing, combustion and exhaust. Almost all car companies use laser-based imaging in order to visualize and measure these flows.

For example, engineers at the Rover company [37,38] have performed time-resolved PIV on airflows within a petrol engine combustion cylinder. Their experiments illustrate many of the compromises involved in high-speed imaging applications, which were as follows:

1. *Choice of camera*. They chose to use the fastest electronic camera (capable of taking at least 360 images) available at the time, the Kodak 4540. A high-speed film camera would have offered a recording bandwidth almost 200 times greater, but the extra time required to use film would have severely reduced the usefulness of the result.
2. *Choice of laser*. The aim of the experiment was to take images with a separation in crank angle of 1°, but at useful engine running speeds (1500 rpm). This meant that a frame rate of 9000 frames per second was required. This restricts the choice of lasers to a copper vapour laser or a CW-pumped Q-switched Nd:YAG laser, but in either case, only a few millijoules of energy per pulse was available (rather than the tens of millijoules more often used in PIV experiments).
3. *Seeding*. In order to achieve sufficient scattering from these relatively low-pulse energies, large (40 μm) seeding particles were required to visualize the flow. However, these particles were incapable of following the detailed turbulent flow structures. However, the low resolution of the camera (256 × 128) at this speed also meant that the detailed turbulent flow structures could not be resolved anyway.

These choices meant that it was the time-resolved behaviour of the bulk flows which was measured, rather than the instantaneous detailed structure. Reeves [37] reported that even in the large-scale flows, complicated spatial and temporal structure was found, and this type of measurement was required to understand the effect of swirl within the cylinder.

25.4.2 Agricultural Spray Characterization

The properties of pesticide sprays in agriculture are essential to the performance of the spraying system. Drop size is a crucial parameter, having a particular influence on the undesirable wind drift of the pesticide. The British Crop Protection Council (BCPC) have defined a set of standard spray nozzles, against which the drop size distributions of other nozzles can be compared [14,39,40], and have reported drop size distributions using a sizing technique based on the analysis of images taken with a high-magnification high-speed imaging system. Murphy [14] has reported how high-speed imaging could also be used to visualize very different spray break-up regimes obtained from various nozzle types, giving an understanding of how the different drop size distributions were produced. Some images are reproduced in Figure 25.5.

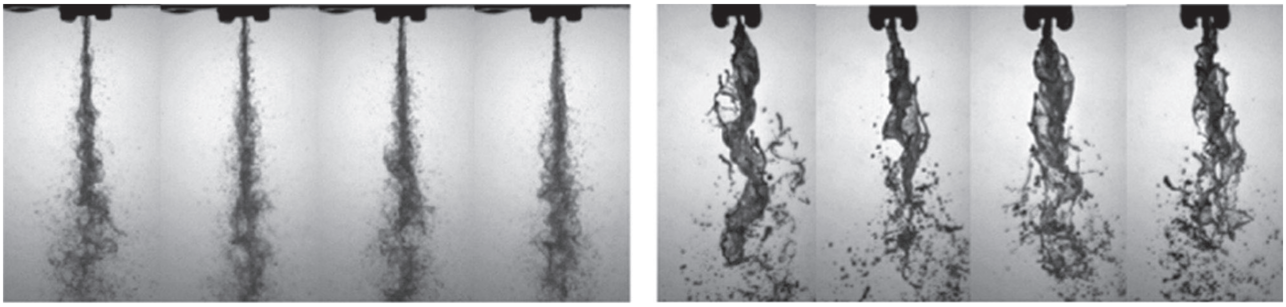

FIGURE 25.5 Sequences of images from high-speed movies showing the different spray break-up properties of agricultural sprays depending on the nozzle type used [14].

25.4.3 Drug Delivery Sprays

Drug delivery directed to the lungs is a well-established tool for the treatment of asthma. MDI is a widely used device for this drug delivery [41]. In order to achieve an efficient delivery to the lungs, drop sizes in the spray cloud must be tightly controlled. Drops smaller than about 1 µm tend to be exhaled, while drops larger than 5 µm tend to stick to the throat rather than reaching the lungs [42]. Also important are the duration, velocity and degree of turbulence of the spray, which affect both throat deposition and patient comfort. In order to check for manufacturing defects and equivalence between innovative and generic devices, it is also necessary to make measurements of the spray pattern and spray plume angle [43]. Measurements of all of these properties (drop size, velocity, duration, turbulence, spray pattern and plume angle) can be made using laser-based high-speed imaging techniques, largely with the same equipment. Figure 25.6 shows an example of a high-resolution image of an MDI spray, illuminated with a laser lightsheet.

- Spray duration can be measured simply by noting the time of appearance and disappearance of the spray in a high-speed movie [44].
- Cone angle (longitudinal) and spray pattern (cross-sectional) can be measured by illumination with a laser lightsheet and combination of the frames from a high-speed movie. Software measurement of the resulting images can yield the cone angle and the spray pattern.
- Drop size distribution can be measured using the image-based particle/droplet image analysis (PDIA) sizing technique.
- For slower sprays (e.g. MDI plumes in spacers which are used to reduce flow velocity and enhance patient comfort), time-resolved PIV at up to 10 000 frames per second is now possible, using the latest generation of CMOS cameras. For faster sprays, more conventional non-time-resolved PIV is required to measure the detailed flow structure, but the bulk flows can be measured with a frame rate of only a few thousand frames per second [44].

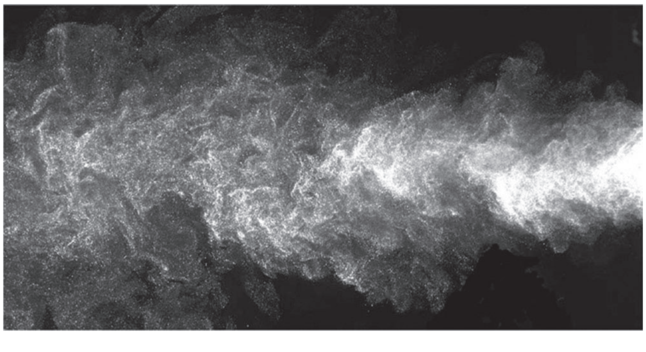

FIGURE 25.6 Spray plume from a metered dose inhaler, illuminated with a laser lightsheet. (Courtesy of Oxford Lasers.)

25.5 Summary

The application of lasers to high-speed imaging applications adds extra capabilities to high-speed cameras, whether electronic or digital. Laser, camera, lighting technique and image analysis tools must all be chosen to complement each other and with the application in mind. Notably, lasers can be used to eliminate motion blur and light-inaccessible regions; slice through complex three-dimensional flow structures, which are seen through explosions, arcs and flames; and make quantitative measurements of velocity and particle/droplet size, yielding temporal and spatial distributions.

REFERENCES

1. Talbot W. H. F. 1852 On the production of Instantaneous photographic images. *Phil. Mag. (4th series)* **3** 73–7.
2. Maiman T. H. 1960 Stimulated optical radiation in ruby masers. *Nature* **187** 493.
3. Fuller P. W. W. 1997 Lighting for cine and high-speed photography. *High Speed Photography and Photonics* ed. S. F. Ray (Oxford: Focal Press) pp. 29–47.
4. Fuller P. W. W. 1997 Flow visualization. *High Speed Photography and Photonics* ed S. F. Ray (Oxford: Focal Press) pp. 254–80.
5. Ray S. F. 1997 *High Speed Photography and Photonics* (Oxford: Focal Press).
6. Errey K. H. E. Pulsed lasers in high-speed imaging. *High Speed Photography and Photonics* ed S. F. Ray (Oxford: Focal Press) pp. 150–63.
7. Hogan D. C. 1990 Applications of copper vapor laser lighting to high-speed motion analysis. *Proc. SPIE* **1346** 324–30.

8. Clowater L., Hamady F. and Schock H. 1992 Fiber optic imaging system for remote location flow visualization studies. *SAE Technical Paper Series 920305, International Congress and Expo*; Detroit, MI, USA, 24–28 February (Warrendale, PA: SAE)
9. Rao K. K., Winterbone D E and Clough E 1992 Laser illuminated photographic studies of the spray and combustion phenomena in a small high speed DI diesel engine. *SAE Technical Paper Series, International Fuel and Lubricants Meeting and Exposition (San Francisco, CA)* (Warrendale, PA: SPIE) Paper 922203.
10. Raffel M. and Willert C. E. 2001 *Particle Image Velocimetry* (Berlin: Springer).
11. Dainty J. C. (ed.) 1975 *Laser Speckle and Related Phenomena* (Springer Topics in Applied Physics 9) (Berlin: Springer).
12. Meinlschmidt P., Hinsch K. D. and Sirohi R. S. (ed.) 1996 *Electronic Speckle Pattern Interferometry: Principles and Practice* (Bellingham, PA: SPIE)
13. Kashdan J. T 2002 Experiments on Intermittent Swirl-Generated Sprays. *PhD Thesis* Imperial College, London.
14. Murphy S. D., Nicholls T., Whybrew A., Tuck C. R. and Parkin C. S. 2001 Classification and imaging of agricultural sprays using a particle/droplet image analyser. *British Crop Protection Council Conference 2001 (BCPC 2001 Weeds) (Brighton)* (British Crop Protection Council).
15. Oxford Lasers 2001 Fluorescent Diffuser GB Patent application GB0117989.4.
16. Krishnaswami K., Tilleman M. M., Choi S. S. and Krivoshlykov S. G. 1997 High speed photographic system for objectives with highly radiant backgrounds. *SPIE* **3108** 50–7.
17. Cordin: https://www.cordin.com.
18. Hadland: https://www.hadland1.demon.co.uk.
19. NAC: https://www.nacinc.com.
20. PCO (Precision Computer Optics): https://www.pco.de.
21. Photec: https://www.photo-sonics.co.uk.
22. Photosonics: https://www.photo-sonics.co.uk.
23. Photron: https://www.photron.com.
24. Roper Scientific: https://www.roperscientific.com.
25. SMD (Silicon Mountain Design): https://www.dalsa.com.
26. Vosskuhler: https://www.vdsvossk.de.
27. Weinberger: https://www.weinberger.ch.
28. Rendell J. and Honour J. High-speed cine systems. *High Speed Photography and Photonics* ed. S. F. Ray (Oxford: Focal Press) pp. 68–80.
29. Bixby J. A. 1982 Fast frame rate sensor readout, US Patent 4,322,752.
30. Wong H.-S. 1999 *Overview of CMOS Image Sensors* NTSC/PAL VHS video (Bellingham, PA: SPIE).
31. Howard N. E., Gardner D. W. and Snyder D. R. 1997 Million frame per second CCD camera with 16 frames of storage in ultrahigh and high speed photography and image based motion measurement. *Proc. SPIE* **3173** 40–7.
32. Etoh T. G., Takehara K. and Takano Y. 2001 High-speed image capturing for PIV. *4th International Symposium Particle Image Velocity* (Göttingen, Germany) Sept 17–19 paper P1155.
33. Honour J. 1994 A new high-speed electronic multi framing camera. *Proc. SPIE* **1801** 643–8.
34. Whybrew A., Nicholls T. R., Boaler J. J. and Booth H. J. 1999 Diode lasers—a cost effective tool for simultaneous visualization, sizing, and velocity measurements of sprays. *ILASS Europe 1999*, Toulouse, France (Inst. for Liquid Atomisation and Spray Systems).
35. Gillespie L., Lawes M., Sheppard C. G. W. and Wolley R. 2000 Aspects of laminar and turbulent burning velocity relevant to SI engines. *Advances in Combustion, SP–1492 SAE Technical Paper Series 2000–01–0192, SAE 2000 World Congress*, Detroit, Michigan, 6–9 March (Warrendale, PA: SAE).
36. Kendall M. A. F., Quinlan N. J., Thorpe S. J., Ainsworth R. W. and Bellhouse B. J. 1999 Particle dynamics of a high-speed needle-free drug delivery system. Paper 3320 *22nd International Symposium on Shock Waves* Imperial College, London.
37. Reeves M., Towers D. T., Tavender B. and Buckberry C. H. 1999 A high-speed all-digital technique for cycle-resolved 2-D flow measurement and flow visualization within SI engine cylinders *Opt. Lasers Eng.* **31** 247–61.
38. Whybrew A., Reeves M., Slagle R. L., Boaler J. J., Baughan A. K., Nicholls T. R., Towers D. P., Tavender B. and Buckberry C. H. 1999 *Two Techniques for All-Digital Time-Resolved PIV* (*Santa Barbara, CA*).
39. Herbst A. 2001 Droplet sizing on agricultural sprays—a comparison of measuring systems using a standard droplet size classification scheme. *2001 ILASS Europe*, Zurich 2–6 September (Inst. for Liquid Atomisation and Spray Systems).
40. Southcombe E. S. E., Miller P. C. H., Ganzelmeier H., van de Zande J. C., Miralles A. and Hewitt A. J. 1997 The international (BCPC) spray classification system including a drift potential factor. *The 1997 Brighton Crop Protection Conference (Weeds, Brighton)* (British Crop Protection Council) pp. 371–80.
41. Purewal T. S. and Grant D. J. W. (eds.) 1998 *Metered Dose Inhaler Technology* (Buffalo Grove, IL: Interpharm) pp. 9–68.
42. Purewal T. S. and Grant D. J. W. (eds.) 1998 *Formulation of Metered Dose Inhalers Metered Dose Inhaler Technology* (Buffalo Grove, IL: Interpharm) pp. 9–68.
43. United States Food and Drug Administration 1998: Metered Dose Inhaler (MDI) and Dry Powder Inhaler (DPI) Drug Products Chemistry, Manufacturing, and Controls Documentation: Draft Guidance for Industry. US FDA, 5600 Fishers Lane, Rockville, MD 20857.
44. Brambilla G., Davies R. J., Ferraris A., Ganderton D., Keay F., Lewis D. A., Meakin B. J., Murphy S. D. and Nicholls T. R. 2001 Plume profiling of Beclomethasone Dipropionate pMDIs. *American Association of Pharmaceutical Sciences (AAPS) Annual Conference.*

FURTHER READING

Ray S. F. 1997 *High Speed Photography and Photonics* (Oxford: Focal Press)

Covers much of the material in this article in greater depth, although lacks the latest developments in electronic camera technology. At the time of writing it is out of print, but the Association of High Speed Photography and Photonics (www.ahspp.com) may have more information about this.

26

Ultrafast Optical Imaging

Jinyang Liang and Lihong V. Wang

CONTENTS

26.1 Introduction 315
26.2 Multiple-shot Ultrafast Optical Imaging 316
  26.2.1 Temporal Scanning 316
    26.2.1.1 Ultrashort Probing 316
    26.2.1.2 Ultrafast Gating 316
  26.2.2 Spatial Scanning 318
    26.2.2.1 Point Scanning 318
    26.2.2.2 Line Scanning 319
26.3 Single-shot Ultrafast Optical Imaging 320
  26.3.1 Active Detection 321
    26.3.1.1 Angle Division 321
    26.3.1.2 Wavelength Division 322
    26.3.1.3 Frequency Division 322
  26.3.2 Passive Detection 323
    26.3.2.1 Direct Imaging 323
    26.3.2.2 Computational Reconstruction 324
26.4 Summary and Outlook 325
References 327

26.1 Introduction

Many transient events, such as electron transfer in electrocatalytic processes (Allen and Larry 2001), electron–phonon interaction in transition-metal oxides (Imada et al. 1998), and structural changes in superheated nanoparticles (Gorkhover et al. 2016), occur at femtosecond to nanosecond timescales. Although imperceptible in daily life, these ultrafast phenomena are major steps in determining fundamental properties of materials and macroscopic chemical reactions. Thus, direct imaging of these transient events is of compelling scientific significance. However, although rapid advances in modern optics and novel electronic imaging devices have significantly increased the imaging speed, nanosecond temporal resolution is still beyond the reach of the state-of-the-art CCD or CMOS cameras (Diels and Rudolph 2006). As a result, the development of novel ultrafast optical imaging techniques holds the key to opening new possibilities for blur-free observation of these ultrafast phenomena.

The scope of ultrafast optical imaging in this chapter is defined by the following three criteria. First, extended from the previous categorization (Fuller 2009), "ultrafast" is defined as speeds at 100 million frames per second (Mfps) or above, which correspond to ≤10-ns inter-frame time intervals. Second, "optical" refers to the detection of photons in the extreme ultraviolet to far-infrared spectral range. Ultrafast imaging using electron beams, X-rays, and terahertz radiations are thus not discussed here. Interested readers can refer to the extensive reviews elsewhere (Zewail 2006; Gaffney and Chapman 2007; Zhang 2002). Thirdly, "imaging" is restricted to two-dimensional (2D, i.e. *x*, *y*). Hence, zero- and one-dimensional (1D) ultrafast optical measurements are excluded.

The structure of this chapter follows the conceptual architecture as shown in Figure 26.1. In general, according to the number of necessary exposures to record a 2D transient (i.e. *x, y, t*) scene, ultrafast optical imaging techniques can be categorized into multiple- and single-shot approaches. Four subcategories are further generated, depending on image acquisition and reconstruction strategies. The multiple-shot approach includes temporal scanning and spatial scanning. While temporal scanning includes ultrashort probing and ultrafast gating, spatial scanning comprises point scanning and line scanning. The single-shot approach is further divided into subcategories: active detection and passive detection. While active detection is represented by angle division, wavelength division, and frequency division, passive detection is embodied in direct imaging and computational imaging. The description of each method includes the basic principles, advantages, and limitations, along with a representative system and its application. Finally, the conclusions and an outlook are given.

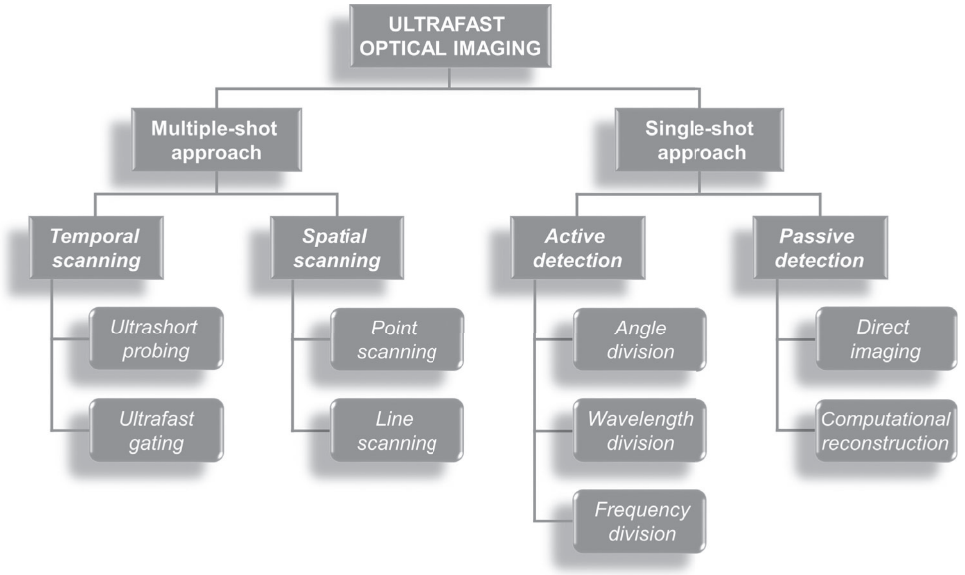

FIGURE 26.1 Categorization of ultrafast optical imaging.

26.2 Multiple-shot Ultrafast Optical Imaging

Multiple-shot ultrafast optical imaging is often implemented in the pump probe arrangement. A pump beam excites the transient event, and a subsequent probe beam records, at a certain pump probe delay time, a temporal slice, i.e. (*x*, *y*) information at the given time point. Temporal scanning, which repeats measurement with a varying delay time, reveals the evolution of the ultrafast phenomenon. Similarly, for spatial scanning, the probe beam is scanned point-by-point or line-by-line, while the temporal information is recorded. Stitching all the measurements together reveals the full spatiotemporal dynamics. As the mainstream in ultrafast optical imaging, the multiple-shot approach usually has superior temporal resolution. However, as the recording of an (*x*, *y*, *t*) datacube requires repetitive measurements, the under-observing transient events must be precisely reproducible, which is a major limitation of this category.

26.2.1 Temporal Scanning

26.2.1.1 Ultrashort Probing

This method uses a probe pulse with an ultrashort pulse width to record a temporal slice. The temporal resolution depends on the pulse width. The imaging speed and sequence depth (i.e. the maximum number of frames in each acquisition) are determined by the step size and range of temporal scanning, respectively. Due to the recent advances in ultrafast laser sciences, ultrashort probing-based optical imaging has the highest temporal resolution, well suited for imaging femtosecond (or even attosecond) transient events (Corkum and Krausz 2007).

As an example, Figure 26.2a shows the experimental setup for imaging spatiotemporally controlled lattice vibrational waves (Feurer et al. 2003). A 50-fs laser pulse is first passed through a beamsplitter to create a pump pulse and a probe pulse. A spatiotemporal pulse shaper (Feurer et al. 2002) converted the pump pulse into many excitation pulses that reached the specified locations of a lithium tantalate single crystal at the specified times. The femtosecond excitation generated coherent lattice vibration waves that propagated away from the excitation point at the light-like speed. Grafting the concept of phased array radars, spatiotemporal control of the excitation patterns allowed coherently manipulating the far-field response of the vibrational waves. The probe pulse, once frequency-doubled by a non-linear crystal, provided a wide-field illumination to the sample. The transmitted probe pulse was imaged onto a CCD camera. Varying the time delay between the pump pulse and the probe pulse enabled monitoring the wave's spatial and temporal evolution. In the example as shown in Figure 26.2b, a series of excitation pulses illuminated distinct spots on the sample, and their times of arrival followed a combined linear and parabolic delay sweep (upper panel of Figure 26.2b). Each exciting pulse generated a spherical wavelet, whose launch time was controlled by the excitation time. Thus, these spherical wavelets, undergoing constructive or destructive interference, produced an upwardly tilted converging wave that focused about 1 mm away from the excitation region (the four lower panels in Figure 26.2b). The propagation speed, directly quantified by these images, was about one-sixth of the speed of light.

26.2.1.2 Ultrafast Gating

Ultrahigh temporal resolution can also be achieved using ultrafast gating—an ultrashort temporal window at detection to record a temporal slice. Ultrafast gating has been demonstrated using various techniques, including non-linear optical gating (Wang et al. 1991) and electronic gating (Patwardhan and Culver 2008). An (*x*, *y*, *t*) datacube is captured by sliding this temporal window. While non-linear optical gating has achieved femtosecond temporal resolution, it imposes

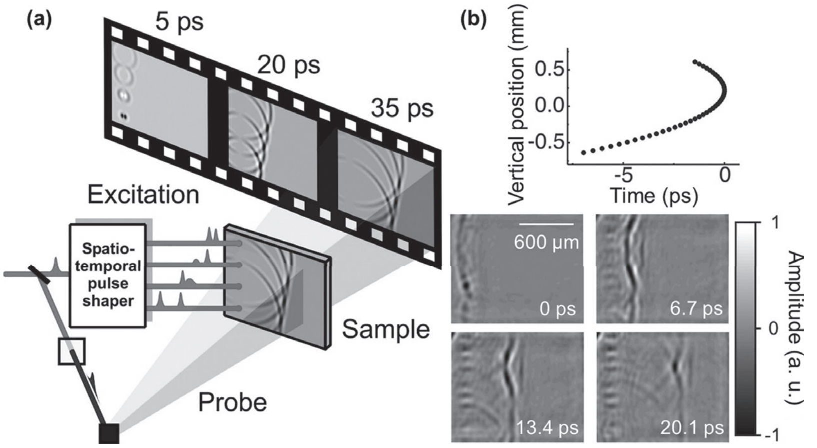
(a)
5 ps
20 ps
35 ps
Excitation
Spatio-temporal pulse shaper
Sample
Probe
(b)
Vertical position (mm)
0.5
0.0
-0.5
-5
0
Time (ps)
600 μm
0 ps
6.7 ps
13.4 ps
20.1 ps
Amplitude (a. u.)
1
0
-1

FIGURE 26.2 Ultrashort-probing-based ultrafast optical imaging of lattice vibrational waves. (a) Schematic of experimental set-up. (b) Pattern of spatiotemporal laser excitation (upper panel) and representative frames of a focusing wave at the far-field (four lower panels). (Reprinted and edited by permission from *Science* (Feurer et al. 2003), copyright 2003.)

requirements on incident light's intensity and polarization. These requirements can be removed by electronic gating. However, its temporal resolution, limited by electronic circuits' response times, is currently clamped to tens to hundreds of picoseconds. In addition, due to passive gated detection, the light throughput is determined by the ratio of the gated time window $\left(\tau_g\right)$ to the total duration of the transient scene $\left(\tau_s\right)$.

Detecting the time-of-flight (ToF) to distinguish ballistic, quasi-ballistic, or diffusive photons, ultrafast gating-based ultrafast optical imaging is well positioned to see through (or into) scattering media. As an example, Figure 26.3a shows the schematic of time-gated optical projection tomography (TGOPT) for imaging zebrafish's internal structures (Fieramonti et al. 2012). A femtosecond laser (800 nm wavelength and 100 fs pulse width) was used as the light source. An output femtosecond pulse was split into a signal pulse and a gate pulse. The signal pulse was sent through a zebrafish's trunk region (marked by the box in the inset of Figure 26.3a). The propagation through the sample broadened the width of the signal pulse to tens of picoseconds due to scattering. The gate pulse went through a delay line and recombined with the signal pulse on a β-barium-borate (BBO) crystal. When the signal and gate pulses were spatiotemporally overlapped, a sum frequency pulse was generated from

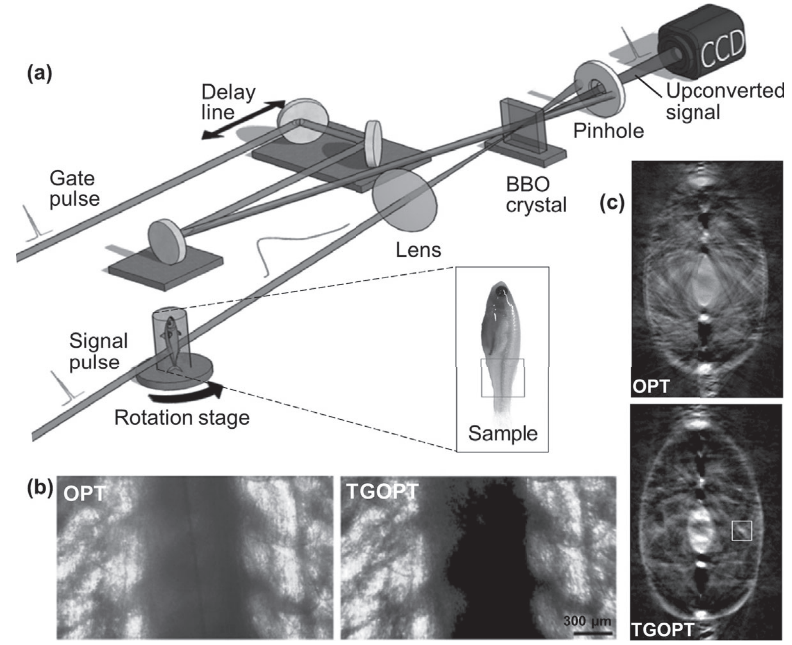
(a)
Delay line
Gate pulse
Lens
BBO crystal
Pinhole
CCD
Upconverted signal
Signal pulse
Rotation stage
Sample
(c)
OPT
TGOPT
(b)
OPT
TGOPT
300 μm

FIGURE 26.3 Time-gated optical projection tomography (TGOPT) for imaging zebrafish's internal structures. (a) Schematic of experimental set-up. BBO: β-barium-borate. The imaged region is marked by the box in the inset. (b) Comparison of projected views acquired by the non-gated OPT and the TGOPT. (c) Comparison of the same transverse slice reconstructed by the non-gated OPT and the TGOPT. The posterior lateral line nerves are marked by the white box in the lower panel. (Reprinted and edited from *PLOS One* (Fieramonti et al. 2012) with permission to use under a Creative Commons license.)

the BBO crystal. By tuning the time delay between the gate and signal pulses, this non-linear optical gate could select the desired types of photons within a 100-fs temporal window. A CCD camera captured the upconverted signal as one projected view. The above process was repeated with different sample rotation angles. The acquired projected views were fed into a back-projection algorithm based on the inverse Radon transformation to reconstruct a volumetric (i.e. x, y, z) image.

Non-linear optical gating enabled TGOPT to enhance resolution and contrast of the projected views (Figure 26.3b). A comparison was drawn on the vertebrate column in the projected views acquired by the non-gated OPT and the TGOPT. Because of its large attenuation properties, practically no ballistic photons would transmit through the vertebrate column. In the non-gated OPT, the projected view, affected by the multiple scattered photons, gave rise to a diffused background (left panel of Figure 26.3b). In TGOPT, a temporal window was placed on the leading edge of the signal pulse, which allowed selecting the quasi-ballistic photons transmitted through the sample. The rejection of multiple scattered photons thus resulted in a dark structure in the projected view (right panel of Figure 26.3b).

The superior quality of TGOPT's projected views led to improved reconstructed images. Figure 26.3c shows the comparison of the reconstructed transverse section of the trunk region using the non-gated OPT and the TGOPT. Without the interference of the diffusive background, TGOPT largely reduced artefacts, which assisted in precisely localizing internal structures, especially nerves and bones due to their distinct scattering and absorption properties from other tissues. For example, while disappearing almost completely in the non-gated OPT image due to a relatively strong background and a large number of artefacts, the zebrafish's posterior lateral line nerves were clearly revealed in the TGOPT's image (marked by the white box in the lower panel of Figure 26.3c).

26.2.2 Spatial Scanning

26.2.2.1 Point Scanning

In this method, an ultrafast point detector records the entire temporal trace at a specific (*x*, *y*) position. By scanning through the 2D space, a full (*x*, *y*, *t*) datacube is acquired. The temporal resolution and the corresponding imaging speed are generally determined by the detector's bandwidth. Mainstream devices include the Geiger-mode avalanche photodiode (APD) and the photomultiplier tube (PMT) with time-correlated single-photon counting (TCSPC). Possessing single-photon sensitivity, these devices are particularly well suited for ultrafast optical imaging under photon-starved conditions. These features have enabled their applications in laser radar (LIDAR) (Pawlikowska et al. 2017), time-resolved positron emission tomography (Szczesniak et al. 2007), and optical communications (Chitnis and Collins 2014). However, the inter-frame time interval and temporal resolution, limited by the response speed of processing electronic circuits, is at tens of picoseconds. In addition, the limited photon processing capability has strained these detectors to reach higher count rates, which could result in a long imaging time even under the high-illumination condition. The light throughput is thus limited by the ratio of the number of processed photons $\left(N_p\right)$ to the total number of emitted photons $\left(N_t\right)$.

As an example, Figure 26.4a shows the schematic of first-photon imaging, which has enabled an accurate ToF volumetric imaging using only the first detected photon (Kirmani et al. 2014). In this set-up, a pulsed laser source (640 nm wavelength, 226 ps pulse width, 10 MHz repetition rate, and 0.6 mW average power) illuminates a scene with quasi-Lambertian reflectivity. In addition, an incandescent lamp emits background light. A two-axis scanning galvanometer raster-scans the laser beam through a 3D object. Each spatial location is illuminated with repeated laser pulses until the first backscattered photon is detected by a Geiger-mode APD. In this device, a reverse-bias voltage, sufficiently higher than the breakdown voltage, is applied to the *p*–*n* junction. When an electron is created by the absorption of the detected photon, it accelerates along the electrical field gradient in the depletion layer. Provided a sufficiently large gradient, this electron can gain a sufficient kinetic energy to knock out more electrons from the atomic lattice—a process termed impact ionization. The generated secondary electrons further intensify this ionization process. As a result, a self-sustained avalanche is caused by a single photon. The avalanche leads to a detectable current, whose leading edge, detected by the following TCSPC set-up, marks the arrival time of the detected photon. The imaging speed, determined by the TCSPC module's bandwidth, is 125 billion frames per second (Gfps).

First-photon imaging used computational techniques to improve the detection accuracy and image quality (Figure 26.4b). Due to the presence of high background light, the estimated depth and surface reflectivity were highly corrupted by using the conventional pointwise maximum-likelihood processing (left column in Figure 26.4b) As a result, in conventional set-ups, hundreds of photons were needed for an accurate calculation of surface reflectivity and depth, even in the absence of background light. First-photon imaging, however, exploited a spatial correlation of the capture photons to circumvent this limitation. First, the reflectivity of the object was reconstructed by minimizing the Poisson noise with a sparsity-promoting regularization function that summed the absolute values of the image's discrete-wavelet-transform (DTW) coefficients. Second, the spatial correlation of the photons' time of arrival was leveraged to censor anomalous ranging values. Finally, a maximum-likelihood 3D estimation, combined with a DTW-based penalty function, was used to further increase the reconstructed image quality (right column in Figure 26.4b). The denoising operation in the post-processing limited the spatial and temporal resolution. The final result had a 4-mm depth resolution, corresponding to an ~30 ps temporal resolution.

Fluorescence lifetime mapping is another popular application using the single-photon ultrafast point-scanning detectors (Becker 2014). In a typical set-up, an ultrafast femtosecond laser delivers pulses to a fluorescent sample through a confocal microscope. The time of arrival of emitted photons, recorded by a PMT-TCSPC detector, is sorted into a histogram that plots the emission counts versus time with respect to the excitation pulse (Figure 26.4c). With the accumulation of a large number of photon counts, the histogram reflects the fluorescence

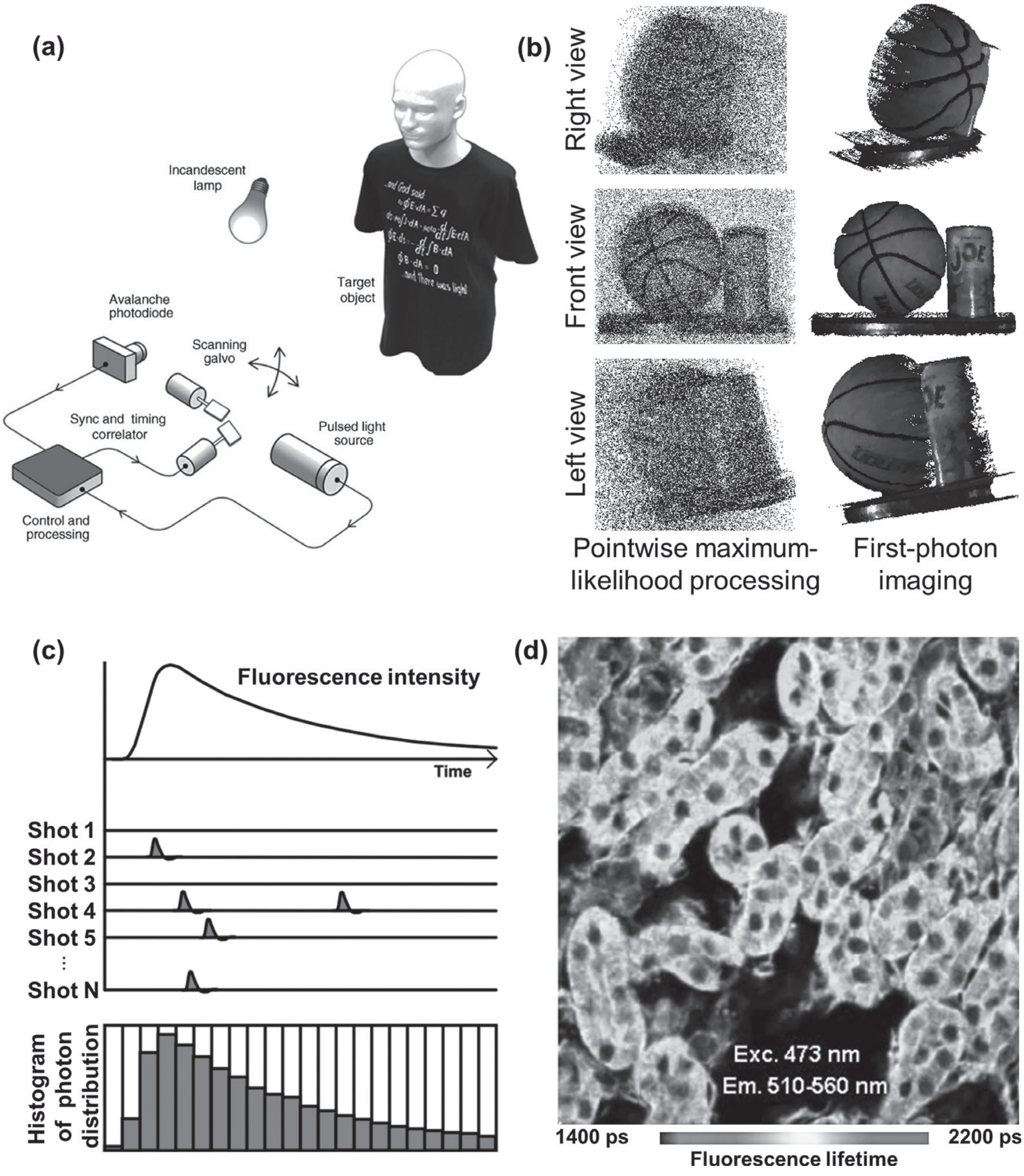
(a)
Incandescent lamp
Target object
Avalanche photodiode
Scanning galvo
Sync and timing correlator
Pulsed light source
Control and processing
(b)
Right view
Front view
Left view
Pointwise maximum-likelihood processing
First-photon imaging
(c)
Fluorescence intensity
Time
Shot 1
Shot 2
Shot 3
Shot 4
Shot 5
Shot N
Histogram of photon distribution
(d)
Exc. 473 nm
Em. 510-560 nm
1400 ps
2200 ps
Fluorescence lifetime

FIGURE 26.4 Point scanning-based ultrafast optical imaging. (a) Experimental set-up of the first-photon imaging technique. (b) Comparison of three different views of a reconstructed volumetric image using the pointwise maximum-likelihood processing (left column) and the first-photon imaging technique (right column). ((a) and (b) are reprinted and edited by permission from *Science* (Kirmani et al. 2014), copyright 2014.) (c) The principle of PMT-TCSPC-based fluorescence lifetime measurements. (d) 2D fluorescence lifetime mapping of a mouse kidney section. ((c) and (d) are reprinted and edited by permission from (Becker 2014), copyright 2014.)

intensity decay, which is used to extract the fluorescence lifetime at this (*x*, *y*) location. A fluorescence lifetime map is acquired by 2D spatial scanning (Figure 26.4d).

26.2.2.2 Line Scanning

This method uses ultrafast line detectors to capture a time-resolved 1D image in a single measurement. By scanning the orthogonal spatial axis, an (*x*, *y*, *t*) datacube is recorded. Compared with the point-scanning counterpart, ultrafast line detectors often have a much higher imaging speed and photon processing ability. However, the underperformed spatial resolution and imaging sensitivity are their current major limitations.

Here, the discussion will be focused on a special ultrafast line imager—the streak camera (Figure 26.5a). Incident photons first pass through a narrow entrance slit (typical width: 50–200 μm), which is imaged onto a photocathode. There, photons are converted into photoelectrons via the photoelectric effect. These photoelectrons accelerate towards a mesh and then pass through a pair of sweep electrodes. A time-varying voltage is applied to the electrodes so that photoelectrons with different arrival times experience different deflections at the spatial direction orthogonal to the entrance slit (y-axis in Figure 26.5a). The deflected photoelectrons, amplified by a micro-channel plate, bombarded a phosphor screen to convert back to photons. The phosphor screen is imaged onto an internal imaging sensor (e.g. a CCD or a CMOS camera), which records an (x, t) streak image. When a synchronous y scanning is carried out on the region of interest, an (x, y, t) datacube is obtained. The state-of-the-art streak camera offers a temporal resolution down to 100 fs with an effective imaging speed of 10 trillion frames per second (Tfps) (Hamamatsu 2017).

The streak camera has recently enabled "seeing around a corner" (Velten et al. 2012). In the set-up (Figure 26.5b), an ultrafast laser delivered pulses of about 50 fs width at a repetition rate of 75 MHz. The laser pulses were focused on a diffuser wall (via path r_1). Then, the wall-scattered photons arrived at the hidden object (via path r_2). The object-scattered photons travelled back to the diffuser wall (via r_3), were scattered, and propagated to a streak camera (via r_4). With an inter-frame time interval of 2 ps, the streak camera sensed the different times of arrival due to the optical path difference. For a fixed laser position, L, and transferred sensor location, W, at a given time t, the allowed values of single scattering positions on the hidden object, s, lied on an ellipsoid with focal points of L and W (Figure 26.5b). By scanning the laser spot, many streak images were recorded (the first panel in Figure 26.5c). For any scattering point at the hidden object, the corresponding ellipses intersected, and the location was determined. By 2D laser beam scanning, the volumetric information of the hidden object was recovered by using computational reconstruction (the second to the fourth panels in Figure 26.5c).

26.3 Single-shot Ultrafast Optical Imaging

Single-shot ultrafast optical imaging can be achieved actively and passively. The active detection methods exploit specially designed pulse trains to probe the transient event. Each pulse in the pulse train carries a unique marker (e.g. incident angle, wavelength, or spatial frequency), which can be extracted at detection and thus allocates related information to a specific time stamp. The passive detection methods are built upon receive-only ultrafast detectors. The transient event is either imaged directly or recovered via computational reconstruction. In general, single-shot ultrafast optical imaging techniques can capture an (x, y, t) datacube in real time (defined as the actual time in which the event occurs), overcoming the requirement of repetitive measurements imposed by the

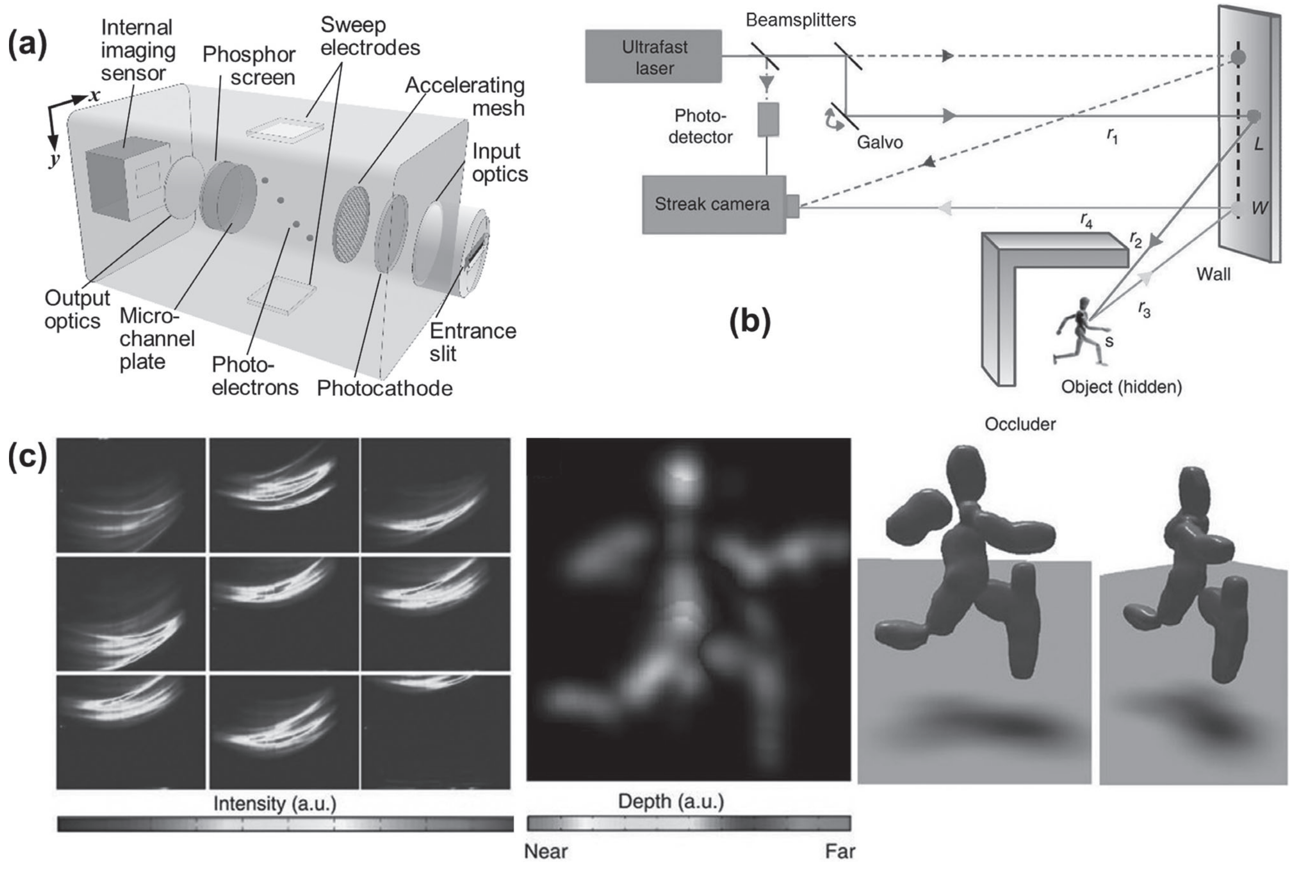

FIGURE 26.5 Line scanning-based ultrafast optical imaging. (a) Schematic of a streak camera. (b) The experimental set-up for imaging a hidden mannequin behind an occluder. (c) Nine representative raw streak images (the first panel); the depth map (the second panel) and two views (the third and fourth panels) of the reconstructed image. ((b) and (c) are reprinted and edited by permission from Macmillan Publishers Ltd: *Nature Communications* (Velten et al. 2012), copyright 2012.)

multiple-shot counterparts (Section 26.2). This unique feature positions these techniques perfectly for imaging non-repetitive or difficult-to-be-reproduced events. However, these methods are in their early development stages.

26.3.1 Active Detection

26.3.1.1 Angle Division

The angle-division approach grafts the concept of computed tomography (CT) on the spatiotemporal domain. Multiple probe pulses illuminate the transient event from different angles. Each records a projected view of the scene. By leveraging the established reconstruction methods in CT, the transient scene can be recovered. This method achieves a large sequence depth by using only a few probe pulses. However, the limited maximum projection angle and the limited number of probe pulses restrict the spatial and temporal resolutions of the reconstructed movie.

The single-shot frequency-domain tomography (SS-FDT) (Li et al. 2014) is a representative imaging technique in this subcategory. In the set-up (Figure 26.6a), an 800-nm, 30-fs pump pulse induces a transient perturbation. Another two pulses (each with a 30-μJ pulse energy), directly split from the pump pulse, are crossed simultaneously at a small adjustable angle in a three-layer structure, in which a BBO crystal is sandwiched between two HZF4 glass plates. By cascaded four-wave mixing and frequency doubling, a fan of five chirped 400-nm probe pulses (600-fs pulse widths) are generated. Imaged by lens L_1, these probe pulses are spatiotemporally overlapped at the scene. The transient event imprints a phase streak on each probe pulse. In addition, a 400-nm reference

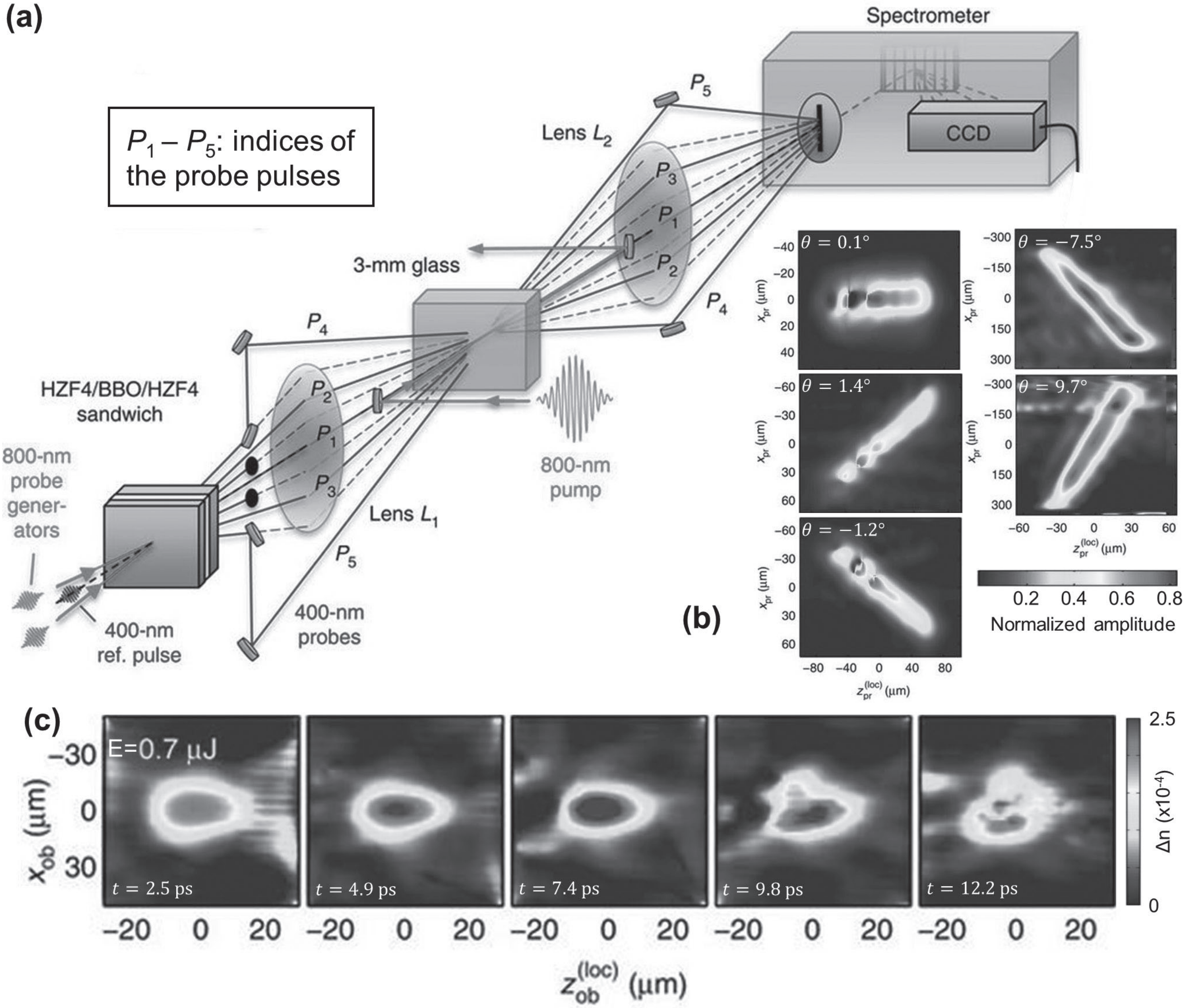
(a)
Spectrometer
CCD
$P_1 - P_5$: indices of the probe pulses
Lens L_2
P_5
P_3
P_1
P_2
P_4
3-mm glass
P_4
HZF4/BBO/HZF4 sandwich
P_2
P_1
P_3
800-nm probe generators
800-nm pump
Lens L_1
P_5
400-nm ref. pulse
400-nm probes
(b)
$\theta = 0.1°$
$\theta = 1.4°$
$\theta = -1.2°$
$\theta = -7.5°$
$\theta = 9.7°$
x_{pr} (μm)
$z_{pr}^{(loc)}$ (μm)
Normalized amplitude
0.2 0.4 0.6 0.8
(c)
E=0.7 μJ
$t = 2.5$ ps
$t = 4.9$ ps
$t = 7.4$ ps
$t = 9.8$ ps
$t = 12.2$ ps
x_{ob} (μm)
$z_{ob}^{(loc)}$ (μm)
Δn (×10⁻⁴)
2.5
0

FIGURE 26.6 Single-shot frequency-domain tomography (SS-FDT) for imaging transient refractive index perturbation. (a) Schematic of the experimental set-up. (b) Phase streaks induced by the evolving refractive index profile. x_{pr} and $z_{\mathrm{pr}}^{(\mathrm{loc})}$, the transverse and the longitudinal coordinates of probe pulses; θ the incident angle of probe pulses. (c) Representative snapshots of the refractive index change (Δn) using a pump energy of $E = 0.7$ μJ. x_{ob} and $z_{\mathrm{ob}}^{(\mathrm{loc})}$, the transverse and the longitudinal coordinates of the object. (Reprinted and edited by permission from Macmillan Publishers Ltd: *Nature Communications* (Li et al. 2014), copyright 2014.)

pulse, advanced temporally by 2–4 ps, records the phase reference. Lens L_2 images both the reference and phase-modulated probe pulses onto an entrance slit of a spectrometer. The reference and probe pulses interfere inside the spectrometer to produce a hologram, which records five projected views of the transient event. Because these probe pulses are incident at different angles, the information carried by them is separated at the reciprocal domain. By windowing, shifting, and inverse transforming the hologram area associated with each probe pulse, five phase streaks are reconstructed. Finally, these phase streaks are used to tomographically reconstruct the evolution of the object. The reconstructed movie has an approximately 3-ps temporal resolution.

The SS-FDT technique has been implemented to image non-linear laser propagation in a fused silica glass (Li et al. 2014). A 0.7-μJ pump pulse induced a propagating refractive index structure due to the pump-generated plasma and non-linear refractive index. The recorded phase streaks at smaller angles (left column in Figure 26.6b) highlighted the evolution of the object's transverse (x_{ob}) profile. Oscillations in transverse radius and peak index change were observed in the last 1/3 of these streaks, indicating a dynamic balance between self-focusing and defocusing. Phase streaks at larger angles (right column in Figure 26.6b) illustrated the evolution of the object's longitudinal $\left(z_{\mathrm{ob}}^{(\mathrm{loc})}\right)$ profile, which remained nearly constant due to the low dispersion of fused silica. The full evolution of the refractive index change was reconstructed by inputting these five streaks into the algebraic reconstruction technique algorithm (Gordon et al. 1970). The representative images (Figure 26.6c) revealed that the pulse was self-focused within 7.4 ps. After that, the substructure started to develop, illustrating as the split-off of the upper spatial lobe at 9.8 ps followed by a steep-walled index "hole" near the centre of the profile at 12.2 ps. This substructure was the result of a negative index change that locally cancelled the laser-induced positive non-linear refractive index change.

26.3.1.2 Wavelength Division

Wavelength division is another approach to assemble a probe pulse train. Developed from the serial time-encoded amplified microscopy (Goda et al. 2009), the general strategy of this approach is to encode the time-resolved 2D image into the spectrum of a broadband laser pulse. The transmitted probe pulses will be spectrally separated, and the spatiotemporal datacube is directly obtained. Without using any computational reconstruction, this approach largely preserved the spatial resolution in each frame. However, this method is restricted by a shallow sequence depth, and it can be used to image only colour-neutral objects. In addition, the trade-off between the pulse width and the spectral bandwidth limits its temporal resolution.

As an example, the sequentially timed all-optical mapping photography (STAMP) system (Nakagawak et al. 2014) is schematically shown in Figure 26.7a. An ultrashort laser pulse first passes through a temporal mapping device, which consists of a pulse stretcher and a pulse shaper. The pulse stretcher can temporally stretch the incident pulse to femtosecond to nanosecond widths by using different materials (e.g. a glass rod, prisms, and a fibre). The pulse shaper is composed of a pair of identical diffraction gratings and two lenses placed in a 4*f* arrangement. A liquid-crystal spatial light modulator is placed at the Fourier plane for phase modulation (Weiner 2011). A pair of polarizing beamsplitters is used with this pulse shaper for amplitude modulation. The output burst consists of six pulses, each of which has an equal intensity but a different spectral band (the left inset in Figure 26.7a). This pulse train is incident on the target as successive "flashes" for stroboscopic image acquisition. The image-encoded pulse train then enters a spatial mapping device, which uses dispersion elements and an imaging system to spatially separate these pulses, which are finally recorded at different areas of an image sensor.

The STAMP system has visualized the dynamics of light–matter interaction. Figure 26.7b illustrates monitoring early-stage dynamics of plasma in a laser-driven micro-explosion at 65.4 Gfps (with an exposure time of 13.8 ps per frame). A focused femtosecond laser pulse (70 fs pulse width and 100 μJ pulse energy) ablated the surface of a glass plate. The STAMP system imaged the generation of plasma filament and the following expansion of a plume. In addition, Figure 26.7c shows a movie of laser-induced electronic response and phonon formation at 4.4 Tfps (with an exposure time of 733 fs per frame). A femtosecond laser pulse (70 fs pulse width and 40 μJ pulse energy) was cylindrically focused into a ferroelectric crystal wafer at room temperature to produce coherent phonon-polariton waves. The STAMP system captured this phenomenon in a polarization-gating configuration. The representative frames showed the irregular and complex electronic response of the excited region in the crystal, followed by the formation of an upward-propagating coherent vibration wave.

26.3.1.3 Frequency Division

Frequency division is realized by attaching different spatial carrier frequencies to probe pulses. The detector records an integrated image which consists of the superimposed transmitted probe pulses from the transient event. The acquired image is then decoded to recover the (x, y, t) datacube. In principle, the generation of the probe pulse train does not rely on dispersion. The preservation of the entire bandwidth of the laser pulse thus allows simultaneously maximizing the frame rate and the temporal resolution. However, this method trades the sequence depth with spatial resolution.

A representative method in this subcategory is the frequency recognition algorithm for multiple exposures (FRAME) imaging (Ehn et al. 2017). In the FRAME imaging system, a pulse from a femtosecond laser is split into four 125-fs subpulses (Figure 26.8a). The intensity profile of each subpulse is modulated by a Ronchi ruling with an identical period but a unique orientation. All Ronchi rulings are placed at the conjugate plane of the measurement volume. The time of arrival for each probe pulse is controlled via separate optical delay lines. As a result, a burst of four structured light-modulated pulses is generated for probing the transient events.

The FRAME imaging system has imaged the propagation of a femtosecond laser pulse through a Kerr-sensitive medium at imaging speeds up to 5 Tfps (Figure 26.8b). An

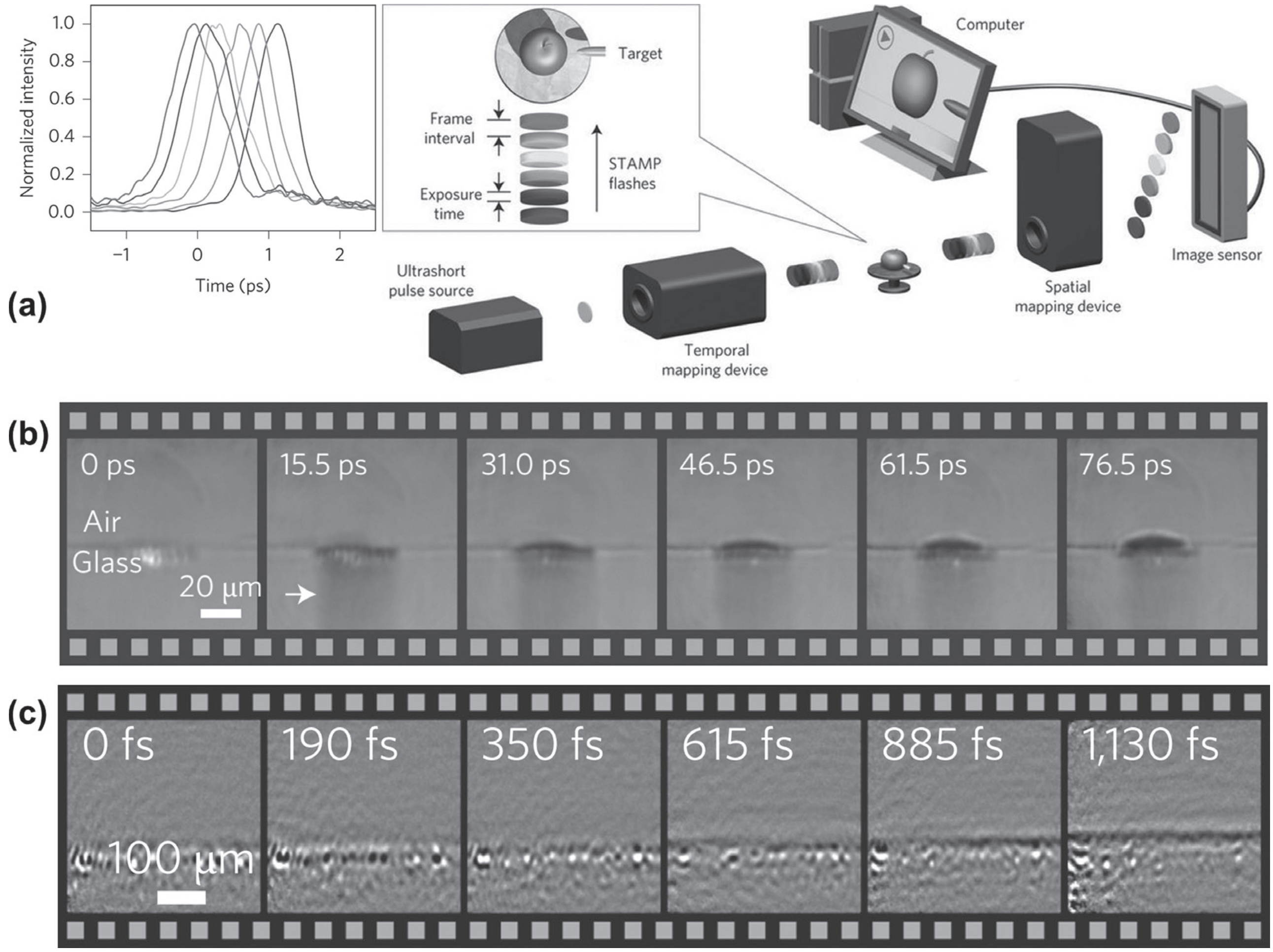

FIGURE 26.7 Sequentially timed all-optical mapping photography (STAMP). (a) Schematic of the STAMP system. The left inset shows the normalized intensity profiles of the six probe pulses with an inter-frame time interval of 229 fs (corresponding to a frame rate of 4.4 Tfps) and an exposure time of 733 fs. (b) Single-shot imaging of plasma dynamics using STAMP at 65.4 Gfps. (c) Single-shot imaging of electronic response and phonon formation at 4.4 Tfps. (Reprinted and edited by permission from Macmillan Publishers Ltd: *Nature Photonics* (Nakagawak et al. 2014), copyright 2014.)

800-nm femtosecond pump pulse was directed through a carbon disulphide (CS_2) medium. The structured light-modulated pulse train probed the CS_2 medium from a direction of propagation orthogonal to the pump pulse. A pair of polarizers, with the polarization axis of 90° from one another, prevented the probe burst from reaching an electron-multiplying CCD camera at the equilibrium state. However, when the arrival time for the pump pulse and the probe burst coincided within the Kerr medium, the transient birefringence caused by the pump pulse allowed the overlapping part of the probe pulse to be transmitted. In image reconstruction, the acquired data was first spatial Fourier-transformed. Because the sinusoidal patterns (from the Ronchi rulings) superimposed on each laser probe pulse had different orientations, the induced carrier frequencies can be well separated at the Fourier domain (Figure 26.8c). Then, by windowing, shifting, and inverse Fourier transforming of information associated with each carrier frequency, the time-resolved 2D images were reconstructed. Figures 26.8d and e show the reconstructed time-resolved images, which captured the laser pulses' propagation.

26.3.2 Passive Detection

26.3.2.1 Direct Imaging

Among the existing 2D ultrafast detectors, the ultrafast framing camera is discussed here because of its high technological maturity, successful commercialization, and wide implementation. In general, the ultrafast framing camera combines the operation of beam splitting with ultrafast gating (Section 26.2.1.2). In an example as shown in Figure 26.9a, a pyramidal beamsplitter with an octagonal base generates eight identical images. Each image is formed onto one time-gated intensified CCD camera. By precisely controlling the time gates of image intensification for each camera (i.e. via electronic gating), successive temporal slices are recorded. The advances of ultrafast electronics have enabled inter-frame time intervals as short as 10 ps and a gate time of 200 ps (Stanford Computer Optics 2017). The implementation of new optical design has increased the sequence depth to as much as 16 frames (Specialised Imaging 2017). The ultrafast framing camera can directly capture transient phenomena without the need for post-processing. However, the camera design imposes a conflict between the light throughput and the sequence depth.

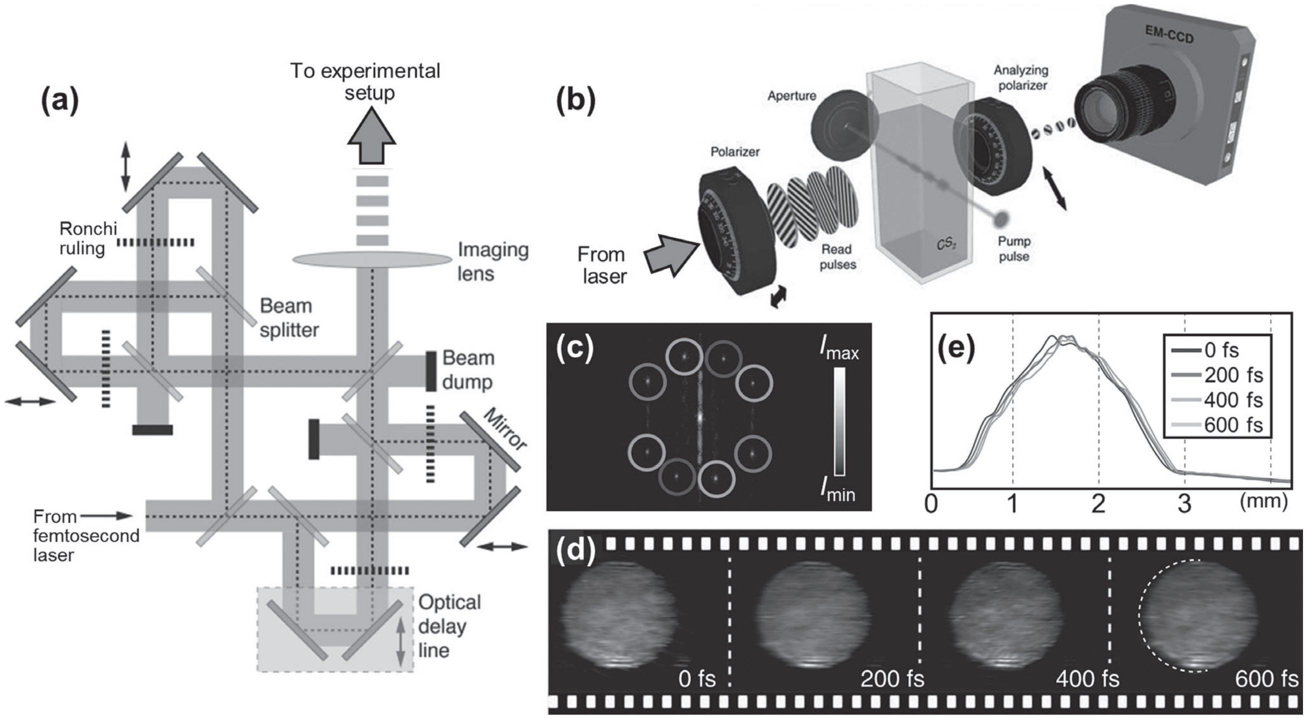

FIGURE 26.8 Frequency recognition algorithm for multiple exposures (FRAME) imaging system. (a) Principle of generating the four structured light-modulated probe pulses with tunable inter-frame time intervals. (b) Experimental set-up of imaging a propagating femtosecond light pulse using FRAME. (c) 2D Fourier transform of an acquired image. (d) Reconstructed images of a propagating laser beam at 5 Tfps. (e) Vertically summed intensity profiles of (d). (Reprinted and edited from Macmillan Publishers Ltd: *Light: Science & Applications* (Ehn et al. 2017) with permission from the authors and under a Creative Commons license.)

The ultrafast framing camera has been widely used in the studies of fluid dynamics, materials science, and ballistic testing (Versluis 2013; Xing et al. 2017). Figure 26.9b shows the process of primary streamer initiation when a 10-μs, 16-kV-voltage electrical pulse was applied to a needle electrode in ultrapure water (Fujita et al. 2013), captured by an ultrafast framing camera at 100 Mfps. The movie revealed that a shadow region was generated at the tip of the electrode before the beginning of the primary streamer, which propagated hemispherically with a constant velocity of 2.5 km s^{-1}.

26.3.2.2 Computational Reconstruction

Computational techniques are teamed up with the existing ultrafast point detector or one-dimensional imagers to enable single-shot 2D ultrafast dynamic imaging. This synergy has significantly enhanced these devices' performance and application scopes. However, computational reconstruction increases the system complexity. In addition, these techniques often trade other system parameters, such as spatial resolution, with sequence depth. As an example, compressed ultrafast photography (CUP) (Gao et al. 2014) is schematically shown in Figure 26.10a. A 2D dynamic scene is first imaged to a digital micromirror device (DMD)—a binary amplitude SLM (Liang et al. 2012). A pseudo-random binary mask is loaded to the DMD for spatial encoding. The spatially encoded scene is then relayed to the entrance port of a streak camera. Different from the conventional operation where the slit has a micrometre-level width (Figure 26.5a), for CUP, the entrance port is fully opened to 5 mm. Inside the streak camera, the scene experiences the same process as described in Section 26.2.2.2. Finally, the spatially encoded, temporally sheared scene is recorded by an internal sensor in the streak camera.

CUP exploits the compressed sensing to add another spatial dimension into the conventional streak camera. The conventional operation of the streak camera forbids any mixture of the spatial information on the *y*-axis and the temporal information, which restricts ultrafast imaging to 1D. CUP, however, uses the spatial encoding and temporal shearing to tag each frame with a spatiotemporal "barcode". This prior information, along with the sparsity in the dynamic scene, facilitates the unmixing of frames in image reconstruction. The resultant CUP provides a single-shot passive 2D ultrafast optical imaging at 100 Gfps and with an effective exposure time of ~50 ps (Zhu et al. 2016). Because of the mixture of spatial and temporal information on the *y*-axis, CUP trades spatial resolution and spatial isotropy with sequence depth.

CUP has been implemented in various applications. First, it has enabled the first-ever real-time visualization of many light-speed phenomena, including single laser pulses' reflection, refraction (Figure 26.10b), and faster-than-light propagation of non-information (Gao et al. 2014). Recently, it has also enabled a single-shot real-time imaging of the formation and propagation of the photonic Mach cone (Figure 26.10c) (Liang et al. 2017). Extended from the (*x*, *y*, *t*) imaging, CUP has enabled 4D imaging. First, a ToF LIDAR has been developed from CUP (Liang et al. 2015). Capturing (*x*, *y*, *z*, *t*) information, the ToF-CUP system has imaged dynamic 3D objects

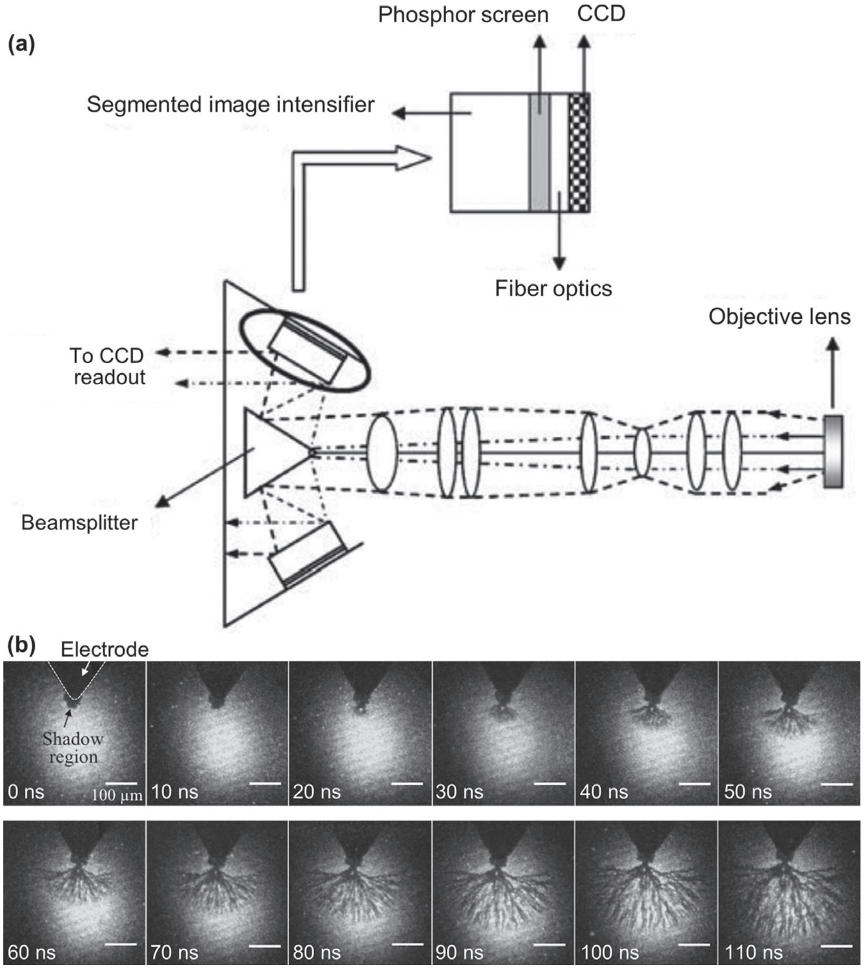

FIGURE 26.9 Ultrafast framing camera. (a) Schematic of the side view. (Reprinted from (Tiwari et al. 2007), with the permission of Springer.) (b) Time-resolved streamer initiation process imaged at 100 Mfps. (Reprinted from (Fujita et al. 2013), with the permission of AIP Publishing.)

at 75 volumes per second, making it one of the fastest single-shot ToF LIDAR cameras. Figure 26.10d illustrates this application using a two-ball object rotating at 150 revolutions per minute. In addition, CUP has been further updated for (x, y, t, λ) imaging. This unique capability enabled a single-shot spectrally resolved fluorescence lifetime mapping (Gao et al. 2014). Figure 26.10e shows a pulsed laser-pumped fluorescence emission process captured by CUP. A single 7-ps laser pulse excited Rhodamine 6G dye in a cuvette. The CUP system clearly captured the fluorescence emission and quantified the fluorescence lifetime.

26.4 Summary and Outlook

This chapter briefly reviews nine representative methods of ultrafast optical imaging from the aspects of their underlying principles, typical systems and applications, as well as their fortes and limitations. This information is summarized in Table 26.1. In practice, researchers could use this table as a general guideline to select the most suitable technique for their specific studies. It is noted that the comparison of spatial resolution is also included for the purpose of completeness. This parameter is not detailed in Sections 26.2 and 26.3 due to its strong dependence on the choice of front optics (such as camera lens and microscope objectives). Here, the comparison lists only the major factors that limit the spatial resolution.

It is undoubted that ultrafast optical imaging will continue evolving in future. Ultrafast optical imaging is established downstream of laser sciences, advanced manufacturing and device sciences, non-linear optics, imaging theory, and novel computational and mathematical modelling. The fast progress in these areas will, therefore, improve the technological levels and foster new imaging techniques. In the following, three future perspectives about the system development are proposed.

First, the advent of new devices will further enhance performances of ultrafast optical imaging systems. For example, novel lasers that generated tunable few-cycle laser pulses across the optical spectral range will enable higher temporal resolution in pump probe experiments (Schmidt et al. 2014). In addition, the development of large-format single-photon avalanche detectors (Gariepy et al. 2015) and multidimensional TCSPC modules (Niehörster et al. 2016) will enable a wide-field fluorescence lifetime imaging and a wide-field Förster resonance energy transfer imaging. Moreover, femtosecond streak camera (Hamamatsu 2017) will significantly improve

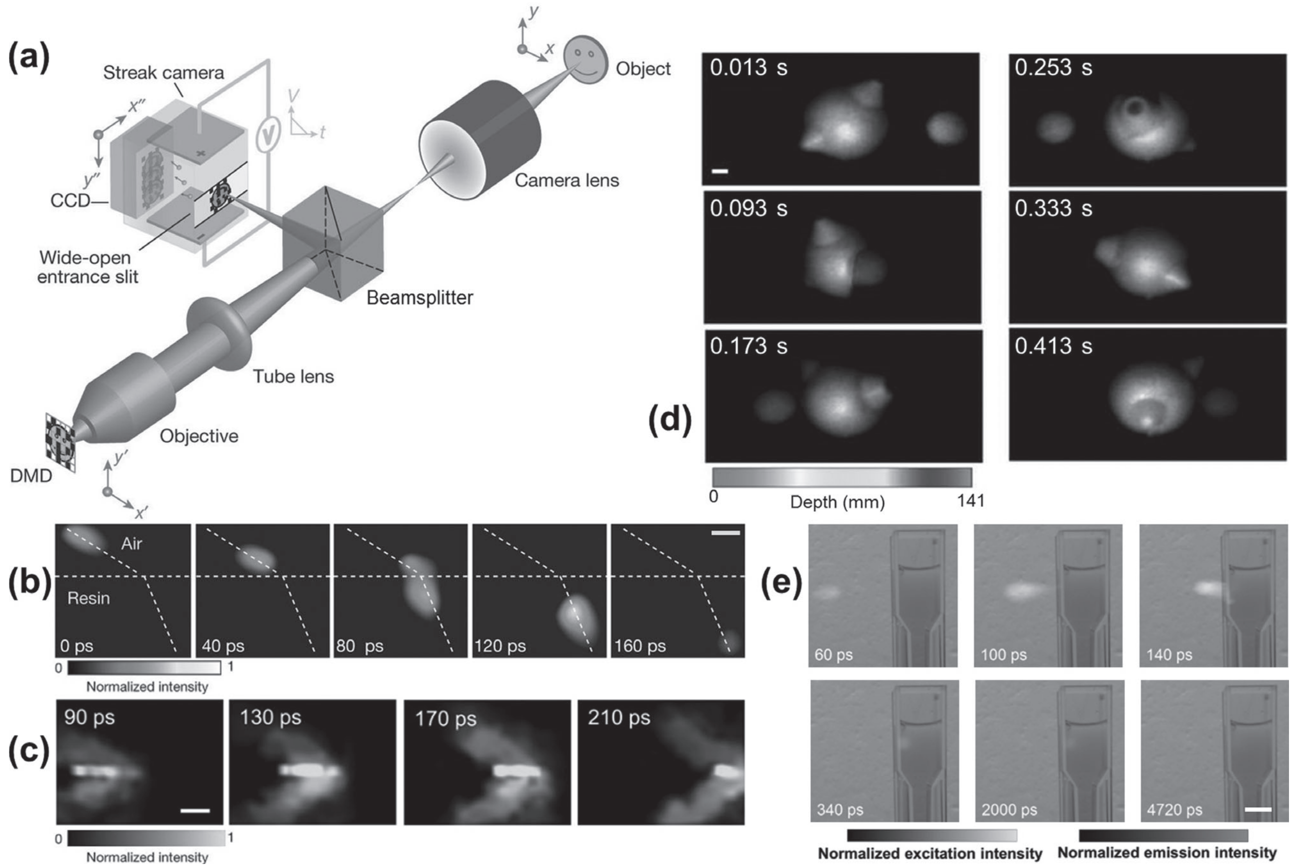

FIGURE 26.10 Compressed ultrafast photography (CUP) for single-shot real-time ultrafast optical imaging. (a) Schematic of CUP. DMD: digital micromirror device. (b) CUP of a single laser pulse's refraction. (c) CUP of a propagating photonic Mach cone. (d) ToF-CUP of dynamic volumetric imaging. (e) CUP of spectrally resolved pulse laser-pumped fluorescence emission. Scale bars in (b–e), 10 mm. ((a), (b), and (e) are reprinted and edited by permission from Macmillan Publishers Ltd: *Nature* (Gao et al. 2014), copyright 2014. (c) is reprinted and edited from *Science Advances* (Liang et al. 2017) with permission to use under a Creative Commons license. (e) is reprinted and edited from *Scientific Report* (Liang et al. 2015) with permission to use under a Creative Commons license.)

the depth resolution in ToF ranging. Finally, the implementation of volume holograms (Hill et al. 1995) and diffraction gratings will largely enhance the sequence depth of the STAMP and the FRAME technologies.

Second, computer-augmented ultrafast optical imaging represents an emerging trend. Optical realization of mathematical models transfers some unique advantages in these models into the ultrafast optical imaging systems and thus could overcome the hardware limitations in imaging size, sensitivity, and speed. In this chapter, six out of nine methods involve computational post-processing to either reconstruct images or improve image quality. It is therefore predicted that many established image reconstruction algorithms that have been implemented in X-ray CT, magnetic resonance imaging, and ultrasound imaging will find applications in the newly developed ultrafast optical imaging instruments.

Finally, high-dimensional ultrafast optical imaging is an important future direction. Many transient events may not be reflected in light intensity. Therefore, the ability to measure other photon tags—for example, the polarization and the propagation direction—will significantly enhance the ability and application scopes of ultrafast optical imaging systems. This requirement will promote the integration of other imaging modality (e.g. volumography, spectroscopy, and light-field photography) into ultrafast optical imaging. The ability to capture high-dimensional datacubes should become the next milestone in system development in ultrafast optical imaging.

Besides the system development, it is envisaged that more novel applications will be enabled with the advances in ultrafast optical imaging. Ultrafast optical imaging used to face a "catch-22" situation: little effort was made to explore applications without the availability of viable ultrafast optical imaging techniques, while no strong motivation in system development could be generated without identifying a "killer application". Recently, blooming of novel ultrafast imaging techniques is vital for improving research capabilities and opening up new research directions. For example, attosecond molecular dynamics (Lépine et al. 2014) can be monitored by brighter attosecond transient absorption imaging. In addition, ultrafast imaging may assist in the investigation of light–matter interaction in transparent media, whose underlying physics remains elusive (Jing et al. 2016). Finally, with an improved sensitivity, the single-shot ultrafast optical imaging may enable the first-ever real-time observation of neural activities (Vogt 2015).

TABLE 26.1

Comparative Summary of Representative Ultrafast Optical Imaging Techniques

Imaging Technique	Number of Exposures	Acquisition Strategy	Reconstruction Strategy	Temporal Resolution	Imaging Speed	Sequence Depth	Spatial Resolution	Light Throughput
Femtosecond pulse probing	Multiple-shot	Active probing	Direct imaging	50 fs	20 Tfps (stitching)	>100[a]	Diffraction-limited	100%
Non-linear optical gating	Multiple-shot	Passive detection	Direct imaging[b]	100 fs	10 Tfps (stitching)	>100[a]	Diffraction-limited	τ_g/τ_s [c]
First-photon imaging	Multiple-shot	Passive detection	Direct imaging[d]	~30 ps	125 Gfps (stitching)	>100[a]	Denoising in reconstruction	N_p/N_t [e]
Streak camera	Multiple-shot	Passive detection	Direct imaging[f]	100 fs	10 Tfps (stitching)	>100[a]	Electronic imaging blurring	100% [g]
SS-FDT	Single-shot	Active probing	Computational reconstruction	~3 ps	>1 Tfps (real time)	50–100[a]	Angular density of probe pulses	100%
STAMP	Single-shot	Active probing	Direct imaging	733 fs	4.4 Tfps (real time)	6[h]	Diffraction-limited	100% [h]
FRAME	Single-shot	Active probing	Computational reconstruction	125 fs	5 Tfps (real time)	4	Spatial frequency bandwidth	100%
Ultrafast framing camera	Single-shot	Passive detection	Direct imaging	200 ps	100 Gfps (real time)	16	Image intensifier blurring	$\frac{\tau_g}{\tau_s}$
CUP	Single-shot	Passive detection	Computational reconstruction	~50 ps	100 Gfps (real time)	>100[a]	Spatiotemporal mixing	100%[i]

[a] Only the general range of the state of the art is given. The specific number is system dependent.

[b] The TGOPT system (Section 26.2.1.2) computationally reconstructs images.

[c] τ_g and τ_s are the width of ultrafast gating and that of the transient event, respectively.

[d] First-photon imaging (Section 26.2.2.1) used computational post-processing to enhance the image quality.

[e] N_p and N_t are the number of processed photons in one acquisition and the total number of emitted photon from the transient event, respectively.

[f] The streak camera-based ultrafast imaging around the corner (Section 26.2.2.2) used computational reconstruction to determine the depth location.

[g] For line illumination and neglect the photon loss due to a limited numerical aperture.

[h] Recently, a sequence depth of 25 is demonstrated in a new STAMP system with, however, a lower light throughput (Suzuki et al. 2017).

[i] The first-generation CUP system has a 12.5% light throughput (Gao et al. 2014). 100% light throughput is achieved in lossless-encoding CUP system (Liang et al. 2017).

REFERENCES

Allen, J. B. & Larry, R. F. 2001. *Electrochemical Methods: Fundamentals and Applications*, John Wiley & Sons, Inc., Hoboken, NJ.

Becker, W. 2014. *The Bh TCSPC Handbook*, Becker & Hickl, Berlin.

Chitnis, D. & Collins, S. 2014. A SPAD-based photon detecting system for optical communications. *Journal of Lightwave Technology* 32: 2028–2034.

Corkum, P. B. & Krausz, F. 2007. Attosecond science. *Nature Physics* 3: 381.

Diels, J.-C. & Rudolph, W. 2006. *Ultrashort Laser Pulse Phenomena*, Academic Press, Cambridge, MA.

Ehn, A., Bood, J., Li, Z., et al. 2017. FRAME: Femtosecond videography for atomic and molecular dynamics. *Light: Science & Applications* 6: e17045.

Feurer, T., Vaughan, J. C., Koehl, R. M. & Nelson, K. A. 2002. Multidimensional control of femtosecond pulses by use of a programmable liquid-crystal matrix. *Optics letters* 27: 652–654.

Feurer, T., Vaughan, J. C. & Nelson, K. A. 2003. Spatiotemporal coherent control of lattice vibrational waves. *Science* 299: 374–377.

Fieramonti, L., Bassi, A., Foglia, E. A., et al. 2012. Time-gated optical projection tomography allows visualization of adult zebrafish internal structures. *PLoS One* 7: e50744.

Fujita, H., Kanazawa, S., Ohtani, K., Komiya, A. & Sato, T. 2013. Spatiotemporal analysis of propagation mechanism of positive primary streamer in water. *Journal of Applied Physics* 113: 113304.

Fuller, P. W. W. 2009. An introduction to high speed photography and photonics. *The Imaging Science Journal* 57: 293–302.

Gaffney, K. J. & Chapman, H. N. 2007. Imaging atomic structure and dynamics with ultrafast X-ray scattering. *Science* 316: 1444–1448.

Gao, L., Liang, J., Li, C. & Wang, L. V. 2014. Single-shot compressed ultrafast photography at one hundred billion frames per second. *Nature* 516: 74–77.

Gariepy, G., Krstajic, N., Henderson, R., et al. 2015. Single-photon sensitive light-in-fight imaging. *Nature Communications* 6: 6021.

Goda, K., Tsia, K. & Jalali, B. 2009. Serial time-encoded amplified imaging for real-time observation of fast dynamic phenomena. *Nature* 458: 1145–1149.

Gordon, R., Bender, R. & Herman, G. T. 1970. Algebraic reconstruction techniques (ART) for three-dimensional electron microscopy and X-ray photography. *Journal of Theoretical Biology* 29: 471IN1477–476IN2481.

Gorkhover, T., Schorb, S., Coffee, R., et al. 2016. Femtosecond and nanometre visualization of structural dynamics in superheated nanoparticles. *Nature Photonics* 10: 93–97.

Hamamatsu 2017. *FESCA-100 Femtosecond streak camera* [Online] Available: https://www.hamamatsu.com/us/en/product/alpha/F/5044/C11853-01/index.html [Accessed 12/31/2017].

Hill, K. B., Purchase, K. G. & Brady, D. J. 1995. Pulsed-image generation and detection. *Optics Letters* 20: 1201–1203.

Imada, M., Fujimori, A. & Tokura, Y. 1998. Metal-insulator transitions. *Reviews of Modern Physics* 70: 1039.

Jing, C., Wang, Z. & Cheng, Y. 2016. Characteristics and applications of spatiotemporally focused femtosecond laser pulses. *Applied Sciences* 6: 428.

Kirmani, A., Venkatraman, D., Shin, D., et al. 2014. First-photon imaging. *Science* 343: 58–61.

Lépine, F., Ivanov, M. Y. & Vrakking, M. J. 2014. Attosecond molecular dynamics: Fact or fiction? *Nature Photonics* 8: 195–204.

Li, Z., Zgadzaj, R., Wang, X., Chang, Y.-Y. & Downer, M. C. 2014. Single-shot tomographic movies of evolving light-velocity objects. *Nature Communications* 5: 3085.

Liang, J., Gao, L., Hai, P., Li, C. & Wang, L. V. 2015. Encrypted three-dimensional dynamic imaging using snapshot time-of-flight compressed ultrafast photography. *Scientific Reports* 5: 15504.

Liang, J., Ma, C., Zhu, L., et al. 2017. Single-shot real-time video recording of photonic Mach cone induced by a scattered light pulse. *Science Advances* 3: e1601814.

Liang, J., Wu, S.-Y., Kohn, R. N., Becker, M. F. & Heinzen, D. J. 2012. Grayscale laser image formation using a programmable binary mask. *Optical Engineering* 51: 108201.

Nakagawa, K., Iwasaki, A., Oishi, Y., et al. 2014. Sequentially timed all-optical mapping photography (STAMP). *Nature Photonics* 8: 695–700.

Niehörster, T., Löschberger, A., Gregor, I., et al. 2016. Multi-target spectrally resolved fluorescence lifetime imaging microscopy. *Nature Methods* 13: 257–262.

Patwardhan, S. V. & Culver, J. P. 2008. Quantitative diffuse optical tomography for small animals using an ultrafast gated image intensifier. *Journal of Biomedical Optics* 13: 011009-1–011009-7.

Pawlikowska, A. M., Halimi, A., Lamb, R. A. & Buller, G. S. 2017. Single-photon three-dimensional imaging at up to 10 kilometers range. *Optics Express* 25: 11919–11931.

Schmidt, B. E., Thiré, N., Boivin, M., et al. 2014. Frequency domain optical parametric amplification. *Nature Communications* 5: 3643.

Specialised Imaging 2017. *SIMD - Ultra High Speed Framing Camera*. [Online] Available: http://specialised-imaging.com/products/simd-ultra-high-speed-framing-camera [Accessed 11/19/2017].

Stanford Computer Optics 2017. *XXRapidFrame: Multiframing ICCD camera* [Online] Available: http://www.stanfordcomputeroptics.com/download/Brochure-XXRapidFrame.pdf [Accessed 11/29/2017].

Suzuki, T., Hida, R., Yamaguchi, Y., et al. 2017. Single-shot 25-frame burst imaging of ultrafast phase transition of Ge2Sb2Te5 with a sub-picosecond resolution. *Applied Physics Express* 10: 092502.

Szczesniak, T., Moszynski, M., Swiderski, L., et al. 2007. Fast photomultipliers for TOF PET. *Nuclear Science Symposium Conference Record, 2007. NSS'07.* IEEE, 2651–2659.

Tiwari, V., Sutton, M. & Mcneill, S. 2007. Assessment of high speed imaging systems for 2D and 3D deformation measurements: Methodology development and validation. *Experimental Mechanics* 47: 561–579.

Velten, A., Willwacher, T., Gupta, O., et al. 2012. Recovering three-dimensional shape around a corner using ultrafast time-of-flight imaging. *Nature Communications* 3: 745.

Versluis, M. 2013. High-speed imaging in fluids. *Experiments in Fluids* 54: 1458.

Vogt, N. 2015. Voltage sensors: challenging, but with potential. *Nature Methods* 12: 921–924.

Wang, L., Ho, P., Liu, C., Zhang, G. & Alfano, R. 1991. Ballistic 2-D imaging through scattering walls using an ultrafast optical Kerr gate. *Science* 253: 769–771.

Weiner, A. 2011. *Ultrafast Optics*, John Wiley & Sons, Hoboken, NJ.

Xing, H., Zhang, Q., Braithwaite, C. H., Pan, B. & Zhao, J. 2017. High-speed photography and digital optical measurement techniques for geomaterials: Fundamentals and applications. *Rock Mechanics and Rock Engineering* 50: 1611–1659.

Zewail, A. H. 2006. 4D ultrafast electron diffraction, crystallography, and microscopy. *Annual Review of Physical Chemistry* 57: 65–103.

Zhang, X. C. 2002. Terahertz wave imaging: Horizons and hurdles. *Physics in Medicine & Biology* 47: 3667.

Zhu, L., Chen, Y., Liang, J., et al. 2016. Space- and intensity-constrained reconstruction for compressed ultrafast photography. *Optica* 3: 694–697.

27

Transient Absorption Microscopy Measurements of Single Nanostructures

Gary Beane, Tuphan Devkota, Brendan S. Brown, and Gregory V. Hartland

CONTENTS

27.1 Introduction 329
27.2 Experimental Methods 330
  27.2.1 Laser Systems for Transient Absorption Microscopy 330
  27.2.2 Optical Components and Signal Detection 331
  27.2.3 Signal-to-Noise Considerations 332
27.3 Dynamics of Single Nanostructures 333
27.4 Summary and Future Directions 335
Acknowledgements 336
References 336

27.1 Introduction

Ultrafast spectroscopy is a valuable tool for studying the properties of materials. For nanomaterials, which are the focus of this chapter, ultrafast transient absorption experiments have generated a unique information about the energy relaxation processes for the excited charge carriers in semiconductor nanocrystals (Klimov 2007), the size dependence of the timescales for electron–electron and electron–phonon coupling in metal nanoparticles (Voisin et al. 2001), and how energy is transferred from the particles to the environment (Hartland 2011). This information is important for applications such as the development of quantum dot lasers (Klimov et al. 2000) and understanding the mechanism of plasmon-enhanced photocatalysis (Brongersma et al. 2015; Linic et al. 2011). The experimental apparatus and the procedure used for ensemble transient absorption measurements of nanomaterials are the same as those for experiments with molecular systems. Nevertheless, there is an important difference between nanomaterial samples compared to molecular samples: for molecular systems, all the entities in the sample are identical, whereas for nanomaterials, there is almost always a distribution of sizes and shapes. This means that experiments on nanomaterials suffer from inhomogeneous broadening effects.

In molecular systems, inhomogeneous broadening can arise from the different environments experienced by different molecules in the sample (Jonas 2003). However, the distribution of sizes in nanoparticle samples adds additional complexity and can often completely obscure information about dynamics. An example from the spectroscopy of metal nanoparticles where inhomogeneous broadening has a significant (and unwanted) effect is studies of the linewidth of the localized surface plasmon resonance (LSPR) (Mock et al. 2002; Sonnichsen et al. 2002). Ensemble spectral measurements can give reliable information about how the frequency of the LSPR depends on the size, shape, and/or surface chemistry of the particles (Sun and Xia 2003), but the linewidths are strongly affected by the sample size distribution (Hartland 2011; Sonnichsen et al. 2002). This means that the linewidth information from ensemble experiments does not give a reliable estimate of the LSPR dephasing time.

In principle, advanced techniques such as two-dimensional spectroscopies can be used to unravel homogeneous and inhomogeneous effects in ultrafast experiments (Mukamel 2000). These experiments have been very successful for the studies of molecular systems, such as dye molecules in solution (Jonas 2003), light-harvesting proteins from photosynthetic systems (Collini et al. 2010; Engel et al. 2007), and 2D semiconductor materials (Pogna et al. 2016). On the other hand, for nanoparticles, a more straightforward approach is to perform ultrafast measurements on single nanostructures (Muskens et al. 2006; van Dijk et al. 2005). This directly removes problems from the distribution of sizes and shapes in the sample, and also removes effects from differences in the environment for different particles. These experiments work for several reasons: firstly, semiconductor and metal nanostructures absorb light very strongly, with absorption cross sections on the order of or exceeding their physical cross sections (Kelly et al. 2003). For example, a 20-nm diameter Au nanoparticle will absorb about 2% of the light from a tightly focused laser beam when the laser is tuned to the maximum of the LSPR. This is sufficient to produce a measurable transient absorption signal (Lo et al. 2013a). As will be discussed in detail below, the small signal levels for single particle experiments mean that many photons have to be counted, which implies that the samples must also be stable. In general, this is not a problem – transient absorption microscopy experiments have been performed on a variety of metal and semiconductor nanostructures, including

Au (van Dijk et al. 2005), Ag (Muskens et al. 2006), II-VI nanowires (Carey et al. 2009), single-walled carbon nanotubes (Gao et al. 2012), Si nanowires (Grumstrup et al. 2014a), and two-dimensional materials such as graphene (Huang et al. 2010) MoS_2 (Shi et al. 2013), and perovskites (Guo et al. 2017).

The remainder of this chapter is arranged as follows: in Section 27.2, a detailed description of the apparatus used for transient absorption microscopy is given. This section includes a discussion of signal averaging considerations for these experiments. In Section 27.3, some selected applications are presented and discussed. The applications include experiments where transient absorption traces from a single nanostructure are recorded to study energy relaxation processes, and imaging experiments that provide information about the motion of electrons and holes in semiconductor nanostructures, and surface plasmon polaritons (SPPs) in metal nanostructures (Beane et al. 2019). Note that transient absorption microscopy is not the only way to study the ultrafast dynamics of single nanoparticles. A number of groups have developed instruments that use X-ray or electron probe beams (Clark et al. 2013; Dabrowsid et al. 2017; Frank et al. 2017; Valley et al. 2016), or that detect the near-field optical signals from the nanoparticles (Nishiyama et al. 2015). These sophisticated measurements can provide an improved spatial resolution compared to transient absorption microscopy, which is limited by diffraction of the pump and probe beams. However, these experiments are harder to implement and are less flexible than transient absorption microscopy, and will not be discussed in detail here. The final section of this chapter describes some future directions for this field of science.

27.2 Experimental Methods

27.2.1 Laser Systems for Transient Absorption Microscopy

Figure 27.1 shows a schematic diagram of the transient absorption microscopy system developed in the authors' laboratory (Devadas et al. 2015). The heart of the system is a high-power ultrafast Ti:Sapphire laser that pumps an optical parametric oscillator (OPO). The Ti:Sapphire laser system at the University of Notre Dame can produce wavelengths between 1080 and 680 nm, and the fundamental can be frequency-doubled to give visible/near-UV laser pulses with wavelengths between 540 and 340 nm. The OPO produces signal and idler beams that have wavelengths between 1320 and 1050 nm (signal), and 3000 and 2200 nm (idler). Visible light between 660 and 525 nm can be produced from the OPO by intracavity second harmonic generation of the signal beam. Thus, this system can produce laser pulses with wavelengths between 3300 and 340 nm, which means that a variety of different materials can, in principle, be studied. Note that a drawback of this system is that the pump and probe wavelengths are not completely independent. For experiments where the second harmonic of the Ti:Sapphire laser is used as a pump and the fundamental is used as a probe, or vice versa, the two wavelengths are obviously related. This is also true for the OPO in the authors' laboratory – which is based on a bulk KTP crystal. For this system, the output wavelength is changed by changing the pump wavelength, which means that only certain wavelength combinations of the Ti:Sapphire fundamental and the OPO output are possible. Although this is not terrible, it illustrates that one needs to carefully consider the design of the laser system to ensure that the desired pump and probe wavelengths can be obtained. Note that improved OPO designs, such as systems based on periodically poled crystals, can generate independently tunable pump and OPO wavelengths.

The laser system at the University of Notre Dame produces high-power outputs (up to 1 W for the OPO and > 3 W for the Ti:Sapphire oscillator), which have to be heavily attenuated before the sample for studies of single nanoparticles. The typical powers used in our experiments are 50–200 μW for the pump and 10–50 μW for the probe at the sample, which correspond to pulse energies of 0.1 – 1 pJ/pulse. These energies are very low compared to the pulse energies in regular ensemble transient absorption experiments. However, the pump and probe beams are typically focused to diffraction-limited spots in transient absorption microscopy experiments, which means that high power densities are created. For example, a 50-μW, 800-nm beam focused to a diffraction-limited spot using a 1.3 numerical aperture (NA) objective has a time-averaged power density of ~70 kW cm^{-2}. This is much higher than what is typically used in confocal microscopic experiments, and increasing the power beyond this range can lead to sample damage. Because low pulse energies have to be used, the best choice of laser systems for these experiments are high repetition rate/low pulse energy systems, rather than low repetition rate/high pulse energy systems (such as amplified Ti:Sapphire lasers). Another advantage of high repetition rate, low pulse energy systems is that they have much lower pulse-to-pulse energy fluctuations than the amplified systems. For example, the root-mean-square (*RMS*) noise from a typical Ti:Sapphire oscillator is < 0.2% for a 20 MHz bandwidth. This is much better than what can be achieved with an amplified system.

A drawback of oscillator/OPO systems is that they cannot be used for materials with long excited-state lifetimes. The majority of commercial Ti:Sapphire oscillator systems produce a pulse every 12 ns or so, which means that the excited nanostructure must relax to its ground state within that time. This is not a problem with metal nanostructures, where the timescales for relaxation of the excited electrons and for energy dissipation into the surroundings are typically fast (Hartland 2011; Voisin et al. 2001). However, it can be an issue for semiconductor materials. For these systems, pulse pickers must be used to reduce the repetition rate of the pump and probe beams (Grumstrup et al. 2014a; Lo et al. 2012). An alternative is to use high repetition rate-amplified system. For example, chirped pulse-amplified (CPA) Yb lasers are now available that operate at 1030 nm with repetition rates up to 1 MHz. The output of these laser systems is very stable (rivalling oscillator systems), and tunable pump and probe beams can be produced using optical parametric amplification (OPA). The noise characteristics of OPAs are not as good as those of oscillator/OPO systems; however, high repetition rate CPA/OPA systems have been successfully used in a number of transient absorption microscopy experiments (Guo, et al. 2017). Thus, these systems are an attractive alternative to oscillator-based systems, especially because it is relatively easy to produce independently tunable pump and probe beams by using two OPAs. Note that transient absorption microscopy experiments have also been performed using a photonic crystal fibre to produce a broadband probe beam (Yi et al. 2017). These sources provide light over a wide range of wavelengths, and different colours in the continuum can be quickly selected with a minimal realignment of the system. This is very useful although these sources are noisier than OPOs or OPAs.

27.2.2 Optical Components and Signal Detection

In the majority of the transient absorption microscopy experiments that have been performed to date, different colour pump and probe beams have been used (Beane et al. 2019). This is because the pump beam can be easily extinguished after the sample using optical filters when the pump and probe wavelengths are different. There have been some experiments with degenerate pump and probe beams where polarization analysis was used to extinguish the pump (Masia et al. 2013). However, these measurements are more challenging to implement than two-colour experiments. For the studies of semiconductor materials, a visible/near-UV pump pulse is typically used with a near-IR probe beam (Carey et al. 2009; Grumstrup et al. 2014b). On the other hand, for the studies of metal nanostructures, a near-IR pump beam is often used in conjunction with a visible/near-UV probe (Beane et al. 2019; Muskens et al. 2006). This is because for metal nanostructures the highest sensitivity is obtained when the probe is tuned to the LSPR of the nanostructure (Hartland 2011). In either case, the pump beam is chopped at high frequency (greater than a few hundred kHz) using an acousto-optic or electro-optic modulator (van Dijk et al. 2005). The timing between the pump beam and the probe beam is controlled by sending one of these beams through a mechanical delay line (the probe beam in Figure 27.1). After the delay line, the pump and probe are recombined by a dichroic beam splitter, and focused at the sample by a high NA objective. It is important in these experiments to achieve a tight focus, which means that the pump and probe beams have to be expanded to fill the back aperture of the objective.

When a nanoparticle is at the focus of the objective, it absorbs pump laser photons, which changes the optical properties of the particle. This creates a small signal on the transmitted or reflected probe beam, and monitoring the signal as a function of pump probe delay time provides information about how energy is redistributed and dissipated in the system. Reflection-mode experiments are pictured in Figure 27.1. Transmission mode measurements can be performed by using a second object to collect and recollimate the probe beam. The polarizations of the pump and probe beams at the sample are controlled using quarter- or half-waveplates. For reflection-mode experiments, the probe beam is typically made circularly polarized using a quarter-waveplate, so that the back-reflected beam can be separated from the input beam with a polarizer. The transmitted or reflected probe beam is sent to a low-noise detector, typically an avalanche photodiode (APD), and the signal from the detector is monitored by a high-frequency lock-in amplifier that is referenced to the modulation frequency for the pump beam. A convenient way to do this is to use the internal reference of the lock-in to drive the device that is used to modulate the pump. The signal from the lock-in amplifier is then recorded as a function of the delay between the pump and probe beams. Note that it is important to completely extinguish the pump beam before the detector, as any pump photons that hit the detector will cause a background signal that increases the noise of the measurement. This can be done using combinations of dichroic mirrors and optical filters. Transient absorption images can be collected by fixing the timing between the pump and probe beams, and scanning the sample through the focus of the beams using a piezo stage. These experiments can provide information about how the dynamics vary spatially within a sample (Huang et al. 2010), which is important for developing devices.

An important application of transient absorption microscopy is to investigate the motion of excited species in different types of nanostructures – such as excitons and/or electrons and holes in semiconductors, or SPPs in metals (Beane et al. 2019).

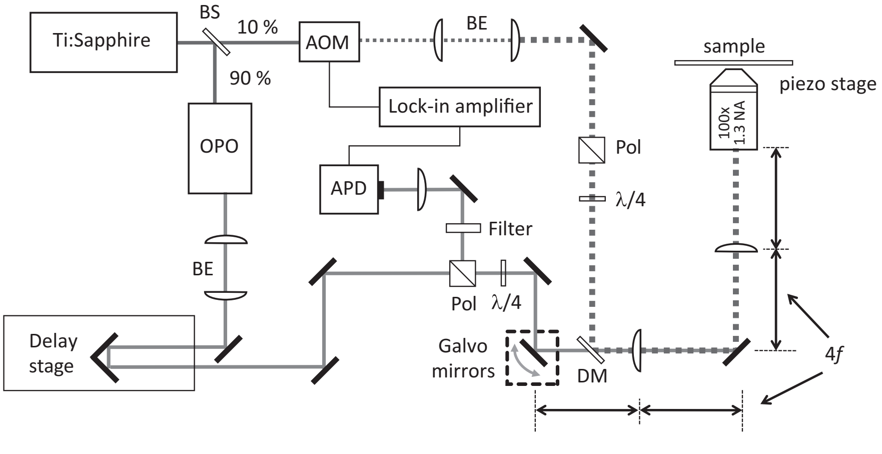

FIGURE 27.1 Diagram of the experimental apparatus for transient absorption microscopy (shown in reflection mode) using a Ti:Sapphire oscillator/OPO laser system. In this scheme, a near-IR pump beam is obtained by splitting off a small portion of the Ti:Sapphire fundamental (~10%) before the OPO. The majority of the fundamental pumps the OPO, and intracavity second harmonic generation is used to create a visible probe beam. BS: 90-10 beam splitter; BE: beam expander; DM: dichroic mirror; Pol: polarizer; $\lambda/4$ and $\lambda/2$: quarter- and half-waveplates, respectively; APD: avalanche photodiode; AOM: acousto-optic modulator; $4f = 4f$ lens system.

An effective way to do this is to perform experiments where the pump laser is focused at a specific point in the structure to generate the excited species, and the probe is scanned over the sample to form an image. For experiments with semiconductor nanostructures, recording images at different times provides information about how the excitons or electrons and holes diffuse away from the excitation region (Cui et al. 2014; Gabriel et al. 2013; Guo et al. 2017). For metal nanostructures, these experiments yield information about the propagation lengths of the SPPs (Yu et al. 2014). The most straightforward way to perform these experiments is to use motorized mirror mounts (Cui et al. 2014; Gabriel et al. 2013) or a galvo-scanning mirror system (Lo et al. 2013b; Yu et al. 2014) to change the angle that the probe beam enters the objective. Figure 27.1 shows the optical scheme for galvo-scanning mirrors. In this scheme, a 4*f* lens system is placed in between the galvo-scanning mirrors and the objective to ensure that the probe beam does not walk off the back aperture of the objective (Lo et al. 2013b). A concern with these experiments is that as the probe beam is scanned over the sample, it will experience different path lengths, which will change the timing. To test this, we performed experiments where the pump laser was focused at the end of a noble metal nanowire to excite propagating SPP modes, and the probe was positioned at different points along the nanowire to record transient absorption traces (Yu et al. 2014). Propagating SPPs move at approximately ½ the speed of light, which is essentially instantaneous in these measurements. The traces show no change in their form for distances up to 25 μm (the length of the nanowire), indicating that there is no change in pump probe timing in these experiments for images recorded over several tens of microns.

27.2.3 Signal-to-Noise Considerations

In a linear absorption experiment with a single nanostructure, the change in power P of the reflected or transmitted probe beam when it is scanned over a nanoparticle is proportional to the absorption cross section of the object being interrogated, divided by the area of the beam: $\Delta P/P = \sigma/A$ (Crut et al. 2014). A 20-nm diameter Au nanoparticle has an extinction cross section of approximately 500 nm^2 at the peak of its LSPR, which will produce a ~2% change in the power of a diffraction-limited probe beam. In transient absorption experiments, the signal is proportional to the change in cross section of the nano-object induced by the pump beam, that is, $\Delta P/P = \Delta\sigma/A$ (Beane et al. 2019; Crut et al. 2014). Given that the transient absorption signals from metal nanoparticles are typically 10^3–10^4 times smaller than the linear absorption of the sample, the signal level for a time-resolved experiment on a single 20-nm diameter Au particle is expected to be $\Delta P/P \approx 10^{-5} - 10^{-6}$. This is very small; however, noise levels of $\Delta P/P \lesssim 10^{-7}$ can be achieved with high repetition rate, low-noise Ti:Sapphire oscillator systems in conjunction with high-frequency modulation and lock-in amplifier detection. This means that a 20-nm diameter gold nanoparticles can be detected with a signal-to-noise ratio (SNR) of several hundred to one (Lo et al. 2013a).

To be more quantitative, there are, in general, four sources of noise in transient absorption experiments: 1/*f* noise from the detection electronics $(\sigma_{1/f})$, "dark" noise from the detector (σ_{det})), fluctuations in the pump and probe laser intensities (σ_{laser}), and "shot noise", which is the statistical noise from counting photons (σ_{shot}). The 1/*f* noise from the detection electronics can be greatly reduced by collecting the signal with high-frequency modulation. Thus, the total noise in a transient absorption microscopy experiment is given by $\sigma = \sqrt{\sigma_{\text{det}}^2 + \sigma_{\text{shot}}^2 + \sigma_{\text{laser}}^2}$ (van Dijk et al. 2007). These different contributions scale with laser power in different ways. The detector noise is independent of the laser power and is defined by the noise-equivalent power (NEP) of the detector. For the APDs used in our experiments, this is on the order of 0.5–1.0 pW/$\sqrt{\text{Hz}}$. The shot noise contribution scales as the square root of the laser power and is given by $\sqrt{2Bh\nu P}$, where B is the measurement bandwidth (van Dijk et al. 2007). For a 530 nm probe wavelength, the shot noise is $\sigma_{\text{shot}} = 0.87\sqrt{P}$ pW/$\sqrt{\text{Hz}}$ for P in μW. The amplification process of the APD also contributes to the shot noise, and can be included by multiplying $(\sigma_{\text{shot}})^2$ by an excess noise factor F (van Dijk et al. 2007). The contribution from laser fluctuations is proportional to the power and can be written as $\sigma_{\text{laser}} = n_{\text{laser}}P$. Laser noise is usually reported by laser manufacturers as a percentage *RMS* noise over a specific bandwidth, which is related to n_{laser} by $n_{\text{laser}} = \left(RMS/\sqrt{B}\right)$, where B is now the bandwidth of the noise measurement. The typical *RMS* noise for a commercial Ti:Sapphire oscillator is 0.15% for a 20 MHz bandwidth, which gives $\sigma_{\text{laser}} = 0.34P$ pW/$\sqrt{\text{Hz}}$ for P in μW.

Transient absorption experiments are always performed at powers well above the NEP of the detector, which means that the noise in the experiments is determined by σ_{shot} and σ_{laser}. Interestingly, these two contributions have similar magnitudes for the typical probe powers used in transient absorption microscopy (several to tens of μW at the detector). Thus, whether the noise is determined by σ_{shot} or σ_{laser} depends on the details of the experiment: the pulse-to-pulse stability of the pump and probe lasers, the excess noise of the APD, and the probe power. As discussed above, the signal in a transient absorption microscopy experiments is given by $\Delta P = (\Delta\sigma/A)P$. Thus, the SNR is given by $\text{SNR} = (\Delta\sigma/A)\sqrt{\Delta t}/\sqrt{2Fh\nu/P + (n_{\text{laser}})^2}$, where Δt is the averaging time. This equation illustrates an important point about these experiments: if the noise is dominated by shot noise, then increasing the probe power increases the SNR (counting more photons improves the SNR). On the other hand, if laser noise is dominant, increasing the probe power has no effect on the noise level (both the signal and the noise are proportional to the probe power). Figure 27.2 shows an example of images of a single CdSe nanowire recorded at different probe laser powers (Lo et al. 2013a). These experiments were performed with 400 nm pump and 800 nm probe wavelengths, using a pulse picker to reduce the repetition rate of the laser system to 5 MHz. In these experiments, the pump and probe beams were spatially and temporally overlapped to give the maximum signal. SNR increases with increasing probe power, demonstrating that the experiments are shot noise-limited. Note that pulse pickers can introduce additional noise into the experiments, which has the same properties as laser noise. This noise can be reduced by splitting the probe into signal and reference beams, and using a balanced detector to divide the signal by the reference (Gabriel et al. 2013).

Note that relatively high probe laser powers were used in the experiments in Figure 27.2. This is possible because the probe

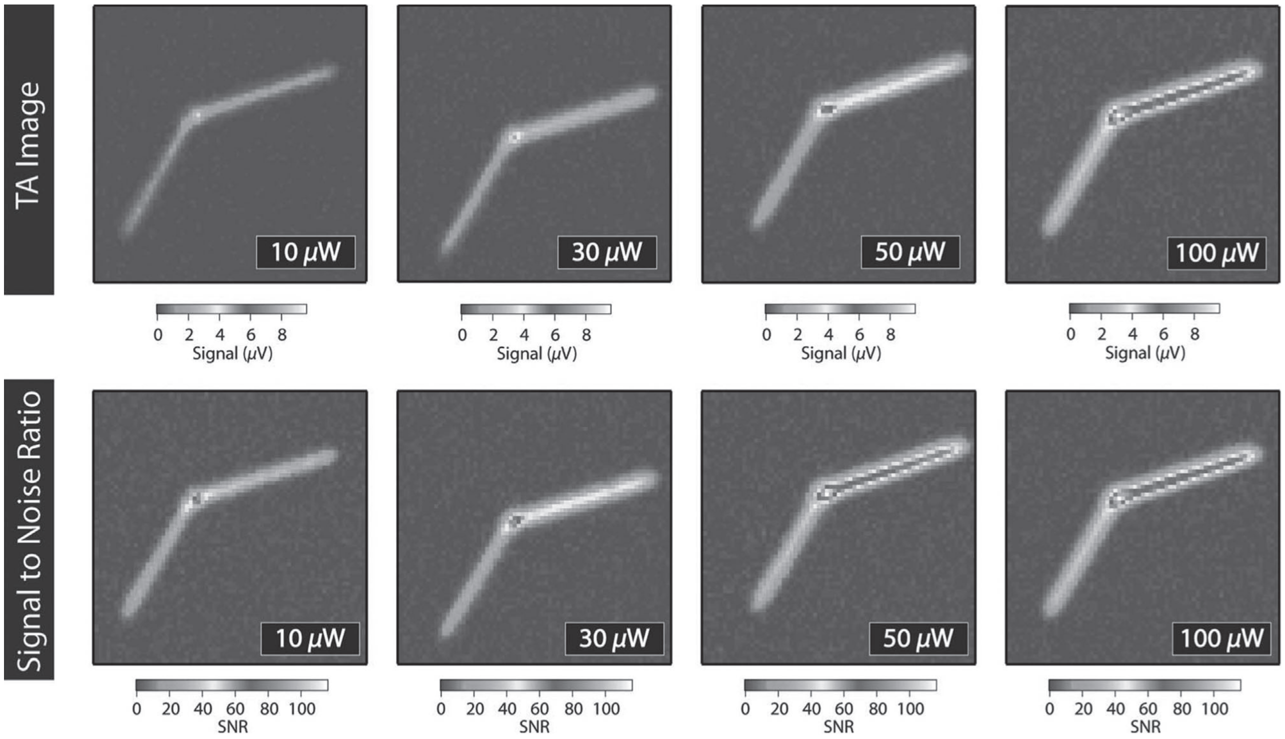

FIGURE 27.2 Transient absorption images ($7 \times 7\,\mu m^2$ image size) of a single-branched CdSe nanowire recorded with 1.5 μW pump power at the sample, and different probe laser powers. Extinction measurements show that the two arms of the nanowire are both ca. 48 nm thick. Top: lock-in signal; bottom: signal-to-noise ratios for the transient absorption images. (Reproduced from Lo et al. 2013a with permission from The Royal Society of Chemistry.)

laser is not resonant to any transitions in the linear absorption spectrum of the nanowire in these experiments (i.e., the probe by itself is not absorbed by the sample and, thus, high probe powers do not lead to photodamage). This is not the case for experiments on metal nanoparticle where the probe is resonant, or nearly resonant, to the LSPR, so that high probe powers can damage the samples. In contrast to the probe beam, the pump laser is always resonant to some feature in the linear absorption spectrum of the sample (there must be some absorption of the pump beam to create a transient absorption signal). Thus, care must be taken to ensure that the pump power is below the damage threshold of the sample.

As discussed earlier, the SNR shows that in general the power of the probe beam should be increased to the point where shot noise becomes irrelevant compared to laser noise (provided this does not damage the sample). Once this is achieved, further increases in the probe power will not change the SNR (Grumstrup et al. 2014b; van Dijk et al. 2007). Increasing the pump power also increases the SNR. However, there are two considerations for the pump beam. Firstly, as noted above, the power must be kept below the damage threshold. Secondly, many photophysical processes in nanomaterials are sensitive to the number of absorbed pump laser photons. For semiconductor nanostructures, the examples of power-dependent processes include Auger recombination (Klimov 2007) and trap state filling (see Figure 27.3). For metals, the timescales for electron–phonon coupling depend on the pump power (Hartland 2011; Voisin et al. 2001). Thus, low pump laser powers should be used to study processes such as electron–phonon coupling in metal nanostructures, or charge carrier trapping in semiconductors.

27.3 Dynamics of Single Nanostructures

Three different types of measurements are possible with transient absorption microscopy: (i) conventional transient absorption experiments where a time-resolved trace is collected from a single nanoparticle, or at a single point in an extended nanostructure, such as a nanowire or a nanoplate; (ii) imaging experiments where the pump and probe are spatially overlapped and the sample is scanned through the focus to form an image; and (iii) measurements where the pump laser is focused at a specific point in the sample, and the probe laser is scanned over the sample to form an image. Conventional transient absorption measurements provide information about energy relaxation processes within nanoparticles, and how energy is transferred to the environment. The imaging experiments generate information about how the dynamics vary spatially within a nanostructure, and can also be used to study the motion of excitons or plasmons within a nanostructure (Beane et al. 2019). In the following, examples are given of the conventional transient absorption experiments where a time-resolved trace is collected at a single point in a nanowire, and fixed pump-scanned probe imaging experiments. Examples of imaging experiments with spatial overlapped pump and probe beams are shown in Figure 27.2.

Figure 27.3 shows transient absorption traces for two different, single CdTe nanowires (Lo et al. 2012). The experiments were performed with near-UV pump and near-IR probe pulses at a 5 MHz repetition rate, similar to the experiments in Figure 27.2. The data shows a biexponential decay plus a background signal

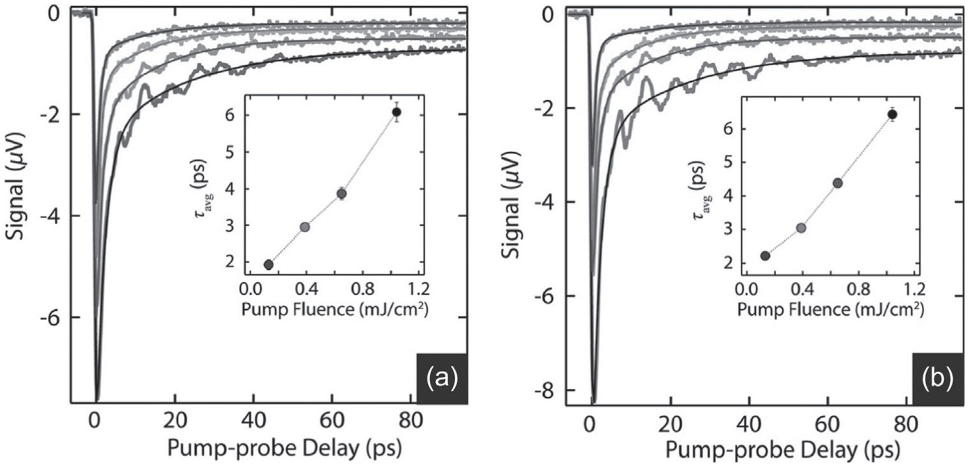

FIGURE 27.3 Transient absorption traces recorded with different pump laser fluences for two different CdTe nanowires. The insets show the amplitude-weighted average lifetimes for the two nanowires, where the colour of the data points corresponds to the colours in the transient absorption traces. (Reprinted with permission from Lo et al. 2012. Copyright (2012) American Chemical Society.)

that decays on a timescale that is much longer than the 100 ps timescale of the experiments. The time constants for the initial decay increase with pump laser fluence, which is opposite to the effect expected if Auger recombination were the dominant decay mechanism for the excited electron–hole pairs (Klimov 2007). The fast decay in the traces is assigned to charge carrier trapping. The dynamics become slower at high pump fluences because charge carrier trapping is a second-order process that depends on the density of free charge carriers and the number of empty trap states. At high pump laser fluences, there are more charge carriers, which fills up the trap states and, thus, reduces the rate of trapping (Lo et al. 2012).

Oscillations can also be seen in the transient absorption traces for both nanowires. These oscillations have a complex pattern and are assigned to coherently excited breathing modes of the nanowires (Lo et al. 2012; Major et al. 2014). Specifically, for the nanowires in Figure 27.3, both the fundamental and the first overtone of the breathing mode are detected. The measured frequencies are in reasonable agreement with calculations where the diameters of the nanowires were estimated from extinction measurements (Lo et al. 2012). Because the periods of these modes depend on the dimensions of the nanoparticle, they suffer strong inhomogeneous damping in ensemble measurements, and are often difficult to observe and analyse. The detailed characterization of the frequencies and energy transfer processes for the acoustic modes of nanoparticles has been one of the major successes of transient absorption microscopy (Beane et al. 2019; Crut et al. 2015).

The breathing modes decay by radiation of sound waves, and the efficiency of this process depends on the difference in acoustic impedance $Z = \rho \times c_L$ between the nanowire and the surroundings, where ρ is the density and c_L is the longitudinal speed of sound (Beane et al. 2019; Devkota et al. 2018; Marty et al. 2011). This decay is usually characterized by the quality factor $Q_{\mathrm{br}} = \pi\tau_{\mathrm{br}}/T_{\mathrm{br}}$, where T_{br} and τ_{br} are the period and damping time of the mode, respectively. For the CdTe nanowires in Figure 27.3, $Q_{\mathrm{br}} = 9 \pm 2$ (averaging the data for the fundamental and overtone modes together). This value is a factor of 2–4 times smaller than what is typically measured for Au nanostructures (Beane et al. 2019). This difference is due to the lower density of CdTe compared to Au, which leads to a smaller difference in the acoustic impedance between the CdTe nanowires and the surroundings (which are glass and microscope immersion oil for the experiments in Figure 27.3). A smaller acoustic impedance difference implies more efficient acoustic energy flow from the nanowire to the surroundings and, consequently, a lower quality factor (Beane et al. 2019; Crut et al. 2015; Devkota et al. 2018).

Figure 27.2 shows examples of transient absorption imaging experiments where the pump and probe beams are spatially overlapped and the sample is scanned through the laser focus. These experiments can provide information about how the dynamics vary spatially within a sample (Huang et al. 2010), but they do not directly probe the motion of the excited species (excitons and/or electrons and holes in semiconductors, or SPPs in metal nanostructures). Examples of transient absorption microscopy imaging experiments where the motion of electrons and holes or propagating SPPs are directly visualized are presented in Figure 27.4. These measurements were performed by holding the pump laser fixed at a specific point in the sample, and scanning the probe beam over the sample to form an image. Figures 27.4a and b shows a scanning electron microscopic (SEM) image and fixed pump-scanned probe transient absorption images for a bent Si nanowire, which has a diameter of approximately 100 nm (Grumstrup et al. 2014b). The transient absorption images in panel (b) were collected at the region of the black circle in the SEM image in panel (a). The signal in this measurement is proportional to the concentration of excited electrons and holes. The images at different times show how the electrons and holes spread out after excitation. Quantitative information about the spatial distribution of the charge carries can be obtained by fitting the distribution to a Gaussian function $\mathrm{Exp}\left(-x^2/2\sigma(t)^2\right)$, where $\sigma(t)$ characterizes the width of the spatial distribution of charge carriers at time t after the pump pulse (Grumstrup et al. 2014b). The time-dependent width of the Gaussian distribution can be written

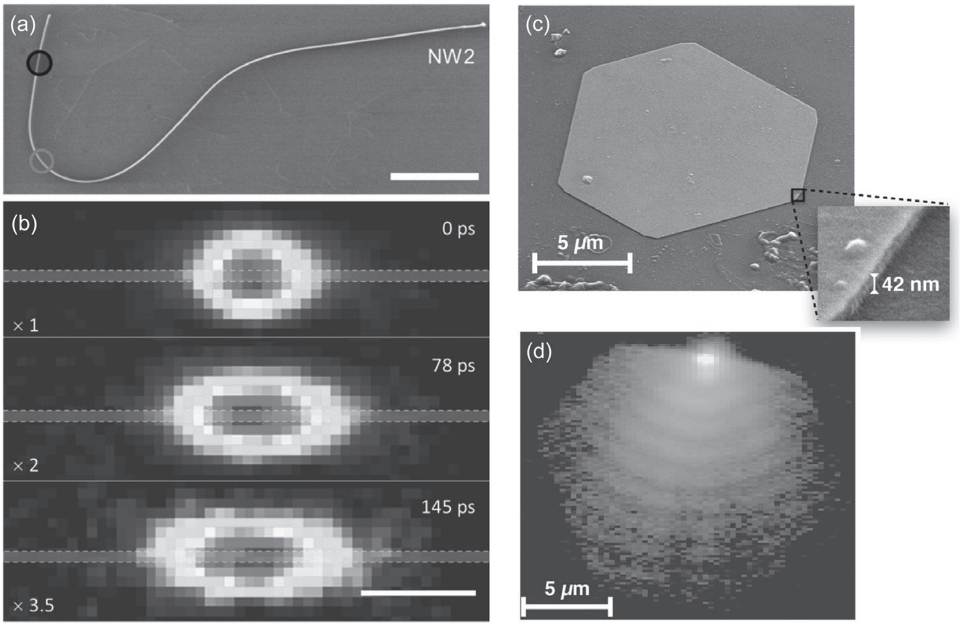

FIGURE 27.4 (a) SEM image of a Si nanowire; the scale bar is 5 μm. (b) Fixed pump-scanned probe images of carrier diffusion in the nanowire at the black circle in (a), the scale bar = 1 μm. (c) SEM image of an Au nanoplate with a thickness of 42 nm. (d) Transient absorption microscopy images of the Au nanoplate where the pump laser has been focused at the top edge of the plate. (Panels (a) and (b) reprinted with permission from Grumstrup et al. 2014b. Copyright (2014) American Chemical Society. Panels (c) and (d) reprinted with permission from Beane et al. 2017. Copyright (2017) American Chemical Society. Further permissions related to the material excerpted should be directed to the American Chemical Society.)

as $\sigma(t)^2 = \sigma_0^2 + L(t)^2$, where σ_0 is the initial width of the distribution created by the pump laser and $L(t)$ is the increase in width from the motion of the charge carriers (Cui et al. 2014; Grumstrup et al. 2015, 2014b). For one-dimensional diffusive motion, the broadening of the spatial distribution of carriers is proportional to $\sqrt{Dt}$, where D is the ambipolar diffusion constant (Grumstrup et al. 2014b). Thus, these experiments provide a way of estimating the diffusion constants for the excited electrons and holes. The diffusion constants for the nanowires in Grumstrup et al. (2014b) were measured to be between 6 and $10\,\text{cm}^2\,\text{s}^{-1}$, which is significantly smaller than the diffusion constant for bulk Si. This was attributed to effects from the high carrier concentration in the single nanowire experiments (Grumstrup et al. 2014b).

Analogous fixed pump-scanned probe transient absorption experiments for an Au nanoplate are shown in Figure 27.4c and d. A tilted SEM image of the nanoplate is presented in Figure 27.4c, which shows that the plate has a thickness of 42 nm. Figure 27.4d shows a transient absorption microscopy image where a 720-nm pump laser beam is focused at the top edge of the nanoplate, and a 560-nm probe beam is scanned over the sample. The pump beam launches SPPs that move away from the excitation region at roughly ½ the speed of light (this motion is effectively instantaneous on the 100–200 fs timescale of these experiments). As the SPPs move, they undergo dephasing processes that create hot electrons. This produces a transient absorption signal from the nanoplate that is proportional to the intensity of the SPP modes (Johns et al. 2017). Thus, transient absorption images like those in Figure 27.4d provide information about the SPP propagation lengths.

A very noticeable feature in the image in Figure 27.4d is the series of concentric rings that radiate away from the excitation spot. This effect arises because the pump laser excites "bound" and "leaky" SPP modes that propagate at the Au–glass and Au–air interfaces, respectively (Johns et al. 2017). These modes have different wavevectors, which creates an interference pattern in the image. The wavelength of the interference pattern is related to the difference in wavevectors by $\lambda = 2\pi/\Delta k$, where $\Delta k = k_{\text{bound}} - k_{\text{leaky}}$. For the nanoplate in Figure 27.4d, the measured wavelength is in excellent agreement with finite element calculations of Δk (Beane et al. 2017). These experiments thus provide wavevector information about bound SPP modes in metal nanostructures, which is unusual as these modes do not directly couple to light in far-field optical measurements (Frank et al. 2017; Johns et al. 2017). Note that in order to observe this interference pattern, the nanoplates must be thin enough that fields from the bound and leaky modes overlap inside the nanoplate. In addition to studies of SPP propagation lengths, these types of experiments have also been used to examine how SPPs couple between nanostructures (Johns et al. 2016; Yu et al. 2014).

27.4 Summary and Future Directions

Transient absorption microscopy is a very versatile technique that can be used to study the photophysics of a variety of different nanostructures. Compared to fluorescence-based measurements, it can be used to interrogate a wider variety of materials (not all materials fluoresce, but all materials absorb at some wavelength), and it is capable of ultrafast time resolution (which is difficult to achieve in fluorescence microscopy experiments). These experiments have led to a new understanding about how nanomaterials interact with their environment (Devkota et al. 2018; Huang et al. 2010; Johns et al. 2017; van Dijk et al. 2005; Yi et al. 2017), the dynamics and motion of charge carriers in semiconductor nanostructures (Carey et al. 2009; Grumstrup et al. 2015, 2014a, b; Guo et al. 2017; Lo et al. 2012; Shi et al. 2013), and the propagation lengths of SPPs in metals (Beane et al. 2019; Johns et al. 2017; Yu et al. 2014). Because transient absorption microscopy is a far-field optical technique, its spatial resolution is limited by diffraction (Beane et al. 2019). Superior spatial resolution can be achieved using electron or X-ray probes (Clark et al. 2013; Dabrowsid et al. 2017; Frank et al. 2017; Valley et al. 2016) or by near-field scanning optical microscopy measurements (Nishiyama et al. 2015). However, these techniques require complex instrumentation and are difficult to implement. They are also extremely challenging to perform in liquid samples. Because of its versatility, we believe that transient absorption microscopy will remain a work-horse tool for ultrafast studies of nanomaterials.

The most important factor for achieving high sensitivity in transient absorption microscopy experiments is to use a low-noise, high repetition rate laser source. Thus, improvements in this technique will come from the development of reliable low-noise ultrafast laser systems that can be easily tuned over a wide range of wavelengths. It would also be nice if competition between laser companies could drive down the price of these systems to make the experiments more affordable! The majority of the transient absorption microscopy experiments that have been reported to date have been performed with 200–300 fs time resolution. It should be possible to improve this by implementing dispersion compensation of the pump and probe laser pulses before the microscope objectives (Squier and Muller 2001). Improvements in time resolution would allow a detailed study of ultrafast processes in single nanostructures, such as electron–electron and/or electron–phonon interactions in metal particles, and Auger recombination is quantum dots. For the studies of slower processes, such as the damping of the acoustic vibrational modes or energy dissipation to the environment, data has to be collected over a long range of pump probe delay times (out to several ns). For the experimental scheme in Figure 27.1 this means that the delay line must be precisely aligned, so that there is no change in the overlap of the pump and probe beams at the sample as the data is collected. This can be challenging. Thus, for these types of studies, asynchronous optical sampling, where two lasers that operate at slightly different repetition rates are used to collect time-resolved data, may be an attractive option (Bartels et al. 2007). Finally, the implementation of 2D ultrafast microscopy experiments would also be an exciting development for the studies of complex materials.

Acknowledgements

This work was supported by the US National Science Foundation through Grant CHE-1502848. The authors are grateful to their collaborators, especially John Sader and Debadi Chakraborty (University of Melbourne), Kuai Yu (Shenzhen University), and Libai Huang (Purdue University).

ORCID:

Gary Beane: 0000-0001-5312-0477
Tuphan Devkota: 0000-0002-0572-5874
Brendan S. Brown: 0000-0002-6421-9330
Gregory V. Hartland: 0000-0002-8650-6891

REFERENCES

Bartels, A., Cerna, R., Kistner, C., et al. 2007. Ultrafast time-domain spectroscopy based on high-speed asynchronous optical sampling. *Rev. Sci. Inst.* 78: 035107.

Beane, G., Yu, K., Devkota, T., et al. 2017. Surface plasmon polariton interference in gold nanoplates. *J. Phys. Chem. Lett.* 8: 4935–41.

Beane, G., Devkota, T., Brown, B. S., Hartland, G. V. 2019. Ultrafast measurements of the dynamics of single nanostructures: A review. *Rep. Prog. Phys.* 82: 016401.

Brongersma, M. L., Halas, N. J., Nordlander, P. 2015. Plasmon-induced hot carrier science and technology. *Nature Nanotech.* 10: 25–34.

Carey, C. R., Yu, Y., Kuno, M., Hartland, G. V. 2009. Ultrafast transient absorption measurements of charge carrier dynamics in single II-VI nanowires. *J. Phys. Chem. C* 113: 19077–81.

Clark, J. N., Beitra, L., Xiong, G., et al. 2013. Ultrafast three-dimensional imaging of lattice dynamics in individual gold nanocrystals. *Science* 341: 56–59.

Collini, E., Wong, C. Y., Wilk, K. E., et al. 2010. Coherently wired light-harvesting in photosynthetic marine algae at ambient temperature. *Nature* 463: 644–47.

Crut, A., Maioli, P., Del Fatti, N., Vallee, F. 2014. Optical absorption and scattering spectroscopies of single nano-objects. *Chem. Soc. Rev.* 43: 3921–56.

Crut, A., Maioli, P., Del Fatti, N., Vallee, F. 2015. Acoustic vibrations of metal nano-objects: Time-domain investigations. *Phys. Rep.* 549: 1–43.

Cui, Q. N., Ceballos, F., Kumar, N., Zhao, H. 2014. Transient absorption microscopy of mono layer and bulk WSe_2. *ACS Nano* 8: 2970–76.

Dabrowsid, M., Dai, Y. N., Petek, H. 2017. Ultrafast microscopy: Imaging light with photoelectrons on the nano-femto scale. *J. Phys. Chem. Lett.* 8: 4446–55.

Devadas, M. S., Devkota, T., Johns, P., et al. 2015. Imaging nano-objects by linear and nonlinear optical absorption microscopies. *Nanotechnology* 26: 354001–01.

Devkota, T., Chakraborty, D., Yu, K., et al. 2018. On the measurement of relaxation times of acoustic vibrations in metal nanowires. *Phys. Chem. Chem. Phys.* 20: 17687–93.

Engel, G. S., Calhoun, T. R., Read, E. L., et al. 2007. Evidence for wavelike energy transfer through quantum coherence in photosynthetic systems. *Nature* 446: 782–86.

Frank, B., Kahl, P., Podbiel, D., et al. 2017. Short-range surface plasmonics: Localized electron emission dynamics from a 60-nm spot on an atomically flat single-crystalline gold surface. *Sci. Adv.* 3: e1700721.

Gabriel, M. M., Kirschbrown, J. R., Christesen, J. D., et al. 2013. Direct imaging of free carrier and trap carrier motion in silicon nanowires by spatially-separated femtosecond pump–probe microscopy. *Nano Lett.* 13: 1336–40.

Gao, B., Hartland, G. V., Huang, L. B. 2012. Transient absorption spectroscopy and imaging of individual chirality-assigned single-walled carbon nanotubes. *ACS Nano* 6: 5083–90.

Grumstrup, E. M., Gabriel, M. M., Cating, E. M., et al. 2014a. Ultrafast carrier dynamics in individual silicon nanowires: Characterization of diameter-dependent carrier lifetime and surface recombination with pump-probe microscopy. *J. Phys. Chem. C* 118: 8634–40.

Grumstrup, E. M., Gabriel, M. M., Pinion, C. W., et al. 2014b. Reversible strain-induced electron-hole recombination in silicon nanowires observed with femtosecond pump-probe microscopy. *Nano Lett.* 14: 6287–92.

Grumstrup, E. M., Gabriel, M. M., Cating, E. E. M., Van Goethem, E. M., Papanikolas, J. M. 2015. Pump-probe microscopy: Visualization and spectroscopy of ultrafast dynamics at the nanoscale. *Chem. Phys.* 458: 30–40.

Guo, Z., Wan, Y., Yang, M. J., et al. 2017. Long-range hot-carrier transport in hybrid perovskites visualized by ultrafast microscopy. *Science* 356: 59–62.

Hartland, G. V. 2011. Optical studies of dynamics in noble metal nanostructures. *Chem. Rev.* 111: 3858–87.

Huang, L. B., Hartland, G. V., Chu, L. Q., et al. 2010. Ultrafast transient absorption microscopy studies of carrier dynamics in epitaxial graphene. *Nano Lett.* 10: 1308–13.

Johns, P., Yu, K., Devadas, M. S., Hartland, G. V. 2016. Role of resonances in the transmission of surface plasmon polaritons between nanostructures. *ACS Nano* 10: 3375–81.

Johns, P., Beane, G., Yu, K., Hartland, G. V. 2017. Dynamics of surface plasmon polaritons in metal nanowires. *J. Phys. Chem. C* 121: 5445–59.

Jonas, D. M. 2003. Two-dimensional femtosecond spectroscopy. *Ann. Rev. Phys. Chem.* 54: 425–63.

Kelly, K. L., Coronado, E., Zhao, L. L., Schatz, G. C. 2003. The optical properties of metal nanoparticles: The influence of size, shape, and dielectric environment. *J. Phys. Chem. B* 107: 668–77.

Klimov, V. I., Mikhailovsky, A. A., Xu, S., et al. 2000. Optical gain and stimulated emission in nanocrystal quantum dots. *Science* 290: 314–17.

Klimov, V. I. 2007. Spectral and dynamical properties of multiexcitons in semiconductor nanocrystals. *Ann. Rev. Phys. Chem.* 58: 635–73.

Linic, S., Christopher, P., Ingram, D. B. 2011. Plasmonic-metal nanostructures for efficient conversion of solar to chemical energy. *Nature Mater.* 10: 911–21.

Lo, S. S., Major, T. A., Petchsang, N., et al. 2012. Charge carrier trapping and acoustic phonon modes in single CdTe nanowires. *ACS Nano* 6: 5274–82.

Lo, S. S., Devadas, M. S., Major, T. A., Hartland, G. V. 2013a. Optical detection of single nano-objects by transient absorption microscopy. *Analyst* 138: 25–31.

Lo, S. S., Shi, H. Y., Huang, L., Hartland, G. V. 2013b. Imaging the extent of plasmon excitation in Au nanowires using pump-probe microscopy. *Opt. Lett.* 38: 1265–67.

Major, T. A., Lo, S. S., Yu, K., Hartland, G. V. 2014. Time-resolved studies of the acoustic vibrational modes of metal and semiconductor nano-objects. *J. Phys. Chem. Lett.* 5: 866–74.

Marty, R., Arbouet, A., Girard, C., et al. 2011. Damping of the acoustic vibrations of individual gold nanoparticles. *Nano Lett.* 11: 3301–06.

Masia, F., Langbein, W., Borri, P. 2013. Polarization-resolved ultrafast dynamics of the complex polarizability in single gold nanoparticles. *Phys. Chem. Chem. Phys.* 15: 4226–32.

Mock, J. J., Barbic, M., Smith, D. R., Schultz, D. A., Schultz, S. 2002. Shape effects in plasmon resonance of individual colloidal silver nanoparticles. *J. Chem. Phys.* 116: 6755–59.

Mukamel, S. 2000. Multidimensional femtosecond correlation spectroscopies of electronic and vibrational excitations. *Ann. Rev. Phys. Chem.* 51: 691–729.

Muskens, O. L., Del Fatti, N., Vallee, F. 2006. Femtosecond response of a single metal nanoparticle. *Nano Lett.* 6: 552–56.

Nishiyama, Y., Imura, K., Okamoto, H. 2015. Observation of plasmon wave packet motions via femtosecond time-resolved near-field imaging techniques. *Nano Lett.* 15: 7657–65.

Pogna, E. A. A., Marsili, M., De Fazio, D., et al. 2016. Photo-induced bandgap renormalization governs the ultrafast response of single-layer MoS_2. *ACS Nano* 10: 1182–88.

Shi, H. Y., Yan, R. S., Bertolazzi, S., et al. 2013. Exciton dynamics in suspended mono layer and few-layer MoS_2 2D crystals. *ACS Nano* 7: 1072–80.

Sonnichsen, C., Franzl, T., Wilk, T., et al. 2002. Drastic reduction of plasmon damping in gold nanorods. *Phys. Rev. Lett.* 88: 077402.

Squier, J., Muller, M. 2001. High resolution nonlinear microscopy: A review of sources and methods for achieving optimal imaging. *Rev. Sci. Inst.* 72: 2855–67.

Sun, Y. G., Xia, Y. N. 2003. Gold and silver nanoparticles: A class of chromophores with colors tunable in the range from 400 to 750 nm. *Analyst* 128: 686–91.

Valley, D. T., Ferry, V. E., Flannigan, D. J. 2016. Imaging intra- and interparticle acousto-plasmonic vibrational dynamics with ultrafast electron microscopy. *Nano Lett.* 16: 7302–08.

van Dijk, M. A., Lippitz, M., Orrit, M. 2005. Detection of acoustic oscillations of single gold nanospheres by time-resolved interferometry. *Phys. Rev. Lett.* 95: 267406.

van Dijk, M. A., Lippitz, M., Stolwijk, D., Orrit, M. 2007. A common-path interferometer for time-resolved and shot-noise-limited detection of single nanoparticles. *Opt. Express* 15: 2273–87.

Voisin, C., Del Fatti, N., Christofilos, D., Vallee, F. 2001. Ultrafast electron dynamics and optical nonlinearities in metal nanoparticles. *J. Phys. Chem. B* 105: 2264–80.

Yi, C. Y., Dongare, P. D., Su, M. N., et al. 2017. Vibrational coupling in plasmonic molecules. *Proc. Nat. Acad. Sci. US* 114: 11621–26.

Yu, K., Devadas, M. S., Major, T. A., Lo, S. S., Hartland, G. V. 2014. Surface plasmon polariton propagation and coupling in gold nanostructures. *J. Phys. Chem. C* 118: 8603–09.

Taylor & Francis
Taylor & Francis Group
http://taylorandfrancis.com

Index

Note: **Bold** page numbers refer to **tables** and *italic* page numbers refer to *figures*.

- ablation efficiency
  - laser micromachining
    - Gaussian beam 55
    - top hat intensity distribution *54,* 54–5
- active pharmaceutical ingredients (APIs) 184
- AFFLAIR® pigment 40
- Agrawal, A. **276**
- Alexandrescu, R 166
- Alikhani, S. **274**
- alloy steels
  - laser cutting process 26
  - PLD techniques 114–15
- Almeida, J. M. P. **275**
- aluminium alloys
  - cutting speeds 31, **32**
  - reflectivity effects 26–7
  - safety note 27
  - to steel 13, *13*
  - thermal conductivity effects 27
- Anija, M. **275**
- anti-Stokes 174
- applications
  - high-speed imaging
    - agricultural spray characterization 312, *313*
    - drug delivery sprays 313, *313*
    - time-resolved PIV 312
  - invasive breast carcinoma 214–17
  - laser-induced breakdown spectroscopy
    - gold fineness 208–9, *209*
    - metal-assisted laser induced plasma *210–12,* 210–17, **215,** *215, 216*
  - laser-induced fluorescence
    - bulk detection *228,* 228–30, *229*
    - single-particle detection 227–8
  - microscopy, coherent diffractive imaging 303–4
  - Raman spectroscopy
    - carbon characterization 182–3, *183*
    - pharmaceutical analysis 184–5, *185*
    - in semiconductors 183–4, *184*
  - SERS 183
- atomic force microscope (AFM) 149–50
- Augustine, A. K. **274**

- Bauer, F. 54, 65
- Bauerle, D. 50
- BD Bioscience 293, *293*
- Beer's law 48, 268
- Bergmann, G. 186
- beta barium borate (BBO) 131
- Bharadwaja, S. S. N. 116
- biological samples
  - laser-induced fluorescence
    - physical principles 220, **220,** *220, 221*
    - special properties 220, **220,** *220, 221*
- biomaterials
  - matrix-assisted pulsed laser evaporation (MAPLE) method 120
  - PLD techniques 120
- Birnbaum, M. 128
- Blatter, A. 50
- Boltaev, G. S. 276
- Bonse, J. 130
- Boyd, G. D. 245
- The British Crop Protection Council (BCPC) 312
- Bureau International des Poids et Mesures (BIPM) 202
- Butet, J. 260

- camera technology
  - electronic cameras 310–11
  - film cameras 310
- Cannon's pioneering laser pyrolysis 161
- carbon dioxide lasers 250
- carbon steels
  - cutting speeds 31, **31**
  - laser cutting process 24–6, *25, 26*
- Castleman, A. W. 143
- ceramics 30
  - laser cutting 30, *30*
  - laser marking 41–2
  - polymers 30, *30*
- Cetin, A. **276**
- charge-coupled device (CCD) sensors 310
- Chatwin, C. 92
- chemical degradation 23
- Cheng, Y. **280**
- Chen, R. **280**
- Chen, Y. H. 146
- Chichkov, B. N. 51
- Choubey, R. K. 276
- CO$_2$
  - laser cutting
    - cut quality 21, *21*
    - cutting speeds 20–1
    - cutting zones 21–2, *22, 23*
    - general notes 28
    - polymers
      - ceramics 30, *30*
      - fibre-reinforced plastics 29
      - glasses 30, *30*
      - thermoplastics 28–9, *29*
      - thermoset plastics 29
      - wood-based products 29–30, *30*
  - laser marking **37,** 37–8, *38*
- coherent anti-stokes Raman scattering (CARS) 181, *296,* 296–7
- coherent diffractive imaging (CDI) 289
  - algorithms 302–3
    - error reduction *302,* 302–3
    - hybrid input/output 303
    - projector notation 303
  - applications 303–4
  - future perspectives 304
  - methods 300–2
    - Fresnel CDI measurement *300,* 301
    - plane-wave CDI experiments *300,* 301, *301*
    - ptychography 301–2
- cold ablation 48
- colony forming unit (CFU) 219
- complementary metal oxide semiconductor (CMOS) 310–11
- compressed ultrafast photography (CUP) 324
- computeraided manufacturing or computer-aided design (CAM/CAD) 90
- computer numerical control (CNC) machining 71
- conduction welding 4, *4*
- cone-like protrusions (CLPs) 60
- confocal laser scanning microscopy (CLSM) 291, *292*
- confocal microscopy, principle 291
- Cong, J. 131
- continuous laser welding 5
- continuous wave (CW) 5
- copper alloys
  - cutting speeds 31, **32**
  - reflectivity effects 26–7
  - safety note 27
  - thermal conductivity effects 27
- *Coriandrum sativum* 278
- Craxton, R. S. 246
- Cruz, A. 128
- crystalline thin films 112

- Dawes, C. 6, 8
- De, A. 7
- de Araujo, C. B. **276**
- De Boni, L. **274**
- DebRoy, T. 7
- defocusing 268, *268*
- Delhaye, M. 187
- desk top manufacturing (DTM) corp 91
- Dhamelincourt, P. 187
- Dhanya, N. P. **274**
- diamond-like carbon (DLC) coatings 119–20
- Diels–Alder photopolymerization 96
- difference frequency generation (GFG)
  - non-linear optics 259
- digital micromirror device (DMD) 324
- Dijkkamp, D. 117
- dioptric systems
  - excimer laser light source **108**
  - monochromatic systems 108
- direct deposition
  - CNC programming approach 72, *72*
- directed light fabrication (DLF)
  - process 72
  - technology 74
    - material properties 75, **76**
    - processing rates 75, **75**

direct laser interference pattering (DLIP) 68
direct laser writing (DLW) techniques 81
discrete-wavelet transform (DTW) coefficients 318
1D laser-induced periodic surface structures (1D-LIPSS) 128–31, *129–31*
Dmitriev, V. G. 246
2D spatial scanning 319, *319*
dual beam welding 11
Ducharme, R. 5
dynamic light scattering (DLS) 169
  angular and concentration effects 200–2, *201*
  principles *198,* 198–200
  size distribution 202–3, *203*
  Stokes–Einstein equation 197
  uncertainty sources 202
dynamic release layer (DRL) 150

EDM *see* electric discharge machining (EDM)
Einstein, A. 255
Ekeberg, T. 304
electric discharge machining (EDM) 76
electromagnetic (EM) radiation 171
electron beam and focused ion beam lithography 149
electronic cameras
  charge-coupled device sensors 310
  complementary metal oxide semiconductor 310–11
  image splitting 311
  on-chip pixel storage 311
electronic polarization 266
electronic speckle pattern interferometry (ESPI) technique 309
electrophoretic deposition (EPD) 142
Elim, H. I. **274**
European Commission 204
evaporation 23; *see also* vaporization cutting
excimer lasers, laser marking **37,** 38–9, *39*
excited-state absorption (ESA) *265,* 265–6
extreme ultraviolet light (EUV) 107, 303

Fabry, C. 255
Fakhri, P. **275**
femtosecond laser
  experimental set-up *126*
  micro-/nanostructuring
    1D laser-induced periodic surface structures 128–31, *129–31*
    2D periodic subwavelength structures 131–4, *131–3*
    irregular nanostructures *127,* 127–8
fibre laser cutting
  cut quality 21, *21*
  cutting speeds 20–1
  cutting zones 21–2, *22, 23*
fibre optic systems 19
fibre-reinforced plastics 29
film cameras
  conventional intermittent-action cine cameras 310
  high-speed cine cameras with rotating prisms 310
  rotating drum cameras 310
  rotating mirror cameras 310
fluorescence microscope, anatomy *293*
Foerster, D. 68
fourier transform infrared (FTIR) spectroscopy 120
Frare, M. C. **275**
free carrier absorption (FCA) *265,* 265–6
frequency recognition algorithm for multiple exposures (FRAME) imaging 322
Frizyuk, K. 260
Fuller, P. W. W. 307
fusion cutting 22–3
Fysikopoulos, A. 13

Gabzdyl, J. 11
Ganeev, R. A. **274–7**
Gao, Y. **274, 280**
Gaussian beam 55
Gaussian blue laser pulse 133
Gaussian decomposition method 272
Gaussian laser beam 269
Geiger-mode avalanche photodiode (APD) 318
genuine multi-photon absorption (MPA) 263–5
George, N. **274**
Gerdova, I. **280**
Ghasemi, F. 214
glasses 30
  laser cutting 30, *30*
  laser marking 41–2
Golightly, J. S. 143
Grehn, M. 52

Hach, A. **280**
harmonic generation
  common laser types
    carbon dioxide lasers 250
    Nd lasers 249–50
    Ti:sapphire lasers 250
  developing and growth areas 250–1
  intra-cavity
    disadvantages 241
    non-linear output coupling 241
    pulsed lasers 242–3
    steady state 242
  non-linear materials
    birefringent materials **247,** 247–8
    quasi-phase-matched materials 248–9
    self-doubling and summing materials 249
  phase matching condition
    birefringent phase-matching *238,* 238–9, *239*
    quasi-phase-matching *239,* 239–40
  second-harmonic generation
    conversion efficiency 235–7, *236, 237*
    intra-cavity 241–3, *242*
    Kleinman conjecture 235
    non-linear polarization *234,* 234–5
    phase-matching 237–40, **238,** *238, 239*
    phase-matching bandwidth 240–1, *241*
    resonant cavity 241–2, *242*
  sum frequency mixing 243–5
    difference frequency mixing 245
    general theories 244
  third- and higher-harmonic generation 245–6, *246*
Hashimoto, S. 145
heat-affected zones (HAZs) 5, 18, 48
heat gun 14
He, T. **275**
high-speed camera technology
  electronic cameras
    charge-coupled device sensors 310
    complementary metal oxide semiconductor 310–11
    image splitting 311
    on-chip pixel storage 311
  film cameras 310
high-speed imaging
  applications
    agricultural spray characterization 312, *313*
    drug delivery sprays 313, *313*
    time-resolved PIV 312
  camera technology
    electronic cameras 310–11
    film cameras 310
  laser choice **311,** 311–12
    illumination techniques 312
  laser radiation properties
    fibre delivery *308,* 308–9
    high-brightness imaging *309,* 309–10
    low divergence 308
    sheet lighting 309, *313*
    short-duration pulses 307–8, *308*
    speckle 309
high temperature, high pressure, and high density (HTHPHD) 138
Hodak, J. H. 146
Honour, J. 310
Hooke, R. 291
Hwang, T. Y. 127
hybrid laser-arc process 9, *9*
hybrid laser welding 9
hybrid systems 19

image splitting 311
indium tin oxide (ITO) 118
inkjet printing 150
International Organization for Standardization (ISO) 202
invasive breast carcinoma (IDC), applications 214–17
Ion, J. C. 4

Jablonski scheme *221*
Jaeggi, B. 62, 63, 68
Jee, Y. 57
Jia, T. **274**
John, J. **274**

Karmakar, B. **275**
Karvonen, L. **275**
Kastler, A. 255
Katoh, T 120
keyhole welding 4, *4*
Kim, S. 163
Kleinman, D. A. 245
Koechner, W. 246
Koenig, J. 65
Kolavekar, S. B. **275**
Kramers–Heisenberg–Dirac (KHD) 176
KrF excimer laser lithography 107–8, **108**
  specifications **108**
Krishnakanth, K. N. **280**
Krishnaswami, K. 310
Kronecker delta function 176
Kumar, A. 214, **275**
Kyoung, M. **274**

- LASER *see* light amplification by stimulated emission of radiation (LASER)
- laser-assisted arc welding 9
- laser cutting process
  - alloy steels 26
  - benefits 18–19, *19*
  - carbon steels 24–6, *25, 26*
    - cutting speeds 31, **31**
  - complementary technologies 18
  - CO_2 *vs.* fibre laser cutting
    - cut quality 21, *21*
    - cutting speeds 20–1
    - cutting zones 21–2, *22, 23*
  - machine types *19,* 19–20, *20*
  - mechanisms
    - chemical degradation 23
    - fusion cutting 22–3
    - oxygen cutting 23
    - vaporization cutting 23
  - mild steels 24–6, *25, 26*
    - cutting speeds 31, **31**
    - with nitrogen 25, *26*
    - with oxygen 24–5
  - non-ferrous metals
    - aluminium alloys 26–7
      - cutting speeds 31, **32**
    - copper alloys 26–7
      - cutting speeds 31, **32**
    - nickel alloys 28
    - other alloys 28
    - titanium alloys 27–8
  - non-metallic materials
    - cutting speeds 31, **32–3**
    - general notes 28
    - other non-metals 30–1
    - polymers 28–30, *30*
  - stainless steels *23,* 23–4, *24*
    - cutting speeds 31, **32**
  - three-dimensional objects
    - fibre optic systems 19
    - hybrid systems 19
    - moving laser systems 20
    - moving optics systems 19
    - moving workpiece systems 19
    - tube cutting systems 19
- laser decal transfer (LDT) 153
- laser-guided and stabilized welding 9
- laser-induced breakdown spectroscopy (LIBS)
  - applications
    - gold fineness 208–9, *209*
    - metal-assisted laserinduced plasma *210–12,* 210–17, **215,** *215, 216*
  - local thermal equilibrium criteria 213
  - signal-to-noise ratio 207
- laser-induced fluorescence (LIF)
  - applications
    - bulk detection *228,* 228–30, *229*
    - single-particle detection 227–8
  - biological fluorophores 220–3, **222,** *223*
  - in biological samples
    - physical principles 220, **220,** *220, 221*
    - special properties 220, **220,** *220, 221*
  - data analysis
    - classification 226
    - discrimination 226
    - identification 226
    - LIDAR Equation 226–7
  - equipment for 225–6, *226*
  - stand-off detection
    - atmospheric aerosols 229–30
    - diluted microbes 228–9
- laser induced forward transfer (LIFT) 1, 81, *85,* 85–6, *86*
  - devices transferred 153–6, *155, 156*
  - future directions 157
  - in industry 156–7
  - liquids 152–3, *153*
  - with a sacrificial layer 150–2, *151*
  - solid films *85*
- laser-induced periodic surface structures (LIPSS) 125
- laser-induced plasmas (LIPs) 142
- laser marking
  - black-and-white laser mark *44*
  - competitive techniques 42–3, *43*
  - decorated packaging 43–5, *44*
  - definition 35
  - equipments
    - CO_2 lasers **37,** 37–8, *38*
    - excimer lasers **37,** 38–9, *39*
    - YAG lasers **37,** *39,* 39–40, *40*
  - materials
    - ceramics 41–2
    - glass 41–2
    - metals 42, *42*
    - plastics 40–1, *41*
    - semiconductors 42
  - multi-coloured green-and-white mark *44*
- laser material processing 1
  - VUV/EUV lasers 1
- laser micromachining
  - alternative approaches 68
  - consequences 56–7, *57*
  - energy transfer 48, *48*
  - heat accumulation 53–4, *54*
  - incubation 57, *58*
  - light absorption 48–9
  - limiting factors
    - heat accumulation *64,* 64–5, *65*
    - plasma/particle shielding 65–6, *66*
  - long (nanosecond) pulses
    - diffusion equation 49
    - enthalpy model 50, *51*
    - homogeneous 3D body 49
    - linear heat conduction 50, *50*
  - machining quality
    - metals 58–60, *60*
    - silicon and germanium 60–2, *61, 62*
  - marking speed 62–4, *63, 64*
  - optimized material removal
    - ablation efficiency 54–5
    - identical problem 54
    - specific removal rate 55, *55, 56*
  - power scale-up 62–4, *63, 64*
  - pulse bursts 66–8, *67, 68*
  - pulse duration 57–8, *57*
  - surface structuring 62, *62*
  - ultra-short pulses
    - dielectrics *52,* 52–3, *53*
    - metals 51–2
    - semiconductors *52,* 52–3, *53*
    - two-temperature model 51
- laser printing
  - laser-induced forward transfer *85,* 85–6, *86*
  - multiphoton polymerization 81–3, *82*
  - stimulated emission depletion 83–5, *84*
- laser pyrolysis
  - challenges 167
  - control parameters 163–4
  - experimental set-up 161–3
  - NPs synthesize
    - compound non-oxide 165–6, *166*
    - compound oxide 166–7, *167*
    - elemental semiconductor 165, *165*
  - operating procedures 164
- laser scanning microscopy 298, **298**
- laser scattering spectroscopy 197–204
- laser spectroscopy 169
- laser welding
  - basic mechanisms
    - continuous welding 5
    - laser sources 5–6
    - light–matter interaction 4–5, *4–5*
    - practical advice 6–7
    - pulsed welding 5
  - benefits 7–8
  - commercial implementations
    - dissimilar materials 8
    - micro-welding 9
    - plastics and transmissive materials 8–9, *9*
    - process developments *9–12,* 9–13
  - diagnostics 13–14, *14*
  - future opportunities 14
  - process set-up 13–14, *14*
- Late, D. J. 119
- Leeuwenhoek, A. van 291
- Lee, Y. H. **274**
- Liang, Y. 144
- Li, C. **274**
- LIFT *see* laser-induced forward transfer (LIFT)
- light amplification by stimulated emission of radiation (LASER) 255
  - in imaging 289
  - microscopy
    - advanced techniques 295–7
    - principles 291–5
- light–matter interaction
  - absorption 4
  - after cooling *5,* 5–6
  - melt pool dynamics 4, *4*
- Link, C. 145
- LIPSS *see* laser-induced periodic surface structures (LIPSS)
- liquid crystal display (LCD) 92
- liquid-phase pulsed laser ablation (LP-PLA)
  - cavitation bubble formation *141,* 141–2, *142*
  - experimental parameters 139–41
  - laser ablation/irradiation 144–6
  - non-reactive 142
  - nucleation and growth
    - early stage 138, *139*
    - intermediate stage 138–9
    - later stage 139
  - reactive pulsed laser ablation 142–4, *143, 144*
- Liu, J. M. 57
- Li, X. 127
- localized surface plasmon resonance (LSPR) 329
- long (nanosecond) pulses
  - laser micromachining
    - diffusion equation 49

- long (nanosecond) pulses (*cont.*)
    - enthalpy model 50, *51*
    - homogeneous 3D body 49
    - linear heat conduction 50, *50*

- Mafune, F. 146
- magnetic resonance imaging (MRI) 89
- Mainman, T. 255, 256
- Majles Ara, M.H. **274**
- Marangoni flow 4
- Martin, A. V. 304
- mass flow controllers (MFCs) 162
- master oscillator power amplifier (MOPA) lasers 6
- Master-Slave Flip Flop 256
- matrix-assisted pulsed laser evaporation-direct write (MAPLE-DW) 153
- matrix-assisted pulsed laser evaporation (MAPLE) 153
- Matsumoto, K. 118
- Matsunawa, A. 4
- Maxwell's equations 256–8
- McWhirter criterion 208
- melting 22–3; *see also* fusion cutting
- melt pool
    - manipulation 9–10, *10, 11*
    - support *12,* 12–13
- MEMS *see* micro-electromechanical system (MEMS)
- Menendez-Manjon, A. 142
- metal–metal welding process 8
- metal nanocomposites **275–7**
- Miao, J. 299
- microbes
    - basic fluorescence behaviour 223–4, *224, 225*
    - LIF stand-off detection *228,* 228–9, **229,** *229*
- micro-electromechanical system (MEMS) 91
- micro-/nanostructuring
    - femtosecond laser
        - 1D laser-induced periodic surface structures 128–31, *129–31*
        - 2D periodic subwavelength structures 131–4, *131–3*
        - irregular nanostructures *127,* 127–8
    - principles 125–6, *126*
- microscopy
    - advanced techniques 295–7
        - coherent anti-stokes raman scattering *296,* 296–7
        - Raman microscopy 295–6, *296*
        - super-resolution microscopy 297, *297*
        - two-photon excitation 295, *295, 296*
    - coherent diffractive imaging
        - algorithms 302–3
        - applications 303–4
        - future perspectives 304
        - methods 300–2
    - confocal dermatology and ophthalmology 295
    - principles
        - confocal laser scanning microscopy 291, *292*
        - fluorescence excitation and emission *292,* 292–3, *293, 294*
        - resolution 293–4
        - scattering and absorption capacity 294–5, *295*
        - wide-field microscopy 291, *292*
- micro-welding 9
- mild steels
    - cutting speeds 31, **31**
    - laser cutting process
        - with nitrogen 25, *26*
        - with oxygen 24–5, *25*
- Milton, M. J. 235
- *Mirabilis jalap*a 278
- modern ArF excimer laser exposure systems, specifications **109**
- modern laser sources, specifications **108**
- Momma, C. 51
- monomodal 200
- Moon, H. Y. 208
- moving laser systems 20
- moving optics systems 19
- moving workpiece systems 19
- MRI *see* magnetic resonance imaging (MRI)
- multimodal 200
- multiphoton lithography
    - applications
        - artificial materials 96
        - biomedical applications 96, *96*
        - optical fibres 96–7
    - experimental set-up 94–5, *95*
    - laser polymerization 95–6
    - sequential and simultaneous two-photon absorption 94, *94*
    - two-photon absorption 94
- multiple beams 11, *12*
- multiple-shots ultrafast optical imaging
    - spatial scanning 318–20, *319*
        - line scanning 319–20, *320*
        - point scanning 318–19, *319*
    - temporal scanning 316–18, *317*
        - ultrafast gating 316–18, *317*
        - ultrashort probing 316, *317*
- multiwall nanotube (MWNT) 143
- Munke, A. 304
- Murphy, S. D. 312
- Muruganandi, G. **276**
- Murugan, G. S. 260

- Nair, A. K. **275**
- nano-electromechanical system (NEMS) 91
- nanoimprint lithography (NIL) 149
- nanomaterials, non-linear optics 259–60, *261–2*
- nanoparticles (NPs) 137–46
    - laser pyrolysis
        - compound non-oxide 165–6, *166*
        - compound oxide 166–7, *167*
        - elemental semiconductor 165, *165*
- nanostructures, femtosecond laser *127,* 127–8
- Nasiadek, M. 214
- NEMS *see* nano-electromechanical system (NEMS)
- Neuenschwander, B. 57, 65, 67, 68
- nickel alloys 28
- Nidya, M. **275**
- NIRFAST software 188
- nitrides, PLD techniques 118–19
- Nolte, S. 51, 52
- non-ferrous metals
    - aluminium alloys, cutting speeds 31, **32**
    - copper alloys, cutting speeds 31, **32**
    - laser cutting process
        - aluminium alloys 26–7
        - copper alloys 26–7
        - nickel alloys 28
        - other alloys 28
        - titanium alloys 27–8
- non-linear optics (NLO)
    - Maxwell's equations 256–8
    - origin 256
    - polarization 256–8
    - scope 281–2
    - second-order
        - difference frequency generation 259
        - nanomaterials 259–60, *261–2*
        - second harmonic generation 258–9
        - sum frequency generation 259
    - third-order
        - excited-state absorption *265,* 265–6
        - free carrier absorption *265,* 265–6
        - genuine multi-photon absorption 263–5
        - metal nanocomposites **275–7,** 278–9
        - metal nanoparticles 274, **274,** 278
        - optical limiting *268,* 268–9, *269,* 273
        - perovskite materials 279–81, **280**
        - refraction index 266–8
        - reverse saturable absorption 260, 263, *263*
        - saturable absorption 260, 263
        - susceptibility 273
        - Z-scan experimental technique 269–73
- non-metallic materials
    - cutting speeds 31, **32–3**
    - laser cutting process
        - general notes 28
        - other non-metals 30–1
        - polymers 28–30, *30*
- nucleation and growth
    - LP-PLA
        - early stage 138, *139*
        - intermediate stage 138–9
        - later stage 139

- odorant-binding proteins (OBPs) 155
- Omidvar, A. **276**
- on-chip pixel storage 311
- operation
    - PLD techniques
        - laser–material interaction 113–14
        - material transport 113, *113*
        - nucleation 113–14, *114*
- optical emission spectroscopy (OES) technique 07
- optical limiters 256
- optical limiting *268,* 268–9, *269,* 273
- optical microscopy 291
- optical parameter oscillator (OPO) 297
- organic lightemitting diodes (OLEDs) 151
- oxidation 23; *see also* oxygen cutting
- oxides, pulsed laser deposition (PLD) techniques 115
- oxygen cutting 23

- Palla Papavlu, A. 155
- paraelectric lanthanum-doped lead titanate (PLT) thin films 116
- particle image velocimetry (PIV) technique 309

particleinduced X-ray emission (PIXE) 208
Perot, A. 255
perovskite nanocrystals 279–81, **280**
Petersen, S. 142
Philip, R. **274**
photoactivatable localization microscopy (PALM) 219
photolithography 149
  cataoptric systems 107
  extreme ultraviolet lithography system 107
  KrF excimer laser lithography 107–8, **108**
  principles *105,* 105–6
  reduction-projection optical systems 106
  scanner *vs.* stepper *108*
  system requirements **106,** 106–7, **107,** *107*
photo multiplier tube (PMT) 318
photon cross-correlation spectroscopy (PCCS) 200, *201*
photorefractive effect 266–7
physical vapour deposition (PVD) 74
Pincon-Roetzinger, N. **275**
plasma-induced plasmas (PIPs) 142
Polloni, R. 275
polycrystalline diamond (PCD) 53
polyether ether ketone (PEEK) 53
polymers
  ceramics 30, *30*
  fibre-reinforced plastics 29
  glasses 30, *30*
  PLD techniques 120
  thermoplastics 28–9, *29*
    polymethyl methacrylate 29
    polyvinyl chloride 29
  thermoset plastics 29
  wood-based products 29–30, *30*
polymethyl methacrylate 29
polyvinyl chloride (PVC) 29
practical advice
  beam delivery 6, *6*
  filler materials 7
  geometric defects 7, *7*
  internal defects 7
  shrouding gas designs 6, *6*
Pradhan, P. **275**
Preuss, S. 49, 52
ptychography 301–2
Pugazhendhi, S. **274**
pulsed laser ablation/irradiation in liquids (PLAL) 137
pulsed laser ablation (PLA) 1
pulsed laser deposition (PLD) techniques 115, 153
  advantages 121
  disadvantages 121
  irradiated zone 112
  operation
    laser–material interaction 113–14
    material transport 113, *113*
    nucleation 113–14, *114*
  target materials
    alloys 114–15
    biomaterials 120
    diamond-like carbon 119–20
    metals 114–15
    nitrides 118–19
    other materials 121
    oxides 115 (*see also* thin films)
    polymers 120
    transition metal dichalcogenides 119, *119*
pulsed laser welding 5
Pyatenko, A. 145

Q-switched lasers 6
quasi-CW (QCW) laser 6

Rahulan, K. M. **275, 276**
Rahulan, M. K. 278
Rajaramakrishna, R. **275**
Raman-induced Kerr effect 266–7
Raman spectroscopy 169
  anti-Stokes 171, *172*
  applications
    carbon characterization 182–3, *183*
    pharmaceutical analysis 184–5, *185*
    in semiconductors 183–4, *184*
  3D imaging 187–8, *188, 189*
  laser 171
  linear *vs.* non-linear processes 171, *172*
  non-invasive depth-resolved studies
    spatially offset 186
    transmission 186–7, *188*
    universal multiple-angle 186
  non-linear spectroscopy
    excited-state planarization dynamics 191–2, *192*
    experimental method 181–2
    photoisomerization reaction *189,* 189–90, *190, 191*
    theory and instrumentation 181, *181*
    ultrafast structural dynamics 190–1
  theory
    classical description 173–5, *174*
    instrument consists 176–8, *177*
    quantum mechanical description 175–6
  ultrafast spectroscopy
    experimental method 181–2
    theory and instrumentation 181, *181*
Rao, K. K. 308
Rao, S. V. **274**
rapid prototyping technology
  advantages 71
  CNC programming approach 72, *72*
  cost advantage 76
  pattern-dependent *vs.* pattern-independent technologies 76, *77*
  technologies and system requirements 72–4, *72–4*
    chemical vapour deposition 74
    diffusion treatments 74
    physical vapour deposition 74
    powder processing 74
    self-propagating high-temperature synthesis 74
Rayleigh light scattering theory 198
Rayleigh scattering 173, 176
Ready, J. F. 4, 50
red-green-blue (RGB) pixels 156
reflection high-energy electron diffraction (RHEED) 118
refraction index 266–8
  NLO
    electronic polarization 266
    electrostriction 267
    molecular orientational effects 267
    photorefractive effect 266–7
    population redistribution 267
    Raman-induced Kerr effect 266–7
    thermo-optic effects 267–8
remote laser welding 13
Rendell, J. 310
reverse saturable absorption (RSA) 260, 263, *263*
Reyhani, A. 210
RHEED *see* reflection high-energy electron diffraction (RHEED)
root mean square (RMS) displacement 197
Ryasnyansky, A. I. **275**

Sabari Girisun, T. C. **276**
Sakho, E. H. M. **275**
Sakka, T. 141
Saouma, F. O. **280**
Saravanan, M. **276**
Sathyavathi, R. **274**
saturable absorption (SA) 260, 263
scanning electron microscopic (SEM) image 334
scanning probe lithography 149–50
Schawlow, A. 255
Schille, J. 52
Schmitt-Rink, S. **280**
Schrader, B. 186
Schuetz, V. 68
screen printing 150
second-harmonic generation
  conversion efficiency
    depleted pump 236–7
    gaussian beams 237
    non-depleted pump beam 236
    photon balance parameter 236
  difference frequency mixing
    Gaussian beams 245
    large intensity ratio 245
    perfect phase-matching 245
    weak non-linear interaction 245
  non-linear optics 258–9
  sum frequency mixing
    large intensity ratio 244
    perfect phase-matching 244
    perfect photon balance 244
    photon number conversion 244
    weak non-linear interaction 244
second-order
  NLO
    difference frequency generation 259
    nanomaterials 259–60, *261–2*
    second harmonic generation 258–9
    sum frequency generation 259
selective laser sintering (SLS) technology 91, *91*
self-focusing 268, *268*
sequentially timed all-optical mapping photography (STAMP) system 322
SERS *see* surface-enhanced Raman scattering (SERS)
Sheik-Bahae, M. 269, 272
short pulse 11, *11*
short wavelength 10–11, *11*
Shoursheini, S. Z. 209
Singh, S. C. 145
single-molecule localization microscopy (SMLM) 297

- single-photon polymerization (1PP) 81
- single-shot frequency-domain tomography (SS-FDT) 321, *321*
- single-shot ultrafast optical imaging
  - active detection
    - angle-division approach *321,* 321–2
    - frequency division 322–3, *323*
    - wavelength division 322, *323*
  - passive detection
    - computational techniques 324–5, *326*
    - direct imaging 323–4, *325*
- Šiškov, K 142
- Smith, H. M. 111, 120
- soft lithography 149
- solid free-form fabrication 71
- spatial light modulators (SLMs) 68, 92
- spatially offset Raman spectroscopy (SORS) 186
- Spence, J. C. H. 299
- Srinivasan, S. M. 188
- stainless steels
  - cutting speeds 31, **32**
  - fusion cutting 23, *23*
- standard operating procedures (SOPs) 164
- STED *see* stimulated emission depletion (STED)
- Steen, W 3, 4
- Steen, W. M. 9
- stepper 107
- stereolithography (SLA) printing *90,* 90–1
- stimulated emission depletion (STED) 83–5, *84,* 297, *297*
  - microscopy implementation 83, 219
- stimulated Raman scattering microscopy (SRS) *296,* 296–7
- stochastic optical reconstruction microscopy (STORM) 219
- Stokes–Einstein equation 197
- Stokes–Einstein relation 139
- Stokes Raman scattering 174
- Stratakis, E. 128
- strontium bismuth tantalate (SBT) films 116
- Sudheesh, P. **275**
- sum frequency generation (SFG), non-linear optics 259
- Sum, T. C. 280
- super-resolution microscopy
  - single-molecule localization microscopy 297
  - stimulated emission depletion 297, *297*
- SuperSoftMark® mark 42
- surface-enhanced Raman scattering (SERS) 96, 178
  - applications 183
  - electromagnetic enhancement 178–9
  - spectrum 180
- surface plasmon polaritons (SPPs) 128, 330

- Talbot W. H. F. 307
- Thermal Fisher 293, *294*
- thermodynamic equilibrium (LTE) 208
- thermo-optic effects 267–8
- thermoplastics
  - polymers 28–9, *29*
    - polymethyl methacrylate 29
    - polyvinyl chloride 29
- thermoset plastics 29
- thin films
  - ferroelectric and multiferroic oxide 115–17, *116, 117*
  - piezoelectric oxides 115–17, *116, 117*
  - PLD techniques
    - advantages 121
    - disadvantages 121
    - operations 112–13, *113, 114*
    - target materials 114–21, *119*
  - superconducting oxides 117–18
  - transparent conducting oxides 118
- third- and higher-harmonic generation
  - periodically poled KTP 248–9
  - periodically poled lithium niobate 248
  - periodically poled lithium tantalate 249
  - periodically poled rubidium titanyl arsenate 249
- third-order
  - NLO
    - excited-state absorption *265,* 265–6
    - free carrier absorption *265,* 265–6
    - genuine multi-photon absorption 263–5
    - metal nanocomposites **275–7,** 278–9
    - metal nanoparticles 274, **274,** 278
    - optical limiting *268,* 268–9, *269,* 273
    - perovskite materials 279–81, **280**
    - refraction index 266–8
    - reverse saturable absorption 260, 263, *263*
    - saturable absorption 260, 263
    - susceptibility 273
    - Z-scan experimental technique 269–73
- three-dimensional (3D) objects
  - fabrication 81, 85
  - laser cutting
    - fibre optic systems 19
    - hybrid systems 19
    - moving laser systems 20
    - moving optics systems 19
    - moving workpiece systems 19
    - tube cutting systems 19
- three-dimensional (3D) printing
  - additive manufacturing technology 89
  - micro-electromechanical system 91
  - multiphoton lithography
    - applications 96–7
    - experimental set-up 94–5, *95*
    - laser polymerization 95–6
    - sequential and simultaneous two-photon absorption 94, *94*
    - two-photon absorption 94
  - nano-electromechanical system 91
  - projection micro-stereolithography 92–3
  - selective laser sintering technology 91, *91*
  - stereolithography *90,* 90–1
  - tomography techniques 89
- three-photon absorption (3PA) 264, *264*
- time-correlated single-photon counting (TCSPC) 318
- time-gated optical projection tomography (TGOPT) 317, *317*
- Ti:sapphire lasers 250
- titanium alloys
  - burning reaction 27
  - commercial note 28
  - safety note 28
- Touloupakis, E. 155
- Townes, C, 255
- transient absorption microscopy
  - experimental methods
    - laser systems for 330–1
    - optical components *331,* 331–2
    - signal detection *331,* 331–2
    - signal-to-noise considerations 332–3, *333*
  - single nanostructures, dynamics 333–5, *334, 335*
- transmission Raman spectroscopy (TRS) 184, 186–7, *188*
- transparent conducting oxides (TCOs) 118
- Tsuji, T. 140
- tube cutting systems 19
- Turner, F. 111, 120
- two-photon absorption (2PA/TPA) 94, 264, *264*
- two-photon absorption polymerization (2PP) 81
- two-photon excitation (TPE) 295, *295, 296*

- Ueda, K. 117
- ultrafast optical imaging
  - categorization 315, *316*
  - comparative summary 325, **327**
  - multiple-shot approach
    - spatial scanning 318–20, *319*
    - temporal scanning 316–18, *317*
  - single-shot approach
    - angle-division approach *321,* 321–2
    - computational techniques 324–5, *326*
    - direct imaging 323–4, *325*
    - frequency division 322–3, *323*
    - wavelength division 322, *323*
- ultrafast Raman loss scattering (URLS) 181
- ultra-short pulsed (USP) laser systems 47
- ultra-short pulses
  - laser micromachining
    - dielectrics *52,* 52–3, *53*
    - metals 51–2
    - semiconductors *52,* 52–3, *53*
    - two-temperature model 51
- universal multiple-angle Raman spectroscopy (UMARS) 186
- USP laser systems 56
- Usui, H. 144, 146
- UV fused silica (UVFS) 58

- van Driel, H. M. 48
- vaporization cutting 23
- Venkatesan, T. 117
- Von Allmen, M. 50
- VUV/EUV lasers 1

- Wang, S. 210
- Wang, W. **275**
- Weber, R. 53
- Wei, K. **280**
- weld monitoring systems 13
- Werner, D. 145
- wobble welding 9
- wood and wood-based products 29–30, *30*

- Xie, Y. **280**
- Xi, P. 295
- X-ray fluorescence spectroscopy (XRF) 208

- YAG lasers
  - integrated circuits *40*
  - laser marking **37,** *39,* 39–40, *40*

Yan, Z. 141, 142
Yariv, A. 246
Yeh, C. S. 146
Yi, J. **280**
You, G. **276**
yttrium barium copper oxide (YBCO) 117
Yue, M. **275**
Yun, Y. K. 117
Zare, R. N. 219
Zewail, A. 181
Zhang, R. **280**
Zhang, Y. 120, **276**
Zhong, J. **276**
Zhu, S. 140
Zimm plot analysis *201,* 202
Zolotovskaya, S. A. 260
Z-scan experimental technique
  NLO 269–73
    closed aperture Z-scan 272–3
    open aperture Z-scan 271, *271*
    wavelength-dependent nonlinear absorption coefficient 271–2
Z-scan method 274
Zulina, N. A. **274**
Zvyagin, A. I. **274**

Taylor & Francis Group
an **informa** business

Taylor & Francis eBooks

www.taylorfrancis.com

A single destination for eBooks from Taylor & Francis with increased functionality and an improved user experience to meet the needs of our customers.

90,000+ eBooks of award-winning academic content in Humanities, Social Science, Science, Technology, Engineering, and Medical written by a global network of editors and authors.

TAYLOR & FRANCIS EBOOKS OFFERS:

- A streamlined experience for our library customers
- A single point of discovery for all of our eBook content
- Improved search and discovery of content at both book and chapter level

REQUEST A FREE TRIAL

support@taylorfrancis.com

Routledge
Taylor & Francis Group

CRC Press
Taylor & Francis Group